

MICROCOPY RESOLUTION TEST CHART
NATIONAL BUREAU OF STANDARDS - 1963 - A

AD-A161 907

AFOSB

SCIEE

USA RESEARCH REPORT

1989

RESEARCH REPORTS

CONDUCTED BY

AFOSB CENTER FOR
AEROSPACE ENGINEERING EDUCATION

AFOSB

AFOSB

AFOSB

AFOSB

ELI

42

14 119

REPORT DOCUMENTATION PAGE

1a. REPORT SECURITY CLASSIFICATION UNCLASSIFIED		1b. RESTRICTIVE MARKINGS AD-A161 907	
2a. SECURITY CLASSIFICATION AUTHORITY		3. DISTRIBUTION / AVAILABILITY OF REPORT APPROVED FOR PUBLIC RELEASE: DISTRIBUTION UNLIMITED	
2b. DECLASSIFICATION / DOWNGRADING SCHEDULE			
4. PERFORMING ORGANIZATION REPORT NUMBER(S)		5. MONITORING ORGANIZATION REPORT NUMBER(S) AFOSR-7-1-1-004	
6a. NAME OF PERFORMING ORGANIZATION The Southeastern Center for Electrical Engineering Education	6b. OFFICE SYMBOL (If applicable)	7a. NAME OF MONITORING ORGANIZATION Air Force Office of Scientific Research/XOT	
6c. ADDRESS (City, State, and ZIP Code) 11th & Massachusetts Ave. St. Cloud, Florida 32769		7b. ADDRESS (City, State, and ZIP Code) Building 410 Bolling AFB, DC 20332-6448	
8a. NAME OF FUNDING / SPONSORING ORGANIZATION AFOSR	8b. OFFICE SYMBOL (If applicable) XOT	9. PROCUREMENT INSTRUMENT IDENTIFICATION NUMBER F49620-82-C-0035	
8c. ADDRESS (City, State, and ZIP Code) Building 410 Bolling AFB, DC 20332-6448		10. SOURCE OF FUNDING NUMBERS	
		PROGRAM ELEMENT NO. 61102F	PROJECT NO. 2301
		TASK NO. D5	WORK UNIT ACCESSION NO.
11. TITLE (Include Security Classification) USAF RESEARCH INITIATION PROGRAM - Volume I			
12. PERSONAL AUTHOR(S) Prof. Warren D. Peele			
13a. TYPE OF REPORT INTERIM	13b. TIME COVERED FROM _____ TO _____	14. DATE OF REPORT (Year, Month, Day) March 1985	15. PAGE COUNT
16. SUPPLEMENTARY NOTATION			
17. COSATI CODES		18. SUBJECT TERMS (Continue on reverse if necessary and identify by block number)	
FIELD	GROUP	SUB-GROUP	
19. ABSTRACT (Continue on reverse if necessary and identify by block number) (SEE BACK)			
20. DISTRIBUTION / AVAILABILITY OF ABSTRACT <input checked="" type="checkbox"/> UNCLASSIFIED/UNLIMITED <input type="checkbox"/> SAME AS RPT. <input type="checkbox"/> DTIC USERS		21. ABSTRACT SECURITY CLASSIFICATION UNCLASSIFIED	
22a. NAME OF RESPONSIBLE INDIVIDUAL AMOS OTIS, Major, Program Manager		22b. TELEPHONE (Include Area Code) (202) 767-4971	22c. OFFICE SYMBOL XOT

DEPT. OF DEFENSE
COLLECTOR
A

For several years prior to 1983, AFOSR conducted a special follow-on funding program for Summer Faculty Research Program (SFRP) participants; this was popularly known as the AFOSR Migrant Program. That program was superseded in 1983 by the Research Initiation Program conducted by SCREE.

To compete for a Research Initiation Program award, SFRP participants must submit a complete proposal and proposed budget either during or promptly after their SFRP appointment periods. Awards to the 1983 participants may extend through 15 December 1984.

Each proposal was evaluated for technical excellence, with special emphasis on relevance to continuation of the SFRP effort, as determined by the Air Force Laboratory/center. The final selection of awards was the responsibility of AFOSR.

The most effective proposals were those which were closely coordinated with the SFRP effort focal point and which followed the SFRP effort with proposed research having strong prospects for later sustained funding by the Air Force Laboratory/center.

The maximum award under the Research Initiation Program is \$12,000 plus cost-sharing up to a matching total amount.

The mechanics of applying for a Research Initiation Program award are as follows:

(1) Research Initiation Program proposals of \$12,000 plus cost-sharing were to be submitted after August 1, 1983 but no later than November 1, 1983.

(2) Proposals were evaluated and the final award decision was the responsibility of AFOSR after consultation with the Air Force Laboratory/center.

(3) The total available funding limited the number of awards to approximately half the number of 1983 SFRP participants.

(4) Subcontracts were negotiated with the employing institution, designating the SFRP participant as Principal Investigator, with the period of award having a start date no earlier than September 1, 1983 and a completion date no later than December 15, 1984.

Employing institutions were encouraged to cost-share since the program was designed as a research initiation procedure. Budgets included, where applicable, Principal Investigator time, graduate assistant and support effort, equipment and expendable supplies, travel and per diem costs, conference fees, indirect costs, and computer charges.

Volumes I and II of the 1983 Research Initiation Program Report contain copies of reports on all 53 of the subcontract efforts awarded under this program.

DISCLAIMER NOTICE

**THIS DOCUMENT IS BEST QUALITY
PRACTICABLE. THE COPY FURNISHED
TO DTIC CONTAINED A SIGNIFICANT
NUMBER OF PAGES WHICH DO NOT
REPRODUCE LEGIBLY.**

AFOSE

1

1983 USAF/SCEEE RESEARCH INITIATION PROGRAM

Conducted by
Southeastern Center for
Electrical Engineering Education
under
USAF Contract Number F49620-82-C-0035

RESEARCH REPORTS

Volume I of II

Submitted to
Air Force Office of Scientific Research
Bolling Air Force Base
Washington, DC

By
Southeastern Center for
Electrical Engineering Education

March 1985

DTIC
ELECTE
S DEC 4 1985 D
A

This document has been approved
for public release and sale; its
distribution is unlimited.

Accession For	
NTIS CRA&I	<input type="checkbox"/>
DTIC TAB	<input type="checkbox"/>
Unannounced	<input type="checkbox"/>
Justification	
By	
Distribution/	
Availability Codes	
Dist	Avail and/or Special
A1	23 bh



SCEEE
©
1985

INTRODUCTION

RESEARCH INITIATION PROGRAM - 1983

For several years prior to 1983, AFOSR conducted a special follow-on funding program for Summer Faculty Research Program (SFRP) participants; this was popularly known as the AFOSR Minigrant Program. That program was superceded in 1983 by the Research Initiation Program conducted by SCEE.

To compete for a Research Initiation Program award, SFRP participants must submit a complete proposal and proposed budget either during or promptly after their SFRP appointment periods. Awards to the 1983 participants may extend through 15 December 1984.

Each proposal was evaluated for technical excellence, with special emphasis on relevance to continuation of the SFRP effort, as determined by the Air Force laboratory/center. The final selection of awards was the responsibility of AFOSR.

The most effective proposals were those which were closely coordinated with the SFRP Effort Focal Point and which followed the SFRP effort with proposed research having strong prospects for later sustained funding by the Air Force laboratory/center.

The maximum award under the Research Initiation Program is \$12,000 plus cost-sharing up to a matching total amount.

The mechanics of applying for a Research Initiation Program award are as follows:

- (1) Research Initiation Program proposals of \$12,000 plus cost-sharing were to be submitted after August 1, 1983 but no later than November 1, 1983.
- (2) Proposals were evaluated and the final award decision was the responsibility of AFOSR after consultation with the Air Force laboratory/center.
- (3) The total available funding limited the number of awards to approximately half the number of 1983 SFRP participants.
- (4) Subcontracts were negotiated with the employing institution, designating the SFRP participant as Principal Investigator, with the period of award having a start date no earlier than September 1, 1983 and a completion date no later than December 15, 1984.

Employing institutions were encouraged to cost-share since the program was designed as a research initiation procedure. Budgets included, where applicable, Principal Investigator time, graduate assistant and support effort, equipment and expendable supplies, travel and per diem costs, conference fees, indirect costs, and computer charges.

Volumes I and II of the 1983 Research Initiation Program Report contain copies of reports on all 53 of the subcontract efforts awarded under this program.

RESEARCH REPORTS

1983 USAF-SCEEE Research Initiation Program

Partial contents

<u>Volume I Report No.</u>	<u>Title</u>	<u>Research Associate</u>
1	A Statistic For Measuring The Balance Of A Sample;	Dr. Richard Andrews
2	Numerical And Analytical Study of High Resolution Limb Spectral Radiance From Non-Equilibrium Atmospheres;	Dr. Pradip Bakshi
3	Electron Waves In The Electrical Breakdown of Gases, With Application To The Dart Leader in Lightning;	Dr. Ernesto Barretto
4	No Title	Dr. Stanley Bashkin
5	Investigation of Liquid Sloshing In Spin-Stabilized Satellites;	Dr. Joseph Baumgarten
6	Surface Potential as a Laser Damage Diagnostic;	Dr. Michael Becker
7	A Study of Slot Waveguides For Electrostatically Variable Saw Delay Lines;	Dr. Henry Bertoni
8	Combustion Modeling of Homogeneous Solid Propellants with Selectively Absorbing Inert Particle Additives;	Dr. M. Quinn Brewster
9	Interim Report Development and Testing of an Animal Model of State Dependent Effects With Atrophine;	Dr. Louis W. Buckalew
10	Combined Blast and Fragment Loading of Reinforced Concrete;	Dr. Chester E. Canada
11	Infrared Spectroscopy of Extrinsic P-Type Silicon;	Dr. Billy Covington
12	Interfacing or Models and Information Systems: A Systematic Approach;	Dr. Donald B. Crouch
13	The Proton in Multisolvant Clusters. 1. The Acetonitrile-Water System;	Dr. Carol A. Deakye
14	Training to Improve the Accuracy and Validity of Performance Ratings;	Dr. Terry L. Dickinson
15	Laser Damage in Crystalline Silicon Observed under RHEED;	Dr. Fred Domann

RESEARCH REPORTS

1983 USAF-SCEEE Research Initiation Program

<u>Volume I</u> <u>Report No.</u>	<u>Title</u>	<u>Research Associate</u>
16	Analysis of Swirling Nozzle Flow by a Time-Dependent Finite Difference Technique	Dr. J. Craig Dutton
17	Analysis of Condensation Phenomena for Conventional Heat Pipes	Dr. Amir Faghri
18	Avionics Reliability Analysis	Dr. Robert Foley
19	Communications Network Simulation Topics with a Computer Network Simulation Model	Dr. Eddie R. Fowler
20	CONFIDENTIAL REPORT	Dr. Victor Frost
21	Development and Evaluation of Scales for the Organizational Assessment Package with Work Groups as the Unit of Analysis	Dr. Samuel B. Green
22	Reinforcement Induced Stereotypy of Sequential Behavior	Dr. Arthur Gutman
23	Neutral Functional Differential Equations and Unsteady Aerodynamics	Dr. Terry Herdman
24	Sensor/Actuator Selection in Linear Systems	Dr. Kathleen C. Howell
25	No Title	Dr. Gwendolyn B. Howze
26	Cycloconverter Modeling for Variable Speed Drives	Dr. Medhat Ibrahim
27	A Novel FDM System For Optical Fiber Communication	Dr. Charles Ih
28	An Experimental Study of the Portable Liquid-Cooled System	Dr. Amir Karimi
29	Short Crack Behavior for Flaws Emanating from Fastener Holes	Dr. George Kirby
<u>Volume II</u>		
30	A Study in the Mechanical Characterization of Advanced Composite Laminates	Dr. William Kyros
31	Modeling of Multi-Echelon and Multi-Indenture Items with Limited Repair and Transportation During War Time Emergencies	Dr. E. Stanley Lee

RESEARCH REPORTS

1983 USAF-SCEEE Research Initiation Program

<u>Volume I Report No.</u>	<u>Title</u>	<u>Research Associate</u>
32	Real-Time Data Quality Assessment Using Linear Prediction	Dr. Siquird Lillevik
33	The Decay of Hydrazine in Air	Dr. Stephen Lin
34	Evaluation of the Chemical Characteristics of Soil Organic Matter in Relationship to the Partitioning Equilibria of Volatile Pollutants	Dr. Leonard Lion
35	Numerical Solution of the Euler Equations On Dynamic Grids	Dr. C. Wayne Mastin
36	Regularity of Feedback Optional Control of Hyperbolic Systems; Minimization of Non-coercive Cost Functionals Over Unbounded Sets; Approximation Methods	Dr. Tapas Mazumdar
37	Removal of Dissolved Hazardous Organics From Contaminated Water Using Extraction/Flotation Process	Dr. Donald L. Michelsen
38	Development of a Computer Program for Calculating Three-Dimensional Transonic Wind Tunnel Wall Interference	Dr. Dale F. Moses
39	Adaptive Array Processing Using Arma Models	Dr. Randolph Moses
40	Raman Spectroscopy of Inhibited and Stimulated Cultured Y-1 Adrenal Cells	Dr. James Mrotek
41	Evaluation of Trichloroethylene Toxicity Using Short Term Exposure And the Amphipod, Gammarus Tigrinus	Dr. Gerald V. Poje
42	Simplification of Nonlinear Systems II	Dr. L. Rai Pujara
43	The Application of an Extended Kalman Filter to Estimate the States of a Bank-to-Turn Missile	Dr. Dallas Russell
44	Improving the Accuracy Enhancement Program for Automatic Network Analyzers	Dr. William Schoggins
45	Poroelectric Models for Spinal Motion Segments	Dr. Bruce R. Simon
46	Neutral Particle Beam Sensing Experiments	Dr. James Steelman

RESEARCH REPORTS

1983 USAF-SCEEE Research Initiation Program

<u>Volume I</u> <u>Report No.</u>	<u>Title</u>	<u>Research Associate</u>
47	The Effect of Moderate to High Pitching Rates on the Aerodynamic Performance of a NACA 0015 Airfoil at a Reynolds No. of 1×10^5	Dr. James Strickland
48	Kinetic Energy Dependence of Ion PolarMolecule Collision Rate Constants by Trajectory Calculations	Dr. Timothy Su
49	No Title	Dr. William Squires
50	A Dynamic Resource Allocation Model	Dr. Patrick Sweeney
51	Electron Paramagnetic Resonance Study of Defects in III-V Semiconductors	Dr. Paul Szydlik
52	No Title	Dr. Enoch Temple
53	Effect of the Graph on Comprehension and Long-Term Recalls of the Text: Eye Movements in Reading	Dr. Shih-sung Wen

1983-84 USAF-SCEEE RESEARCH INITIATION PROGRAM

Sponsored by the

AIR FORCE OFFICE OF SCIENTIFIC RESEARCH

Conducted by the

SOUTHEASTERN CENTER FOR ELECTRICAL ENGINEERING EDUCATION

FINAL REPORT

A STATISTIC FOR MEASURING THE BALANCE OF A SAMPLE

Prepared by: Dr. Richard Andrews

Academic Rank: Associate Professor

Department and
University: Statistics Department
University of Michigan

Research Location: Air Force Logistics Management Center

Date: January 1985

A STATISTIC FOR MEASURING THE BALANCE OF A SAMPLE

Richard W. Andrews

The University of Michigan

ABSTRACT

Consider a finite population for which the values of many variables are known on every unit. The sampling units for a multipurpose sample have been selected. A statistic based on the principal components of the auxiliary variables is proposed to measure the balance of the sample. The mean and variance of this statistic are derived. Calculations for two simple examples demonstrate the behavior of this measure with both simple random and purposive sampling. The statistic is then used to check the balance of various samples from a U. S. Air Force supply database.

1. INTRODUCTION

The population of interest consists of N units, labelled $1, 2, \dots, N$. Associated with each unit there are V variables, x_1, x_2, \dots, x_V . The x 's are the auxiliary variables and their values are known on all N units. Also associated with each unit are numerous variables which are not available without sampling. We refer to these variables as target variables and use the symbol Y to denote any one of them. The target variable Y could be a vector. A sample s , of n units, will be selected. The values of Y for these n units sampled will be available for observation. The n units sampled will constitute a database (or data bank). Requests for data on Y will be made. The nature of the requests are unknown at the time of sampling. The resulting Y data from the n units will be used to make inferences about the entire N units. The r^{th} ($r = 1, 2, \dots, R$) population and sample moments about the origin for the v^{th} auxiliary variable ($v = 1, 2, \dots, V$) are:

$$\mu_r(v) = N^{-1} \sum_N x_v^r.$$

and

$$m_r(v) = n^{-1} \sum_s x_v^r.$$

The \sum_N indicates a summation over all units in the population, \sum_s indicates a summation over sampled units.

In Royall and Herson(1973) a balanced sample is defined to have $\mu_r(v^*) = m_r(v^*)$ for $r = 1, 2, \dots, R$, for some R . However most of their results consider the case in which $V^* = 1$, i.e. there is one auxiliary variable. More than one auxiliary variable is considered in Royall and Pfeffermann(1982).

In Royall and Herson(1973), an approximately balanced sample is defined to be a sample for which the values of Δ_r are small, where

$$\Delta_r = \frac{m_r(v^*) - \mu_r(v^*)}{\mu_r(v^*)} \text{ for } r = 1, 2, \dots, R.$$

Again a single variable ($V^* = 1$) is considered. The ratio estimator is shown to be approximately unbiased when the sample is approximately balanced. Royall and Herson(1973) state that conditions that yield an approximately balanced sample are easy to obtain but they do not elaborate on how to achieve those conditions.

The three purposes of this report are (i) to define a statistic, based on the principle components of the auxiliary variables which measures the balance of a sample; (ii) to find the mean and standard deviation of that statistic, and (iii) to recommend that this statistic along with its mean and standard deviation be reported for multipurpose samples.

The literature in finite population sampling has reported some theoretical results for balanced samples (i.e. perfectly balanced). For example, Royall and Herson(1973) state the following result:

$$\text{If } m_1(v^*) = \mu_1(v^*) \text{ for } v^* = 1, 2, \dots, V^*$$

and

$$Y_k = \beta_0 + \beta_1 x_{1k} + \beta_2 x_{2k} + \dots + \beta_{V^*} x_{V^*k} + \epsilon_k \text{ for } k = 1, 2, \dots, N$$

with $\epsilon_k \sim (0, \sigma^2 \eta(x))$, $\eta(x) = \sum_{j=0}^{V^*} a_j x_j$ and, a_j 's are constants, then $\frac{N}{n} \sum y$ is the best linear unbiased estimator of $\sum_N Y$. Royall and Herson(1973) also give similar results in which there is a single auxiliary variable and the function for Y is a polynomial in x .

Royall and Pfeffermann(1982) show that there are no affects on the posterior distribution of the parameter of interest due to misspecification if the sample is balanced on both \tilde{x}_1 and \tilde{x}_2 . The misspecified model is a linear relationship between Y and \tilde{x}_1 only, which they term the working model. The 'true model' has Y as a linear function of both \tilde{x}_1 and \tilde{x}_2 . They use this result to conclude that there is a role for random sampling in Bayesian inference because a random sample will, with some probability, provide balance on some of the components of \tilde{x}_2 .

The results of this work suggest that a restricted random sample be used. The restriction being that the sample is approximately balanced on the principal components of the known auxiliary variables.

The sampling environment for which the results of this work are appropriate have three characteristics:(1)The sampling units are large with respect to the entire population, and there is no

practical way to subsample, (2) The sample will be used for many purposes which are not known at the time of sampling, and (3) There are many auxiliary variables.

It is common for decision makers in large businesses and governments to maintain what is called a data bank, which is a sample with the above three characteristics. In addition to the auxiliary variables, the data bank contains the values of many target variables, but these values are available only for the units in the sample. In section 3 an Air Force Supply Data Bank is described. It has the three characteristics listed above.

The balancing statistic is defined in section 2 and its mean and variance are derived. Section 3 contains 3 examples, one of these being samples taken from Air Force supply data. The last section gives concluding remarks concerning the use of the balancing statistic.

2. BALANCING STATISTIC

We consider the case in which there are many auxiliary variables which may be strongly correlated. We employ principle components methodology to replace the x 's by uncorrelated auxiliary variables. Without loss of generality we can assume that $\tilde{X} = (x_1, x_2, \dots, x_V)'$ has mean $\tilde{0}$ and variance-covariance matrix Σ . Let the eigenvalues of Σ be $\delta_1, \delta_2, \dots, \delta_V$ and the corresponding eigenvectors be $\tilde{g}_1, \tilde{g}_2, \dots, \tilde{g}_V$; $G = (\tilde{g}_1, \tilde{g}_2, \dots, \tilde{g}_V)$. Then

$$\Sigma = G\Delta G'$$

where $\Delta = \text{diagonal}(\delta_1, \delta_2, \dots, \delta_k)$. The principle components are

$$z_i = \tilde{g}_i' \tilde{X}.$$

Let the V principle components, (z_1, z_2, \dots, z_V) , corresponding to the V largest eigenvalues, be the auxiliary variables on which the sample will be approximately balanced. The z 's are uncorrelated. The r^{th} ($r = 1, 2, \dots, R$) population and sample moments about the origin for the v^{th} principle component ($v = 1, 2, \dots, V$) are:

$$\mu_r(v) = N^{-1} \sum_N z_v^r$$

and

$$m_r(v) = n^{-1} \sum_n z_v^r.$$

Under simple random sampling

$$E[m_r(v)] = \mu_r(v).$$

If N is large relative to n , the population size can be considered infinite and the finite population correction can be ignored. From Kendall and Stuart (1963, p.229),

$$\text{Var}[m_r(v)] = n^{-1} [\mu_{2r}(v) - \mu_r^2(v)]. \quad (2.1)$$

As a measure of balance we define:

$$B = \sum_{r=1}^R B_r$$

where

$$B_r = \sum_{v=1}^k \frac{n[m_r(v) - \mu_r(v)]^2}{\mu_{2r}(v) - \mu_r^2(v)}$$

The quantity B measures the squared error between the sample and population moments for V principle components and for R moments. The purpose of the remaining part of this section is to derive the mean and variance of B .

The result is:

$$E[B] = kR \quad (2.2)$$

and

$$\begin{aligned} \text{Var}[B] = & 2kR \\ & + 2 \sum_r \sum_{r \neq s} \sum_i (\mu_{2r} - \mu_r^2)^{-1} (\mu_{2s} - \mu_s^2)^{-1} (\mu_{r+s} - \mu_r \mu_s)^2; \\ & - n^{-1} \sum_r \sum_s \sum_i (\mu_{2r} - \mu_r^2)^{-1} (\mu_{2s} - \mu_s^2)^{-1} f(\mu) \end{aligned} \quad (2.3)$$

where

$$f(\mu) = \mu_{2r+2s} - \mu_{2r}\mu_{2s} - 2\mu_{2r+s}\mu_s + 2\mu_{2r}\mu_s^2 - 2\mu_{2s+r}\mu_r + 2\mu_{2s}\mu_r^2 - 2\mu_{r+s}^2 + 8\mu_{r+s}\mu_r\mu_s - 6\mu_r^2\mu_s^2.$$

The innermost summation is over the V principal components and the notation of showing that the population moments are for variable v has been deleted for brevity of presentation.

The main steps in deriving this result are as follows. For (2.2),

$$E(B_r) = \sum_{i=1}^k \frac{nE(m_r - \mu_r)^2}{\mu_{2r} - \mu_r^2} = k;$$

$$E(B) = \sum_{r=1}^R E(B_r) = kR.$$

The main steps for showing (2.3) are:

$$\begin{aligned} \text{Var}(B_r) = & \sum_{i=1}^k \frac{n^2 \text{Var}(m_r - \mu_r)^2}{(\mu_{2r} - \mu_r^2)^2} \\ = & \sum_{i=1}^k \frac{n^2 [\text{Var}(m_r^2) + 4\mu_r^2 \text{Var}(m_r) - 4\mu_r \text{Cov}(m_r^2, m_r)]}{(\mu_{2r} - \mu_r^2)^2}. \end{aligned} \quad (2.4)$$

$$\text{Var}(m_r^2) = E(m_r^4) - [E(m_r^2)]^2. \quad (2.5)$$

$$E(m_r^2) = n^{-1}\mu_{2r} + (1 - n^{-1})\mu_r^2. \quad (2.6)$$

$$E(m_r^4) = n^{-4} [n\mu_{4r} + 4n(n-1)\mu_{3r}\mu_r + 3n(n-1)\mu_{2r}^2 + 6n(n-1)(n-2)\mu_{2r}\mu_r^2 + n(n-1)(n-2)(n-3)\mu_r^4] \quad (2.7)$$

Substituting (2.6) and (2.7) into (2.5) yields

$$\begin{aligned} Var(m_r^2) &= n^{-3}\mu_{4r} + 4(n^{-2} - n^{-3})\mu_{3r}\mu_r + (2n^{-2} - 3n^{-3})\mu_{2r}^2 \\ &\quad + (4n^{-1} - 16n^{-2} + 12n^{-3})\mu_{2r}\mu_r^2 - (4n^{-1} - 10n^{-2} + 6n^{-3})\mu_r^4. \end{aligned} \quad (2.8)$$

$$Cov(m_r^2, m_r) = n^{-2}\mu_{3r} + (2n^{-1} - 3n^{-2})\mu_{2r}\mu_r - (2n^{-1} - 2n^{-2})\mu_r^3. \quad (2.9)$$

Substituting (2.1), (2.8), and (2.9) into (2.4) yields

$$\begin{aligned} Var(B_r) &= 2k \\ &\quad - n^{-1} \sum_{i=1}^k (\mu_{2r} - \mu_r^2)^{-2} (\mu_{4r} - 4\mu_{3r}\mu_r - 3\mu_{2r}^2 + 12\mu_{2r}\mu_r^2 - 6\mu_r^4) \\ Var(B) &= \sum_{r=1}^R Var(B_r) + 2 \sum_{r < s} Cov(B_r, B_s) \\ &= 2kR \\ &\quad + n^{-1} \sum_{i=1}^k (\mu_{2r} - \mu_r^2)^{-2} (\mu_{4r} - 4\mu_{3r}\mu_r - 3\mu_{2r}^2 + 12\mu_{2r}\mu_r^2 - 6\mu_r^4) \\ &\quad - 2 \sum_{r < s} [E(B_r B_s) - k^2] \end{aligned} \quad (2.10)$$

$$\begin{aligned} E(B_r B_s) &= k^2 \\ &\quad + \sum_{i=1}^k (\mu_{2r} - \mu_r^2)^{-1} (\mu_{2s} - \mu_s^2)^{-1} [2\mu_r^2 \mu_s^2 + 2\mu_{rs}^2 - 4\mu_{r+s} \mu_r \mu_s + n^{-1} f(\mu)] \end{aligned} \quad (2.11)$$

Substituting (2.11) into (2.10) gives (2.3).

3. EXAMPLES

In this section, the statistic B is calculated for samples from 3 populations. In all cases the first four moments are used ($R = 4$). A population is defined by its N units and the known values of the V^* auxiliary variables. Based on the V^* auxiliary variables, V principal components are found.

For each population and its associated principal components the mean and standard deviation of B are stated. Several samples of different sizes are taken. Some of the samples are selected by simple random sampling. Other samples are purposively selected. The value of B is reported for each sample. Reflecting on the resulting values of B lead to the concluding remarks which are given in the next section.

Population I This example demonstrates the variation in B pictorially. Population I has 100 units ($N = 100$) and a single auxiliary variable X ($V^* = 1$). Furthermore, the values of X are the unit indices, i.e. $X_i = i$ ($i = 1, \dots, 100$). Five simple random samples of size 2 were taken. The samples are depicted in Figure 3.1. A blackened strip indicates a sampled index. The corresponding value of B is given directly above the chart. From the 5 simple random samples, the best balanced sample had a B of 0.38. That sample consisted of indices 17 and 85.

For this population and a sample of size 2, the mean and standard deviation of B are 8.00 and 4.46, respectively. It is interesting to note that the sample with indices 3 and 99 has a larger value of B than the (77, 98) sample. Obviously, the (3, 99) sample is better balanced on the first moment. However, the second and fourth moments cause the value of B for the (3, 98) sample to be large. Both of these samples have a value of B larger than its mean. It is reasonable not to use any sample with a B value larger than its mean. This recommendation will be discussed further in the next section.

For this population, it is easy to select all possible samples of size 2. There are 4950 possible samples. The value of B was calculated for all these samples. Five samples are shown in Figure 3.2. Two samples provide the smallest value of B . They are (19, 81) shown at the top of Figure 3.2 and (20, 82), not shown. The largest value of B is 41.76, which results with either sample (99, 100) (not shown) or (1, 2), shown at the bottom of Figure 3.2

Figure 3.3 consists of charts for 5 simple random samples of size 6. The mean and standard deviation of B for $n = 6$ is 4.00 and 4.08, respectively. Figure 3.4 consists of 5 purposively selected samples. It is interesting to note that the second sample in Figure 3.4 was chosen purposively and with some care towards balance. However, the value of its B was higher than 3 of the 5 random samples from Figure 3.3. The implications of this observation will be further discussed in the next section.

Population II This population was taken from Press and Wilson(1978). The units are the 50 states of the U.S. The 3 variables we will consider are X_1^* (per capita income in \$1000), X_2^* (birth rate), and X_3^* (death rate).

The output of the principal components analysis is given in Table 3.1. Table 3.2 gives the values of B for a sample of size 2. The computations for B were based on both the first principal component only ($k = 1$) and the first two principal components ($k = 2$). For $k = 1$ the mean and standard deviation of B are 4.00 and 9.11; for $k = 2$ the mean and standard deviation of B are 8.00 and 17.99.

The first five entries in Table 3.2 are simple random samples and all except one (Nebraska and South Dakota) have a value of B below its mean. Of the 5 purposive samples the first (Arkansas, Delaware) and the last (Louisiana, South Dakota) were selected based on a complete enumeration of all possible samples of size 2. The (Arkansas, Delaware) sample resulted in the

smallest value of B for the $k = 1$ case. The (Louisiana, South Dakota) sample resulted in the largest value of B . The other 3 samples were chosen as interesting cases. For example, (New York, California) is the sample of the 2 most populous states.

The values in Table 3.2 indicate that a single sampling unit can greatly influence the value of B . The state of South Dakota is in the 2 samples which have large B values. From the original data the death rate for South Dakota is 2.4. The next largest death rate is 1.3. The implications of a single sample point will be discussed further in the next section.

In Table 3.3 the Population II data was again used but this time with a sample of size 6. The mean and standard deviation of B are 4.00 and 6.36, respectively. The first 5 entries are simple random samples. The last 4 entries are purposively selected. The first 2 of these consist of the 6 most populous states and the 6 least populous states. The 50 states were stratified by population into 6 strata with 8 states in each stratum except for the last stratum which had the 10 states with the smallest population. The third purposive sample chose the state from each stratum which had the largest population. The last purposive sample chose the state from each stratum with the smallest population.

Those samples which include South Dakota again yield large values of B . The only sample which provided a very small value of B was the third purposive sample, which was purposively selected from a stratified design. The implications of this observation will be discussed further in the next section.

Population III The final population to be discussed is the population that led to the author's inquiry into the question of balancing. This population consists of 96 units. The units are the 96 U.S. Air Force bases which belong to the six major commands. A list of these 96 bases and the commands to which they belong is given in Table 3.4. Twelve supply variables have been chosen as auxiliary variables. They are reported for each base every month. A list of these variables is given in Table 3.5. The data is from April, 1982.

A principal components analysis yielded the output given in Table 3.6. The first 3 eigenvectors were used to develop scores on the 96 units, so $V = 3$.

Five simple random samples of size 2 were selected and their values of B are reported in Table 3.7. The $E[B] = 12.00$ and $SD[B] = 26.59$.

All possible samples of size 2 were selected and their values of B calculated. The smallest value of B is 0.56 as reported in the first purposive sample in Table 3.7. The largest is 225.21 which is also reported in Table 3.7.

Table 3.8 gives the values of B for the Air Force supply data using a sample size of 6 ($E[B] = 12.00$ and $SD[B] = 16.84$). The first 5 entries are simple random samples.

The sixth entry in Table 3.8 is a purposively selected sample which consists of one base from each major command. This sample was selected by Air Force personnel and put forth as repre-

sentative. These 6 bases provide additional data in the form of Y or target variables to the Air Force Logistics Management Center. The value of the Y variables observed at these six bases are used as input into stockage policy analysis. This additional data is not observed at the other 90 bases. The choice of these 6 bases has been previously investigated by Andrews and Gentner(1983) and the concepts of a representative sample as discussed by Kruskal and Mosteller(1979a,b,c,1980) have been considered.

The next two purposive samples were selected based on the values of the variable V_1 , which is a measure of size of the base. The second purposive sample took the 6 largest bases out of the 96. The third purposive sample selected the 6 smallest bases. For the last 2 samples in Table 3.8 the population of bases was stratified by major command as given in Table 3.4. The largest and smallest in each stratum refer to variable V_1 .

The obvious conclusion based on Table 3.8 is that the sample purposively chosen by Air Force personnel is well balanced. Additional remarks on the values of B calculated in this and previous tables will be discussed in the next section.

4. CONCLUDING REMARKS

(1) Balancing on X seems to makes sense only if the target variable Y is correlated with X . In the first population the X values are just indicies and balancing on X might seem to be worthless. However a sample is taken to be used. It is my contention that a user will not put as much credence in a poorly balanced sample on the indices as one without obvious balancing problems. For example, if (1,2) was the sample from population I, would a user proceed without hesitation? Therefore I take the extreme position that even if one knows (one could be wrong) that X is uncorrelated with Y , I still recommend a restricted random sample. The restriction being that only values of B less than $E\{B\} - \delta SD\{B\} (\delta \geq 0)$ are acceptable.

(2) Figures 3.3 and 3.4 demonstrate that caution is in order if one uses a purposive sample. The second sample from the top in Figure 3.4 was selected with the idea that it would be well balanced. However, 3 of the 5 simple random samples had a smaller B . That comparison supports the suggestion to use a restrictive random sample.

(3) As demonstrated with the Press and Wilson data, one unit in a sample may be responsible for a large value of B . Does a sampling unit which causes imbalance adversely affect the inference? The answer is not obvious and it will depend on the type of inference procedure used. However, it would be wise to treat such a situation with caution and to possibly exclude that unit from the population.

(4) The statistic B equally weights each principal component used in developing scores. It also weights each of the R moments equally. This is reasonable unless additional information is available about the the components or moments. Another approach would be to report a vector of balance

measures based on moments and/or variables but comparison of samples would be difficult.

(5) A restrictive random sample allows the sample to be irregularly spaced throughout the auxiliary variable space. The sample of size 6 at the top of Figure 3.4 is not ideal even though it has a low value for B . It is too regular. Choosing a sample by minimizing B would set higher order inclusion probabilities for adjacent items to zero. A random sample with an adequately small value of B is preferable. Randomness avoids the pitfalls of regularly but unrestricted randomness may result in misleading inferences.

ACKNOWLEDGMENT

This research was supported by the Air Force Office of Scientific Research and the Southeastern Center for Electrical Engineering Education under contract F49620-82-C-0035.

References

- Andrews, R.W., and Gentner, F.J., (1983), "Testing the Representativeness of the Supply Data Bank," Final Report for 1983 USAF-SCEEE Summer Faculty Research Program.
- Kendall, M.G., and Stuart, A., (1963), The Advanced Theory of Statistics, Volume I, 2nd ed. Charles Griffen & Co., London.
- Kruskal, W. and Mosteller, F., (1979a) "Representative Sampling, I: Non-scientific Literature, International Statistical Review, Vol. 47, pp. 13-24.
- Kruskal, W. and Mosteller, F., (1979b) "Representative Sampling, II: Scientific Literature, Excluding Statistics," International Statistical Review, Vol. 47, pp. 111-127.
- Kruskal, W. and Mosteller, F., (1979c) "Representative Sampling, III: the Current Statistical Literature," International Statistical Review, Vol. 47, pp. 245-265.
- Kruskal, W. and Mosteller, F., (1980) "Representative Sampling, IV: the History of the Concept in Statistics, 1985-1939," International Statistical Review, Vol. 48, pp. 169-195.
- Press, S. James and Wilson, S., (1978) "Choosing Between Logistic Regression and Discriminant Analysis," Journal of the American Statistical Association, Vol. 73, pp. 699-705.
- Royall, R.M. and Herson, J., (1973) "Robust Estimation in Finite Populations," Journal of the American Statistical Association, Vol. 68, pp. 880-9.
- Royall, R.M. and Pfeffermann, D., (1982) "Balanced Samples and Robust Bayesian Inference in Finite Population Sampling," Biometrika, Vol. 69, pp. 401-409.

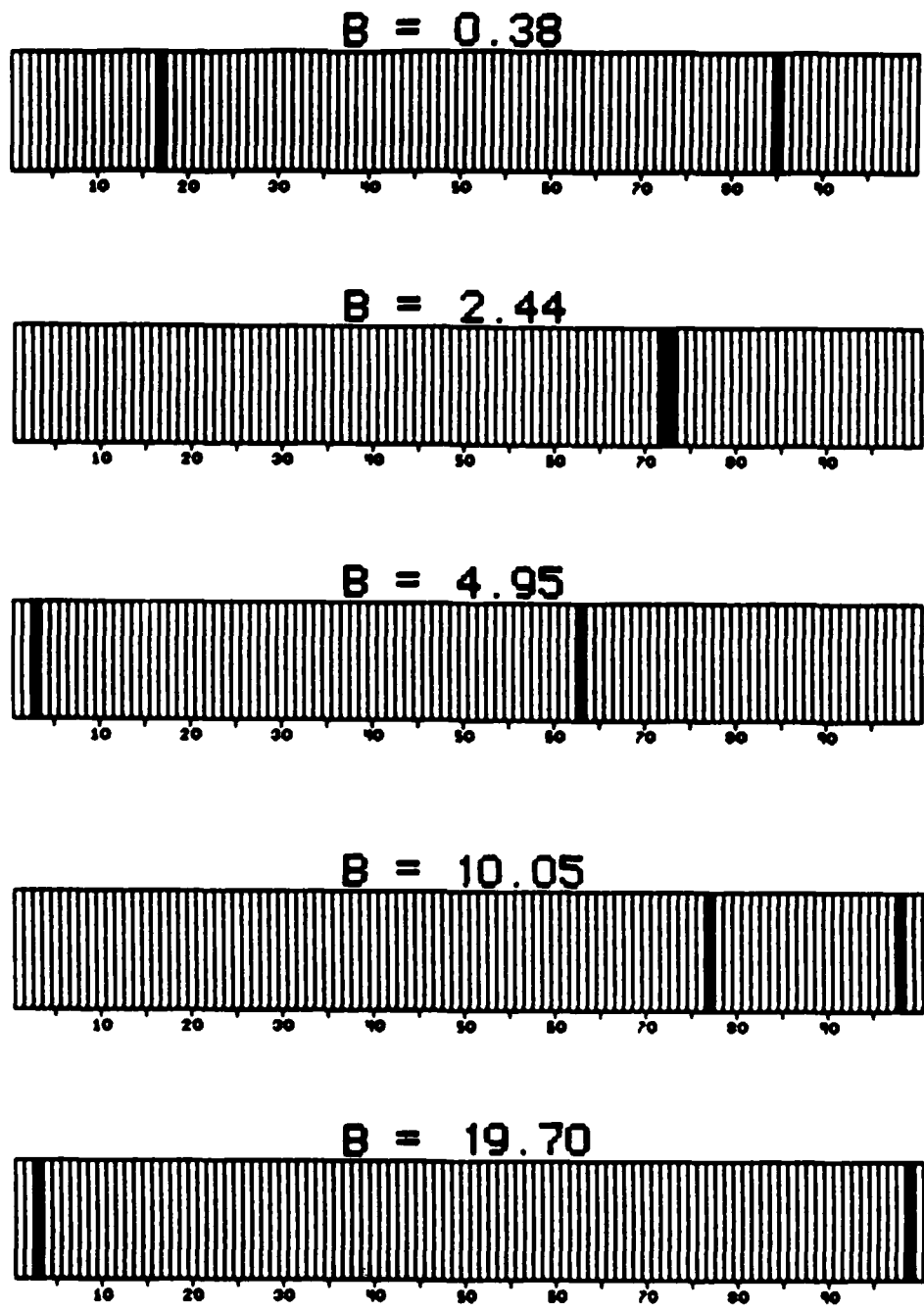
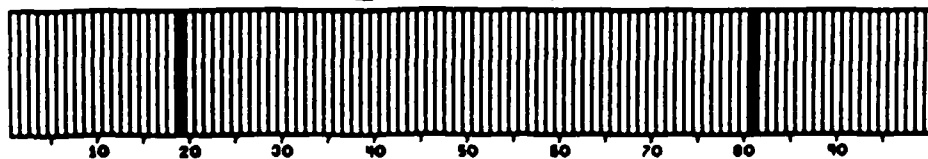
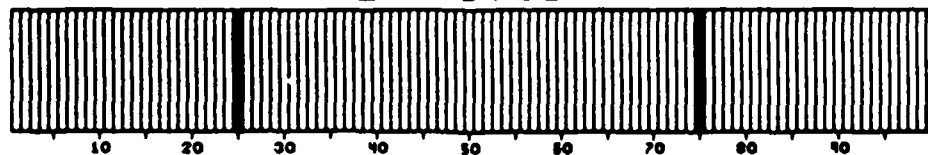


Figure 3.1
 Balance Charts for Simple Random Samples
 (Sample Size=2)

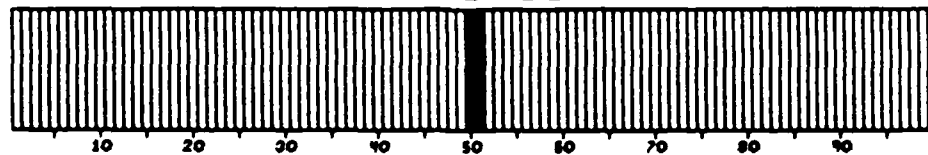
$B = 0.14$



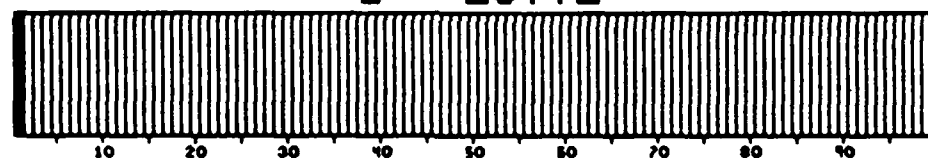
$B = 0.69$



$B = 3.63$



$B = 25.72$



$B = 41.76$

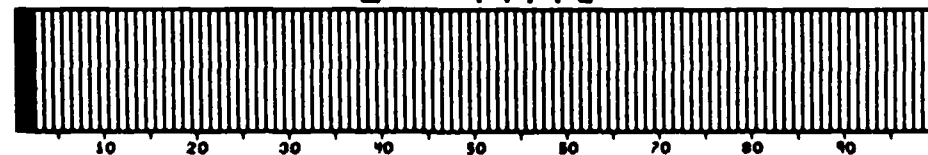
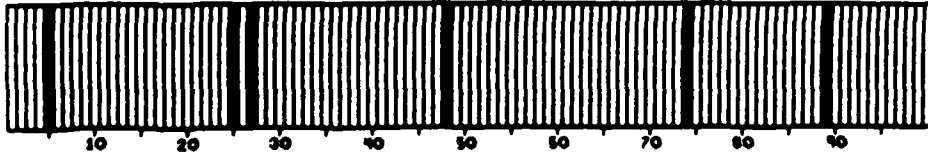
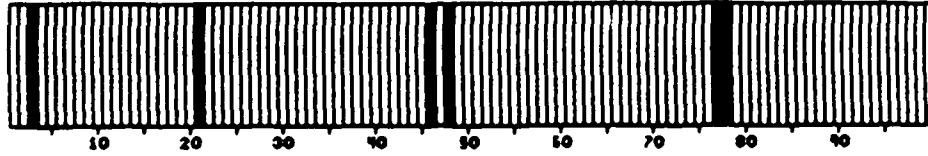


Figure 3.2
Balance Charts for Purposive Samples
(Sample Size=2)

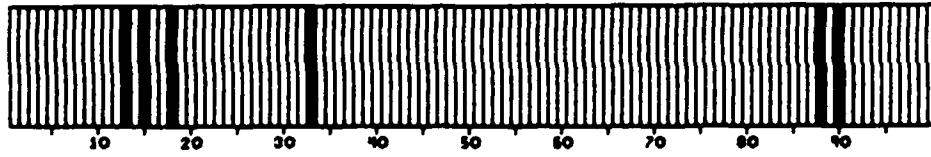
$B = 0.49$



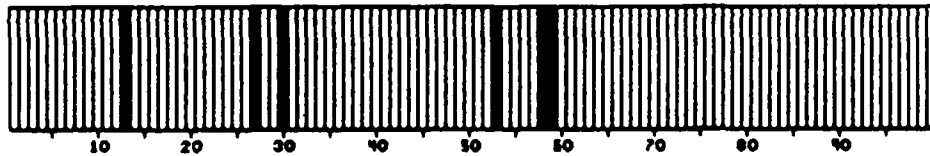
$B = 0.90$



$B = 1.83$



$B = 4.57$



$B = 15.88$

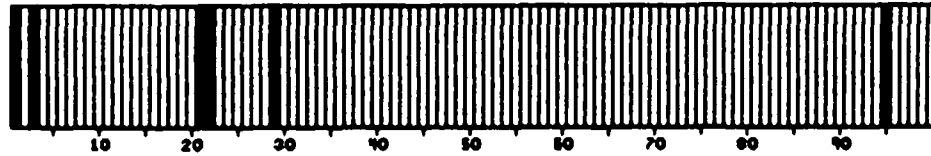
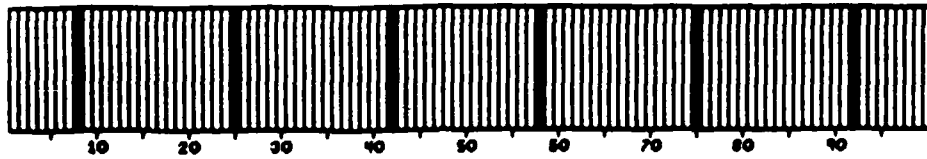
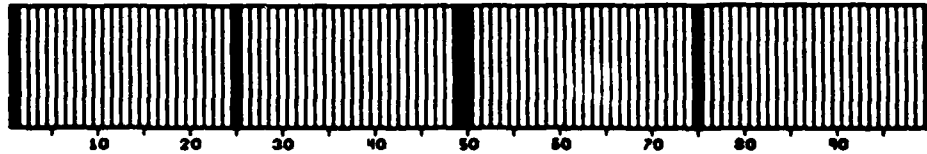


Figure 3.3
Balance Charts for Simple Random Samples
(Sample Size=6)

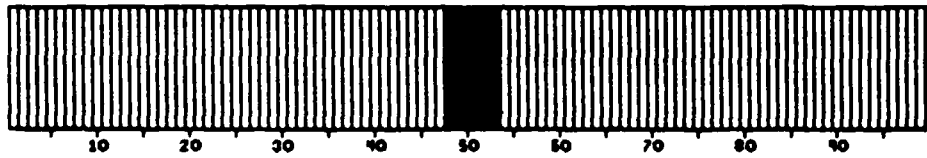
$B = 0.02$



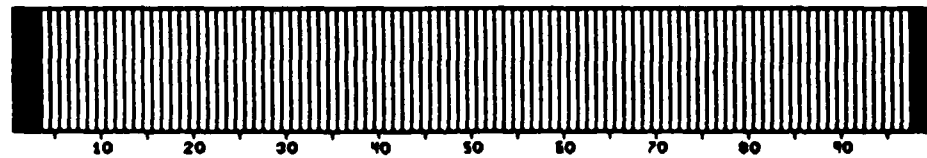
$B = 2.09$



$B = 10.83$



$B = 64.82$



$B = 94.79$

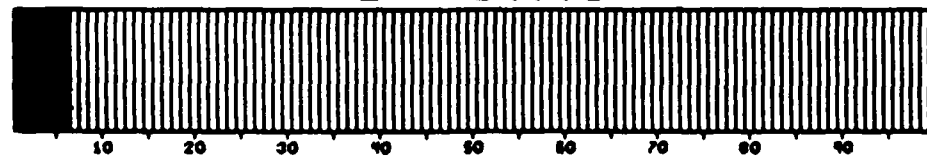


Figure 3.4
Balance Charts for Purposive Samples
(Sample Size=6)

	(1)	(2)	(3)
EIGENVALUES	1.3406	1.1470	.51244
% VARIANCE	44.69	82.92	100.00
1. INCOME	-.76723	.00962	.64129
2. BIRTHS	.46464	.69759	.54542
3. DEATHS	.44211	-.71644	.53968

=====

TABLE 3.1

Output from Principal Components for Press and Wilson Data

STATES		METHOD OF SELECTION	VALUES OF B	
			(k=1)	(k=2)
Maine	Colorado	SRS	0.74	0.93
Virginia	Alabama	SRS	0.52	0.93
Nebraska	South Dakota	SRS	27.35	103.49
Alaska	Colorado	SRS	1.03	3.50
Illinois	Delaware	SRS	2.26	2.54
Arkansas	Delaware	Purposive	0.12	0.40
New York	California	Purposive	4.86	5.13
Hawaii	Alaska	Purposive	1.09	10.76
Texas	Rhode Island	Purposive	0.95	1.13
Louisiana	South Dakota	Purposive	123.96	194.66

TABLE 3.2
 Values of B for Press and Wilson Data
 (n=2)

STATES		METHOD OF SELECTION	VALUES OF B (k=1)	VALUES OF B (k=2)
Nevada	Mississippi			
Missouri	South Dakota	SRS	14.00	34.52
Nebraska	Tennessee			
Georgia	New York			
Delaware	Rhode Island	SRS	2.15	2.66
Ohio	Indiana			
Michigan	Maine			
New Jersey	Washington	SRS	2.70	3.48
Nevada	North Carolina			
Nebraska	South Carolina			
Louisiana	North Carolina	SRS	7.31	8.00
New York	North Dakota			
Texas	Iowa			
Georgia	Nebraska	SRS	2.60	3.78
New Mexico	North Carolina			
California	New York	Purposive:		
Texas	Pennsylvania	Most	3.92	4.78
Illinois	Florida	Populous		
Alaska	Wyoming	Purposive:		
Vermont	Delaware	Least	5.34	23.87
North Dakota	South Dakota	Populous		
California	New Jersey	Purposive:		
Tennessee	S. Carolina	Largest in	0.67	1.48
Arkansas	N. Hampshire	Stratum		
Alaska	Rhode Island	Purposive:		
West Va.	Colorado	Smallest in	6.01	6.93
Louisiana	North Car.	Stratum		

TABLE 3.3
 Values of B for Press and Wilson Data
 (n=6)

<u>Index</u>	<u>Base</u>	<u>Major Command</u>	<u>Index</u>	<u>Base</u>	<u>Major Command</u>
1	Keesler	Air Training Command	25	McGuire	Military Airlift Command
2	Chanute	Air Training Command	26	Lajes	Military Airlift Command
3	Sheppard	Air Training Command	27	Pope	Military Airlift Command
4	Columbus	Air Training Command	28	Dover	Military Airlift Command
5	Vance	Air Training Command	29	K.I. Sawyer	Strategic Air Command
6	Williams	Air Training Command	30	Minot	Strategic Air Command
7	Lackland	Air Training Command	31	Wurtsmith	Strategic Air Command
8	Lowry	Air Training Command	32	Offutt	Strategic Air Command
9	Reese	Air Training Command	33	Barksdale	Strategic Air Command
10	Mather	Air Training Command	34	Vandenberg	Strategic Air Command
11	Maxwell	Air Training Command	35	F.E. Warren	Strategic Air Command
12	Randolph	Air Training Command	36	Plattsburg	Strategic Air Command
13	Laughlin	Air Training Command	37	Griffis	Strategic Air Command
14	Scott	Military Airlift Command	38	Farichild	Strategic Air Command
15	Hurlburt	Military Airlift Command	39	McConnell	Strategic Air Command
16	Charleston	Military Airlift Command	40	Pease	Strategic Air Command
17	Altus	Military Airlift Command	41	Whiteman	Strategic Air Command
18	Rhein Main	Military Airlift Command	42	Malmstrom	Strategic Air Command
19	Andrews	Military Airlift Command	43	Blytheville	Strategic Air Command
20	Travis	Military Airlift Command	44	Grissom	Strategic Air Command
21	Norton	Military Airlift Command	45	Grand Fork	Strategic Air Command
22	Little Rock	Military Airlift Command	46	Dyess	Strategic Air Command
23	Kirtland	Military Airlift Command	47	March	Strategic Air Command
24	McChord	Military Airlift Command	48	Castle	Strategic Air Command

<u>Index</u>	<u>Base</u>	<u>Major Command</u>	<u>Index</u>	<u>Base</u>	<u>Major Command</u>
49	Loring	Strategic Air Command	74	Clark	Pacific Air Force
50	Beale	Strategic Air Command	75	Taegu	Pacific Air Force
51	Carswell	Strategic Air Command	76	Hickam	Pacific Air Force
52	Ellsworth	Strategic Air Command	77	Kadena	Pacific Air Force
53	Langley	Tactical Air Command	78	Kunsan	Pacific Air Force
54	Holloman	Tactical Air Command	79	Osan	Pacific Air Force
55	Shaw	Tactical Air Command	80	San Vito	U.S. Air Force - Europe
56	England	Tactical Air Command	81	Mildenhall	U.S. Air Force - Europe
57	Myrtle Beach	Tactical Air Command	82	Zweibrucken	U.S. Air Force - Europe
58	S. Johnson	Tactical Air Command	83	UpperHeyford	U.S. Air Force - Europe
59	Howard	Tactical Air Command	84	Torrejon	U.S. Air Force - Europe
60	George	Tactical Air Command	85	Lakenheath	U.S. Air Force - Europe
61	MacDill	Tactical Air Command	86	Sembach	U.S. Air Force - Europe
62	Tyndall	Tactical Air Command	87	Bitburg	U.S. Air Force - Europe
63	Keflavik	Tactical Air Command	88	Ramstein	U.S. Air Force - Europe
64	Homestead	Tactical Air Command	89	Hahn	U.S. Air Force - Europe
65	Moody	Tactical Air Command	90	Springdahlm	U.S. Air Force - Europe
66	Nellis	Tactical Air Command	91	Alconbury	U.S. Air Force - Europe
67	Cannon	Tactical Air Command	92	Bentwaters	U.S. Air Force - Europe
68	Bergstrom	Tactical Air Command	93	Aviano	U.S. Air Force - Europe
69	D-Monthan	Tactical Air Command	94	Incirlik	U.S. Air Force - Europe
70	Luke	Tactical Air Command	95	Hellenikon	U.S. Air Force - Europe
71	Mt. Home	Tactical Air Command	96	Camp NewAust	U.S. Air Force - Europe
72	Yokota	Pacific Air Force			
73	CIRF Kadena	Pacific Air Force			

TABLE 3.4
AIR BASES AND MAJOR COMMANDS

CATEGORY 1: MEASURES OF SIZE

- V1 - Number of Items Records
Overall Total (Repair Cycle)

CATEGORY 2: ACTIVITY MEASURES

- V2 - Total Transactions (Supplies)
- V3 - Total Issues (Supplies)
- V4 - Total Due-Outs (Supplies)
- V5 - Total Receipts (Supplies)
- V6 - Total Overall Requisitions
Total Number

CATEGORY 3: EFFECTIVENESS MEASURES

- V7 - Recoverable Issue Effectiveness
- V8 - Recoverable Release Effectiveness
- V9 - Total Item Records with Requisition Objective, Zero Accessible Assets - Overall Total

CATEGORY 4: REPAIR CYCLE INFORMATION

- V10 - Average RCT for Total RTS
Total All Organizations
- V11 - Average RCT for Total NRTS
Total All Organizations
- V12 - Average RCT for Total Condemned
Total All Organizations

TABLE 3.5

AIR FORCE SUPPLY VARIABLES

	(1)	(2)	(3)
EIGENVALUES	6.2337	2.2224	1.1653
% VARIANCE	51.95	70.47	80.18
1.V1	.34247	-.01612	-.08775
2.V2	.39357	.04980	.00980
3.V3	.36595	.09850	.02281
4.V4	.38871	.02107	.00005
5.V5	.38961	.03858	-.00622
6.V6	.38939	.03312	.03650
7.V7	.00740	.04892	.83608
8.V8	-.02456	.42394	.34685
9.V9	.35714	.00777	-.08464
10.V10	.03946	-.53931	.09781
11.V11	.03875	-.60602	-.01550
12.V12	.09005	-.37979	.39244

=====

TABLE 3.6

Output from Principal Components for Air Force Supply Data

BASES		METHOD OF SELECTION	VALUES OF B (k=3)
Grissom	Incirlik	SRS	2.06
San Vito	Torrejon	SRS	17.58
Lowry	Cannon	SRS	44.68
McChord	Lajes	SRS	10.27
D-Monthan	Maxwell	SRS	3.47
Howard	Osan	Purposive	0.56
Carswell	Aviano	Purposive	225.21

TABLE 3.7
 Values of B for Air Force Supply Data
 (n=2)

BASES		METHOD OF SELECTION	VALUES OF B (k=3)
Columbus	McGuire		
Mildenhall	Altus	SRS	4.77
Randolph	Zweibrucken		
Norton	Castle		
Camp NewAmst	Mather	SRS	4.12
Plattsburg	Howard		
McChord	Osan		
Plattsburg	Langley	SRS	19.43
Taegu	Clark		
F.E.Warren	Mildenhall		
Rhein Main	Blytheville	SRS	5.32
Loring	Norton		
Bergstrom	Loring		
Taegu	Shaw	SRS	4.76
Maxwell	Upper Heyford		
Randolph	Little Rock	Purposive:	
Minot	England	Data Bank	2.18
Kunsan	Upper Heyford	Bases	
Nellis	Clark	Purposive:	
Offutt	Kadena	Largest	125.39
Langley	Travis	by V1	
Lackland	Maxwell	Purposive:	
Chanute	San Vito	Smallest	45.95
Hellenikon	Columbus	by V1	
Keesler	Travis	Purposive:	
Offutt	Nellis	Largest in	158.49
Clark	Ramstein	Stratum	
Lackland	Lajes	Purposive:	
F.E.Warren	Howard	Smallest in	32.85
Taegu	San Vito	Stratum	

TABLE 3.8
 Values of B for Air Force Supply Data
 (n=6)

1983-84 USAF-SCEEE RESEARCH INITIATION PROGRAM

Sponsored by the

AIR FORCE OFFICE OF SCIENTIFIC RESEARCH

Conducted by the

SOUTHEASTERN CENTER FOR ELECTRICAL ENGINEERING EDUCATION

FINAL REPORT

NUMERICAL AND ANALYTICAL STUDY OF HIGH RESOLUTION LIMB SPECTRAL

RADIANCE FROM NON-EQUILIBRIUM ATMOSPHERES

Prepared by: Dr. Pradip Bakshi

Academic Rank: Research Professor of Physics

Department and
University: Physics Department
Boston College

Research Location: Air Force Geophysics Laboratory

Date: October 1984

Abstract-Emission lineshapes are calculated numerically for isolated optically thick infrared lines in the earth limb as a function of tangent height using a general non-local thermodynamic equilibrium (non-LTE) upper-atmospheric line-by-line radiation transport code. It is also shown that the exact integral form of the transport equation can be written in a form that is easily amenable to analytical approximation of high accuracy. In this form the limb spectral radiance I_ν appears as a weighted average of n_u/n_l , the ratio of upper-state to lower-state population density, multiplied by the absorptivity $1 - \exp[-\tau(\nu)]$, where $\tau(\nu)$ is the total optical path along the line-of-sight. In the wings the variation of I_ν is governed by the absorptivity, while in the core of the optically-thick line I_ν is determined by the averaged population ratio. The analytical forms enable one to calculate all the important features of the self-absorbed line and agree remarkably well with the more time-intensive numerical calculation. We illustrate these results by calculations on the $15 \mu\text{m CO}_2 \nu_2(01^10 - 00^00)$ vibrational transition for tangent heights ranging through the mesosphere and lower thermosphere. Even though the collision linewidth is less than 1% of the Doppler width at these altitudes, we show that it is essential to use the Voigt line profile in this calculation rather than the Doppler profile. Failure to do so leads to a total band radiance in error by up to a factor of three, as well as incorrect bandshapes and lineshapes.

SECTION 1: INTRODUCTION

Probing the earth's high-altitude atmosphere by observing emitting species in the earth limb from balloon, rocket, or satellite platforms has become increasingly popular in recent years¹⁻⁶. By scanning the earth limb as a function of tangent height, one obtains a radiance profile which can be inverted to yield species concentration and temperature information^{7,8}. This technique is capable of high vertical resolution and large area coverage. The large limb optical paths available compared to upward-looking or downward-looking probes and the very low background radiation from space contribute to high signal-to-noise ratio and allow the identification of weak emitters. These techniques have been successfully employed in measuring and analyzing the diurnal^{6,9}, latitudinal, and seasonal¹⁰ behavior of the infrared emissions from the earth's mesosphere and thermosphere.

The calculation of the propagation of light from a high-altitude molecular emitter viewed in the limb of a planetary atmosphere is accompanied by many complications, especially in the infrared region of the spectrum where the vibration-rotation bands of most atmospheric molecular species lie. The optical path is inhomogeneous, with the atmosphere becoming less dense and the mixing ratio and temperature of the emitting species changing as one proceeds outward from the tangent point along the path in either direction. At sufficiently high altitude, and certainly by the time one has reached 65 km, collisions are insufficiently frequent to maintain the vibrational populations in equilibrium, and the atmosphere deviates from the condition of local thermodynamic equilibrium (LTE). In the non-LTE region absorption of sunshine and earthshine, chemiluminescent processes, and radiation to space, in addition to collisional processes, determine the vibrational population

distribution. Additional difficulties are contributed by the presence of hot bands and isotopic bands, the overlapping of bands, and especially by the fact that strong lines become optically thick.

Most infrared atmospheric radiation analyses have used band models because of the increase in computational speed which they allow¹¹. Nevertheless, the increased accuracy possible with the more time-consuming line-by-line calculations is well-known, and various methods have been proposed to increase computing speed¹²⁻¹⁴. In this paper we present a general numerical treatment of non-LTE infrared earthlimb emission lineshapes, using a recently developed computer code¹⁵, and also show how various analytical approximations of high accuracy can be used to provide important insights and to significantly shorten computation time. We express the solution of the radiation transport equation for the spectral radiance within non-overlapping lines in the form $I_{\nu} \sim \langle R \rangle [1 - \exp[-\tau(\nu)]]$, where $\langle R \rangle$ is essentially a weighted average of the ratio of upper-level to lower-level populations n_u/n_l of the emitter and $\tau(\nu)$ is the total optical path along the line-of-sight (LOS). This expression can be approximated in different ways in the line wings and in the line-center region. The expression for I_{ν} is determined primarily by the variation of $\mathcal{T}(\nu)$ in the wings and by the variation of $\langle R \rangle$ in the central region. We show that in the line-center region the variation of $\langle R \rangle$, and hence of I_{ν} , as a function of frequency reflects the variation in n_u/n_l as a function of height. This suggests the possibility of inverting the radiance profile for a single line to obtain upper-level populations.

We concentrate in this paper on mesospheric emissions and show the critical importance of using the Voigt emission lineshape rather than the Doppler for optically thick lines in this part of the high-altitude atmosphere to predict properly band and line radiances, as well as the spectral radiance variation I_{ν} within a single line. This is true despite the fact that the Doppler linewidth is more than 100 times the collision width everywhere above 65-70 km altitude. The extremely slow $(\Delta \nu)^{-2}$ fall-off of the wings of the

Lorentzian is responsible for this effect. The observation that for very strong absorbers the wings of the line determine the absorption coefficient has been known for a long time in the field of atomic resonance radiation¹⁶. However, the manifestation of this effect in molecular vibration-rotation bands in the atmosphere is particularly striking. The wings of the Voigt profile are of importance not only in the calculation of mesospheric infrared limb emission, as pointed out in this paper, but also in the calculation of mesospheric infrared radiative cooling rates¹⁷.

High-resolution line-by-line limb emission spectra have been calculated by Rebourts and Rabache recently^{18, 19}; however, their code has been optimized for stratospheric calculations, where LTE conditions prevail and line broadening is predominantly Lorentzian, and they have concentrated on the far-infrared region (wavelength $< 100 \text{ cm}^{-1}$). A number of other slant-path line-by-line transmission and emission codes are optimized for the lower atmosphere where LTE conditions exist (for example²⁰).

We begin in Sec. 2 with a discussion of the general features of the emission lineshape. Section 3 discusses the earthlimb viewing geometry. In Sec. 4 we present the integrated radiative transfer equation for I_ν and recast it into the form of a product of $\langle R \rangle$ and the absorptivity. The numerical solution of this equation is discussed in Sec. 5, and the inadequacy of using the Doppler line profile in the 70-85 km altitude range is shown. Analytical approximations to the spectral radiance I_ν in the line-center and line-wing regions are presented in Sec. 6, and Sec. 7 presents some concluding remarks.

SECTION 2: GENERAL EMISSION LINESHAPE CONSIDERATIONS

The following discussion and results are generally applicable for non-overlapping spectral lines; however, for clarity we use the specific example of the CO₂ bending mode $\Delta v_2 = 1$ (01¹0-00⁰0) vibration-rotation transitions viewed in a limb look near 70 km tangent height.

In the presence of both Doppler and collision broadening, the lineshape for a homogeneous path is described by the familiar Voigt profile²¹, which is a convolution of the Doppler and Lorentz profiles (Appendix A). (The collision lineshape is Lorentzian in the impact approximation.) The use of a Voigt profile assumes that the Doppler and collisional broadening are independent broadening mechanisms which do not interfere. When the molecular mean free path between collisions is much shorter than the wavelength, $l_f \ll \lambda$, such destructive interference occurs and gives rise to the phenomenon of collisional or Dicke narrowing (for example 22, 23). In the mesosphere and thermosphere at infrared wavelengths, the mean free path is long enough that this condition is never satisfied, and we assume that Doppler and collisional broadening are independent for the remainder of this paper.

At 70 km altitude the Doppler linewidth (half-width at half-maximum) $\alpha_D = (\nu \bar{v}/c) (\ln 2)^{1/2}$ is about $5.3 \times 10^{-4} \text{ cm}^{-1}$ in the 15 μm spectral region, where ν is the frequency expressed in wavenumbers, \bar{v} is the most probable molecular speed, and c is the speed of light. At this altitude the collisional width α_c is $4.8 \times 10^{-6} \text{ cm}^{-1}$, or only 1/110 times the Doppler width. The shape of the line close to line center near 70 km altitude is expected to be Gaussian with a half-width given by α_D . A few (approximately three) Doppler widths away from line center, the shape of the line becomes Lorentzian. This is due to the fact that, no matter how much larger α_D is than α_c , the Gaussian (Eq. A-1) decreases much more rapidly than the asymptotic form of the Lorentzian $\pi^{-1} \alpha_c (\nu - \nu_0)^{-2}$ (Eq. A-2), and the latter dominates sufficiently far from line center ν_0 .

Still further from line center, perhaps several tens of thousand Doppler widths away, the condition $c\Delta\nu \approx t_c^{-1}$ is achieved, where t_c is the duration of a collision²³. Then the impact approximation fails, and the details of the short-range part of the intermolecular potential and of the molecular trajectory during the collision dominate the lineshape. In this far-line-wing region, in simplest approximation, the lineshape falls off exponentially. Although this part of the molecular lineshape has raised several points, which so far have not been completely resolved, in this paper we need not be concerned with the shape of the line more than about twenty Doppler linewidths from line center, well within the region where the impact approximation is valid.

Suppose we have a detector with infinite resolution and negligible noise looking at the earth limb emission in the $15 \mu\text{m}$ spectral region and near 70 km tangent height. This detector will record emission from the fundamental of the bending mode of various isotopes of carbon dioxide. The observed emission will involve transitions in the various branches of bands ending not only in the ground vibrational level but also in higher vibrational levels. The detector will also resolve isotopic emissions and reveal the details of the lineshape of each vibration-rotation transition.

The shape of optically thin lines seen by our detector is a composite of lines obtained from different altitudes weighted by the density of emitters and the element of geometric path length at that altitude. The Doppler linewidth is independent of pressure and increases weakly with temperature $\alpha_D \sim T^{1/2}$, because the average speed increases with temperature. The Lorentz part

of the lineshape in the extreme wings may permit us to deduce the collisional linewidth α_c . Because of the weak dependence of α_c on the temperature and because $\alpha_c \sim$ density, it may be possible to invert the lineshape in the extreme wings to obtain the density.

In the rest of this paper, we focus on the transmitted CO_2 (ν_2) lineshape or spectral radiance in the domain where self-absorption becomes important. Under the influence of self-absorption, the lineshape can be altered dramatically, and the relative importance of the Doppler center portion of the line and the Lorentzian wings can be changed. We will examine the spectral radiance in various regions of a single line and the variation of line radiance from line to line in the band. The way in which the spectral radiance and line radiance depend on the properties of the radiative transfer process and on atmospheric parameters will be investigated.

SECTION 3: LIMB GEOMETRY

The geometry of a detector making earthlimb radiance measurements is illustrated in Fig. 1. The detector is in the exosphere above the spherical earth at an altitude $h_d \approx 300$ km. The point where the LOS of the detector meets the line from the center of the earth at right angles is called the tangent point, and the altitude of this point h_t is called the tangent height. Looking at the earthlimb at tangent height h_t , the detector collects radiation from all altitudes h such that $h_t \leq h$. The position along the LOS is characterized by its distance s measured from the tangent point. The path increment Δs along the LOS for an altitude increment Δh above altitude h is given by

$$\Delta s = (2R + h + h_t)^{1/2} [(h - h_t + \Delta h)^{1/2} - (h - h_t)^{1/2}], \quad (3-1)$$

where R is the radius of the earth. For h_t near 70 km and altitudes h within a few tens of kilometers of h_t , we have

$$\Delta s \approx 113.5 \text{ km}^{1/2} [(h - h_t + \Delta h)^{1/2} - (h - h_t)^{1/2}]. \quad (3-2)$$

The point of Eq. (3-2) is that altitudes closer to the tangent height have longer path lengths along the LOS than those farther away. In fact, the path along the LOS within 1 km above h_t is $2\Delta s \approx 227$ km, whereas the next 1 km increase in altitude contributes only 94 km. We thus emphasize that not all altitudes through which the LOS traverses make equal contributions to the path length along the LOS and that the contribution of altitudes close to the tangent height predominates. Of course, the contribution to the total radiance from a given altitude region is determined by weighting the path length Δs by appropriate parameters characteristic of the radiating species, such as the upper-state density or the transmissivity. We discuss these factors in the next section.

SECTION 4: PATH SPECTRAL RADIANCE - GENERAL EXPRESSION

In this section we develop some analytical results for the general line profile for limb radiance observations. The limb spectral radiance I_ν [photons/cm² sec sr cm⁻¹] at wavenumber ν is given by²⁴

$$I_\nu = \frac{A}{4\pi} \int_{-\infty}^{\infty} ds \, g[\nu - \nu_0, h(s)] n_u[h(s)] \times \exp \left\{ -\frac{h\nu}{c} B_{1 \rightarrow u} \int_s^{\infty} ds' \, g[\nu - \nu_0, h(s')] n_l[h(s')] (1 - \gamma[h(s')]) \right\}, \quad (4-1)$$

where A [sec⁻¹] is the Einstein coefficient for spontaneous emission, $B_{1 \rightarrow u}$ is the Einstein absorption coefficient [cm³/erg sec² molecule = cm/gm molecule], h multiplying ν is Planck's constant, and $n_l(h)$ and $n_u(h)$ are the densities [cm⁻³] of the lower state and upper state of the emitting species, respectively, at altitude h . The function $g(\nu - \nu_0, h)$ [cm] is the normalized lineshape function centered at ν_0 , that is

$$\int_{-\infty}^{\infty} d\nu \, g(\nu - \nu_0, h) = 1. \quad (4-2)$$

It depends on altitude h through the temperature T and the pressure p . (See Appendix A for functional forms.) The population factor $\gamma(h)$ is given by

$$\gamma(h) = g_l n_u(h) / g_u n_l(h), \quad (4-3)$$

where g_u and g_l are the statistical weights of the upper and lower states. Note that ds and dh are related by the infinitesimal limit of Eq. (3-1), namely

$$ds/dh = (1/2) [(2R + h + h_t)/(h-h_t)]^{1/2} . \quad (4-4)$$

Equation (4-1) has very simple and basic physics as its foundation. The number of photons emitted per unit volume at h over the whole vibration-rotation line per second per steradian is $(A/4\pi)n_u$. Of these, the number emitted at frequency ν is obtained by multiplying by $g(\nu - \nu_0, h)$, and the fraction reaching the detector is obtained by multiplication by the exponential transmissivity factor. Finally, the resulting number is integrated over the whole optical path. Equation (4-1) assumes that the detector height h_d is above the whole radiating atmosphere, so that the upper limit on the s integral can be set to $+\infty$ and that there is no flux from space into the atmosphere. The equation also ignores scattering of any kind. The derivation of Eq. (4-1) also assumes a steady-state atmosphere which need not be in thermal equilibrium and includes stimulated emission through the factor $[1 - \gamma(h)]$.

If we define the integrand of the exponential term in Eq. (4-1), that is the absorption coefficient, by

$$f[\nu, h(s)] = (h\nu/c) B_{1 \rightarrow u} g(\nu - \nu_0, h) n_1(h) [1 - \gamma(h)] \quad (4-5)$$

and define a weighting factor

$$F[\nu, h(s), s] = f[\nu, h(s)] \exp \left\{ - \int_s^\infty ds' f[\nu, h(s')] \right\} , \quad (4-6)$$

then (using the relation between the Einstein A and B coefficients and the definition of γ), Eq. (4-1) can be rewritten

$$I_\nu = 2c\nu_0^2 \int_{-\infty}^{\infty} ds \left(\gamma[h(s)] / \{1 - \gamma[h(s)]\} \right) F[\nu, h(s), s]. \quad (4-7)$$

Further substitution of

$$R(h) = \gamma(h)/[1 - \gamma(h)] \quad (4-8)$$

in Eq. (4-7) gives

$$I_\nu = 2c \nu_0^2 \int_{-\infty}^{\infty} ds R[h(s)] F[\nu, h(s), s]. \quad (4-9)$$

Note that $2c \nu_0^2 R(h)$ is equal to the blackbody spectral radiance at a temperature equal to the vibrational temperature T_{vib} for the Q branch. In this case T_{vib} is related to γ by

$$T_{\text{vib}}(h) = -hc \nu_0/k \ln \gamma(h). \quad (4-10)$$

For P and R branches an additional factor depending on the rotational temperature must be included to account for the population difference between lower and upper rotational states. The vibrational temperature T_{vib} need not be equal to the common temperature T characterizing the translational and rotational distributions. Furthermore, the interpretation of $2c \nu_0^2 R(h)$ as a blackbody spectral radiance does not require that the whole vibrational distribution be in equilibrium at T_{vib} .

Clearly the dimensionless factor F is a positive quantity (because f is everywhere positive) and can be used as a measure with which to average R over the LOS. The integral of the weight factor F over the whole path is easily shown to be the absorptivity

$$\int_{-\infty}^{\infty} ds F[\nu, h(s), s] = 1 - \exp[-\tau(\nu)], \quad (4-11)$$

where $\tau(\nu)$ is the total optical path,

$$\tau(\nu) = \int_{-\infty}^{\infty} ds f[\nu, h(s)]. \quad (4-12)$$

Equation (4-9) can now be written

$$I_{\nu} = 2c \nu_0^2 \langle R \rangle \left\{ 1 - \exp[-\tau(\nu)] \right\}, \quad (4-13)$$

where

$$\langle R \rangle = \frac{\int ds R[h(s)] F[\nu, h(s), s]}{\int ds F[\nu, h(s), s]}, \quad (4-14)$$

the range of the integrals being $(-\infty, \infty)$.

The radiative transport equation, Eq. (4-13), is the central result of this paper. The radiance at frequency ν can be viewed as the effective blackbody radiance $2c \nu_0^2 \langle R \rangle$, averaged over the LOS with weighting function F , multiplied by the total absorptivity.

Note that $\langle R \rangle$ depends on the Einstein absorption coefficient $B_{1 \rightarrow u}$, or the line strength, only through the optical path. In two particular cases, namely (1) optically thin lines and (2) R independent of height, the average value $\langle R \rangle$ is independent of the B coefficient or the line strength. In the former case,

$$\langle R \rangle = \frac{g_1 \int ds n_u g}{g_u \int ds n_1 g(1-\gamma)} \quad (4-15)$$

while in the latter case $\langle R \rangle = R = \text{constant}$.

In the next section we discuss computer solutions of Eq. (4-13) for $\text{CO}_2(\nu_2)$ spectral lines and for a LOS intersecting the earth limb.

SECTION 5: NUMERICAL SOLUTION OF TRANSFER EQUATION

The integral in Eq. (4-9) is approximated by partitioning the atmosphere above the tangent height with spherical shells and summing over the n path segments, $n/2$ on each side of the tangent point, resulting from the partition ¹⁵,

$$I_\nu \cong \sum_{i=1}^n R_i \int_{s_i}^{s_{i+1}} ds F[\nu, h(s), s] \quad (5-1)$$

Each atmospheric layer is chosen to correspond to a 1 km change in altitude. A constant value R_i is assumed for the slowly varying function $R(h)$ in each layer, based on the mean value within the layer of vibrational temperature (and also rotational temperature for the P and R branches). The positions s_i and s_{i+1} bound the LOS in the i th layer on the far and near sides, respectively, relative to the detector. A value of $n/2$ equal to 50 was sufficient for the calculations reported here. Integration over the perfect differential $F ds$ for each layer gives

$$I_\nu \cong \sum_{i=1}^n R_i [1 - \exp(-\tau_{\nu i})] \exp(-\sum_{j=i+1}^n \tau_{\nu j}), \quad (5-2)$$

where $\tau_{\nu i}$, the optical path along the LOS in the i th layer, is approximated by

$$\tau_{\nu i} \cong f_{\nu i} \Delta s_i \quad (5-3)$$

Here Δs_i is the LOS distance in the i th layer determined from Eq. (3-2), and $f_{\nu i}$ is the linear absorption coefficient of Eq. (4-5), assumed constant within the layer,

$$f_{\nu i} = \left(\frac{h\nu}{c}\right) B_{l \rightarrow u} g_{\nu i} n_{li} (1 - \gamma_i) \quad (5-4)$$

The subscripted parameters $g_{l,i}$, $n_{l,i}$, and γ_i are mean values of $g(r - r_0, h)$, $n_l(h)$, and $\gamma(h)$ calculated from mean values of temperature and number density in the i th layer [compare Eq. (4-5)].

In practice, the linear absorption coefficient was calculated using the line strength from the AFGL line parameters compilation²⁵. The tabulated line strength $S(T_s)$ [cm/molecule] is given for conditions of LTE at the standard temperature T_s , which is 296 K, and is related to $B_{l \rightarrow u}$ by

$$\frac{h\nu}{c} B_{l \rightarrow u} = \frac{S(T_s)}{P_l(T_s)} [1 - \exp(-C_2 \nu_0 / T_s)]^{-1} \quad (5-5)$$

where $C_2 = 1.4388 \text{ K/cm}^{-1}$ is the second radiation constant and $P_l(T_s)$ is the probability of finding the lower vibration-rotation state occupied. In general, $P_l = n_l/n$, where n is the total number density of the species. The exponential term in Eq. (5-5) takes into account the stimulated emission at 296 K and, in fact, is simply γ evaluated under conditions of LTE at T_s . Equation (5-4) can now be rewritten

$$f_{l,i} = S(T_s) \frac{P_l(T_i)}{P_l(T_s)} \frac{1 - \gamma_i}{1 - \exp(-C_2 \nu_0 / T_s)} g_{l,i} n_i \quad (5-6)$$

The spectral radiance was calculated for lines in the $\text{CO}_2 \nu_2$ (01¹0 - 00⁰0) band. Total pressure (p) and kinetic temperature (T) profiles were based on the 1976 U.S. Standard Atmosphere²⁶. The vibrational temperature profile used was based on preliminary results from a code currently under development, and is shown in Fig. 2, along with the kinetic temperature profile. Similar profiles have been shown by Kumer²⁷. The rotational temperature T_{rot} is taken to be equal to the kinetic temperature $T_{\text{kin}} = T$ at all altitudes of interest. The vibrational temperature is less than the kinetic temperature for $h > 65 \text{ km}$ because collisional excitation is insufficiently frequent to overcome radiative loss. The CO_2 density profile was based on a constant mixing ratio of 322 ppmv²⁶ extrapolated to $h > 125 \text{ km}$ from the data of Trinks and Fricke²⁸, and is shown along with the total pressure in Fig. 3. In Fig. 4 we show the altitude profile of the weighted population ratio R , along with the corresponding vibrational temperature profile repeated from Fig. 2.

Examples of spectral radiance calculated for the Q14 line at tangent heights between 70 and 85 km are shown in Fig. 5. The calculations were performed using both Voigt²⁹ and Doppler lineshape. Out to approximately 0.0015 cm^{-1} (or three Doppler widths at 70 km) from line center the calculations are identical for the two lineshape options used. This is because the Voigt and Doppler lineshapes are not significantly different from each other this close to line center at these altitudes. Further from line center the Voigt and Doppler lineshapes do differ, and the calculations using the Doppler lineshape deviate from those using the Voigt lineshape at altitudes below 85 km. At 70 km tangent height, the integrated line radiance calculated with the Voigt lineshape is more than three times that calculated using the Doppler lineshape, even though (as noted in Sec. 2) the collisional linewidth is less than one hundredth of the Doppler linewidth. The very slight line intensity in the Lorentzian wings of the Voigt profile is nevertheless sufficient to give rise to significant band radiance for the strong transition and long path lengths involved.

Within about 0.0013 cm^{-1} of line center, the spectral radiance and its variation as a function of distance from line center are remarkably similar at the various tangent heights. As will be shown quantitatively in Sec. 6, in this spectral region, the spectral radiance is approximately that of a blackbody at a temperature T_{vib} at the altitude where the radiation first becomes optically thick and the atmosphere becomes opaque, proceeding inward from the detector along the LOS. The initial decrease in T_{vib} as a function of altitude h , its minimum near 95 km, and its subsequent increase as a function of h (see Fig. 4) are tracked by the radiances seen looking inward along the LOS as one moves out from line center in Figure 5. This is due to the fact that the more opaque center of the line samples the atmosphere closer to the detector, and hence at a higher altitude, than does the more transparent portion of the line at larger $\nu - \nu_0$. The minimum in the calculated

radiance is 5.0×10^{13} photons/cm² sec sr cm⁻¹ in reasonable agreement with a radiance of 4.0×10^{13} photons/cm² sec sr cm⁻¹ for a blackbody at the vibrational temperature minimum of 148 K. For an extremely thick line in limb-looking geometry, the altitude where the atmosphere becomes opaque to a given frequency of radiation is fairly independent of tangent height. Consequently, the resulting spectral radiance is also not strongly dependent on tangent height. This situation leads to the similarity in appearance of the central spectral region at various tangent heights.

In the optically thin frequency range sufficiently far from line center, the radiance is proportional to both upper-state column density and absolute line strength. The line strength sufficiently far from line center is, in turn, proportional to the pressure. Hence, the radiance rises rapidly in the wings at successively lower altitudes below a critical altitude (approximately 85 km for the Q14 line).

Integrated line radiances for the fundamental transition of the most common isotope $^{12}\text{C}^{16}\text{O}_2$ in the spectral range 620-720 cm⁻¹, again using both Voigt and Doppler lineshapes, are shown in Fig. 6. (Note that an actual spectrum would show additional lines for hot bands and other isotopes.) Examination of these radiances shows qualitatively different behavior for the two lineshapes. The Doppler shape gives almost constant values of radiance for all except very weak lines. The Voigt-shape calculation matches the Doppler for weaker lines, but the radiance from stronger lines shows a distinct correlation with line strength. The additional contribution in the Voigt calculation for strong lines corresponds to the spectral radiance arising in the optically thinner collision-broadened wing region, where radiance is dependent on absolute line strength.

SECTION 6: ANALYTICAL APPROXIMATIONS

As shown in Sec. 4, the path spectral radiance was expressible through Eq. (4-13) as a product of two factors, (i) the absorptivity along the LOS, Eq. (4-11), and (ii) the averaged R, Eq. (4-14), which essentially reflects the average of the ratio of populations in the upper and lower levels in the region where the weight factor F of Eq. (4-6) is significant. Various analytical approximations or simplifications are now feasible for the evaluation of these two factors, depending on the frequency range and other parameters of interest. Many of the salient features of the lineshapes can be inferred from these analytical approximations.

A. Determination of Optical Path $\tau(\nu)$

From Eq. (4-12), the optical path along the LOS is given by

$$\tau(\nu) = \frac{h\nu}{c} B_{1 \rightarrow 0} \int_{-\infty}^{\infty} ds \, g(\nu - \nu_0, h) \, n_1(h)[1 - \gamma(h)], \quad (6-1)$$

where $h = h(s)$. For the Voigt profile, a convenient integral representation is³⁰

$$g(\xi) \approx \frac{(1n2)^{1/2}}{\pi a_D} \int_0^{\infty} dx \, \cos \xi x \exp(-ax - x^2/4), \quad (6-2)$$

where ξ and a are defined in Eqs. (A-5) and (A-6). Since $a \ll 1$ for our parameters, one can use the small- a expression³⁰.

$$g(\xi) \approx (1n2/\pi)^{1/2} a_D^{-1} \left\{ \exp(-\xi^2) - 2a\pi^{-1/2} [1 - 2F(\xi)] + \dots \right\} \quad (6-3)$$

with

$$F(\xi) = \exp(-\xi^2) \int_0^{\xi} dx \exp(x^2) \quad (6-4)$$

being Dawson's integral. The function $F(\xi)$ has been tabulated by Abramowitz and Stegun³¹. We note here the small- ξ and large- ξ expansions for the second term in Eq. (6-3).

$$2\pi^{-1/2}[1 - 2\xi F(\xi)] = 2\pi^{-1/2}(1 - 2\xi^2 + \frac{4}{3}\xi^4 - \frac{8}{15}\xi^6 + \dots), \quad \xi \ll 1 \quad (6-5a)$$

$$= -\frac{1}{\pi^{1/2}\xi^2} (1 + \frac{3}{2}\xi^{-2} + \frac{15}{4}\xi^{-4} + \dots), \quad \xi \gg 1. \quad (6-5b)$$

The representation for the line profile, Eq. (6-3), allows the evaluation of the optical path of Eq. (6-1) by a simple quadrature. Since the main contribution arises from $s \approx 0$ where the density has a maximum, one can set $\alpha_D = \alpha_D^0$, its value at the tangent height, in Eq. (6-3) as a first approximation. This is permissible since the Doppler width is a slowly varying function of altitude, and one obtains an explicit ν dependence in terms of $\xi = (\ln 2)^{1/2}(\nu - \nu_0)/\alpha_D^0 = \eta/\alpha_D^0$,

$$\tau(\nu) = \frac{h\nu}{c} B_{1 \rightarrow u} \frac{(\ln 2)^{1/2}}{\pi^{1/2} \alpha_D^0} [I_0 \exp(-\xi^2) - I_1 \{2\pi^{-1/2} [1 - 2\xi F(\xi)]\}], \quad (6-6)$$

where

$$I_0 = \int_{-\infty}^{\infty} ds n_1(h)[1 - \nu(h)],$$

$$I_1 = \int_{-\infty}^{\infty} ds a(h)n_1(h)[1 - \nu(h)].$$

The first term in Eq. (6-6) represents the Doppler profile contribution, and the second term is the additional correction due to the Voigt profile. The optical path in the wing is governed by the second term.

A further improvement is achieved by expanding the Doppler term as

$$\exp[-\eta^2/\alpha_D^2] = \exp[-\eta^2/(\alpha_D^0)^2] \{1 - \eta^2 [\alpha_D^{-2} - (\alpha_D^0)^{-2}] + \dots\} \quad (6-7)$$

before integration in Eq. (6-1) and including the factor $1/\alpha_D$ in the quantity in the integrand of I_0 , rather than approximating it by $1/\alpha_D^0$. Figure 7 displays the optical path calculated (a) numerically from Eq. (6-1), as described in Sec. 5, (b) approximately based on Eq. (6-6), and (c) approximately based on Eq. (6-7). In all three cases, summation over 1 km thick layers replaces the integrals. The three curves for tangent height 70 km are practically indistinguishable. Curve (b) differs at most by 11% and curve (c) by 3% from curve (a). Even for greater tangent heights such as 110 km, the differences in the three curves are not significant.

Thus, we can conclude that the simple forms of Eqs. (6-6) or (6-7) are an adequate representation for the optical path over the entire lineshape for the tangent heights of interest. The absorptivity factor $1 - \exp[-\tau(\nu)]$ is then easily evaluated for all ν ; the only required quadratures over the LOS are the integrals I_0 and I_1 for Eq. (6-6) or the only slightly more involved quadratures for Eq. (6-7). Hence, a considerable saving of computation time is realized by using Eq. (6-6) or Eq. (6-7) instead of Eq. (6-1).

B. Determination of $\langle R \rangle$

The other factor to be evaluated across the line profile is the averaged R , Eq. (4-14). Different approximations are required, depending on the frequency domain.

(1) Line Center

For thick lines, the line center is characterized by $\tau \gg 1$, and Eq. (4-13) reduces to

$$I_\nu = 2c\nu^2 \langle R \rangle . \quad (6-8)$$

The average $\langle R \rangle$ can be estimated by applying the method of steepest descent to evaluate the numerator in Eq. (4-14),

$$\langle R \rangle \approx R[h(s_0)] = R(h_0), \quad (6-9)$$

where s_0 , the location along the LOS at which F attains its peak value, is given by

$$df/ds = -f^2. \quad (6-10)$$

As we move away from the line center, s_0 moves closer to the tangent point, and h_0 moves toward the tangent height h_t . This is illustrated in Fig. 8 which shows the weighting function F for several values of $\nu - \nu_0$ at 70 km tangent height. Thus the variation of I_ν near the center reflects the variation of R with altitude. (The normalization for F is given by Eq. (4-11); however, only the shape of F is significant for the evaluation of $\langle R \rangle$.)

(2) Line Wing

The wing region is characterized by little or no absorption, $\tau \ll 1$ and $F \rightarrow f$, leading to

$$\langle R \rangle_{\text{wing}} = \frac{g_l \int ds g_{n_u}}{g_u \int ds g_{n_l} (1 - \tau)} \quad (6-11)$$

For thin lines (where $\tau \ll 1$ for all ν), this is valid for the entire lineshape as already stated in Eq. (4-15).

For the Doppler profile, there are no pronounced wings due to the fast Gaussian decline of $g(\nu)$. For the Voigt profile, when the Lorentzian width $\alpha_c \ll \alpha_0$ the Doppler width, or $a \ll 1$, one can employ Eq. (6-3); for $\xi \gg 1$ only the second term survives in Eq. (6-3) and it has the asymptotic form

$$g(\xi, h) = [\alpha_c(h)/\pi] [B/(\nu - \nu_0)^2], \quad (6-12)$$

based on Eq. (6-5b), where

$$B = 1 + \frac{3}{21n2} \frac{\alpha_0^2}{(\nu - \nu_0)^2} + \frac{15}{4(1n2)^2} \frac{\alpha_0^4}{(\nu - \nu_0)^4} + \dots \quad (6-13)$$

The primary ν dependence is the explicit $(\nu - \nu_0)^{-2}$ factor in Eq. (6-12), while the space dependence is mainly through α_c ; the factor B is only weakly dependent on ν and h.

The approximate separability of g into a function of h multiplied by a function of ν renders $\langle R \rangle_{\text{wing}}$ in Eq. (6-11) almost independent of ν , and if we set $B = 1$, we obtain the far-wing limit,

$$\langle R \rangle_{\infty} = \frac{g_1}{g_u} \frac{\int ds \alpha_c n_u}{\int ds \alpha_c n_1 (1 - \nu)} \quad (6-14)$$

The integrals in Eq. (6-14) can be evaluated from the input data specifying n_u , n_1 , and the pressure p, which determines α_c , as functions of altitude. Thus $\langle R \rangle_{\infty}$ is easily evaluated by quadratures.

The weak dependence of $\langle R \rangle$ on ν in the wings can be recovered by using higher-order terms for B in Eq. (6-13) to represent g in Eq. (6-11) and by retaining the lowest-order absorption effects in F in Eq. (4-14). It is convenient to express these corrections to Eq. (6-14) in the form

$$\langle R \rangle / \langle R \rangle_{\infty} = [1 + b_1 (\nu - \nu_0)^{-2} + b_2 (\nu - \nu_0)^{-4} + \dots] \times (1 - q^{-1} \tau^2 + \dots), \quad (6-15)$$

where

$$b_1 = (3/2 \ln 2) [\langle \alpha_D^2 \rangle_u - \langle \alpha_D^2 \rangle_1] \quad (6-16)$$

with the averages over the upper-level and lower-level populations defined by

$$\langle A \rangle_u = \frac{\int ds n_u \alpha_c A}{\int ds n_u \alpha_c} \quad (6-17a)$$

$$\langle A \rangle_1 = \frac{\int ds n_1 (1 - \nu) \alpha_c A}{\int ds n_1 (1 - \nu) \alpha_c} \quad (6-17b)$$

while

$$\frac{1}{q} = \frac{1}{24} - \frac{1}{8} \frac{\langle [\int_0^s ds' n_1 (1 - \nu) \alpha_c]^2 \rangle_u}{[\int_0^{\infty} ds' n_1 (1 - \nu) \alpha_c]^2} \quad (6-18)$$

The first factor in Eq. (6-15) represents the successive corrections due to the higher-order terms in B in Eq. (6-13), and the second factor represents the lowest-order absorption effects. The mixed representation in Eq. (6-15) can be converted into a pure $(\nu - \nu_0)^{-2}$ expansion by noting from Eqs. (6-1), (6-3), and (6-5b) that

$$T = \left\{ (h\nu B_{1 \rightarrow 0} / \pi c) \int ds n_1 (1 - \gamma) \alpha_0 \right\} (\nu - \nu_0)^{-2} + O[(\nu - \nu_0)^{-4}] \quad (6-19)$$

in the far-wing region.

C. Comparison with Numerical Results

It is convenient to express the path spectral radiance in the normalized form

$$\tilde{I}(\nu) = I_\nu / (2c \nu_0^2 \langle R \rangle_\infty) = \{1 - \exp[-\tau(\nu)]\} \langle R \rangle / \langle R \rangle_\infty \quad (6-20)$$

Near the line center, when the absorption is strong, the absorptivity factor approaches unity, and $\tilde{I}(\nu)$ is simply the ratio of $\langle R \rangle$ to $\langle R \rangle_\infty$. On the other hand, in the wing region, the second factor approaches unity and $\tilde{I}(\nu)$ is simply the absorptivity factor. Further simplification occurs in the wing domain for $\tau(\nu) \ll 1$, where $\tilde{I}(\nu) = 1 - e^{-\tau(\nu)} \rightarrow \tau(\nu)$. The solid line in Fig. 9a is a plot of the exact (numerically obtained) $\tilde{I}(\nu)$ for the Q14 line observed at a tangent height of 70 km. The dashed and dotted lines represent, respectively, the exact first and second factors of $\tilde{I}(\nu)$ indicated in Eq. (6-20).

The analytical expression of Eq. (6-6) for $\tau(\nu)$ provides an accuracy of better than 0.5% over the entire range of ν for the absorptivity factor $1 - e^{-\tau}$, and no further improvement is achieved in this strong-line case by employing Eq. (6-7). Thus the first factor of $\tilde{I}(\nu)$ is predicted analytically to high accuracy over the entire spectral range.

The second factor $\langle R \rangle / \langle R \rangle_\infty$ of $\tilde{I}(\nu)$ departs from its asymptotic value rather gradually. The analytical approximation for this factor, Eq. (6-15), keeping only the leading corrections of order $(\nu - \nu_0)^{-2}$ and τ^2 involving b_1 and q , is represented by the dotted line in Fig. 9b.

The agreement with the numerical result (solid line) is quite remarkable for $|v - v_0| \geq 0.002 \text{ cm}^{-1}$, or $\tau \leq 4$, with a maximum error of less than 2%. Furthermore, we find that the τ^2 term in Eq. (6-15) accounts for the main departure from the asymptotic value, as b_1 happens to be quite small; even at $|v - v_0| = 0.002 \text{ cm}^{-1}$, or $\xi = 3.12$, the error in neglecting b_1 is only 0.05%.

Under these conditions, we have the simple result

$$\tilde{I}(\nu) \approx (1 - e^{-\tau}) (1 - \tau^2/q), \quad (6-21)$$

and the peak occurs at $d\tilde{I}/d\tau = 0$, or at τ satisfying

$$q = 2\tau(e^{\tau} - 1) + \tau^2. \quad (6-22)$$

Knowledge of q in terms of the atmospheric density and temperature distributions through Eq. (6-18) allows us to predict the optical path τ at the peak, and hence also the magnitude of $\tilde{I}(\nu)$ at the peak. When $q \gg 1$, as is the case here, we can simplify Eqs. (6-21) and (6-22), obtaining

$$q \approx 2\tau e^{\tau} \quad (6-23a)$$

and

$$\tilde{I}_{\text{peak}} \approx 1 - (1 + \tau/2) e^{-\tau} \approx 1 - \tau(\tau + 2)/q. \quad (6-23b)$$

Thus, we can infer that the peak value of \tilde{I} is only slightly below unity as long as $q \gg 1$. At 70 km tangent height, $q = 187$, and according to Eq. (6-22) the predicted τ at the peak spectral radiance is 3.32, in excellent agreement with the actual value of $\tau \approx 3.3$ inferred from Figs. 9a and 7. For this tangent height, \tilde{I}_{peak} assumes the value 0.92, and it is predicted within 2% by Eq. (6-23b).

As we move towards the line center, τ increases very rapidly and the higher-order absorption corrections become significant in Eq. (6-15). This domain is well represented by Eq. (6-8) or by just the second factor in Eq. (6-20). The average R in the central domain can be determined from Eq. (6-9), or suitable extensions of that approach. Even the simple analytical result of Eq. (6-9), represented in Fig. 9b by the dashed line remains within 20% of the numerically obtained result, and the qualitative behavior, including the occurrence of the minimum of $\tilde{I}(\nu)$, is very well represented.

Further improvements indicated in subsection E below bring the agreement to within 6% over the entire range from the line center to the peak.

In Fig. 9c the predicted results for the absorptivity and $\langle R \rangle / \langle R \rangle_\infty$ factors are combined to obtain the analytically predicted $\tilde{I}(\nu)$, represented by the dashed line. The discontinuity in the dashed line near the peak is associated with the transition from the central to the wing approximation for $\langle R \rangle / \langle R \rangle_\infty$. The solid line represents the exact numerically obtained result, which was already displayed in Fig. 9a.

We see from Fig. 9c that the spectral radiance for the Q14 line at tangent height 70 km is well represented by the analytical results. Similar agreement between the analytical and actual results is obtained for other tangent heights as well. Figure 10 represents the corresponding results for 85 km. We will not discuss the latter case in detail. However, we note that the peak of $\tilde{I}(\nu)$ occurs for smaller ξ at 85 km, making the Doppler contribution in Eq. (6-3) significant in the vicinity of the peak. Hence, the simple form of Eq. (6-21) which only employs the asymptotic wing profiles needs to be modified.

D. General Comments

(1) The analytical results can be used to obtain the integrated radiance in approximate closed form; these results compare well with the numerically obtained results.

(2) At 70 km tangent height $\langle R \rangle_0$, the average R at line center, is much smaller than $\langle R \rangle_\infty$, and the radiance profile has one maximum and one minimum. As the tangent height is increased, the variation in $\langle R \rangle$ is reduced, and when $\langle R \rangle_0$ substantially exceeds $\langle R \rangle_\infty$, the radiance profile will increase monotonically from line wing to center. Such is the case for tangent heights above 88 km. Thus the determination of the two limiting values of $\langle R \rangle$ is useful to assess the general characteristics of the radiance profile.

(3) Whether the radiance profile will be monotonic or undulating can also be seen from the line-wing results, which are governed by b_1 and q . The absorption effects (τ^2 term) dominate for strong lines. It can be shown

easily that $q^{-1} \rightarrow 0$ if R as a function of altitude approaches flatness in the vicinity of the tangent height. The lineshape effects (b_1 term) also vanish in this situation, and $\langle R \rangle$ is essentially flat over the line-wing region. This can be expected to occur around $h_t \approx 90$ to 95 km (see Fig. 4). The radiance profile, however, already will have become monotonic at a slightly lower tangent height due to the effect of the absorptivity factor. For larger tangent heights, q^{-1} becomes negative, and the radiance profile increases monotonically both due to the τ^2 effects in $\langle R \rangle$ and the rise in the absorptivity factor from the wing to the line center.

(4) Decrease in the line strength will push the peak in the radiance profile towards line center.

(5) The radiance at line center I_0 can be shown to be almost independent of the tangent height for the range of tangent heights where $\tau \gg 1$.

(6) A systematic study of the shape of a single isolated line as a function of tangent height h_t , the line strength or the Einstein coefficient $B_{1 \rightarrow 0}$, and the width ratio a will be given in a subsequent paper. The corresponding results for integrated radiances will also be given elsewhere. The basic framework for these studies has been developed here.

E. Further Analytical Results for Radiance Profiles

The wing region is very well represented by the approximations given so far. Agreement between the analytical and numerical results in the central region can be improved by a better determination of $\langle R \rangle$. Some of the attempts made to improve the line-center profile are described in the following paragraphs.

(1) Instead of applying the method of steepest descent in terms of integration over s , one can change the variable to the altitude h and evaluate R at the peak \hat{h}_0 of the new weighting function $\hat{F} = F(ds/dh)$, that is $\langle R \rangle = R(\hat{h}_0)$. However, the results in this case are poorer approximations of the exact $\langle R \rangle$ of Fig. 9 than is $R(h_0)$ corresponding to the peak of F . The reason for the poor results lies in the much greater asymmetry of the weight functions \hat{F} (Fig. 11) compared to the weight function F shown in Fig. 8.

(2) Since the range of s or h which makes the main contribution to R is also the range where the line first becomes optically thick as one proceeds inward from the detector along the LOS, one can use the criterion $\mathcal{T}(\nu, h_1) = \ln 2$ to define h_1 , and set $\langle R \rangle = R(h_1)$. The quantity $\mathcal{T}(\nu, h_1)$ is the optical path from position s_1 defined as in Eq. (4-12) with the lower limit of the s -integration taken to be $s_1 = s(h_1)$. The point s_1 is the median point of the weighting function F as a function of s for optically thick lines.

(3) Alternative (2) above provides some improvement in part of the frequency range as compared to the simple procedure used in Eq. (6-9). But the above methods cannot be expected to give a uniformly accurate description of $\langle R \rangle$, since they all evaluate R at a single height. Further improvement is achieved in these methods, for instance, by expanding R in a Taylor series around s_0 or h_0 and keeping the first few moments over the distribution F or \hat{F} . This procedure recognizes explicitly the curvature of R as a function of h . Keeping terms up to the second moment provides a uniformly good approximation to $\langle R \rangle$ within 6% for the entire domain from the center to the peak for the Q14 line at 70 km tangent height. The domain beyond the peak is described by the wing approximation.

SECTION 7: CONCLUDING REMARKS

In this paper we have discussed the emission lineshape for an isolated line, including self-absorption, in a planetary atmosphere viewed in the limb as a function of tangent height. Numerical results were described in Sec. 5 and analytical approximations and insights were presented in Sec. 6. The representation of the spectral radiance in the product form, as an averaged density ratio $\langle R \rangle$ times the absorptivity factor $[1 - \exp(-\tau)]$ provides a clear understanding of the main features of the lineshape.

Besides these insights regarding the formation of the lineshape, the analytical results provide a reasonably accurate approach for practical calculations at a considerable saving of computer time compared to the numerical approach. Since the optical path along the LOS $\tau(\nu)$ can be calculated as an explicit function of frequency by simply computing a few global averages of the atmospheric parameters, the determination of the absorptivity factor takes very little computing time. The asymptotic form for $\langle R \rangle$ in the wing region also requires only a few global averages. Thus the lineshape for frequencies beyond the peak of I_ν is easily computed without any serious loss of accuracy. In the central region the simple steepest-descent methods provide $\langle R \rangle$ without consuming much computing time, if we are satisfied with a 10-20% accuracy. To increase the accuracy one can, for instance, include the higher moments as mentioned in Sec. 6E. That, however, does take considerable computing time (perhaps almost as much as the direct numerical approach), and further analytical improvements in that domain with the aim of reducing the computing time should still be attempted.

If we consider a single lineshape at a single tangent height, the atmospheric parameters appear only through global averages along the LOS. Viewing along a different LOS (that is, varying the tangent height) provides a numerically different average, and inverting these averages provide a means of deciphering the atmospheric parameters from limb-viewing observations.

The density profiles, both for the lower level and the upper level, were monotonically decreasing functions of the altitude for the species (CO_2) and altitude regime discussed here. For certain other species, peaked distributions of upper-state and lower-state densities as a function of altitude will prevail, perhaps substantially altering the F and R(h) profiles. These effects can give rise to lineshapes with significantly different features. The methods developed here are, however, general enough to encompass such distributions, and corresponding studies will be described elsewhere.

ACKNOWLEDGMENTS

M.K.B. gratefully acknowledges the support of the U.S. Air Force Geophysics Scholar Program, conducted by the Southeast Center for Electrical Engineering Education (SCEEE), for the period during which this research was carried out. P.M.B. would like to thank Dr. R. Armstrong for his kind hospitality at the Air Force Geophysics Laboratory during the summer of 1983, when this research was initiated under the AFOSR/SCEEE Summer Faculty Research Program, supported by Contract F49620-82-C-0035. A follow-up Research Initiation Program supported by AFOSR/SCEEE at Boston College under the same contract is also gratefully acknowledged.

APPENDIX A: VOIGT LINESHAPE FUNCTION

The lineshape function for the Doppler line profile has the form

$$g_D(\nu - \nu_0, h) = \frac{(\ln 2)^{1/2}}{\pi^{1/2} \alpha_D} \exp [-(\ln 2)(\nu - \nu_0)^2 / \alpha_D^2], \quad (\text{A-1})$$

where $\alpha_D = (\nu_0/c)[(2(\ln 2)kT/m)]^{1/2}$ is the half-width at half maximum. Here m is the molecular mass, k is Boltzmann's constant, and ν_0 is the line center. The width α_D depends weakly on temperature, which in turn gives α_D an implicit dependence on altitude h .

The Lorentz lineshape function g_L is given by

$$g_L(\nu - \nu_0, h) = \frac{1}{\pi} \frac{\alpha_c + \alpha_N}{(\nu - \nu_0)^2 + (\alpha_c + \alpha_N)^2} \quad (\text{A-2})$$

where $\alpha_N = A/2\pi c$ is the natural linewidth and α_c is the collision linewidth $\alpha_c = n \sigma v/2\pi c$, n being the total density, σ the species-weighted average collision cross-section, and v the relative velocity. The radiative width α_N can be neglected because it is normally very small for infrared transitions. For example, for the $15\mu\text{m CO}_2$ transition $\alpha_N \approx 10^{-11} \text{ cm}^{-1}$, while as mentioned above $\alpha_D \approx 10^{-3} \text{ cm}^{-1}$ at room temperature and $\alpha_c \approx 10^{-5} \text{ cm}^{-1}$ at 70 km altitude. Since $n \sim T^{-1}$ and $v \sim T^{1/2}$, for constant pressure and a velocity-independent cross section we have $\alpha_c \sim T^{-1/2}$. Once again, α_c depends weakly on temperature but more strongly on pressure. The result is a strong altitude dependence for α_c , since p varies exponentially with altitude.

The Voigt lineshape function is a convolution of Doppler and Lorentz profiles and is given by

$$g_V(\nu - \nu_0, h) = \int_{-\infty}^{\infty} d\nu' g_L(\nu - \nu', h) g_D(\nu' - \nu_0, h). \quad (\text{A-3})$$

If we introduce y and ξ , the frequency intervals from line center corresponding to ν and ν' , and a , the ratio of Lorentz to Doppler widths, by

$$y = (1n2)^{1/2} (\nu' - \nu_0) / \alpha_D \quad (A-4)$$

$$a = (1n2)^{1/2} (\alpha_C + \alpha_N) / \alpha_D \quad (A-5)$$

$$\xi = (1n2)^{1/2} (\nu - \nu_0) / \alpha_D, \quad (A-6)$$

Eq. (A-3) becomes

$$g_V(\xi, h) = \frac{a (1n2)^{1/2}}{\pi^{3/2} \alpha_D} \int_{-\infty}^{\infty} dy \frac{\exp(-y^2)}{a^2 + (\xi - y)^2} \quad (A-7)$$

REFERENCES

1. A. Girard and M. P. Lemaitre, *Appl. Opt.* 9, 903 (1970).
2. J. C. Gille, P. L. Bailey, and J. M. Russell III, *Phil. Trans. R. Soc. London, Ser. A* 296, 205 (1980).
3. J. C. Gille, P. L. Bailey, R. A. Craig, F. B. House, and G. P. Anderson, *Science* 208, 397 (1980).
4. P. B. Hays, *Appl. Opt.* 21, 1136 (1982).
5. C. A. Barth, D. W. Rusch, R. J. Thomas, G. H. Mount, G. J. Rottman, G. E. Thomas, R. W. Sanders, and G. M. Lawrence, *Geophys. Res. Lett.* 10, 237 (1983).
6. A. T. Stair, Jr., R. D. Sharma, R. M. Nadile, D. J. Baker, and W. Grieder, *J. Geophys. Res.* (in press).
7. J. C. Gille and F. B. House, *J. Atmos. Sci.* 28, 1427 (1971).
8. C. D. Rodgers, *Revs. Geophys. Space Phys.* 14, 609 (1976).
9. R. D. Sharma and A. Zachor, *Appl. Opt.* 22, 2665 (1983).
10. R. J. Thomas, C. A. Barth, G. J. Rottman, D. W. Rusch, G. H. Mount, G. M. Lawrence, R. W. Sanders, G. E. Thomas, and L. E. Clemens., *Geophys. Res. Lett.* 10, 245 (1983).

11. For example, S. N. Tiwari, *Adv. Geophys.* 20, 1 (1978).
12. T. G. Kyle, *J. Opt. Soc. Am.* 58, 192 (1968).
13. N. A. Scott, *JQSRT* 14, 691 (1974).
14. V. G. Kunde and W. C. Maguire, *JQSRT* 14, 803 (1974).
15. R. D. Sharma, R. D. Siani, M. K. Bullitt, and P. P. Wintersteiner, "A Computer Code to Calculate Emission and Transmission of Infrared Radiation Through Non-Equilibrium Atmospheres," AFGL-TR-83-0168 (NTIS No. ADA137162). Air Force Geophysics Laboratory, Bedford, MA 01731 (1983).
16. A. C. G. Mitchell and M. W. Zemansky, Resonance Radiation and Excited Atoms, p. 104. The University Press, Cambridge (1971).
17. R. E. Dickinson, "Infrared Radiative Cooling in the Mesosphere and Lower Thermosphere," NCAR Ms. 0901-84-01. National Center for Atmospheric Research, Boulder, CO 80307 (1984).
18. B. Rebours and P. Rabache, *JQSRT* 24, 517 (1980).
19. B. Rebours and P. Rabache, *JQSRT* 29, 173 (1983).
20. S. A. Clough, F. X. Kneizys, L. S. Rothman, and W. O. Gallery, *Proc. SPIE* 277, 152 (1981).

21. S. S. Penner, Quantitative Molecular Spectroscopy and Gas Emissivities. Addison-Wesley, Reading, Massachusetts (1959).
22. F. Herbert, JQSRT 14, 943 (1974).
23. P. R. Berman, Appl. Phys. 6, 283 (1975).
24. R. M. Goody, Atmospheric Radiation. Clarendon Press, Oxford (1964).
25. L. S. Rothman, R. R. Gamache, A. Barbe, A. Goldman, J. R. Gillis, L. R. Brown, R. A. Toth, J.-M. Flaud, C. Camy-Peyret, Appl. Opt. 22, 2247 (1983).
26. U. S. Standard Atmosphere, 1976. National Oceanic and Atmospheric Administration, Washington (1976).
27. J. B. Kumer, J. Geophys. Res. 82, 2195 (1977).
28. H. Trinks and K. H. Fricke, J. Geophys. Res. 83, 1983 (1978).
29. B. H. Armstrong and R. W. Nicholls, Emission, Absorption and Transfer of Radiation in Heated Atmospheres. Pergamon, Oxford (1972).
30. Reference 21, pp. 45-47.
31. M. Abramowitz and I. A. Stegun, Handbook of Mathematical Functions, p. 319. U. S. Government Printing Office, Washington, D.C. 20402 (1964).

FIGURE CAPTIONS

Fig. 1. Earthlimb viewing geometry for an exoatmospheric detector [R = earth radius, h_t = tangent height, h ($h + \Delta h$) = height at position s ($s + \Delta s$) along line-of-sight].

Fig. 2. Profiles of kinetic temperature $T = T_{kin} = T_{rot}$ and $CO_2 \nu_2$ vibrational temperature T_{vib} vibrational temperature used in model calculations.

Fig. 3. Altitude profiles of total pressure p and CO_2 density used in model calculations.

Fig. 4. Vibrational temperature profile T_{vib} for ν_2 mode of CO_2 , along with profile of R corresponding to this vibrational temperature profile. Equation (4-8) defines R , which is proportional to the affective blackbody radiance at temperature T_{vib} .

Fig. 5. Limb spectral radiance for Q14 line of $CO_2 \nu_2$ fundamental band at four different tangent heights. The line is symmetric in frequency ν about its center frequency ν_0 , and only half of the line is shown. In each case the results are shown for the Voigt (solid line) and Doppler (dashed line) lineshapes.

Fig. 6. Integrated line radiance for lines of $CO_2 \nu_2$ fundamental band at 70 km tangent height for two cases: (a) Voigt profile (b) Doppler profile.

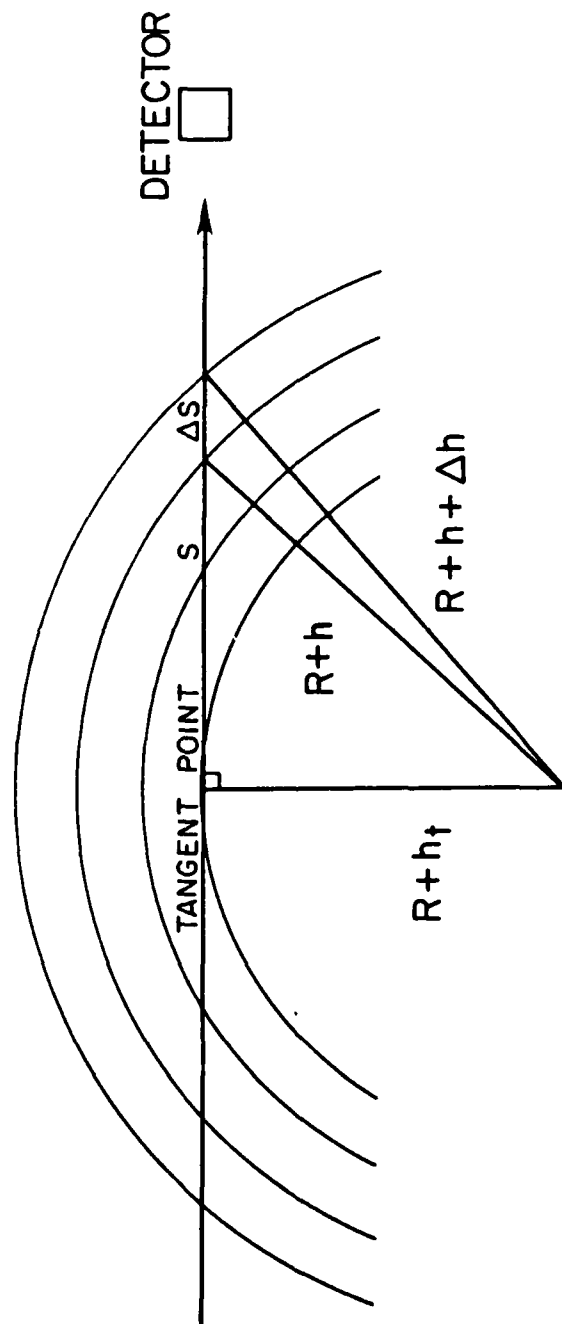
Fig. 7. Optical path $\mathcal{T}(\nu)$ for the Q14 line of the $\text{CO}_2 \nu_2$ transition:
 (a) _____ exact calculation from Eq. (6-1); (b) approximation based on Eq. (6-6); (c) ----- approximation based on Eq. (6-7), expanding the Doppler term. The results are shown at 70, 90, and 110 km altitude. Over large ranges of frequency and altitude the approximate results coincide with the exact solution and are not shown separately.

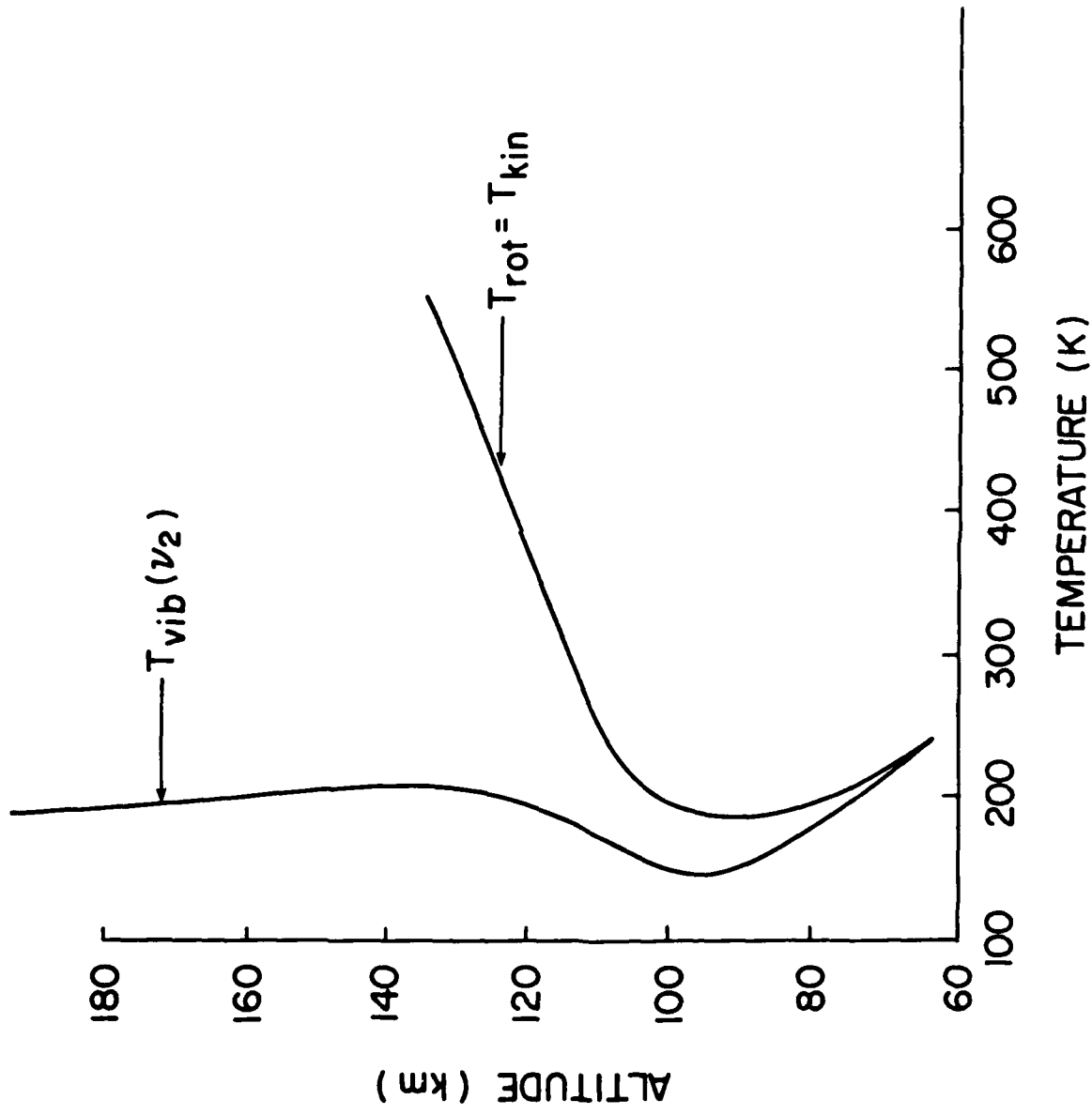
Fig. 8. Weighting function $F[\nu, h(s), s]$ for several values of $\nu - \nu_0$ in Q14 line of $\text{CO}_2 \nu_2$ fundamental as a function of distance s at a tangent height of 70 km.

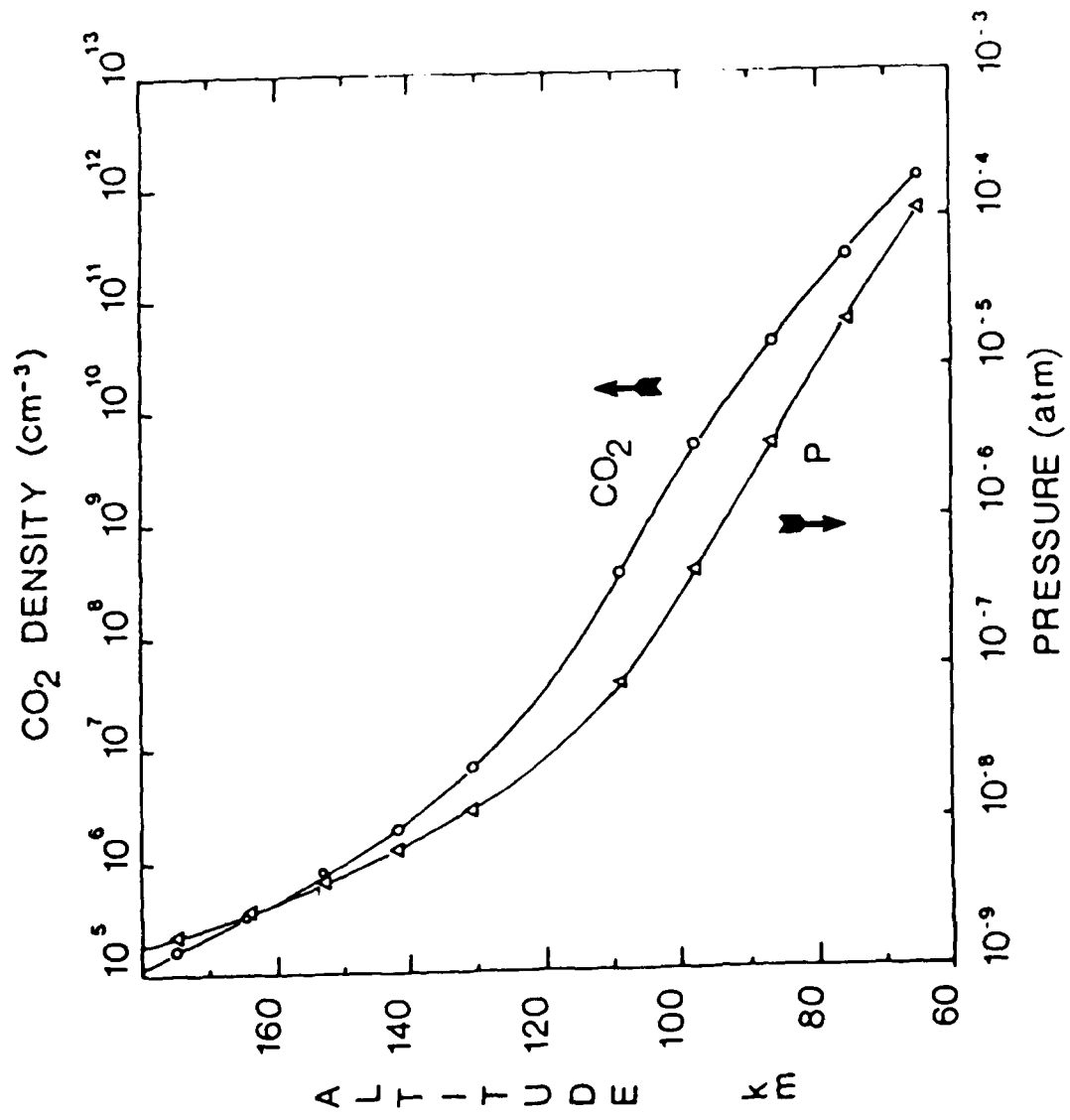
Fig. 9. (a) Exact normalized spectral radiance $\tilde{I}(\nu)$ for the Q14 line of $\text{CO}_2 \nu_2$ at 70 km tangent height (solid curve) along with its factors [Eq. (6-20)]. The dashed curve represents the absorptivity factor $1 - \exp(-\mathcal{T})$, and the dotted curve shows the behavior of $\langle R \rangle / \langle R \rangle_{\infty}$. (b) Exact result for $\langle R \rangle / \langle R \rangle_{\infty}$ (solid curve) along with approximate calculations based on peak of weighting function F (dashed curve) and based on expansion of Eq. (6-15) (dotted line). (c) Normalized spectral radiance $\tilde{I}(\nu)$ calculated exactly (solid curve) and on basis of approximate $\mathcal{T}(\nu)$ and $\langle R \rangle / \langle R \rangle_{\infty}$.

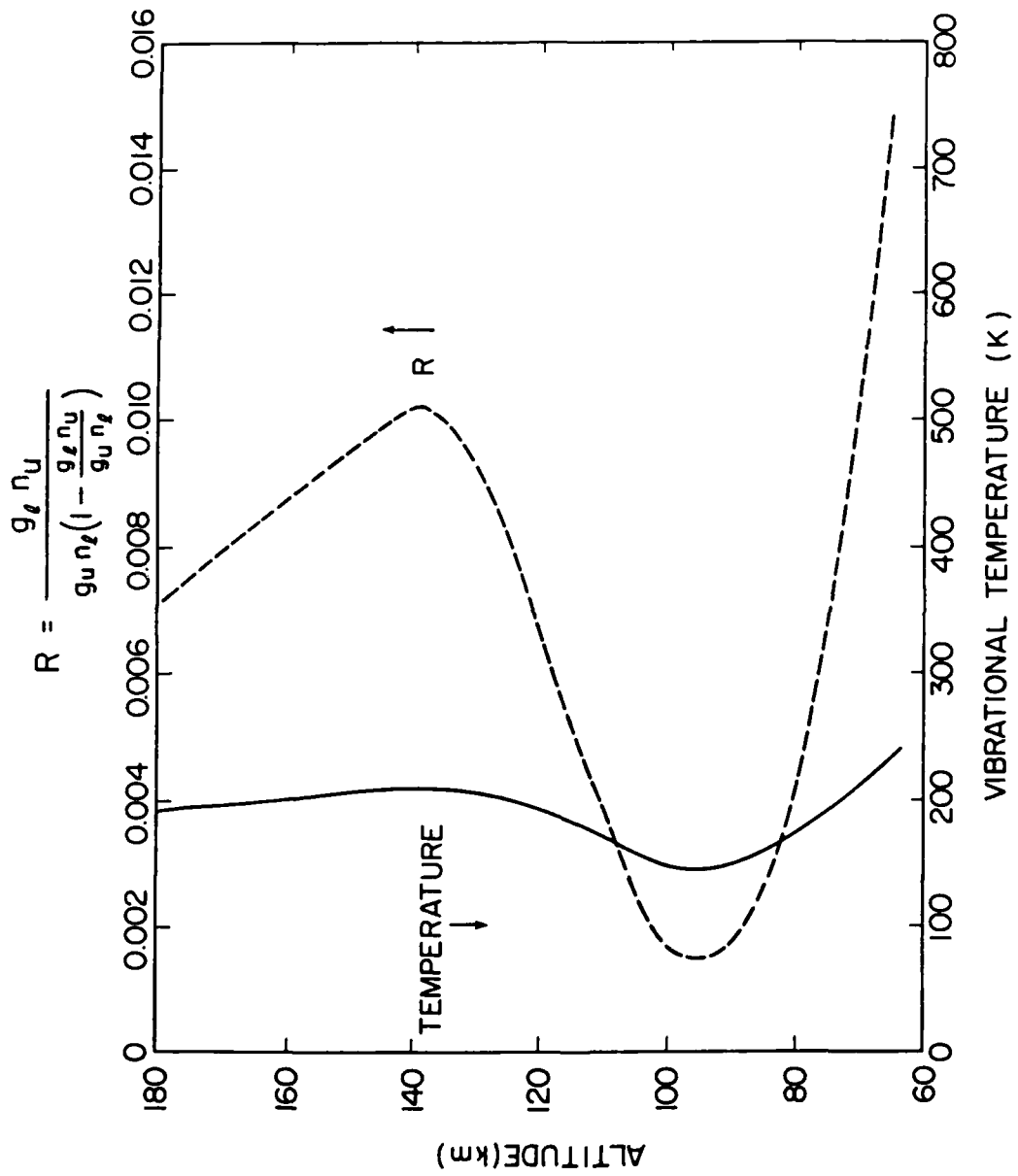
Fig. 10. Corresponding results for $\tilde{I}(\nu)$ at 85 km. Format is same as in Fig. 9.

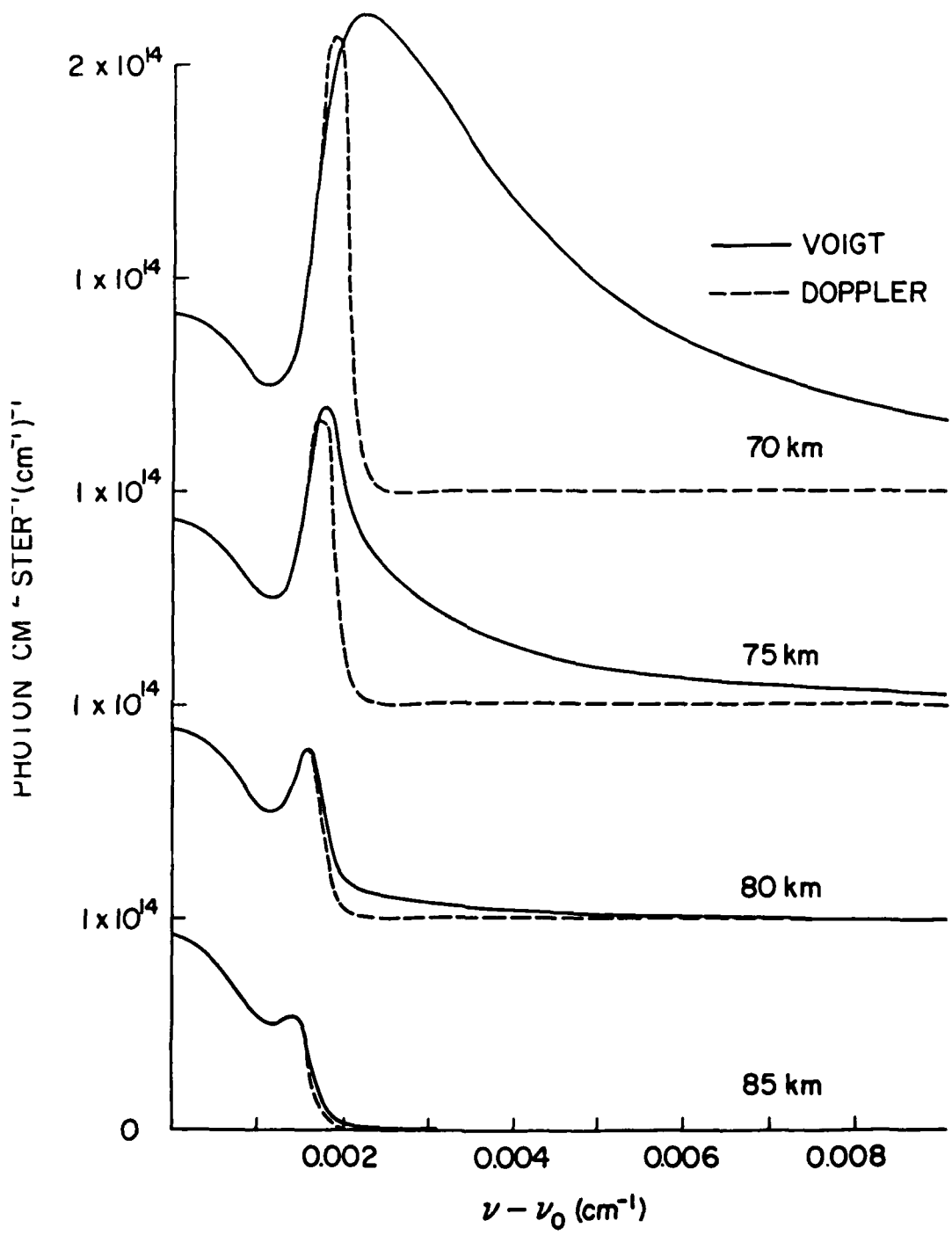
Fig. 11. Weighting function \hat{F} plotted versus altitude h for several values of $\nu - \nu_0$. Tangent height is 70 km, and values of \hat{F} to the left of $h = 70$ km correspond to points on the far side of the tangent point, as viewed from the detector. Rest of parameters are as in Fig. 8.

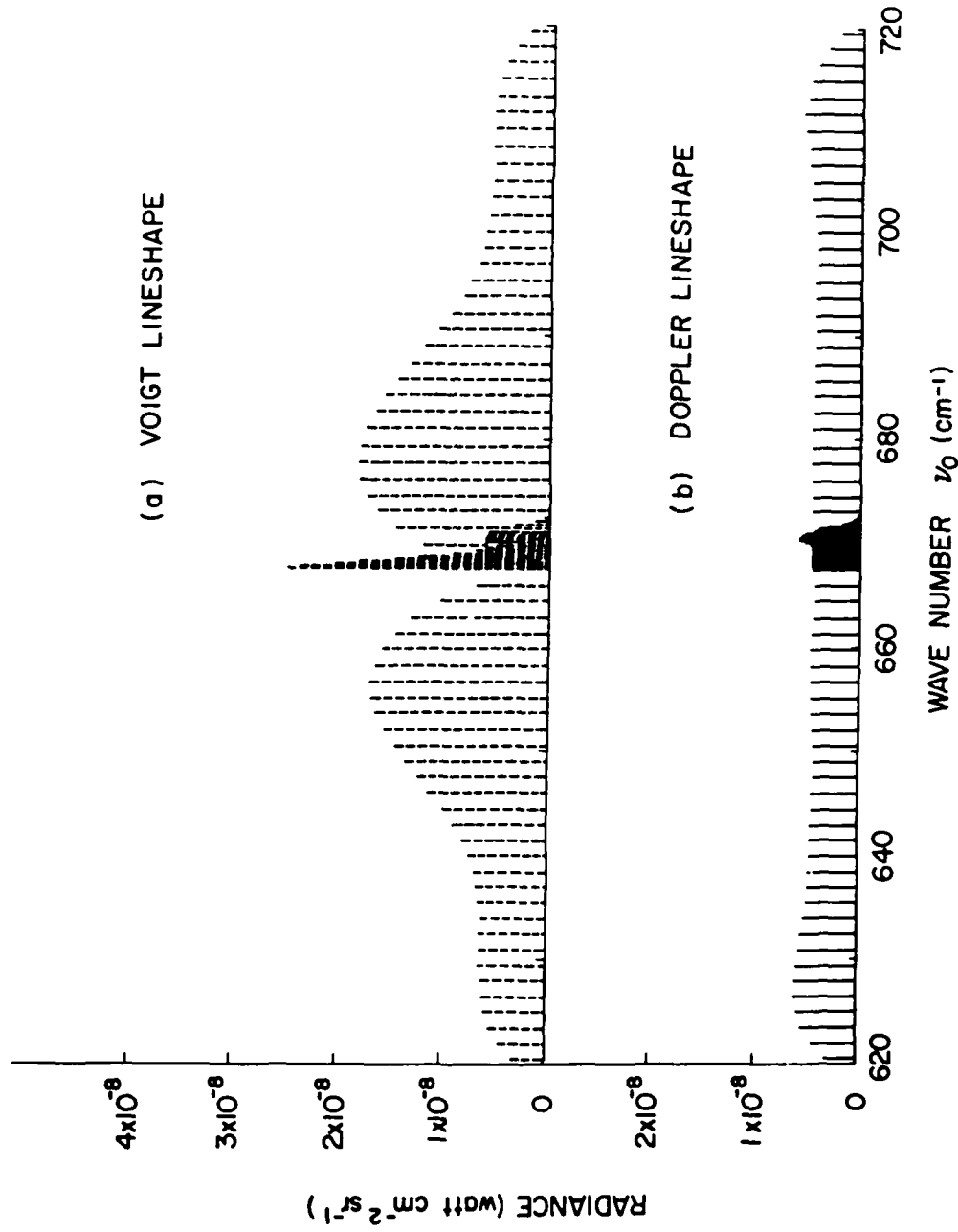


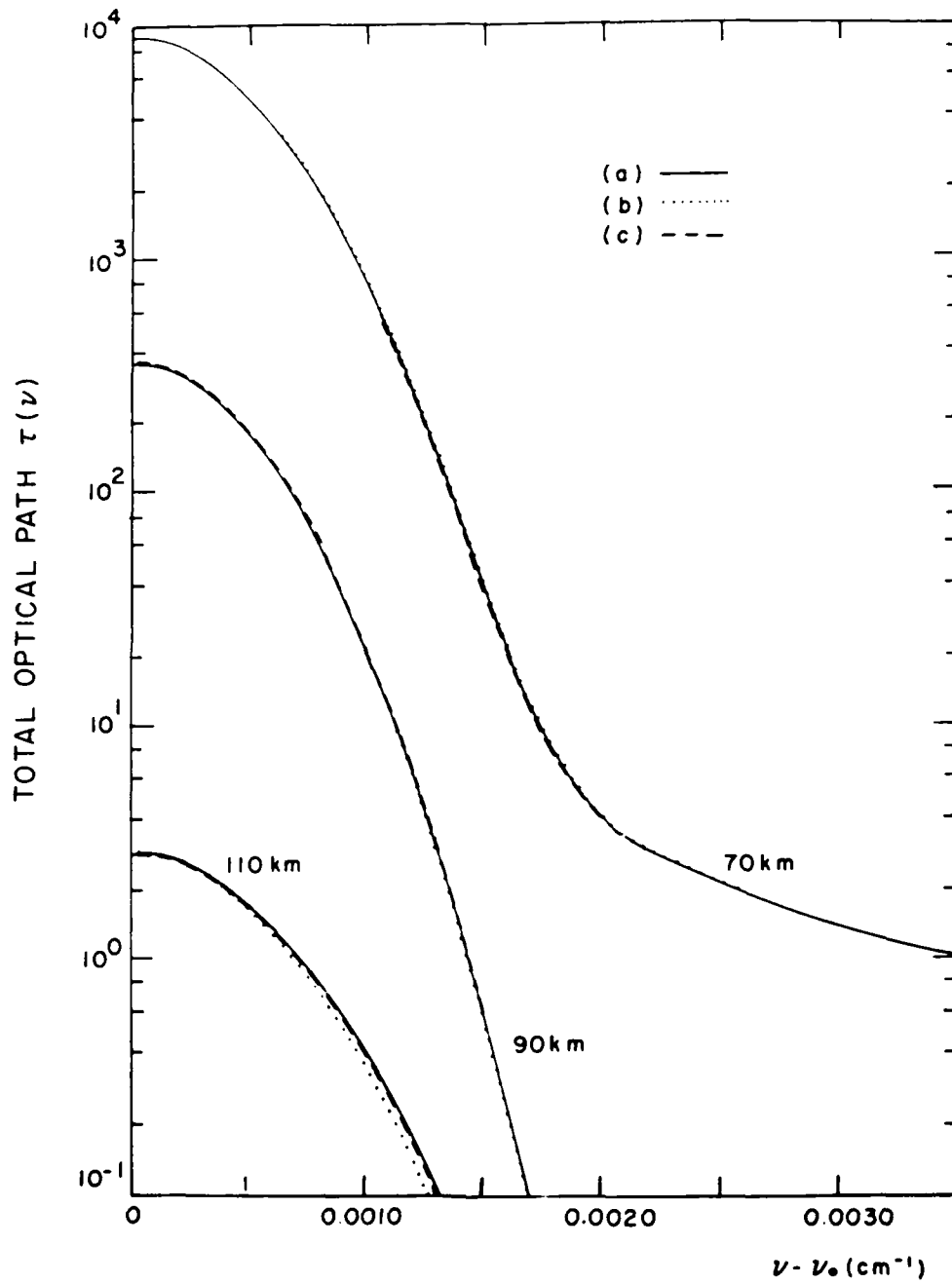


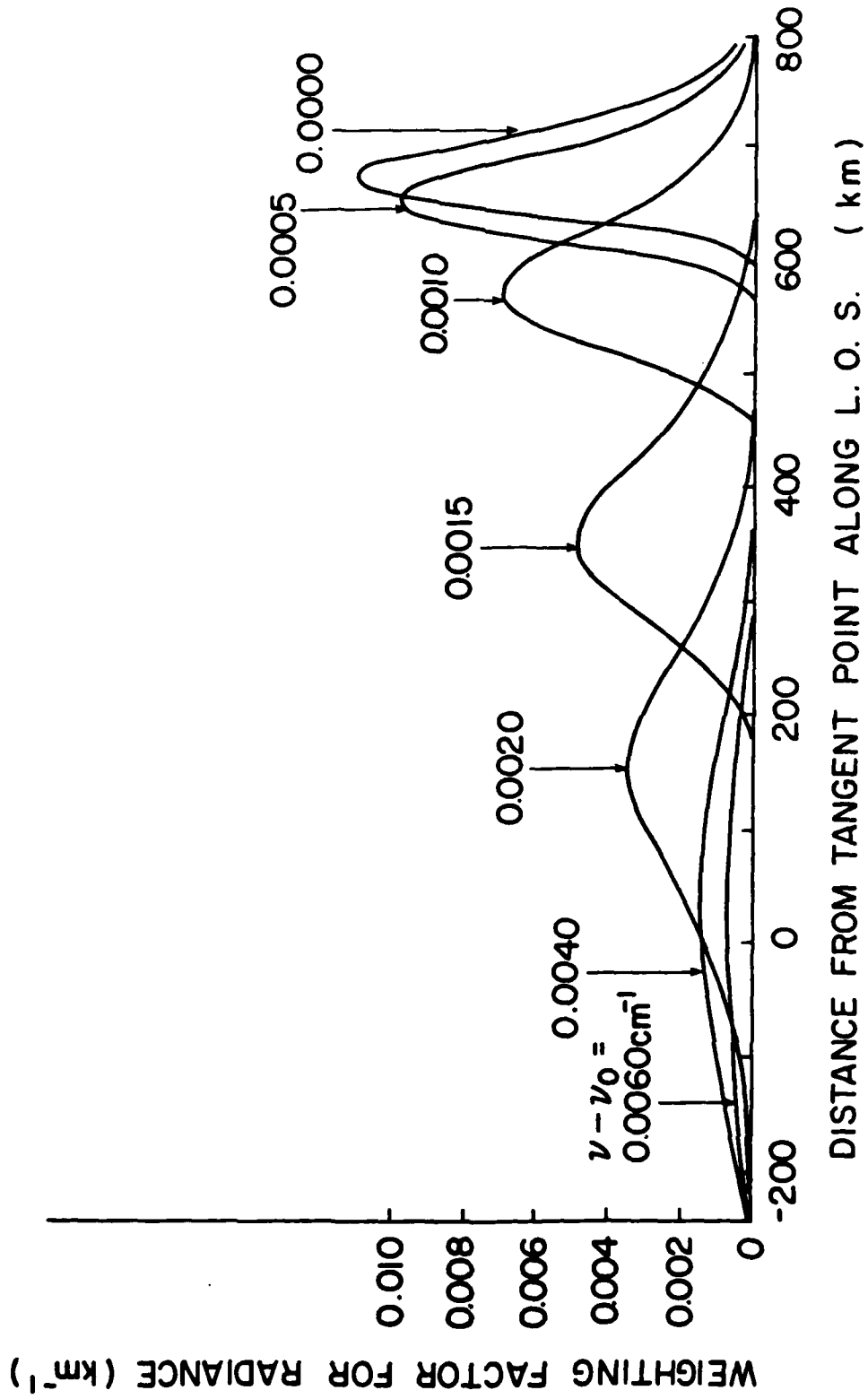


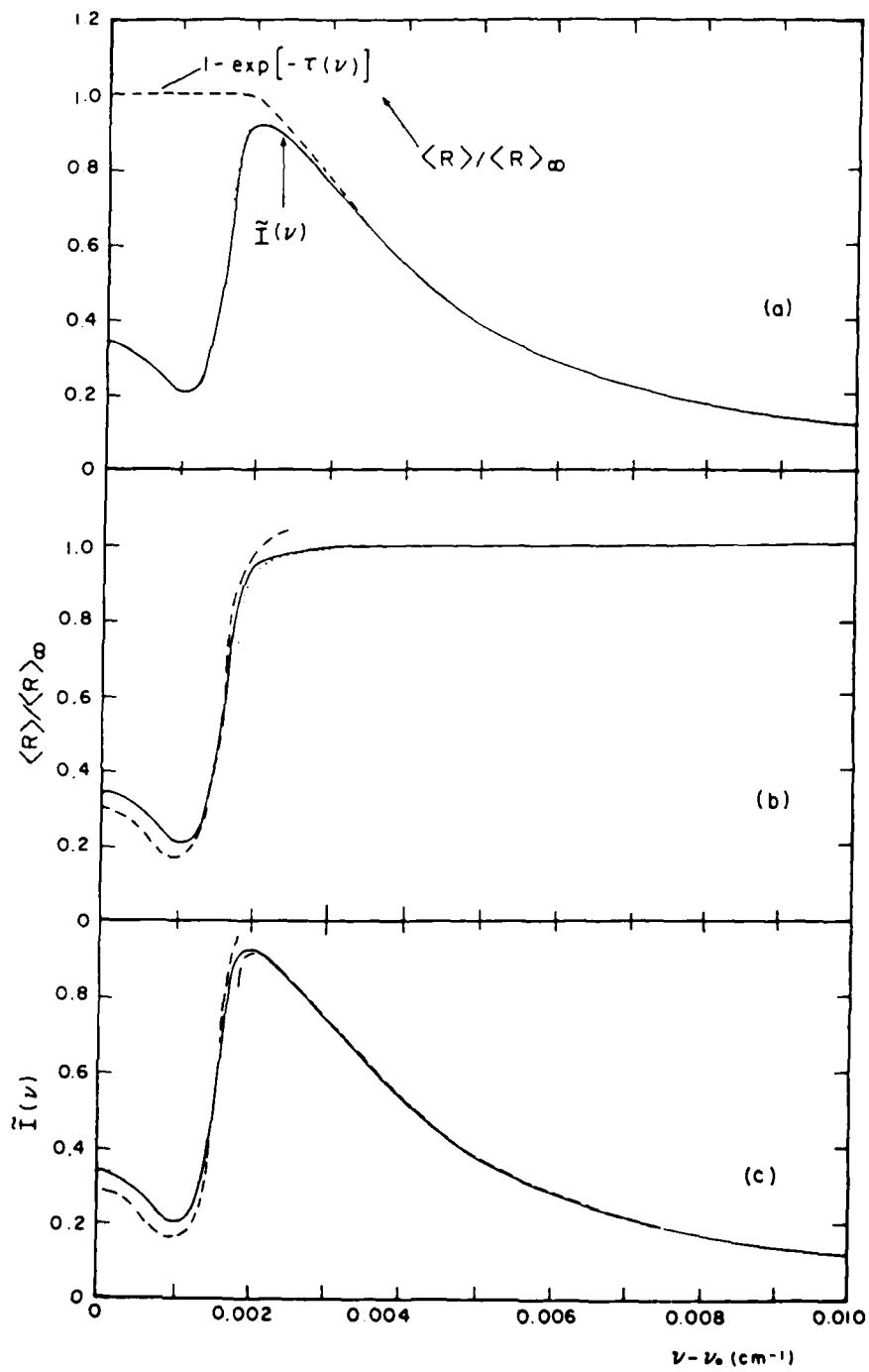


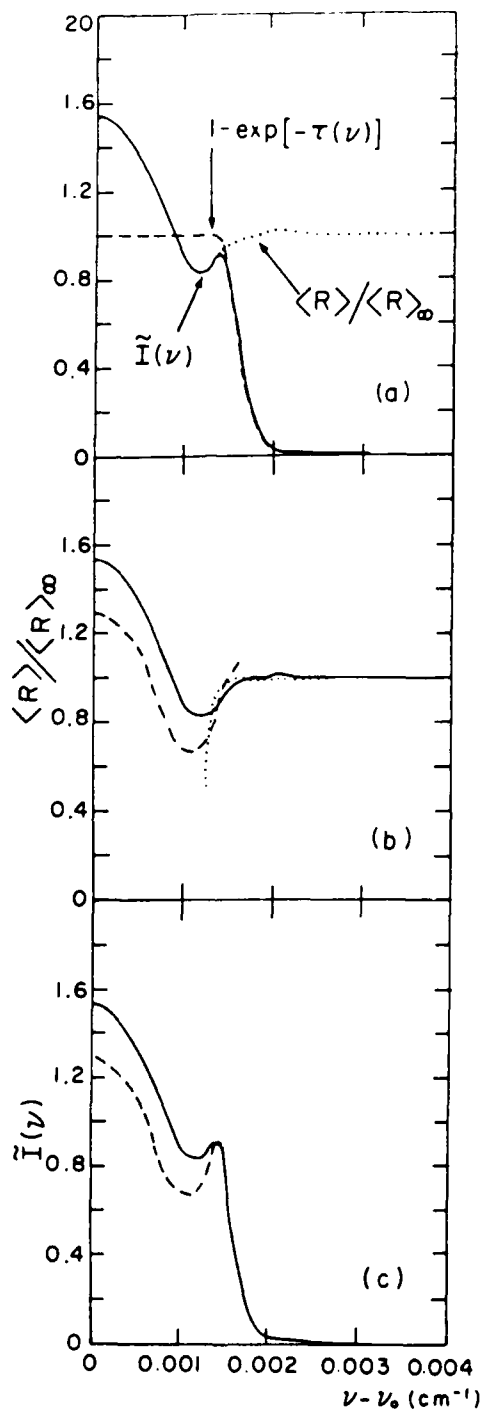


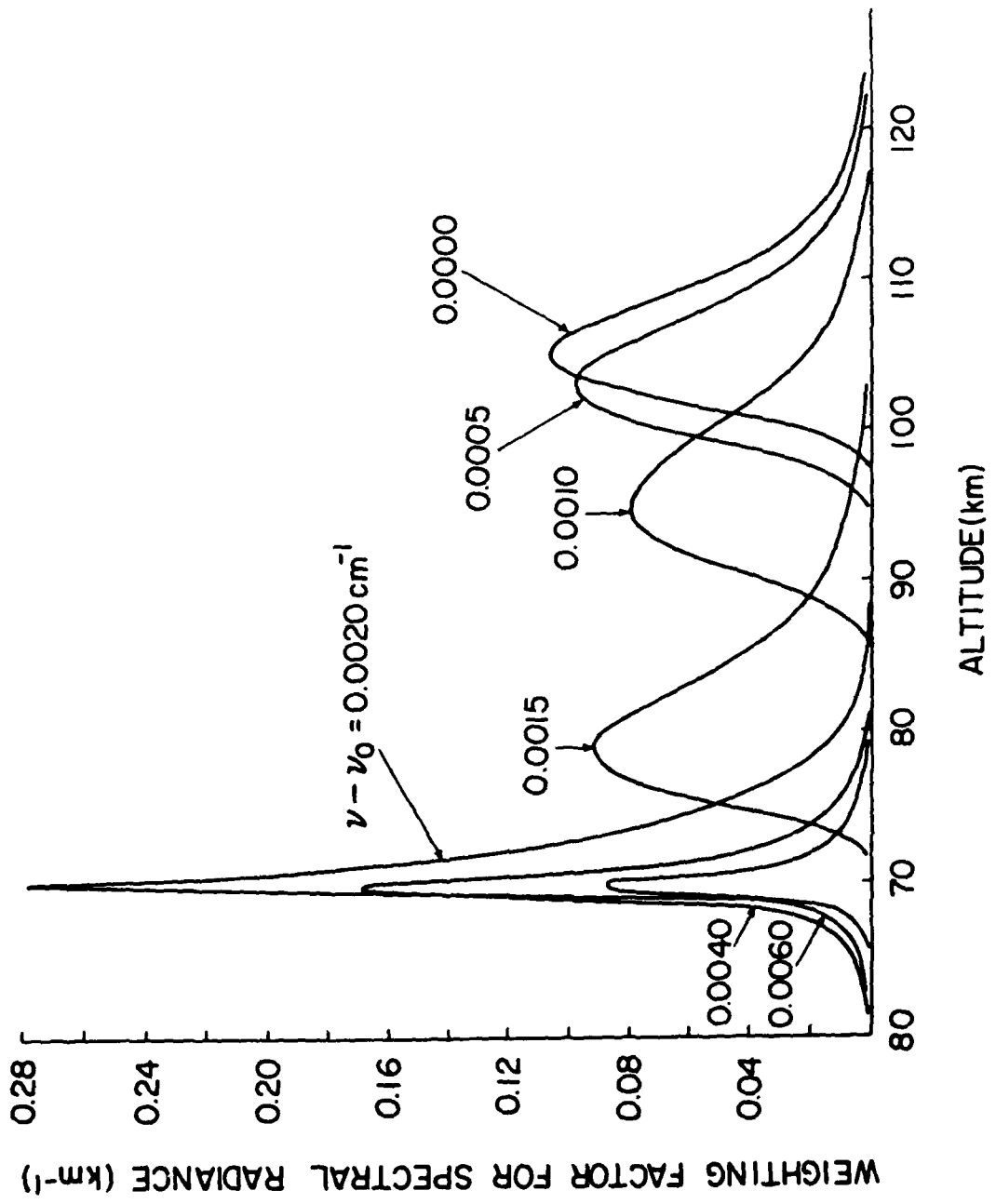












1983-84 USAF-SCEEE RESEARCH INITIATION PROGRAM

Sponsored by the

AIR FORCE OFFICE OF SCIENTIFIC RESEARCH

Conducted by the

SOUTHEASTERN CENTER FOR ELECTRICAL ENGINEERING EDUCATION

FINAL REPORT

ELECTRON WAVES IN THE ELECTRICAL BREAKDOWN OF GASES, WITH

APPLICATION TO THE DART LEADER IN LIGHTNING

Prepared by: Dr. Ernesto Barreto

Academic Rank: Senior Research Assistant

Department and

University: Atmospheric Sciences Research Center
State University of New York/Albany

Research Location: Air Force Flight Dynamics Laboratory

Date: October 1984

Electrical Gas Heating and Combustion*

Ernesto Barreto

Atmospheric Sciences Research Center
State University of New York at Albany
Albany, New York USA

Abstract

Stored electrical energy of 0.20 mJ can produce an ignition in a propane-air combustible mixture of quenching distance (2.00 mm). The spark and ignition proper are sequential but individually different physical events. The first is related to the general problem of rapid gas heating by electrical discharges ($\sim 10^{-7}$ sec), the second to the onset of a flame by enhanced chemical reactions due to the temperature increase ($\sim 10^{-3}$ sec). Only the first event is considered, and it is assumed that, since the hydrocarbon does not appreciably change the breakdown voltage, the same energy is sufficient to heat air or gases like N_2 and O_2 . In uniform fields, for all these gases, a critical avalanche is larger than the discharge gap used, thus no streamers are produced. There is, however, preliminary ionization that guarantees the existence of a transient glow capable of concentrating all electrical forces into narrow sheaths. Depending on the electronegativity of the gas and on the conditions at the cathode surface, it is possible to produce either diffuse cone-shaped or filamentary discharges. Both heat the gas as confirmed by their ability to ignite. Diffuse discharges exhibit only molecular lines and the energy deposition takes a time (~ 35 nsec) which is larger than that for filamentary discharges. The cone produced is consistent with the concept of a subsonic submerged jet expansion of electrons from the cathode spot. The gas temperature calculated agrees with both the value for ignition and that predicted for positive streamers in point-to-plane geometries. Filamentary discharges are associated with the standard formation of a strongly ionized plasma and the procurement of a critical electron density (10^{17} to 10^{18} cm^{-3}). They are very hot as evidenced by atomic nitrogen lines and by very rapid energy deposition (~ 10 nsec).

*Work supported by the Office of Naval Research and the Air Force Office of Scientific Research.

Objectives and Definitions

The purpose of this study is to clarify the manner in which available potential energy is rapidly converted into heat in a small discharge at atmospheric pressure. The problem is one of long standing and has been traditionally neglected.¹ This is because dielectric breakdown constitutes a series of irreversible events that, if undisturbed, automatically lead into each other. For example, recording the onset of field directed ionization in a uniform field between metal electrodes guarantees a subsequent rapid collapse of the applied voltage. Experimentally, accurate recording of any one item in the breakdown sequence, say an initial barely luminous avalanche, requires very different instrumentation and/or calibration than, say the strongly luminous final collapse of voltage associated with the onset of an arc. The spark we study has a 2 mm gap between metal electrodes. The total time elapsed between ionization onset and gas heating is ≈ 1 usec. However, within this microsecond, depending on gap geometry and gas used, one may have avalanches, a transient glow, streamers, interaction with electrodes, space waves of ionization, cathode spot formation, and metal evaporation and its ionization. Exactly what each one of these processes is and how they blend into each other is not clear, and it is not uncommon for people to refer to physically different events by the same name.

The best known mechanisms are, of course, initial avalanches and streamers. In order to clarify our nomenclature, we define these two as follows: An avalanche starts ionization in a neutral gas. Its onset requires the existence of at least one free electron and a critical electric field (potential difference) characteristic of the gas and geometry used. If the free electron is not artificially produced, the onset of an avalanche incorporates a statistical time delay that is longer for smaller gaps.

Because of the smaller volume, there is a correspondingly smaller probability for a random electron to be produced in the electrically stressed region. Avalanches multiply electrons exponentially with distance, x , as $n_e/n_0 = \exp(\alpha - \eta)x$. α and η are, respectively, the number of electrons made by collision and those lost by attachment per unit length of electron travel in the field direction. In an avalanche, each charged particle interacts independently with the applied electric field. Electrons collide and exchange energy almost exclusively with neutral molecules, and, even at peak ionization rates, the great majority of collisions are elastic. The avalanche velocity is of the order of the drift velocity of electrons in the field direction. This velocity is small compared to the random thermal motion of the electrons. The head of an avalanche grows as a result of electron diffusion due to their high density, not due to electrostatic forces. Using a cloud chamber, avalanches can be verified to be conically shaped. The projected cone angles are consistent with simple diffusion theory and are of the order of two to five degrees in air and gases such as N_2 and O_2 .

Avalanches are intrinsically unstable: they must either cease or change to a more stable discharge. The final stage of an avalanche is influenced by space charge effects, resulting from the high degree of ionization obtained, and by the possible transformation to a non-equipartition plasma. At critical E/p values in N_2 (~ 50 V/cm-Torr), avalanches grow until electron multiplication (n_e/n_0) reaches a value $\sim 10^8$. This corresponds to a distance ~ 12 mm, a head diameter ~ 30 μ m and a time interval ~ 90 nsec.² The space charge at the head of the avalanche produces a local field that is much stronger than the applied field. The discharge accelerates to velocities much larger than the electron drift velocity and thus changes into a streamer. While an avalanche is being produced, optically excited

molecules may decay and produce photoelectrons at the cathode. Thus, successive avalanches can extend the discharge over the cathode surface. Even in this case, a final streamer grows from the space charge left by the avalanches in sufficiently long gaps (> 2 cm). In highly overvolted gaps, a single avalanche can be transformed into a streamer that crosses the whole gap. In gaps smaller than those required to produce a critical avalanche, photosuccessors can fill the gap with a glow. This glow can also be produced in longer gaps by coating the cathode with a substance that lowers the work function of the metal³ (e.g. CuI on Cu) or also by using very clean gases with low photoattachment coefficients (e.g. N_2).

Streamers are filamentary channels that grow from a critical avalanche and propagate toward the electrodes at speeds exceeding the electron drift velocity. In very inhomogeneous fields, streamers propagate from the electrically stressed region into the neutral gas. This is particularly evident for cathode-directed streamers in positive coronas.⁴ For their propagation into a neutral gas, positive streamers require strategically located electrons ahead of the positive propagating front. The source of these electrons has never been clarified.^{5,6} In uniform fields, the luminosity near a critical avalanche exhibits a contraction at the region where streamers start propagating toward both electrodes. However, except for discharges in O_2 , cloud chambers exhibit a knob-shaped expanded cloud at the same location. The reason for this behavior is again unknown.⁷ At any other location, luminosity and ionization profiles are well correlated in time and space. Streamer channels are of the diameter of the critical avalanche (~ 70 μm in diameter) and contain electron densities of the order of 10^{13} to 10^{15} cm^{-3} . In molecular nitrogen the average electron energy is limited by vibrational excitation² to values between 2 and 4 eV. Although the electrons collide

primarily with neutral molecules (they are collision dominated), they first exchange energy among themselves ($T_e > T_n$), due to their small mass and the long range of Coulomb forces at this high electron density. Consequently, their distribution is not only primarily isotropic but also Maxwellian. This model of a streamer as a weakly ionized plasma capable of producing shielding sheaths is not consistent with those where a significant charge separation is due to independent interaction of the electrons with the applied field (e.g. the Loeb-Raether and Dawson-Winn models). However, the assumed conducting nature of a streamer leads to a consistent computer model⁸ that agrees with both the very small shielding distances ($< 1 \mu\text{m}$) and the large plasma frequencies ($> 10^{10} \text{ sec}^{-1}$) that must be inferred from the electron densities and temperatures involved.⁹ In a streamer, the energy of all electrons is very small compared to the energy of the neutrals, which stays at values close to room temperature. A low temperature is verified by molecular line radiation and is supported by the inability of streamers to ignite combustible mixtures. The glow-like nature is verified by the fact that when streamers bridge a positive point-to-plane discharge gap, the current is significantly reduced,^{9,10} whereas in uniform fields, it becomes saturated.² A conducting glow model also complements the observation¹¹ that streamers propagate for distances of the order of one meter in an originally uniform field which is much weaker than that required to start ionization between parallel electrodes (~ 7 vs 30 kV/cm). This suggests field intensification by induction. Also, it has been shown that successive small voltage pulses along a streamer channel lead to increased ionization and actual gas heating.¹² This suggests wave propagation and attenuation in a plasma.

This rather meticulous description of both avalanches and streamers is presented to clarify our point of view and the work to be discussed.

It is clear that only the early stages of an avalanche ($n_e/n_0 \lesssim 10^6$) are in uncontested agreement with theory. It is also clear that, in small gaps ($\lesssim 1.50$ cm), the whole interelectrode gap is bridged by the discharge before actual gas heating occurs and, as will be shown, even before a significant portion of the available potential energy is used. That is, the applied voltage does not change, the gas remains at room temperature and ionization is maintained by interaction with the electrodes, as in a steady positive glow. Fortunately, this high pressure, abnormal glow state constitutes the longest stage in the breakdown sequence, and its existence has been clearly demonstrated in discharges with or without streamers.¹⁰ In a point-to-plane gap in air (300 μ m, 2.0 mm), there is a glow lasting ~ 2.0 μ sec after a streamer crosses the gap but before the voltage collapses.⁹ In the same gap with a uniform field, there is an initial succession of avalanches lasting between 0.2 and 0.5 μ sec before the voltage collapses. This final stage of the discharge is the object of the work presented here, and it is all that will be discussed henceforth. Also, it must be noted that thermalized leaders and return strokes^{13,14} are not present in small discharges (< 10 cm) having just sufficient available energy to heat the gas.

Using a photomultiplier we have established a time relationship between gas heating by a spark and the onset of ignition by chemical reactions.¹⁵ It is shown that sparks get hot in very short times (5 to 50 nsec), and that the onset of a combustion flame follows after a few milliseconds. This is because combustion requires the existence of a hot volume. This must be sufficiently large to guarantee that the heat produced by chemical reactions is accumulated and not lost through its surface. This volume has a characteristic dimension of the order of the cube of the quenching distance

for the combustible mixture used (hence, our 2.00 mm gap). Its formation is associated with heat transfer from the spark channel to its surroundings.¹⁶ It is then clear that, in time and space, the spark and the onset of a flame are, again, sequential but very different physical events. However, ignition guarantees gas heating to, at least, the self-ignition temperature of the combustible mixture ($\sim 500^{\circ}\text{K}$). The amount of hydrocarbon is smaller than 8% by volume, and its presence does not significantly change the experimental breakdown voltage. Actually, we observe larger variations due to meteorological pressure changes. Consequently, we can safely assume that, in gases like air, N_2 and O_2 , minimum ignition energies of the order of ~ 0.2 mJ are also capable of heating the gas even in the absence of a hydrocarbon. As will be discussed below, current traces and spark luminosities are the same as in air.

The present work deals with an experiment in which the gas heating stage alone has been isolated. We have found that, depending on the gas used and the conditions at the cathode, the electron number density can change in such a way that thermalization and rapid gas heating are due to either electron-neutral collisions or electron-ion interactions. That is, given the same minimum energy, there are two types of sparks capable of heating the gas. We will show that both are consistent with the concept of an electron fluid.

Experimental

The experiment itself is done using a small discharge gap (2.00 mm) with interchangeable electrodes.¹⁵ One of the electrodes is machined to fit the stage of an electron microscope. In the gap, one electrode is connected to a high voltage supply through a very high resistance and the other to a small grounded resistor with an inductance that matches

the lines and equipment used (50Ω). The high resistance isolates the power supply during the time of a discharge. The ungrounded side of the small resistor is connected to either a fast oscilloscope (Tektronix 7904) or a transient digitizer (Tektronix 7912AD). Because of the small capacitance used (5-60 pF), RC times are small enough (< 0.3 nsec) to guarantee that the current recorded corresponds to events occurring in the gap. (The recording instrumentation has 0.5 GHz capability). The discharge itself is photographed through an electronic camera supplemented by an additional image intensifier (TRW/Quantrad 1D; EMI 9914 1S). The gain of the image intensifier is not sufficient to see avalanches or streamers. These can be recorded by their luminosity or by their characteristic current trace. Streamers do not occur when using uniform fields, because the gap is smaller than a critical avalanche. Unless specifically noted the field should be considered to be uniform.

We have developed a model to explain gas heating that is summarized as follows: during the glow stage, electrical forces concentrate near the electrodes. The electron density is high enough ($10^{12} \ll n_e \ll 10^{17} \text{ cm}^{-3}$) to guarantee that the electron collision frequency, ν_{ee} , falls in the range $(m_e/m_n) \nu_{en} \ll \nu_{ee} \ll \nu_{en}$. Consequently, the electrons in the glow constitute an ideal fluid characterized by $T_e \gg T_n = T_i$ and by an equation of state $p_e = n_e k T_e$. The electron temperature value is fixed by vibrational excitation losses,^{14,17} and a small amount of energy must be supplied to the glow discharge in order to maintain it for the long times observed. This probably occurs through a standard cathode fall phenomenon. During the long lasting glow stage, ions can drift and accumulate at a dielectric oxide layer that invariably covers any metal surface exposed to even traces of O_2 . (Its equilibrium vapor pressure over Cu is $\sim 10^{-10}$ Torr).¹⁸ Since these layers

are very thin (50-500 Å), the capacities involved are very large. The electric field at the surface of the metal, more properly, at an asperity on the surface, can reach field emission magnitudes.^{19,20,21} The emitted electrons interact with those in the gap as a fluid driven primarily by electron pressure gradients.

Experimental evidence for this model is most clearly demonstrated by a discharge in N₂. The results are shown as the current trace in Figure 1a, the photograph of a corresponding single cathode cell in a Cu electrode, Figure 2a, and the luminosity in the gas, Figure 2b. There is gas flow of ~ 100 m/sec perpendicular to the discharge, thus ionization lasting for times compatible with gas motion is evidenced by the asymmetry of luminosity near the cathode spot in Figure 2b. Notice, however, that the integral of the current with respect to time (Figure 1a) raises from zero to the CV value in about 25 nsec. That is, within this short time, practically all the available charge and energy goes into the gap. The stored energy is 0.23 mJ, and only a single cathode spot is produced. Its diameter is about 3 μm, and the peak current value is 6.8 Amp. The maximum current density is then 9.6×10^7 A/cm². This value is very large but agrees with that for electron emission from a single cathode cell (a Kesaev cell) as reported by others.^{22,23} Thus, it is concluded that practically all the stored charge goes into the gap through a single cathode cell (sometimes two next to each other). This agrees with the well known fact that, in small gaps between metal electrodes, a spark does not materialize unless a cathode spot is formed.^{9,15,24} In vacuum arc studies, as well as in our previous work with ignitions, it has been established that electrons from the cathode contribute to ionization only after their thermalization.^{9,22} Consequently, the region near the cathode

is one of high electron pressure.

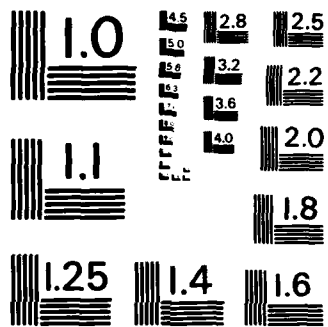
The conical luminosity in Figure 2b is associated with the formation of the cathode spot and its inherent high electron pressure. A very important fact confirming this assertion is that the luminosity has an average vertex angle of 25° . This value is an order of magnitude larger than the "wedge angle" for avalanches in N_2 which, as noted must have also subsided by the time the cone is produced. However, a 25° angle corresponds precisely to the value for turbulent mixing of a submerged jet. This angle has been verified in fluid dynamic studies²⁵ to be practically constant (25° to 30°) and independent of the fluid used. It follows that the increase in ionization and, of course, its associated excitation and luminosity, is due to energy gained by the electrons in the gap as they mix turbulently with those emitted from the cathode.

Further evidence for the validity of an electron fluid model has been obtained by increasing the capacity to demonstrate that such an increase corresponds to a higher electron pressure near the cathode, and, consequently, to an underexpanded jet expansion.²⁶ That is, one in which the pressure near the cathode (the exit pressure if it were a nozzle) far exceeds that of the region into where the expansion occurs, namely, the glow region in the gap. Such an expansion is characterized by the existence of a normal shock and of an inviscid convergent core that protrudes into the divergent region of turbulent mixing and incorporates a series of diamond shaped shock waves. An example of the formation of waves inside the core in N_2 is shown in Figure 2e, which is a streak photograph of a discharge with higher capacity (23 pF). The camera is triggered by the signal from a photomultiplier. This allows us to estimate that the, t_0 , time in the figure corresponds to about 110 nsec from the onset of ionization. A cone

like that in Figure 2b is probably produced in the first two nanoseconds after t_0 as evidenced by luminosity near the anode region in Figure 2e. Then about 3 nanoseconds later, two brightly luminous regions appear above the bright cathode spot. Their sudden appearance involves times of a fraction of a nanosecond, hence the speed of the phenomenon is so high ($10^{-3} \text{ m}/10^{-9} \text{ sec} \approx 10^6 \text{ m/sec}$) that it can only be explained in terms of electron waves.

We have shown that the position of the normal shock changes with capacity, and that the length of the inviscid core is, as expected, proportional to the area of cathode activity at the metal surface. Furthermore, the length of waves inside the core but after the normal shock, remains constant, increasing in number for a longer core. These are characteristic properties of an underexpanded jet. It has been tacitly assumed that changes in the electron population are very fast compared to changes recorded by the current trace. That is, it is assumed that a steady state expansion can be established in times small compared to the recorded current changes. This is justified because equilibrium between electrons is obtained in times $\nu_{ee}^{-1} \approx 10^{-10} \text{ sec}$ for $n_e = 10^{15} \text{ cm}^{-3}$. It is also assumed that the inelastic collisions of frequency ν_{Ne} that make the flow visible do not affect its inviscid quality. This is justified because $\nu_{Ne} \ll \nu_{ee}$. Both theoretical and experimental evidence for the existence of a supersonic electron fluid expansion have been reported in detail.^{26,27,28}

While working in a combustible mixture using minimum ignition energies, or with the same energy in air, N_2 and O_2 , we noted that there are two different types of sparks that we call diffuse and filamentary because of their photographic appearance (e.g. Fig. 2b vs. Fig. 2c). Diffuse discharges are the cone shaped sparks discussed above and filamentary the more familiar



MICROCOPY RESOLUTION TEST CHART
NATIONAL BUREAU OF STANDARDS - 1963 - A

narrow channel sparks that are always present in longer gaps or with streamer induced sparks. In air and in a combustible propane-air mixture, diffuse discharges are almost the same as those in pure N_2 with only slight differences in the current trace. Also, when either diffuse or filamentary discharges occur in a sequence, they exhibit a high degree of reproducibility. For instance, Figure 1b shows the average current trace of 20 diffuse sparks in air together with the standard deviation that had to be multiplied by a factor of ten in order to be noticeable. Such reproducibility is remarkable because there were five sequences of four sparks at four different sections of the same Cu cathode, and observation with an optical microscope made evident that each spark produced its own separate spot. We know diffuse discharges can not be very hot because they exhibit only molecular line radiation. However, in combustible mixtures, they are more likely to produce ignition when compared to filamentary discharges which are louder, brighter and hotter as evidenced by atomic N lines. The difference in combustion ability is then clearly related to a more efficient transfer of electrical potential energy into translational energy of the heavy particles. For the same stored value, less energy goes into shock waves, dissociation and excitation.

Consider the current trace for the diffuse discharge in Figure 1a. If we assume that all the stored charge becomes uniformly distributed in a cone 2 mm high with a 25° vertex angle we obtain an average charge density of $7.7 \times 10^{14} \text{ cm}^{-3}$. This number is at least two orders of magnitude smaller than the value required to bring about effective Coulomb interactions between electrons and ions ($\geq 10^{17} \text{ cm}^{-3}$), but it is compatible with the densities of positive streamers.²⁹ Now, assuming all the stored energy goes into the cone and becomes thermal energy of the neutrals, then

$$\left(\frac{1}{2}\right) CV^2 = n_n (\pi r^2 L / 3) (3/2) k T_n$$

$$T_n = CV^2 / (n_n \pi r^2 L k)$$

Taking $n_n = 2.7 \times 10^{25} \text{ m}^{-3}$, C and V from Figure 1a and r and L from Figure 2b, we obtain a temperature $T_n = 1.01 \times 10^3 \text{ }^\circ\text{K}$. This value is clearly an overestimate because no losses are considered. However, it is an order of magnitude smaller than the temperature reported in normal filamentary sparks ($\sim 10^4 \text{ }^\circ\text{K}$). Nevertheless, we know the temperature is high enough to produce ignitions with propane, therefore $T_n > 500 \text{ }^\circ\text{K}$.

The point made is that under the most optimistic assumptions, the diffuse sparks never reach the electron density required for transformation into a strongly ionized gas, but the gas does reach a temperature between 500 and 1000 $^\circ\text{K}$. The lower estimate also agrees with temperatures calculated for positive streamers. Electrons can interact strongly among themselves, but Coulomb interactions with ions are not important (v_{ee} is always much smaller than v_{en}). Thus, energy is given to the electrons and is gradually lost to the neutrals in times of the order of that for the whole current trace. It is interesting to note that using $v_{en} = 1.5 \times 10^{12} \text{ sec}^{-1}$ and $(m_e/m_n) = 1.5 \times 10^{-5}$ for N_2 , the electron thermalization time is $(v_{en} m_e/m_n)^{-1} = 34 \text{ nsec}$; that is of the same order as the current duration. As shown in Figure 3a and b the current trace becomes much larger in He ($\sim 100 \text{ nsec}$) but not in Ar ($\sim 10 \text{ nsec}$), thus indicating a molecule mass effect associated with the current flow in gases that are unaffected by rotation or vibration. This is true even though we cannot say anything about the neutral gas temperature for He and Ar.

As suggested by the luminous region just before the bright supersonic waves and near the anode in Figure 2e, we believe the actual formation of the

cone occurs near the current peak in times smaller than 10 nsec. However, this has to be clarified using better recording instrumentation. Finally, it must be emphasized that in air, diffuse discharges appear together with filamentary ones in an unpredictable manner. They may actually alternate or be of the same nature for a whole day; we have not been able to control their behavior in air. However, we find that in N_2 they are always diffuse while in O_2 they are always filamentary. There are no stable negative N_2 ions, but dissociative attachment efficiently produces O^- ions simultaneously with ionization. Consequently, it is clear that negative ions in the gas do play a role. The erratic behavior in air nevertheless indicates that other phenomena must also play a role. We will show that, as expected, the nature of the spark is affected by events occurring at the cathode.

Figure 1c and 2c show current traces and the luminosity associated with filamentary discharges in oxygen. The oscillations after the current trace should be real according to the sensitivity of the equipment. They may represent subsonic electron wave reflections at the electrodes that travel 2 mm in 8 nsec; that is, with a velocity 0.25×10^6 m/sec which is subsonic compared to the electron acoustic speed $(5 kT_e/3m_e)^{1/2} \approx 0.77 \times 10^6$ m/sec. The true diameter of the spark is not well defined because of halation effects. Nevertheless, according to Figure 2c, it is of the order of 50 μ m. This is an overestimate, but it compares favorably with that for a more diffuse streamer in air, namely ~ 70 μ m. If we assume that all the stored charge goes into a cylinder 25 μ m in radius and 2 mm high, we obtain an underestimated electron charge density of 6.5×10^{16} cm^{-3} . This value is larger than the number we have predicted⁹ for the propagation of non-linear waves $n_e \approx 2.9 \times 10^{16}$ cm^{-3} and very close to the 10^{17} cm^{-3} required for effective electron-ion interaction. If we put all the energy into this

cylinder we obtain $T_n = 6.7 \times 10^4 \text{ }^\circ\text{K}$, which is an overestimate but of the order of the values² observed in longer filamentary sparks in N_2 (5 to 6 x $10^4 \text{ }^\circ\text{K}$ in 2.0 cm gaps). Since the electron density is underestimated, it is fair to conclude that filamentary discharges are heated because $v_{ee} \rightarrow v_{en}$. Consequently, the thermalization of the electrons is associated with the change in the plasma to a strongly ionized one. This is the more standard accepted mechanism for gas heating in sparks, even though it is also poorly understood. The appearance of atomic N lines confirm the high gas temperature.

The difference between a diffuse discharge in N_2 , like that in Figure 2b, and a filamentary one in O_2 , like that in Figure 2c, has been ascribed in the previous paragraphs to the ability of negative ions to be rapidly produced by dissociative attachment ($\text{O}_2 + e \rightarrow \text{O}^- + \text{O}$) in the early stages of ionization. Thus it is inferred that the O^- ions produced confine the diffusion of electrons injected into the gap at later times. This can result in a local high electron pressure. If the electron pressure gradient becomes sufficiently steep, non-linear waves can propagate into the ion confined electron fluid. These waves provide the mechanism by which the degree of ionization increases to the thermalization value associated with $v_{ee} \rightarrow v_{en}$. This point of view is confirmed by the fact that many electronegative molecules (Cl_2 , NO_2 , NO , Cl_2F_2 , SO_2 , CO_2) are also able to confine the discharge and to produce filamentary channels. Recent experiments by Goshō³⁰ report a large increase in streamer current associated with an increase in partial pressure of the electronegative gas used. For instance, in a positive point-to-plane-gap in air (2.0 mm radius, 2.0 cm gap), an initially steady glow discharge progressively disappears, and streamer formation is enhanced as the partial pressure of NO is increased. At a partial pressure of 0.16

Torr, the discharge goes "directly" into a spark. A strongly electronegative gas such as Cl_2 produces the same effect at just 0.01 Torr partial pressure.

If a local electron pressure increase leads to filamentary discharges, it should be possible to do the same even in N_2 by enhancing the local emission and accumulation of electrons near the cathode using a small surface protrusion. Thus by polishing the metal surface, we left a protrusion about 25 μm high, which is large compared to a natural asperity ($< 5.0 \mu\text{m}$ in steel and Al).²⁰ However, it is also too small to produce a regular negative corona, even though it does lower the breakdown voltage by 1.5 kV. This is evidenced by the fact that we obtain the filamentary bright spark shown in Figure 2d with a single current trace that indicates the deposition of all the stored charge in a single rapid event as shown in Figure 3c (no corona pulses). Also note that in Figure 2d, there is an extended faint glow around the cathode spot on the metal surface which supports the concept of a non localized discharge. The high current phase lasts about 10 nsec which is of the same duration as that for a discharge in O_2 (c.f. Figure 1c) but is much shorter than the 35 nsec for a diffuse discharge in N_2 (c.f. Figure 1a). Notice that the region near the cathode spot towards the anode is not very bright. This would be expected if it takes a longer distance to accumulate the electrons. As always, it is also possible that the anode may be playing a role. It is nevertheless clear that ionization near the protrusion enhances the local accumulation of electrons, and that a discharge very much like one in O_2 , but without stable negative ions, is produced by the high electron pressure gradient.

We have previously indicated that the local accumulation of electrons can also be provided by surface streamers over a charged dielectric.¹⁵ There is no accurate way of obtaining a reliable oscilloscope trace, but

an example of this effect is clearly demonstrated in Figure 2f. The cathode is cleaned and then covered with the coating provided to fix Polaroid pictures. This coating is of the order of $10 \mu\text{m}$: thick enough to significantly lower the capacity when compared to that provided by the thinner natural oxide layer on the metal surface. Consequently, initial ionization cannot increase the surface field to produce electron emission or a cathode spot. Instead charge accumulates on the Polaroid coating, lowers the field in the gap and stops the ionization. Progressive increases in voltage eventually lead to a surface streamer system that resembles a miniature lightning discharge, when looked at facing the cathode, or just like a bright line over the surface, when looking sideways, as in Figure 2f. Note the existence of a characteristic expansion cone, indicating electron turbulent mixing, and the lack of luminosity at the location where the cathode spot is shown in Figures 2b, c and d. Thus, we conclude that a system of surface streamers can also collect charge fast enough to provide sufficient electron pressure to form an underexpanded jet across the electrodes. Clearly, this type of discharge is closely related to hazards as well as to gas heating not strongly influenced by the metallic properties of the electrodes.

Conclusions

The main purpose of this paper is to demonstrate that in small sparks, probably in larger sparks as well, heating of the heavy particles occurs after the region to be heated has changed into a non-equipartition, weakly ionized plasma of high electron temperature ($T_e > T_n$). Consequently, outside electrical forces must affect the plasma through narrow sheaths at its boundaries or through macroscopic electron fluid motion and waves. The plasma is primarily neutral ($|n_e - n_i| \ll n_e$) and isotropic with all transport

processes small compared to random properties. The electrons constitute an independent fluid that is bound both weakly to the neutrals, by elastic electron-neutral collisions, and also very weakly to the ions, because of the low concentration and heavy mass of the ions. That is, the electrons are collision dominated, and binary collisions are a good approximation to the kinetics of the gas. However, because of their small mass, electrons effectively exchange momentum among themselves through long range Coulomb interactions, even though they collide primarily with neutrals: $(m_e/m_n)v_{en} \ll v_{ee} \ll v_{en}$. (Changes in the electron population occur much faster than in any other species. Inelastic collisions resulting in ionization are always very few even at peak ionization rates. In molecular gases like nitrogen, inelastic collisions, resulting in vibrational excitation, limit the average energy of the electrons, but rotational states are considered to be in equilibrium with translational motion.)

It has been shown that small sparks are associated with the formation of a cathode spot or with a system of surface streamers on a positively charged dielectric over the cathode. These are associated effects that feed electrons to a region near the cathode at the point where a spark is produced across the gap. In both cases, experimental evidence is presented to show that breakdown is produced by a resulting electron pressure increase that leads to either subsonic or supersonic expansions, with reference to the electron acoustic speed.

Depending on both the nature of the gas molecules and the efficiency of the associated mechanism (cathode spot or surface streamers) to raise the electron pressure, the gas may become hot in two different ways. In N_2 with just sufficient energy to heat the gas, turbulent electron mixing produces a characteristic 25° conical jet. Practically all the stored energy is transferred into the gap just before and just after this jet is

produced, and the current trace indicates a total time compatible with the energy relaxation time for the electrons $(v_{en} m_e/m_n)^{-1}$. The gas is gradually heated to temperatures estimated to be between 500 and 1000 °K. Ion-electron interactions do not occur because of the low ion density obtained.

In O_2 and in other electronegative gases, electrons are rapidly captured in the initial ionization events with the result that electron diffusion is subdued and the electron pressure gradient enhanced. Filamentary discharges are produced, and the stored charge goes into the gap in times that are small compared to the energy relaxation time of the electrons. In this case, there is a rapid electron population increase associated with compression heating of the electrons by supersonic waves. Evidence of this supersonic event has been reported. The gas becomes very hot as evidenced by atomic radiation. In air, either filamentary or diffuse discharges are possible, and in N_2 it is possible to produce a filamentary hot discharge by enhancing the electron pressure gradient using a small cathode protrusion.

Finally, a word must be said regarding the temperature of positive streamers. These are not present in our uniform field discharges, but Marode, Bastien and Bakker²⁹ have computed the same neutral temperature range as in our diffuse discharges (500-1000 °K) using the same basic system of fluid equations. Furthermore, although there are basic differences in the assumptions made, we believe that, regardless of the validity of Marode's physical model, we may be actually providing experimental support for his computations. The plasma in a streamer channel is basically the same as in our diffuse discharges with the same molecular radiation, density $n_e \approx 10^{15} \text{ cm}^{-3}$ and temperature $T_e \approx 2-4 \text{ eV}$. Marode considers a section of a streamer that has bridged the discharge gap. There are no electrode effects, and the applied electric field is not completely shielded in the plasma.

Consequently, the temperature of the neutrals increases due to current flow. This produces a low density core where enhanced ionization leads to a large current increase that occurs after a delay of 60 to 120 nsec and which depends on the initial current amplitude of the streamer. Axial properties are considered homogeneous and the radial changes computed from the conservation equations of mass, momentum and energy supplemented by ideal gas laws and the inter-linking collision terms between the species. The number density of electrons at the axis changes by over two orders of magnitude between 40 and 94 nsec. But the radial electron velocity exceeds the ion velocity significantly after only 40 nsec. Thus, a line source of electrons which plays the same role as our experimental cathode spot, may be implicitly assumed. The inability of streamers to ignite combustible propane-air mixtures can be easily explained by their small crosssection. A streamer has a large surface to volume ratio, and, just as in a nucleation problem, it cannot raise the temperature in a volume of quenching size. Conversely, our diffuse sparks involve a much larger volume. The smaller surface losses account for their good ability to produce ignitions at just the self-ignition temperature ~ 500 °K. Clearly much more work is required to study the transition from a small discharge, controlled by the electrodes, to one in which electrodes play only a minor role.

Acknowledgements. I would like to thank Mr. J. Hughes of ONR and the RISE program of AFOSR for support that made this work possible. Also, G. Barreto and M.L. Hewitt, for their help with the manuscript.

REFERENCES

- (1) Barreto, E. "The Gas Heating Phase in Electrical Breakdown." Air Force Technical Report AFWAL-TR-83-3124.
- (2) Stritzke, P., I. Sander and H. Raether. "Spatial and Temporal Spectroscopy of a Streamer Discharge in Nitrogen." J. Phys. D: Appl. Phys., 10, 2285-2300 (1977).
- (3) Koppitz, J. "Nitrogen Discharges of Large Cross section at High Overvoltage in a Homogeneous Field." J. Phys. D: Appl. Phys., 6, 1494-1503 (1973).
- (4) Loeb, L.B. Electrical Coronas. Univ. Cal. Press, Berkeley (1965).
- (5) Sigmond, R.S. and M. Goldman. "Corona Discharge Physics and Applications" in Electrical Breakdown and Discharges in Gases. E.E. Kunhardt and L.H. Luessen Eds. NATO Adv. Ser. B, Vol. 89b, Plenum Press, NY (1983).
- (6) Fernsler, R.F. "General Model of Streamer Propagation." Phys. Fluids, 27, 1005-1012 (1984).
- (7) Allen, K.R. and K. Phillips. "Cloud Chamber Study of Electron Avalanche Growth." Proc. Roy. Soc. A, 274, 163-186 (1963).
- (8) Geary, J.M. and G.W. Penney. "Charged Sheath Model of Cathode-Directed Streamer Propagation." Phys. Rev. A, 17, 1483-1489 (1978).
- (9) Barreto, E., H. Jurenka and S.I. Reynolds. "The Formation of Small Sparks." J. Appl. Phys., 48, 4510-4520 (1977).
- (10) Marode, E. "The Glow-to-Arc Transition" in Electrical Breakdown and Discharges in Gases. E.E. Kunhardt and L.H. Luessen, Eds. NATO Adv. Series B., Vol. 89b, Plenum Press, NY (1983).
- (11) Phelps, C.T. "Field Enhanced Propagation of Corona Streamers." J. Geophys. Res., 76, 5799-5806 (1971).
Phelps, C.T. and R.F. Griffiths. "Dependence of Positive Corona Streamer Propagation on Air Pressure and Water Vapor Content." J. Appl. Phys., 47, 2929-2934 (1976).
- (12) Acker, F.E. and G. Penney. "Influence of Previous Positive Streamers on Streamer Propagation and Breakdown in Positive Point-to-Plane Gap." J. Appl. Phys., 39, 2363-2369 (1968).
"Temperature as a Mechanism for the Buildup of Successive Streamers in Low-Voltage Breakdown." Ibid. 45, 126-134 (1974).
- (13) Kekez, M.M. and P. Savic. "Contributions to Continuous Leader Channel Development" in Electrical Breakdown and Discharges in Gases. E.E. Kunhardt and L.H. Luessen, Eds. NATO Adv. Ser. B, Vol. 89a, Plenum Press, NY (1983).

- (14) Gallimberti, I. "The Mechanism of the Long Spark Formation." *J. de Physiq. Colloque C7*; 40, C7-193 to C7-249 (1979).
- (15) Barreto, E., S.I. Reynolds and H. Jurenka. "Ignition of Hydrocarbons and the Thermalization of Electrical Discharges." *J. Appl. Phys.*, 45, 3317-3327 (1974).
- Barreto, E. "Electrostatic Hazards: Basic Concepts" in *Encyclopedia of Chem. Processing and Design*. J.J. McKetta and W.A. Cunningham, Eds., 17, 426-468, Marcel Dekker, New York (1983).
- (16) Lewis, B. and G. von Elbe. "Combustion Flames and Explosion of Gases." Acad. Press, New York (1961), p. 346.
- (17) Brunet, H. and P. Vincent. "Predicted Electron Transport Coefficients at High E/N Values. I. Hydrogen." *J. Appl. Phys.*, 50, 4700-4707 (1979).
- "Predicted Electron Transport Coefficients at High E/N Values. II. Nitrogen." *Ibid*, 4708-4713 (1979).
- (18) Roberts, M.W. and C.S. McKee. *Chemistry of the Metal Gas Interface*. Clarendon Press, Oxford (1978), p. 439.
- (19) Guile, A.E. and B. Jüttner. "Basic Erosion Processes of Oxidized and Clean Metal Cathodes by Electric Arcs." *IEEE Trans. Plasma Science*, PS-8, 3, 259-269 (1980).
- (20) Farrall, G.A. "Electrical Breakdown in Vacuum" in *Vacuum Arcs*, J.M. Lafferty, Ed., John Wiley, New York (1980).
- (21) Loeb, L.B. *Static Electrification*. Springer-Verlag, Berlin (1958), Chp. IV.
- (22) Ecker, G. "Theoretical Aspects of the Vacuum Arc" in *Vacuum Arcs*, J.M. Lafferty, Ed. John Wiley, NY (1980).
- (23) Kesaev, I.G. "Cathode Processes in the Mercury Arc". Consultants Bureau, New York (1964).
- (24) Lutz, M.A. "The Glow to Arc Transition - A Critical Review". *IEEE Trans. Plasma Sci.*, PS-2, 1-10 (1974).
- (25) Landau, L.D. and E.M. Lifshitz. *Fluid Mechanics*. Pergamon Press, London (1959), p. 113.
- (26) Jurenka, H. "The Existence of an Electron Shock Structure in the Electrical Breakdown of Nitrogen." *J. Appl. Phys.*, 53, 6115-6120 (1982).
- (27) Barreto, E. "Ignition by Electric Sparks." *Electrostatics 1979*. Conf. Ser. No. 48, Inst. of Phys., London (1979), p. 135-144.

- (28) Jurenka, H. and E. Barreto. "Study of Electron Waves in Electrical Discharge Channels." J. Appl. Phys., 53, 3581-3590 (1982).
- (29) Marode, E., F. Bastien and M. Bakker. "A Model of the Streamer Induced Spark Formation Based on Neutral Dynamics." J. Appl. Phys., 50, 140-146 (1979).
- (30) Gosho, Y. "Enhancement of D.C. Positive Streamer Corona in a Point-plane Gap in Air due to the Addition of a Small Amount of an Electronegative Gas." J. Phys. D: Appl. Phys., 14, 2035-2046 (1981).

FIGURE LEGENDS

- Figure 1. Current traces corresponding to discharges in N_2 , Air and O_2 . Uniform field 2.00 mM gap. Top figure shows current pulse, integral of the current with respect to time, and stored charge value CV. All traces are preceded by a glow discharge.
- Figure 2. (a) and (b) show the cathode spot and the luminosity associated with a discharge like that on Figure 1a.
(c) Discharge in O_2 with a uniform field and associated with current traces like those in Figure 1c.
(d) Discharge in N_2 with a 25 μm protrusion at the cathode. The corresponding current trace is shown in Figure 3c.
(e) Streak picture of a 23 pF discharge in N_2 . Note luminosity near the anode before the rapid onset of the electron waves.
(f) Discharge in air using a cathode covered by a thin ($\sim 10 \mu m$) dielectric coating of Polaroid fixer.
- Figure 3. (a) and (b) Discharges in atomic gases. Note that because of the low breakdown voltage the capacitor does not completely discharge to the CV value.
(c) Discharges in N_2 with a 25 μm protrusion at the cathode. Because of the energy used the gas is hot and the capacitor discharges to the CV value (not shown) as in Figure 1a. The corresponding luminosity is shown as Figure 2d.

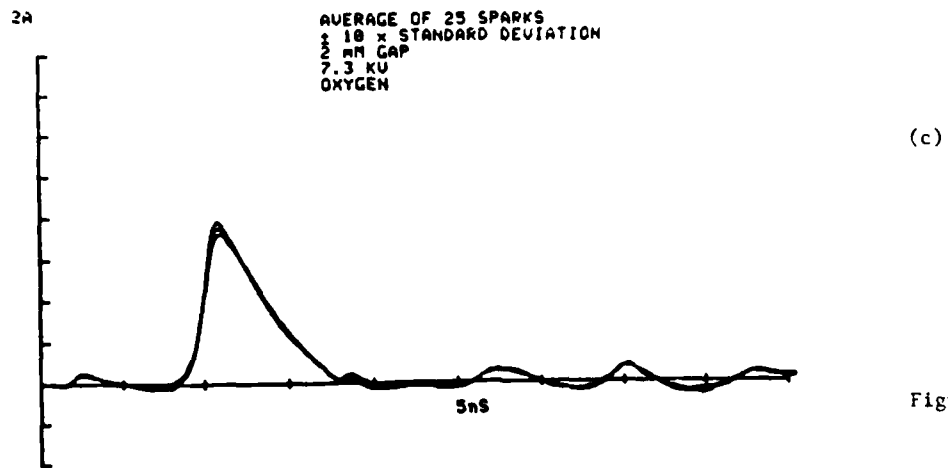
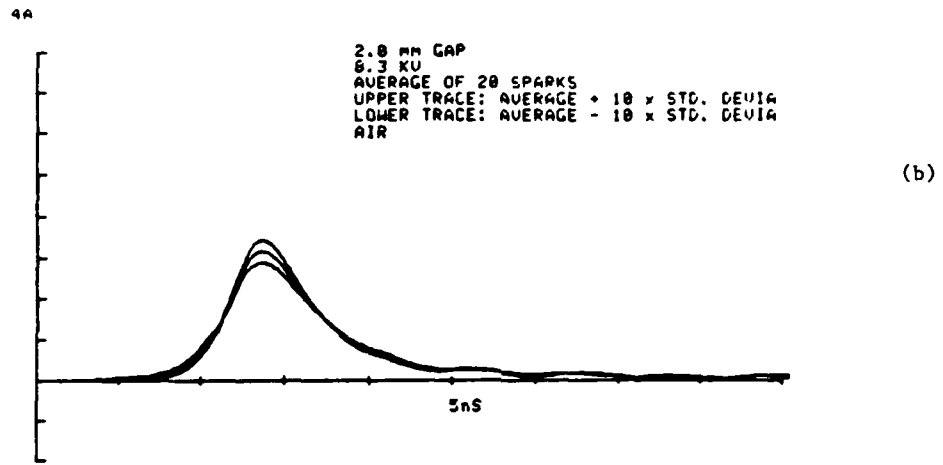
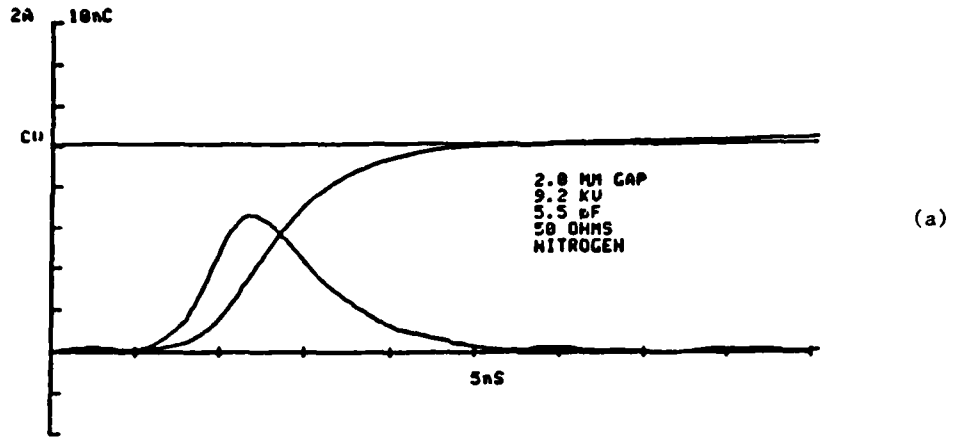
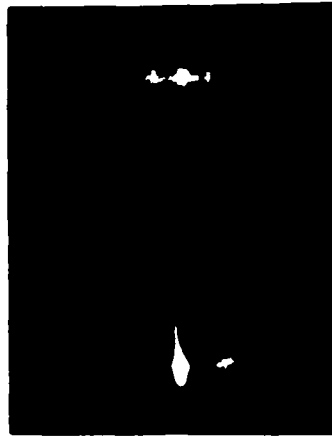


Figure 1



a

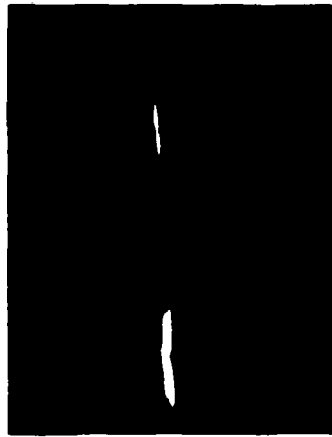
3 μ m



b

(+)

(-)



c

(+)

(-)



d

(+)

(-)



e

(nsec) 9 6 3 t_0

(+)

(-)

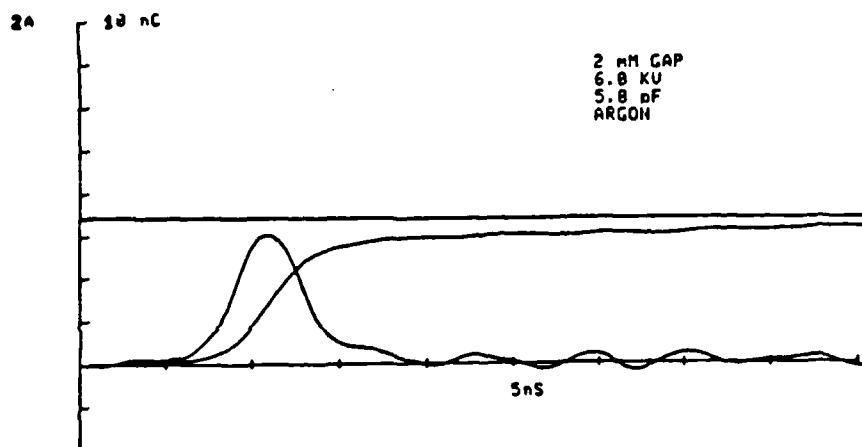


f

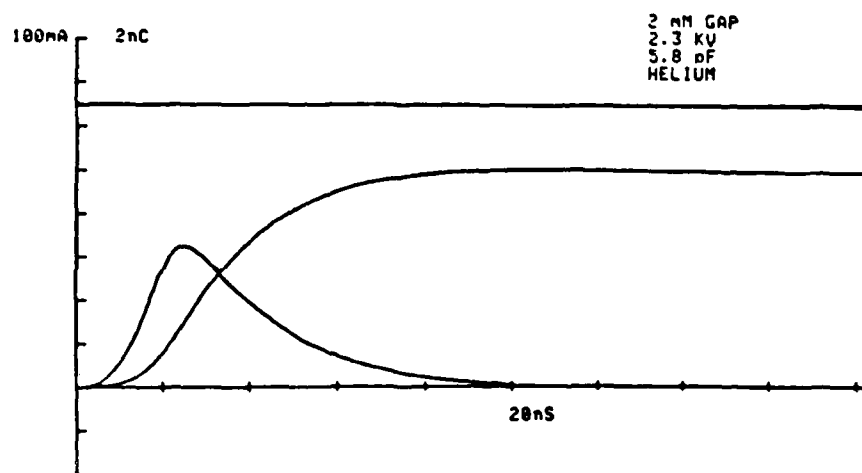
(+)

(-)

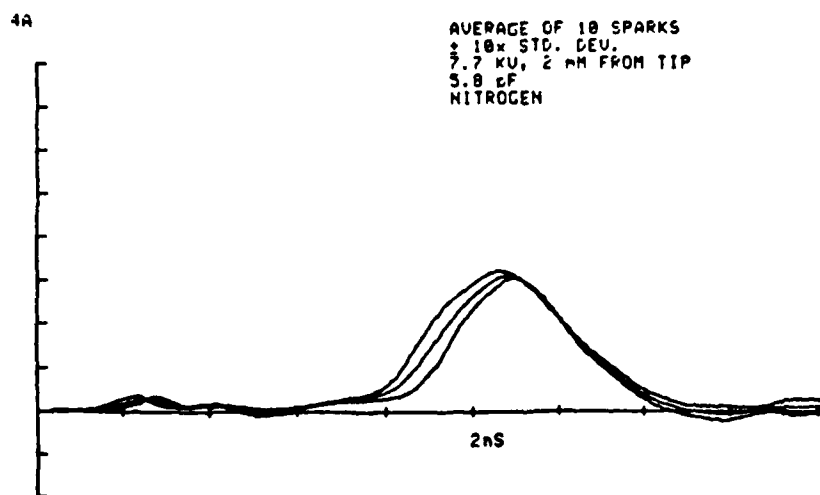
FIGURE 2



(a)



(b)



(c)

Figure 3

1983-84 USAF-SCEEE RESEARCH INITIATION PROGRAM

Sponsored by the

AIR FORCE OFFICE OF SCIENTIFIC RESEARCH

Conducted by the

SOUTHEASTERN CENTER FOR ELECTRICAL ENGINEERING EDUCATION

FINAL REPORT

Prepared by: Dr. Stanley Bashkin

Academic Rank: Professor

Department and
University: Physics Department
University of Arizona

Research Location: Air Force Geophysics Laboratory

Date: February 1985

Subcontract SCEEE RIP 23

Final Report

Professor Stanley Bashkin

Principal Investigator

Introduction

According to this contract, it was intended to search for infrared emissions generated by the passage of protons and other heavy ions through atmospheric gases. The particles were to be delivered by a 2 MV Van de Graaff accelerator. While the initial observations were to be made in the optical region, using apparatus in the Department of Physics, the intention was to have one or more representatives from the Air Force Geophysical Laboratory collaborate with us in the later, infrared phases of the work. That collaboration was to include the use of AFGL apparatus for the venture into the infrared region of the spectrum.

The Experiment

In order to carry out the experiments, a differentially-pumped gas target chamber was constructed and mounted on one of the beam lines in the Van de Graaff Laboratory. Some of the light generated in the gas when the particles went through went via a window into the entrance slit of an Interactive Technology high-resolution air spectrometer, equipped with a grating blazed at 500 nm. At the exit of the spectrometer, a photomultiplier tube detected the light, the intensity of which was converted into an electrical signal in conventional manner. The signals were recorded with a multichannel analyzer, with the stepping pulse to

successive channels being provided by time. Since the particle beam was quite steady, this was a satisfactory technique for the initial experiments.

The wavelength range covered in these initial experiments extended from 300 to 700 nm. We studied two different gases, N_2 and O_2 . We used several bombarding energies from 250 keV to 1 MeV, and also investigated the separate effects of protons, diatomic hydrogen ions, and triatomic hydrogen ions.

The grating we used was blazed at 500 nm, and this might explain why our work up to 700 nm gave few signals at the longer wavelengths. The region beyond 550 nm should be reexamined with a grating better suited to the region of long wavelengths. It would then be possible to gauge better whether a further excursion into the infrared would be profitable. With such information, the direct participation of AFGL personnel and equipment in the experiments would be worth pursuing.

Please note that a proposal has been submitted to AFGL to request additional support for this work.

Results

Some of the results we obtained are presented in Figs. 1, 2, and 3. Those figures make several conclusions clear, namely,

a) A number of interesting features were seen, particularly in the case of nitrogen. From the nitrogen data, we could qualitatively infer the relative combined effects of changing the type of incident particle and the particle velocity. Thus, we tabulate the yield for the most intense lines, normalized to the number of nucleons in the incident H_2^+ beam:

λ (nm)	H^+	H_2^+	H_2^+
357.7	2.5	1	2.2
391.4	1.5	1	1.3
427.8	1.9	1	1.4

It appears from this that protons have a higher cross section than either H_2^+ or H_3^+ for the excitation of these spectral lines. This is somewhat surprising in light of the fact that the particle velocity, relative to that of H^+ , is reduced by factors of 1.4 and 1.7 for H_2^+ and H_2^+ , respectively, and one would expect that slower particles would be intrinsically more effective in generating excited states. Clearly further - and more quantitative - work is needed to investigate this dependence on particle type and velocity.

b) There is a substantial difference between the excitation cross sections for nitrogen and oxygen, the former being by far the larger. This may well account for the fact that little has been reported in the literature on the excitation of oxygen by hydrogenic ions. Of course, our work covered only one portion of the entire spectral range, and it would be valuable to extend the observations, especially towards the infrared.


c) Our resolving power, which is displayed in Fig. 2, was considerably better than that used in the several experiments reported in the literature. Thus, in a number of the regions seen in Fig. 1 to show severe blending, it is possible for us to separate out the several spectral features. Particular attention should be paid to the regions near 388.4 and 405.9 nm, and further work to study those regions is indicated.

d) The foregoing give a clear direction in which additional experiments should go.

The Budget

All the funds provided under the contract were spent.

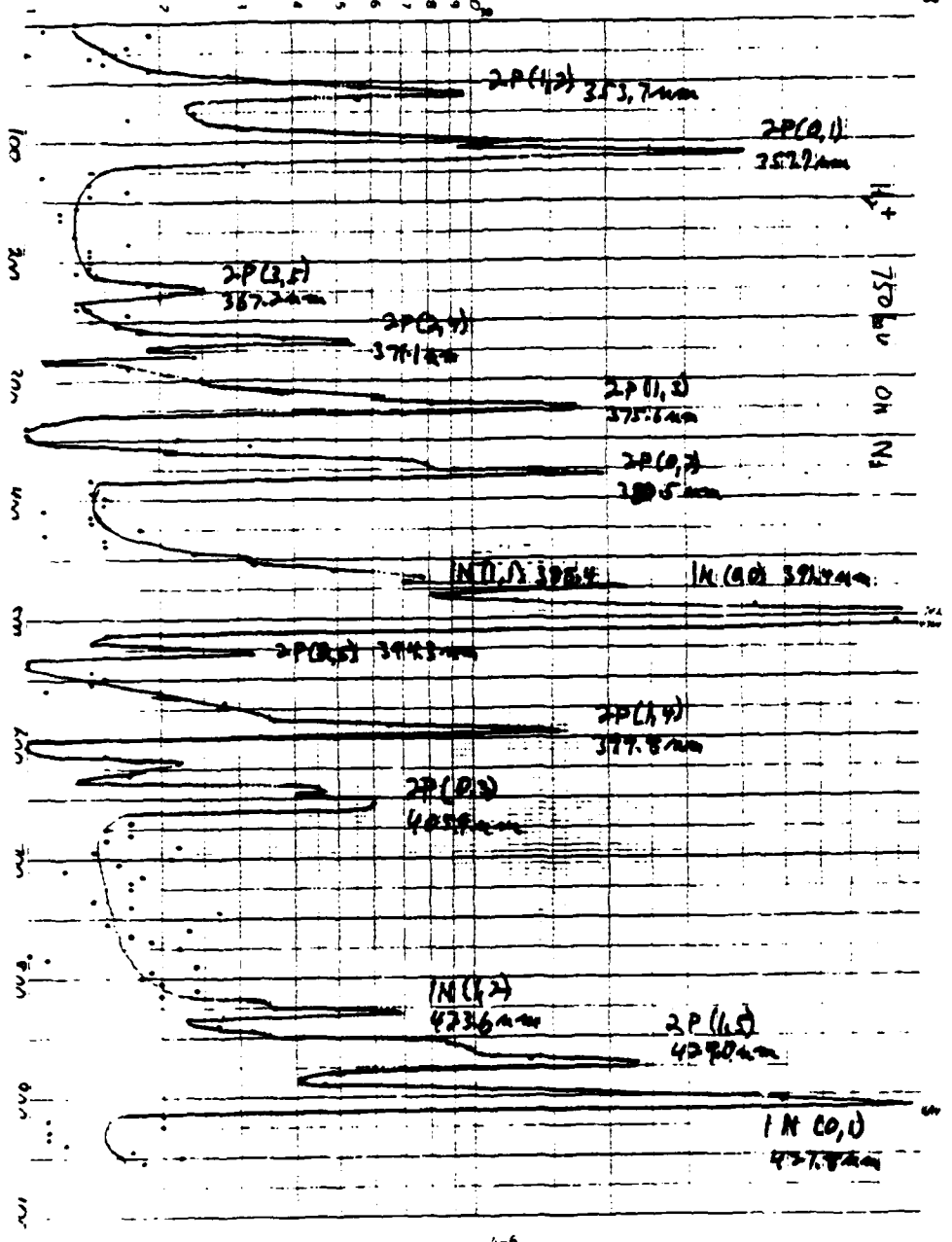
Respectfully submitted,


Stanley Bashkin
Principal Investigator
February 6, 1985

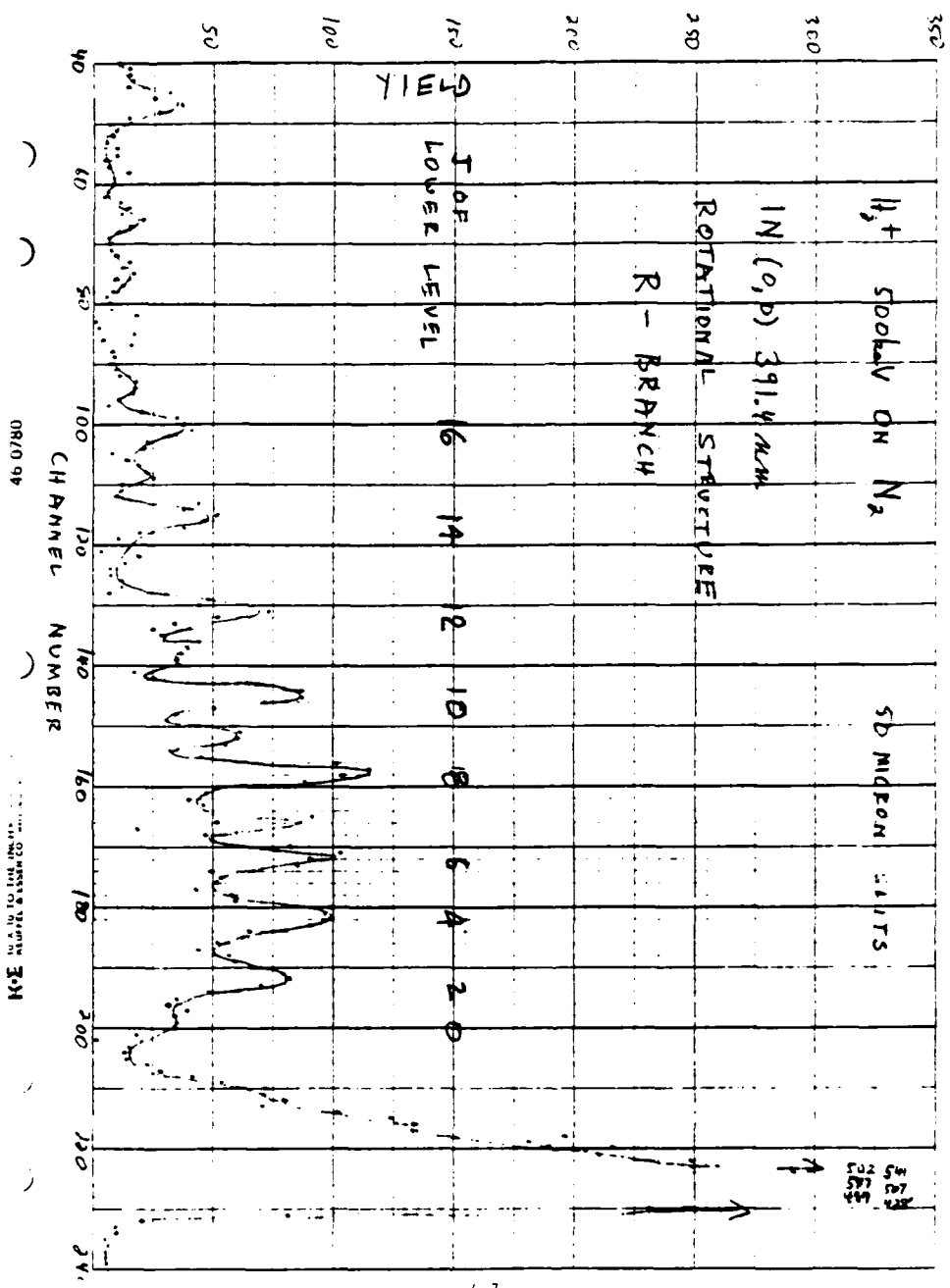
Approved for the University:


Charles Peyton
Associate Vice President, Research

YIELD



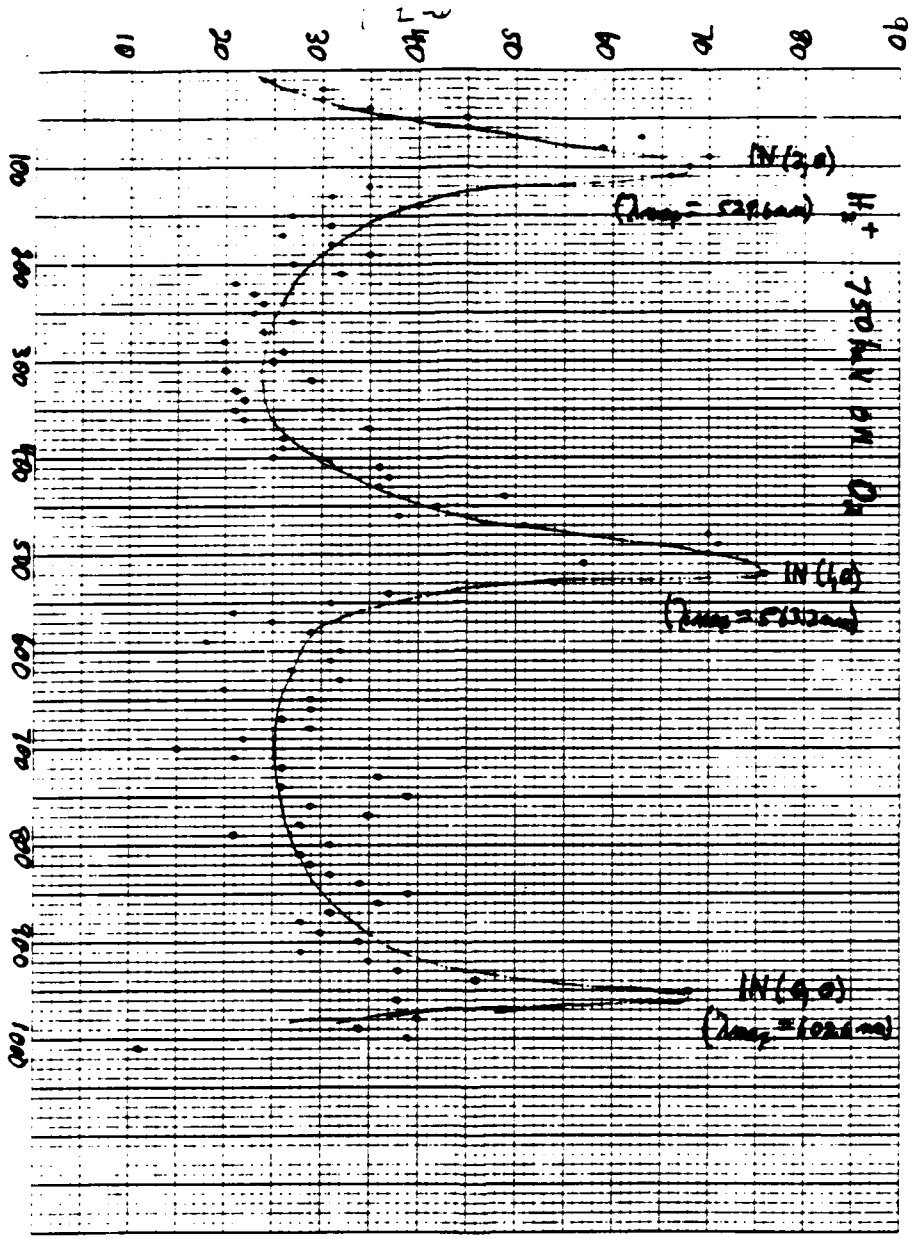
46 5250



CH 8780 94

CHANNEL NUMBER

DEPTH



K-E 3 X 3 TO THE CENTER IN X 34 CM
 46 1610

1983-84 USAF-SCEEE RESEARCH INITIATION PROGRAM

Sponsored by the

AIR FORCE OFFICE OF SCIENTIFIC RESEARCH

Conducted by the

SOUTHEASTERN CENTER FOR ELECTRICAL ENGINEERING EDUCATION

FINAL REPORT

INVESTIGATION OF LIQUID SLOSHING IN SPIN-STABILIZED SATELLITES

Prepared by: Dr. Joseph R. Baumgarten

Academic Rank: Professor

Department and
University: Mechanical Engineering Department
Iowa State University

Research Location: Air Force Arnold Engineering Center

Date: November 1984

ABSTRACT

Certain configurations of spin-stabilized spacecraft consistently develop a coning or nutating motion during the perigee burn. This motion consists of sinusoidal oscillations about the pitch and yaw axes at the same frequency, but with a 90° phase difference. The sloshing of liquid fuel stores is suspected as a source of these nutations. The moving liquid in its spherical containers has been modeled as an equivalent pendulum, pivoted with the main body of the payload, and moving relative to it in the rotating constraint. The equations of motion of the spacecraft with a compound pendulum system have been derived. Numerical solution is accomplished on the digital computer. Comparison is made to flight test data of actual spacecraft.

INTRODUCTION

Launchings of several of the STAR 48 Communication Satellites from the Space Shuttle have consistently resulted in a nutating motion of the spacecraft. Flight data from roll, spin, and yaw axis rate gyros indicate a constant frequency, equal amplitude, sinusoidal oscillation about the yaw and pitch axis. The vector combination of these two components of vibration results in a coning motion of the satellite about its spin axis. The vehicle is spin stabilized at launch, having a 1 rev/sec spin velocity imparted to it.

After launching from the Shuttle, in the perigee phase of its orbit, the satellite's power assist module (PAM) fires its thruster to establish a geosynchronous earth orbit. It is this axial thrust that gives rise to the coning which predominates after PAM-motor burnout. Consistently, flight data from rate gyros indicates the steady-state coning and a 0.5 cps small amplitude disturbance superimposed on the 1 rev/sec spin velocity.

Combustion instabilities in the PAM rocket motor were thought to be the source of a side force which would induce the coning motion. In order to investigate the presence of any such combustion instabilities, a STAR 48 motor was fired at the Engine Test Facility, AEDC, Arnold AFS. A test rig having lateral and axial load cells was utilized, and the rig allowed the PAM to be spun at 1 rev/sec during the firing. A spectral analysis was completed of the resulting load cell records obtained during firing. The test results indicated no significant forces at the required frequency (one-half cycle per second) and it was concluded that combustion instabilities could not be the source of moments about the principal axes of the spacecraft causing coning motion.

A preliminary analysis of the payload (the communication satellite) was completed indicating that a 55 ft-lb external moment at one-half cycle/sec would sustain the coning motion. It was suspected that sloshing motion of liquid stored in the vehicle is the mechanism for creating and sustaining the nutation of the spacecraft. Previous work in modeling of sloshing fluids [1,2]* indicated that equivalent solid pendulum systems could be found to represent the periodic motion of the fluid in the container.

THEORY

This investigation has been initiated in order to study the general problem of the dynamic effects of moving parts on the motion of a spin-stabilized spacecraft. The problem has been formulated from various points of view by Roberson [3], Grubin [4], Kane and Sobala [5], and Edwards and Kaplan [6]. Roberson modeled a rigid main body with an arbitrary number of moving components. He chose the composite center of mass of the system as the reference point. This formulation resulted in time varying moments of inertia and a moving reference point. Grubin avoided this problem by choosing the vehicle center of mass as the reference point. He could easily identify the instantaneous position of the moving mass with reference to the vehicle. Kane and Sobala investigated the problem of attitude control through controlled motion of an internal mass in the spacecraft. Edwards and Kaplan studied the detumbling of a spacecraft by the programmed motion of a movable internal mass. The equations of motion of the spacecraft were derived with the origin of a coordinate set fixed in the principal

*Numbers in brackets designate references.

coordinates of the main mass of the spacecraft. Thus, a fixed reference point was defined at the body center of mass and the instantaneous position of the movable mass was defined relative to the main mass. This is the approach taken here in this present study.

Let a satellite with some even number of semi-spherical fuel tanks be represented as shown in Figure 1. The sloshing fuel can be represented in this first approximation as a spherical pendulum with some equivalent mass oscillating, at some identifiable radius [1,2]. The reference frames $X_1X_2X_3$, $B_1B_2B_3$, and $(n_1n_2n_3)^i$ are inertial and body coordinates fixed to the main body and pendulum respectively. The equations of motion were derived using both D'Alembert's Form of Lagrange's Equations (also known as Kane's equations, [7]) and a Lagrangian formulation. These two different formulations provide a check on the equations of motion because of their differences in form. Kane's equations are much simpler to formulate than the classical Lagrangian approach because of the differentiations needed in the Lagrangian formulation.

The two methods can be summarized for this problem by the results which follow.

1. General Derivations

For Kane's equations,

$$F_r + F_r^* = 0 \quad r = 1, \dots, n$$

$$F_r^* = (F_r^*)_B + (F_r^*)_{mi} \quad r = 1, \dots, n \text{ degrees of freedom}$$

$$(F_r^*)_B = \dot{v}_{qr} \cdot \underline{F}^* + \omega_{qr} \cdot \underline{T}^* \quad r = 1, \dots, n$$

$$(F_r^*)_{mi} = \dot{v}_{qr} \cdot \underline{F}_{mi}^* \quad r = 1, \dots, n$$

$qr \stackrel{\Delta}{=} \text{generalized coordinate}$

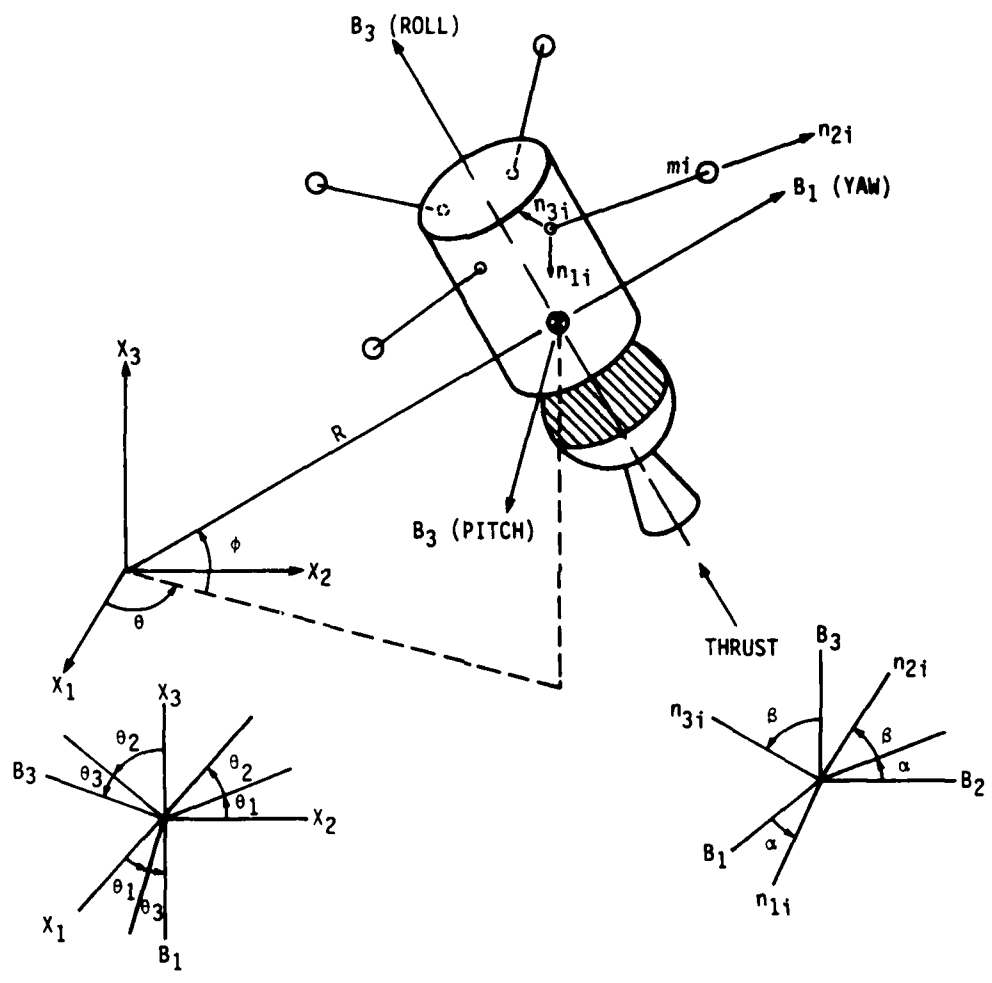


Fig. 1. Model of spacecraft with spherical pendulum.

$\underline{v} \triangleq$ velocity vector

$\underline{\omega} \triangleq$ angular velocity vector

$\dot{q} \triangleq$ first derived coordinate with respect to time

$$\frac{\underline{v}}{\underline{q}r} \triangleq \frac{\partial \underline{v}}{\partial \dot{q}r}$$

$$\frac{\underline{\omega}}{\underline{q}r} \triangleq \frac{\partial \underline{\omega}}{\partial \dot{q}r}$$

$$\underline{F}^* = - M_B \underline{a}_B$$

$M_B \triangleq$ mass of main body

$\underline{a}_B \triangleq$ acceleration of main body

$$\underline{T}^* = - \dot{\underline{I}} \cdot \underline{R}^B + (\underline{I} \cdot \underline{\omega}^B) \times \underline{R}^B - \underline{I} \cdot \frac{d\underline{\omega}^B}{dt}$$

$\underline{I} \triangleq$ inertia tensor

$$\underline{F}_{mi}^* = - m_i \underline{a}_{mi}$$

$m_i \triangleq$ mass of pendulum i

$\underline{a}_{mi} \triangleq$ acceleration of m_i

$F_r \triangleq$ generalized active force

$$(F_r)_B = \underline{v}_{\dot{q}r} \cdot (\underline{F}_G + \underline{F}_T) + \underline{R}_{\dot{q}r}^B \cdot (\underline{T}_T) + \underline{R}_{\dot{q}r}^{mi} \cdot \underline{T}_{mi} \dots$$

$\underline{F}_G \triangleq$ gravitational force vector

$\underline{F}_T \triangleq$ thrust vector

$\underline{T}_{mi} \triangleq$ spring and damper torque vector i on m_i

$\underline{T}_T \triangleq$ thrust torque vector

$\underline{R}^B \triangleq$ angular velocity of body B in the inertial frame

$\underline{R}^{mi} \triangleq$ angular velocity of body m_i in the inertial frame

For the Lagrangian formulation:

$$\frac{d}{dt} \frac{\partial K}{\partial \dot{q}r} - \frac{\partial K}{\partial q_r} = F_r \quad r = 1, \dots, n$$

$K \triangleq$ kinetic energy

$$K = \frac{1}{2} \underline{R}^B \cdot \underline{I} \cdot \underline{R}^B + \frac{1}{2} \sum_{i=1}^N m_i \underline{v}_{mi} \cdot \underline{v}_{mi} + \frac{1}{2} M_{B-G} \underline{v}_G \cdot \underline{v}_G$$

$\underline{v}_{mi} \triangleq$ velocity of mass m_i

$\underline{v}_G \triangleq$ velocity of main body mass center

The generalized coordinates chosen to describe the position of the system were (see Figure 1),

x_1, x_2, x_3 - cartesian location of main body mass center

$\theta_1, \theta_2, \theta_3$ - angles for the orientation of the main body relative to x_1, x_2, x_3

α_i, β_i - angles for the orientation of m_i relative to the main body B_1, B_2, B_3

The system has $n = 6 + 2N$ degrees of freedom where,

$N \triangleq$ number of spherical pendulums

$n \triangleq$ degrees of freedom.

2. Definition of Variables and Parameters

The equation variables and parameters;

$$a_{11} \equiv \cos\theta_1 \cos\theta_3 - \sin\theta_1 \sin\theta_2 \sin\theta_3$$

$$a_{12} \equiv -\sin\theta_1 \cos\theta_2$$

$$a_{13} \equiv \cos\theta_1 \sin\theta_3 + \sin\theta_1 \sin\theta_2 \cos\theta_3$$

$$a_{21} \equiv \sin\theta_1 \cos\theta_3 + \cos\theta_1 \sin\theta_2 \sin\theta_3$$

$$a_{22} \equiv \cos\theta_1 \cos\theta_2$$

$$a_{23} \equiv \sin\theta_1 \sin\theta_3 - \cos\theta_1 \sin\theta_2 \cos\theta_3$$

$$a_{31} \equiv -\cos\theta_2 \sin\theta_3$$

$$a_{32} \equiv \sin\theta_2$$

$$a_{33} \equiv \cos\theta_2 \cos\theta_3$$

$$t_{11} \equiv \cos\alpha_i$$

$$t_{12} \equiv \sin\alpha_i$$

$$L_1^i \equiv -L_i \sin\alpha_i \cos\beta_i$$

$$L_2^i \equiv L_i \cos\alpha_i \cos\beta_i$$

$$L_3^i \equiv L_i \sin\beta_i$$

$$L_i \equiv \text{pendulum length}$$

$$r_1^i, r_2^i, r_3^i \equiv \text{distance from main body mass center to pendulum attachment point}$$

$$u_1 \equiv a_{11}$$

$$u_2 \equiv a_{12}$$

$$u_3 \equiv a_{13}$$

$$u_4 \equiv a_{21}$$

$$u_5 \equiv a_{22}$$

$$u_6 \equiv a_{23}$$

$$u_7 \equiv a_{31}$$

$$u_8 \equiv a_{32}$$

$$u_9 \equiv a_{33}$$

$$u_{10} \equiv (r_3 + L_3)a_{32} - (r_2 + L_2)a_{33}$$

$$\sin\theta \equiv \text{sn}\theta \quad \cos\theta \equiv \text{cs}\theta$$

$$u_{11} \equiv (r_1 + L_1)a_{33} - (r_3 + L_3)a_{31}$$

$$u_{12} \equiv (r_2 + L_2)a_{31} - (r_1 + L_1)a_{32}$$

$$u_{13} \equiv - (r_2 + L_2)\text{sn}\theta_3$$

$$u_{14} \equiv (r_1 + L_1)\text{sn}\theta_3 - (r_3 + L_3)\text{cs}\theta_3$$

$$u_{15} \equiv (r_2 + L_2)\text{cs}\theta_3$$

$$u_{16} \equiv r_3 + L_3$$

$$u_{17} \equiv 0$$

$$u_{18} \equiv - (r_1 + L_1)$$

$$u_{19} \equiv L_3 t_{12}$$

$$u_{20} \equiv - L_3 t_{11}$$

$$u_{21} \equiv L_2 t_{11} - L_1 t_{12}$$

$$u_{22} \equiv - L_2$$

$$u_{23} \equiv L_1$$

$$u_{24} \equiv 0$$

$$R_{\omega_1}^B \equiv \dot{\theta}_1 a_{31} + \dot{\theta}_2 \text{cs}\theta_3 \quad R_{\omega_1}^{mi} = R_{\omega_1}^B + \dot{\beta} t_{11}$$

$$R_{\omega_2}^B \equiv \dot{\theta}_1 a_{32} + \dot{\theta}_3 \quad R_{\omega_2}^{mi} = R_{\omega_2}^B + \dot{\beta} t_{12}$$

$$R_{\omega_3}^B \equiv \dot{\theta}_1 a_{33} + \dot{\theta}_2 \text{sn}\theta_3 \quad R_{\omega_3}^{mi} = R_{\omega_3}^B + \dot{\alpha}$$

$$e_1 \equiv \dot{\theta}_1 \dot{\theta}_2 a_{32} \text{sn}\theta_3 - \dot{\theta}_1 \dot{\theta}_3 a_{33} - \dot{\theta}_2 \dot{\theta}_3 \text{sn}\theta_3$$

$$e_2 \equiv \dot{\theta}_1 \dot{\theta}_2 \text{cs}\theta_2$$

$$e_3 \equiv - \dot{\theta}_1 \dot{\theta}_2 a_{32} \text{cs}\theta_3 + \dot{\theta}_1 \dot{\theta}_3 a_{31} + \dot{\theta}_2 \dot{\theta}_3 \text{cs}\theta_3$$

$$d_1 \equiv - (I_{11}e_1 + I_{12}e_2 + I_{13}e_3) - (\dot{i}_{11}\omega_1 + \dot{i}_{12}\omega_2 + \dot{i}_{13}\omega_3) \\ + I_{12}\omega_1\omega_3 + I_{22}\omega_2\omega_3 + I_{23}\omega_3^2 - (I_{13}\omega_1\omega_2 + I_{23}\omega_2^2 + I_{33}\omega_2\omega_3)$$

$$d_2 \equiv - (I_{12}e_1 + I_{22}e_2 + I_{23}e_3) - (\dot{i}_{12}\omega_1 + \dot{i}_{22}\omega_2 + \dot{i}_{23}\omega_3) \\ + I_{13}\omega_1^2 + I_{23}\omega_1\omega_2 + I_{33}\omega_1\omega_3 - (I_{11}\omega_1\omega_3 + I_{12}\omega_2\omega_3 + I_{13}\omega_3^2)$$

$$d_3 \equiv - (I_{13}e_1 + I_{23}e_2 + I_{33}e_3) - (\dot{i}_{13}\omega_1 + \dot{i}_{23}\omega_2 + \dot{i}_{33}\omega_3) \\ + I_{11}\omega_1\omega_2 + I_{12}\omega_2^2 + I_{13}\omega_2\omega_3 - (I_{12}\omega_1^2 + I_{22}\omega_1\omega_2 + I_{23}\omega_1\omega_3)$$

$$B_1 \equiv (r_3 + L_3)e_2 - (r_2 + L_2)e_3 + L_3 (\dot{\beta}(\dot{\tau}_{12} + \tau_{11}\omega_3) - \dot{\alpha}\omega_1) \\ - L_2(\dot{\beta}(\tau_{12}\omega_1 - \tau_{11}\omega_2)) + \omega_1\omega_2 r_2 - r_1(\omega_2^2 + \omega_3^2) \\ + \omega_1\omega_3 r_3 + (\omega_1\omega_2 L_2 - L_1(\omega_2^2 + \omega_3^2) + \omega_1\omega_3 L_3)^{mi} \\ - 2(\omega_2 \dot{r}_3 - \omega_3 \dot{r}_2) - \ddot{r}_1$$

The superscript mi denotes the angular velocity used in the brackets must be ω^{mi} otherwise ω^B .

$$B_2 \equiv (r_1 + L_1)e_3 - (r_3 + L_3)e_1 + L_1(\dot{\beta}(\tau_{12}\omega_1 - \tau_{11}\omega_2)) \\ - L_3(\dot{\beta}(\dot{\tau}_{11} - \tau_{12}\omega_3) + \dot{\alpha}\omega_2) + \omega_2\omega_3 r_3 - r_2(\omega_1^2 + \omega_3^2) \\ + \omega_1\omega_2 r_1 + (\omega_2\omega_3 L_3 - L_2(\omega_1^2 + \omega_3^2) + \omega_1\omega_2 L_1)^{mi} \\ - 2(\omega_3 \dot{r}_1 - \omega_1 \dot{r}_3) - \ddot{r}_2$$

$$\begin{aligned}
B_3 \equiv & (r_2 + L_2)e_1 - (r_1 + L_1)e_2 + L_2(\dot{\beta}(\dot{t}_{11} - t_{12}\omega_3) + \dot{\alpha}\omega_2) \\
& - L_1(\dot{\beta}(\dot{t}_{12} + t_{11}\omega_3) - \dot{\alpha}\omega_1) + \omega_1\omega_3r_1 - r_3(\omega_1^2 + \omega_2^2) \\
& + \omega_2\omega_3r_2 + (\omega_1\omega_3L_1 - L_3(\omega_1^2 + \omega_2^2) + \omega_2\omega_3L_2)mi \\
& - 2(\omega_1\dot{r}_2 - \omega_2\dot{r}_1) - \ddot{r}_3
\end{aligned}$$

$K_G \equiv$ gravitational constant

$F_1, F_2, F_3 \equiv$ thrust force components in $\beta_1\beta_2\beta_3$ reference frame

$T_1, T_2, T_3 \equiv$ thrust moment components in $\beta_1\beta_2\beta_3$ reference frame

$K_1, D_1 \equiv$ spring and damping coefficients with respect to α coordinate

$K_2, D_2 \equiv$ spring and damping coefficients with respect to β coordinate

2. Motion Equations

Using both Kane's formulation (A) and Lagrangian formulation (B), the equations of motion were formulated as,

$$\begin{aligned}
& [-M - \sum_{mi}] \ddot{x}_1 + [0] \ddot{x}_2 + [0] \ddot{x}_3 \\
& + [- \sum_{mi} \{u_1u_{10} + u_2u_{11} + u_3u_{12}\}] \ddot{\theta}_1 \\
& + [- \sum_{mi} \{u_1u_{13} + u_2u_{14} + u_3u_{15}\}] \ddot{\theta}_2 \\
& + [- \sum_{mi} \{u_1u_{16} + u_3u_{18}\}] \ddot{\theta}_3 \\
& + [- \sum_{mi} \{u_1u_{19} + u_2u_{20} + u_3u_{21}\}] \ddot{\beta}_1 \\
& + [- \sum_{mi} \{u_1u_{22} + u_2u_{23}\}] \ddot{\alpha}_1
\end{aligned}$$

$$\begin{aligned}
& + [- \sum_{mi} \{u_1 B_1 + u_2 B_2 + u_3 B_3\}] + a_{11} F_1 + a_{12} F_2 + a_{13} F_3 \\
& - \frac{K_G x_1}{[x_1^2 + x_2^2 + x_3^2]^{3/2}} = 0 \quad (1)
\end{aligned}$$

$$\begin{aligned}
& [0] \ddot{x}_1 + [-M - \sum_{mi}] \ddot{x}_2 + [0] \ddot{x}_3 \\
& + [- \sum_{mi} \{u_4 u_{10} + u_5 u_{11} + u_6 u_{12}\}] \ddot{\theta}_1 \\
& + [- \sum_{mi} \{u_4 u_{13} + u_5 u_{14} + u_6 u_{15}\}] \ddot{\theta}_2 \\
& + [- \sum_{mi} \{u_4 u_{16} + u_6 u_{18}\}] \ddot{\theta}_3 \\
& + [- \sum_{mi} \{u_4 u_{19} + u_5 u_{20} + u_6 u_{21}\}] \ddot{\beta}_i \\
& + [- \sum_{mi} \{u_4 u_{22} + u_5 u_{23}\}] \ddot{\alpha}_i \\
& + [- \sum_{mi} \{u_4 B_1 + u_5 B_2 + u_6 B_3\}] + a_{21} F_1 + a_{22} F_2 + a_{23} F_3 \\
& - \frac{K_G x_2}{[x_1^2 + x_2^2 + x_3^2]^{3/2}} \quad (2)
\end{aligned}$$

$$\begin{aligned}
& [0] \ddot{x}_1 + [0] \ddot{x}_2 + [-M - \sum_{mi}] \ddot{x}_3 + [0] \ddot{\theta}_1 \\
& + [- \sum_{mi} \{u_7 u_{13} + u_8 u_{14} + u_9 u_{15}\}] \ddot{\theta}_2 \\
& + [- \sum_{mi} \{u_7 u_{16} + u_9 u_{18}\}] \ddot{\theta}_3 \\
& + [- \sum_{mi} \{u_7 u_{19} + u_8 u_{20} + u_9 u_{21}\}] \ddot{\beta}_i \\
& + [- \sum_{mi} \{u_7 u_{22} + u_8 u_{23}\}] \ddot{\alpha}_i \\
& + [- \sum_{mi} \{u_7 B_1 + u_8 B_2 + u_9 B_3\}] + a_{31} F_1 + a_{32} F_2 + a_{33} F_3
\end{aligned}$$

$$-\frac{K_G x_3}{[x_1^2 + x_2^2 + x_3^2]^{3/2}} = 0 \quad (3)$$

$$\begin{aligned}
& [- \sum_{mi} (u_{10} u_1 + u_{11} u_2 + u_{12} u_3)] \ddot{x}_1 \\
& + [- \sum_{mi} (u_{10} u_4 + u_{11} u_5 + u_{12} u_6)] \ddot{x}_2 \\
& + [- \sum_{mi} (u_{10} u_7 + u_{11} u_8 + u_{12} u_9)] \ddot{x}_3 \\
& + [(- I_{11} a_{31}^2 - 2I_{12} a_{31} a_{32} - 2I_{13} a_{31} a_{33} - I_{22} a_{32}^2 \\
& - 2I_{23} a_{32} a_{33} - I_{33} a_{33}^2)] \\
& - \sum_{mi} (u_{10}^2 + u_{11}^2 + u_{12}^2)] \ddot{\theta}_1 \\
& + [(- I_{11} a_{31} \text{cs}\theta_3 - I_{12} a_{32} \text{cs}\theta_3 - I_{13} (a_{33} \text{cs}\theta_3 + a_{31} \text{sn}\theta_3) \\
& - I_{23} a_{32} \text{sn}\theta_3 - I_{33} a_{33} \text{sn}\theta_3)] \\
& - \sum_{mi} [u_{10} u_{13} + u_{11} u_{14} + u_{12} u_{15}] \ddot{\theta}_2 \\
& + [(- I_{12} a_{31} - I_{22} a_{32} - I_{23} a_{33} \\
& - \sum_{mi} [u_{10} u_{16} + u_{12} u_{18}]) \ddot{\theta}_3 \\
& + [- \sum_{mi} (u_{10} u_{19} + u_{11} u_{20} + u_{12} u_{21})] \ddot{\theta}_4 \\
& + [- \sum_{mi} (u_{10} u_{22} + u_{11} u_{23})] \ddot{\alpha}_1 \\
& + [- \sum_{mi} (u_{10} B_1 + u_{11} B_2 + u_{12} B_3)] \\
& + d_1 a_{31} + d_2 a_{32} + d_3 a_{33} + a_{31} T_1 + a_{32} T_2 + a_{33} T_3 = 0 \quad (4)
\end{aligned}$$

$$\begin{aligned}
& [- \sum_{mi} [u_{13}u_1 + u_{14}u_2 + u_{15}u_3]] \ddot{x}_1 \\
& + [- \sum_{mi} [u_{13}u_4 + u_{14}u_5 + u_{15}u_6]] \ddot{x}_2 \\
& + [- \sum_{mi} [u_{13}u_7 + u_{14}u_8 + u_{15}u_9]] \ddot{x}_3 \\
& + [- I_{11}a_{31}cs\theta_3 - I_{12}a_{32}cs\theta_3 - I_{13}(a_{33}cs\theta_3 + a_{31}sn\theta_3) \\
& - I_{23}a_{32}sn\theta_3 - I_{33}a_{33}sn\theta_3 \\
& - \sum_{mi} [u_{13}u_{10} + u_{14}u_{11} + u_{15}u_{12}]] \ddot{\theta}_1 \\
& + [- I_{11}cs^2\theta_3 - 2I_{13}cs\theta_3sn\theta_3 - I_{33}sn^2\theta_3 \\
& - \sum_{mi} [u_{13}^2 + u_{14}^2 + u_{15}^2]] \ddot{\theta}_2 \\
& + [- I_{12}cs\theta_3 - I_{23}sn\theta_3 - \sum_{mi} (u_{13}u_{16} + u_{15}u_{18})] \ddot{\theta}_3 \\
& + [- \sum_{mi} [u_{13}u_{19} + u_{14}u_{20} + u_{15}u_{21}]] \ddot{\beta}_i \\
& + [- \sum_{mi} [u_{13}u_{22} + u_{14}u_{23}]] \ddot{\alpha}_i \\
& + [- \sum_{mi} [u_{13}B_1 + u_{14}B_2 + u_{15}B_3]] \\
& + d_1cs\theta_3 + d_3sn\theta_3 + T_1cs\theta_3 + T_3sn\theta_3 = 0 \quad (5)
\end{aligned}$$

$$\begin{aligned}
& [- \sum_{mi} [u_{16}u_1 + u_{18}u_3]] \ddot{x}_1 \\
& + [- \sum_{mi} [u_{16}u_4 + u_{18}u_6]] \ddot{x}_2 \\
& + [- \sum_{mi} [u_{16}u_7 + u_{18}u_9]] \ddot{x}_3 \\
& + [- I_{12}a_{31} - I_{22}a_{32} - I_{23}a_{33} - \sum_{mi} [u_{16}u_{10} + u_{18}u_{12}]] \ddot{\theta}_1 \\
& + [- I_{12}cs\theta_3 - I_{23}sn\theta_3 - \sum_{mi} [u_{16}u_{13} + u_{18}u_{15}]] \ddot{\theta}_2
\end{aligned}$$

$$\begin{aligned}
& + [-I_{22} - \sum_{mi} (u_{16}^2 + u_{18}^2)] \ddot{\theta}_3 \\
& + [-\sum_{mi} (u_{16}u_{18} + u_{18}u_{21})] \ddot{\beta} \\
& + [-\sum_{mi} (u_{16}u_{22})] \ddot{\alpha}_i \\
& + [-\sum_{mi} (u_{16}^{B_1} + u_{18}^{B_3})] + d_2 + T_2 = 0 \quad (6)
\end{aligned}$$

$$\begin{aligned}
& [-mi (u_{19}u_1 + u_{20}u_2 + u_{21}u_3)] \ddot{x}_1 \\
& + [-mi (u_{19}u_4 + u_{20}u_5 + u_{21}u_6)] \ddot{x}_2 \\
& + [-mi (u_{19}u_7 + u_{20}u_8 + u_{21}u_9)] \ddot{x}_3 \\
& + [-mi (u_{19}u_{10} + u_{20}u_{11} + u_{21}u_{12})] \ddot{\theta}_1 \\
& + [-mi (u_{19}u_{13} + u_{20}u_{14} + u_{21}u_{15})] \ddot{\theta}_2 \\
& + [-mi (u_{19}u_{16} + u_{21}u_{18})] \ddot{\theta}_3 \\
& + [-mi (u_{19}^2 + u_{20}^2 + u_{21}^2)] \ddot{\beta}_1 \\
& + [0] \ddot{\alpha}_i + [-mi (u_{19}^{B_1} + u_{20}^{B_2} + u_{21}^{B_3})] - (k_2(\beta - \beta_0))^3 \\
& + D_2 \dot{\beta} = 0 \quad (7)
\end{aligned}$$

$$\begin{aligned}
& [-mi (u_{22}u_1 + u_{23}u_2)] \ddot{x}_1 \\
& + [-mi (u_{22}u_4 + u_{23}u_5)] \ddot{x}_2 \\
& + [-mi (u_{22}u_7 + u_{23}u_8)] \ddot{x}_3 \\
& + [-mi (u_{22}u_{10} + u_{23}u_{11})] \ddot{\theta}_1 \\
& + [-mi (u_{22}u_{13} + u_{23}u_{14})] \ddot{\theta}_2
\end{aligned}$$

$$\begin{aligned}
& + [-mi [u_{22}u_{16}]] \ddot{\theta}_3 \\
& + [0] \ddot{\beta}_1 \\
& + [-mi [u_{22}^2 + u_{23}^2]] \ddot{\alpha}_1 \\
& + [-mi [u_{22}^{B_1} + u_{23}^{B_2}]] - (k_1(\alpha - \alpha_0)^3 + D_1\dot{\alpha}) = 0 \quad (8)
\end{aligned}$$

Equations (7) and (8) occur for each pendulum.

The equations of motion can be expressed in state variable form as,

$$\begin{array}{cccc}
y_1 = x_1 & y_7 = \theta_1 & y_{13} = \beta_1 & y_{2N-3} = \beta_n \\
y_2 = \dot{x}_1 & y_8 = \dot{\theta}_1 & y_{14} = \dot{\beta}_1 & y_{2N-2} = \dot{\beta}_n \\
y_3 = x_2 & y_9 = \theta_2 & y_{15} = \alpha_1 & y_{2N-1} = \alpha_n \\
y_4 = \dot{x}_2 & y_{10} = \dot{\theta}_2 & y_{16} = \dot{\alpha}_1 & y_{2N} = \dot{\alpha}_n \\
y_5 = x_3 & y_{11} = \theta_3 & \cdot & \\
y_6 = \dot{x}_3 & y_{12} = \dot{\theta}_3 & \cdot &
\end{array}$$

$$\begin{bmatrix}
1 & 0 & 0 & \dots & \dots & \dots \\
0 & 0 & 1 & 0 & \dots & \dots \\
0 & 0 & 0 & 0 & 1 & 0 & \dots & \dots \\
\vdots & \vdots & \vdots & \vdots & \vdots & \vdots & \vdots & \vdots \\
\vdots & \vdots & \vdots & \vdots & \vdots & \vdots & \vdots & \vdots \\
\vdots & \vdots & \vdots & \vdots & \vdots & \vdots & \vdots & \vdots
\end{bmatrix}
\begin{bmatrix}
\dot{y}_1 \\
\dot{y}_2 \\
\dot{y}_3 \\
\dot{y}_4 \\
\dot{y}_5 \\
\dot{y}_6 \\
\vdots \\
\vdots \\
\vdots \\
\vdots
\end{bmatrix}
=
\begin{bmatrix}
y_2 \\
- \\
y_4 \\
- \\
y_6 \\
- \\
\vdots \\
\vdots \\
\vdots \\
\vdots
\end{bmatrix} \quad (9)$$

The left hand side matrix is symmetric and a set of $2(6 + 2N)$ nonlinear equations come about from the formulation and can be solved by various

numerical schemes.

Rocket motor thrust properties were modeled using a cubic spline fit of data supplied from the manufacturer. The curve fit is shown in Figure 2. These data provide the F and T thrust force and thrust torque terms of Equations (1) through (8). Spacecraft inertial data required in the motion equations is shown in Figure 3.

SOLUTION

1. Numerical Solution of Equations of Motion

An arbitrary initial state of the free surface fluid was set and the thrust data of the Power Assist Module, as shown in Figure 2, was applied to the structure. The digital computer solution of Equations (1) through (8) yielded roll, pitch, and yaw rates versus time as shown in Figure 4. As time advances into the burn phase, the pitch and yaw oscillations begin. With continued thrusting, the small amplitude 0.5 Hz variation in the 1 rev/sec spin velocity is seen to appear. With the completion of the ninety second booster thrust, the approximate equal amplitude, quarter cycle phase shifted oscillations about the pitch and about the yaw axis is sustained. This is the physical manifestation of the coning mode of the spacecraft.

Considerable study is needed to find an efficient algorithm to accomplish the numerical quadrature of the motion equations. This set of nonlinear, coupled differential equations possesses a time varying Jacobian and shows traits of systems with stiff coefficient matrices.

2. Flight Test Data

Figure 5 shows the flight test data from roll, pitch, and yaw rate gyros of the RCA-C' vehicle thrust phase. Approximately ten seconds before

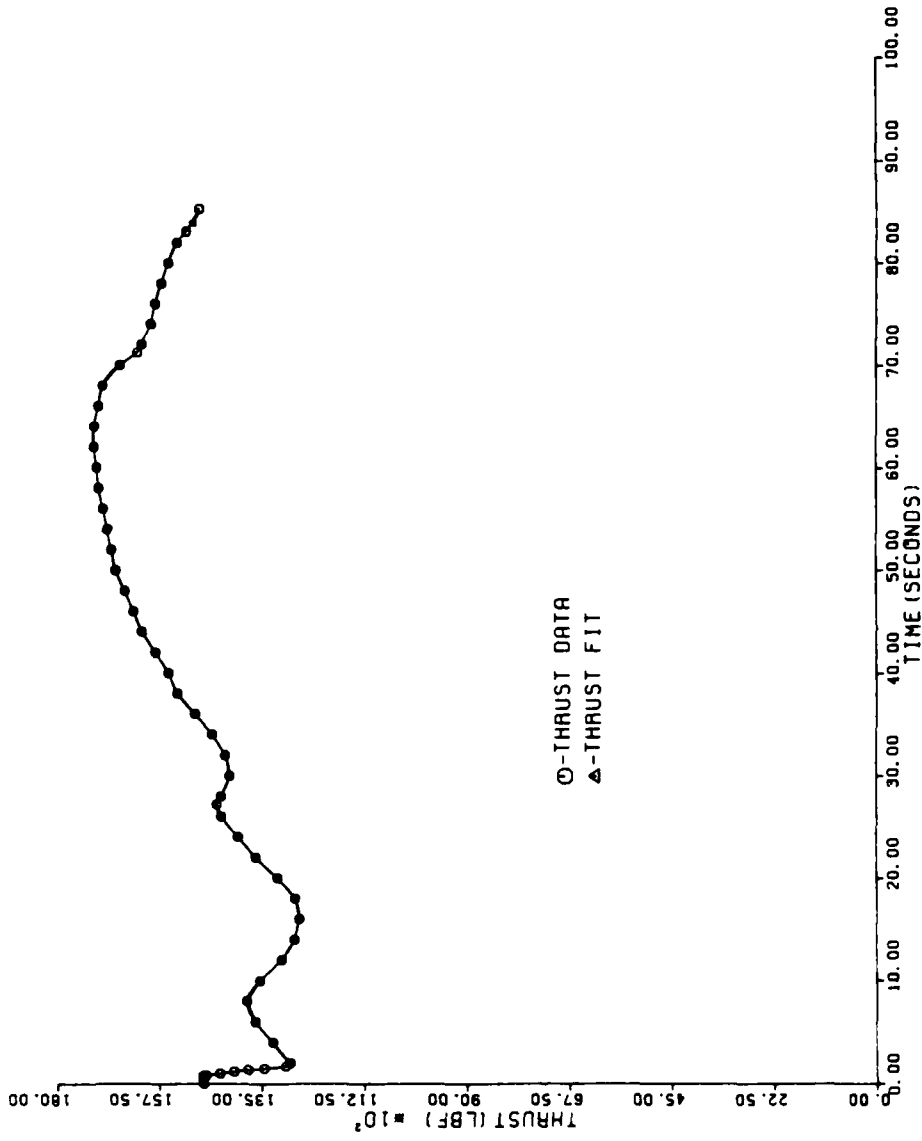


Fig. 2. Thiokol upper stage motor thrust versus time.

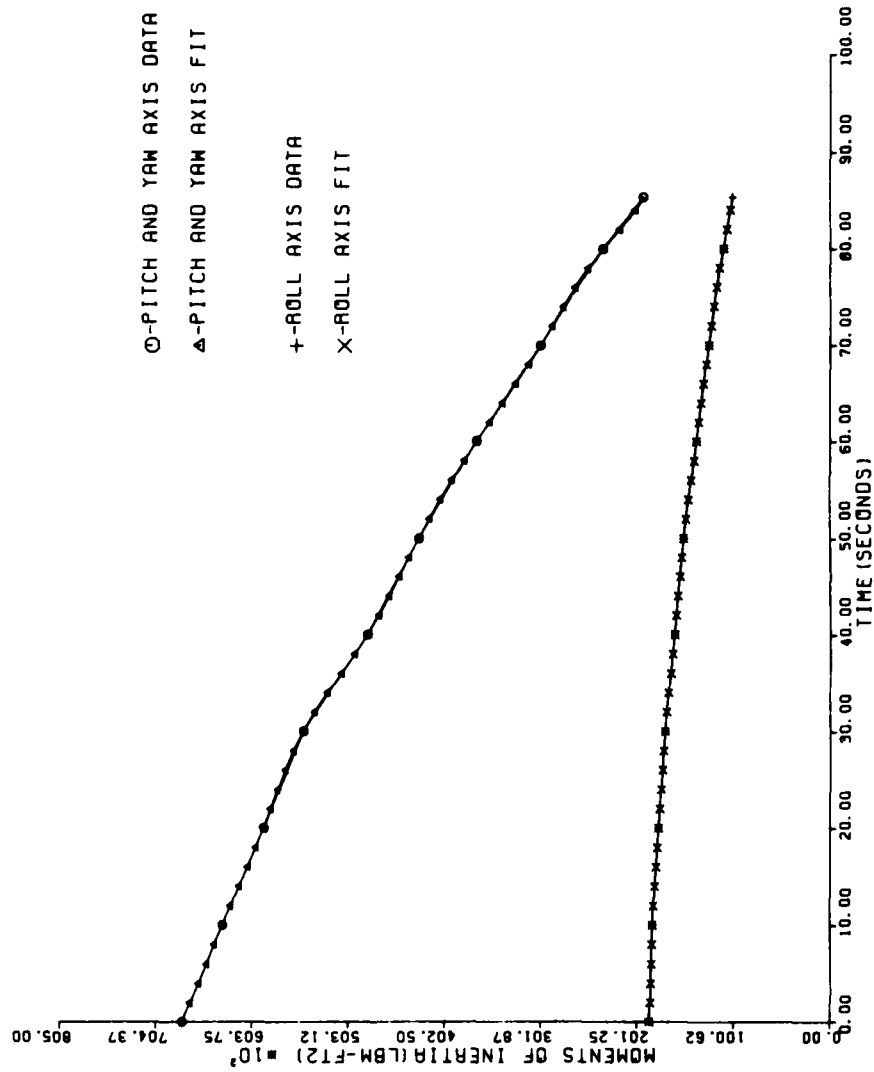


Fig. 3. Typical moments of inertia during burn.

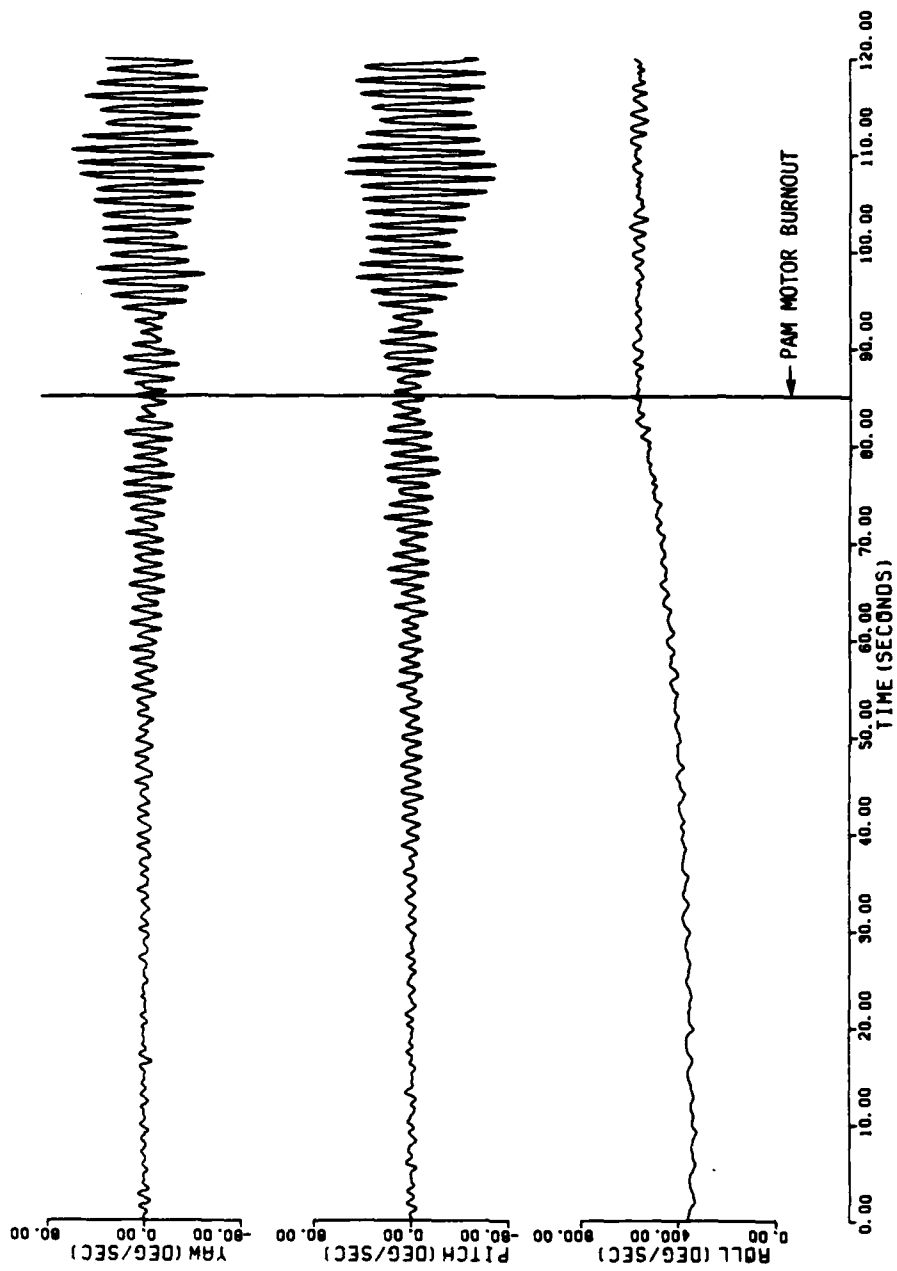


Fig. 4. Spacecraft Flight Simulation

DEFINITION OF CONING PROBLEM

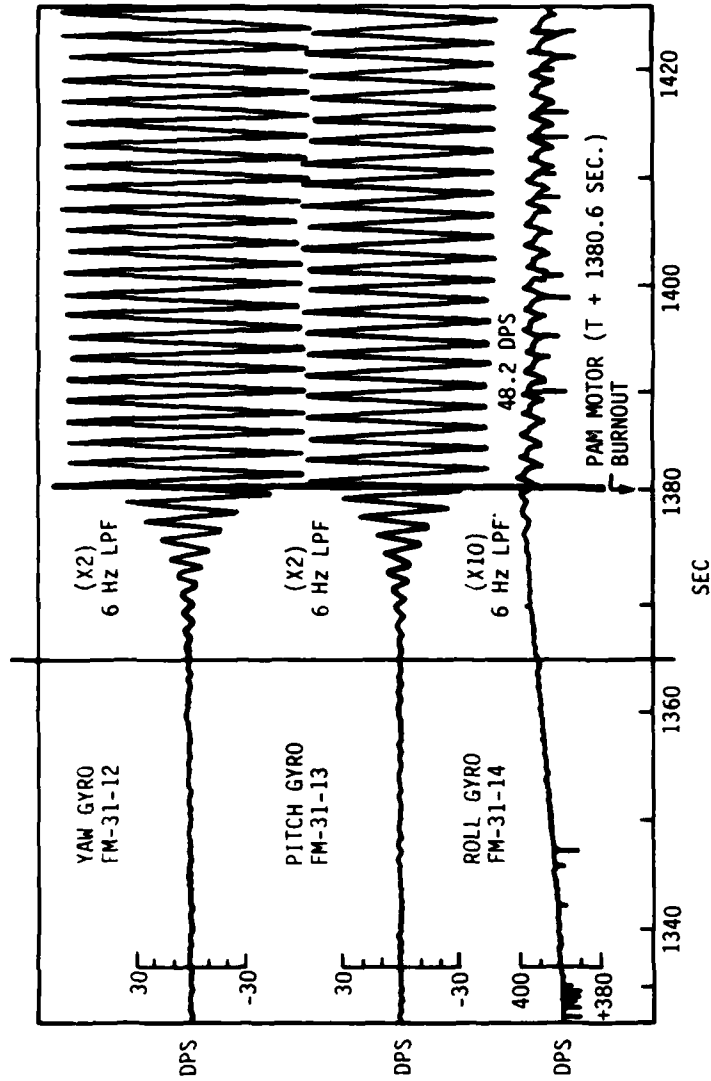


Fig. 5. Flight data--RCA-C'.

burnout, the onset of coning motion is evident. At burnout, the half-cycle/sec. variation in spin velocity is now sustained. The results of analysis have shown that the initial state of the sloshing liquid markedly affects the steady state oscillations in roll rate. Close examination of Figure 5 shows some beating superimposed on the coning motion, having a period of about 20 seconds. This is borne out from analysis. It is again evident from the numerical solution that the initial state of the fluid affects the magnitude and frequency of the beat phenomenon just mentioned.

The implication of the effect of the fluid stores initial state is an interesting research question. Study of varying initial conditions could yield the knowledge that one particular induced state of the fluid could yield reduced coning motion. The controlled sloshing state of the fluid produces challenging opportunities to optimally control the spacecraft attitude.

PROPOSED RESEARCH

The next topic which should be investigated after modeling the system dynamics is the control of the vehicle to reduce or eliminate the coning without expending large amounts of station keeping fuel. This can be studied by formulating and solving an optimal control problem which minimizes the fuel expended by the vehicle subject to thrust constraints. This is known as a nonlinear two point boundary value problem.

An alternative control scheme would use the fluid on board as a control mass to minimize the deviation from the desired state of spin by solving the nonlinear two point boundary value problem.

This type of optimal control would provide a baseline from which to determine how closely other control laws perform. These controls are not

practical to implement because they are not in so-called feedback form. A more practical control law would be generated by linearizing the system and control equations and solving the linear regulator problem. This consists of minimizing a functional containing the state and control variables. This control law is in feedback form and linear in the system states but will be time varying. A drawback lies in the fact that all the state variables must be known. This is not feasible in this system because only the location relative to the earth and the roll, pitch, and yaw signals can be obtained for control purposes. This problem may be overcome by using an observer or state estimator to estimate the unknown states.

The solution to the linear regulator problem combined with the state estimator gives a linear feedback control law which minimizes the deviations from the desired state with minimal control effort. Control performance of the linear feedback controller can then be compared to the solution of the nonlinear two point boundary value problem (NLTBPV) because the system is inherently nonlinear.

The study proposed requires the solution of a large number of ordinary differential equations which can seriously overload many computers. Previous work done with ISU's AS/6 mainframe proved to be marginal and a faster machine would be more ideal to solve the NLTBPV.

In summary the proposed research would,

- 1) Solve a NLTBPV using the on board thrusters as control variables.
- 2) Solve a NLTBPV using the fuel as a control mass.
- 3) Solve the linear regulator problem using the on board thrusters as control variables.

- 4) Solve the linear regulator problem using the fuel as a control mass.
- 5) Develop a state estimator.
- 6) Compare the performance of the linear regulator with state estimator to the NLTBPVP solution.

REFERENCES

1. Sayar, B. A., and Baumgarten, J. R. "Pendulum Analogy for Nonlinear Fluid Oscillations in Spherical Containers," ASME Trans., Journal of Applied Mechanics, December 1981, Vol. 48, pp. 769-772.
2. Sayar, B. A. and Baumgarten, J. R. "Linear and Nonlinear Analysis of Fluid Slosh Dampers," AIAA Journal, Vol. 20, No. 11, Nov. 1982, pp. 1534-1538.
3. Roberson, R. E. "Torques on a Satellite Vehicle from Internal Moving Ports," Trans. ASME, Journal of Applied Mechanics, Vol. 25, June 1958, pp. 196-200.
4. Grubin, C. "Dynamics of a Vehicle Containing Moving Parts," Trans. ASME, Journal of Applied Mechanics, Vol. 29, September 1962, pp. 486-488.
5. Kane, T. R. and Sobala, D. "A New Method for Attitude Stabilization," AIAA Journal, Vol. 1, No. 6, June 1963, pp. 1365-1367.
6. Edwards, T. L. and Kaplan, M. H. "Automatic Spacecraft Detumbling by Internal Mass Motion," AIAA Journal, Vol. 12, No. 4, April 1974, pp. 496-502.
7. Kane, T. R., Dynamics, Holt, Rinehart, and Winston, N.Y., 1968.

1983-84 USAF-SCEEE RESEARCH INITIATION PROGRAM

Sponsored by the

AIR FORCE OFFICE OF SCIENTIFIC RESEARCH

Conducted by the

SOUTHEASTERN CENTER FOR ELECTRICAL ENGINEERING EDUCATION

FINAL REPORT

SURFACE POTENTIAL AS A LASER DAMAGE DIAGNOSTIC

Prepared by: Dr. Michael Becker

Academic Rank: Associate Professor

Department and
University: Electrical & Computer Engineering Department
University of Texas

Research Location: Air Force Weapons Laboratory

Date: March 1985

OBJECTIVE

The objective both proposed and attained in this project was to investigate the relationship between surface potential changes, including free surface charge accumulation, and laser induced damage on a wide variety of optical surfaces. This is the first such investigation relating surface potential and laser damage. The Kelvin technique for surface potential measurement was adapted from work in other areas of surface science. Unanticipated results were found for dielectric materials where extensive surface charging followed by a slow decay was observed. A detailed account of our experimental findings is presented in Appendix I.

SCOPE OF WORK

All the experimental work was completed during the one year grant period and one technical conference presentation was made. After the termination date of the grant, work continued on a second conference presentation and two written papers for the respective conference proceedings. These contributions are listed in the following section. The more detailed of these two papers serves as the technical report on this work and is attached as Appendix I.

Conferences and Publications

Conference Presentations:

"Surface Potential as a Laser Damage Diagnostic," 16th ASTM Laser Damage Symposium, Boulder CO, October 1984.

"Surface Potential as a Laser Damage Diagnostic," Southwest Conference on Optics, Albuquerque, N.M., March 1985.

Publications:

M. F. Becker, J. A. Kardach, A. F. Stewart, and A. H. Guenther, "Surface Potential as a Laser Damage Diagnostic," 16th ASTM Laser Laser Damage Symposium, NBS Special Publication, Boulder CO, 1985.

M. F. Becker, J. A. Kardach, A. F. Stewart, and A. H. Guenther, "Surface Potential as a Laser Damage Diagnostic," Proceedings of the Southwest Conference on Optics, SPIE, Bellingham WA, 1985.

Appendix I

Surface Potential as a Laser Damage Diagnostic

M. F. Becker

Electrical and Computer Engineering Department
The University of Texas
Austin, TX 78712

J. A. Kardach, A. F. Stewart, and A. H. Guenther

Air Force Weapons Laboratory
Kirtland, NM 87117

We investigated the relationship between surface potential changes and N-on-1 laser surface damage on a wide range of materials. The surface potential or work function difference was measured as a function of position by a small non-contacting Kelvin type probe. This design and operation of the probe is described. Using this probe, the change in surface potential due to laser irradiation was mapped with a ~ 1 mm resolution. Although no consistent pre-damage changes in potential were observed, all larger damage features had surface potential changes associated with them. The insulating materials studied, fluoride and oxide thin films, bare fused silica and magnesium fluoride substrates, all showed the accumulation of negative charge in areas more than ten times larger in diameter than the laser beam spot or damage area. This initial charge was observed to decay on the time scale of hours to a lower fixed value of potential associated with permanent damage to the surface.

Key words: laser damage, N-on-1 damage, surface potential, contact potential, work function, surface charge, charge decay.

1. Introduction

This is the first reported study of the relationship between surface potential and laser induced damage of insulating and semiconducting optical materials, and the first such study for metals damaged at wavelengths shorter than 10.6 microns [1]. By surface potential we simply mean the difference in work functions or the contact potential between two materials. Usually one material is employed as a reference; stainless steel was used in this study. Surface potential is related to a number of material surface properties which may be of interest in the study of laser damage. For metals and semiconductors, surface potential is sensitive to band bending at the surface which can be related to surface preparation procedures, fixed surface states, or adsorbates. For dielectric materials, surface potential is sensitive to these same effects as well as to fixed charge either in the form of surface or volume charge distributions or even permanent electric dipole states.

Our interest in surface potential was aroused by our previous experiments utilizing charge emission into vacuum as a diagnostic for the onset of laser damage or more importantly as a precursor to laser induced damage [2-4]. Although no charge emission was observed prior to damage in N-on-1 tests for silicon and ThF_4 thin films in these earlier experiments, all other materials, including copper mirrors and several types of oxide thin films, showed charge emission at fluences as low as 1/20 of the 1-on-1 damage threshold. The copper mirrors exhibited a reduction of emission for repeated shots to the same site (N-on-1) as one would expect in a conditioning or cleaning effect. To further complicate the situation, all of these materials showed either accumulation or hardening in N-on-1 tests. The idea of a non-contacting charge sensitive technique which could measure changes in the surface state of a sample appeared an attractive method to study these N-on-1 effects.

Previously, Porteus, et al. [1] used Auger electron imaging as a qualitative measure of laser induced changes in work function. In our experiments we have applied a different technique which is capable of giving spatially resolved quantitative maps of surface potential over the region in and around the laser interaction area. This technique utilizes what is known as a Kelvin probe or the Kelvin method to measure surface potential without making physical contact with the surface, and as such is also non-intrusive.

In this paper we first describe the Kelvin probe apparatus used in our experiments as well as the other diagnostics. The sample set was chosen to include a wide variety of optical material classes, including copper mirrors, silicon crystals, dielectric thin films and bare dielectric

substrates. After the experimental samples and cleaning procedures are described, data taken by the Kelvin probe from a series of N-on-1 experiments will be presented. Finally, the implications of these measurements for the understanding of laser induced damage will be discussed.

2. Experimental

2.1 Kelvin Probe

The Kelvin method for measuring surface potential is essentially one of adjusting the dc voltage on the test capacitor formed by the sample surface and the reference electrode so as to null out ac variations in the capacitor voltage caused by physically dithering the reference electrode. In these experiments, we used a feedback technique which would adjust the dc voltage for an ac null automatically [5,6]. The probe assembly is shown in figure 1. The probe electrode tip is 1 mm in diameter and is on a carrier which may be positioned over the laser beam axis and adjusted in spacing from the sample or may be withdrawn when laser irradiation takes place. The sample location is also mechanically controlled in order to position it to new irradiation sites and to scan the sample under the probe in a raster pattern for measuring surface potential contours. Typical raster scans were squares of either 5 mm or 10 mm on a side. Data points were taken at 0.25 mm intervals on each row while the scan rows were separated by 0.25 mm for the small squares and 0.5 mm for the large squares. The scan rate of the stepper motors was the chief factor limiting data acquisition speed. A magnetic drive is used to dither the probe at 88 Hz with a peak-to-peak amplitude of 0.1 mm. It requires a drive signal at 44 Hz of about 5 W.

In operation, the probe tip is placed so that its closest approach to the sample surface is about 25 μ m as viewed by a long working distance Questar microscope with a CCTV system. This view is shown in figure 2. Since the capacitance between the probe and a grounded sample is about 0.1 pF and the capacitance with a dielectric sample 9.5 mm thick backed by a ground plane is considerably less, eliminating stray capacitance was crucial [7,8]. To do this we mounted a low input capacitance electrometer op-amp directly to the end of the probe arm. Other metallic objects were kept as far away as possible from the oscillating probe tip. As a result, the probe sensitivity to surface potential changes was less than 10 mV. This level is also of the same order as the noise level and the reproducibility of the measurements.

The feedback circuit used to automatically adjust the probe dc voltage to be equal to the surface potential is shown in figure 3. The preamp has an ac voltage gain of 11 while the lock-in amplifier is adjusted for the maximum gain possible without oscillation with a 0.3 sec damping time. The dc output of the lock-in is fed back through a high impedance path to supply the surface potential to the probe. The dc output is also read by a digital voltmeter which was interfaced to the laboratory mini-computer used for automatic data reduction. Only the critical adjustment of setting the probe height above the sample surface was done manually. The probe was always scanned over the unirradiated site to obtain a background potential map which was later subtracted from the data to obtain the laser produced change in surface potential. The probe was next removed, the sample irradiated, and the probe returned to scan for the data. Sequences of scans over time could also be programmed in order to monitor the time decay of laser induced effects. The time needed to scan a 10 mm square was 16 minutes, and about half that for the 5 mm square.

2.2 Diagnostics

The optical and diagnostic layout is shown in figure 4. The fundamental 1.06 μ m wavelength of a Molelectron Q-switched Nd:YAG laser was used at a rep rate of 10 Hz. It was focused on the sample with a 2 m focal length lens. Time and space profiles were checked regularly. The pulse length was 18 ns FWHM, and the focused spot was typically 0.39 mm in diameter at the $1/e^2$ points. The beam was scanned in both the vertical and horizontal directions with a narrow slit at the focal plane. An electromechanical shutter was used by the computer to control the irradiations. Pulse energy for every shot was recorded and statistics were computed. The standard deviation in pulse energies for 10 to 100 pulses was typically 1% or less and never greater than 3%.

After a sequence of sites had been tested on a sample it was examined under a Nomarski microscope to determine the corresponding damage morphology. Although exact damage thresholds were not measured, data was generally taken at fluences between 1/2 and 2 times threshold with an exposure of 10 or more pulses in order to attempt to observe pre-threshold as well as permanent damaging effects.

2.3 Samples

The sample set consisted of OFMC diamond turned copper mirrors, single crystal [111] silicon substrates, MgF₂ half wave (at 1.06 μ m) thin films on fused silica, HfO₂ half wave thin films on fused silica, ThF₄ half wave thin films on fused silica, bare oriented crystalline MgF₂ substrates, crystalline quartz and bare fused silica substrates. The silicon and fused silica substrates used

in this study were fabricated using the controlled grinding technique. Total integrated scattering (TIS) measurements on witness samples indicated an average surface roughness of $5 \pm 2 \text{ \AA}$ RMS for both substrate types. TIS measurements were repeated on fused silica witness substrates after film deposition. The measured surface roughness of half wave MgF_2 films on fused silica was found to be $5 \pm 1.5 \text{ \AA}$ RMS. In contrast, half wave MgF_2 films on fused silica were found to have an average roughness of $10 \pm 1.5 \text{ \AA}$ RMS. In subsequent examination of these samples under the Nomarski microscope, only the MgF_2 films were observed to have a definite microstructure and a "parquet tiled" appearance resulting presumably from columnar growth.

The cleaning procedure did not require touching the sample surfaces with any solid object. The samples were cleaned in a photoresist spinner with deionized water and high purity acetone and blown off with dry nitrogen. The dielectric samples were pre-cleaned by spinning on a collodion layer and subsequently lifting it off to remove any tenaciously held particulates.

3. Experimental Data

In this section, we present a selection of typical data obtained by the Kelvin probe and correlations with microscopically observed damage morphology.

3.1 Dielectric thin films

Figures 5 and 6 illustrate the two graphic formats we used for data presentation. Figure 5 is a three dimensional projection plot of the potential change with a small, unscaled contour plot below, and figure 6 is a full size contour plot. The large contour plots and the raw data arrays were used to extract all numerical data since small changes in surface potential were readily apparent. However, the three dimensional projections are more easily viewed, especially when the change in potential is in an upward direction. For this reason, we show only projection plots in the remainder of this paper with their potential axis polarities oriented such that the change in potential at the damage site is always upwards.

The data in figures 5 and 6 is for an MgF_2 thin film irradiated with 10 pulses at 69 J/cm^2 . It is representative of all the thin films studied in these experiments. Note that the observed potential change is negative for this sample. Subsequent microscopic examination showed large scale damage covering the entire beam footprint. The profile of the change in surface potential was 4 to 6 mm in diameter with a magnitude of nearly half a volt. This diameter is distinctly larger than both the laser spot and the resolution of the Kelvin probe. In addition, all large scale damaging events were detected by a similar potential change. No potential changes were detected when laser damage was not observed. In these N-on-1 experiments, small damage pits were observed only on the MgF_2 film. About 50% of these small damage sites were detected by the Kelvin probe as small changes in surface potential, while the remaining sites resulted in no observable change. The surface potential change on these thin film samples was observed to decay with time. This effect and its relation to surface charge will be discussed in a later section.

3.2 Conductors

The surface potential changes on damaged silicon and copper, although similar to each other in diameter and magnitude, were opposite in polarity. In fact, copper was the only material that showed a positive surface potential change when damaged. (Bare MgF_2 substrates also showed a positive potential change but only when bulk cracking was created by exit surface damage.) A typical surface potential plot for single crystal silicon is shown in figure 7. The object to the left in the field is the adjacent, previous damage site.

For silicon, not all microscopically observed surface damage could be detected by the Kelvin probe. When pits were formed, indicating a more severe degree of damage, the potential changed as shown in figure 7. However, when only melting and resolidification occurred with the accompanying formation of ripples or ridges, no change in surface potential could be observed. No pre-damage changes in surface potential were ever detected.

The OFHC diamond turned copper was always observed to damage by melt pit formation, and these pits were detected by their accompanying changes in surface potential. As for the silicon, the observed diameter was limited by the 1 mm resolution of the Kelvin probe tip. One case of pre-damage change in the surface potential was observed for copper. In three other cases near the threshold fluence where no observable surface damage occurred, no surface potential change could be detected.

The surface potential change for the conductive samples was found to be constant and reproducible over time. In this case, no decaying component was observed as was for the dielectric samples.

3.2 Bare dielectric substrates

The bare dielectric substrates seemed to be more unpredictable in their behavior. Experimental difficulty was experienced due to their tendency to damage on the exit surface. In N-on-1 experiments for large enough N, damage would propagate from the rear to the front surface before surface damage was initiated on the front surface. Experiments were thus limited to less than 10-20 pulses per site.

A typical potential contour plot for bare SiO₂ is shown in figure 8. Both fused silica and the polycrystalline MgF₂ substrates showed similar behavior. The surface potential change was 4 to 6 mV in diameter but smaller in magnitude than for the thin films. The Kelvin probe noise level seemed to increase in the vicinity of the damage sites.

Microscopy of the damage sites on the bare substrates showed less distinct damage features which resembled surface erosion. Larger diameter surface damage sites were detected by the Kelvin probe while several smaller diameter damage sites and all undamaged sites showed no surface potential change. These surface potential changes were observed to decay with time just like those for the thin film samples, and will be discussed later.

The MgF₂ substrates showed unusual behavior when a crack from the rear surface propagated to the front. The arrival of the crack at the front surface would be accompanied by a sudden strong positive change in the surface potential. This change may be associated with the piezoelectric properties of the material or with the exoemission of electrons from the crack which leaves the substrate positively charged [9].

4. Discussion

4.1 Surface charge density

One of the most interesting and unexpected findings in these experiments was the significance of surface charge effects on the dielectric samples. First it will be necessary to relate the surface potential measurements to surface charge density. In measuring contact potential as between two conducting samples, the Kelvin probe separation from the surface does not affect the potential difference so long as the increase in distance can be compensated for by an increase in the gain in the feedback loop. The case of free charge on the surface of a dielectric material is entirely different. It resembles very closely the case of fixed charge in a Schottky or MOS device. The potential required to place an equal and opposite charge on the probe tip is now dependent on the tip to surface distance. The surface potential is related to the surface charge density (ignoring fringing field effects) by the parallel plate capacitor formula:

$$Q_s/A = \epsilon_0 V/d \quad (1)$$

where Q_s is the total surface charge under the probe, V is the surface potential, and d is the mean probe height over the surface. Typically, d was 70 μm so that a charge density of $1.26 \times 10^{-11} \text{ C/cm}^2$ per volt of potential change was measured in these experiments. As an example, a spot 4 mm in diameter with a potential change of 0.1 V would represent about 1.3×10^6 negative charges. A rather large amount of charge is spread from the 1/3 mm diameter laser damage site to a distance of several mm.

Closer analysis of the surface potential contour maps reveals that the effect is even more widespread. The shape of the potential change peak is flat topped with a sharp drop at a diameter of 4 to 6 mm. The drop is not to zero however, since there is about 10% remaining change in surface potential which decreases slowly with distance for another several mm. This might lead an investigator to rethink the problem of site spacing for laser damage experiments on dielectric samples. The charge related effects of a damaging event extend across the sample surface much further than would be expected from either the observed damage morphology or even the incident beam diameter.

4.2 Charge decay

Detailed measurements of the surface potential decay as a function of time were made on the HfO₂ thin film and on the MgF₂ bare substrate. The results for the two were similar and the thin film data will be presented in detail.

Figures 9a-c show selected surface potential maps of the damage site at $t=0$, 1 hour, and 2 hours respectively. Note that each scan took about 16 min so that there was an initial delay of 8 min to scan to the beam center. Subsequent scans of the center were spaced by intervals equal to the scan time plus a programmed inter-scan delay time.

In figure 9, the potential change is observed to decay without significant migration of the charge. Presumably recombination, not diffusion, is responsible for the decay. It is not certain whether the recombination charge comes from the air or the material, however, these sites could be discharged artificially with airborne charge by using a static charge gun or by creating another charge cloud from a nearby laser damage site.

The decay of the surface potential peak values obtained from the scans shown in figure 9 is plotted in figure 10. From the simple linear graph, we infer a single exponential decay process with a time constant of 62 min. The decay asymptote is not zero potential change. There is permanent damage, and some fixed change is expected. In this case the fixed part of the potential change is -25 mV as compared to the initial peak of -100 mV. As indicated previously, similar data was obtained for the MgF₂ bare substrate for which a 30 min time constant was observed.

4.3 Conductors

Obviously no such free charge effects will be observed for conductive samples. An earlier study using Auger analysis of damage sites on OFHC copper surfaces demonstrated the effects of surface shape changes (pit formation) on the work function [1]. We also observed these effects on copper with 1.06 μ m illumination. There is no way of telling if the sign of the change observed by the authors of reference [1] matches that measured by the Kelvin probe since they used a different method which measured only qualitative potential changes. Similar potential changes were observed at damage pits on silicon but of opposite polarity. There is no obvious reason why such a polarity difference should exist.

4.4 Pre-damage effects

One of the objectives for undertaking these experiments was to observe sub-damage threshold changes in the surface potential on those materials which emitted charge at 1/10 to 1/20 of the threshold fluence, or showed accumulation or cleaning effects. In this respect we were unsuccessful. One possible pre-threshold event was observed for copper out of four total observations. If a sub-threshold surface potential effect exists, it is not large.

5. Conclusions

We observed distinct surface potential signatures associated with laser damage. For conductors, silicon and OFHC copper, small diameter surface potential changes were detected in conjunction with pit formation. No surface potential change was seen on silicon when only surface ripples or ridges formed. Copper differed from silicon and all other materials in that the sign of the surface potential change was positive.

All of the insulating materials showed surprisingly large diameter surface potential changes around the laser damage spots. These potential changes were observed to extend over an area 4 to 6 mm in diameter as compared to the 1 mm diameter Kelvin probe resolution and the 1/3 mm laser beam spot diameter. These charged areas contained as many as 10⁷ negative charges. In light of this large diameter charging effect, the spacing of adjacent sites in laser damage experiments on insulating substrates and thin films should be carefully reexamined.

The charge on the insulators' surfaces was observed to decay with time constants on the order of an hour to a constant level whose value is 1/4 or less of the initial value. We associated this change with recombination, and the fixed change in potential with the effect of surface geometry and damage morphology on surface potential.

No consistent pre-damage potential changes were observed indicating that the charge emission and surface cleaning observed in previous experiments do not have a significant effect on surface potential. Evidently these effects are not appropriate for study by surface potential methods.

This research was supported by an AFOSR/SCEE/RIP grant and by the DoD Joint Services Electronics Program at The University of Texas.

6. References

- [1] J.O. Porteus, D.L. Decker, D.J. Grandjean, S.C. Seitel, and W.N. Faith, "Defect-Damage Resistant Copper Mirrors," in 11th ASTM Symposium on Optical Materials for High Power Lasers, NBS Special Publication #568, Boulder CO (1979).

- [2] M.F. Becker, F.E. Domann, A.F. Stewart, and A.H. Guenther, "Charge Emission and Related Precursor Events Associated with Laser Damage," 15th ASTM Symposium on Materials for High Power Lasers, NBS Special Publication, Boulder CO (1984).
- [3] J.K. Jhee, M.F. Becker, and R.M. Walser, "Charge Emission and Accumulation in Multiple-Pulse Damage of Silicon," 16th ASTM Symposium on Materials for High Power Lasers (elsewhere in these proceedings), NBS Special Publication, Boulder CO (1985).
- [4] M.F. Becker, Y.K. Jhee, M. Bordelon, and R.M. Walser, "Charged Particle Exoemission from Silicon During Multi-Pulse Laser Induced Damage," 14th ASTM Symposium on Optical Materials for High Energy Lasers, NBS Special Publication #669, Boulder CO (1983).
- [5] Y. Petit-Clerc and J.D. Carette, "New Feedback Kelvin Probe," Rev. Sci. Inst. 39, 933 (1968).
- [6] J.C. Campuzano and R.G. Greenler, "Instrument for Combining Reflection-Absorption Infrared Spectroscopy with other Surface-Sensitive Techniques," Rev. Sci. Inst. 52, 678 (1981).
- [7] R.J. D'Arcy and N.A. Surplice, "The Effects of Stray Capacitance on the Kelvin Method for Measuring Contact Potential Difference," J. Phys. D: Appl. Phys. 3, 482 (1970).
- [8] N.A. Surplice and R.J. D'Arcy, "A Critique of the Kelvin Method of Measuring Work Functions," J. Phys. E: Sci. Inst. 3, 477 (1970).
- [9] P. Braunlich, "Exoelectron Emission from Optical Surfaces," 2nd ASTM Symposium: Damage in Laser Materials, NBS Special Publication #341, Washington, D.C. (1970).

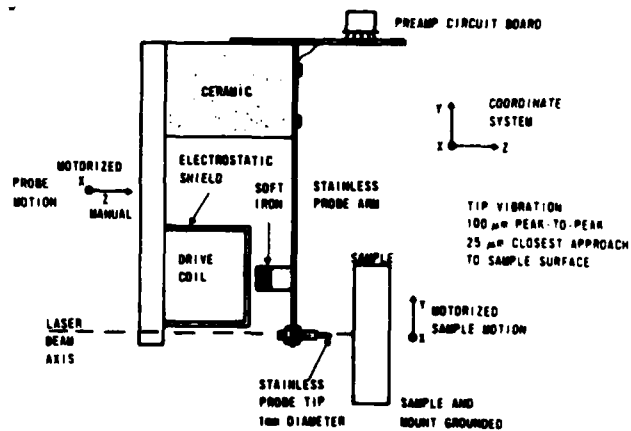


Figure 1. Mechanical diagram of the Kelvin probe.



Figure 2. Photograph of the Kelvin probe over a silicon sample. The probe is higher than its usual operating distance above the sample surface.

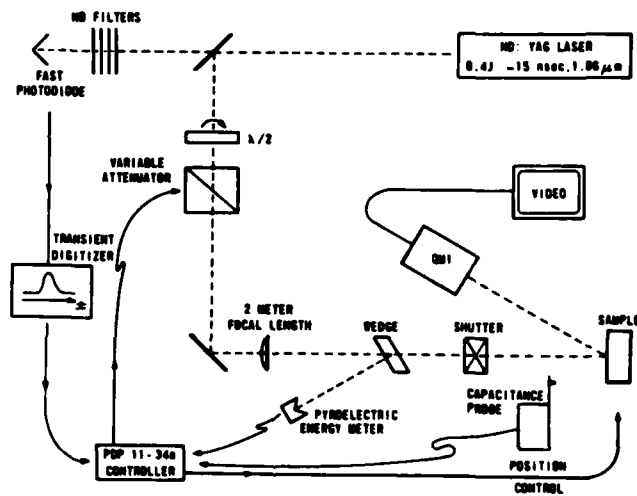


Figure 4. Optical layout and laser diagnostics.

KELVIN PROBE INSTRUMENTATION

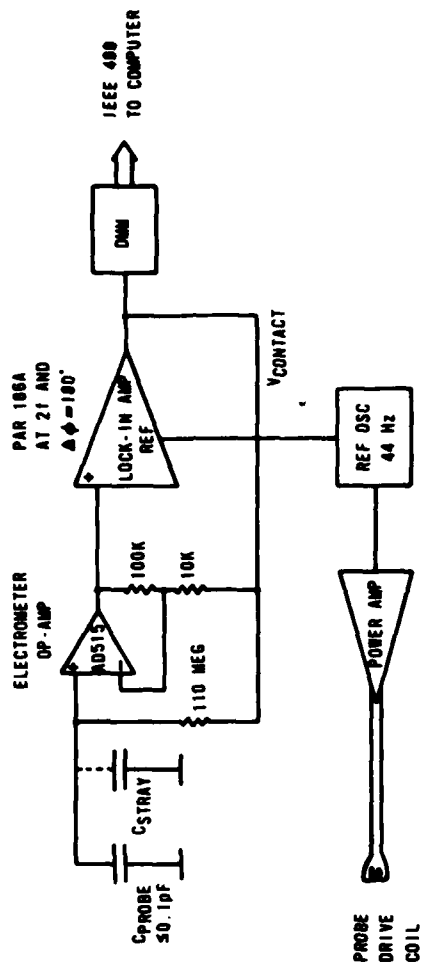


Figure 3. Schematic diagram of the Kelvin probe instrumentation.

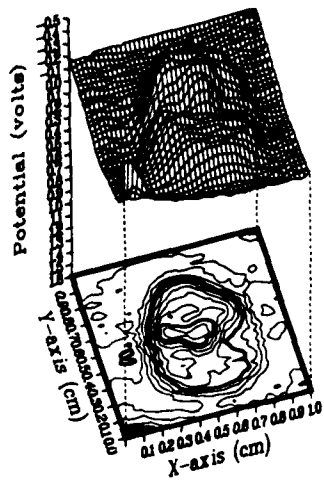


Figure 5. Surface potential change contour plot for the MgF₂ thin film irradiated by 10 pulses at 69 J/cm². The format is discussed further in the text.

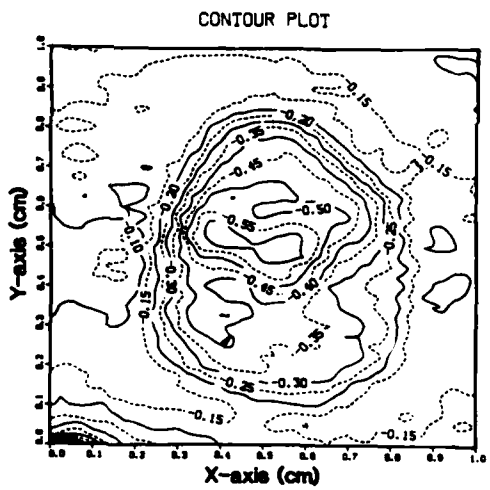


Figure 6. Same subject as figure 5, but plotted in a different format (see text).

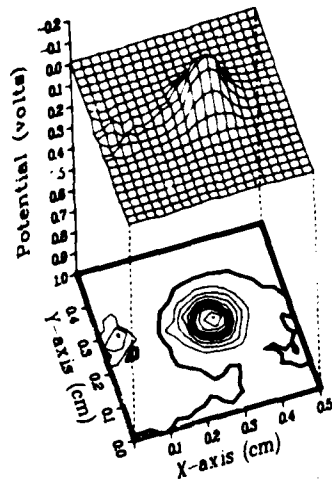


Figure 7. Surface potential change map for single crystal silicon irradiated by 1 pulse at 3.7 J/cm^2 . The feature at the left is the adjacent previous damage site.

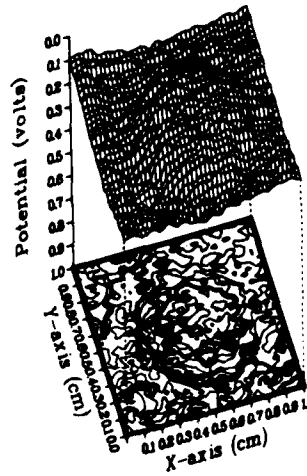


Figure 8. Surface potential change map for bare fused silica irradiated by 10 pulses at 140 J/cm^2 .

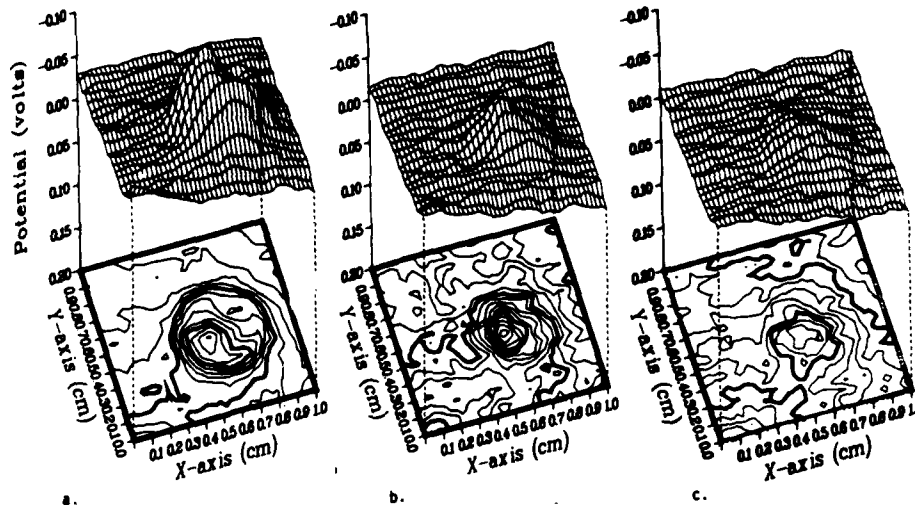


Figure 9. Surface potential maps for the HfO_2 thin film irradiated by 10 pulses at 50 J/cm^2 showing the peak decay at times; a. $t=0$; b. $t=1$ hour; c. $t=2$ hours; (left to right).

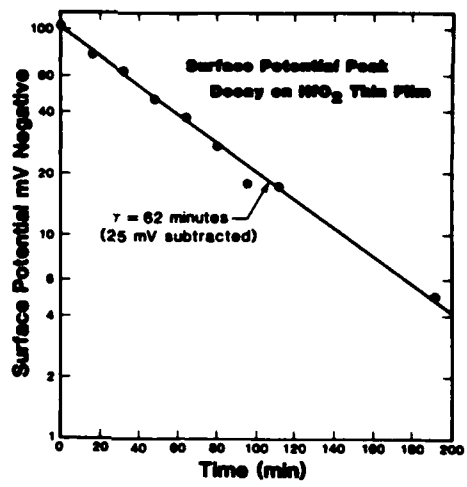


Figure 10. Surface potential peak height versus time for the same site on HFO₂ as Figure 9. The constant -25mV has been subtracted since it is the asymptotic value for the exponential decay.

1983-84 USAF-SCEEE RESEARCH INITIATION PROGRAM

Sponsored by the

AIR FORCE OFFICE OF SCIENTIFIC RESEARCH

Conducted by the

SOUTHEASTERN CENTER FOR ELECTRICAL ENGINEERING EDUCATION

FINAL REPORT

A STUDY OF ALOT WAVEGUIDES FOR ELECTROSTATICALLY

VARIABLE SAW DELAY LINES

Prepared by: Dr. Henry Bertoni

Academic Rank: Professor

Department and
University: Electrical Engineering and Computer Science
Polytechnic Institute of New York

Research Location: Air Force Rome Air Development Center

Date: July 1984

Abstract

Electrostatically variable SAW delay has been demonstrated for the in-plane configuration where the D.C. electrodes are placed on the same surface as the SAW and on either side of the propagation path. In this study we investigate the properties of the guided waves when the electrodes are covered with an AlN layer to form a slot waveguide. Both semi-infinite and finite width electrodes are considered, with the former giving superior performance, but the latter employing a thinner AlN layer. Use of slot waveguides for frequencies in the vicinity of 1 GHz are found to permit close electrode spacing, for high voltage sensitivity, with path loss only a few dB greater than the free-surface attenuation.

<u>Table of Contents</u>	<u>Page</u>
I. Introduction	1
II. Guided Waves	5
A. Straight- Crested Surface Waves	5
B. Dispersion Relations for the Guided Waves	10
III. Guided Waves for Semi-Infinite Electrodes	13
IV. Guided Waves for Electrodes of Finite Width	26
A. Guided Waves for $Rek_1 \geq Rek_2 > Rek_3$	27
B. Guided Waves for $Rek_2 > Rek_1 > Rek_3$	34
C. Comparison of Semi-Infinite and Narrow Electrodes	43
V. Delay Line Path Loss	46
A. Field Miss-Match Factor R_V for Semi-Infinite Electrodes	47
B. Field Miss-Match Factor R_V for Finite Width Electrodes	51
VI. Conclusion	58
VII. References	60

LIST OF FIGURES

- Figure 1. Top view of the electrodes for the in-plane field configuration.
- Figure 2. Cross-section view of the slot waveguides; a) guide having semi-infinite electrodes; b) guide having finite width electrodes.
- Figure 3. Frequency variation of the SAW attenuation constants on LiNbO_3 for a free surface ($\text{Im } k_1$) and for a surface covered with 600 Angstroms of Al ($\text{Im } k_2$).
- Figure 4. Geometrical construction for finding the solution of the dispersion equation for slot waveguide having semi-finite electrodes.
- Figure 5. Dependence of the propagation constants $\text{Re } \kappa$ on slot width $2a$ for the modes of a waveguide with semi-infinite electrodes ($f=1\text{GHz}$, $H=0.677 \mu\text{m}$).
- Figure 6. Dependence on slot width $2a$ of the attenuation due to the metalization $\text{Im}(\kappa-k_1)$ for the modes of a waveguide with semi-infinite electrodes ($f=1\text{GHz}$, $H=0.677 \mu\text{m}$).
- Figure 7. Frequency dependence of the propagation constants $\text{Re } \kappa \leq \text{Re } \kappa_1$ of the various modes for $2a=20 \mu\text{m}$ and $H=0.677 \mu\text{m}$ plotted as the deviation $\text{Re}(k_1-\kappa)$.
- Figure 8. Frequency dependence of the attenuation due to the metalization $\text{Im}(\kappa-k_1)$ of the various modes for $2a=20 \mu\text{m}$ and $H=0.677 \mu\text{m}$.
- Figure 9. Frequency dependence of the propagation constant $\text{Re } \kappa \leq \text{Re } \kappa_1$ for $2a=10 \mu\text{m}$ and $H=0.677 \mu\text{m}$ plotted as the deviation $\text{Re}(k_1-\kappa)$.
- Figure 10. Frequency dependence of the attenuation due to the metalization $\text{Im}(\kappa-k_1)$ for $2a=20 \mu\text{m}$ and $H=0.677 \mu\text{m}$.
- Figure 11. Variation with AlN layer thickness H of the propagation constant $\text{Re } \kappa \leq \text{Re } \kappa_1$ for $f=1\text{GHz}$ and guides of width $2a=10, 20 \mu\text{m}$.
- Figure 12. Construction for finding solutions to the dispersion relation in the absence of loss for waveguides having finite width electrodes when $k_1 \geq k_2 > k_3$.
- Figure 13. Variation of the propagation constants $\text{Re } \kappa$ with slot width $2a$ for the modes of slot guide having electrode width $w=5 \mu\text{m}$, $H=0.6 \mu\text{m}$ and $f=1 \text{GHz}$.
- Figure 14. Variation of the propagation constant $\text{Re } \kappa$ with slot width $2a$ for the modes of slot guide having electrode width $w=10 \mu\text{m}$, $H=0.6 \mu\text{m}$ and $f=1 \text{GHz}$.

- Figure 15. Dependence on slot width $2a$ of the attenuation due to the electrode metalization for modes of a slot guide having $w=5 \mu\text{m}$, $H=0.6 \mu\text{m}$ and $f=1 \text{ GHz}$.
- Figure 16. Construction for finding solutions to the dispersion relation in absence of loss for waveguides having finite width electrodes when $k_2 > k_1 > k_3$.
- Figure 17. Dependence on slot width $2a$ of the propagation constants $\text{Re}k$ for the modes of slot guide having $w=5 \mu\text{m}$, $H=0.2 \mu\text{m}$ and $f=1 \text{ GHz}$.
- Figure 18. Dependence on slot width $2a$ of the attenuation due to electrode metalization for modes of slot guide having $w=5 \mu\text{m}$, $H=0.6 \mu\text{m}$ and $f=1 \text{ GHz}$.
- Figure 19. Dependence on slot width $2a$ of the propagation constants $\text{Re}k$ for the modes of slot guide having $w=10 \mu\text{m}$, $H=0.6 \mu\text{m}$ and $f=1 \text{ GHz}$.
- Figure 20. Dependence on slot width $2a$ of the attenuation due to electrode metalization for modes of slot guide having $w=5 \mu\text{m}$, $H=0.6 \mu\text{m}$ and $f=1 \text{ GHz}$. For the $n=-1$ mode $\text{Im}(\kappa-k_1) \approx 6.5 \times 10^{-5} \mu\text{m}^{-1}$.
- Figure 21. Frequency dependence of the propagation constants of slot guide having $w=10 \mu\text{m}$, $2a=20 \mu\text{m}$ and $H=0.2 \mu\text{m}$, plotted as the deviation $\text{Re}(\kappa-k_1)$.
- Figure 22. Frequency dependence of the attenuation due to metalization for the modes of slot guide having $w=10 \mu\text{m}$, $2a=20 \mu\text{m}$ and $H=0.2 \mu\text{m}$.
- Figure 23. Dependence on transducer width $2b$ of the field miss-match factor for slot guides having semi-infinite electrodes for $2a=10, 20 \mu\text{m}$, $H=0.677 \mu\text{m}$ and $f = 1 \text{ GHz}$.
- Figure 24. Dependence on transducer width $2b$ of the field miss-match factor for the two propagating modes for guide width $2a=40 \mu\text{m}$, $H=0.677 \mu\text{m}$ and $f = 1 \text{ GHz}$.
- Figure 25. Frequency dependence of the field miss-match factor for the cases $2a=2b=10, 20 \mu\text{m}$ of slot guides with semi-infinite electrodes and $H=0.677 \mu\text{m}$.
- Figure 26. Dependence on transducer width $2b$ of the field miss-match factor for the modes of slot guide having finite width electrodes ($2a=w=10 \mu\text{m}$, $H=0.2 \mu\text{m}$, $f=1 \text{ GHz}$).
- Figure 27. Dependence on transducer width $2b$ of the field miss-match factor for the modes of slot guide having finite width electrodes ($2a=20 \mu\text{m}$, $w=10 \mu\text{m}$, $H=0.2 \mu\text{m}$, $f=1 \text{ GHz}$).

I. Introduction

Studies have shown that the time delay of a surface acoustic wave (SAW) delay line is changed by the application of a D.C. bias field [1-4]. For some crystal orientations, the change in delay is proportional to the applied field [4,5]. While the change in delay time is not large, with sufficient path length and/or applied voltages it should be possible to achieve a delay change of $\pm 1/2$ of an R.F. cycle. This effect can serve as the basis for phase shifters, such as those employed in phased array radar antennas. SAW phase shifters, fabricated by photolithographic techniques, would be much less expensive than the current latching ferrite phase shifters.

It is desirable that the path loss in the device be low, and that the voltage V_{DC} necessary to achieve a change in delay time of $\pm 1/2$ an R.F. cycle be as low as possible. One method that has been proposed to achieve low values of V_{DC} is the in-plane configuration [3] shown in Figure 1. Here the D.C. electrodes are placed on either side of the path of propagation. Reducing the electrode separation $2a$ lowers the D.C. voltage needed to achieve a given field strength in the gap. The presence of the electrodes however results in an increase in the path loss due to diffraction effects and attenuation in the metal film [6].

The velocity change with applied in-plane field has been measured for various materials. Of these, the 38-X cut of LiNbO_3 has been found to have the highest sensitivity [3]. This cut is also attractive because its piezoelectric coupling allows for low transducer insertion loss over a wide band of frequencies. Measurements for this material lead to the relationship $V_{DC} = (2a/L)(3.3 \times 10^5/f)$ for the voltage need to change the delay time by $1/2$ an R.F. cycle, where f is the frequency

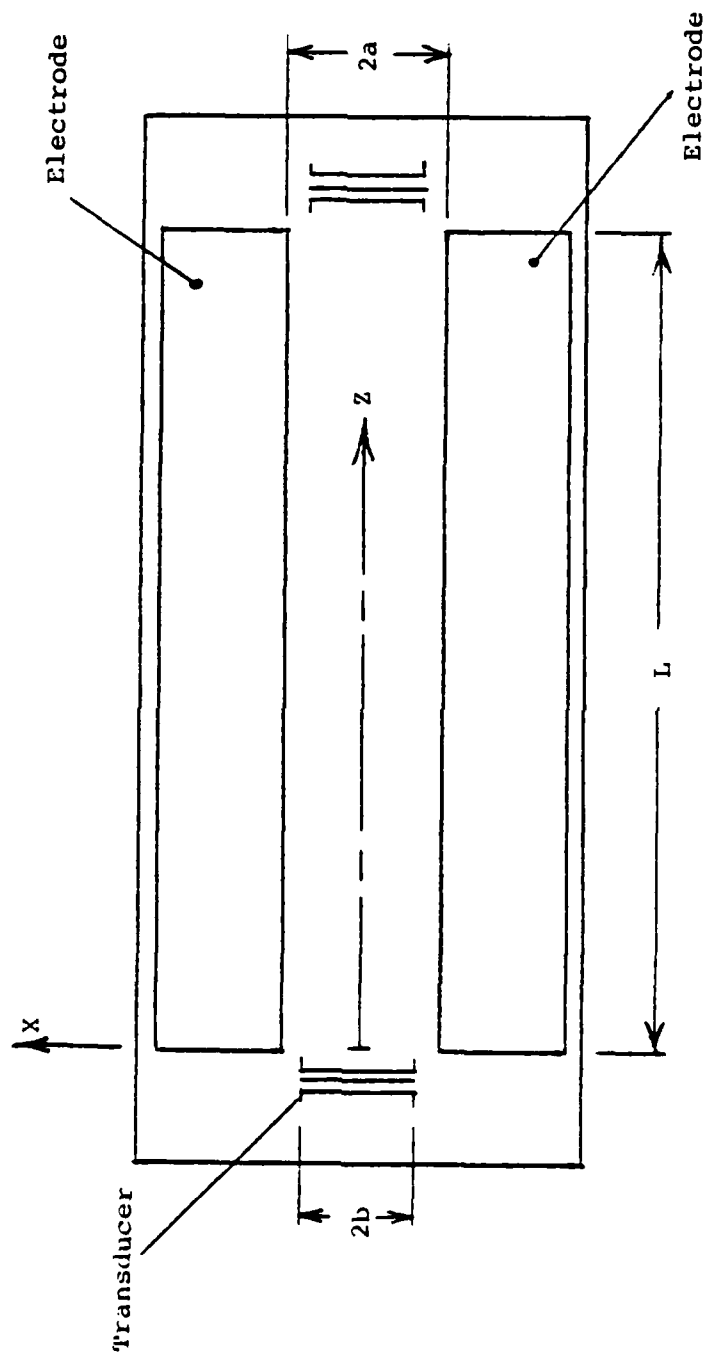


Figure 1. Top view of the electrodes for the in-plane field configuration.

in GHz. For example, if $V_{DC} = 100$ volts, then at 1 GHz the path length L must be $3.3 \times 10^3(2a)$. For a gap $2a = 10 \mu\text{m}$, $L = 3.3 \text{ cm}$. It is thus seen that narrow gaps and long paths are required to prevent V_{DC} from becoming large, which implies the need for some type of waveguiding structure.

Deposition of a fast material, such as aluminum nitride (A₂N) over the electrodes of Figure 1 has been proposed as one method for overcoming the electrode loss. In this case, the coated electrode configuration would act as a slot waveguide [7-10], with the energy of the guided waves primarily confined to the free surface region between the electrodes.

In this study we investigate the characteristics of the two types of slot waveguides shown in cross-section in Figure 2, with the substrate assumed to be the 38-X cut of LiNbO₃. The waveguide shown in Figure 2a has electrode and A₂N layer that are semi-infinite on either side of the gap. For the guide shown in Figure 2b, the electrodes have been reduced to strips of finite width w , while the A₂N layer is semi-infinite on either side of the gap.

The propagation and attenuation constants are computed for the modes of both guiding structures as a function of the various geometrical parameters and frequencies in a band centered about 1 GHz. In addition to attenuation, the insertion loss will depend on the mismatch between the profile of the fields radiated by the transducer, which is assumed to be rectangular, and the profile of the modal fields. A factor describing the effect of field mismatch is also computed for various modes of the two waveguides. These studies show the potential of waveguides for use in electrostatic phase shifters.

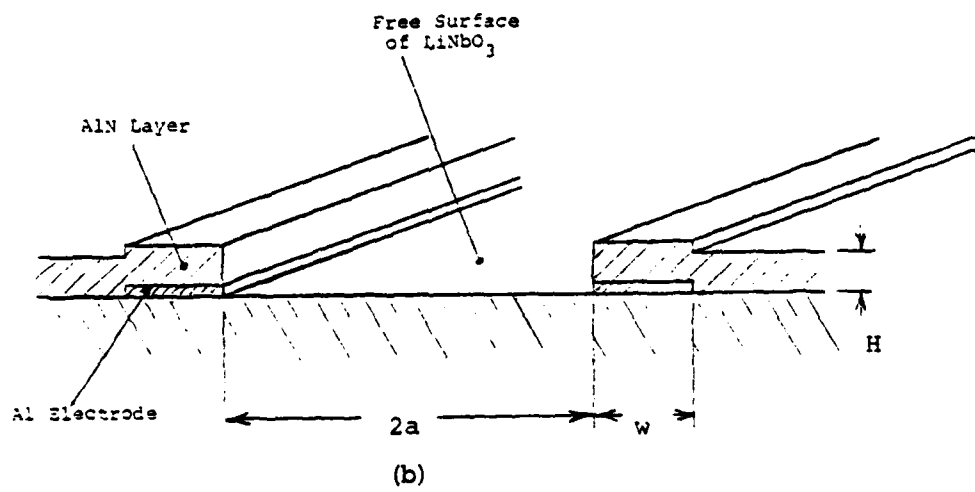
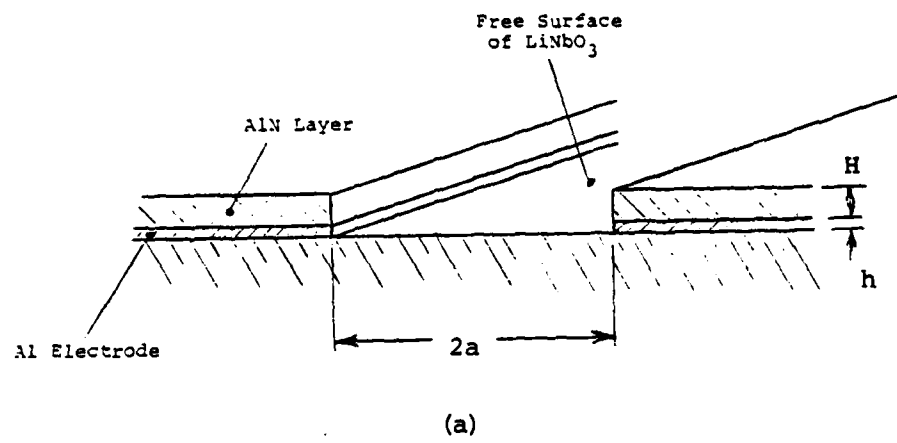


Figure 2. Cross-section view of the slot waveguides; a) guide having semi-infinite electrodes; b) guide having finite width electrodes.

II. Guided Waves

In order to construct the solutions for guided waves, it is first necessary to understand SAW propagation in the various surface regions of Figure 2.

A. Straight-Crested Surface Waves

With the coordinate system shown in Figure 1, and assuming harmonic time dependence $\exp(-i\omega t)$, straight-crested surface waves have x-z dependence of the form

$$e^{i\eta x} e^{i\kappa z} \quad (1)$$

where η, κ and ω are related via the SAW dispersion relation. Because the SAW velocities in the various surface regions are all close together, guiding will take place only when the constituent straight-crested SAW propagate at small angles to the z-axis. As a result, we may use the parabolic approximation [11]. Using this approximation, the SAW dispersion relation has the quadratic form

$$\alpha_j^2 \eta^2 + \kappa^2 = k_j^2 \quad (2)$$

where k_j is the wavenumber for SAW propagation along z, and α_j is related to the anisotropy parameter $\gamma = d^2V(\theta)/d\theta^2$ of Reference [11] via

$$\alpha_j^2 = 1 + \gamma_j \quad (3)$$

The index $j = 1$ refers to the free surface, $j = 2$ to the metalized surface covered with AlN, and $j = 3$ is for a surface having only the AlN layer.

For the 38-X cut of LiNbO_3 (crystal X axis along z in Figure 1), α_1 obtained from the computed Rayleigh velocity [12] is 0.8916. In the absence of loss $k_1 = \omega/V_1$, where $V_1 = 3.9913 \times 10^9$ $\mu\text{m/s}$ is the Rayleigh velocity for propagation along z [12]. On well prepared samples, Rayleigh wave attenuation has been found to be [13]

$$- 2.5f^2 + 0.54f \text{ db/cm} \quad (4)$$

where f is the wave frequency in GHz. Converting (4) into units of μm^{-1} ,

$$k_1 = 1.5742f + i[2.9 \times 10^{-5}f^2 + 0.6 \times 10^{-5}f] \mu\text{m}^{-1} \quad (5)$$

where f is in GHz.

If a thin metal plating is deposited on the LiNbO_3 surface, shorting of the piezoelectric field at the surface causes a slowing of the SAW by an amount $\Delta V/V_1 = 0.0268$, as well as an increase in attenuation. Davis and Weller [14] have measured SAW attenuation in the frequency range 270-730 MHz for Al films on YZ LiNbO_3 . For their best films the data is given approximately by

$$9.5f^{2.2}(h/600)^{0.4} \text{ db/cm} \quad (6)$$

where h is the film thickness in \AA .

To produce a slot waveguide it is necessary to increase the velocity of the SAW above V_1 for those portions of the surface in the range $|x| \rightarrow \infty$. Such a speed-up of the SAW can be accomplished by stiffening the surface with a layer of material such as AlN.

In the case of the semi-infinite electrodes of Figure 2a, the stiffening layer must overcome the slowing effect due to the conducting

electrodes. For thin electrode platings h , the mechanical perturbation of the surface will be due only to the stiffening layer. To first order, the electrical shorting and mechanical perturbation are additive effects. For a layer of thickness H of a hexagonal material, such as AlN, with C axis normal to the surface, the SAW velocity V_2 can be found from the relation [15]

$$\frac{V_1}{V_2} = 1 + \frac{\Delta V}{V_1} + \frac{V_1 H}{P} \left[\left(\rho' - \frac{1}{V_1^2 s_{66}} \right) |v_x|^2 + \rho' |v_y|^2 + \left(\rho' - \frac{1}{V_1^2} \frac{s_{11}}{s_{11}^2 - s_{12}^2} \right) |v_z|^2 \right] \quad (7)$$

Here $\Delta V/V_1$ is the change due to shorting of the piezoelectric field, ρ' is the mass density of the layer material, and s_{ij} is the elastic stiffness constant in the coordinate system where Z is along the C axis. Finally, v_x , v_y and v_z are the particle velocity components at the surface $y = 0$ of a Rayleigh wave carrying power along z of P watts (per meter along x).

Using the compliances C_{ij} given in Reference [16] for AlN, and neglecting the piezoelectric constants, $1/s_{66} = 1.10 \times 10^{11} (\text{m}^2/\text{N})$ and $s_{11}/(s_{11}^2 - s_{12}^2) = 1.35 \times 10^{11} (\text{m}^2/\text{N})$. Also, $\rho' = 3.26 \times 10^3 \text{ kg/m}^3$ and using $|v_x|^2/P$, $|v_y|^2/P$ and $|v_z|^2/P$ from Reference [12] for the 37-X cut of LiNbO₃, expression (7) becomes

$$\frac{V_1}{V_2} = 1.0268 - 0.0556 fH \quad (8)$$

where H in (8) is measured in μm and f in GHz. For $f = 1$, a layer thickness H slightly greater than 0.4 is necessary to overcome the slowing due to the conducting film. Greater values of H will cause the SAW velocity to be greater than V_1 .

The AlN plating can be expected to contribute to SAW attenuation, although we are not aware of any reliable measurements. Because one goal of the study is to assess the effects of film attenuation on path loss, we assume the attenuation to be the same as found for a metal film alone on LiNbO₃. With this assumption, we find from (6) and (8) that the SAW wavenumber k_2 for $h = 600\text{\AA}$ of Al covered by AlN is

$$k_2 = (1.6164f - 0.08756f^2H) + i(11 \times 10^{-5}f^{2.2}) \quad (9)$$

In the case of the slot guide of Figure 2b, guiding is achieved if the SAW velocity for the AlN layer placed directly on LiNbO₃ is faster than the free surface SAW velocity. Neglecting piezoelectric and dielectric effects in the AlN layer, the perturbation in the SAW velocity is given by the last term in (7). Assuming the SAW attenuation to be the same as on a free surface, the wavenumber k_3 of the SAW for an AlN layer on LiNbO₃ is

$$k_3 = k_1 - 0.08756f^2H \quad (10)$$

The imaginary parts of k_1 , k_2 and k_3 are plotted in Figure 3 as a function of frequency.

A more accurate approximation for k_2 and k_3 requires a full wave analysis of the two layered structures. Such an analysis is beyond the scope of this study, and would only modify details of the results obtained here using (9) and (10). Similarly, computing anisotropy parameters α for the layered structures would require a full wave analysis. For simplicity, we assume all α 's to have the free surface value.

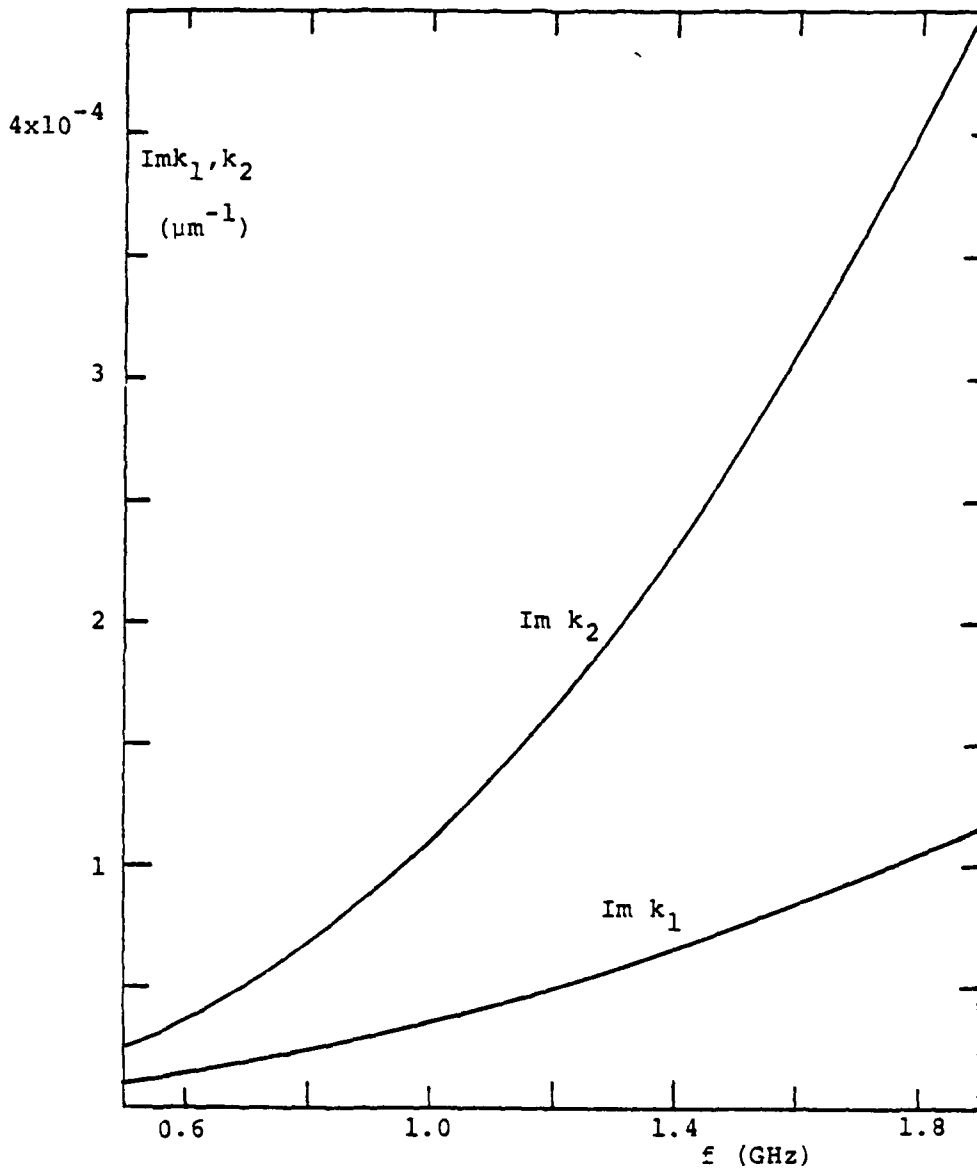


Figure 3. Frequency variation of the SAW attenuation constants on LiNbO_3 for a free surface ($\text{Im } k_1$) and for a surface covered with 600 Angstroms of Al ($\text{Im } k_2$).

B. Dispersion Relations for the Guided Waves

When solving for the waves guided by surface platings on isotropic substrates, various authors have used the two-dimensional amplitude approximation [7-10]. With this approximation one solves for the SAW amplitude $\psi(x,z)$ that satisfies the two-dimensional wave equation. As applied to a substrate with parabolic anisotropy, the wave equation becomes

$$(\alpha^2 \frac{\partial^2}{\partial x^2} + \frac{\partial^2}{\partial z^2} + k^2_j) \psi(x,z) = 0 \quad (11)$$

Boundary conditions at the edges of the various platings require that particle velocity and stress be continuous. Within the amplitude approximation, the boundary conditions require that ψ and $\partial\psi/\partial x$ be continuous. One consequence of the boundary conditions is that the amplitude must have the same z dependence in each region. Thus if κ is the wavenumber along z of the guided wave, then in each region of the surface the solution to (11) is of the form

$$\psi(x,z) = (V_j^+ e^{i\eta_j x} + V_j^- e^{-i\eta_j x}) e^{i\kappa z} \quad (12)$$

where η_j and κ satisfy the dispersion relation of Eq. (2).

The derivative $\partial\psi/\partial x$ is of the form

$$\frac{\partial\psi}{\partial x} = \eta_j (V_j^+ e^{i\eta_j x} - V_j^- e^{-i\eta_j x}) e^{i\kappa z} \quad (13)$$

Expressions (12) and (13) have x dependence of the same form as found for voltage and current on a transmission line [17] of impedance $1/\eta_j$. As a result, the transmission line formalism may be used to find the properties of the guided waves.

Let Z_{in} be the impedance seen looking to the right at $x = a$ in either Figure 2a or 2b. Recalling the time dependence $e^{-i\omega t}$, it is easily shown that

$$Z_{in} = \begin{cases} \frac{1}{\eta_2} & \text{for Fig. 2a} \\ \frac{1}{\eta_2} \frac{(1/\eta_3) - i(1/\eta_2)\tan\eta_2 w}{(1/\eta_2) - i(1/\eta_3)\tan\eta_2 w} & \text{for Fig. 2b} \end{cases} \quad (14)$$

The transverse resonance condition for the guide modes requires that the sum of the impedance seen looking to the left at $x = a$ and Z_{in} should vanish. For even modes $\partial\psi/\partial x = 0$ at $x = 0$, corresponding to an open circuit, while for odd modes $\psi = 0$ at $x = 0$, corresponding to a short circuit. Using the impedance seen looking to the left at $x = a$ for open and short circuits at $x = 0$, the dispersion equation for guided waves is

$$\begin{aligned} Z_{in} + i \frac{1}{\eta_1} \cot \eta_1 a &= 0 && \text{for even modes} \\ Z_{in} - i \frac{1}{\eta_1} \tan \eta_1 a &= 0 && \text{for odd modes} \end{aligned} \quad (15)$$

For transducers that are symmetrical about $x = 0$, as in Figure 1, only the even modes are excited. Because of this, we treat only the even modes for the remainder of this report. Simplifying the first equation in (15) gives the even mode dispersion relation

$$i\eta_1 \tan \eta_1 a = \begin{cases} \eta_2 & \text{for Fig. 2a} \\ \eta_2 \frac{\eta_3 - i\eta_2 \tan\eta_2 w}{\eta_2 - i\eta_3 \tan\eta_2 w} & \text{for Fig. 2b} \end{cases} \quad (16)$$

Solution of the dispersion equation is discussed separately for the semi-infinite electrodes and for the finite width electrodes.

III. Guided Waves for Semi-Infinite Electrodes

The solution of (16) for the modes of the slot waveguide with semi-infinite electrodes can be obtained by solving (2) for η_2 in terms of η_1 . Observing that in the absence of loss η_2 must be positive imaginary in order for the guided wave fields to decay for $|x| \rightarrow \infty$, we obtain from (2)

$$\eta_2 = i \frac{1}{\alpha} \sqrt{k_1^2 - k_2^2 - \alpha^2 \eta_1^2} \quad (17)$$

thus the dispersion equation becomes

$$\eta_1 \tan \eta_1 a = \frac{1}{\alpha} \sqrt{k_1^2 - k_2^2 - \alpha^2 \eta_1^2} \quad (18)$$

which may be solved for η_1 .

The right and left-hand sides of (18) are plotted in Figure 4 for the case of k_1 and k_2 real. It is seen that the lowest $n = 0$ mode will exist for all frequencies and all guide widths $2a$. Higher modes are obtained as the width $2a$ decreases or frequency increases. The cutoff condition for the higher modes is

$$\frac{1}{\alpha} \sqrt{k_1^2 - k_2^2} = n \frac{\pi}{a} \quad (n = 1, 2, \dots) \quad (19)$$

When loss is present, the higher modes will not have a sharp cutoff. However, they will exhibit large attenuation for frequencies near and below that for which (19) is satisfied with $\text{Re}k_1$ and $\text{Re}k_2$ substituted for k_1 and k_2 .

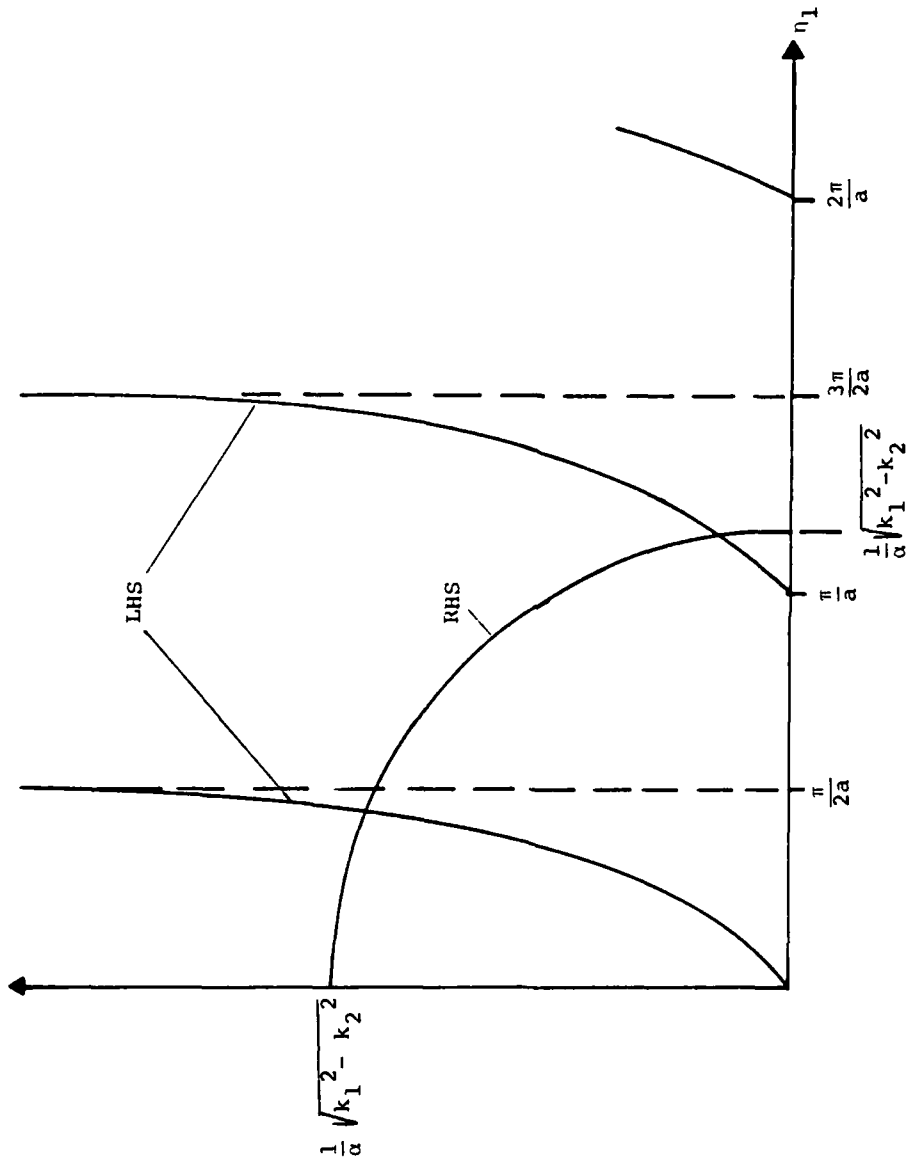


Figure 4. Geometrical construction for finding the solution of the dispersion equation for slot waveguide having semi-finite electrodes.

Solutions of (18) for η_1 were obtained numerically for a number of cases, and corresponding value of κ was obtained from (2). In Figure 5 we have plotted $\text{Re}\kappa$ for the various symmetric modes as a function of the slot width $2a$ for $f = 1$ GHz and an AlN film thickness $0.677 \mu\text{m}$. At cutoff for each mode $\text{Re}\kappa = \text{Re}\kappa_2 = 1.5571$. As $2a$ increases $\text{Re}\kappa$ increases towards $\text{Re}\kappa_1 = 1.5742$. To four decimal place accuracy, the same results were obtained when (18) was solved assuming k_1 and k_2 were real with the values cited above. Thus, SAW attenuation does not affect $\text{Re}\kappa$.

The additional attenuation of the guided wave, over and above the free surface attenuation, due to the electrodes is indicated in Figure 6 for $f = 1$ GHz and $H = 0.677 \mu\text{m}$. The value of $\text{Im}(\kappa - k_1)$ is plotted as a function of guide width $2a$. The additional attenuation was computed two ways, with agreement to two significant figures. First, κ was computed with k_1 and k_2 having the complex values given in (5) and (9). Next, the imaginary part of k_1 was set to zero and the imaginary part of k_2 was reduced to 7.5×10^{-5} by subtracting $\text{Im}k_1 = 3.5 \times 10^{-5}$. Because of the agreement between the two methods, guided wave attenuation for other values of film loss can be found by scaling the additional attenuation presented in Figure 6.

It is seen from Figure 6 that the attenuation is large for each mode near its cutoff, but decreases rapidly away from cutoff. For example, at $2a = 20$, the additional attenuation has fallen to about 13% of the free surface value.

Because the frequency dependence of $\text{Re}\kappa_2$ is not linear, changing frequency does not have the same effect on the dispersion relation as does changing guide width $2a$, which has been found to be the case for

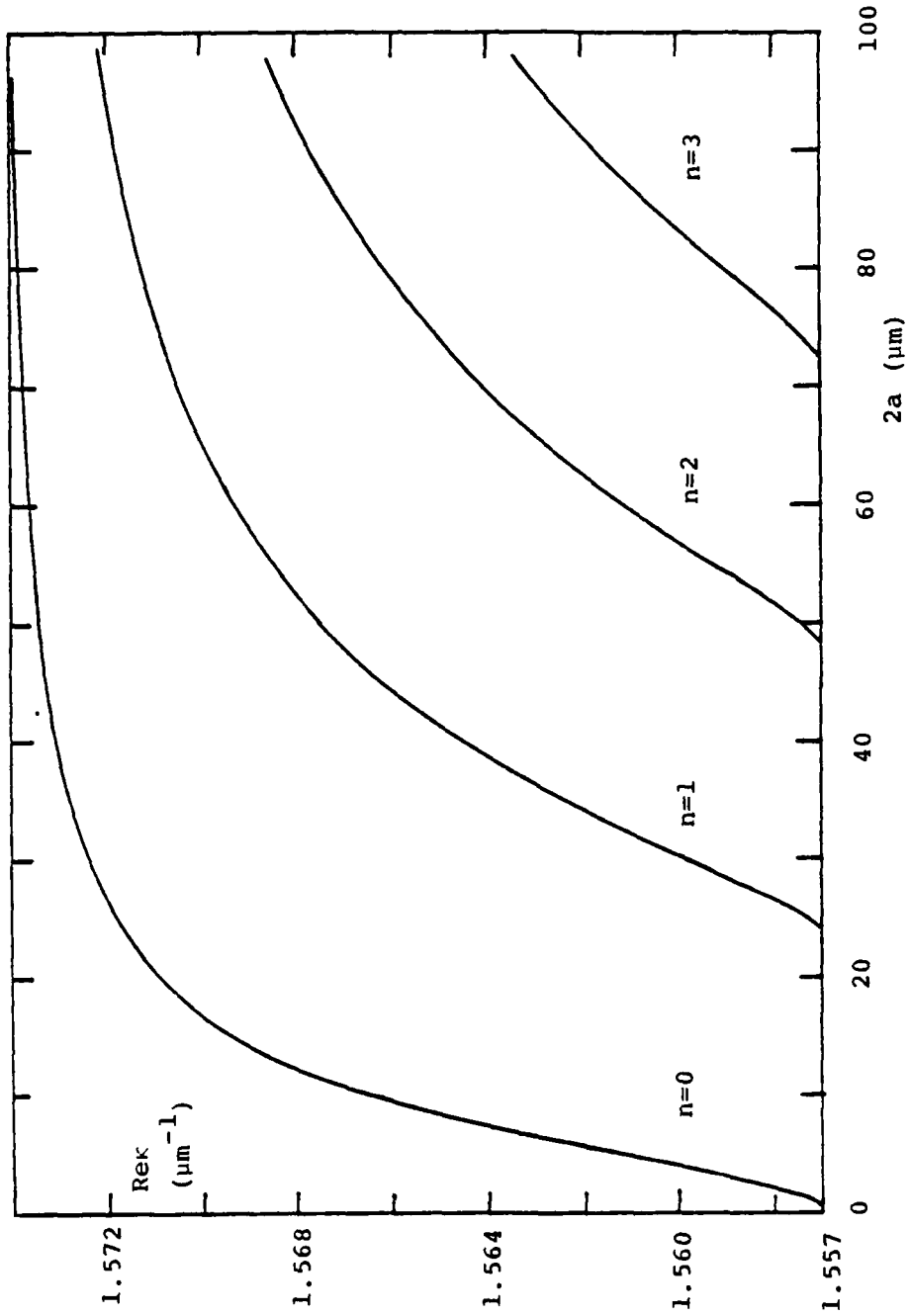


Figure 5. Dependence of the propagation constants $Re k$ on slot width $2a$ for the modes of a waveguide with semi-infinite electrodes ($f=1GHz$, $H=0.677 \mu m$)

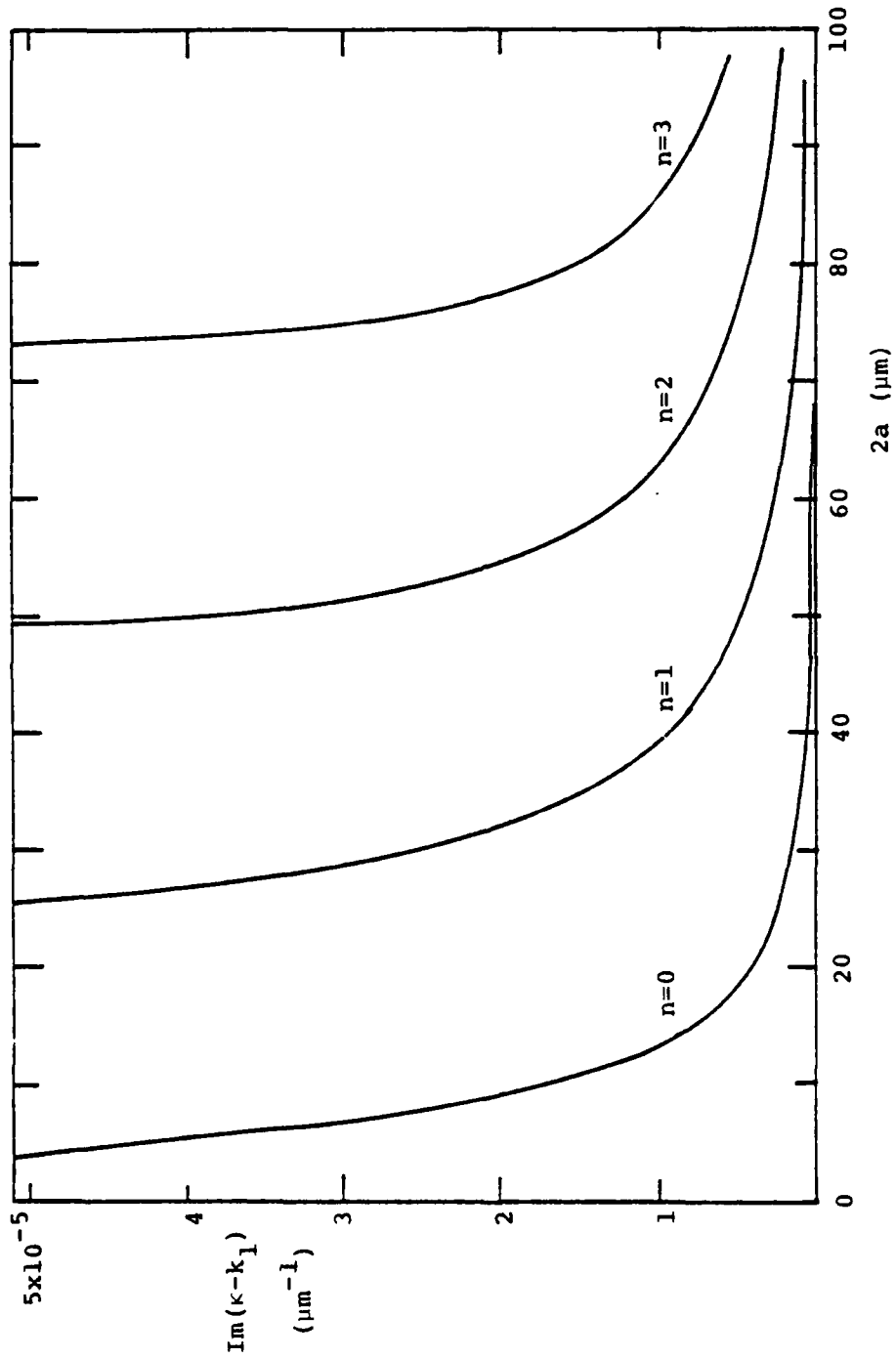


Figure 6. Dependence on slot width $2a$ of the attenuation due to the metalization $\text{Im}(\kappa - k_1)$ for the modes of a waveguide with semi-infinite electrodes ($f=1\text{GHz}$, $H=0.677\mu\text{m}$).

$\Delta V/V$ waveguides [9]. The dependence of the modal κ on frequency has been calculated, and the results plotted in Figures 7 and 8 for the case of $H = 0.677 \mu\text{m}$ and a guide width of $2a = 20 \mu\text{m}$. In Figure 7, the deviation of $\text{Re}k$ from $\text{Re}k_1$ is plotted on a logarithmic scale to accommodate the large range of variation. Note that $\text{Re}k_1 > \text{Re}k$ for these modes.

The lowest mode ($n = 0$) has a cutoff frequency $f = 0.712 \text{ GHz}$ corresponding to the value of f at which $\text{Re}k_1 = \text{Re}k_2$. For lower frequencies, it is seen from the dependence in (9) that the mechanical stiffening of the A2N layer is too small to overcome the slowing effect of the conducting film. As a result, the SAW under the electrodes has lower velocity than the free surface Rayleigh wave so that no guided wave exists. Above 0.712 GHz , $\text{Re}(k_1 - \kappa)$ for the $n = 0$ mode increases rapidly to about 3×10^{-3} , and remains close to this value for frequencies up to 2 GHz . The near constancy of $\text{Re}(k_1 - \kappa)$ is due to competing phenomena. If k_2 were proportional to frequency, one would expect $\text{Re}k$ to approach $\text{Re}k_1$ as frequency increases. However, the difference between $\text{Re}k_1$ and $\text{Re}k_2$ increases as f^2 , and inhibits $\text{Re}k$ from approaching the limit.

The higher modes ($n = 1, 2, 3$) shown in Figure 7 have a cutoff frequency, which in the absence of loss is given by the solution of (19) for f . Were it not for loss, $\kappa = k_2$ at cutoff so that at cutoff $k_1 - \kappa = k_1 - k_2$. Because of the dependence of k_1 and k_2 on f , the value of $k_1 - \kappa$ will be different for each mode. It is seen from Figure 7 that the value of $k_1 - \kappa$ for the higher modes does not change significantly from cutoff through $f = 2 \text{ GHz}$.

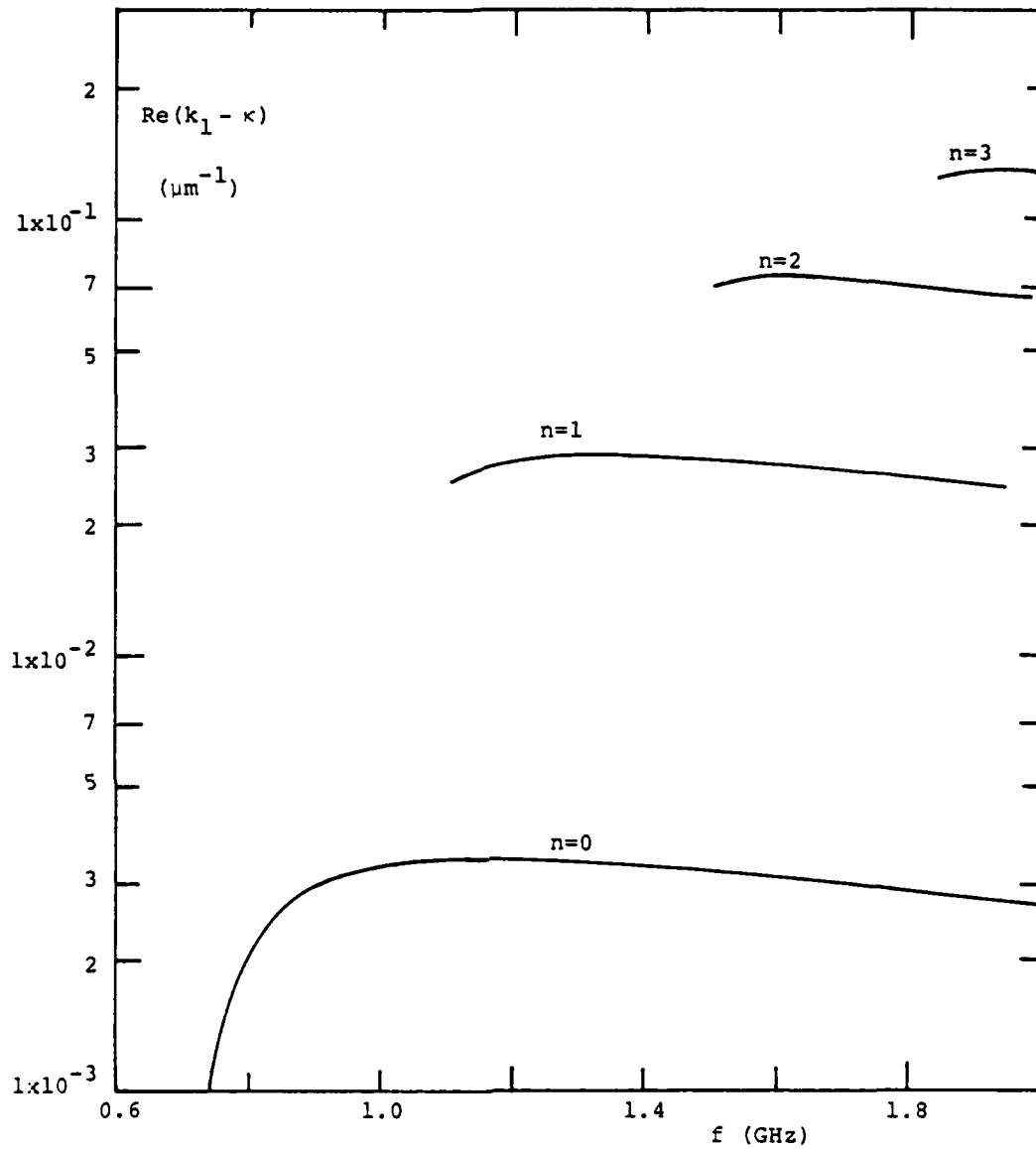


Figure 7. Frequency dependence of the propagation constants $\text{Re} \kappa \leq \text{Re} k_1$ of the various modes for $2a=20 \mu\text{m}$ and $H=0.677 \mu\text{m}$ plotted as the deviation $\text{Re}(k_1 - \kappa)$.

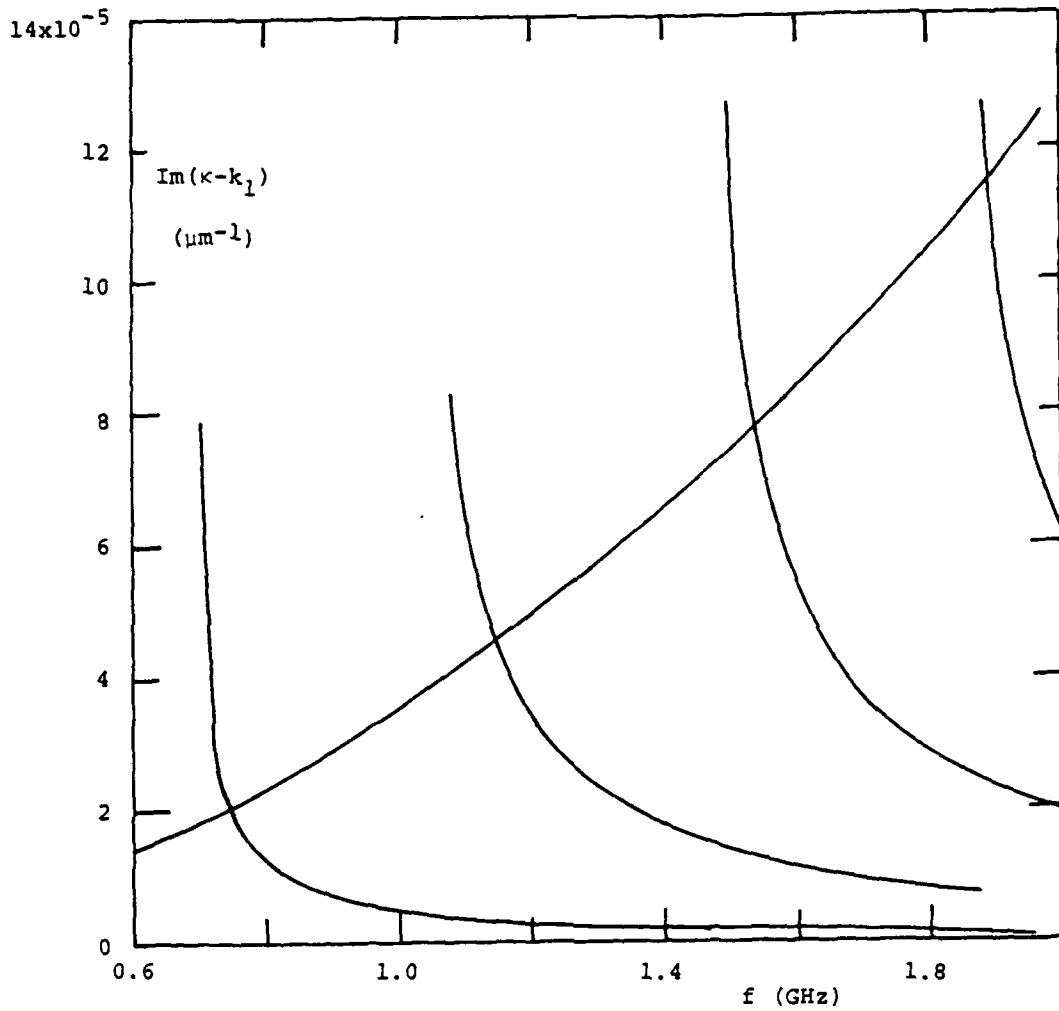


Figure 8. Frequency dependence of the attenuation due to the metalization $\text{Im}(\kappa-k_1)$ of the various modes for $2a=20 \mu\text{m}$ and $H=0.677 \mu\text{m}$.

Figure 8 shows the variation of the guided wave attenuation due to plating loss in the vicinity of the cutoff frequency. The free surface attenuation $\text{Im}k_1$ has also been plotted for comparison. Attenuation due to plating loss, $\text{Im}(\kappa - k_1)$, is seen to drop rapidly for frequencies above cutoff, and ultimately become small compared to $\text{Im}k_1$.

Modal dispersion characteristics for the lowest mode ($n = 0$) of a narrow slot width of $2a = 10 \mu\text{m}$ and A λ N layer thickness $H = 0.677 \mu\text{m}$ is shown in Figure 9. Here $\text{Re}(k_1 - \kappa)$ is plotted on a linear scale as a function of frequency over the range for which the slot guide has a single propagating mode. The frequency dependence is similar to that of the lowest mode for a slot width of $2a = 20 \mu\text{m}$.

Figure 10 shows the contribution to the attenuation constant $\text{Im}\kappa$ due to plating loss for the lowest mode of the $2a = 10 \mu\text{m}$ guide. The decrease in $\text{Im}(\kappa - k_1)$ with increasing frequency results from the fact that the fields of the guided wave penetrate a smaller distance under the plating. This decrease partially compensates for the increase in $\text{Im}k_1$ with frequency. For example, in the band $0.9 < f < 1.1$, the Rayleigh wave attenuation $\text{Im}k_1$ increases from 2.9×10^{-5} to 4.2×10^{-5} , whereas the guided wave attenuation $\text{Im}\kappa$ has a much smaller variation from 5.1×10^{-5} to $5.6 \times 10^{-5} \mu\text{m}^{-1}$.

The value $H = 0.677$ used for the previous calculation was chosen to place k_2 midway between k_1 and the wavenumber of the slowest shear wave propagating along the crystal x axis at $f = 1 \text{ GHz}$. To investigate the effect of changing H we have plotted the variation of $\text{Re}(k_1 - \kappa)$ with H at $f = 1 \text{ GHz}$ in Figure 11 for $2a = 10 \mu\text{m}$ and $2a = 20 \mu\text{m}$. At $H = 0.482$, $\text{Re}k_2 = \text{Re}k_1$ for $f = 1 \text{ GHz}$, so that H must be greater than this value for guiding to take place. This condition is evident from

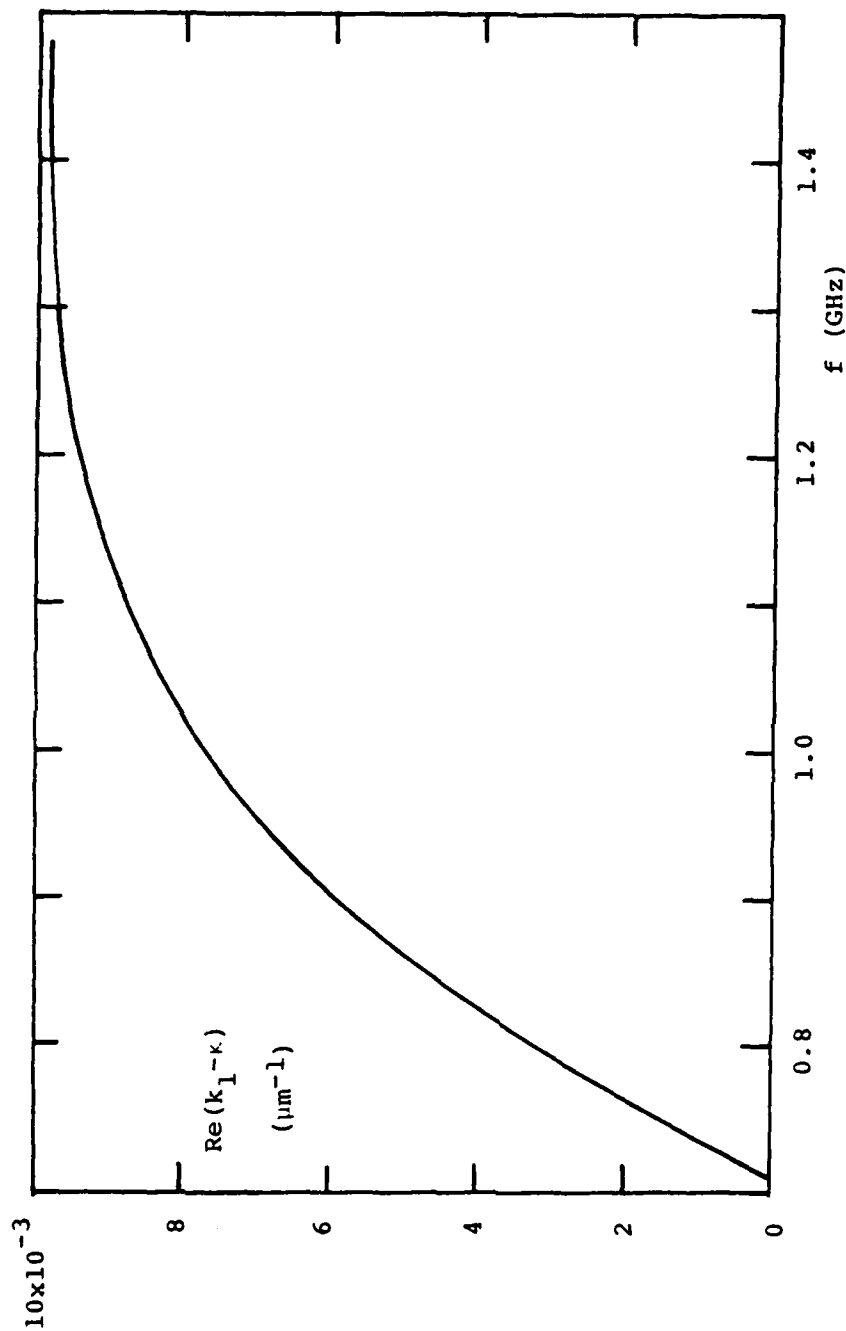


Figure 9. Frequency dependence of the propagation constant $\text{Re} k_1$ for $2a=10 \mu\text{m}$ and $H=0.677 \mu\text{m}$ plotted as the deviation $\text{Re}(k_1 - \kappa)$.

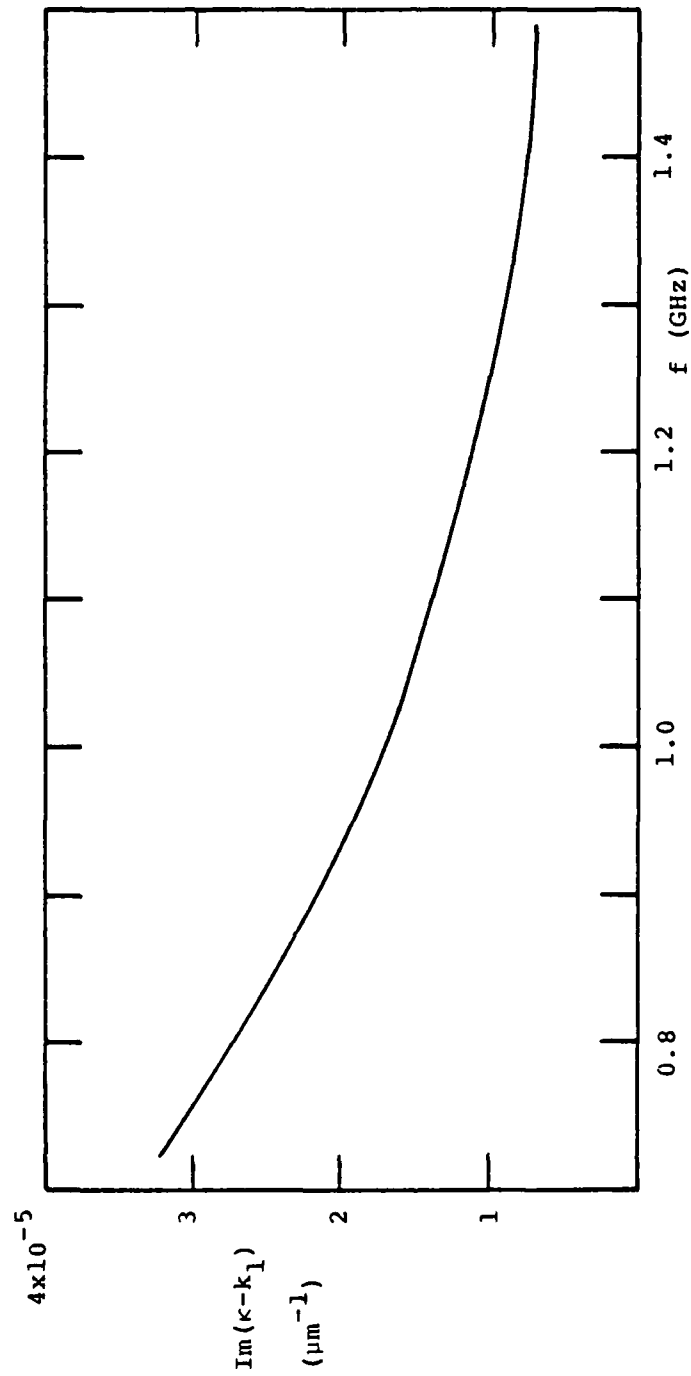


Figure 10. Frequency dependence of the attenuation due to the metalization $\text{Im}(\kappa - k_1)$ for $2a = 20 \mu\text{m}$ and $H = 0.677 \mu\text{m}$.

the curve for $2a = 10$ and from the lowest mode ($n = 0$) for $2a = 20$ in Figure 11.

Thicker layers allow more modes to propagate, although only one mode propagates for guide width $2a = 10$ over the entire range of H shown.

When H is greater than about 0.87 for $f = 1$ GHz, the SAW on the layered surface is faster than the slowest shear wave, so that a straight-crested surface wave would leak into the substrate. However, in the case of the slot waveguide, the modal fields in the layered portion of the surface are not those of a straight-crested surface wave, and hence need not leak into the substrate even for $H > 0.87$. Provided that $\text{Re}k$ for the guided wave is greater than the wavenumber of the slowest bulk wave, all fields will decay into the substrate and the wave will be of the bound variety. Thus the guided wave characteristics may legitimately be computed for $H \rightarrow 1.0$, as indicated in Figure 11.

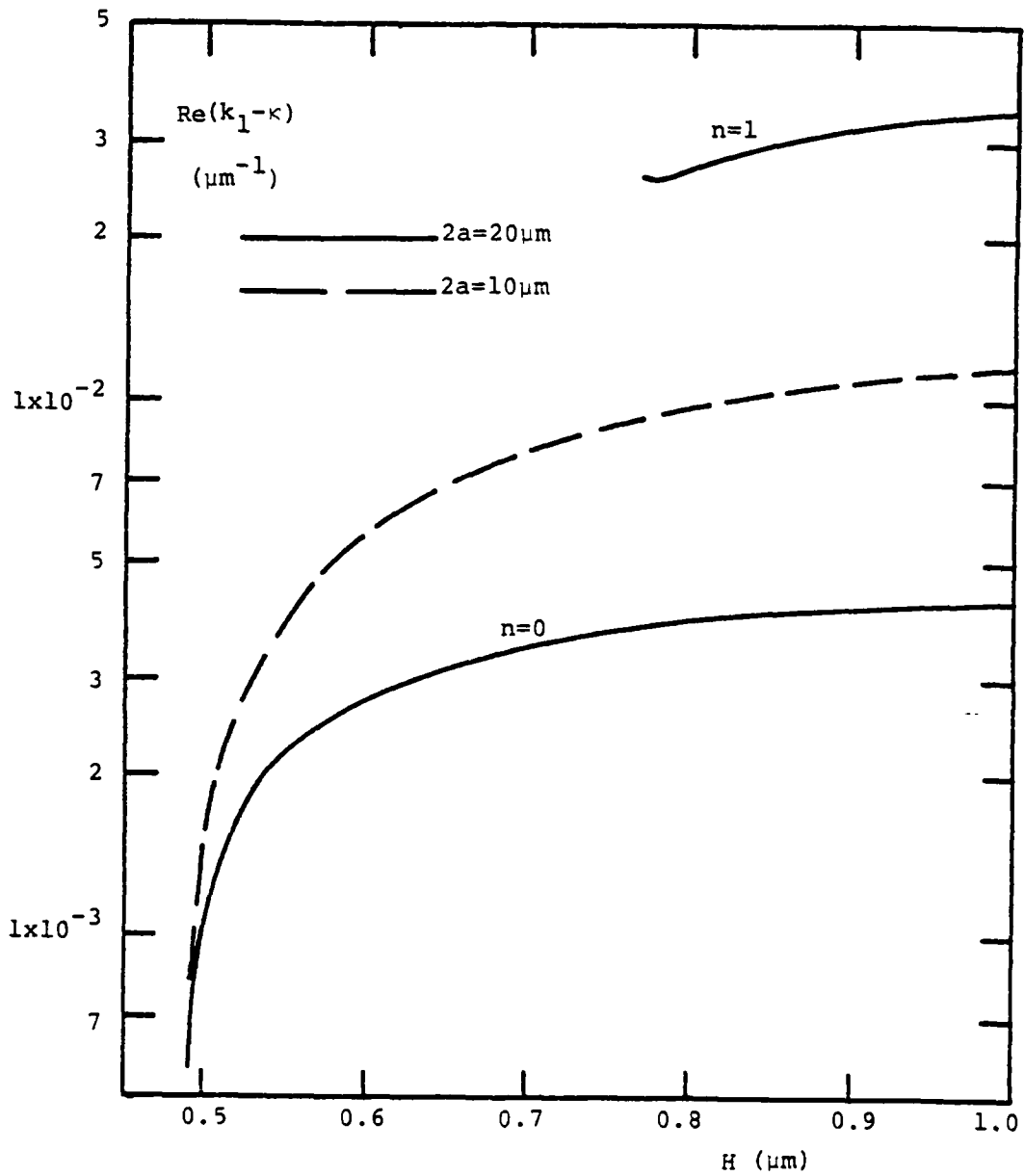


Figure 11. Variation with A2N layer thickness H of the propagation constant $Re \kappa \leq Re k_1$ for $f=1GHz$ and guides of width $2a = 10, 20 \mu m$.

IV. Guided Waves for Electrodes of Finite Width

Single step deposition of the A₂N layer is expected to give the same thickness over the electrodes as over the LiNbO₃ surface. We therefore assume that H has the same value when computing k₂ from (9) as when computing k₃ from (10), with the result that Re k₂ > Re k₃. Depending on the value of H, Re k₂ may be less than Re k₁, or greater. In the former case, the slot acts as the primary guiding region, while for Re k₂ > Re k₁ either the electrodes or the slot can act as the primary guiding region.

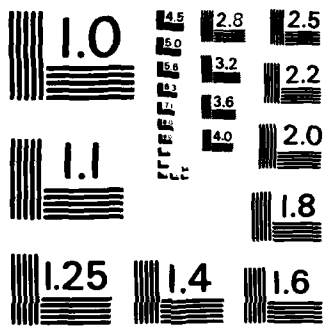
A graphical construction indicating the character of the roots of the dispersion equation can be obtained by defining

$$\theta = \tan^{-1} \left(\frac{i\eta_2}{\eta_3} \right) \quad (20)$$

In the absence of loss, η_3 of the guided waves must be pure imaginary so that the fields will decay as $|x| \rightarrow \infty$. Thus θ in (20) will be real or imaginary depending on η_2 being real or imaginary. Using this definition in (16) for the case of Figure 2b, the dispersion equation for the symmetric modes becomes

$$\eta_1 \tan \eta_1 a = \frac{\eta_2}{\tan(\eta_2 w + \theta)} \quad (21)$$

Comparing (5) and (9), it can be shown that for $fH \geq 0.482$, $\text{Re } k_1 \geq \text{Re } k_2$ and guided wave solutions of (21) will have η_1 real in the absence of loss, but η_2 may be real or imaginary. For $fH < 0.482$, η_2 will be real, but η_1 can be real or imaginary. These cases are discussed separately below.



MICROCOPY RESOLUTION TEST CHART
NATIONAL BUREAU OF STANDARDS-1963-A

A. Guided Waves for $\text{Re}k_1 \geq \text{Re}k_2 > \text{Re}k_3$

The right and left-hand sides of (21) are sketched in Figure 12 for η_1 real, and neglecting loss. If η_1 were imaginary, the left-hand side of (21) would be negative real. For $\text{Re}k_1 \geq \text{Re}k_2$, η_2 and θ would also be imaginary, and the right-hand side of (21) would be positive real. Thus, no solution to (21) exists for $\text{Re}k_1 \geq \text{Re}k_2$ that has η_1 imaginary.

In the range $0 \leq \eta_1 \leq \sqrt{k_1^2 - k_2^2}/\alpha$, both η_2 and θ are imaginary and the right-hand side of (21) decreases monotonically, as shown in Figure 12. Note that for $w \rightarrow \infty$, this portion of the curve approaches that for the right-hand side of (18) for semi-infinite electrodes. In the range $\sqrt{k_1^2 - k_2^2}/\alpha < \eta_1 \leq \sqrt{k_1^2 - k_3^2}/\alpha$, η_2 and θ are real so that the right-hand side of (21) undergoes variations like those of the cotangent function. For $\eta_1 > \sqrt{k_1^2 - k_3^2}/\alpha$, η_3 will be real, as well as η_2 , so that θ is imaginary and hence the right-hand side of (21) will be complex. As a result, no solutions with η_1 real will be found.

Figure 12 has been sketched in a way indicating four solutions to (21). The number of solutions depends on both the size of w and a , as well as H and frequency. No simple formula can be used to express the cutoff condition of the modes. Actual cutoff is determined numerically by tracing along the branches of the dispersion curve.

Solutions to the dispersion equation (21) were obtained numerically and the wavenumber κ of the guided waves were obtained from (2). The phase constants $\text{Re}k$ are plotted as a function of slot width $2a$ in Figure 13 for $f = 1$ GHz, $w = 5$ μm and a layer thickness $H = 0.6$ μm . The lowest $n = 0$ mode starts as the mode of a $\Delta V/V$ waveguide of width $2w = 10$ μm when the two electrodes are next to each other ($2a = 0$).

IV. Guided Waves for Electrodes of Finite Width

Single step deposition of the A2N layer is expected to give the same thickness over the electrodes as over the LiNbO₃ surface. We therefore assume that H has the same value when computing k₂ from (9) as when computing k₃ from (10), with the result that Re k₂ > Re k₃. Depending on the value of H, Re k₂ may be less than Re k₁, or greater. In the former case, the slot acts as the primary guiding region, while for Re k₂ > Re k₁ either the electrodes or the slot can act as the primary guiding region.

A graphical construction indicating the character of the roots of the dispersion equation can be obtained by defining

$$\theta = \tan^{-1} \left(\frac{i\eta_2}{\eta_3} \right) \quad (20)$$

In the absence of loss, η_3 of the guided waves must be pure imaginary so that the fields will decay as $|x| \rightarrow \infty$. Thus θ in (20) will be real or imaginary depending on η_2 being real or imaginary. Using this definition in (16) for the case of Figure 2b, the dispersion equation for the symmetric modes becomes

$$\eta_1 \tan \eta_1 a = \frac{\eta_2}{\tan(\eta_2 w + \theta)} \quad (21)$$

Comparing (5) and (9), it can be shown that for $fH \geq 0.482$, $\text{Re } k_1 \geq \text{Re } k_2$ and guided wave solutions of (21) will have η_1 real in the absence of loss, but η_2 may be real or imaginary. For $fH < 0.482$, η_2 will be real, but η_1 can be real or imaginary. These cases are discussed separately below.

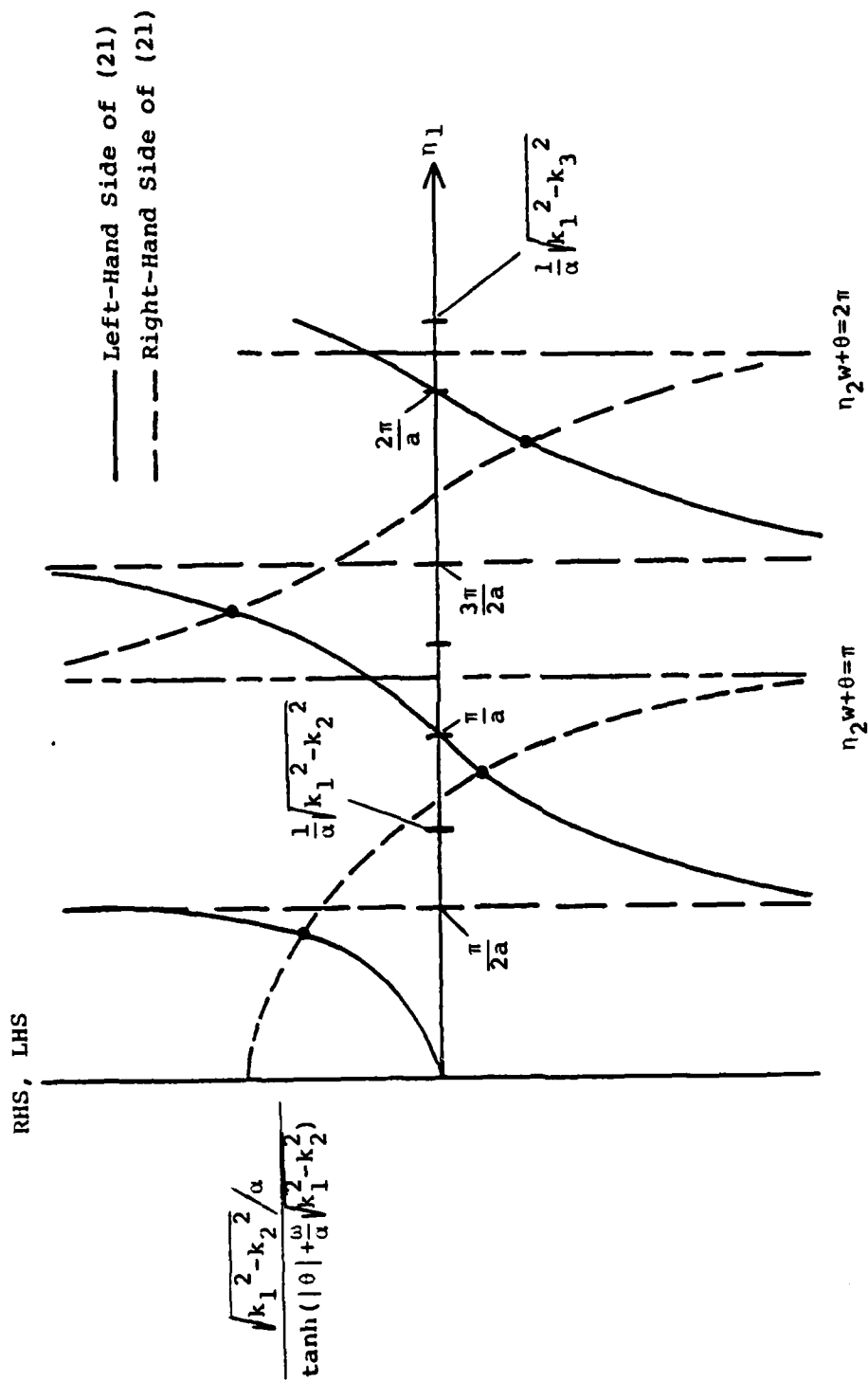


Figure 12. Construction for finding solutions to the dispersion relation in the absence of loss for waveguides having finite width electrodes when $k_1 \geq k_2 > k_3$.

Higher modes ($n=1,2,\dots$) start at $\text{Re}k = \text{Re}k_3$. For all modes, $\text{Re}k$ approaches $\text{Re}k_1$ as $2a$ becomes large.

Comparing Figure 13 with Figure 5 for semi-infinite electrodes, it is seen that more modes can propagate for a given value of $(2a)$ in the structure having finite width electrodes, even though H is nearly the same in both cases. This property can be understood by comparing the wavenumber k_1 in the central guiding region with that for $|x| \rightarrow \infty$, which is k_2 in the case of Figure 5 and k_3 for Figure 13. The number of modes increases with the difference between the real parts of k_1 and the wavenumber for $|x| \rightarrow \infty$. Since $\text{Re}(k_1 - k_2) > \text{Re}(k_1 - k_3)$ for the same H , one would expect more mode for the finite width electrodes, as is found to be the case.

Conversely, to have the same number of modes for the case of finite width electrodes as for semi-infinite electrodes, the value of H must be made smaller for the finite width electrodes. For example, if $H = 0.677$ is used for the semi-infinite electrodes, then to have the same number of modes for finite width electrodes one should use $H \approx 0.2$. For this value of layer thickness however, $\text{Re}k_2 > \text{Re}k_1$ changing somewhat the character of the lowest modes. This situation is discussed in the next section.

The effect of changing the electrode width w can be seen from Figure 14. Here we have plotted the phase constants $\text{Re}k$ for the various modes as a function of slot width $2a$ for $f = 1$ GHz and $H = 0.6 \mu\text{m}$, but for an electrode width $w = 10 \mu\text{m}$ that is double the width used for Figure 13. It is seen that two modes are guided by the $\Delta V/V$ guide formed by the electrodes when $2a = 0$. The curves for $w = 10$ are similar to those for $w = 5$, except that the wider electrode introduces one additional mode.

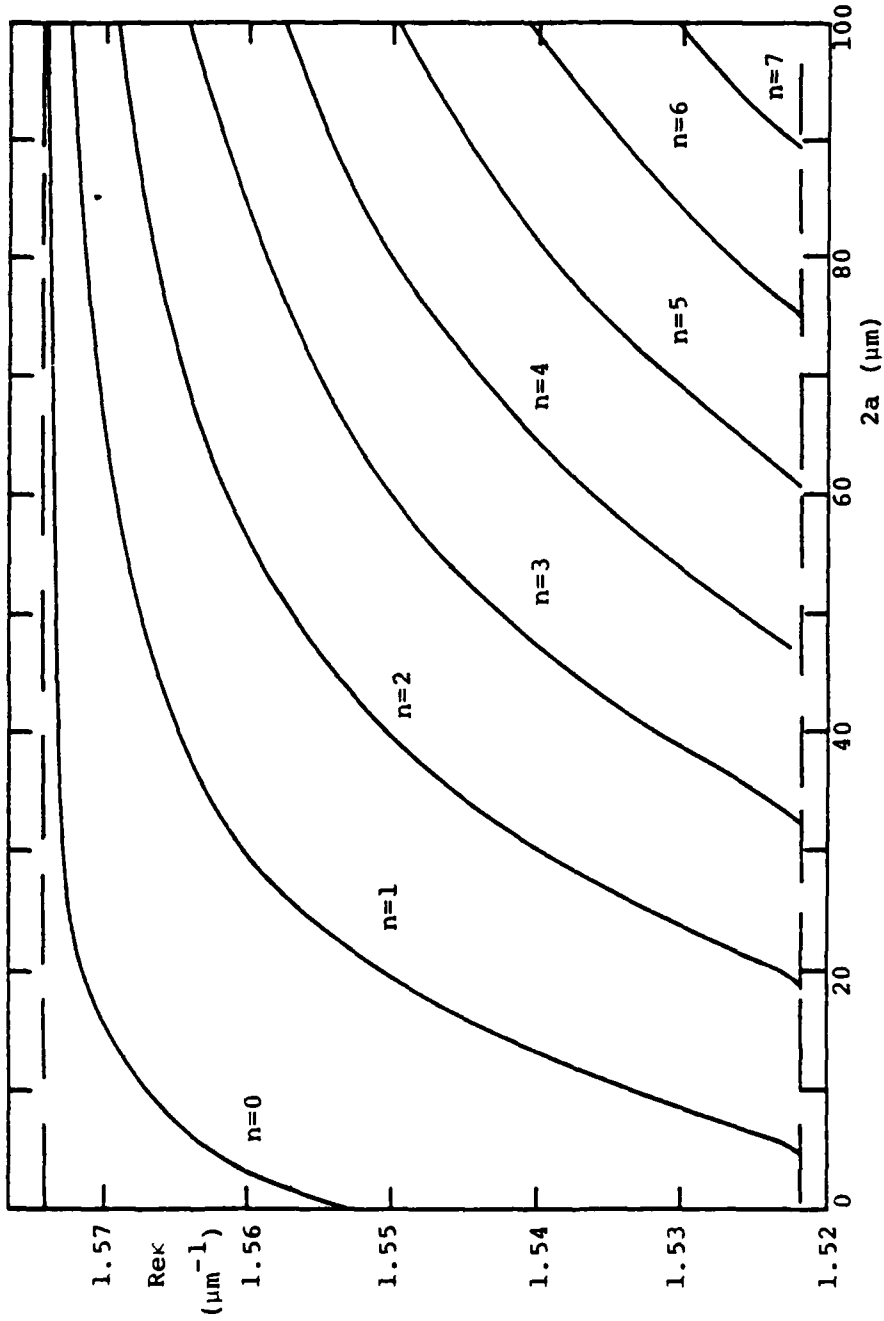


Figure 13. Variation of the propagation constants $\text{Re}\kappa$ with slot width $2a$ for the modes of slot guide having electrode width $w=5 \mu\text{m}$, $H=0.6 \mu\text{m}$ and $f=1 \text{ GHz}$.

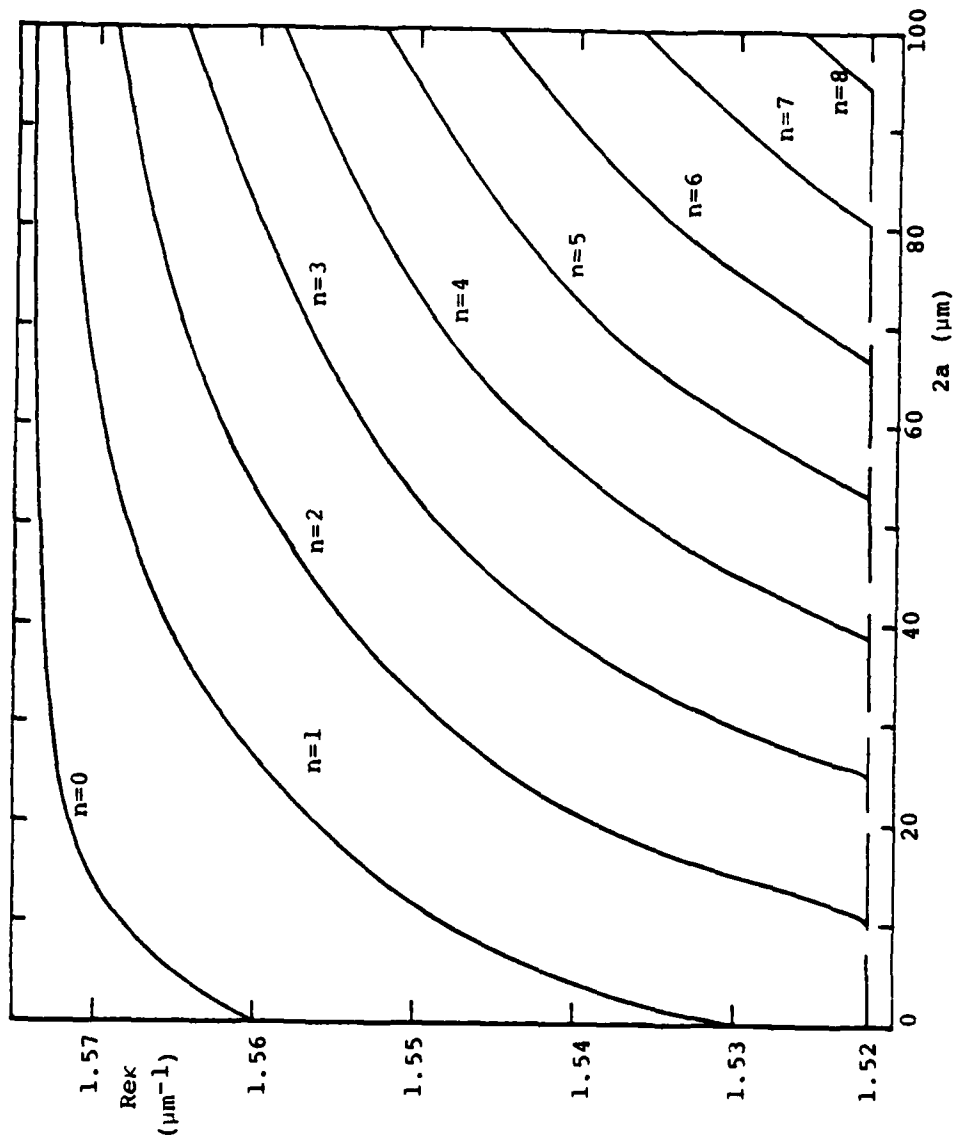


Figure 14. Variation of the propagation constant $\text{Re } \kappa$ with slot width $2a$ for the modes of slot guide having electrode width $w=10 \mu\text{m}$, $H=0.6 \mu\text{m}$ and $f=1 \text{ GHz}$.

Surface wave attenuation was found to have no effect on $\text{Re}k$ to the accuracy shown in Figures 13 and 14. The contribution to the guided wave attenuation due to loss in the electrodes is depicted in Figure 15 as a function of $2a$ for $f = 1$ GHz, $H = 0.6 \mu\text{m}$ and the electrode width $w = 5$ of Figure 13. Here we have plotted the difference between the guided wave attenuation constant $\text{Im}k$ and free-surface Rayleigh wave attenuation $\text{Im}k_1 = 3.5 \times 10^{-5} \mu\text{m}^{-1}$.

Attenuation of the lowest mode ($n = 0$) is high for $2a$ small, since this is a wave guided by the metal film, which is much more lossy than the free surface. The loss quickly decreases as $2a$ increases. Higher modes ($n = 1, 2, \dots$) near cutoff have $\text{Re}k$ close to $\text{Re}k_3$, and hence their fields extend far from the guiding structure on the $A\lambda N$ layered portion of the surface. Because the fields extend well away from the metal electrodes, their effect on the attenuation is small. Above cutoff, the fields are more concentrated under the electrodes and attenuation is higher. Finally, well above cutoff the fields become concentrated in the free-surface region between the electrodes and the loss becomes small again. Similar curves for $\text{Im}(\kappa - k_1)$ are obtained for $w = 10 \mu\text{m}$, corresponding to the propagation constant $\text{Re}k$ of Figure 14.

Comparing Figures 5 and 6 with 13 and 15, it is seen that for the same thickness of $A\lambda N$, narrow electrodes produce a more complex mode structure than do semi-infinite electrodes. Attenuation for the $n = 0$ modes is about the same for both electrode structures, but single mode operation is obtained over a wider range of electrode separation $2a$ for the semi-infinite electrodes. In short, narrow electrodes, which are more difficult to fabricate, appear to offer no advantage over semi-infinite electrodes when the same thickness $A\lambda N$ layer is used for both,

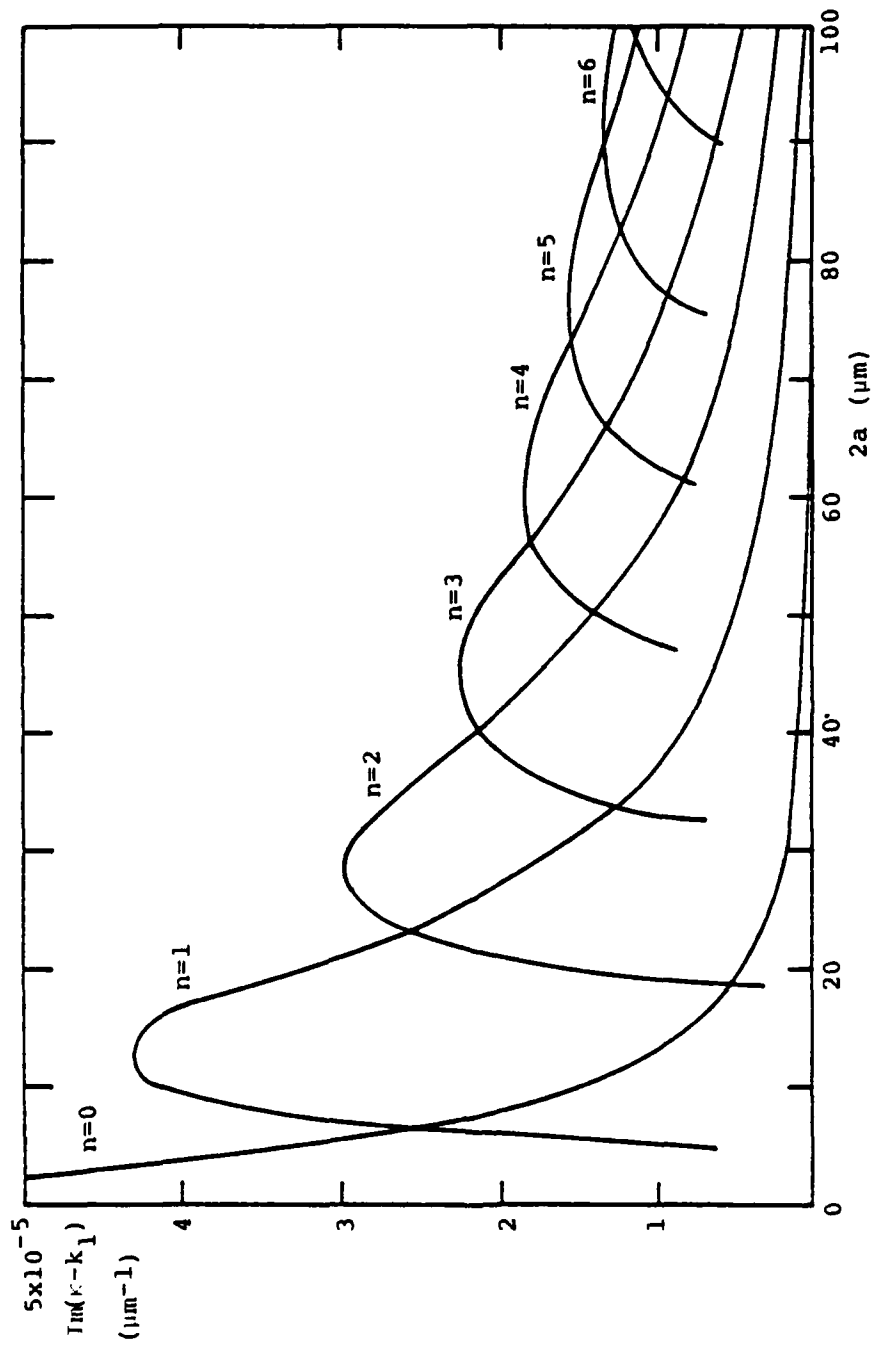


Figure 15. Dependence on slot width $2a$ of the attenuation due to the electrode metalization for modes of a slot guide having $w=5 \mu\text{m}$, $H=0.6 \mu\text{m}$ and $f=1 \text{ GHz}$.

and the thickness is great enough to allow guiding in the case of the semi-infinite electrodes. The guided wave properties obtained for reduced layer thickness are treated in the next section.

B. Guided Waves for $\text{Re}k_2 > \text{Re}k_1 > \text{Re}k_3$

When $\text{Re}k_2 > \text{Re}k_1$, a range of real values of η_2 exists over which η_1 is imaginary in the absence of loss. In this range of η_2 , the left-hand side of (21) is negative for η_2 positive and real. Since $\tan(\eta_2 w + \theta)$ can be negative for η_2 positive and real, a solution to (21) is possible in this range of η_2 . However, no solution of (21) is possible for which both η_1 and η_2 are imaginary, as discussed in the previous section.

In the absence of loss, when η_1 is imaginary with magnitude in the range $0 \leq |\eta_1| \leq \sqrt{k_2^2 - k_1^2}/\alpha$, then η_2 is real and η_3 imaginary. For η_1 real and in the range $0 \leq \eta_1 \leq \sqrt{k_1^2 - k_3^2}/\alpha$, then η_3 is imaginary but η_2 is real. These two ranges are plotted as the left-hand axis and right-hand axis in Figure 16, respectively. The two sides of (21) are sketched as a function of η_1 real, or of η_1 imaginary, in Figure 16. The intersection points, of which there are four in Figure 16, give the roots of (21).

The intersection points in the range where η_1 is imaginary correspond to perturbations of the modes that would be guided by the $\Delta V/V$ waveguide formed if the free surface in Figure 2b were to extend to $x \rightarrow -\infty$. Figure 16 has been drawn for w small enough so that only one such mode exists. For larger values of w more than one solution will exist for η_1 imaginary.

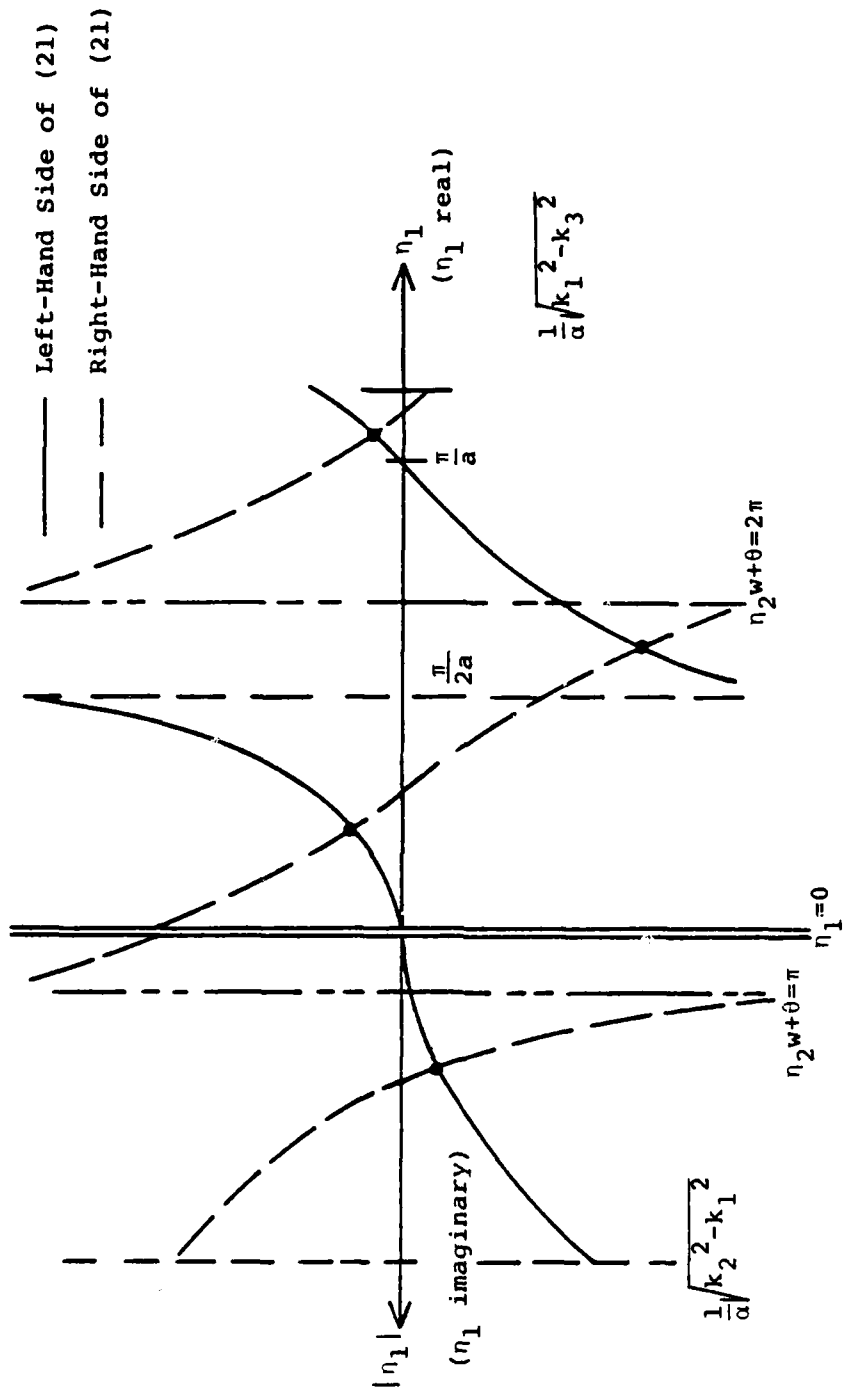


Figure 16. Construction for finding solutions to the dispersion relation in the absence of loss for waveguides having finite width electrodes when $k_2 > k_1 > k_3$.

Numerical solutions of (12) for the case $\text{Re}k_2 > \text{Re}k_1$ have been obtained by assuming $H = 0.2 \mu\text{m}$. The phase constant $\text{Re}k$ for the guided waves is plotted in Figure 17 as a function of slot width $2a$ for frequency $f = 1 \text{ GHz}$ and electrode width $w = 5 \mu\text{m}$. The contribution to the guided wave attenuation due to loss in the metal electrodes is plotted in Figure 18 as a function of $2a$ for the same parameters as used for figure 17.

For $2a$ large, the mode labeled $n = -1$ corresponds to a perturbation of the $\Delta V/V$ waveguide mode for a structure obtained by letting the free surface region in Figure 2b extend to $x \rightarrow -\infty$. When $2a \rightarrow 0$, this mode approaches that of a $\Delta V/V$ waveguide of width $2w$ and covered with an AlN layer. The $n = -1$ mode comes from the solution to (21) having η_1 imaginary. Because this mode is guided by the electrodes, its attenuation will be large compared to that of a free-surface Rayleigh wave, as seen from $\text{Im}(\kappa - k_1)$ in Figure 18.

The other modes in Figure 17 arise from the solutions to (21) having η_1 real. At cutoff they correspond to SAW propagation along z on the AlN layered surface. Above cutoff, the guided wave fields are larger under the electrodes, while well above cutoff the guided wave field is concentrated in the slot region and $\text{Re}k$ approaches $\text{Re}k_1$. As a result of this change in the modal field pattern, the contribution to the attenuation due to the electrodes, $\text{Im}(\kappa - k_1)$, is seen in Figure 18 to be zero at cutoff. It increases initially with $2a$, but decreases again for $2a$ large.

The effect of changing electrode width is seen from Figures 19 and 20, which have been plotted for an electrode width $w = 10 \mu\text{m}$ that is twice the width for Figures 17 and 18. As in the case of $w = 5$, one

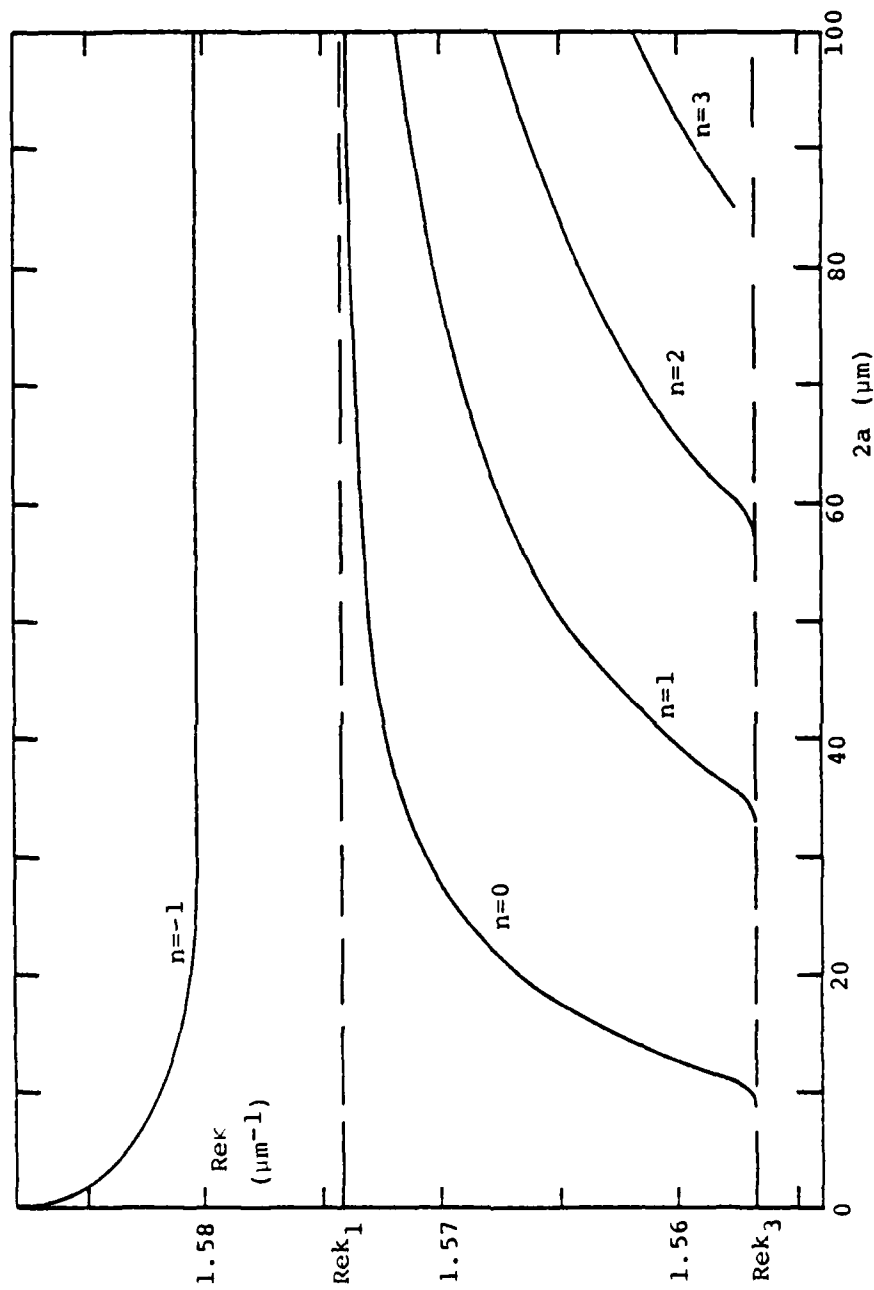


Figure 17. Dependence on slot width $2a$ of the propagation constants Re_k for the modes of slot guide having $w=5 \mu\text{m}$, $H=0.2 \mu\text{m}$ and $f=1\text{GHz}$.

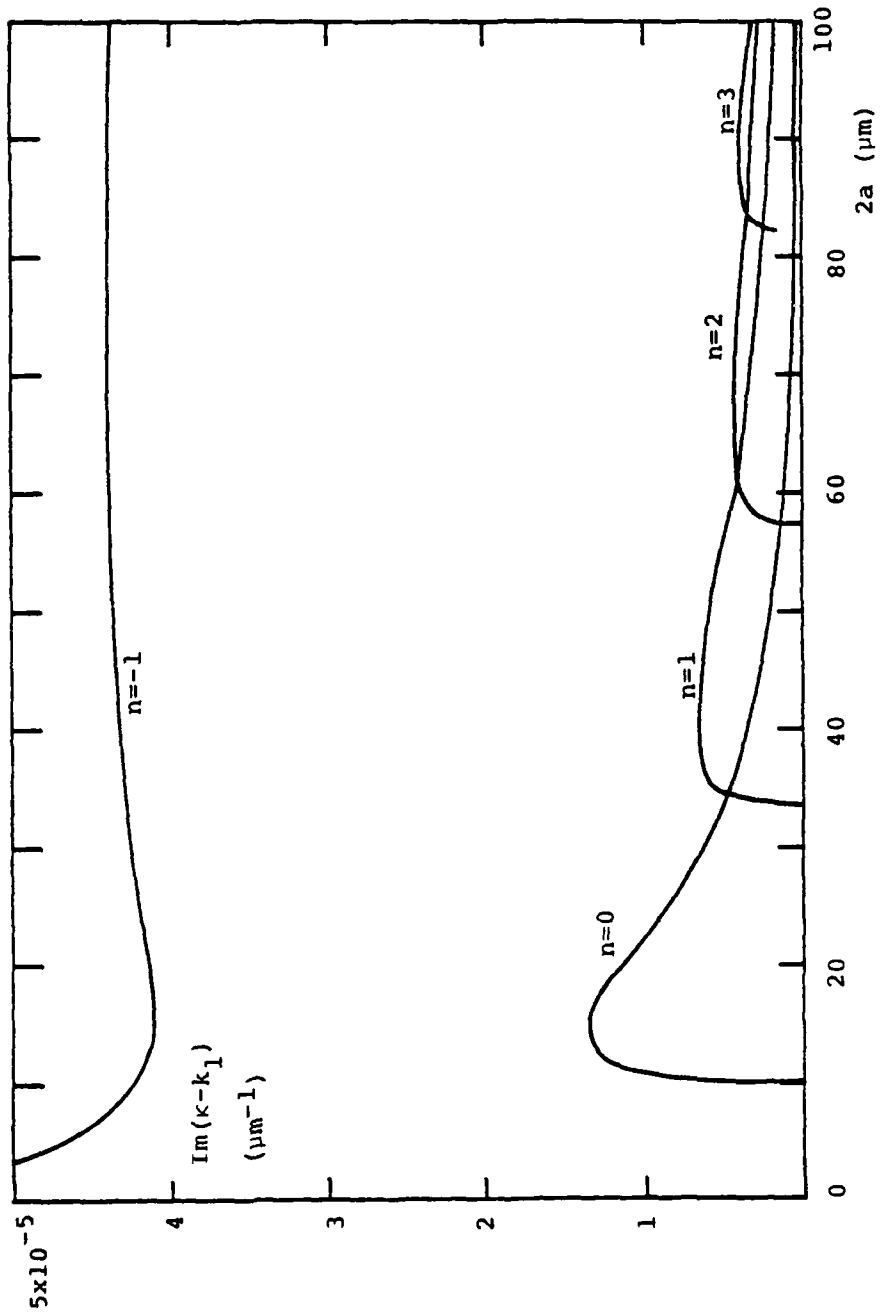


Figure 18. Dependence on slot width $2a$ of the attenuation due to electrode metalization for modes of slot guide having $w=5 \mu m$, $H=0.6 \mu m$ and $f=1$ GHz.

mode exists for which η_1 is imaginary. The propagation constant of this mode is shown in Figure 19. The attenuation constant of the mode $\text{Im}\kappa$ varies from a minimum of $9.82 \times 10^{-5} \mu\text{m}^{-1}$ at $2a = 8 \mu\text{m}$ to $10.06 \times 10^{-5} \mu\text{m}^{-1}$ at $2a = 100 \mu\text{m}$. Because $\text{Im}\kappa$ is large, the difference $\text{Im}(\kappa - k_1)$ does not fit on the scale of Figure 20, and is not shown.

The mode labeled $n = 0$ in Figure 19 is seen to exist for $2a \rightarrow 0$. In the limit $2a = 0$, the guiding structure consist of a $\Delta V/V$ waveguide of width $2w = 20 \mu\text{m}$, covered with an A2N layer. This structure guides a second mode for which $\text{Re}\kappa = 1.566 \mu\text{m}^{-1}$. However, for $2a$ large, the $\Delta V/V$ guide of width $w = 10 \mu\text{m}$ support only one mode, which is close to the $n = -1$ mode shown in Figure 19. Thus as $2a$ increases from zero, the $n = 0$ mode in Figure 19 gradually changes from a mode of $\Delta V/V$ guide to a mode of the slot guide. Corresponding to the change in the modal field pattern, the attenuation $\text{Im}(\kappa - k_1)$ due to the electrodes is large for $2a$ small, and decreases with increasing slot width $2a$. Higher modes ($n = 1, 2, \dots$) in Figures 19 and 20 have behavior that is similar to that of the higher modes for $w = 5 \mu\text{m}$.

Variation of the propagation constant with frequency is shown in Figure 21 for a slot width $2a = 20 \mu\text{m}$ and electrode width $w = 10 \mu\text{m}$. Here we have plotted $\text{Re}(\kappa - k_1)$ on a linear scale to accommodate positive and negative values. The $n = -1$ mode is slower than the free-surface Rayleigh wave and hence $\text{Re}(\kappa - k_1) > 0$. Waves guided by the slot are fast, so that $\text{Re}(\kappa - k_1) < 0$ for $n = 0, 1, 2, 3$. The $n = 0$ mode is similar to the first higher symmetric mode on a $\Delta V/V$ waveguide of width $2w$. As such the mode has a finite cutoff frequency. Numerically, the cutoff frequency of the $n = 0$ mode is found to be just under 0.6 GHz, at which frequency the fields on the A2N layered surface are

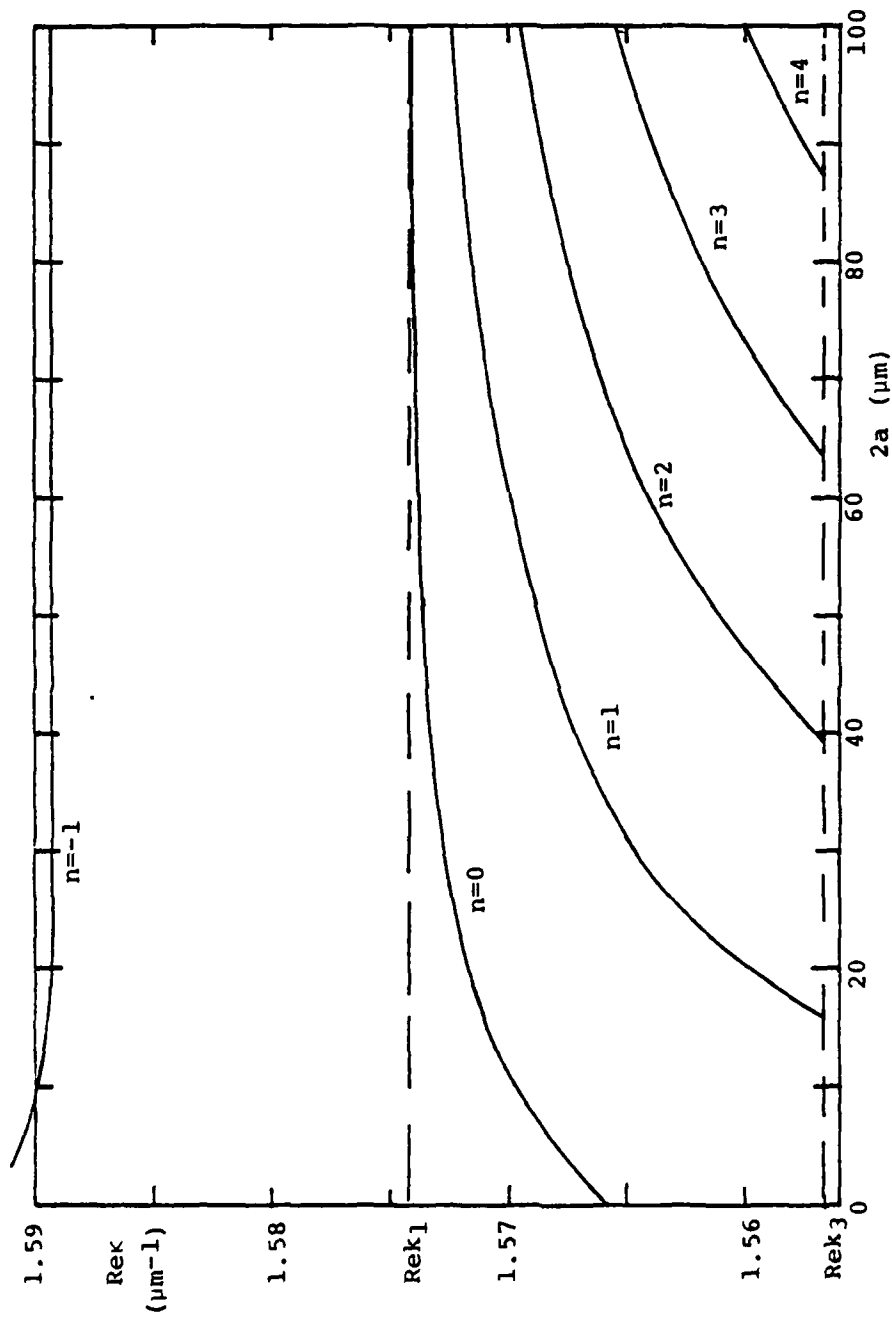


Figure 19. Dependence on slot width $2a$ of the propagation constants Re_k for the modes of slot guide having $w=10 \mu\text{m}$, $H=0.6 \mu\text{m}$ and $f=1 \text{ GHz}$.

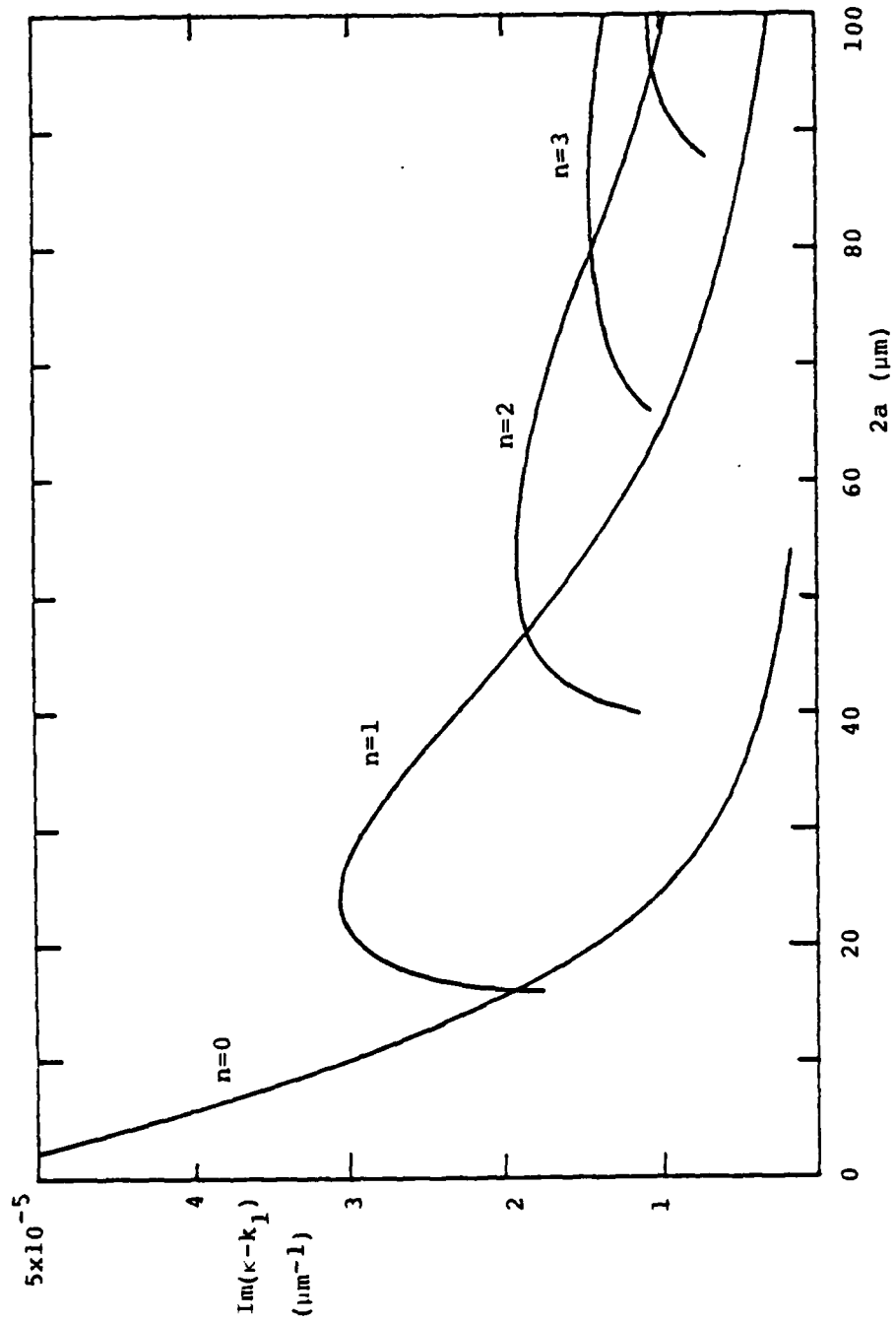


Figure 20. Dependence on slot width $2a$ of the attenuation due to electrode metalization for modes of slot guide having $w=5 \mu\text{m}$, $H=0.6 \mu\text{m}$ and $f=1 \text{ GHz}$. For the $n=-1$ mode $\text{Im}(\kappa - k_1) \approx 6.5 \times 10^{-5} \mu\text{m}^{-1}$.

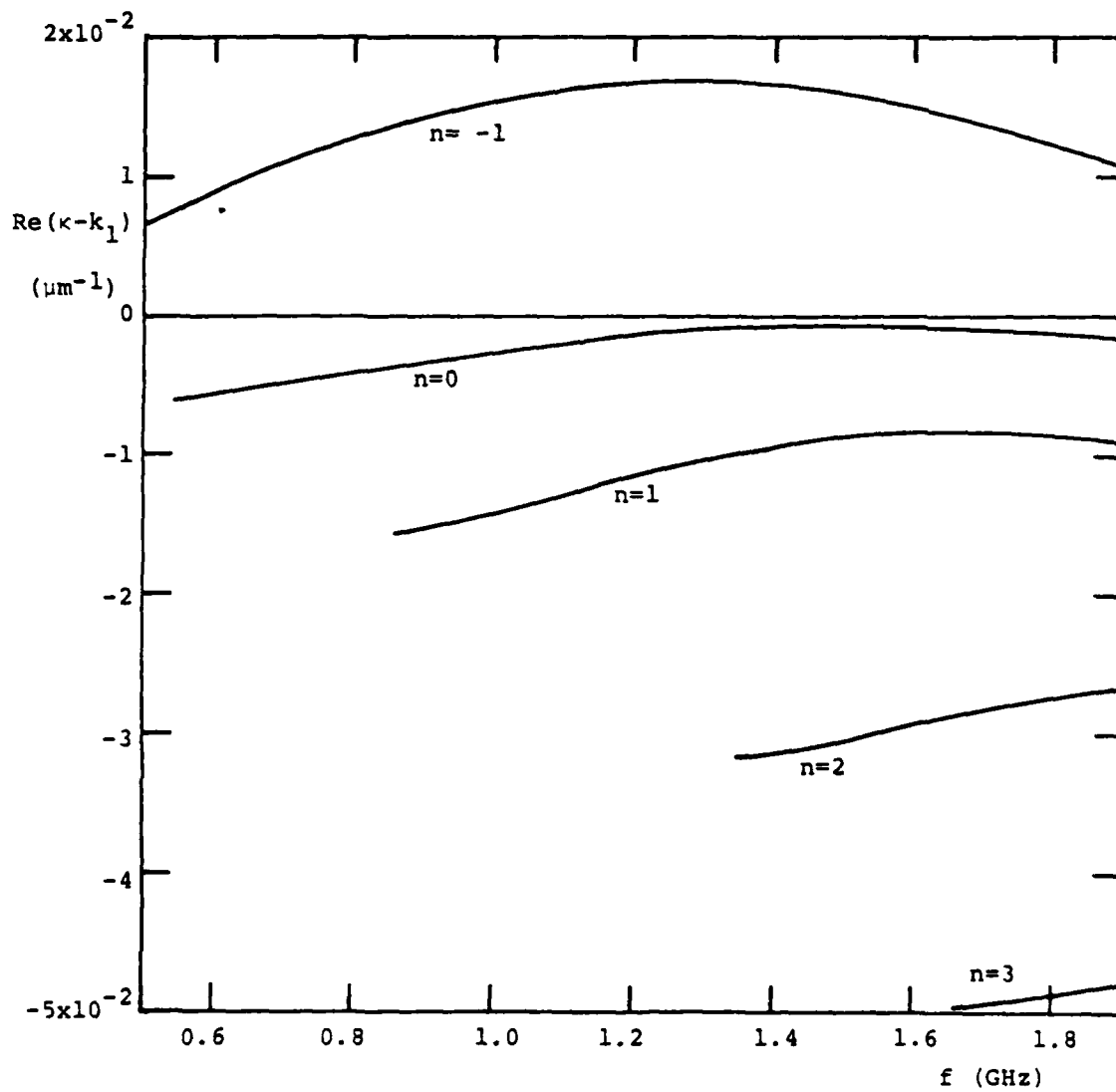


Figure 21. Frequency dependence of the propagation constants of slot guide having $w=10 \mu\text{m}$, $2a=20 \mu\text{m}$ and $H=0.2 \mu\text{m}$, plotted as the as the deviation $\text{Re}(\kappa-k_1)$.

those of a SAW propagating along z with wavenumber k_3 . The higher modes ($n = 1, 2, 3$) each have a cutoff frequency at which the fields on the layered surface are those of a SAW propagating with wavenumber k_3 at the cutoff frequency.

The contribution from the electrodes to the attenuation of the guided waves, $\text{Im}(\kappa - k_1)$, is plotted as a function of frequency in Figure 22 for the waveguide geometry shown in Figure 21. For comparison, $\text{Im}k_1$ is also plotted. The additional attenuation $\text{Im}(\kappa - k_1)$ of the $n = -1$ mode is nearly twice $\text{Im}k_1$, while for the $n = 0$ mode $\text{Im}(\kappa - k_1)$ is about one-half of $\text{Im}k_1$. Higher modes have $\text{Im}(\kappa - k_1) = 0$ at cutoff, but this quantity rapidly increases above $\text{Im}k_1$.

C. Comparison of Semi-Infinite and Narrow Electrodes

As pointed out previously, $\text{Re}k_3$ for $H = 0.2$ is approximately equal to $\text{Im}k_2$ for $H = 0.677$. One might therefore expect a similarity between the modes for the semi-infinite electrode structure with $H = 0.677$, and those for the finite width electrodes when $H = 0.2$. The similarity can be observed by comparing Figure 5 with Figures 17 and 19. Aside from the $n = -1$ mode, the $n = 0, 1, \dots$ modes have a similar dependence on $2a$, except for the cutoff value of $2a$ and the behavior of the $n = 0$ mode for $2a \rightarrow 0$. The mode numbering in Figures 17 and 19 is purely arbitrary, and made to facilitate comparison with figure 5. For wider electrodes, two or more modes with η_1 imaginary will exist. These modes have $\text{Re}k > \text{Re}k_1$ and, like the $n = -1$ mode in Figures 17 and 19, have no counterpart in Figure 5.

Attenuation for the $n = 0, 1, \dots$ modes is less for the finite width electrodes very near to cutoff, but is elsewhere greater than for the

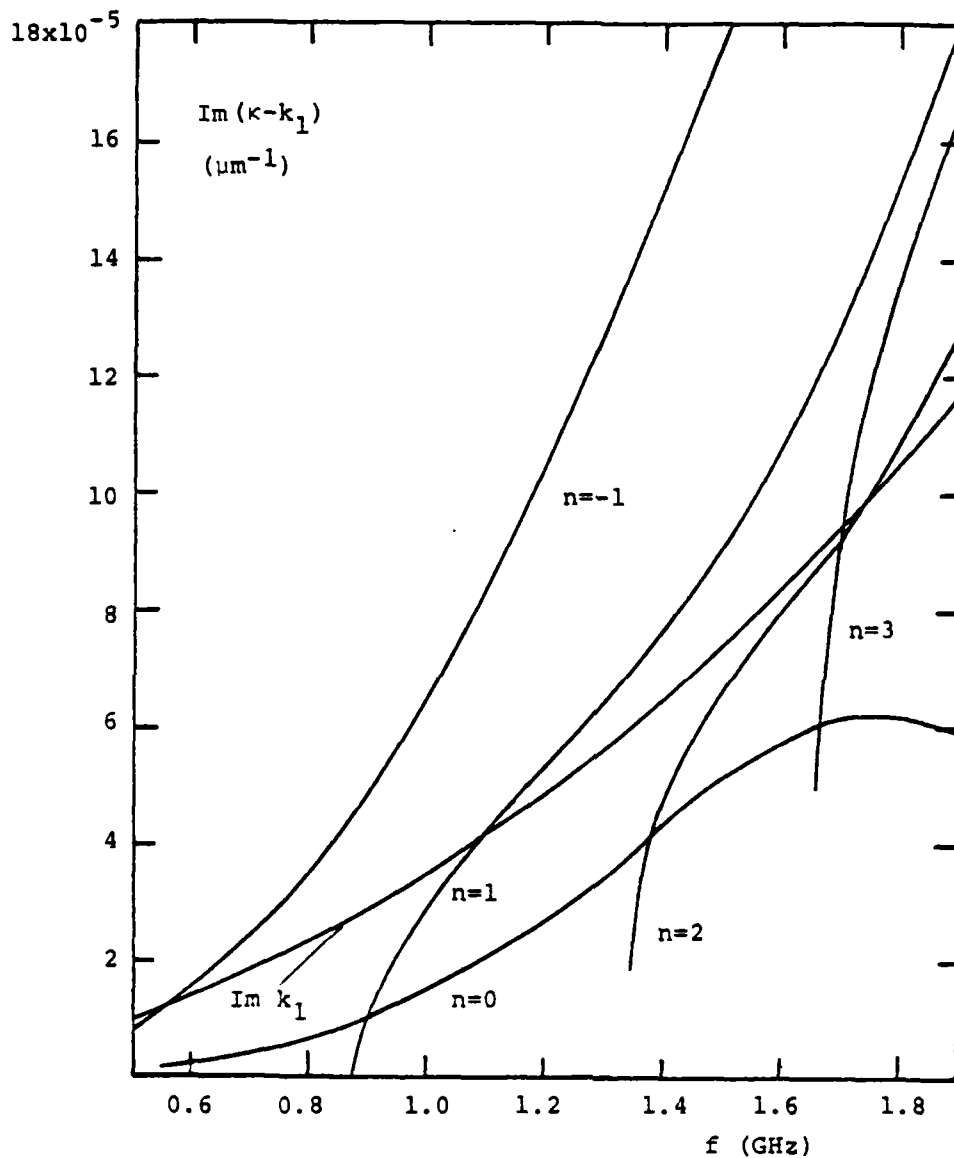


Figure 22. Frequency dependence of the attenuation due to metalization for the modes of slot guide having $w=10 \mu\text{m}$, $2a=20 \mu\text{m}$ and $H=0.2 \mu\text{m}$.

semi-infinite electrodes, as seen by comparing Figures 18 and 20 with Figure 6. This is due to the fact that for $H = 0.2$, the fields under the electrodes have sinusoidal dependence on x and fill the region under the electrodes. However, for $H = 0.677$ the fields under the electrodes decay exponentially with x away from the edge.

Frequency dependence of the phase constant for guides of slot width $2a = 20\mu\text{m}$ can be compared from Figure 7 for semi-infinite electrodes and from Figure 21 for $w = 10\mu\text{m}$. Aside from the differences in scales used, and the fact that $\text{Re}(\kappa - k_1)$ is plotted in one while $\text{Re}(k_1 - \kappa)$ is plotted in the other, the dependence is similar for the $n = 0, 1, \dots$ modes away from cutoff. Higher modes have higher values of $\text{Re}(k_1 - \kappa)$ and this quantity is a slowly varying function of frequency away from cutoff. The frequency dependence of $\text{Im}(\kappa - k_1)$ is however seen from Figures 8 and 22 to be considerably different for the two guiding structures.

In summary, for the same layer thickness H and slot width $2a$, the finite width electrode structure has more propagating modes than does the structure with semi-infinite electrodes - compare Figures 13 and 14 with Figure 5. Moreover, the attenuation of the modes is greater for the finite width electrodes - compare Figures 6 and 15. With the exception of the $n = -1$ mode, the modes for semi-infinite electrodes with $H = 0.677$ are similar to the modes for finite width electrodes with $H = 0.2$, although the latter generally have higher attenuation. Unless thickness of the AlN layer is critical for fabrication or other reasons not now apparent, the simple slot guide using semi-infinite electrodes appears to be the preferable geometry. Fabrication should be simpler, and the modes are fewest, as well as having the lowest attenuation away from cutoff.

V. Delay Line Path Loss

Insertion loss between the transducers of Figure 1 can be approximated as the product of three factors. The first is the electro-mechanical coupling efficiency of the transducers, which would give the total insertion loss if the two transducers were located close together on a free surface. The second factor gives the efficiency with which the aperture distribution of the fields radiated by the transducer couple to the transverse variation of the guided wave field. Guided wave attenuation, which was discussed in the last section, gives the third factor. In this section we treat the effect of mismatch between transverse distribution of modal fields and the aperture field of the transducer.

At the input transducer, the transverse field mismatch will result in a portion of the radiated power being carried away by the continuous spectrum of fields, rather than the guide waves. Thus, only a fraction of the radiated power will go into the guided waves. At the output transducer only a fraction of the power carried by a guided wave will couple out, e.g., some of the guided wave fields lie outside of the transducer aperture [18]. For identical input and output transducers, reciprocity implies that the fraction of the power coupled to a guided wave at the input is equal to the fraction of the power coupled to the transducer at the output.

Waldron [18] treated the problem of finding the output power resulting from the illumination of the transducer by a SAW having nonuniform amplitude. The mismatch of fields was found to effect the output power by the factor

$$\frac{\left| \int_{-b}^b \psi(x) dx \right|^2}{2b \int_{-\infty}^{\infty} |\psi(x)|^2 dx} \quad (22)$$

for a transducer of width $2b$. Here $\psi(x)$ is the transverse variation of the incident SAW amplitude, or in our case the transverse variation of the guided wave. Note that this factor is unity when $\psi(x)$ is uniform over the aperture $-b \leq x \leq b$ of the transducer, and zero outside the aperture. For all other $\psi(x)$, this factor is less than unity.

In the case of guided waves, the same factor (22) gives the field mismatch effect at the input, as well as the output. Thus the ratio of output to input power will involve the square of (22). Alternatively, the ratio of output to input voltage will include the first power of the factor (22) to account for field mismatch at both input and output. We define this factor as R_V , and evaluate it below for the various waveguide modes.

A. Field Mismatch Factor R_V for Semi-Infinite Electrodes

The amplitude variation of the symmetric modes of the slot waveguide of Figure 2a is given by

$$\psi(x) = \begin{cases} \cos\eta_1 a e^{i\eta_2(x-a)} & \text{for } x > a \\ \cos\eta_1 x & \text{for } -a \leq x \leq a \\ \cos\eta_1 a e^{-i\eta_2(x+a)} & \text{for } x < -a \end{cases} \quad (23)$$

In (23), η_1 is any one of the solutions to the dispersion equation (18) and η_2 is given by (17). Neglecting loss, η_1 is real and η_2 pure imaginary.

For each mode we may define the field mismatch factor R_V . As discussed above, R_V is obtained by substituting (23) into (22). Neglecting the imaginary part of η_1 and the real part of η_2 , after some manipulation one obtains

$$R_V = \frac{2/(\eta_1 b)}{|\eta_2| a + 1} \begin{cases} \frac{|\eta_2|}{\eta_1} \sin^2 \eta_1 b & \text{for } b \leq a \\ \frac{[\eta_1^2 + |\eta_2|^2 - \eta_1^2 e^{-|\eta_2|(b-a)}]^2}{\eta_1 |\eta_2| (\eta_1^2 + |\eta_2|^2)} & \text{for } b > a \end{cases} \quad (24)$$

The factor R_V has been computed as a function of transducer aperture $2b$ for various guide widths $2a$ at $f = 1$ GHz. For guide widths $2a = 10$ and $20 \mu\text{m}$, only the lowest mode propagates. We have plotted R_V for this mode in Figure 23 for the two guide widths, with abscissa b/a . For guide width $2a = 20 \mu\text{m}$, R_V peaks at 0.9 for aperture $2b$ equal to the guide width. In the case of the narrow guide $2a = 10 \mu\text{m}$, the fields extend a greater distance on the layered portions of the surface. In this case R_V has a maximum value for $2b = 15 \mu\text{m}$, which is $1\frac{1}{2}$ times the guide width. The maximum is broad so that even for $2b = 20 \mu\text{m}$, R_V is close to its maximum value.

In the case of a guide of width $2a = 40 \mu\text{m}$, two modes ($n = 0, 1$) can propagate at $f = 1$ GHz. The variation of R_V for each mode is plotted as a function of b/a in Figure 24. The value of R_V for the lowest mode peaks when the aperture $2b$ is about $9/10$ of the guide width, at which point R_V for the $n = 1$ mode is small. The zero of R_V for the $n = 1$ mode at $b/a \approx 0.8$ corresponds to an aperture $2b$ that covers one full cycle of $\cos \eta_1 x$ in (23), with the result that the integral of $\psi(x)$ in (22) vanishes.

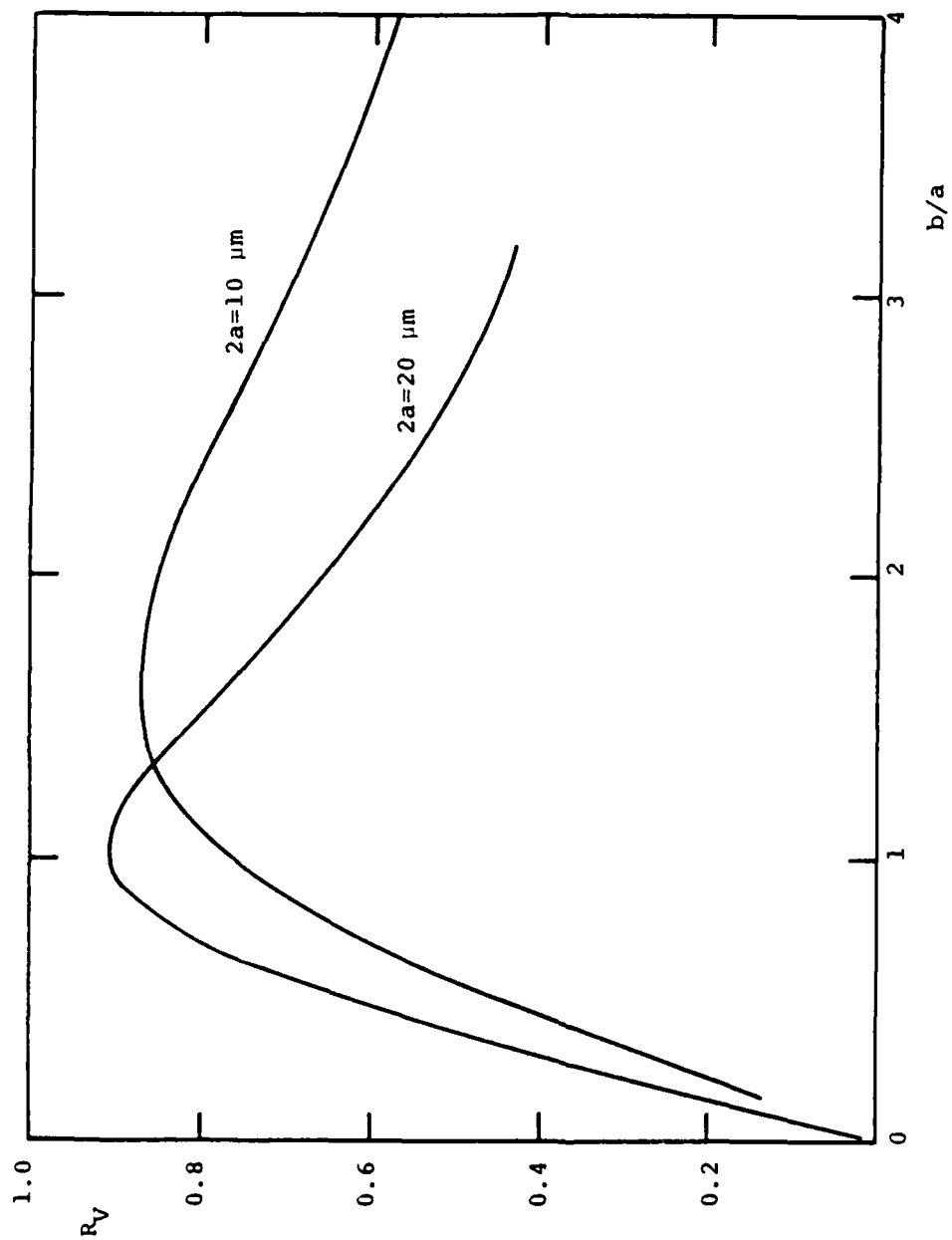


Figure 23. Dependence on transducer width $2b$ of the field miss-match factor for slot guides having semi-infinite electrodes for $2a=10, 20 \mu\text{m}$, $H=0.677 \mu\text{m}$ and $f = 1 \text{ GHz}$.

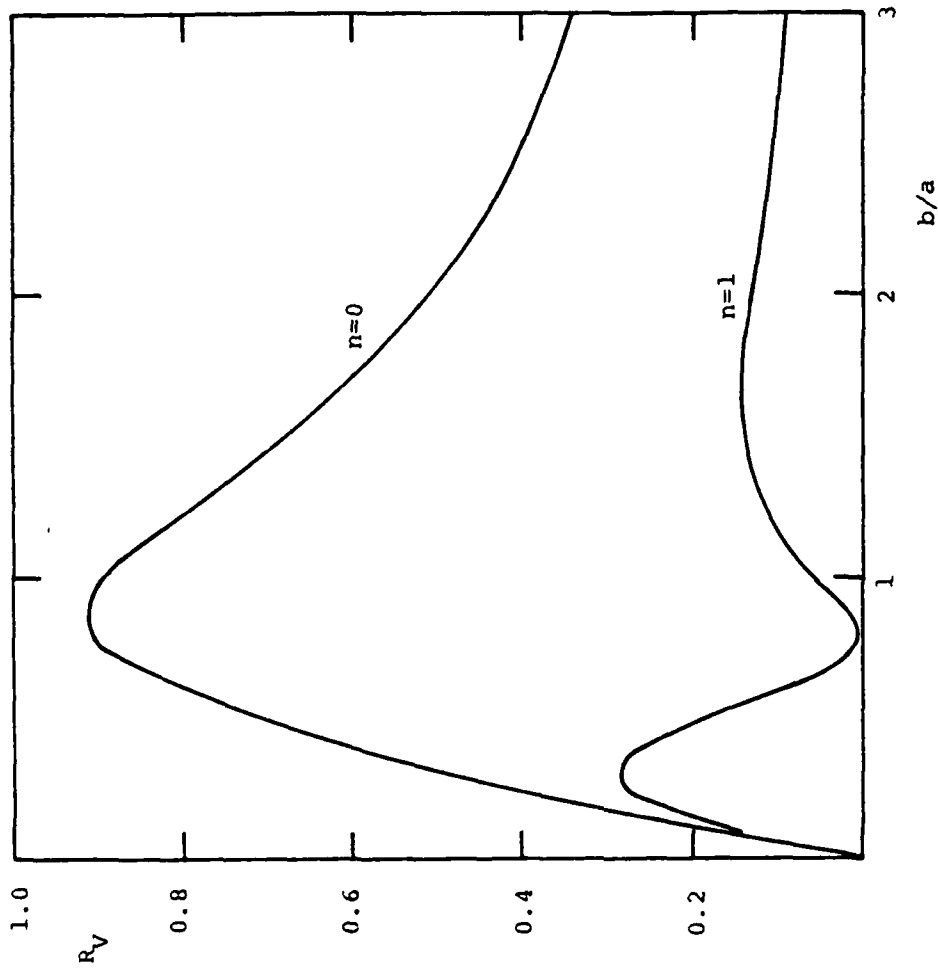


Figure 24. Dependence on transducer width $2b$ of the field miss-match factor for the two propagating modes for guide width $2a=40 \mu\text{m}$, $H=0.677 \mu\text{m}$ and $f = 1 \text{ GHz}$.

When two guided modes are present, as is the case for $2a = 40 \mu\text{m}$, the output voltage will show interference ripple when the frequency is scanned. The amplitude of the ripple can be estimated from the relative size of R_V for the two modes, and from their attenuation over the guide length L . Assuming $2b = 2a = 40 \mu\text{m}$, it is seen from Figure 24 that the ratio $R_V(n=1)/R_V(n=0)$ is 0.05/0.9. From Figure 6 for $2a = 40 \mu\text{m}$, it is seen that $\text{Im}\kappa(n=1) - \text{Im}\kappa(n=0)$ is approximately $0.9 \times 10^{-5} \mu\text{m}^{-1}$. For a short guide length L , so that the guided wave attenuation is not significant, the interference ripple is ± 0.5 db about the average. For a long path $L = 4$ cm, the attenuation difference reduces the ripple to ± 0.3 db.

The variation of R_V with frequency has been computed for several values of $a = b$. Results for $2a = 2b = 10$ and $20 \mu\text{m}$ are plotted in Figure 25. As frequency increases from cutoff, R_V for these $n = 0$ modes seen to approach 0.9. Over the same frequency range with $2a = 2b = 40 \mu\text{m}$, little variation was found for R_V of the $n = 0$ and $n = 1$ modes.

B. Field Mismatch Factor R_V for Finite Width Electrodes

In the various regions, the transverse variation of the amplitude for the symmetric modes can be expressed in the following form. For $0 \leq x \leq a$,

$$\psi(x) = \cos \eta_1 x \quad (25a)$$

Under the electrodes $a < x \leq a + w$

$$\psi(x) = \cos \eta_1 a \frac{\eta_2 \cos \eta_2 (x-a-w) + i \eta_3 \sin \eta_2 (x-a-w)}{\eta_2 \cos \eta_2 w - i \eta_3 \sin \eta_2 w} \quad (25b)$$

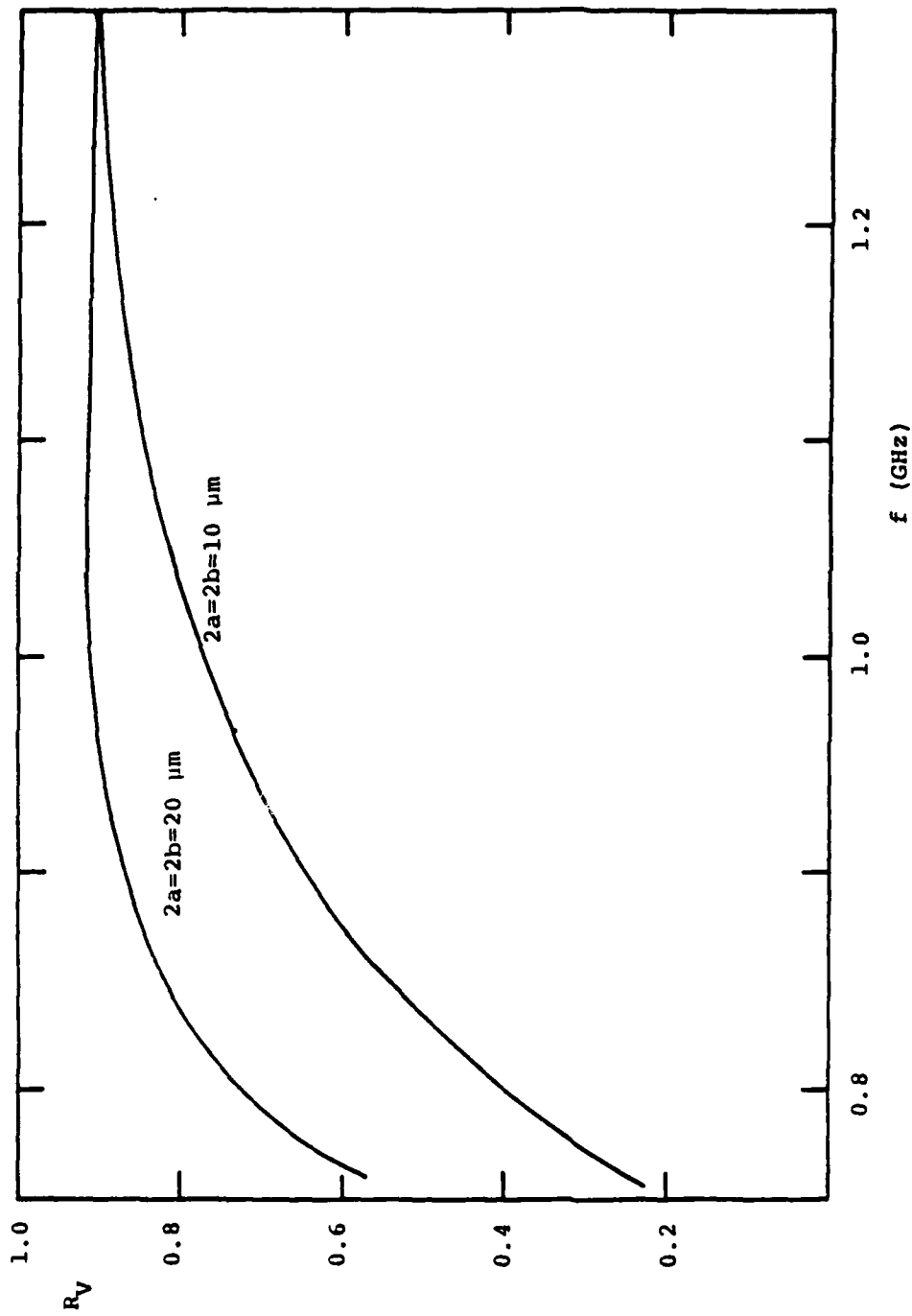


Figure 25. Frequency dependence of the field miss-match factor for the cases $2a=2b=10$, $20 \mu\text{m}$ of slot guides with semi-infinite electrodes and $H=0.677 \mu\text{m}$.

while for $x > a + w$

$$\psi(x) = \frac{\eta_2 \cos \eta_1 a e^{i\eta_3(x-a-w)}}{\eta_2 \cos \eta_2 w - i\eta_3 \sin \eta_2 w} \quad (25c)$$

These expressions directly satisfy continuity of $\psi(x)$ at $x = a$ and $x = a + w$, and continuity of $\partial\psi/\partial x$ at $x = a + w$. For η_1 satisfying the dispersion relation (21) and η_2, η_3 expressed in terms of η_1 , continuity of $\partial\psi/\partial x$ is also satisfied at $x = a$. For these symmetric modes, the amplitude in the region $x < 0$ is obtained by replacing x in (25) with $|x|$.

The factor R_V can be found by straight forward evaluation of the integrals in (22) making use of the expressions (25). As suggested by the transform approach to computing path loss used in Reference 6, it can be shown that neglecting loss

$$\begin{aligned} \int_{-\infty}^{\infty} |\psi|^2 dx &= \\ &= \frac{\cos^2 \eta_1 a}{\eta_1} \frac{d}{d\eta_1} \left[\eta_1 \tan \eta_1 a + \eta_2 \frac{i\eta_3 + \eta_2 \tan \eta_2 w}{\eta_2 - i\eta_3 \tan \eta_2 w} \right] \end{aligned} \quad (26)$$

In (26) η_3 is imaginary and both η_2 and η_3 must be expressed in terms of η_1 before the derivative is taken. Because the derivative can easily be computed numerically, this form for the denominator of (22) facilitates numerical evaluation.

The integral in the numerator of (22) must be evaluated for different ranges of b relative to a and $a + w$. For $0 < b \leq a$

$$\int_{-b}^b \psi dx = \frac{2}{\eta_1} \sin \eta_1 b \quad (27a)$$

For b in the range $a < b \leq a + w$,

$$\int_{-b}^b \psi dx = 2 \left(\frac{1}{\eta_1} - \frac{\eta_1}{\eta_2^2} \right) \sin \eta_1 a + 2 \frac{\cos \eta_1 a [\eta_2 \sin \eta_2 (b-a-w) - i \eta_3 \cos \eta_2 (b-a-w)]}{\eta_2 (\eta_2 \cos \eta_2 w - i \eta_3 \sin \eta_2 w)} \quad (27b)$$

Finally, for $b > a + w$

$$\int_{-b}^b \psi dx = 2 \left(\frac{1}{\eta_1} - \frac{\eta_1}{\eta_2^2} \right) \sin \eta_1 a - 2 \frac{\cos \eta_1 a \{ i \eta_3 + (\eta_2^2 / i \eta_3) [1 - e^{i \eta_3 (b-a-w)}] \}}{\eta_2 (\eta_2 \cos \eta_2 w - i \eta_3 \sin \eta_2 w)} \quad (27c)$$

The forgoing expressions were used to compute R_V for several cases.

The field mismatch factor is plotted in Figure 26 as a function of transducer width $2b$ for a slot guide of width $2a = 10 \mu\text{m}$, electrode width $w = 10 \mu\text{m}$ and layer thickness $H = 0.2 \mu\text{m}$. For these dimensions and for $f = 1 \text{ GHz}$ only the $n = -1, 0$ modes propagate. It is seen that the $n = -1$ mode guided by the electrodes can be more strongly excited than the desired $n = 0$ mode, whose fields are more nearly confined within the slot region. Even for $2b \approx 2a$, where R_V is maximum for the $n = 0$ mode, substantial excitation of the $n = -1$ mode will occur. If $b = a$, excitation of the $n = -1$ mode will result in ripple of $\pm 1.9 \text{ db}$ over a band of frequencies for short path lengths L . However, the large attenuation of the $n = -1$ mode compared to the $n = 0$ mode will reduce this ripple to $\pm 0.5 \text{ db}$ for a path length $L = 4 \text{ cm}$.

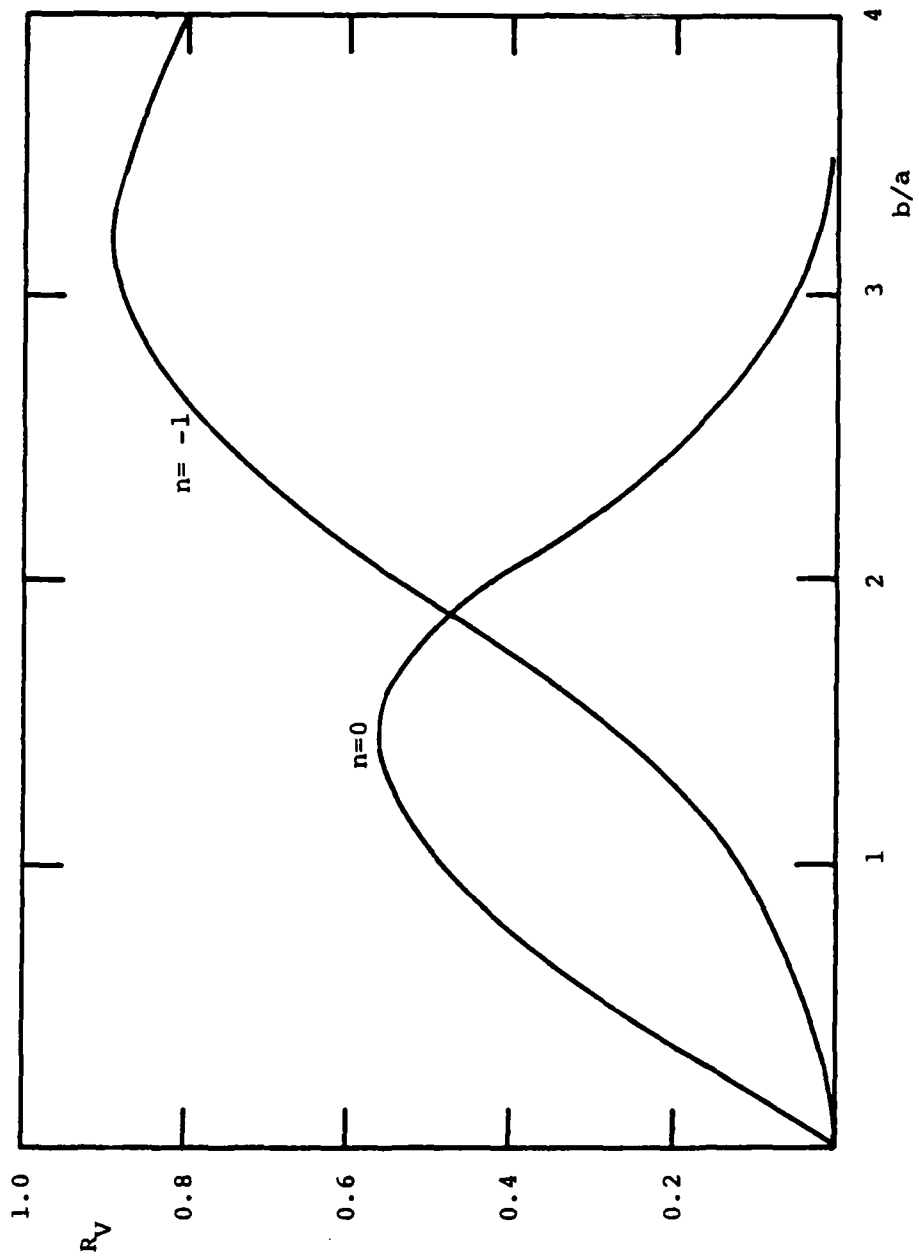


Figure 26. Dependence on transducer width $2b$ of the field miss-match factor for the modes of slot guide having finite width electrodes ($2a=w=10 \mu\text{m}$, $H=0.2 \mu\text{m}$, $f=1 \text{ GHz}$).

Figure 27 shows the field mismatch factor R_V for the three propagating modes of a guide whose width $2a = 20 \mu\text{m}$ is twice that of Figure 26, but whose other dimensions are the same. For $2b = 2a = 20 \mu\text{m}$ the $n = 0$ mode is more strongly excited than for $2b = 2a = 10 \mu\text{m}$. The presence of the $n = \pm 1$ modes however leads to ripple as frequency varies. For long paths L , the ripple is due to the $n = 1$ mode, since the high attenuation of the $n = -1$ mode significantly reduces its amplitude at the output. As an example, if $L = 4 \text{ cm}$, the ripple is $\pm 0.6 \text{ db}$.

Comparing Figures 26 and 27 with Figure 23, it is seen that simple slot guides having semi-infinite electrodes gives higher excitation efficiency for the $n = 0$ mode. further, they are free of the problems associated with having more than one propagating mode. This latter property is very significant in the case of narrow guides $2a = 10 \mu\text{m}$, where it may be convenient to use long transducers $2b > 2a$. Excitation of the $n = -1$ mode in guides having finite width electrodes would lead to severe multimode problems.

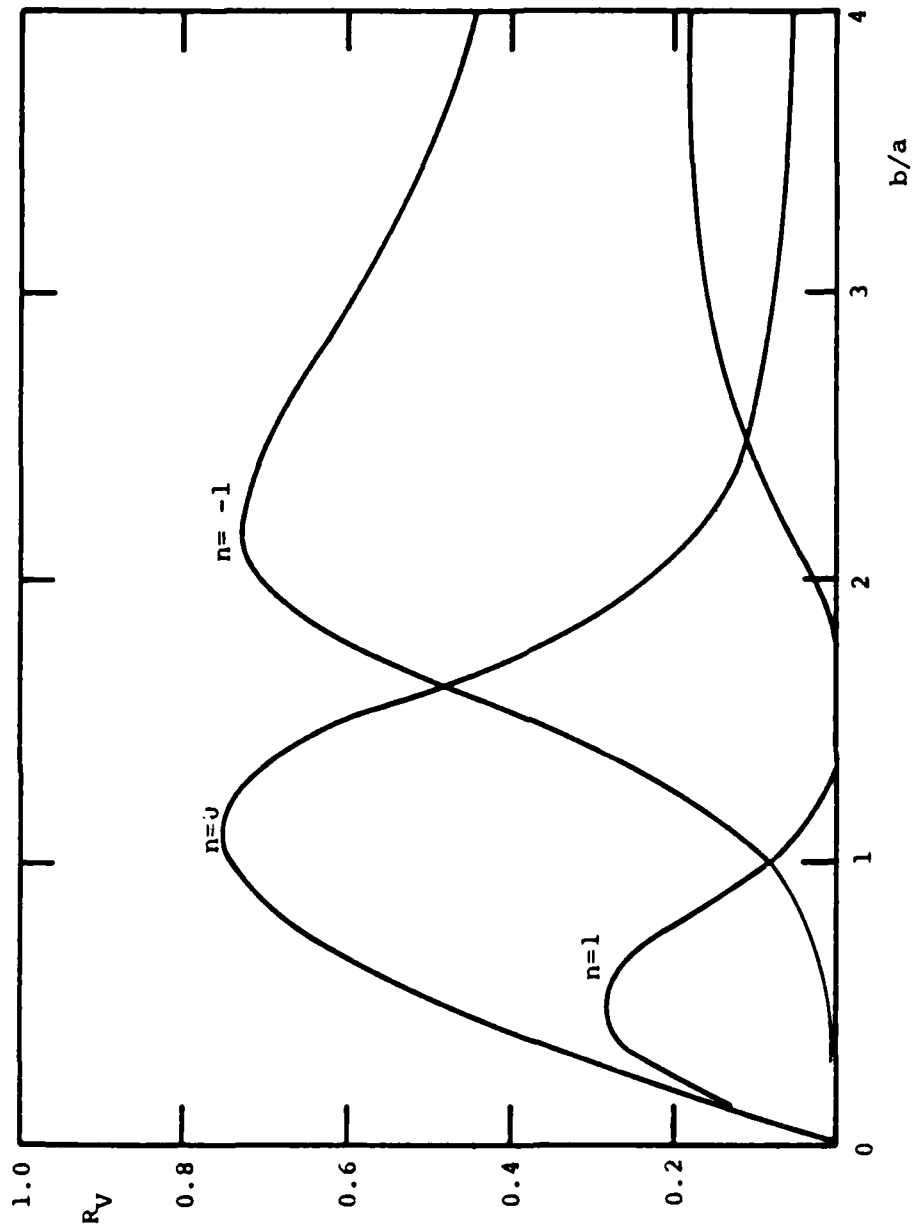


Figure 27. Dependence on transducer width $2b$ of the field miss-match factor for the modes of slot guide having finite width electrodes ($2a=20 \mu\text{m}$, $w=10 \mu\text{m}$, $H=0.2 \mu\text{m}$, $f=1 \text{ GHz}$).

VI. Conclusion

Simple slot waveguides having semi-infinite electrodes covered with AlN and slot width $2a$ in the range of 10-20 μm have only one propagating mode for frequencies in the vicinity of 1 GHz. Attenuation of this lowest mode is in the range 1.5-1 times that of the free-surface Rayleigh wave, i.e., between 4.6 and 3 dB/cm at 1 GHz. Loss due to mismatch between the transducer aperture and the modal field can be made close to 1 dB by using transducers of length $2b \approx 20 \mu\text{m}$.

The use of wider guides has disadvantages besides requiring higher D.C. voltage and/or greater path length to achieve $\frac{1}{4}$ cycle change in time delay. Because two or more symmetric modes can propagate, their interference gives rise to ripple in the frequency response that is of the order of 1 dB peak-to-peak. Since the modes have different transverse dependence, they will experience differently the D.C. electric field, which is nonuniform in the vicinity of the electrode edges. Thus the change in delay with applied voltage will be different, which will give rise to phase and amplitude variations with applied voltage.

More complex guides having finite width electrodes do not appear to offer any performance advantages. The lowest mode is confined beneath the electrodes, and thus has attenuation approaching that of the SAW on the metalized surface, which is at least 9.5 dB/cm for 600Å thick metalization at 1 GHz. For small electrode widths ($w \lesssim 10 \mu\text{m}$), the next higher symmetric mode is similar to the lowest mode of the simple slot guide, but with somewhat higher attenuation. It is this mode which will respond to the D.C. field between the electrodes. However, the presence of the mode concentrated beneath the electrodes will cause ripple in the response as a function of frequency.

Waveguides using semi-infinite electrodes require an A2N layer thickness of about 0.6 μm , as opposed to 0.2 μm for the case of finite width electrodes. However, deposition of the thicker layers does not appear to be a limitation [16,19], so that the simple slot guide appears to be the most desirable choice for an electrostatically variable SAW delay line.

VII. References

1. S.G. Jshi and B.B. Dasgupta, "Electronically Variable Surface Acoustic Wave Time Delay Using a Biasing Electric Field," Proc. 1981 IEEE Ultrasonics Symp., pp. 319-323.
2. S.G. Joshi, "A Temperature Compensated High Voltage Probe Using Surface Acoustic Waves," Proc. 1982 IEEE Ultrasonics Symp., pp. 317-320.
3. A.J. Budreau, P.H. Carr and J.H. Silva, "New Configuration for Electronically Variable SAW Delay Line," Proc. 1982 IEEE Ultrasonics Symp., pp. 399-400.
4. A.J. Budreau, P.H. Carr and H.L. Bertoni, "Highest Sensitivity Electrically Variable SAW Delay Line," Proc. 1983 IEEE Ultrasonics Symp.
5. A.J. Budreau, G.J. Scalzi, P.H. Carr and H.L. Bertoni, "Electrostatically Variable SAW Delay Lines - Theory and Experiment," IEEE Trans., SU, accepted for publication.
6. H.L. Bertoni, Propagation Loss in Electrostatically Variable SAW Delay Lines, Final Report of the 1983 USAF-SCEEE Summer Faculty Research Program, Contract No.: F49620-82-C-0035. Also issued as Rome Air Development Center report No. RADC-TR-84-6.
7. H.F. Tiersten, "Elastic Surface Waves Guided by Thin Films," JAP, 40 (1969), pp. 770-789.
8. B.K. Sinha and H.F. Tiersten, "Elastic and Piezoelectric Surface Waves Guided by Thin Films, JAP, 44 (1973), pp. 4831-4854.
9. R.V. Schmidt and L.A. Coldren, "Thin Film Acoustic Surface Waveguides on Anisotropic Media," IEEE Trans., SU-22 (1975), pp. 115-122.
10. L.A. Coldren and D.H. Smithgall, "Thin Film slot Waveguides of Arbitrary Cross Section," IEEE Trans., SU-22 (1975), pp. 123-130.
11. T.L. Szabo and A.J. Slobodnik, Jr., "The Effect of Diffraction on the Design of Acoustic Surface Wave Devices," IEEE Trans., SU-20 (1973), pp. 240-251.
12. A.J. Slobodnik, Jr., E.D. Conway and R.T. Delmonico, Microwave Acoustics Handbook-Vol. 2, AFCRL, Hanscom AFB, MA 01739, unpublished.
13. A.J. Slobodnik, Jr., P.H. Carr and A.J. Budreau, "Microwave Frequency Acoustic Surface-Wave Loss Mechanism on LiNbO₃," JAP, 41, (1970), pp. 4380-4387.
14. K.L. Davis and J.F. Weller, "SAW Attenuation in Metal Film-Coated Delay Lines," Proc. 1979 IEEE Ultrasonics Symp., pp. 659-662.

15. B.A. Auld, Acoustic Fields and Waves in Solids, Vol. II, Wiley and Sons, New York (1973), pp. 274-278.
16. K. Tsubouchi, K. Sugari, and N. Midoshiba, "Zero Temperature Coefficient Surface-Acoustic-Wave Devices Using Epitaxial AlN Films," Proc. 1982 IEEE Ultrasonics Symp., pp. 340-345.
17. A.A. Oliner, H.L. Bertoni and R.C.M. Li, "A Microwave Network Formalism for Acoustic Waves in Isotropic Media, Proc. IEEE, 60 (1972), pp. 1503-1512.
18. R.A. Waldron, "Power Transfer Factors for Nonuniformly Irradiated Interdigital Piezoelectric Transducers," IEEE Trans., SU-19 (1972), pp. 448-453.
19. S. Onishi, M. Eschwei, S. Bielaczy, and W-C. Wang, "Colorless, transparent, C-oriented aluminum nitride films grown at low temperature by a modified sputter gun," APL, 39 (1981), pp. 643-645.

1983-84 USAF-SCEEE RESEARCH INITIATION PROGRAM

Sponsored by the

AIR FORCE OFFICE OF SCIENTIFIC RESEARCH

Conducted by the

SOUTHEASTERN CENTER FOR ELECTRICAL ENGINEERING EDUCATION

FINAL REPORT

COMBUSTION MODELING OF HOMOGENEOUS SOLID PROPELLANTS

WITH SELECTIVELY ABSORBING INERT PARTICLE ADDITIVES

Prepared by: Dr. M. Quinn Brewster

Academic Rank: Assistant Professor

Department and
University: Mechanical & Industrial Engineering
University of Utah

Research Location: Air Force Rocket Propulsion Laboratory

Date: January 1985

Abstract

A two phase model has been developed to study aluminum (Al) particle preheating through selective radiation absorption in composite solid propellants. The two phases considered are one strongly absorbing particle (Al) phase and another weakly absorbing matrix (Ammonium Perchlorate (AP) and binder) phase surrounding the particle phase. Separate energy balance equations for the particle and matrix phases are developed. Both the matrix and the particle phase are assumed to be non-emitting, anisotropically scattering, absorbing media. The parameters identified which inhibit Al pre-heating and melting are Al size, mass fraction, burn rate and level of incident radiant flux. Smaller Al particles and larger Al mass fractions promote lower Al temperatures. These results should prove useful to propellant formulators in trying to reduce the problem of unwanted Al agglomeration.

INTRODUCTION

It has been observed that during the combustion of aluminized composite solid propellants, some of the aluminum particles agglomerate before they leave the surface of the propellant [1-3]. Typically, aluminum particles with mean diameters of 5-30 μ m may be mixed in the propellant formulation. Yet combustion bomb studies [1-3] indicate that aluminum agglomerates as large as 300 μ m leave the burning propellant surface. This agglomeration results in two kinds of loss. The first loss is the energy that escapes due to the fact that the large agglomerates have insufficient residence time to burn completely. The second loss is the two phase flow loss incurred in dragging the large agglomerates out through the nozzle. Both types of loss reduce the specific impulse of the rocket motor.

It is conceivable that the problem of unwanted aluminum agglomeration could be substantially reduced by maintaining the temperature of the aluminum particles below the melting temperature (933K for pure aluminum). To study the factors which influence the temperature variation of the aluminum particles, a heat transfer model has been developed. Among the factors investigated which influence the aluminum particle temperature are aluminum particle size and mass fraction, the level of radiant flux incident from the rocket motor, and the nature of the propellant matrix surrounding the aluminum.

The type of propellant studied was an Ammonium Perchlorate (AP)/hydrocarbon/aluminum (Al) composite propellant with properties similar to Morton-Thiokol space shuttle propellant. Bi-modal AP was considered. Taken together the AP oxidizer and hydrocarbon binder constitute the matrix which surrounds the Al particles (see Fig. 1). Since the matrix is relatively transparent to thermal radiation and since significant levels of radiant

flux are likely to be present in aluminized propellant motors due to the abundance of Al and Al₂O₃ particles suspended in the gas phase it is quite possible for the Al particles embedded in the propellant to be preferentially heated and become hotter than the surrounding matrix. Furthermore the low thermal conductivity of AP ($k_{AP} = 0.04186 \text{ W/m K}$, $10^{-4} \text{ cal/cm s K}$) inhibits heat conduction between the Al particles and matrix and thus preserves separate and distinct matrix and Al particle temperatures. By tailoring the propellant's thermal radiative absorption and scattering properties it should be possible, in theory at least, to control the sub-surface Al particle temperature profile and maintain Al particle temperatures below the matrix temperatures. Perhaps it would be possible to maintain the Al particles below the melting temperature. These considerations are the basis for this theoretical study.

Definition of Model

The model developed consists of two phases, one strongly absorbing particle phase consisting of Al particles and another weakly absorbing matrix phase (AP plus hydrocarbon binder) (Fig. 1). The incident radiation was assumed to be blackbody radiation at a temperature T_R . For theoretical purposes all particles (AP and Al) were treated as spherical and monodisperse. Both phases were assumed to be non-emitting, anisotropically scattering, absorbing media.

Analysis

As the propellant is assumed to be non-emitting the radiative transfer equation is decoupled from the energy equations and solved by the two-flux method [4].

The two-flux radiative transfer equations are

$$\frac{dI_{\lambda}^{+}}{dx} = -(\bar{a}_{\lambda} + \bar{\sigma}_{\lambda}) I_{\lambda}^{+} + \bar{\sigma}_{\lambda} \bar{I}_{\lambda} \quad (1)$$

$$-\frac{dI_{\lambda}^{-}}{dx} = -(\bar{a}_{\lambda} + \bar{\sigma}_{\lambda}) I_{\lambda}^{-} + \bar{\sigma}_{\lambda} I_{\lambda}^{+} \quad (2)$$

where

$$\bar{a}_{\lambda} = 2(a_{\lambda B} + a_{\lambda AP_1} + a_{\lambda AP_2} + a_{\lambda AI}) \quad (3)$$

$$\bar{\sigma}_{\lambda} = 2(\sigma_{\lambda AP_1} B_{AP_1} + \sigma_{\lambda AP_2} B_{AP_2} + \sigma_{\lambda AI} B_{AI}) \quad (4)$$

$$a_{\lambda i} = \frac{1.5 f_{vi} Q_{ai}}{D_i} \quad \text{except } a_{\lambda B} = \frac{f_{vB} 4\pi k_B}{\lambda} \quad (5)$$

$$\sigma_{\lambda i} = \frac{1.5 f_{vi} Q_{si}}{D_i} \quad (6)$$

$$B_i = \frac{1}{2} \int_0^1 \int_{-1}^0 P_i(\mu, \mu') d\mu' d\mu \quad (7)$$

$$P_i(\mu, \mu') = \frac{1}{\pi} \int_{\theta_0}^{\theta_{\pi}} \frac{p(\theta) \sin\theta d\theta}{[(1-\mu^2)(1-\mu'^2) - (\cos\theta - \mu\mu')^2]^{1/2}} \quad (8)$$

$p(\theta)$ - single scatter phase function

θ_0 and θ_{π} are defined as:

$$\cos\theta_0 = \mu\mu' + (1-\mu^2)^{1/2} (1-\mu'^2)^{1/2} \quad (9)$$

$$\cos\theta_{\pi} = \mu\mu' - (1-\mu^2)^{1/2} (1-\mu'^2)^{1/2} \quad (10)$$

Directions for I^{+} and I^{-} are as shown in Figure 2.

Solution of equations (1) and (2) with the boundary conditions

$$(1) \text{ at } x \rightarrow -\infty: I_{\lambda}^{+} \rightarrow \text{finite value} \quad (11)$$

$$(2) \text{ at } x = 0: I_{\lambda}^{-}(0) = (1-R) \frac{q_{R\lambda}}{\pi} + R I_{\lambda}^{+}(0) \quad (12)$$

(where R is the hemispherical spectral reflectivity and $q_{R\lambda}/\pi =$ (uniform) incident intensity)

$$2\pi[I_{\lambda}^{+}(x) + I_{\lambda}^{-}(x)] = 2C_{\lambda} \exp[\gamma_{\lambda}x] \quad (13)$$

where,

$$\gamma_{\lambda} = \bar{a}_{\lambda} (\bar{a}_{\lambda} + 2\bar{\sigma}_{\lambda}) \quad (14)$$

$$C_{\lambda} = \pi C_1 \left[1 + \frac{1}{\bar{\sigma}_{\lambda}} \bar{a}_{\lambda} (\bar{a}_{\lambda} + 2\bar{\sigma}_{\lambda}) + \frac{1}{\bar{\sigma}_{\lambda}} (\bar{a}_{\lambda} + \bar{\sigma}_{\lambda}) \right] \quad (15)$$

$$C_1 = \frac{(1-R) q_{R\lambda}/\pi}{\frac{1}{\bar{\sigma}_{\lambda}} [\bar{a}_{\lambda} (\bar{a}_{\lambda} + 2\bar{\sigma}_{\lambda})]^{1/2} + \frac{1}{\bar{\sigma}_{\lambda}} (\bar{a}_{\lambda} + \bar{\sigma}_{\lambda}) - R} \quad (16)$$

In equation [13] the term $2\pi[I_{\lambda}^{+}(x) + I_{\lambda}^{-}(x)]$ has the interpretation of the radiant power incident on a differential slab element of propellant per unit volume per unit wavelength. Weighted by the appropriate absorption coefficients this term will appear as a source term in the particle and matrix energy equations.

Separate steady state energy equations for the matrix and particle phase are written.

$$(\rho C)_{\infty} (f_{vB} + f_{vAP}) r \frac{dT_{\infty}}{dx} = k_{\infty} (f_{vB} + f_{vAP}) \frac{d^2T_{\infty}}{dx^2} + \pi \frac{2}{D_{A1}} \left(\frac{2k_{\infty}}{D_{A1}} \right) (T_p - T_{\infty}) N_{A1} + \pi \int_0^{\infty} (\bar{a}_{B\lambda} + \bar{a}_{AP\lambda}) (I_{\lambda}^{+} + I_{\lambda}^{-}) d\lambda \quad (17)$$

$$f_{vAL} \rho_{A1} C_{A1} r \frac{dT_p}{dx} = \pi \frac{2}{D_{A1}} \left(\frac{2k_{\infty}}{D_{A1}} \right) (T_{\infty} - T_p) N_{A1} + \pi \int_0^{\infty} \bar{a}_{A1\lambda} (I_{\lambda}^{+} + I_{\lambda}^{-}) d\lambda \quad (18)$$

where

$$k_{\infty} = \frac{f_{vB} k_B + f_{vAP} k_{AP}}{f_{vB} + f_{vAP}} \quad (19)$$

$$(\rho C)_{\infty} = \frac{f_{vB} \rho_B C_B + f_{vAP} \rho_{AP} C_{AP}}{(f_{vB} + f_{vAP})} \quad (20)$$

$$N_{A1} = \frac{6 f_{vA1}}{\pi D_{A1}} \quad (21)$$

The above equations are coupled through the conduction term $h (T_p - T_{\infty})$:
 $h = 2k_{\infty}/D_{A1}$. In this equation the limiting result for spherical conduction, $Nu = 2$, is used [5]. Also the particle temperature has been lumped due to the poor matrix conductivity.

$$\text{Biot No.} = h (D_{A1}/3)/k_{A1} = 2/3 k_{\infty}/k_{A1} \ll 0.1$$

The coupled energy and transfer equations are reduced to:

$$\frac{d^3 T_{\infty}}{dx^3} + a_2 \frac{d^2 T_{\infty}}{dx^2} + a_1 \frac{dT_{\infty}}{dx} + a_0 \int_0^{\infty} \bar{a}_{\lambda} C_{\lambda} e^{\gamma_{\lambda} x} d\lambda + \frac{1}{k_{\infty}(f_{vB} + f_{vAP})} \int_0^{\infty} (\bar{a}_{B\lambda} + \bar{a}_{AP\lambda}) C_{\lambda} e^{\gamma_{\lambda} x} d\lambda = 0 \quad (22)$$

where:

$$a_0 = \frac{12}{\rho_{A1} D_{A1}^2 C_{A1} r (f_{vB} + f_{vAP})} \quad (23)$$

$$a_1 = \frac{-12(\rho C)_{\infty}}{\rho_{A1} D_{A1}^2 C_{A1}} - \frac{12 f_{vA1}}{D_{A1}^2 (f_{vB} + f_{vAP})} \quad (24)$$

and

$$a_2 = \frac{-(\rho C)_{\infty} r}{k_{\infty}} + \frac{12 k_{\infty}}{D_{A1}^2 \rho_{A1} C_{A1} r} \quad (25)$$

The solution of this equation is

$$T_{\infty}(x) = [T_s - T_0 - \int_0^{\infty} C_{0\lambda} d\lambda] e^{\alpha_1 x} + \int_0^{\infty} C_{0\lambda} e^{\gamma_{\lambda} x} d\lambda + T_0 \quad (26)$$

where the boundary conditions used are

$$(1) T_{\infty}(0) = T_S \quad (27)$$

$$(2) T_{\infty}(x \rightarrow -\infty) = T_0 \quad (28)$$

$$(3) dT_{\infty}/dx (x \rightarrow \infty) = 0 \quad (29)$$

The constants appearing in the solution for $T_{\infty}(x)$ are

$$C_{0\lambda} = \frac{-C_{\lambda} \left[a_0 \bar{a}_{\lambda} + \left(\frac{\bar{a}_{B\lambda} + \bar{a}_{AP\lambda}}{k_{\infty}(f_{VB} + f_{VAP})} \right) \gamma_{\lambda} \right]}{\gamma_{\lambda}^3 + \gamma_{\lambda}^2 a_2 + \gamma_{\lambda} a_1} \quad (30)$$

and

$$a_1 = \frac{-a_2 + \sqrt{a_2^2 - 4a_1}}{2} \quad (31)$$

The particle temperature can then be determined as

$$\begin{aligned} T_p(x) = T_{\infty}(x) + \frac{D_{A1}^2 (\rho C)_{\infty} r (f_{VB} + f_{VAP})}{12 k_{\infty} f_{VA1}} \left\{ a_1 (T_{\infty}(x) - T_0) \right. \\ \left. + \int_0^{\infty} C_{0\lambda} e^{\gamma_{\lambda} x} (\gamma_{\lambda} - a_1) d\lambda \right\} - \frac{D_{A1}^2 (f_{VB} + f_{VAP})}{12 f_{VA1}} \left\{ a_1^2 \right. \\ \left. (T_{\infty}(x) - T_0) + \int_0^{\infty} C_{0\lambda} e^{\gamma_{\lambda} x} (\gamma_{\lambda}^2 - a_1^2) d\lambda \right\} \\ - \frac{D_{A1}^2}{12 k_{\infty} f_{VA1}} \int_0^{\infty} (\bar{a}_{B\lambda} + \bar{a}_{AP\lambda}) C_{\lambda} e^{\gamma_{\lambda} x} d\lambda \quad (32) \end{aligned}$$

Radiative Properties

The absorption and scattering efficiencies $Q_{a\lambda i}$ and $Q_{s\lambda i}$ for the AP and Al particles were determined from the fundamental optical constants $\tilde{n} = n - ik$. The values for the Al particles were taken to be $\tilde{n} = 1.7 - i 0.1$ for all wavelengths, which is characteristic of the oxide which coats the aluminum particles [6]. The optical constants for AP were determined from the dispersion equations [7-8]

$$n^2 - k^2 = 1.4833 + \sum_{i=1}^3 \frac{N_i e^2}{m \epsilon_0} \frac{\omega_{0i}^2 - \omega^2}{(\omega_{0i}^2 - \omega^2)^2 + \gamma_i^2 \omega^2} \quad (33)$$

$$2nk = \sum_{i=1}^3 \frac{N_i e^2}{m \epsilon_0} \frac{\gamma_i \omega}{(\omega_{0i}^2 - \omega^2)^2 + \gamma_i^2 \omega^2} \quad (34)$$

where

$$N_1 = 0.252 \times 10^{19} \text{ cm}^{-3}$$

$$N_2 = 0.188 \times 10^{19}$$

$$N_3 = 0.405 \times 10^{19}$$

$$\omega_{01} = 58.7 \times 10^{13} \text{ s}^{-1}$$

$$\omega_{02} = 25.4 \times 10^{13}$$

$$\omega_{03} = 19.8 \times 10^{13}$$

$$\gamma_1 = 1.66 \times 10^{13} \text{ s}^{-1}$$

$$\gamma_2 = 1.76 \times 10^{13}$$

$$\gamma_3 = 0.746 \times 10^{13}$$

which is valid over the range of wavelengths from 0.4 to 14 μm . Over this range of wavelengths it was determined from Fourier-Transform Infrared Spectrometer (FTIR) measurements that the AP transmits between 0.4 and 2.7 μm , 3.8 and 4.3 μm , and 11.8 and 14.0 μm . The AP absorbs between 2.7 and 3.8 μm and 4.3 and 11.8 μm . Since the AP dispersion equations give small non-zero values for k in the known transmissive regions k is set equal to zero in those regions.

Absorption and scattering efficiencies are determined either by Mie theory or the laws of geometric optics. For opaque regions of wavelength (all wavelengths for AI and selective as noted above for AP) the efficiencies and single-scatter phase function are calculated from Mie theory for $x = \pi D n_p / \lambda < 5$. For $x > 5$ the geometric optics results are used assuming a diffusely-reflecting particle with the hemispherical reflectivity equal to normal reflectivity [9]. For transmissive wavelength regions (AP only) Mie theory is used for values of $x < 50$. For $x > 50$ geometric optics results

are used with the Fraunhofer diffraction contribution to forward scatter removed.

The binder was assumed to be non-absorbing with a refractive index of $n_B = 1.6$. This is a reasonable representation of most hydrocarbon binders which have a few very narrow infrared absorption bands and refractive indices ranging between 1.4 and 1.7.

Asymptotic Solution

To clarify the roles of some of the major parameters and to help debug the computer program of the full solution an asymptotic solution was developed using the following assumptions.

- (1) Transparent matrix phase ($\bar{a}_A = \bar{a}_B = 0$)
- (2) Grey medium
- (3) F_{VA1} very small
- (4) No scattering ($\bar{\sigma} = 0$)
- (5) No interface reflectance ($R = 0$)
- (6) $\alpha_1 \gg \gamma$
- (7) $|a_1/\bar{a}| \gg |a_2|, |\bar{a}|$

Assumptions (6) and (7) may be verified by substituting realistic propellant properties into the definitions of those constants. With the above assumptions the modified constants are obtained as

$$\alpha_1 = \frac{(\rho C)_{\infty} r}{k_{\infty}} \quad (35)$$

$$C_0 = \frac{-q_R a_0 \bar{a}}{\gamma^3 + \gamma^2 a_2 + \gamma a_1} \quad (36)$$

$$\gamma = \bar{a} \quad (37)$$

and equation (32) evaluated at the surface $x = 0$ reduces to

$$T_{P_0} - T_s = \frac{q_R Q_{aA1} D_{A1}}{4 k_m} \quad (38)$$

Also, for large black ($\sigma = 0$) Al particles ($D_{A1} \geq 10 \mu\text{m}$) $Q_{aA1} \rightarrow 1$, giving

$$T_{P_0} - T_s = \frac{q_R D_{A1}}{4 k_m} \quad (39)$$

Now the influence of the key parameters can be easily seen. The temperature difference between the selectively absorbing particles and transparent matrix is larger for large incident fluxes, small matrix conductivities and large particle diameters. Assuming values of $T_R = 3000\text{K}$, $k_m = 0.04186 \text{ W/m K}$ ($10^{-4} \text{ cal/cm s K}$) gives the following results from the limiting case.

$D_{A1} (\mu\text{m})$	$T_{P_0} - T_s (\text{K})$
10	275
30	826
100	2750

Results and Discussion

A formulation similar to the space shuttle solid rocket booster (SRB) propellant manufactured by Morton-Thiokol was chosen as a baseline case against which to test variations in various parameters. The parameters for the baseline formulation were as follows:

$D_{AP_1} = 24 \mu\text{m}$	$D_{AP_2} = 180 \mu\text{m}$	$D_{A1} = 30 \mu\text{m}$
$m_{AP_1} = 0.21$	$m_{AP_2} = 0.49$	$m_{A1} = 0.16$
$r = 0.9347 \text{ cm/s}$	$n_B = 1.6$	$k_B = 0$
$T_R = 3000\text{K}$	$T_s = 1000\text{K}$	$T_0 = 300\text{K}$
$n_{A1} = 1.7$	$k_{A1} = 0.1$	

The predicted particle and matrix temperature profiles for this case, T_p and T_m , are depicted in Figure 3. The selectively absorbing Al particles main-

tain a consistently hotter temperature profile. For this case the Al particles would reach 933K, the melting temperature of pure Al, at or very near the surface. In other cases that follow, for comparison, the baseline formulation will also appear as a solid curve.

To test which parameters most strongly influenced the Al particle temperature each parameter in the baseline formulation was varied keeping all others the same. In Figure 4 the total AP mass fraction was held constant at 70% but the split between large and small AP varied. Little effect was noticed on T_p . In Figure 5 the small AP size was varied. To some degree smaller diameters reduced the Al particle temperature due to the enhanced scattering by smaller particles.

Variation of the large AP size (Figure 6) did not produce any significant changes in T_p . This is because the AP radiative properties are dominated by the small AP. Variation of the total AP mass fraction (Figure 7) keeping the small/large ratio the same (30/70) made no significant difference either.

The surface temperature T_s is a parameter over which the propellant formulator really has no control but its effect was tested anyway (Figure 8) and found to be insignificant. Because of uncertainty in the optical constants of the oxidized Al particles k_{Al} was varied in Figure 9 and also found to be relatively unimportant.

Of the parameters over which the propellant formulator has control the two which indicated promise for use in reducing the Al particle temperature were the Al diameters (Figure 10) and mass fraction (Figure 11). Both small diameters and large mass fractions favor lower Al temperatures. Temperature reductions of approximately 200K are predicted by merely reducing the Al size from 30 to 10 μm .

Finally, two parameters which had a large effect on T_p but which are difficult to control independent of other ballistic considerations are the characteristic blackbody temperature of the incident radiation T_R (Figure 12) and the burn rate r (Figure 13). For obvious reasons low incident fluxes and high burn rates favor lower Al temperatures. While little is known about the level of radiant flux present in aluminized propellant motors and controlling that flux would be difficult, it is important to recognize that it is a major parameter in determining the temperature of the Al particles.

One final case, presented in Figure 14 shows the effect of varying several parameters simultaneously to achieve minimal Al temperatures. By reducing D_{A1} to $20\mu\text{m}$, increasing m_{A1} to 0.25, reducing D_{Ap1} to $20\mu\text{m}$, changing the small/large AP split to 50/50, increasing the burn rate to 2.0 cm/s and decreasing T_R to 2000K the Al temperature was reduced by approximately 400-500K.

Conclusions

A realistic model for radiative pre-heating of aluminum particles in AP composite propellants has been developed. The model predicts melting of the aluminum near the propellant surface for parameters corresponding to the space shuttle solid rocket booster propellant. The model also identifies which parameters have a strong influence on the aluminum particle temperature. These are aluminum size and mass fraction, burn rate and level of radiant flux. Smaller aluminum particles and larger Al mass fractions promote lower temperatures. The model was used to predict that certain combinations of parameters may be chosen to inhibit heating and melting of the aluminum. Parameters were also identified which have little effect on Al temperature. These were total AP mass fraction, small/large AP split,

surface temperature, Al extinction coefficient, and large AP size. In addition the size of small AP had a weak effect. These results should prove useful in formulating propellants which minimize the problem of unwanted Al agglomeration.

Acknowledgements

Support for this work from the Southeastern Conference on Electrical Engineering Education and the Air Force Office of Scientific Research under subcontract 83 RIP 42 is gratefully acknowledge. Additional support from the University of Utah Research Committee was also appreciated.

Figure Captions

- Fig. 1. Aluminized Composite Propellant with Bi-Modal AP Blend
- Fig. 2. Radiative Flux Convention for Two-Flux Model
- Fig. 3. Particle and Matrix Temperatures for Baseline Propellant Formulation
- Fig. 4. Effect of AP Split on Particle and Matrix Temperatures
- Fig. 5. Effect of Small AP Size on Particle and Matrix Temperatures
- Fig. 6. Effect of Large AP Size on Particle and Matrix Temperatures
- Fig. 7. Effect of Total AP Mass Fraction on Particle and Matrix Temperatures
- Fig. 8. Effect of Propellant Surface Temperature
- Fig. 9. Effect of Aluminum Extinction Coefficient
- Fig. 10. Effect of Aluminum Particle Diameters
- Fig. 11. Effect of Aluminum Mass Fraction
- Fig. 12. Effect of Blackbody Incident Radiation Temperature
- Fig. 13. Effect of Propellant Burn Rate
- Fig. 14. Results of Special Non-Agglomeration Formulation

References

- (1) Sambamurthi, J. K., Price, E. W., and Sigman, R. K., "Aluminum Agglomeration in Solid-Propellant Combustion," AIAA J., Vol. 22, No. 8, August 1984, pp. 1132-1138.
- (2) Brundige, W. N., and Caveny, L. H., "Low Burning Rate Aluminized Propellants in Acceleration Fields", AIAA J., Vol. 22, No. 5, May 1984, pp. 638-646.
- (3) Beckstead, M. W., Richards, R. S., and Brewster, B. S., "Distributed Combustion Effects on Particle Damping," AIAA J., Vol. 22, No. 3, March 1984, pp. 383-387.
- (4) Brewster, M. Q., and Tien, C. L., "Examination of the Two-Flux Model for Radiative Transfer in Particulate Systems," Int. J. of Heat and Mass Transfer, Vol. 25, No. 12, December 1982, pp. 1905-6.
- (5) Bird, R. B., Stewart, W. E., and Lightfoot, E. N., Transport Phenomena, John Wiley & Sons, 1960, p. 409.
- (6) Rieger, T. J., "On the Emmissivity of Alumina/Aluminum Composite Particles," J. Spacecraft and Rockets, Vol. 16, No. 6, December 1979, pp. 438-439.
- (7) Moss, T. S., Optical Properties of Semi-Conductors, Butterworths Scientific Publications, 1959, p. 16.
- (8) Patel, R. S., and Brewster, M. Q., "Infrared Optical Constants of Ammonium Perchlorate," In preparation for submission to AIAA J.
- (9) Siegel, R., and Howell, J. R., Thermal Radiation Heat Transfer, McGraw-Hill, 1981, 2nd Ed., p. 581.

NOMENCLATURE

Upper Case

C	Specific Heat (Cal/gm K or kJ/kg K)
C_1	Constant defined by equation (15) (watts/cm ² μm)
C_λ	Constant defined by equation (16) (watts/cm ² μm)
$C_{0\lambda}$	Constant defined by equation (30) (K/μm)
D	Diameter (μm)
I	Intensity (watts/cm ² μm)
N	Number density of particles (cm ⁻³)
N_1, N_2, N_3	Parameters in equation (33) (cm ⁻³)
P	Phase function in slab geometry
Q	Scattering or absorption efficiency
R	Hemispherical spectral reflectivity
T	Temperature (K)

Lower Case

a	Absorption coefficient (cm ⁻¹)
a_c	Constant defined by equation (23) (K/watt)
a_1	Constant defined by equation (24) (cm ⁻²)
a_2	Constant defined by equation (25) (cm ⁻¹)
e	Charge of electron
f_v	Volume fraction
h	Heat transfer coefficient (watts/m ² K)
k	Imaginary part of refractive index ($\tilde{n} = n - ik$), also thermal conductivity (watts/m K)
m	Mass fraction, also mass of electron
n	Real part of refractive index ($\tilde{n} = n - ik$)

p Single scatter phase function
 r Rate of burning (cm/s)

Greek Symbols

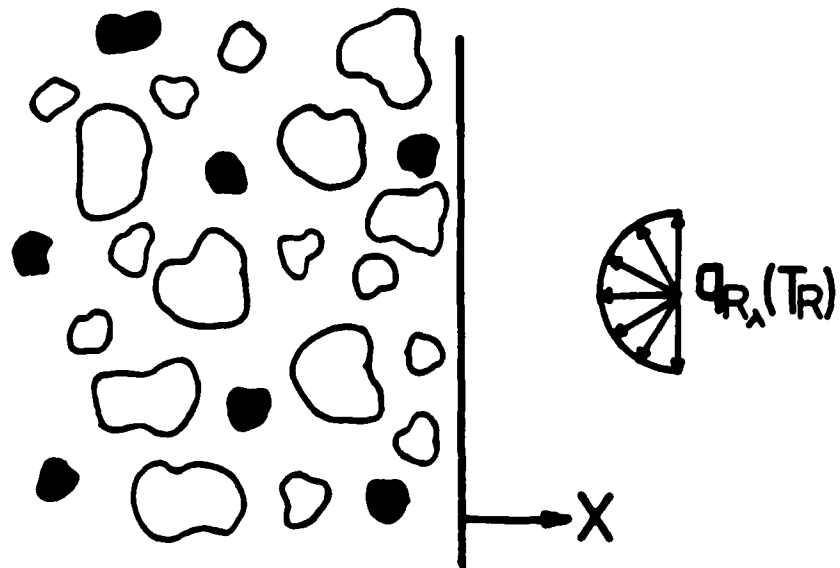
α_1 Constant defined by equation (31) (cm^{-1})
 γ_λ Constant defined by equation (14) (cm^{-1})
 γ Constant defined by equation (37) (cm^{-1})
 $\gamma_1, \gamma_2, \gamma_3$ Parameter defined in equation (33) (S^{-1})
 ϵ_0 Permittivity of free space
 θ Polar angle in single particle geometry
 μ Cosine of polar angle in slab geometry for incoming ray
 μ' Cosine of polar angle in slab geometry for outgoing ray
 ρ Density (kg/m^3)
 σ Scattering coefficient (cm^{-1})
 ω Angular frequency (S^{-1})
 $\omega_{01}, \omega_{02}, \omega_{03}$ Parameters defined in equation (33) (S^{-1})




Subscripts

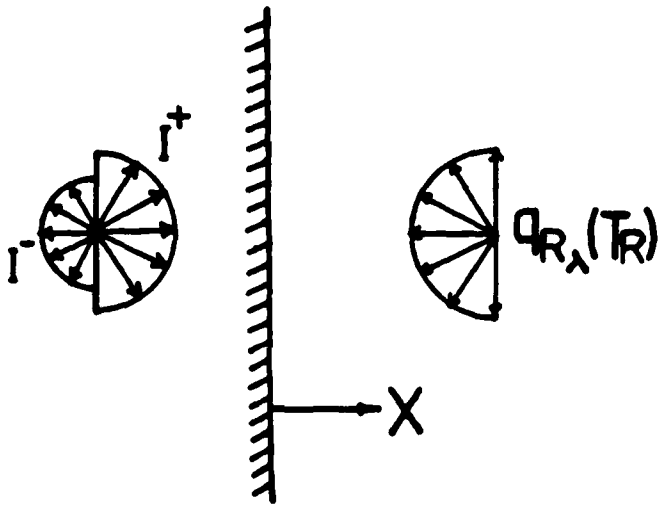
A1 Aluminum
 AP Ammonium perchlorate
 B Binder
 P Particle
 P_0 Particle at $x = 0$
 R Incident radiation
 S Surface (at $x = 0$), also scattering
 a Absorption
 i Index used for $AP_1, AP_2, A1$ and B
 - Matrix
 λ Monochromatic

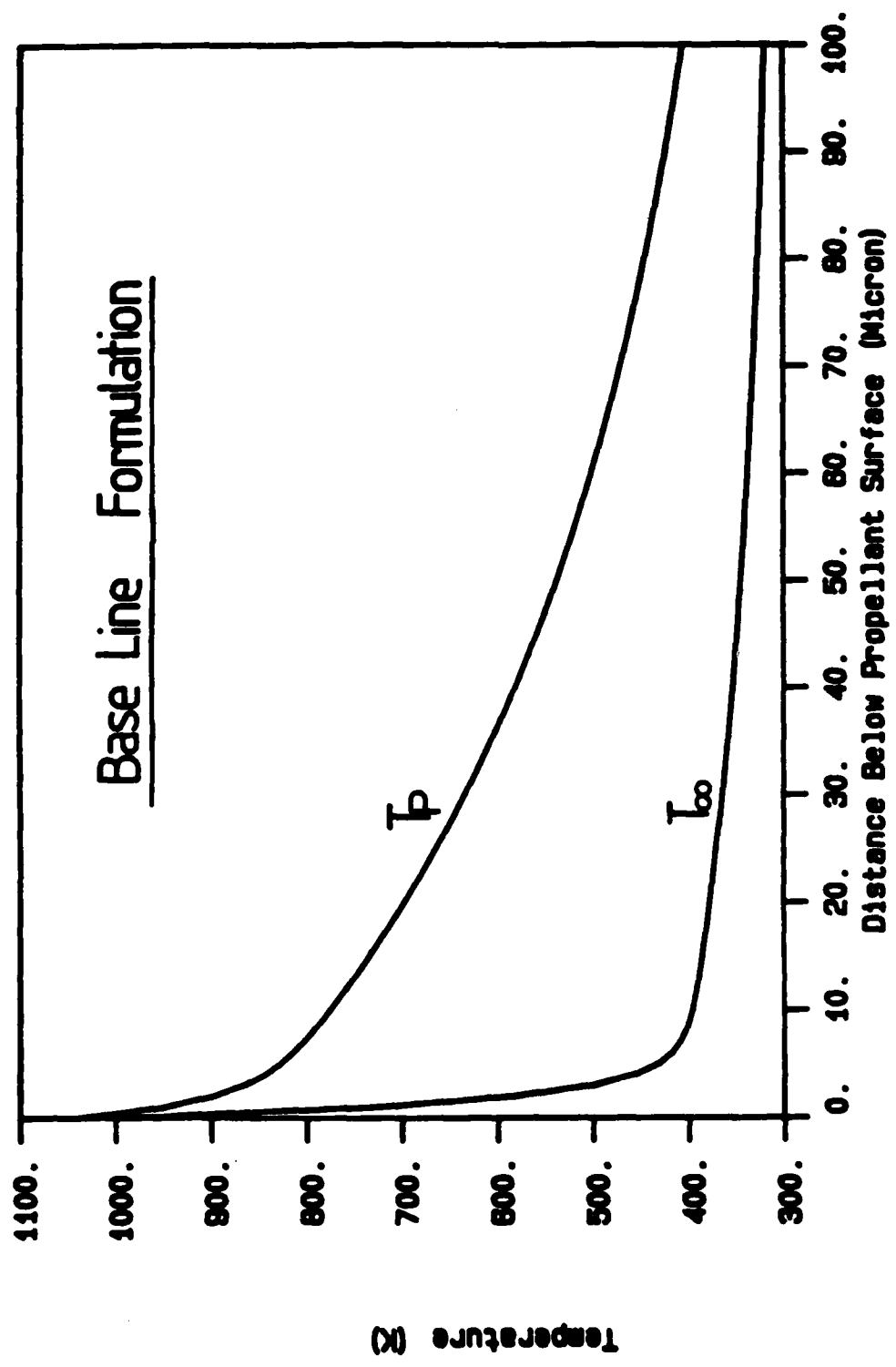
Superscripts

- ± Forward and backward direction
- (Overbar) two flux value

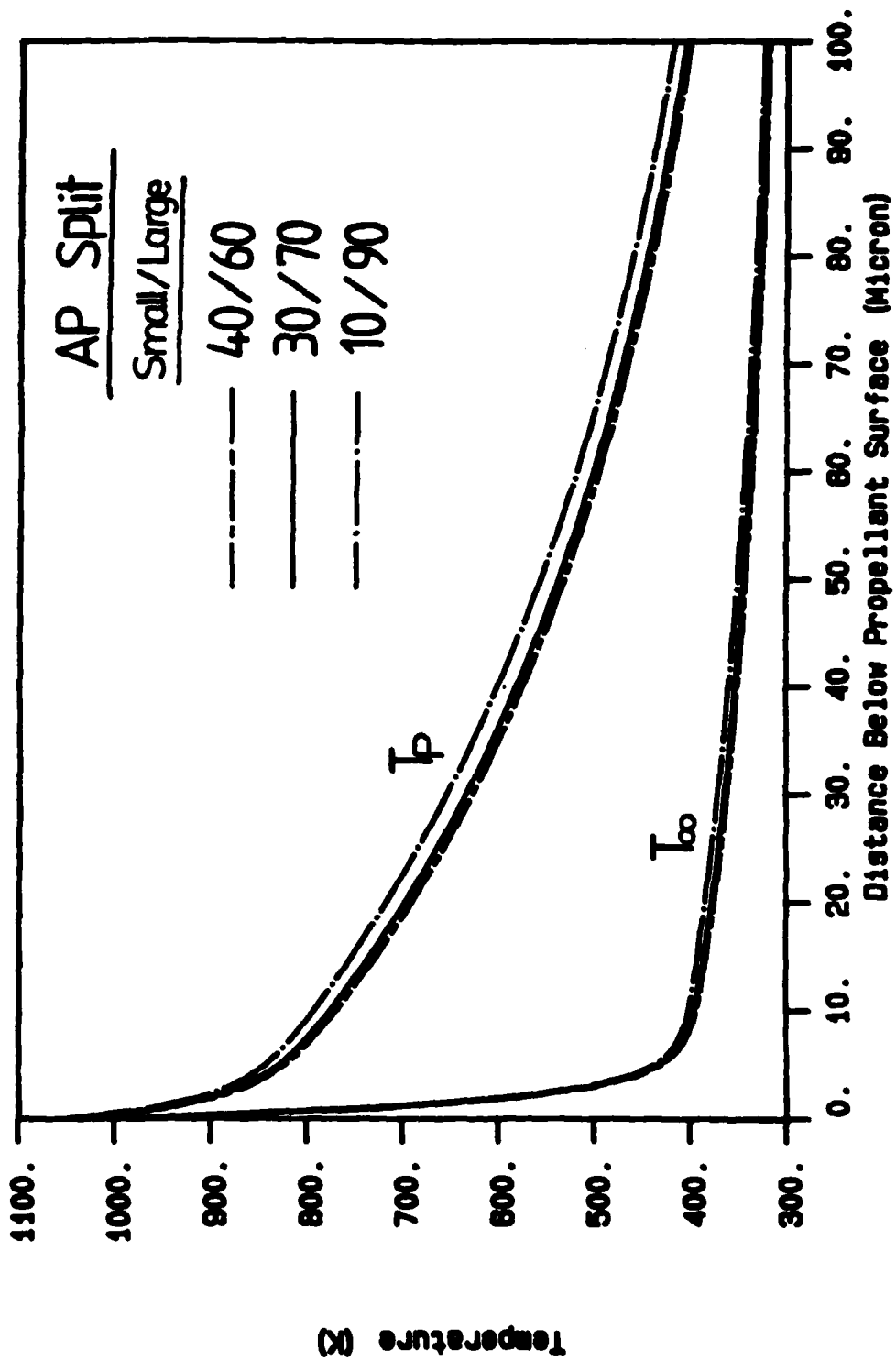


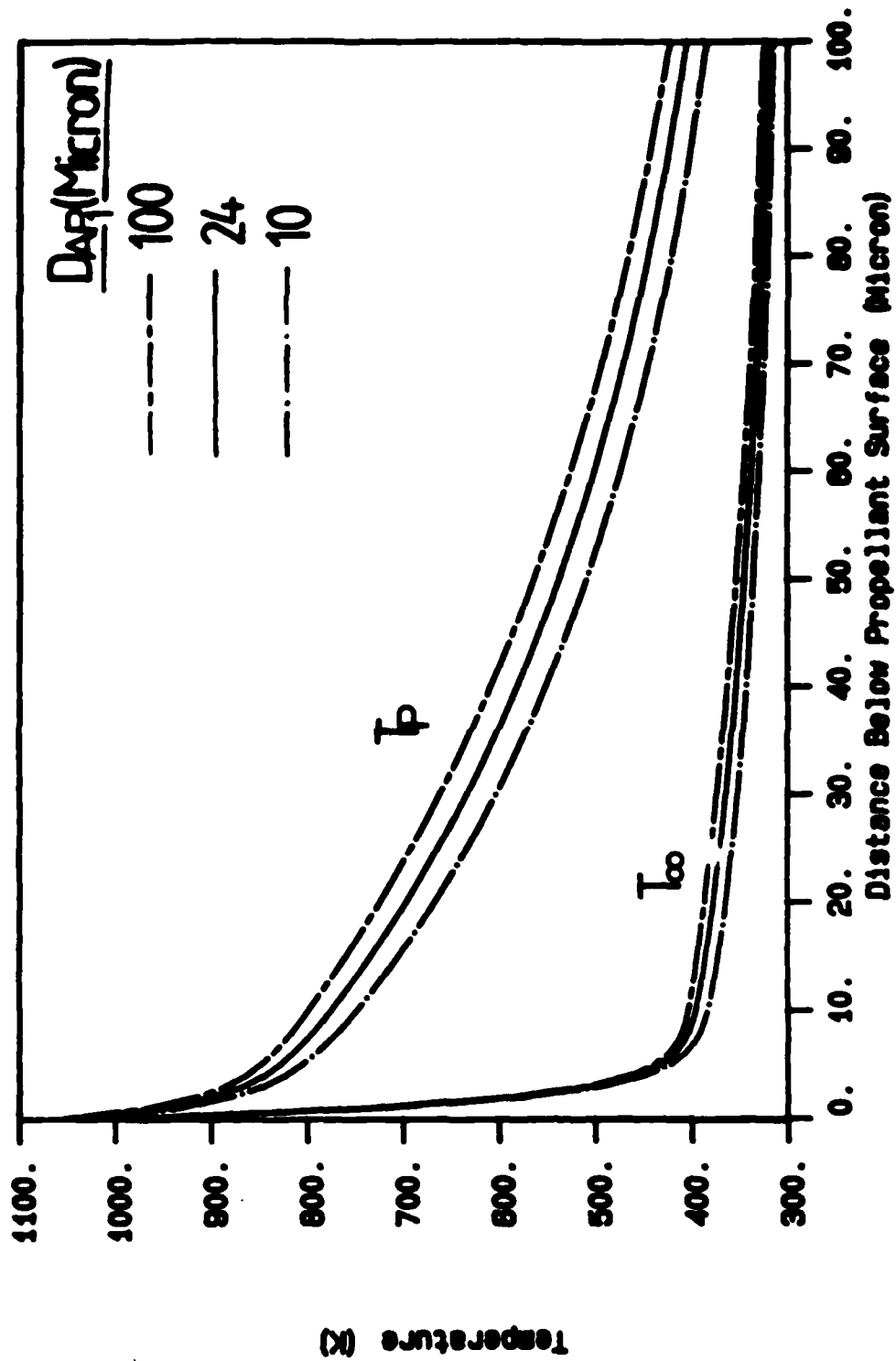
-  Large AP Particles
-  Small AP Particles
-  Aluminum Particles
- Remainder Is Binder

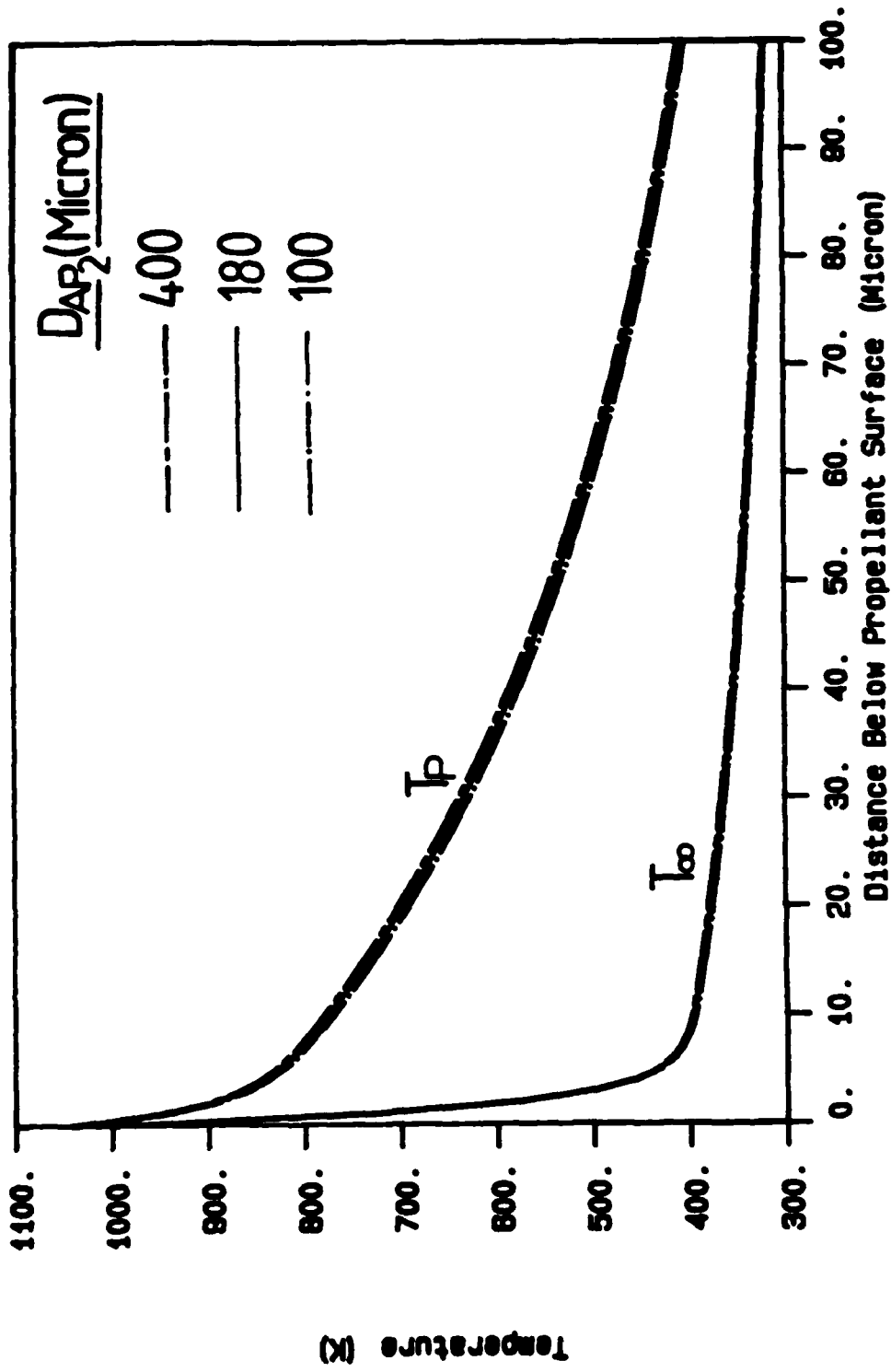


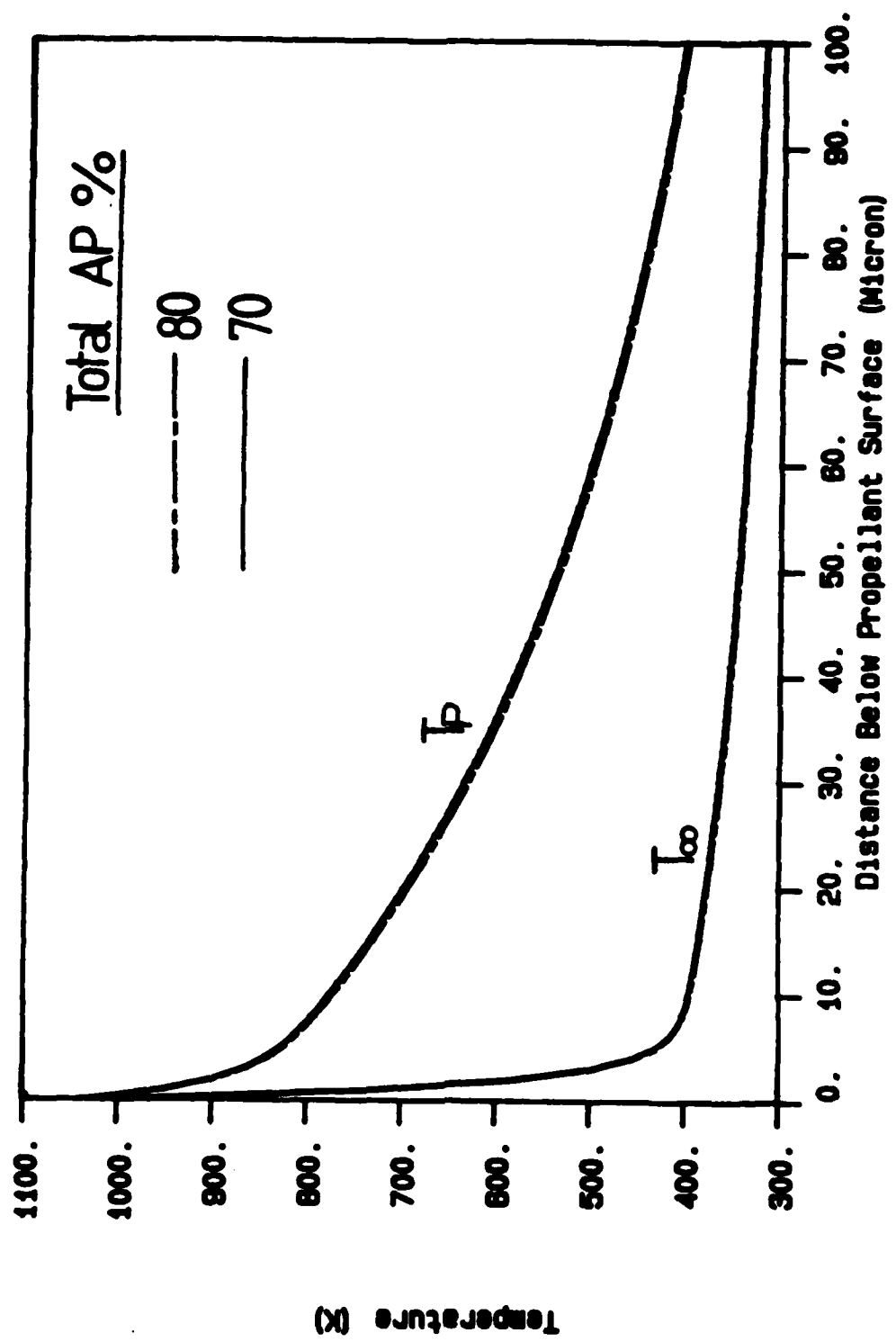


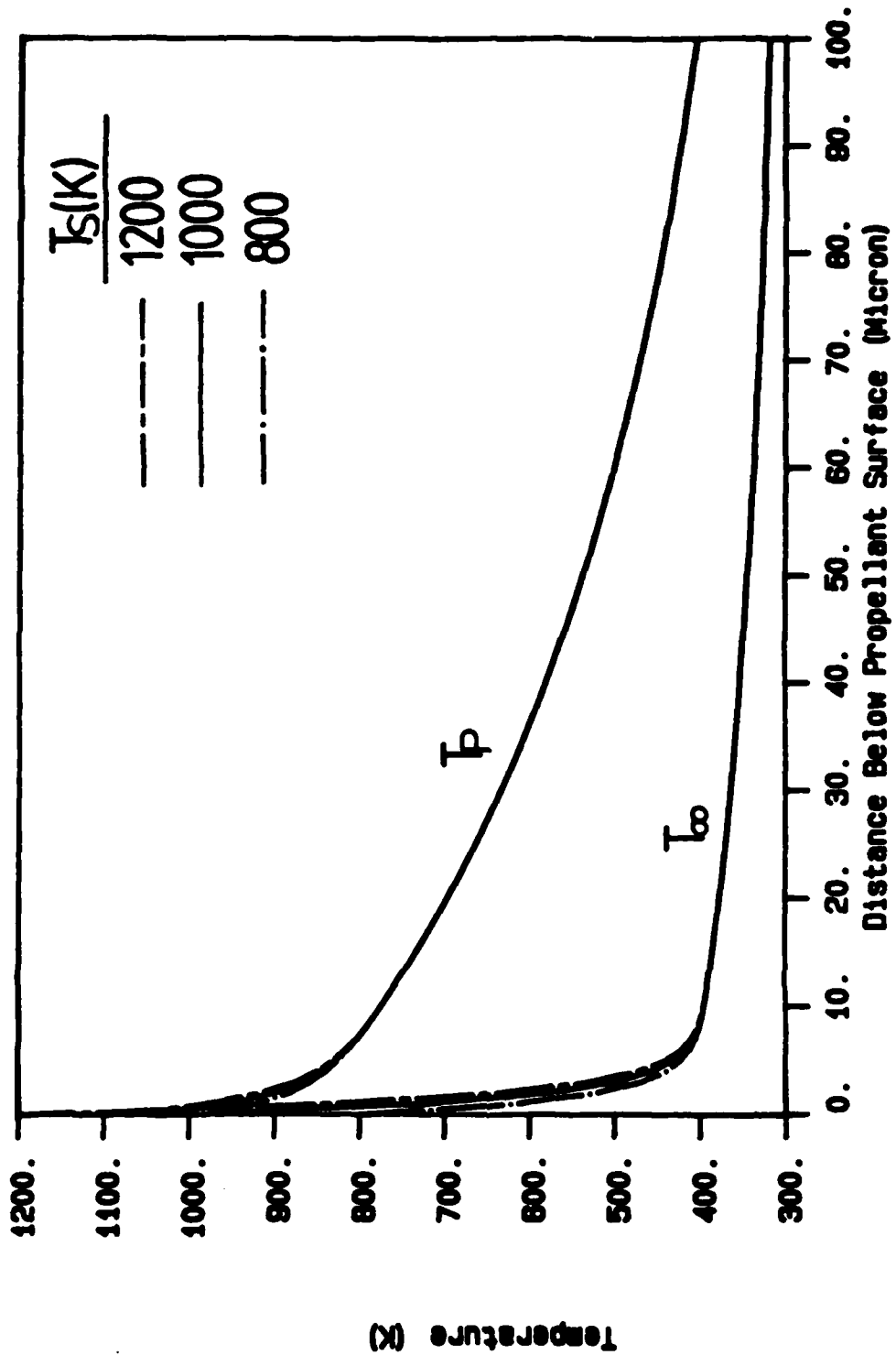
Temperature (K)

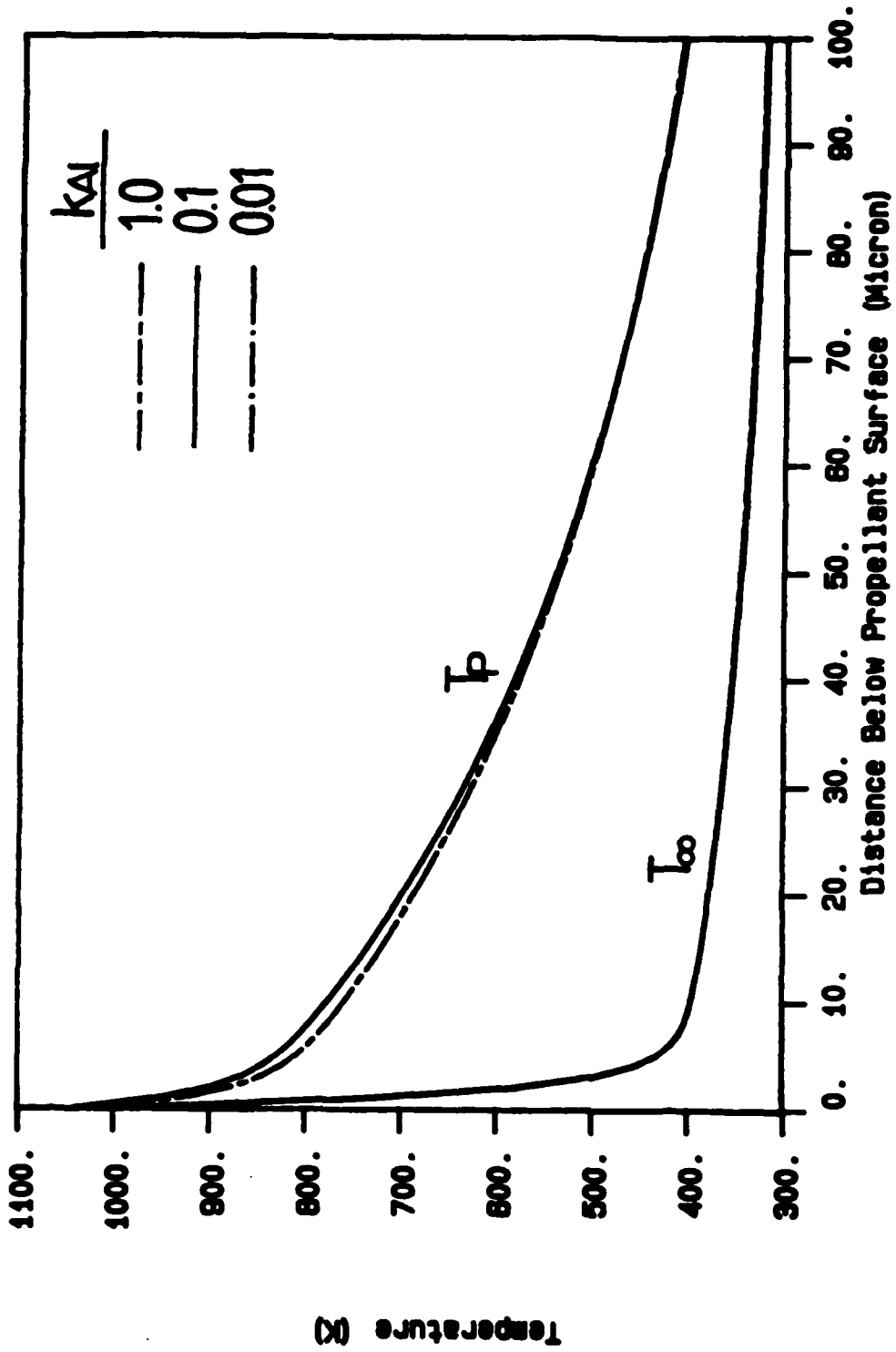


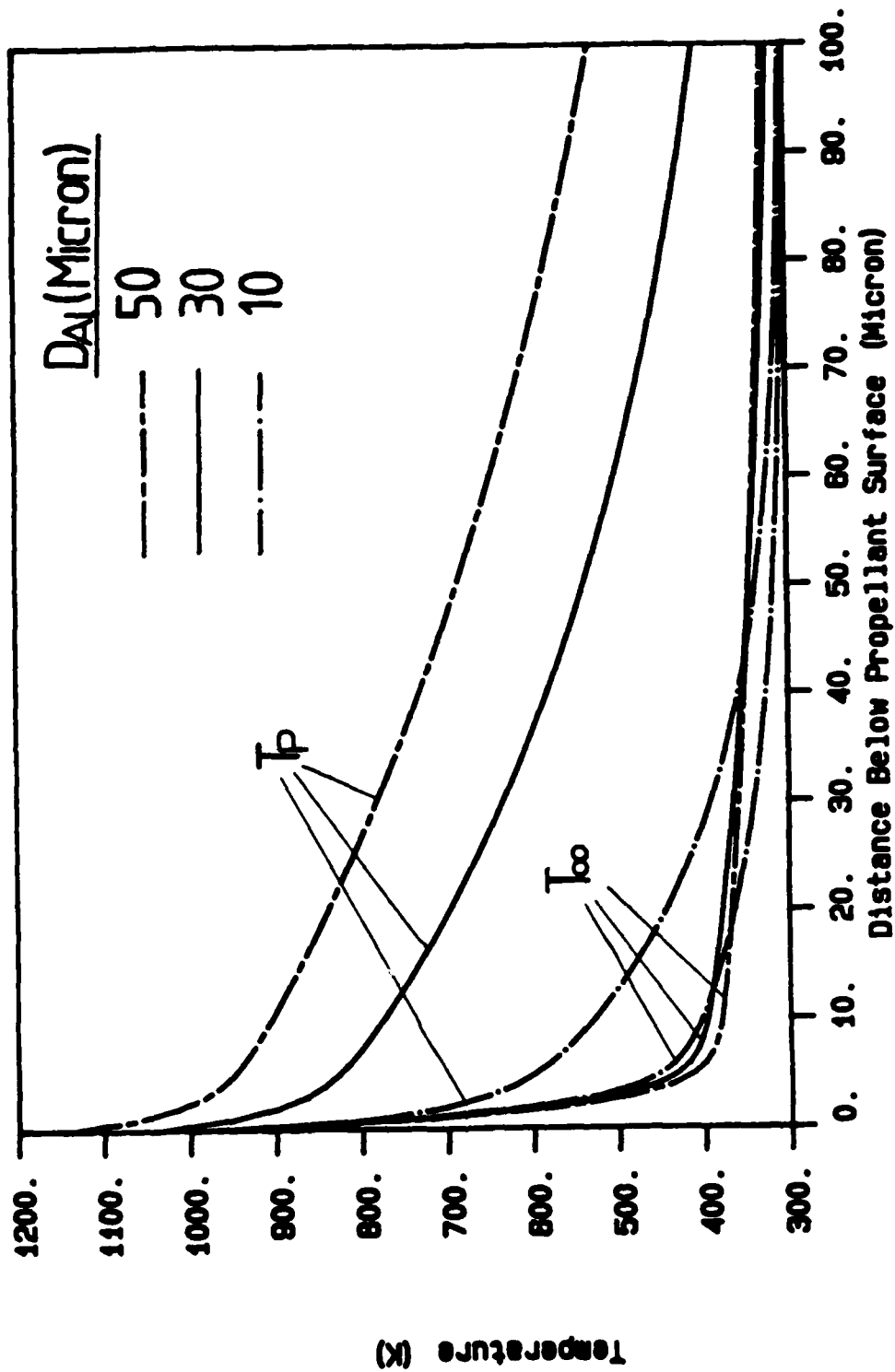


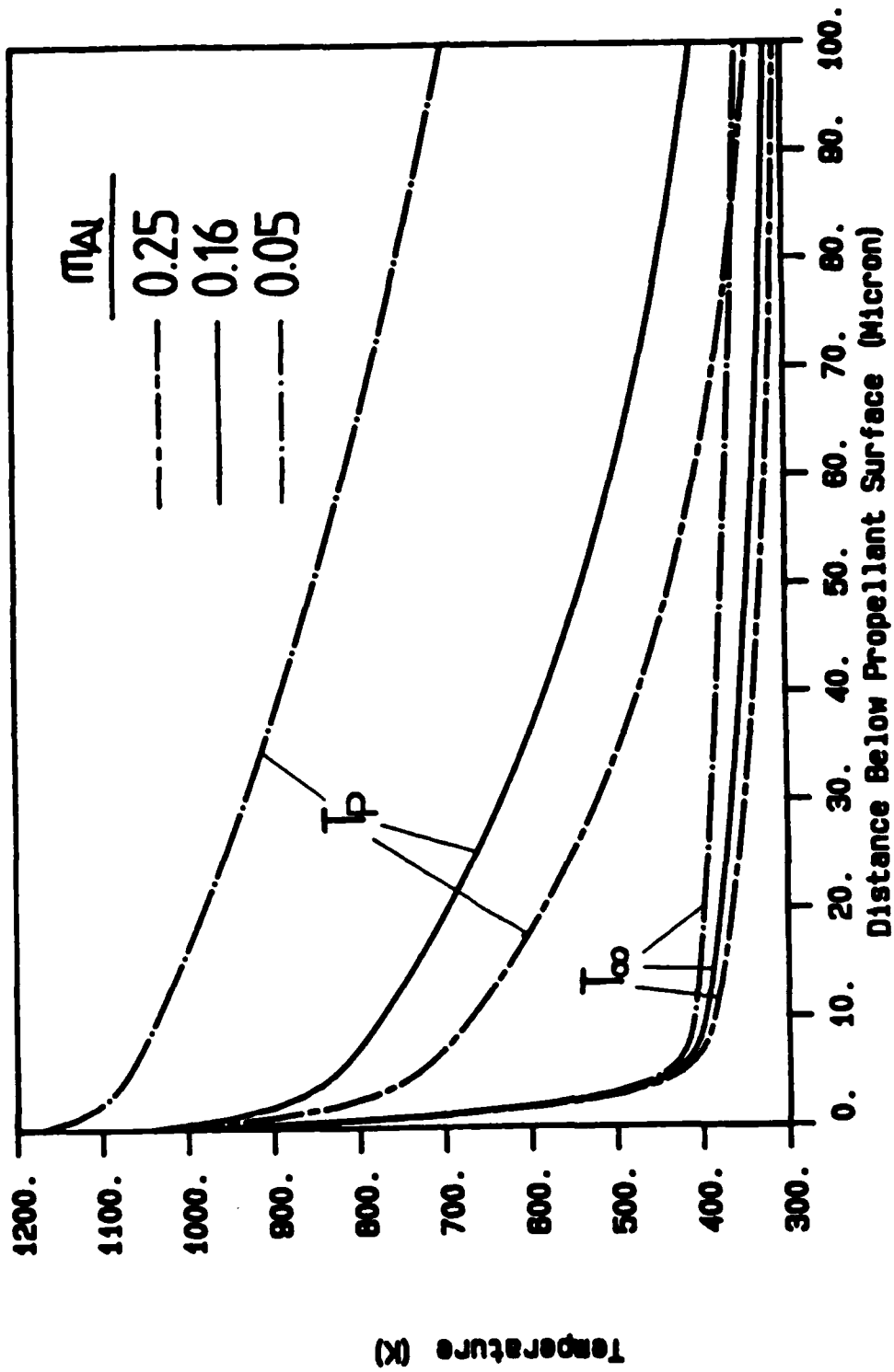


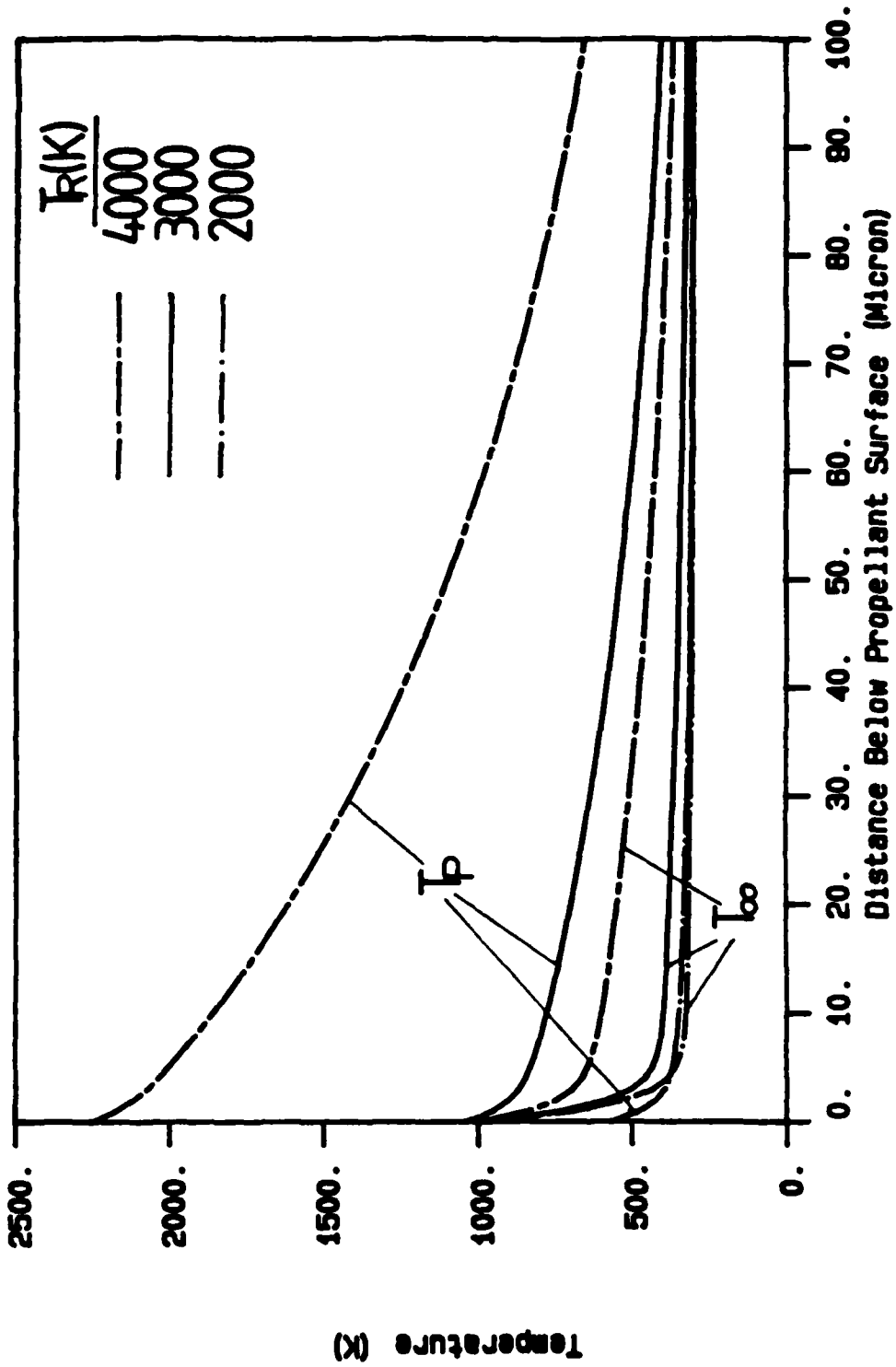


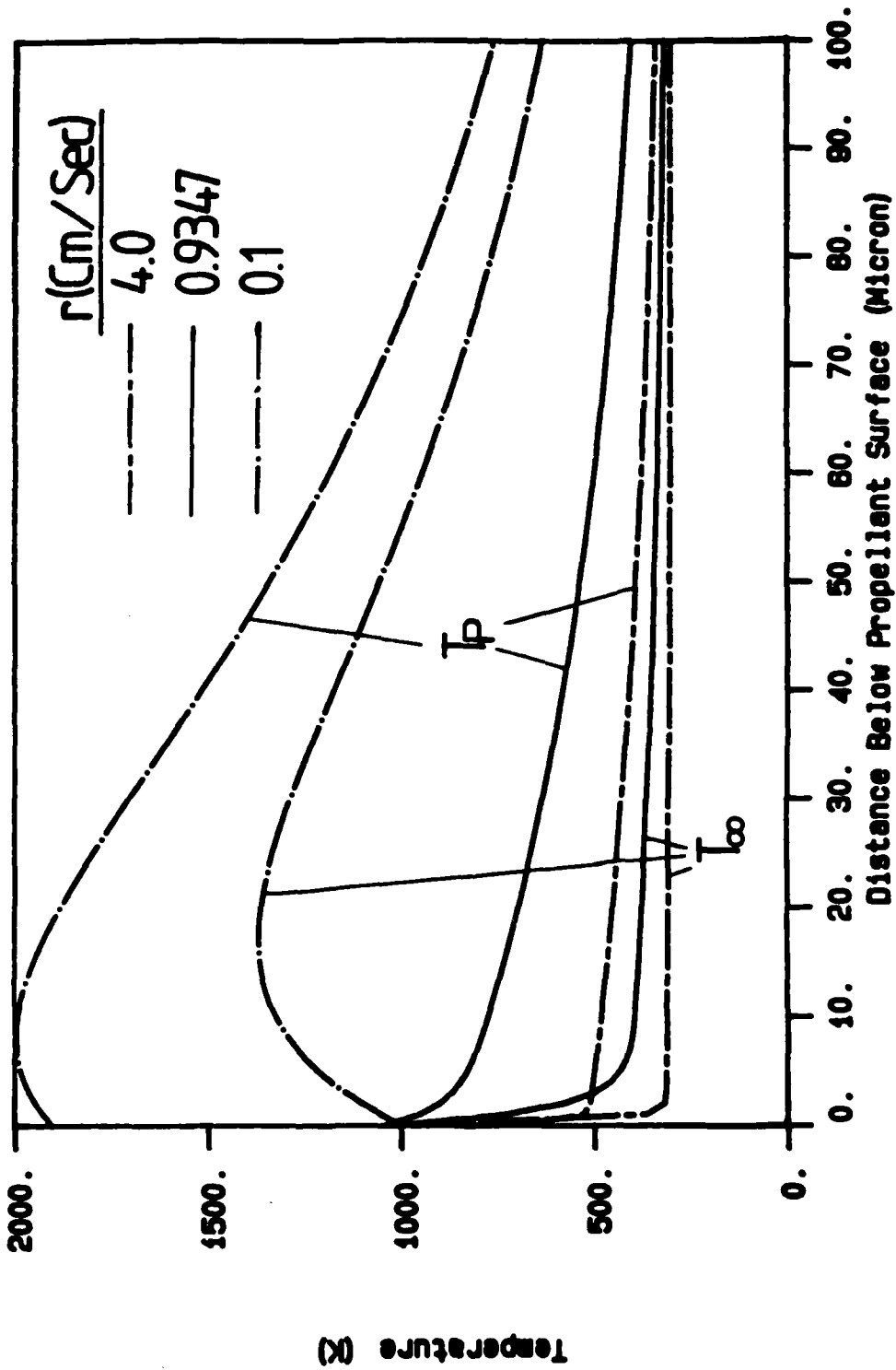


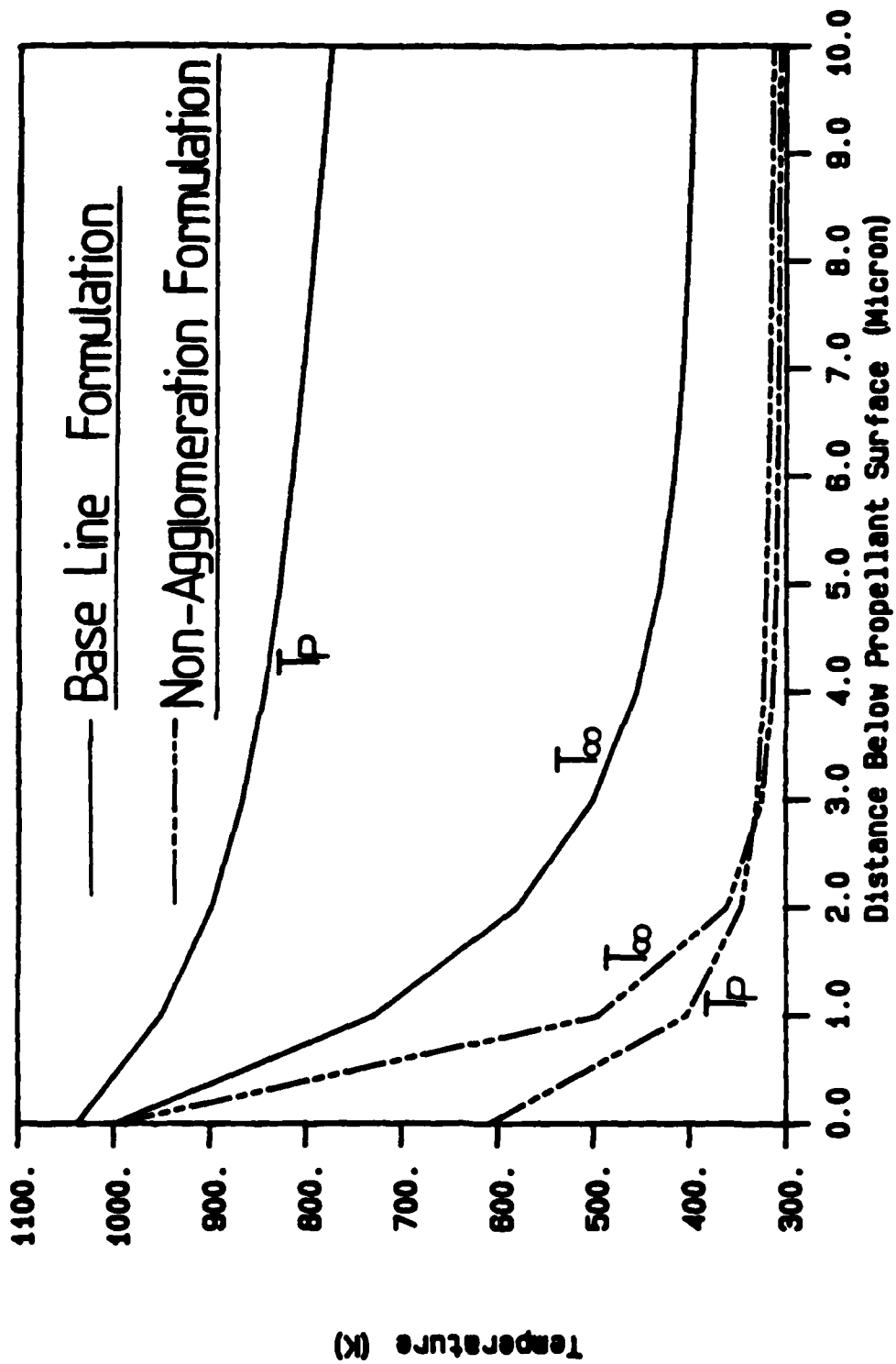


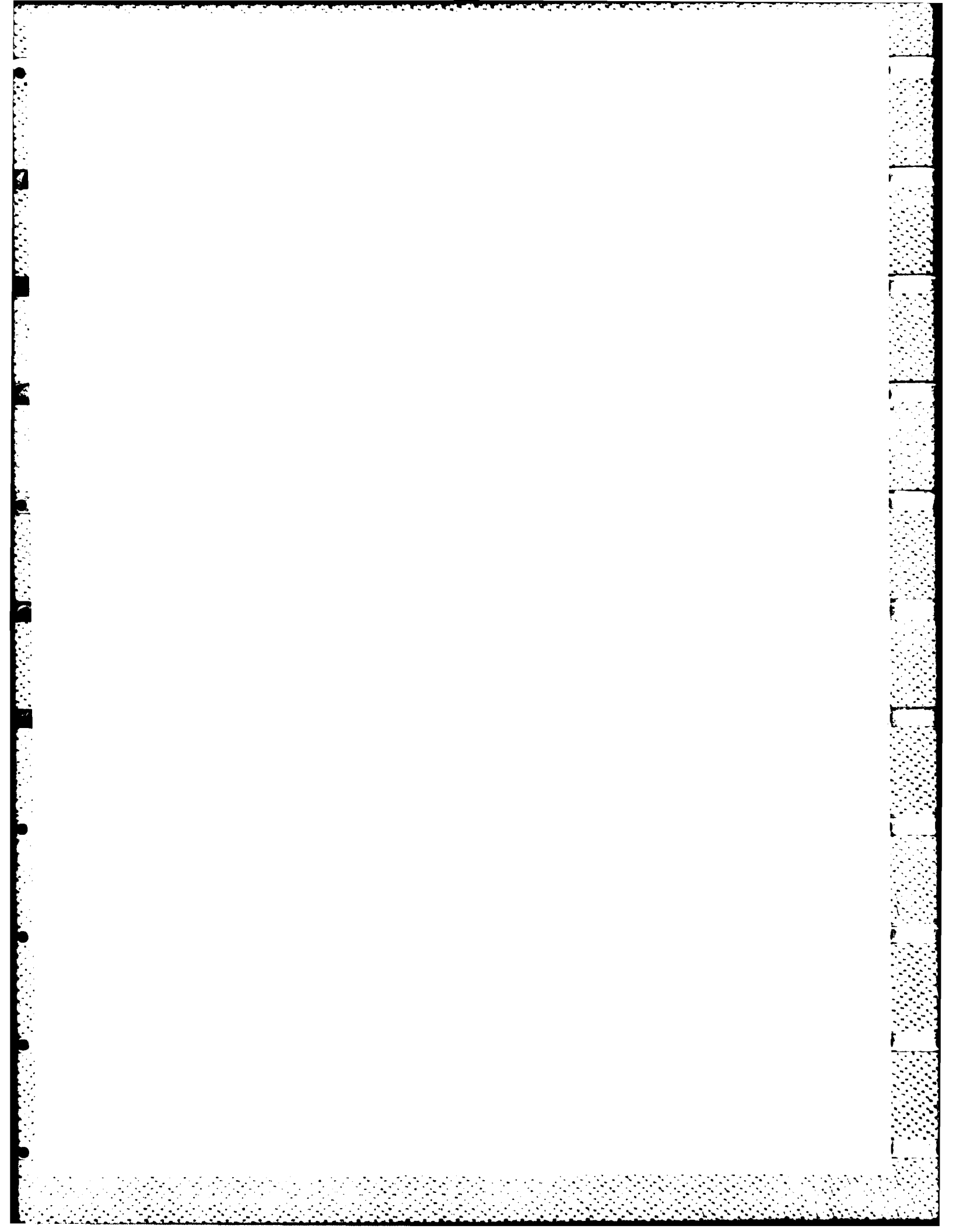












1983-84 USAF-SCEEE RESEARCH INITIATION PROGRAM

Sponsored by the

AIR FORCE OFFICE OF SCIENTIFIC RESEARCH

Conducted by the

SOUTHEASTERN CENTER FOR ELECTRICAL ENGINEERING EDUCATION

FINAL REPORT

INTERIM REPORT DEVELOPMENT AND TESTING OF AN ANIMAL MODEL

OF STATE DEPENDENT EFFECTS WITH ATROPHINE

Prepared by: Dr. Louis W. Buckalew

Academic Rank: Associate Professor

Department and
University: Psychology Department
Alabama A&M University

Research Location: Air Force School of Aerospace Medicine

Date: April 1985

DEVELOPMENT AND TESTING OF AN ANIMAL MODEL
OF STATE DEPENDENT EFFECTS WITH ATROPINE

by

L. W. Buckalew

ABSTRACT

This project attempted to 1) design and validate a small animal model for determining state dependent effects with a CD agent, and 2) explore the possibility of a state dependent effect with atropine, a CNS-acting CD agent. Relevant literature is reviewed and a model developed which required experimentation to determine appropriate drug dose levels, route of injection, and time to peak effect. The evolved model and suggested procedure accompanying it are recommended for use in future small animal experimentation with atropine. This agent was found to yield decrements in performance during training though no definitive conclusion as to state dependency was warranted due to complications encountered during testing and the resultant small number of cases available. However, trends would suggest the viability of a state dependent effect with atropine in small animals, and further more extensive research is strongly encouraged due to the important implications for combat-conditions (CD) behavioral efficiency, as discussed. Presently reported research efforts are continuing, stimulated by this opportunity as reported, and further results will be made available to USAF.

I. INTRODUCTION:

The threat of chemical (drug) weapons appears very real, accentuated by recent reports of field deployment in Central and Southeast Asia. There appears a growing possibility of military personnel encountering chemical environments in any future conflict, a realization which has stimulated concerted research interest. A major defensive/protective thrust now exists for the evaluation of potential CD agents in order to preserve the viability of military operations, with USAF concerns for flight line operations in particular.

The discovery of German nerve agent (anticholinesterase) stockpiles after World War II rapidly stimulated interest in developing, testing, and making available to field forces appropriate pre-treatment or antidote CD agents.¹ These agents (anticholinergics), such as atropine, were first studied in organized fashion in the 1950s, with particular concern for determination of therapeutic doses.¹ Since then, considerable research has been conducted, primarily by the British, on atropine drug effects in humans. Relatively comprehensive overviews of the pharmacology and pharmacodynamics of anticholinergics are available.^{2,3,4} For two anticholinergic CD agents, atropine and benactyzine, extensive investigations have been conducted on their physiological effects,^{1,5,6,7,8,9} with particular emphasis on dose effects. Many fewer efforts have been directed at determining performance effects, both psychomotor and cognitive, of CD agents in humans, though some research exists.^{1,6,10} A review of atropine's physiological and performance effects in humans, with specific concern for USAF interests, is available.¹¹

A majority of available research on atropine, both for humans and animals, has been concentrated on the investigation of physiological effects. While certainly important considerations in evaluating the effects of any drug, these effects must ultimately be related to behavioral changes and

efficacy, concerns particularly relevant to the operational readiness, combat efficiency, and mission integrity needed in USAF personnel. Given that such personnel, and particularly those on the flight line, have been highly trained, a major concern emerges as to the influence of atropine, as a CD agent, on learned behavior, learning phenomena, and memory. Obviously, disruption within these processes induced by a CD agent could prove disastrous to combat operations and mission integrity. However, few studies have been devoted to exploring atropine's effects in these areas. One early study¹² did report passive avoidance learning, extinction, and retrieval in rats as impaired by atropine sulphate, though the consolidation and storage of memory traces were not adversely influenced. A recent major review¹³ reported that anticholinergics alter learning and memory performance, though memory storage itself is rarely affected by these drugs. In essence, while the process of learning and memory storage are relatively free from anticholinergic influence, performance relying on these processes is impaired. The question emerges, then, if input processes are undisturbed by atropine, though output (performance) is impaired, how can this impairment be minimized so as to maintain behavioral integrity?

Particularly relevant to this question is the concept of state dependent learning. In typical studies, subjects learn a set of materials in one particular state (e.g., under the influence of a drug) and are then tested either in that same state or in some other (e.g., atropine-free). Although the results are controversial, some studies have shown that retention, and hence performance, are better when the learning and test states are the same.¹⁴ Mixing the states (e.g., learning while atropine-free and recalling/performing under the influence) can result in poorer retention/performance. This last scenario would typify the concerns of the USAF in its contemplated use of atropine as a CD agent. Of note, much of the research on humans with atropine was accomplished

prior to "the increasing experimental evidence that responses acquired under one drug condition and tested under another may result in a response decrement independent of the specific actions of the drug employed,"¹⁵ i.e. the state dependent effect. Hence, the question evolves as to whether atropine lends itself to state dependent effects, knowledge of which could be used to minimize the drug effect, per se, of atropine employed as a CD agent. Experimentation exploring this parameter, however, is hampered by the toxicity of atropine.

Due to the toxic nature of CD agents, in vivo human testing is often precluded, thus necessitating use of animals to estimate human performance decrements. Examples of this orientation are reflected in previous USAF efforts.^{16,17,18} However, while advantageous if not necessary, there are some important problems associated with the use of animals in CD research, as addressed by a recent USAF report.¹⁹ One such problem is the development and validation of animal models for drug effects. A second and related problem is validating animal performance measures/tasks as analogs to human behaviors, a consideration further defined by necessity to approximate flight line, aircrew operations. With resolution of these basic problems, and assuming the validity of aircrew performance decrements associated with treatment by a CD agent as suggested by previous studies, there remains the untested possibility of state dependent effects associated with administration of atropine. The implications of this phenomenon, if demonstrated, extend to training conditions and practices for aircrews, as performance decrements shown to exist for atropine might be minimized if performance training operations methodologically compensated for state dependent effects of this drug. Given appropriate testing and empirical demonstration of state dependent effects for atropine, efforts could be readily undertaken during initial aircrew training to compensate for anticipated performance

decrements when exposed to this CD agent.

II. OBJECTIVES:

It was a major objective of this research to design and develop an animal model which would facilitate testing for state dependent effects with anticholinergic drugs. A portion of this development involved determination of survivable dose levels of atropine and levels which did not compromise behavioral integrity. A second major objective was to employ this model to explore whether the pharmacological and behavioral effects of atropine, a primary CD agent, lend themselves to state dependent effects associated with other CNS-acting drugs such as alcohol.²⁰ In essence, the state dependent phenomenon involves the fact that, for a given agent, performance under that agent's influence is maximized if training was also under the same agent's effect. This phenomenon allows that performance decrements will be minimized as a result of an agent's influence providing that similar physiological conditions existed during both training and performance phases.

Animals are frequently used in drug studies because they allow a degree of control not possible in retrospective or prospective human studies, and animal investigations allow a greater range of tests than possible with humans.²¹ Hence, pre-clinical drug development research and much medical and psychological research uses animals. The efficacy of such research is predicated on the design and validity of specific animal models, the most prevalent of which involve rodents and primates, and basic drug research methodological considerations.²² The present effort considered rodents (rats) in an escape learning paradigm involving a noxious (shock) stimulus such as has been discussed in drug research reviews.¹³ This scenario was operationally equated with emergency aircrew operations during highly stressful and combat-related operations. Of note, a state dependent effect has been demonstrated for a number of CNS-acting agents, most notably

alcohol, marihuana, nicotine, and amphetamines.

Given that atropine, alone or in combination with benactyzine, is the primary pre-treatment or antidote agent indicated for CD, the development of a model for and the demonstration of state dependent effects with this drug should have appreciable implications for both training and indications. If state dependent effects can be tested for and demonstrated with atropine, and recognizing performance decrements generally associated with the administration of this agent to naive subjects, these decrements could be minimized if training procedures involved an atropine-influenced condition. This phase of training, if indicated, would contribute appreciably towards the maintenance of aircrew viability during treatment for suspected chemical warfare agents. Any effort to preserve the integrity of aircrew operations under chemical warfare conditions may be regarded as a major contribution to insuring the operational readiness and ultimate combat efficacy of USAF personnel and missions.

III. METHODS AND MATERIALS:

a. Subjects

The subjects were 24 adult male albino rats; four groups of six each. Rats were obtained from an animal supply company and were naive to any drug administration or previous experimentation. Animals were obtained at an age equivalent to human adolescence and were matured in the laboratory over a two month period to facilitate laboratory acclimation. At the beginning of drug testing, the mean weight of animals was approximately 230 gm.

b. Apparatus and Materials

To facilitate injections, a 5cc disposable syringe was used. The agent employed was atropine sulphate (1ml = .5mg), and injectable sodium chloride (.9%) was used for the control condition. Dose quantities were determined by animal weight which was measured by a Hanson Model 1440 500g scale. A Lafayette Model A-586 one-way shuttle system facilitating

the administration of shock and use of a light discriminative stimulus was employed to test/train avoidance behavior. This apparatus allows provision, with or without discriminative stimulus presentation, provision of a mild shock via a grid floor. Avoidance is accomplished by the animal jumping to a higher, nonelectrified portion of the apparatus. Animals were housed individually in standard galvanized cages which had 200 ml water bottles and drinking tubes attached. Purina Lab Chow was used for feeding, supplemented by 20% protein chunk dog food.

c. Procedure

The operational procedure of this research was multifaceted due to two distinct, though related, objectives. One objective involved the design, development, and testing of an animal (rodent) model for detecting state dependent effects with a CD agent (atropine). This effort included experimentation to determine a survivable and appropriate dose level of atropine for subjects. The second objective entailed specific drug-testing to determine the existence, if any, of a reliable state dependent effect using the evolved model.

Objective 1. A number of animal models for testing drug effect exist, though differences may be noted between models based on the animal being used and the nature of the agent employed. As atropine is a CNS-acting agent, review of models was restricted to this category. Further, while a general paradigm for testing state dependent effects exists, it was necessary to experiment with methodology to determine the most appropriate methodological procedures. The major concerns requiring actual experimentation for resolution were: dose level, type of injection (IV, IP, IM, subcutaneous), avoidance learning criterion (performance), and determination of a standard interval period between training trials and testing (drug effect and/or state dependent effect) trials. As indicated, the appropriate procedure(s) for resolving these issues entailed review of the literature and actual

experimentation. Based on outcomes of meeting Objective 1, actual testing for a state dependent effect (Objective 2) was instituted. Figure 1 reflects the procedural model designed.

Objective 2. The model on which initial experimentation has begun involves three distinct phases: 1) training, 2) interim period, and 3) testing. During training, subjects were conditioned to escape (initially) or avoid (finally) the shock. Early training essentially reflected an escape learning situation in that animals had to learn to attend to the light discriminative stimulus. This stimulus was turned on 5 seconds prior to shock. Once this stimulus acquired meaning, training became traditional avoidance learning, with trials continuing until a criterion was met. This criterion was pre-determined to be 3 successive successful avoidance trials. Once an animal completed this phase, no further training or even experience in the apparatus was allowed for a 3-week period (interim phase). The testing phase entailed recording the number of trials needed for an animal to regain training (criterion) performance levels. One half of the animal population underwent training under atropine exposure and one half under saline exposure. Testing, or phase 3 trials were accomplished under either atropine or saline conditions. The specific drug conditions of any group of animals may be seen in Figure 1.

IV. RESULTS:

As this project entailed two major objectives, results are reported individually for each. The design and development of a state dependent model for testing CD agent effects in rodents is reflected in Figure 1, which incorporates both specific treatments and the sequence thereof.

The design and development of this procedural model, to include specific subject treatments, entailed a number of trial-and-error experimentations. The relative poverty of research with atropine on rats¹³ necessitated experimenting with dose levels and routes of injection. A consultant

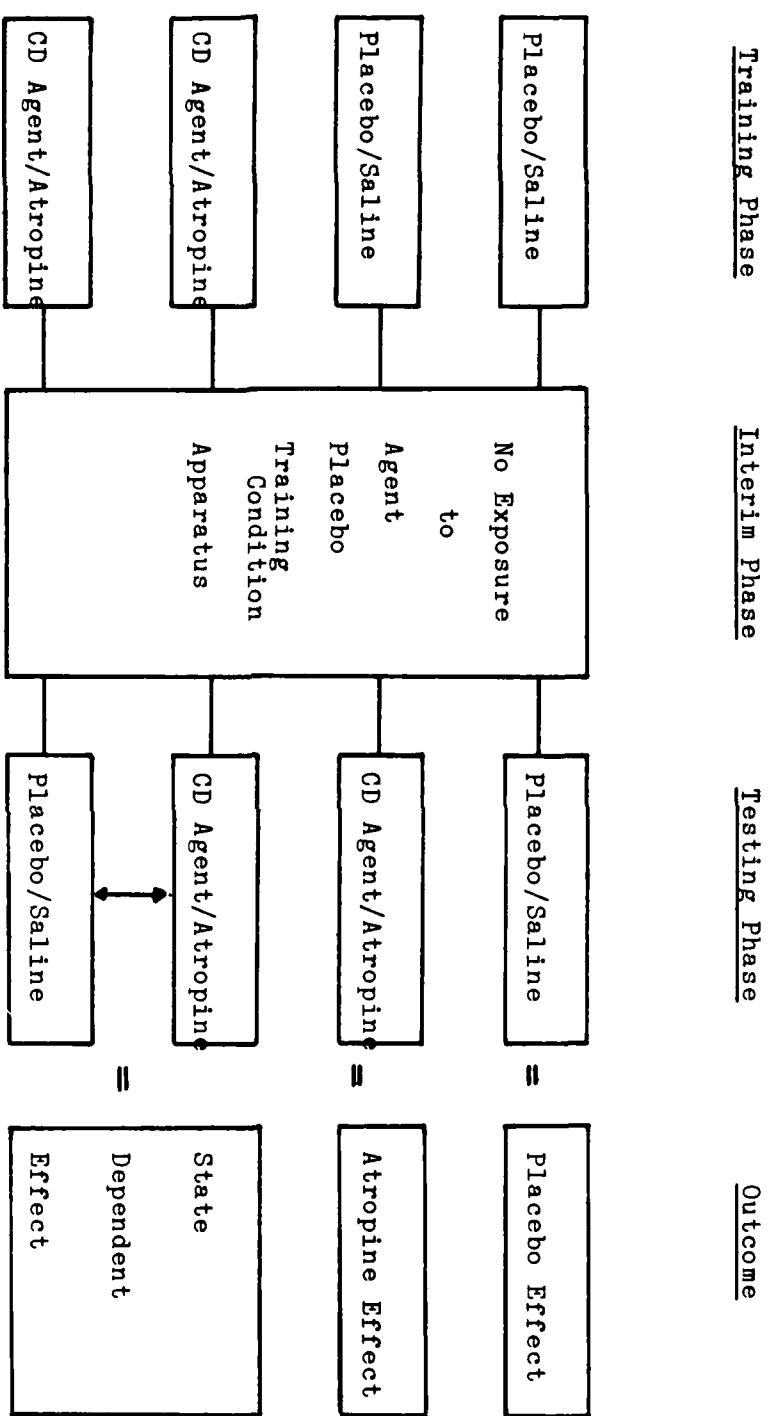


Figure 1. A model for state dependent learning effect testing in small animals using prophylactic doses of atropine. Dose level, peak effect time, injection route, and learning/performance task are discussed in text.

veterinarian aided in experimenting with route and dose determinations. While the prescribed CD human route of administration is IM, or at worst, subcutaneous, this mode proved inefficient with rats due to 1) typical needle length, 2) small size of muscle groups readily accessible, and 3) difficulty of injection. Hence, and in accord with some previous relevant research,¹² an IP (intraperitoneal) route was established as the most efficacious accomplishable. Determination of dose level proved both difficult and costly. A major regional school of veterinary science consulted was unable to indicate any precise rat-equivalent of the conventional human dose. Of note, not only is the rat much smaller but metabolism and drug assimilation rates are appreciably different than in humans. Unfortunately, experimentation with a narrowing range of atropine doses resulted in the premature demise of some animals, thus reducing the number of subjects available for actual state dependent testing. The atropine dose of 1 cc/100 gm of 50% solution of atropine sulphate proved as the most viable dose level to approximate the behavioral decrement noted in humans for a CD dose. It was also determined, through trial-and-error, that this animal dose achieved essentially peak effect in 20 minutes following IP injection. The determination of an avoidance learning criterion was based on preliminary testing of non-injected (atropine or saline) animals: 3 consecutive trials of successful avoidance behavior in a discriminant stimulus situation. The 3-week interim (between training and testing) period was selected arbitrarily. Collectively, the model of Figure 1 and the foregoing experimentally-based information constituted completion of Objective 1.

Objective 2 entailed the actual controlled testing of animals using the paradigm evidenced in Figure 1. Several intervening variables operated to severely limit the conduct of this portion of the research project. As previously noted, an unexpected number of animals were lost to the study in

the process of exploring dose levels, either as a direct and relatively immediate result of atropine administration or as a suspected side/after effect within several days of injection. A second unforeseen situation further detracted from experimental efforts and opportunities: a wild rat managed to gain entry into the animal housing area. Before it could be eliminated, it had destroyed several laboratory animals or sufficiently injured them so as to require humane sacrifice. Hence, the total number of available and surviving animals naive to atropine exposure was sufficiently reduced to require curtailment of using the full state dependent paradigm of Figure 1. Consequently, the data obtained must be considered limited and/or preliminary. In essence, the N's for experimental groups (4) with insufficient statistically to allow drawing definitive conclusions. However, preliminary/guarded data indicated the following: 1) the administration of atropine did disrupt the learning/training process, as control (saline) subjects required an average of 14 trials to criterion while experimental (atropine) subjects took an average of 23 (22.7) trials to reach criterion; and 2) while no definitive statement on a state dependent effect is warranted (n = 3 per group), a trend was evidenced supporting the phenomenon, i.e. atropine/training rats returned to criterion level performance during testing with atropine in fewer trials than did either rats trained under saline conditions. Again, this data must be considered tentative, and continuing, larger-N, experimentation is in progress.

V. RECOMMENDATIONS:

Despite the recounted problems encountered in pursuing Objective 2, several suggestions and recommendations seem warranted.

1. The developed model (Figure 1) appears viable for atropine experimentation with small animals respecting a CD orientation.

2. The atropine dose level and peak effect time period and mode of injection appear viable and adequate, and should

be considered for future and/or continuing research efforts.

3. The present research, coupled with previous related efforts using rodents,^{12,13} strongly supports performance decrements associated with atropine exposure. Such knowledge is a necessary precursor to testing for state dependency.

4. The trend evidenced presently, along with results of other research on CNS-acting drugs, endorses the probability of state dependent effects with atropine. The clear establishment of this phenomenon should be a high priority in USAF research interests due to the implications on combat (CD) efficiency. A reliable and clear establishment of such an effect would encourage special training (under atropine influence) for all essential flightline personnel which could deter any significant loss of behavioral efficiency in CD conditions.

5. The research herein reported is continuing at personal (researcher)/institutional (university) expense, stimulated by this RIP grant and inherent opportunities. As larger amounts and more definitive data become available, journal publication is envisioned and all results will be made readily available to AFOSR.

REFERENCES

1. Headley, D. B., "Effects of Atropine Sulfate and Pralidoxime Chloride on Visual, Physiological, Performance, Subjective, and Cognitive Variables in Man: a Review," Military Medicine, Vol. 147, pp. 122-132, 1982.
2. Julien, R. M., A Primer of Drug Action (3rd ed.), San Francisco, W. H. Freeman, 1981.
3. Kalser, S. C., and McLain, P. L., "Atropine Metabolism in Man," Clinical Pharmacology and Therapeutics, Vol. 11, pp. 214-227, 1970.
4. Ketchum, J. S., Sidell, F. R., Crowell, E. B., Aghajanian, G. K., and Hayes, A. H., "Atropine, Scopolamine, and Ditran: Comparative Pharmacology and Antagonists in Man," Psychopharmacologia, Vol. 28, pp. 121-145, 1973.
5. Brown, B., Haegerstrom-Portnoy, G. Jones, R., and Jampolsky, A., "Investigation of Visual Performance After Administration of Cholinergic Blocking Agents, II. Atropine," US Army Medical Research and Development Command, Ft. Detrick, Maryland, 1982.
7. Cullumbine, H., McKee, W. H. E., and Creasey, N. H., "The Effects of Atropine Sulphate upon Healthy Male Subjects," Quarterly Journal of Experimental Physiology, Vol. 40, pp. 309-319, 1955.
8. Mirakhur, R. K., "Comparative Study of the Effects of Oral and I.M. Atropine and Hyocine in Volunteers," British Journal of Anaesthetics, Vol. 50, pp. 591-598, 1978.
9. Perry, D. J., and Mount, E., "A Comparison of the Effect of Atropine and Placebo on the Galvanic Skin Response," Journal of Investigative Dermatology, Vol. 22, pp. 497-501, 1954.

10. Moylan-Jones, R., "The Effect of a Large Dose of Atropine Upon the Performance of Routine Tasks," British Journal of Pharmacology, Vol. 37, pp. 301-305, 1969.
11. Lobb, M. L., Phillips, J. D., and Winter, A. S., "Aircrew Performance Effects of Atropine Sulfate with and Without an Anticholinesterase Challenge: Review and Interpretation," USAF Contract No. F33615-83-RO611, USAF School of Aerospace Medicine, Brooks AFB, Texas, 1983.
12. Buresova, O., Bures, J., Bohdanecky, Z., and Weiss, T., "Effect of Atropine on Learning, Extinction, Retention and Retrieval in Rats," Psychopharmacologia, Vol. 5, pp. 255-263, 1964.
13. Spencer, D. G., and Lal, H., "Effects of Anticholinergic Drugs on Learning and Memory," Drug Development Research, Vol. 3, pp. 489-502.
14. Houston, J. P., Fundamentals of Learning, New York, New York, Academic Press, 1976.
15. Belleville, R. E., "Control of Behavior by Drug-produced Internal Stimuli," Psychopharmacologia, Vol. 5, pp. 95-105, 1964.
16. Bennett, C. T., Lof, N. E., Farrer, D. N., and Mattsson, J. L., "Equilibrium Performance Changes Produced by Atropine in M. Mulatta and M. Fascicularis," SAM-TR-81-29, USAF School of Aerospace Medicine, Brooks AFB, Texas, 1981.
17. Farrer, D. N., Yochmowitz, M. G., Mattsson, J. L., Barnes, D. J., Log, N. E., Bachman, J. A., and Bennett, C. T., "Behavioral Effects of Benactyzine on Equilibrium Maintenance and a Multiple Response Task," SAM-TR-79-19, USAF School of Aerospace Medicine, Brooks AFB, Texas, 1979.

18. Farrer, D. N., Yochmowitz, M. G., Mattsson, J. L., Lof, N. E., and Bennette, C. T., "Effects of Benactyzine on an Equilibrium and Multiple Response Task in Rhesus Monkeys," Pharmacology Biochemistry and Behavior, Vol. 16, pp. 605-609, 1982.
19. Buckalew, L. W., "Aircrew-Relevant Man-Monkey Analogs for Evaluation of CD Agents: Pitch and Alcohol," USAF Contract No. F49620-82-C-0035, USAF School of Aerospace Medicine, Brooks AFB, Texas, 1983.
20. Wenger, J. R., Tiffany, T. M., Bombardier, C., Nicholls, K., and Woods, S. C., "Ethanol Tolerance in the Rat is Learned," Science, Vol. 213, pp. 575-577, 1981.
21. Riley, E., "Ethanol as a Behavioral Teratogen: Animal Models," in Biomedical Processes and Consequences of Alcohol Use, DHHS Publication No. (ADM) 82-1191, 1982.
22. Buckalew, L. W., "Methodological Issues in Drug Assessment Research," Drug Development Research, Vol. 5, pp. 103-110, 1985.

1983-84 USAF-SCEEE RESEARCH INITIATION PROGRAM

Sponsored by the

AIR FORCE OFFICE OF SCIENTIFIC RESEARCH

Conducted by the

SOUTHEASTERN CENTER FOR ELECTRICAL ENGINEERING EDUCATION

FINAL REPORT

COMBINED BLAST AND FRAGMENT LOADING OF REINFORCED CONCRETE

Prepared by: Dr. Chester E. Canada

Academic Rank: Associate Professor

Department and
University: Civil Engineering Department
Oklahoma State University

Research Location: Air Force Engineering & Services Center

Date: September 1984

COMBINED BLAST AND FRAGMENT LOADING
OF REINFORCED CONCRETE

by

Dr. Chester E. Canada

ABSTRACT

The loading and response of an aboveground, blast-resistant, reinforced concrete structure to the nearby detonation of an air-delivered bomb is addressed. The resulting load on an adjacent structural element is due both to blast waves and to the impacts of high-velocity metal fragments. The loading profile from a metal-cased charge is found to differ significantly from that of a bare explosive charge because of these high-velocity fragments, which cause direct spall from the front face of a concrete element and modify the shock wave that propagates into the concrete. Overpressure magnitudes are larger, and the spatial gradient behind the front is increased. Larger structural deformations and a higher probability of spalling at the back face of the concrete element are to be expected. Consequently, a structure that provides desired protection against a bare charge may prove inadequate for protecting against a metal-cased charge.

ACKNOWLEDGEMENTS

This research was sponsored by the Air Force Systems Command and the Air Force Office of Scientific Research under contract No. F49620-82-C-0035 through the Southeastern Center for Electrical Engineering Education. The effort evolved from work at the Engineering and Services Center of Tyndall Air Force Base during the summer of 1983. The work at Tyndall, which involved personnel from both Tyndall AFB and Waterways Experiment Station, was supported by the same sponsors listed above.

The author wishes to thank personnel from both Tyndall and WES for their contributions to this effort. Specifically the encouragement and guidance of Lt. Tom Hilferty, Capt. Paul Rosengren, and Major John Centrone of Tyndall and the technical discussions with Dave Coltharp and Sam Kiger of WES are acknowledged.

I. INTRODUCTION: Aboveground reinforced concrete structures are widely used by the Air Force to protect equipment and personnel from the near-miss detonations of air-delivered ordinance. The design of these structures has historically been based on conservative procedures such as those outlined in Reference 1. Recent tests (2-4) were conducted to investigate the degree of conservatism inherent in these accepted design procedures. These tests confirmed that an acceptable protective structure satisfying the shear and flexural requirements imposed by the detonation of a bare charge can be met with a design using less steel than is recommended by the conservative procedures. These tests were conducted using structures with concrete wall thicknesses consistent with the accepted procedures but with variations in both the flexural and shear reinforcing.

Unfortunately, a new area of concern became evident because of these tests. Reinforced concrete walls that were capable of resisting the nearby explosion of a bare explosive charge without significant damage could spall or even breach when subjected to a metal-cased charge of the same weight. Hader (5) reported that cased charges caused perforation in walls at distances up to ten times larger and thicknesses up to three times greater than a bare charge of the same weight. Fig. 1, which shows the effect, is taken from Hader's paper. Obviously the loading caused by the high-velocity missiles modify the total loading profile to enhance the probability of spall or perforation.

Additional work conducted at Tyndall AFB (6) has demonstrated workable methods to mitigate the loading of the fragments thereby reducing the likelihood of spall or perforation. All tested methods have involved the insertion of a barrier between the charge and structural wall so that direct fragment impact was prevented. An earth cover, a tile wall, or a decoupled concrete barrier wall were all effective for mitigating the case charge effect. Simply increasing the wall thickness was not practical for eliminating spall. It was found necessary to decouple a

solid barrier.

Considerable effort has been historically expended in both understanding and in predicting the response of a structure to the blast wave loading of a bare explosive charge. Unless the charge is in contact or very close to the concrete element of concern, loading magnitudes are generally not sufficient to cause crushing of the concrete on the front face nor spalling of the concrete on the back face. As a result, most of the experimental literature addresses structural rather than material response.

Both spall and breaching are early-time, across-the-plate effects caused by localized material failure. The later-time flexural response of the structure depends on the overall geometry as well as material strength properties. Early-time effects such as spall or breaching that cause removal of material from a structural element obviously adversely effect the response of that element at later times. It is noted, however, that if spall or even some limited breaching should occur, the affected structural element should not be considered as totally failed. Reserve strength in the element or in the structure may well be adequate to carry the subsequent dynamic flexural response as well as the post-event dead loads.

II. OBJECTIVE: The purpose of this study is to develop a quantitative rationale to predict the response of a reinforced concrete structure to the detonation of a metal-cased explosive charge. As explained, considerable effort has been expended in understanding response mechanisms due to detonations of bare charges. The emphasis of this work will be to identify and quantitate differences in the loading magnitudes and profiles arising from the high-velocity fragments that cause enhanced across-the-plate effects and perturbations of the subsequent flexural behavior. Where possible, predictions based on these across-the-plate effects will simply be incorporated as modifications into existing predictions of structural behavior.

Ref. 7 contains a computer program, herein called "REICON" that predicts structural behavior from the detonation of a bare charge. Predictive rationale developed here will use flexural response algorithms contained in this existing program. For the situation to be considered, a direct line-of-sight path from the charge to the element is assumed. The structural element is thus loaded by both the blast wave and the high-velocity missiles from the fragmented case.

III. DISCUSSION: For this study, a vertically oriented explosive charge of known weight and cylindrical geometry is used. The charge is located a prescribed, unobstructed distance from the structural element to be analyzed. Loads from bare and metal-cased charges are examined. When cased, the outside dimensions of the charge are assumed equal to the inside dimensions of the case.

On detonation, a nearby structure is externally loaded by both a blast wave and, if the charge is cased, high-velocity fragments. Parameters of the loading on the front face of the structural element due to the blast wave and the fragments are estimated from empirical data and theory (1, 8-9). If present, the numerous high-velocity fragments crush and penetrate the concrete on the front face thereby causing the removal of some concrete from this surface. In addition this external loading induces a shock wave into the concrete which propagates across the element, interacts with the free surface at the back face, and causes potential spall at this surface. These early-time phenomena may adversely affect the capacity of the element to resist later-time flexural requirements.

A typical blast-resistant structure has concrete walls containing flexural reinforcement. In most cases this reinforcing steel spans both the horizontal and vertical directions. If the anticipated overload is sufficiently severe, web reinforcement, most often stirrups but sometimes lacing, is provided. A concrete cover of prescribed thickness is used to protect and contain the reinforcing steel. As explained below, the mechanism for spall used herein is a direct function of this concrete cover thickness.

A post-test examination of the structures and a review of the photographic records taken during the testing at Tyndall AFB and described by Colthorp (4) provide insight for understanding the mechanisms leading to spall, perforation, and flexural responses.

For these tests, metal-cased charges were detonated at ground level at prescribed distances from several model structures. The load carrying capacities of the various concrete walls were varied so that a wide range of structural responses and material failure modes would be observed. At one extreme, for a weak wall, early-time spall and perforation failures followed by later-time flexural deformation failures, all occurred in a single test. At the other extreme, for a wall designed so that excessive flexural deformations were prevented, spalling on the back face still resulted. One effect common to all walls was the removal of concrete from the front face due to the impacting, high-velocity metal fragments. The amount of concrete removed was directly dependent on the depth of penetration of the high-velocity fragments.

The high-speed photographic records (4) indicate, when all failure modes occur during a single test, that the time sequence of failure events is first spalling, then breaching, and then excessive flexural deformation. Dimensions of individual, spalled concrete pieces were found to be strongly dependent on the concrete cover thickness and the spacing between the horizontal and vertical flexural steel. When spall occurred, the pattern of first cracking of the concrete on the back face formed a rectangular array directly over the location of the adjacent flexural steel. The presence of the flexural steel apparently serves to focus the shock wave thereby producing the observed cracking array. As a result, the preferred lateral dimensions and thickness of a spalled concrete piece equals the spacing of the steel array and the thickness of the concrete cover respectively. It will be assumed herein that, if spall occurs, only one spalling plane is formed and this plane is near the centroid of the flexural steel for the back face. Of course, additional spalling planes may form between the front and back faces, but the prescribed flexural and shear steel confines the concrete in this region thereby resisting the separation of material across a spall plane.

The crushing and removal of concrete from the front face by the impacting fragments and the potential spall from the back face both cause a reduction in thickness of the structural element that is to resist breaching and flexural deformations at later times.

a. LOADING DUE TO BLAST WAVE: Prediction of the parameters for the free-field blast wave, as it approaches the element of concern is based on curves in Ref. 1 and 8 for the detonation of a hemispherical charge at ground level. No pressure reduction mechanisms due to the metal case are considered. Pressure-time loading applied to the element depends on the angle of incidence of the blast wave and the magnitude of the free-field side-on overpressure. Empirical data in Ref. 9 is used to convert the free-field parameters to actual pressure-time loading.

Necessary numerical values, from Ref. 1 and 9, to compute the loading profile at a point on a surface are stored as data in the computer program. These data include values from the scaled distance, side-on overpressure, peak reflected overpressure, scaled reflected impulse, scaled duration, and scaled time-of-arrival curves of Fig. 4.12 (1) and the side-on overpressure, angle of incidence, and reflection coefficient curves of Ref. 9. Because of incomplete knowledge concerning wave pressure-time histories, a simple triangular profile will be assumed throughout this analysis.

When the loading profile at a point on the surface is desired, the approaching free-field, side-on overpressure (P_{S0}) and the angle of incidence for this location is determined. The peak loading pressure P_b is then computed from the corresponding reflection coefficient C_{ra} of Ref. 9. In order to estimate a wave profile, this value of loading pressure P_b is used to establish a scaled distance-reflected overpressure point on the empirical curve of Ref. 1. The corresponding value of reflected impulse I_r is assumed to equal the impulsive load I_b at the point in question. The duration of the load is determined from the assumed triangular profile.

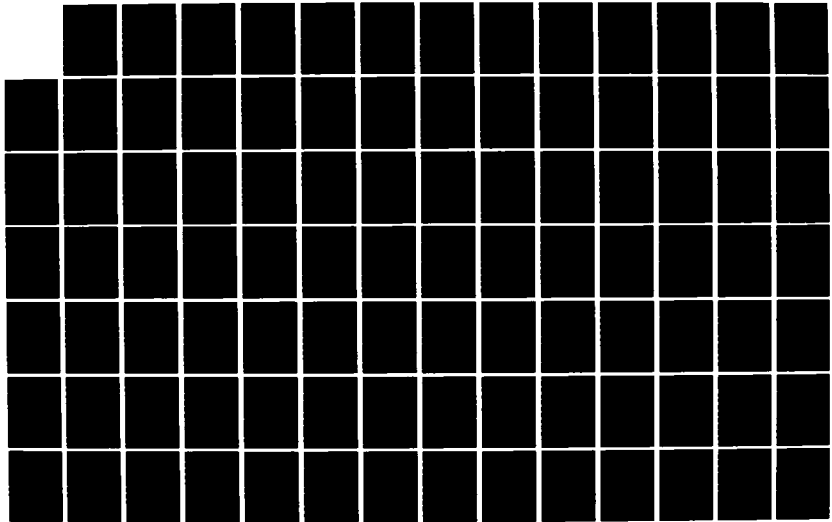
The procedure used to compute the average loading on an area of the surface of interest differs from that given above for a point in that average impulse and duration of loading are established

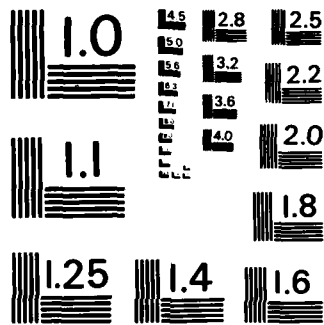
NO-A161 907

USAF/SCEEE (UNITED STATES AIR FORCE/SOUTHEASTERN CENTER 4/12
FOR ELECTRICAL EN. (U) SOUTHEASTERN CENTER FOR
ELECTRICAL ENGINEERING EDUCATION INC S. W D PEELE
MAR 85 AFOSR-TR-85-0904 F49620-82-C-0035 F/G 9/3

UNCLASSIFIED

ML





MICROCOPY RESOLUTION TEST CHART
NATIONAL BUREAU OF STANDARDS - 1963 - A

first. The peak loading pressure is then computed using the assumption of a triangular loading profile. The average impulse for an area is computed numerically. The duration of this effective loading is obtained from an equation of the form of Eq. 4.1 of Ref. 1, namely

$$t_b = t_{Af} - t_{An} + t_{Of} \quad (1)$$

where the subscripts "n" and "m" refer to near and far points on the area of interest. A listing of these symbols and their definitions are given in Appendix A.

The loading profile for a point or an area on the surface of interest has the form

$$p = p_b*(1 - t/t_b), \quad (2)$$

where the parameters are obtained as described above.

b. LOADING DUE TO FRAGMENTS: The rationale developed in Ref. 1 is used herein to predict the velocity, mass, and number distributions of fragments from a metal-cased charge. A homogeneous, cylindrical, metal-cased charge is assumed. For this analysis the charge is oriented vertically. All initial fragment motion will then be horizontal at a velocity

$$v_0 = (2E')^{1/2} (2W_{HE} / (2W_C + W_{HE}))^{1/2}. \quad (3)$$

This velocity decays with distance as

$$v = v_0 \exp((-1.59 E^{-3}) r / W_f^{1/3}). \quad (4)$$

From the Mott theory (8) the median weight of a fragment is

$$W_f = (B * t_C^{5/6} * d_C^{1/3} * (1 + t_C / d_C) * (\ln(.5)))^2, \quad (5)$$

with the symbols defined in Appendix A.

The depth of penetration of a fragment traveling at velocity v and striking a concrete wall at a normal angle is

$$z_f = (5.61 E^{-8} * k' * (5000 / f'_c)^{1/2} * W_f^{0.4} * v^{1.8}), \quad (6)$$

where k' is 0.7 for mild steel and 1.0 for armor piercing steel. The depth of penetration of a fragment approaching the wall at an angle other than normal is estimated by using the normal component of velocity. The concrete material removed by this process reduces wall thickness and the capacity of the element to resist breaching and flexure as will be more fully addressed below.

The total number of fragments from the case is

$$N_T = ((\ln 0.5)^2 / 2) * W_C / W_f. \quad (7)$$

The number of fragments striking a region of the concrete wall subtending an angle "a" at the metal case is simply

$$N_a = N_T * (a/360). \quad (8)$$

The momentum imparted to this region by the fragments is then

$$M_f = m_f * v_{nf} \quad (9)$$

where v_{nf} is the normal component of the fragment velocity at the region of interest. The fragment impulse for an area in the region of interest is obtained from

$$i_f = M_f / A. \quad (10)$$

c. COMBINED BLAST WAVE and FRAGMENT LOADING: The loading on a surface resulting from both blast waves and fragment impacts is certainly a sequence of complex wave interactions. A complete description requires a knowledge of the pressure-time histories of both sources as well as their interaction times with each other and the surface of interest. This information is most often not available.

A reasonable estimate of the pressure-time history from the blast wave acting alone is possible. This estimate gives values of p_b , t_b , and i_b . The impacting fragments impart analogous loading parameters to the element of interest. Unfortunately for this situation, the applied impulse i_f is the only parameter that is predictable with a reasonable degree of confidence.

The duration of a load from an individual impacting fragment will be a function of the time required for rarefaction waves within the metal fragments to relieve stresses at the impact interface. For the problem of interest here, this time will be small relative to the duration of the blast load. For this study, it will be assumed that the impulses from the two sources combine linearly and that the duration of the loading is controlled by the value of t_b . This approximation is sufficiently accurate as long as the natural period of the element of interest is long enough to consider the loading as an "impulsive loading" event.

The combined loading profile at a point or an area on the surface consistent with the assumptions stated above is

$$i_{APP} = i_b + i_f, \quad (11)$$

$$t_{APP} = t_b, \quad (12)$$

and
$$p_{APP} = 2 * i_{APP} / t_b. \quad (13)$$

This loading profile is used as the initial state on the front face of the concrete element.

d. ATTENUATION OF SHOCK WAVE: The pressures associated with a shock wave certainly decrease as the shock propagates through a structural element. However, as long as internal stresses do not exceed material strengths, little attenuation occurs and this decay process is often simply ignored for design considerations. For the problem of concern here, induced stresses are often larger than material strengths. As a result, the shock decay process becomes significant and is included in the analysis.

Quite often when dynamic stresses exceeding material strengths are applied at an interface, two shock waves emanate from that interface to relieve the unbalanced condition. The first wave has a pressure determined by the material strength while the second wave has a magnitude governed by the applied loading. The first wave is generally an elastic wave whereas the second wave is a plastic wave. Pressures associated with the plastic wave exceed material strengths so the attenuation of this wave is significant. By comparison, the attenuation of the elastic wave is negligible and will be ignored here.

Since concrete is a somewhat porous material, the theory of Herrmann (10), which contains a (p, α) -model as an equation of state to compute the attenuation of shock waves in porous materials, will be used. In this theory the magnitude of the slope of the unloading path in pressure-volume space is significantly larger than that of the loading path. As a result, the local speed of sound behind the shock front, which is a function of this slope, is large enough so that disturbances behind the front quickly overtake it thereby causing attenuation. Read and Malden (11) list equation of state parameters and material strength characteristics required to apply the technique. These values are directly applied in this analysis.

Fig. 2 illustrates the analysis for attenuation. The initial position of the shock front is at x_1 at time t_1 . The separation between the shock front and point "P" at t_1 is $\Delta x'$ while the relative velocity between the shock front and the point is Δv where

$$\Delta v = (C + u_p) - U_s. \quad (14)$$

The time of overtaking and attenuation of the shock front to the pressure of point "P" is

$$t = \Delta v / \Delta x'. \quad (15)$$

The position of the shock front at this new time is

$$x_t = x_1 + U_s * \Delta t. \quad (16)$$

These steps are repeated until either the back face is encountered or the pressure decays to the elastic limit P_E at which time further attenuation is negligible.

Values of the local speed of sound for pressure along the tail of the shock wave profile are required by this analysis scheme. The local speed of sound behind the shock front is

$$C = (-v^2 * \partial p / \partial v)_s, \quad (17)$$

where the equation is to be evaluated along an isentrope. Sufficient information is not currently available to evaluate this partial differential equation except at points near zero pressure where the Hugoniot and the isentrope are nearly identical.

These speeds of sound are estimated as follows: The speeds of sound for two zero pressure porosity states are determined. The first state is at the zero pressure of the Hugoniot for the initial porosity. The speed of sound for this state (C_0) is nearly equal to that at the Hugoniot elastic limit (p_E, v_E). The second state is at the zero pressure of the Hugoniot for concrete having zero porosity. The speed of sound at this state is conservatively equated to that which occurs at the intersection of the two Hugoniot as shown in Fig. 3. The speeds of sound for points on the actual loading curve between P_E and P_S are simply assumed to vary linearly with porosity so that

$$C = C_0 + 4.505*(C_0 - C_1)*(\alpha - 1.222). \quad (18)$$

Functional relationships between particle velocity and shock velocity and between porosity and pressure are obtained directly from equation of state parameters listed in Ref. (11).

e. SPALLING OF CONCRETE: Concrete spalling is a dynamic phenomena. It has no static counterpart. It results from the interaction of two rarefaction waves which produce a net tensile stress within the material. Several models for spalling have been proposed (12) to predict the behavior of various classes of materials. Unfortunately, insufficient data are available to utilize most of these models. One of the more simple models will be used here. For this model, spall occurs at the instant the tensile stress at a plane in the concrete exceeds the tensile strength S_u . The phenomena is treated as a brittle process.

Fig. 4 illustrates the model and shows conditions in the concrete at two points in time. When the shock front first contacts the back face, the peak overpressure is that predicted from the attenuation analysis. The back face is treated as a free surface. A rarefaction wave must be propagated backwards into the concrete to maintain this plane as a free-surface.

At a later time, the interaction between left-going rarefaction wave and the tail of the right-going compressive wave produces a net tensile stress S_t at the plane of interest. If the tensile stress exceeds the tensile strength, spall occurs and material on the right of this plane has a larger velocity than material on the left. If no external restraint is provided, material on the two sides of the plane will increasingly separate with time. As previously explained, if the plane is located within the concrete cover, no external restraints exist and the separation of material is complete. If the spall plane is located between the positive and negative flexural steel, additional restraint is eventually provided and the total separation of material on the two sides of the spalling plane is inhibited.

The type of structure of concern here will contain both positive and negative flexural steel and, quite often, shear reinforcing as well. Relative material motion between these two planes is thus inhibited and only one spall plane located at the depth of the centroid of flexural steel for the back face will be considered. If spall occurs

$$S_t > S_u, \quad (19)$$

and the impulse trapped in the spalled region, assuming a triangular profile, is

$$i_T = p \cdot t_S \cdot (1 - t_S / (2 \cdot t_b)). \quad (20)$$

Correct values to be used for the dynamic tensile strength are certainly higher than the static tensile strength but questions of absolute value remain. Kot (9) reports evidence of dynamic tensile strengths equal to one-half the compressive strength while other investigators use values as low as 13% of the compressive strength. The value used for the test cases reported here is 14% of the compressive strength. However, due to questions of correct magnitude for this variable, it is treated as an input parameter in the computer program and can be changed according to the needs of the user.

Kot (9) also reports that spalling is highly dependent on the angle of incidence of the shock wave at the front surface. He predicts that spalling will not occur for angles of incidence exceeding 45 degrees. This limiting angle is used in this analysis.

The spalling process both removes impulse trapped in the concrete cover and reduces the wall thickness available to resist breaching and flexural response. The momentum associated with this trapped impulse is computed and removed from that available to cause subsequent breaching and flexural response.

An effective wall thickness is defined as a linear function of the volume of material spalled or

$$H_{eff} = H - (A_{SPALL}/A_{TOTAL}) * \Delta Z, \quad (21)$$

where the subscripts refer to the spalled area and the total area of the wall respectively.

In addition, the fragments that impact the front face also remove material and decrease the resistance to breaching and flexure. An effective wall thickness is defined relative to this process that is also linearly related to the volume of material removed or

$$H_{eff} = H - (A_{FRAG}/A_{TOTAL}) * \Delta Z, \quad (22)$$

where the subscripts refer to the area subjected to fragment impacts and the total surface area respectively.

f. COMPUTATIONAL PROCEDURE: The physical models described above were inserted into the basic framework of the computer program "REICON" (7). "REICON" was written to study the shear failure of soil covered structures subjected to the pressure loading of a small localized explosion. The initial program treated both beams and plates and used a centrally located charge. An analytical power function with empirical coefficients was used to define the pressure loading on the surface of concern. The resulting response was computed using yield line and traveling hinge mechanisms together with both linear and rotational motion of the structural element. The program is modified here to address the combined loading of fragments and blast waves. A listing of the modified program is given in Appendix B. Changes are highlighted where practical. A partial listing of the symbols is in Appendix C.

The number of input data to run the program has been reduced and times for listing the output data are internally computed. The algorithm for computing blast pressure loading is completely changed and a spalling model with attendant changes in the effective wall thickness is employed. In addition, output data from the modified program are changed to reflect parameters of interest for a vertical concrete wall. The existing algorithms for computing rotational and linear response based on yield lines and traveling hinges are used intact. Subroutines that are contained in "REICON" but that are not applicable to this analysis are deleted from the listing in Appendix B.

IV. RESULTS and DISCUSSION: The limited studies reported here are intended to demonstrate comparative differences between the effects for cased and uncased charges. Comparisons are made for spalling, breaching, and flexural response. A reference standard consisting of a 100-pound cylindrical charge and a 12-inch thick concrete wall is used. The wall thickness of the metal case for the reference standard is 1/4-inch. The length-to-diameter ratio of the charge is three and the surface dimensions of the concrete wall are 10 feet by 10 feet. Parameters for other comparative conditions are scaled from this geometry.

a. BREACHING: Fig. 5-7 illustrate the increased likelihood of breaching for metal-cased charges over bare charges as a function of scaled standoff distance. Two charge weights, 10 and 100 pounds, are examined. The criteria used for breaching of a concrete wall is based on the impulse applied to a specified surface area on that wall as explained in Ref. 7. If the average impulse applied to the area exceeds a critical impulse, breaching is predicted. The relationship for critical impulse as a function of parameters of the concrete wall is,

$$I_{CR} = (2^{1.5}/3) * H * (((1-Q) * \rho_C + Q * \rho_R) * (((1-Q) * 1.9 * (f'_C)^{.5} + (Q+Q_1) * D * f_y * 1.5/H)))^{0.5}. \quad (23)$$

A value of 0.01 was used for Q and 0.0025 was used for Q₁. The critical impulse I_{CR} is almost linear with wall thickness as shown in Fig. 8.

Fig. 7 confirms that the impulsive loading and the relative difference between a cased and bare charge are scalable.

Conclusions made for one charge weight are thus applicable for all charge weights as long as scaled geometries are involved.

The minimum surface area evaluated for breaching in Ref. 7 was circular with a radius equal to the thickness of the wall. The minimum surface area used to develop Fig. 5-7 is rectangular but contains the same area as that of Ref. 7. The reason for this difference is because numerical integration techniques of this work involve rectangular coordinates while those of Ref. 7 involved circular coordinates.

Although the results of Fig. 5-7 support the claim that a cased charge is more effective for causing breaching than a bare charge of the same geometry and weight, the difference in the breaching capability is not as great as would be expected from the results of Ref. 5. From Fig. 7, a 12-inch thick wall is expected to breach if the applied impulse is 5.73 psi-ms. A bare charge provides this impulse at a standoff distance of about $0.6 \text{ ft/lb}^{1/3}$ while a cased charge provides the impulse at $0.86 \text{ ft/lb}^{1/3}$. For this condition, a cased charge causes breaching at a standoff of about 1.4 times that of a bare charge. This is considerably less than the factor of 10 found in Ref. 5. The difference is unexplained.

b. SPALLING: Fig. 9 illustrates the increased likelihood of spalling for a cased charge over that of a bare charge as a function of scaled standoff distance. This figure is a graph of the tensile stress at the spalling plane as a function of scaled standoff distance. The features exhibited by this figure are scalable between homologous conditions so conclusions made are also valid for different charges involving scaled geometries. If the critical tensile stress for spall is 750 psi, then spall is predicted at a standoff of 0.72 for a bare charge and 0.92 for a cased charge. For this defined condition, a cased charge is about 1.3 times more effective for producing spall. This multiplicative constant would not change significantly if spalling criteria different from 750 psi were assumed.

A linear and a nonlinear region is evident on each of the curves

displayed in Fig. 9. These curves are based on an average load over the minimum surface area discussed above. At small standoff distances, the loading is large enough over the entire reference area for attenuation of the shock wave to occur within the wall. At the larger standoff dimensions, the pressure applied to the reference area is small enough so that attenuation does not occur. For standoff distances between these extremes, only part of the reference area is loaded with pressure sufficient for attenuation. The exact shape of the nonlinear regions are somewhat dependent on the minimum surface area used while the shape of the linear region is independent of the reference area.

The concrete cover thickness used for the curves of Fig. 9 was 1.5 inches. The net tensile stress at the spalling plane is a direct function of the concrete cover thickness as indicated by Fig. 4. In the region where attenuation is not large, doubling the cover thickness will also double the tensile stress at the new spalling plane. The resulting spall will be significantly different.

In addition, if a particular test situation is causing spall, simply increasing the wall thickness a limited amount is not effective for eliminating spall. In the region where attenuation is small, increasing the distance the wave travels by changing the wall thickness will not cause a significant difference in the net tensile stress at the new spalling plane. For the region of behavior where attenuation is important, considerable crushing of the concrete is occurring due to the attendant large pressures and potential breaching rather than spalling is of the greater concern. This process may serve to quantify why increasing the wall thicknesses a limited amount in the tests at Tyndall (6) reduced the degree of spalling but did not eliminate it.

c. FLEXURE: Selected output from two wall response calculations

are listed in Appendix D. A charge weight of 100 pounds and the standard wall defined above are used. One calculation is for a bare charge and the other one is for a cased charge. A scaled standoff of $0.8 \text{ ft/lb}^{1/3}$ is used because this standoff separates the spall and no-spall conditions for bare and cased charges when the critical tensile stress is 750 psi. The output listing of Appendix D can be scaled for other charge weights of scaled geometries.

Two response calculations are conducted for the metal cased, 100-pound charge because breaching has occurred for this situation. The second set of data defines the response of the element after removal of the mass and momentum associated with the breached and spalled material. Differences in the dynamic behavior are evident.

V. CONCLUSIONS: A computer program that addresses the response of a concrete structure subjected to the nearby detonation of a metal cased charge is described. Physical models included in the program are fragmentation of the metal case, crushing of concrete due to fragment impacts, near-field blast wave loading, attenuation of the shock wave in concrete, and spalling from the backface.

Limited experimental data are available to compare predictions with the prediction model. Trends that are predictable by this model are consistent with empirical findings. However, those experimental data which are available (5) suggest that greater breaching damage will occur than is predicted by this analysis. For example, the theory developed here predicts that a cased charge is about 1.4 times more effective than a bare charge for causing breaching. By comparison, the experimental data of Hader (5) indicates that a cased charge is up to ten times more effective for causing breaching. More experimental data and more highly refined computational models for breaching and for spall will be required to attain agreement between theory and experiment.

REFERENCES

1. AFM 88-22, Department of the Air Force Manual "Structures to Resist the Effects of Accidental Explosions," Department of the Army, the Navy, and the Air Force (June 1969).
2. D. R. Coltharp, "Blast Response Tests of Reinforced Concrete Box Structures," Symposium proceedings of the interaction of non-nuclear munitions with structures, U.S. Air Force Academy, Colorado (May 10-13, 1983).
3. H. Pahl and M. Kropatscheck, "Explosive Tests on Reinforced Concrete Elements Performed on Test Site 91 of the Federal Armed Forces at Meppen," Infrastrukturstab der Bundeswehr, WWTB-80-17 (Summer 1980).
4. G. Loos and H. Pahl, "Explosive Tests on Under-Reinforced Model Structures in Incirlik (Republic of Turkey) and Meppen (Federal Republic of Germany)," Infrastrukturstab der Bundeswehr, TB-82-01 (Jan 1982).
5. H. Hader, "Effects of Bare and Cased Explosive Charges on Reinforced Concrete Walls," Symposium proceedings of the interaction of non-nuclear munitions with structures, U.S. Air Force Academy, Colorado (May 10-13, 1983).
6. Private communication with Lt. Tom Hilferty of Tyndall Air Force Base.
7. C. A. Ross et al, "Concrete Breaching Analysis," AFATL-TR-81-105 (Dec 81).
8. DOE/TIC-11268, "A Manual for the Prediction of Blast and Fragment Loading on Structures," U. S. Department of Energy, Albuquerque Operations Office, Amarillo Area Office, Amarillo, Texas (Nov 1980).
9. C. A. Kot, "Effects of Air Blasts on Power Plant Structures and Components," NUREG/CR-0442, ANL-CT-78-41, Argonne National Laboratory (Oct 1978).
10. H. E. Read and C. J. Malden, "The Dynamic Behavior of Concrete," 3 SR-707, Systems Science and Software, P. O. Box 1620, La Jolla, California (Aug 1971).
11. W. Herrmann, "Constitutive Equation for the Dynamic Compaction of Ductile Porous Materials," J. Appl. Phys., Vol. 40, 6 1969, p. 2490.
12. J. H. Oscarson and K. F. Graff, "SPALL Fracture and Dynamic Response of Materials Report #BAT-197A-4-3," (March 1968).

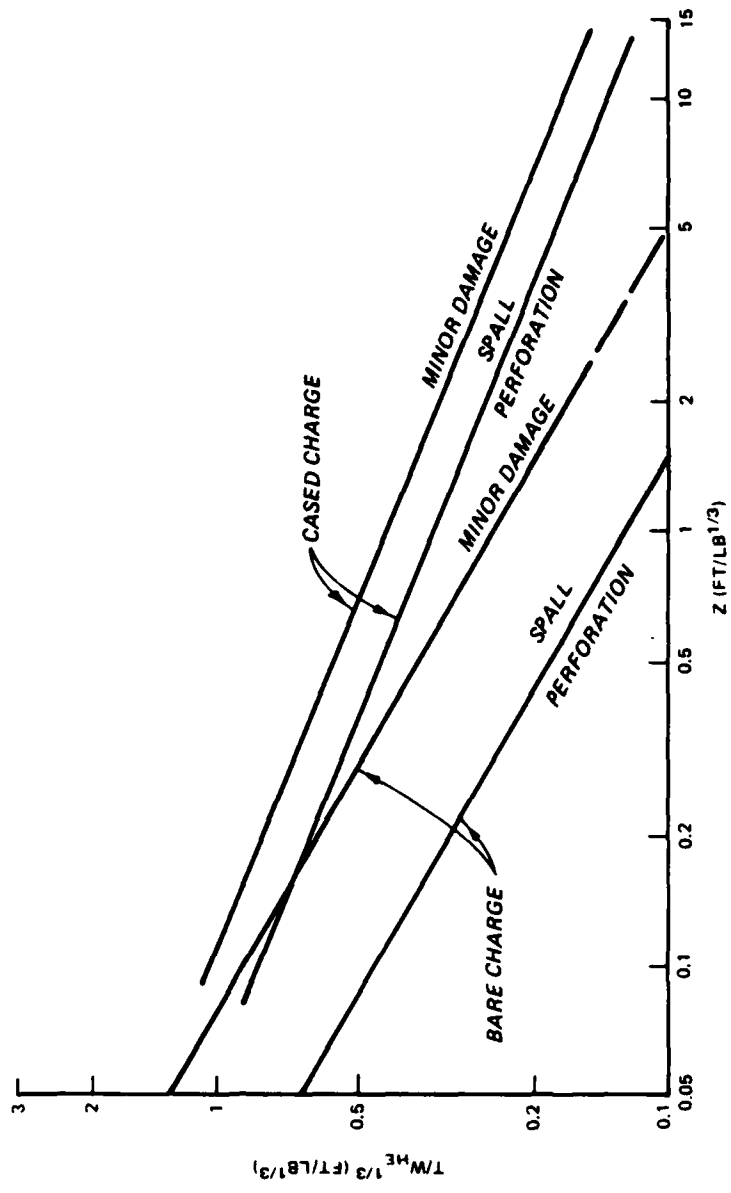


FIG. 1. COMPARISON OF CASED AND BARE CHARGE EFFECTS

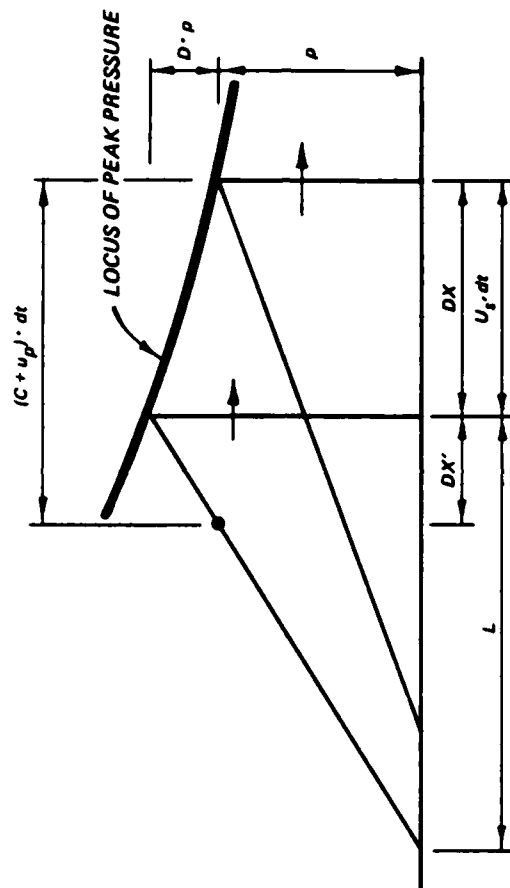


FIG. 2. ATTENUATION OF SHOCK WAVE IN CONCRETE

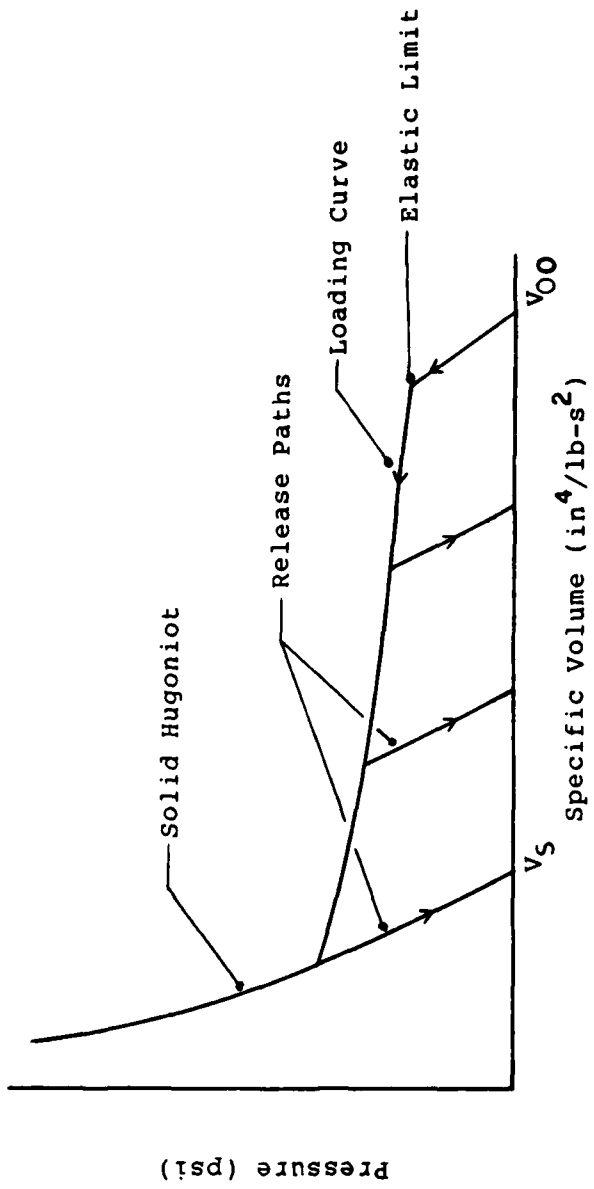


Fig.3. Hugoniot for (p,Q)-model

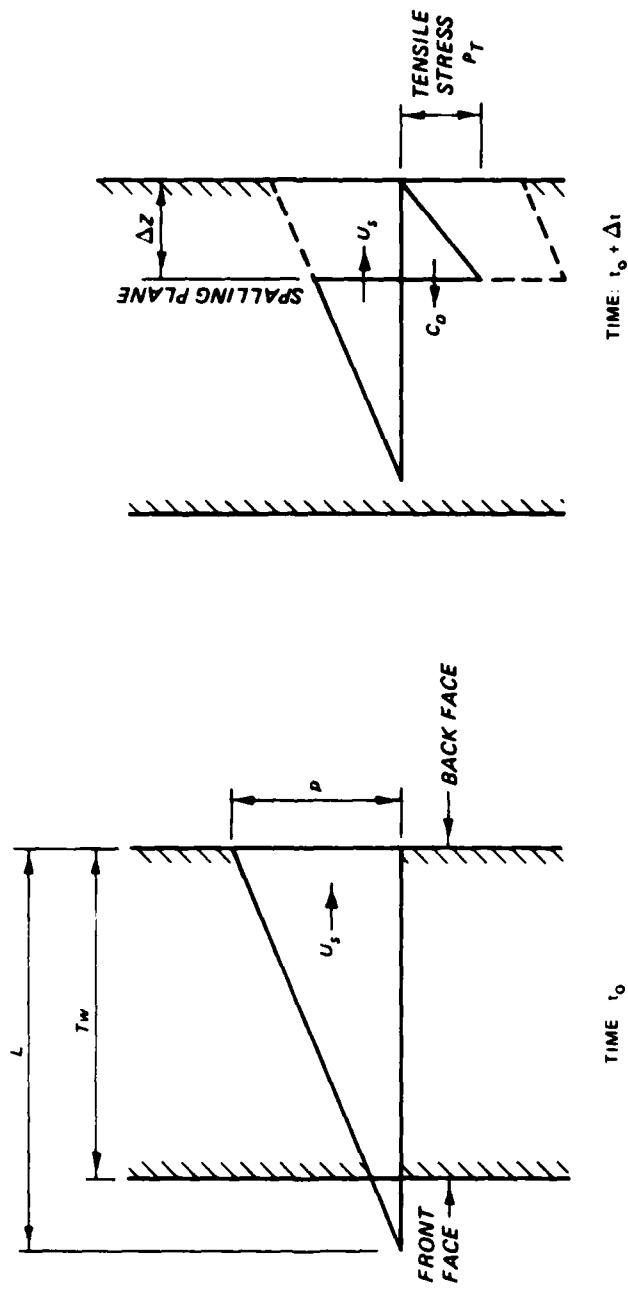


FIG. 4. MECHANISM FOR SPALLING AT BACK FACE

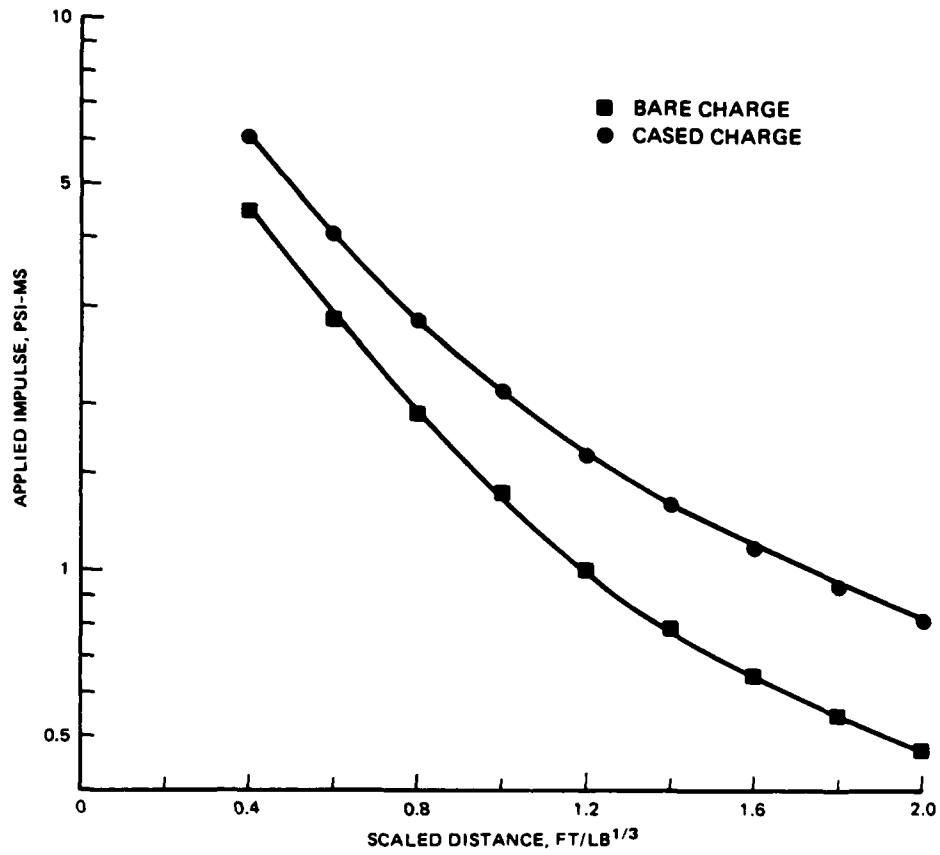


FIG. 5. INITIAL IMPULSE AS A FUNCTION OF SCALED STAND OFF DISTANCES FOR A 10-POUND CHARGE

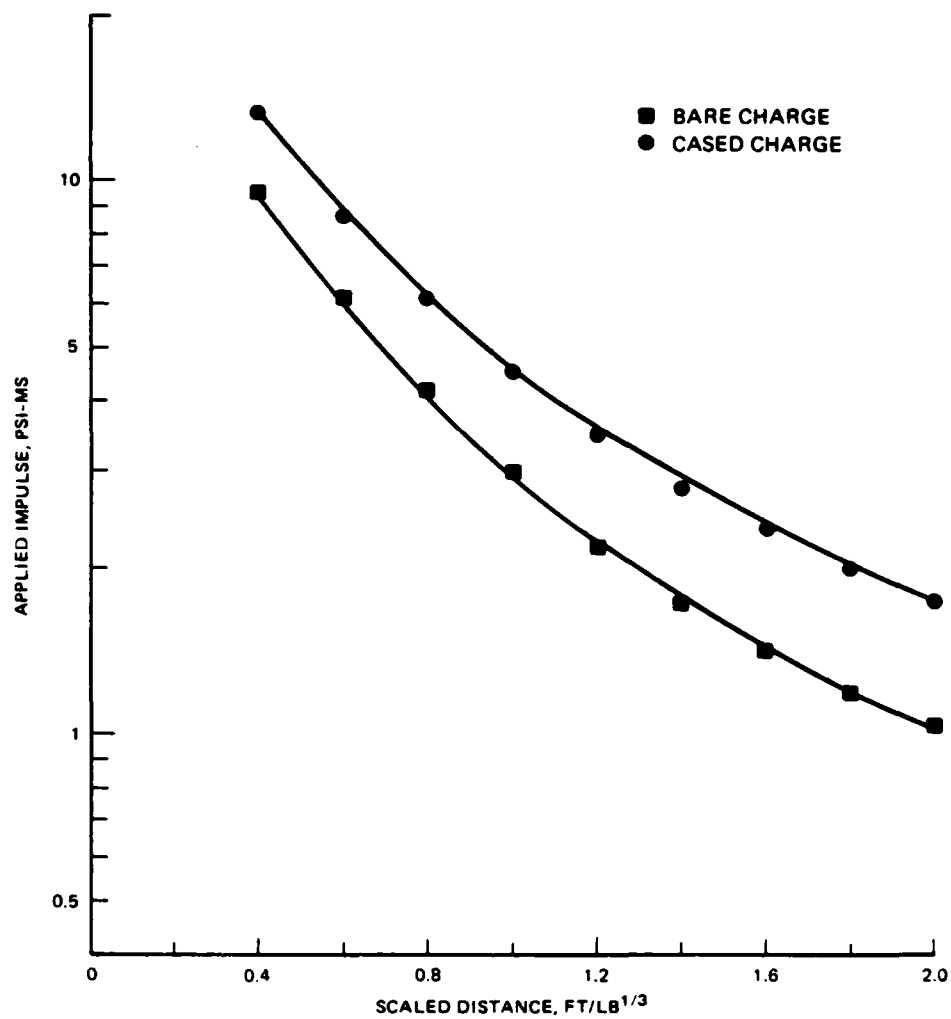


FIG. 6. INITIAL IMPULSE AS A FUNCTION OF SCALED STAND OFF DISTANCES FOR A 100-POUND CHARGE

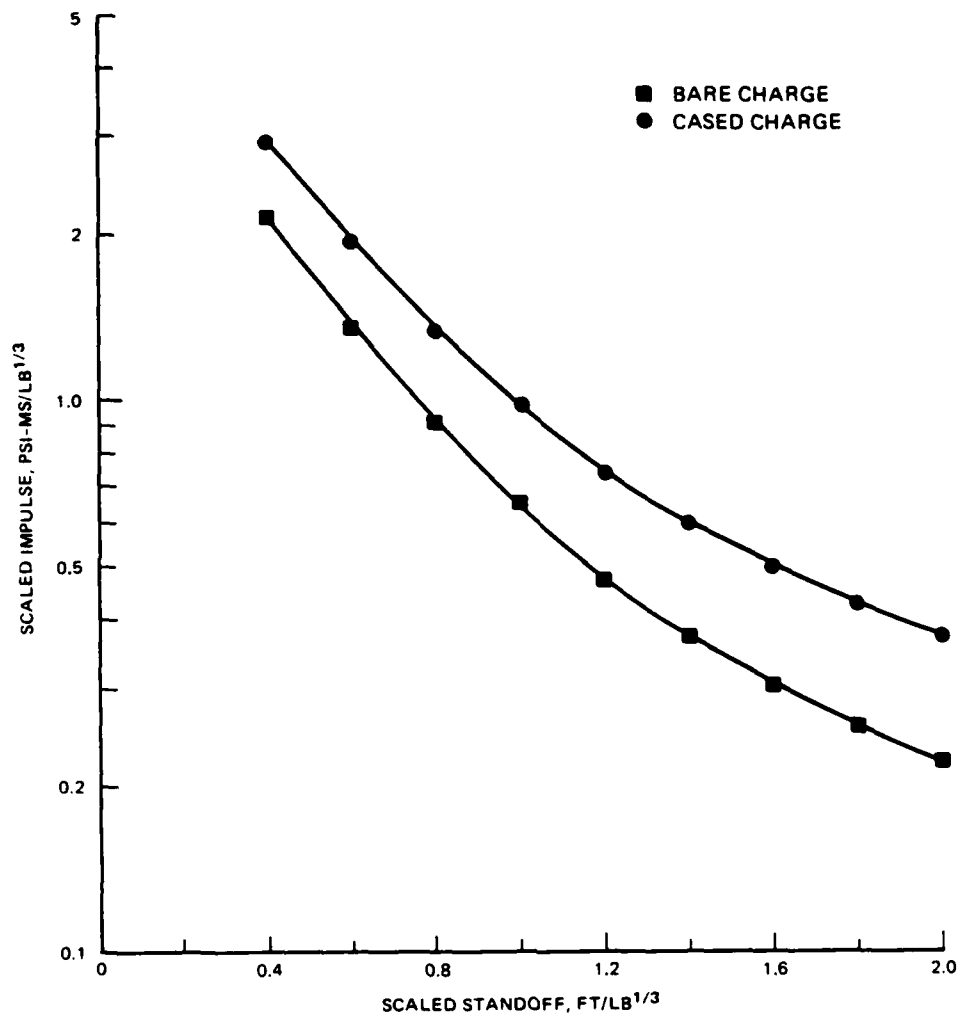


FIG. 7. INITIAL SCALED IMPULSE AS A FUNCTION OF SCALED STAND OFF DISTANCES

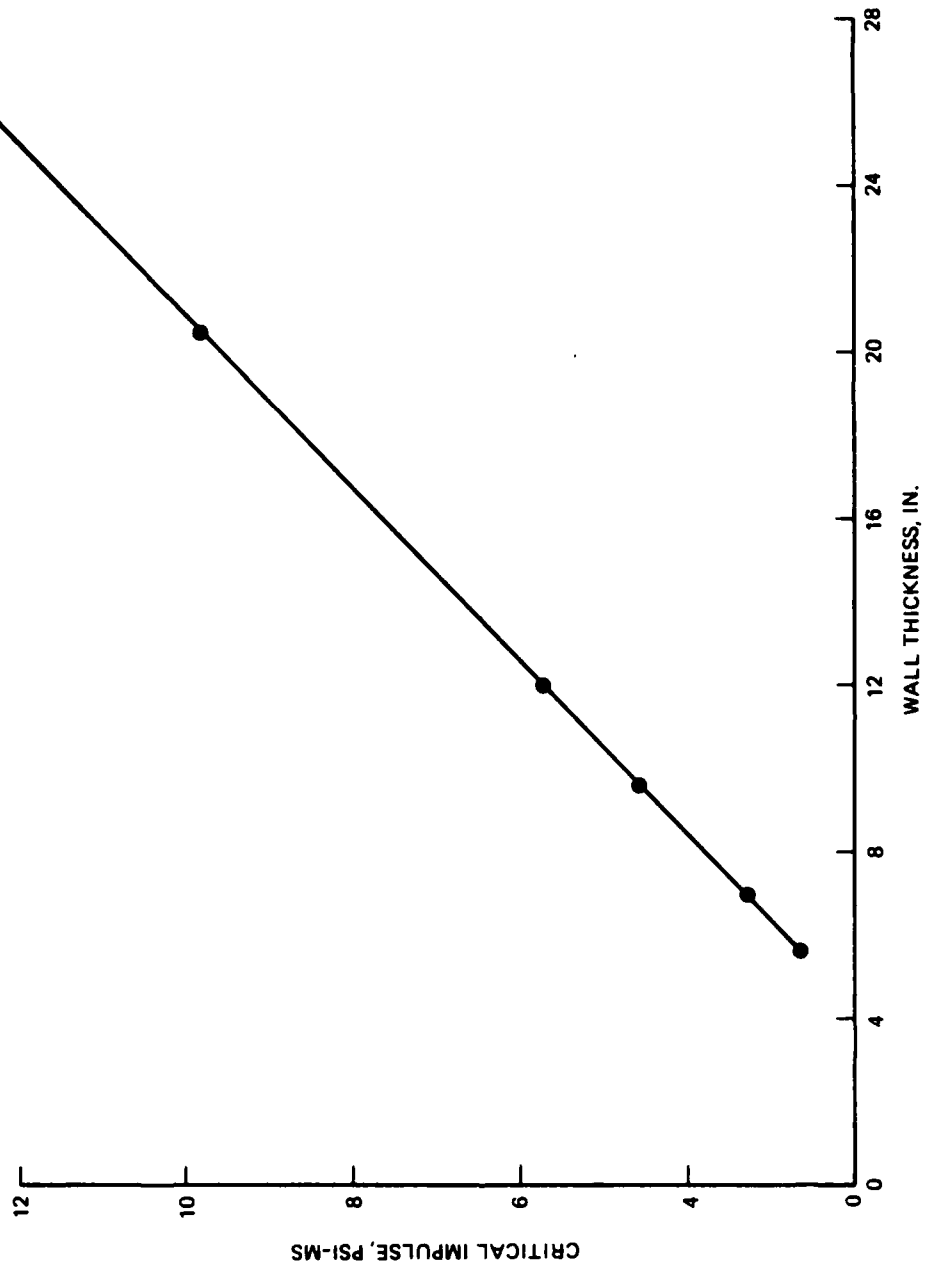


FIG. 8. CRITICAL IMPULSE FOR BREACHING VERSUS WALL THICKNESS

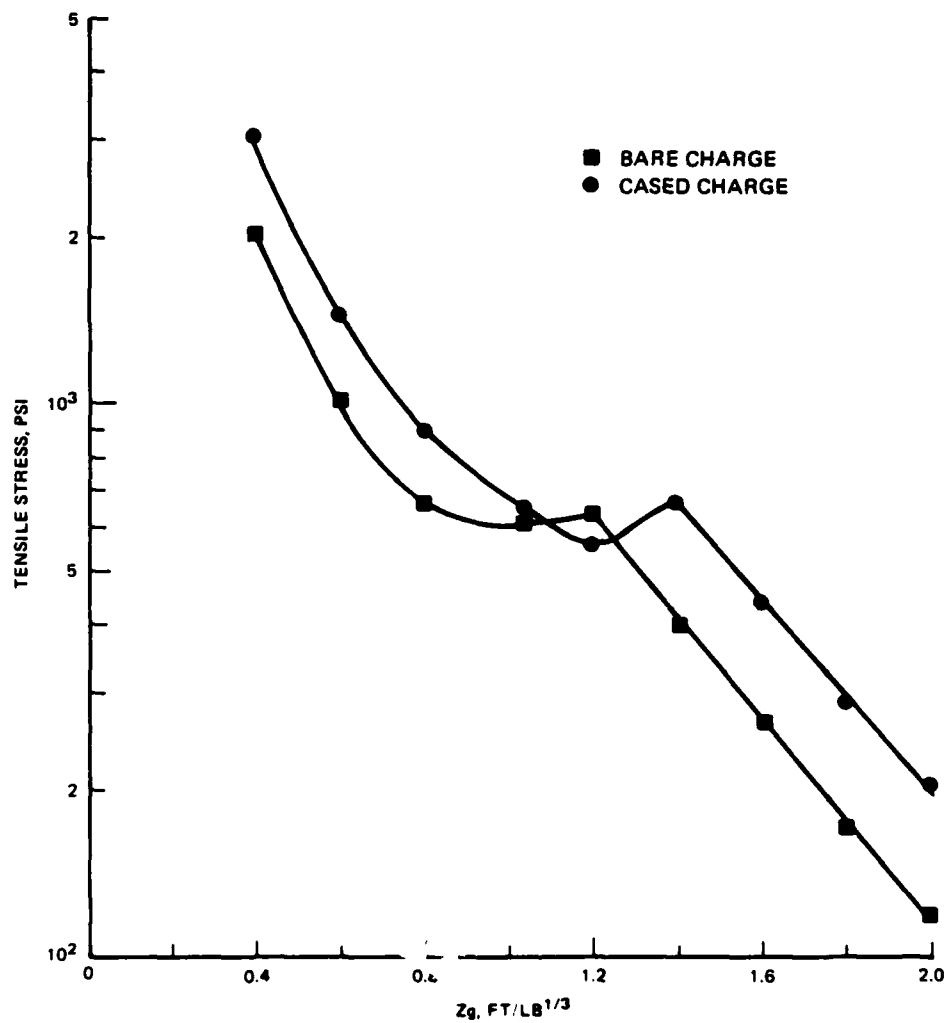


FIG. 9. TENSILE STRESS AT PRESCRIBED SPALL PLANE FOR SCALED STAND OFF DISTANCES AND GEOMETRIES

APPENDIX A

SYMBOLS FOR PHYSICAL MODELS

APPENDIX A

A	Surface area on wall	(in ²)
A _{SPALL}	Surface area affected by spalling	(in ²)
A _{TOTAL}	Total surface area	(in ²)
B	Fragmentation parameter	(lb ^{.5} /in ^{7/6})
C	Variable speed of sound	(in/s)
C ₀	Speed of sound at initial porosity	(in/s)
C ₁	Speed of sound at zero porosity	(in/s)
D	Effective depth of wall	(in)
H	Variable wall thickness	(in)
H _{REF}	Initial wall thickness	(in)
I _{CR}	Critical impulse	(psi-ms)
M _f	Momentum of fragments	(lb-s)
N _a	Number of fragments per subtended angle "a"	
Q	Area ratio of flexural steel	
Q ₁	Area ratio of shear steel	
S _t	Tensile stress at spall plane	(psi)
S _u	Critical tensile stress	(psi)
U _p	Particle velocity	(in/s)
U _s	Shock velocity	(in/s)
V	Specific volume	(in ⁴ /lb-s ²)
W _C	Weight of metal case	(lb)
W _f	Weight of average fragment	(lb)
W _{HE}	Weight of explosive charge	(lb)
Z _f	Depth of penetration of fragment	(in)
(2E') ^{.5}	Gurney constant	(in/s)
d _C	Diameter of metal case	(in)

APPENDIX A

f_C	Compressive strength of concrete	(psi)
f_y	Tensile strength of steel	(psi)
i_{APP}	Applied impulsive load	(psi-ms)
i_f	Impulse due to fragments	(psi-ms)
i_T	Trapped impulse due to spalling	(psi-ms)
k'	Hardness parameter for metal fragment	
m_f	Mass of fragment	(lb-s ² /in)
p	Variable pressure	(psi)
p_{APP}	Effective loading pressure	(psi)
p_b	Effective loading pressure	(psi)
r	Variable distance	(ft)
t	Variable time	(s)
t_{Af}	Time of arrival at far point	(s)
t_{An}	Time of arrival at near point	(s)
t_{APP}	Duration of applied load	(s)
t_b	Duration of load	(s)
t_C	Thickness of metal caes	(in)
t_S	Time of spalling	(s)
t_{Of}	Duration at far point	(s)
v	Variable velocity of fragments	(in/s)
v_0	Initial velocity of fragments	(in/s)
v_{nf}	Normal velocity of fragments	(in/s)
x	Coordinate in wall	(in)
a	Measure of porosity	
ρ_C	Mass density of concrete	(lb-s ² /in ⁴)
ρ_R	Mass density of steel	(lb-s ² /in ⁴)

APPENDIX B

LISTING OF COMPUTER PROGRAM

```

JJJ
10000C PROGRAM REICON (INPUT,OUTPUT)
10001C
10002C *****
10003C *****
10004C PROGRAM MODIFIED BY C. E. CANADA AND W. P. CHEN
10005C OF OKLAHOMA STATE UNIVERSITY, MAY 1984
10006C *****
10007C *****
10008C WRITTEN BY C. C. SCHAUBLE FOR C. A. ROSS
10009C UNIVERSITY OF FLORIDA GRADUATE ENGINEERING CENTER
10010C EGLIN AIR FORCE BASE, FLORIDA 904-882-5614
10011C JULY, 1981 (MODIFIED 18 JANUARY 1982)
10012C
10013C THIS PROGRAM, REICON, COMPUTES THE DEFLECTION OF
10014C THE CENTER OF A REINFORCED CONCRETE BEAM OR PLATE
10015C CAUSED BY A UNIFORM OR BLAST LOAD.
10016C
10017C THIS MAIN PROCEDURE CALLS THE SYSTEM LIBRARY
10018C ROUTINES, DATE AND TIME, TO INITIALIZE THE CURRENT
10019C DATE AND TIME. IT ALSO CALLS THE SUBPROCEDURE,
10020C DRIVER, TO HANDLE THE READING AND PROCESSING OF
10021C EACH CASE.
10022C
10023C THIS PROGRAM HAS BEEN WRITTEN IN CDC FORTRAN
10024C VERSION 5. THE INPUT UNIT SPECIFIED IN READ
10025C STATEMENTS BY AN ASTERICK IS THE NORMAL INPUT
10026C FILE IN 80-COLUMN CARD FORMAT. THE OUTPUT
10027C UNIT SPECIFIED BY AN ASTERICK IS THE LISTING
10028C OR PRINT FILE ALLOWING 133 CHARACTERS PER LINE,
10029C INCLUDING THE CARRIAGE-CONTROL CHARACTER.
10030C
10031C
10032C INTEGER BADXFG, BPFLAG, BRHFG, DONEFG, EOFLAG, FLGX, FLGY,
10033C & BRHFG1
10034C COMMON / FLAGS / BADXFG, BPFLAG, BRHFG, DONEFG, EOFLAG,
10035C & IERRFG, LOADFG, MECHFG, M1STFG, NCONFG, FLGX, FLGY,
10036C & BRHFG1
10037C COMMON / PRINTS / LITTLN, MAXLIN, NF, NUMLIN, NUMPAG,
10038C & NWAVER, STEPCT
10039C CHARACTER FLAG*1, TIMNOW*10, TITLE*75, TODAY*10, TYPE*5
10040C COMMON / PRINTC / FLAG, TIMNOW, TITLE, TODAY, TYPE
10041C COMMON / CONC / A, ALPHA, AR, BIGD, BIGL, EX1, EX2, EY1,
10042C & EY2, EZ1, EZ2, RHOR, RHOC, SMALLM, TAU, TCR, TINC,
10043C & TMAX, TPRINT
10044C COMMON / CONSTS / ACUBE, AFOUR, ARSQ, ARSZP1, ARZSP1,
10045C & ARZF1, ARZS, ASQ, B, BIGRB, BIGMU, DELTAK, EPSLNU,
10046C & FOURTH, HALF, ONEMZ, ONEPZ, SIXTH, THETU1, THIRD,
10047C & TWELFH, W, Z, ZB, ZCUBE, ZFOUR, ZSQ
10048C CHARACTER *10 DATE, TIME
10049C

```



```

      JJJ
10050C      INITIALIZATION
10051C
10052C      GET DATE AND TIME
10053C      SET MAXIMUM NUMBER OF LINES PER PAGE
10054C      CLEAR END-OF-FILE FLAG
10055C      SET UP CONSTANTS
10056C
10057      MAXLIN = 54
10058      EOFLAG = 0
10059C
10060      HALF = 1.0 / 2.0
10061      THIRD = 1.0 / 3.0
10062      FOURTH = 1.0 / 4.0
10063      SIXTH = 1.0 / 6.0
10064      TWELFH = 1.0 / 12.0
10065      EPSLNU = 0.2
10066C
10067C      DO WHILE END-OF-FILE FLAG IS CLEAR
10068C
10069      100 IF (EOFLAG .NE. 0) GO TO 110
10070      CALL DRIVER
10071      GO TO 100
10072C
10073C      CLEAN UP LOOSE ENDS
10074C
10075      110 WRITE (*,120)
10076      STOP
10077C
10078      120 FORMAT ('1')
10079C
10080      END

```

```

JJJ
10081 SUBROUTINE DRIVER
10082C
10083C THIS SUBROUTINE DRIVES ONE CASE FROM BEGINNING
10084C (READING OF DATA) TO END (COMPLETION OF EXECUTION
10085C OR ERRONEOUS TERMINATION). IT CALLS SUBROUTINES
10086C NXTCAS, TO HANDLE THE READING OF THE DATA FOR THE
10087C NEXT CASE, AND TCNTRL, TO CONTROL THE CASE THROUGH
10088C THE TIME STEP PROCESSING, FROM INITIALIZING FOR
10089C TIME ZERO THROUGH PROCESSING EACH TIME STEP UNTIL
10090C TIME-MAX OR UNTIL NORMAL COMPLETION.
10091C
10092C IT IS CALLED BY THE MAIN PROGRAM, REICON.
10093C
10094 INTEGER BADXFG, BPFLAG, BRHFG, DONEFG, EOFLAG, FLGX, FLGY,
10095 & BRHFG1
10096 COMMON / FLAGS / BADXFG, BPFLAG, BRHFG, DONEFG, EOFLAG,
10097 & IERRFG, LOADFG, MECHFG, MISTFG, NCONFG, FLGX, FLGY,
10098 & BRHFG1
10099C
10100C
10101C CLEAR INPUT-ERROR-FLAG, READ NEXT CASE
10102C
10103 IERRFG = 0
10104 CALL NXTCAS
10105C
10106C CHECK INPUT OR END-OF-FILE ERRORS
10107C
10108C IF END OF FILE FOUND
10109C THEN TERMINATE CASE
10110C
10111 IF (EOFLAG .NE. 0) GO TO 140
10112C
10113C ELSE IF INPUT ERROR FOUND
10114C
10115 IF (IERRFG .EQ. 0) GO TO 100
10116C
10117C THEN PRINT MESSAGE, PROCEED TO TERMINATE CASE
10118 WRITE (*,150)
10119 GO TO 140
10120C
10121C ELSE CONTINUE
10122C
10123C CLEAR CASE-IS-DONE-FLAG, NUMBER-OF-TRIES-COUNT
10124C
10125 100 CALL INIT
10126 110 DONEFG = 0
10127 NTRIES = 0
10128C
10129C DO WHILE CASE-IS-DONE-FLAG IS CLEAR
10130C

```

```
      JJJ
10131 120 IF ( .NOT. (DONEFG .EQ. 0)) GO TO 130
10132C
10133      CALL TCNTRL(NTRIES)
10134      GO TO 120
10135C
10136C      END WHILE (DONEFG)
10137C
10138C      REPEAT FOR BREACH OUTPUT, IF NECESSARY
10139C
10140 130 IF (BPFLAG .EQ. 2 .AND. BRHFG .EQ. 1) GO TO 110
10141C
10142C      END IF (IERRFG)
10143C
10144C      END IF (EOFLAG)
10145C
10146 140 RETURN
10147C
10148C      FORMAT STATEMENT
10149C
10150 150 FORMAT ('OINPUT ERRORS FOUND--CASE TERMINATED')
10151C
10152      END
```

```

JJJ
10153      SUBROUTINE NXTCAS
10154C
10155C      THIS SUBROUTINE OBTAINS THE INPUT FOR THE NEXT
10156C      CASE, SETS UP THE OUTPUT HEADINGS, AND LISTS THE
10157C      INPUT.
10158C
10159C      THE BEAM-PLATE-FLAG (BPFLAG) IS SET TO SHOW
10160C      WHETHER THE CASE IS A BEAM OR A PLATE CASE. THE
10161C      END-OF-FILE FLAG (EOFLAG) IS SET IF AN END-OF-FILE
10162C      INDICATOR IS FOUND WHEN DATA IS EXPECTED.
10163C
10164C      THIS ROUTINE CALLS TWO SUBROUTINES
10165C      GETITL          TO LOOK FOR FIRST INPUT CARD FOR CASE,
10166C      A TYPE&TITLE CARD (ALPHABETIC INPUT)
10167C      RWDATA          TO READ AND PRINT OUT NUMERIC INPUT
10168C      VALUES, AS WELL AS ANY INPUT ERRORS.
10169C
10170C      THIS SUBROUTINE IS CALLED BY THE ROUTINE, DRIVER.
10171C
10172C
10173      INTEGER BADXFG, BPFLAG, BRHFG, DONEFG, EOFLAG, FLGX, FLGY,
10174      & BRHFG1
10175      COMMON / FLAGS / BADXFG, BPFLAG, BRHFG, DONEFG, EOFLAG,
10176      & IERRFG, LOADFG, MECHFG, M1STFG, NCONFG, FLGX, FLGY,
10177      & BRHFG1
10178      COMMON / PRINTS / LITTLN, MAXLIN, NF, NUMLIN, NUMPAG,
10179      & NWAVER, STEPCT
10180      CHARACTER FLAG*1, TIMNOW*10, TITLE*75, TODAY*10, TYPE*5
10181      COMMON / PRINTC / FLAG, TIMNOW, TITLE, TODAY, TYPE
10182C
10183C      CLEAR THE BEAM-OR-PLATE FLAG
10184C
10185      BRHFG = 0
10186      BPFLAG = 0
10187C
10188C      DO WHILE END-OF-FILE & BEAM-OR-PLATE FLAGS CLEAR
10189C      (I.E., UNTIL FIRST CARD OF NEW CASE IS READ)
10190C
10191      100 IF ( .NOT. (BPFLAG .EQ. 0 .AND. EOFLAG .EQ. 0)) GO TO 110
10192C
10193      CALL GETITL
10194      GO TO 100
10195C
10196C      END WHILE (BPFLAG AND EOFLAG)
10197C
10198C      IF THE END-OF-FILE HAS NOT YET BEEN REACHED
10199C
10200      110 IF (EOFLAG .NE. 0) GO TO 120
10201C
10202C      THEN READ AND PRINT DATA FOR THE NEW CASE

```

```
JJJ  
10203C  
10204      CALL RWDATA  
10205C  
10206C      ELSE CONTINUE  
10207C      END IF (NOT EOF)  
10208C  
10209 120 RETURN  
10210C  
10211      END
```

```

JJJ
10212 SUBROUTINE GETITL
10213C
10214C THIS SUBROUTINE SEARCHES THE INPUT FILE FOR THE
10215C NEXT CARD (OR RECORD) WHICH CONTAINS THE CHAR-
10216C ACTERS 'BEAM ' OR 'PLATE' IN THE FIRST FIVE
10217C POSITIONS OF THE CARD, INDICATING A TYPE & TITLE
10218C INPUT CARD, THE FIRST INPUT CARD FOR A CASE.
10219C WHEN SUCH A CARD IS FOUND, THE INPUT INFORMATION
10220C IS STORED IN THE COMMON BLOCK, PRINTS, TO BE
10221C USED LATER IN PRINTING OUTPUT HEADINGS FOR THE
10222C CASE. ANY CARDS FOUND WITHOUT 'BEAM ' OR 'PLATE'
10223C IN THE FIRST FIVE COLUMNS ARE CONSIDERED ERRONEOUS
10224C OR OUT-OF-ORDER AND ARE PRINTED OUT AS ERRORS.
10225C
10226C THE END-OF-FILE FLAG IS SET WHEN END-OF-FILE INDI-
10227C CATOR IS DETECTED. THE BEAM-OR-PLATE-FLAG IS SET
10228C ACCORDING TO THE TYPE OF TYPE&TITLE CARD FOUND.
10229C
10230C THIS SUBROUTINE IS CALLED BY THE PROCEDURE NXCAS.
10231C IT CALLS NO SUBPROCEDURES.
10232C
10233C
10234C INTEGER BADXFG, BPFLAG, BRHFG, DONEFG, EOFLAG, FLGX, FLGY,
10235C & BRHFG1
10236C COMMON / FLAGS / BADXFG, BPFLAG, BRHFG, DONEFG, EOFLAG,
10237C & IERRFG, LOADFG, MECHFG, M1STFG, NCONFG, FLGX, FLGY,
10238C & BRHFG1
10239C COMMON / PRINTS / LITTLN, MAXLIN, NF, NUMLIN, NUMPAG,
10240C & NWAUF, STEPCT
10241C CHARACTER FLAG*1, TIMNOW*10, TITLE*75, TODAY*10, TYPE*5
10242C COMMON / PRINTC / FLAG, TIMNOW, TITLE, TODAY, TYPE
10243C CHARACTER *5 BEAM, PLATE
10244C DATA BEAM/'BEAM '//, PLATE/'PLATE'//
10245C
10246C
10247C READ NEXT RECORD
10248C
10249C READ (*,130,END = 110) TYPE, TITLE
10250C
10251C CONTINUE BY CHECKING TYPE
10252C
10253C IF BEAM CASE, SET FLAG FOR BEAM (1)
10254 100 IF (TYPE .EQ. BEAM) THEN
10255 BPFLAG = 1
10256C IF PLATE CASE, SET FLAG FOR PLATE (2)
10257 ELSEIF(TYPE.EQ.PLATE)THEN
10258 BPFLAG = 2
10259 ELSE
10260C THIS IS A BAD TYPE&TITLE CARD
10261 WRITE (*,140) TYPE, TITLE

```

```
    JJJ
10262     END IF
10263     GO TO 120
10264C
10265C     END OF FILE FOUND, SET E-O-F FLAG
10266C
10267 110 EOFLAG = 1
10268C
10269C
10270 120 RETURN
10271C
10272C     FORMAT STATEMENTS
10273C
10274 130 FORMAT (A5, A75)
10275 140 FORMAT ('1' / '0' / 'ORAD TYPE & TITLE CARD FOUND' / 5X,
10276     &      A5, A75 / ' CARDS MAY BE OUT OF ORDER')
10277     END
```

JJJ
10278C
10279C
10280C
10281
10282C
10283C
10284C
10285C
10286C
10287C
10288C
10289C
10290C
10291C
10292C
10293C
10294C
10295C
10296C
10297C
10298C
10299C
10300C
10301C
10302C
10303C
10304C
10305
10306
10307
10308
10309
10310
10311
10312
10313
10314
10315
10316
10317
10318
10319
10320C
10321C
10322C
10323C
10324C
10325
10326
10327

SUBROUTINE RWDATA

THIS SUBROUTINE READS DATA CARDS # 2 THRU 6 FOR THE CURRENT CASE AND PRINTS THE INPUT DATA OUT ON THE LISTING. IF INPUT ERRORS OCCUR, THEY ARE COUNTED AND THE NUMBER OF ERRORS IS PRINTED AFTER THE LISTING OF THE INPUT VALUES. IF AN END-OF-FILE IS FOUND, AN ERROR MESSAGE IS PRINTED AND THE END-OF-FILE FLAG IS SET.

THIS ROUTINE ALSO USES THE NEWLY-READ VALUES OF F, SMALLN, AND WAVE-FUNCTION-CODE, IF THEY ARE VALID, TO SET UP SUBSCRIPTS FOR THE TYPE OF CASE DESCRIPTION TO BE INCLUDED IN THE OUTPUT PAGE HEADINGS.

ALL INPUT DATA READ IS PLACED IN THE COMMON BLOCK, INPUTS. THE PRINT HEADING SUBSCRIPTS ARE PLACED IN THE COMMON BLOCK, PRINTS.

THIS SUBROUTINE IS CALLED BY THE NXCAS PROCEDURE. IT CALLS THE SUBPROCEDURE, PAGE, TO SET UP THE HEADINGS ON A FRESH PAGE FOR THE NEW CASE.

```
INTEGER BADXFG, BPFLAG, BRHFG, DONEFG, EOFLAG, FLGX, FLGY,  
      & BRHFG1  
COMMON / FLAGS / BADXFG, BPFLAG, BRHFG, DONEFG, EOFLAG,  
      & IERRFG, LOADFG, MECHFG, M1STFG, NCONF, FLGX, FLGY,  
      & BRHFG1  
COMMON / INPUTS / BLEN, BHGT, HREF, BIGW, RATLD, Z0,  
      & TCASE, D, F, Q, Q1, COVER, TE, SIGMAC, SIGMAR, SMALLN,  
      & WAVEFN  
COMMON / CONC / A, ALPHA, AR, BIGD, BIGL, EX1, EX2, EY1,  
      & EY2, EZ1, EZ2, RHOR, RHOC, SMALLM, TAU, TCR, TINCR,  
      & TMAX, TPRINT  
COMMON / PRINTS / LITTLN, MAXLIN, NF, NUMLIN, NUMPAG,  
      & NWAVER, STEPCT  
CHARACTER FLAG*1, TIMNOW*10, TITLE*75, TODAY*10, TYPE*5  
COMMON / PRINTC / FLAG, TIMNOW, TITLE, TODAY, TYPE
```

SET UP OUTPUT HEADINGS ON A NEW PAGE AND
INITIALIZE COUNT OF INPUT ERRORS TO LAST COUNT

```
LOADFG = 0  
NUMPAG = 0  
CALL PAGE
```



```

      JJJ
10328C
10329C          READ REMAINING CARDS FOR CASE
10330C          AND PRINT OUT INPUT VALUES
10331C
10332          READ (*,170,IOSTAT=IO) BLEN, BHGT, HREF, BIGW, RATLD, Z0,
10333          & TCASE, D, F, Q, Q1, COVER, TE, SIGMAC, SIGMAR, SMALLN,
10334          & WAVEFN
10335 100 WRITE (*,180) BLEN, BHGT, HREF
10336          WRITE (*,190) BIGW, RATLD, Z0, TCASE
10337          WRITE (*,200) D, F, Q, Q1, COVER, TE
10338          WRITE (*,210) SIGMAC, SIGMAR, SMALLN, WAVEFN
10339C
10340C
10341C          IF THICKNESS OF WALL IS TOO LARGE
10342C
10343C
10344          IF ((HREF .GE. BLEN/2.) .OR. (HREF .GE. BHGT/2.)) THEN
10345          EOFLAG = 1
10346          WRITE (*,120)
10347          WRITE (*,140)
10348          GO TO 110
10349          END IF
10350C
10351C          CALCULATE CONSTANTS TO BE USED IN COMMON BLOCK 'CONC'
10352C
10353          IF ((BPFLAG .EQ. 2) .AND. (BLEN .LE. BHGT)) THEN
10354          B = BHGT / 2.
10355          A = BLEN / 2.
10356          ELSE
10357          B = BLEN / 2.
10358          A = BHGT / 2.
10359          END IF
10360          IF (BPFLAG .EQ. 1) THEN
10361          A = BLEN / 2.
10362          B = BHGT / 2.
10363          END IF
10364          AR = B / A
10365          EX1 = 0.
10366          EX2 = 0.
10367          EY1 = 0.
10368          EY2 = 0.
10369          EZ1 = Z0 * 12.
10370          EZ2 = Z0 * 12.
10371          RHOR = .7250E - 03
10372          RHOC = .2250E - 03
10373C
10374C          IF END-OF-FILE FOUND
10375C
10376          IF (IO .LT. 0) THEN
10377C

```

```

JJJ
10378C      SET END-OF-FILE FLAG & PRINT ERROR MESSAGE
10379C
10380      EOFLAG = 1
10381      WRITE (*,130)
10382      WRITE (*,150)
10383C
10384C      IF ANY INPUT ERRORS WERE FOUND
10385C
10386      ELSEIF(IO.GT.0)THEN
10387C
10388C          SET INPUT-ERROR FLAG & PRINT ERROR MESSAGE
10389C
10390      IERRFG = 1
10391      WRITE (*,140) IO
10392      WRITE (*,150)
10393C
10394      ELSE
10395C
10396C          IF SMALLN, F, OR WAVEFN ARE WITHIN RANGE
10397C
10398      IF ((SMALLN .GE. -1.0 .AND. SMALLN .LE. 1.0) .AND. (F .EQ.
10399      & 1.0 .OR. F .EQ. 2.0) .AND. (WAVEFN .EQ. 1.0 .OR.
10400      & WAVEFN .EQ. 2.0)) THEN
10401C
10402C          SET UP PRINTING SUBSCRIPTS
10403C
10404      LITTLN = SMALLN + 2.0
10405      NF = F
10406      NWAVEF = WAVEFN
10407C
10408      ELSE
10409C          SET ERROR FLAG AND PRINT ERROR MESSAGE
10410C
10411      IERRFG = 1
10412      WRITE (*,160)
10413C
10414      END IF
10415      END IF
10416C
10417      110 CONTINUE
10418      RETURN
10419C
10420C          FORMAT STATEMENTS
10421C
10422      120 FORMAT ('0' / 'OWALL THICKNESS IS TOO LARGE')
10423      130 FORMAT ('0' / 'OEND OF FILE FOUND DURING INPUT OF DATA' /
10424      & ' CASE IS TERMINATED AS NOT ALL DATA IS PRESENT')
10425      140 FORMAT ('0' / '0', I4, ' DATA ERROR(S) WERE FOUND IN INPUT'
10426      & / ' CASE IS TERMINATED AS DATA IS IN INCORRECT FORM')
10427      150 FORMAT ('OSOME OF THE VALUES LISTED ABOVE MAY ACTUALLY BE '

```

```

JJJ
10428      &      , 'FROM PREVIOUS CASE')
10429 160 FORMAT ('0' /
10430      &      'OVALUES OF SMALLN, F, OR WAVEFN ARE OUT OF RANGE' /
10431      &      'CASE IS TERMINATED')
10432 170 FORMAT (3F12.0 / , 4F12.0 / , 6F12.0 / , 4F12.0)
10433 180 FORMAT ('OPLATE LENGTH OR BEAM SPAN, IN.', T53, '(BLEN)'
10434      &      , G15.8 / 1X, 'PLATE HEIGHT OR BEAM WIDTH, IN.', T53,
10435      &      '(BHGT)', G15.8 / 1X, 'BEAM OR PLATE THICKNESS, IN.'
10436      &      , T56, '(H)', G15.8)
10437 190 FORMAT (1X, 'EXPLOSIVE WEIGHT, LBS.', T53, '(BIGW)', G15.8 /
10438      &      1X, 'LENGTH TO DIAMETER RATIO, DIMENSIONLESS', T52,
10439      &      '(RATLD)', G15.8 / 1X, 'ZO OF EXPLOSIVE, IN.', T55,
10440      &      '(ZO)', G15.8 / 1X, 'THICKNESS OF METAL CASE, IN.',
10441      &      T52, '(TCASE)', G15.8)
10442 200 FORMAT (1X, 'REINFORCING DISTANCE, IN.', T56, '(D)', G15.8 /
10443      &      1X, 'SUPPORT FACTOR      1=SIMPLY, 2=CLAMPED', T56,
10444      &      '(F)', G15.8 / 1X,
10445      &      'REINFORCEMENT RATIO IN TENSION, DIMENSIONLESS', T56,
10446      &      '(Q)', G15.8 / 1X, 'SHEAR STIRRUP REINFORMENT RATIO'
10447      &      , T55, '(Q1)', G15.8 / 1X,
10448      &      'CONCRETE COVER ON BACK FACE, IN.', T52, '(COVER)',
10449      &      G15.8 / 1X, 'TENSILE SPALLING STRENGTH, PSI.', T43,
10450      &      '(SPALL STRENGTH)', G15.8)
10451 210 FORMAT (1X, 'CONCRETE COMPRESSIVE STRENGTH, PSI.', T51,
10452      &      '(SIGMAC)', G15.8 / 1X,
10453      &      'REINFORCED STEEL YIELD STRESS, PSI.', T51, '(SIGMAR)'
10454      &      , G15.8 / 1X,
10455      &      'WEIGHT VECTOR      0=VERT, 1=EXP BLW, -1=EXP ABV',
10456      &      T51, '(SMALLN)', G15.8 / 1X,
10457      &      'WAVE FUNCTION      1=GENERAL, 2=SQUARE', T51,
10458      &      '(WAVEFN)', G15.8)
10459C
10460      END

```

```

JJJ
10461C
10462C
10463C
10464C *****
10465C *****
10466C *****
10467 SUBROUTINE INIT
10468C THIS ROUTINE TAKES INPUT FROM 'RWDATA' AND COMPUTES
10469C SPALLING, BREACHING, AND LOADING OF A CONCRETE BEAM
10470C OR PLATE DUE TO BARE OR METAL CASED CYLINDRICAL
10471C CHARGES.
10472C
10473C AN ATTENUATION MODEL IS INCLUDED TO COMPUTE THE DECAY
10474C OF THE SHOCK WAVE AS IT TRANSITS THE CONCRETE MATERIAL.
10475C
10476C THE LONGITUDINAL AXIS OF THE CYLINDRICAL CHARGE IS
10477C VERTICAL. A SURFACE BURST IS ASSUMED. RELATIVE TO
10478C THE STRUCTURAL ELEMENT, THE CHARGE IS SITUATED AT A
10479C MIDSPAN POINT IN ONE DIRECTION AND ALONG A BOARDER
10480C IN THE OTHER DIRECTION.
10481C
10482C FOR SPALLING AND BREACHING, THE LOADING FROM A
10483C LOCALIZED DETONATION IS USED. FOR SUBSEQUENT FLEXURAL
10484C CALCULATIONS, THE ROUTINE COMPUTES AN EFFECTIVE BEAM
10485C OR PLATE THICKNESS AND AN EFFECTIVE UNIFORM LOAD.
10486C THESE EFFECTIVE PARAMETERS ARE PROVIDED TO THE EXISTING
10487C ROUTINES OF 'REICON' FOR A FLEXURAL ANALYSIS.
10488C INTEGER BADXFG, BPFLAG, BRHFG, DONEFG, EOFLAG, FLGX, FLGY,
10489C & BRHFG1
10490C COMMON / FLAGS / BADXFG, BPFLAG, BRHFG, DONEFG, EOFLAG,
10491C & IERRFG, LOADFG, MECHFG, MISTFG, NCONFG, FLGX, FLGY,
10492C & BRHFG1
10493C COMMON / INPUTS / BLEN, BHGT, HREF, BIGW, RATLD, ZO,
10494C & TCASE, D, F, Q, Q1, COVER, TE, SIGMAC, SIGMAR, SMALLN,
10495C & WAVEFN
10496C COMMON / CONC / A, ALPHA, AR, BIGD, BIGL, EX1, EX2, EY1,
10497C & EY2, EZ1, EZ2, RHOR, RHOC, SMALLM, TAU, TCR, TINCR,
10498C & THAX, TPRINT
10499C COMMON / PRINTS / LITTLN, MAXLIN, NF, NUMLIN, NUMPAG,
10500C & NWAVEF, STEPCT
10501C CHARACTER FLAG*1, TIMNOW*10, TITLE*75, TODAY*10, TYPE*5
10502C COMMON / PRINTC / FLAG, TIMNOW, TITLE, TODAY, TYPE
10503C COMMON / CONSTS / ACUBE, AFOUR, ARSQ, ARSZP1, ARZSP1,
10504C & ARZP1, ARZS, ASQ, B, BIGRB, BIGMU, DELTAK, EPSLNU,
10505C & FOURTH, HALF, ONEMZ, ONEPZ, SIXTH, THETU1, THIRD,
10506C & TWELFH, W, Z, ZB, ZCUBE, ZFOUR, ZSQ
10507C COMMON / RES1 / WC, VI, FPAR, WFRG, FRGT
10508C COMMON / RES2 / VR, FRGN, FRGM, VN, ZF1
10509C COMMON / RES3 / AE, VO, VE, UE, TSPL
10510C COMMON / RES4 / PU, H

```

```

      JJJ
10511      DATA PI/3.14159/, ERR/1E-4/
10512      DATA RHOHE/0.0574/, PE/14700./
10513C     COMPUTE CHARGE DIAMETER
10514      100 H = HREF
10515      THOM = 0.
10516      ZZ = 0.
10517      XB = 0.
10518      YB = 0.
10519      FLGX = 0
10520      FLGY = 0
10521      BRHFG1 = 0
10522      BIGD = ((4./(PI*RATLD)) * (BIGW / RHOHE)) ** THIRD
10523      BIGL = RATLD * BIGD
10524C
10525C
10526C     COMPUTE COORDINATES OF WALL WITH CHARGE AT (0,0,Z0)
10527C
10528C
10529C     DIMENSIONS OF LENGTH ARE 'INCHES'
10530C
10531C
10532      XP = BLEN / 2.
10533      YP = BHGT - BIGL / 2.
10534      YM = - BIGL / 2.
10535C
10536C
10537C     COMPUTE THE COORDINATES OF SPALL AND FRAGMENTS
10538C
10539C
10540      IF ((XP/12.) .GT. Z0) THEN
10541      X SPL = Z0 * 12.
10542      ELSE
10543      X SPL = XP
10544      END IF
10545      IF ((YP/12.) .GT. Z0) THEN
10546      Y SPL = Z0 * 12.
10547      ELSE
10548      Y SPL = YP
10549      END IF
10550      IF (TCASE .EQ. 0.) THEN
10551      XF = 0.
10552      YF = 0.
10553      ELSE
10554      XF = XP
10555      YF = BIGL / 2.
10556      END IF
10557C
10558C
10559C     SELECTING THE STARTING AREA
10560C

```

```

JJJ
10561C
10562      XE = SQRT(PI/4.) * HREF
10563      YE = SQRT(PI/4.) * HREF
10564      YI = - YE
10565      IF (BIGL / 2. .LT. HREF) YI = YM
10566C
10567C
10568C      DIVIDE THE SURFACE BY SELECTING THE SMALLER OF TWO INCREMENTS
10569C
10570C
10571      IF (XE .LT. (XP-XE)) THEN
10572      DX = (XE / 10.)
10573      ELSE
10574      DX = (XP - XE) / 10.
10575      END IF
10576      IF (YE .LT. (YP-YE)) THEN
10577      DY = (YE / 10.)
10578      ELSE
10579      DY = (YP - YE) / 10.
10580      END IF
10581C
10582C
10583C      THE VALUE OF XSPL MUST BE GREATER THAN XE OR
10584C
10585C
10586      IF (XSPL .LT. XE) THEN
10587      XS = 0.
10588      YS = 0.
10589      FLGX = 1
10590      FLGY = 1
10591      SS = 0.
10592      WRITE (*,250)
10593      END IF
10594C
10595C
10596C      COMPUTE PARAMETERS AT THE HUGONIOT LIMIT
10597C
10598C
10599      CALL HUGPAR
10600C
10601C
10602C      COMPUTE THE CONSTANTS OF FRAGMENTATION
10603C
10604C
10605      CALL FRGCON
10606C
10607C
10608C      COMPUTE AVERAGE LOADING ON A REFERENCE AREA
10609      110 DP = XE / 2.
10610      BQ = (YE - YI) / 2.

```

```

      JJJ
10611      CALL AVGLD(DP, DQ, PB, APPIMP, YI)
10612      IF ((TCASE .EQ. 0.)) GO TO 120
10613      R = SQRT(ZO**2+(XE/24.）**2)
10614      DT = ATAN(XE/(12.*ZO))
10615      CALL FRGLD(R, DT)
10616      AJ = BIGL * XE
10617      IF (BIGL / 2. .GE. YE) THEN
10618      FRGIMP = FRGM * VN / AJ
10619      ELSE
10620      FRGIMP = (FRGM * VN / AJ) * (BIGL / 2. - YI) / (YE - YI)
10621      END IF
10622      APPIMP = APPIMP + FRGIMP
10623      120 CALL TLD1(XE, YE, TF, TB)
10624      PB = 2. * APPIMP / TB
10625C
10626C
10627C DETERMINE IF SPALL OCCURS:-FIRST IN THE X-, THEN IN THE Y-DIR
10628C
10629C
10630      IF ((FLGX .EQ. 1) .AND. (FLGY .EQ. 1)) GO TO 180
10631      IF (FLGX .EQ. 1) GO TO 160
10632      R = SQRT(ZO**2+(XE/12.）**2)
10633      ZDIS = R / (BIGW ** (THIRD))
10634      CALL LDFAR(ZDIS, R, REFIMP, PO, CRA)
10635      REFIMP = REFIMP * (BIGW ** (THIRD))
10636      CALL TLD2(ZDIS, TA, TO)
10637      TR = TO * (BIGW ** (THIRD)) / 1000.
10638C
10639C
10640C COMPUTE FRAGMENT IMPULSE AT A POINT
10641C
10642C
10643      IF ((TCASE .EQ. 0.)) THEN
10644      FRGIMP = 0.
10645      GO TO 130
10646      END IF
10647      R = SQRT(ZO**2+(((2*XE-DX)/24.）**2))
10648      DT = ATAN(XE/(12.*ZO)) - ATAN((XE-DX)/(12.*ZO))
10649      CALL FRGLD(R, DT)
10650C
10651C
10652C SYMMETRY ASSUMED IN X-DIRECTION
10653C
10654C
10655      DA = DX * BIGL
10656      FRGIMP = FRGM * VN / DA
10657      130 PR = 2. * (REFIMP + FRGIMP) / TR
10658C
10659C
10660C      IF PR < PE THEN NO ATTENUATION OCCURS

```

```

      JJJ
10661C
10662C
10663      IF (PR .LE. PE) THEN
10664      P = PR
10665      GO TO 140
10666      END IF
10667C
10668C
10669C COMPUTE ATTENUATION THROUGH WALL
10670C
10671C
10672      CALL ATTEN(PR, TR, P)
10673C
10674C
10675C      SS IS THE TENSILE STRESS AT THE SPALL PLANE
10676C
10677C
10678      140 SS = P * (TSPL / TR) * P / PR
10679      IF ((SS .LT. TE) .AND. (ZZ .EQ. 0.)) THEN
10680      XS = 0.
10681      YS = 0.
10682      FLGX = 1
10683      FLGY = 1
10684      GO TO 180
10685      END IF
10686      IF (SS .LT. TE) THEN
10687      XS = XE - DX
10688      FLGX = 1
10689      GO TO 160
10690      END IF
10691      XS = XE
10692      TIMP = P * TSPL * (1 - (TSPL / 2.) / TR)
10693      IF (ZZ .EQ. 0.) THEN
10694      DA = (XE * YE * 2.)
10695      GO TO 150
10696      END IF
10697      IF (YE .LT. ABS(YM)) THEN
10698      DA = DX * (YE - DY) * 2.
10699      ELSE
10700      DA = DX * ((YE-DY) + BIGL / 2.)
10701      END IF
10702      150 TMOM = TMOM + TIMP * DA
10703C
10704C
10705C CHECK SPALL IN Y-DIR.
10706C
10707C
10708      160 IF ((FLGY .EQ. 1)) GO TO 180
10709      R = SQRT(ZO**2+(YE/12.）**2)
10710      ZDIS = R / (BIGW ** THIRD)

```



```

      JJJ
10711      CALL LDPAR(ZDIS, R, REFIMP, PO, CRA)
10712      REFIMP = REFIMP * BIGW ** THIRD
10713C
10714C
10715C FIND DURATION AT A POINT
10716C
10717C
10718      CALL TLD2(ZDIS, TA, TO)
10719      TR = TO * (BIGW ** THIRD) / 1000.
10720C
10721C
10722C COMPUTE FRAGMENT IMPULSE AT A POINT
10723C IF YE < BIGL/2 THEN THE IMPULSE DUE TO FRAGMENTS IN
10724C THE Y-DIR IS THE SAME AS IN THE X-DIR, ELSE FRGIMP = 0
10725C
10726C
10727      IF ((TCASE .EQ. 0.) .OR. (BIGL/2. .LT. YE)) THEN
10728      FRGIMP = 0.
10729      END IF
10730      PR = 2. * (REFIMP + FRGIMP) / TR
10731      IF (PR .LE. PE) THEN
10732      P = PR
10733      GO TO 170
10734      END IF
10735      CALL ATTEN(PR, TR, P)
10736C SPALL IN Y-DIR.
10737      170 SS = (P * TSPL / TR) * P / PR
10738      IF (SS .LT. TE) THEN
10739      FLGY = 1
10740      YS = YE - DY
10741      GO TO 180
10742      END IF
10743      YS = YE
10744      TIMP = P * TSPL * (1. - (TSPL / 2.)) / TR)
10745      IF (ZZ .EQ. 0.) GO TO 180
10746      IF (YE .LT. ABS(YM)) THEN
10747      DA = (DY * XE) * 2.
10748      ELSE
10749      DA = (DY * XE)
10750      END IF
10751      TMOM = TMOM + TIMP * DA
10752C
10753C
10754C CHECK BREACH AND EFFECTIVE WALL THICKNESS
10755C IF FLGX, FLGY, AND BRHFG1 ARE ONE
10756C THEN PROCEED TO FLEXURE CALCULATION
10757C
10758C
10759      180 IF ((FLGX .EQ. 1) .AND. (FLGY .EQ. 1) .AND. (BRHFG1 .EQ.
10760      &      1)) GO TO 210

```

```

      JJJ
10761 IF (YE .LT. ABS(YM)) GO TO 190
10762 IF ((FLGX .EQ. 0) .AND. (FLGY .EQ. 0)) THEN
10763 H = HREF - COVER
10764 GO TO 200
10765 END IF
10766 IF ((FLGX .EQ. 0) .AND. (FLGY .EQ. 1)) THEN
10767 H = HREF - ((YS+BIGL/2.) / (YE + BIGL / 2.)) * COVER
10768 GO TO 200
10769 END IF
10770 IF ((FLGX .EQ. 1) .AND. (FLGY .EQ. 0)) THEN
10771 H = HREF - (XS / XE) * COVER
10772 GO TO 200
10773 END IF
10774 IF ((FLGX .EQ. 1) .AND. (FLGY .EQ. 1)) THEN
10775 H = HREF - (XS * (YS + BIGL / 2.)) / (XE * (YE + BIGL /
10776 & 2.)) * COVER
10777 GO TO 200
10778 END IF
10779 190 IF ((FLGX .EQ. 0) .AND. (FLGY .EQ. 0)) THEN
10780 H = HREF - COVER
10781 GO TO 200
10782 END IF
10783 IF ((FLGX .EQ. 0) .AND. (FLGY .EQ. 1)) THEN
10784 H = HREF - (YS / YE) * COVER
10785 GO TO 200
10786 END IF
10787 IF ((FLGX .EQ. 1) .AND. (FLGY .EQ. 0)) THEN
10788 H = HREF - (XS / XE) * COVER
10789 GO TO 200
10790 END IF
10791 IF ((FLGX .EQ. 1) .AND. (FLGY .EQ. 1)) THEN
10792 H = HREF - (YS / YE) * (XS / XE) * COVER
10793 GO TO 200
10794 END IF
10795 200 IF (YE .GT. ABS(YM)) THEN
10796 AREA = (XE * YE + XE * BIGL / 2.)
10797 ELSE
10798 AREA = XE * YE * 2.
10799 END IF
10800C
10801C
10802C COMPUTE CRITICAL IMPULSE
10803C
10804C
10805 BIGICR = (2.0 ** 1.5) * THIRD * H *
10806 & SQRT(((1.0-Q)*RHOC+Q*RHOR)*((1.0-Q)*1.9*SIGMAC**HALF+(
10807 & Q+Q1)*D*SIGMAR*1.5/H))
10808 TIMP = (TMOM / AREA)
10809 BIGIBR = APPIMP - TIMP
10810C

```

```

      JJJ
10811C
10812C DETERMINE IF BREACH OCCURS
10813C
10814C
10815      IF (BIGIBR .GE. BIGICR) THEN
10816      XB = XE
10817      YB = YE
10818      RY = YE - YI
10819      ELSE
10820      BRHFG1 = 1
10821      END IF
10822      XE = XE + DX
10823      YE = YE + DY
10824      YI = - YE
10825      IF (ABS(YM) .LT. YE) YI = YM
10826      IF (((XE .GT. XSPL-ERR) .OR. (YE .GT. YSPL-ERR)) .AND.
10827      &      ((FLGY .EQ. 0) .OR. (FLGX .EQ. 0))) THEN
10828      FLGX = 1
10829      FLGY = 1
10830      XS = XSPL
10831      YS = YSPL
10832      END IF
10833      IF ((XE .GE. XP) .OR. (YE .GE. YP) .AND. (BRHFG1 .EQ. 0))
10834      &      THEN
10835      IF (XP .GT. YP) THEN
10836      BRHFG1 = 1
10837      XB = XP
10838      YB = YP
10839      ELSE
10840      BRHFG1 = 1
10841      XB = YP
10842      YB = YP
10843      END IF
10844      END IF
10845      ZZ = 1.
10846      GO TO 110
10847C
10848C
10849C COMPUTE AVERAGE DEPTH OF PENERATION AND IMPULSE
10850C ON THE FRONT FACE
10851C
10852C
10853      210 DX = XP / 10.
10854      ZF = 0.
10855      FRGMOM = 0.
10856      IF (TCASE .EQ. 0.) GO TO 230
10857      XX = - DX / 2.
10858      II = 0
10859      DO 220 I = 1, 10
10860      II = II + 1

```

```

      JJJ
10861      XX = XX + DX
10862      R = SQRT(ZO**2+(XX/12.)**2)
10863      DT = ATAN((XX+DX/2.)/(12.*ZO)) -
10864      &      ATAN((XX-DX/2.)/(12.*ZO))
10865      CALL FRGLD(R, DT)
10866      ZF = ZF + ZF1
10867      FRGMOM = FRGMOM + FRGM * VN
10868 220 CONTINUE
10869      ZF = ZF / FLOAT(II)
10870C
10871C
10872C FRGMOM IS MOMENTUM DUE TO FRAGMENTS
10873C COMPUTE AVERAGE IMPULSE AND DURATION OF
10874C BLAST LOAD FOR THE ENTIRE WALL
10875C
10876C
10877 230 DP = XP / 2.
10878      DQ = (YP - YM) / 2.
10879      XE = XP
10880      YI = YM
10881      YE = YP
10882      CALL AVGLD(DP, DQ, FB, APPIMP, YI)
10883      APPIMP = APPIMP + (FRGMOM - TMOM) / (XP * (YP - YI))
10884      CALL TLD1(XE, YE, TF, TB)
10885C
10886C
10887C TB IS DURATION OF LOAD ON ENTIRE WALL
10888C COMPUTE EFFECTIVE WALL THICKNESS OF WALL
10889C FOR FLEXURAL RESPONSE
10890C
10891C
10892 240 IF (TCASE .EQ. 0.) THEN
10893      ZF = 0.
10894      END IF
10895      IF (YS .LE. BIGL / 2.) THEN
10896      H = HREF - (ZF * XF * (YF + BIGL / 2.) + (COVER * XS * 2. *
10897      &      YS)) / (XP * (YP - YM))
10898      ELSE
10899      H = HREF - (ZF * XF * (YF + BIGL / 2.) + COVER * XS * (YS +
10900      &      BIGL / 2.)) / (XP * (YP - YM))
10901      END IF
10902      PU = FB
10903      BIGRB = SQRT(2.*XB*RY/PI)
10904C
10905C
10906C      RESET BRHFG1 FLAG
10907C
10908C
10909      IF (XB .EQ. 0.0) BRHFG1 = 0
10910      ALPHA = 0.

```

```

      JJJ
10911      SMALLM = RHOC * H
10912C
10913C
10914C      COMPUTE TIMES FOR TZERO
10915C
10916C
10917      TAU = TB
10918      TCR = TAU
10919      CALL TSCALE
10920C
10921C
10922 250 FORMAT ('0', / , 'THE VALUE OF XSPL IS LESS THAN XE', / )
10923      WRITE (*,260)
10924 260 FORMAT ('0', 10X, 'COMPUTED VALUES OF MATERIAL RESPONSE',
10925      & / )
10926      WRITE (*,270) XS
10927 270 FORMAT ('0LIMIT OF SPALL IN X-DIR, IN', T59, G15.8)
10928      WRITE (*,280) YS
10929 280 FORMAT (1X, 'LIMIT OF SPALL IN Y-DIR, IN', T59, G15.8)
10930      WRITE (*,290) XB
10931 290 FORMAT (1X, 'LIMIT OF BREACH IN X-DIR, IN', T59, G15.8)
10932      WRITE (*,300) YB
10933 300 FORMAT (1X, 'LIMIT OF BREACH IN Y-DIR, IN', T59, G15.8)
10934      WRITE (*,310) THOM
10935 310 FORMAT (1X, 'TOTAL TRAPPED MOMENTUM, LB-S', T59, G15.8)
10936      WRITE (*,320) APPIMP
10937 320 FORMAT (1X, 'IMPULSE FOR FLEXURE, PSI-MS', T59, G15.8)
10938      WRITE (*,330) TB
10939 330 FORMAT (1X, 'DURATION OF LOAD ON WALL, S', T59, G15.8)
10940      PB = 2. * APPIMP / TB
10941      WRITE (*,340) PB
10942 340 FORMAT (1X, 'AVERAGE PRESSURE ON WALL, PSI', T59, G15.8)
10943      WRITE (*,350) H
10944 350 FORMAT (1X, 'EFFECTIVE WALL THICKNESS, IN', T59, G15.8)
10945      WRITE (*,360) BIGRB
10946 360 FORMAT (1X, 'EFFECTIVE BREACH RADIUS, IN', T59, G15.8)
10947      RETURN
10948      END

```

JJJ
10949C
10950C
10951C
10952
10953C
10954C
10955C
10956C
10957C
10958
10959
10960
10961
10962
10963
10964
10965
10966
10967
10968
10969
10970
10971
10972
10973
10974
10975
10976
10977
10978
10979
10980
10981
10982
10983
10984
10985
10986
10987
10988
10989
10990
10991
10992
10993
10994
10995
10996
10997
10998

SUBROUTINE HUGPAR

COMPUTE PARAMETERS FROM THE HUGONIOT EQUATION OF STATE

```
COMMON / CONSTS / ACUBE, AFOUR, ARSQ, ARSZP1, ARZSP1,  
  & ARZP1, ARZS, ASQ, B, BIGRB, BIGMU, DELTAK, EPSLNU,  
  & FOURTH, HALF, ONEMZ, ONEPZ, SIXTH, THETU1, THIRD,  
  & TWELFH, W, Z, ZB, ZCUBE, ZFOUR, ZSQ  
COMMON / INPUTS / BLEN, BHGT, HREF, BIGW, RATLD, ZO,  
  & TCASE, D, F, Q, Q1, COVER, TE, SIGMAC, SIGMAR, SMALLN,  
  & WAVEFN  
COMMON / CONC / A, ALPHA, AR, BIGD, BIGL, EX1, EX2, EY1,  
  & EY2, EZ1, EZ2, RHOR, RHOC, SMALLM, TAU, TCR, TINC, R,  
  & TMAX, TPRINT  
COMMON / RES3 / AE, VO, VE, UE, TSPL  
DATA A0/1.222000/, VS/3998.0000/, CO/1.673E5/  
DATA A1/1.6670E7/, A2/-4.2307E7/, A3/5.7462E7/  
DATA PM/1.7640E6/, PE/14.700E3/, B0/-4.145270/, B1/1.19068/  
DATA B2/-0.10530/, B3/2.959E-3/, N/100/  
X8 = 0.  
T1 = 0.  
X1 = A2 / A3  
X2 = A1 / A3  
X3 = - PE / A3  
X4 = X2 - (X1 ** 2) / 3.  
X5 = X3 - X2 * X1 / 3. + 2. * ( - ( - X1 / 3.) ** 3)  
X6 = - X5 / 2. + SQRT((X5/2.)**2+(X4/3.)**3)  
IF (X6 .GE. 0.) THEN  
  X6 = X6 ** (THIRD)  
ELSE  
  X6 = - ( - X6) ** (THIRD)  
END IF  
X7 = - X5 / 2. - SQRT((X5/2.)**2+(X4/3.)**3)  
IF (X7 .GE. 0.) THEN  
  X7 = X7 ** THIRD  
ELSE  
  X7 = - ( - X7) ** THIRD  
END IF  
X3 = X6 + X7 - X1 / 3.  
AE = A0 - 1.3605E - 7 * PE  
VO = A0 * VS  
VE = AE * VS / (1. + X3)  
UE = SQRT(PE*(VO-VE))  
TSPL = 2. * COVER / CO  
RETURN
```

```

JJJ
10999      END
11000C
11001C
11002C
11003C
11004      SUBROUTINE FRGCON
11005C
11006C
11007C COMPUTE CONSTANT PARAMETERS OF FRAGMENTATION
11008C
11009C
11010      COMMON / INPUTS / BLEN, BHGT, HREF, BIGW, RATLD, ZO,
11011      & TCASE, D, F, Q, Q1, COVER, TE, SIGMAC, SIGMAR, SMALLN,
11012      & WAVEFN
11013      COMMON / CONC / A, ALPHA, AR, BIGD, BIGL, EX1, EX2, EY1,
11014      & EY2, EZ1, EZ2, RHOR, RHOC, SMALLM, TAU, TCR, TINC,
11015      & TMAX, TPRINT
11016      COMMON / CONSTS / ACUBE, AFOUR, ARSQ, ARSZP1, ARZSP1,
11017      & ARZP1, ARZS, ASQ, B, BIGRB, BIGMU, DELTAK, EPSLNU,
11018      & FOURTH, HALF, ONEMZ, ONEPZ, SIXTH, THETU1, THIRD,
11019      & TWELFH, W, Z, ZB, ZCUBE, ZFOUR, ZSQ
11020      COMMON / RES1 / WC, VI, FPAR, WFRG, FRGT
11021      DATA GC/1.1520E+5/, FP/0.0531/, G/386.4/, PI/3.14159/
11022      IF (TCASE .EQ. 0.) GO TO 100
11023      WC = ((PI/4*G) * ((BIGD+2.*TCASE) ** 2 - BIGD ** 2) *
11024      & BIGL) * RHOR
11025      VI = GC * (2. * BIGW / (2. * WC + BIGW)) ** (HALF)
11026      FPAR = (FP * TCASE ** (5. / 6.) * BIGD ** (THIRD) * (1. +
11027      & TCASE / BIGD))
11028      WFRG = (FPAR * ALOG(.5)) ** 2
11029      FRGT = (ALOG(.5)) ** 2 * (WC / WFRG) / 2.
11030      100 RETURN
11031      END

```

```

JJJ
11032C
11033C
11034C
11035C
11036C
11037      SUBROUTINE AVGLD(DP, DQ, PB, APPIMP, YI)
11038C
11039C
11040C SUBROUTINE TO CALCULATE AVERAGE IMPULSE ON AN AREA
11041C
11042C
11043      COMMON / INPUTS / BLEN, BHGT, HREF, BIGW, RATLD, Z0,
11044      & TCASE, D, F, Q, Q1, COVER, TE, SIGNAC, SIGMAR, SMALLN,
11045      & WAVEFN
11046      COMMON / CONC / A, ALPHA, AR, BIGD, BIGL, EX1, EX2, EY1,
11047      & EY2, EZ1, EZ2, RHOR, RHOC, SMALLM, TAU, TCR, TINC,
11048      & THAX, TPRINT
11049      COMMON / CONSTS / ACUBE, AFOUR, ARSQ, ARSZP1, ARZSP1,
11050      & ARZP1, ARZS, ASQ, B, BIGRB, BIGMU, DELTAK, EPSLNU,
11051      & FOURTH, HALF, ONEMZ, ONEPZ, SIXTH, THETU1, THIRD,
11052      & TWELFH, W, Z, ZB, ZCUBE, ZFOUR, ZSQ
11053      N = 2
11054      T4 = 0.
11055      T5 = 0.
11056      T6 = 0.
11057 100 T1 = 0.
11058      T2 = 0.
11059      T3 = 0.
11060      XX = - DP / 2.
11061      DO 120 I = 1, N
11062          YY = YI - DQ / 2.
11063          XX = XX + DP
11064          DO 110 J = 1, N
11065              YY = YY + DQ
11066              R = SQRT((XX/12.)**2+(YY/12.)**2+Z0**2)
11067              ZDIS = R / BIGW ** THIRD
11068              CALL LDPAR(ZDIS, R, REFIMP, P0, CRA)
11069              T1 = T1 + P0
11070              T2 = T2 + P0 * CRA
11071              T3 = T3 + REFIMP
11072 110 CONTINUE
11073 120 CONTINUE
11074      P0 = T1 / FLOAT(N**2)
11075      PR = T2 / FLOAT(N**2)
11076      REFIMP = T3 / FLOAT(N**2)
11077      IF (ABS(P0-T4) / P0 .LT. .02) GO TO 140
11078      T4 = P0
11079      T5 = PR
11080      T6 = REFIMP
11081      N = N + 1

```



```
JJJ
11082C ESTABLISH A LIMIT FOR A NUMBER OF ITERATIONS
11083     IF (N .GT. 5) THEN
11084     WRITE (*,130)
11085 130 FORMAT (1X, 'CAUTION FOR THE VALUE OF THE REFLECT IMPULSE')
11086     GO TO 140
11087     END IF
11088     DP = DP * FLOAT(N-1) / FLOAT(N)
11089     DQ = DQ * FLOAT(N-1) / FLOAT(N)
11090     GO TO 100
11091 140 PB = PR
11092     APPIMP = REFIMP * BIGW ** THIRD
11093     RETURN
11094     END
```

```

JJJ
11095C
11096C
11097C
11098      SUBROUTINE FRGLD(R, DT)
11099C
11100C
11101C      COMPUTE FRAGMENT LOADING OF AN AREA
11102C
11103C
11104      COMMON / INPUTS / BLEN, BHGT, HREF, BIGW, RATLD, ZO,
11105      &      TCASE, D, F, Q, Q1, COVER, TE, SIGMAC, SIGMAR, SMALLN,
11106      &      WAVEFN
11107      COMMON / CONC / A, ALPHA, AR, BIGD, BIGL, EX1, EX2, EY1,
11108      &      EY2, EZ1, EZ2, RHOR, RHOC, SMALLN, TAU, TCR, TINC,
11109      &      TMAX, TPRINT
11110      COMMON / CONSTS / ACUBE, AFOUR, ARSQ, ARSZP1, ARZSP1,
11111      &      ARZP1, ARZS, ASQ, B, BIGRB, BIGMU, DELTAK, EPSLNU,
11112      &      FOURTH, HALF, ONEMZ, ONEPZ, SIXTH, THETU1, THIRD,
11113      &      TWELFH, W, Z, ZB, ZCUBE, ZFOUR, ZSQ
11114      COMMON / RES1 / WC, VI, FPAR, WFRG, FRGT
11115      COMMON / RES2 / VR, FRGN, FRGM, VN, ZF1
11116      DATA PI/3.14159/, G/386.4/, CP/.7/
11117      IF (TCASE .EQ. 0.) GO TO 100
11118      VR = VI * EXP(-1.59E-3*R/(WFRG**THIRD))
11119      FRGN = (FRGT / (2. * PI)) * DT
11120      FRGM = (WC / G) * (DT / (2 * PI))
11121      VN = VR * ZO / R
11122      ZF1 = (CP * 5.61E - 8) * SQRT(5000./SIGMAC) * (WFRG **
11123      &      .4) * (VN ** 1.8)
11124      100 RETURN
11125      END

```

```

JJJ
11126C
11127C
11128C
11129      SUBROUTINE TLD1(XE, YE, TF, TB)
11130C
11131C      COMPUTE THE EFFECTIVE LOADING DURATION ON AN AREA
11132C
11133C
11134C
11135      COMMON / INPUTS / BLEN, BHGT, HREF, BIGW, RATLD, ZO,
11136      & TCASE, D, F, Q, Q1, COVER, TE, SIGMAC, SIGMAR, SMALLN,
11137      & WAVEFN
11138      COMMON / CONC / A, ALPHA, AR, BIGD, BIGL, EX1, EX2, EY1,
11139      & EY2, EZ1, EZ2, RHOR, RHOC, SMALLM, TAU, TCR, TINC,
11140      & TMAX, TPRINT
11141      COMMON / CONSTS / ACUBE, AFOUR, ARSQ, ARSZP1, ARZSP1,
11142      & ARZP1, ARZS, ASQ, B, BIGRB, BIGMU, DELTAK, EPSLNU,
11143      & FOURTH, HALF, ONEMZ, ONEPZ, SIXTH, THETU1, THIRD,
11144      & TWELFH, W, Z, ZB, ZCUBE, ZFOUR, ZSQ
11145      ZDIS = ZO / (BIGW ** THIRD)
11146      CALL TLD2(ZDIS, TA, TO)
11147      TN = TA * (BIGW ** THIRD) / 1000.
11148      ZDIS = SQRT(ZO**2+(XE/12.)**2+(YE/12.)**2) / (BIGW **
11149      & THIRD)
11150      CALL TLD2(ZDIS, TA, TO)
11151      TF = TA * (BIGW ** THIRD) / 1000.
11152      TO = TO * (BIGW ** THIRD) / 1000.
11153      TB = TF - TN + TO
11154      RETURN
11155      END

```

```

JJJ
11156C
11157C
11158C
11159C
11160C
11161C
11162      SUBROUTINE LDPAR(ZDIS, R, REFIMP, PO, CRA)
11163C
11164C
11165C      COMPUTE THE OVERPRESSURE, REFLECTION COEFFICIENT,
11166C      AND REFLECTED IMPULSE AT A POINT.
11167C
11168C
11169      COMMON / INPUTS / BLEN, BHGT, HREF, BIGW, RATLD, ZO,
11170      & TCASE, D, F, Q, Q1, COVER, TE, SIGMAC, SIGMAR, SMALLN,
11171      & WAVEFN
11172      COMMON / CONC / A, ALPHA, AR, BIGD, BIGL, EX1, EX2, EY1,
11173      & EY2, EZ1, EZ2, RHOR, RHOC, SMALLM, TAU, TCR, TINCR,
11174      & TMAX, TPRINT
11175C
11176C
11177      DIMENSION X(20), P(20), PR(20), RI(20), PA(10), AL(12),
11178      & C(10,12)
11179C
11180C
11181      DATA X/.3000, .4000, .5000, .6000, .7000, .8000, .9000,
11182      & 1.000, 1.100, 1.200, 1.300, 1.500, 1.600, 1.800,
11183      & 2.000, 2.500, 3.000, 3.500, 4.000, 5.000/
11184      DATA P/4.600, 3.400, 2.620, 2.080, 1.700, 1.400, 1.200,
11185      & 1.020, .9000, .7800, .6900, .5450, .4900, .3950,
11186      & .3300, .2100, .1400, .1100, .0700, .0410/
11187      DATA PR/55.00, 38.00, 27.00, 20.60, 16.20, 13.00, 10.40,
11188      & 8.600, 7.400, 6.300, 5.400, 4.100, 3.600, 2.800,
11189      & 2.200, 1.240, .7500, .4500, .3100, .1550/
11190      DATA RI/3.500, 2.500, 1.900, 1.450, 1.160, .9600, .8000,
11191      & .6700, .5500, .4800, .4200, .3400, .3100, .2600,
11192      & .2200, .1600, .1250, .1000, .0840, .0600/
11193      DATA PA/7.00, 3.00, 1.00, .500, .200, .050, .030, .010,
11194      & .005, .001/
11195      DATA AL/0.00, 10.0, 20.0, 30.0, 35.0, 40.0, 45.0, 50.0,
11196      & 60.0, 70.0, 80.0, 90.0/
11197      DATA C/12.7, 11.0, 8.50, 7.30, 6.00, 4.20, 3.50, 2.50,
11198      & 2*2., 12.2, 10.6, 8.30, 7.20, 5.90, 4.10, 3.50, 2.50,
11199      & 2*2., 11.3, 9.80, 7.90, 6.80, 5.60, 4.00, 3.40, 2.40,
11200      & 2*2., 10.0, 8.80, 7.30, 6.10, 5.10, 3.60, 3.30, 2.40,
11201      & 2*2., 9.40, 8.20, 6.90, 5.80, 4.90, 3.60, 3.30, 2.40,
11202      & 2*2., 8.50, 7.50, 6.20, 5.70, 5.10, 4.10, 3.50, 2.50,
11203      & 2*2., 8.50, 7.80, 6.40, 5.80, 4.90, 3.70, 3.30, 2.60,
11204      & 2*2., 8.80, 7.30, 5.80, 5.00, 4.00, 2.90, 2.50, 2.20,
11205      & 2*1.9, 5.00, 4.30, 3.60, 3.00, 2.50, 2*2.1, 3*1.8,

```

```

      JJJ
11206      3.00, 2.70, 2.30, 2.10, 3*1.8, 3*1.7, 2.00, 1.90,
11207      3*1.8, 2*1.7, 3*1.6, 10*1.5/
11208      DATA PI/3.14159/
11209      DO 100 I = 1, 20
11210          IF (X(I) .GT. ZDIS) THEN
11211              N1 = I
11212              N2 = I - 1
11213              GO TO 110
11214          END IF
11215      100 CONTINUE
11216          WRITE (*,180)
11217      110 SLOPE = ALOG(P(N1)/P(N2)) / ALOG(X(N1)/X(N2))
11218          P0 = P(N2) * (ZDIS / X(N2)) ** SLOPE
11219          ANGLE = Z0 / R
11220          IF ((1.-ANGLE) .LT. 1.E - 4) THEN
11221              ANGLE = 0.
11222          ELSE
11223              ANGLE = ATAN(SQRT((R/Z0)**2-1.)) * 360. / (2. * PI)
11224          END IF
11225          DO 120 I = 1, 10
11226              IF (PA(I) .LT. P0) THEN
11227                  N1 = I
11228                  N2 = I - 1
11229                  GO TO 130
11230              END IF
11231      120 CONTINUE
11232          WRITE (*,190)
11233      130 DO 140 I = 1, 12
11234          IF (AL(I) .GT. ANGLE) THEN
11235              N3 = I
11236              N4 = I - 1
11237              GO TO 150
11238          END IF
11239      140 CONTINUE
11240          WRITE (*,200)
11241      150 SLOPE = (C(N1,N3) - C(N2,N3)) / ALOG(PA(N1)/PA(N2))
11242          C1 = C(N2,N3) + SLOPE * ALOG(P0/PA(N2))
11243          SLOPE = (C(N1,N4) - C(N2,N4)) / ALOG(PA(N1)/PA(N2))
11244          C2 = C(N2,N4) + SLOPE * ALOG(P0/PA(N2))
11245          SLOPE = (C1 - C2) / (AL(N3) - AL(N4))
11246          CRA = C2 + (ANGLE - AL(N4)) * SLOPE
11247          PR1 = CRA * P0
11248          DO 160 I = 1, 20
11249              IF (PR(I) .LE. PR1) THEN
11250                  N1 = I
11251                  N2 = I - 1
11252                  GO TO 170
11253              END IF
11254      160 CONTINUE
11255          WRITE (*,210)

```

```
      JJJ
11256 170 SLOPE = ALOG(RI(N1)/RI(N2)) / ALOG(PR(N1)/PR(N2))
11257       REFIMP = RI(N2) * (PR1 / PR(N2)) ** SLOPE
11258       PO = PO * 1000.
11259       RETURN
11260 180 FORMAT ('OLIMIT EXCEEDED IN LDPAR, ZDIS')
11261 190 FORMAT ('OLIMIT EXCEEDED IN LDPAR, PO')
11262 200 FORMAT ('OLIMIT EXCEEDED IN LDPAR, AL')
11263 210 FORMAT ('OLIMIT EXCEEDED IN LDPAR, PR1')
11264       END
```

```

JJJ
11265C
11266C
11267C
11268C
11269      SUBROUTINE TLD2(ZDIS, TA, TO)
11270C
11271C
11272C      COMPUTE THE DURATION AND TIME OF ARRIVAL AT A POINT
11273C
11274C
11275      DIMENSION X(20), TA1(20), T(20)
11276      DATA X/.3000, .4000, .5000, .6000, .7000, .8000, .9000,
11277      &      1.000, 1.100, 1.200, 1.300, 1.500, 1.600, 1.800,
11278      &      2.000, 2.500, 3.000, 3.500, 4.000, 5.000/
11279      DATA T/.0490, .0510, .0540, .0570, .0600, .0630, .0660,
11280      &      .0690, .0730, .0770, .0820, .0890, .0950, .1080,
11281      &      .1200, .1750, .2700, .4000, .6000, .9800/
11282      DATA TA1/.0075, .0150, .0225, .0300, .0380, .0470, .0580,
11283      &      .0700, .0820, .0930, .1080, .1360, .1650, .1900,
11284      &      .2250, .3400, .4750, .6300, .8100, 1.230/
11285      100 FORMAT (1X, 'LIMIT EXCEEDED IN TLD2')
11286      IF (ZDIS .LT. X(1)) GO TO 120
11287      DO 110 I = 2, 20
11288          IF (X(I) .GT. ZDIS) THEN
11289              N1 = I
11290              N2 = I - 1
11291              GO TO 130
11292          END IF
11293      110 CONTINUE
11294      120 WRITE (*,100)
11295          GO TO 140
11296      130 FACT = ALOG(TA1(N1)/TA1(N2)) / ALOG(X(N1)/X(N2))
11297          TA = TA1(N2) * ((ZDIS/X(N2)) ** FACT)
11298          FACT = ALOG(T(N1)/T(N2)) / ALOG(X(N1)/X(N2))
11299          TO = T(N2) * ((ZDIS/X(N2)) ** FACT)
11300      140 RETURN
11301      END

```

```

JJJ
11302C
11303C
11304C
11305      SUBROUTINE ATTEN(PR, TR, P)
11306C
11307C
11308C COMPUTE ATTENUATION OF SHOCK WAVE THROUGH THE CONCRETE
11309      COMMON / INPUTS / BLEN, BHGT, HREF, BIGW, RATLD, ZO,
11310      & TCASE, D, F, Q, Q1, COVER, TE, SIGMAC, SIGMAR, SMALLN,
11311      & WAVEFN
11312      COMMON / CONC / A, ALPHA, AR, BIGD, BIGL, EX1, EX2, EY1,
11313      & EY2, EZ1, EZ2, RHOR, RHOC, SMALLM, TAU, TCR, TINCR,
11314      & TMAX, TPRINT
11315      COMMON / CONSTS / ACUBE, AFOUR, ARSQ, ARSZP1, ARZSP1,
11316      & ARZP1, ARZS, ASQ, B, BIGRB, BIGMU, DELTAK, EPSLNU,
11317      & FOURTH, HALF, ONENZ, ONEPZ, SIXTH, THETU1, THIRD,
11318      & TWELFH, W, Z, ZB, ZCUBE, ZFOUR, ZSQ
11319      COMMON / RES3 / AE, VO, VE, UE, TSPL
11320      COMMON / RES4 / PU, H
11321      DATA A0/1.222000/, VS/3998.0000/, C0/1.673E5/
11322      DATA A1/1.6670E7/, A2/-4.2307E7/, A3/5.7462E7/
11323      DATA PM/1.7640E6/, PE/14.700E3/, B0/-4.145270/, B1/1.19068/
11324      DATA B2/-0.10530/, B3/2.959E-3/, N/100/
11325      X8 = 0.
11326      T1 = 0.
11327      DO 120 I = 1, N
11328          P = (PR / FLOAT(2*N)) * FLOAT(2*(N-I)+1)
11329          IF ((PR .GT. PE) .AND. (P .LE. PE)) THEN
11330              P = PE
11331              GO TO 130
11332          END IF
11333          T = (TR / FLOAT(2*N)) * FLOAT(2*I-1)
11334          F5 = ALOG(P)
11335          APAR = EXP(B0+B1*F5+B2*F5**2+B3*F5**3)
11336          IF (APAR .LT. 1.) APAR = 1.
11337C FROM J. V. USPENSKY PP 84-89
11338          X1 = A2 / A3
11339          X2 = A1 / A3
11340          X3 = - P / A3
11341          X4 = X2 - (X1 ** 2) / 3.
11342          X5 = X3 - X2 * X1 / 3. + 2. * ((X1/3.) ** 3)
11343          X6 = - X5 / 2. + SQRT((X5/2.)**2+(X4/3.)**3)
11344          IF (X6 .GE. 0.) THEN
11345              X6 = X6 ** THIRD
11346          ELSE
11347              X6 = - ( - X6) ** THIRD
11348          END IF
11349          X7 = - X5 / 2. - SQRT((X5/2.)**2+(X4/3.)**3)
11350          IF (X7 .GE. 0.) THEN
11351              X7 = X7 ** THIRD

```



```

    JJJ
11352     ELSE
11353     X7 = - ( - X7) ** THIRD
11354     END IF
11355     X3 = X6 + X7 - X1 / 3.
11356     V = APAR * VS / (1. + X3)
11357     C1 = SQRT(A1*VS)
11358     C = C0 + (C1 - C0) * (APAR - A0) / (1. - A0)
11359     IF (P .GT. PM) GO TO 100
11360     US = UE + VE * ((P-PE) / (VE - U)) ** HALF
11361     UP = UE + ((P-PE) * (VE - U)) ** HALF
11362     GO TO 110
11363 100   US = V0 * (P / (V0 - V)) ** HALF
11364     UP = (P * (A * VS - V)) ** HALF
11365 110   IF (US .GT. C) GO TO 130
11366     X9 = (X8 - (T1 - T) * US) / (1. - US / (C + UP))
11367     T2 = T1 + (X9 - X8) / US
11368     IF (X9 .GE. H) GO TO 130
11369     X8 = X9
11370     T1 = T2
11371 120 CONTINUE
11372 130 RETURN
11373     END

```

```

    JJJ
11374C
11375C
11376      SUBROUTINE TSCALE
11377C
11378C
11379C      SUBROUTINE COMPUTES TIME VALUES TO BE USED IN TSTEP
11380C
11381C
11382      COMMON / CONC / A, ALPHA, AR, BIGD, BIGL, EX1, EX2, EY1,
11383      &      EY2, EZ1, EZ2, RHOR, RHOC, SMALLM, TAU, TCR, TINCR,
11384      &      TMAX, TPRINT
11385C
11386C
11387      TMAX = 20. * TAU
11388      TINCR = TMAX / 200.
11389      FACT = 1.
11390      DO 100 I = 1, 10
11391          TVAR = FACT * TINCR
11392          TVAR = IFIX(TVAR)
11393          IF (TVAR .GT. 0) GO TO 110
11394          FACT = 10. * FACT
11395      100 CONTINUE
11396      110 TINCR = 1. / FACT * TVAR
11397      TPRINT = 5. * TINCR
11398      RETURN
11399      END

```

JJJ
11400C
11401C
11402C
11403C
11404C
11405C
11406
11407C
11408C
11409C
11410C
11411C
11412C
11413C
11414C
11415C
11416C
11417C
11418C
11419C
11420C
11421C
11422C
11423C
11424C
11425C
11426C
11427C
11428C
11429C
11430C
11431C
11432C
11433C
11434C
11435C
11436C
11437C
11438C
11439C
11440C
11441C
11442C
11443C
11444
11445
11446
11447
11448
11449

SUBROUTINE TCNTRL(NTRIES)

THIS SUBROUTINE STARTS WITH EACH CASE AT TIME T=0 AND AFTER SOME INITIALIZATION, PUSHES THE CASE THRU THE TIME STEPS, USING TINCR AS THE TIME STEP INCREMENT AND TMAX, AS THE TIME STOP INDICATOR.

THE BAD-HINGE-LOCATION-FLAG IS SET IF A BAD VALUE FOR THE HINGE LOCATION IS DISCOVERED BY THE SUB-PROCEDURE, CHEKXH, THE LOOP-CONTROL-FLAG IS SET WHEN THE SUBPROCEDURE, TSTEP, FINDS THE TIME-STEP-LOOP SHOULD BE TERMINATED FOR ANY REASON. THE CASE-IS-DONE-FLAG CAN BE SET AS FOLLOWS

- 1 IF THE TIME-STEP-LOOP HAS BEEN ATTEMPTED MAXTRI TIMES (SET IN TCNTRL)
- 2 IF THE ORIGINAL CONSTANTS FOR THE CASE ARE NEGATIVE OR NONCONVERGENT (SET IN TZERO)
- 3 IF THE MAXIMUM DEFLECTION HAS BEEN FOUND OR IF THE TIME MAXIMUM HAS BEEN EXCEEDED (SET IN TSTEP).

THE PARAMETER, NTRIES, IS INCREMENTED BY THIS ROUTINE, WHENEVER THE TIME-STEP-LOOP IS TERMINATED, TO INDICATE THE NUMBER OF TIMES THE LOOP HAS BEEN TRIED. IN THE CASE OF AN UNSUCCESSFUL TERMINATION, THE LOOP WILL BE TRIED AGAIN UP TO MAXTRI TIMES, WITH THE TIME STEP HALVED EACH TIME.

THIS SUBROUTINE CALLS THE FOLLOWING SUBPROCEDURES
TZERO TO INITIALIZE CONSTANTS AND VARIABLES FOR THE CASE
TSTEP TO COMPUTE THE DESIRED VARIABLES AT EACH TIME STEP, FROM TIME = TINCR THRU THE TIME, T = TMAX.

THIS ROUTINE IS CALLED BY THE PROCEDURE, DRIVER.

INTEGER BADXFG, BPFLAG, BRHFG, DONEFG, EOFLAG, FLGX, FLGY,
1 BRHFG1
COMMON / FLAGS / BADXFG, BPFLAG, BRHFG, DONEFG, EOFLAG,
1 IERRFG, LOADFG, MECHFG, M1STFG, NCONFG, FLGX, FLGY,
1 BRHFG1
COMMON / INPUTS / BLEN, BHGT, HREF, BIGW, RATLD, ZO,

```

      JJJ
11450      TCASE, D, F, Q, Q1, COVER, TE, SIGMAC, SIGMAR, SMALLN,
11451      WAVEFN
11452      COMMON / CONC / A, ALPHA, AR, BIGD, BIGL, EX1, EX2, EY1,
11453      EY2, EZ1, EZ2, RHOR, RHOC, SMALLM, TAU, TCR, TINC,
11454      TMAX, TPRINT
11455      COMMON / RESULT / DELTA, PE, T, THETA, THETAD, VEL, WF,
11456      WK, WP, BIGX, XH
11457      COMMON / PRINTS / LITTLN, MAXLIN, NF, NUMLIN, NUMPAG,
11458      NWAVER, STEPCT
11459      CHARACTER FLAG*1, TIMNOW*10, TITLE*75, TODAY*10, TYPE*5
11460      COMMON / PRINTC / FLAG, TIMNOW, TITLE, TODAY, TYPE
11461      CHARACTER BLANK*1
11462      DATA BLANK/' ', MAXTRI/2/
11463C
11464C
11465C      SET MECHANISM-FLAG FOR MECHANISM 2 TO CHECK XHO
11466C      CLEAR BAD-HINGE-LOCATION AND LOOP-CONTROL FLAGS
11467C      SET FIRST-TIME-FLAG FOR 1ST 2 PASSES THRU COMP
11468C      CLEAR NON-CONVERGENT-FLAG FOR PLATE CASE
11469C      CLEAR FAILURE FLAG FOR PRINTOUT
11470C      SET TYPE-OF-LOAD FLAG TO EFFECTIVE UNIFORM LOAD
11471C      INITIALIZE TIME VARIABLES, COMPUTE CASE CONSTANTS
11472C      AND PRINT T=0 RESULTS ON NEW PAGE (TZERO).
11473C
11474      MECHFG = 2
11475      BADXFG = 0
11476      LOOPFG = 0
11477      MISTFG = 2
11478      NCONFG = 0
11479      LOADFG = 1
11480C
11481      T = 0.0
11482      THETA = 0.0
11483      THETAD = 0.0
11484      DELTA = 0.0
11485      VEL = 0.0
11486      WF = 0.0
11487      WP = 0.0
11488      PE = 0.0
11489      WK = 0.0
11490C
11491      FLAG = BLANK
11492      NUMLIN = MAXLIN
11493      CALL TZERO(NTRIES)
11494C
11495C      IF ORIGINAL CONSTANTS ARE OKAY
11496C
11497      IF (DONEFG .EQ. 1) GO TO 120
11498C
11499C      THEN

```

```

      JJJ
11500C      DO WHILE LOOP-CONTROL-FLAG IS CLEAR
11501C      (I.E., WHILE TIME<TIME MAX & BADXFG IS CLEAR)
11502C
11503      100 IF (LOOPFG .NE. 0) GO TO 110
11504C
11505      CALL TSTEP(LOOPFG)
11506      GO TO 100
11507C
11508C      END WHILE
11509C
11510C      ADD 1 TO NUMBER OF TRIES
11511C
11512      110 NTRIES = NTRIES + 1
11513C
11514C      IF THIS WAS THE LAST TRY ALLOWED,
11515C      THEN SET CASE-IS-DONE-FLAG
11516C
11517      IF (NTRIES .GE. MAXTRI) DONEFG = 1
11518C
11519C      ELSE CONTINUE, SKIPPING CALCULATIONS
11520C
11521C      END IF (ORIGINAL CONSTANTS)
11522C
11523      120 RETURN
11524C
11525      END

```

JJJ
11526
11527C
11528C
11529C
11530C
11531C
11532C
11533C
11534C
11535C
11536C
11537C
11538C
11539C
11540C
11541C
11542C
11543C
11544C
11545C
11546C
11547C
11548C
11549C
11550C
11551C
11552C
11553C
11554C
11555C
11556
11557
11558
11559
11560
11561
11562
11563
11564
11565
11566
11567
11568
11569
11570
11571
11572
11573
11574C
11575C

SUBROUTINE TZERO(NTRIES)

THIS SUBROUTINE COMPUTES AND PRINTS CASE CONSTANTS FROM THE GIVEN INPUT VALUES. IT ALSO PROVIDES FOR THE FIRST LINE OF OUTPUT (T=0) TO BE PRINTED OUT ON A NEW PAGE WITH HEADINGS.

THIS SUBROUTINE IS CALLED BY THE PROCEDURE TCNTRL AND CALLS THE FOLLOWING SUBPROCEDURES

BTZERO INITIALIZES BEAM CONSTANTS & VARIABLES
PTZERO INITIALIZES PLATE CONSTANTS
& VARIABLES
CALXHO FINDS THE ORIGINAL HINGE LOCATION, XHO
CHEKXH CHECKS THE ORIGINAL LOCATION OF THE HINGE, XHO, AT TIME = 0
PRINTR PRINTS OUT THE INITIAL VALUES FOR THE GIVEN CASE AT TIME = 0

THE INPUT PARAMETER, NTRIES, IS USED TO PREVENT THE CALCULATION AND PRINTING OF THE COMPUTED CONSTANTS FOR THE CASE ON THE SECOND AND SUCCEEDING TRIES. THE PARAMETER WILL NOT BE ALTERED IN ANY WAY.

THE CASE-IS-DONE-FLAG MAY BE SET IN TWO WAYS FIRST, WHEN THE PLATE CONSTANT, Z, CANNOT BE FOUND OR DOES NOT CONVERGE, AND SECOND, IF NEGATIVE CONSTANTS ARE COMPUTED.

INTEGER BADXFG, BPFLAG, BRHFG, DONEFG, EOFLAG, FLGX, FLGY,
& BRHFG1
COMMON / FLAGS / BADXFG, BPFLAG, BRHFG, DONEFG, EOFLAG,
& IERRFG, LOADFG, MECHFG, M1STFG, NCONFG, FLGX, FLGY,
& BRHFG1
COMMON / INPUTS / BLEN, BHGT, HREF, BIGW, RATLD, ZO,
& TCASE, D, F, Q, Q1, COVER, TE, SIGMAC, SIGMAR, SMALLN,
& WAVEFN
COMMON / RESULT / DELTA, PE, T, THETA, THETAD, VEL, WF,
& WK, WP, BIGX, XH
COMMON / CONC / A, ALPHA, AR, BIGD, BIGL, EX1, EX2, EY1,
& EY2, EZ1, EZ2, RHOR, RHOC, SMALLM, TAU, TCR, TINC,
& THAX, TPRINT
COMMON / CONSTS / ACUBE, AFOUR, ARSQ, ARSZP1, ARZSP1,
& ARZP1, ARZS, ASQ, B, BIGRB, BIGMU, DELTAK, EPSLNU,
& FOURTH, HALF, ONEMZ, ONEPZ, SIXTH, THETU1, THIRD,
& TWELFH, W, Z, ZB, ZCUBE, ZFOUR, ZSQ
COMMON / RES4 / PU, H

```

      JJJ
11576C      IF THIS IS THE FIRST TIME THRU TZERO FOR THIS CASE
11577C
11578      IF (NTRIES .EQ. 0 .AND. BRHFG .EQ. 0) THEN
11579C
11580C          USE INPUT VALUES TO COMPUTE CONSTANTS
11581C
11582      BIGMU = 0.9 * D ** 2 * Q * SIGMAR * (1.0 - 0.59 * Q *
11583      &      (SIGMAR / SIGMAC))
11584      ASQ = A * A
11585      ACUBE = A ** 3
11586      AFOUR = A ** 4
11587      ARSQ = AR * AR
11588      W = 386.4 * SMALLM
11589      DELTAK = SMALLN * 386.4
11590      RHOC = SMALLM / H
11591      THETU1 = (4.0 * H * EPSLNU) / D ** 2
11592C
11593C          SET TYPE OF CASE CONSTANTS
11594C
11595C              BEAM CASE
11596      IF (BPFLAG .EQ. 1) CALL BTZERO
11597C              PLATE CASE
11598      IF (BPFLAG .EQ. 2) CALL PTZERO
11599C
11600C          FIND VALUE OF ORIGINAL HINGE LOCATION
11601C          AND PRINT OUT COMPUTED CONSTANTS
11602C
11603      CALL CALXHO(X0, XH0)
11604C
11605      IF (BPFLAG .EQ. 1) WRITE (*,110) B, BIGMU, W, XH0
11606      IF (BPFLAG .EQ. 2) WRITE (*,120) B, Z, BIGMU, W, XH0
11607C
11608C          IF NEGATIVE CONSTANTS, PRINT MESSAGE
11609C
11610      IF (B .LE. 0.0 .OR. BIGMU .LT. 0.0 .OR. W .LE. 0.0) THEN
11611C
11612      WRITE (*,130)
11613      DONEFG = 1
11614C
11615      ELSE
11616C          SET BREACH FLAG
11617      BRHFG = BRHFG1
11618      END IF
11619C
11620C          IF THIS IS THE 1ST TIME THRU FOR BREACH ENTRY
11621C
11622      ELSEIF(NTRIES.EQ.0.AND.BRHFG.EQ.1)THEN
11623C
11624C          SET UP CONSTANTS FOR BREACH OUTPUT
11625C

```

```

      JJJ
11626      CALL FIXBRH
11627      BRHFG = 2
11628C
11629      END IF
11630C
11631C      IF CASE CONSTANTS APPEAR OKAY
11632C
11633      IF (DONEFG .NE. 0) GO TO 100
11634C
11635C      THEN SET BIGX AND XH TO ORIGINAL HINGE LOCATION,
11636C      CHECK MECHANISM AND PRINT TIME ZERO RESULTS
11637C
11638      BIGX = X0
11639      XH = XH0
11640      CALL CHEKXH
11641      CALL PRINTR
11642C
11643C      ELSE CONTINUE
11644C      END IF (CONSTANT OKAY)
11645C
11646      100 RETURN
11647C
11648C      FORMAT STATEMENTS
11649C
11650      110 FORMAT ('0' / '0', 2X, 'COMPUTED CONSTANT VALUES' / '0',
11651      &          6X, 'BEAM HALF WIDTH, IN.', T56, '(B)', G15.8 / 7X,
11652      &          'HINGE MOMENT, IN.-LBS./IN.', T52, '(BIGMU)', G15.8 /
11653      &          7X, 'WEIGHT PER UNIT AREA, LBS./IN.SQ.', T56, '(W)',
11654      &          G15.8 / 7X, 'ORIGINAL HINGE LOCATION, IN.', T55,
11655      &          '(XH)', G15.8)
11656      120 FORMAT ('0' / '0', 2X, 'COMPUTED CONSTANT VALUES' / '0',
11657      &          6X, 'PLATE HALF LENGTH, IN.', T56, '(B)', G15.8 / 7X,
11658      &          'RATIO OF FINAL HINGE LOC TO B, DIMENSIONLESS', T56,
11659      &          '(Z)', G15.8 / 7X, 'HINGE MOMENT, IN.-LBS./IN.', T52,
11660      &          '(BIGMU)', G15.8 / , 7X,
11661      &          'WEIGHT PER UNIT AREA, LBS./IN.SQ.', T56, '(W)',
11662      &          G15.8 / 7X, 'ORIGINAL HINGE LOCATION, IN.', T55,
11663      &          '(XH)', G15.8)
11664      130 FORMAT ('0' /
11665      &          'OSOME COMPUTED CONSTANTS FOR THIS CASE ARE NEGATIVE.'
11666      &          / 1X, 'SOME INPUT VALUES MUST BE IN ERROR.' / 1X,
11667      &          'CASE IS TERMINATED.' / )
11668C
11669      END

```



```

JJJ
11670 SUBROUTINE BTZERO
11671C
11672C THIS SUBROUTINE CALCULATES THE INITIAL VALUES OF
11673C CONSTANTS AND VARIABLES TO BE USED BY THE GIVEN
11674C BEAM CASE.
11675C
11676C ALL OF THE CONSTANTS AND VARIABLES INITIALIZED ARE
11677C PASSED TO THE OTHER PROCEDURES THROUGH THE COMMON
11678C BLOCKS, COMPS, FLAGS, AND CONSTS.
11679C
11680C THIS SUBROUTINE IS CALLED BY THE PROCEDURE, TZERO.
11681C IT CALLS NO SUBPROCEDURES.
11682C
11683C
11684 EXTERNAL FXBO, PXY
11685 INTEGER BADXFG, BPFLAG, BRHFG, DONEFG, EOFLAG, FLGX, FLGY,
11686 & BRHFG1
11687 COMMON / FLAGS / BADXFG, BPFLAG, BRHFG, DONEFG, EOFLAG,
11688 & IERRFG, LOADFG, MECHFG, MISTFG, NCONFG, FLGX, FLGY,
11689 & BRHFG1
11690 COMMON / COMPS / ATHED1, ATHED2, APEDOT, AWFDOT, DELDOT,
11691 & PEDOT, THEDT1, THEDT2, THEDT3, WFDOT, WPDOT
11692 COMMON / CONSTS / ACUBE, AFOUR, ARSQ, ARSZP1, ARZSP1,
11693 & ARZP1, ARZS, ASQ, B, BIGRB, BIGMU, DELTAK, EPSLNU,
11694 & FOURTH, HALF, ONEMZ, ONEPZ, SIXTH, THETU1, THIRD,
11695 & TWELFH, W, Z, ZB, ZCUBE, ZFOUR, ZSQ
11696 COMMON / INPUTS / BLEN, BHGT, HREF, BIGW, RATLD, ZO,
11697 & TCASE, D, F, Q, Q1, COVER, TE, SIGMAC, SIGMAR, SMALLN,
11698 & WAVEFN
11699 COMMON / CONC / A, ALPHA, AR, BIGD, BIGL, EX1, EX2, EY1,
11700 & EY2, EZ1, EZ2, RHOR, RHOC, SMALLM, TAU, TCR, TINCR,
11701 & TMAX, TPRINT
11702 COMMON / RESULT / DELTA, PE, T, THETA, THETAD, VEL, WF,
11703 & WK, WP, BIGX, XH
11704 COMMON / RES4 / PU, H
11705C
11706C
11707C SET UP BEAM CONSTANTS
11708C
11709 B = A * AR
11710 THEDT2 = 3.0 * HALF * DELTAK / A
11711 THEDT3 = 3.0 * F * BIGMU / (SMALLM * ACUBE)
11712 WFDOT = 4.0 * ASQ * B
11713 WPDOT = 4.0 * B * F * BIGMU
11714 PEDOT = 4.0 * ASQ * B * SMALLN * W
11715 ATHED2 = THEDT2 + THEDT3
11716 APEDOT = PEDOT * HALF
11717C
11718C IF THIS IS A UNIFORM LOAD
11719C

```

```

      JJJ
11720      IF (LOADFG .EQ. 1) THEN
11721C
11722C          DETERMINE UNIFORM LOAD CONSTANTS FOR COMP
11723C
11724      DELDOT = PU / SMALLM
11725      THEDT1 = 3.0 * DELDOT * HALF / A
11726      ANFDOT = WFDOT * PU * HALF
11727C
11728      ELSE
11729C          DETERMINE BLAST LOAD CONSTANTS FOR COMP
11730C
11731      DELDOT = 1.0 / (SMALLM * A * B)
11732      THEDT1 = 3.0 / (SMALLM * ACUBE * B)
11733      XH = A
11734      CALL DBLNC(0, XH, FXBO, PXY, ANSX)
11735      ATHED1 = THEDT1 * ANSX
11736      ANFDOT = 4.0 * ANSX
11737C
11738      END IF
11739C
11740      RETURN
11741C
11742      END

```

```

      JJJ
11743      SUBROUTINE PTZERO
11744C
11745C      THIS SUBROUTINE COMPUTES INITIAL VALUES OF VARI-
11746C      ABLES AND CONSTANTS TO BE USED BY THE GIVEN PLATE
11747C      CASE.  THE PLATE CONSTANT Z IS FOUND USING THE
11748C      ROOT-FINDING ROUTINE, BISECT, WITH THE DERIVATIVE
11749C      FUNCTION, DFZ.  A MESSAGE IS PRINTED AND THE CASE
11750C      IS TERMINATED IF Z CANNOT BE FOUND.
11751C
11752C      THIS SUBROUTINE IS CALLED BY THE PROCEDURE, TZERO,
11753C      AND CALLS THE FOLLOWING SUBPROCEDURES
11754C          BISECT          TO SOLVE FOR Z (THE FUNCTION, DFZ, IS
11755C          CARRIED TO BISECT AS A PARAMETER)
11756C          DBLNC          TO COMPUTE THE DOUBLE INTEGRALS
11757C      WITHIN
11758C          P(X,Y) TO COMPUTE CONSTANTS FOR THE
11759C          MECHANISM 1 CASE (THE FUNCTIONS, FXPO,
11760C          FYPO, AND PXY ARE CARRIED TO DBLNC AS
11761C          PARAMETERS).
11762C
11763C      THE NON-CONVERGENT-FLAG IS RETURNED TO THIS ROU-
11764C      TINE BY THE ROUTINE, BISECT, AS SET, IF THE MIN
11765C      FOR THE Z FUNCTION CANNOT BE FOUND.  THIS IS
11766C      PASSED THROUGH THE COMMON BLOCK, FLAGS, BACK TO
11767C      THE CALLING PROCEDURE, TZERO.
11768C
11769C      ALL THE CONSTANTS AND VARIABLES INITIALIZED ARE
11770C      STORED AND PASSED TO THE OTHER PROCEDURES BY THE
11771C      COMMON BLOCKS, COMPS, AND CONSTS.
11772C
11773C
11774      EXTERNAL DFZ, FXPO, FYPO, PXY, PYX
11775      INTEGER BADXFG, BPFLAG, BRHFG, DONEFG, EOFLAG, FLGX, FLGY,
11776      & BRHFG1
11777      COMMON / FLAGS / BADXFG, BPFLAG, BRHFG, DONEFG, EOFLAG,
11778      & IERRFG, LOADFG, MECHFG, M1STFG, NCONFG, FLGX, FLGY,
11779      & BRHFG1
11780      COMMON / COMPS / ATHED1, ATHED2, APEDOT, AWFDOT, DELDOT,
11781      & PEDOT, THEDT1, THEDT2, THEDT3, WFDOT, WPDOT
11782      COMMON / INPUTS / BLEN, BHGT, HREF, BIGW, RATLD, ZO,
11783      & TCASE, D, F, Q, Q1, COVER, TE, SIGMAC, SIGMAR, SMALLN,
11784      & WAVEFN
11785      COMMON / CONC / A, ALPHA, AR, BIGD, BIGL, EX1, EX2, EY1,
11786      & EY2, EZ1, EZ2, RHOR, RHOC, SMALLM, TAU, TCR, TINCR,
11787      & TMAX, TPRINT
11788      COMMON / CONSTS / ACUBE, AFOUR, ARSQ, ARSZP1, ARZSP1,
11789      & ARZP1, ARZS, ASQ, B, BIGRB, BIGMU, DELTAK, EPSLNU,
11790      & FOURTH, HALF, ONEMZ, ONEPZ, SIXTH, THETU1, THIRD,
11791      & TWELFH, W, Z, ZB, ZCUBE, ZFOUR, ZSQ
11792      COMMON / RES4 / PU, H

```

```

      JJJ
11793C
11794C
11795C          SOLVE FOR Z
11796C
11797          B = A * AR
11798          NCONFG = 0
11799          IF (LOADFG .EQ. 1) THEN
11800          CALL BISECT(.0000001, 1.0000001, Z, NCONFG, DFZ)
11801          ELSE
11802          CALL BISECT(.00000001, 1.0, Z, NCONFG, DFZ)
11803          END IF
11804C
11805C          ASSUME Z = 1 IF MINIMUM NOT IN (0,1)
11806C
11807          IF (NCONFG .EQ. 1) THEN
11808          Z = 1.0
11809          NCONFG = 0
11810          WRITE (*,100)
11811          END IF
11812C
11813C          ASSUME Z CONVERGES AFTER 100 ITERATIONS
11814C
11815          IF (NCONFG .EQ. - 1) THEN
11816          NCONFG = 0
11817          WRITE (*,110)
11818          END IF
11819C          COMPUTE Z CONSTANTS
11820C
11821C
11822          ZB = Z * B
11823          ZSQ = Z * Z
11824          ZCUBE = Z ** 3
11825          ZFOUR = Z ** 4
11826          ARZS = AR * ZSQ
11827          ARZP1 = AR * Z + 1.0
11828          ARSZP1 = ARSQ * Z + 1.0
11829          ARZSP1 = ARZS + 1.0
11830          ONEMZ = 1.0 - Z
11831          ONEPZ = 1.0 + Z
11832C
11833C          DETERMINE CONSTANTS FOR COMP
11834C
11835C
11836          THEDT2 = DELTAK / A
11837          THEDT3 = F * BIGMU * (AR + 1.0) / (SMALLM * AR * ACUBE)
11838          ATHDEM = ARZSP1 * THIRD - Z * FOURTH * ARZP1
11839          THWORK = ARZS * SIXTH + HALF - Z * THIRD
11840          ATHED2 = (THEDT2 * THWORK + THEDT3) / ATHDEM
11841C
11842          WPDOT = 4.0 * F * BIGMU * A * ARSZP1 / (Z * AR)

```

```

      JJJ
11843      PEDOT = 4.0 * SMALLN * W * AR * ACUBE
11844      APEDOT = PEDOT * (HALF - Z * SIXTH)
11845C
11846C          IF THIS IS A UNIFORM CASE
11847C
11848      IF (LOADFG .EQ. 1) THEN
11849C
11850C          DETERMINE UNIFORM LOAD COMP CONSTANTS
11851C
11852      THEDT1 = PU / (SMALLM * A)
11853      ATHED1 = THEDT1 * THWORK / ATHDEM
11854      DELDOT = PU / SMALLM
11855      WFDOT = 4.0 * AR * ACUBE * PU
11856      AMFDOT = WFDOT * (HALF - Z * SIXTH)
11857C
11858      ELSE
11859C          DETERMINE BLAST LOAD COMP CONSTANTS
11860C
11861      CALL DBLNC(0, A, FXPO, PXY, ANSX)
11862      CALL DBLNC(0, ZB, FYPO, PYX, ANSY)
11863C
11864      THEDT1 = (1.0) / (SMALLM * AFOUR * AR)
11865      ATHED1 = (ANSX + ANSY) * THEDT1 / ATHDEM
11866      DELDOT = 1.0 / (SMALLM * A * B)
11867      AMFDOT = 4.0 * (A * ANSY / ZB + ANSX)
11868C
11869      END IF
11870C
11871      RETURN
11872C
11873C          FORMAT STATEMENTS
11874C
11875      100 FORMAT ( /
11876      &          'OTHE ROOT OF THE EQUATION FOR Z WAS NOT BETWEEN ZERO '
11877      &          , ' AND ONE' / 6X, 'Z IS ASSUMED TO BE 1.0')
11878      110 FORMAT ( /
11879      &          'OTHE MINIMUM OF THE EQUATION FOR Z DID NOT CONVERGE '
11880      &          , 'AFTER 100 ITERATIONS' /
11881      &          '0      LAST VALUE OF Z IS ASSUMED CORRECT')
11882C
11883      END

```

```

      JJJ
11884      SUBROUTINE CALXHO(XO, XHO)
11885C
11886C      THIS SUBROUTINE HANDLES CALLING THE METHOD FOR
11887C      SOLVING WHATEVER FUNCTION IS NECESSARY TO FIND
11888C      THE ORIGINAL HINGE LOCATION FOR THE CASE--OR
11889C      PRINTING AN ERROR MESSAGE IF IT CANNOT BE FOUND
11890C      EXACTLY.
11891C
11892C      THIS ROUTINE IS CALLED BY THE SUBROUTINE, TZERO.
11893C      THE ONLY SUBPROCEDURE CALLED BY THIS ROUTINE IS
11894C      THE ROOT-FINDING SUBPROCEDURE, BISECT, WHICH
11895C      USES THE FUNCTION, BFTNX OR PFTNX, DEPENDING ON
11896C      THE TYPE OF CASE.
11897C
11898C      THE PARAMETERS RELATING TO THE COMPUTED HINGE
11899C      LOCATION, XO AND XHO, ARE RETURNED TO THE CALLING
11900C      PROCEDURE, TZERO.
11901C
11902C
11903      EXTERNAL BFTNX, PFTNX
11904      INTEGER BADXFG, BPFLAG, BRHFG, DONEFG, EOFLAG, FLGX, FLGY,
11905      & BRHFG1
11906      COMMON / FLAGS / BADXFG, BPFLAG, BRHFG, DONEFG, EOFLAG,
11907      & IERRFG, LOADFG, MECHFG, M1STFG, NCONFG, FLGX, FLGY,
11908      & BRHFG1
11909      COMMON / INPUTS / BLEN, BHGT, HREF, BIGW, RATLD, ZO,
11910      & TCASE, D, F, Q, Q1, COVER, TE, SIGMAC, SIGMAR, SMALLN,
11911      & WAVEFN
11912      COMMON / CONC / A, ALPHA, AR, BIGD, BIGL, EX1, EX2, EY1,
11913      & EY2, EZ1, EZ2, RHOR, RHOC, SMALLM, TAU, TCR, TINCR,
11914      & THAX, TPRINT
11915C
11916C
11917C      COMPUTE XHO IN THE INTERVAL (0,A)
11918C
11919C      DETERMINE TYPE OF CASE FOR CORRECT XHO FUNCTION
11920C
11921C      IF BEAM CASE
11922      IF (BPFLAG .EQ. 1) CALL BISECT(0.00001, 0.99999, XO,
11923      & NCONFG, BFTNX)
11924C
11925C      IF PLATE CASE
11926      IF (BPFLAG .EQ. 2) CALL BISECT(0.00001, 0.99999, XO,
11927      & NCONFG, PFTNX)
11928C
11929C      END CASE OF TYPE OF CASE FOR XHO CALCULATION
11930C
11931      XHO = XO * A
11932C
11933C      CHECK CONVERGENCE

```

```

JJJ
11934C
11935C          CASE 1          DID NOT FIND ROOT IN THE INTERVAL (0,A)
11936C
11937          IF (NCONFIG .NE. 1) GO TO 100
11938C          ASSUME XHO = A
11939          WRITE (*,120)
11940          NCONFIG = 0
11941          XO = 1.0
11942          XHO = A
11943C
11944C          CASE 2          DID NOT CONVERGE AFTER 100 ITERATIONS
11945C
11946          100 IF (NCONFIG .NE. - 1) GO TO 110
11947C          ASSUME ROOT FOUND IS CORRECT
11948          WRITE (*,130) XHO
11949          NCONFIG = 0
11950C
11951C          END CASE ON CONVERGENCE
11952C
11953          110 RETURN
11954C
11955C          FORMAT STATEMENTS
11956C
11957          120 FORMAT ( /
11958          &          'OND VALUE OF THE ORIGINAL HINGE LOCATION, XHO, WAS '
11959          &          , 'FOUND IN THE INTERVAL (0,A).' /
11960          &          ' IT IS ASSUMED TO BE THE VALUE OF A.' )
11961          130 FORMAT ( /
11962          &          'OTHE BISECTION METHOD USED TO FIND THE ORIGINAL '
11963          &          , 'HINGE LOCATION, XHO, DID NOT CONVERGE AFTER 100 '
11964          &          , 'ITERATIONS.' /
11965          &          ' THE RESULT OF THE LAST ITERATION WILL BE ASSUMED '
11966          &          , 'CORRECT XHO = ', G15.8, '.' )
11967C
11968          END

```

```

JJJ
11969 SUBROUTINE BISECT(GUESS1, GUESS2, ROOT, ERRFLG, FTN)
11970C
11971C THIS SUBROUTINE TRIES TO FIND A ZERO ROOT FOR THE
11972C GIVEN FUNCTION WITHIN THE INTERVAL (GUESS1,GUESS2)
11973C USING THE BISECTION METHOD. GUESS 1 MUST BE LESS
11974C THAN GUESS 2.
11975C NOTE THIS ROUTINE MAY BLOW UP IF THE FUNCTION,
11976C FTN, HAS A DISCONTINUITY IN THE GIVEN INTERVAL.
11977C
11978C THE INPUT PARAMETERS ARE DEFINED AS FOLLOWS
11979C GUESS1 THE LOWER END OF THE GIVEN INTERVAL
11980C GUESS2 THE UPPER END OF THE GIVEN INTERVAL
11981C FTN THE EXTERNAL FUNCTION SUBPROCEDURE
11982C WHICH COMPUTES THE FUNCTION FOR WHICH
11983C BISECT IS ATTEMPTING TO FIND A ROOT.
11984C
11985C THE OUTPUT PARAMETERS ARE DEFINED AS FOLLOWS
11986C ROOT THE ROOT FOR THE FUNCTION,
11987C FTN, IN TH GIVEN INTERVAL , IF FOUND
11988C THE MIDPOINT OF THE INTERVAL, IF THE
11989C ROOT WAS NOT FOUND
11990C
11991C ERRFLG 0, THE ROOT WAS FOUND SUCCESSFULLY
11992C -1, THE ROOT FAILED TO CONVERGE
11993C AFTER 100 ITERATIONS
11994C +1, THE ROOT COULD NOT BE FOUND AS
11995C FTN(GUESS1) AND FTN(GUESS2) HAVE
11996C THE SAME SIGN, INFERRING THAT
11997C THERE IS EITHER NO ROOT OR MORE
11998C THAN ONE ROOT FOR THE FUNCTION IN
11999C THIS INTERVAL.
12000C
12001C THIS ROUTINE IS CALLED BY THE SUBPROCEDURES,
12002C PTZERO AND CALXHO. IT CALLS THE SUBPROCEDURE,
12003C FTN, WHICH MAY BE ONE OF THE FOLLOWING FUNCTIONS
12004C DFZ CALLED BY PTZERO, FINDS THE VALUE OF
12005C BFTNX CALLED BY CALXHO, FINDS XHO, BEAM CASE
12006C PFTNX CALLED BY CALXHO, FINDS XHO,
12007C PLATE CASE
12008C
12009C
12010 INTEGER ERRFLG
12011 EXTERNAL FTN
12012C
12013C
12014C CLEAR ERROR-FLAG AND INITIALIZE END POINT VALUES
12015C INITIALIZE EPSILON AND PUT DUMMY VALUE IN F3
12016 ITER = 0
12017 X1 = GUESS1
12018 X2 = GUESS2

```



```

      JJJ
12019      EPSILN = ABS(X2-X1) * 0.00000001
12020      F3 = 1.0
12021      SF3 = SIGN(1.0,F3)
12022C
12023      F1 = FTN(X1)
12024      F2 = FTN(X2)
12025      SF1 = SIGN(1.0,F1)
12026      SF2 = SIGN(1.0,F2)
12027C
12028C      IF THE SIGNS OF F1 AND F2 ARE THE SAME
12029C
12030      IF (SF1 .NE. SF2) GO TO 100
12031C
12032C      THEN THERE IS AN EVEN NUMBER OF ROOTS IN GIVEN
12033C      INTERVAL (0,2,4,...)--SET THE ERROR FLAG
12034C
12035      ERRFLG = 1
12036      ROOT = (X2 - X1) / 2.0 + X1
12037      GO TO 150
12038C
12039C      ELSE CONTINUE
12040C
12041C      DO WHILE F3 IS NOT ZERO AND ITER < 100
12042C      AND (X2 - X1) IS NOT ZERO
12043C
12044      100 IF ((SF3*F3) .LT. EPSILN .OR. (X2-X1) .LT. EPSILN) GO TO 140
12045      ITER = ITER + 1
12046      IF (ITER .GT. 100) GO TO 130
12047C
12048C      FIND X3 BETWEEN X1 AND X2. COMPUTE F3.
12049C
12050      X3 = X1 + (X2 - X1) / 2.0
12051      F3 = FTN(X3)
12052      SF3 = SIGN(1.0,F3)
12053C
12054C      IF NO ROOT BETWEEN X1 AND X3
12055C
12056      IF (SF3 .NE. SF1) GO TO 110
12057C
12058C      THEN MOVE X1 TO X3
12059C
12060      X1 = X3
12061      F1 = F3
12062      SF1 = SF3
12063      GO TO 120
12064C
12065C      ELSE MOVE X2 TO X3
12066C
12067      110 X2 = X3
12068      F2 = F3

```

```
JJJ
12069      SF2 = SF3
12070C
12071C          END IF
12072C
12073 120 GO TO 100
12074C
12075C          END WHILE
12076C
12077C          TAKE CARE OF ERROR--DID NOT CONVERGE IN 100 TRIES
12078C
12079 130 ERRFLG = - 1
12080      ROOT = (X2 - X1) / 2.0 + X1
12081      GO TO 150
12082C
12083C          ROOT HAS BEEN FOUND
12084C
12085 140 ROOT = X3
12086C
12087C          END IF
12088C
12089 150 RETURN
12090C
12091      END
```

```

JJJ
12092      FUNCTION BFTNX(TRIALX)
12093C
12094C      THIS FUNCTION CALCULATES A VALUE OF THE BEAM ORI-
12095C      GINAL HINGE LOCATION EQUATION FOR THE GIVEN TRIAL
12096C      X (WHICH IS A GUESS AT THE CORRECT VALUE). IF THE
12097C      RESULT RETURNED IS ZERO, THE GUESS IS CORRECT.
12098C
12099C      THIS FUNCTION IS CALLED BY THE ROOT-FINDING SUB-
12100C      PROCEDURE, BISECT. IT CALLS NO SUBPROCEDURES.
12101C
12102C
12103      EXTERNAL F1B0, FXB0, PXY
12104      INTEGER BADXFG, BPFLAG, BRHFG, DONEFG, EOFLAG, FLGX, FLGY,
12105      & BRHFG1
12106      COMMON / FLAGS / BADXFG, BPFLAG, BRHFG, DONEFG, EOFLAG,
12107      & IERRFG, LOADFG, MECHFG, M1STFG, NCONFG, FLGX, FLGY,
12108      & BRHFG1
12109      COMMON / COMPS / ATHED1, ATHED2, APEDOT, AWFDOT, DELDOT,
12110      & PEDOT, THEDT1, THEDT2, THEDT3, WFDOT, WPDOT
12111      COMMON / CONSTS / ACUBE, AFOUR, ARSQ, ARSZP1, ARZSP1,
12112      & ARZP1, ARZS, ASQ, B, BIGRB, BIGMU, DELTAK, EPSLNU,
12113      & FOURTH, HALF, ONEMZ, ONEPZ, SIXTH, THETU1, THIRD,
12114      & TWELFH, W, Z, ZB, ZCUBE, ZFOUR, ZSQ
12115      COMMON / INPUTS / BLEN, BHGT, HREF, BIGW, RATLD, ZO,
12116      & TCASE, D, F, Q, Q1, COVER, TE, SIGMAC, SIGMAR, SMALLN,
12117      & WAVEFN
12118      COMMON / CONC / A, ALPHA, AR, BIGD, BIGL, EX1, EX2, EY1,
12119      & EY2, EZ1, EZ2, RHOR, RHOC, SMALLM, TAU, TCR, TINC,
12120      & TMAX, TPRINT
12121      COMMON / RESULT / DELTA, FE, T, THETA, THETAD, VEL, WF,
12122      & WK, WP, BIGX, XH
12123C
12124C
12125      TRXSQ = TRIALX * TRIALX
12126      TRXCUB = TRIALX * TRXSQ
12127      XH = A * TRIALX
12128C
12129C      USE EQUATION DEPENDING ON TYPE OF LOAD FOR BEAM
12130C
12131C      IF UNIFORM LOAD
12132      IF (LOADFG .EQ. 1) THEN
12133C
12134      THEDD = (THEDT1 - THEDT2) / TRIALX - THEDT3 / TRXCUB
12135      DELDD = DELDOT - DELTAK
12136C
12137C
12138C      IF BLAST LOAD
12139      ELSE
12140C
12141      CALL DBLNC(XH, A, F1B0, PXY, ANS1)

```

```
    JJJ
12142 CALL DBLNC(0, XH, FXBO, PXY, ANSX)
12143 THEDD = (ANSX * THEDT1 - THEDT3) / TRXCUB - THEDT2 / TRIALX
12144 DELDD = DELDOT * ANS1 / (1.0 - TRIALX) - DELTAK
12145C
12146 END IF
12147C     END OF CASE ON TYPE OF LOAD
12148C
12149 BFTNX = XH * THEDD - DELDD
12150C
12151 RETURN
12152 END
```

```

JJJ
12153      FUNCTION PFTNX(TRIALX)
12154C
12155C      THIS FUNCTION CALCULATES A VALUE OF THE PLATE ORI-
12156C      GINAL HINGE LOCATION EQUATION FOR THE GIVEN TRIAL
12157C      X (WHICH IS A GUESS AT THE CORRECT VALUE). IF THE
12158C      RESULT RETURNED IS ZERO, THE GUESS IS CORRECT.
12159C
12160C      THIS FUNCTION IS CALLED BY THE ROOT-FINDING PRO-
12161C      CEDURE, BISECT.
12162C
12163C
12164      EXTERNAL F1P0, FXP0, FYP0, PXY, PYX
12165      INTEGER BADXFG, BPFLAG, BRHFG, DONEFG, EOFLAG, FLGX, FLGY,
12166      & BRHFG1
12167      COMMON / FLAGS / BADXFG, BPFLAG, BRHFG, DONEFG, EOFLAG,
12168      & IERRFG, LOADFG, MECHFG, M1STFG, NCONFG, FLGX, FLGY,
12169      & BRHFG1
12170      COMMON / COMPS / ATHED1, ATHED2, APEDOT, AMFDOT, DELDOT,
12171      & PEDOT, THEDT1, THEDT2, THEDT3, WFDOT, WPDOT
12172      COMMON / CONSTS / ACUBE, AFOUR, ARSQ, ARSZP1, ARZSP1,
12173      & ARZP1, ARZS, ASQ, B, BIGRB, BIGMU, DELTAK, EPSLNU,
12174      & FOURTH, HALF, ONEMZ, ONEPZ, SIXTH, THETU1, THIRD,
12175      & TWELFH, W, Z, ZB, ZCUBE, ZFOUR, ZSQ
12176      COMMON / INPUTS / BLEN, BHGT, HREF, BIGW, RATLD, ZO,
12177      & TCASE, D, F, Q, Q1, COVER, TE, SIGMAC, SIGMAR, SMALLN,
12178      & WAVEFN
12179      COMMON / CONC / A, ALPHA, AR, BIGD, BIGL, EX1, EX2, EY1,
12180      & EY2, EZ1, EZ2, RHOR, RHOC, SMALLM, TAU, TCR, TINC,
12181      & TMAX, TPRINT
12182      COMMON / RESULT / DELTA, PE, T, THETA, THETAD, VEL, WF,
12183      & WK, WP, BIGX, XH
12184C
12185C
12186      TRXSQ = TRIALX * TRIALX
12187      XH = A * TRIALX
12188C
12189C      IF UNIFORM LOAD
12190C
12191C      IF (LOADFG .EQ. 1) THEN
12192C
12193      THEDD = ((THEDT1-THEDT2) * (ARZS * (HALF - TRIALX * THIRD) +
12194      & HALF - TRIALX * Z * THIRD) - THEDT3 / TRXSQ) /
12195      & (TRIALX * (ARZSP1 * THIRD - ARZP1 * Z * TRIALX *
12196      & FOURTH))
12197      DELDD = DELDOT - DELTAK
12198C
12199      ELSE
12200C      MUST BE A BLAST LOAD
12201C
12202      CALL DBLNC(0, XH, FXP0, PXY, ANSX)

```

```

JJJ
12203 CALL DBLNC(0, ZB*XH/A, FYPO, PYX, ANSY)
12204 CALL DBLNC(XH, A, F1PO, PXY, ANS1)
12205C
12206C
12207 THEDD = ((ANSX+ANSY) * THEDT1 - THEDT3 - THEDT2 * TRXSQ *
12208 & (ARZS * (HALF - TRIALX * THIRD) + HALF - Z * TRIALX *
12209 & THIRD)) / (TRIALX ** 3 * (THIRD * ARZSP1 - TRIALX *
12210 & Z * FOURTH * ARZP1))
12211C
12212 DELDD = ANS1 * DELDOT / ((1.0-TRIALX) * (1.0 - TRIALX *
12213 & Z)) - DELTAK
12214C
12215 END IF
12216C
12217 PFTNX = XH * THEDD - DELDD
12218C
12219 RETURN
12220 END

```

```

JJJ
12221      FUNCTION DFZ(TRIALZ)
12222C
12223C      THIS FUNCTION SUBPROCEDURE COMPUTES THE VALUE OF
12224C      THE DERIVATIVE OF THE Z FUNCTION AT THE VALUE OF
12225C      TRIALZ. IT USES THE SECANT LINE APPROXIMATION TO
12226C      DETERMINE THE DERIVATIVE.
12227C
12228C      THIS FUNCTION IS CALLED BY THE ROOT-FINDING PRO-
12229C      CEDURE, BISECT, IN ORDER TO DETERMINE THE MINIMUM
12230C      VALUE OF Z IN THE GIVEN INTERVAL. IT CALLS THE
12231C      FUNCTION, FTNZ.
12232C
12233      EXTERNAL FTNZ
12234      INTEGER BADXFG, BPFLAG, BRHFG, DONEFG, EOFLAG, FLGX, FLGY,
12235      & BRHFG1
12236      COMMON / FLAGS / BADXFG, BPFLAG, BRHFG, DONEFG, EOFLAG,
12237      & IERRFG, LOADFG, MECHFG, MISTFG, NCONFG, FLGX, FLGY,
12238      & BRHFG1
12239      COMMON / CONSTS / ACUBE, AFOUR, ARSQ, ARSZP1, ARZSP1,
12240      & ARZP1, ARZS, ASQ, B, BIGRB, BIGMU, DELTAK, EPSLNU,
12241      & FOURTH, HALF, ONEMZ, ONEPZ, SIXTH, THETU1, THIRD,
12242      & TWELFH, W, Z, ZB, ZCUBE, ZFOUR, ZSQ
12243      DATA EPSILN/.0000001/
12244C
12245C
12246C      IF UNIFORM LOAD
12247C
12248      IF (LOADFG .EQ. 1) THEN
12249C
12250      DFZ = (ARSQ * TRIALZ + 2.0) * TRIALZ - 3.0
12251C
12252      ELSE
12253C      IF BLAST LOAD
12254C
12255      DFZ = (FTNZ(TRIALZ+EPSILN) - FTNZ(TRIALZ-EPSILN)) / (2.0 *
12256      & EPSILN)
12257C
12258      END IF
12259C
12260      RETURN
12261      END

```

```

JJJ
12262      FUNCTION FTNZ(TRIALZ)
12263C
12264C      THIS FUNCTION CALCULATES A VALUE FOR THE PLATE Z
12265C      FUNCTION FOR THE GIVEN TRIAL Z.
12266C
12267C      THIS FUNCTION IS CALLED BY THE SUBPROCEDURE, DFZ,
12268C      WHICH CALCULATES THE DERIVATIVE OF THE Z FUNCTION.
12269C      IT CALLS THE DOUBLE INTEGRATION ROUTINE, DBLNC,
12270C      IN ORDER TO DETERMINE THE TWO DOUBLE INTEGRALS IN
12271C      THE DENOMINATOR.
12272C
12273C
12274      EXTERNAL FXPO, FYPO, PXY, PYX
12275      INTEGER BADXFG, BPFLAG, BRHFG, DONEFG, EOFLAG, FLGX, FLGY,
12276      & BRHFG1
12277      COMMON / FLAGS / BADXFG, BPFLAG, BRHFG, DONEFG, EOFLAG,
12278      & IERRFG, LOADFG, MECHFG, M1STFG, NCONFG, FLGX, FLGY,
12279      & BRHFG1
12280      COMMON / CONSTS / ACUBE, AFOUR, ARSQ, ARSZP1, ARZSP1,
12281      & ARZP1, ARZS, ASQ, B, BIGRB, BIGMU, DELTAK, EPSLNU,
12282      & FOURTH, HALF, ONEMZ, ONEPZ, SIXTH, THETU1, THIRD,
12283      & TWELFH, W, Z, ZB, ZCUBE, ZFOUR, ZSQ
12284      COMMON / INPUTS / BLEN, BHGT, HREF, BIGW, RATLD, ZO,
12285      & TCASE, D, F, Q, Q1, COVER, TE, SIGMAC, SIGMAR, SMALLN,
12286      & WAVEFN
12287      COMMON / CONC / A, ALPHA, AR, BIGD, BIGL, EX1, EX2, EY1,
12288      & EY2, EZ1, EZ2, RHOR, RHOC, SMALLM, TAU, TCR, TINCR,
12289      & TMAX, TPRINT
12290C
12291C
12292      ZB = B * TRIALZ
12293C
12294      CALL DBLNC(O, ZB, FYPO, PYX, ANSY)
12295      CALL DBLNC(O, A, FXPO, PXY, ANSX)
12296C
12297      FTNZ = (ANSY / ZB + ANSX / A) / (A / ZB + AR)
12298C
12299      RETURN
12300      END

```



```

JJJ
12301      SUBROUTINE FIXBRH
12302C
12303C      THIS SUBROUTINE RECALCULATES THE CONSTANTS TO BE
12304C      USED FOR THIS PLATE CASE WHICH HAS SHOWN LOCALIZED
12305C      LOAD SHEAR FAILURE.  THESE NEW CONSTANTS WILL
12306C      SUBTRACT THE LOAD WHICH IS GOING THROUGH THE
12307C      HOLE THROUGH THE CENTER OF THE PLATE (OR RADIUS
12308C      BIGRB).
12309C
12310C      THIS ROUTINE IS CALLED BY THE PROCEDURE, TZERO,
12311C      AND CALLS THE DOUBLE INTEGRATION SUBPROCEDURE,
12312C      DBLNC, TO COMPUTE SEVERAL DOUBLE INTEGRALS.
12313C
12314C      ALL CONSTANTS AND VARIABLES USED ARE STORED IN
12315C      THE COMMON BLOCKS, INPUTS, CONSTS, AND COMPS.
12316C
12317C
12318      EXTERNAL FXP1, FYP1, FZ, FZSQ, FZPXY, FZPYX, F1P2, F1P3,
12319      & PXY, PYX
12320      INTEGER BADXFG, BPFLAG, BRHFG, DONEFG, EOFLAG, FLGX, FLGY,
12321      & BRHFG1
12322      COMMON / FLAGS / BADXFG, BPFLAG, BRHFG, DONEFG, EOFLAG,
12323      & IERRFG, LOADFG, MECHFG, M1STFG, NCONFG, FLGX, FLGY,
12324      & BRHFG1
12325      COMMON / COMPS / ATHED1, ATHED2, APEDOT, AWFDOT, DELDOT,
12326      & PEDOT, THEDT1, THEDT2, THEDT3, WFDOT, WPDOT
12327      COMMON / CONSTS / ACUBE, AFOUR, ARSQ, ARSZP1, ARZSP1,
12328      & ARZP1, ARZS, ASQ, B, BIGRB, BIGMU, DELTAK, EPSLNU,
12329      & FOURTH, HALF, ONEMZ, QNEPZ, SIXTH, THETU1, THIRD,
12330      & TWELFH, W, Z, ZB, ZCUBE, ZFOUR, ZSQ
12331      COMMON / INPUTS / BLEN, BHGT, HREF, BIGW, RATLD, ZO,
12332      & TCASE, D, F, G, Q1, COVER, TE, SIGMAC, SIGMAR, SMALLN,
12333      & WAVEFN
12334      COMMON / CONC / A, ALPHA, AR, BIGD, BIGL, EX1, EX2, EY1,
12335      & EY2, EZ1, EZ2, RHOR, RHOC, SMALLN, TAU, TCR, TINC,
12336      & TMAX, TPRINT
12337C
12338C
12339C      RESET MECHANISM-FLAG AND Z, WRITE MESSAGE
12340C
12341      MECHFG = 1
12342      Z = 1.0
12343C
12344      WRITE (*,100)
12345C
12346C      RECOMPUTE CONSTANTS TO BE USED
12347C
12348      ARP1 = AR + 1.0
12349      ARSQP1 = ARSQ + 1.0
12350      ARSZP1 = ARSZP1

```

```

JJJ
12351 ARZSP1 = ARP1
12352 ARZP1 = ARP1
12353 ARZS = AR
12354C
12355 AARB = A + AR * B
12356 XBAR = (AARB - SQRT(AARB**2-ARSQP1*(A*A+B*B-BIGRB**2))) /
12357 & ARSQP1
12358 YBAR = XBAR * AR
12359C
12360 CALL DBLNC(0.0, A, FXP1, PXY, ANSX)
12361 CALL DBLNC(0.0, B, FYP1, PYX, ANSY)
12362C
12363 CALL DBLNC(YBAR, B, F1P2, FZPYX, ANSPX)
12364 CALL DBLNC(XBAR, A, F1P3, FZPXY, ANSPY)
12365C
12366 CALL DBLNC(YBAR, B, F1P2, FZ, ANSZX)
12367 CALL DBLNC(XBAR, A, F1P3, FZ, ANSZY)
12368C
12369 CALL DBLNC(YBAR, B, F1P2, FZSQ, ANSZX2)
12370 CALL DBLNC(XBAR, A, F1P3, FZSQ, ANSZY2)
12371C
12372 THEDT1 = ANSX + ANSY - ANSPX - ANSPY
12373 THEDT2 = SMALLN * W * (ACUBE * AR * ARP1 * SIXTH - ANSZX -
12374 & ANSZY)
12375 THEDT3 = F * BIGMU * (ARP1 * A - 2.0 * BIGRB)
12376C
12377 ATHDEM = SMALLM * (AFOUR * AR * ARP1 * TWELFH - ANSZX2 -
12378 & ANSZY2 / AR)
12379 ATHED1 = THEDT1 / ATHDEM
12380 ATHED2 = (THEDT2 + THEDT3) / ATHDEM
12381C
12382 WPDOT = 4. * F * BIGMU * (B + A / AR - ARP1 * BIGRB / AR)
12383 APEDOT = 4. * SMALLN * W * (AR * ACUBE * THIRD - ANSZX -
12384 & ANSZY / AR)
12385 AWFDOT = 4. * (ANSY / AR + ANSX - ANSPX - ANSPY / AR)
12386C
12387 RETURN
12388C
12389C FORMAT STATEMENT
12390C
12391 100 FORMAT ('0' /
12392 & 'BECAUSE THIS PLATE HAS SHOWN LOCALIZED LOAD SHEAR '
12393 & ', 'FAILURE,' /
12394 & ' A SECOND SET OF CALCULATIONS WILL BE DONE WITH '
12395 & ', 'THE BREACH AREA MASS AND LOADING REMOVED' /
12396 & ' Z IS RESET TO 1.0, AND WE ASSUME THE PLATE TO BE IN '
12397 & ', 'MECHANISM 1' / )
12398C
12399 END

```

```

      JJJ
12400  SUBROUTINE TSTEP(LOOPFG)
12401C
12402C      THIS SUBROUTINE CONTAINS THE LOOP OF OPERATIONS
12403C      PERFORMED ON THE GIVEN VARIABLES FOR THE CASE FOR
12404C      ONE TIME STEP.
12405C
12406C      THIS SUBROUTINE IS CALLED BY THE TIME-LOOP-CONTROL
12407C      PROCEDURE, TCNTRL. IT CALLS THE FOLLOWING SUB-
12408C      PROCEDURES
12409C          CHEKXH          TO CHECK THE LOCATION OF THE HINGE,
12410C          XH, DURING MECHANISM TWO OF A CASE
12411C          PRINTR          TO PRINT OUT A LINE OF RESULTS FOR THE
12412C          GIVEN TIME STEP
12413C          RUNGEK          TO PERFORM THE RUNGE-KUTTA COMPUTATION
12414C          OF VARIABLES AT THE CURRENT TIME STEP.
12415C
12416C      THE PARAMETER, LOOPFG, IS THE LOOP-CONTROL-FLAG,
12417C      WHICH IS SET BY THIS ROUTINE IF THE LOOP SHOULD BE
12418C      TERMINATED FOR ANY REASON.
12419C
12420C      THE CASE-IS-DONE-FLAG, DONEFG, IS SET IN TWO WAYS
12421C      1   IF EITHER VELOCITY, DELTA DOT OR THETA DOT,
12422C          GO NEGATIVE INDICATING THAT THE MAXIMUM
12423C          DEFLECTION HAS BEEN REACHED OR THE PRESSURE
12424C          WAS NOT SUFFICIENT TO SHOW A RESPONSE AND
12425C          THE CASE CAN BE TERMINATED
12426C      2   IF THE TIME MAXIMUM (TMAX) FOR THE CASE TO
12427C          BE RUN HAS BEEN REACHED, IN WHICH CASE THE
12428C          CASE MUST BE ENDED.
12429C
12430C      INTEGER BADXFG, BPFLAG, BRHFG, DONEFG, EOFLAG, FLGX, FLGY,
12431      & BRHFG1
12432      COMMON / FLAGS / BADXFG, BPFLAG, BRHFG, DONEFG, EOFLAG,
12433      & IERRFG, LOADFG, MECHFG, M1STFG, NCONFG, FLGX, FLGY,
12434      & BRHFG1
12435      COMMON / INPUTS / BLEN, BHGT, HREF, BIGW, RATLD, Z0,
12436      & TCASE, D, F, Q, Q1, COVER, TE, SIGMAC, SIGNAR, SMALLN,
12437      & WAVEFN
12438      COMMON / CONC / A, ALPHA, AR, BIGD, BIGL, EX1, EX2, EY1,
12439      & EY2, EZ1, EZ2, RHOR, RHOC, SMALLM, TAU, TCR, TINCR,
12440      & TMAX, TPRINT
12441      COMMON / RESULT / DELTA, PE, T, THETA, THETAD, VEL, WF,
12442      & WK, WP, BIGX, XH
12443      COMMON / PRINTS / LITTLN, MAXLIN, NF, NUMLIN, NUMPAG,
12444      & NWAVEF, STEPCT
12445      CHARACTER FLAG*1, TIMNOW*10, TITLE*75, TODAY*10, TYPE*5
12446      COMMON / PRINTC / FLAG, TIMNOW, TITLE, TODAY, TYPE
12447      COMMON / CONSTS / ACUBE, AFOUR, ARSQ, ARSZP1, ARZSP1,
12448      & ARZP1, ARZS, ASQ, B, BIGRB, BIGMU, DELTAK, EPSLNU,
12449

```

```

      JJJ
12450      &    FOURTH, HALF, ONEMZ, ONEPZ, SIXTH, THETU1, THIRD,
12451      &    TWELFH, W, Z, ZB, ZCUBE, ZFOUR, ZSQ
12452      CHARACTER STAR*1
12453      DATA STAR/'*'/
12454C
12455C
12456C          COMPUTE MOTION & WORK EQUATIONS FOR NEXT TIME STEP
12457C
12458      CALL RUNGEK
12459      WK = WF - WP - PE
12460      T = T + TINCR
12461      STEPCT = STEPCT + TINCR
12462C
12463C          IF MECHANISM 1
12464C
12465C          IF (MECHFG .NE. 1) GO TO 100
12466C
12467C          THEN COMPLETE VEL AND DELTA CALCULATIONS
12468C
12469      VEL = THETAD * A
12470      DELTA = THETA * A
12471C
12472C          ELSE CONTINUE
12473C          END IF (MECH 1)
12474C
12475C          IF EITHER VELOCITY IS ZERO
12476C
12477      100 IF (VEL .GE. 0.0 .AND. THETAD .GE. 0.0) GO TO 130
12478C
12479C          THEN WRITE MESSAGE AND SET
12480C          CASE-IS-DONE-FLAG TO TERMINATE CASE
12481C
12482C          IF THIS IS THE FIRST TIME STEP
12483      IF (T .NE. TINCR) GO TO 110
12484C          THEN WRITE NO RESPONSE MESSAGE
12485      WRITE (*,200)
12486      GO TO 120
12487C          ELSE WRITE MAXIMUM DEFLECTION FOUND
12488      110 WRITE (*,180) DELTA, T
12489C
12490C          END IF (1ST TIME STEP)
12491C
12492      120 LOOPFG = 1
12493      DONEFG = 1
12494      WRITE (*,210)
12495      GO TO 170
12496C
12497C          ELSE CONTINUE COMPUTATIONS
12498C
12499C          IF MECHANISM 2, GET NEW HINGE LOCATION (XH)

```

```

JJJ
12500 130 IF (MECHFG .EQ. 2) CALL CHEKXH
12501C
12502C      IF HINGE LOCATION IS OKAY
12503      IF (BADXFG .NE. 0) GO TO 150
12504C
12505C      THEN CHECK FOR FAILURE WITH THETA U
12506C      PRINT RESULTS IF END OF TIME STEP INTERVAL
12507C
12508      THETAU = D * (SQRT(THETAU1*XH+1.0) - 1.0) / XH
12509      IF (THETA .GT. THETAU) FLAG = STAR
12510      IF ((STEPCT+TINCR) .GT. TPRINT) CALL PRINTR
12511C
12512C      IF TIME HAS REACHED THE LIMIT (TMAX)
12513C
12514      IF (TMAX .GE. (T+TINCR)) GO TO 140
12515C
12516C      THEN SET LOOP-CONTROL- AND CASE-IS-DONE-FLAGS
12517C      AND WRITE TIME-EXCEEDED MESSAGE
12518      LOOPFG = 1
12519      DONEFG = 1
12520      WRITE (*,190)
12521      WRITE (*,210)
12522C      ELSE CONTINUE
12523C      END IF (T=TMAX)
12524C
12525 140 GO TO 160
12526C
12527C      ELSE SET LOOP CONTROL FLAG TO TERMINATE TRY
12528C      BECAUSE OF A BAD HINGE LOCATION
12529 150 LOOPFG = 1
12530C
12531C      END IF (GOOD XH)
12532C
12533 160 GO TO 170
12534C
12535C      END IF (ZERO VELOCITIES)
12536C
12537 170 RETURN
12538C
12539C      FORMAT STATEMENTS
12540C
12541 180 FORMAT ('0', 20X, 'MAXIMUM DEFLECTION = ', G15.8,
12542      & ' AT TIME = ', G15.8)
12543 190 FORMAT ('0', 30X, 'TIME EXCEEDED')
12544 200 FORMAT ('0', 20X,
12545      & ' INSUFFICIENT PRESSURE TO GIVE A RESPONSE')
12546 210 FORMAT ('0', 20X,
12547      & ' AN ASTERISK INDICATES THAT A REINFORCING ELEMENT HAS '
12548      & ' FRACTURED')
12549C

```

```

      JJJ
12550      END
12551      SUBROUTINE CHEKXH
12552C
12553C      THIS SUBROUTINE CHECKS THE VALUE OF THE HINGE
12554C      LOCATION, XH, TO SEE THAT IT IS WITHIN RANGE, AND
12555C      TO SEE IF IT HAS MOVED FROM A MECHANISM 2 TO A
12556C      MECHANISM 1 POSITION.
12557C
12558C      IF THE HINGE LOCATION IS NEGATIVE (OFF THE END OF
12559C      THE BEAM OR PLATE), THE DATA MUST BE BAD. IF THE
12560C      HINGE LOCATION HAS MOVED WITHIN TWO PERCENT OF THE
12561C      CENTER OF THE BEAM OR PLATE, IT IS CONSIDERED TO
12562C      BE AT THE CENTER, WHICH IS THE MECHANISM 1 POSI-
12563C      TION, AND THE MECHANISM FLAG IS CHANGED TO REFLECT
12564C      THIS. IF THE HINGE LOCATION HAS MOVED PAST THE
12565C      CENTER OF THE BEAM OR PLATE BY MORE THAN TWO PER-
12566C      CENT, THE COMPUTATION IS CONSIDERED TOO IMPRECISE,
12567C      AND SO THE TIME INCREMENT, TINCR, IS HALVED, A
12568C      MESSAGE IS PRINTED, AND FLAGS ARE SET TO SHOW THAT
12569C      THIS HAS HAPPENED AND TO RUN THROUGH THE COMPUTA-
12570C      TION AGAIN WITH THE SMALLER TIME STEP. THE MAX-
12571C      IMUM NUMBER OF TIMES WHICH THIS CAN BE ATTEMPTED
12572C      IS TWO (AND IS STORED IN THE CONSTANT, MAXTRI, IN
12573C      THE SUBROUTINE, TCNTRL).
12574C
12575C      THE BAD-HINGE-LOCATION-FLAG, BADXFG, IS SET IF
12576C      THE HINGE LOCATION FOUND IS NEGATIVE OR PAST
12577C      THE CENTER POINT BY MORE THAN TWO PERCENT.
12578C
12579C      THE CASE-IS-DONE-FLAG, DONEFG, IS SET IF THE HINGE
12580C      LOCATION IS NEGATIVE.
12581C
12582C      THE MECHANISM-FLAG, MECHFG, IS CHANGED FROM 2 TO 1
12583C      IF THE HINGE LOCATION HAS MOVED TO THE CENTER OF
12584C      THE BEAM OR PLATE.
12585C
12586C      THIS SUBROUTINE IS CALLED BY THESE PROCEDURES
12587C      TCNTRL          TO CHECK THE ORIGINAL HINGE
12588C      LOCATION AT
12589C      TIME ZERO
12590C      TSTEP          TO COMPUTE AND CHECK THE HINGE
12591C      LOCATIO
12592C      AT EACH SUCCESSIVE TIME STEP.
12593C      THIS ROUTINE CALLS NO SUBPROCEDURES.
12594C
12595C      INTEGER BADXFG, BPFLAG, BRHFG, DONEFG, EOFLAG, FLGX, FLGY,
12596      & BRHFG1
12597      COMMON / FLAGS / BADXFG, BPFLAG, BRHFG, DONEFG, EOFLAG,
12598      & IEKRF, LOADFG, MECHFG, M1STFG, NCONF, FLGX, FLGY,
12599

```

```

      JJJ
12600      & BRHFG1
12601      COMMON / INPUTS / BLEN, BHGT, HREF, BIGW, RATLD, ZO,
12602      & TCASE, D, F, Q, Q1, COVER, TE, SIGHAC, SIGMAR, SMALLN,
12603      & WAVEFN
12604      COMMON / CONC / A, ALPHA, AR, BIGD, BIGL, EX1, EX2, EY1,
12605      & EY2, EZ1, EZ2, RHOR, RHOC, SMALLM, TAU, TCR, TINCR,
12606      & TMAX, TPRINT
12607      COMMON / RESULT / DELTA, PE, T, THETA, THETAD, VEL, WF,
12608      & WK, WP, BIGX, XH
12609C
12610C
12611C      IF THIS IS NOT THE FIRST TIME STEP (T/=0)
12612C
12613      IF (T .EQ. 0.0 .OR. THETA .EQ. 0.0) GO TO 100
12614C
12615C      THEN COMPUTE HINGE LOCATION FROM LAST RESULTS
12616      XH = DELTA / THETA
12617      BIGX = XH / A
12618C
12619C      ELSE CONTINUE
12620C      END IF (T)
12621C
12622C      IF THE HINGE HAS NOT REACHED THE FINAL HINGE LOC
12623      100 IF (BIGX .GT. 0.98) GO TO 120
12624C
12625C      THEN CASE IS STILL WITHIN MECHANISM 2
12626C      IF HINGE LOCATION IS NEGATIVE
12627C
12628      IF (XH .GT. 0.0) GO TO 110
12629C
12630C      THEN DATA MUST BE BAD
12631C      SET BAD-HINGE & CASE-IS-DONE FLAGS TO END CASE
12632C
12633      WRITE (*,170)
12634      BADXFG = 1
12635      DONEFG = 1
12636C
12637C      ELSE CONTINUE--HINGE LOCATION IS WITHIN MECH 2
12638C
12639C      END IF (NEG XH)
12640C
12641      110 GO TO 150
12642C
12643C      ELSE HINGE HAS MOVED TO MECHANISM 1 LOCATION
12644C      NEED TO CHECK RANGE
12645C
12646C      IF HINGE IS WITHIN 2% OF FINAL HINGE LOCATION
12647      120 IF (BIGX .GT. 1.02) GO TO 130
12648C
12649C      THEN SET HINGE TO FINAL HINGE LOC & SET FLAGS

```

```

      JJJ
12650C      TO SHOW MECH 1 HAS BEEN SUCCESSFULLY REACHED
12651C
12652      XH = A
12653      BIGX = 1.0
12654      MECHFG = 1
12655      GO TO 140
12656C
12657C      ELSE HINGE HAS OVERSHOT THE FINAL HINGE LOC
12658C      NEED TO DECREASE TIME STEP AND TRY AGAIN
12659C
12660      130 TINCRC = TINCRC / 2.0
12661      BADXFG = 1
12662      WRITE (*,160) A, XH
12663C
12664C      END IF (2% OF FINAL HINGE LOC)
12665C
12666      140 GO TO 150
12667C
12668C      END IF (XH REACHED FINAL HINGE LOC)
12669C
12670      150 RETURN
12671C
12672C      FORMAT STATEMENTS
12673C
12674      160 FORMAT ('HINGE LOCATION HAS OVERSHOT FINAL HINGE LOCATION'
12675      & / ' FINAL HINGE LOCATION = ', G15.8,
12676      & / ' HINGE IS AT ', G15.8 /
12677      & / ' TIME INCREMENT HAS BEEN HALVED--CASE WILL BE RERUN')
12678      170 FORMAT ('HINGE LOCATION IS NEGATIVE--CASE IS TERMINATED'
12679      & / ' CHECK INPUT DATA VALUES')
12680C
12681      END

```


AD-A161 907

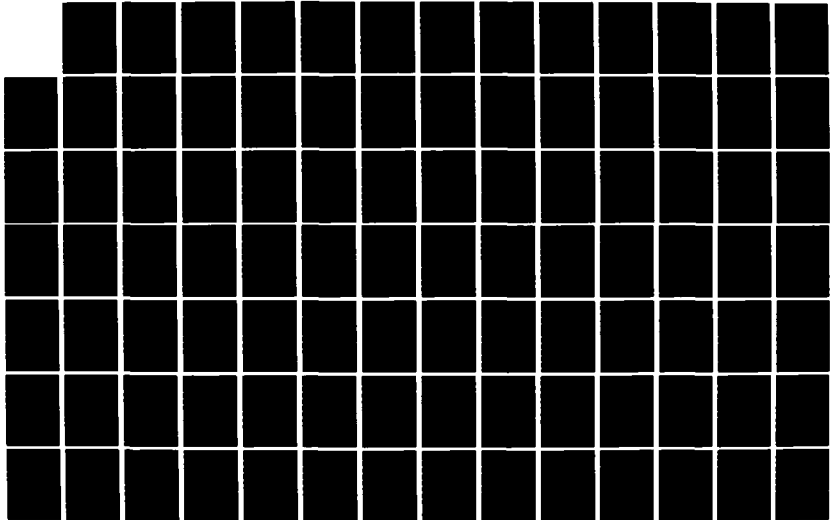
USAF/SCEEE (UNITED STATES AIR FORCE/SOUTHEASTERN CENTER 5/12
FOR ELECTRICAL EN. (U) SOUTHEASTERN CENTER FOR
ELECTRICAL ENGINEERING EDUCATION INC S... W D PEELE

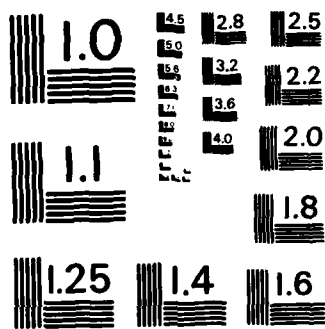
UNCLASSIFIED

MAR 85 AFOSR-TR-85-0904 F49620-82-C-0035

F/G 9/3

NL





MICROCOPY RESOLUTION TEST CHART
NATIONAL BUREAU OF STANDARDS-1963-A

JJJ
12682
12683C
12684C
12685C
12686C
12687C
12688C
12689C
12690C
12691C
12692C
12693C
12694C
12695C
12696C
12697C
12698C
12699C
12700C
12701C
12702C
12703C
12704C
12705C
12706C
12707C
12708C
12709C
12710C
12711C
12712C
12713C
12714C
12715C
12716C
12717C
12718C
12719C
12720C
12721C
12722C
12723C
12724C
12725C
12726C
12727C
12728
12729
12730
12731

SUBROUTINE RUNGEK

THIS SUBROUTINE SOLVES FIRST AND SECOND ORDER SIMULTANEOUS DIFFERENTIAL EQUATIONS USING THE RUNGE-KUTTA FOURTH-ORDER METHOD.

THE FIRST ORDER SOLUTIONS OF THE DIFFERENTIAL EQUATIONS OF THE HIGHEST ORDER (WHICH CAN BE FIRST OR SECOND) ARE STORED IN THE ARRAY CALLED Y. THE FINAL SOLUTIONS FOR THE DIFFERENTIAL EQUATIONS (WHICH ARE ACTUALLY THE FIRST ORDER RESULTS STORED IN THE ARRAY, Y) ARE IN THE ARRAY U, WITH MATCHING SUBSCRIPT.

THE ARRAY, ARG, HOLDS THE VALUES TO BE USED IN EACH STEP OF COMPUTING THE FUNCTION. THE FIRST ELEMENT OF ARG, ARG(1), IS ALWAYS USED FOR THE TIME ARGUMENT, T.

THE ARRAYS, DX AND DXDX, ARE USED FOR THE VALUES OF THE FIRST AND SECOND ORDER CHANGE (DELTA) DETERMINED FOR EACH VARIABLE BY THE RUNGE-KUTTA METHOD. THESE ARE ADDED TO EACH ELEMENT OF Y AND U, RESPECTIVELY, TO DETERMINE THE NEW VALUES OF THE VARIABLES AT THE END OF THE TIME STEP.

THIS SUBROUTINE CALLS THE SUBPROCEDURE, COMP, WHICH ACTUALLY COMPUTES THE PROPER FUNCTIONS AT EACH POINT OF THE RUNGE-KUTTA CALCULATION.

THE ARRAYS, A0, A1, A2, AND A3, HOLD THE INTERMEDIATE RESULTS OF THE RUNGE-KUTTA CALCULATION, SHOWING THE VALUE OF EACH FUNCTION AT EACH POINT OF THE CALCULATION. THESE VALUES ARE COMBINED TO FORM THE VALUES OF THE ARRAYS, DX AND DXDX, ACCORDING TO THE RUNGE-KUTTA FORMULA.

FOR FURTHER INFORMATION ON THE METHOD USED HERE, THE READER IS DIRECTED TO THE TEXT, INTRODUCTION TO NUMERICAL ANALYSIS BY HILDEBRAND (NEW YORK MCGRAW-HILL, 1956), PP. 233-239.

THIS SUBROUTINE IS CALLED BY THE PROCEDURE, TSTEP. IT CALLS THE SUBPROCEDURE, COMP.

INTEGER BADXFG, BPFLAG, BRHFG, DONEFG, EOFLAG, FLGX, FLGY,
& BRHFG1
COMMON / FLAGS / BADXFG, BPFLAG, BRHFG, DONEFG, EOFLAG,
& IERRFG, LOADFG, MECHFG, M1STFG, NCONFG, FLGX, FLGY,

```

JJJ
12732      &      BRHFG1
12733      COMMON / INPUTS / BLEN, BHGT, HREF, BIGW, RATLD, ZO,
12734      &      TCASE, D, F, Q, Q1, COVER, TE, SIGMAC, SIGMAR, SMALLN,
12735      &      WAVEFN
12736      COMMON / CONC / A, ALPHA, AR, BIGD, BIGL, EX1, EX2, EY1,
12737      &      EY2, EZ1, EZ2, RHOR, RHOC, SMALLN, TAU, TCR, TINCRC,
12738      &      TMAX, TPRINT
12739      COMMON / RESULT / DELTA, PE, T, THETA, THETAD, VEL, WF,
12740      &      WK, WP, BIGX, XH
12741C
12742C
12743      DIMENSION Y(5), U(2), DX(5), DXDX(2), A0(5), A1(5), A2(5),
12744      &      A3(5), ARG(5)
12745C
12746C
12747C      INITIALIZE VALUES OF 1ST AND 2ND ORDER EQUATIONS
12748C
12749      Y(1) = VEL
12750      U(1) = DELTA
12751      Y(2) = THETAD
12752      U(2) = THETA
12753      Y(3) = WF
12754      Y(4) = WP
12755      Y(5) = PE
12756C
12757C      SET UP ARGUMENTS FOR FIRST STEP OF RUNGE-KUTTA
12758C
12759      ARG(1) = T
12760      ARG(2) = DELTA
12761      ARG(3) = VEL
12762      ARG(4) = THETA
12763      ARG(5) = THETAD
12764      CALL COMP(ARG, A0)
12765C
12766C      SET UP ARGUMENTS FOR THE SECOND STEP
12767C
12768      HALFTI = 0.5 * TINCRC
12769      ARG(1) = T + HALFTI
12770      ARG(2) = DELTA + HALFTI * VEL
12771      ARG(3) = VEL + 0.5 * A0(1)
12772      ARG(4) = THETA + HALFTI * THETAD
12773      ARG(5) = THETAD + 0.5 * A0(2)
12774      CALL COMP(ARG, A1)
12775C
12776C      SET UP ARGUMENTS FOR THE THIRD STEP
12777C
12778      ARG(2) = DELTA + HALFTI * VEL + 0.5 * HALFTI * A0(1)
12779      ARG(3) = VEL + 0.5 * A1(1)
12780      ARG(4) = THETA + HALFTI * THETAD + 0.5 * HALFTI * A0(2)
12781      ARG(5) = THETAD + 0.5 * A1(2)

```

```

JJJ
12782 CALL COMP(ARG, A2)
12783C
12784C SET UP ARGUMENTS FOR THE FOURTH AND LAST STEP
12785C
12786 ARG(1) = T + TINCR
12787 ARG(2) = DELTA + TINCR * VEL + HALFTI * A1(1)
12788 ARG(3) = VEL + A2(1)
12789 ARG(4) = THETA + TINCR * THETAD + HALFTI * A1(2)
12790 ARG(5) = THETAD + A2(2)
12791 CALL COMP(ARG, A3)
12792C
12793C PUT PIECES TOGETHER
12794C
12795 DO 100 I = 1, 2
12796 DXDX(I) = TINCR * Y(I) + TINCR * (A0(I) + A1(I) + A2(I)) /
12797 6.0
12798 100 U(I) = U(I) + DXDX(I)
12799C
12800 DO 110 I = 1, 5
12801 DX(I) = (A0(I) + 2.0 * A1(I) + 2.0 * A2(I) + A3(I)) / 6.0
12802 110 Y(I) = Y(I) + DX(I)
12803C
12804C COMPUTATION COMPLETE
12805C
12806 VEL = Y(1)
12807 DELTA = U(1)
12808 THETAD = Y(2)
12809 THETA = U(2)
12810 WF = Y(3)
12811 WP = Y(4)
12812 PE = Y(5)
12813C
12814 RETURN
12815 END

```

JJJ
12816
12817C
12818C
12819C
12820C
12821C
12822C
12823C
12824C
12825C
12826C
12827C
12828C
12829C
12830C
12831C
12832C
12833C
12834C
12835C
12836C
12837C
12838C
12839
12840
12841
12842
12843
12844
12845
12846
12847
12848
12849
12850
12851
12852
12853
12854
12855
12856
12857
12858
12859
12860
12861C
12862C
12863C
12864C
12865

SUBROUTINE COMP(ARG, AA)

THIS SUBROUTINE ACTUALLY COMPUTES ONE OF EIGHT POSSIBLE SETS OF FUNCTIONS WHICH DESCRIBE THE SIMULTANEOUS DIFFERENTIAL EQUATIONS BEING SOLVED FOR EACH TIME STEP. THE SET OF EQUATIONS USED DEPENDS ON THE TYPE OF CASE AND TYPE OF LOAD AS WELL AS THE CURRENT STATE (OR MECHANISM) OF THE CASE.

THE INPUT AND OUTPUT PARAMETER ARRAYS ARE DEFINED AS FOLLOWS

ARG INPUT TO THE PROCEDURE, CONTAINS THE ARGUMENTS TO BE USED IN COMPUTING THE FUNCTIONS
AA OUTPUT RESULTS TO BE RETURNED TO THE CALLING PROCEDURE, RUNGEK.

IT USES THE SYSTEM LIBRARY ROUTINE, EXP. THIS ROUTINE IS CALLED BY THE RUNGE-KUTTA SUBPROCEDURE, RUNGEK.

EXTERNAL F1B0, F1P0, FXB0, FXP0, FY0, PXY, PYX
INTEGER BADXFG, BPFLAG, BRHFG, DONEFG, EOFLAG, FLGX, FLGY,
: BRHFG1
COMMON / FLAGS / BADXFG, BPFLAG, BRHFG, DONEFG, EOFLAG,
: IERRFG, LOADFG, MECHFG, M1STFG, NCONFG, FLGX, FLGY,
: BRHFG1
COMMON / COMPS / ATHED1, ATHED2, APEDOT, AWFDOT, DELDOT,
: PEDOT, THEDT1, THEDT2, THEDT3, WFDOT, WPDOT
COMMON / INPUTS / BLEN, BHGT, HREF, BIGW, RATLD, Z0,
: TCASE, D, F, Q, Q1, COVER, TE, SIGMAC, SIGMAR, SMALLN,
: WAVEFN
COMMON / CONC / A, ALPHA, AR, BIGD, BIGL, EX1, EX2, EY1,
: EY2, EZ1, EZ2, RHOR, RHOC, SMALLN, TAU, TCR, TINC, T
: THAX, TPRINT
COMMON / RESULT / DELTA, PE, T, THETA, THETAD, VEL, WF,
: WK, WP, BIGX, XH
COMMON / CONSTS / ACUBE, AFOUR, ARSQ, ARSZP1, ARZSP1,
: ARZP1, ARZS, ASQ, B, BIGRB, BIGMU, DELTAK, EPSLNU,
: FOURTH, HALF, ONEHZ, ONEPZ, SIXTH, THETU1, THIRD,
: TWELFH, W, Z, ZB, ZCUBE, ZFOUR, ZSQ
COMMON / RES4 / PU, H
DIMENSION ARG(5), AA(5)

DETERMINE FTNT

CALL FT(ARG(1), FTNT)

```

JJJ
12866C
12867C      IF FIRST TIME OR SECOND TIME THROUGH THIS ROUTINE
12868C
12869      IF (M1STFG .EQ. 0) GO TO 100
12870C
12871C      THEN, TO AVOID ZERO DIVISION AND TO INITIALIZE
12872C      THE FIRST TIME STEP FOR THE RUNGE-KUTTA METHOD,
12873C      SET THE SECOND AND FOURTH ARGUMENTS SUCH THAT
12874C      CURRX WILL REFLECT THE VALUE OF THE ORIGINAL
12875C      HINGE LOCATION. THIS WILL BE DONE THE FIRST AND
12876C      SECOND TIME THE PROCEDURE COMP IS CALLED
12877C      IS, FOR THE CALCULATION OF THE FIRST TWO PARA-
12878C      METERS OF THE RUNGE-KUTTA FOR THE FIRST TIME
12879C      STEP ONLY.
12880C
12881      ARG(2) = XH
12882      ARG(4) = 1.0
12883      M1STFG = M1STFG - 1
12884C
12885C      ELSE CONTINUE
12886C      END IF (1ST OR SECOND TIME THRU)
12887C
12888C
12889C      CASE ON LOAD-, MECHANISM-, & BEAM-PLATE-FLAGS
12890C
12891      100 IF (BPFLAG .EQ. 1 .AND. LOADFG .EQ. 1 .AND. MECHFG .EQ. 1)
12892      &      THEN
12893C
12894C      UNIFORM LOAD CASES
12895C
12896C      THIS IS A BEAM CASE, MECHANISM 1, UNIFORM LOAD
12897C
12898      CURRX = 1.0
12899      AA(1) = 0.0
12900      AA(2) = FTNT * THEDT1 - ATHED2
12901      AA(3) = FTNT * ARG(5) * AMFDOT
12902      AA(4) = WPDOT * ARG(5)
12903      AA(5) = APEDOT * ARG(5)
12904C
12905      ELSEIF (BPFLAG.EQ.1.AND.LOADFG.EQ.1.AND.MECHFG.EQ.2) THEN
12906C
12907C      THIS IS A BEAM CASE, MECHANISM 2, UNIFORM LOAD
12908C
12909      CURRX = ARG(2) / (A * ARG(4))
12910      AA(1) = FTNT * DELDOT - DELTAK
12911      AA(2) = (FTNT * THEDT1 - THEDT2) / CURRX - THEDT3 /
12912      &      (CURRX ** 3)
12913      AA(3) = FTNT * ARG(5) * WFDOT * CURRX * PU * (1.0 - CURRX *
12914      &      HALF)
12915      AA(4) = WPDOT * ARG(5)

```

```

JJJ
12866C
12867C           IF FIRST TIME OR SECOND TIME THROUGH THIS ROUTINE
12868C
12869           IF (M1STFG .EQ. 0) GO TO 100
12870C
12871C           THEN, TO AVOID ZERO DIVISION AND TO INITIALIZE
12872C           THE FIRST TIME STEP FOR THE RUNGE-KUTTA METHOD,
12873C           SET THE SECOND AND FOURTH ARGUMENTS SUCH THAT
12874C           CURRX WILL REFLECT THE VALUE OF THE ORIGINAL
12875C           HINGE LOCATION. THIS WILL BE DONE THE FIRST AND
12876C           SECOND TIME THE PROCEDURE COMP IS CALLED
12877C           IS, FOR THE CALCULATION OF THE FIRST TWO PARA-
12878C           METERS OF THE RUNGE-KUTTA FOR THE FIRST TIME
12879C           STEP ONLY.
12880C
12881           ARG(2) = XH
12882           ARG(4) = 1.0
12883           M1STFG = M1STFG - 1
12884C
12885C           ELSE CONTINUE
12886C           END IF (1ST OR SECOND TIME THRU)
12887C
12888C
12889C           CASE ON LOAD-, MECHANISM-, & BEAM-PLATE-FLAGS
12890C
12891           100 IF (BPFLAG .EQ. 1 .AND. LOADFG .EQ. 1 .AND. MECHFG .EQ. 1)
12892           &       THEN
12893C
12894C           UNIFORM LOAD CASES
12895C
12896C           THIS IS A BEAM CASE, MECHANISM 1, UNIFORM LOAD
12897C
12898           CURRX = 1.0
12899           AA(1) = 0.0
12900           AA(2) = FTNT * THEDT1 - ATHED2
12901           AA(3) = FTNT * ARG(5) * AMFDOT
12902           AA(4) = WPDOT * ARG(5)
12903           AA(5) = APEDOT * ARG(5)
12904C
12905           ELSEIF(BPFLAG.EQ.1.AND.LOADFG.EQ.1.AND.MECHFG.EQ.2)THEN
12906C
12907C           THIS IS A BEAM CASE, MECHANISM 2, UNIFORM LOAD
12908C
12909           CURRX = ARG(2) / (A * ARG(4))
12910           AA(1) = FTNT * DELDOT - DELTAK
12911           AA(2) = (FTNT * THEDT1 - THEDT2) / CURRX - THEDT3 /
12912           &       (CURRX ** 3)
12913           AA(3) = FTNT * ARG(5) * WFDOT * CURRX * PU * (1.0 - CURRX *
12914           &       HALF)
12915           AA(4) = WPDOT * ARG(5)

```



```

JJJ
12916 AA(5) = PEDOT * ARG(5) * CURRX * (1.0 - CURRX * HALF)
12917C
12918 ELSEIF(BPFLAG.EQ.2.AND.LOADFG.EQ.1.AND.MECHFG.EQ.1)THEN
12919C
12920C     THIS IS A PLATE CASE, MECHANISM 1, UNIFORM LOAD
12921C
12922     CURRX = 1.0
12923     AA(1) = 0.0
12924     AA(2) = FTNT * ATHED1 - ATHED2
12925     AA(3) = FTNT * ARG(5) * AMFDOT
12926     AA(4) = WPDOT * ARG(5)
12927     AA(5) = APEDOT * ARG(5)
12928C
12929 ELSEIF(BPFLAG.EQ.2.AND.LOADFG.EQ.1.AND.MECHFG.EQ.2)THEN
12930C
12931C     THIS IS A PLATE CASE, MECHANISM 2, UNIFORM LOAD
12932C
12933     CURRX = ARG(2) / (A * ARG(4))
12934     CURRXS = CURRX * CURRX
12935     AA(1) = FTNT * DELDOT - DELTAK
12936     AA(2) = ((FTNT*THEDT1-THEDT2) * (ARZS * (HALF - CURRX *
12937 &     THIRD) + HALF - Z * CURRX * THIRD) - THEDT3 / CURRXS) /
12938 &     (CURRX * (ARZSP1 * THIRD - Z * FOURTH * CURRX *
12939 &     ARZP1))
12940     AA(3) = FTNT * ARG(5) * WPDOT * CURRX * (1.0 - CURRX *
12941 &     HALF * ONEPZ + Z * THIRD * CURRXS)
12942     AA(4) = WPDOT * ARG(5)
12943     AA(5) = PEDOT * ARG(5) * CURRX * (1.0 - ONEPZ * HALF *
12944 &     CURRX + Z * THIRD * CURRXS)
12945C
12946 ELSEIF(BPFLAG.EQ.1.AND.LOADFG.EQ.2.AND.MECHFG.EQ.1)THEN
12947C
12948C     BLAST LOAD CASES
12949C
12950C     THIS IS A BEAM CASE, MECHANISM 1, BLAST LOAD
12951C
12952     CURRX = 1.0
12953     AA(1) = 0.0
12954     AA(2) = FTNT * ATHED1 - ATHED2
12955     AA(3) = FTNT * ARG(5) * AMFDOT
12956     AA(4) = WPDOT * ARG(5)
12957     AA(5) = APEDOT * ARG(5)
12958C
12959 ELSEIF(BPFLAG.EQ.1.AND.LOADFG.EQ.2.AND.MECHFG.EQ.2)THEN
12960C
12961C     THIS IS A BEAM CASE, MECHANISM 2, BLAST LOAD
12962C
12963     CURRX = ARG(2) / (A * ARG(4))
12964     CALL DBLNC(CURRX*A, A, F1B0, PXY, ANS1)
12965     CALL DBLNC(0, CURRX*A, FXB0, PXY, ANSX)

```

```

JJJ
12966 AA(1) = FTNT * DELDOT * ANS1 / (1.0 - CURRX) - DELTAK
12967 AA(2) = (FTNT * ANSX * THEDT1 - THEDT3) / CURRX ** 3 -
12968 & THEDT2 / CURRX
12969 AA(3) = FTNT * 4.0 * ARG(5) * (ANSX + A * CURRX * ANS1)
12970 AA(4) = WPDOT * ARG(5)
12971 AA(5) = PEDOT * ARG(5) * CURRX * (1.0 - CURRX * HALF)
12972C
12973 ELSEIF(BPFLAG.EQ.2.AND.LOADFG.EQ.2.AND.MECHFG.EQ.1)THEN
12974C
12975C THIS IS A PLATE CASE, MECHANISM 1, BLAST LOAD
12976C
12977 CURRX = 1.0
12978 AA(1) = 0.0
12979 AA(2) = FTNT * ATHED1 - ATHED2
12980 AA(3) = FTNT * ARG(5) * AWFDOT
12981 AA(4) = WPDOT * ARG(5)
12982 AA(5) = APEDOT * ARG(5)
12983C
12984 ELSEIF(BPFLAG.EQ.2.AND.LOADFG.EQ.2.AND.MECHFG.EQ.2)THEN
12985C
12986C THIS IS A PLATE CASE, MECHANISM 2, BLAST LOAD
12987C
12988 CURRX = ARG(2) / (A * ARG(4))
12989 CURRXS = CURRX * CURRX
12990 CALL DBLNC(0, CURRX*A, FXPO, PXY, ANSX)
12991 CALL DBLNC(0, ZB*CURRX, FYPO, PYX, ANSY)
12992 CALL DBLNC(CURRX*A, A, F1PO, PXY, ANS1)
12993 AA(1) = FTNT * ANS1 * DELDOT / ((1.0-CURRX) * (1.0 - Z *
12994 & CURRX)) - DELTAK
12995 AA(2) = (FTNT * (ANSX + ANSY) * THEDT1 - THEDT3 - THEDT2 *
12996 & CURRXS * (ARZS * (HALF - CURRX * THIRD) + HALF - Z *
12997 & CURRX * THIRD)) / (CURRX ** 3 * (THIRD * ARZSP1 -
12998 & CURRX * Z * FOURTH * ARZP1))
12999 AA(3) = FTNT * 4.0 * ARG(5) * (A * ANSY / ZB + ANSX +
13000 & CURRX * A * ANS1)
13001 AA(4) = WPDOT * ARG(5)
13002 AA(5) = PEDOT * ARG(5) * CURRX * (1.0 - ONEPZ * HALF *
13003 & CURRX + Z * THIRD * CURRXS)
13004C
13005C END CASE ON LOADFG, BPFLAG & MECHFG
13006C
13007 END IF
13008C
13009C MULTIPLY EACH TERM BY THE TIME STEP INCREMENT
13010C
13011 DO 110 I = 1, 5
13012 110 AA(I) = TINC * AA(I)
13013C
13014 RETURN
13015 END

```

JJJ
13016
13017C
13018C
13019C
13020C
13021C
13022C
13023C
13024C
13025C
13026C
13027C
13028C
13029C
13030C
13031C
13032C
13033C
13034C
13035C
13036C
13037C
13038C
13039C
13040C
13041C
13042C
13043C
13044C
13045C
13046C
13047C
13048C
13049C
13050C
13051C
13052C
13053C
13054C
13055C
13056C
13057C
13058C
13059C
13060C
13061C
13062C
13063C
13064C
13065C

SUBROUTINE DBLNC(A1, B1, FTN1, FTN2, ANS)

THIS STAND-ALONE PROCEDURE PERFORMS A DOUBLE INTEGRATION USING A COMPOSITE NEWTON-COTES (N=2) FORMULATION.

THIS COMPOSITE NEWTON-COTES (N=2) METHOD COMPUTES THE INTEGRAL AS FOLLOWS

$$\text{INTEGRAL}(X0, X2K) F(X)DX = (H/3)[F(X0) + 4F(X1) + 2F(X2) + \dots + 4F(X2K-1) + F(X2K)]$$

WHERE 2K IS THE NUMBER OF INTERVALS TAKEN OVER THE FUNCTION IN DETERMINING THE INTEGRAL AND H IS THE SIZE OF THE EQUALLY SPACED INTERVALS, THAT IS, H IS EQUAL TO THE RANGE OF INTEGRATION DIVIDED BY THE QUANTITY 2K. FOR MORE INFORMATION, THE READER IS DIRECTED TO THE TEXT ANALYSIS BY HILDEBRAND, PP. 71,76.

FOR THIS PARTICULAR ROUTINE, WE HAVE ARBITRARILY CHOSEN 2K = 20, WHICH CAUSES H = (X2K-X0)/20.

THE PARAMETERS ARE DEFINED AS FOLLOWS

A1 LOWER LIMIT OF OUTER INTEGRAL
B1 UPPER LIMIT OF OUTER INTEGRAL
FTN1 F(X1), INSIDE OF OUTER INTEGRAL
FTN2 F(X1,X2), INSIDE OF INNER INTEGRAL
ANS THE ANSWER OR RESULT.

THE SUBPROCEDURE, FTN1, COMPUTES THE VALUE OF THE OUTER INTEGRAL AND RETURNS IT AS THE ARRAY, ANSF1. ALSO COMPUTED ARE THE LIMITS OF THE INNER INTEGRAL WHICH MAY DEPEND ON THE VALUE OF THE VARIABLE IN THE OUTER INTEGRAL. THE ARGUMENTS PASSED TO THIS PROCEDURE ARE DEFINED AS FOLLOWS

X1 CURRENT VALUE OF OUTER VARIABLE
A2 LOWER LIMIT OF INNER INTEGRAL
B2 UPPER LIMIT OF INNER INTEGRAL
ANSF1 ANSWER OR RESULT.

THE SUBPROCEDURE, FTN2, COMPUTES THE INNER PORTION OF THE INNER INTEGRAL, RETURNING THE VALUES TO THE ARRAY, ANSF2, AT EACH STEP OF THE INNER INTEGRAL. THE ARGUMENTS PASSED TO THIS PROCEDURE ARE DEFINED BELOW

X1 CURRENT VALUE OF OUTER VARIABLE
X2 CURRENT VALUE OF INNER VARIABLE
ANSF2 ANSWER OR RESULT.

```

      JJJ
13066      EXTERNAL FTN1, FTN2
13067      DIMENSION COEFF(020)
13068      DATA COEFF/1., 4., 2., 4., 2., 4., 2., 4., 2., 4., 2., 4.,
13069      &      2., 4., 2., 4., 2., 4., 2., 4., 1./
13070C
13071C
13072C          DETERMINE VALUE OF H1
13073C
13074      H1 = (B1 - A1) / 20.
13075C
13076C          SET OUTER INTEGRAND SUMS TO ZERO
13077C
13078      S1 = 0.0
13079C
13080C          DO OUTER INTEGRAL
13081C
13082      DO 110 I1 = 0, 20
13083C
13084          X1 = A1 + I1 * (B1 - A1) / 20.
13085          CALL FTN1(X1, A2, B2, ANSF1)
13086C
13087          H2 = (B2 - A2) / 20.
13088          S2 = 0.0
13089C
13090C          DO INNER INTEGRAL
13091C
13092          DO 100 I2 = 0, 20
13093              X2 = A2 + I2 * (B2 - A2) / 20.
13094              CALL FTN2(X1, X2, ANSF2)
13095      100  S2 = S2 + COEFF(I2) * ANSF2
13096C
13097      110  S1 = S1 + COEFF(I1) * ANSF1 * (H2 / 3.) * S2
13098C
13099C          PUT ANSWER TOGETHER
13100C
13101      ANS = (H1 / 3.0) * S1
13102C
13103      RETURN
13104      END

```

```

JJJ
13105 SUBROUTINE FXB0(X, A2, B2, ANS)
13106C
13107C THIS PROCEDURE DETERMINES THE VALUES OF THE OUTER
13108C PART OF THE DOUBLE INTEGRAL WITH RESPECT TO X
13109C WHICH IS USED TO COMPUTE THE PRESSURE FUNCTION.
13110C
13111C
13112 COMMON / CONSTS / ACUBE, AFOUR, ARSQ, ARSZP1, ARZSP1,
13113 & ARZP1, ARZS, ASQ, B, BIGRB, BIGMU, DELTAK, EPSLNU,
13114 & FOURTH, HALF, ONEHZ, ONEPZ, SIXTH, THETU1, THIRD,
13115 & TWELFH, W, Z, ZB, ZCUBE, ZFOUR, ZSQ
13116 COMMON / INPUTS / BLEN, BHGT, HREF, BIGW, RATLD, ZO,
13117 & TCASE, D, F, Q, Q1, COVER, TE, SIGMAC, SIGMAR, SMALLN,
13118 & WAVEFN
13119 COMMON / CONC / A, ALPHA, AR, BIGD, BIGL, EX1, EX2, EY1,
13120 & EY2, EZ1, EZ2, RHOR, RHOC, SMALLM, TAU, TCR, TINCR,
13121 & TMAX, TPRINT
13122C
13123C
13124 A2 = 0
13125 B2 = B
13126 GO TO 100
13127C
13128C
13129 ENTRY FXP0(X, A2, B2, ANS)
13130C
13131 A2 = ZB * X / A
13132 B2 = B
13133 GO TO 100
13134C
13135C
13136 ENTRY FXP1(X, A2, B2, ANS)
13137C
13138 A2 = X * AR
13139 B2 = B
13140C
13141C
13142 100 ANS = X
13143C
13144 RETURN
13145 END

```

```

JJJ
13146 SUBROUTINE FYPO(Y, A2, B2, ANS)
13147C
13148C THIS PROCEDURE DETERMINES THE VALUE OF THE OUTER
13149C PART OF THE DOUBLE INTEGRAL WITH RESPECT TO Y
13150C WHICH IS USED TO COMPUTE THE PRESSURE FUNCTION.
13151C
13152C
13153 COMMON / CONSTS / ACUBE, AFOUR, ARSQ, ARSZP1, ARZSP1,
13154 & ARZP1, ARZS, ASQ, B, BIGRB, BIGMU, DELTAK, EPSLNU,
13155 & FOURTH, HALF, ONEMZ, ONEPZ, SIXTH, THETU1, THIRD,
13156 & TWELFH, W, Z, ZB, ZCUBE, ZFOUR, ZSQ
13157 COMMON / INPUTS / BLEN, BHGT, HREF, BIGW, RATLD, Z0,
13158 & TCASE, D, F, Q, Q1, COVER, TE, SIGMAC, SIGMAR, SMALLN,
13159 & WAVEFN
13160 COMMON / CONC / A, ALPHA, AR, BIGD, BIGL, EX1, EX2, EY1,
13161 & EY2, EZ1, EZ2, RHOR, RHOC, SMALLM, TAU, TCR, TINC,
13162 & TMAX, TPRINT
13163C
13164C
13165 A2 = A * Y / ZB
13166 B2 = A
13167 GO TO 100
13168C
13169C
13170 ENTRY FYP1(Y, A2, B2, ANS)
13171C
13172 A2 = Y / AR
13173 B2 = A
13174C
13175C
13176 100 ANS = Y
13177C
13178 RETURN
13179 END

```

```

JJJ
13180 SUBROUTINE F1B0(X, A2, B2, ANS)
13181C
13182C THIS PROCEDURE DETERMINES THE VALUES OF THE OUTER
13183C PART OF THE DOUBLE INTEGRAL WITH RESPECT TO X
13184C WHICH IS USED TO COMPUTE THE PRESSURE FUNCTION.
13185C
13186C
13187 COMMON / CONSTS / ACUBE, AF0UR, ARSQ, ARSZP1, ARZSP1,
13188 & ARZP1, ARZS, ASQ, B, BIGRB, BIGMU, DELTAK, EPSLNU,
13189 & FOURTH, HALF, ONEMZ, ONEPZ, SIXTH, THETU1, THIRD,
13190 & TWELFH, W, Z, ZB, ZCUBE, ZFOUR, ZSQ
13191 COMMON / INPUTS / BLEN, BHGT, HREF, BIGW, RATLD, ZO,
13192 & TCASE, D, F, Q, Q1, COVER, TE, SIGMAC, SIGMAR, SMALLN,
13193 & WAVEFN
13194 COMMON / CONC / A, ALPHA, AR, BIGD, BIGL, EX1, EX2, EY1,
13195 & EY2, EZ1, EZ2, RHOR, RHOC, SMALLH, TAU, TCR, TINCR,
13196 & TMAX, TPRINT
13197 COMMON / RESULT / DELTA, PE, T, THETA, THETAD, VEL, WF,
13198 & WK, WP, BIGX, XH
13199C
13200C
13201 A2 = 0
13202 B2 = B
13203 GO TO 110
13204C
13205C
13206 ENTRY F1P0(X, A2, B2, ANS)
13207C
13208 A2 = ZB * XH / A
13209 B2 = B
13210 GO TO 110
13211C
13212C
13213 ENTRY F1P1(Y, A2, B2, ANS)
13214C
13215 B2 = A
13216 GO TO 100
13217C
13218C
13219 ENTRY F1P2(Y, A2, B2, ANS)
13220C
13221 B2 = Y / AR
13222 100 RADIX = BIGRB ** 2 - (B - Y) ** 2
13223 IF (RADIX .LT. 0.0) RADIX = 0.0
13224 A2 = A - SQRT(RADIX)
13225 GO TO 110
13226C
13227C
13228 ENTRY F1P3(X, A2, B2, ANS)
13229C

```

```
JJJ
13230 RADIX = B1GRB ** 2 - (A - X) ** 2
13231 IF (RADIX .LT. 0.0) RADIX = 0.0
13232 A2 = B - SQRT(RADIX)
13233 B2 = X * AR
13234C
13235 110 ANS = 1.0
13236C
13237 RETURN
13238 END
```


JJJ
13239
13240C
13241C
13242C
13243C
13244C
13245C
13246
13247C
13248
13249

SUBROUTINE FZ(Z1, Z2, ANS)

THIS PROCEDURE DETERMINES THE VALUE OF THE INNER
PART OF THE DOUBLE INTEGRAL WITH RESPECT TO Z2,
WHERE $F(Z1, Z2) = Z2$.

ANS = Z2

RETURN
END

JJJ
13250
13251C
13252C
13253C
13254C
13255C
13256C
13257
13258C
13259
13260

SUBROUTINE FZSQ(Z1, Z2, ANS)

THIS PROCEDURE DETERMINES THE VALUE OF THE INNER
PART OF THE DOUBLE INTEGRAL WITH RESPECT TO Z2,
WHERE $F(Z1, Z2) = Z2 * Z2$.

ANS = Z2 ** 2

RETURN
END

```

JJJ
13261 SUBROUTINE PXY(X, Y, ANS)
13262
13263C THIS PROCEDURE DETERMINES THE VALUES OF THE INNER
13264C PART OF THE DOUBLE INTEGRAL WHICH IS USED TO
13265C COMPUTE THE PRESSURE FUNCTION. THE NORMAL ENTRY,
13266C PXY, IS PERFORMING THE INNER INTEGRAL WITH
13267C RESPECT TO Y, WHILE THE SECOND ENTRY, PYX,
13268C PERFORMS THE INNER INTEGRAL WITH RESPECT TO X.
13269C SIMILARILY, THE ENTRY, FZPXY, COMPUTES THE INNER
13270C INTEGRAL OF Y*P(X,Y) WITH RESPECT TO Y, AND THE
13271C ENTRY, FZPYX, COMPUTES X*P(X,Y) WITH RESPECT TO X.
13272C
13273C
13274 INTEGER BADXFG, BPFLAG, BRHFG, DONEFG, EOFLAG, FLGX, FLGY,
13275 & BRHFG1
13276 COMMON / FLAGS / BADXFG, BPFLAG, BRHFG, DONEFG, EOFLAG,
13277 & IERRFG, LOADFG, MECHFG, MISTFG, NCONFG, FLGX, FLGY,
13278 & BRHFG1
13279 COMMON / CONSTS / ACUBE, AFOUR, ARSQ, ARSZP1, ARZSP1,
13280 & ARZP1, ARZS, ASQ, B, BIGRB, BIGMU, DELTAK, EPSLNU,
13281 & FOURTH, HALF, DNEMZ, ONEPZ, SIXTH, THETU1, THIRD,
13282 & TWELFH, W, Z, ZB, ZCUBE, ZFOUR, ZSQ
13283 COMMON / INPUTS / BLEN, BHGT, HREF, BIGW, RATLD, ZO,
13284 & TCASE, D, F, Q, Q1, COVER, TE, SIGNAC, SIGMAR, SMALLN,
13285 & WAVEFN
13286 COMMON / CONC / A, ALPHA, AR, BIGD, BIGL, EX1, EX2, EY1,
13287 & EY2, EZ1, EZ2, RHOR, RHOC, SMALLM, TAU, TCR, TINCR,
13288 & TMAX, TPRINT
13289 COMMON / RESULT / DELTA, PE, T, THETA, THETAD, VEL, WF,
13290 & WK, WP, BIGX, XH
13291 COMMON / RES4 / PU, H
13292C
13293C
13294C ENTRY PYX(Y, X, ANS)
13295C
13296C TERM = 1.0
13297C GO TO 100
13298C
13299C ENTER HERE FOR DOUBLE INTGRAL--1ST MOMENT
13300C
13301C ENTRY FZPXY(X, Y, ANS)
13302C
13303C TERM = Y
13304C GO TO 100
13305C
13306C
13307C ENTRY FZPYX(Y, X, ANS)
13308C
13309C TERM = X
13310C

```

```
JJJ
13311C
13312C      COMPUTE P(X,Y) WITH VALUES GIVEN
13313C
13314      100 ANS = PU
13315C
13316C
13317      ANS = ANS * TERM
13318C
13319      RETURN
13320      END
```

JJJ
13321
13322C
13323C
13324C
13325C
13326C
13327C
13328C
13329C
13330C
13331C
13332C
13333C
13334C
13335C
13336C
13337C
13338C
13339C
13340C
13341C
13342C
13343C
13344C
13345C
13346C
13347C
13348C
13349C
13350C
13351C
13352C
13353C
13354C
13355C
13356C
13357C
13358
13359
13360
13361
13362C
13363C
13364C
13365C
13366
13367C
13368C
13369C
13370

SUBROUTINE SINGNC(A1, B1, FTN, ANS)

THIS STAND-ALONE PROCEDURE PERFORMS A SINGLE INTEGRATION USING A COMPOSITE NEWTON-COTES (N=2) FORMULATION.

THIS COMPOSITE NEWTON-COTES (N=2) METHOD COMPUTES THE INTEGRAL AS FOLLOWS

$$\text{INTEGRAL}(X0, X2K) F(X)DX = (H/3)[F(X0) + 4F(X1) + 2F(X2) + \dots + 4F(X2K-1) + F(X2K)]$$

WHERE 2K IS THE NUMBER OF INTERVALS TAKEN OVER THE FUNCTION IN DETERMINING THE INTEGRAL AND H IS THE SIZE OF THE EQUALLY SPACED INTERVALS, THAT IS, H IS EQUAL TO THE RANGE OF INTEGRATION DIVIDED BY THE QUANTITY 2K. FOR MORE INFORMATION, THE READER IS DIRECTED TO THE TEXT ANALYSIS BY HILDEBRAND, PP. 71,76.

FOR THIS PARTICULAR ROUTINE, WE HAVE ARBITRARILY CHOSEN 2K = 20, WHICH CAUSES H = (X2K-X0)/20.

THE PARAMETERS ARE DEFINED AS FOLLOWS

A1 LOWER LIMIT OF INTEGRAL
B1 UPPER LIMIT OF INTEGRAL
FTN F(X1), INSIDE OF INTEGRAL
ANS THE ANSWER OR RESULT.

THE SUBPROCEDURE, FTN, COMPUTES THE INNER PORTION OF THE INTEGRAL, RETURNING THE VALUES TO THE ARRAY, ANSF1, AT EACH STEP OF THE INTEGRAL. THE ARGUMENTS PASSED TO THIS PROCEDURE ARE DEFINED BELOW

X1 CURRENT VALUE OF VARIABLE
ANSF1 ANSWER OR RESULT.

EXTERNAL FTN

DIMENSION COEFF(020)

DATA COEFF/1., 4., 2., 4., 2., 4., 2., 4., 2., 4., 2., 4., 2., 4., 2., 4., 2., 4., 2., 4., 1./

DETERMINE VALUE OF H1

H1 = (B1 - A1) / 20.

SET INTEGRAND SUMS TO ZERO

S1 = 0.0

```
    JJJ
13371C
13372C      DO INTEGRAL
13373C
13374      DO 100 I1 = 0, 20
13375C
13376          X1 = A1 + I1 * (B1 - A1) / 20.
13377          CALL FTN(X1, ANSF1)
13378C
13379 100 S1 = S1 + COEFF(I1) * ANSF1
13380C
13381C      PUT ANSWER TOGETHER
13382C
13383      ANS = (H1 / 3.0) * S1
13384C
13385      RETURN
13386      END
```

```

    JJJ
13387   SUBROUTINE FT(T, FTNT)
13388C
13389C   THIS PROCEDURE DETERMINES THE VALUE OF F(T) FOR
13390C   THE GIVEN VALUE OF T. IT IS USED IS DETERMINING
13391C   THE INTEGRAL OF F(T) FROM T=0 TO T=TCR WHICH IS
13392C   USED TO COMPUTE IBAR.
13393C
13394C
13395   COMMON / INPUTS / BLEN, BHGT, HREF, BIGW, RATLD, ZO,
13396   & TCASE, D, F, Q, Q1, COVER, TE, SIGMAC, SIGMAR, SMALLN,
13397   & WAVEFN
13398   COMMON / CONC / A, ALPHA, AR, BIGD, BIGL, EX1, EX2, EY1,
13399   & EY2, EZ1, EZ2, RHOR, RHOC, SMALLM, TAU, TCR, TINC,
13400   & TMAX, TPRINT
13401C
13402C   DETERMINE F(T) USING
13403C   CASE ON RATIO OF T
13404C
13405C
13406   FTNT = 0.0
13407   TRATIO = T / TAU
13408   IF (TRATIO .LE. 1.0 .AND. WAVEFN .EQ. 1.0) FTNT = (1.0 -
13409   & TRATIO) * EXP(-ALPHA*TRATIO)
13410   IF (TRATIO .LE. 1.0 .AND. WAVEFN .EQ. 2.0) FTNT = 1.0
13411C
13412   RETURN
13413   END

```

```

JJJ
13414 SUBROUTINE PRINTR
13415C
13416C THIS SUBROUTINE PRINTS THE LINE OF RESULTS FOR THE
13417C TIME, T. IT IS CALLED BY THE SUBPROCEDURES, TZERO
13418C AND TSTEP. IT CALLS SUBPROCEDURE, PAGE, TO HEAD A
13419C NEW PAGE, IF THE CURRENT LINE COUNT FOR THE
13420C PRINTED PAGE EXCEEDS THE MAXIMUM NUMBER OF LINES
13421C PER PAGE.
13422C
13423C
13424 COMMON / PRINTS / LITTLN, MAXLIN, NF, NUMLIN, NUMPAG,
13425 & NWAVER, STEPCT
13426 CHARACTER FLAG*1, TIMNOW*10, TITLE*75, TODAY*10, TYPE*5
13427 COMMON / PRINTC / FLAG, TIMNOW, TITLE, TODAY, TYPE
13428 COMMON / RESULT / DELTA, PE, T, THETA, THETAD, VEL, WF,
13429 & WK, WP, BIGX, XH
13430C
13431C
13432C IF LINE COUNT EXCEEDS MAX/PAGE
13433C THEN HEAD A NEW PAGE
13434C
13435C IF (NUMLIN .GE. MAXLIN) CALL PAGE
13436
13437C ELSE CONTINUE
13438C END IF (LINECOUNT)
13439C
13440C PRINT LINE OF RESULTS, ADD 1 TO LINE COUNT,
13441C AND ZERO STEP COUNT
13442C
13443C WRITE (*,100) T, THETA, FLAG, VEL, DELTA, WF, WP, WK, XH
13444 NUMLIN = NUMLIN + 1
13445 STEPCT = 0.0
13446
13447C RETURN
13448
13449C
13450C FORMAT STATEMENT
13451C
13452 100 FORMAT (1X, G14.8, 2X, G14.8, A1, 6(2X,G14.8))
13453C
13454 END

```


JJJ
13455C
13456C
13457C
13458
13459C
13460C
13461C
13462C
13463C
13464C
13465C
13466C
13467C
13468C
13469
13470
13471
13472
13473
13474
13475
13476
13477
13478C
13479
13480
13481
13482
13483
13484
13485
13486
13487
13488
13489
13490
13491
13492
13493C
13494C
13495C
13496C
13497
13498C
13499C
13500C
13501
13502
13503C
13504

SUBROUTINE PAGE

THIS SUBROUTINE PUSHES THE OUTPUT TO A NEW PAGE AND PROVIDES ALL HEADINGS, INCLUDING CURRENT DATE AND TIME. IT IS CALLED BY THE SUBPROCEDURE, RWDATA, TO PRINT HEADINGS FOR THE FIRST PAGE OF THE NEW CASE AND BY THE SUBPROCEDURE, PRINTR, FOR EACH ADDITIONAL PAGE OF INPUT THAT FOLLOWS FOR THAT CASE. IT CALLS NO SUBPROCEDURES.

```
INTEGER BADXFG, BPFLAG, BRHFG, DONEFG, EOFLAG, FLGX, FLGY,  
& BRHFG1  
COMMON / FLAGS / BADXFG, BPFLAG, BRHFG, DONEFG, EOFLAG,  
& IERRFG, LOADFG, MECHFG, M1STFG, NCONFG, FLGX, FLGY,  
& BRHFG1  
COMMON / PRINTS / LITTLN, MAXLIN, NF, NUMLIN, NUMPAG,  
& NWAVER, STEPCT  
CHARACTER FLAG*1, TIMNOW*10, TITLE*75, TODAY*10, TYPE*5  
COMMON / PRINTC / FLAG, TIMNOW, TITLE, TODAY, TYPE  
CHARACTER TYPSTP(2)*7, TYPWAV(2)*12, TYPSTB(3)*32,  
& TYPLOA(2)*7, TOPLIN(2, 5)*31, BLANK*1  
DATA TYPSTP/' SIMPLY', 'CLAMPED', TYPWAV/'GENERAL TIME',  
& ' SQUARE WAVE', TYPLOA/'UNIFORM', ' BLAST',  
& TYPSTB/'HORIZONTAL SLAB, EXPLOSIVE ABOVE',  
& ' VERTICAL WALL',  
& 'HORIZONTAL SLAB, EXPLOSIVE BELOW'  
DATA TOPLIN/'EDGE SHEAR CALCULATION', ' ',  
& 'LOCALIZED SHEAR FAILURE CALCULATION', 'TION',  
& 'FLEXURAL RESPONSE ASSUMING NO E', 'DGE SHEAR',  
& 'FLEXURAL RESPONSE ASSUMING NO L',  
& 'LOCALIZED SHEAR FAILURE',  
& 'FLEXURAL RESPONSE WITH SHEAR FAILURE',  
& 'ILURE MASS AND LOADING REMOVED', BLANK/' '/
```

IF WE ARE COMPLETING THE FIRST PAGE FOR CASE

IF (NUMPAG .EQ. 1) THEN

PRINT SUPPORT, WAVE, WEIGHT TYPES

```
WRITE (*,140) TYPSTP(NF), TYPWAV(NWAVER), TYPSTB(LITTLN),  
& TYPLOA(LOADFG)
```

ELSEIF (NUMPAG.GT.2) THEN

```

JJJ
13505C
13506C          PRINT * MESSAGE AT BOTTOM OF PAGE
13507C
13508          WRITE (*,150)
13509C
13510          END IF
13511C
13512C          ADD ONE TO PAGE NUMBER AND
13513C          PRINT TOP TWO LINES ON NEXT PAGE
13514C
13515          NUMPAG = NUMPAG + 1
13516C
13517          IF (NUMPAG .EQ. 1) THEN
13518          WRITE (*,100) TYPE, BLANK, BLANK, NUMPAG, TITLE, TODAY,
13519          &      TIMNOW
13520          WRITE (*,130)
13521C
13522C          ELSEIF (BRHFG.LT.2) THEN
13523          WRITE (*,100) TYPE, (TOPLIN(I,LOADFG+2), I = 1, 2), NUMPAG,
13524          &      TITLE, TODAY, TIMNOW
13525          WRITE (*,140) TYPSTP(NF), TYPWAV(NWAVEF), TYPSTB(LITTLN),
13526          &      TYPSTO(LOADFG)
13527          WRITE (*,120)
13528          NUMLIN = 12
13529
13530C          ELSE
13531          WRITE (*,100) TYPE, TOPLIN(1,5), TOPLIN(2,5), NUMPAG,
13532          &      TITLE, TODAY, TIMNOW
13533          WRITE (*,140) TYPSTP(NF), TYPWAV(NWAVEF), TYPSTB(LITTLN),
13534          &      TYPSTO(LOADFG)
13535          WRITE (*,120)
13536          NUMLIN = 12
13537
13538C          END IF
13539
13540C
13541C          RETURN
13542
13543C
13544C          FORMAT STATEMENTS
13545C
13546C          100 FORMAT ('1' / '0' / 11X, 'CALCULATIONS ON A CONCRETE ',
13547          &      A5, 5X, A31, A30, 14X, 'PAGE', I3 // 7X, A75, 25X,
13548          &      A10, 4X, A9)
13549          110 FORMAT ('0' / '0', 2X, 'BREACH RADIUS', 4X, 'I BAR', 10X,
13550          &      'I CRITICAL' / )
13551          120 FORMAT ('0' / 5X, 'TIME', 10X, 'THETA', 10X, 'MIDPT. VEL.',
13552          &      , 4X, 'MIDPT. DELTA', 4X, 'PRESSURE WORK', 3X,
13553          &      'PLASTIC WORK', 3X, 'KINETIC ENERGY', 3X,

```

```
JJJ
13555      &      'HINGE LOCATION' / 3X, '(SECONDS)', 5X, '(RADIAN)',
13556      &      9X, '(IN./SEC.)', 6X, '(INCHES)', 1X,
13557      &      3(6X, '(IN.-LBS.)'), 7X, '(INCHES)' / )
13558 130 FORMAT ('0' / '0', 2X, 'INPUT VALUES')
13559 140 FORMAT ('0', 10X, A7, '-SUPPORTED', 10X, A12, ' FUNCTION'
13560      &      , 10X, A32, 10X, A7, ' LOAD')
13561 150 FORMAT ('0', 20X,
13562      &      'AN ASTERISK INDICATES THAT A REINFORCING ELEMENT HAS '
13563      &      , ' FRACTURED')
13564C
13565      END
```

APPENDIX C

LIST OF SYMBOLS FOR COMPUTER PROGRAM

APPENDIX C

A0	INITIAL POROSITY OF CONCRETE
A1-A3	HUGONIOT COEFFICIENTS FOR CONCRETE(PSI)
AL	INCIDENT ANGLE ARRAY(DEG)
APAR	VARIABLE POROSITY OF CONCRETE
APPIMP	AVERAGE IMPULSE ON AN AREA(PSI-S)
AREA	REFERENCE AREA ON PLATE (IN**2)
B0-B3	HUGONIOT COEFFICIENTS FOR CONCRETE
BHGT	WIDTH OF PLATE OR WIDTH OF BEAM(IN)
BIGD	DIAMETER OF EXPLOSIVE CHARGE(IN)
BIGIBR	IMPULSE TO CAUSE BREACH (PSI-S)
BIGICR	CRITICAL IMPULSE FOR BREACHING(PSI-S)
BIGL	LENGTH OF EXPLOSIVE CHARGE(IN)
BIGW	WEIGHT OF EXPLOSIVE CHARGE (LB)
BLEN	LENGTH OF PLATE OR SPAN OF BEAM(IN)
BRHFG1	FLAG TO INDICATE BREACH OF CONCRETE
C	LOCAL SPEED OF SOUND AT PRESSURE(IN/S)
C0	BULK SPEED OF SOUND FOR CONCRETE(IN/S)
CL	BULK SPEED OF SOUND FOR VOIDLESS CONCRETE(IN/S)
CL-C2	PARAMETERS TO COMPUTE AVERAGE PRESSURE
COVER	CONCRETE COVER THICKNESS(IN)
CP	FRAGMENTATION PARAMETER FOR CASE MATERIAL
CRA	REFLECTION COEFFICIENT FOR BLAST WAVE
DP	PARAMETER TO CALCULATE AVERAGE PRESSURE
DQ	PARAMETER TO CALCULATE AVERAGE PRESSURE
DT	DIFFERENCE BETWEEN TWO ANGLES(RAD)
DX	INCREMENT FOR SPALL IN X-DIR(IN)
DY	INCREMENT FOR SPALL IN Y-DIR(IN)
F1-F2	PARAMETERS TO COMPUTE AVERAGE PRESSURE
F5	PARAMETER TO COMPUTE PRESSURE DECAY
FACT	PARAMETER TO COMPUTE AVERAGE PRESSURE
FLGX	FLAG TO INDICATE SPALL OF CONCRETE IN X-DIR
FLGY	FLAG TO INDICATE SPALL OF CONCRETE IN Y-DIR
FP	FRAGMENTATION PARAMETER
FPAR	PARAMETER FOR FRAGMENT DISTRIBUTIO (LB**HALF)
FRGIMP	AVERAGE IMPULSE FROM FRAGMENTS ON AN AREA(PSI-S)
FRGM	MASS OF FRAGMENTS IMPACTING AN AREA (LB-S**2/IN)
FRGMOM	MOMENTUM OF FRAGMENTS STRIKING AN AREA(LB-S)
FRGN	NUMBER OF FRAGMENTS IN A REFERENCE AREA
FRGT	TOTAL NUMBER OF FRAGMENTS
G	CONSTANT
GC	GURNEY CONSTANT(IN/S)
H	VARIABLE PLATE THICKNESS (IN)
HREF	INITIAL PLATE THICKNESS (IN)
P	VARIABLE SHOCK OVERPRESSURE IN CONCRETE(PSI)
P0	PEAK SIDE-ON OVERPRESSURE(PSI)
PA	INCIDENT OVERPRESSURE ARRAY(PSI)
PB	OVERPRESSURE DUE TO BLAST AND FRAGMENTS(PSI)
PE	HUGONIOT YIELD STRENGTH OF CONCRETE(PSI)
PI	CONSTANT
PM	REFERENCE POINT ON HUGONIOT OF CONCRETE(PSI)
PR	PEAK REFLECTED OVERPRESSURE(PSI)
Q	DENSITY RATIO OF FLEXURAL STEEL TO CONCRETE
Q1	DENSITY RATIO OF SHEAR STEEL TO CONCRETE

APPENDIX C

R VARIABLE DISTANCE FROM CENTER OF CHARGE(FT)
 RATLD LENGTH TO DIAMETER RATIO FOR THE EXPLOSIVE CHARGE
 REFIMP IMPULSE IN REFLECTED BLAST WAVE(PSI-S)
 RHOC MASS DENSITY OF CONCRETE (LB-S**2/IN**4)
 RHOHE WEIGHT DENSITY OF EXPLOSIVE CHARGE (LB/IN**3)
 RHOR MASS DENSITY OF STEEL (LB-S**2/IN**4)
 RI REFLECTED IMPULSE ARRAY(PSI-S)
 SIGMAC COMPRESSIVE STRENGTH OF THE CONCRETE(PSI)
 SIGMAR TENSILE STRENGTH OF THE STEEL REINFORCING(PSI)
 SS VARIABLE TENSILE STRESS AT SPALL PLANE(PSI)
 T REFERENCE TIME ON SHOCK WAVE PROFILE(S)
 T1-T6 PARAMETER TO CALCULATE AVERAGE PRESSURE
 TB DURATION OF LOADING ON AN AREA (S)
 TCASE THICKNESS OF THE METAL CASE(IN)
 TE CRITICAL TENSILE STRENGTH FOR CONCRETE(PSI)
 TF DURATION AT FAR POINT ON PLATE(S)
 TIMP TRAPPED IMPULSE IN SPALLED CONCRETE(PSI-S)
 TMOM MOMENTUM TRAPPED IN SPALLED CONCRETE
 TN DURATION AT NEAR POINT ON PLATE(S)
 TSPL TIME FOR TRAVEL FROM FREE SURFACE TO SPALL PLANE(S)
 UE PARTICLE VELOCITY OF CONCRETE AT PE(IN/S)
 UP PARTICLE VELOCITY IN LABORATORY COORDINATES(IN/S)
 US SHOCK VELOCITY IN LABORATORY COORDINATES(IN/S)
 V SPECIFIC VOLUME OF CONCRETE (IN**4/(LB-S**2))
 V0 INITIAL SPECIFIC VOLUME OF CONCRETE (IN**4/(LB-S**2))
 VE SPECIFIC VOLUME OF CONCRETE AT PE (IN**4/(LB-S**2))
 VI INITIAL FRAGMENT VELOCITY(IN/S)
 VN NORMAL IMPACT VELOCITY FOR FRAGMENTS(IN/S)
 VR VELOCITY OF FRAGMENT AT DISTANCE R(IN/S)
 VS SPECIFIC VOLUME OF VOIDLESS CONCRETE (IN**4/(LB-S**2))
 WC WEIGHT OF THE METAL CASE(LBS)
 WFRG WEIGHT OF A MEDIAN FRAGMENT(LBS)
 X SCALED DISTANCE ARRAY(FT/LB**THIRD)
 X1-X7 PARAMETERS TO COMPUTE VALUES AT PE OF CONCRETE
 X8 POSITION OF SHOCK FRONT IN PLATE (IN)
 X9 LOCATION OF SHOCK FRONT IN CONCRETE(IN)
 XB X-DIMENSION OF BREACHING IN CONCRETE(IN)
 XE COORDINATE POSITION ON PLATE (IN)
 XF X-DIMENSION FOR EFFECTS OF FRAGMENTATION(IN)
 XP ONE-HALF OF PLATE OR BEAM SPAN IN X-DIR (IN)
 XS X-DIM OF SPALL(IN)
 XSPL MAX POSSIBLE DIMENSION OF SPALLING IN THE X-DIR(IN)
 YB Y-DIMENSION OF BREACHING IN CONCRETE(IN)
 YE COORDINATE POSITION ON PLATE (IN)
 YF Y-DIMENSION FOR EFFECTS OF FRAGMENTATION(IN)
 YI COORDINATE POSITION ON PLATE (IN)
 YM MIN DIMENSION OF PLATE OR BEAM IN Y-DIR(IN)
 YP MAX DIMENSION OF PLATE OR BEAM IN Y-DIR(IN)
 YSPL MAX POSSIBLE DIMENSION OF SPALLING IN THE Y-DIR(IN)
 Z0 STANDOFF FROM PLATE TO CENTER OF CHARGE (FT)
 ZDIS SCALED DISTANCE TO POINT ON PLATE (FT/LB**THIRD)
 ZF AVERAGE DEPTH OF PENETRATION FOR FRAGMENTS(IN)

APPENDIX D

SELECTED OUTPUT OF ANALYSIS

CALCULATIONS ON A CONCRETE PLATE

PAGE 1

TEST FOR 100 POUNDS (BARE) AT Z= 0.8

PLATE LENGTH OR BEAM SPAN, IN.	(BLEN)	120.00000
PLATE HEIGHT OR BEAM WIDTH, IN.	(BHGT)	120.00000
BEAM OR PLATE THICKNESS, IN.	(H)	12.000000
EXPLOSIVE WEIGHT, LBS.	(BIGW)	100.00000
LENGTH TO DIAMETER RATIO, DIMENSIONLESS	(RATLD)	3.000000
Z0 OF EXPLOSIVE, IN.	(Z0)	3.7130000
THICKNESS OF METAL CASE, IN.	(TCASE)	0.00000000
REINFORCING DISTANCE, IN.	(D)	10.500000
SUPPORT FACTOR 1=SIMPLY, 2=CLAMPED	(F)	2.0000000
REINFORCEMENT RATIO IN TENSION, DIMENSIONLESS	(Q)	0.10000000E-01
SHEAR STIRRUP REINFORCEMENT RATIO	(Q1)	0.25000000E-02
CONCRETE COVER ON BACK FACE, IN.	(COVER)	1.5000000
TENSILE SPALLING STRENGTH, PSI.	(SPALL STRENGTH)	750.00000
CONCRETE COMPRESSIVE STRENGTH, PSI.	(SIGMAC)	5000.0000
REINFORCED STEEL YIELD STRESS, PSI.	(SIGMAR)	60000.000
WEIGHT VECTOR 0=VERT, 1=EXP BLW, -1=EXP ABV	(SMALLN)	0.00000000
WAVE FUNCTION 1=GENERAL, 2=SQUARE	(WAVEFN)	1.0000000

COMPUTED VALUES OF MATERIAL RESPONSE

LIMIT OF SPALL IN X-DIR, IN	0.00000000
LIMIT OF SPALL IN Y-DIR, IN	0.00000000
LIMIT OF BREACH IN X-DIR, IN	0.00000000
LIMIT OF BREACH IN Y-DIR, IN	0.00000000
TOTAL TRAPPED MOMENTUM, LB-S	0.00000000
IMPULSE FOR FLEXURE, PSI-MS	1.6141986
DURATION OF LOAD ON WALL, S	0.18963297E-02
AVERAGE PRESSURE ON WALL, PSI	1702.4451
EFFECTIVE WALL THICKNESS, IN	12.000000
EFFECTIVE BREACH RADIUS, IN	0.00000000

COMPUTED CONSTANT VALUES

PLATE HALF LENGTH, IN.	(B)	60.000000
RATIO OF FINAL HINGE LOC TO B, DIMENSIONLESS	(Z)	1.0000000
HINGE MOMENT, IN.-LBS./IN.	(BIGMU)	55319.922
WEIGHT PER UNIT AREA, LBS./IN.SQ.	(W)	1.0432800
ORIGINAL HINGE LOCATION, IN.	(XH)	13.488254

CLAMPED-SUPPORTED	GENERAL TIME FUNCTION
VERTICAL WALL	UNIFORM LOAD

CALCULATIONS ON A CONCRETE PLATE
 FLEXURAL RESPONSE ASSUMING NO EDGE SHEAR
 PAGE 2

TEST FOR 100 POUNDS (BARE) AT Z= 0.8

CLAMPED-SUPPORTED
 VERTICAL WALL

GENERAL TIME FUNCTION
 UNIFORM LOAD

TIME (SECONDS)	THETA (RADIAN)	MIDPT. VEL. (IN./SEC.)	MIDPT. DELTA (INCHES)
0.00000000	0.00000000	0.00000000	0.00000000
0.50000000E-03	0.12244307E-01	660.91300	0.17359172
0.99999999E-03	0.41823604E-01	1121.1029	0.62745914
0.15000000E-02	0.78739063E-01	1380.5695	1.2612407
0.20000000E-02	0.11407618	1443.6713	1.9747283
0.25000000E-02	0.14261876	1443.6713	2.6965640
0.30000001E-02	0.16517906	1443.6713	3.4183996
0.35000001E-02	0.18303673	1443.6713	4.1402352
0.40000001E-02	0.19717247	1443.6713	4.8620710
0.45000001E-02	0.20833058	1443.6713	5.5839068
0.50000002E-02	0.21707755	1443.6713	6.3057426
0.55000002E-02	0.22384774	1443.6713	7.0275784
0.60000002E-02	0.22897709	1443.6713	7.7494142
0.65000003E-02	0.23272765	1443.6713	8.4712498
0.70000003E-02	0.23530539	1443.6713	9.1930853
0.75000003E-02	0.23687304	1443.6713	9.9149208
0.80000003E-02	0.23755950	1443.6713	10.636756

MAXIMUM DEFLECTION = 10.925490 AT TIME = 0.82000001E-02

AN ASTERISK INDICATES THAT A REINFORCING ELEMENT HAS FRACTURED

CALCULATIONS ON A CONCRETE PLATE

PAGE 1

TEST FOR 100 POUNDS (CASED) AT Z= 0.8

PLATE LENGTH OR BEAM SPAN, IN.	(BLEN)	120.00000
PLATE HEIGHT OR BEAM WIDTH, IN.	(BHGT)	120.00000
BEAM OR PLATE THICKNESS, IN.	(H)	12.000000
EXPLOSIVE WEIGHT, LBS.	(BIGW)	100.00000
LENGTH TO DIAMETER RATIO, DIMENSIONLESS	(RATLD)	3.0000000
ZO OF EXPLOSIVE, IN.	(ZO)	3.7130000
THICKNESS OF METAL CASE, IN.	(TCASE)	0.25000000
REINFORCING DISTANCE, IN.	(D)	10.500000
SUPPORT FACTOR 1=SIMPLY, 2=CLAMPED	(F)	2.0000000
REINFORCEMENT RATIO IN TENSION, DIMENSIONLESS	(Q)	0.10000000E-01
SHEAR STIRRUP REINFORMENT RATIO	(Q1)	0.25000000E-02
CONCRETE COVER ON BACK FACE, IN.	(COVER)	1.5000000
TENSILE SPALLING STRENGTH, PSI.	(SPALL STRENGTH)	750.00000
CONCRETE COMPRESSIVE STRENGTH, PSI.	(SIGMAC)	5000.0000
REINFORCED STEEL YIELD STRESS, PSI.	(SIGMAR)	60000.000
WEIGHT VECTOR 0=VERT, 1=EXP BLW, -1=EXP ABV	(SMALLN)	0.00000000
WAVE FUNCTION 1=GENERAL, 2=SQUARE	(WAVEFN)	1.0000000

COMPUTED VALUES OF MATERIAL RESPONSE

LIMIT OF SPALL IN X-DIR, IN	22.332909
LIMIT OF SPALL IN Y-DIR, IN	12.761662
LIMIT OF BREACH IN X-DIR, IN	15.952078
LIMIT OF BREACH IN Y-DIR, IN	15.952078
TOTAL TRAPPED MOMENTUM, LB-S	248.59576
IMPULSE FOR FLEXURE, PSI-MS	1.8433026
DURATION OF LOAD ON WALL, S	0.18963297E-02
AVERAGE PRESSURE ON WALL, PSI	1944.0739
EFFECTIVE WALL THICKNESS, IN	11.531472
EFFECTIVE BREACH RADIUS, IN	17.313197

COMPUTED CONSTANT VALUES

PLATE HALF LENGTH, IN.	(B)	60.000000
RATIO OF FINAL HINGE LOC TO B, DIMENSIONLESS	(Z)	1.0000000
HINGE MOMENT, IN.-LBS./IN.	(BIGMU)	55319.922
WEIGHT PER UNIT AREA, LBS./IN.SQ.	(W)	1.0025461
ORIGINAL HINGE LOCATION, IN.	(XH)	13.488254

CLAMPED-SUPPORTED
VERTICAL WALL

GENERAL TIME FUNCTION
UNIFORM LOAD

CALCULATIONS ON A CONCRETE PLATE
 FLEXURAL RESPONSE ASSUMING NO EDGE SHEAR
 PAGE 2

TEST FOR 100 POUNDS (CASED) AT Z= 0.8

CLAMPED-SUPPORTED
 VERTICAL WALL

GENERAL TIME FUNCTION
 UNIFORM LOAD

TIME (SECONDS)	THETA (RADIAN)	MIDPT. VEL. (IN./SEC.)	MIDPT. DELTA (INCHES)
0.00000000	0.00000000	0.00000000	0.00000000
0.50000000E-03	0.12741798E-01	687.76617	0.18064482
0.99999999E-03	0.43522915E-01	1166.6537	0.65295307
0.15000000E-02	0.81938264E-01	1436.6627	1.3124855
0.20000000E-02	0.11871114	1502.3283	2.0549623
0.25000000E-02	0.14841341	1502.3283	2.8061264
0.30000001E-02	0.17189035	1502.3283	3.5572906
0.35000001E-02	0.19047358	1502.3283	4.3084548
0.40000001E-02	0.20518366	1502.3283	5.0596190
0.45000001E-02	0.21679513	1502.3283	5.8107833
0.50000002E-02	0.22589750	1502.3283	6.5619475
0.55000002E-02	0.23294276	1502.3283	7.3131118
0.60000002E-02	0.23828052	1502.3283	8.0642760
0.65000003E-02	0.24218347	1502.3283	8.8154399
0.70000003E-02	0.24486595	1502.3283	9.5666039
0.75000003E-02	0.24649729	1502.3283	10.317768
0.80000003E-02	0.24721164	1502.3283	11.068932

MAXIMUM DEFLECTION = 11.369397 AT TIME = 0.82000001E-02

AN ASTERISK INDICATES THAT A REINFORCING ELEMENT HAS FRACTURED

BECAUSE THIS PLATE HAS SHOWN LOCALIZED LOAD SHEAR FAILURE,
 A SECOND SET OF CALCULATIONS WILL BE DONE WITH
 BREACH AREA MASS AND LOADING REMOVED
 Z IS RESET TO 1.0, AND WE ASSUME THE PLATE TO BE IN MECHANISM 1

CALCULATIONS ON A CONCRETE PLATE
 FLEXURAL RESPONSE WITH SHEAR FAILURE MASS AND LOADING REMOVED
 PAGE 3

TEST FOR 100 POUNDS (CASED) AT Z= 0.8

CLAMPED-SUPPORTED VERTICAL WALL		GENERAL TIME FUNCTION UNIFORM LOAD	
TIME (SECONDS)	THETA (RADIAN)	MIDPT. VEL. (IN./SEC.)	MIDPT. DELTA (INCHES)
0.00000000	0.00000000	0.00000000	0.00000000
0.50000000E-03	0.64925087E-02	1479.7093	0.38955052
0.99999999E-03	0.23353608E-01	2488.4617	1.4012165
0.15000000E-02	0.46658656E-01	3026.2571	2.7995194
0.20000000E-02	0.72489015E-01	3103.3216	4.3493409
0.25000000E-02	0.98054231E-01	3032.3301	5.8832538
0.30000001E-02	0.12302785	2961.3387	7.3816710
0.35000001E-02	0.14740988	2890.3473	8.8445924
0.40000001E-02	0.17120031	2819.3559	10.272018
0.45000001E-02	0.19439914	2748.3644	11.663948
0.50000002E-02	0.21700638	2677.3730	13.020383
0.55000002E-02	0.23902202	2606.3816	14.341321
0.60000002E-02	0.26044607	2535.3902	15.626764
0.65000003E-02	0.28127852	2464.3988	16.876711
0.70000003E-02	0.30151938	2393.4073	18.091163
0.75000003E-02	0.32116865	2322.4159	19.270119
0.80000003E-02	0.34022632	2251.4245	20.413579
0.85000000E-02	0.35869239	* 2180.4331	21.521543
0.89999997E-02	0.37656687	* 2109.4417	22.594012
0.94999994E-02	0.39384975	* 2038.4502	23.630985
0.99999992E-02	0.41054104	* 1967.4588	24.632462
0.10499999E-01	0.42664073	* 1896.4674	25.598444
0.10999999E-01	0.44214883	* 1825.4760	26.528930
0.11499998E-01	0.45706533	* 1754.4846	27.423920
0.11999998E-01	0.47139024	* 1683.4931	28.283414
0.12499998E-01	0.48512355	* 1612.5017	29.107413
0.12999998E-01	0.49826527	* 1541.5103	29.895916
0.13499997E-01	0.51081540	* 1470.5189	30.648924
0.13999997E-01	0.52277392	* 1399.5275	31.366435
0.14499997E-01	0.53414085	* 1328.5360	32.048451
0.14999996E-01	0.54491618	* 1257.5446	32.694971
0.15499996E-01	0.55509994	* 1186.5532	33.305996
0.15999996E-01	0.56469207	* 1115.5618	33.881525
0.16499997E-01	0.57369263	* 1044.5704	34.421557
0.16999997E-01	0.58210158	* 973.57893	34.926095
0.17499997E-01	0.58991894	* 902.58755	35.395136
0.17999998E-01	0.59714470	* 831.59616	35.828682
0.18499998E-01	0.60377888	* 760.60477	36.226733
0.18999998E-01	0.60982145	* 689.61339	36.589287
0.19499999E-01	0.61527243	* 618.62200	36.916346
.19999999E-01	0.62013182	* 547.63062	37.207909
.20499999E-01	0.62439961	* 476.63924	37.463976

AN ASTERISK INDICATES THAT A REINFORCING ELEMENT HAS FRACTURED

CALCULATIONS ON A CONCRETE PLATE
 FLEXURAL RESPONSE WITH SHEAR FAILURE MASS AND LOADING REMOVED
 PAGE 4

TEST FOR 100 POUNDS (CASED) AT Z= 0.8

CLAMPED-SUPPORTED
 VERTICAL WALL

GENERAL TIME FUNCTION
 UNIFORM LOAD

TIME (SECONDS)	THETA (RADIAN)		MIDPT. VEL. (IN./SEC.)	MIDPT. DELTA (INCHES)
0.21000000E-01	0.62807580	*	405.64785	37.684548
0.21500000E-01	0.63116041	*	334.65646	37.869625
0.22000000E-01	0.63365341	*	263.66508	38.019205
0.22500000E-01	0.63555483	*	192.67369	38.133290
0.23000001E-01	0.63686464	*	121.68231	38.211878
0.23500001E-01	0.63758287	*	50.690925	38.254972

MAXIMUM DEFLECTION = 38.263890 AT TIME = 0.23900001E-01

AN ASTERISK INDICATES THAT A REINFORCING ELEMENT HAS FRACTURED

=

1983-84 USAF-SCEEE RESEARCH INITIATION PROGRAM

Sponsored by the

AIR FORCE OFFICE OF SCIENTIFIC RESEARCH

Conducted by the

SOUTHEASTERN CENTER FOR ELECTRICAL ENGINEERING EDUCATION

FINAL REPORT

INFRARED SPECTROSCOPY OF EXTRINSIC P-TYPE SILICON

Prepared by: Dr. Billy Covington

Academic Rank: Assistant Professor

Department and
University: Physics Department
Sam Houston University

Research Location: Air Force Materials Laboratory

Date: August 1984

Abstract

We present the initial results of a project to investigate, as a function of annealing temperature and irradiation time, the infrared optical properties of neutron transmutation doped (NTD) silicon which has been conventionally doped with gallium. Comparisons are made between the silicon:gallium absorption data and previously obtained data for other NTD silicon samples. The observation of a broadband absorption region and an unknown absorption line at 2960 cm^{-1} is discussed. Recommendations for additional research are made.

Acknowledgement

The author would like to thank the Air Force Office of Scientific Research, the Southeastern Center for Electrical Engineering, and Sam Houston State University for providing the funding for this research project. He wishes to thank graduate students Tom Gregg and Herman Trivilino for their efforts in obtaining the data.

INFRARED SPECTROSCOPY OF EXTRINSIC P-TYPE SILICON

Introduction

The development and spectral characterization of high quality extrinsic silicon material for fabrication of infrared detectors for use in missile, satellite, and aircraft imaging systems is of continuing importance to the Air Force. One area in which extensive research is presently being conducted, is in the development of methods for rendering optically and electrically inactive the residual boron present in all silicon material. The residual boron is present in sufficient concentrations (10^{12}cm^{-3}) to degrade detector efficiency and to require colder detector operating temperature. Neutron transmutation-doping of silicon is proving to be the best method for rendering the boron inactive.

The NTD process employs the (n,γ) reaction to convert ^{30}Si to ^{31}P , which then compensates the boron. Compensation involves the recombination of a phosphorous (donor) electron with a boron (acceptor) hole. The electron which then remains at the boron lattice site completes the covalent bond and thus renders the boron inactive.

A major disadvantage of the NTD process is that it produces undesirable, radiation induced defects in the silicon crystal structure. These defects produce unwanted absorption centers as well as rendering the ^{31}P optically and electrically inactive. In order to remove the radiation damage and to activate the ^{31}P , the crystal must be annealed at high temperature (800°C) for times ranging from fifteen minutes to one hour.

Covington^{1,2}, Watson and Covington³, and Kainer and Covington⁴ have initiated a study of the effects of annealing on the infrared absorption properties of neutron irradiated pure silicon, neutron irradiated silicon doped with boron, and neutron irradiated silicon doped with gallium. The work with pure silicon has provided information about the annealing temperature dependence of the optically active damage centers as well as information about damage or defect concentrations as a function of irradiation time. Information about the interaction of defects with impurities such as boron and gallium or the transmationally added phosphorous have also been obtained. The fact that thermal neutron irradiation provides a novel method for adding the impurity phosphorous to silicon via transmutation provides additional incentive for studying neutron irradiated silicon. Not only does the opportunity exist for studying lattice damage but it is also possible to study impurity interactions as a function of annealing temperature.

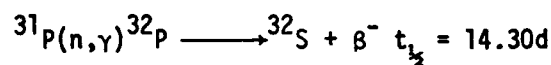
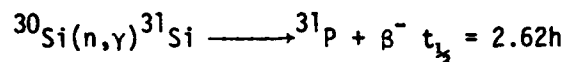
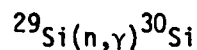
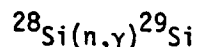
The objectives of the research were (1) to obtain high resolution absorption spectra as a function of annealing temperature for two silicon (gallium) samples neutron doped to $5 \times 10^{13} \text{ P cm}^{-3}$ and containing $3 \times 10^{16} \text{ Ga cm}^{-3}$ and (2) initiate comparison of this data to previously obtained NTD pure silicon and NTD silicon (boron) data.

NTD Theory

For many years impurities have been introduced (doped) into the silicon crystal during growth. The major problems associated with this method are (1) lack of close control of impurity concentrations (2) nonuniform distribution of the impurities and (3) difficulty in

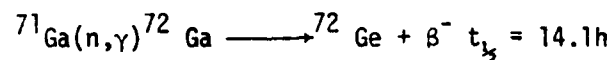
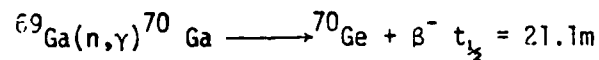
avoiding unwanted impurities which are present in the dopant material.

The possibility of doping semiconductor materials by nuclear transmutation was first suggested by Lark-Horovitz.⁵ Later Tanenbaum and Mills⁶ discussed the basic process of neutron transmutation doping in silicon. They verified experimentally that the only significant nuclear reaction for silicon in a thermal neutron flux is the (n, γ) reaction. This reaction involves the following nuclear reactions.



The ^{31}P reaction is important from the standpoint that it is the primary source of radioactivity. This is due to the extended half-life of this reaction with respect to the ^{30}Si reaction half-life.

The major nuclear reactions for gallium present in the silicon are given by



The amount of gallium lost in this process is insignificant when compared to the total gallium concentration. Thus, it is possible to assume that the gallium concentration remains essentially unchanged. The germanium, which is also produced in an insignificant amount, is optically and

electrically neutral due to its having the same valence electron configuration as silicon.

The major advantages of doping silicon by neutron transmutation are close control of the dopant concentration and uniform distribution of the dopant in the silicon crystal. The dopant concentration depends on the relative abundance of the ^{30}Si isotope, the thermal neutron flux, the thermal neutron cross section, and the time of irradiation. All of these quantities are well known or can be accurately determined so that the dopant concentration (^{31}P for silicon) can be determined to 1% or better.

The dopant uniformity is a direct result of a uniform distribution of the silicon isotopes and the long thermal neutron diffusion length as compared to typical silicon ingot size.

As previously mentioned, the major disadvantage of neutron transmutation doping is the radiation damage suffered by the silicon crystal. This damage results mainly from fast neutron collisions, gamma recoil, and beta recoil. Meese⁷ has done extensive studies of the various types of damage processes and has calculated the concentration of defects produced by each process.

The types of defects produced during irradiation are vacancies (resulting from silicon atoms being knocked from lattice sites), divacancies (two vacancies at adjacent lattice sites), vacancy complexes (multiple vacancies grouped together), interstitials, (atoms not in lattice positions), interstitial complexes (multiple grouping of interstitials), and impurity-vacancy centers (an impurity and a vacancy on adjacent lattice sites).

Previous studies^{1-4, 7-12} have shown that many of the defects listed above are infrared active in the spectral range 4000 to 200 cm^{-1} . Thus a spectral study of these defects as a function of annealing temperature provides information about defect bonding strengths, formation and destruction of defect complexes, and interactions between the defects and phosphorous or interaction with other impurities such as oxygen.

The strength of interaction between two adjacent defects, defect clusters, or between defects and other atoms in the crystal can be approximated by determining the annealing temperature at which the infrared absorption line or lines associated with the defect system disappear.

Experimental

The samples presently being studied are two float-zoned samples containing 3×10^{16} Ga cm^{-3} , 1×10^{13} B cm^{-3} and both have been NTD to 5×10^{13} P cm^{-3} . In addition, we are studying a non NTD sample that has the same gallium and boron concentrations. The sample size is $1/2" \times 1/2" \times 2$ mm thick. These samples were donated by the Air Force Materials Laboratory and were NTD at the Texas A&M University Research Reactor.

The experimental method consisted of obtaining prior to annealing the room temperature and 10K absorption spectra in the range 4000 to 200cm^{-1} for each irradiated sample. The spectra were obtained on a Perkin-Elmer Model 599B spectrophotometer. The samples were cooled in a Cryo-Cal helium refrigerator. The samples were mounted to the cold

finger with copper impregnated vacuum grease. Only one edge of the sample was greased in order to avoid stressing the sample when cooling to 10 K. The samples were annealed at 200°C for 30 minutes. This was followed by room temperature and 10 K spectral scans. The process continues in steps of 100°C until 1000°C is reached. The samples were annealed in a Lindburg tube furnace that was purged with argon gas.

Results and Conclusions

The results obtained to date agree for the most part with previous investigations.¹³⁻¹⁸ As previously reported¹¹⁻¹⁵, divacancies at 2767 and 2890 cm^{-1} are present in both unannealed NTD samples. The absorption spectra at 10 K in the region 4000 to 2000 cm^{-1} for samples 1156 and 1157 (NTD) are shown in Figures 1 and 2. The broad feature at 3200 cm^{-1} in both figures is due to water vapor which has condensed as ice on the sample surface. The absorption spectrum at 40 K for sample 1156 is shown in Figure 3. Comparison with Figure 1 shows that the strength of the absorption lines is certainly temperature dependent as is expected for an electronic excitation absorption process.

The absorption spectrum for sample 1159 (no NTD) is shown in Figure 4. Once again the broad feature near 3200 cm^{-1} is present. The overall increase in absorption with increasing wavelength is an unexpected phenomena. The spectra for sample 1159 in the spectral region 2000 to 1400 cm^{-1} and 1400 to 200 cm^{-1} are shown in Figures 5 and 6, respectively.

We are unsure of how to explain the tremendously broad band absorption taking place in this sample and not occurring in the NTD samples. At 10 K and with only 10^{16} gallium atoms present, we do not believe the absorption is due to free carriers. One possibility is that we are seeing

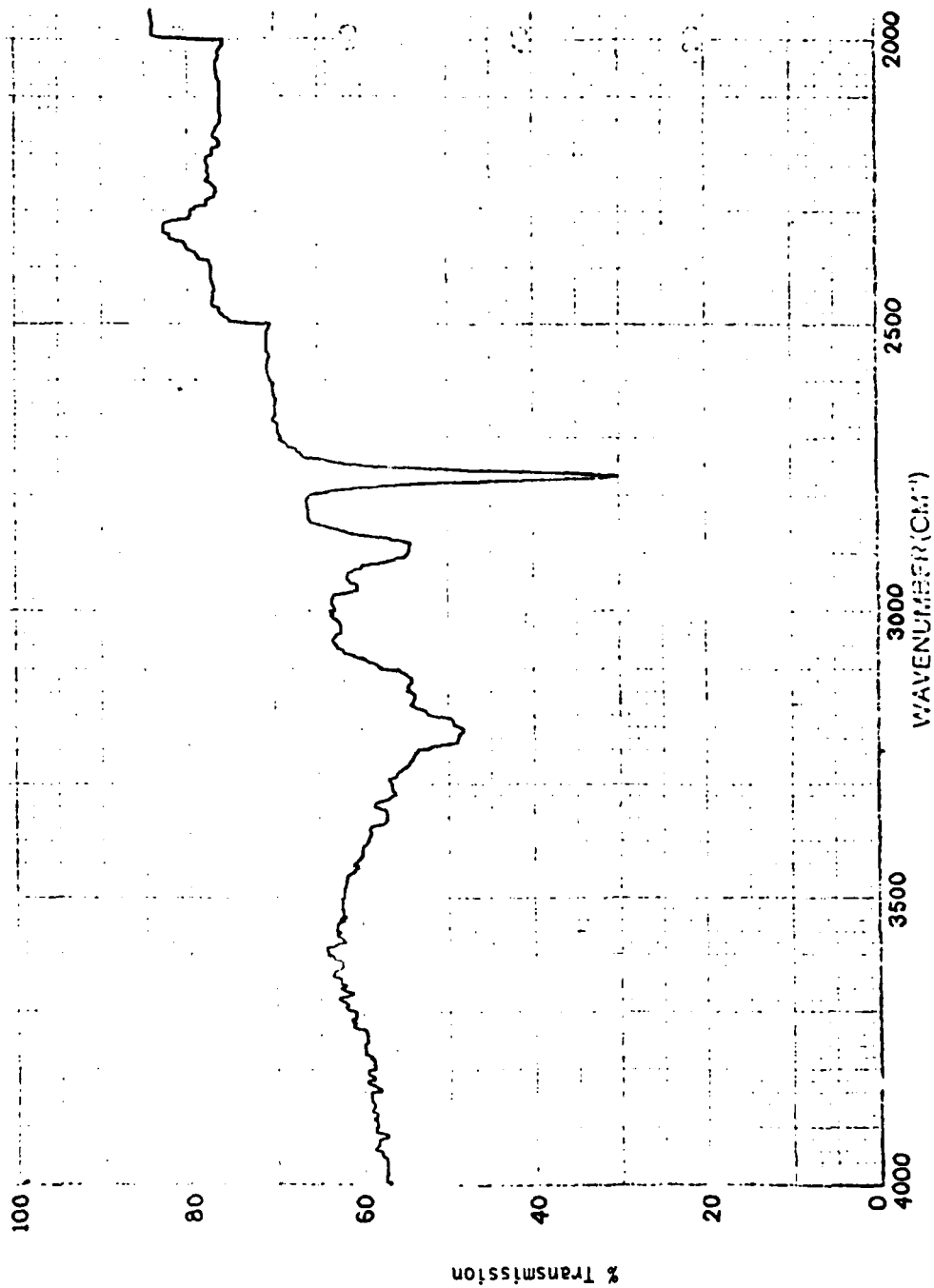


Figure 1. Absorption Spectrum for sample 1156
No anneal. T = 10K.

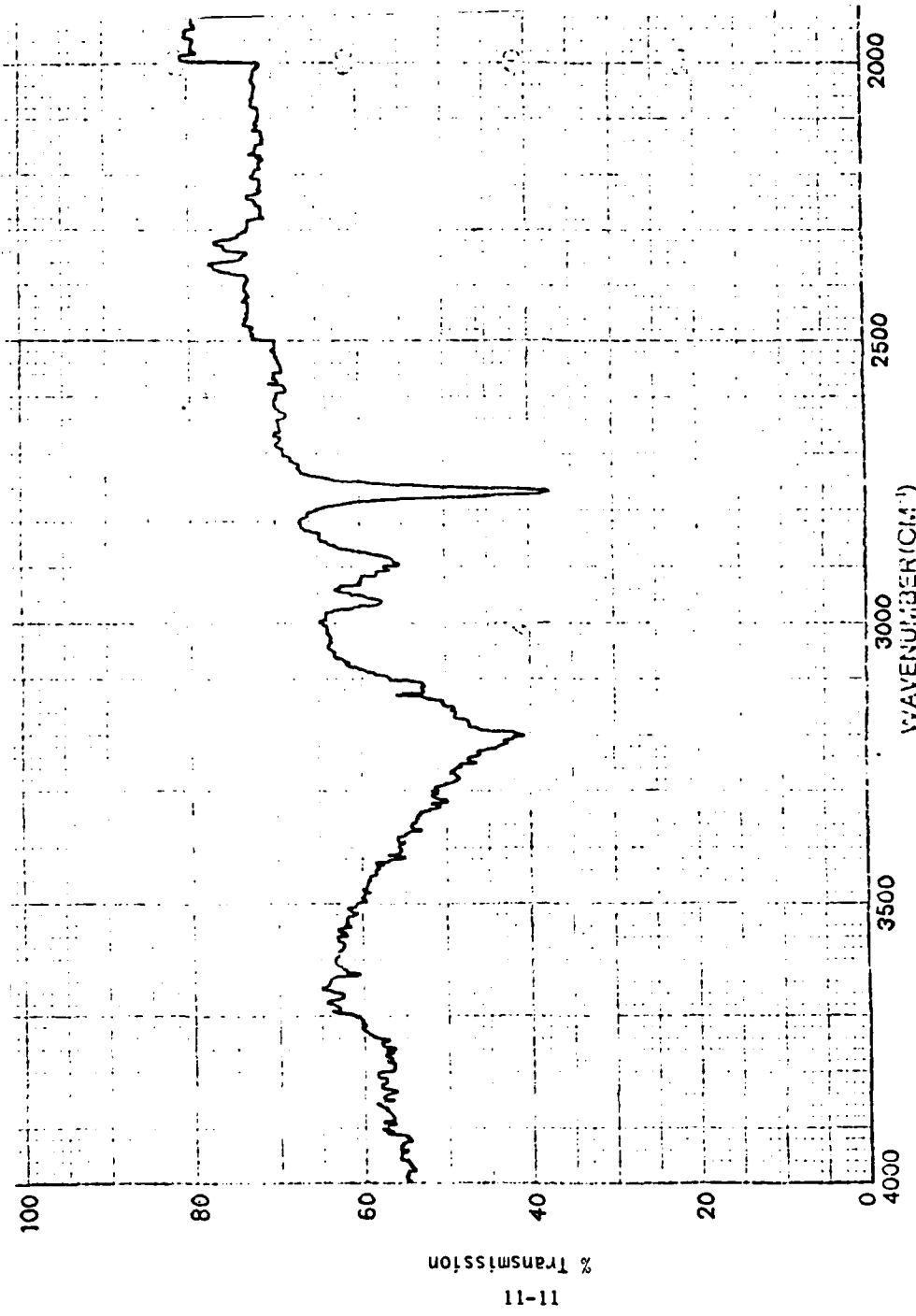


Figure 2. Absorption Spectrum for sample 1157.
No anneal. T = 10K

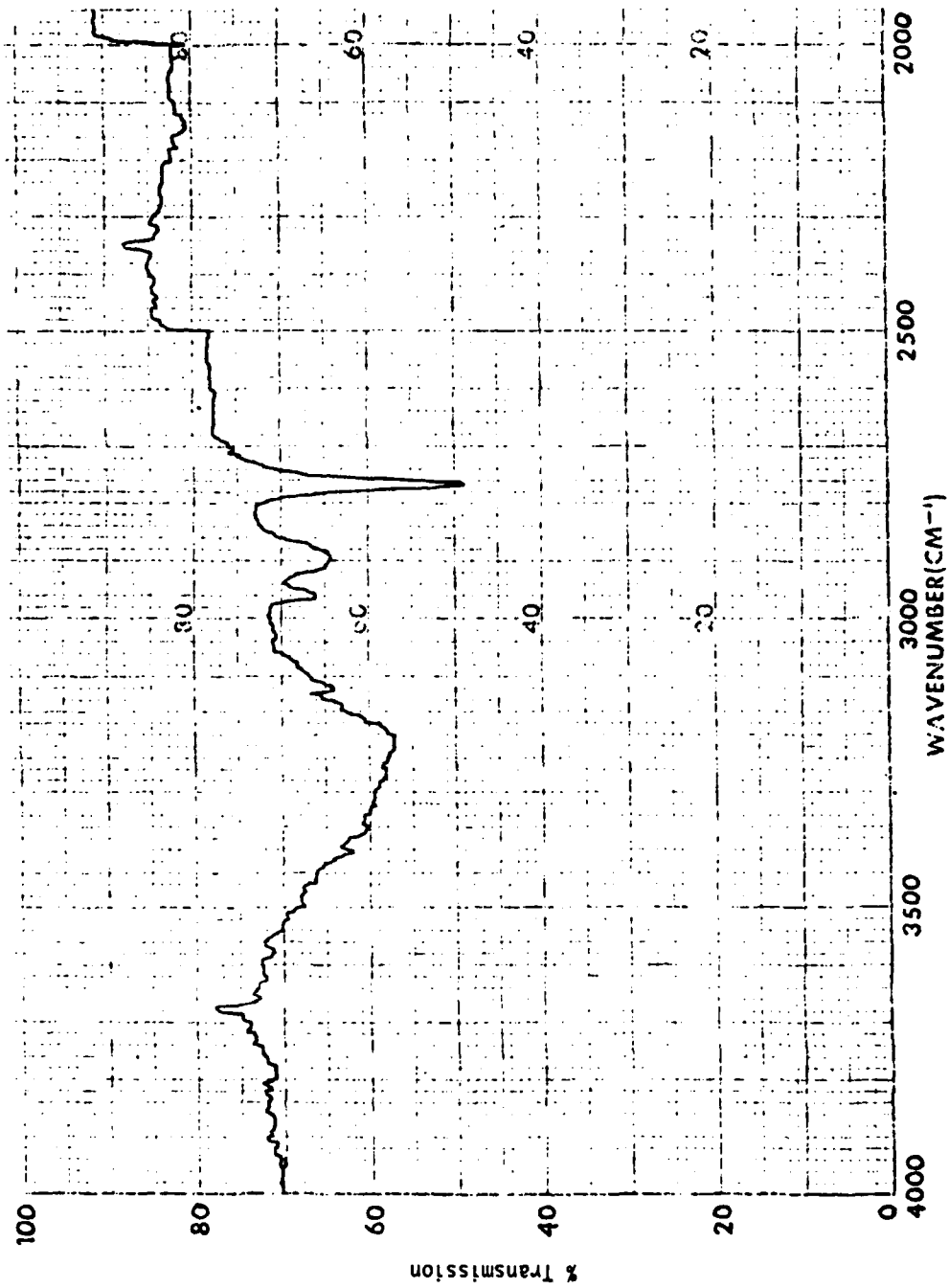


Figure 3. Absorption Spectrum for sample 1156.
No anneal. T = 40K

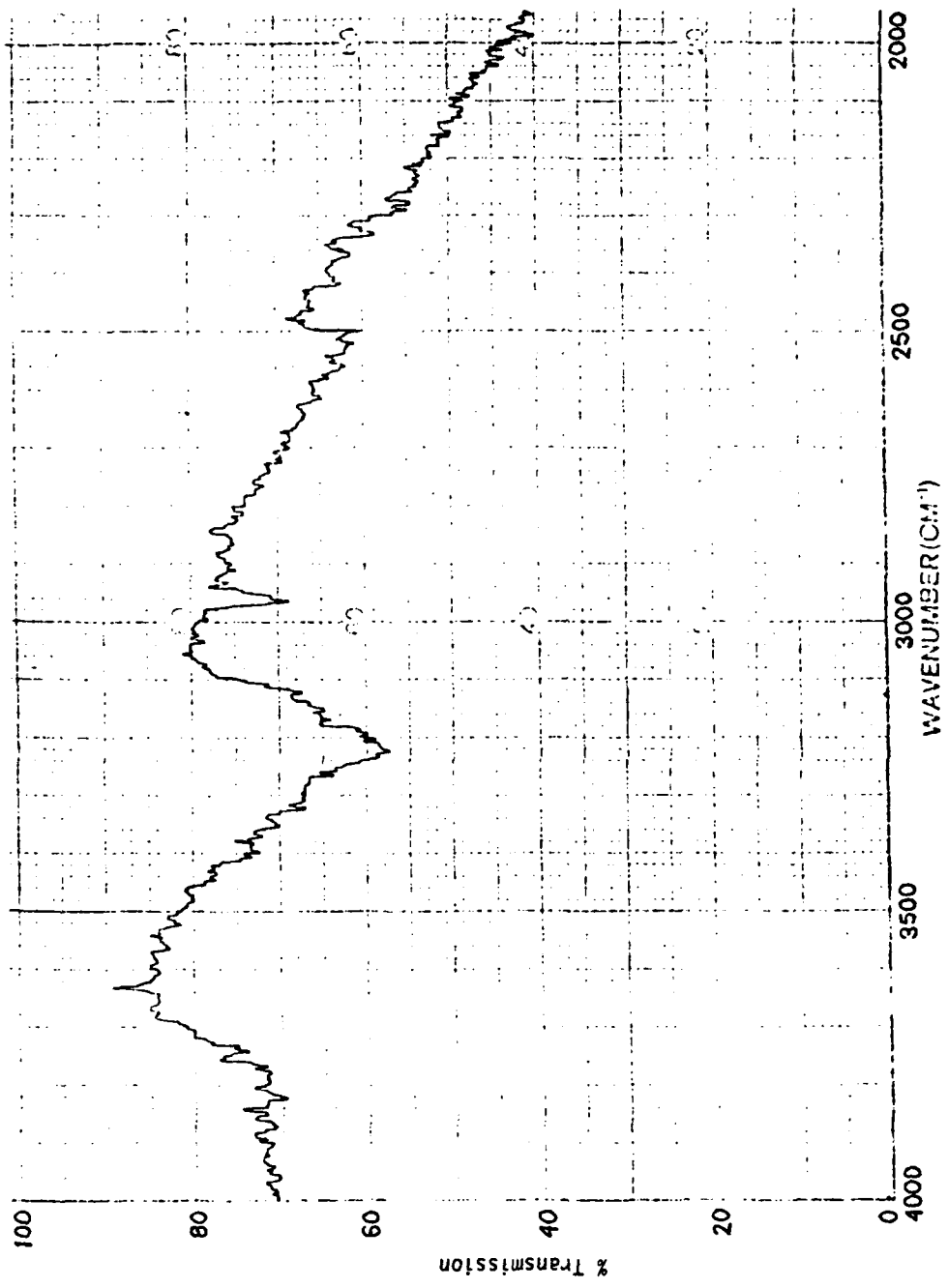


Figure 4. Absorption Spectrum for sample 1159.
No anneal. T = 10K

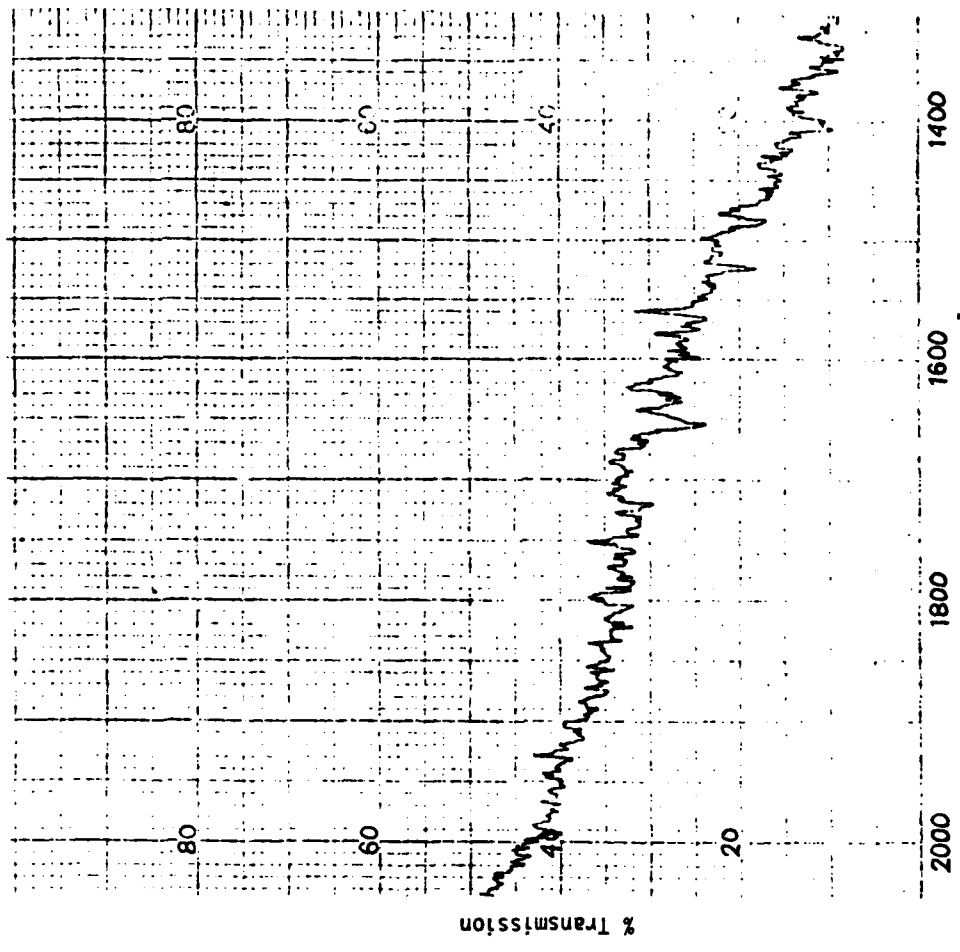


Figure 5. Absorption Spectrum for sample 1159.
No anneal. T = 10K.

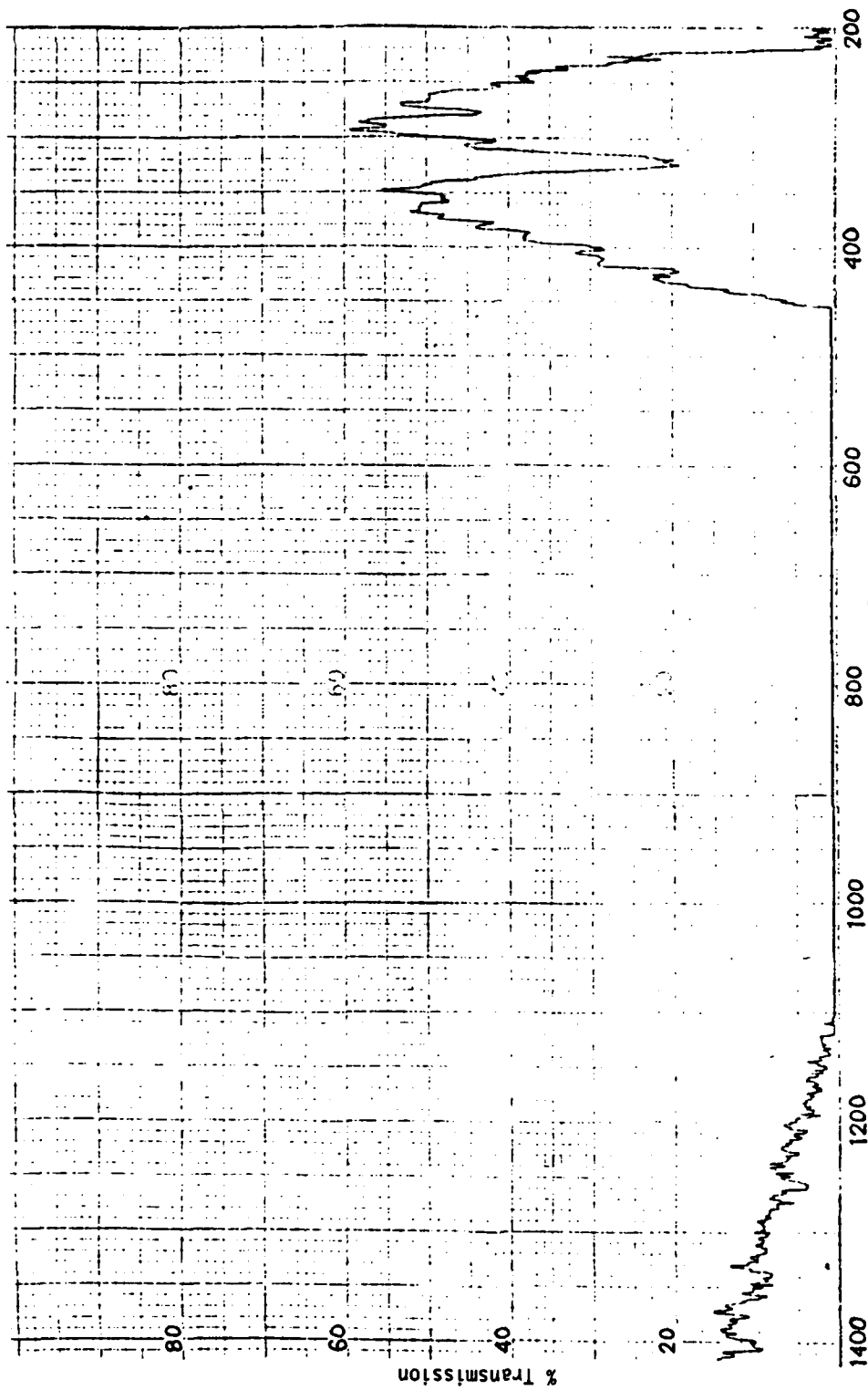


Figure 6. Absorption Spectrum for sample 1159.
No anneal. T = 10K.

the continuum absorption associated with the gallium impurity. Since the majority of the gallium atoms are rendered optically inactive by defects introduced by the NTD process this would explain why we are not seeing this absorption in the NTD samples. We are somewhat surprised by this broad band absorption in samples with such low impurity concentration. Additional studies are planned to try and determine if this absorption is the gallium continuum.

In all three samples, we are seeing an absorption line at 2960 cm^{-1} . Since this line occurs in the non-NTD sample it is not associated with a defect produced by the NTD process. We have observed this line in other gallium doped silicon samples which were grown by different techniques. We believe that this line may be associated with the water vapor that has condensed as ice on the sample surface. Tests are presently being conducted to determine the source of this absorption.

We are at present beginning to anneal the samples and collect absorption data. As anneals are made at higher temperature, the gallium absorption lines should become visible. After these higher temperature anneals, we will focus our efforts on the spectral region which contains the gallium absorption lines (approximately $400 - 500 \text{ cm}^{-1}$).

Recommendations

In order to explain the broad band absorption occurring in the non-NTD sample and the absorption line at 2960 cm^{-1} in all samples, we have planned the following studies:

- (1) 2960 cm^{-1} line - To determine whether this line is due to gallium or water vapor condensed as ice on the sample surface we are going

to reduce the thickness of one of the samples by 50 percent. Also, in an attempt to drive any condensate off the surface we are going to heat the sample slightly after lowering the temperature to 10 K. We believe that these two procedures will provide the information needed to determine the source of the 2960 cm^{-1} line.

2. Broad band absorption - To determine if gallium is the source of this absorption we will investigate the sample whose thickness has been reduced by 50 percent. Hopefully, this will allow the recording of data in the spectral region that is at present completely off scale. This should allow for viewing the gallium lines and the gallium continuum. In addition, we hope to obtain samples that have a gallium concentration lower than 10^{16} cm^{-3} . Obtaining the spectra of samples with a lower gallium concentration, should immediately indicate if the broad band absorption is gallium related.

References

1. Billy C. Covington, Air Force Technical Report, August 1980.
2. Billy C. Covington, Air Force Technical Report, August 1983.
3. Jeffrey B. Watson and B. C. Covington, Proceedings for the Fourth International Neutron Transmutation Doping Conference, June 1982, Plenum Press, in press.
4. John Kainer and Billy C. Covington, Air Force Technical Report, August, 1983.
5. K. Lark-Horovitz, Semiconducting Materials, Edited by H. K. Henisch (Butterworths Scientific Publications, Ltd., London, 1951) p. 47.
6. M. Tanenbaum and J. Mills, J. Electrochem. Soc. 108, 171 (1961).
7. J. M. Meese, Air Force Technical Report AFML-TR-77-178, Feb. 1978.
8. R. C. Newman and D. H. J. Totterdell, J. Phys. C. 8, 3944 (1978).
9. J. W. Corbett, G. D. Watkins, R. M. Chrenko and R. S. McDonald, Phys. Rev. 121(4), 1015 (1960).
10. L. J. Cheng, J. C. Corelli, J. W. Corbett, and G. D. Watkins, Phys. Rev. 152(2), 73 (1966).
11. C. S. Chen and J. C. Corelli, Phys. Rev. B. 5(4), 1505 (1971).
12. D. H. J. Totterdell and R. C. Newman, J. Phys. C. 8, 589 (1974).
13. H. Y. Fan and A. K. Ramdas, "Infrared Absorption and Photoconductivity in Irradiated Silicon," J. Apply. Phys., 30, 1127 (1959).
14. L. J. Cheng, J. C. Corelli, J. W. Corbett, and G. D. Watkins, "1.8-, 3.3-, and 3.9-u Bands in Irradiated Silicon: Correlations with the Divacancy," Phys. Rev., 152, 761 (1966).
15. C. S. Chen and J. C. Corelli, "Infrared Spectroscopy of Divacancy-Association Radiation-Induced Absorption Bands in Silicon," Phys. Rev. B5(4), 1505 (1972).
16. F. Carton-Merlet, B. Pajot, D. T. Don, C. Porte, B. Clerjaud, and P. M. Mooney, "Photo-induced Changes in the Charge State of the Divacancy in Neutron and Electron Irradiated Silicon," J. Phys. C: Solid State Phys. 15 2239 (1982).

17. M. Balkanski and W. Nazarewics, "Single PHonon Absorption Bands in Fast Neutron Irradiated Silicon," J. Phys. Chem. Solids, 23, 573 (1961).
18. M. E. Rolle and J. C. Corelli, "Study of Atomic Disorder Produced by Fast Neutrons in Silicon Using Infrared Spectroscopy," J. Appl. Phys., 47, 37 (1976).

1983-84 USAF-SCEEE RESEARCH INITIATION PROGRAM

Sponsored by the

AIR FORCE OFFICE OF SCIENTIFIC RESEARCH

Conducted by the

SOUTHEASTERN CENTER FOR ELECTRICAL ENGINEERING EDUCATION

FINAL REPORT

INTERFACING OR MODELS AND INFORMATION SYSTEMS: A SYSTEMATIC APPROACH

Prepared by: Dr. Donald B. Crouch

Academic Rank: Associate Profesor

Department and
University: Computer Science Department
Cornell University

Research Location: Air Force Armament Division

Date: August 1984

INTERFACING OR MODELS AND INFORMATION SYSTEMS:
A SYSTEMATIC APPROACH

Donald B. Crouch
Department of Computer Science
Cornell University

ABSTRACT

Successful implementation of an OR model within an information system occurs only when the model becomes an integral part of the system. The process of incorporating a model into a system not only necessitates a detailed analysis of the model's informational requirements, which must be satisfied once the model is introduced into the system, but also requires an analysis of the information system with respect to these requirements. Such analyses may reveal that both the model and the system must be perturbed in order to effect a feasible interface. In determining the extent of the modifications to be made to each, the total cost of the various alternatives and the resulting effects on optimality must be established.

This research resulted in the development of informational models and procedures for performing these interface operations and the definition of a basis by which optimal or near optimal modifications and adjustments of the OR model and information system may be determined.

TABLE OF CONTENTS

LIST OF TABLES	iv
LIST OF FIGURES.	iv
INTRODUCTION	1
RELATED WORK	2
THE GENERAL INTERFACE PROCEDURE.	3
OR INFORMATION MODEL	6
IS RESOURCE MODEL	12
FEASIBILITY STUDY	17
CONCLUSION	19
ACKNOWLEDGMENTS	20
APPENDIX	21
REFERENCES	26

LIST OF TABLES

Table	Page
1. Algorithm for Creating an OR Information Model	22
2. Algorithm for Creating an IS Resource Model.	23
3. Procedure for Performing a Feasibility Study	24

LIST OF FIGURES

Figure	Page
1. OR-IS Interface Procedure	7
2. OR Information Model - Data Requirements	8
3. Data Requirements for OR Inventory Problem	10
4. Binary Tree of OR Information Model.	13
5. OR Information Model	14
6. IS Resource Model.	16

INTERFACING OR MODELS AND INFORMATION SYSTEMS:
A SYSTEMATIC APPROACH

INTRODUCTION

One of the fundamental tasks of an executive information system is to provide the means by which knowledge embedded within the system's databases can be successfully extracted and applied toward the organization's goals and objectives. In order to develop a system which accomplishes this task, techniques for integrating and converting data into useful information which can aid in problem-solving and effective decision-making must be defined and incorporated into an organization's existing management information system [1]. Furthermore, the information system must be provided with additional data on a regular basis for conversion into information in order to support timely decision-making.

For middle and upper level management, the type of information needed from such a system is that which supports the identification of potential consequences of decisions or future business or economic conditions; thus, management desires information that may be used to answer "what if" type questions. Management information systems can generate this type of information by utilizing OR modeling techniques in conjunction with mathematical analyses of data contained within the system.

Unfortunately, incorporation of OR models within an existing information system is not a trivial operation; it involves much more than just implementing additional processes and generating additional data. The complexity of the problem lies in the fact that the optimal solution to an OR model may not be optimal when the cost of incorporating the model into the system is considered.

Successful implementation of an OR model within an information system occurs only when the model becomes an integral part of the system. The process of incorporating a model into a system not only necessitates a detailed analysis of the model's informational requirements, which must be met once the model is introduced into the system, but also requires an analysis of the degree to which the information system satisfies these requirements. Such analyses may well

reveal that both the model and the system must be perturbed in order to effect a feasible interface. In determining the extent of the modifications to be made to each, the total cost of the various alternatives and the resulting effects must be established.

The purpose of this report is to describe a systematic procedure for interfacing OR models and information systems and to define a basis for modifying and adjusting the model and system during the feasibility analysis. The objective of the interface operations is to obtain overall optimality with respect to both the model and the system.

RELATED WORK

Despite the interest in decision support systems and the technological advances which have occurred in information systems in general during the last twenty years, and despite the fact that over the past few years literature in the field has been quite prolific, both the theoretical and practical problems associated with the incorporation of OR decision models into existing information systems have largely been ignored. Some authors contribute this to the existence of a so-called "practicality gap" between operations researchers and practitioners [2,3]. In fact, one author noted that the gap has widened to the point that operations researchers now consider the computer representation or implementation of the results derived from the OR models as a secondary consideration to the development of the models and implications therein [4].

Most research relating to the implementation of decision support systems tends to focus on the development of such systems in toto, not on the problems involved in building support systems out of existing information systems. In particular, previous research has been primarily concerned with the approaches to deriving management information requirements for decision support systems [5,6,7], measuring the effectiveness of such systems [8,9,10], and the general building of these systems [11,12].

Yet, the majority of the organizations desiring to "improve the effectiveness of decision-making by supplying (computer) aids to the decision-maker" will meet this objective by building OR modeling

techniques into their information systems [13]. To do so without evaluating the impact of the system on the optimal theoretical solution of the model or the model's potential impact on the system's resources may well lead to poor and unreliable management tools.

This problem was first raised by Crouch and Crouch in [14] and the ramifications of the problem were explored by Crouch and Mjosund in [15] and [16]. Dyer and Mulvey [17] discuss one aspect of this general area, namely the selection of an appropriate optimizing model for a specific decision-making process. They specify five criteria to be considered when evaluating alternative models: performance, realism/complexity, computational cost, information requirements, and ease of use. They do not consider the impact of the optimizing model on the information system, nor do they attempt to interface the operations research model and the information system such that a basis is created for total optimality.

Implementation of decision support systems involves the incorporation of certain modeling and analysis techniques into existing, large-scale management information systems. Before such implementation takes place, an impact and feasibility study must be conducted. A framework is needed within which a systematic evaluation of the mapping of the OR models onto the information system can be performed without disturbing the actual information system. The research described in this report is directed toward that goal.

THE GENERAL INTERFACE PROCEDURE

In order to incorporate the optimal solution of an OR model into an information system, the symbolic representation of the solution must be restructured into a form amenable to computer implementation. During this transformation process, the model's data and processing requirements must be defined. Such requirements include

- data to estimate model parameters,
- data to fit distributions to model variables,
- data to determine values of constants, and
- computations to obtain the optimal solution.

To ensure model validity and functionality, OR models also require

time-varying information to be provided by the system once the model is introduced into the system. The actual type of information needed must be defined during the transformation process. Such requirements include

- periodic information needed in order to determine whether the solution continues to hold or whether an updated solution must be provided, and
- information which will result in actions dictated by the solution.

The specification of the informational and processing needs of the model's optimal solution is generally perceived as the only requirement necessary for establishing an effective OR-IS interface. Regrettably, for the case when the model's requirements cannot be met by the existing information system, one cannot assume that the system can and will be modified to meet the requirements. In fact, in practice, the system is seldom modified to provide the resources necessary to support an optimal solution due to the costs involved and the impact that such system modifications may have on existing system applications.

Neither can it be assumed that if an OR-solution cannot be implemented without additional system capability, then the OR-model can be modified to produce a solution which not only satisfies the constraints of the information system but also meets the decision support needs of the user of the system. If that were the case, one would conclude that the specification of the informational resources and processing capability of the system is the only requirement in establishing an effective IS-OR interface.

Obviously both views are narrow in their scope and will lead to successful interfacing of the OR model and the information system only in the rare case in which the OR informational needs are a subset of the system's informational resources and processing capabilities and, additionally, in which the cost constraints are met. In reality, perturbations of both the system and the model are usually necessary to effect an optimal or near optimal interface. In determining the extent of the modifications to be made to each, it becomes necessary to determine the total cost of the various alternatives. If the cost of increasing the capacity of the information system is less than the loss that would incur from utilization of a modified OR solution, the system

should obviously be augmented, and vice versa. Admittedly, as with shortage cost in inventory control, the estimation of the cost of not having certain data available is in most cases difficult; but in all likelihood, an awareness in itself of just how that cost component fits into the perturbation decision is extremely valuable.

It should be noted that it is incorrect to assume that the incorporation of a single OR model into the system should bear the full economic burden of an increase in the capacity of the information system. Other applications will normally benefit from such an expansion. What suggests itself here is an accumulation of losses due to modification in OR models and solutions (or other type applications) until such time that these exceed the cost of an expansion that would eliminate these losses.

The tasks involved in interfacing OR models and information systems include:

- establishing a basis for comparison of the OR model's requirements and the information system's resources,
- establishment of the OR model's data requirements, information requirements and processing requirements,
- establishment of the information system's processing capabilities and data resources,
- comparison of the OR model's requirements and the information system's resources using the established basis,
- determining feasible alternatives for the OR model and the information system based on the comparison of the OR model's and the information system's requirements, and
- assigning cost figures to the alternatives.

What are needed are systematic procedures to follow in performing these operations.

To solve the interface problem, we propose the creation of two formal information models which fully describe the OR model and the information system:

- an OR Information Model representing the information requirements necessary to implement the OR solution on a computer, and
- an IS Resource Model representing the resources available within the information system which will support the implementation of the OR model.

These two models must be formulated on a common basis in order to provide a framework within which a systematic evaluation of the mapping

of the OR model onto the information system can be performed. The purpose of the evaluation process is to ensure overall optimality after implementation. The evaluation must be done without disturbing the actual information system.

We envision that during the evaluation process to ascertain the degree of interface feasibility there will be feedback from the OR Information Model to the OR model and from the IS Resource Model to the information system. Thus, one might say that the formal information models permit the OR model and the information system to "fight it out" before an actual implementation is undertaken. Graphically, the general interface procedure may be visualized as in figure 1.

OR INFORMATION MODEL

The objective of defining an OR Information Model is to establish the totality of information necessary to transfer the optimal solution of the OR model into an operational computerized representation of the model. To facilitate the understanding of this operation, the OR Information Model in figure 1 may first be considered to consist of only the data requirements of the OR model. In this case, the OR Information Model specifies the informational needs of the OR model in terms of elemental data items which define broad information categories corresponding to the OR model's parameters and controllable and noncontrollable variables.

The Model may be thought of conceptually as a tree structure (figure 2). Nodes on the first level correspond to the categories which define the primary needs of the OR model. Intermediate, non-terminal nodes define the components of these categories or further refine those components which appear at a higher level in the tree. The terminal nodes represent elemental data items which compose the components and for which the information system must ultimately provide values. When actual values are assigned to the data elements, the data values will be processed to produce values for the components. Since each information category is a function of its components, the values produced for the components may be subsequently processed to generate values for the categories.

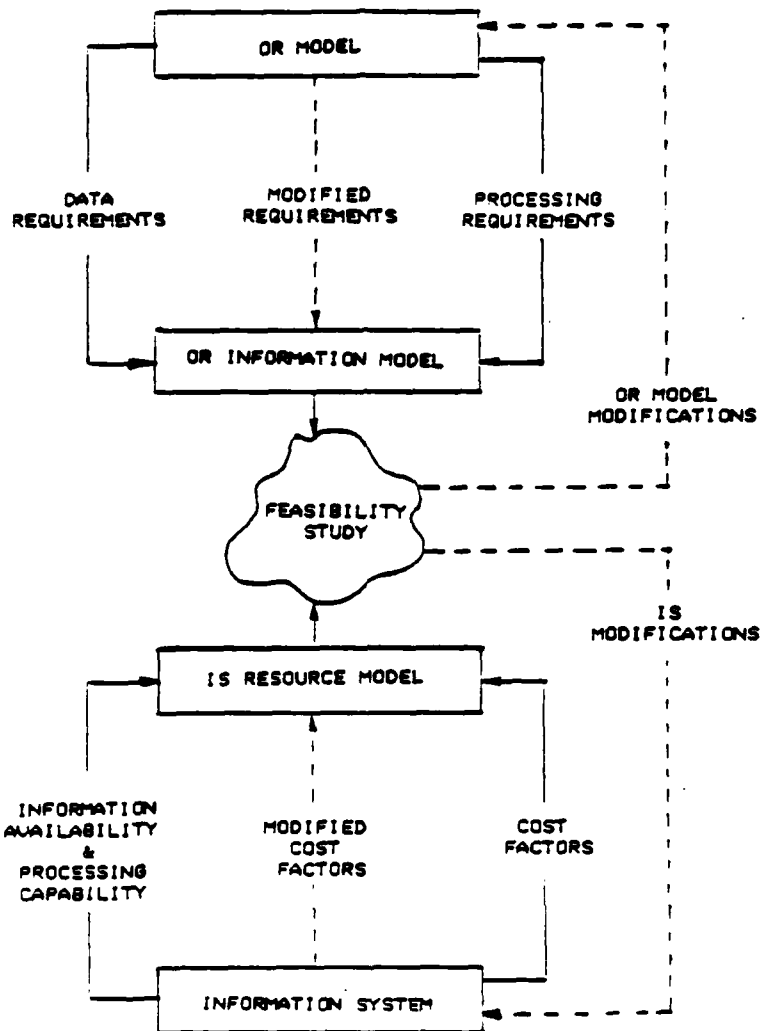
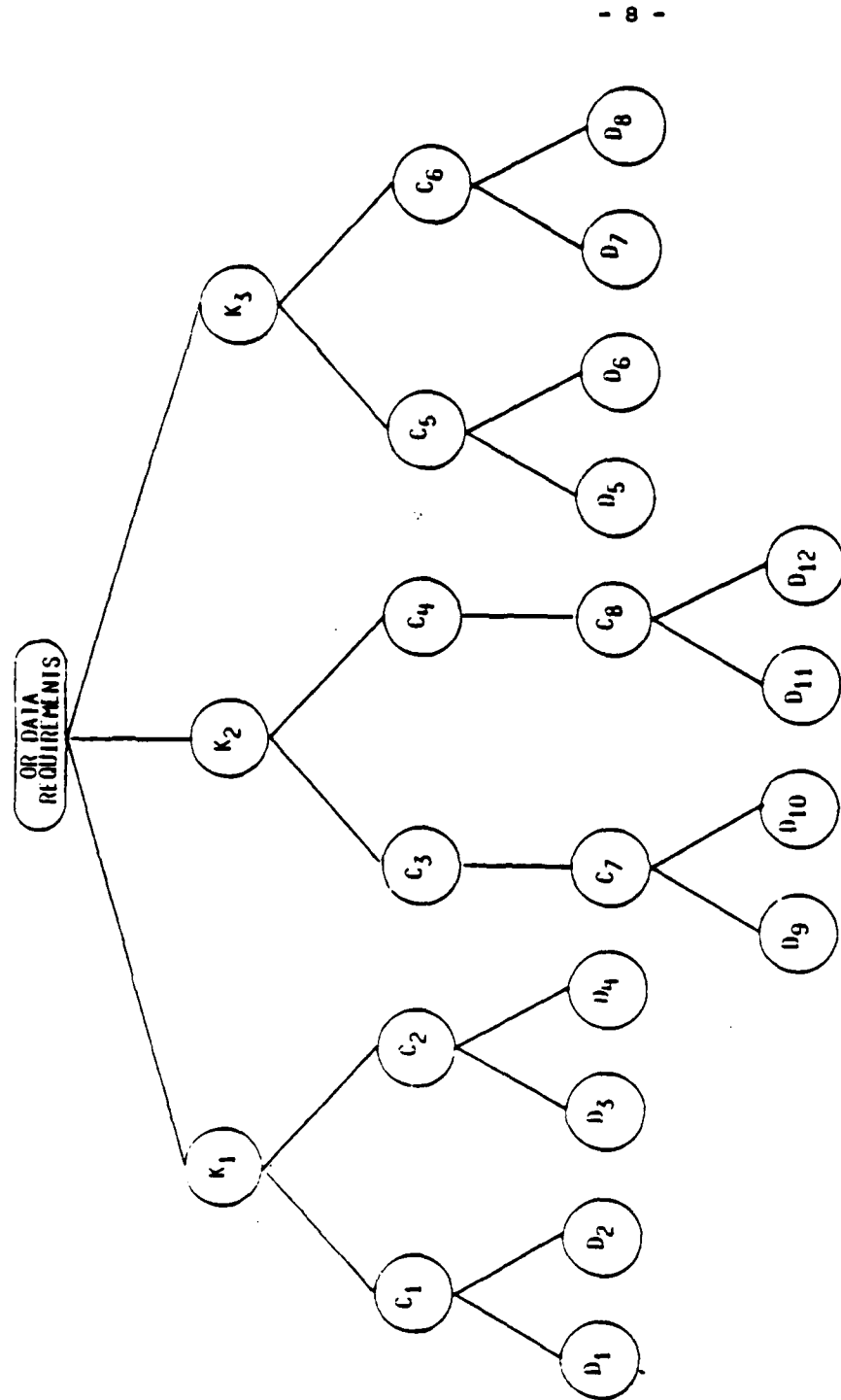


Fig. 1. OR-IS Interface Procedure



LEGEND:

- K_i - Information Category
- C_i - Information Component
- D_i - Data Element

Fig. 2. OR Information Model - Data Requirements

The purpose of the OR Information Model is to facilitate the process of establishing the basic data requirements necessary to transform the symbolic solution of the OR model to a numerical solution which can be implemented. Initially the broad categories defining the model are established (level 1). Next, each category is defined in terms of its basic components (level 2). Each component may be defined in subsequent levels in terms of even more basic components. Ultimately, the basic components are defined in terms of the most elemental data items needed to produce the components (terminal level).

The tree representation provides a structured means by which one can accomplish in a systematic procedure the specification of all informational needs of the OR model. One does not attempt to determine all needs at once but rather proceeds down each branch independently until all terminal nodes for the root of that subtree (that is, category) are generated.

As an example consider an OR-model which represents a deterministic inventory system with the following cost equation:

$$C = \frac{S^2h}{2Q} + \frac{(Q-S)^2b}{2Q} + \frac{ad}{Q}$$

where

- C - total cost per year
- Q - order size
- S - maximum inventory level
- b - cost of being short one unit one year
- h - cost of carrying one unit in inventory per year
- d - annual demand
- a - ordering cost.

Figure 3 illustrates how the data requirements portion of the OR Information Model for this example might look. Thus, for this inventory model, the categories of the OR Information Model would include such items as holding cost, ordering cost, annual demand, and shortage cost.

To continue this example, consider the leftmost subtree in figure 3 whose root is the holding cost category. Assuming that holding cost is a function of insurance cost, capital cost, warehouse cost, damage loss and theft loss, these five factors would be the components (that is, children) of the node representing holding cost. Since the information system must ultimately provide values for each of these components, each

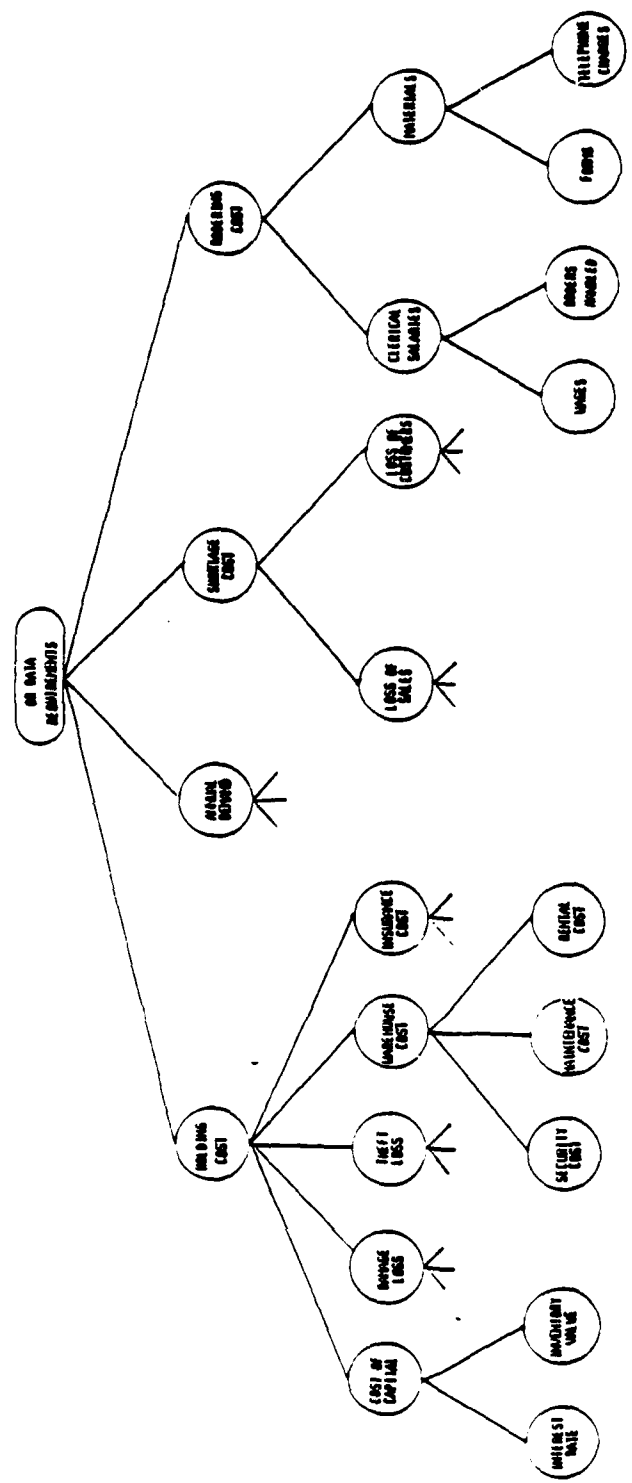


Fig. 3. Data Requirements for OR Inventory Problem

such component must be further expanded until the elemental data items composing the component are specified. For example, warehouse cost may be a function of maintenance, security and rental costs. If so, then these three items would represent the elemental data items for the node corresponding to the warehouse component.

It should be noted that the values to be assigned to the elemental data items by the information system may either be known exactly or may be uncertain and subject to variation. In most modeling situations, the values for such items are not readily available; substantial time and cost must be expended to arrive at values which at best are only good estimates. The time required to collect the actual values for the data elements and the errors involved in the data generation procedure are a critical part of the quantitative decision making process. These factors, however, are taken into account in the IS Resource Model. At this point, we are concerned only with specifying the informational needs of the OR model, not with specifying the means by which the values of the data elements will be estimated or generated by the system.

Establishing the data requirements in the OR Information Model is only one of the major tasks involved in defining the OR model's informational requirements. The other major task is establishment of the OR model's processing requirements. The processing requirements include the following:

- aggregative processes which when applied to the data elements produce the information components,
- informational processes which when applied to the components produce the categories, and
- a functional process which when applied to the categories produces a solution of the OR model.

Thus, the processing requirements are those processes which are necessary to transform the elemental data items into a solution of the OR Model. The processes may range from collection procedures (to capture data necessary to produce the desired information) or simple summations of data to complex mathematical calculations.

In order to incorporate the OR model's processing requirements into the tree structured OR Information Model, we need first to transform the tree containing the data requirements into a binary tree using the

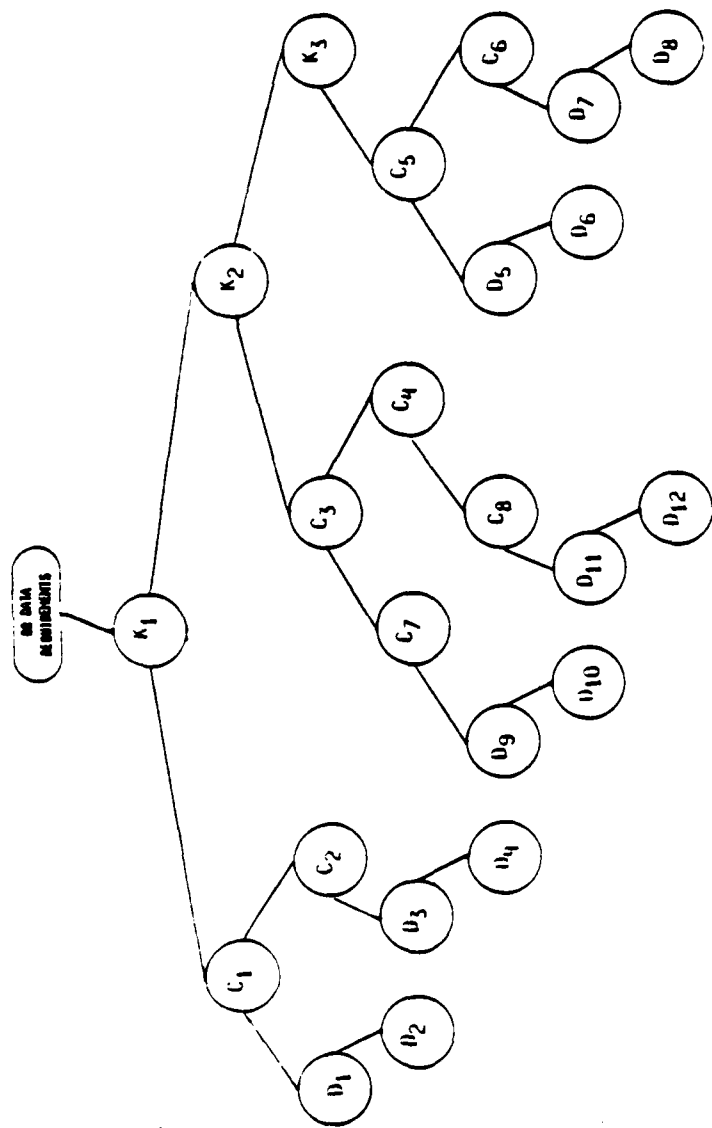
"natural correspondence" between forests and trees [18]. The binary tree corresponding to the data requirements of the OR Information Model of figure 2 is contained in figure 4. In this form, the left subtree of a node represents the entire set of data needed to define the node. What is missing are the processes to be applied to the nodes to produce the parental nodes. In order to define completely the OR Information Model, the left child of each nonterminal node in the binary tree is replaced with a processing node whose left child is null and whose right child is the subtree defined by the node being replaced. The resulting tree represents the OR Information Model (figure 5).

The OR Information Model for a given OR model is conceptually simple to understand and relatively easy to construct; computational algorithms are well defined for creating, traversing, and processing binary trees [18]. Each node in the OR Information Model represents either a process to be performed or an informational item to which a process will be applied. A process node is always a left child of a node; the set of informational nodes to which a process will be applied are always connected along the right branch of the process node. Application of a process node to its informational nodes results in the definition of the process node's parent, that is, an information component, information category, or the root node, the optimal solution.

Table 1 of the Appendix contains a detailed specification of the general procedure for creating an OR Information Model for a given OR model. Each major step of the procedure involves creation of a subtree consisting of a processing node and the informational nodes associated with it. Each new subtree becomes the left child of one of the informational nodes in the current tree configuration.

IS RESOURCE MODEL

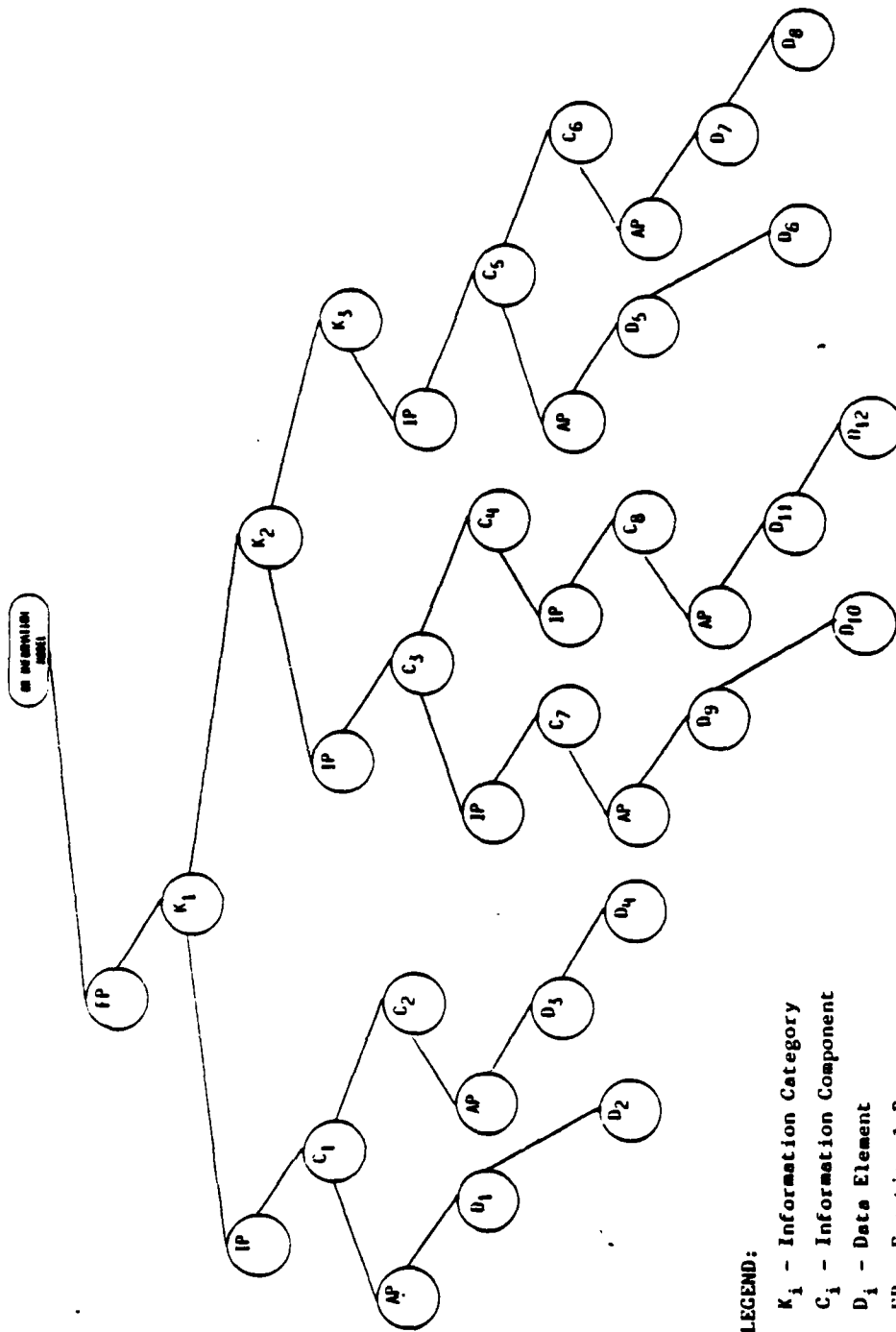
The IS Resource Model in the OR-IS interface procedure reflected in figure 1 is an abstract of the information system. This Model specifies the availability (within the information system) of the informational requirements of the OR model for its implementation in the system and the costs associated with providing such information to the OR model. The needs of the OR model are specified by the OR Information Model of



LEGEND:

- K_i - Information Category
- C_i - Information Component
- D_i - Data Element

Fig. 4. Binary Tree of OR Information Model - Data Requirements



- LEGEND:**
- K₁ - Information Category
 - C_i - Information Component
 - D_i - Data Element
 - IP - Functional Process
 - IP - Informational Process
 - AP - Aggregative Process

Fig. 5. OR Information Model

figure 5. The abstract of the information system describes the availability and costs of both the data elements and processes of the OR Information Model.

The IS Resource Model has a structure identical to the OR Information Model. Moreover, each node in the binary tree of the IS Resource Model consists of two additional value fields: namely,

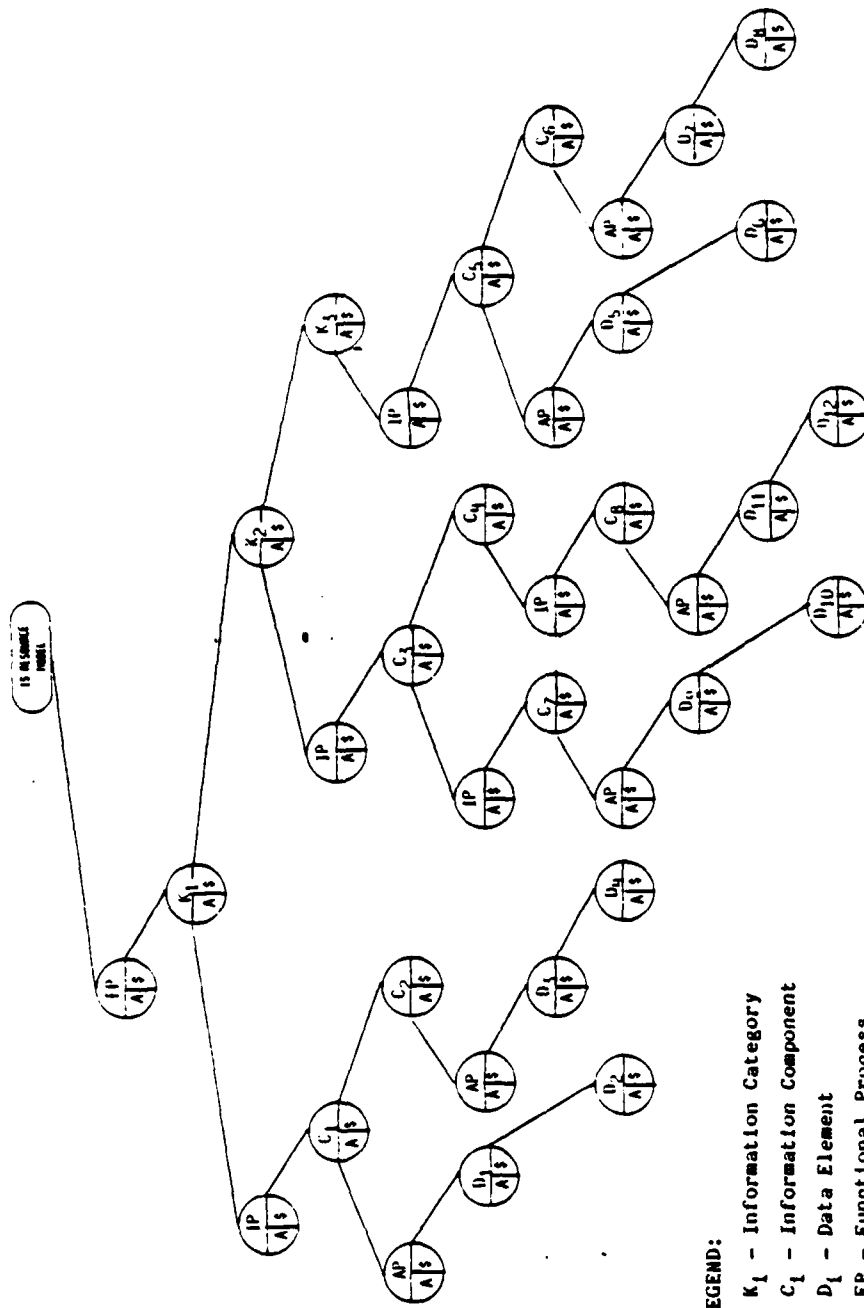
- a yes/no response indicating the capability of the information system to meet the informational need of the OR model as designated by the corresponding OR Information Model's node, and
- the information system's cost in meeting this information requirement.*

The relationship between the OR model's informational needs and the information system's resources as represented by the IS Resource Model is shown schematically in figure 6.

The specifics of the procedure to be followed in creating an IS Resource Model is contained in Table 2 of the Appendix. The creation of the Model is straightforward and, as may be noted, does not necessarily require that the value fields be completed for each and every node in the tree. In fact, if the value fields are known for an informational type node (that is, a category node or a component node), then each node in the subtree defined by the informational node's child may be ignored.

The purpose of creating the OR Information Model and the IS Resource Model is to avoid the inconsistencies that normally arise in the incorporation of OR models into information systems. In the past, systems have been developed in a piece-meal fashion with little thought being given to the ramifications of the OR Model on the system or the system on the optimal solution of the model. These systems are now proving to be inadequate as effective administrative tools. The OR

*In order to balance cost of nonoptimality of the OR solution versus cost of information, a cost analysis scheme for the information system must be developed. The general development of such a scheme falls outside the scope of this paper. It should be noted that the cost aspect of information system design is of great importance regardless of design strategy and is an area where more work is needed. In this discussion we assume that the cost of data processing for the existing information system is known and that the cost of additional data collection and processing can be estimated. With regard to the OR model, we assume that sensitivity analyses are performed before information requirements for the optimal solution are determined such that excessive data collection is avoided for robust parameters.



- LEGEND:**
- K₁ - Information Category
 - C₁ - Information Component
 - D₁ - Data Element
 - FP - Functional Process
 - IP - Informational Process
 - AP - Aggregative Process
 - A - Availability
 - \$ - Cost

Fig. 6. IS Resource Model

Information Model consolidates the functional requirements and data specifications of the optimal solution of the OR model into a single, coherent structure; the IS Resource Model reflects the ability of the information system to meet these requirements and the cost of doing so. The Models, being formulated on a common basis, serve as coordination and communication media for performing successful implementation of OR models. The Feasibility Study of the interface procedure of figure 1 performs the comparative analysis of the two Models.

FEASIBILITY STUDY

The purpose of the feasibility study, the third phase of the OR-IS Interface, is three-fold:

- to compare the information requirements of the OR model and the information availability within the information system,
- to establish feasibility and costs of alternative models, and
- to estimate associated loss for nonoptimality.

As reflected in figure 1, this phase supports an analysis of the ramifications of modifying the OR model and the system in an attempt to obtain overall optimality. The feasibility study can perform such an analysis due to the fact that the two formal Models, that is, the OR Information Model and the IS Resource Model, are formulated on a common basis. This evaluation can, of course, be made without disturbing the actual information system.

The comparison of the two formal tree-structured Models is simple to perform; one needs only to evaluate the functional processing node on the first level of the IS Resource Model and all the information component nodes connected along the right branch emanating from the process node. One of two basic situations will occur during this evaluation: either all information requirements will be met by the existing information system (that is, all the aforementioned nodes will have a positive response for availability) or only a subset of the requirements will be met (in which case at least one of the nodes will have a negative response).

If, in the former case, more than one OR model is available for the

same decision problem (an example of the occurrence of this type of situation is given by Dyer and Mulvey [17]), the cost of meeting the information requirements for each of these models may be calculated. Once an OR model has been selected, or if only one model is available which is more likely to be the case, a cost evaluation is performed to determine whether the OR solution is optimal when the data requirements are considered. For this evaluation an heuristic approach is proposed in which one information category is removed at a time from the IS Resource Model, starting with the node possessing the largest information cost. The OR model is subsequently modified to a simpler, less realistic model, the corresponding OR Information Model is reconfigured, and the associated loss for nonoptimality is estimated. As long as the resulting loss is less than the corresponding savings in information cost, the process continues.

In the situation in which only a subset of the information requirements can be met by the existing information system, the procedure is reversed; the OR model is gradually enhanced by the addition of information categories to the OR Information Model. The cost of adding information categories (that is, the cost associated with modifying the information system such that it may provide the requirements needed for a category) is estimated for additional categories one at a time. This cost is compared with the estimated gain obtained from the corresponding increase in model realism. As long as this gain exceeds the added information cost, the information category is added to the OR Information Model and the corresponding data collection and processing costs are included in the IS Resource Model.

The feasibility study provides a means of determining the extent of the modifications which may be made to both the OR model and the information system in an attempt to effect a feasible interface, that is, an interface considered optimal with respect to both entities. The systematic procedure to follow in performing the feasibility study is contained in Table 3 of the Appendix.

As an example of the feasibility analysis phase, consider the inventory problem previously presented. Let us assume that the OR model is realistic, that the symbolic solution is optimal, and that the

information requirements can be met. Suppose that cost analysis subsequently reveals that the OR model is not optimal when the cost of the required information is considered. Assume further that the information cost associated with the information category "shortage cost" is the highest of all information category costs. If this category is removed, the model can be modified to a less realistic EOQ model. The OR Information Model and the IS Resource Model for the EOQ model could be readily obtained from the original Models by pruning the subtree defined by the "shortage cost node" and by modifying the functional process node on level 1 of the tree. If the estimated loss incurred by using the EOQ model (rather than the more realistic model with shortage) turns out to be less than the cost of providing shortage cost information, the EOQ model should be chosen.

As another example, assume that the original optimal model is one with probabilistic rather than deterministic demand and that the current information system is not capable of providing the probability distribution and the processing to obtain an optimal solution for the probabilistic model. If the cost of including these capabilities in the information system is greater than the loss of using a deterministic model instead of a probabilistic model, the deterministic model should be chosen.

It is clear that the approach we have proposed here requires substantial cost analysis and cost evaluation of alternatives. We believe strongly, however, that the problem with many information systems has been a lack of cost consciousness and a haphazard adding on of information as needs arise. A systematic approach to the development of decision support systems where data requirements and data costs are continuously balanced will undoubtedly lead to more effective decision-making systems. We also believe that once such a systematic approach is adopted, it will lead to the formation of a cost information system as a part of the overall information system.

CONCLUSION

Management in business, industry, and governmental organizations is always seeking ways to increase efficiency and to bring order to the

chaos created by the increased complexities of the problem-solving and decision-making environment. Proposed solutions include the creation and utilization of decision support systems or executive information systems as management tools. However, due to the proliferation of management information systems during the last decade and due to the expense associated with the creation and maintenance of such systems, it is only natural that new management tools will be built onto the existing systems. Furthermore, the information accumulated within the MIS's databases is needed for effective decision-making.

To incorporate OR decision models into an existing MIS without ascertaining in advance the impact such actions will have on the optimal solutions of the models and on the MIS itself will in all likelihood result in poor decision support systems. The systematic procedures described in this paper provide a solution to this problem and, thus, will enable computational support organizations to move more readily toward the use of reliable decision support systems.

Research now needs to be directed toward the development of a methodology of implementation of these procedures.

ACKNOWLEDGMENTS

The author would like to thank Professor Arne Mjosund of Mississippi State University for his advice and collaboration on this project and Dr. Bob Braswell, Director of Computer Sciences at Eglin AFB, for giving him the opportunity to explore this area of research under the auspices of the 1983 AFOSR Summer Faculty Research Program as conducted by the Southeastern Center for Electrical Engineering Education.

APPENDIX

This appendix contains algorithms for creating the OR Information Model and the IS Resource Model and for performing the Feasibility Study.

NOTATION

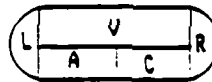
Node:

A tree node consists of five fields: namely,

- L: pointer to the root of the node's left subtree
- R: pointer to the root of the node's right subtree
- V: description of the node
- A: availability within the information system of the informational needs of the node (yes/no value)
- C: cost of providing the needed information.

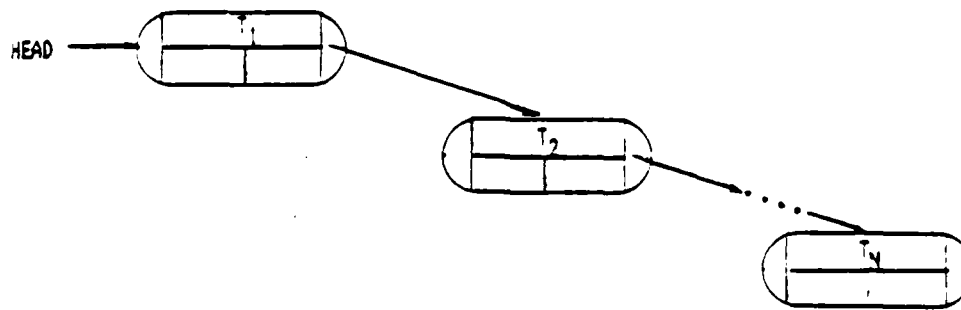
NOTE: In the OR Information Model, fields A and C are null.

Schematic Representation of a Node:



Procedure Subtree (T):

This routine builds a tree for the ordered list of elements (T) and stores a pointer to the tree in the variable HEAD. Schematically, the subtree produced is as follows:



Stack Operations:

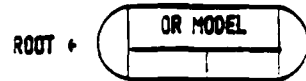
$P \uparrow S$ - pop item P from the stack S

$P \downarrow S$ - push item P onto the stack S

TABLE 1

ALGORITHM FOR CREATING AN OR INFORMATION MODEL

S1. [Create the root node.]



S2. Extract the broad information categories (parameters and controllable and noncontrollable variables) from the OR model, say list (ICAT), and define the process FP which, when applied to (ICAT), produces the optimal value for the OR model.

S3. [Create a subtree for the data.]

SUBTREE ((FP,(ICAT))).

S4. P ← ROOT.

S5. [Attach the subtree to the OR Information Model.]

L(P) ← HEAD

S6. [Push each information category node onto the stack S.]

1. P ← R(L(P))
2. P ↓ S
3. P ← R(P)
4. If P = null, then go to step 2.

NOTE: The remainder of the algorithm expands each information node in the stack into a process and its elemental information items (components or data elements) until the informational nodes become terminal nodes.

S7. If the stack S is empty, terminate the algorithm. Otherwise,

P ↑ S.

S8. Can the informational item U(P) be further refined? If not, go to step S7.

S9. Expand U(P) into a process P (an aggregative process or information process) and its list of informational items T (information components or data elements).

S10. [Create a subtree for the new informational items.]

SUBTREE ((P,(T))).

S11. Go to step S5.

TABLE 2

ALGORITHM FOR CREATING AN IS RESOURCE MODEL

- S1. [Push the functional processing node and each information category node in the OR Information Model onto the stack.]
1. $P \leftarrow L(\text{ROOT})$
 2. $P \downarrow S$
 3. $P \leftarrow R(P)$.
 4. If $P \neq \text{null}$, then go to step 2.
- S2. If the stack S is empty, then terminate the algorithm. Otherwise,
- $P \uparrow S$.
- S3. If the information concerning availability is not known for node P , then go to step S4. Otherwise,
1. $A(P) \leftarrow \text{yes}$
 2. $C(P) \leftarrow \text{estimated cost}$
 3. Go to step S2.
- S4. [Has node P been previously analyzed?]
- If $A(P) = \text{no}$, then go to step S2.
- S5. [Indicate information unavailable for node P .]
- $A(P) \leftarrow \text{no}$
 $C(P) \leftarrow \text{estimated cost to modify system}$
- S6. [Can this node be expanded?]
- If $L(P) = \text{null}$, then go to step S2.
- S7. [Push P onto the stack.]
- $P \downarrow S$
- S8. [Push P 's left child onto the stack S and the informational nodes along the right branch of this child.]
1. $P \leftarrow L(P)$
 2. $P \downarrow S$
 3. $P \leftarrow R(P)$
 4. If $P \neq \text{null}$, then go to step 2.
- S9. [Iterate.]
- Go to step S2.

TABLE 3

PROCEDURE FOR PERFORMING FEASIBILITY STUDY

S1. [Determine extent of feasibility.]

1. $P \leftarrow L(\text{ROOT})$
2. If $A(P) = \text{no}$, then go to step S6.
3. $P \leftarrow R(P)$
4. If $P = \text{null}$, then go to step 2.

CASE 1: All information requirements are met by the information system. Perform cost evaluation analysis.

S2. [Determine information category with highest cost.]

1. $BN - BP \leftarrow L(\text{ROOT})$
2. $N \leftarrow P \leftarrow R(BP)$
3. $MAX \leftarrow C(N)$
4. If $R(N) = \text{null}$, then go to step S3.
5. $BN \leftarrow N$
6. $N \leftarrow R(N)$
7. If $MAX < C(N)$, then
 - 7.1 $MAX \leftarrow C(N)$
 - 7.2 $P \leftarrow N$
 - 7.3 $BP \leftarrow BN$
8. Go to step 4.

S3. [Remove node P.]

$$R(BP) \leftarrow R(P)$$

S4. Modify $L(\text{ROOT})$ to reflect characteristic of less realistic OR model.

S5. Estimate loss for nonoptimality. If loss is less than the cost savings MAX , then iterate the process beginning with step S2. Otherwise, terminate the feasibility study.

CASE 2: Some information requirements are not met by the information system.

S6. Modify $L(\text{ROOT})$ to reflect the characteristics of the less realistic OR model corresponding to the set of informational items currently available within the information system.

TABLE 3 (Continued)

- S7. [Determine information category with lowest cost whose requirements are not presently met by the information system.]
1. $N + P + R(L(ROOT))$
 2. If $A(N) = \text{no}$, then
 - 2.1 $MIN + C(N)$
 - 2.2 $P + N$
 - 2.3 Go to step 4.
 3. If $R(N) = \text{null}$, then terminate the feasibility study.
Otherwise,
 - 3.1 $N + R(N)$
 - 3.2 Go to step 2.
 4. If $R(N) = \text{null}$, then go to step S8.
 5. $N + R(N)$
 6. If $A(N) = \text{yes}$, then go to step 4.
 7. If $MIN > C(N)$, then
 - 7.1 $MIN + C(N)$
 - 7.2 $P + N$
 8. Go to step 4.
- S8. Estimate the gain which would be obtained in model realism if the information represented by node P were available. If the gain is less than the cost MIN, then terminate the feasibility study.
- S9. [Insert node P.]
- $A(P) = \text{yes}$
- S10. Modify $L(ROOT)$ to reflect characteristics of the more realistic model. Iterate process beginning with step S7.

REFERENCES

1. W. Van de Bogert, Concept formation - a fundamental element of an information system. Inf. Mgmt., 39-41 (April 1983).
2. A. Mjosund, The synergy of operations research and computers. Oper. Res., Vol. 11, No. 5, 1057-1064 (1972).
3. J. P. C. Kleijnen, Operations research and computers. In Encyclopedia of Computer Science and Technology, J. Belzer, et. al. (eds.), Marcel Dekker, Inc., New York (1977).
4. R. E. Nance, Stylistism, synergism and syncretism: the interface of computer science and operations research. ACM Annual Conference, Washington, D. C., December 1978.
5. A. Mjosund, Toward a strategy for information needs analysis. Comput. & Ops. Res., Vol. 2, No. 1, 39-47 (1975).
6. V. Chachra and R. C. Heterick, Anatomy of a decision support system. Cause/Effect, Vol. 5, 6-11 (Sept. 1982).
7. M. P. Martin, Determining information requirements for DSS. J. Sys. Mgmt., Vol. 33, 14-21 (1982).
8. R. S. John, D. von Winterfeldt and W. Edwards, The quality and user acceptance of decision analysis performed by computer vs. analyst. Tech. Rep. AD-A105, NTIS (JUNE 1981).
9. R. J. Thierauf, Decision Support Systems for Effective Planning and Control. Prentice-Hall, Englewood Cliffs, N. J. (1982).
10. M. Lasden, Computer-aided decision-making. Comp. Dec., Vol. 14, 156-158 (Nov. 1982).
11. R. H. Sprague, Jr. and E. Carlson, Building effective decision support systems. Prentice-Hall, Englewood Cliffs, N.J. (1982).
12. J. Bennett, (ed.), Building Decision Support Systems. Addison-Wesley, Reading, Massachusetts (1983).
13. L. B. Methlie, Data management for decision support systems. ACM SIGOA Newsletter, 40-46 (Sept.-Nov. 1980).
14. C. J. Crouch and D. Crouch, Interrelations of O. R. models and information systems. ORSA National Meeting, San Diego, 1973.

15. D. B. Crouch and A. Mjosund, Mapping the OR model onto the information system. ORSA National Meeting, San Diego, 1977.
16. D. B. Crouch and A. Mjosund, Operations research - information systems: a computerized interface. Third National Conference for Computers and Industrial Engineering, Orlando, 1980.
17. J. S. Dyer and J. M. Mulvey, Integrating optimization models with information systems for decision support. In Building Decision Support Systems, J. Bennet (ed.), Addison-Wesley, Reading, Massachusetts (1983).
18. D. Knuth. The Art of Computer Programming: Fundamental Algorithms. Addison-Wesley, Reading, Massachusetts (1972).

1983-84 USAF-SCEEE RESEARCH INITIATION PROGRAM

Sponsored by the

AIR FORCE OFFICE OF SCIENTIFIC RESEARCH

Conducted by the

SOUTHEASTERN CENTER FOR ELECTRICAL ENGINEERING EDUCATION

FINAL REPORT

THE PROTON IN MULTISOLVENT CLUSTERS. 1.

THE ACETONITRILE-WATER SYSTEM

Prepared by: Dr. Carol A. Deakyne

Academic Rank: Assistant Professor

Department and
University: Chemistry Department
College of the Holy Cross

Research Location: Air Force Geophysics Laboratory

Date: April 1985

THE PROTON IN MULTISOLVENT CLUSTERS. I. THE ACETONITRILE-WATER SYSTEM.

Carol A. Deakyne,* Air Force Geophysics Laboratory,
Hanscom AFB, Bedford, MA 01731

Michael Meot-Ner (Mautner), Chemical Kinetics Division,
Center for Chemical Physics, National Bureau of Standards,
Gaithersburg, MD 20899

Cynthia L. Campbell, Michael G. Hughes, and Sean P. Murphy,
Department of Chemistry, College of the Holy Cross,
Worcester, MA 01610

Abstract: Experimental and ab initio dissociation energies of the $(\text{H}_2\text{O})_n(\text{CH}_3\text{CN})_m\text{H}^+$ ions are reported. The energies range from 10-35 kcal/mol. The proton is best stabilized by placing the maximum number of acetonitrile molecules close to the protonated center in such a way that the formation of a network of strong hydrogen bonds is still possible. Other results from this work are: 1) Distinct solvent shells can be distinguished in these complex ions. 2) Mixtures of several isomeric structures are unlikely for $n \leq 4$. 3) When a solvent molecule clusters with $(\text{H}_2\text{O})(\text{CH}_3\text{CN})\text{H}^+$, the proton is transferred from the acetonitrile to the water. 4) Although electrostatic interactions make the dominant contribution to the bonding in these systems, polarization and charge transfer effects contribute also. 5) There is a cooperativity effect among the hydrogen bonds that leads to extensive changes in geometry and charge distribution as successive hydrogen bonds are formed. 6) The relative complexation energies along a series of reactions correlate with many properties of the electron donor and with several properties of the proton donor.

*Air Force Geophysics Scholar.

Introduction

Information on the properties of clusters incorporating several solvent molecules about a proton is of interest from the point of view of both understanding the structure of acidic solutions and understanding planetary ionospheric chemistry. Clusters comprising several different solvent molecules, ie, complexes of mixed solvents, are of interest because (1) they simulate multicomponent solvent systems, (2) studying them can clarify the structure of hydrogen-bonded networks about a protonated solute ion, and (3) such clusters have been observed in the ionosphere.

We are interested in the following questions concerning the buildup of a complex ion:

- (1) What combination of solvent molecules about the proton best stabilizes the charged proton?
- (2) Do clusters build up through the filling of distinct solvent shells?
- (3) Can complexes with a given composition assume several isomeric structures?
- (4) Starting with a protonated solute molecule, can a group of solvent molecules "pull away" the proton from the solute molecule?
- (5) To what degree does clustering simulate bulk solvation?
- (6) How much do charge transfer and electrostatic interactions contribute to the bonding in the supermolecules?
- (7) How much does clustering affect the geometry and charge distribution of the components?
- (8) What is the relationship between structure, charge transfer, and energetics for the complex ions?

We shall address these questions as they pertain to supersystems containing several different solvent molecules about the proton.

In order to address similar questions, Kebarle and coworkers,¹ Castleman

and coworkers,² and Meot-Ner³ have looked at the thermochemistry of cluster dissociation, ie, reactions of the general type:



With respect to the atmosphere, the complex ions of significance contain such ubiquitous planetary atmospheric species as H₂O, NH₃, CH₃OH, HCN, CH₃CN, etc. The clustering of each of these molecules about the proton in single-component complexes has been investigated.² In contrast, the only protonated mixed clusters composed of the above atmospheric or similar molecules that have been studied experimentally are the (NH₃)_m(H₂O)_nH⁺⁴ and the ((CH₃)₂O)_m(H₂O)_nH⁺ systems.⁵ In the present series of papers, we shall examine a variety of multicomponent supermolecules containing the above atmospheric species.

The present paper deals with (H₂O)_n(CH₃CN)_mH⁺ (denoted W_nAc_mH⁺). In addition to their atmospheric relevance (see below), water-acetonitrile clusters may be important in HPLC-chemical ionization mass spectrometry.

Recently balloon-borne mass spectrometers have been utilized to determine the ionic composition of the earth's ionosphere.⁶⁻⁹ Two types of positive ions found in the stratosphere are proton hydrates, (H₂O)_nH⁺, and (H₂O)_nX_mH⁺ ions, where X has a mass of 41 amu and must have a proton affinity greater than 175 kcal/mole and an abundance greater than 7 x 10⁴ cm⁻³ in order to enter into the ion chemistry. The most viable candidate for X to date is acetonitrile.⁷⁻¹⁴ Part of the evidence in support of CH₃CN as X has been provided by the selected ion flow tube (SIFT) experiments of Smith et al.¹⁴ These workers have shown that CH₃CN rapidly replaces H₂O in the

cluster ions $(\text{H}_2\text{O})_n\text{H}^+$, $n=2-4$, with the exception of the last H_2O in $(\text{H}_2\text{O})(\text{CH}_3\text{CN})_2\text{H}^+$ and $(\text{H}_2\text{O})(\text{CH}_3\text{CN})_3\text{H}^+$. Equally significantly, ions with masses equivalent to those of the $(\text{H}_2\text{O})_n(\text{CH}_3\text{CN})_m\text{H}^+$ cations observed by Smith et al.¹⁴ have been observed in the atmosphere.^{7,8,11,12} In addition to the objectives mentioned above, a particular objective of this work was to determine why the last H_2O molecule in the $(\text{H}_2\text{O})(\text{CH}_3\text{CN})_m\text{H}^+$, $m=2,3$, cations is not readily replaced.

Experimental and Computational Details

The experimental measurements were performed using the NBS pulsed high pressure mass spectrometer and standard techniques^{3,15} Reactions in the ion source were initiated by a 1 msec pulse of 500-1000 eV electrons, and equilibria in the clustering reactions were observed to 2-4 msec after the pulse.

The reaction mixtures were 0.1% - 10% CH_3CN in H_2O , at total source pressures of 0.2-1.0 torr. Checks were performed to verify that the equilibrium constants were independent of pressure in this range. Furthermore, some equilibria were replicated with CH_4 as the main carrier gas, with 10-20% H_2O and CH_3CN added. The thermochemical data obtained from the latter experiments agreed with those obtained with neat H_2O as the carrier gas within experimental error. However, the same equilibria are observed over a somewhat lower temperature range in the CH_4 mixtures than in the H_2O mixtures. The agreement indicates that thermal cluster dissociation outside the ion source is not significant.

The theoretical calculations were carried out ab initio using the Gaussian

80 series of programs¹⁶ on a VAX 11/780 computer. Optimized structures were obtained using the 3-21G basis set by the force relaxation method.¹⁷ Reported bond lengths represent convergence to 0.001 Å and bond angles to 0.1°. Since the 4-31G basis has been shown to yield reliable trends in solvation energies for related molecules,¹⁸⁻²² the 3-21G optimum structures were utilized to compute total energies at the 4-31G level, ie, HF/4-31G//HF/3-21G calculations were performed. In order to check the accuracy of the HF/4-31G//HF/3-21G solvation energies and to compare 3-21G and 4-31G optimum geometries, we optimized the structure of (H₂O)(CH₃CN)H⁺ at the 4-31G basis set level. The 4-31G structures of H₂O,²³ H₃O⁺,²³ CH₃CN,¹⁹ CH₃CNH⁺,¹⁹ (H₂O)_nH⁺, n=2-4,^{20,21} and (CH₃CN)_nH⁺, n=2,3,¹⁹ have been calculated, also. The total energies (E_T) obtained were then used to compute stabilization energies (ΔE_{n-1,n}) according to the following equations, where W = H₂O and Ac = CH₃CN.

$$\Delta E_{n-1,n} = E_T(W_n Ac_m H^+) - E_T(W_{n-1} Ac_m H^+) - E_T(W) \quad (2)$$

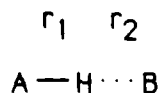
$$\Delta E_{m-1,m} = E_T(W_n Ac_m H^+) - E_T(W_n Ac_{m-1} H^+) - E_T(Ac) \quad (3)$$

No zero-point or basis-set superposition error (BSSE) corrections were made for any of the calculated energies. The BSSE obtained at the 4-31G level is small (1-2 kcal) and similar in magnitude for many supersystems.²⁴⁻²⁶ Zero-point energy effect generate ΔE's of only about 2 kcal also.^{20,26}

Geometry Optimization. The molecules investigated in the theoretical portion of this work are H₂O, H₃O⁺, CH₃CN, CH₃CNH⁺, (H₂O)_nH⁺, n=2-4, (CH₃CN)_mH⁺, m=2,3, (H₂O)_n(CH₃CN)H⁺, n=1-3, (H₂O)(CH₃CN)_mH⁺, m=2,3, and

$(\text{H}_2\text{O})_2(\text{CH}_3\text{CN})_2\text{H}^+$. The geometries of H_2O ,²¹ H_3O^+ ,²¹ CH_3CN ,²¹ CH_3CNH^+ , $(\text{H}_2\text{O})_2\text{H}^+$, and symmetric $(\text{CH}_3\text{CN})_2\text{H}^+$ were optimized completely. Partial geometry optimizations were carried out for all of the other complexes. With the exceptions noted below, the optimum structures of H_2O , H_3O^+ , CH_3CN , and CH_3CNH^+ were retained in the complexes and only selected bond lengths and bond angles (indicated in the Results and Analysis of Results section) between them were varied. For several $(\text{H}_2\text{O})_n(\text{CH}_3\text{CN})_m\text{H}^+$ ions, different isomers were considered (i.e., branched (I) and straight-chain (II)) and an optimum geometry and total energy were obtained for each isomer. The procedure of preserving the monomer structure in hydrogen-bonded systems has been utilized by many other research groups.^{18-22,27,28}

All hydrogen-bonded distances r_1 and r_2 (defined below) were varied.



Each $\text{A}-\text{H} \cdots \text{B}$ angle was optimized also in $(\text{H}_2\text{O})_2\text{H}^+$, $(\text{CH}_3\text{CN})_2\text{H}^+$, $(\text{H}_2\text{O})(\text{CH}_3\text{CN})\text{H}^+$, $(\text{H}_2\text{O})_2(\text{CH}_3\text{CN})\text{H}^+$ (I) and (II), and $(\text{H}_2\text{O})(\text{CH}_3\text{CN})_2\text{H}^+$ (I) and (II) and found to be 180° . Therefore, all of the hydrogen bonds in the remaining clusters were assumed to be linear.

For the cations where H_3O^+ is the central ion, the H_3O^+ was assumed to be planar and all three of the O-H bond lengths were optimized. When an H_2O molecule is both a hydrogen donor and acceptor, both O-H bond lengths were optimized. The H-O-H angles of H_3O^+ were not optimized. Calculations on $(\text{H}_2\text{O})_3\text{H}^+$, $(\text{H}_2\text{O})_2(\text{CH}_3\text{CN})\text{H}^+$, and $(\text{H}_2\text{O})(\text{CH}_3\text{CN})_2\text{H}^+$ with and without this

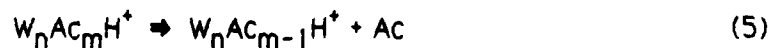
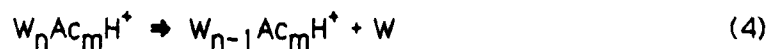
optimization showed that although the H-O-H angles changed by as much as 4°, the total energies changed by less than 0.2 kcal and the optimum bond lengths changed by less than 0.003Å. Clearly, the total energies, stabilization energies, and geometries of these complexes are relatively insensitive to variations in the H₃O⁺ H-O-H angles.

Several different orientations of the hydrogens in W₂H⁺, WAcH⁺, and Ac₂H⁺ were studied. It was determined for W₂H⁺ that the conformation with the two water planes perpendicular to each other is the most stable, in agreement with an earlier study at the 4-31G basis set level.¹³ The most stable conformation of WAcH⁺ is the one where the angle between the plane containing the H₂O molecule and the plane containing the NCCH atoms is 0° (or 90°). The total energy of Ac₂H⁺ is independent of the orientation of the methyl hydrogens.

Based on the above results, the following assumptions were made. (1) In all of the ions involving water hydrogen-water hydrogen and/or methyl hydrogen-water hydrogen nonbonded interactions, the hydrogens are oriented as they are in W₂H⁺ and WAcH⁺, respectively. (2) In all of the ions involving methyl hydrogen-methyl hydrogen nonbonded interactions, the hydrogens are staggered.

Results and Analysis of Results

A. Structures and Energetics. The cluster dissociation equilibria are of type (4) and (5).



The experimental thermochemical results are summarized in Table I and Figure 1. Table I lists the experimental dissociation enthalpies and the computed 3-21G//3-21G, 4-31G//3-21G, and 4-31G//4-31G total energies and dissociation energies. Figure 1 shows the specific dissociation reactions examined. The experimental error usually associated with these measurements is ± 1 kcal/mol for ΔH° and ± 2 cal/mol for ΔS° . The errors in the measurements involving ACH^+ , Ac_2H^+ , Ac_2WH^+ , and AcWH^+ in Figure 1 and Table I are consistent to this degree.

The structures obtained from the 3-21G and 4-31G optimizations are displayed in Figure 2. Only the values of the bond lengths and bond angles varied in the calculations are included in the figure. The 4-31G parameters are given in parentheses. The values of the remaining bond lengths and bond angles are those of the relevant parameters in H_2O ,^{20,23} CH_3CN ,^{19,23} and CH_3CNH^+ .

H_2O , H_3O^+ , CH_3CN , and CH_3CNH^+ . It has been pointed out previously²⁹ that 3-21G and 4-31G equilibrium geometries of one and two heavy atom systems are very similar. We find that this is true also for CH_3CN , for CH_3CNH^+ , and, in general, for r_1 and r_2 in the cluster ions we compared. Let $\Delta(\text{OH}) = r_{\text{OH}}(4-31\text{G}) - r_{\text{OH}}(3-21\text{G})$ and $\Delta(\angle\text{HOH}) = \angle\text{HOH}(4-31\text{G}) - \angle\text{HOH}(3-21\text{G})$. Then a negative value of Δ indicates that the magnitude of the O-H bond length or H-O-H bond angle is larger for the 3-21G basis set. For H_2O ,^{20,23} $\Delta(\text{OH}) = -0.017 \text{ \AA}$ and $\Delta(\angle\text{HOH}) = 3.7^\circ$; for H_3O^+ ,^{20,23} $\Delta(\text{OH}) = -0.015 \text{ \AA}$, $\Delta(\angle\text{HCH}) = 0.2^\circ$ and the average deviation in bond length is 0.002 \AA for CH_3CN ,^{20,24} while $\Delta(\angle\text{HCH}) = 0.2^\circ$ and the average deviation in bond length is 0.004 \AA for CH_3CNH^+ . The 4-31G//3-21G and 4-31G//4-31G total energies are in good agreement as well for these species, varying by at most 0.43 kcal.

$(\text{H}_2\text{O})_n\text{H}^+$, $(\text{CH}_3\text{CN})_m\text{H}^+$, and $(\text{H}_2\text{O})(\text{CH}_3\text{CN})\text{H}^+$. The structure of the

protonated water dimer calculated with the 3-21G basis set is close to that calculated with the 4-31G basis.²⁰ Both have a symmetric hydrogen bond with an H-O...O-H dihedral angle of 90°. $\Delta r_1 = \Delta r_2 = -0.010$ Å and $\Delta(\angle HOH) = 0.8^\circ$. As noted earlier,²⁰ the hydrogen bonds in W_3H^+ are asymmetric such that the complex essentially consists of a central H_3O^+ group interacting with two H_2O molecules.

Two isomers were considered for W_4H^+ . $W_4H^+(I)$ has a branched structure, ie, the fourth water molecule forms a hydrogen bond with the free hydrogen of the central H_3O^+ moiety, and is the more stable of the two (Table I). $\Delta r_1 = -0.016$ Å and $\Delta r_2 = 0.055$ Å for this ion. $W_4H^+(II)$ has a straight-chain structure, ie, the fourth water molecule forms a hydrogen bond with one of the outer water molecules rather than with the H_3O^+ moiety. For the latter cluster, addition of the last H_2O leads to structural rearrangements that make the central ion more properly represented as $H_5O_2^+$ rather than as H_3O^+ . When the geometry of $W_4H^+(II)$ was optimized using the 4-31G basis set,²⁰ the ion was constrained to be symmetric. That constraint was not imposed in this work, and the central hydrogen bond was found to be slightly asymmetric. Consequently, some of the Δr values are fairly large, with the largest being 0.070 Å.

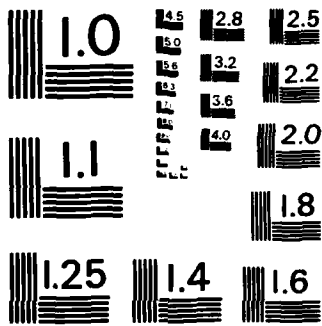
The dimer of $(CH_3CN)_2H^+$ with an asymmetric hydrogen bond is more stable at both basis set levels.¹⁹ However, the symmetric form is less than a kcal higher in energy. Thus, calculations that include polarization functions in the basis set and take electron correlation into account could reverse the relative stabilities of symmetric and asymmetric Ac_2H^+ as occurs for $OH^-(H_2O)$.³⁰ For the asymmetric system, $\Delta r_1 = -0.011$ Å and $\Delta r_2 = -0.040$ Å. Again, the magnitudes of Δr_1 and Δr_2 are noticeably higher in the complex than the Δr

values are in the subunits. However, part of the discrepancy may be due to the 4-31G structure not being completely optimized, since the 4-31G//4-31G total energy¹⁹ is higher than the 4-31G//3-21G total energy for the dimer.

Linear (to C-H) and T-shaped models of Ac_3H^+ were examined. The linear system is more stable, primarily due to the sizeable exchange repulsion in the T-shaped trimer.¹⁹ A comparison of the 4-31G//4-31G and 3-21G//3-21G equilibrium geometries of the Ac_3H^+ isomers is not useful, since not all of the hydrogen-bond bond lengths were varied in the 4-31G calculations.

$(\text{H}_2\text{O})(\text{CH}_3\text{CN})\text{H}^+$ has the hydrogen-bonded proton associated more closely with the acetonitrile, in accordance with the relative proton affinities of water and acetonitrile.³¹ The 3-21G results, however, show a hydrogen bond with a much longer r_1 (by 0.078 Å) and a much shorter r_2 (by 0.136 Å). The difference (acetonitrile - water) in the 3-21G//3-21G, 4-31G//4-31G, and experimental proton affinities is 7.3, 15.1, and 16.7 kcal, respectively. The incorrectly small difference obtained from the 3-21G//3-21G calculations leads to a more symmetric hydrogen bond, which accounts for the unusually large disparity in the two sets of r_1 and r_2 values.

Overall, the 4-31G r_1 distances tend to be shorter and the 4-31G r_2 distances tend to be longer, which is consistent with the weaker solvation energies obtained with this basis set (see below). Nevertheless, although the differences in the 4-31G//4-31G and 3-21G//3-21G equilibrium geometries of these systems are not always trivial, the differences in the 4-31G//3-21G and 4-31G//4-31G total energies (Table I) are quite small. The largest ΔE_T is 2.25 kcal (for $\text{W}_4\text{H}^+(\text{II})$) and most of them are less than 1 kcal. Not reoptimizing the geometries has even less effect on ΔE_D ; the largest $\delta\Delta E_D$ is 1.0 kcal (for WACH^+). Clearly, reoptimization of the 3-21G structures is unnecessary.



MICROCOPY RESOLUTION TEST CHART
NATIONAL BUREAU OF STANDARDS-1963-A

$(\text{H}_2\text{O})_n(\text{CH}_3\text{CN})_m\text{H}^+$. When either H_2O or CH_3CN is added to the H_2O group of WACH^+ to form $\text{W}_2\text{ACH}^+(\text{I})$ or $\text{WAC}_2\text{H}^+(\text{I})$, the proton that is associated with the CH_3CN group in WACH^+ moves along the hydrogen-bond axis such that both hydrogen-bonded protons in the trimers are associated with the central water molecule. In other words, these complexes consist of a central H_3O^+ moiety interacting with two solvent molecules, as was found for W_3H^+ . The result for $\text{W}_2\text{ACH}^+(\text{I})$ is consistent with the observation that the combined proton affinity of two water molecules ($166.5 + 32.9 = 199.4 \text{ kcal/mol}^{31,32}$) is greater than the proton affinity of CH_3CN ($189.2 \text{ kcal/mol}^{31}$). The other, less stable isomer considered for W_2ACH^+ and WAC_2H^+ has the additional solvent molecule forming an unconventional linear $\text{C-H}^{\delta+} \cdots \text{X}$ hydrogen bond. For $\text{W}_2\text{ACH}^+(\text{II})$ and $\text{WAC}_2\text{H}^+(\text{II})$ the proton remains on the central acetonitrile.

Since the latter isomers of W_2ACH^+ and WAC_2H^+ are so much less stable than the former (Table I), no clusters containing $\text{C-H}^{\delta+} \cdots \text{X}$ hydrogen bonds were investigated for the tetramers. Thus, only the branched structure of WAC_3H^+ and the branched (I) and straight-chain (II) structures of W_3ACH^+ and $\text{W}_2\text{AC}_2\text{H}^+$ were studied. Again, the straight-chain systems are higher in energy and have a slightly asymmetric H_5O_2^+ group interacting with two solvent molecules. In fact, the $\text{W}_4\text{H}^+(\text{II})$, $\text{W}_3\text{ACH}^+(\text{II})$, and $\text{W}_2\text{AC}_2\text{H}^+(\text{II})$ r_1 and r_2 values for the H_5O_2^+ moiety are very similar.

B. Population Analysis. The charge distributions obtained from Mulliken population analysis³³ are presented in Figure 2. The figure shows that there is no extensive delocalization of the positive charge in these complexes, with the exception of H_5O_2^+ . They are best represented as a central cation bonded to one or more solvent molecules. The positive charge on the central ion,

H_3O^+ or H_5O_2^+ , does decrease as the number of solvent molecules increases; however, the charge transferred from a given solvent molecule decreases as their number increases. Overall, the central cation retains 70-80% of the positive charge. The charge changes observed in this work for the individual atoms or groups of atoms upon hydrogen-bond formation are consistent with those observed by other researchers.^{19,21,22}

Table II tabulates the charge gain on the proton-donating atom Δq_A and the electron-donating atom Δq_B , the charge loss on the atom(s) directly bonded to the electron-donating atom Δq_{BL} (BL = C or H), the charge transfer Δq_{CT} , and the charge on the hydrogen-bonded proton before q_H and after $q_{H,HB}$ the hydrogen bond is formed for the reactions studied. Table III shows r_1 , r_2 , R , r_1/R , and the A-H and H...B overlap populations. The reactions are arranged from highest to lowest ΔE_D . The data in the tables are from the 3-21G results.

C. Trends in ΔE_D and ΔH° . The ΔE_D values are generally too high compared to the ΔH° values at both the 3-21G and 4-31G basis set levels, although the 4-31G ΔE_D 's are consistently closer to the experimental ΔH° 's. Much of the disparity in the two sets of theoretical data and some of the disparity in the theoretical and experimental data is accounted for by BSSE.²⁴⁻²⁶ There are several reasons the corrected ΔE_D 's are overestimated. They are the poor quality of the calculated multipole moments of CH_3CN and H_2O ,^{25,34,35} neglecting zero-point energies, and not including polarization functions or electron correlation in the calculations. Latajka and Scheiner³⁵ have shown that it is necessary to add a set of diffuse polarization functions to a DZ+P basis in order to properly reproduce the electrical properties of the subunits, to evaluate accurate electron correlation effects, and to obtain solvation energies in good agreement with experimental solvation enthalpies.

For both basis sets, the value of $\Delta E_D - \Delta H^\circ$ is considerably bigger when the electron donor is H_2O . Two factors that contribute to this result are the following. First, and more importantly, the poorer computed charge distribution for H_2O than for CH_3CN , as reflected in the larger deviation in the experimental and calculated dipole moment for H_2O than for CH_3CN (0.708 D vs. 0.167 D for the 4-31G basis), will produce more exaggerated ΔE_D 's when H_2O is the electron donor. Second, results from other systems suggest that the BSSE will be larger for clusters made by adding H_2O than by adding CH_3CN , since H_2O is a smaller molecule.^{24,25}

The trends in the ΔH° values are reproduced reasonably well by the calculations for each series of reactions involving a given electron donor, especially by the 4-31G basis set. However, the experimental and calculated trends are not the same when one compares the stabilization achieved when water versus acetonitrile is added to a specific cation. In some cases, the experimental results show that the complex should be stabilized more by CH_3CN and the theoretical results show the opposite. An examination of the 4-31G data for these cases (ACH^+ , $WACH^+$, and Ac_2H^+), yields that $\Delta E_D - \Delta H^\circ$ for H_2O solvation is approximately 6.7 kcal higher than for CH_3CN solvation. Thus, the error is consistent. It is also not unexpected due to the larger overestimation of ΔE_D values mentioned above for the H_2O series of reactions.

From the comparison of the 4-31G//3-21G and 3-21G//3-21G ΔE_D 's and ΔH° 's with respect to the ΔH° 's and ΔH° 's, one concludes that either the 3-21G energies should be corrected for BSSE or 4-31G//3-21G energies should be computed. Both methods yield more accurate stabilization energies and relative energies than are obtained from the simple 3-21G//3-21G

calculations.

The relative dissociation energies of the cluster ions correlate with a number of properties of the ions. The data in Tables II and III demonstrate that for a given electron donor, regardless of the type of proton-donating atom (ie, C, N, or O), there is a direct relationship between the differences in the complexation energies and the charge gain on the proton-accepting atom Δq_B , the charge loss on the atom(s) directly bonded to the proton-accepting atom Δq_{BL} (BL = C or H), the charge transfer Δq_{CT} , the charge on the hydrogen-bonded proton after the hydrogen bond is formed $q_{H,HB}$, r_1/R , and the H...B overlap population (with the exception of the overlap population of $WACH^+$ which is too high). There is an indirect relationship between the energy differences and r_2 . These results indicate that delocalization effects as well as electrostatic effects contribute to the stability of the clusters.

It should be noted that all of the above are properties of the electron donor. As a result of the different types of proton-donating atoms and the large charge and structural rearrangements in some proton-donating molecules brought about by hydrogen-bond formation (Figure 2), it is not unreasonable that there is no correlation between the proton donor properties and relative stabilization energies when all of the proton donors are compared. On the other hand, if only clusters with the same type of A atom are compared, the $\delta\Delta E_D$'s also correlate directly with the charge on the hydrogen-bonded proton before the hydrogen bond is formed q_H and indirectly with the A-H overlap population and R. The only exceptions to the former relationship are the reactions where a solvent molecule is added to the H_2O moiety in $WACH^+$. The q_H for these cases is too low because the water is essentially neutral in $WACH^+$. Other researchers have seen similar correlations in other hydrogen-bonded systems.^{20,21,28,36}

D. Cooperativity Effects. The transfer of electron density to the

proton-donating molecule when a hydrogen bond is formed makes that molecule a poorer proton donor for subsequent hydrogen bonds.^{20,21,27} Thus, when a molecule serves as a multiple proton donor, ΔE_D decreases as successive solvent molecules are added (Figure 1 and Table I). However, the structural changes that occur within the proton donor indicate that the subsequent hydrogen bonds are not as weak as they could be, ie, there is a cooperativity effect among the hydrogen bonds. When a second hydrogen bond is formed, r_1 shortens and r_2 lengthens for the first hydrogen bond. A compromise is reached whereby the first hydrogen bond is weakened relative to its strength in the dimer to allow the second hydrogen bond to strengthen somewhat. Thus, it is more favorable to make two moderately strong, partially protonated, hydrogen bonds than to make one strong, essentially fully protonated, and one weak, essentially neutral, hydrogen bond. Similar results are observed for larger clusters as well.

When straight-chain isomers are formed, the structural changes are even more pronounced. As noted above, in these cases the central ion is converted from essentially H_3O^+ to essentially $H_5O_2^+$. There is also an increase in r_2 and a decrease in r_1 for the other hydrogen bond to the H_3O^+ . When a second shell water molecule acts as a proton donor, it improves its capacity to serve as an electron donor. Therefore, the interaction between it and the H_3O^+ ion is strengthened at the expense of the other hydrogen bond involving the H_3O^+ .

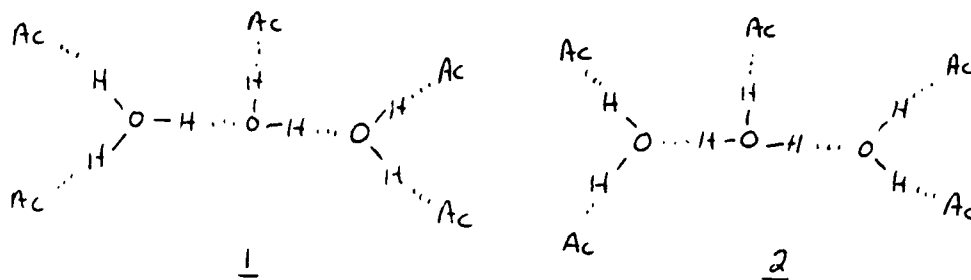
E. Isomers. In order to explore the possibility that more than one isomeric form exists for some of the $n + m = 4$ complexes, branched (I) and straight-chain (II) structures were examined for W_3ACH^+ , $W_2AC_2H^+$, and WAC_3H^+ . The branched isomer is universally more stable than the straight-chain isomer. The lower stability of the straight-chain clusters results from 1) a smaller q_H , r_1 , r_1/R , and $H \cdots B$ overlap population, 2) a larger R and $A-H$ overlap population, and 3) less polarization of the electron

donor and slightly less charge transfer to the proton donor. However, the straight-chain form is only about 2-5 kcal higher in energy than the branched form of a specific ion depending on the basis set employed. Since the 4-31G basis yields more reliable ΔE_D 's and $\delta\Delta E_D$'s, that data will be used here. The differences in the 4-31G stabilization energies are 4-5 kcal, suggesting that mixtures of ions will not be present for these systems. This is consistent with the experimental enthalpy data which shows that for the $W_nAc_mH^+$ ions there is a significant drop in $\Delta H^*_{k,k-1}$ ($k = m + n$) for reactions after $k=3$ (for $n = 0$). We have found that these criteria fulfill the quantitative requirements for the filling of the second solvent shell at $k = 3$.

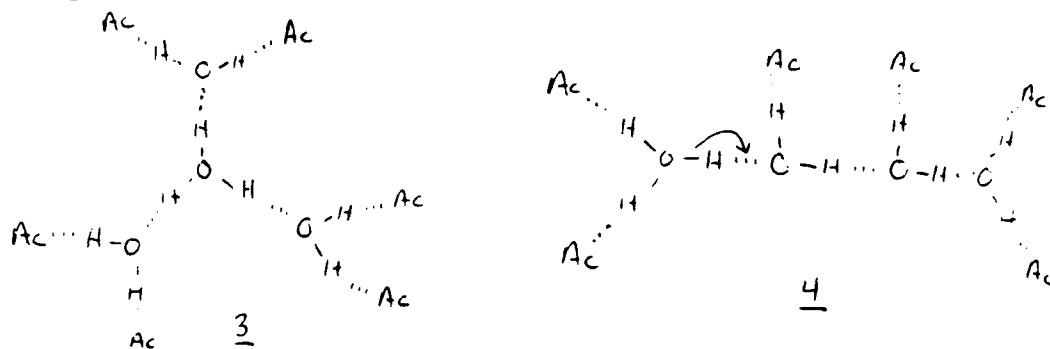
F. Rule on Relative Cluster Stability. With respect to the stability of the clusters, two factors appear to be important: the high proton affinity of CH_3CN compared to H_2O and the hydrogen bonding of water. Thus, the most stable dimer in terms of the total enthalpy of dissociation is Ac_2H^+ (Figure 1 and Table I). However, since in Ac_3H^+ the second hydrogen bond is a weak unconventional $C-H^{\delta+} \cdots N$ bond, the most stable trimer is WAc_2H^+ , ie, the complex with the highest acetonitrile content for which an optimal hydrogen-bonding configuration is still allowed. The same rule yields WAc_3H^+ as the most stable tetramer, and $W_2Ac_3H^+$ as the most stable pentamer. WAc_4H^+ , which could not be observed, requires a hydrogen-bonded structure blocked by methyl groups. Therefore, the following rule seems to apply to all of the observed water-acetonitrile complexes: the most stable clusters are those with the highest acetonitrile content which still allows the formation of a network of strong, eg. $N-H \cdots O$ and $O-H \cdots O$, hydrogen bonds.

The general formula for clusters with n water molecules containing the maximum amount of acetonitrile molecules is $W_nAc_{n+2}H^+$. For $n = 2$ and 3, only two isomers each are possible, and these differ only by a shift of the

proton as illustrated schematically in ions 1 and 2. (Acetonitrile is denoted by Ac.)

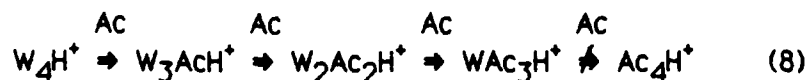
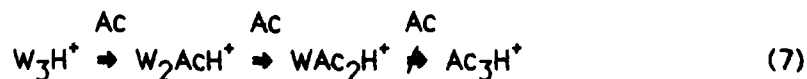


For $n \geq 4$ several isomers are possible, the extreme of which are illustrated schematically by ions 3 and 4. In 3 the acetonitrile molecules are pushed to the periphery such that ultimately the proton is solvated by a neat water environment. In 4 two acetonitrile molecules are placed close to the protonated center, or at least one acetonitrile molecule is attached to the protonated center if the proton moves as indicated, while some are even further away from the protonated center than they are in 3. The trends observed in the smaller clusters suggest that acetonitrile molecules proximal to the protonated center are stabilizing, and, therefore, that linear configurations such as 4 would be preferred to globular configurations such as 3.



We note that the structures in the acetonitrile-water systems are similar to those in the dimethyl ether-water systems. For these two cases the relative proton affinities and methyl blocking effects are comparable.⁵

G. SIFT Results. Smith et al.¹⁴ have carried out studies using a selected ion flow tube (SIFT) that show that CH₃CN rapidly replaces H₂O in the (H₂O)_nH⁺ ions according to the following reactions.



One question that arises from this work is why the last water molecule cannot be replaced in the last two sequences of reactions. The results are readily explained by the observations that 1) the central ion in these complexes is H₃O⁺ and 2) only the outer water molecules are replaced by the acetonitrile molecules. However, Smith and Adams³⁷ also found that when WAc₂H⁺ and WAc₃H⁺ are broken apart no H₃O⁺ is obtained, which is in apparent disagreement with observation 1). In actuality, the structures we calculated are not ruled out by the latter result because Smith and Adams broke the complexes apart stepwise. Thus, the last hydrogen bond broken is the one in WAcH⁺. Recall that in WAcH⁺ the more stable position for the proton is on the acetonitrile rather than on the water. No H₃O⁺ will be observed if there is time for the proton to migrate from the H₂O to the CH₃CN before the dissociation occurs.

Summary

Analysis of the theoretical and experimental data reported in this article answers some of the questions posed in the Introduction. First, the charged proton is best stabilized by placing the maximum number of acetonitrile molecules proximate to the protonated center in such a way that the

formation of a network of strong hydrogen bonds is still allowed. Second, distinct solvent shells can be distinguished in these cluster ions. Third, mixtures of several isomeric structures are unlikely for $n \leq 4$. Fourth, a group of solvent molecules can "pull away" the proton from a protonated solute molecule. Fifth, although electrostatic interactions make the dominant contribution to the bonding in these systems, polarization and charge transfer effects contribute also. Sixth, there is a cooperativity effect among the hydrogen bonds that leads to extensive changes in geometry and charge distribution as successive hydrogen bonds are formed. Seventh, the relative stabilization energies along a series of reactions correlate with many properties of the electron donor and with several properties of the proton donor. Eighth, the fact that the last water molecule in WAc_mH^+ , $m = 2$ and 3 , is not replaced by acetonitrile, yet no H_3O^+ ions are observed when the clusters are broken apart in a stepwise manner, is explained by our structural results.

Acknowledgment

The support of the Holy Cross Data Processing Center and of the Air Force Geophysics Laboratory Information Resources Center is gratefully acknowledged. This work was sponsored by the Air Force Office of Scientific Research, Bolling AFB, Washington, D. C.

References

1. Kebarle, P. Ann. Rev. Phys. Chem. 1977, **28**, 445.
2. A review of clustering data is given in Keesee, R. G. ; Castleman, A. W. J. Phys. Chem. Ref. Data 1985, in press.
3. Meot-Ner (Mautner), M. J. Am. Chem. Soc. 1984, **106**, 1265.
4. Payzant, J. D. ; Cunningham, A. J. ; Kebarle, P. Can. J. Chem. 1973, **51**, 3242.
5. Hiraoka, K. ; Grimsrud, E. P. ; Kebarle, P. J. Am. Chem. Soc. 1974, **96**, 3359.
6. Arnold, F. ; Krankowsky, D. ; Marien, K. H. Nature 1977, **267**, 30.
7. Arnold, F. ; Bohringer, H. ; Henschen, G. Geophys. Res. Lett. 1978, **5**, 653.
8. a) Arijs, E. ; Ingels, J. ; Nevejans, D. Nature 1978, **271**, 642. b) Arijs, E. ; Nevejans, D. ; Ingels, J. ibid. 1980, **288**, 684.
9. a) Arijs, E. ; Nevejans, D. ; Ingels, J. Nature 1983, **303**, 314. b) Arijs, E. ; Nevejans, D. ; Ingels, J. ; Frederick, P. Ann. Geophys. 1983, **1**, 161.
10. Ferguson, E. E. ; Arnold, F. Acc. Chem. Res. 1981, **14**, 327.
11. Arnold, F. "Physics and Chemistry of Atmospheric Ions," Atmospheric Chemistry, ed. E. D. Goldberg, Springer-Verlag, New York, 1982.
12. Arnold, F. ; Henschen, G. ; Ferguson, E. E. Planet. Space Sci. 1981, **29**, 185.
13. Bohringer, H. ; Arnold, F. Nature 1981, **290**, 321.
14. Smith, D. ; Adams, N. G. ; Alge, E. Planet. Space Sci. 1981, **29**, 449.
15. Meot-Ner (Mautner), M. ; Sieck, L. W. J. Am. Chem. Soc. 1983, **103**, 2956.
16. a) Binkley, J. S. ; Whiteside, R. A. ; Krishnan, R. ; Seeger, R. ; DeFrees, D. J. ; Schlegel, H. B. ; Topiol, S. ; Kahn, L. R. ; Pople, J. A. QCPE 1981, **13**, 406. b) Krogh-Jespersen, K., private communication.
17. a) Pulay, P. Molec. Phys. 1969, **17**, 197. b) Schlegel, H. B. ; Wolfe, S. ; Bernardi, F. J. Chem. Phys. 1975, **63**, 3632.
18. Hirao, K. ; Sano, M. ; Yamabe S. Chem. Phys. Lett. 1982, **95**, 7939.
19. Hirao, K. ; Yamabe, S. ; Sano, M. J. Phys. Chem. 1982, **86**, 2626.

20. Newton, M. D. ; Ehrenson, S. J. Am. Chem. Soc. 1971, 93, 4971.
21. Newton, M. D. J. Chem. Phys. 1977, 67, 5535.
22. Hirao, K. ; Fujikawa, T. ; Konishi, H. ; Yamabe, S. Chem. Phys. Lett. 1984, 104, 184.
23. Whiteside, R. A. ; Frisch, M. J. ; Binkley, J. S. ; DeFrees, D. J. ; Schlegel, H. B. ; Raghavachari, K. ; Pople, J. A. "Carnegie-Mellon Quantum Chemistry Archives," Department of Chemistry, Carnegie-Mellon University, Pittsburgh, PA 15123.
24. Hobza, P. ; Zahradnik, R. Chem. Phys. Lett. 1981, 82, 473.
25. Sokalski, W. A. ; Hariharan, P. C. ; Kaufman, J. J. J. Phys. Chem. 1983, 87, 2803.
26. Meot-Ner (Mautner), M. ; Deakyne, C. A. Submitted for publication.
27. Kollman, P. A. "Hydrogen Bonding and Donor-Acceptor Interactions," Applications of Electronic Structure Theory, ed. H. F. Schaefer III, Plenum Press, New York, pp. 109-152, 1977.
28. Desmeules, P. J. ; Allen, L. C. J. Chem. Phys. 1980, 72, 4731.
29. Binkley, J. S. ; Pople, J. A. ; Hehre, W. J. J. Am. Chem. Soc. 1980, 102, 939.
30. Rohlfing, C. M. ; Allen, L. C. ; Cook, C. M. ; Schlegel, H. B. J. Chem. Phys. 1983, 78, 1498.
31. Lias, S. G. ; Liebman, J. F. ; Levin, R. D. J. Phys. Chem. Ref. Data 1984, 13, 695.
32. Lau, Y. K. ; Ikuta, S. ; Kebarle, P. J. Am. Chem. Soc. 1982, 104, 462.
33. Mulliken, R. S. J. Chem. Phys. 1955, 23, 1833.
34. Sokalski, W. A. ; Hariharan, P. C. ; Kaufman, J. J. J. Comput. Chem. 1983, 4, 506.
35. Latajka, Z. ; Scheiner, S. J. Phys. Chem. 1984, 81, 4014.
36. Deakyne, C. A. "Conventional and Unconventional Ionic Hydrogen Bonds. Theoretical Calculations," in Methods in Stereochemical Analysis: Molecular Structures and Energetics - IV, eds. J. F. Liebman and A. Greenberg, Verlag Chemie International, in press.

37. Smith, D. ; Adams, N. G. Personal communication.

38. Meot-Ner(Mautner),M. J. Am. Chem. Soc. 1978, 100,4694.

Table I. Total Energies (E_T , a.u.), Dissociation Energies (ΔE_D , kcal), and
Dissociation Enthalpies (ΔH° , kcal) of $W_nAc_mH^+$ Complexes.

Molecule	$E_T(3-21G)$	$E_T(4-31G)^a$	$\Delta E_D(3-21G)$	$\Delta E_D(4-31G)^a$	ΔH°
W	-75.58596	-75.90792 (-75.9086)			
WH ⁺	-75.89123	-76.20001 (-76.2006)	191.6	183.3 (183.2)	166.5 ^D
W ₂ H ⁺	-151.56094	-152.17852 (-152.1791)	52.6	44.3 (43.6)	32.9
W ₃ H ⁺	-227.20350	-228.13549 (-228.1370)	35.5	30.8 (30.9)	19.0
W ₄ H ⁺ (I)	-302.83597	-304.08475 (-304.0872)	29.2	25.9 (26.1)	17.6
W ₄ H ⁺ (II)	-302.83059	-304.07611 (-304.07970)	25.8	20.5 (21.4)	
Ac	-131.19180	-131.72823 (-131.7283)			
AcH ⁺	-131.50875	-132.04445 (-132.0445)	198.9	198.4 (198.4)	189.2 ^D
Ac ₂ H ⁺ (asym)	-262.75653	-263.82175 (-263.8213)	35.1	30.8 (30.4)	30.2 ^C
Ac ₂ H ⁺ (sym)	-262.75605	-263.82035	34.8	29.9	
Ac ₃ H ⁺ (C-H)	-393.96994	-395.56985 (-395.56843)	13.6	12.5 (11.9)	9.3 ^C
Ac ₃ H ⁺ (T-shape)	-393.96059	-395.56095	7.7	6.9	
WAcH ⁺	-207.15909	-208.00161 (-208.0040) ^d	40.4	30.9 (31.9) ^d	24.8
W ₂ AcH ⁺ (I)	-282.80158	-283.95391	35.5	27.9	17.5
W ₂ AcH ⁺ (II)	-282.76855	-283.92840	14.7	11.8	
W ₃ AcH ⁺ (I)	-358.43436	-359.90209	29.4	25.3	15.6
W ₃ AcH ⁺ (II)	-358.42985	-359.89495	26.5	20.8	

Table I cont.

Molecule	$E_T(3-21G)$	$E_T(4-31G)^a$	$\Delta E_D(3-21G)$	$\Delta E_D(4-31G)^b$	ΔH^c
$WAc_2H^+(I)$	-338.39989	-339.77294	30.7 ^d	27.1 ^e	23.4 ^f
			36.0	27.2	15.9
$WAc_2H^+(II)$	-338.37242	-339.75026	13.5 ^d	12.9 ^e	
			18.8	13.0	
WAc_3H^+	-469.63126	-471.53831	24.8	23.3	20.6
$W_2Ac_2H^+(I)$	-414.03312	-415.72040	29.7	24.8	15.3
$W_2Ac_2H^+(II)$	-414.02960	-415.71413	27.5	20.9	

^aThe number in parentheses is the 4-31G//4-31G value; the other number is the 4-31G//3-21G value. The 4-31G//4-31G results for the W_nH^+ ions are from reference 20; the 4-31G//4-31G results for the Ac_mH^+ ions are from reference 19. ^bReference 31. ^cReference 38. ^dThis work. ^eThe top number is the value obtained when WAc_2H^+ dissociates into $WAcH^+ + Ac$; the bottom number is the value obtained when WAc_2H^+ dissociates into $Ac_2H^+ + W$.

Table II. Properties of the Hydrogen-Bonded Clusters from Population Analysis.^a

Reaction	ΔE_D	Δq_A	Δq_B	$\Delta q_{B,BL}$	Δq_{CT}	q_H	$q_{H,HB}$
$ACH^+ \Rightarrow AC_2H^+{}^D$	35.1	-0.019	-0.242	0.270	0.148	0.519	0.580
$WACH^+ \Rightarrow WAC_2H^+(I)$	30.7	-0.070	-0.218	0.230	0.117	0.471	0.562
$W_2H^+ \Rightarrow W_2ACH^+(I)$	30.6	-0.061	-0.218	0.227	0.114	0.499	0.559
$W_2ACH^+(I) \Rightarrow W_2AC_2H^+(I)$	24.9	-0.049	-0.177	0.185	0.091	0.486	0.534
$WAC_2H^+(I) \Rightarrow WAC_3H^+$	24.8	-0.047	-0.178	0.188	0.093	0.489	0.538
$W_2ACH^+(I) \Rightarrow W_2AC_2H^+(II)$	22.7	-0.076	-0.168	0.172	0.084	0.456	0.514
$WACH^+ \Rightarrow WAC_2H^+(II)$	13.5	-0.064	-0.102	0.101	0.051	0.335	0.414
$AC_2H^+ \Rightarrow AC_3H^+(I \text{ near to C-H})$	13.2	-0.063	-0.102	0.101	0.051	0.336	0.414

$WH^+ \Rightarrow W_2H^+{}^C$	52.6	-0.080	-0.061	0.133	0.500	0.571	0.591
$ACH^+ \Rightarrow WACH^+$	40.4	-0.018	-0.043	0.105	0.167	0.519	0.591
$W_2H^+ \Rightarrow W_3H^+$	35.5	-0.070	-0.046	0.093	0.140	0.499	0.554
$WACH^+ \Rightarrow W_2ACH^+(I)$	35.5	-0.079	-0.043	0.090	0.137	0.471	0.559
$W_2ACH^+(I) \Rightarrow W_3ACH^+(I)$	29.4	-0.059	-0.032	0.073	0.114	0.486	0.532
$W_3H^+ \Rightarrow W_4H^+(I)$	29.2	-0.055	-0.036	0.075	0.114	0.482	0.528
$W_2ACH^+(I) \Rightarrow W_3ACH^+(II)$	26.5	-0.089	-0.030	0.068	0.106	0.456	0.513
$W_3H^+ \Rightarrow W_4H^+(II)$	25.8	-0.083	-0.029	0.068	0.106	0.459	0.509
$WACH^+ \Rightarrow W_2ACH^+(II)$	14.7	-0.073	-0.002	0.041	0.080	0.335	0.412

^aThe data is from the 3-21G results. A negative value means the parameter is more negatively charged after the reaction than before. ^bReactions where CH_3CN is one of the reactants. ^cReactions where H_2O is one of the reactants.

Table III. Structural Properties of the Hydrogen-Bonded Clusters.

Reaction	ΔE_D	r_1	r_2	R	r_1/R	A-H	H...B overlap population
$\text{AcH}^+ \rightleftharpoons \text{Ac}_2\text{H}^+ \text{ } ^{\text{b}}$	35.1	1.115	1.456	2.571	0.434	0.298	0.261
$\text{WAcH}^+ \rightleftharpoons \text{WAc}_2\text{H}^+(1)$	30.7	1.031	1.538	2.569	0.401	0.366	0.184
$\text{W}_2\text{H}^+ \rightleftharpoons \text{W}_2\text{AcH}^+(1)$	30.6	1.028	1.549	2.577	0.399	0.370	0.181
$\text{W}_2\text{AcH}^+(1) \rightleftharpoons \text{W}_2\text{Ac}_2\text{H}^+(1)$	24.9	1.000	1.655	2.655	0.377	0.416	0.152
$\text{WAc}_2\text{H}^+(1) \rightleftharpoons \text{WAc}_3\text{H}^+$	24.8	1.003	1.643	2.646	0.379	0.412	0.155
$\text{W}_2\text{AcH}^+(1) \rightleftharpoons \text{W}_2\text{Ac}_2\text{H}^+(11)$	22.7	0.996	1.699	2.695	0.370	0.435	0.134
$\text{WAcH}^+ \rightleftharpoons \text{WAc}_2\text{H}^+(11)$	13.5	1.090	2.094	3.184	0.342	0.591	0.104
$\text{Ac}_2\text{H}^+ \rightleftharpoons \text{Ac}_3\text{H}^+(\text{linear to C-H})$	13.2	1.090	2.091	3.181	0.343	0.592	0.104

$\text{WH}^+ \rightleftharpoons \text{W}_2\text{H}^+ \text{ } ^{\text{c}}$	52.6	1.190	1.190	2.380	0.500	0.260	0.260
$\text{AcH}^+ \rightleftharpoons \text{WAcH}^+$	40.4	1.159	1.292	2.451	0.473	0.269	0.269
$\text{W}_2\text{H}^+ \rightleftharpoons \text{W}_3\text{H}^+$	35.5	1.052	1.390	2.442	0.431	0.343	0.211
$\text{WAcH}^+ \rightleftharpoons \text{W}_2\text{AcH}^+(1)$	35.5	1.054	1.384	2.438	0.432	0.343	0.209
$\text{W}_2\text{AcH}^+(1) \rightleftharpoons \text{W}_3\text{AcH}^+(1)$	29.4	1.018	1.476	2.494	0.408	0.389	0.185
$\text{W}_3\text{H}^+ \rightleftharpoons \text{W}_4\text{H}^+(1)$	29.2	1.016	1.485	2.501	0.406	0.390	0.186
$\text{W}_2\text{AcH}^+(1) \rightleftharpoons \text{W}_3\text{AcH}^+(11)$	26.5	1.012	1.517	2.529	0.400	0.408	0.169
$\text{W}_3\text{H}^+ \rightleftharpoons \text{W}_4\text{H}^+(11)$	25.8	1.010	1.527	2.537	0.398	0.412	0.167
$\text{WAcH}^+ \rightleftharpoons \text{W}_2\text{AcH}^+(11)$	14.7	1.095	1.908	3.003	0.365	0.535	0.150

^aThe data is from the 3-21G results. ^bReactions where CH_3CN is one of the reactants. ^cReactions where H_2O is one of the reactants.

Figure Captions

Figure 1. $-\Delta H^\circ$ (kcal/mol, top number) and $-\Delta S^\circ$ (cal/mol K, bottom number) of clustering reactions, where $\text{AcH}^+ \rightleftharpoons \text{Ac}_2\text{H}^+$ indicates $\text{AcH}^+ + \text{Ac} \rightleftharpoons \text{Ac}_2\text{H}^+$, etc. The number under the ions indicates the total dissociation enthalpy for $\text{W}_n\text{Ac}_m\text{H}^+ \rightleftharpoons \text{WH}^+ + m\text{Ac} + (n-1)\text{W}$. The proton affinities are from reference 32. The data for the neat water clusters are from the present authors (unpublished data) for $n = 1-4$ and from reference 33 for $n = 5-7$. The data for the neat acetonitrile clusters are from reference 38. For $\text{WAc}_3\text{H}^+ \rightleftharpoons \text{W}_2\text{Ac}_3\text{H}^+$, ΔS° was estimated and ΔH° was obtained from the measured $\Delta G^\circ(316) = -2.8$ kcal/mol. For $\text{W}_4\text{AcH}^+ \rightleftharpoons \text{W}_4\text{Ac}_2\text{H}^+$, ΔH° was obtained from $\Delta G^\circ(318) = -7.4$ kcal/mol.

Figure 2. Structures calculated from 3-21G and 4-31G optimizations. Only the values of the bond distances and bond angles varied in the computations are included. The 4-31G parameters are given in parentheses. Charge distributions from population analysis (3-21G basis set level) are displayed, also.

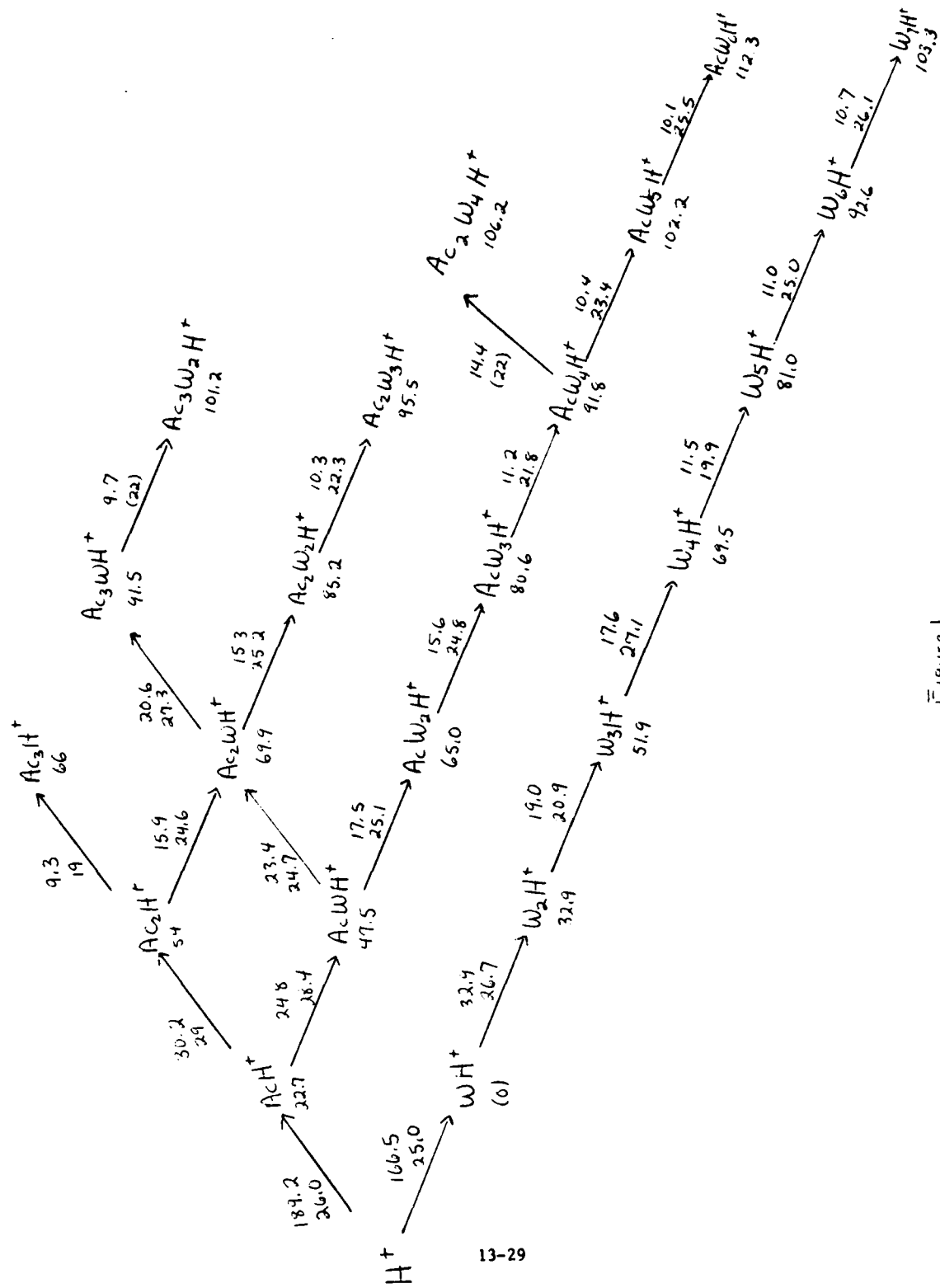


Figure 1

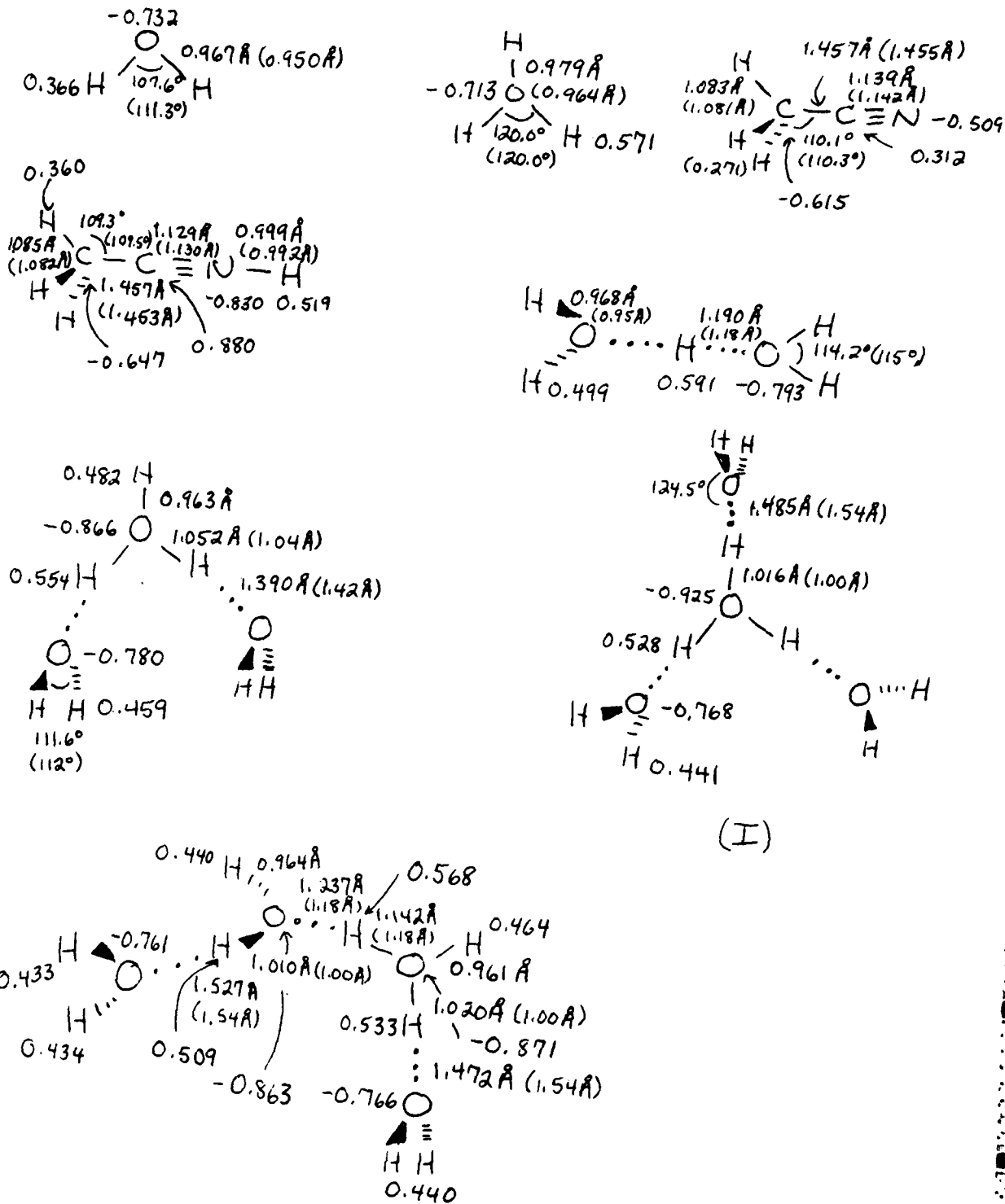


Figure 2 13-30

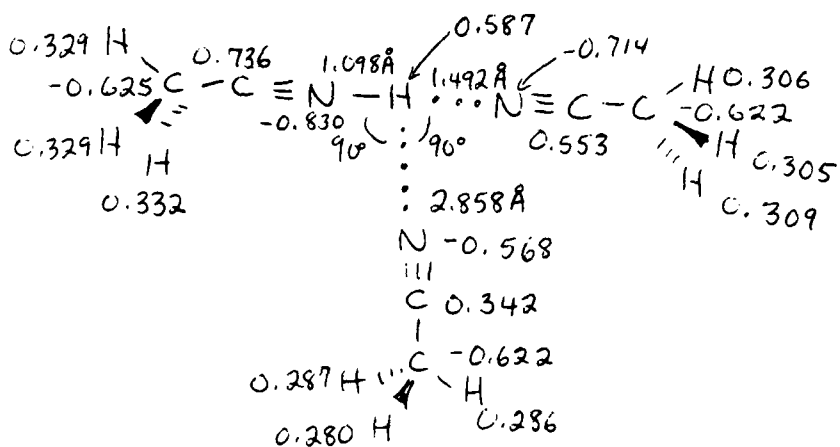
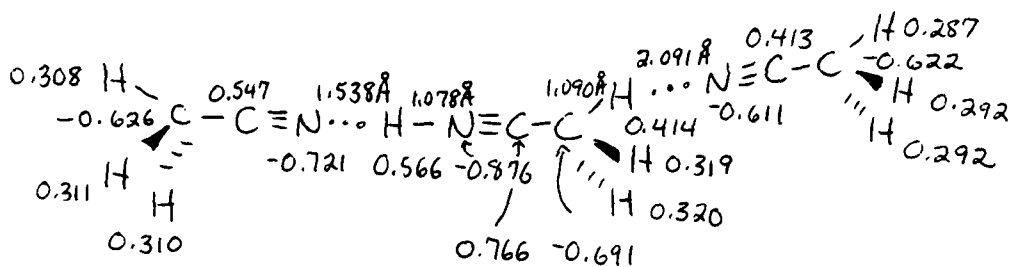
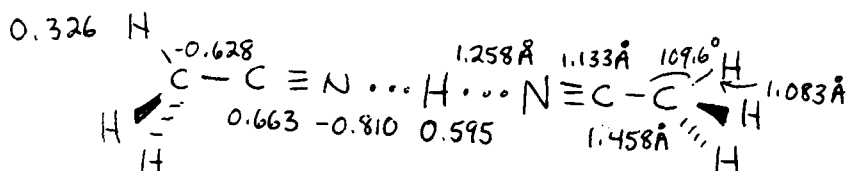
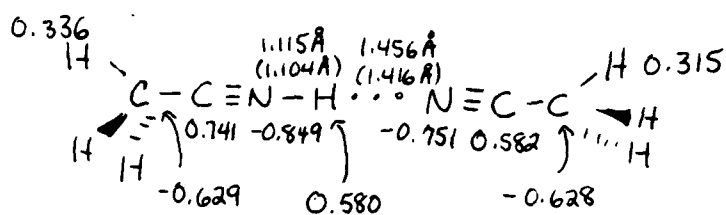
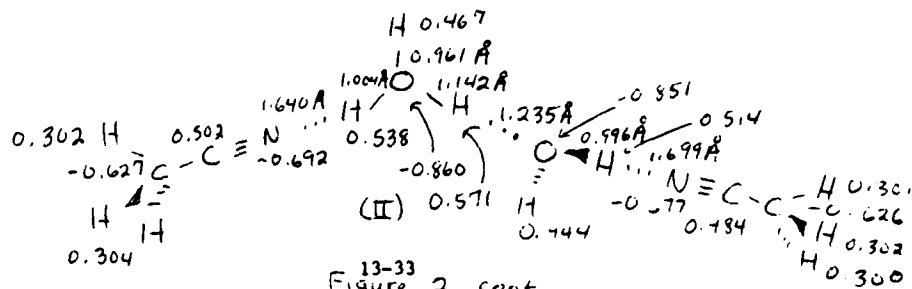
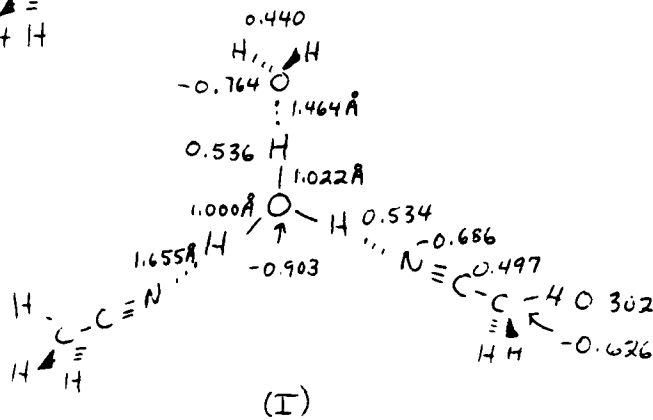
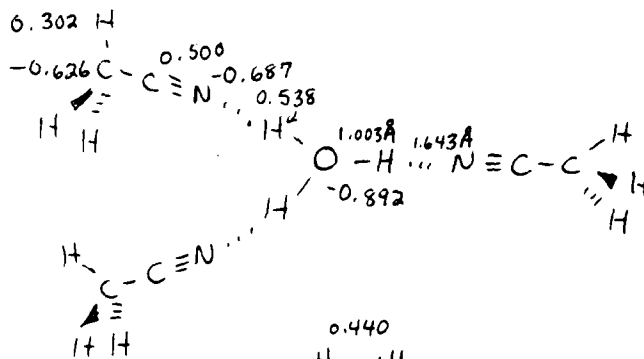
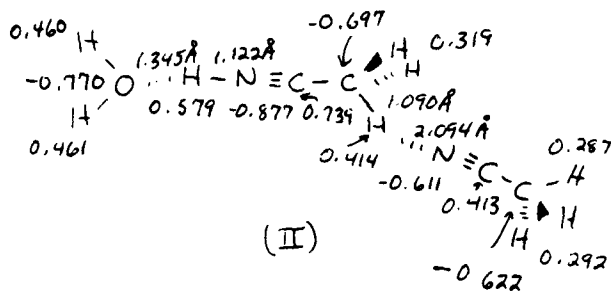
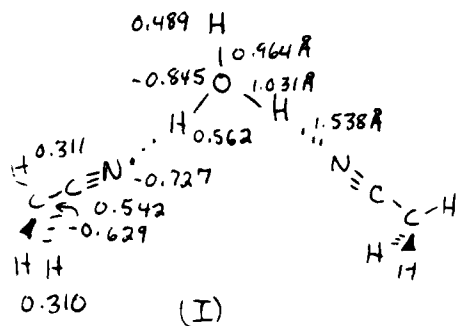


Figure 2 cont.
13-31



13-33
 Figure 2 cont

1983-84 USAF-SCEEE RESEARCH INITIATION PROGRAM

Sponsored by the

AIR FORCE OFFICE OF SCIENTIFIC RESEARCH

Conducted by the

SOUTHEASTERN CENTER FOR ELECTRICAL ENGINEERING EDUCATION

FINAL REPORT

TRAINING TO IMPROVE THE ACCURACY AND VALIDITY OF PERFORMANCE RATINGS

Prepared by: Dr. Terry L. Dickinson

Academic Rank: Professor

Department and
University: Psychology Department
Old Dominion University

Research Location: Air Force Human Resources Laboratory/Brooks AFB

Date: September 1983

Abstract

This study applied the research design that was developed at the Air Force Human Resources Laboratory during the tenure of the Principal Investigator as a Fellow under the 1983 Summer Faculty Research Program. This design provides an analysis of the accuracy of performance ratings in terms of the logical requirements of the multitrait-multimethod design and the deviations from target ratings in the person perception design.

A review of the literature indicated that the current emphasis of research on the accuracy of performance ratings is on the development of training programs to improve accuracy. Although several programs show promise, no research study has considered the accuracy of performance ratings in the framework of the logical requirements for performance measures. The purpose of the present study was to compare several training programs for improving the accuracy of performance ratings. An emphasis of the study was to determine how well performance ratings meet logical criteria for performance measures as well as meet traditional requirements for rating accuracy.

Participants were assigned to one of five training conditions (i.e., rater bias, observation, frame of reference, combination of observation and frame of reference, and control). The videotaped performances of employment interviewers were viewed and rated with both a behaviorally anchored rating scale and mixed standard scale formats. The results indicated that

Accuracy and Validity

while the training programs did not differentially impact on the accuracy of the performance ratings, the training was effective across conditions. Furthermore, format differences with respect to accuracy were found, and it was argued that purpose for ratings must be considered in choosing a rating format.

Training to Improve the Accuracy and Validity
of Performance Ratings

In an effort to meet the Air Force's mandate from Congress to develop job performance measures that reflect hands-on performance, the Air Force Human Resources Laboratory has initiated a program of research and development (Kavanagh, Borman, Hedge & Gould, 1983). The short range goal of this program is to research and develop performance measures with which to validate the Air Force's selection and classification procedures. The longer range goal is to institutionalize the procedures for developing job performance measures so that these measures are continually updated and available for the Air Force to use in research on human resources.

Although the Air Force has been mandated by Congress to develop hands-on performance measures, some circumstances warrant the use of surrogate measures such as performance ratings. In many work contexts, ratings are the only reasonable method for measuring performance. Instances of job performance may occur too infrequently or be too dangerous and, therefore, require the use of ratings. Furthermore, the development of hands-on performance measures is quite expensive. Ratings may be substituted to cut costs if their technical quality is high. Finally, there are few jobs that possess performance measures that are devoid of judgments about job performance. Except for the most mundane jobs, humans must observe, report, and perhaps

rate job performance.

Despite the potential utility of performance ratings, these measures must be developed with care. Distortions in human judgments reduce their actual utility. These distortions have been addressed with research into the quality of performance ratings.

The multitrait-multimethod design has been used to evaluate performance ratings against criteria that are logical requirements for performance measures (Boruch, Larkin, Wolins, & MacKinney, 1970). In particular, the criteria require that performance measures reflect differences between people that are due to the traits of performance and not due to the method for rating. Variance components and intraclass correlation indexes are used to describe the degree to which the ratings meet the logical requirements.

The person perception design (Cronbach, 1955) has also been used to evaluate performance ratings. These traits are compared against target ratings that are defined as undistorted measures of performance. Statistics are computed from discrepancies between the target and performance ratings to describe the inaccuracies in the performance ratings.

Recently, Dickinson (1984) developed a combination design to guide investigations on both the validity and accuracy of performance ratings. The combination design extends the multitrait-multimethod and person perception designs to consider their relationships. For example, differential accuracy in the

Accuracy and Validity

person perception design also reflects differential discriminant validity for the rater compared to the discriminant validity possessed by the target ratings. Both interpretations describe the rater's ability to rate the individual ratee on each of the traits. Furthermore, the combination design expands the assessment of performance ratings to define additional sources that reduce the validity and accuracy of the ratings. One source is differential elevation accuracy by methods. It reflects the ability of the rater to order ratees with each of the methods compared to the target ratings. Of course, a logical property for target ratings is to order ratees the same with each of the methods for rating. Since the investigator can design the research so that the target ratings meet this requirement, differential elevation accuracy by methods is a source of inaccuracy in the performance ratings. An accurate rater should order the ratees the same with each method and this ordering should be identical to the order provided by the target ratings.

Another unwanted source that is defined in the combination design is differential discriminant validity by methods. It reflects a different pattern of ordering the ratees on the traits for each of the methods. A logical requirement for performance ratings is that the same pattern of discriminant validity should be obtained with each method of rating. If the investigator designs the research so that the target ratings order the ratees on the traits in the same patterns for each

method, this source of invalidity reflects the raters' inability to duplicate the patterns in the target ratings. A rater should order the rates on the traits with the same patterns of ratings for each of the methods, and these patterns should be identical to those provided by the target ratings.

The combination design provides a broader strategy for assessing the quality of performance ratings than either the multitrait-multimethod or person perception designs. It emphasizes the assessment of accuracy in the framework of logical requirements for performance measures. The design allows the investigator to specify the amounts of multitrait-multimethod properties possessed by the target ratings. Such a research strategy provides a meaningful theory within which to interpret the accuracy of performance ratings.

Background

Several models suggest variables that influence the accuracy of ratings (DeCotiis & Petit, 1978; Kavanagh, et al., 1983; Landy & Farr, 1980). They include variables such as the purpose for the ratings, race and sex of the ratees, ability of the rater and training programs to improve the accuracy of the performance ratings. However, none of the models emphasize the influence of logical requirements for the performance ratings in understanding accuracy. These models represent a myopic strategy for research on accuracy (Cronbach, 1955).

Research on the accuracy of performance ratings has focused on the effects of rater training (Bernardin & Pence, 1980;

Borman, 1977; 1979; Hedge, 1982; McIntyre, Smith, & Hassett, 1984). This research has typically been concerned with providing raters with experiences to improve the quality of their ratings. For example, raters have attended lectures on the nature of distortions in ratings, participated in small group discussions of distortions in ratings, and learned the performance behaviors associated with target ratings.

Borman (1979) used an elaborate procedure of training to investigate the accuracy of performance ratings and the distortion of halo error in the ratings. He included participants in workshops in which they discussed the nature of halo error, formulated ways to avoid it, and practiced rating videotapes of ratees performing as managers in a problem-solving session with a troublesome subordinate or performing as recruiters in employment interviews.

Borman (1979) measured halo error and differential accuracy in ratings that were obtained from trained and untrained participants. Training did reduce halo error, but it had no effect on the accuracy of the performance ratings. Borman (1979) suggested that teaching people to avoid halo error is not equivalent to teaching them to make accurate ratings. In a further analysis of the data, Borman (1977) also measured leniency and range restriction errors and found little correspondence between these errors and differential accuracy.

Bernardin and Pence (1980) also investigated the effects of training on rating errors and the accuracy of performance

ratings. The authors provided participants with two types of training. One group received an hour-long training program that provided in-depth lectures on how to avoid leniency and halo errors. They were also lectured on the multidimensionality of performance in most jobs and the importance of distinguishing these dimensions when making ratings. Raters were also lectured on the importance of fair, unbiased and accurate ratings. Finally, they were urged to discuss and seek consensus on stereotypes of effective and ineffective ratee performance. The second group received a much shorter training program. They were informed of leniency and halo errors and admonished to avoid them in their performance ratings.

The two training groups and a no-training group evaluated two written vignettes describing the performance of two ratees. Ratings from the training groups had significantly less leniency and halo errors in the ratings. However, these groups were significantly less accurate than the control group. Bernardin and Pence (1980) suggested that training to avoid errors fosters a response set in raters that does reduce these errors but also reduces the accuracy of the ratings. In addition, they suggested the development of training programs that increase accuracy rather than induce response sets.

A recent study by McIntyre, Smith, and Hassett (1984) investigated the influence of training programs and perceived purpose for the ratings on the accuracy of ratings and the occurrence of leniency and halo errors. Participants in the

study rated videotapes of the lecture performance of three instructors. They were informed that their ratings would remain anonymous.

The authors employed four programs of training. Rater error training consisted of a 15 minute presentation and discussion of halo and leniency errors followed by a short group discussion of how to avoid making these errors. Frame of reference training was developed from suggestions by Bernardin (1981). Participants were shown a videotape of the performance of one ratee and were told the specific aspects of the ratee's performance that were considered in determining target ratings as well as the actual values of the target ratings. The third group combined the rater error and frame of reference training programs, while the fourth group served as a control and received no training.

Three purposes for the ratings were included in the research design. In the research purpose condition, participants were informed that the purpose was to evaluate students' abilities to rate lecturers accurately by comparing their ratings to those of experts. In the course improvement condition, participants were told that the purpose was to give feedback to lecturers with the performance ratings that were obtained from them. Instructions informed the participants that they should not be biased for or against a particular lecturer because they were not students in courses taught by any of the lecturers. Finally, in the hiring purpose condition,

Accuracy and Validity

participants were told that their ratings would serve as the basis for selecting lecturers to teach the next semester.

McIntyre, et al. (1984) found that the frame of reference and combination training groups were more accurate than the rater error and no training groups. Furthermore, the group with research as the purpose for rating tended to be more accurate than the groups with hiring decision or course improvement as their purpose. Leniency and halo errors were committed by all groups of participants. Performance ratings tended to underestimate the target ratings and show less variance than these ratings. In particular, the research purpose group was more severe in underestimating the target ratings than the other groups, while the frame of reference training group displayed less halo than the rater error and combination training groups. McIntyre, et al. (1984) suggested that the results of their study supported frame of reference training as a strategy for improving the accuracy of performance ratings. They also suggested that rater error training is not effective in improving accuracy or in reducing halo and leniency errors. Finally, they suggested that the purpose for the ratings in their study was a weak effect and accounted only for small differences in accuracy and rating errors.

In another study of the effects of training, Hedge (1982) studied the influence of several training programs on accuracy and leniency, halo, and range restriction errors in performance. Prior to and approximately one week after the training programs,

participants rated videotapes of the performance of five managers dealing with a problem employee. Subsequent to training, participants also rated the performance of their own subordinates using their organization's questionnaire. Ratings of the subordinates that were made prior to training were obtained from personnel files.

Participants were assigned to one of three training programs or to receive no training. One program focused on the rating errors of leniency, halo, and range restriction. The program included a videotaped lecture about the rating errors. The lecture was followed up with illustrations and graphs of the errors. Next, a written description of two case studies was presented which was followed by a discussion of the errors committed in the cases. A second program was training to improve observational skills. This program also included two parts. A videotaped lecture was presented that instructed participants to observe carefully and look for specific behaviors as well as to avoid errors in their observations and not be influenced by prior, irrelevant information or rely only on a single source of information. The third program provided training to improve decision-making skills. A videotaped lecture explained the use of judgmental heuristics in decision making, inappropriate causal inferences, and inappropriate weighting of observed behavior. The lecture was followed by a discussion of two exercises. One exercise involved reading two scenarios that presented irrelevant information about two interviewers whose

performance in recruiting an applicant was subsequently presented on videotape. A discussion focused on the effect of the scenerios on the ratings. The second exercise involved viewing pictures of people in a work setting, listing behaviors observed in the pictures, and listing inferences drawn from these behaviors. After the exercise, a discussion focused on the differences between behaviors and inferences as well as on the potential errors in inferences.

The ratings of the videotapes of managerial performance showed a decrease in leniency and halo errors from pre- to post-training for the rater error group, while the observation group increased in halo and range restriction errors and the no training group increased in range restriction. Decision making training had no effect on these errors. Furthermore, the rater error and control groups decreased in their accuracy of the ratings, while the decision making and observation groups increased in accuracy.

The ratings by the participants of their own subordinates differed from prior ratings of those subordinates that were obtained from personnel files. The rater error training decreased leniency, halo and range restriction errors from pre- to post-training. In contrast, observation training increased leniency error, and decision making training increased range restriction error.

The results of Hedge's (1982) study indicate that training to improve decision making can be used to increase the accuracy

of performance ratings without increasing rating errors such as halo and leniency. Although training to improve observational skills also can increase accuracy, it appears to do so at the expense of increasing rating errors.

The review of the literature on training to improve accuracy suggests several directions for future research. Most studies indicate that training to avoid rating errors does not improve accuracy. This type of training should be replaced with other programs in future studies. However, several programs show promise for improving accuracy. Frame-of-reference, decision making, and observation training have been successful in improving accuracy, but their success at reducing rating errors has been mixed.

A major weakness with the literature on accuracy training is that it does not include an analysis of logical requirements for performance ratings. The investigation of accuracy requires the development of a standard in the form of a set of target ratings that specify the performance scores of several rates. These target ratings are usually developed from the judgments of job experts or other decision making groups. Unless the target ratings themselves meet criteria for logical requirements for performance measures, performance ratings cannot be expected to meet those requirements. For example, the target ratings should possess discriminant validity if performance ratings are to reflect distinct aspects of job performance. A training program that successfully improves rater accuracy may do nothing more

than produce performance ratings that contain redundancies and ambiguities.

The purpose of this study was to compare several training programs for improving the accuracy of performance ratings. An emphasis of the study was to assess how well the performance ratings meet logical criteria for performance measures as well as meet traditional requirements for rating accuracy (e.g., McIntyre, et al., 1984).

Methods

Participants

The participants in this study were 91 undergraduate students from Old Dominion University who were enrolled in introductory psychology courses. Students received extra course credit as well as ten dollars for participating in the two to three hour study. Due to incomplete data, one participant was not included in the analyses.

Stimulus Materials

All participants viewed five videotapes of interviews between an interviewer and college senior interested in applying for work. Videotaped performances with established target scores were utilized because of their amenability to calculations of accuracy. For detailed information concerning development of the videotapes, the rating scales, and the generation of target scores refer to Borman (1977). Five of the six dimensions developed by Borman (1977) were utilized in this study, one being eliminated because of apparent overlap with

another of the dimensions. The dimensions were: (1) organizing the interview; (2) providing appropriate information about the company; (3) asking relevant questions; (4) answering applicant's questions; and (5) establishing rapport with the applicant.

Rating Formats

The videotaped performances were rated with two rating formats by each participant. The rating formats were developed by utilizing adaptations of the 7-point behaviorally anchored rating scales (BARS) provided by Borman (1977). The BARS format consisted of Borman's (1977) rating scales with minor rewording of the behavioral statements. In addition, a mixed standard scale (MSS) format was developed by using behavioral statements which represented low, medium, and high levels of performance on each of the performance dimensions. These 15 statements (three levels x five dimensions) were obtained by using the behavioral anchors on the BARS format which corresponded to the scale points 2, 4, and 6 for each of the dimensions. The statements were organized hierarchically by dimension into a questionnaire format. The order in which the rating formats were completed was counterbalanced within conditions.

Procedures

Volunteers signed-up for participation during one of five time periods. The time periods were assigned randomly to five treatment conditions. The treatment conditions and number of participants in each were: (1) rater bias training, n = 18; (2)

Accuracy and Validity

observation training, n = 17; (3) frame of reference training, n = 15; (4) combination observation and frame of reference training, n = 20; and (5) no training control, n = 20.

Each experimental session began with a discussion of the importance and difficulty of performance appraisal. Participants were informed that the purpose of the study was to assess the effects of rating formats on the accuracy of performance ratings. Instructions were then given for the use of the two rating formats. For the BARS, it was explained that the seven behavioral statements were meant to represent various levels of behavior, and the participants were to pick the number corresponding to the level of behavior that they observed on each of the dimensions. In addition to reading aloud definitions of the dimensions, the experimenter read three of the behavioral statements for each dimension (one high, one average, and one low) to familiarize participants with the scale. Furthermore, participants were asked to read the remaining statements themselves, before the experimenter proceeded to the next dimension.

For the MSS, it was explained that each dimension's three statements represented high, medium, and low performance. For each statement participants were told to record a "+" if the level of performance they observed was better than the statement, a "0" if the level of performance was the same as the statement, and a "-" if what they observed was worse than the statement. In order to illustrate this rating system, a schema

was presented in which participants were shown a continuum of possible performance on any dimension ranging from poor to excellent. Three points along this continuum were illustrated which corresponded to the three behavioral statements. Participants were then asked to place mentally the performance they observed along that continuum and then determine its relation to each of the three statements. If the observed performance was further along the continuum in the positive direction than a statement then a "+" should be given, further along the continuum in the negative direction then a "-" should be given, and if on the same point a "0" should be given. After the schema was described, participants received practice in assigning ratings when the observed performance was located at various points on the continuum.

Following the format training and a five minute break, rater training was administered and the videotaped interviews were viewed and rated. Upon completion of ratings, participants were debriefed as to the details of the study. The procedures involved in each of the five rater training treatments are described below.

Rater Bias Training. This training consisted of a lecture describing common rating biases and means of avoiding them. The rating biases included in the lecture were halo, leniency/severity, and similarity error. In addition, hypothetical ratings which illustrated positive halo, negative halo, leniency, and severity were presented. The five

videotaped interviews were then viewed. At the completion of each interview the rating formats were distributed and the participants rated the performance of the interviewer. Participants were asked not to record information as they watched the interviews.

Observation Training. This training consisted of instruction in using a coding scheme to systematically record relevant behaviors as they were observed during the interviews. The coding scheme was described to the participants as a memory aid which would be used to refresh their memories at the end of an interview, before ratings were assigned. The coding scheme consisted of a set of abbreviations for the dimensions and for independently observable components of each dimension's definition. All of the abbreviations were organized into an observation coding form. The observation coding form was used to record behaviors as they were observed by circling the appropriate abbreviations and listing key phrases which would help to recall each incident. After the abbreviations and coding form were described, an example coding form was presented to illustrate proper use of the coding scheme. The videotaped interviews were then viewed. Participants were instructed to record pertinent behaviors on the observation coding form as they watched an interview and then refer to it before assigning their ratings. It was emphasized that the purpose of the observation coding form was to refresh their memories but they would have to take additional information into consideration

when actually assigning ratings. At the completion of each interview, the rating formats were distributed and the participants rated the performance of the interviewer. After ratings were assigned a "target" observation coding form was distributed by the experimenter and described to illustrate the behaviors that should have been recorded. The "target" form had been constructed by the experimenter from a content analysis of the videotapes.

Frame of Reference Training. This training condition was similar to the training described by Bernardin (1981), and McIntyre, et al., (1984). It consisted of the presentation of target scores after each interview was viewed and rated. For the BARS format, Borman's (1977) mean expert ratings were presented. These mean expert ratings were converted into logical response patterns (Saal, 1979) and used as target feedback for the MSS format. In addition, a behavioral rationale for the ratings was provided. This rationale was presented by replaying specific segments from the videotapes along with verbal descriptions of pertinent behaviors. These behaviors were discussed in terms of their relevance to the expert ratings.

Combination Observation and Frame of Reference Training. This training condition combined all aspects of the observation training and frame of reference training as described above.

No Training Control. This condition consisted of no additional training subsequent to the description of the rating

formats. Participants viewed the five videotaped interviews. At the completion of each interview, the rating formats were distributed and the performance of the interviewer was rated.

Results

Two approaches were utilized in analyzing the data for this study. These were (1) examining the quality of ratings with traditional measures of accuracy and (2) determining the extent to which logical requirements were satisfied by the ratings. The quality of ratings approach included the dependent measures of leniency, halo, correlational accuracy per rater, correlational accuracy per dimension, and distance accuracy. Dickinson's (1984) combination design was utilized to assess the extent to which the logical requirements of rating were met.

Quality of Ratings Analysis

Leniency. This measure was calculated as the mean difference between target scores and the observed ratings over the five videotaped interviews and the five behavioral dimensions. A two-way analysis of variance resulted in a significant main effect for training ($F(4,85)=5.674, p<.001$), and a significant main effect for formats ($F(1,85)=8.106, p<.01$). The training by formats interaction was not found to be significant ($F(4,85)=0.692, p>.05$).

Post hoc analyses of the means for the training conditions indicated that a contrast of the mean leniency scores for the observation and combination conditions was significantly different than the mean leniency score for the control

condition. Examination of the means for the formats effect indicated that the ratings with the BARS format underestimated the target scores ($M = -.044$) while the MSS format overestimated the target scores ($M = .034$).

Halo. Two measures of halo were investigated. The first of these was obtained by computing the mean differences in the variance of a ratee's dimension scores between target scores and ratings across the five videotaped interviews. A two-way analysis of variance indicated a significant main effect for training ($F(4,85)=2.720, p<.05$), and a significant main effect for formats ($F(1,85)=61.455, p<.001$). The training by formats interaction was not found to be significant ($F(4,85)=0.868, p>.05$). Post hoc analyses resulted in no meaningful contrasts among the means.

Examination of the means for the formats effect indicated that for the BARS format the variance of a ratee's dimension scores was greater in the ratings than in the target scores ($M = -.101$), while with the MSS format there was less variance in the ratings than the target scores ($M = .087$).

The second measure of halo was obtained by computing the mean differences in the variance of a dimension's ratee scores between target scores and ratings across the five videotaped interviews. The results of a two-way analysis of variance suggested a significant main effect for formats ($F(1,85)=158.228, p<.001$), however, the effect for training and the training by formats interaction were not found to be

significant ($F(4,85)=1.76, p>.05$, and $F(4,85)=1.38, p>.05$, respectively). Examination of the means indicated that while ratings with both formats had negative halo (i.e. more variance in the ratings than the target scores) the difference between the variance of a dimension's ratee scores in the ratings and target scores was greater with the BARS format ($M = -.371$) than with the MSS format ($M = -.016$).

Correlational Accuracy Per Ratee. This measure is an index of the extent to which ratees can be differentiated by raters using behavioral dimensions. It was calculated by computing the mean across the five videotaped interviews for the r-to z-transformed correlations of the ratings with the target scores for each rater. A two-way analysis of variance yielded a significant main effect for formats ($F(1,85)=27.762, p<.05$), with no significant effect for training ($F(4,85)=0.322, p>.05$) or the training by format interaction ($F(4,85)=0.318, p>.05$). Comparison of the means for the format effect indicated that ratings with the BARS format ($\bar{r} = .47$) were more accurate than those with the MSS format ($\bar{r} = .29$).

Correlational Accuracy Per Dimension. This is a measure of how well a rater used behavioral dimensions to rate a group of ratees. It was calculated for each rater by computing the mean of the r-to z-transformed correlations of the ratings with the target scores across the five behavioral dimensions. Overall, the raters were quite accurate ($\bar{r} = .63$). However, the results of a two-way analysis of variance indicated no significant

effects for training ($F(4,85)=1.035, p>.05$), formats ($F(1,85)=0.184, p>.05$), or the training by formats interaction ($F(4,85)=1.419, p>.05$).

Distance Accuracy. This measure is an index of the similarity between the profiles of target scores and ratings (Nunnally, 1978). This index takes into consideration the differences between target and rating profiles in means and variances, as well as their correlation. Thus, distance accuracy is a composite measure that reflects leniency, halo, and correlational accuracy. It was computed for each rater as the mean across videotaped interviews of the mean absolute differences between target scores and ratings for the five behavioral dimensions.

A two-way analysis of variance yielded a significant effect for formats ($F(1,85)=66.911, p<.001$), with no significant effects for training ($F(4,85)=0.195, p>.05$), or the training by formats interaction ($F(4,85)=0.712, p>.05$). Examination of the means indicated that ratings with the MSS format were more accurate ($M = 1.01$) than with the BARS format ($M = 1.17$).

Combination Design

Each participant's ratings on the five dimensions across the five videotaped interviews were individually analyzed with a three-way analysis of variance with rater (interviewers), traits (dimensions), and methods (formats) as the independent variables. For each source of variance in the combination design an intraclass correlation coefficient (ICC) was computed

to describe the proportion of variance accounted for by that source. Subsequently, the ICCs were used as dependent variables in one-way analyses of variance for each of the sources of variance to assess the effects of training. Results of the analyses of variance indicated significant effects due to training for convergent validity ($F(4,85)=2.939, p<.05$) and trait bias ($F(4,85)=5.952, p<.001$). The F values, significance levels, and the grand means for the ICCs for each of the sources of variance in the design are shown in Table 1.

Post hoc analyses of the means with Newman-Keuls tests suggested that for convergent validity, the ICC for the no training control condition ($M = .382$) was significantly greater than all of the other conditions ($M = .290$). In addition, a Newman-Keuls analysis for trait bias suggested that the ICCs for the observation ($M = -.029$) and combination ($M = -.046$) training groups were significantly greater than the other training conditions ($M = -.015$).

Discussion

The results of this study indicate that the training strategies impacted minimally on the accuracy and validity of the performance ratings. The analyses of the quality of ratings resulted in significant differences between training groups only on the leniency measure and the measure of halo for a ratee's dimension scores. No significant differences were found on the correlational or distance measures of accuracy. In addition, results from the analysis of combination design measures yielded

differences due to training only for convergent validity and trait bias.

The results from the combination design analysis indicated that the training, for all groups, was quite effective. The mean ICC values indicated that four sources accounted for significant proportions of rating variance (i.e., convergent validity, differential elevation accuracy, discriminant validity, and differential accuracy). The amount of variance accounted for by each of the remaining sources was negligible. These results are favorable when considering logical requirements for ratings. Under ideal circumstances large proportions of variance should be accounted for in the ratings by convergent and discriminant validity, whereas little variance should be accounted for by the remaining sources. The only discrepancies from the ideal were that differential elevation accuracy and differential accuracy both accounted for relatively large amounts of variance. Future research will have to determine what factors influence the interactions (i.e., rating source x ratees and rating source x ratees x traits) to explain these findings. The factors to investigate may include experimental treatments (e.g., other types of rater training) or ratee characteristics (e.g., motivation).

The general effectiveness of the training was also supported by the traditional accuracy measures. Specifically, the correlational accuracy per dimension measure resulted in a mean correlation across training and no training groups of

notable strength (i.e., $\bar{r} = .63$). This correlation compares favorably with those obtained in similar studies: Borman (1977) reported $\bar{r} = .73$ for rater bias training and $\bar{r} = .69$ for no training; and McIntyre, et al. (1984) reported $\bar{r} = .49$ for no training, $\bar{r} = .46$ for rater error training, and $\bar{r} = .62$ for frame of reference training.

Comparisons of the present study to previous research on rater training are inconclusive. For example, Borman (1979) also found that rater bias training did not improve the accuracy of ratings when compared to a control group. The results of the present study, however, do not agree with those of Bernardin and Pence (1980), or McIntyre et al. (1984). While the present study found no differences on the accuracy measures between any of the training groups, Bernardin and Pence's (1980) rater error training group was actually less accurate than a control group in terms of distance accuracy, and McIntyre et al.'s (1984) frame of reference training group was significantly more accurate than a no-training control in terms of distance and correlational accuracy per dimension.

One explanation for these inconsistent findings may be the nature of the control group used in the present study. Perhaps, the control group was not a true no-training control group since participants received extensive orientation in which they were familiarized with detailed behavioral definitions of the dimensions and the behavioral statements comprising the rating formats. These procedures were included in the study because

the investigator believed they would provide a realistic baseline for comparison. The extent to which raters have been familiarized with the rating formats in previous studies is not adequately described by their procedures. In light of the high level of accuracy of the no training group ($\bar{r} = .67$), it seems likely that a true no-training control would have rated less accurately than the training groups.

The analyses conducted also allowed for a comparison of the effects of rating formats on the quality of performance ratings. For leniency and the halo of a ratee's dimension scores, there were no significant differences between formats. The magnitudes of leniency and halo measures were similar across formats although the signs were in opposite directions. Also, with the correlational accuracy per dimension measure, accurate ratings were obtained which did not significantly differ due to formats. On each of the remaining measures, the results indicated that one of the formats resulted in superior ratings. The BARS format was significantly more accurate on the correlational accuracy per ratee's dimensions measure. In contrast, the MSS format resulted in ratings with less halo for variance of a dimension's ratee scores, and it was more accurate on the distance accuracy measure.

The results with regard to formats are not consistent with previous conclusions that the study of formats is a futile endeavor (Landy & Farr, 1980). It is suggested that depending on the purpose for rating, different formats will be preferred.

Accuracy and Validity

For example, if the purpose for rating is to differentiate between ratees, then the BARS and MSS formats are equally accurate, and none is preferable. Ratings that are used to make administrative decisions (e.g., compensation, selection, promotion) can be made with either format. In contrast, if the purpose for ratings is to differentiate between traits within ratees, then the BARS format yields more accurate ratings, and it is preferred over the MSS format. Ratings that are used to diagnose individual strengths and weaknesses (e.g., vocational guidance, performance feedback) should be made with the BARS format.

Finally, the results of this study indicate that distance accuracy is a complex measure of accuracy. It is a composite of the components of leniency, halo, and correlational accuracy. Although the mathematics have not been derived to describe the exact contribution of the components to the composite measure, the results of the present study suggest that the halo for variance of a dimension's ratee scores is a major contributor. Because of the complex nature of distance accuracy, the present author suggests that its use to describe ratings should be avoided. Researchers will obtain more useful information by looking at each of the components separately to locate the exact sources of accuracy and inaccuracy.

References

- Bernardin, H. J. (1981, August). Improving rater training. Paper presented at the 89th Annual Meeting of the American Psychological Association. Bernardin, H. J., & Pence, E. C. (1980). Effects of rater training: Creating new response sets and decreasing accuracy. Journal of Applied Psychology, 65, 60-66.
- Borman, W. C. (1977). Consistency of rating accuracy and rating errors in the judgment of human performance. Organizational Behavior and Human Performance, 20, 258-272.
- Borman, W. C. (1979). Format and training effects on rating accuracy, and rater errors. Journal of Applied Psychology, 64, 410-421.
- Boruch, R. F., Larkin, J. D., Wolins, L., & MacKinney, A. C. (1970). Alternative methods of analysis: Multitrait-multimethod data. Educational and Psychological Measurement, 30, 833-853.
- Cronbach, L. J. (1955). Processes affecting scores on understanding of others and assuming "similarity". Psychological Bulletin, 52, 177-193.
- DeCotiis, T. A., & Petit, A. (1978). The performance appraisal process: A model and some testable propositions. Academy of Management Review, 3, 635-646.
- Dickinson, T. L. (1984, August). A design for evaluating the validity and accuracy of performance ratings. Paper presented at the 92nd Annual Meeting of the American

Psychological Association.

- Hedge, J. W. (1982). Improving the accuracy of performance evaluations: A comparison of the methods of performance appraiser training. Unpublished doctoral dissertation, Old Dominion University.
- Kavanaugh, M. J., Borman, W. C., Hedge, J. W., & Gould, R. B. (1983). A model of performance measurement quality for validation research in the military. AFHRL Technical Paper, Brooks Air Force Base, Tx: Manpower and Personnel Division, Air Force Human Resources Laboratory.
- Landy, F., & Farr, J. (1980). Performance rating. Psychological Bulletin, 87, 72-107.
- McIntyre, R. M., Smith, D. E., & Hassett, C. E. (1984). Accuracy of performance ratings as affected by rater training and perceived purpose of rating. Journal of Applied Psychology, 69, 147-156.
- Nunnally, J. C. (1978). Psychometric theory. New York: McGraw Hill.
- Saal, F. E. (1979). Mixed standard rating scale: A consistent system for numerically coding inconsistent response combinations. Journal of Applied Psychology, 64, 422-428.

Table 1

F Values, Significance Levels, and the Grand Means for ICCs

Source	Psychometric Interpretation	F-Ratio	Sign. Level	Mean ICC
Rating Source (S)	Elevation Accuracy	2.061	0.093	-0.009
Ratees (R)	Convergent Validity	2.939	0.025	0.311
Traits (T)	Trait Bias	5.952	0.000	-0.024
Methods (M)	Scale Bias	0.321	0.863	0.001
S x R	Differential Elevation Accuracy	2.162	0.080	0.148
S x T	Stereotype Accuracy	0.732	0.573	-0.008
S x M	Differential Scale Bias by Source	1.478	0.216	-0.001
R x T	Discriminant Validity	2.176	0.079	0.256
R x M	Method Bias	2.063	0.093	0.001
T x M	Trait by Scale Bias	0.407	0.803	-0.001
S x R x T	Differential Accuracy	0.241	0.914	0.196
S x R x M	Differential Elevation Accuracy by Methods	2.074	0.091	0.020
S x T x M	Differential Stereotype Accuracy by Methods	2.321	0.063	0.001
R x T x M	Differential Discriminant Validity by Methods	0.240	0.915	0.006

1983-84 USAF-SCEEE RESEARCH INITIATION PROGRAM

Sponsored by the

AIR FORCE OFFICE OF SCIENTIFIC RESEARCH

Conducted by the

SOUTHEASTERN CENTER FOR ELECTRICAL ENGINEERING EDUCATION

FINAL REPORT

LASER DAMAGE IN CRYSTALLINE SILICON OBSERVED UNDER RHEED

Prepared by: Dr. Fred Domann

Academic Rank: Assistant Professor

Department and
University: Department of Physics
University of Wisconsin

Research Location: Air Force Weapons Laboratory

Date: October 1984

ABSTRACT

In this work, the experimental apparatus necessary to make laser damage studies of single crystalline silicon have been nearly completed. The electron diffraction system is now operative, the pulsed dye laser (on loan from AFWL) has been installed and is working, the laser beam handling optics and the beam diagnostic system is still in development. To date, no damage data have been collected, but we anticipate that we will have these data by January 1, 1985.

In the remainder of this report we give a chronological description of our activities to date.

REPORT OF RESEARCH ACTIVITY FROM January 1, 1984 through October 31, 1984.

January 9, 1984 - February 28, 1984. The first two months of research effort was spent designing the experimental arrangement and determining what type of laser and beam diagnostics would be needed to carryout the project. Although \$9,695.00 were budgeted for a pulsed N₂ laser and energy meter, we decided instead to accept AFWL's offer to loan us a laser for a three year period. We were advised by AFWL that an HF-DF pulsed laser was available and was to be cleaned, rejuvenated, and shipped to us about April 15, 1984. During this time AFWL also advised us that they would lend us an energy meter in lieu of us purchasing one.

On January 12 my student assistant (Norman Troullier) began working on the project (7 hrs/wk) for 2 academic credits of undergraduate research in lieu of a salary, and said that he was willing to commit to a summer

'84 work schedule calling for a total of not less than 107.5 hrs as specified in the budget.

In early January '84 we decided to try cleaning the 60 l/s ion pump ourselves instead of contracting with Varian Associated as called for in our budget. On January 21 the ion pump maintenance was complete and the pump was reinstalled, and was found to operate successfully. From January 22 - February 4 the vacuum system was checked for leaks with a He leak detector; several small leaks were found and repaired. From February 15-22 the vacuum system was baked at approximately 150°C. After removing the oven the ambient pressure dropped to 10^{-8} Torr.

March. From March 1-14 we tried repeatedly to obtain an electron diffraction pattern and were unsuccessful. We experienced severe difficulties with the electron beams focus and concluded that the problem was 60 Hz pickup in the e-gun circuitry. This resulted in a major task of rebuilding the e gun control circuit to incorporate extensive shielding. This shielding project lasted until early May. On March 28 Allen Stewart of AFWL called and advised us that the HF-DF laser was inoperable, but that a smaller dye laser would be sent instead, and would arrive in late May '84. On March 28 I ordered optical support components, rhodamine dye, and Photrex methanol to be used with the dye laser. The total cost for these orders: \$1,886.60.

May. Having completed the task of rebuilding the e-gun control system we again tried to obtain a RHEED pattern but again were unsuccessful. The e-gun control power supply developed a H.V. arcing problem and was sent to the UW-Platteville electronic technician for repair.

On May 24 the power supply was returned and we again attempted to obtain a diffraction pattern with no success. On May 29 we decided to purchase a new e-gun control from Physical Electronics for \$6,400.00. The delivery date was set (by Physical Electronics) at September 15, 1984.

On or about May 25 the dye laser arrived from AFWL.

June. June 1-8 was spent bringing up the laser, which fired successfully on June 8th. The next several days were spent optimizing the Rhodamine 590 dye concentration. The optimum concentration appears to be about 1.7×10^{-4} moles/liters. On June 11 David Johnson (an Electrical Engineering student) joined the research effort for two academic credits of Independent Study. His assignment was to develop a beam diagnostics system which would employ a linear diode array (i.e., RETICON ARRAY) to measure the laser beam profile and diameter. On June 20 Mr. Johnson demonstrated that the diode array was operative with a small He-Ne laser, and proceeded to add a KIM-I micro processor to acquire and store the beam profile data.

June 17-30 was spent making changes in the vacuum chamber to accommodate the input of the laser beam to the Si target. The pumpdown recycling process required about one week.

July. July 6-10 were spent measuring the optical density of 26 neutral density filters which will be used to attenuate the dye laser beam for processing with the RETICON array. On July 19 the Si sample holder was removed from the vacuum chamber for the purpose of installing an improved heating system used to clean the sample. On July 27 the new sample heating unit was installed and the vacuum system recycled.

August. Having completed their summer term commitments on August 3, 1984, the two student research assistants departed for the remainder of the summer. Suspecting that the vacuum system had again developed several small leaks, I spent August 2-10 using a He leak detector to locate them. I concluded that in fact no leaks were present. On August 11 I left for vacation to return September 1.

September. September 1-15 was devoted to introducing a He-Ne laser beam through the flashlamp of the dye laser to be used as an aiming device for the larger laser. This required a reasonable amount of building and construction of mirror mounting system and the purchase of several translation stages. A fair amount of difficulty was encountered in making the He-Ne beam coaxial with the dye laser beam. Also in September the spark gap assembly of the dye laser suffered an electrical breakdown and required the machining of a new (nylon) replacement collar.

On or about Sept 20 the new e-beam controller arrived from Physical Electronics, but was not operative until several weeks after arrival due to an incorrect cable fitting supplied with the instrument.

October. Early in October the proper cable arrived from Physical Electronics. The e-beam controller was checked out and operated successfully. The electron beam current was measured and found to be 22.9 μA at the maximum allowable filament temperature. This amount of current is more than 100 times the amount needed for RHEED. The e-beam controller also offered the advantage of a 5 KV maximum instead

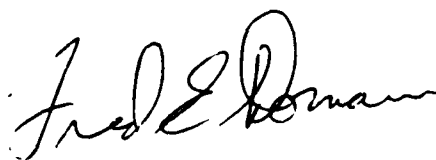
of the 3 KV limit with the previous controller. On October 25 we again attempted to obtain a RHEED pattern and this time we were successful. The RHEED pattern of (100) Si was observed to last 20 minutes from the time of cleaning the Si sample until it became unresolved due to the adsorption of residual gases in the vacuum chamber.

Much time in October has been spent in completing the beam handling optics and RETICON diode array diagnostic system.

Concluding Remarks.

The contract period has seemingly vanished and we have no data to report. All components of the apparatus however are either operative or very nearly so at this time. The RETICON diagnostics are perhaps the farthest from completion, but I am extremely optimistic that we will have data by January 1, 1985. I will make my visitation to AFWL on February 6, 1985 to present our data as required.

Finally, when the results are published, we will gratefully acknowledge SCEE, AFOSR, and AFWL for supporting this effort.



1983-84 USAF-SCEEE RESEARCH INITIATION PROGRAM

Sponsored by the

AIR FORCE OFFICE OF SCIENTIFIC RESEARCH

Conducted by the

SOUTHEASTERN CENTER FOR ELECTRICAL ENGINEERING EDUCATION

FINAL REPORT

ANALYSIS OF SWIRLING NOZZLE FLOW BY A TIME-DEPENDENT FINITE

DIFFERENCE TECHNIQUE

Prepared by: Dr. J. Craig Dutton

Academic Rank:

Department and
University: Mechanical Engineering Department
Texas A&M University

Research Location: Air Force Aero Propulsion Laboratory

Date: December 1984

ANALYSIS OF SWIRLING NOZZLE FLOW BY A
TIME-DEPENDENT FINITE DIFFERENCE TECHNIQUE

ABSTRACT

As a continuation and extension of research conducted during the 1983 AFOSR/SCEEE Summer Faculty Research Program, a time-dependent finite difference technique for analyzing swirling flow in propulsion nozzles has been developed. The geometries which may be analyzed with this code (SNAP) include convergent nozzles, convergent-divergent nozzles, and nozzles with centerbodies. As indicated by preliminary results, the inlet boundary condition has been reformulated in terms of the swirl angle instead of the tangential velocity component, and this inlet condition has been thoroughly investigated. In addition, the time-dependent code has been validated both by internal calculation of conserved quantities and by comparison with experimental measurements. This data has been obtained in a parallel effort in the Ramjet Technology Branch at Wright-Patterson Air Force Base, and the agreement between the experimental and numerical results is excellent. Once the code had been developed and validated, it was used to compute the flowfield in several nozzle configurations at various levels of swirl with several inlet swirl profiles. Reductions in the discharge coefficient and vacuum stream thrust efficiency of up to 11 and 13 percent, respectively, have been calculated. At moderate and higher levels, the effect of swirl has also been found to have a very strong influence on the computed nozzle flowfields. Using the many cases calculated in this study, a universal curve has been developed which can be employed to predict the reduction in the discharge coefficient due to swirl.

ACKNOWLEDGMENTS

The author would like to extend his thanks to the U.S. Air Force Office of Scientific Research and the Southeastern Center for Electrical Engineering Education for support of this work under the 1983-84 Research Initiation in Science and Engineering (RISE) Program. In addition, the continuing support and encouragement of Dr. F. Don Stull, Branch Chief, Dr. Roger R. Craig, Technical Area Manager, and the other members of the Ramjet Technology Branch at Wright-Patterson Air Force Base are greatly appreciated. In particular, Edward Y. Hahn had primary responsibility for design of the hardware and performance of the experiments which comprised an important part of this research effort. The careful and accurate typing of this report by Ms. Bich-N. Ho is also gratefully acknowledged.

TABLE OF CONTENTS

	Page
LIST OF TABLES	iv
LIST OF FIGURES	v
NOMENCLATURE	ix
I. INTRODUCTION	1
II. THEORETICAL FORMULATION	4
III. NUMERICAL TECHNIQUE	8
A. Interior Points	8
B. Boundary Points	8
1. Inlet Points	8
2. Exit Points	10
3. Wall and Centerbody Points	11
4. Free Jet Boundary Points	13
IV. RESULTS AND DISCUSSION	15
A. Converging - Diverging Nozzle	16
B. Centerbody Nozzle	31
C. Converging Nozzle	38
D. Code Validation	46
1. Convergence/Conservation Checks	46
2. Comparison to Experiment	62
E. Correlation of Results	80
V. SUMMARY AND CONCLUSIONS	87
VI. REFERENCES	89

LIST OF TABLES

	Page
Table 1: Computational Details	61
Table 2: Computed Performance Parameters for Experimental Cases	77

LIST OF FIGURES

	Page
Fig. 1 Converging-diverging nozzle geometry	17
Fig. 2 Swirl angle inlet conditions for converging-diverging nozzle calculations	18
Fig. 3 Dependence of integral performance parameters on inlet swirl number for converging-diverging nozzle cases	20
Fig. 4 Total Mach number contours for unswirled converging- diverging nozzle flow	22
Fig. 5 Total Mach number contours for highly swirled, constant angle, converging-diverging nozzle flow	23
Fig. 6 Total Mach number contours for highly swirled, forced vortex, converging-diverging nozzle flow	24
Fig. 7 Total Mach number contours for highly swirled, free vortex, converging-diverging nozzle flow	25
Fig. 8 Comparisons of axis and wall total Mach number distributions for unswirled and highly swirled, forced vortex, converging- diverging nozzle flow	26
Fig. 9 Tangential velocity profiles at inlet, throat, and exit of highly swirled, constant angle, converging-diverging nozzle flow	28
Fig. 10 Tangential velocity profiles at inlet, throat, and exit of highly swirled, forced vortex, converging-diverging nozzle flow	29
Fig. 11 Tangential velocity profiles at inlet, throat, and exit of swirled, free vortex, converging-diverging nozzle flow	30
Fig. 12 Annular nozzle geometry	32

	Page
Fig. 13 Dependence of integral performance parameters on inlet swirl number for annular nozzle cases	33
Fig. 14 Total Mach number contours for unswirled annular nozzle flow	35
Fig. 15 Total Mach number contours for highly swirled, constant angle, annular nozzle flow	36
Fig. 16 Comparisons of inner and outer wall total Mach number distributions for unswirled and highly swirled, constant angle, annular nozzle flow	37
Fig. 17 Tangential velocity profiles at inlet, throat, and exit of highly swirled, constant angle, annular nozzle flow	39
Fig. 18 Converging nozzle geometry	40
Fig. 19 Dependence of integral performance parameters on inlet swirl number for converging nozzle cases	42
Fig. 20 Total Mach number contours for unswirled converging nozzle flow	43
Fig. 21 Total Mach number contours for highly swirled, constant angle, converging nozzle flow	44
Fig. 22 Comparisons of axis and wall total Mach number distributions for unswirled and highly swirled, constant angle, converging nozzle flow	45
Fig. 23 Tangential velocity profiles at inlet, exit, and in the plume of highly swirled, constant angle, converging nozzle flow	47
Fig. 24 Mass flow conservation for a highly swirled, constant angle, converging-diverging nozzle flow	49
Fig. 25 Mass flow conservation for a highly swirled, constant angle, annular nozzle flow	50

	Page
Fig. 26 Mass flow conservation for a highly swirled, constant angle, converging nozzle flow	51
Fig. 27 Wall angular momentum conservation for a highly swirled, constant angle, converging-diverging nozzle flow	53
Fig. 28 Outer wall angular momentum conservation for a highly swirled, constant angle, annular nozzle flow	54
Fig. 29 Inner wall angular momentum conservation for a highly swirled, constant angle, annular nozzle flow	55
Fig. 30 Wall angular momentum conservation for a highly swirled, constant angle, converging nozzle flow	56
Fig. 31 Comparison of mass flow conservation for 41 x 11 and 81 x 21 calculations of highly swirled, constant angle, converging-diverging nozzle flow	58
Fig. 32 Comparison of wall angular momentum conservation for 41 x 11 and 81 x 21 calculations of highly swirled, constant angle, converging-diverging nozzle flow	59
Fig. 33 Experimental converging-diverging nozzle geometry	63
Fig. 34 Experimental inlet stagnation pressure profiles for unswirled and swirling, converging-diverging nozzle flow	65
Fig. 35 Experimental inlet swirl angle profiles for swirling converging-diverging nozzle flow	66
Fig. 36 Total Mach number contours for unswirled, experimental, converging-diverging nozzle flow	68
Fig. 37 Total Mach number contours for CA3 swirler/experimental converging-diverging nozzle flow	69
Fig. 38 Total Mach number contours for CA5 swirler/experimental converging-diverging nozzle flow	70

Fig. 39	Comparisons of axis and wall total Mach number distributions for unswirled and CA3 swirler/experimental converging-diverging nozzle flow	71
Fig. 40	Comparisons of axis and wall total Mach number distributions for unswirled and CA5 swirler/experimental converging-diverging nozzle flow	72
Fig. 41	Comparison of SNAP computations with experimental wall static pressure measurements for unswirled converging-diverging nozzle flow	74
Fig. 42	Comparison of SNAP computations with experimental wall static pressure measurements for CA3 swirler/converging-diverging nozzle flow	75
Fig. 43	Comparison of SNAP computations with experimental wall static pressure measurements for CA5 swirler/converging-diverging nozzle flow	76
Fig. 44	Tangential velocity profiles at inlet, throat, and exit of CA3 swirler/experimental converging-diverging nozzle flow ...	78
Fig. 45	Tangential velocity profiles at inlet, throat, and exit of CA5 swirler/experimental converging-diverging nozzle flow ...	79
Fig. 46	Universal correlation for reduced discharge coefficient as a function of throat swirl number S_{1t} for swirling nozzle flow	83
Fig. 47	Quasi-universal correlation for reduced vacuum stream thrust efficiency as a function of throat swirl number S_{1t} for swirling nozzle flow	85

NOMENCLATURE

<u>Symbol</u>	<u>Meaning</u>
a	speed of sound
A	area
CA3	constant angle, S = 0.3 swirler designation
CA5	constant angle, S = 0.5 swirler designation
C_D	discharge coefficient, defined in Eq. (44)
D	diameter
D/Dt	substantial derivative
L	length
\dot{m}	mass flowrate
M	Mach number
P	pressure
$(\Delta P/P)_{rms}$	rms value over the grid of the fractional static pressure change from one time plane to the next, defined in Eq. (48)
S_1	inlet swirl number, defined in Eq. (47)
S_1, S_2, \dots, S_{12}	swirl numbers defined in Eqs. (49)
t	time
T	temperature or vacuum stream thrust
u	axial velocity component
v	radial velocity component
\bar{v}	transformed radial velocity component, defined in Eq. (18)
w	tangential velocity component

SymbolMeaning

x axial coordinate
y radial coordinate

Greek

α quantity defined in Eq. (15)
 α^* quantity defined in Eq. (36)
 β quantity defined in Eq. (16)
 γ gas specific heat ratio
 δ quantity defined in Eq. (17)
 ξ transformed axial coordinate, defined in Eq. (7)
 η transformed radial coordinate, defined in Eq. (8)
 η_{SI} specific impulse efficiency, defined in Eq. (46)
 η_{VS} vacuum stream thrust efficiency, defined in Eq. (45)
 \bar{n} quantity defined in Eq. (19)
 θ meridian plane streamline angle, $\theta \equiv \tan^{-1}(v/u)$
 ρ density
 τ transformed time coordinate, defined in Eq. (9)
 ϕ swirl angle, $\phi \equiv \tan^{-1}(w/u)$
 $\psi_1, \psi_2, \dots, \psi_{10}$ source terms defined in Eqs. (21)-(23), (29)-(30), (37)-(41)

Subscripts

amb ambient
ave average
c centerbody

<u>Symbol</u>	<u>Meaning</u>
CL	centerline
e	exit
i	inlet
i,j	referring to axial and radial gridpoint location
id	ideal
max	maximum
o	stagnation or zero swirl condition
t	throat
w	wall

Superscripts

n	referring to time plane number
*	conditions at M = 1
—	rms value over the computational grid

I. INTRODUCTION

Swirling flow in nozzles occurs in a number of applications of importance in the aero-propulsion field including the flow in turbofan and turbojet engines and in spin-stabilized rockets. In the former case the tangential velocity component results from the motion of the turbine blades which are immediately upstream, and in the latter by the rocket spin. Another primary application is the exhaust nozzle of integral rocket/ramjets where the swirl is induced by fixed vanes located upstream in the combustor inlet in order to improve combustor performance. Recent studies such as Ref. [1] have demonstrated that higher combustion efficiencies, significantly lower total pressure losses, and shorter combustor lengths are possible for swirled combustors relative to typical flameholder configurations. In each of these applications it is obvious that swirl generated upstream will persist at some level to the inlet of the exhaust nozzle. It is therefore imperative that the effect of swirl on the nozzle flowfield be examined so that important design parameters such as nozzle thrust, mass flow-rate, and specific impulse can be accurately determined.

Although it is well known that the qualitative effect of swirl is to reduce the mass flow and thrust of nozzles at given stagnation conditions, the magnitude of these reductions and the effects of swirl on the flowfield details have not been thoroughly investigated. This is particularly true for configurations typical in ramjet and turbojet applications where the nozzles tend to be short, steep, and highly curved so that the flowfield is very nonuniform and the magnitude of the radial velocity component is significant. In other words, in the applications of interest here it is expected that all three velocity components, axial, radial, and tangential, are of importance.

The majority of previous investigations concerned with swirling nozzle flow have been quasi-one-dimensional theoretical studies [2-21] in which the swirl velocity component has been included in an otherwise conventional one-dimensional nozzle analysis. Each of these investi-

gators generally employs a different choking criterion and makes different assumptions about the swirl velocity distribution. As pointed out in Refs. [6] and [17], several of the quasi-one-dimensional formulations were overspecified, and the fact that each of these studies is confined to certain classes of tangential velocity profiles limits their generality. However, the most serious shortcoming of the quasi-one-dimensional approach is that it neglects the radial velocity component and all of its derivatives. As just mentioned, this is a poor assumption for nozzle geometries typical in ramjet and turbojet applications. Based on these considerations, it is concluded that the quasi-one-dimensional theories are inadequate for the applications of interest here.

A limited number of two-dimensional calculations for inviscid, swirling, converging-diverging nozzle flow have been performed. Guderley and his colleagues [22-25] obtained an approximate numerical solution for transonic throat flow with swirl in order to provide a starting line for the method of characteristics analysis of the supersonic diverging portion of the nozzle. Rao's method was employed to determine wall contours for maximum thrust in the presence of swirl. Only the supersonic portion of the flowfield is treated exactly in this analysis; no consideration is given to the subsonic portion of the flow, and the transonic region is treated only approximately. Boerner, et al. [26] have also developed approximate series solutions for swirling flow in the throat region of axisymmetric nozzles. The weak swirl solution includes the effect of the nozzle wall curvature while the strong swirl solution does not and, therefore, cannot be used for short, highly curved nozzles. Pandolfi [27] has obtained two-dimensional, time-dependent calculations of swirling flow in a converging-diverging nozzle with and without a centerbody. In each case only a single level of swirl was considered and since the computations were terminated just downstream from the sonic line, no thrust calculations were reported. The reduction in mass flow due to swirl was computed only for the no-centerbody case. The principal investigator is unaware of any attempts at a two-dimensional solution of swirling flow in convergent nozzles. However, swirling

supersonic free jet calculations, which are generally incorporated in converging nozzle analyses, have been performed. Smith [28] employed the method of characteristics in his calculations, while Carpenter [29] utilized a linearized theory in an investigation of swirling jet noise.

In addition, there is a dearth of experimental measurements of swirling nozzle flow. Norton, et al. [11] and Dunlap [30] used a spinning test apparatus to simulate spin-stabilized rockets. Norton measured only the mass flow reduction due to spin while Dunlap's investigation concentrated on the flowfield in the spinning combustion chamber immediately upstream from the nozzle. Batson and Sforzini [31] and Sforzini and Essing [32] experimentally investigated swirling nozzle flow in single and multiple converging-diverging nozzles. The swirl was generated by injecting cold gas tangentially to a cylindrical chamber upstream from the nozzle test section. For the case of a single nozzle, limited mass flowrate, thrust, and velocity profile data were obtained. Boerner [26] obtained wall static pressure measurements on the inner and outer walls of an annular nozzle which were compared with the results of his series solutions. The swirl velocity component was induced by the passage of the air radially inward between vanes which were set in a tangential direction. The air was then turned into the axial direction by means of a contoured passageway before passing through the annular nozzle test section. Qualitative agreement between the theoretical and experimental results was obtained. Other than the measurements obtained as part of the current investigation, there is no known data available for swirled nozzle flow generated by fixed or rotating vanes where the predominant flow direction through the vanes is axial. This, of course, is the case for the ramjet and turbojet applications mentioned previously.

II. THEORETICAL FORMULATION

As a result of the preceding discussion, the computational method chosen to analyze swirling flow through the nozzles of interest must include the calculation of all three velocity components and should correctly consider the entire subsonic/transonic/supersonic regions of the nozzle flowfield. For non-swirling flow, the most successful nozzle analysis method has been the time-dependent technique. In this method the unsteady form of the governing equations is used to avoid the mixed, elliptic/hyperbolic nature of the steady flow equations. An initial value surface for the nozzle flowfield is guessed, the steady flow boundary conditions are applied, and the solution is advanced in time until it converges to the steady state. A disadvantage of this method is the long computing times which are sometimes required. If only the steady state solution is desired, several hundred or thousand time planes must be calculated before this limit is reached. On the other hand, its major advantages are its ability to analyze mixed flowfields and its obvious ability to handle truly transient flows.

Based on these considerations, the approach adopted in this research has been to properly include the effects of swirl in an otherwise conventional time-dependent, non-swirling nozzle flow analysis. As a starting point, a version of the widely used "NAP" code [33-36] written by M.C. Cline has been used. This program has been demonstrated to accurately and efficiently calculate non-swirling nozzle flowfields.

In this analysis it is assumed that the nozzle contains the inviscid, non-heat conducting, axisymmetric flow of a thermally and calorically perfect gas. In this context, "axisymmetric" denotes that all derivatives in the tangential direction vanish while the tangential velocity component, of course, does not. Under these assumptions and using Cartesian coordinate notation where x and y are the axial and radial coordinates and u , v , and w are the axial, radial, and tangential velocity components, respectively, the governing equations can be written in nonconservation form as:

Continuity: $\rho_t + u\rho_x + v\rho_y + \rho u_x + \rho v_y + \frac{\rho v}{y} = 0$ (1)

Euler Equations:

Axial: $u_t + uu_x + vu_y + \frac{P_x}{\rho} = 0$ (2)

Radial: $v_t + uv_x + vv_y - \frac{w^2}{y} + \frac{P_y}{\rho} = 0$ (3)

Tangential: $w_t + uw_x + vw_y + \frac{vw}{y} = 0$ (4)

Energy: $(P_t + uP_x + vP_y) - a^2(\rho_t + u\rho_x + v\rho_y) = 0$ (5)

where P , ρ , a , t are pressure, density, speed of sound, and time, respectively, and the subscripts denote partial differentiation.

The inclusion of the swirl velocity component, w , requires the integration of an additional momentum equation, the tangential Euler equation (4), as well as the appearance of the centripetal acceleration term, w^2/y , in the radial momentum equation, (3). The result is a set of five coupled, nonlinear partial differential equations in the five dependent variables: u , v , w , P , and ρ . Knowing these variables and using the ideal gas equation of state, any other quantity of interest can be determined in the flowfield. A point of interest is that the tangential momentum equation can be integrated to:

$$\frac{D}{Dt}(yw) = 0 \quad (6)$$

i.e., the angular momentum of the flow is constant along pathlines. This integrated form could be used to avoid the finite difference solution of equation (4). However, to obtain a solution which is consistent in time, pathlines would have to be projected from each gridpoint on the current time plane to the previous time plane and a bivariate spatial interpolation performed to determine w . Since this procedure would be numerically inefficient, the tangential momentum equation has

been solved using the same time-dependent finite difference technique as for the other four equations.

In order that the finite difference calculations be performed on a rectangular grid, the governing equations are transformed from (x, y, t) coordinates to (ζ, η, τ) coordinates where the η coordinate varies from zero at the nozzle centerline (or centerbody wall) to unity at the outer wall,

$$\zeta \equiv x \quad (7)$$

$$\eta \equiv \frac{y - y_c(x)}{y_w(x, t) - y_c(x)} \quad (8)$$

$$\tau \equiv t \quad (9)$$

The "c" subscript refers to the centerbody while the "w" subscript to the nozzle wall. Under this transformation, the governing equations corresponding to Eqs. (1) - (5) become

$$\rho_\tau + u\rho_\zeta + \bar{v}\rho_\eta + \rho u_\zeta + \rho\alpha u_\eta + \rho\beta v_\eta + \rho v/\bar{\eta} = 0 \quad (10)$$

$$u_\tau + uu_\zeta + \bar{v}u_\eta + P_\zeta/\rho + \alpha P_\eta/\rho = 0 \quad (11)$$

$$v_\tau + uv_\zeta + \bar{v}v_\eta + \beta P_\eta/\rho - w^2/\bar{\eta} = 0 \quad (12)$$

$$w_\tau + uw_\zeta + \bar{v}w_\eta + vw/\bar{\eta} = 0 \quad (13)$$

$$P_\tau + uP_\zeta + \bar{v}P_\eta - a^2(\rho_\tau + u\rho_\zeta + \bar{v}\rho_\eta) = 0 \quad (14)$$

where

$$\alpha \equiv \frac{\partial \eta}{\partial x} = -\beta \frac{dy_c}{dx} - \eta\beta \left(\frac{\partial y_w}{\partial x} - \frac{dy_c}{dx} \right) \quad (15)$$

$$\beta \equiv \frac{\partial \eta}{\partial y} = \frac{1}{y_w - y_c} \quad (16)$$

$$\delta \equiv \frac{\partial \eta}{\partial t} = -\beta \eta \frac{\partial y_w}{\partial t} \quad (17)$$

$$\bar{v} \equiv \alpha u + \beta v + \delta \quad (18)$$

$$\bar{\eta} \equiv y_c + \eta/\beta = y \quad (19)$$

The numerical solution of these equations together with the appropriate boundary conditions is discussed in the next section.

III. NUMERICAL TECHNIQUE

The ζ - η computational plane is rectangular and has uniform spacing in the ζ and η directions although $\Delta\zeta$ and $\Delta\eta$ are not necessarily equal. At present the SNAP code is dimensioned to accept a maximum of 41 points in the ζ direction and 21 in the η direction.

A. Interior Points

The interior points in the flowfield are calculated using MacCormack's [37] well known, second order accurate, explicit, predictor-corrector method. First order accurate backward spatial differences are used for the predictor while first order forward spatial differences are employed on the corrector step. When used in this predictor-corrector fashion, the differencing procedure produces second order accuracy in both space and time. Solution of the interior mesh points is very straightforward and occupies only a small fraction of the coding in SNAP.

B. Boundary Points

Even though the boundary points are far fewer in number than the interior points, it is well known that an accurate evaluation of them is a necessity in obtaining valid time-dependent solutions, particularly in transonic flowfields. In the present work an accurate reference-plane characteristics scheme is used at all boundary points. In this method, the spatial derivatives in the coordinate direction along each boundary are approximated by finite differences and are treated as source terms in the governing equations. The resulting unsteady, one-dimensional problem normal to the boundary is then solved by a second order accurate method of characteristics scheme.

1. Inlet Points For subsonic flow at the nozzle inlet, there is only one compatibility equation available which applies along a characteristic originating from inside the computational mesh on the previous time plane,

$$dP - \rho a du = (\psi_4 + a^2 \psi_1 - \rho a \psi_2) d\tau \quad \text{along } d\zeta = (u - a) d\tau \quad (20)$$

The equation on the left is the compatibility equation which applies along the characteristic, whose equation is on the right. The ψ_1 , ψ_2 , ψ_4 quantities are source terms which involve η derivatives,

$$\psi_1 \equiv -\bar{v}\rho_\eta - \rho\alpha u_\eta - \rho\beta v_\eta - \rho v/\bar{\eta} \quad (21)$$

$$\psi_2 \equiv -\bar{v}u_\eta - \alpha P_\eta/\rho \quad (22)$$

$$\psi_4 \equiv -\bar{v}P_\eta + a^2\bar{v}\rho_\eta \quad (23)$$

Since only one compatibility equation is available and there are five unknown flow properties, assumptions must be made about the values of four flow properties at each inlet point, and both the choice of the specified properties, as well as their assumed distributions, are crucial to obtaining accurate solutions. For non-swirling flow Serra [38], Moretti [39], and Cline [33, 34] recommend specifying the stagnation pressure, P_0 , the stagnation temperature, T_0 , and the meridian plane streamline angle, $\theta = \tan^{-1}(v/u)$. As an alternative, Cline also suggests the specification of the axial and radial velocities, u and v , and the density, ρ . For swirling flow another property must be specified, and in initial computations [40] the author added the specification of the tangential velocity component, w , to the (P_0, T_0, θ) inlet boundary condition. However, for highly swirled nozzle flows this led to presumably unrealistic conditions at the nozzle inlet such as very large swirl angles in the inlet wall region. For this reason, the swirling nozzle flow inlet condition has been reformulated in terms of specified values of P_0 , T_0 , θ , and ϕ where $\phi = \tan^{-1}(w/u)$ is the swirl angle. From a purely physical standpoint, it is much more likely that a reasonable assumption about the ϕ distribution can be made as opposed to the detailed distribution of the w velocity component, especially when the swirl is induced by fixed or rotating vanes.

An iterative technique is required to determine the five dependent variables u , v , w , P , and ρ from the compatibility condition and the four specified properties P_0 , T_0 , θ , and ϕ at each inlet point. The

procedure is to assume a value for the Mach number and then to use the specified values of P_0 and T_0 , together with isentropic relations, to calculate the static pressure and temperature, P and T . The density, ρ , is then calculated from the equation of state and the axial velocity component, u , from the compatibility condition, Eq. (20). The radial and tangential velocity components may then be determined from the specified values of θ and ϕ by $v = u \tan\theta$ and $w = u \tan\phi$. A new value for the Mach number may now be calculated, and the whole procedure is repeated until convergence is achieved. In solving the compatibility equation, a second order accurate predictor-corrector characteristics technique is used. On the predictor step the coefficients in the compatibility condition are based only on property values from the previous time plane, while on the corrector they are based on average values of properties from the old time plane and predicted properties from the new time plane. The specified properties P_0 , T_0 , θ , and ϕ need not be constant across the inlet, but rather can vary arbitrarily. This is in direct contrast to the quasi-one-dimensional theories which generally make assumptions about the distributions of one or more of these properties.

In some cases, particularly for nozzles with long diverging sections, the nozzle flowfield calculation has been done in two parts: a subsonic/transonic calculation of the nozzle throat region followed by a supersonic calculation of the diverging section. This has been done since the supersonic computations have been found to converge to the steady state much faster than the subsonic/transonic computations. The inlet boundary conditions used for the supersonic section are fixed values of u , v , w , P , and ρ where the values are obtained from the last axial location of the converged subsonic/transonic analysis.

2. Exit Points For all of the nozzle computations reported herein, supersonic flow at the exit occurs. In this case the method of characteristics analysis demonstrates that five compatibility conditions must be simultaneously satisfied: three along the pathline and one each along left- and right-running Mach lines, where all of these characteristics

originate from inside the mesh on the previous time plane. Thus, the physically consistent result is obtained that supersonic flow at the exit is completely determined by upstream conditions, and no assumptions about the outflow boundary conditions need be made. The five compatibility equations and the corresponding characteristic equations are given by

$$dv = \psi_3 d\tau \quad (24)$$

$$dP - a^2 d\rho = \psi_4 d\tau \quad \text{along } d\zeta = u d\tau \quad (25)$$

$$dw = \psi_5 d\tau \quad (26)$$

$$dP + \rho a du = (\psi_4 + a^2 \psi_1 + \rho a \psi_2) d\tau \quad \text{along } d\zeta = (u + a) d\tau \quad (27)$$

$$dP - \rho a du = (\psi_4 + a^2 \psi_1 - \rho a \psi_2) d\tau \quad \text{along } d\zeta = (u - a) d\tau \quad (28)$$

where

$$\psi_3 \equiv -\bar{v} v_{\bar{n}} - \beta P_{\bar{n}} / \rho + w^2 / \bar{n} \quad (29)$$

$$\psi_5 \equiv -\bar{v} w_{\bar{n}} - v w / \bar{n} \quad (30)$$

and ψ_1 , ψ_2 , and ψ_4 are defined in Eqs. (21)-(23). The simultaneous solution of the five compatibility equations yields the five dependent variables of interest. A second order accurate, predictor-corrector reference plane characteristics technique similar to that employed at the inlet is used. Because disturbances cannot propagate upstream in a supersonic flow, many previous investigators [33, 34, 38] have simply used extrapolation to obtain the properties at supersonic exit points. However, when nozzle thrust calculations are based on the exit property values, or when the exit conditions from the throat region calculation are used as the fixed inlet conditions for the diverging section computation, the more accurate and physically consistent reference plane characteristics technique is preferred [35, 36].

3. Wall and Centerbody Points For the wall and centerbody boundary points, the ζ derivatives along the boundaries are approximated by finite differences and treated as source terms. The characteristics analysis

shows that three compatibility equations must be satisfied along the wall pathline and one compatibility condition must be satisfied along either a right- or left-running Mach line depending on whether an outer wall or centerbody point is being analyzed,

$$\beta du - \alpha dv = (\beta \psi_7 - \alpha \psi_8) d\tau \quad (31)$$

$$dP - a^2 d\rho = \psi_9 d\tau \quad (32)$$

$$dw = \psi_{10} d\tau \quad (33)$$

along $d\eta = \bar{v} d\tau$

$$dP + \frac{\rho \alpha a}{\alpha^*} du + \frac{\rho \beta a}{\alpha^*} dv = (\psi_9 + a^2 \psi_6 + \frac{\rho \alpha a}{\alpha^*} \psi_7 + \frac{\rho \beta a}{\alpha^*} \psi_8) d\tau \quad (34)$$

$$\text{along } d\eta = (\bar{v} + \alpha^* a) d\tau$$

$$dP - \frac{\rho \alpha a}{\alpha^*} du - \frac{\rho \beta a}{\alpha^*} dv = (\psi_9 + a^2 \psi_6 - \frac{\rho \alpha a}{\alpha^*} \psi_7 - \frac{\rho \beta a}{\alpha^*} \psi_8) d\tau \quad (35)$$

$$\text{along } d\eta = (\bar{v} - \alpha^* a) d\tau$$

$$\text{where } \alpha^* \equiv (\alpha^2 + \beta^2)^{\frac{1}{2}} \quad (36)$$

For an outer wall point, the four compatibility equations available are Eqs. (31)-(34) while for a centerbody point, Eqs. (31)-(33) and (35) are used. The ψ source terms are defined by

$$\psi_6 \equiv -u\rho_\zeta - \rho u_\zeta - \rho v/\bar{\eta} \quad (37)$$

$$\psi_7 \equiv -uu_\zeta - P_\zeta/\rho \quad (38)$$

$$\psi_8 \equiv -uv_\zeta + w^2/\bar{\eta} \quad (39)$$

$$\psi_9 \equiv -uP_\zeta + a^2 u\rho_\zeta \quad (40)$$

$$\psi_{10} \equiv -uw_\zeta - vw/\bar{\eta} \quad (41)$$

In addition to the four compatibility conditions, the wall tangency boundary condition is applied for inviscid flow,

$$v = u \tan \theta_w \text{ or } c + \frac{\partial y_w}{\partial t} \quad (42)$$

This, then, gives five simultaneous equations for the five unknowns u , v , w , P , and ρ which are solved for at each wall point. A predictor-corrector characteristics technique is again used.

For nozzles without centerbodies, the nozzle centerline points are calculated using the interior point algorithm with the proper symmetry conditions enforced. Second order backward differences are used to set the η derivatives of the symmetric quantities u , P , and ρ to zero. The anti-symmetric quantities v and w must vanish on the centerline.

4. Free Jet Boundary Points For the swirling, underexpanded, converging nozzle calculations reported in the next section, it is convenient to continue the calculations into the exhaust plume until an axial location is reached where the flow is supersonic at all mesh points. This procedure avoids the mixed subsonic/supersonic flow conditions which occur at the nozzle exit if the computations are terminated there. As previously mentioned, supersonic exit points are uniquely determined by upstream flow conditions, so that no assumptions need be made about the outflow boundary conditions in that case. However, continuation of the calculations into the exhaust plume requires the solution of free jet boundary points. These points are computed iteratively by the wall point routine in order to satisfy the static pressure boundary condition

$$P = P_{amb} \quad (43)$$

This is done by assuming an initial shape for the plume boundary and using the wall routine to calculate the static pressure. The location of each boundary point is then iterated using the secant method until the calculated boundary pressure and the specified ambient pressure agree within a specified tolerance. The plume boundary location is therefore seen to be a function of time which is the reason for the inclusion of the time dependence of y_w in Eqs. (8), (17), (18), and (42).

Of special interest when making free jet calculations is the nozzle exit lip point which is a singularity in the flowfield. An "upstream" solution is first calculated at this point using the wall tangency boundary condition and backward ζ derivatives on both the initial and solution planes in the evaluation of the ψ source terms. A "downstream" solution is then computed using the specified pressure boundary condition, and the stagnation pressure, stagnation temperature, and tangential velocity from the upstream solution. The upstream solution is used when computing the wall grid point immediately upstream from the exit, while the downstream solution is employed for the free jet boundary point immediately downstream from the exit. A third exit lip solution is used for calculating interior points. This solution is obtained by averaging the meridian plane Mach numbers and flow angles of the upstream and downstream solutions and using the stagnation pressure, stagnation temperature, and tangential velocity of the upstream solution to obtain the other properties.

An additional point of interest regarding the numerical technique is that explicit artificial viscosity has not been included in any of the calculations reported herein. Further details concerning the numerical technique, including the method for deriving the compatibility and characteristic equations used at the boundaries, may be found in Refs. [34] and [35].

IV. RESULTS AND DISCUSSION

Before proceeding to a detailed discussion of the results, the integral parameters used to judge the nozzle performance will be defined. Results have been obtained for the discharge coefficient, C_D , the vacuum stream thrust efficiency, η_{vs} , the specific impulse efficiency, η_{SI} , and the nozzle flowfield as functions of the inlet swirl number, S_i , where

$$C_D \equiv \frac{\dot{m}}{\dot{m}_{id}} = \frac{2 \int_{y_c}^{y_w} \rho u y dy}{(y_{wt}^2 - y_{ct}^2) (\rho^* u^*)_{id}} \quad (44)$$

$$\eta_{vs} \equiv \frac{T}{T_{id}} = \frac{2 \int_{y_{we}}^{y_{ce}} (P + \rho u^2) y dy}{(y_{we}^2 - y_{ce}^2) (P_e + \rho_e u_e^2)_{id}} \quad (45)$$

$$\eta_{SI} \equiv \frac{(T/\dot{m})}{(T/\dot{m})_{id}} = \frac{\eta_{vs}}{C_D} \quad (46)$$

$$S_i \equiv \frac{\int_{y_{ci}}^{y_{wi}} \rho u w y^2 dy}{y_{wi} \int_{y_{ci}}^{y_{wi}} \rho u^2 y dy} \quad (47)$$

The subscripts i, t, e, and id are used to denote inlet, throat, exit, and ideal conditions, respectively, and \dot{m} and T are the mass flowrate and vacuum stream thrust. The ideal conditions are defined as one-dimensional, isentropic values at the same stagnation conditions as the actual flow.

Note that the inlet swirl number can be interpreted as the axial flux of angular momentum divided by the inlet wall radius times the axial flux of axial momentum, and is therefore a measure of the level of swirl at the nozzle inlet. As will be discussed in a succeeding section, use of this swirl number definition evaluated at the nozzle inlet is not an optimal choice for correlating the performance of various nozzle geometries with different swirl profiles. However, from a practical viewpoint, the design engineer is concerned with knowing the nozzle performance when a certain level of swirl is imposed at the inlet by upstream conditions and, in addition, the definition given in Eq. (47) is in wide use, e.g. [1] and [41]. For these reasons the results will be presented as a function of the inlet swirl number, S_i .

A. Converging-Diverging Nozzle

The nozzle geometry used in the first series of computations is shown in Fig. 1. It is a conventional converging-diverging nozzle with a cylindrical inlet, a circular arc transition to a 35° conical convergent section, a circular arc throat region, and an 18.5° conical divergent section. The area contraction ratio between the nozzle inlet and throat is $A_t/A_i = 0.668$. This nozzle design is typical of those presently under development for integral rocket/ramjet systems.

In addition to a nozzle geometry, inlet conditions must also be specified. As discussed previously, the specified inlet properties have been chosen as P_o , T_o , θ , and ϕ . In the present computations it has been assumed that P_o , T_o , and $\theta = 0$ are uniform across the nozzle inlet ($x = -0.9$), and the three ϕ distributions shown in Fig. 2 have been used. Away from the centerline, the "constant angle" swirl profile has $\tan \phi = \text{constant}$, while for the "forced vortex" profile $\tan \phi$ is proportional to y and for the "free vortex" profile $\tan \phi$ is proportional to $1/y$. The rationale for these choices is that if the axial velocity component, u , is uniform across the inlet these ϕ profiles would translate directly into corresponding tangential velocity profiles, w . Since one of the fundamental assumptions of the numerical technique

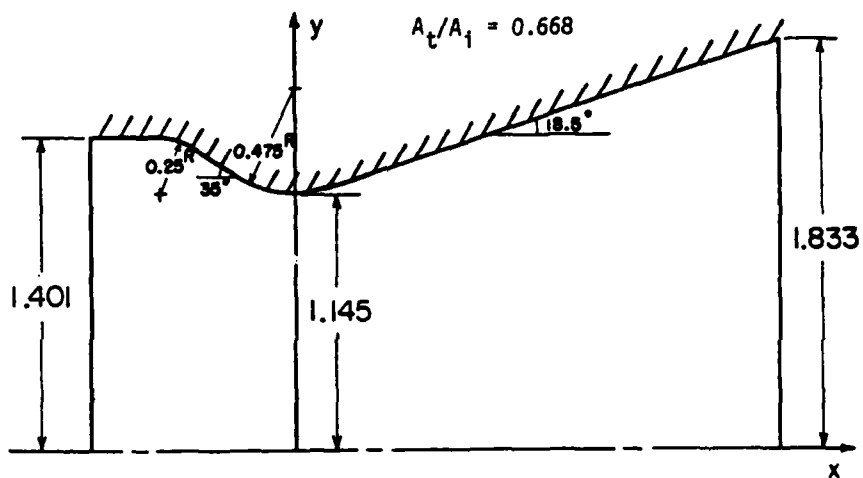
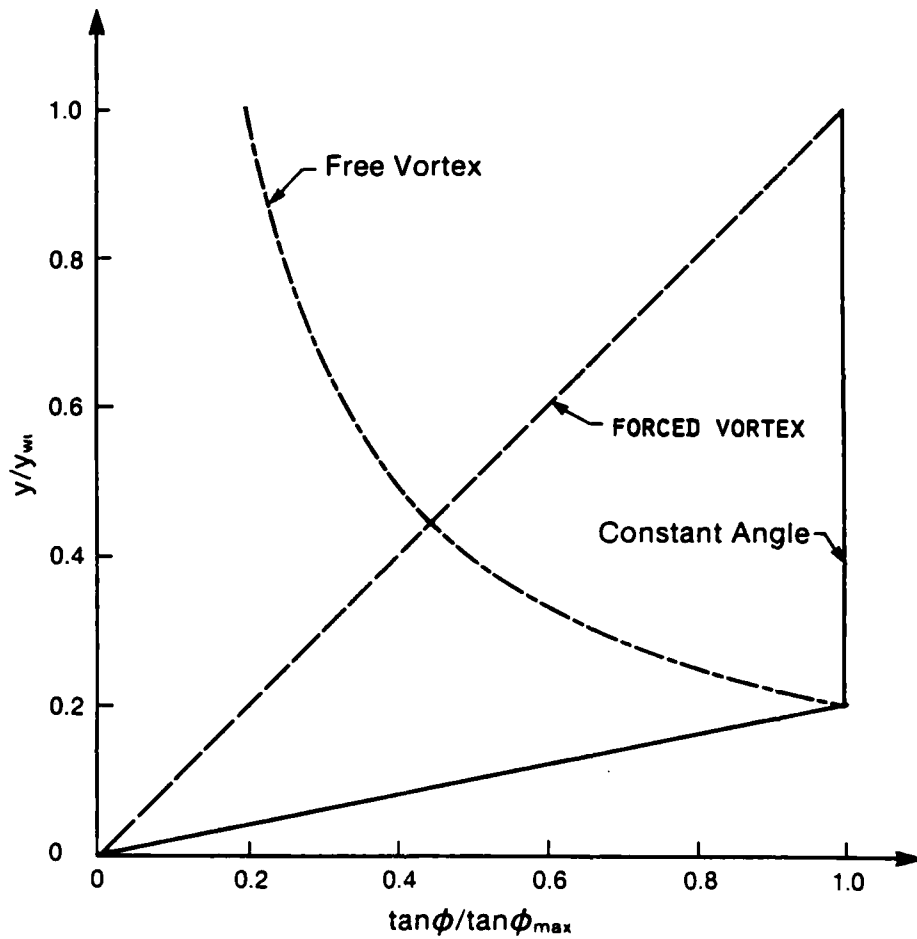


Figure 1. Converging-diverging nozzle geometry

SWIRL ANGLE INLET CONDITIONS



$P_o, T_o, \phi=0$ Assumed Uniform Across Inlet

Figure 2. Swirl angle inlet conditions for converging-diverging nozzle calculations

is that the flow is spatially axisymmetric, w must vanish on the axis. A linear, forced vortex profile has been used in the centerline region for the constant angle and free vortex profiles in order to enforce this symmetry condition. The radius ratio chosen for the "matching point", $y/y_{wi} = 0.2$, is typical of the radius ratio of the hub of fixed vane swirlers [1]. In order to increase the level of swirl in the nozzle flowfield, the numerical value of ϕ_{max} is simply increased. Another point of importance is that since the swirl number is proportional to the area under the curve in Fig. 2, for given S_i the numerical value of ϕ_{max} must be largest near the centerline for the free vortex profile. In these and all succeeding calculations a specific heat ratio of $\gamma = 1.4$ has been used.

Results for the discharge coefficient and vacuum stream thrust efficiency as a function of the inlet swirl number are shown in Fig. 3. For given S_i the reductions in C_D and η_{VS} are largest for the free vortex profile, followed by the constant angle and forced vortex profiles. As will be shown shortly, the major effect of swirl on the nozzle flowfield is to cause a large increase in the axial velocity near the nozzle centerline. Since large values of ϕ_{max} are required near the centerline to achieve a given S_i for the free vortex profile, even moderate values of S_i result in a very nonuniform throat flowfield due to the centerline sensitivity effect. This causes the steep decrease in C_D and η_{VS} as a function of S_i shown in Fig. 3 for the free vortex swirl profile. Interestingly, the specific impulse efficiency, η_{SI} , is very nearly constant for the entire range of cases shown in Fig. 3. This result suggests that for a choked, swirling nozzle flow with fixed stagnation conditions, the reduction in thrust is due solely to the reduction in mass flow through the nozzle. For a constant mass flow device like a ramjet, on the other hand, the introduction of swirl entails essentially no loss in thrust but rather results in an increased combustor pressure. This increased pressure, in turn, requires that more diffusion occur in the inlet. To avoid the loss in mass flow and thrust or the increased diffusion requirement, the nozzle throat may be

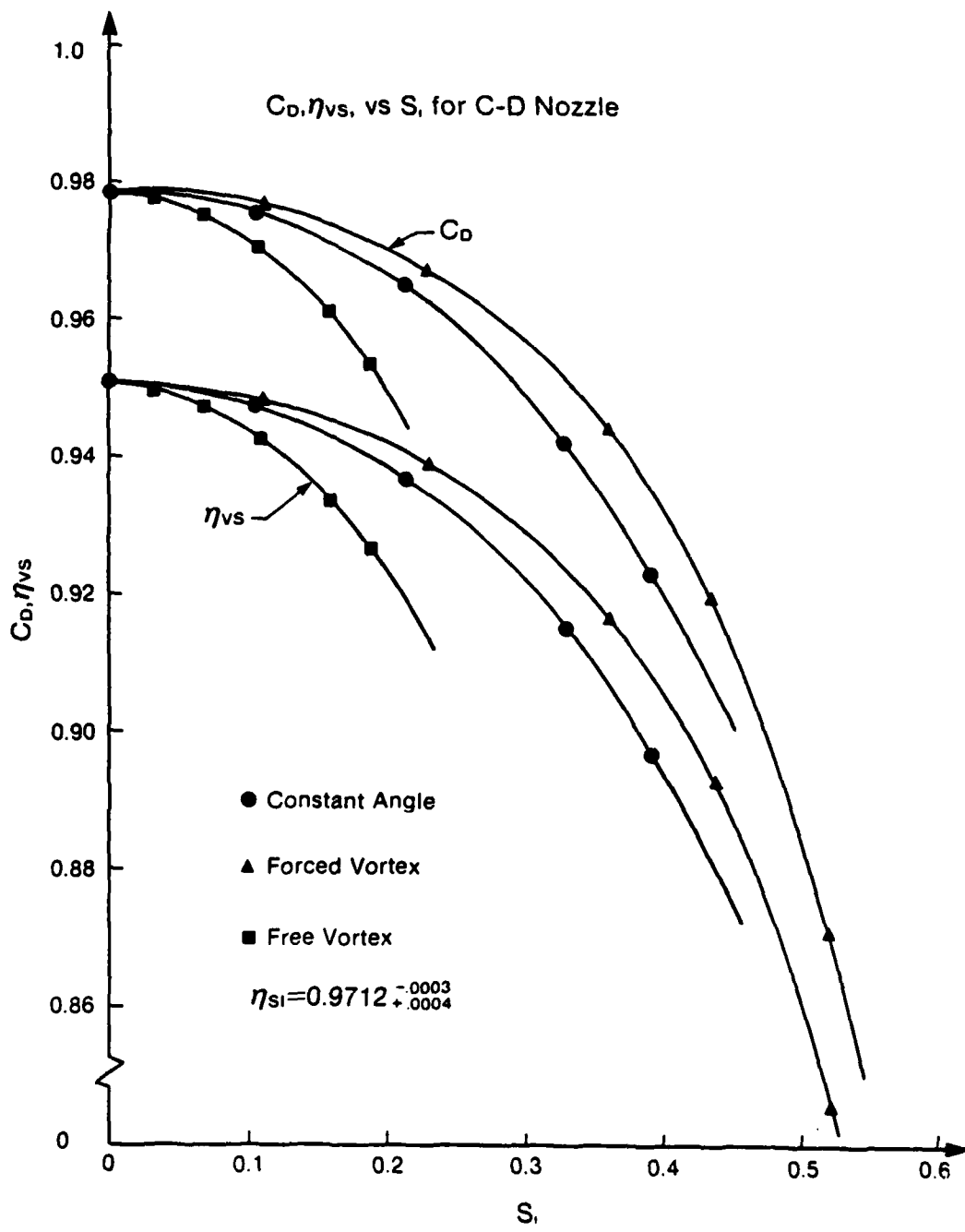


Figure 3. Dependence of integral performance parameters on inlet swirl number for converging-diverging nozzle cases

appropriately enlarged. However, an analysis such as the present one must still be performed to determine the magnitude of the throat enlargement in the presence of swirl.

Each of the three series of calculations presented in Fig. 3 were performed at increasing levels of swirl until sonic axial velocities in the inlet centerline region were generated. Under these conditions the characteristics analysis described in the preceding section reveals that all five dependent variables u , v , w , P , and ρ should be specified at the nozzle inlet. However, an a priori specification of these properties, or even a prediction of which inlet mesh points will be supersonic for a given swirl profile, is virtually impossible. In any event, it is unlikely that in actual applications the combustor will impose supersonic axial velocities in the centerline region of the nozzle inlet.

Total Mach number contour plots are shown for various cases in Figs. 4-7, where $M \equiv (u^2 + v^2 + w^2)^{1/2}/a$. The flowfield shown in Fig. 4 for the no swirl case is typical of that for a conical nozzle. Due to the relatively small wall radius of curvature, a strong expansion of the flow occurs in the throat wall region which greatly leads the expansion occurring along the nozzle centerline. The "wiggles" in the $M = 2.0$ and 2.25 contours are due to an oblique shock wave which originates at the tangency point between the circular arc and conical divergent wall sections ($x = 0.15$). A discontinuity in the curvature of the wall contour occurs at this point, leading to a compression of the flow in this region. Comparing the unswirled case, Fig. 4, to highly swirled constant angle, forced vortex, and free vortex cases, Figs. 5-7, the most notable effect is seen to be an upstream shifting of the Mach number contours near the nozzle centerline. In other words, the predominant effect of swirl on the nozzle flowfield is a large increase in the axial velocity near the centerline as compared to the unswirled case. The influence of the tangential velocity component on the flowfield near the wall, on the other hand, is weak. These effects can be seen more clearly in Fig. 8 where the axial distributions of the Mach

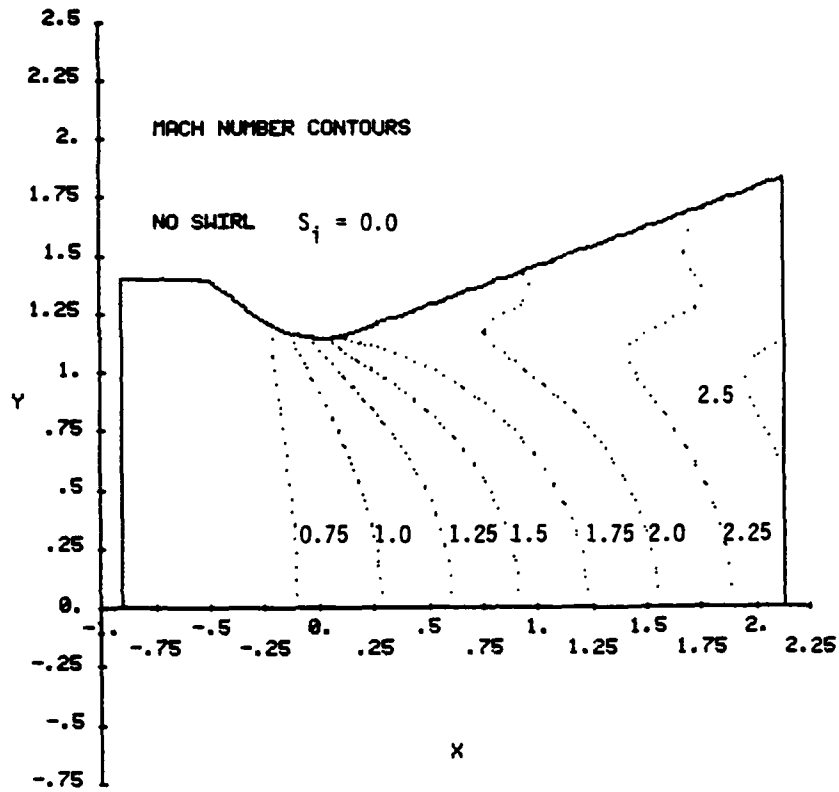


Figure 4. Total Mach number contours for unswirled converging-diverging nozzle flow

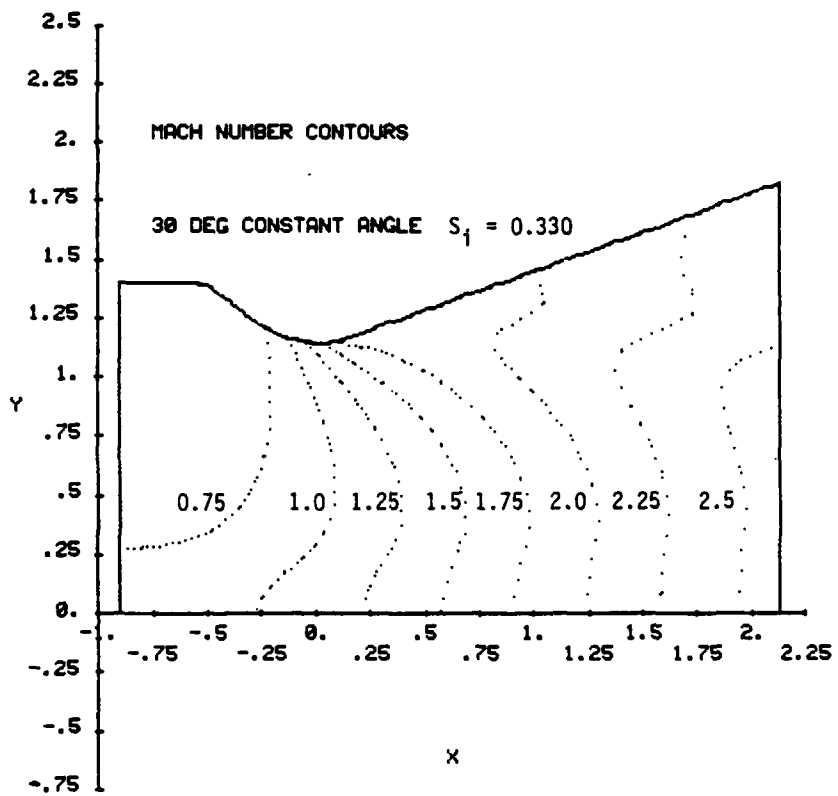


Figure 5. Total Mach number contours for highly swirled, constant angle, converging-diverging nozzle flow

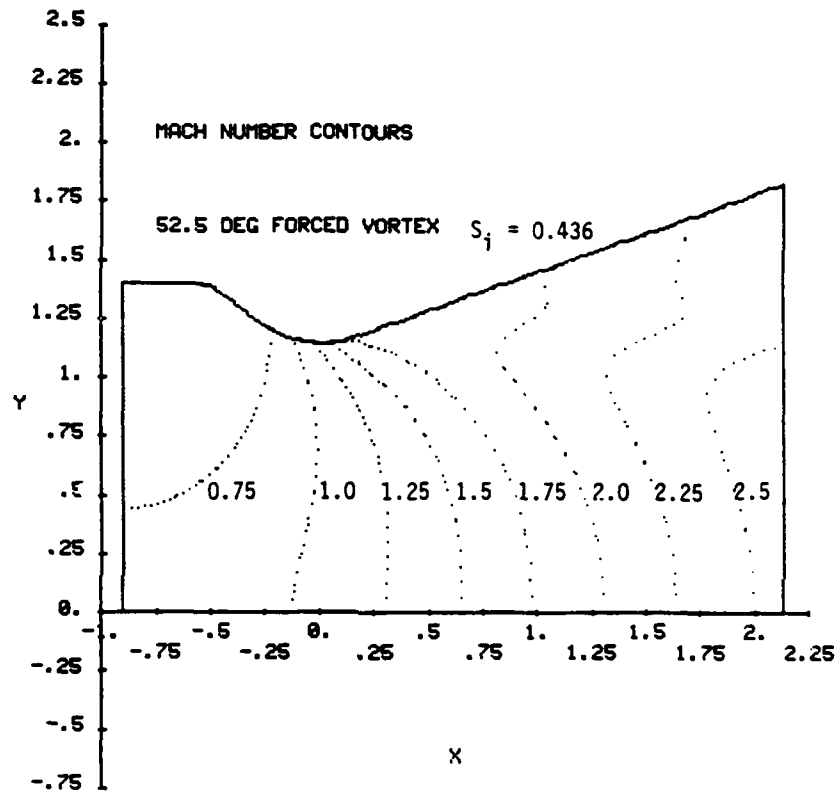
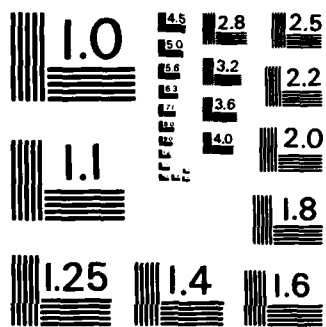


Figure 6. Total Mach number contours for highly swirled, forced vortex, converging-diverging nozzle flow



MICROCOPY RESOLUTION TEST CHART
NATIONAL BUREAU OF STANDARDS - 1963 - A

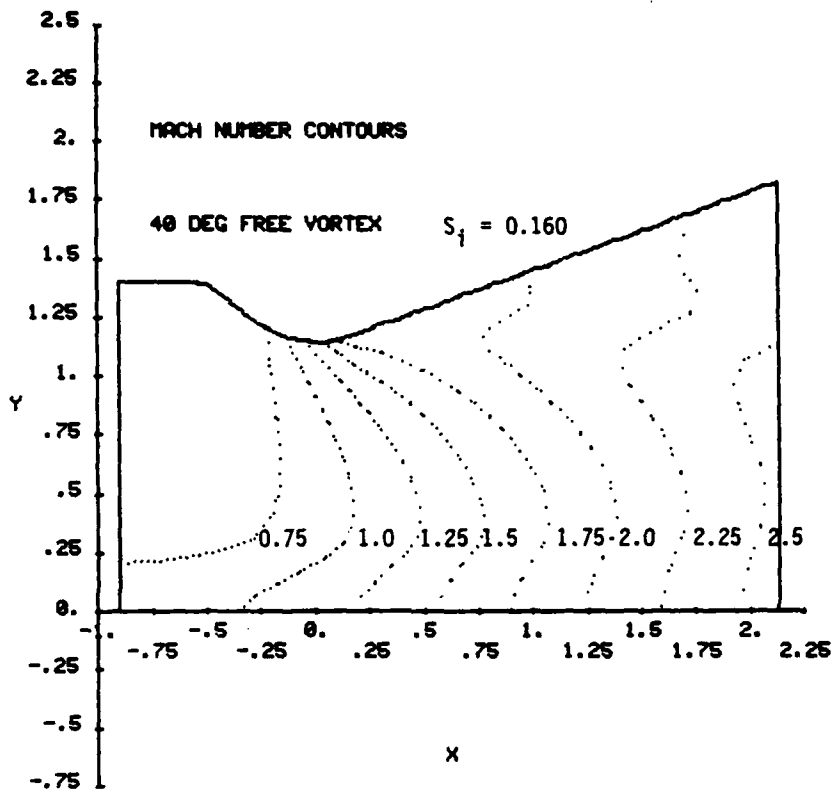


Figure 7. Total Mach number contours for highly swirled, free vortex, converging-diverging nozzle flow

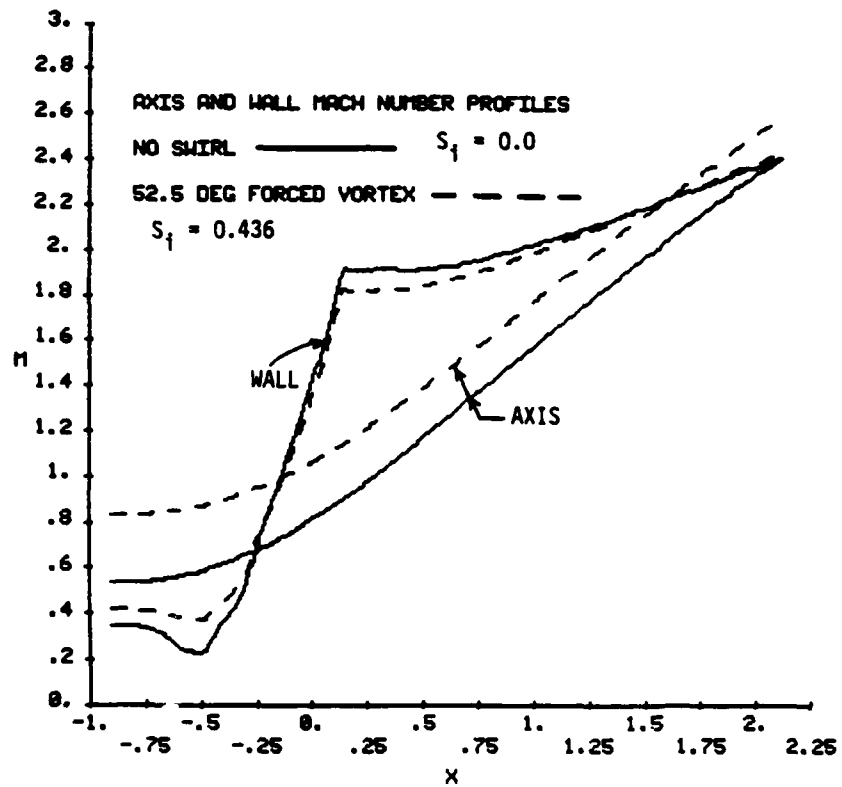


Figure 8. Comparisons of axis and wall total Mach number distributions for unswirled and highly swirled, forced vortex, converging-diverging nozzle flow

number along the nozzle centerline and wall are plotted for the unswirled nozzle flow (Fig. 4) and for the highly swirled forced vortex flow (Fig. 6). Along the axis the flow is smoothly accelerated from subsonic to supersonic conditions, although the axial velocity for the swirling flow is significantly higher than that for the non-swirling flow. At the wall the effect of swirl is very much reduced. In addition, the forced vortex case shown in Fig. 8 is the one for which the effect of swirl at the wall is the greatest; for the constant angle and free vortex cases the effect is even smaller. The discontinuity in the slope of the wall Mach number plots in Fig. 8 is due to the previously mentioned oblique shock wave which originates from the tangency point between the circular arc nozzle throat and the conical divergent section.

The tangential velocity profiles across the inlet, throat, and exit for the highly swirled constant angle, forced vortex, and free vortex flows are plotted in Figs. 9-11, respectively. In each case the local wall radius, y_w , has been used to normalize the radial coordinate, and the maximum value of w at the nozzle inlet has been used to normalize the tangential velocity. With the previously described inlet boundary conditions and nozzle geometry, the axial velocity, u , is found to decrease from the axis to the wall across the inlet in each case. Therefore, the constant swirl angle profile does not result in constant tangential velocity across the inlet, but rather w falls as the wall is approached. In a similar manner, w does not increase linearly across the inlet for the forced vortex case, and w decreases faster than $1/y$ across the inlet for free vortex swirl. In each case, however, the profiles at the throat and exit are similar in shape to that at the inlet. Based on the conservation of angular momentum, Eq. (6), it is also expected that the general level of the tangential velocity should be inversely proportional to the wall radius at a given location. Referring to the dimensions given in Fig. 1, it is seen that the profiles presented in Figs. 9-11 confirm this expectation.

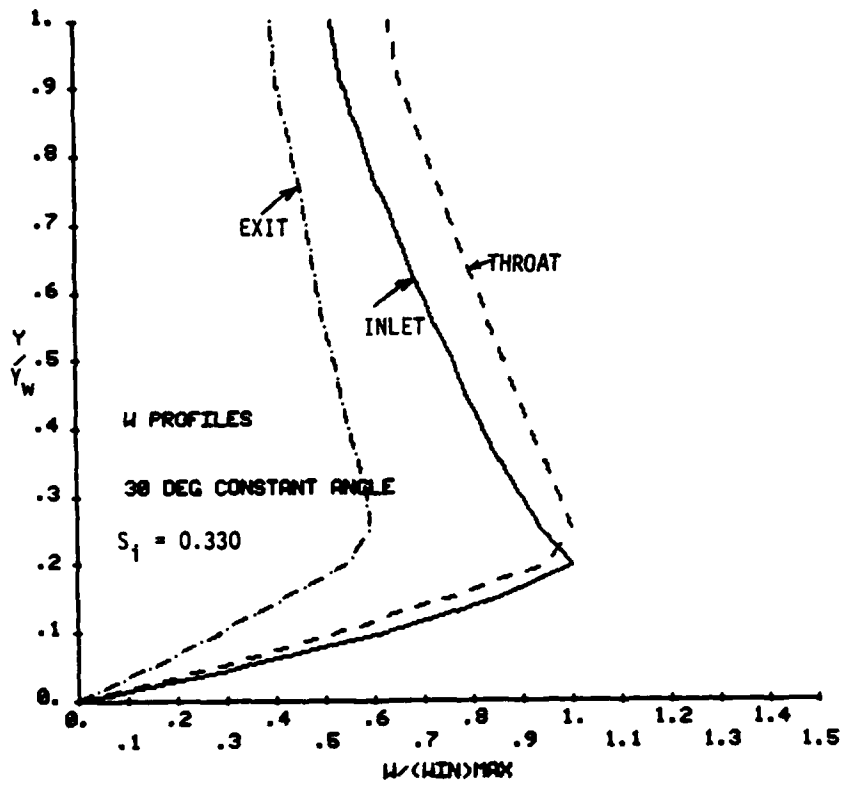


Figure 9. Tangential velocity profiles at inlet, throat, and exit of highly swirled, constant angle, converging-diverging nozzle flow

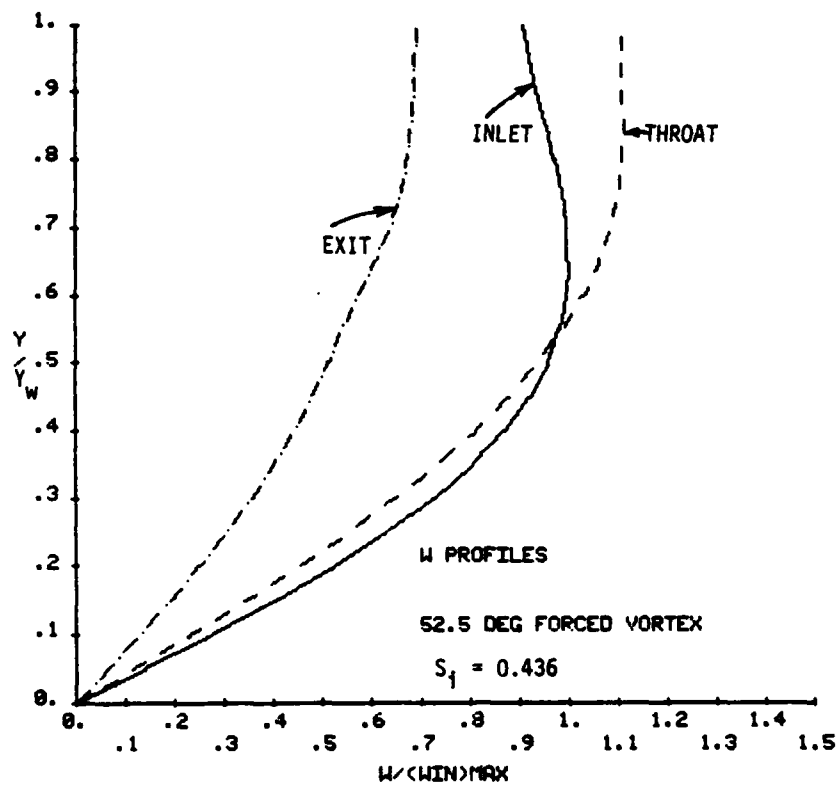


Figure 10. Tangential velocity profiles at inlet, throat, and exit of highly swirled, forced vortex, converging-diverging nozzle flow

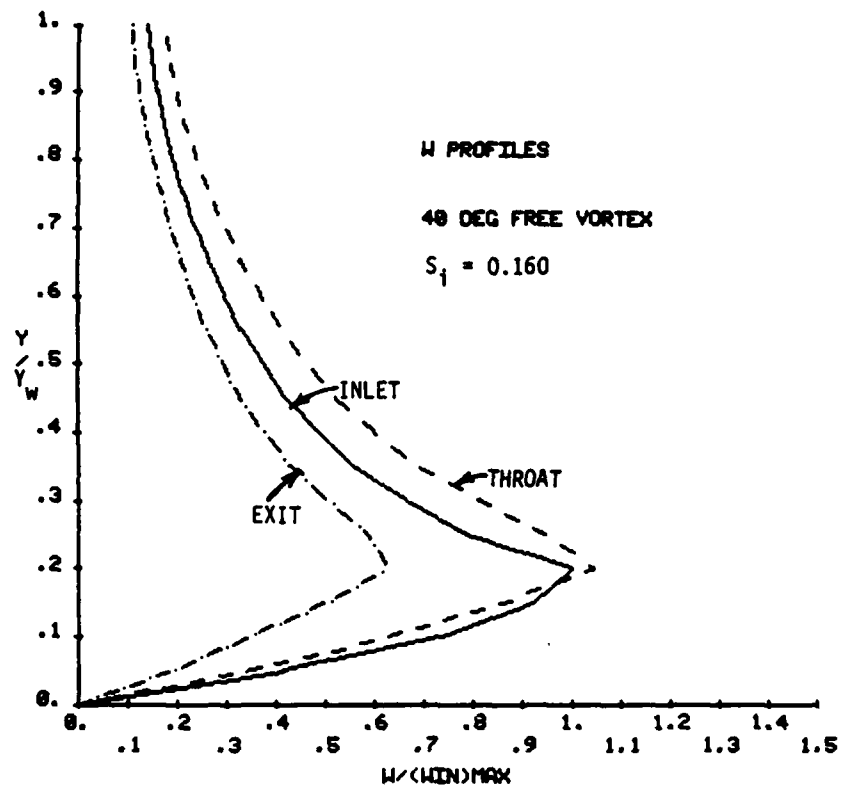


Figure 11. Tangential velocity profiles at inlet, throat, and exit of swirled, free vortex, converging-diverging nozzle flow

B. Centerbody Nozzle

In order to demonstrate the ability of the SNAP code to compute swirling flow in annular nozzles with centerbodies, the geometry shown in Fig. 12 has been analyzed. This is the turbojet plug nozzle geometry investigated experimentally under non-swirl conditions by Bresnahan and Johns [42]. The outer wall is a straight, cylindrical one while the inner wall has a circular arc transition to a circular arc throat and a 10° conical plug section. The area contraction ratio in this case is $A_t/A_i = 0.327$. As mentioned in a previous section, the inner and outer walls are both treated using a reference plane characteristics technique identical to that used for the wall of a conventional c-d nozzle. This geometry is an interesting one since the computed results are quite different from those of the just discussed c-d nozzle. For the converging-diverging nozzle the swirl velocity component along the wall increases from the inlet to the throat and then decreases to the exit as the wall radius first decreases and then increases (conservation of angular momentum). For the plug nozzle in Fig. 12, however, w should be constant along the outer wall since its radius is constant, and w should first decrease and then increase as the flow traverses from the inlet to the throat to the exit along the inner wall. The contraction in area from inlet to throat is also significantly larger for the annular nozzle than for the c-d nozzle. For the computations reported here the boundary conditions have been taken as P_0 , T_0 , ϕ , and $\theta = 0$ uniform across the nozzle inlet.

The results for the integral performance parameters as a function of the swirl level are presented in Fig. 13. Over the range of swirl numbers investigated, the reductions in the discharge coefficient and vacuum stream thrust efficiency as compared to the unswirled case are approximately 11% and 13%, respectively. These are the largest reductions computed for any of the cases investigated to date. In addition, the specific impulse efficiency is not constant as for the c-d nozzle, but instead decreases by 2.3% at the highest S_i computed. Of particular

PLUG NOZZLE GEOMETRY

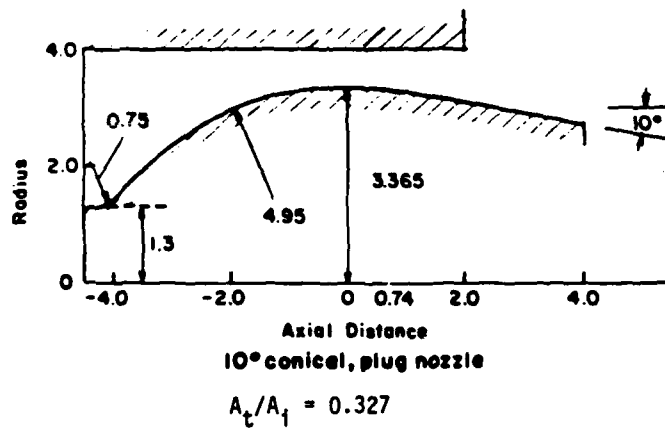


Figure 12. Annular nozzle geometry

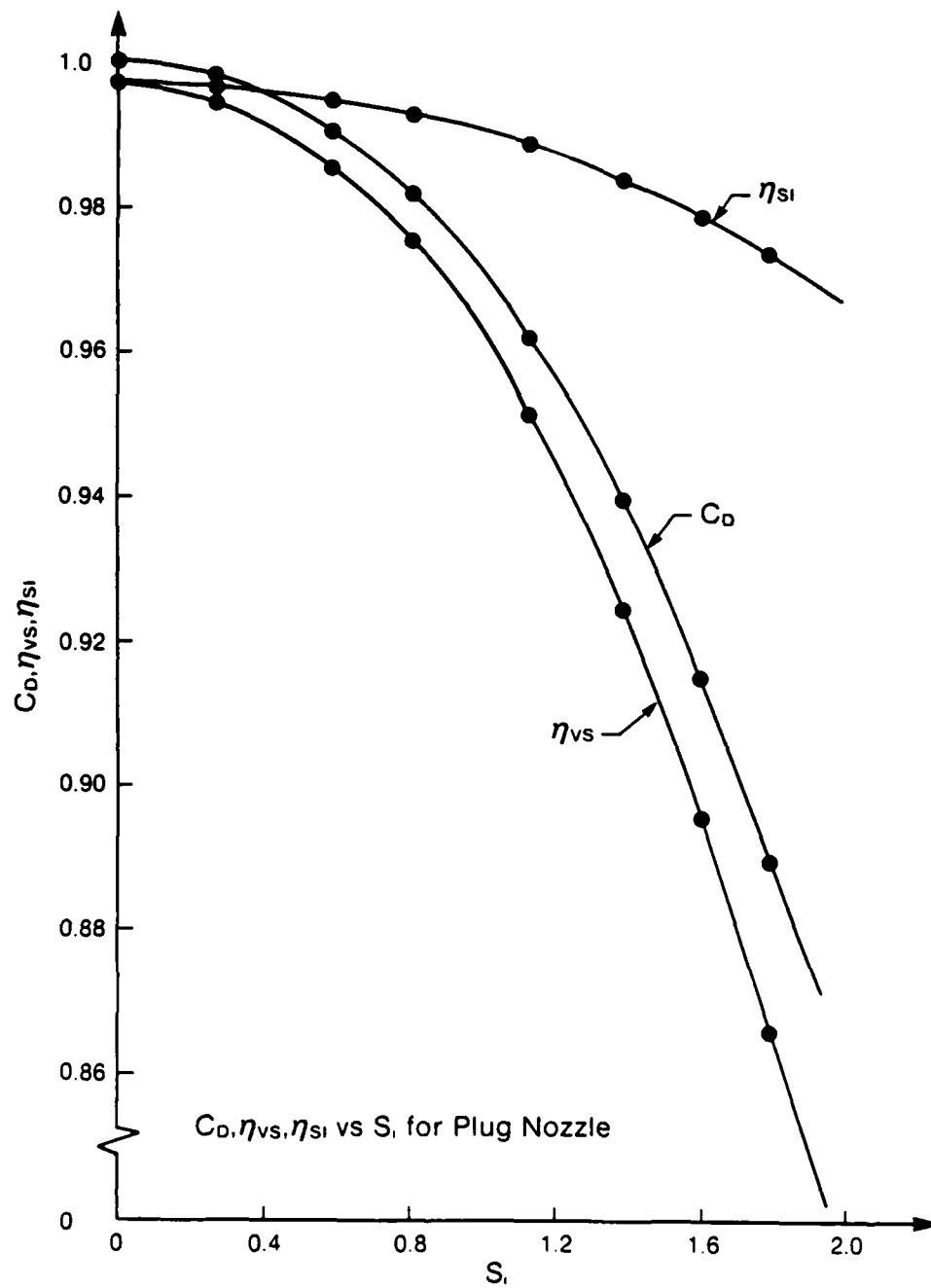


Figure 13. Dependence of integral performance parameters on inlet swirl number for annular nozzle cases

interest is the magnitude of the swirl numbers along the abscissa in Fig. 13, values roughly four times those along the S_1 axis in Fig. 3 for the c-d nozzle. Because of the large contraction in area, which causes a large increase in the axial velocity from the inlet to throat, and because the tangential velocity decreases from the inlet to throat, the flow must be very strongly swirled at the plug nozzle inlet in order to have a significant effect on the performance parameters. In fact, for the most highly swirled case plotted in Fig. 13, the constant value of ϕ across the inlet is 70° . Thus, for this case $w = 2.74u$ across the inlet, and the tangential velocity is clearly the dominant component in the inlet region.

Contours of constant total Mach number are plotted in Figs. 14 and 15 for the unswirled and highly swirled cases, respectively. The contours for the unswirled case are fairly uniform in the throat region due to the relatively large throat wall radius of curvature. The difference in shape of the $M = 1.4$ and 1.6 contours near the inner wall is again due to a weak oblique shock which propagates into the flow from the tangency point between the circular arc throat and the 10° conical section ($x = 0.860$). A discontinuity in the curvature of the inner wall occurs at this point. For the highly swirled flow, the Mach number contours in the inlet region are vastly different from those for the no swirl case. As the flow progresses along the inner wall near the inlet, the total Mach number decreases, i.e. the flow is actually being compressed, because the tangential velocity, which is the dominant component, is decreasing (conservation of angular momentum). As the throat is approached, however, the axial velocity eventually becomes the largest component, such that in the throat region the Mach number contours become more conventional in shape. These features are clearly seen in Fig. 16 where the axial Mach number distributions along the inner and outer walls are compared for the unswirled and highly swirled cases. Along the outer wall the flow experiences a monotonic acceleration from subsonic to supersonic conditions. The Mach number distribution for the swirled case is higher than that for the unswirled flow,

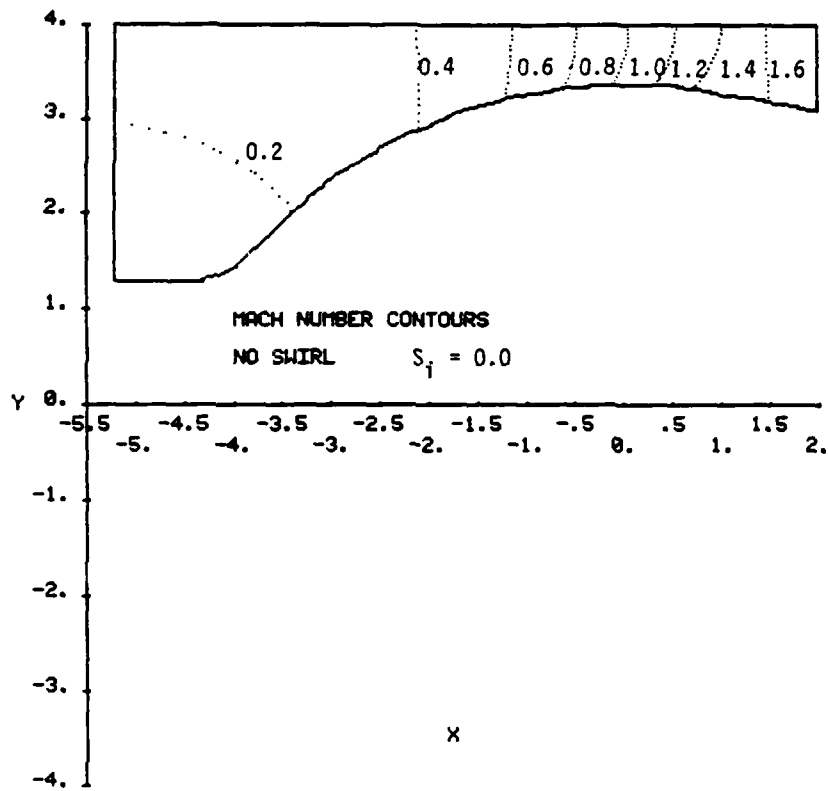


Figure 14. Total Mach number contours for unswirled annular nozzle flow

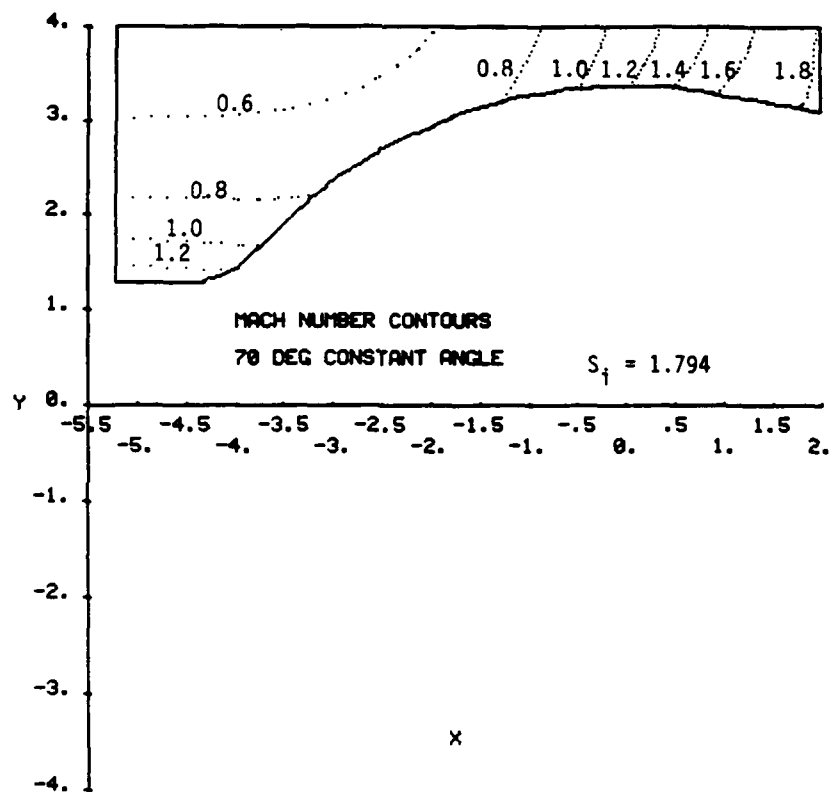


Figure 15. Total Mach number contours for highly swirled, constant angle, annular nozzle flow

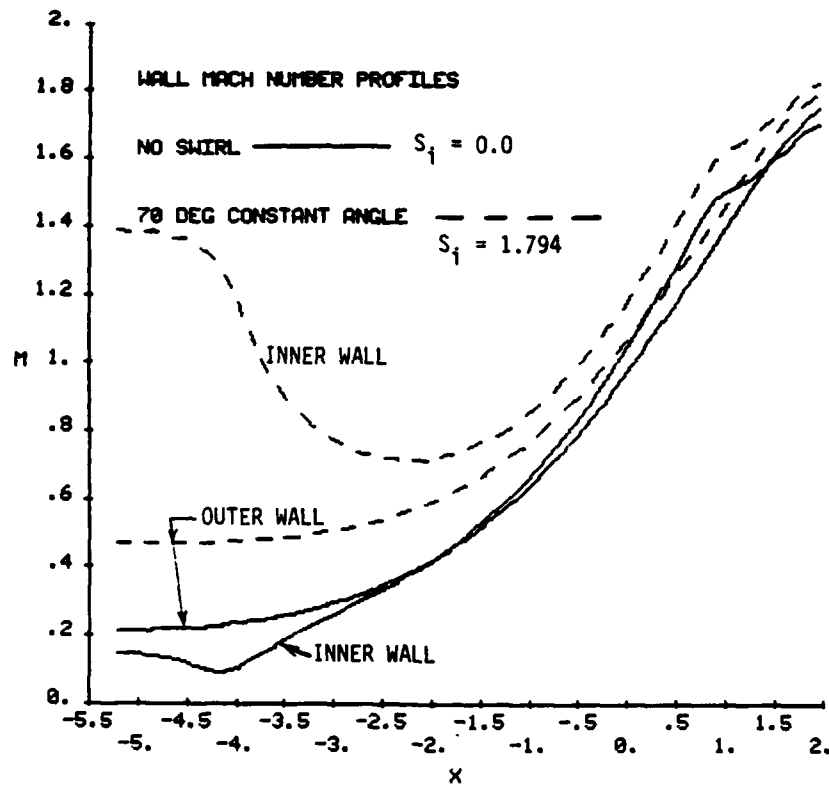


Figure 16. Comparisons of inner and outer wall total Mach number distributions for unswirled and highly swirled, constant angle, annular nozzle flow

especially in the inlet region. Along the inner wall near the inlet, the Mach number for the swirling case is over 7 times that for the no swirl case, and the compression which occurs for $x \leq -2$ with swirl is clearly evident. The slight change in slope of the inner wall Mach number profiles at $x = 0.860$ marks the location of the circular arc throat/ 10° conical section tangency point.

The tangential velocity profiles at the inlet, throat, and exit locations are presented in Fig. 17 for the highly swirled nozzle flow. For this nozzle geometry and assumed inlet conditions, the axial velocity component at the inlet is computed to decrease from the inner to the outer wall. Since a constant swirl angle inlet condition has been used, the tangential component, w , decreases across the inlet in a similar way. Interestingly, however, the w profiles across the throat and exit are found to be virtually uniform. Conservation of angular momentum is also seen to be at least qualitatively satisfied since the centerbody radius is smallest at the inlet, largest at the throat, and intermediate at the exit.

C. Converging Nozzle

The first known two-dimensional calculations of swirling flow in a converging nozzle are presented and discussed next. The geometry which has been analyzed, Fig. 18, has a cylindrical inlet with a circular arc transition to an elliptically contoured converging section. Except for the small circular arc section, this nozzle is identical to the 0.5 contraction ratio nozzle used at AFWAL/PORT in ramjet combustor tests. The circular arc transition has been added to avoid the infinite wall slope which would otherwise occur at the junction between the cylindrical and elliptical sections. The inlet boundary conditions used in this case are P_0 , T_0 , and $\theta = 0$ uniform across the inlet and a "constant angle" swirl profile similar to the one sketched in Fig. 2. In this case, however, the "matching point" between the linear and constant portions of the $\tan \phi$ profile is located at $y/y_{wi} = 0.214$. A stagnation-to-ambient pressure ratio of 3.0 has been used in all of the

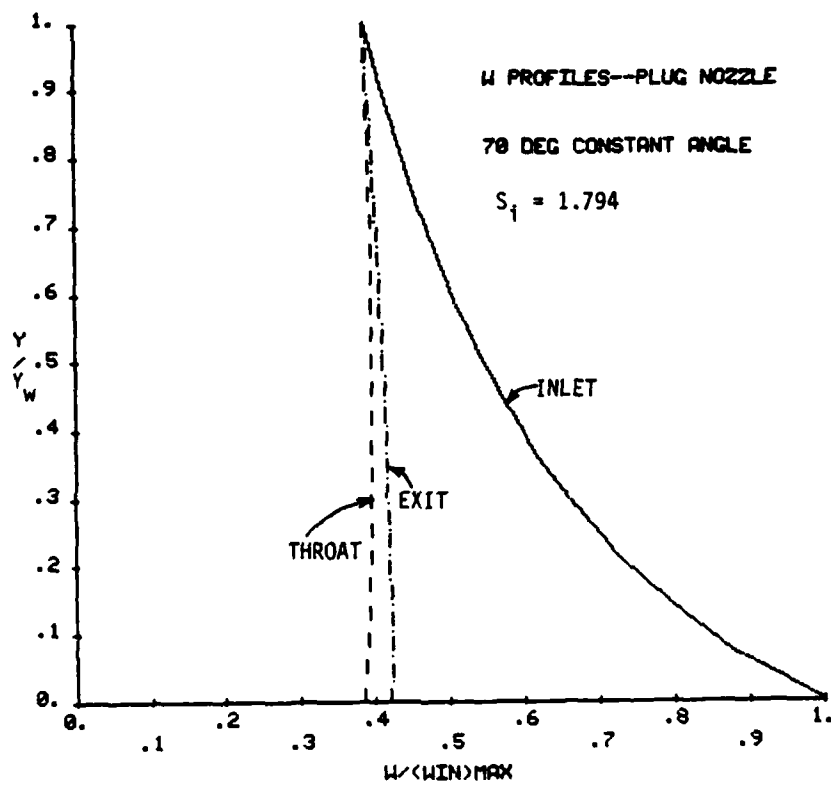


Figure 17. Tangential velocity profiles at inlet, throat, and exit of highly swirled, constant angle, annular nozzle flow

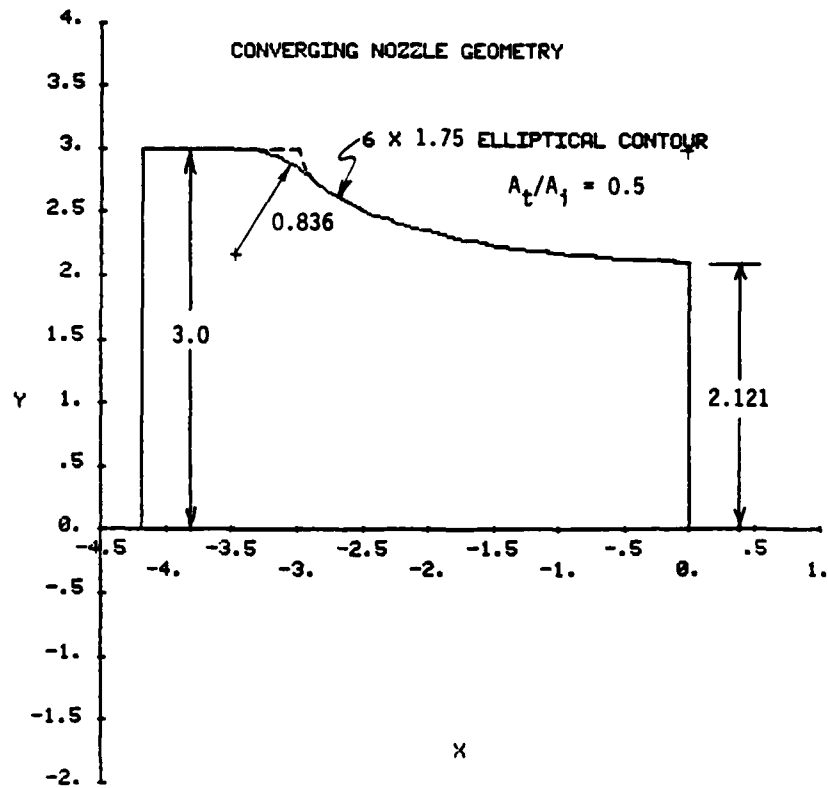


Figure 18. Converging nozzle geometry

calculations to be presented. A few of the calculations were repeated at $P_0/P_{amb} = 5.0$ with virtually identical results, demonstrating the back pressure independent nature of this flow. A portion of the swirling exhaust plume has been calculated such that the flow at all the downstream boundary mesh points is supersonic due to the aforementioned advantages of this exit condition. Iterative use of the wall point routine to satisfy the $P = P_{amb}$ boundary condition for the free jet points was therefore required.

The swirl number dependence of the discharge coefficient, vacuum stream thrust efficiency, and specific impulse efficiency is plotted in Fig. 19. As for previous cases, C_D and η_{VS} decrease rather rapidly with S_i , reaching values 8.5% and 9.6% less than for the non-swirling case at the highest swirl level investigated. In this instance the specific impulse efficiency is not constant, but rather decreases by approximately 1.3% over the range of S_i studied.

Unswirled and highly swirled total Mach number contours are plotted for this converging nozzle in Figs. 20 and 21. In many respects, the comments made earlier in connection with the converging-diverging nozzle results also apply here. Comparing Figs. 20 and 21, the most obvious difference is the strong upstream shift in the contours near the centerline for the swirled flow, i.e. much higher axial velocities in the centerline region in this case. For the non-swirling case, the flow in the nozzle exit plane is seen to be mixed, i.e. subsonic near the axis and supersonic near the wall. Use of the nozzle exit plane as the downstream computational boundary would therefore complicate treatment of the outflow boundary condition. Another interesting result is that, even at this high level, the effect of swirl has virtually no effect on the plume shape.

The axis and wall Mach number distributions for these same two cases are shown in Fig. 22. As for the c-d nozzle, the flow experiences a smooth acceleration along the axis with the swirled case having significantly higher Mach numbers at a given axial location than

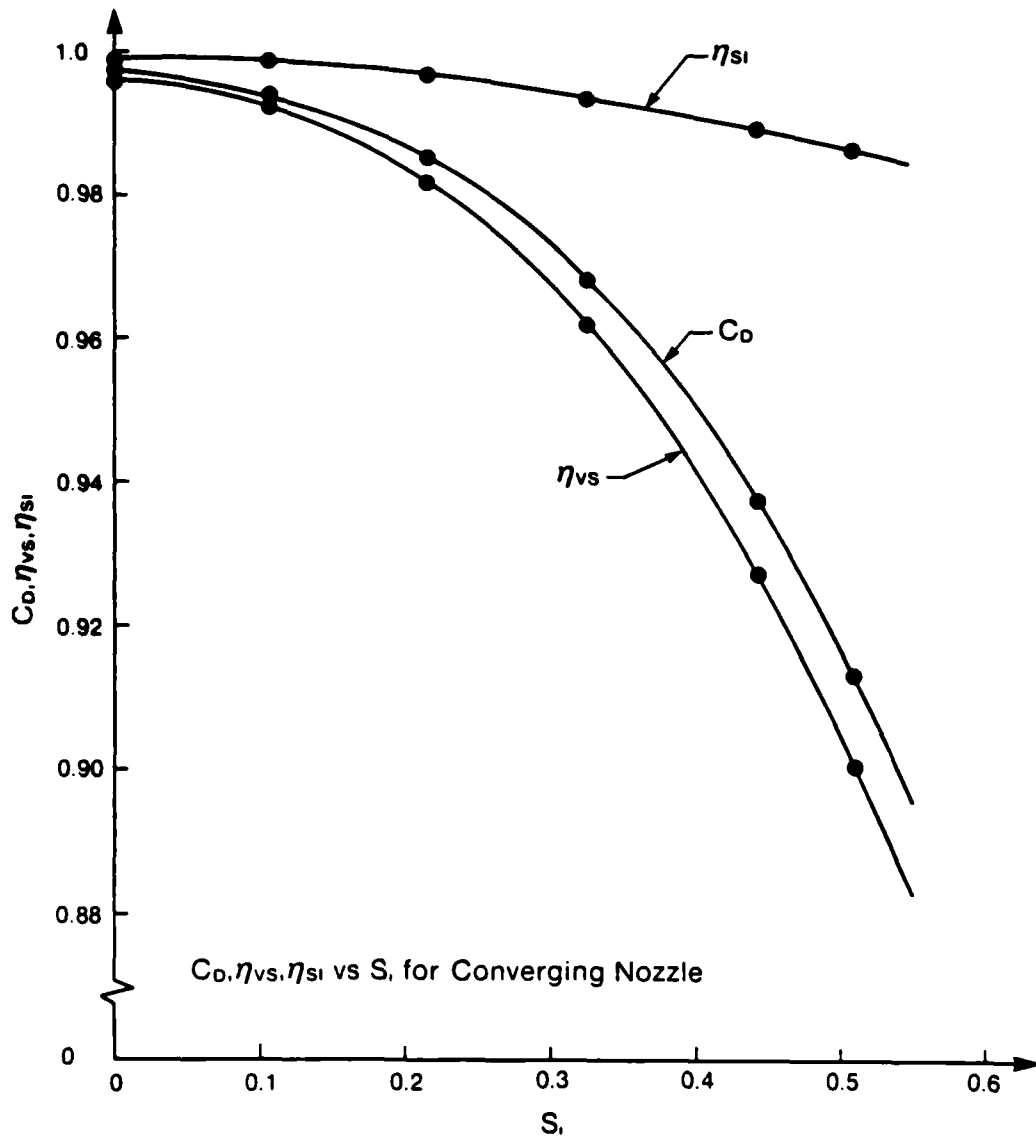


Figure 19. Dependence of integral performance parameters on inlet swirl number for converging nozzle cases

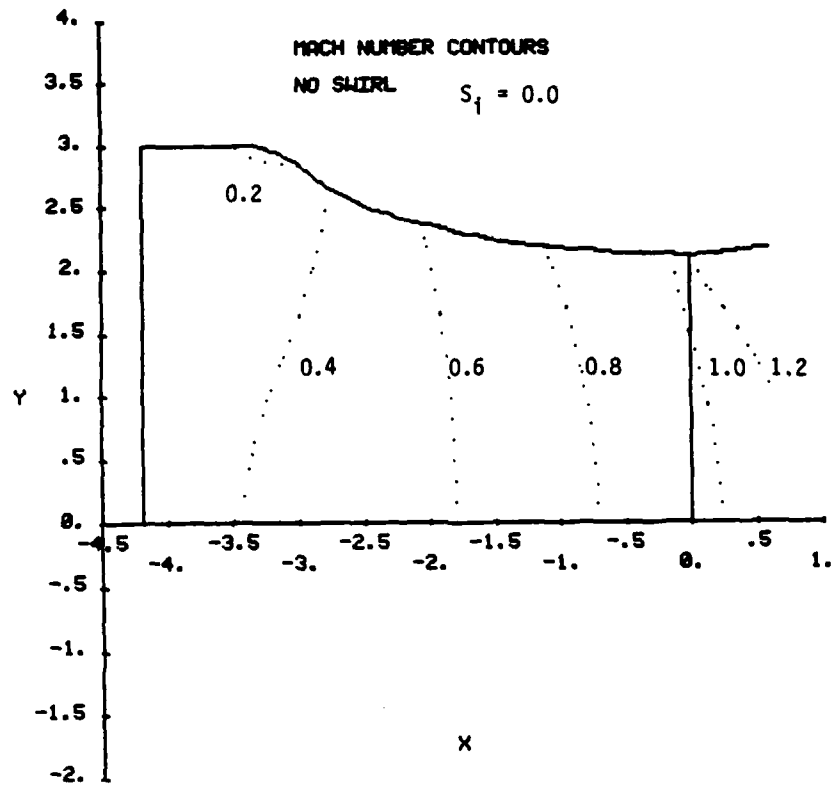


Figure 20. Total Mach number contours for unswirled converging nozzle flow

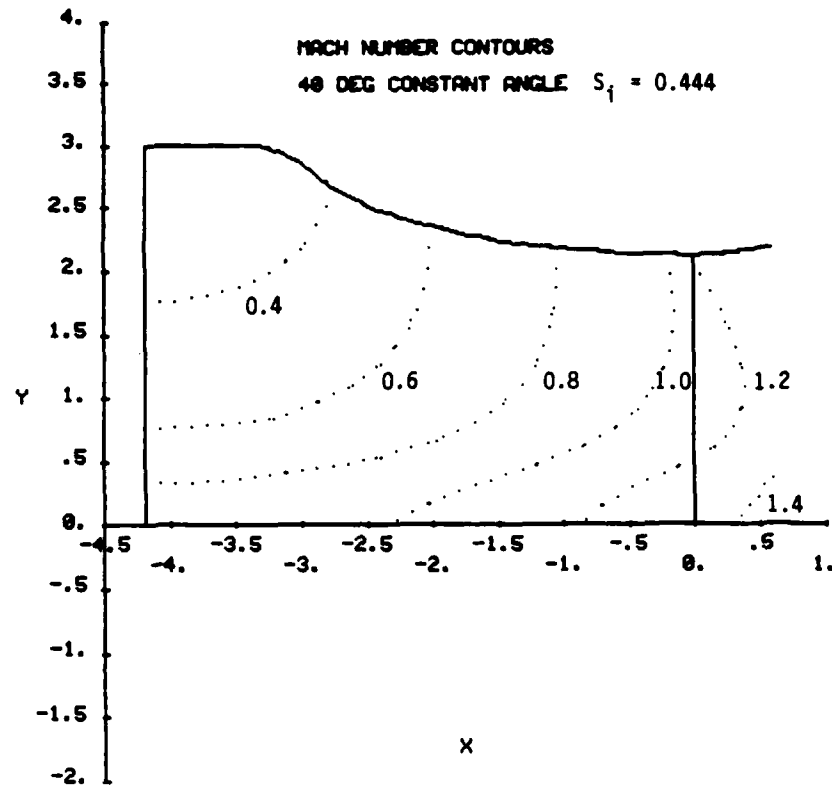


Figure 21. Total Mach number contours for highly swirled, constant angle, converging nozzle flow

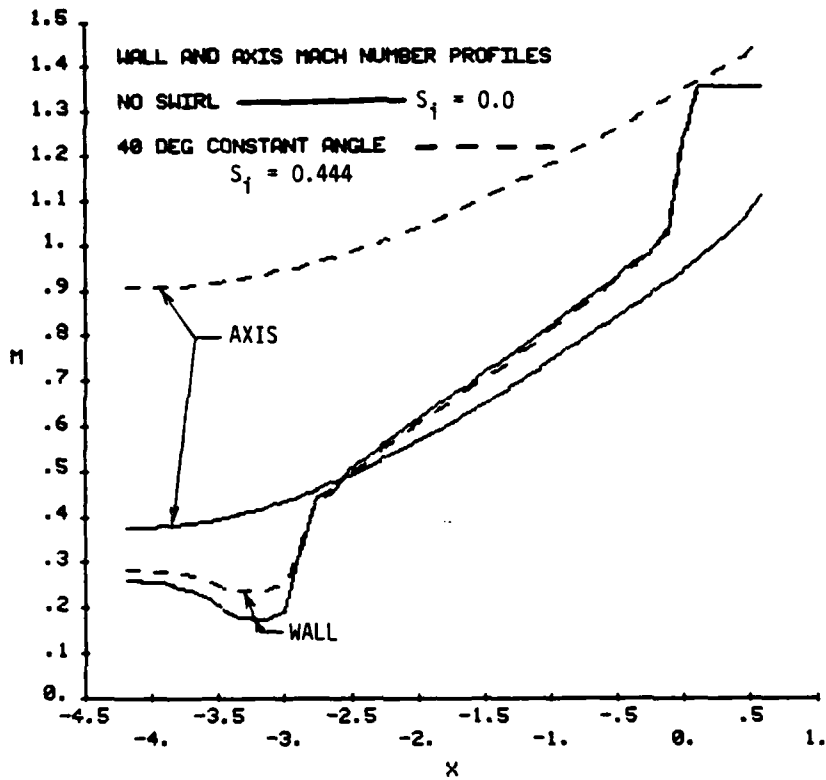


Figure 22. Comparisons of axis and wall total Mach number distributions for unswirled and highly swirled, constant angle, converging nozzle flow

the unswirled case. At the nozzle wall the effect of the tangential velocity component is minor. The relatively strong expansion occurring at the exit lip point ($x = 0$) is clearly evident, as is the correct prediction of a constant total Mach number along the free jet boundary.

Figure 23 presents the swirl velocity profiles at the nozzle inlet, exit, and across the plume at the last axial station. As in previous cases, the computed results predict a decrease in the axial velocity component from the axis to the wall across the inlet. For this reason, the "constant ϕ " inlet condition does not correspond to a "constant w " inlet condition, but rather to the profile shown in Fig. 23. The profiles at the exit and in the plume are qualitatively similar in shape to that at the inlet, although the magnitude of w is generally larger in both cases. This is consistent with the conservation of angular momentum principle since the boundary radius at the exit and in the plume is smaller than that at the inlet, Fig. 18.

D. Code Validation

In order to thoroughly validate the SNAP code, an extensive series of calculations of conserved quantities has been added to the program, and these quantities were monitored during the converging-diverging, annular, and converging nozzle calculations previously discussed. In addition, the numerical predictions from SNAP have been compared to experimental data obtained in the Ramjet Technology Branch (AFWAL/PORT) at Wright-Patterson Air Force Base for swirling flow through a converging-diverging nozzle. The results of these studies are discussed below.

1. Convergence/Conservation Checks Because they are quantities of fundamental importance, the stagnation pressure, P_0 , and stagnation temperature, T_0 , are calculated and printed at each gridpoint in the flowfield. In the steady state limit for inviscid, adiabatic, shockless flow, and assuming uniform P_0 and T_0 across the nozzle inlet as in the previously described computations, the stagnation pressure and stagnation temperature should be constant through the entire flowfield.

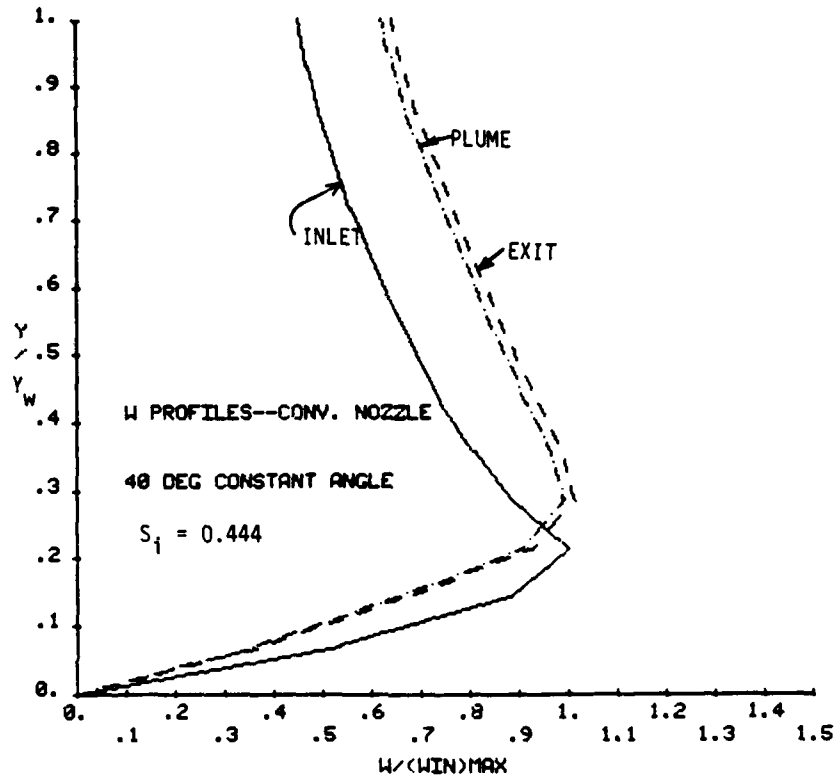


Figure 23. Tangential velocity profiles at inlet, exit, and in the plume of highly swirled, constant angle, converging nozzle flow

However, since these conservation conditions are not automatically satisfied by the nonconservation form of the governing equations employed in the numerical technique, their calculation provides a self-check on the accuracy of the finite difference computations. In all of the cases presented so far, P_0 and T_0 have been very well conserved, usually being within 0.1% of the prescribed values at the nozzle inlet. Not surprisingly, the largest variations generally occur at the boundaries of the computational mesh. In addition, if large variations in P_0 and T_0 were experienced after a given number of time planes, this result usually indicated that the steady state limit had not yet been reached. Therefore, the calculation of the stagnation quantities can also be used as a measure of the convergence to the steady state.

In addition to the stagnation properties, the axial distribution of mass flowrate, \dot{m} , and the flow angular momentum along streamlines, yw , should be constant in steady state. For this reason, \dot{m} and yw along the inner (if present) and outer wall boundaries (as well as thrust and swirl number) are calculated for every axial station in the grid for the final time plane. Statistical quantities including the mean and standard deviation of \dot{m} and $(yw)_{wall}$ are also calculated and printed. Note that the mass flowrate used in the discharge coefficient and specific impulse efficiency results presented previously is the mean value for the grid calculated in this way.

Conservation of mass is demonstrated in Figs. 24-26 where the mass flow deviation, $\dot{m}/\dot{m}_{ave} - 1$, is plotted as a function of the axial coordinate through the nozzle. Although results have been generated and plotted for each of the cases computed, an interesting result is that mass flow conservation is virtually independent of both the swirl level and swirl profile. Therefore, just a single, highly swirled case is presented for each nozzle geometry. Figure 24 is for the converging-diverging nozzle shown in Fig. 1, while Figs. 25 and 26 are for the annular and converging nozzles of Figs. 12 and 18, respectively. As can be seen in these figures, mass flow is very well

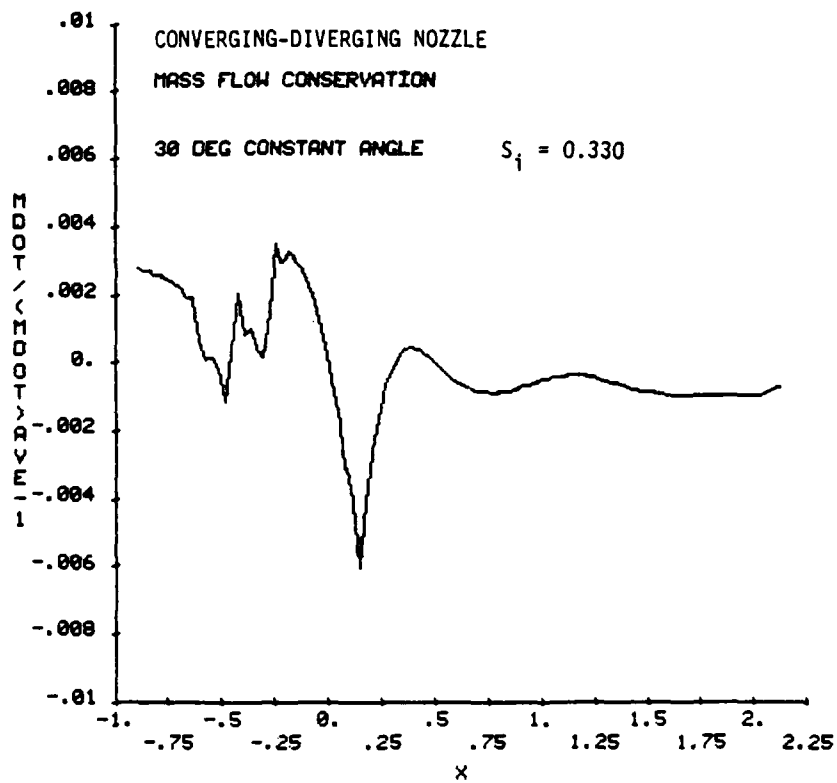


Figure 24. Mass flow conservation for a highly swirled, constant angle, converging-diverging nozzle flow

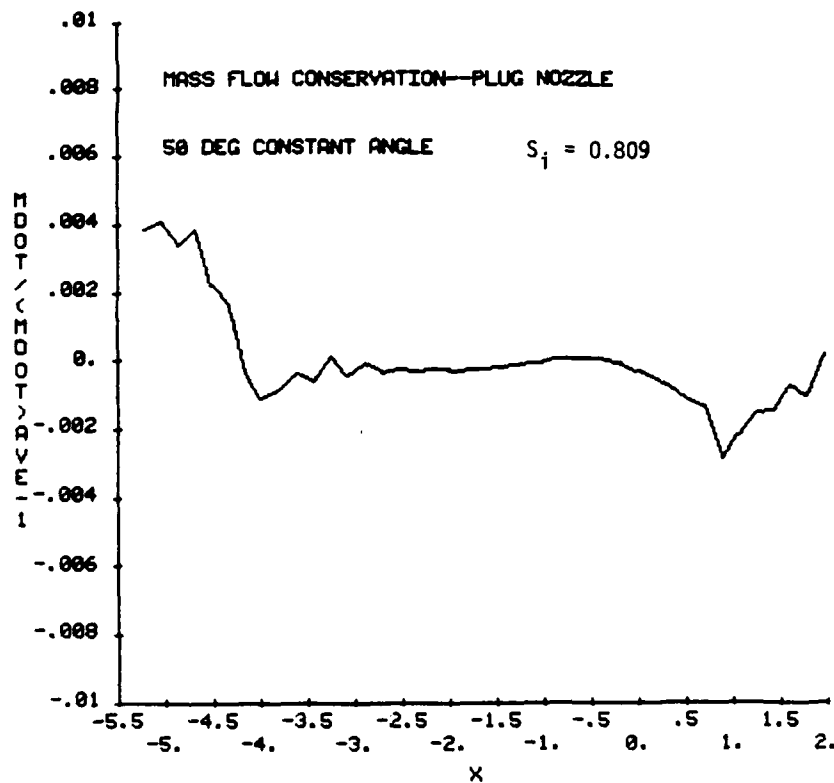


Figure 25. Mass flow conservation for a highly swirled, constant angle, annular nozzle flow

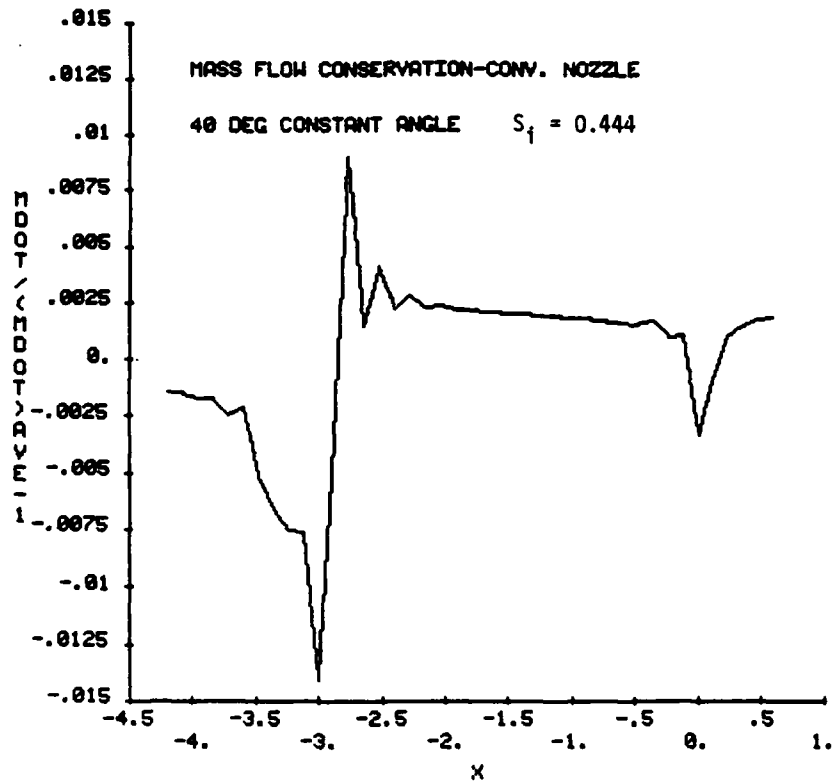


Figure 26. Mass flow conservation for a highly swirled, constant angle, converging nozzle flow

conserved in each case with the fluctuations generally being less than $\pm 0.5\%$. The fluctuations are usually larger in the subsonic region near the inlet than further downstream. The "spikes" which occur are at transitions in the nozzle wall geometry. The negative spike which occurs at $x = 0.15$ in Fig. 24 is at the tangency point between the circular arc throat and the 18.5° divergent section for the c-d nozzle; the small negative spike at $x = 0.860$ is at the tangency point between the circular arc throat and the 10° conical plug for the annular nozzle; and the spikes at $x = -3$ in Fig. 26 mark the circular arc transition from the cylindrical inlet to the elliptical converging section for the converging nozzle. In the two former cases an oblique shock wave originates from the tangency point, while in the latter case the slope of the wall contour changes rapidly in a relatively short distance. The negative spike occurring at the exit, $x = 0$, in Fig. 26 for the converging nozzle is due to the relatively strong expansion at the exit lip point, see Fig. 22. In each of these cases the spikes in the mass flow conservation plots are a direct result of the strong flow property gradients present near these points.

Figures 27-30 present the wall angular momentum deviation, $(yw)/(yw)_{ave} - 1$, for the same three cases shown in Figs. 24-26. There are two plots for the annular nozzle; the outer wall is shown in Fig. 28 and the inner wall in Fig. 29. Essentially identical remarks apply in this case as just made for mass flow conservation. The flow angular momentum is well conserved by the numerical computations, and the fluctuations which do occur can generally be associated with transitions in the wall boundary contours. The angular momentum fluctuations in the nozzle inlet region vary more rapidly spatially, but their magnitude is of the same order or less than the mass flow fluctuations for the same case. Note that the flow angular momentum along the outer wall of the plug nozzle, Fig. 28, is virtually constant. Because this wall is straight, it is an "easy" boundary to deal with computationally.

Not only does the monitoring of the axial variations of \dot{m} and $(yw)_{wall}$ yield information about the accuracy and truncation error

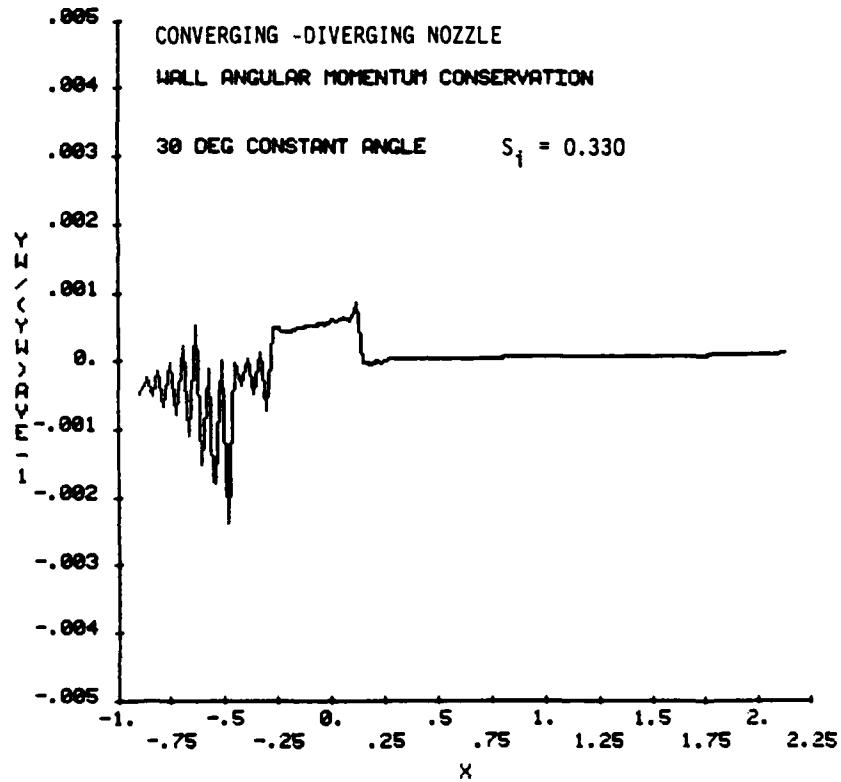


Figure 27. Wall angular momentum conservation for a highly swirled, constant angle, converging-diverging nozzle flow

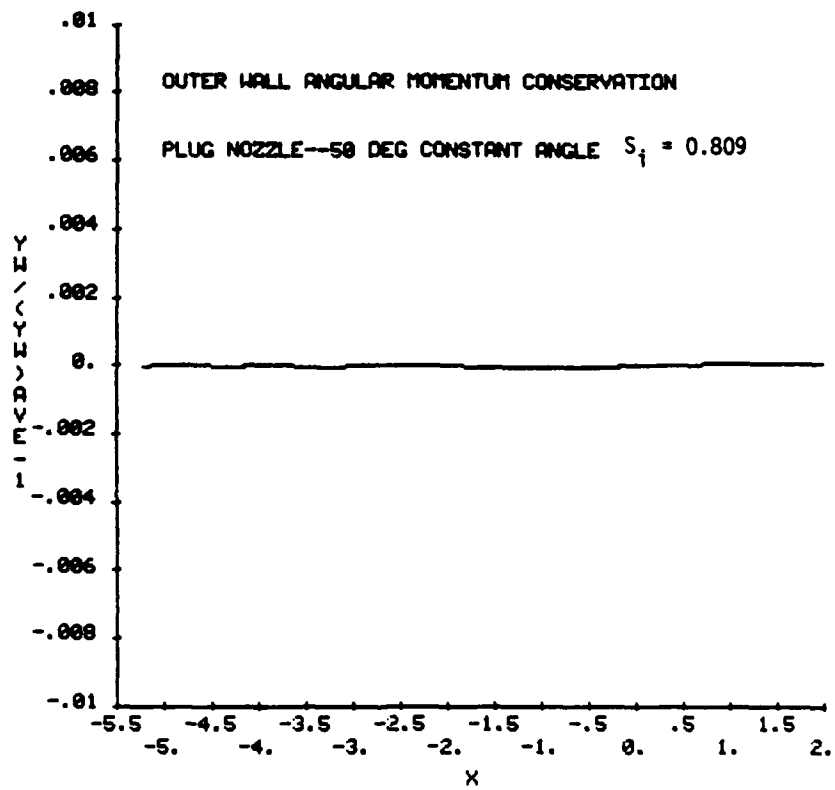


Figure 28. Outer wall angular momentum conservation for a highly swirled, constant angle, annular nozzle flow

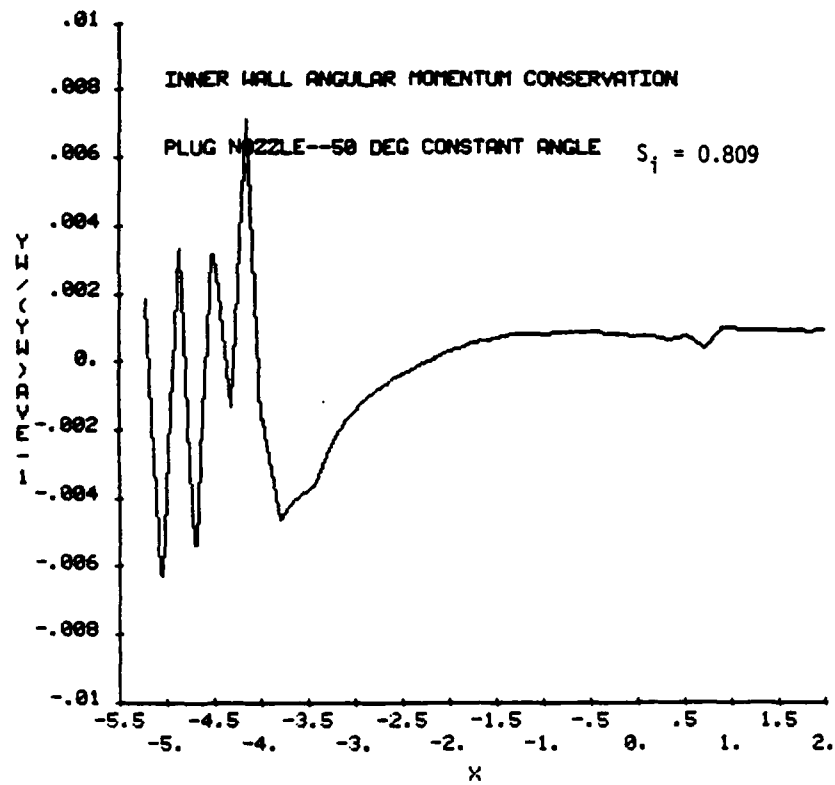


Figure 29. Inner wall angular momentum conservation for a highly swirled, constant angle, annular nozzle flow

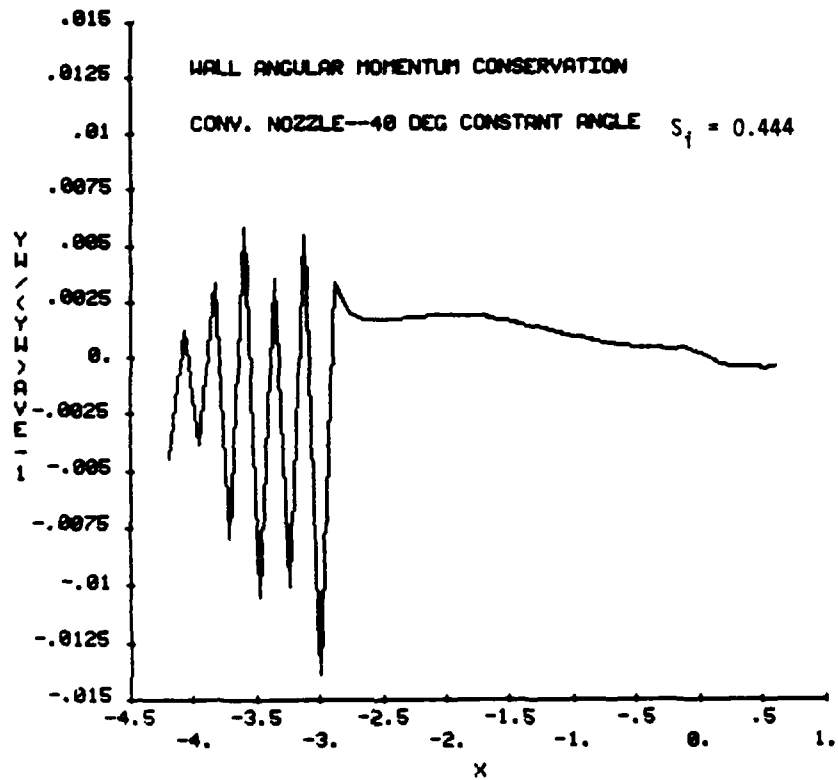


Figure 30. Wall angular momentum conservation for a highly swirled, constant angle, converging nozzle flow

of the computations, but it is also informative in terms of convergence to steady state conditions. Large variations in these quantities are usually indicative of the fact that the steady state limit has not yet been reached in the time-dependent computations. The flow angular momentum has been found to be particularly sensitive in this regard.

Along the same lines, it is of interest to point out that for every time plane the mass flowrate, vacuum stream thrust, and swirl number at the inlet, throat, and exit planes are calculated and printed. If one is only interested in these performance parameters, significantly fewer time planes need be calculated than if the entire flowfield is of interest. This is because, as integral parameters, these quantities converge to limiting values much more quickly than do the flowfield details.

In order to assess the effects of grid refinement, a highly swirled, constant angle, converging-diverging nozzle calculation, originally done using an 81 x 21 grid, has been repeated using a coarser, 41 x 11 grid. The original 81 x 21 calculations have previously been presented in Figs. 5, 9, 24, and 27. The results demonstrate that the gross performance parameters, including C_D , η_{VS} , η_{SI} , and S_f , are within 0.15% of each other using the two grids. However, the 41 x 11 calculation gives local Mach numbers which are consistently 2-3% higher than for the 81 x 21 grid. Mass flow and wall angular momentum conservation for the two meshes are compared in Figs. 31 and 32, respectively. For both grids the mass flow and particularly the wall angular momentum are well conserved, although the 81 x 21 calculation is clearly superior. This result is expected due to the smaller truncation error associated with the finer grid. These results, however, do point out the possibility of obtaining results of acceptable engineering accuracy using a relatively coarse, and therefore computationally efficient, mesh.

The primary quantity used in monitoring convergence to steady state is the rms value over the entire grid of the fractional static

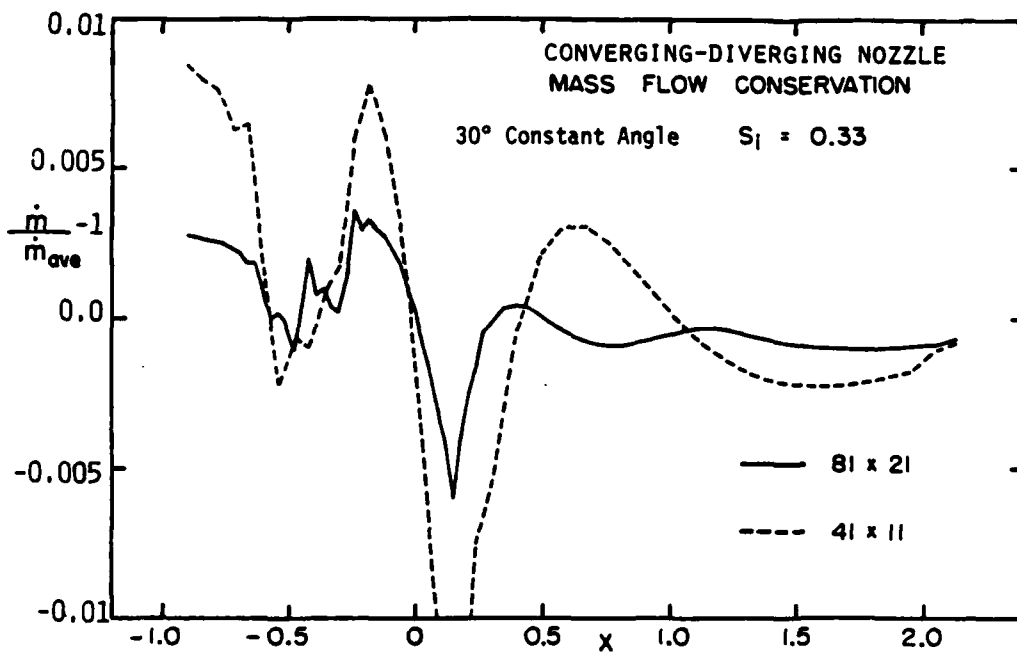


Figure 31. Comparison of mass flow conservation for 41 x 11 and 81 x 21 calculations of highly swirled, constant angle, converging-diverging nozzle flow

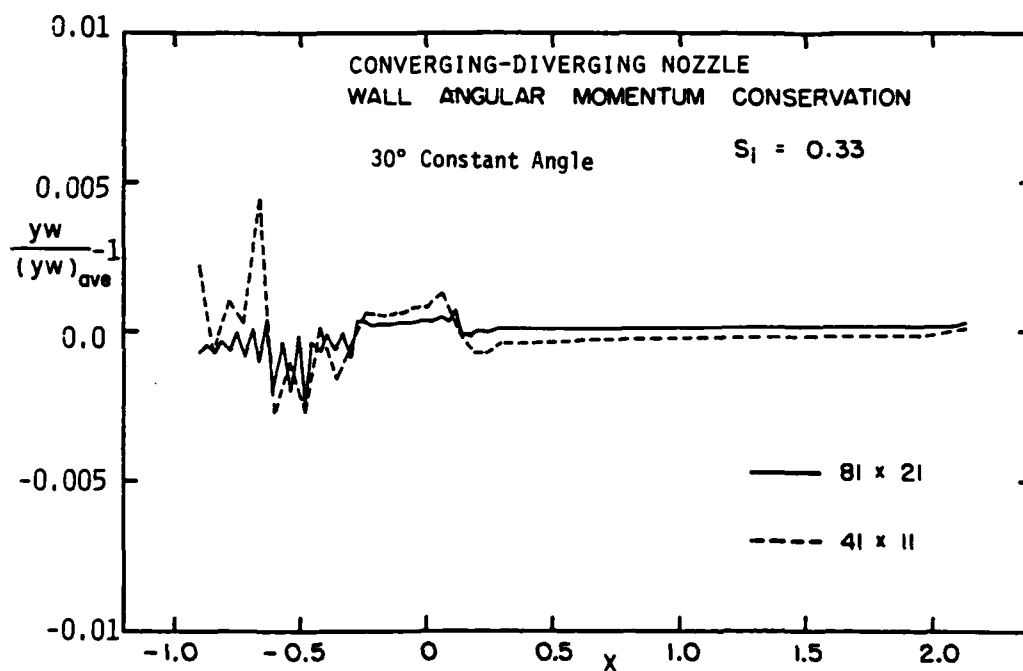


Figure 32. Comparison of wall angular momentum conservation for 41 x 11 and 81 x 21 calculations of highly swirled, constant angle, converging-diverging nozzle flow

pressure change from one time plane to the next, i.e.

$$\left(\frac{\Delta P}{P}\right)_{\text{rms}} \equiv \overline{\left(\frac{p_{i,j}^{n+1} - p_{i,j}^n}{p_{i,j}^{n+1}}\right)} \quad (48)$$

In this expression the standard practice of using the (i,j) subscripts to indicate the axial and radial mesh point locations and the superscript to denote the time plane number is adopted. The bar is used to signify that an rms value of the quantity in parentheses is to be found over the grid, i.e. for all (i,j). Rather than continuing computations in the time domain until $(\Delta P/P)_{\text{rms}}$ falls to a specified critical value, Cline's suggestion [43] has been adopted that a fixed number of time planes be calculated to ensure that an "average" fluid particle passes through the computational domain at least 5 times. The quantity defined in Eq. (48) has simply been monitored to see that it falls to an acceptably low value after this number of time planes.

Some details concerning the computations are presented in Table 1. For computational efficiency each converging-diverging nozzle calculation has been done in two parts: a 41 x 21 subsonic-transonic computation followed by a 41 x 21 calculation of the supersonic region. In each case data from the last axial plane of the transonic computation has been used as the fixed inlet condition for the supersonic calculation. Obviously, a 41 x 21 grid will require less computer central memory than an 81 x 21 grid but, in addition, the supersonic calculations converged more than twice as fast as the subsonic-transonic computations. Each transonic calculation was continued through 1000 time planes, and at this point $(\Delta P/P)_{\text{rms}}$ averaged approximately 1.7×10^{-5} . In contrast only 500 time planes were computed for each supersonic case and $(\Delta P/P)_{\text{rms}}$ was about 2.2×10^{-9} at this point. Since the plug and converging nozzle geometries do not have long supersonic diverging sections, each of these nozzles was analyzed using a single 41 x 15 grid. The annular nozzle computations were continued for 2000 time planes for which

TABLE 1: COMPUTATIONAL DETAILS

	NUMBER OF TIME PLANES	$\left(\frac{\Delta P}{P}\right)^*$	CYBER 74/825 * CPU TIME (SEC)
CONVENTIONAL C-D NOZZLE: 41 X 21 SUBSONIC- TRANSONIC COMPUTATION	1000	1.7×10^{-5}	1350
41 X 21 SUPERSONIC COMPUTATION	500	2.2×10^{-9}	650
PLUG NOZZLE 41 X 15 COMPUTATION (ENTIRE FLOWFIELD)	2000	3.9×10^{-6}	1950
CONVERGING NOZZLE 41 X 15 COMPUTATION (ENTIRE FLOWFIELD)	1000	3.8×10^{-6}	1050

* Average values for each series of calculations

$(\Delta P/P)_{\text{rms}} = 3.9 \times 10^{-6}$, while 1000 time planes were calculated for the converging nozzle yielding $(\Delta P/P)_{\text{rms}} = 3.8 \times 10^{-6}$. In each case, therefore, the convergence to steady state is excellent.

Average computational times on the Texas A&M University CDC Cyber 74/825 are also shown in Table 1. While these times appear to be relatively long, the Cyber 74/825 is a slow machine in comparison to most mainframes. The SNAP code has also been run on a CDC Cyber 175, and computation times approximately one-sixth of those listed in Table 1 were required. Therefore, on a Cyber 175 the CPU times shown in Table 1 translate to more modest (and reasonable) values of 3-5½ minutes.

2. Comparison to Experiment In order to further verify the numerical method described herein, results calculated using SNAP have been compared to wall static pressure measurements obtained in the Ramjet Technology Branch at Wright-Patterson Air Force Base for swirling and non-swirling flow through a converging-diverging nozzle. As mentioned in the introduction, this is the first known swirling nozzle data in which the tangential velocity is produced by axial-flow vanes, which is the case for both ramjet and turbofan/turbojet engines.

The nozzle design which has been built and tested is shown in Fig. 33. It is very similar to the c-d nozzle previously discussed with a cylindrical inlet, a circular arc transition to a 35° conical converging section, a circular arc throat, and an 18.5° conical divergent section. The contraction in area occurring between the nozzle inlet and throat is somewhat larger in this case, however, $A_t/A_i = 0.249$. The short circular arc section near the inlet has been added to the computational geometry to provide a smooth transition between the cylindrical inlet and conical convergent portions of the nozzle.

In all of the experiments discussed here, the nozzle was mounted immediately downstream from a sudden enlargement (dump) combustor with a length-to-diameter ratio of $L/D = 3$. Cold, dry, compressed air was supplied to the combustor facility from centrifugal compressors, and this air passed through the nozzle test section before entering the

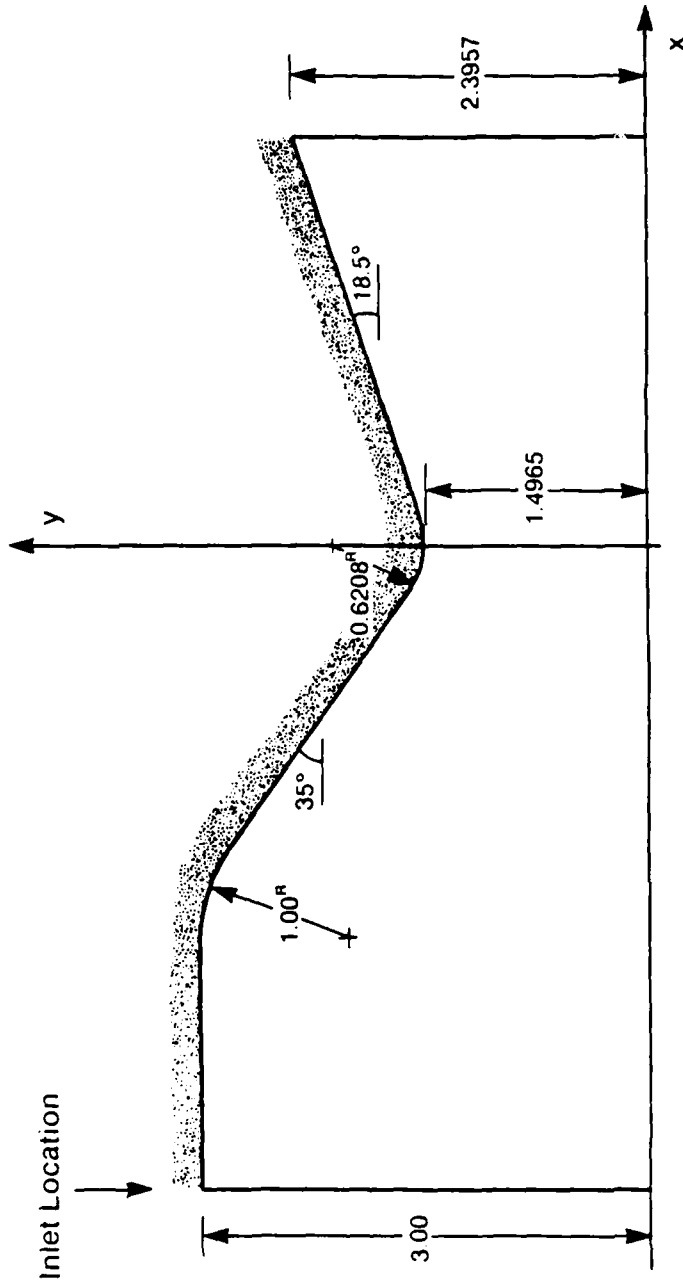


Figure 33. Experimental converging-diverging nozzle geometry

exhauster system. Fixed vane swirlers, located in the inlet to the dump combustor, were used to produce the tangential velocity component. A five-hole Pitot probe was traversed across the nozzle inlet in order to measure the inlet profiles of stagnation pressure and swirl angle. The wall static pressure distributions have been determined by means of 22 pressure taps, each 0.010" in diameter, which were carefully drilled normal to the nozzle wall at various axial locations. Individual pressure transducers were connected to each of the wall static taps. Further details concerning the Ramjet Combustor Test Facility at AFWAL/PORT, its instrumentation, and data acquisition and reduction capabilities may be found in Ref. [1].

Numerical computations have been compared to the experimental measurements for three cases: (1) no swirl, (2) moderate swirl, denoted by CA3 (constant angle, $S = 0.3$), and (3) high swirl, referred to as CA5 (constant angle, $S = 0.5$). In the swirler designation the swirl number is the nominal, design value based on Eq. (47) evaluated in the combustor inlet not at the inlet to the nozzle. The boundary conditions used in the computations were T_0 and $\theta = 0$ uniform across the nozzle inlet, together with the measured inlet distributions of P_0 and ϕ . The experimental inlet stagnation pressure profiles for the three cases and the swirl angle profiles for the two swirled cases are presented in Figs. 34 and 35, respectively. In each case the flow has been probed from one wall, through the centerline, to the opposite wall, so that conclusions regarding the symmetry of the inlet flow can be drawn. As shown in Fig. 34, the P_0 distributions are relatively symmetric for the three cases, and for the unswirled and moderately swirled cases the variation in P_0 from the centerline to the nozzle wall is small ($< 3\%$). Interestingly, however, the total pressure decreases from the centerline to the wall for the unswirled case while it increases for the two swirled flows. The P_0 distribution is also fairly nonuniform for the highly swirled case, approaching a 10% variation from the centerline to the wall. The swirl angle profiles in Fig. 35 demonstrate that while ϕ is relatively symmetric, some fairly large asymmetries were also

Inlet Stagnation Pressure Profiles

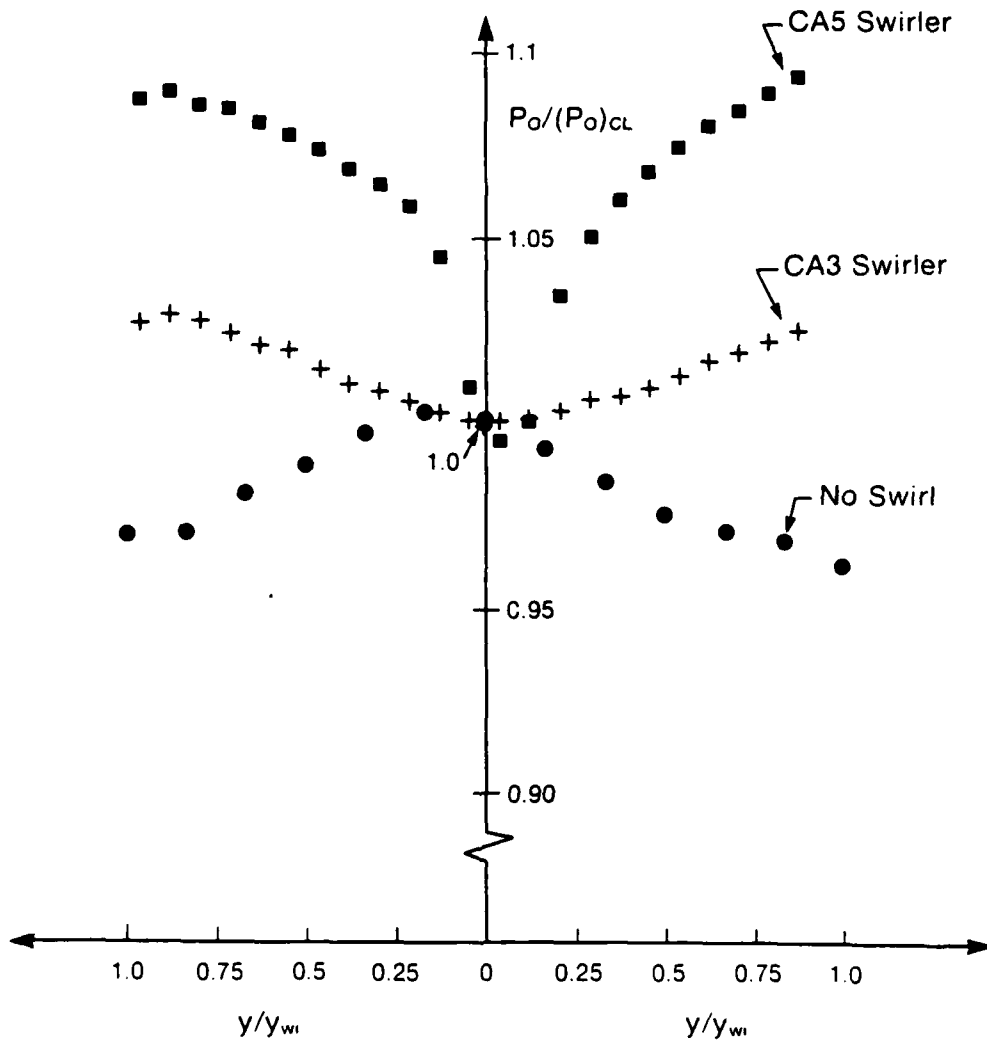


Figure 34. Experimental inlet stagnation pressure profiles for unswirled and swirling, converging-diverging nozzle flow

Inlet Swirl Angle Profiles

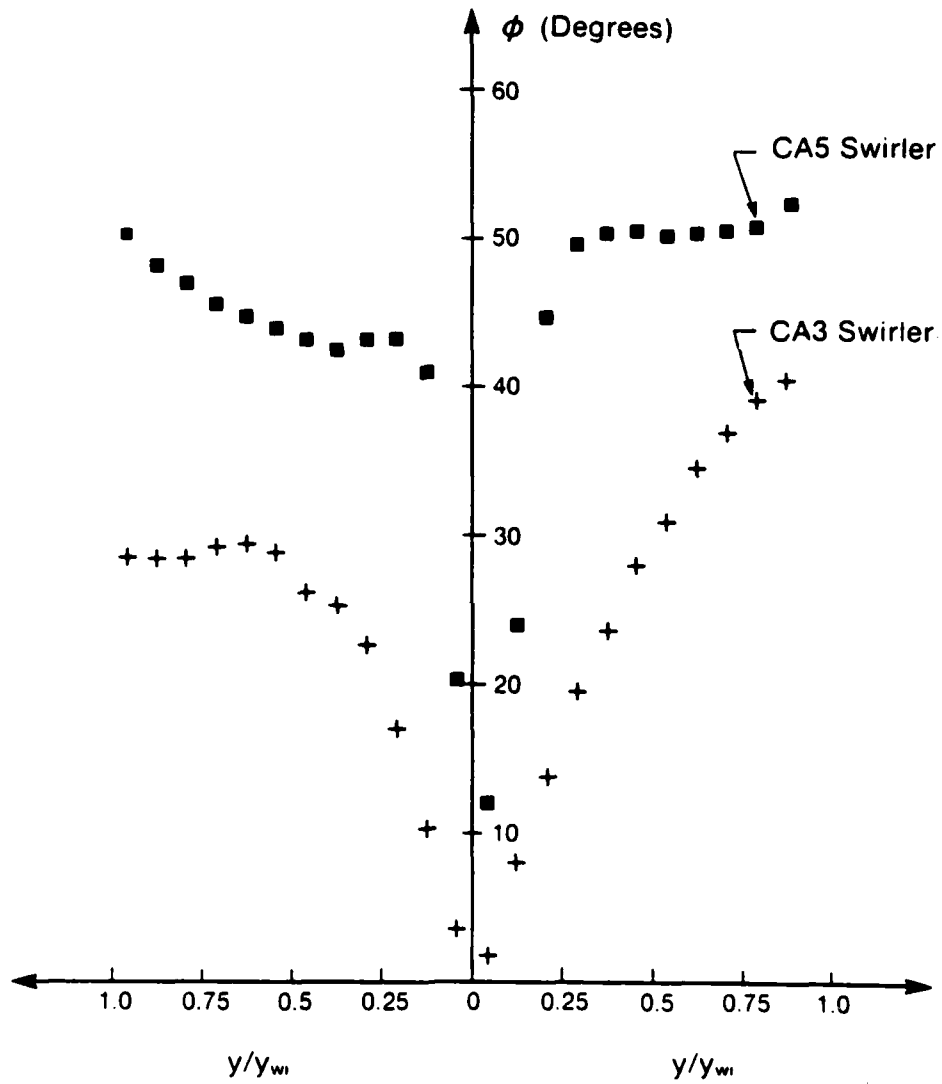


Figure 35. Experimental inlet swirl angle profiles for swirling converging-diverging nozzle flow

measured, particularly near the nozzle wall for the CA3 swirler. These P_0 and ϕ distributions were used as input for the axisymmetric SNAP code by averaging the two centerline-to-wall profiles for each case and using linear interpolation as necessary.

The experimental results presented in Figs. 34 and 35 are important in their own right because they provide needed information concerning assumptions which can be made for the inlet flow property distributions for swirling nozzle flow calculations. In particular, at least for the case in which the nozzle is just downstream from a relatively short dump combustor, the axisymmetric assumption is reasonable, although for highly swirled flow the uniform P_0 assumption may not be adequate. This latter assumption is inherent in most of the previous quasi-one-dimensional theories. Another point of importance is that the swirlers employed in these experiments were designed [1] to produce "constant angle" swirl profiles in the combustor inlet. Figure 35 shows that, except for one of the CA3 profiles, approximately constant angle swirl profiles have survived to the nozzle inlet.

The Mach number contours computed for the three experimental cases are shown in Figs. 36-38. Qualitatively, these contours are quite similar to those for the previously discussed c-d nozzle, since the two designs are so similar. Except in the inlet region, there is little difference between the contours for the non-swirling and CA3 swirler flows. For the highly swirled CA5 case, on the other hand, the characteristic upstream shift of the contours at the centerline is seen. This again indicates larger centerline axial velocities for the swirled case as compared to unswirled flow. These details can be seen more clearly in Figs. 39 and 40 where the axial distributions of Mach number along the nozzle axis and wall are compared for each of the swirled cases with the unswirled nozzle flow. Figure 39 shows that for the CA3 swirler the effect of swirl is significant only in the inlet region ($x \leq -0.5$), although it is at least as large at the wall as at the centerline. In addition, the unswirled centerline Mach numbers are larger in the inlet region than for the swirled flow.

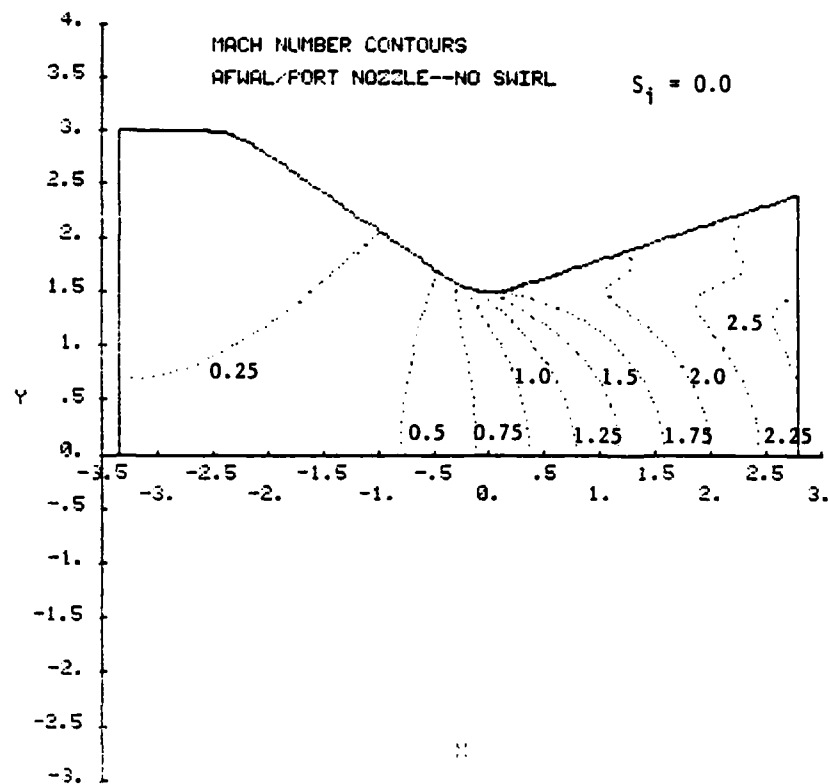


Figure 36. Total Mach number contours for unswirled, experimental, converging-diverging nozzle flow

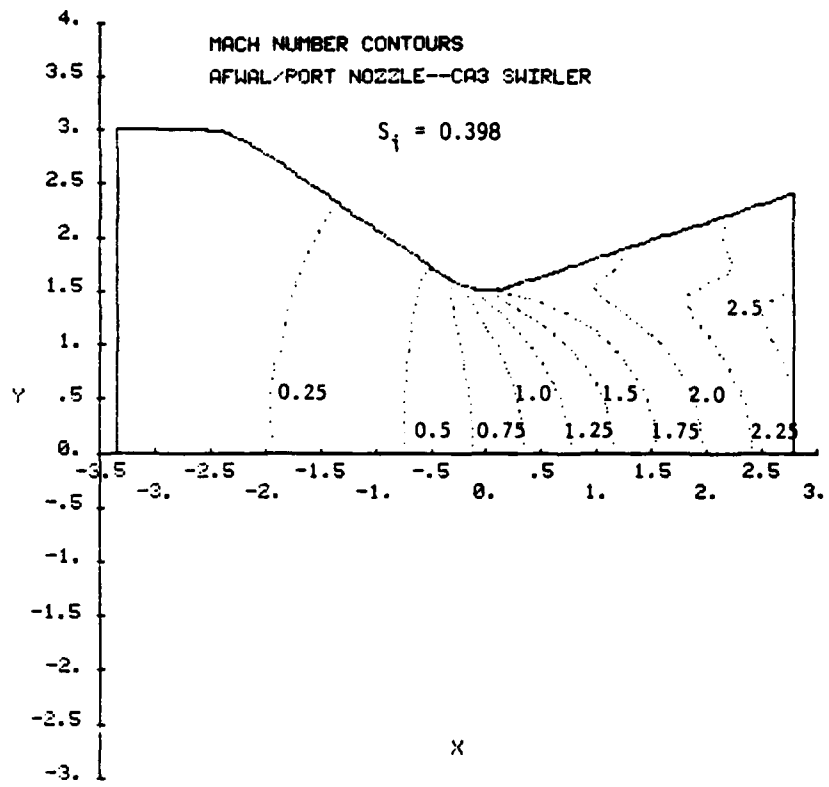


Figure 37. Total Mach number contours for CA3 swirler/experimental converging-diverging nozzle flow

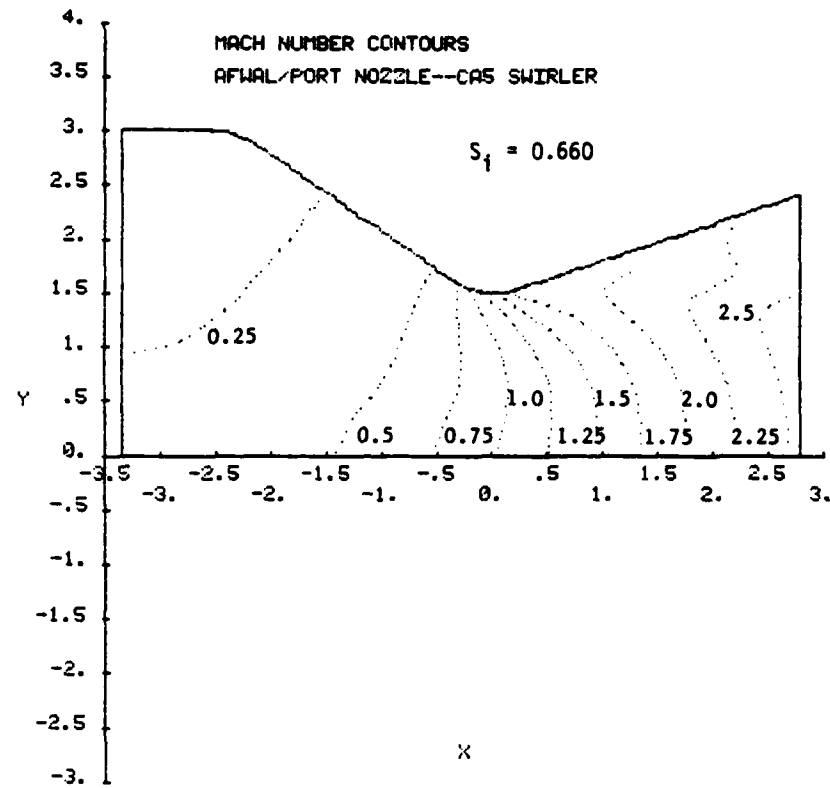


Figure 38. Total Mach number contours for CA5 swirler/experimental converging-diverging nozzle flow

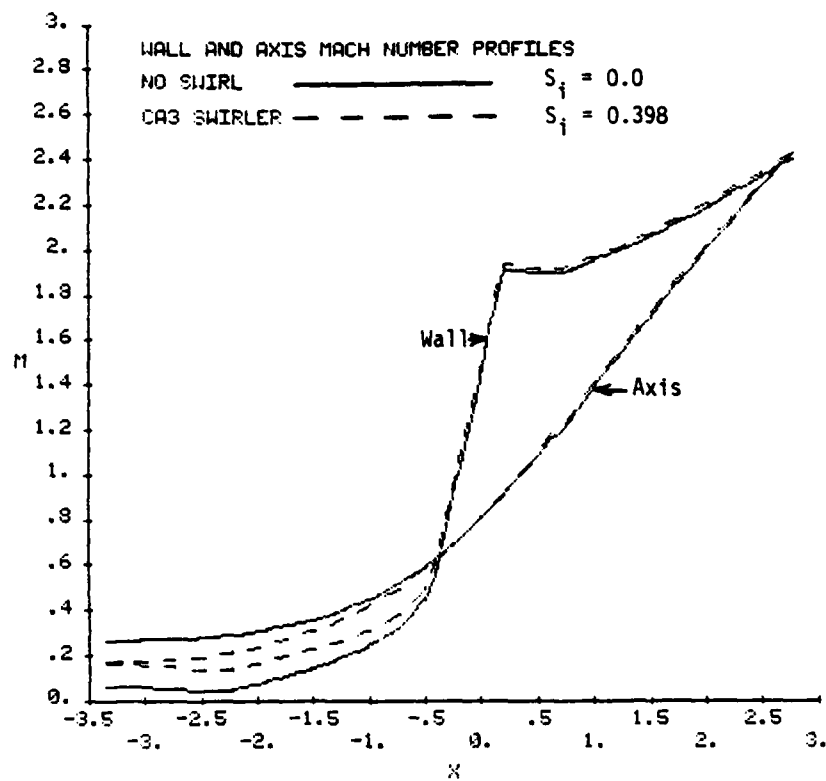


Figure 39. Comparisons of axis and wall total Mach number distributions for unswirled and CA3 swirler/experimental converging-diverging nozzle flow

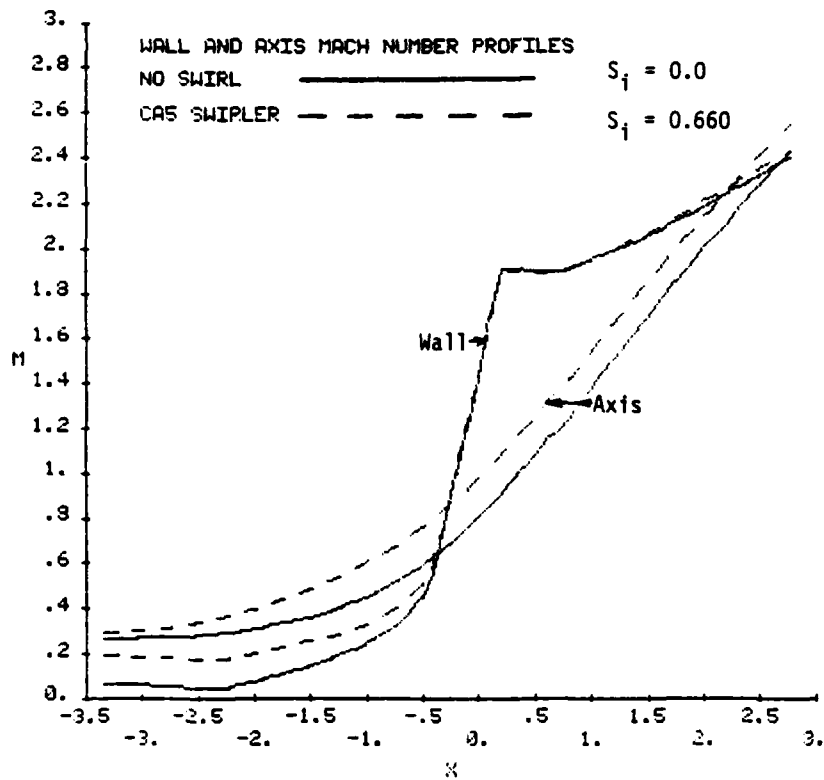


Figure 40. Comparisons of axis and wall total Mach number distributions for unswirled and CAS swirler/experimental converging-diverging nozzle flow

Although these results are different from those discussed previously, one must remember that a uniform inlet stagnation pressure profile has not been assumed for these cases. Instead, the measured, nonuniform profiles presented in Fig. 34 have been employed as the inlet P_0 boundary condition. The results in Figure 40 demonstrate that the effect of swirl is significant near the inlet for the wall Mach numbers and for the entire length of the nozzle for the centerline Mach numbers. In contrast to the CA3 case, the Mach numbers for the CA5 swirler are larger than those for no swirl along both the centerline and wall.

The computed and measured wall static pressures are compared in Figs. 41-43 for the three cases. The static pressures have been non-dimensionalized with the stagnation pressure at the nozzle inlet centerline location. As a reference, the conventional, non-swirling, isentropic, one-dimensional solution has also been included. Clearly this solution is in serious disagreement with the data, especially just downstream from the throat. On the other hand, the SNAP-computed results agree very well with the data in all three cases. There is a slight underprediction of the wall pressure downstream of the tangency point between the circular arc throat and conical divergent section ($x = 0.2$). As previously mentioned, a weak oblique shock originates at this location, which results in the discontinuity in slope of the wall pressure distributions in Figs. 41-43. The underprediction may be due to inadequate numerical resolution of the gradients which occur near the shock or to a rapid thickening of the wall boundary layer in this region of neutral pressure gradient. The growth of this boundary layer would act to reduce the effective nozzle area, thereby raising the wall pressure over the predicted inviscid value. The excellent agreement between the numerical and experimental results near the nozzle inlet ($x \leq -0.5$) is particularly gratifying since it indicates that the effects of swirl are being correctly predicted by the numerical method reported here.

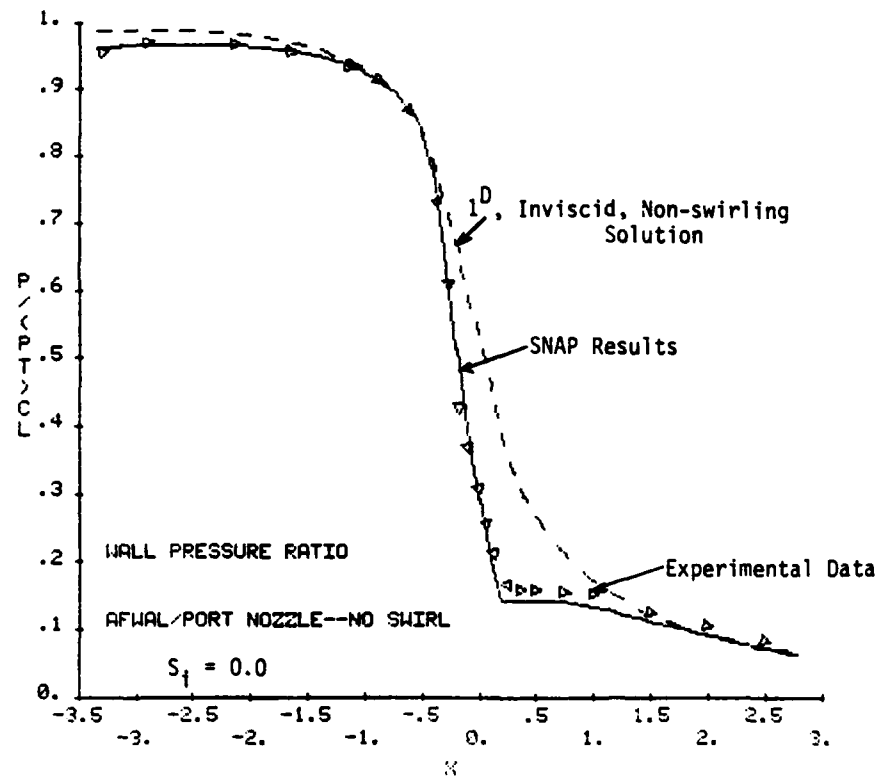


Figure 41. Comparison of SNAP computations with experimental wall static pressure measurements for unswirled converging-diverging nozzle flow

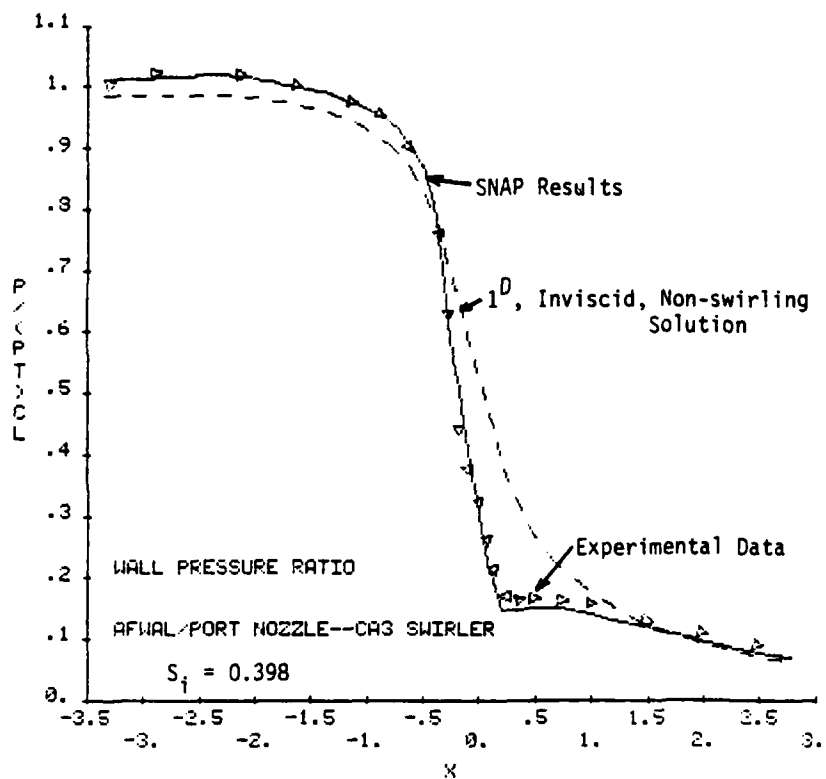


Figure 42. Comparison of SNAP computations with experimental wall static pressure measurements for CA3 swirler/converging-diverging nozzle flow

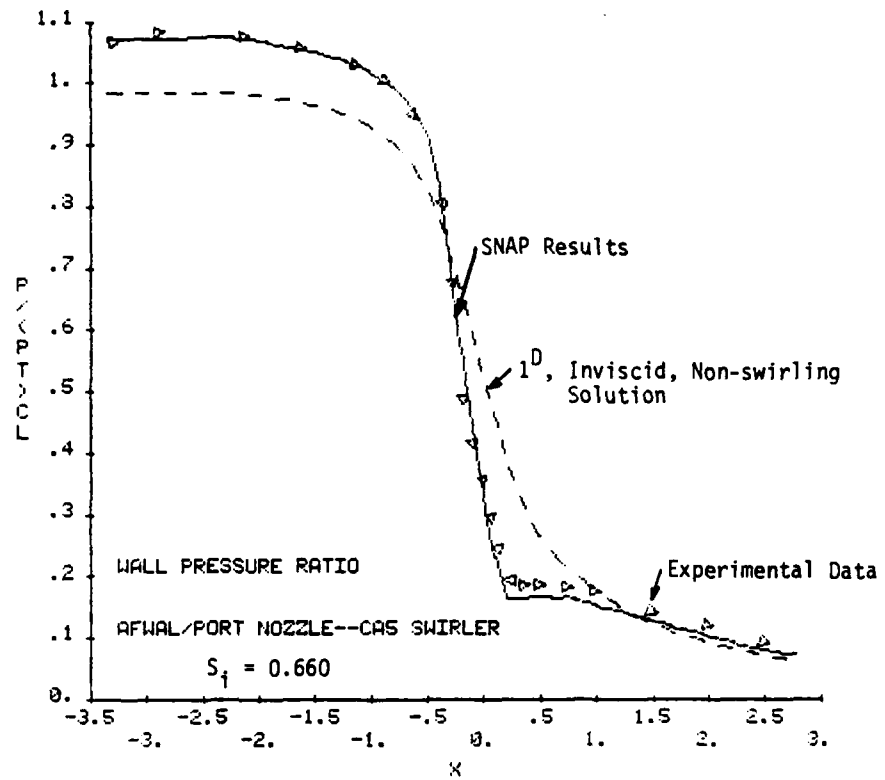


Figure 43. Comparison of SNAP computations with experimental wall static pressure measurements for CA5 swirler/converging-diverging nozzle flow

The computed tangential velocity profiles across the inlet, throat, and exit of the nozzle are shown in Figs. 44 and 45 for the two swirling flows. For the CA3 swirler the tangential velocity increases monotonically from the centerline to the wall at all three axial locations. However, for the CA5 swirler the swirl velocity component is relatively constant in the region away from the nozzle centerline. Therefore, for this nozzle geometry and the measured inlet P_0 and ϕ distributions shown in Figs. 34 and 35, the CA5 "constant angle" swirler is predicted to produce relatively uniform w profiles throughout the nozzle. As for the previous converging and c-d nozzle cases, the w profile retains approximately the same shape as the flow progresses through the nozzle. The magnitude of w , however, first increases and then decreases from the inlet to the throat to the exit in agreement with the conservation of angular momentum principle.

The computed integral performance parameters for the three experimental cases are presented in Table 2. The specific impulse efficiency is again found to be virtually constant, which is the same result obtained for the previously discussed c-d nozzle geometry. For the CA3

Table 2: Computed Performance Parameters for Experimental Cases

	C_D	η_{vs}	η_{SI}	S_i
No Swirl	0.9792	0.9501	0.9703	0.0
CA3 Swirler	0.9636	0.9355	0.9709	0.3976
CA5 Swirler	0.9389	0.9115	0.9708	0.6596

swirler the discharge coefficient and vacuum stream thrust efficiency are both reduced by about 1.6% over the unswirled case while for CA5 the reduction is about 4.1%. For both swirled cases the swirl number at the nozzle inlet is significantly higher than the nominal, design

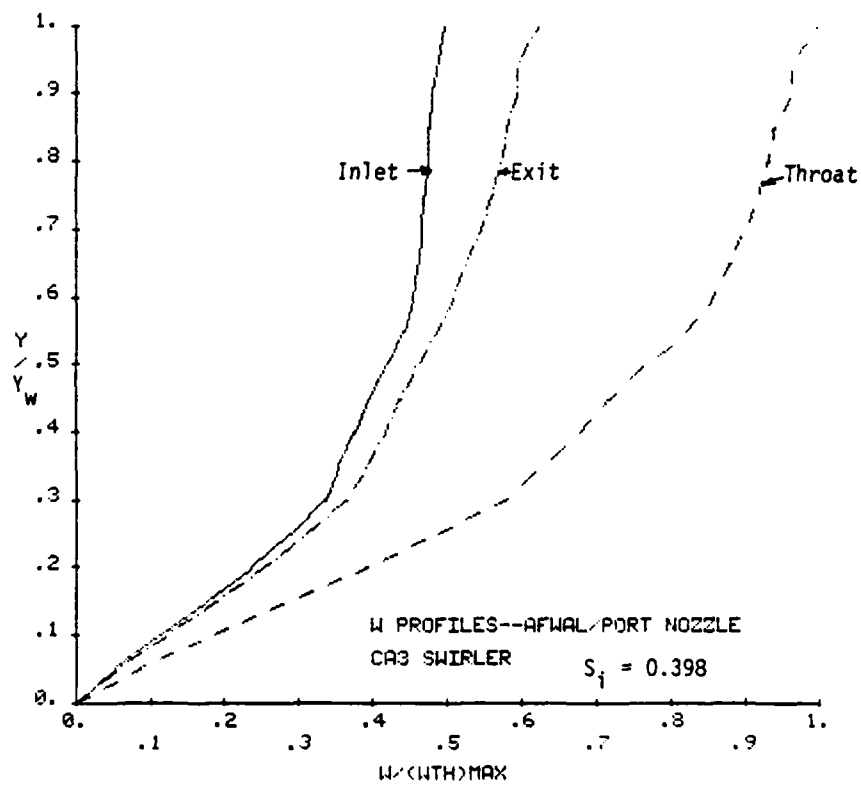


Figure 44. Tangential velocity profiles at inlet, throat, and exit of CA3 swirler/experimental converging-diverging nozzle flow

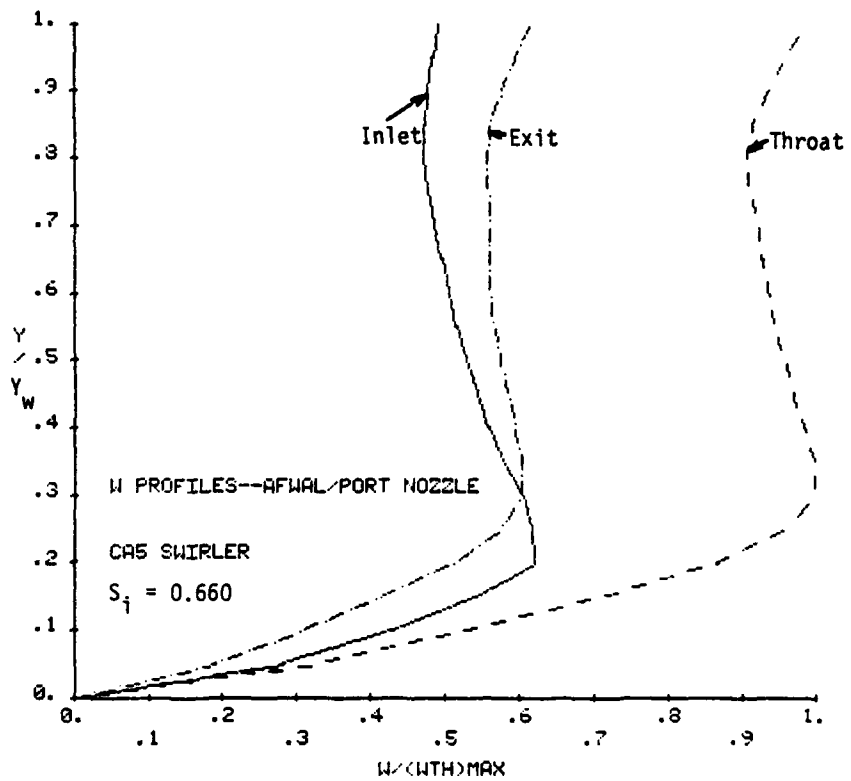


Figure 45. Tangential velocity profiles at inlet, throat, and exit of CAS swirler/experimental converging-diverging nozzle flow

value in the combustor inlet (0.3 and 0.5, respectively). This result is expected since the axial velocity in the combustor inlet is higher than that at the inlet to the nozzle. The swirl angles plotted in Fig. 35 and the inlet swirl numbers given in Table 2 are relatively high, although the reductions in C_D and η_{VS} due to swirl are very moderate. This result is due to the large contraction in area which occurs between the inlet and throat for the experimental nozzle geometry. Because of this contraction, the axial velocity at the throat is very much larger than at the inlet, so that the relative effects of swirl at the throat, and in the rest of the nozzle, are much weaker than at the inlet.

The calculations described above were performed on a 63 x 21 grid in two parts with a 41 x 21 subsonic-transonic computation followed by a 23 x 21 calculation of the supersonic diverging portion of the nozzle. The transonic computations were continued over 2000 time planes while the supersonic calculations required only 500 time planes to reach the steady state. As usual, the mass flowrate and flow angular momentum at the nozzle wall were well conserved by the calculations.

E. Correlation of Results

Using the results from the many swirling nozzle flow calculations which have been performed during this investigation, an attempt has been made to identify a "universal" swirl number. Ideally, this parameter would collapse the discharge coefficient, thrust efficiency, and specific impulse efficiency curves for the various swirl profiles and nozzle geometries investigated onto single curves when it is used as the independent variable. At the outset it is expected that the inlet swirl number S_i defined in Eq. (47) will not be appropriate in this regard. This is because, in addition to S_i , the nozzle area contraction ratio also has a strong effect on the discharge coefficient and vacuum stream thrust efficiency. If such a correlation parameter can be discovered and the universal curves developed, the mass flow and thrust penalties for any geometry and swirl profile can be estimated. Obviously, this would be an extremely useful result.

The 12 swirl number definitions shown below have been investigated:

$$\begin{aligned}
 S_1 &\equiv \frac{2 \int_{y_c}^{y_w} \frac{w}{a^*} y dy}{(y_w^2 - y_c^2)} & S_7 &\equiv \frac{\int_{y_c}^{y_w} \rho u \frac{w}{a^*} y dy}{\int_{y_c}^{y_w} \rho u y dy} \\
 S_2 &\equiv \frac{\int_{y_c}^{y_w} w y dy}{\int_{y_c}^{y_w} u y dy} & S_8 &\equiv \frac{\int_{y_c}^{y_w} \rho u w y dy}{\int_{y_c}^{y_w} \rho u^2 y dy} \\
 S_3 &\equiv \frac{2 \int_{y_c}^{y_w} \left(\frac{w}{a^*}\right)^2 y dy}{(y_w^2 - y_c^2)} & S_9 &\equiv \frac{\int_{y_c}^{y_w} \rho u \left(\frac{w}{a^*}\right)^2 y dy}{\int_{y_c}^{y_w} \rho u y dy} \\
 S_4 &\equiv \frac{\int_{y_c}^{y_w} w^2 y dy}{\int_{y_c}^{y_w} u^2 y dy} & S_{10} &\equiv \frac{\int_{y_c}^{y_w} \rho u w^2 y dy}{\int_{y_c}^{y_w} \rho u^3 y dy} \\
 S_5 &\equiv \frac{2 \int_{y_c}^{y_w} \frac{w}{a^*} y^2 dy}{y_w (y_w^2 - y_c^2)} & S_{11} &\equiv \frac{\int_{y_c}^{y_w} \rho u \frac{w}{a^*} y^2 dy}{y_w \int_{y_c}^{y_w} \rho u y dy}
 \end{aligned} \tag{49}$$

$$S_6 \equiv \frac{\int_{y_c}^{y_w} wy^2 dy}{y_w \int_{y_c}^{y_w} udy} \qquad S_{12} \equiv \frac{\int_{y_c}^{y_w} \rho uwy^2 dy}{y_w \int_{y_c}^{y_w} \rho u^2 y dy}$$

The physical interpretation of the swirl number pairs on each line is identical except that area averaging is used for the definitions on the left and mass averaging on the right. Note that swirl number S_1 has been used by Boerner et al. [26], S_3 is recommended by Carpenter [18-21], and S_{12} is commonly used in swirling combustor work [1, 41]. Swirl number S_{12} evaluated at the nozzle inlet is also the one which has been used in the presentation of all of the previously discussed results.

Presumably the mass flowrate is determined at the nozzle throat. Therefore, the reduced discharge coefficient (discharge coefficient divided by no swirl discharge coefficient for the same geometry) has been plotted against each of the 12 swirl numbers evaluated at the throat for each of the 28 swirling nozzle flow cases computed during this study. Swirl numbers S_1 and S_7 have proven to do the best job of collapsing the results onto a single curve. Interestingly, the commonly used swirl number S_{12} is very poor in this regard. Since its definition is somewhat simpler, the reduced discharge coefficient results are shown plotted against S_1 in Fig. 46. Considering the variety of geometries and swirl profiles embodied in these results, the curve defined in Fig. 46 can be considered to be at least reasonably "universal". Obviously, a larger number of cases would help to verify this conclusion.

In contrast very little success has been obtained in correlating the thrust and specific impulse results. The reduced vacuum stream thrust and specific impulse efficiencies have been plotted as functions of each of the 12 swirl numbers evaluated at both the throat and exit for the 28 cases of interest. In no case was a correlation obtained as good as that presented in Fig. 46 for the discharge coefficient. The

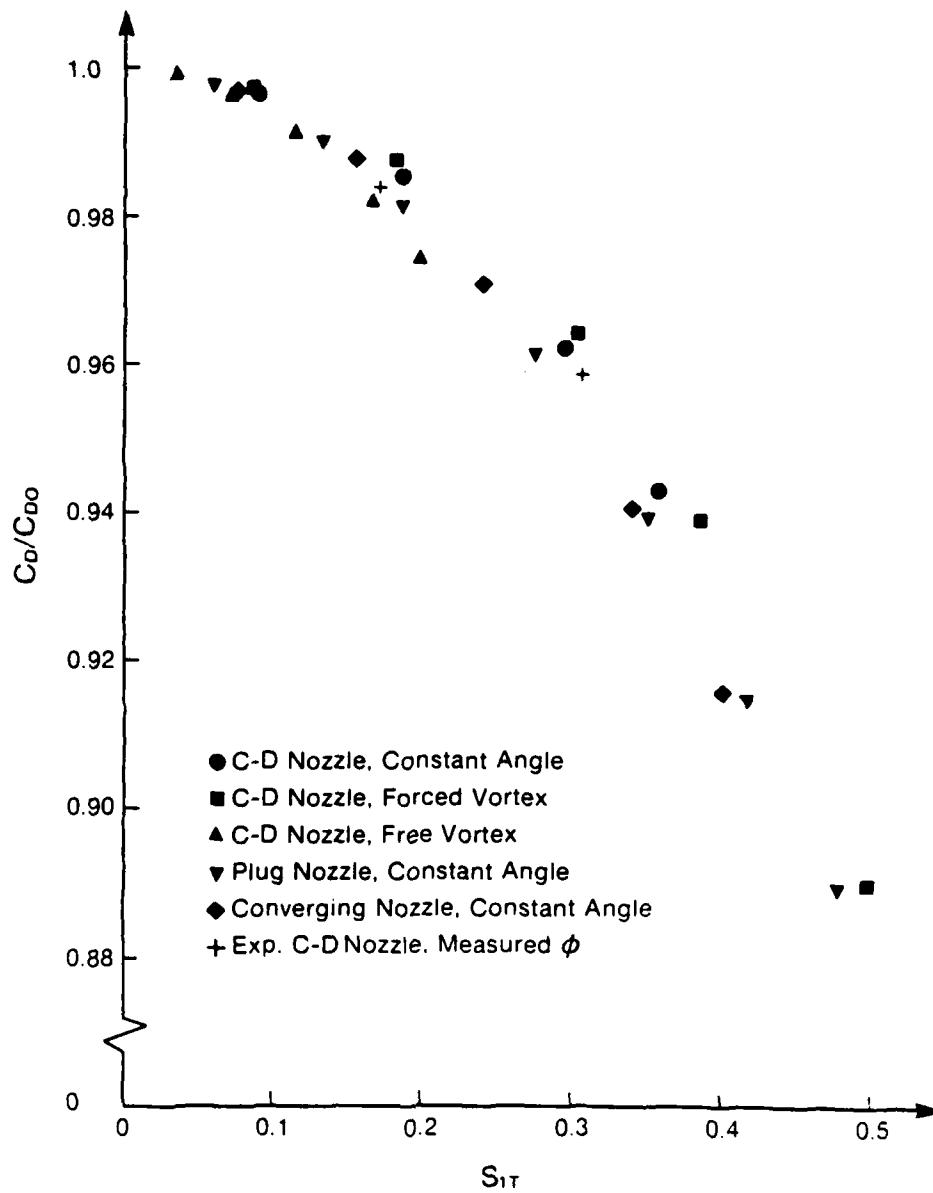


Figure 46. Universal correlation for reduced discharge coefficient as a function of throat swirl number S_{1t} for swirling nozzle flow

specific impulse results were anticipated since η_{S_1} was found to be nearly independent of swirl for the converging-diverging geometries while it monotonically decreased with swirl for the annular and converging nozzles. As shown in Fig. 47, the best (although not particularly good) correlation for the reduced vacuum stream thrust efficiency has been obtained using S_1 evaluated at the throat. The increased scatter in Fig. 47 compared to that in Fig. 46 is due to the just mentioned variations in the specific impulse for the converging and plug nozzle geometries.

In comparison, Boerner [26] found from his approximate series analyses that S_1 evaluated at the throat gave a nearly universal correlation for the reduced discharge coefficient for various swirl profiles in a conventional c-d nozzle. However, when he analyzed an annular nozzle geometry, the annular and c-d nozzle results did not coincide. Figure 46, on the other hand, demonstrates a good correlation for converging-diverging, annular, and converging nozzle geometries with several swirl profiles. In addition, the results of Fig. 46 predict a somewhat less rapid decrease in the reduced discharge coefficient with swirl than predicted by Boerner's c-d nozzle analyses. The present results are generally in better agreement with Boerner's annular nozzle predictions and with the c-d nozzle data of Farquhar [44] (quoted in [26]). Carpenter [18] has used a quasi-one-dimensional theory and found that swirl number definition S_3 , Eq. (49), correlated the reduced discharge coefficient very well for various swirl profiles. The reduced specific impulse coefficient, however, was not universally correlated using S_3 . Carpenter's results are similar to those obtained here although swirl number S_1 has been found to be somewhat superior to S_3 in defining a universal curve for the reduced discharge coefficient. In addition, Carpenter predicts a much greater rate of decrease of C_D/C_{D0} with S_3 than that obtained with the present method. It is to be emphasized that the time-dependent computations reported here consider the entire subsonic/transonic/supersonic regions of the nozzle and correctly treat the two-dimensional details of the nozzle geometry including the effects of the nozzle wall curvature. These aspects are

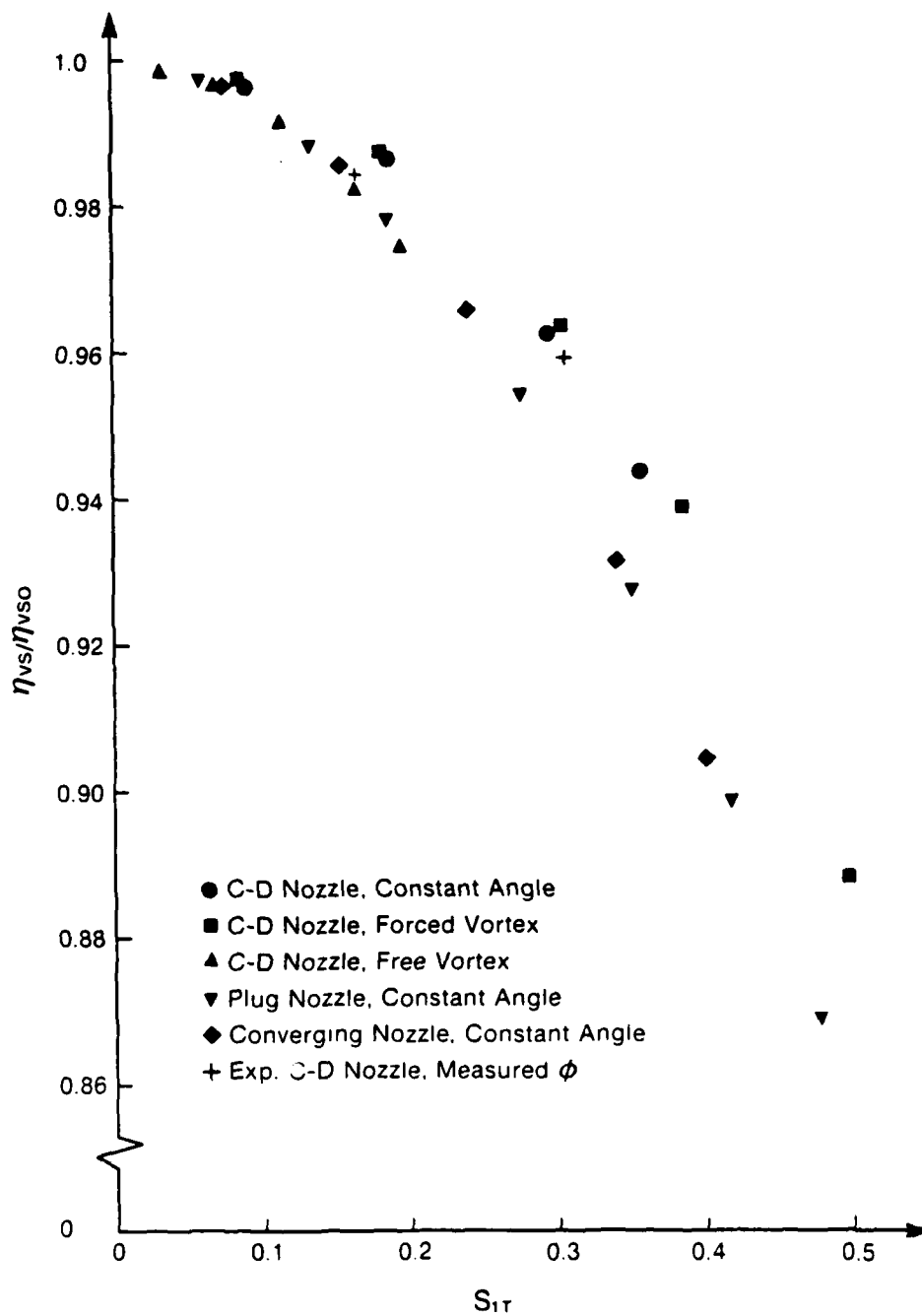


Figure 47. Quasi-universal correlation for reduced vacuum stream thrust efficiency as a function of throat swirl number S_{1t} for swirling nozzle flow

treated either only approximately or not at all by the analytical methods of Boerner [26] and Carpenter [18].

As a result of this study, it is concluded that Fig. 46 may be employed to obtain a good estimate of the reduction in the discharge coefficient due to swirl. Figure 47 may be used with much less confidence to obtain a first approximation to the reduction in the vacuum stream thrust efficiency. The preferred approach, however, is to use the time-dependent SNAP code to determine the thrust results. To use either Fig. 46 or Fig. 47, however, swirl number S_1 must be known at the nozzle throat. In contrast, the nozzle designer is more likely to be faced with the problem of knowing the swirl level imposed at the nozzle inlet and therefore having to estimate the throat swirl number from this information. As previously mentioned, this is one of the reasons the commonly used swirl number definition S_{12} evaluated at the nozzle inlet has been used in the presentation of the results.

V. SUMMARY AND CONCLUSIONS

The results and conclusions of this investigation of swirling nozzle flow can be summarized as follows:

- (1) A time-dependent finite difference code (SNAP) for analyzing inviscid swirling flow in converging, converging-diverging, and annular/plug nozzle geometries has been developed, and computations have been performed over a range of geometries, inlet swirl angle profiles, and swirl levels.
- (2) For the cases considered, reductions in discharge coefficient and vacuum stream thrust efficiency as large as 11% and 13%, respectively, have been calculated. For a given inlet swirl number, the free vortex swirl angle profile has been found to cause the largest reductions, followed by the constant angle and forced vortex profiles.
- (3) For the conventional c-d nozzle cases investigated, the specific impulse efficiency has been found to be essentially constant regardless of the swirl angle profile or swirl level. For the converging and plug nozzles, however, increased swirl resulted in reductions in specific impulse efficiency of up to 1.3% and 2.3%, respectively.
- (4) For the converging and converging-diverging geometries the major effect of swirl on the flowfield is to cause a large increase in the axial velocity near the centerline while the effect of swirl at the nozzle wall is much less pronounced. As a result, the nozzle flowfield and performance are sensitive to the tangential velocity magnitude in the vicinity of the centerline.
- (5) The nozzle area contraction ratio is an important parameter affecting the flowfield and performance. For a nozzle whose throat area is much smaller than its inlet area, very strongly swirled conditions must exist at the inlet to cause significant changes from the unswirled case.

- (6) For the converging and converging-diverging nozzle cases little distortion of the tangential velocity profile shapes occurs as the flow progresses through the nozzle. The magnitude of w at a particular axial station is generally inversely proportional to the wall radius in agreement with the conservation of flow angular momentum principle.
- (7) Conservation checks reveal that stagnation pressure, stagnation temperature, mass flowrate, and wall angular momentum are all well conserved by the computational method.
- (8) Calculations on 41×11 and 81×21 grids for a converging-diverging nozzle case give nearly identical results for gross performance parameters such as C_D , η_{VS} , and S_i . However, local flowfield information, such as the Mach number, may differ by a few percent between the two computations.
- (9) Experimental measurements of the stagnation pressure and swirl angle profiles across the nozzle inlet for a non-swirling and two swirling cases indicate that the flow is fairly axisymmetric, although for highly swirled conditions the uniform stagnation pressure assumption may not be adequate. In these experiments a conventional c-d nozzle was located immediately downstream from a relatively short ($L/D = 3$) dump combustor.
- (10) Excellent agreement has been obtained between the present time-dependent finite difference calculations and experimental wall static pressure measurements for an unswirled and two swirling c-d nozzle flows.
- (11) Using the many cases calculated here, a universal curve has been developed which can be employed to predict the reduction in the discharge coefficient due to swirl. The swirl number used in this correlation is the area-averaged tangential velocity component non-dimensionalized with respect to the critical speed of sound and evaluated at the nozzle throat.

VI. REFERENCES

1. Buckley, P.L., Craig, R.R., Davis, D.L., and Schwartzkopf, K.G., "The Design and Combustion Performance of Practical Swirlers for Integral Rocket/Ramjets," AIAA Paper No. 80-1119, 1980.
2. Binnie, A.M., "The Passage of a Perfect Fluid Through a Critical Cross-Section or Throat," Proceedings of the Royal Society, Series A, Vol. 197, 1949, pp. 545-555.
3. Mager, A., "Approximate Solution of Isentropic Swirling Flow Through a Nozzle," ARS Journal, Vol. 31, Aug. 1961, pp. 1140-1148.
4. Bastress, E.K., "Interior Ballistics of Spinning Solid-Propellant Rockets," Journal of Spacecraft and Rockets, Vol. 2, No. 3, May - June 1965, pp. 455-457.
5. Manda, L.J., "Spin Effects on Rocket Nozzle Performance," Journal of Spacecraft and Rockets, Vol. 3, No. 11, Nov. 1966, pp. 1695-1696.
6. King, M.K., "Comment on 'Spin Effects on Rocket Nozzle Performance'," Journal of Spacecraft and Rockets, Vol. 3, No. 12, Dec. 1966, pp. 1812-1813.
7. Manda, L.J., "Reply by Author to M. King," Journal of Spacecraft and Rockets, Vol. 3, No. 12, Dec. 1966, pp. 1813-1814.
8. King, W.S., "On Swirling Nozzle Flows," Journal of Spacecraft and Rockets, Vol. 4, No. 10, Oct. 1967, pp. 1404-1405.
9. Glick, R.L., and Kilgore, M.S., "Effect of Specific-Heat Ratio on Mass Flow for Swirling Nozzle Flow," Journal of Spacecraft and Rockets, Vol. 4, No. 8, Aug. 1967, pp. 1098-1099.
10. Lewellen, W.S., Burns, W.J., and Strickland, H.J., "Transonic Swirling Flow," AIAA Journal, Vol. 7, No. 7, July 1969, pp. 1290-1297.
11. Norton, D.J., Farquhar, B.W., and Hoffman, J.D., "An Analytical and Experimental Investigation of Swirling Flow in Nozzles," AIAA Journal, Vol. 7, No. 10, Oct. 1969, pp. 1992-2000.

12. Hsu, C.T., "Swirling Nozzle Flow Equations from Crocco's Relation," AIAA Journal, Vol. 9, No. 9, Sept. 1971, pp. 1866-1868.
13. Hsu, C.T., "Errata: 'Swirling Nozzle Flow Equations from Crocco's Relation'," AIAA Journal, Vol. 10, No. 3, March 1972, p. 368.
14. Hsu, C.T., "Mass Blocking of Swirling Flow in Nozzles," Journal of Spacecraft and Rockets, Vol. 8, No. 12, Dec. 1971, pp. 1232-1234.
15. Hsu, C.T., and DeJooode, A.D., "Inviscid Swirling Flows Through a Choked Nozzle," AIAA Journal, Vol. 11, No. 11, Nov. 1973, pp. 1564-1566.
16. Wolfram, W.R., and Walker, W.F., "Swirling Flow of a Dissociated Gas," ASME Journal of Fluids Engineering, Vol. 97, March 1975, pp. 122-124.
17. Carpenter, P.W., and Johannesen, N.H., "An Extension of One-Dimensional Theory to Inviscid Swirling Flow through Choked Nozzles," Aeronautical Quarterly, Vol. 26, May 1975, pp. 71-87.
18. Carpenter, P.W., "A General One-Dimensional Theory of Compressible Inviscid Swirling Flows in Nozzles," Aeronautical Quarterly, Vol. 27, Aug. 1976, pp. 201-216.
19. Carpenter, P.W., "Effects of Swirl on the Subcritical Performance of Convergent Nozzles," AIAA Journal, Vol. 18, No. 5, May 1980, pp. 600-602.
20. Carpenter, P.W., "Supercritical Swirling Flows in Convergent Nozzles," AIAA Journal, Vol. 19, No. 5, May 1981, pp. 651-660.
21. Carpenter, P.W., "The Effects of Swirl on the Performance of Supercritical Convergent-Divergent Nozzles," Aeronautical Quarterly, Vol. 32, May 1981, pp. 126-152.
22. Guderley, K.G., and Tabak, D., "On the Determination of Optimum Supersonic Thrust Nozzles of Given Length for a Flow with Swirl: Theoretical Part," Aerospace Research Laboratories Report No. ARL 66-0013, Jan. 1966.

23. Guderley, K.G., and Breiter, M.C., "Approximation for Swirl Flows in the Vicinity of the Throat of a Laval Nozzle," Aerospace Research Laboratories Report No. ARL 70-0009, Jan. 1970.
24. Guderley, K.G., and Breiter, M.C., "On the Determination of Optimum Thrust Nozzles of a Given Length for a Flow with Swirl: Numerical Results," Aerospace Research Laboratories Report No. ARL 70-0161, Aug. 1970.
25. Guderley, K.G., Tabak, D., Breiter, M.C., and Bhutani, O.P., "Continuous and Discontinuous Solutions for Optimum Thrust Nozzles of Given Length," Journal of Optimization Theory and Applications, Vol. 12, Dec. 1973, pp. 588-628.
26. Boerner, C.J., Sparrow, E.M., and Scott, C.J., "Compressible Swirling Flow through Convergent-Divergent Nozzles," Wärme- and Stoffübertragung, Vol. 5, No. 2, 1972, pp. 101-115.
27. Pandolfi, M., "Transonic Swirling Flow in Axisymmetric Nozzles," Meccanica, Vol. 11, Sept. 1976, pp. 157-161.
28. Smith, R., "An Investigation of Supersonic Swirling Jets," Aeronautical Quarterly, Vol. 24, 1973, pp. 167-178.
29. Carpenter, P.W., "A Linearized Theory for Swirling Supersonic Jets and Its Application to Shock-Cell Noise," AIAA Paper No. 80-1449, July 1980.
30. Dunlap, R., "An Investigation of the Swirling Flow in a Spinning End-Burning Rocket," AIAA Journal, Vol. 7, No. 12, Dec. 1969, pp. 2293-2300.
31. Batson, J.L., and Sforzini, R.H., "Swirling Flow through a Nozzle," Journal of Spacecraft and Rockets, Vol. 7, No. 2, Feb. 1970, pp. 159-163.
32. Sforzini, R.H., and Essing, J.E., "Swirling Flow through Multiple Nozzles," Journal of Spacecraft and Rockets, Vol. 7, No. 11, Nov. 1970, pp. 1366-1369.

33. Cline, M.C., "NAP: A Computer Program for the Computation of Two-Dimensional, Time-Dependent, Inviscid Nozzle Flow," Los Alamos Scientific Laboratory Report No. LA-5984, Jan. 1977.
34. Cline, M.C., "VNAP: A Computer Program for Computation of Two-Dimensional, Time-Dependent, Compressible, Viscous, Internal Flow," Los Alamos Scientific Laboratory Report No. LA-7326, Nov. 1978.
35. Stiles, R.J., and Hoffman, J.D., "Analysis of Steady, Two-Dimensional Chemically Reacting Nonequilibrium Flow by an Unsteady, Asymptotically Consistent Technique, Volume I - Theoretical Development," AFWAL-TR-81-2127, Vol. I, Sept. 1982.
36. Stiles, R.J., and Hoffman, J.D., "Analysis of Steady, Two-Dimensional Chemically Reacting Nonequilibrium Flow by an Unsteady, Asymptotically Consistent Technique, Volume II - Computer Program Manual," AFWAL-TR-81-2127, Vol. II, Sept. 1982.
37. MacCormack, R.W., "The Effect of Viscosity in Hypervelocity Impact Cratering," AIAA Paper No. 69-354, April 1969.
38. Serra, R.A., "Determination of Internal Gas Flows by a Transient Numerical Technique," AIAA Journal, Vol. 10, No. 5, May 1972, pp. 603-611.
39. Moretti, G., "A Physical Approach to the Numerical Treatment of Boundaries in Gas Dynamics," Numerical Boundary Condition Procedures, NASA Conf. Pub. 2201, Oct. 1981, pp. 73-95.
40. Dutton, J.C., "Time-Dependent Calculations of Swirling Nozzle Flow," Final Report for 1983 USAF-SCEEE Summer Faculty Research Program, Contract No. F49620-82-C-0035, Aug. 1983.
41. Beer, J.M., and Chigier, N.A., Combustion Aerodynamics, Halsted Press, New York, 1972.
42. Bresnahan, D.L., and Johns, A.L., "Cold Flow Investigation of a Low Angle Turbojet Plug Nozzle with Fixed Throat and Translating Shroud at Mach Numbers from 0 to 2.0," NASA TM X-1619, Aug. 1968.

43. Cline, M.C., "VNAP2: A Computer Program for Computation of Two-Dimensional, Time-Dependent, Compressible, Turbulent Flow," Los Alamos National Laboratory Report No. LA-8872, Aug. 1981.
44. Norton, D.J., Farquhar, B.W., and Hoffman, J.D., "An Analytical and Experimental Investigation of Swirling Flow in Nozzles," Report No. F-67-9, Jet Propulsion Center, Purdue University, West Lafayette, Indiana, Oct. 1967.

1983-84 USAF-SCEEE RESEARCH INITIATION PROGRAM

Sponsored by the

AIR FORCE OFFICE OF SCIENTIFIC RESEARCH

Conducted by the

SOUTHEASTERN CENTER FOR ELECTRICAL ENGINEERING EDUCATION

FINAL REPORT

ANALYSIS OF CONDENSATION PHENOMENA FOR CONVENTIONAL HEAT PIPES

Prepared by: Dr. Amir Faghri

Academic Rank: Associate Professor

Department and
University: Mechanical Systems Engineering Department
Wright State University

Research Location: Air Force Aero Propulsion Laboratory

Date: December 1984

Analysis of Condensation Phenomena for Conventional Heatpipes

by

ABSTRACT

Experimental investigation concerning the local heatflux variation along the condenser section of different heatpipes were undertaken to obtain better understanding of the condensation phenomenon inside heatpipes. The design consists of installing circular fins along the condenser section of double-wall, conventional and axially-grooved heatpipes. The trends for heatflux, heat transfer coefficient, and the wall temperature were obtained and show a random behavior. In general the trend for local heat flux variation is more uniform for axially grooved heat pipes compared to double-wall heatpipes. The experimental results show an over-all energy balance.

ACKNOWLEDGEMENT

The author would like to thank the Air Force Wright Aeronautical Laboratories, Air Force office of Scientific Research and the Southeastern center for Electrical Engineering Education for providing the support for this project. Appreciation is expressed to Dr. Tom Mahafkey and Jerry Beam of the Thermal Energy Lab, Aeropropulsion Lab, Wright Patterson Air Force Base for valuable advice and technical assistance.

1. Introduction

Since the invention of heat pipes in 1963 by Grover [1] a dramatic growth in the development and research in this area has taken place. The majority of investigators have used a water circulating cooling jacket in experimental evaluation of the condenser performance. Using this conventional technique, no information can be obtained on local values. Other cooling systems such as droplet/forced air evaporation or fins were used with heat pipes, but no cooling rate in the condenser was measured. A new technique was developed very recently [2] to experimentally measure local heat flux along the condenser section of a heat pipe. This design consists of installing circular fins along the condenser section of a double wall heat pipe. There have been numerous experimental and theoretical studies [3] concerning the effect of non condensible gases on the condensation phenomena of heat pipes. In general, experimental observation which indicates the effect of non condensible gases on the local variation of heat flux are lacking. This information is very important, because one purposefully introduces a non condensible gas into the heat pipe for the control of the temperature. In the early stage of heat pipe development, Musselt theory [5] was used to describe the condensation phenomena in heat pipes. Because of the liquid flow in the conventional wick (porous media) or axially grooved wicks, as well as its interaction with the gas flow, the above model is too simplified to be used considering the fact that the heat pipe is also a closed system. Seban and Faghri [6] considered the laminar reflux condensation in a closed two phase thermosyphon (gravity assisted wickless heat pipe) for both constant wall temperature and constant heat flux at the wall by accounting for

the shear stress at the interface due to vapor friction and suction. Theoretical prediction was compared with experimental prediction and shows a good agreement. Unfortunately theoretical prediction for turbulent flow does not exist for closed systems. The theory of condensation was also extended for axially grooved heat pipes [7,8,9]. In axially grooved heat pipe analysis, the following assumptions were made:

- a. Zero-gravity condition.
- b. Vapor mainly condenses in the land area between the grooves where the liquid film thickness is lowest.
- c. Liquid condensed is sucked into grooves by capillary action and then flows along the groove to the evaporator section.

In both the gravity assisted wickless heat pipe and the axially grooved heat pipes the results were compared with overall heat transfer coefficients which were obtained by a cooling jacket.

The problem of heat pipes with porous wick with an annular liquid flow between the wick and the solid pipe wall was considered by H. Hwang-Bo and W.E. Hilding [10]. Not only are the assumptions made in solving the problems not true, but because of the annular liquid flow and reduction of total resistance, it is not of practical interest. An effort is now underway to analyze and make a parametric study of the condensation phenomena in the condenser section of a conventional heat pipe accounting for the porous media structure as well as the variation of the contact angle along the axial direction.

It is interesting to note that for axially grooved heat pipes the liquid thickness is decreasing along the axial direction toward the end of the condenser. Therefore the heat flux, or heat transfer, has an

increasing effect in the same direction. The trend is completely the opposite for conventional heat pipes because the resistance thickness is fixed by the thickness of the wick; however, the effective thermal conductivity is decreasing toward the end of the condenser.

2.A. Previous experimental investigation by the author summer 1983.

Introduction

A new, simple technique was developed by the author for the prediction of the axial variation of local heat flux along the condenser section of a double-wall artery high capacity heat pipe. This work was performed by the author while he was working as a visiting scientist at the Thermal Energy Lab, Aero Propulsion Lab, Wright Patterson AFB, in the summer of 1983 for ten weeks. The work was presented at the Fifth International Heat Pipe Conference in Japan [2] and will be duplicated in part here for completion of this report.

2.B. Experiments

The heat pipe experimental set-up consists of three main components. These are the heat pipe itself, the power supply and monitoring equipment, and the instrumentation and data collection devices. The basic setup is the same as that reported by R. Ponnappan and E.T. Mahefkey [4]. The only difference is in the design and instrumentation of the condenser section.

This double-wall artery high capacity heat pipe incorporates two concentric copper tubes. The inner tube has axial external grooves, the outer tube has internal circumferential grooves, and finally, there is an interannular screenmesh wick. The pipe itself is 1.2 m long with an 0.2 m evaporator and condenser section.

Since the overall experimental objective was to investigate the behavior of the local heat transfer coefficient along the condenser section, we had to design a completely new instrumentation package to measure the local heat flux. This consists of circular fins clamped to the heat pipe and instrumented to measure the temperature gradient along the radius at the base of the fin. This design is shown in Figures 1 and 2. The heat flux for each fin was calculated using

$$q_x = K \left. \frac{dT}{dr} \right|_{r=r_1}$$

where K is the thermal conductivity, and $\left. \frac{dT}{dr} \right|_{r=r_1}$ is the temperature gradient at the base of the fin. This temperature gradient was also obtained analytically for a constant wall temperature. It was shown that this temperature gradient was linear up to 0.1 inches from the base of the fin for most metals and boundary conditions considered.

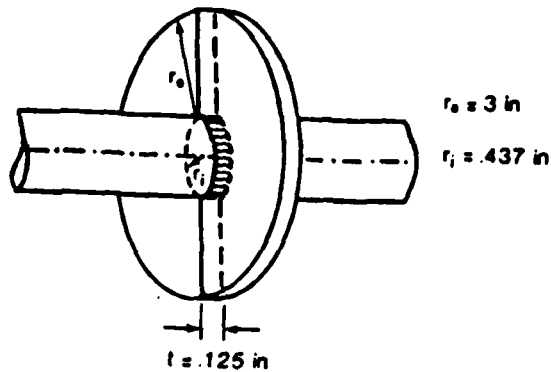


Figure 1. Fin Orientation on pipe

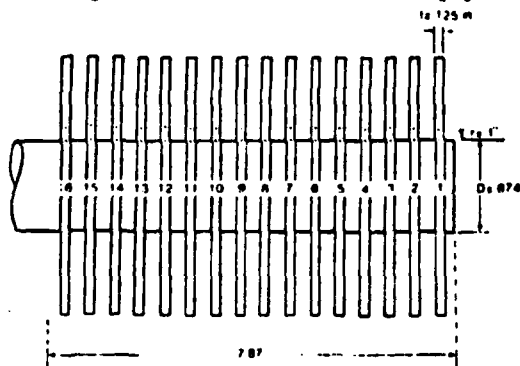


Figure 2. Condenser Section Orientation

Analytical results for the temperature distribution, fin effectiveness and fin efficiency were obtained for a circular fin for constant wall temperature at the base of the fin. The applicable differential equation with the appropriate boundary conditions for this case are the following

$$\frac{d^2T}{dr^2} + \frac{1}{r} \frac{dT}{dr} - \frac{2h}{Kt} (T - T_\infty) = 0$$

$$r = r_i \quad T = T_0$$

$$r = r_o \quad \frac{dT}{dr} = 0$$

The result of the above analysis for constant heat transfer coefficients h , was only used for the purpose of design analysis to find the best appropriate fin dimensions and material.

There were several advantages to this design. First was the relative simplicity to manufacture the fins. Second was the ability to measure an actual local heat flux. Energy balance is the only method of checking the validity of the data. In other words, the power entering the evaporation section should be equal to the sum of the heat going out of each fin. It was also shown theoretically, using fin effectiveness, that the amount of power loss through the part which is not covered with fin was negligible.

For design analysis, we considered an overall transport capacity limit of 1500 W-m for the present heat pipe which was used for our investigation. Based on design limitation and the fin efficiency calculations, we decided to use aluminum fins, .125 inches thick and 3.0 inches in radius. This radius is defined as the distance between the pipe wall and the tip of the fin. We also assumed that the effects of the steel clamp at the edge of the fin was negligible.

A Dynatech Model 316 TIG welder was used for obtaining uniform beads from 0.005 inch (36 fine gage), type J, thermocouple wires. This method brought the ability to keep the wire insulation right up to the bead to prevent extra junctions between the wires themselves or between

the wires and the fin. Each fin was drilled with 0.0225 inch holes. One was at 0.1 inch and 0.0625 inches deep. The second hole was drilled through the side of the fin to the wall of the heat pipe. The thermocouples were dipped in glyptal to provide extra insulation to prevent extra junctions. These were then held in place using Dow Corning Silastic Silicon Rubber. Finally, Dow Corning 340 heat sink material was used between the fin and the pipe to improve thermal contact.

2.C. Results and Discussion

Figures 3, 4, and 5 show the wall temperature profile for 8, 15 and 13 fins respectively. Each of these graphs show a concave shape with Figure 6 showing this phenomenon most clearly. This is probably due to the better thermal contact afforded by using the aluminum putty as the interstitial material.

In the book, Heat Pipes by Dunn and Reay [5], they list several different failure modes of a heat pipe. In certain of these failure modes it is mentioned that stagnant water in the end of the condenser section serves as an insulation blanket resulting in cooler wall temperatures and lower heat flux in the condenser. Based on this observation and the profile in Figure 5, it is hypothesized that the higher wall temperatures at the end of the condenser section were due to lower water levels in that end of the condenser section. In other words, the end of the condenser section is not being optimally used.

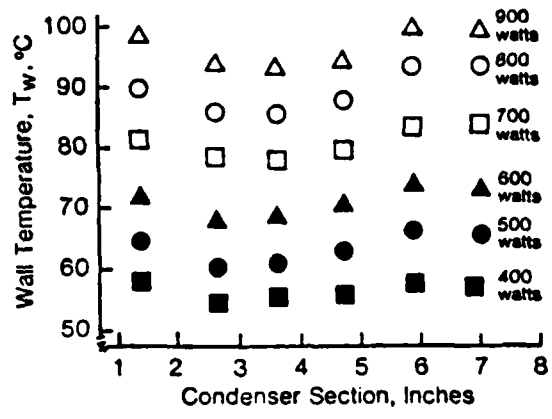


Figure 3. Wall Temperature profile in Condenser Section, 8 fins

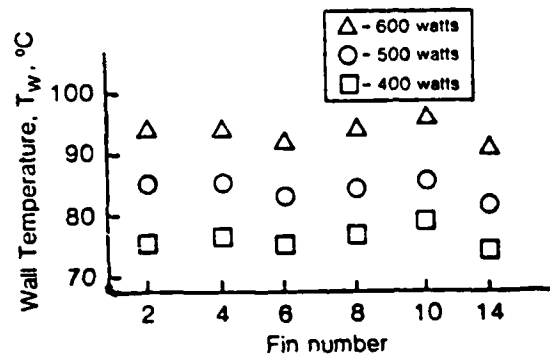


Figure 4. Wall Temperature Profile in Condenser Section, 15 fins

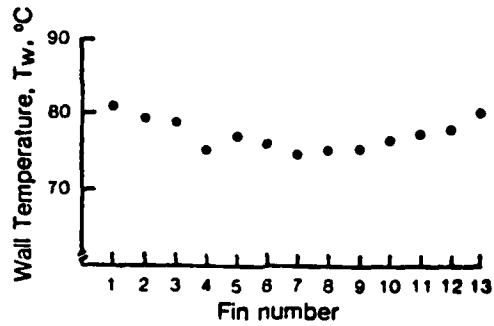


Figure 5. Wall Temperature Profile in Condenser Section, 13 fins.

If this was true, a negative tilt angle test, where the condenser section is lower than the evaporator section, should force water to stay in that region of the condenser. This is because the capillary pressure in the wick has to fight against gravity to return the water back to the evaporator section. Then the additional water in the end of the condenser should bring these end temperatures down and slightly raise the temperatures at the beginning of the condenser. The results of this experiment are shown in Figure 6 for 250W and 400W. The results were exactly as predicted.

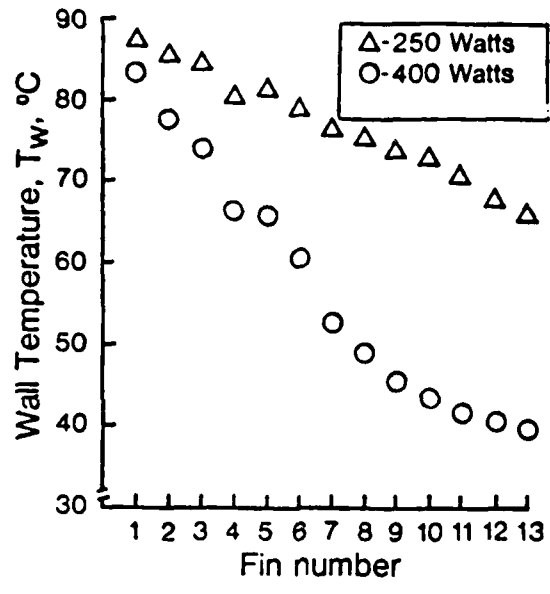


Figure 6. Wall Temperature Profile in Condenser Section, 13 fins, -2° tilt

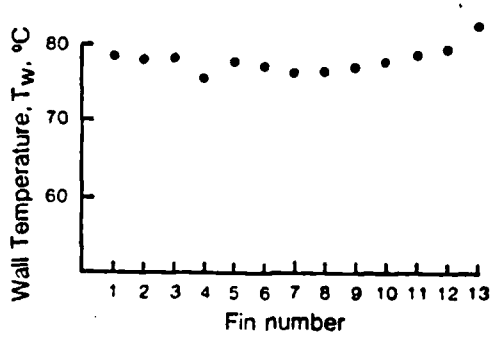


Figure 7. Wall Temperature Profile in Condenser Section, 13 fins, +2° tilt.

A positive tilt experiment was also performed at +2° tilt. The wall temperature profile is shown in Figure 7. The positive tilt had the affect of leveling out the temperature profile, however, you can still observe the concave behavior prevalent in the other tests.

The most important general trend is axial variation of local heat flux. Heat flux variation is shown for 8 fins, 15 fins, and 13 fins for various power settings in Figures 8, 9, and 10 respectively. From these graphs it can be seen that there is a general trend from high value to low value of the heat flux. There is about a 10 percent drop in heat flux at the end of the condenser section compared to that at the beginning of the section. This seems to be a valuable conclusion since it existed for each power setting and shows a basic characteristic of the condenser section for this cooling method. In addition the heat transfer coefficient

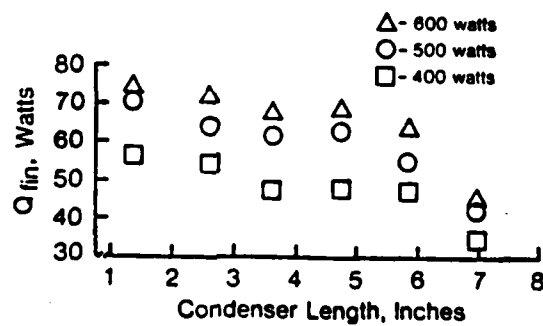


Figure 8. Local Heat Flux Variation in Condenser Section, 8 fins.

along the condenser length showed proportional results to the heat flux. It should also be noted that the total heat loss calculated from all the fins are within 10 percent of the energy input in the evaporator. This energy balance was shown for eight, fifteen, and thirteen fins.

The results of the negative tilt tests for the variation of the local heat flux along with condenser section is shown in Figure 11 for 250W and 400W. The 400W curve is much steeper than the 250W curve as would be expected. The heat flux follows the same general trend as the wall temperature profile shown in Figure 6. The positive tilt test results showing the local heat flux variation is shown in Figure 12. Note once again for the positive tilt the leveling affect that corresponds to the trend in the wall temperatre shown in Figure 7.

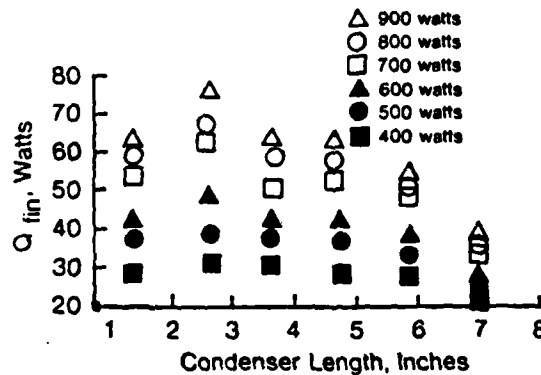


Figure 9. Local Heat Flux Variation in Condenser Section, 15 fins

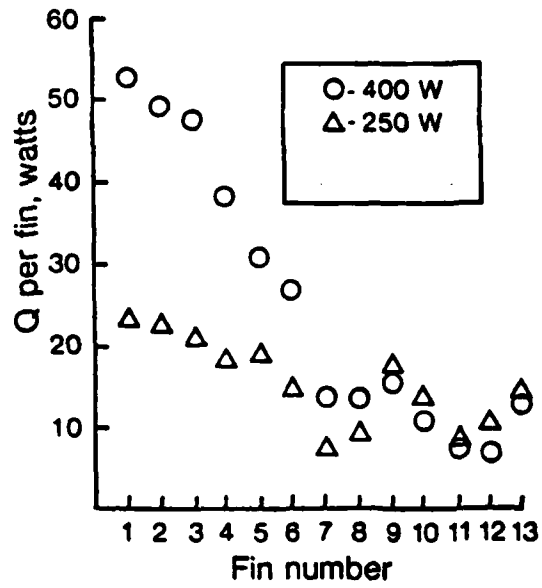


Figure 10. Local Heat Flux Variation in Condenser Section, 13 fins

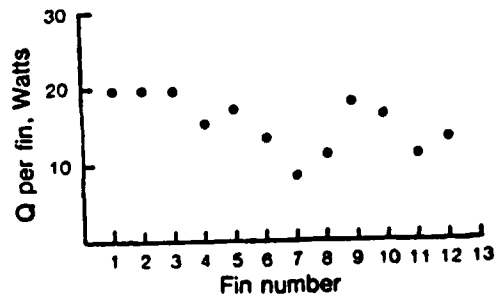


Figure 11. Local Heat Flux Variation in Condenser Section, 13 fins, -2° tilt

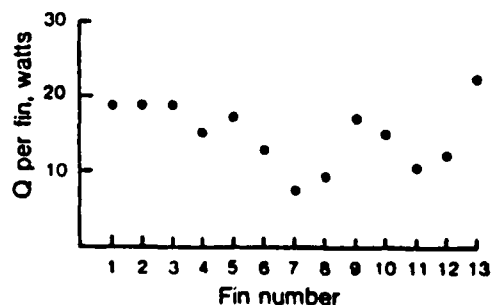


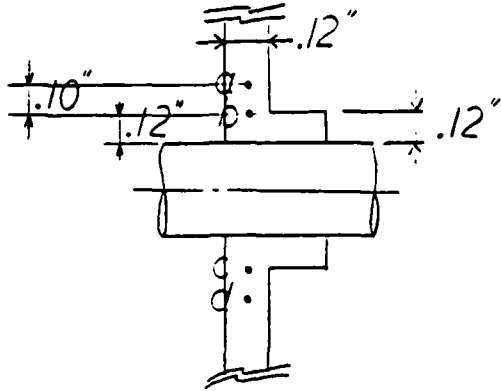
Figure 12. Local Heat Flux Variation in Condenser Section, 13 fins, +2° tilt

- 3. Previous experimental investigation by the author summer of 1984
- 3.A. Experimental design, setup and performance

Four different heat pipes were designed and built in order to test and compare the result of local variation of heat flux along the condenser section. These heat pipes are conventional heat pipes with screen-mesh wick, axially grooved heat pipe and two gravity assisted wickless heat pipes. The major part for the summer of 1984 was spent in designing the heat pipes, base construction and leveling of the heat pipes, calibration of thermocouples and the both boards of the Fluke 2280A, calibration of measuring equipment for power and building the heating parts for the evaporation section of the heat pipes.

The heat pipes were made of copper, were 1.2 m long with .2 m evaporation and condenser sections. Eighteen circular fins of aluminum were press fitted according to Figure 13. The heat flux and heat transfer coefficient for each fin was calculated using

Installation of thermocouples



Every thermocouples in fins are installed by using aluminum putty after 0.5 mm drilled. The others are just used aluminum putty.

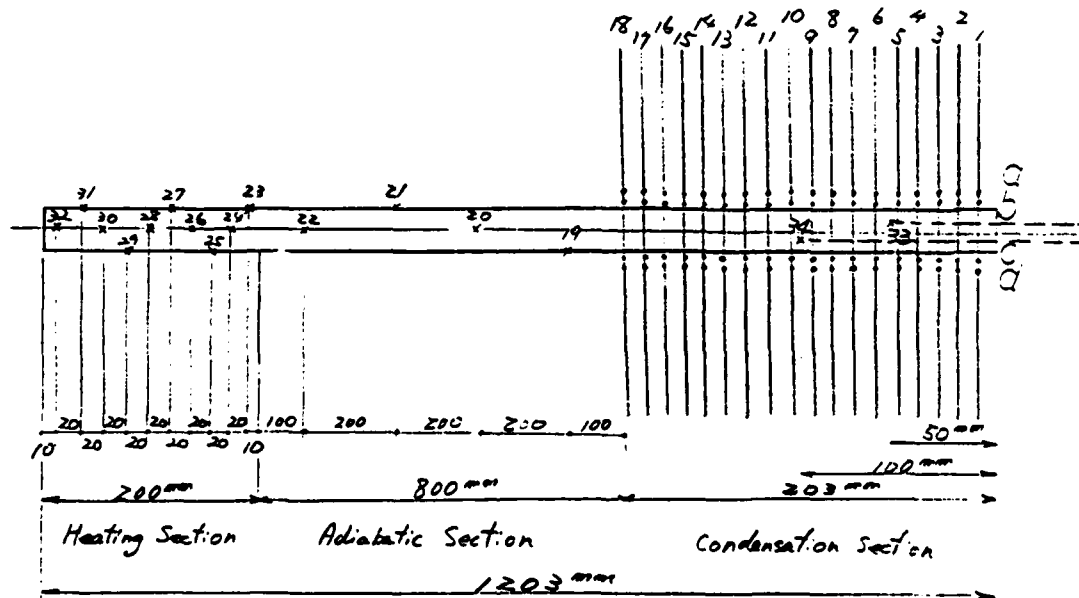


Figure -13

$$q_x = k \frac{T_{\text{wall}} - T_u}{\Delta r}$$

$$h = \frac{q_x}{T_{\text{wall}} - T_{\text{sat}}}$$

where T_{wall} is the wall temperature of the pipe, t_u is the temperature at .1" from the base of a fin along the radial direction of the fin, T_{sat} is the vapor temperature inside the heat pipe and $\Delta r = .1$ ". Four thermocouples were installed in each fin to analyze the effect of heat flux circumferentially.

For design analysis, we considered an overall capacity limit of 1200 W-m for all the heat pipes. Since all of the analysis used to evaluate the heat flux were based on the assumption of one dimensional flow. This was obviously a very important criteria. Physically, the longer the fin is relative to the width, the more accurate this assumption will be. On the other hand, however, there are practical considerations such as buckling limits and thermoangle attachments.

Based on these considerations and fin efficiency calculation, we decided to use aluminum fins 3mm thick at 76mm in radius. This radius is defined as the distance between the pipe wall and the tip of the fin. All pipes have an approximate outside diameter of 25mm.

Experimental setup such as leveling, insulation, calibration etc. are given in the interim report. The experimental procedure, however, should be included here. The basic idea was to obtain steady state data for each pipe at power input ranges from 100-1000 watts. Steady state conditions were determined by negligible temperature change over a 40 minute period; commonly, it took 2 1/2 hrs to reach steady conditions. Data was taken on a 40 channel Fluke DVH(2280A). The

first few tests, we choose to record only one thermocouple pair per of fin, on all 18 fins, but due to the scatter encountered, we later decided to record both TC pairs on every other fin, and average their results. In addition the vapor core temperature was measured at two locations, 50 and 100mm from the condenser end. The adiabatic section wall temperature was recorded at two locations. The evaporation wall temperature was measured with thermocouples embedded in the ceramic case surrounding the heating coils. These measurements lead to unexpectedly large differences in the evaporation wall temperature, and a large axial scatter in the evaporation section. The reading of the evaporator section thermocouples were deemed unreliable due to their close and variable proximity to the heating coils. The power supply is a staco 5020-P variac, with output of 0-240 volts and 0-28 amps. The watt meter and ammeter are Weston Mirror Meters and the voltage is measured by a Keithly digital multimeter. The overall energy balance was made by calculating heat per fin, as mentioned above, using an average $\frac{dT}{dx}$ for every fin when possible, then linearly interpolating across unmeasured fins, and taking the resulting sum over all fins. This total was of course, compared with the input power.

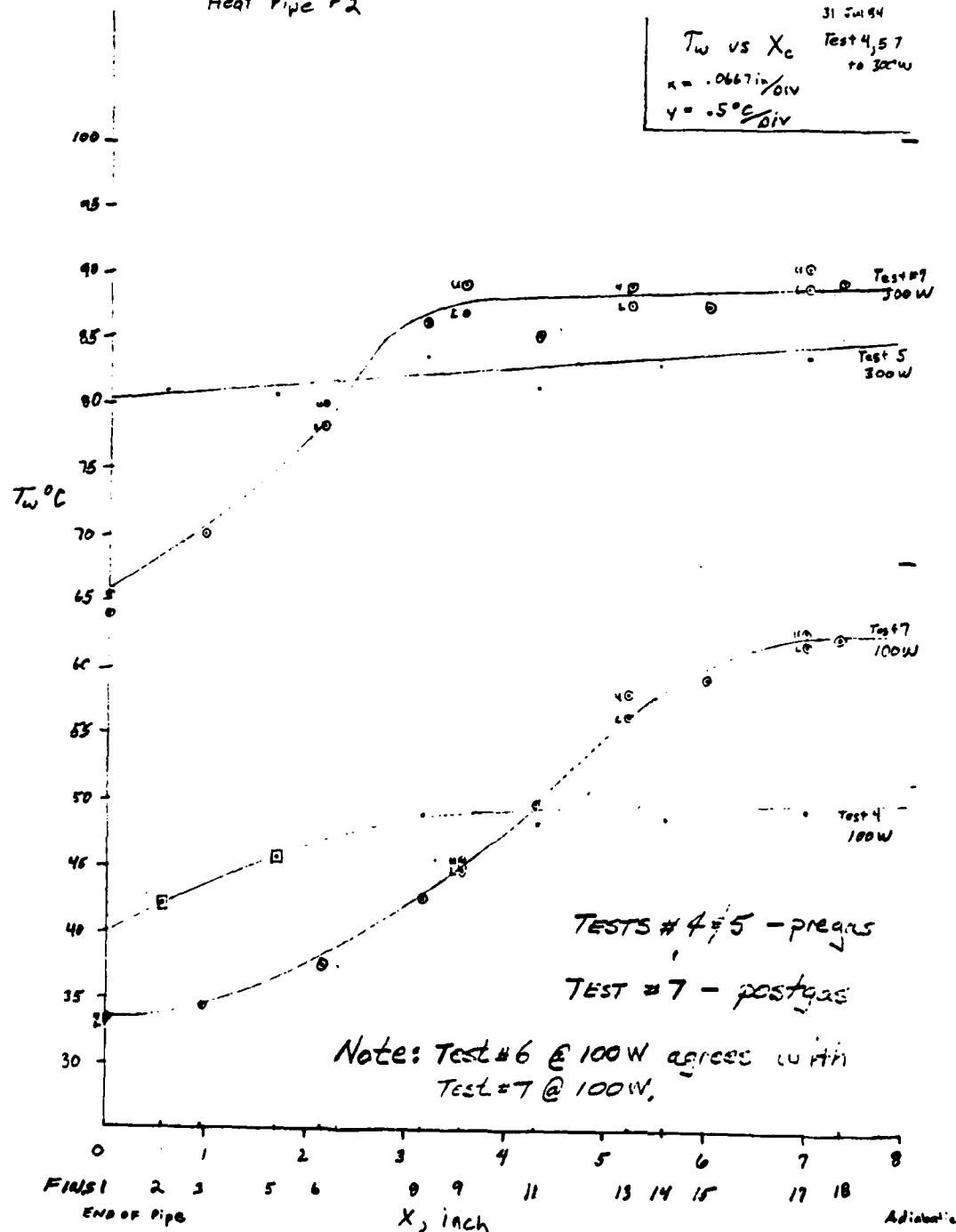
3.B. Result and Discussion

Up to now, seven experimental tests were performed only with the axially grooved heat pipes. The first five tests were done on low power inputs and the last two at high power. Unfortunately, some amount of gas was discovered in the last two tests. This was observed by the small differences between the two temperatures in the vapor core of the condenser section.

Heat Pipe #2

31 Jul 64

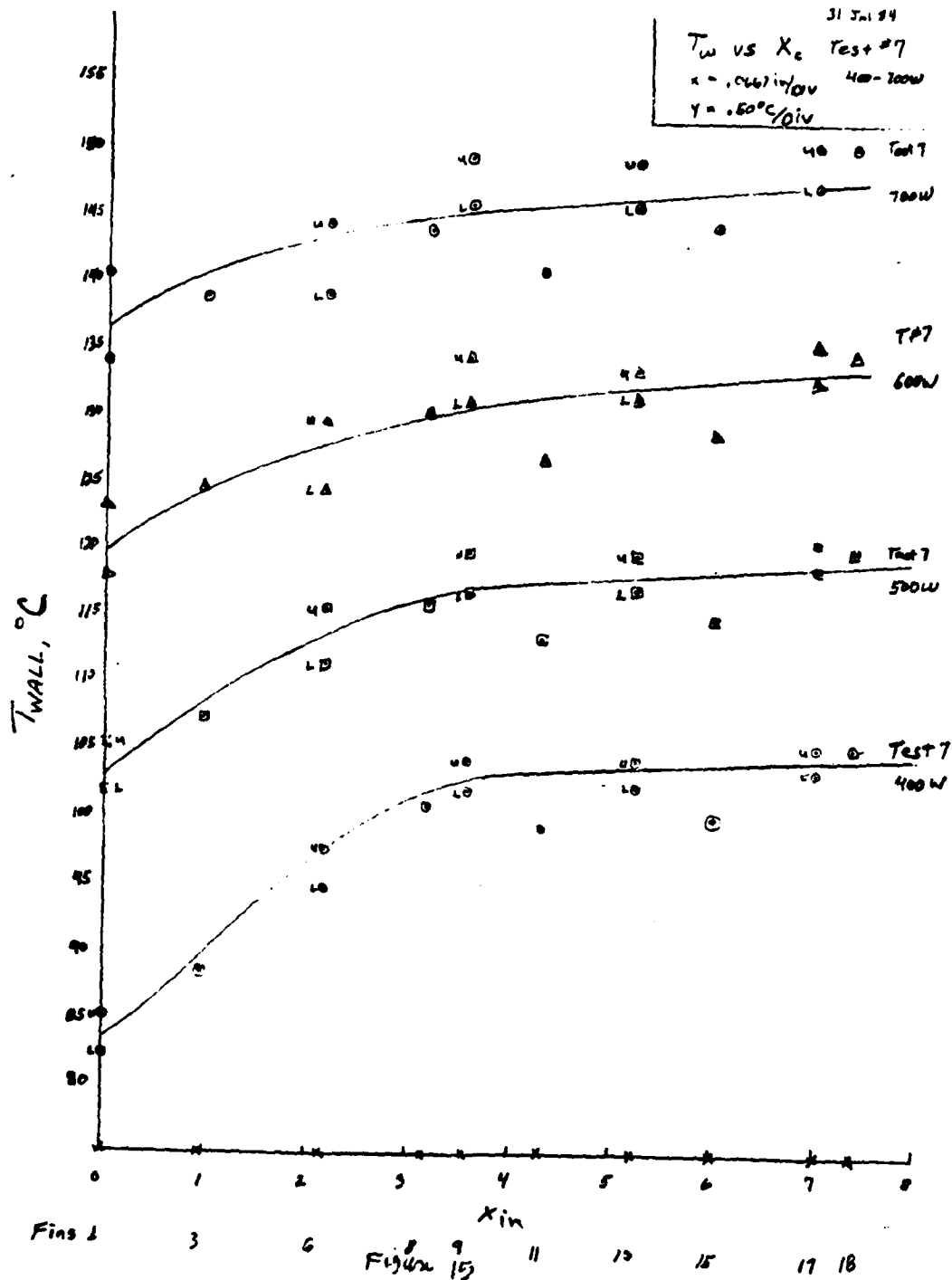
T_w vs X_c Test 4, 5, 7
 to 300W
 $x = .0667 \text{ in/div}$
 $y = .5^\circ\text{C/div}$



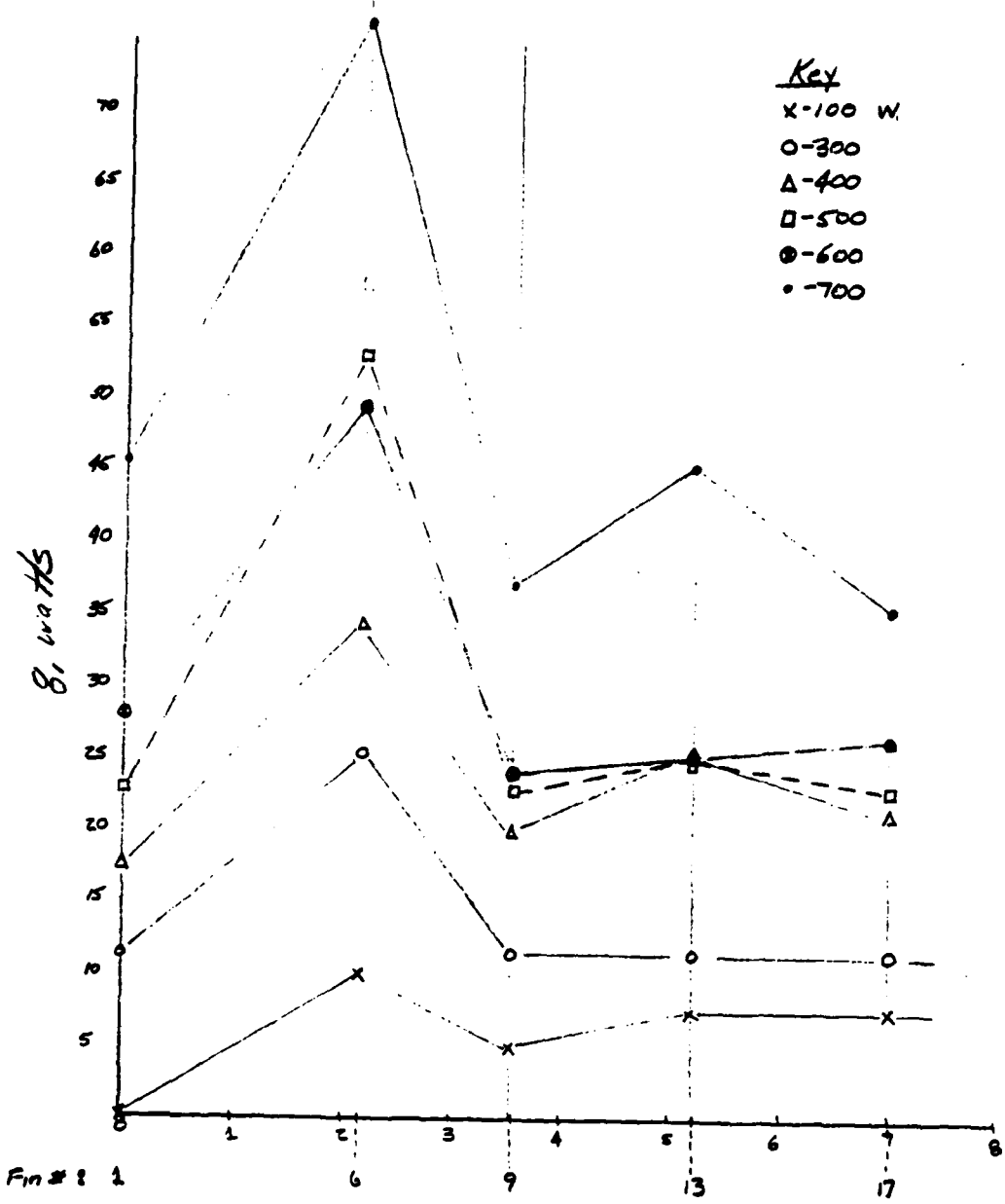
Note: Test # 6 @ 100W agrees with Test # 7 @ 100W.

Figure 14
 17-21

Fig. 11. The effect of fin spacing on the wall temperature of a
 750 Watts (Heat Sink)



Title: *Time vs. Power for TC pairs A & B*
 Date: *10-9-57*
 TC pairs A & B and C-D



X, inches
 Figure-1b

The wall temperature distributions along the condenser section of axially grooved heat pipe is shown in Figure (14) and (15) for all the tests. Existence of some gas in the heat pipe can be seen from the wall temperature distribution. The variation of heat flux is shown in Figure (16) for the same tests. The following conclusions can be made concerning these tests.

1. Gas did leak into the system between test 5 and 6, as shown by the temperature distribution.
2. The energy balance error is a maximum of 20%.
3. Heat flux shows some random scatter. This scatter is minimized by using 4 thermocouples per fin and averaging.
4. Heat flux and heat transfer coefficient are generally higher for the upper half of the fin.

4. References

1. G.M. Glover, T.P. Cotter and G.F. Erickson, "Structures of Very High Thermal Conductance," J. App. Phys. Vol. 35, p. 1990, 1964.
2. A. Faghri, R. Stewart and C.L. Rainey, "Axial Variation of Local Heat Flux Along the Condenser Section of a Double-Wall Artery High Capacity Heat Pipe", Proceedings of the V International Heat Pipe Conference, Japan, May 1984.
3. J.V. McAllan, and B.C. Bassani, "Oscillations in Gas Controlled Heat Pipes at Low Pressure", Proceedings of the V International Heatpipe Conference, May 1984.
4. R. Ponnappan and E.T. Mahefkey, "Performance Characteristics of the Double-Wall Artery Capacity Heat Pipe," Paper No. AIAA-83-0318, AIAA/ASME 21st Aerospace Science Meeting, Reno, Nevada, January 10-13, 1983.
5. P. Dunn and D.A. Reay, Heat Pipes. (Pergamon, New York, 1976), p. 76-78.
6. R.A. Seban and A. Faghri, "Film Condensation in a Vertical Tube with a Closed Top," International Journal of Heat and Mass Transfer. Vol. 27, No 6, pp. 944-948, 1984.
7. Y. Kamontani, "Analysis of Axially Grooved Heat Pipe Condensers," Paper No. AIAA-76-147, 1976.
8. V.A. Babenko, M.M. Levitan and D.K. Khrustalev, J. Eng. Phys., Vol. 40, p. 6. 1981.
9. L.I. Vassilev, L.P. Grakovich and D.K. Khrustalev, "Low-Temperature Axially Grooved Heat Pipes," Proceedings of the IV International Heat Pipe Conference, London, Sept. 1981.
10. Hwang-Bo and W.E. Hilding, "Optimization of a Heat Pipe with a Wick and Annulus Liquid Flow," J. Heat Transfer, May 1972.

1983-84 USAF-SCEEE RESEARCH INITIATION PROGRAM

Sponsored by the

AIR FORCE OFFICE OF SCIENTIFIC RESEARCH

Conducted by the

SOUTHEASTERN CENTER FOR ELECTRICAL ENGINEERING EDUCATION

FINAL REPORT

AVIONICS RELIABILITY ANALYSIS

Prepared by: Dr. Robert Foley

Academic Rank: Assistant Professor

Department and
University: Industrial Engineering Department
Virginia Polytechnic Institute & State University

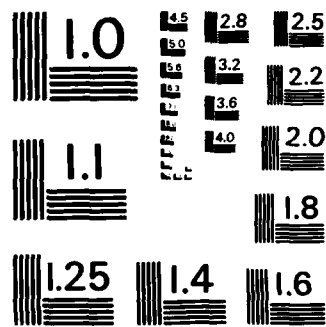
Research Location: Air Force Human Resources Laboratory/Wright-Patterson AFB

Date: December 1984

Abstract

The U.S. Air Force is developing an integrated communications, navigation, and identification avionics system known as ICNIA for use in tactical aircraft. Designers of ICNIA as well as the Air Force need to be informed of the reliability of proposed designs. Hence, the Air Force contracted The Analytic Sciences Corporation (TASC) to develop a model of ICNIA and to develop algorithms for determining various system performance measures such as the system reliability. TASC developed the ICNIA model and developed MIREM which analyzes ICNIA. Unfortunately, due to the complexity of ICNIA, the developers of MIREM were forced to incorporate several approximations in MIREM. In Foley (1983), we showed that these approximations may grossly overestimate the system reliability in some simple examples. Their accuracy on realistic examples is unknown.

We have developed and implemented two algorithms for analyzing ICNIA. The algorithms do not use any approximations and are computationally feasible on realistic sized examples. It is recommended that MIREM be modified to use the algorithms described in this paper.



MICROCOPY RESOLUTION TEST CHART
NATIONAL BUREAU OF STANDARDS-1963-A

1. Introduction

Overview. The U.S. Air Force is developing an integrated communication, navigation, and identification avionics (= aviation electronics) system known as the ICNIA system for use in tactical aircraft. Design work is currently being done at both ITT and TRW. Designers of ICNIA as well as the Air Force need to know the reliability of proposed designs. Hence, the Air Force contracted The Analytic Sciences Corporation (TASC) to develop a model of the ICNIA system and to develop algorithms for computing various performance measure such as the system reliability.

TASC developed a model of ICNIA and a computer package MIREM which computes various performance measures. Unfortunately due to the complexity of ICNIA, the direct ways of analyzing ICNIA were computationally impossible. Hence, the designers of ICNIA were forced to incorporate several approximations in MIREM to reduce the amount of computation to a reasonable level. In Foley (1983), we showed that these approximations may grossly overestimate the system reliability in some simple examples. Their accuracy on realistic examples is unknown. By realistic examples, we mean the systems being developed at ITT and TRW.

We have developed two algorithms for analyzing ICNIA neither of which uses approximations. The algorithms have been implemented and tested on several examples including the ITT and the TRW designs. The design details of the ITT and TRW systems are proprietary information and cannot be disclosed in this document. The algorithms required little computational effort even on realistic examples. In fact, the computational effort was so small that we always used WATFIV and the "// Quickie job card" for small batch jobs of less than 20 seconds.

Reader's Guide. In the remainder of this section, we briefly describe the performance measures of interest, our results, and our recommendations. We urge the reader to look over these topics before jumping ahead. Section 2 describes the ICNIA model in detail. Readers who are familiar with the ICNIA model may choose to skim or skip Section 2. Readers who wish to know none of the details of ICNIA should skip to Section 6, the Summary.

We cannot take credit for the model described in Section 2. TASC devoted an enormous amount of time poring over blueprints and discussing the problem with the U.S. Air Force, TRW, and ITT in developing the model. We merely describe the model for the reader's convenience. Sections 3 and 4 are the heart of this document. They describe the mathematical basis for our Algorithms I and II. Readers who wish to take mathematics on faith may jump to Section 5 in which we report our computational results on a variety of examples. Section 6 contains a summary and suggests further research topics.

There is little literature devoted to the reliability of ICNIA. Veatch, Calvo, and Myers (1983) and Veatch (1983) describe the ICNIA model and the mathematical basis of MIREM. Foley (1983) describes some of the assumptions of the ICNIA model, points out the difficulties with MIREM's approximations, describes an approach to the mission-phasing problem which will be described later, and makes some initial suggestions for improving the algorithms analyzing ICNIA.

Performance Measures of Interest. There are three basic performance measures: the system reliability, the mean time until system failure, and a measure of the fault tolerance of the system. We assume that the ICNIA system is initially in perfect working condition. During the course of a mission various components may fail until eventually the ICNIA system is unable to

perform its tasks satisfactorily. Let T be the length of time that ICNIA is working. The designers of ICNIA and the Air Force wish to be able to compute the system reliability

$$R(t) = P\{T > t\}. \quad (1.1)$$

$R(t)$ gives the probability that the ICNIA system performs satisfactorily on a mission of length t hours. It would be nice if a closed form expression for the function $R(t)$ could be found. Unfortunately that seems impossible. The best that can be done seems to be to have a computer program which given the ICNIA system specification and the length of the mission t , computes a single number $R(t)$.

The next performance measure of interest is the mean time until the ICNIA system fails

$$E[T]. \quad (1.2)$$

Since

$$E[T] = \int_0^{\infty} R(t)dt, \quad (1.3)$$

the reliability function $R(t)$ determines $E[T]$. However, since we do not have a closed form expression for $R(t)$, we are forced to numerically integrate the r.h.s. of (1.3) over $[0, \infty)$ which is difficult especially without qualitative knowledge of the behavior of $R(t)$ for large t . Thus, we would prefer to avoid numerically integrating the r.h.s. of (1.3) if possible.

A third performance measure of interest known as the failure resiliency attempts to capture the amount of fault tolerance of the system. The ICNIA system is intelligent enough to detect failures of components and reconfigure itself in order to continue performing required tasks. The failure resiliency is defined as the mean time until system failure $E[T]$ divided by the mean time

until the first component failure. Large failure resiliency values are supposed to correspond to systems with more fault tolerance. However, the failure resilience does not really capture the fault tolerance. For example, one could add superfluous components which would decrease the mean time until the first component failure without affecting the time until system failure resulting in an increased failure resiliency. A better measure of fault-tolerance which we call the modified failure resilience and defined roughly as the mean time until system failure divided by the mean time until system failure without allowing ICNIA to detect errors and reconfigure itself. We will define it more precisely later.

Results. We have developed and implemented two Algorithms, I and II, which analyze an ICNIA model. Algorithm I requires as input the specifications of the ICNIA system and the length of the mission t . The algorithm determines the exact system reliability $R(t)$ without using approximations. The only source of error is computer round-off error.

Algorithm II requires as input only the specifications of the ICNIA system. Algorithm II determines two functions $a(\cdot)$ and $b(\cdot)$ such that for every t

$$a(t) < R(t) < b(t).$$

Algorithm II also determines two number u and v such that

$$u < E[T] < v.$$

Thus we have upper and lower bounds for the system reliability function $R(t)$ and for the mean time until system failure $E[T]$. In practice the upper and lower bounds have been extremely close to each other. In addition, the functions $a(t)$ and $b(t)$ are simple closed form equations which can be evaluated on a hand-held calculator.

Both algorithms have been implemented and used on a variety of examples including the ITT and TRW architectures. In all cases, the algorithms have required little computational effort.

Recommendations. MIREM should be modified to use Algorithms I and II in analyzing ICNIA models. In addition, instead of computing the failure resiliency MIREM should compute the modified failure resiliency.

2. Model Description

We give a top-down description of the ICNIA model. At the top level ICNIA is a black box which performs all of the navigation, identification, and communication avionics functions. A subset of these functions is designated as the set of critical functions. The ICNIA system attempts to support all of the critical functions for as long as possible. The time at which ICNIA can no longer support all of the critical functions is the time at which ICNIA fails and is denoted by T. The set of critical functions may change from one mission to another or even within the different phases of a single mission. However, we will assume in this paper that the set of critical functions does not change during a mission, i.e., a single-phase mission. Multi-phase mission can be analyzed as described in Foley (1983) once single phase missions can be analyzed.

At the next level, we divide the ICNIA system into s stages as shown in Figure 2.1. The critical functions must be supported at each stage in order for ICNIA to be working.

Each stage consists of either a single chain or a parallel chain as shown in Figures 2.2a and 2.2b. In a parallel chain, each critical function is assigned to either the upper or lower chain. In a single chain, all critical functions are assigned to the only chain in that stage. Thus, each critical function is routed through ICNIA. At each parallel stage, there are 2^c ways of allocating where c is the number of critical functions. There are 2^n ways of allocating functions through ICNIA where n is the number of parallel chain stages.

Each chain contains several pools. A pool contains several components of the same type. We assume that each pool in a parallel chain has a

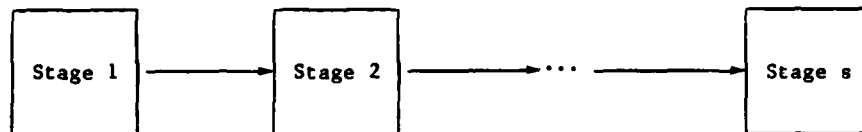
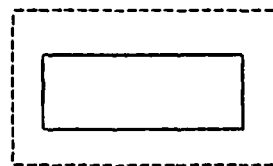
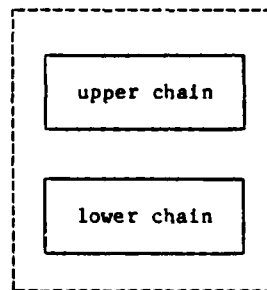


Figure 2.1. The s Stages of ICNIA.



(a)



(b)

Figure 2.2. (a) Single chain and (b) Parallel chain.

corresponding pool in the other chain which contains components of the same type but not necessarily the same number. In reality, there may not be a corresponding pool containing components of the same type. In this case, we assume that there is, but it is empty.

The components are the basic resources required by the critical functions. Each critical function has some requirement, possibly zero, for each of the types of components. Pools are classified into several different types depending on how the functions compete for the components in that pool. A contending pool is a pool in which the pool must have sufficient working components to satisfy the sum of all the requirements for that component by all of the critical functions assigned to that chain. Thus, if there are two critical functions assigned to that chain and one needs 3 units of a particular type of component and the other needs 4.7 units of that component, there needs to be at least 8 working components to satisfy the demand of the two critical functions. The opposite of a contending pool is a non-contending pool in which the critical functions can use the same components in a pool without interference. Thus, if we have the same example with only two critical functions, one requiring 3 and the other 4.7 units of a particular component, there only needs to be five working components. Thus, with non-contending pools, there only needs to be a sufficient number of components to meet the demand of the critical function placing the highest demand on the pool.

In a parallel chain, some of the corresponding pairs of pools may be physically linked to each other, e.g., through a data bus, such that critical functions allocated to one of the parallel chains can use the components in the corresponding pool in the other chain. Pools physically linked in this

fashion are called sharing pools. In theory, there could either be sharing, contending pools and sharing, non-contending pools. In practice, we have only encountered sharing, contending pools.

The last pool type has to do with the power supply. Each chain has a power supply and if the power supply fails, none of the components in that chain can be used. The power supply is treated as a non-contending pool containing a single component, and every critical function allocated to that chain needs one unit of power supply. We have to be especially careful of the sharing pools. A critical function allocated to one chain in a parallel chain can use components in sharing pools in the other parallel chain only so long as the power supply is working in the other parallel chain. Thus, in order for any critical function to take advantage of the sharing feature, both power supplies in the parallel chains must be working.

Now we can classify the four pool types in ICNIA

C - contending, but not sharing

N - non-contending, excluding the power supply

S - sharing, contending pools

F - the power supply.

Since we have not encountered sharing, non-contending pools, we have not bothered to include them.

We assume that all of the components are initially working. The components have independent, exponentially distributed lifetimes. All of the components within a pool have identically distributed lifetimes. To describe the system, we need to know the number of stages, whether each stage is a single or parallel chain, the number of pools (or pairs of pools in parallel chains), the number of components in each pool, the parameter for the

distribution of the lifetimes in each pool, the type of each pool, the number of critical functions, the requirements of each critical function from each pool or (pair of pools in parallel chains), any any special restrictins on the allocation of functions in parallel chains. That is, there may be special restrictions requiring a particular critical function to be allocated through a particular chain of a parallel chain.

3. Algorithm I

The goal of this section is to develop a computationally feasible algorithm for determining the reliability of the model described in Section 2. To give a rough idea of the size of the problem, Realistic examples might have 50 to 100 pools and anywhere from 4 to 8 critical functions. With 8 critical functions, there are $2^8 = 1024$ ways of allocating the critical functions in each parallel chain stage.

The first step in analyzing the system is to note that each stage can be analyzed separately. Since each of the stages behave independently, the reliability of the system is the product of the reliabilities at each stage.

Single-chain stage. The reliability of a single-chain stage can be computed without too much difficulty as follows. Assume that stage i is a single-chain stage. Let $R_i(t)$ denote the reliability of stage i , n the number of pools in stage i , c the number of critical functions, and r_{jk} the requirement on pool j by critical function k . The total demand d_j on pool j is

$$d_j = \begin{cases} \left\lceil \sum_{k=1}^c r_{jk} \right\rceil & \text{for type C pools,} \\ \left\lceil \max_{1 \leq k \leq c} \{r_{jk}\} \right\rceil & \text{for type N or F pools,} \end{cases}$$

where $\lceil x \rceil$ denotes the least integer greater than or equal to x . In a single-chain pool, there are no type S pools. Let $N_j(t)$ denote the number of working components in pool j and $1/\lambda_j$ the mean lifetime of each component in pool j . Note that $N_j(0)$ is the number of components in pool j . Then

$$P\{N_j(t)=k\} = \binom{N_j(0)}{k} \left(e^{-\lambda_j t} \right)^k \left(1 - e^{-\lambda_j t} \right)^{N_j(0)-k}$$

and

$$R_1(t) = \prod_{j=1}^n P(N_j(t) > d_j).$$

Parallel chain stage. Parallel chain stages are substantially more complicated than single-chain stages. Assume that i is a parallel chain stage and that there are c critical functions. Then there are 2^c possible allocations of the critical functions since each function can be assigned either to the upper or lower parallel chain stages. A feasible allocation is an allocation that satisfies all of the constraints at each of the pools and any special restrictions. The allocations create dependencies among the pairs of pools. A particular allocation might appear to be feasible when considering only one pool but turn out to be infeasible after considering another. A feasible allocation must simultaneously satisfy the constraints at each pair of pools. Let A_k denote the event that allocation k is feasible.

Then in Foley (1983), the reliability of stage i was expressed as

$$R_1(t) = P(A_1 \text{ or } A_2 \text{ or } \dots \text{ or } A_{2^c}) \quad (3.1)$$

where 2^c is the number of allocations. Equation (3.1) was rewritten as

$$\begin{aligned} R_1(t) = & P(A_1) + P(A_2) + \dots + P(A_a) \\ & - P(A_1 A_2) - P(A_1 A_3) - \dots - P(A_{a-1} A_a) \\ & + P(A_1 A_2 A_3) + \dots + P(A_{a-2} A_{a-1} A_a) \\ & \vdots \\ & + (-1)^{a+1} P(A_1 A_2 \dots A_a) \end{aligned} \quad (3.2)$$

where $a = 2^c$. Each one of the terms in (3.2) can be evaluated with roughly the same amount of work as analyzing a single-chain stage. Unfortunately, the

number of terms on the r.h.s of (3.2) is $2^a = 2^{2^c}$ where c is the number of critical functions. Since c might vary from 4 to 8, the amount of work evaluating the r.h.s. of (3.2) may vary substantially as can be seen from Table 3.1

c	2^c	2^{2^c}
4	16	65,536
5	32	4,294,967,296
6	64	$\approx 1.8 \times 10^9$
7	128	$\approx 3.4 \times 10^{38}$
8	256	$\approx 1.1 \times 10^{77}$

Table 3.1. 2^{2^c} is the number of terms on the r.h.s. of (3.2).

Clearly, evaluating the r.h.s. of (3.2) becomes doubtful very quickly. It was hoped that (3.2) might be computed cutting down on the number of terms in realistic examples through using only feasible allocations instead of all possible allocations, through truncating (3.2) after an entire row is zero, or through truncating (3.2) in order to obtain bounds on the reliability. These measures proved unnecessary since a rather simple measure, to be described shortly, dramatically reduced the number of terms.

To analyze this parallel chain stage 1, we will first eliminate a couple of easy cases. If both power supplies are down, stage 1 is down. If one power supply is up and the other is down, the chain with the working power supply can be treated as a single chain stage. Note that none of the sharing pools in the other chain can be used, and all of the critical functions must be allocated to the chain with the working power supply. In the remainder of

this section, we assume that and use an asterisk to emphasize that $R_1^*(t)$ is the reliability of stage conditional on both power supplies working.

Let n_s denote the number of sharing pools in stage i . The demand on the j th pair of sharing pool is

$$d_j^s = \left\lceil \sum_{k=1}^c r_{jk} \right\rceil$$

where $\lceil x \rceil$ denotes the least integer greater than or equal to x and r_{jk} the requirement on pool-pair j by critical function k . Let $N_j^s(t)$ denote the total number of working components, upper plus lower, in the j th pair of sharing pools. Then

$$P\{N_j^s(t) = \ell\} = \binom{N_j(0)}{\ell} \left(e^{-\lambda_j t} \right)^\ell \left(1 - e^{-\lambda_j t} \right)^{N_j(0) - \ell}$$

and

$$R_j^*(t) = \left[\prod_{j=1}^{n_s} P\{N_j^s(t) > d_j^s\} \right] P\{\text{a feasible allocation exists on the contending and non-contending pools}\}. \quad (3.3)$$

Thus we need to determine the $P\{\text{a feasible allocation exists on the contending and non-contending pools}\}$. Let us redefine A_k as the event that the k th allocation is feasible on for the contending and non-contending pools. Let $d_j^u(k)$ denote the demand on the upper pool of pool-pair j under allocation k . We have

$$d_j^u(k) = \begin{cases} \left\lceil \sum_{m=1}^c r_{jm}^u \right\rceil & j \text{ is contending,} \\ \left\lceil \max_{1 \leq m \leq c} \{r_{jm}\} \right\rceil & j \text{ is non-contending,} \end{cases}$$

where r_{jm}^u is the demand on the upper pool of pool-pair j by the m th critical function. Similarly on the lower pool

$$d_j^l(k) = \begin{cases} \left[\sum_{m=1}^c r_{jm}^l \right] & \text{pool } j \text{ is contending,} \\ \left[\max_{1 \leq m \leq c} (r_{jm}^l) \right] & \text{pool } j \text{ is non-contending.} \end{cases}$$

Now,

$$P\{\text{a feasible allocation exists on the contending and non-contending pools}\} = P(A_1 \text{ or } A_2 \text{ or } \dots \text{ or } A_c) \quad (3.4)$$

which can be expanded as in (3.2). Terms such as $P(A_k)$ can be computed

$$P(A_k) = \prod_{j=1}^{n_c+n} [P\{N_j^u(t) > d_j^u(k)\} P\{N_j^l(t) > d_j^l(k)\}] \quad (3.5)$$

where n_{c+n} is the number of contending and non-contending pools. More complicated terms are computed as

$$P(A_{k_1} A_{k_2} \dots A_{k_m}) = \prod_{j=1}^{n_c+n} [P\{N_j^u(t) > \bigvee_{r=1}^m d_j^u(k_r)\} P\{N_j^l(t) > \bigvee_{r=1}^m d_j^l(k_r)\}]$$

where \bigvee denotes "maximum of".

Thus, in principal, we can determine the system reliability using the above approach but we have not yet eliminated the problem of too many terms to evaluate. The problem occurs only when trying to evaluate the r.h.s. of (3.4) using the expansion shown in (3.2). Again, since the number of allocation is 2^c , the total number of terms to be evaluated is 2^{2^c} where c is the number of critical functions. The number of allocations can be reduced by noting that two allocations may result in the same demands on the contending and non-contending pools. That is, two events A_{k_1} and A_{k_2} are substantively identical if for every contending or non-contending pool j in the parallel chain

$$d_j^u(k_1) = d_j^u(k_2) \text{ and } d_j^l(k_1) = d_j^l(k_2).$$

If two allocations are substantively identical, one of the allocations can be eliminated from the r.h.s. of (3.4). This rather simple observation dramatically reduced the allocations that need to be considered. On the realistic examples with 6 critical functions, the number of allocations was reduced from $2^6 = 64$ to anywhere between 3 and 8. This reduces the number of terms that need to be evaluated from $2^{2^6} \approx 1.8 \times 10^{19}$ to anywhere between $2^3 = 8$ and $2^8 = 256$. Thus, eliminating substantively identical allocations from the r.h.s. of (3.4) reduces the number of terms that needs to be computed from an unreasonable level to a relatively small number which can be computed without much difficulty.

A rough sketch of Algorithm I. In order to implement the algorithm, one needs to know the substantively different allocations. The easiest way is to simply build a small data structure which will contain the demands $d_j^u(k)$ and $d_j^l(k)$ on the contending and non-contending pools of the substantively different allocations. To build the data structure, loop through all possible allocations. With each allocation check if it is substantively identical to an allocation already in the data structure. If it is, throw it away; if it isn't, insert it in the data structure. Conveniently, the substantively different allocations do not depend on the number of components in a pool or the reliability of the components in a pool. Thus the data structure does not need to be modified if the number of components in a pool or the reliability of the components is changed. In addition, if the algorithm is capable of computing the reliability a particular system, the algorithm should still be able to compute the reliability after changing the reliability of the components or the number of components in various pools since this has very little effect on the computational effort. The small number of substantively

different allocations has other implications which will be discussed in the Summary.

A rough sketch of the Algorithm is:

For $i = 1$ to s stages;

If stage i is a single chain stage then compute

$R_i(t)$ as described in the beginning of this section;

If stage i is a parallel chain stage then

Begin break it into 4 cases depending on the states of the 2 power supplies;

Compute the reliability in 3 of the 4 cases easily;

in the fourth case (both power supplies are up)

build the data structure;

determine the reliability of the sharing pools;

compute the reliability of the contending and

non-contending pools;

compute the reliability of the fourth case as the

product of the reliability of the sharing pools with the contending and non-contending pools;

compute the reliability of the parallel stage as the

weighted sum of the reliabilities of the 4 cases;

End;

Endloop;

Compute the system reliability as the product of the stage reliabilities.

Algorithm I has been implemented and has computed the reliability in all of the examples as described in Section 4.

4. Algorithm II

Algorithm II was initially developed since we thought that Algorithm I would prove to be computationally infeasible on some realistic problems. Even though Algorithm I has proved to be computationally feasible on all problems attempted so far, Algorithm II is still useful and, in fact, may be the more valuable of the two.

Algorithm II requires as input the description of the ICNIA model. It does not require the length of the mission t . It produces two functions $a(\cdot)$ and $b(\cdot)$ such that for all $t > 0$

$$a(t) < R(t) < b(t).$$

and two numbers u, v such that

$$u < E[T] < v.$$

That is, it produces upper and lower bounds on the reliability function of the system and on the mean lifetime of the system. More specifically, there exists two sequences of functions $a_1, a_2, \dots, b_1, b_2, \dots$ such that

$$a_1(t) < a_2(t) < R(t) < b_2(t) < b_1(t)$$

and two sequences of numbers $u_1, u_2, \dots, v_1, v_2, \dots$, such that

$$u_1 < u_2 < \dots < E[T] < \dots < v_2 < v_1$$

and, in addition,

$$R(t) = \lim_{n \rightarrow \infty} a_n(t) = \lim_{n \rightarrow \infty} b_n(t)$$

$$E[T] = \lim_{n \rightarrow \infty} u_n = \lim_{n \rightarrow \infty} v_n.$$

In our implementation, we have computed $a_2(\cdot)$, $b_2(\cdot)$, u_2 , and v_2 which have provided very good bounds on the quantities of interest. Algorithm's II advantages over I is that it gives functions which provide good bounds on the

system reliability over all times t rather than simply the reliability at one point in time. In addition, the bounds on the mean system lifetime can be obtained without numerical integration.

Our approach is as follows. Assume that in the j th pool there are n_j components and each components' lifetime is exponentially distributed with mean $1/\lambda_j$. Suppose that each component has a bell which rings according to a Poisson process with rate λ_j . The first bell rings at a component when the component fails. Even when it is broken, the bell still goes off according to a Poisson process. The Poisson processes at each component are mutually independent. Since the superposition of independent Poisson processes is a Poisson process, the bell process in the j th pool is a Poisson process with rate $n_j \lambda_j$. We can either analyze the entire system or a stage. We will assume that we are analyzing stage i ; the extension to an entire system is straightforward. The bell process for the stage i is a Poisson process with rate $\lambda = \sum_j n_j \lambda_j$ where the summation is over all pools j in the subsystem. The reliability of the i th stage can be expressed as

$$R_i(t) = \sum_{k=0}^{\infty} \frac{e^{-\lambda t} (\lambda t)^k}{k!} p_k \quad (4.1)$$

where p_k is the probability that stage i is still working at time t given that k bells were heard from stage i during $(0, t]$. If k bells have been heard, there may have been anywhere from 1 to k failures. The functions $a_n(\cdot)$ and $b_n(\cdot)$ are defined by

$$a_n(t) = \sum_{k=0}^n \frac{e^{-\lambda t} (\lambda t)^k}{k!} p_k \quad (4.2)$$

and

$$\begin{aligned}
b_n(t) &= \sum_{k=0}^n \frac{e^{-\lambda t} (\lambda t)^k}{k!} p_k + \sum_{k=n+1}^{\infty} \frac{e^{-\lambda t} (\lambda t)^k}{k!} p_n \\
&= \sum_{k=0}^n \frac{e^{-\lambda t} (\lambda t)^k}{k!} p_k + p_n \left(1 - \sum_{k=0}^n \frac{e^{-\lambda t} (\lambda t)^k}{k!} \right) \quad (4.3)
\end{aligned}$$

The function $a_n(t)$ is clearly a lower bound since we are merely truncating the series in (4.1) and all of the terms are non-negative. The function $b_n(t)$ is an upper bound since p_k is non-increasing in k . The functions $a_n(\cdot)$ and $b_n(\cdot)$ can be easily computed once p_k can be computed. Suppose there are m pools in stage i . Let k_1, \dots, k_m be non-negative integers such that $k_1 + \dots + k_m = k$. Let $p_{k_1, \dots, k_m | k}$ denote the probability that k_j bells were heard from pool j given k bells were heard from stage i during $[0, t]$. Then $p_{k_1, \dots, k_m | k}$ has a multinomial distribution

$$p_{k_1, \dots, k_m | k} = \binom{k}{k_1, \dots, k_m} \left(\frac{n_1 \lambda_1}{\lambda} \right)^{k_1} \dots \left(\frac{n_m \lambda_m}{\lambda} \right)^{k_m} \quad (4.4)$$

where $k_1 + \dots + k_m = k$. Now let $f_{r_j | k_j}^{n_j}$ denote the probability that r_j components failed in a pool given that k_j bells were heard from a pool with n_j components. Clearly, if $k_j > 0$, then $1 < k_j < r_j$, and if $k_j = 0$, then $r_j = 0$.

$$p_k = \sum_{\substack{k_1, \dots, k_m \\ k_1 + \dots + k_m = k}} p_{k_1, \dots, k_m | k} \sum_{\substack{r_1, \dots, r_m \\ 0 < r_j < k_j}} \prod_{j=1}^m f_{r_j | k_j}^{n_j} \phi(n_1 - r_1, n_2 - r_2, \dots, n_m - r_m) \quad (4.5)$$

where $\phi(x_1, x_2, \dots, x_m)$ is 1 if stage i can function with x_j working components in pool j for each of the pools, and zero otherwise. The only terms left to compute is $f_{r_j | k_j}^{n_j}$ which is the probability of r_j real failures given that k_j bells were heard from a pool with n_j components.

Clearly,

$$f_{r_j|0}^{n_j} = \begin{cases} 1 & \text{if } r_j = 0 \\ 0 & \text{if } r_j \neq 0 \end{cases}$$

$$f_{r_j|1}^{n_j} = \begin{cases} 1 & \text{if } r_j = 1 \\ 0 & \text{if } r_j \neq 1 \end{cases}$$

Other values can be computed from the recurrence relation

$$f_{r_j|k_j+1}^{n_j} = \frac{r_j}{n_j} f_{r_j|k_j}^{n_j} + \frac{n_j - r_j + 1}{n_j} f_{r_j-1|k_j}^{n_j}.$$

Thus, the p_k 's can be computed from (4.5) and inserted in (4.2) and (4.3) to get the bounds. The amount of effort in computing p_k grows quickly in k . Hence, it's hoped that we can use small values of n in (4.2) and still get good bounds.

As mentioned the above procedure can be implemented on the whole system or on each stage. We implemented the procedure on each stage in order to get bounds on the reliability and the expected lifetime of each stage. The results for each stage can be combined in the following fashion to get the results for the system. Basically, we need to compute the corresponding quantities p_k for the system from the information at each stage. Let p_k^i denote the probability that stage is still working given that k bells were heard from stage i . The quantities p_k^i can be computed by using (4.5) on stage i . Let p_k^* denote the reliability of the entire system given k bells were heard from the system during $[0, t]$. If we let λ_i denote the total rate at which bells ring in stage i , p_k^* can be expressed as

$$p_k^* = \sum_{\substack{k_1, \dots, k_s \\ k_1 + \dots + k_s = k}} \binom{k}{k_1 \dots k_s} \left(\frac{\lambda_1}{\lambda}\right)^{k_1} \dots \left(\frac{\lambda_s}{\lambda}\right)^{k_s} p_{k_1}^1 \dots p_{k_s}^s$$

where $\lambda = \lambda_1 + \dots + \lambda_s$. Now using p_k^* in place of p_k in (4.2) and (4.3) and letting λ denote the total rate at which bells ring in the system yields upper and lower bounds for the reliability of the entire system.

Bounds on the mean lifetime. Now we will describe how upper and lower bounds on the mean lifetime of either a stage or the system can be computed without numerical integration. Assume that we already have upper and lower bounds $a_n(\cdot)$ and $b_n(\cdot)$ such that

$$a_n(t) < R(t) < b_n(t) \quad (4.6)$$

where $a_n(\cdot)$ and $b_n(\cdot)$ are defined in (4.2) and (4.3). We are trying to find u_n and v_n such that

$$u_n < E[T] = \int_0^\infty R(t) dt < v_n. \quad (4.7)$$

We haven't specified whether we are bounding the mean lifetime of a stage or the system since in either case we have an expression of the form where

$$a_n(t) = \sum_{k=0}^n \frac{e^{-\lambda t} (\lambda t)^k}{k!} p_k$$

and

$$b_n(t) = \sum_{k=0}^n \frac{e^{-\lambda t} (\lambda t)^k}{k!} p_k + p_n \sum_{k=n+1}^{\infty} \frac{e^{-\lambda t} (\lambda t)^k}{k!}.$$

From (4.6) and (4.7), we have

$$\int_0^\infty a_n(t) dt < E[T] < \int_0^\infty b_n(t) dt.$$

Now

$$\begin{aligned}
\int_0^{\infty} a_n(t) dt &= \int_0^{\infty} \sum_{k=0}^n \frac{e^{-\lambda t} (\lambda t)^k}{k!} p_k dt \\
&= \sum_{k=0}^n p_k \int_0^{\infty} \frac{e^{-\lambda t} (\lambda t)^k}{k!} dt \quad (\text{Tonelli's Theorem}) \\
&= \frac{1}{\lambda} \sum_{k=0}^n p_k.
\end{aligned}$$

Thus we have a lower bound with a rather pleasant form

$$u_n = \frac{1}{\lambda} \sum_{k=0}^n p_k. \quad (4.8)$$

Repeating the procedure for the upper bound yields

$$\begin{aligned}
\int_0^{\infty} b_n(t) dt &= \int_0^{\infty} \left[\sum_{k=0}^n \frac{e^{-\lambda t} (\lambda t)^k}{k!} p_k + p_n \sum_{k=n+1}^{\infty} \frac{e^{-\lambda t} (\lambda t)^k}{k!} \right] dt \\
&= \frac{1}{\lambda} \sum_{k=0}^n p_k + p_n \sum_{k=n+1}^{\infty} \int_0^{\infty} \frac{e^{-\lambda t} (\lambda t)^k}{k!} dt \\
&= \frac{1}{\lambda} \sum_{k=0}^n p_k + \infty \\
&= \infty
\end{aligned}$$

which does not help a whole lot. Our upper bound on the reliability is too coarse to obtain an upper bound on the mean lifetime. We can refine our upper bound on the system reliability to obtain $b_n^*(\cdot)$ as follows.

From Brown (1983) $p_k^{1/k}$ is non-increasing in k . Hence

$$p_{n+k} < p_n^{(n+k)/n}.$$

Thus,

$$\begin{aligned}
R(t) &= \sum_{k=0}^{\infty} \frac{e^{-\lambda t} (\lambda t)^k}{k!} p_k \\
&= \sum_{k=0}^n \frac{e^{-\lambda t} (\lambda t)^k}{k!} p_k + \sum_{k=1}^{\infty} \frac{e^{-\lambda t} (\lambda t)^{n+k}}{(n+k)!} p_{n+k} \\
&< \sum_{k=0}^n \frac{e^{-\lambda t} (\lambda t)^k}{k!} p_k + \sum_{k=1}^{\infty} \frac{e^{-\lambda t} (\lambda t)^{n+k}}{(n+k)!} p_n^{(n+k)/n} = b_n^*(t).
\end{aligned}$$

We could have used $b_n^*(t)$ as our upper bound since

$$R(t) < b_n^*(t) < b_n(t)$$

except that $b_n(t)$ worked sufficiently well in practice and is simpler to compute than $b_n^*(t)$. However, $b_n^*(t)$ works rather well for obtaining an upper bound on the mean lifetime

$$\begin{aligned} \int_0^{\infty} b_n^*(t) dt &= \frac{1}{\lambda} \sum_{k=0}^n p_k + \sum_{k=1}^{\infty} \int_0^{\infty} \frac{e^{-\lambda t} (\lambda t)^{n+k}}{(n+k)!} p_n^{(n+k)/n} dt \\ &= \frac{1}{\lambda} \sum_{k=0}^n p_k + \frac{1}{\lambda} \sum_{k=1}^{\infty} p_n^{(n+k)/n} \\ &= \frac{1}{\lambda} \left(\sum_{k=0}^n p_k + \frac{p_n^{(1+1/n)}}{(1-p_n^{1/n})} \right). \end{aligned}$$

Thus, we have a relatively simple upper bound on the mean lifetime

$$v_n = \frac{1}{\lambda} \left(\sum_{k=0}^n p_k + \frac{p_n^{(1+1/n)}}{(1-p_n^{1/n})} \right).$$

A rough sketch of Algorithm II is to compute the p_k 's at each stage, obtain upper and lower bounds on the reliability and mean lifetime of each stage, combine the p_k 's to get bounds for the system reliability, and lastly, obtain bounds on the mean lifetime of the system.

5. Implementation and Examples

Implementation. Both algorithms were implemented and tested on a variety of problems including the realistic examples, i.e., the TRW and ITT architectures. The algorithms were implemented in WATFIV-S, a dialect of FORTRAN which produces relatively inefficient code but good diagnostics, and run on an IBM 3081 computer at Virginia Tech. Double precision was used throughout. We made little effort to be clever and write efficient code. Basically, we faithfully implemented the equations appearing in the previous sections. For the bounds, we computed $a_2(\cdot)$, $b_2(\cdot)$, u_2 , and v_2 . The examples were run under "// Quickie" which handles small batch jobs of less than 20 seconds. The longest example required only 3.77 seconds of execution time to execute both algorithms. In other words, we made virtually no effort to implement the algorithms efficiently, yet in all of the examples, little computational effort was required.

Example 1. Example 1 appeared in Foley (1983). The system consists of two parallel chains containing n pools in each chain. There is a single component in each pool and a single critical function which requires one component from each of the n pools in the chain that it is allocated to as shown in Figure 5.1.

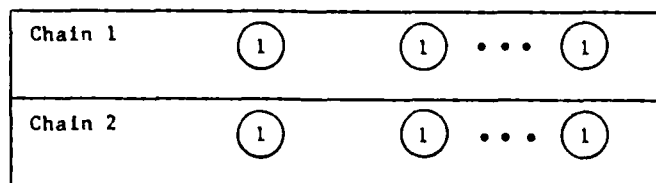


Figure 5.1. Example 1 contains n pairs of pools.

The failure rate of each component is $-\frac{1}{3} \ln .9$. Hence the reliability of each component during a 3 hour mission is .9. We reported the results of MIREM's approximation¹ and the true system reliability, which can be analytically determined, for a 3 hour mission in Foley (1983), and the results are shown in Table 5.1 along with the true mean lifetime E[T].

<u>n</u>	<u>MIREM's Approximations¹</u>	<u>R(3)</u>	<u>E[T]</u>
1	.9900	.9900	42.7
2	.9801	.9639	21.4
3	.9703	.9266	14.2
4	.9606	.8817	10.7
5	.9506	.8323	8.5
10	.9044	.5758	4.3
15	.8601	.3694	2.8
20	.8179	.2284	2.1

Table 5.1. MIREM's approximation vs. the correct answer for Example 1.

The results we obtained using Algorithms I and II are shown in Table 5.2.

<u>n</u>	<u>a₂(3)</u>	<u>R(3)</u>	<u>b₂(3)</u>	<u>u₂</u>	<u>v₂</u>
1	.9896	.9900	.9904	35	53
2	.9617	.9639	.9663	17	26
3	.9205	.9266	.9337	11	18
4	.8696	.8817	.8967	8	14
5	.8128	.8323	.8580	7	11
10	.5127	.5758	.6889	3	6
15	.2823	.3694	.5882	2	4
20	.1427	.2284	.5385	1.7	2.7

Table 5.2. Results from Algorithms I and II on Example 1.

Note that the computed values for R(3) in Table 5.2 agree with the true

¹For this simple example, the current version of MIREM would be able to compute the system reliability. However, this same behavior would occur on slightly more complicated examples. Rather than complicate the example, we will stick with the simple example to illustrate the problem.

values appearing in Table 5.1. In addition, the computed value for $R(3)$ always lies between the upper and lower bounds $a_2(3)$ and $b_2(3)$, and the true value for $R(T)$ always lies between the bounds u_2 and v_2 .

Example 2. The following example appears in Veatch (1983). The system architecture is shown in Figure 5.2.

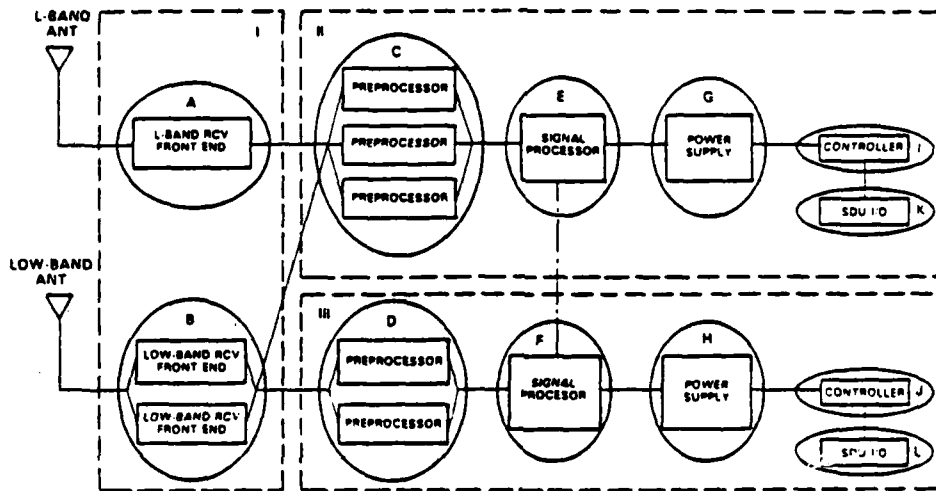


Figure 5.2. A Simplified Fault-Tolerant Architecture (Receive Functions) - from Veatch (1983).

The input data appears in Table 5.3.

Veatch (1983) uses MIREM to analyze the system under two different mission scenarios. In Scenario A, only UHF and SINGARS are critical functions. In Scenario B, all three functions are critical functions. From Figure 1, it appears that GPS (Global Positioning System) must be allocated to the upper chain, Chain II, since GPS uses Pool A and the line going out of pool A goes directly to pool C. However, this is not mentioned in the text,

POOL	CHAIN	DESCRIPTION	UTILIZATION			CAPACITY	COMPONENT FAILURES PER 10 ⁶ HRS	POOL TYPE
			GPS	UHF	SINGARS			
A	I	L-Band Receive Front End	1	-	-	1	50	N
B	I	Low-Band Receive Front End	-	1	1	2	100	N
C	II	Preprocessor	2	1	1	3	300	C
D	III					2		
E	II	Signal Processor	0.8	0.1	0.4	1	100	S
F	III					1		
G	II	Power Supply	1	1	1	1	20	F*
H	III					1		
I	II	Secure Data Unit I/O	-	-	1	1	20	N
J	III					1		
K	II	Controller	1	1	1	1	100	N
L	III					1		

*In Veatch (1983), this F was an N. We assume that was a typo.

Table 5.3. Input Data - from Veatch (1983).
The three functions are GPS, UHF, and SINGARS.

so we are not sure if Scenario B has the extra constraint or not. We will divide Scenario B into two cases: Scenario BW which is Scenario 3 with the constraint, and Scenario BWO which is Scenario B without the extra constraint. In Veatch (1983), the system reliability and mean time until system failure are reported as shown in Table 5.4.

	R(3)	E[T]
Scenario A	.999999	3,357 hrs.
Scenario B	.9989	448 hrs.

Table 5.4. MIREM's results - from Veatch (1983).

Our results for the same system are shown in Table 5.5.

	$a_2(3)$	R(3)	$b_2(3)$	u_2	v_2
Scenario A	.99987912	.999879158	.99987916	1,304 hrs.	11,980 hrs.
Scenario BW	.99852275	.998522759	.99852276	904 hrs.	1,004 hrs.
Scenario BWO	.998522919	.998522920	.998522924	907 hrs.	1,012 hrs.

Table 5.5. Our results for the same system.

Our bounds for the mean time in Scenario A are quite loose, but tighten up substantially in Scenarios BW and BWO. These are a function of p_2 . The smaller p_2 is; the tighter the bounds.

Now in comparing Tables 5.4 and 5.5, note that the system reliability is consistently overestimated by MIREM and clearly falls above the upper bound under both scenarios. The difference appears to be substantially larger than the amount of round-off error occurring. These results are consistent with

Foley (1983) which points out that MIREM's approximations result in overestimating the system reliability. In comparing MIREM's mean time until system failure with our bounds in Scenario B, note that MIREM's approximation of 448 hours falls way below our lower bound of roughly 900 hrs. This is a little surprising. First, since the system reliability is overestimated, one would guess that the mean lifetime would be overestimated. However, the mean lifetime has been grossly underestimated. The reason for this is that even though the reliability is overestimated, the numerical approximations used in integrating the reliability do not overestimate the integral. Hence, it is not clear whether the mean lifetime will be over or underestimated in general.

Example 3. This is one of the realistic examples which cannot be described in detail since the information is proprietary. There were 6 critical functions. It took .27 seconds of execution time, and our results are shown in Table 5.6.

$a_2(3)$	$R(3)$	$b_2(3)$	u_2	v_2
.9977345036	.9977345037	.9977345038	1,257 hrs.	1,305 hrs.

Table 5.6. Our results for Example 3.

Example 4. This is another realistic example on a different architecture than Example 3. Again there were 6 critical functions, and the execution time was 3.77 seconds. Our results appear in Table 5.7.

$a_2(3)$	$R(3)$	$b_2(3)$	u_2	v_2
.997378100	.997378109	.997378115	753 hrs.	1,122 hrs.

Table 5.7. Our results for Example 4.

6. Summary

The existing version of MIREM should be modified to incorporate both of the algorithms described in this paper. The system reliability currently produced by MIREM should only be considered as an upper bound on the system reliability, and the mean lifetime of the system produced by MIREM should only be considered as a rough approximation. The algorithms described in this paper appear to work well, require little computational effort, and should be used.

As we pointed out in Section 3, many of the allocations of the critical functions between the upper and lower chains were substantively identical; i.e., they resulted in exactly the same amount of resources being needed from each pool. In fact, eliminating substantively identical allocations in the realistic examples resulted in the number of allocations decreasing from $2^6 = 64$ to anywhere from 3 to 8. Even some of the remaining allocations may be eliminated since they are infeasible. There are several implications of this large decrease in the number of allocations. The first we used in order to calculate the exact system reliability in Section 3. The second and third implications concerns reallocating functions between parallel chains when errors occur. If there are few substantively different allocations and even fewer feasible, substantively different allocations, it will be much simpler to reallocate functions than had been anticipated. Instead of having to develop a clever algorithm to quickly locate another allocation supporting all of the critical functions, the few feasible, substantively different allocations can be checked. With so few, there should be no need to be fancy. The third implication is that there may be little reason to reallocate functions between parallel chains. That is, the cost of having the ability

to reallocate functions between parallel chains may exceed the benefit of a slight increase in reliability. This can be investigated in the following way.

Define a minor reallocation to be a reallocation which allows critical functions to be reallocated among the components in a pool but does not allow reallocating critical functions between parallel chains. Define a major reallocation to be a reallocation which allows reallocating functions both between parallel chains and among components in pools. A measure of the increase in reliability due to allowing major reallocations is the modified failure resiliency mentioned in the introduction. The modified failure resiliency is the ratio of the mean system lifetime allowing major reallocations to the mean system lifetime without allowing any reallocations. The mean lifetime without reallocations is not yet well defined since it depends on the initial allocation. It seems reasonable to start with a best allocation initially. A best allocation is easy to find since the mean lifetime is the inverse of the sum of the failure rates of all the components used in the allocation. The modified failure resiliency is a more accurate measure of the ability of the system to overcome failures of components.

Similarly we can compute the modified failure resiliency allowing minor reallocations which is the mean system lifetime allowing only minor reallocations. The denominator is the same as in the previous paragraph. The mean lifetime allowing minor reallocations can be computed by restricting critical functions to the chains that they are initially allocated to. Again we should start off with a best initial allocation. In this case, we will probably have to check the mean lifetime of all substantively different allocations without allowing major reallocations in order to locate a best

initial allocation between parallel chains.

If the two ratios are close to each other, then there would be little advantage in allowing major reallocations over minor reallocations. If the ratios are close to each other and close to one, then there would be little advantage in allowing reallocations at all.

The two algorithms are clearly useful for designers of ICNIA. They can see the affect of adding a component to a pool or changing a pair of pools from contending to sharing, etc. However, these changes are discrete. It would also be useful to know the partial derivative of the system reliability $R(t)$ with respect to the failure rate of components in the j th pool, i.e., $\partial R(t)/\partial \lambda_j$. These quantities would allow designers to know which components should have their reliability improved in order to obtain greatest increase in the system reliability. This approach is philosophically more in step with the overall concept of ICNIA since ICNIA was designed in order to use fewer components reducing the weight and volume of the avionics system.

Acknowledgements

We would like to thank Jim McManus of AFHRL and Mike Veatch of TASC for their help. In particular, Mike Veatch's comments on and insights into the behavior of ICNIA led us to develop Algorithm II. We would also like to thank the Southeastern Center for Electrical Engineering Education and the Air Force Office of Scientific Research for supporting this work under Contract F49620-82-C-0035 Subcontract No. 83 RIP 32.

References

- Brown, Mark and N. R. Chaganty (1983) On the first passage time distribution for a class of Markov chains. Annals of Probability, 11, 1000-1008.
- Foley (1983) MIREM and mission phasing. Technical Report 8404, Department of Industrial Engineering and Operations Research, Virginia Polytechnic Institute and State University, Blacksburg, Virginia.
- Veatch (1983) Reliability of integrated, fault-tolerant avionics. Presented at the 1983 ORSA/TIMS conference in Orlando. The Analytic Sciences Corporation.
- Veatch, M. H., Calvo, A. B. and J. B. Myers (1983) Logistics engineering design techniques for fault-tolerant avionics. The Analytic Sciences Corporation, TIM-4128-1.

1983-84 USAF-SCEEE RESEARCH INITIATION PROGRAM

Sponsored by the

AIR FORCE OFFICE OF SCIENTIFIC RESEARCH

Conducted by the

SOUTHEASTERN CENTER FOR ELECTRICAL ENGINEERING EDUCATION

FINAL REPORT

COMMUNICATIONS NETWORK SIMULATION TOPICS WITH A COMPUTER

NETWORK SIMULATION MODEL

Prepared by: Dr. Eddie R. Fowler

Academic Rank: Associate Professor

Department and
University: Electrical & Computer Engineering
Kansas State University

Research Location: Air Force Weapons Laboratory

Date: April 1985

Contract No. F49620-82-C-0085

FINAL REPORT 83 RIP 48

COMMUNICATIONS NETWORK SIMULATION TOPICS - With A Computer
Network Simulation Model

by

Dr. Eddie R. Fowler

ABSTRACT

This report presents an executive summary followed by three sections that cover four communications network simulation topics. Section I discusses computer network graphical methods, network measures of effectiveness (MOE), and a computer network simulation model with a User's Manual and example "run". Section II discusses simulation validation, network MOE, and the DELPHI sequence to identify and prioritize network MOE. Section III discusses network MOE and the applicability of factor analysis to analyze MOE.

ACKNOWLEDGEMENTS

The author would like to thank the Air Force Office of Scientific Research and the Southeastern Center for Electrical Engineering Education for providing him with the opportunity to research communications network simulation topics.

He wishes to thank Russell Thomas, Kurt Ziegler, and Ron Hightower, his graduate students, for their research contributions, many late nights spent on the computer terminals, and researching topics that they may not have chosen if they were given a choice.

Finally, he wishes to thank his wife, Patricia Ann, for typing, proof reading, and collating this report.

1.0 Introduction. This is an executive summary of the topics presented in considerable detail in the three sections that follow. The executive summary topics presented are: communications network measures of effectiveness (MOE), MOE development methodology using DELPHI techniques and factor analysis, and communications network simulations. This portion of the report summarizes the research efforts of three graduate students [8, 11, 12] and the author.

1.1 Research Motivation. The military mission of the United States Air Force (USAF) requires it to have a research interest in communications network degradation resulting from nuclear detonations and/or electronic warfare (EW). This research interest can further be defined as desiring to develop improved analysis techniques to: quantify degradation levels and effects; and, suggest mitigation techniques to reduce the level of degradation.

1.1.1 The present analytical techniques for quantifying network degradation are time consuming, costly, and yield results with high levels of uncertainty. Two specific analytical technique problems are: massive computer simulation programs that defy validation; and, non-standard MOE upon which to structure the simulation program.

1.1.2 These two problems are created by the following situations.

1.1.2.1 There exists only limited or no empirical data to use for simulation validation purposes. Atmospheric testing of nuclear weapons has been outlawed for many years and the atmospheric test substitutes have been very poor.

1.1.2.2 No Department of Defense (DoD) agency has developed a set of standard analytical validation procedures for massive computer simulation programs.

1.1.2.3 No DoD agency has approved a standard set of MOE upon which to structure a massive simulation.

1.1.2.4 For massive simulations, serially interfaced modules have orders of magnitude differences in simulation levels of resolution so that output errors in one module may become primary input data for a follow-on module.

1.1.2.5 High resolution modeling for massive simulations require an excessive number of simulation parameters for some (or all) modules and these cause the simulation to manifest the "chaos factor".

1.1.2.6 High resolution modeling for massive simulations require excessive pre- and post-processing times (man-months) along with excessive CPU run time and cost.

1.1.2.7 Results from massive simulation runs are so slow coming that they have no significant impact on early system

design and procurement.

1.1.2.8 No approved "quick and dirty" (Q&D) computer simulations exist.

1.2 Research Objectives. Based on the motivations described in Para. 1.1.2, the following research objectives were established and are discussed in this report.

1.2.1 Review and become familiar with some present USAF communications network degradation simulations. From this review, identify presently used simulation MOEs, structures, techniques, levels of resolution, input & output parameters, run times, pre- and post-processing times, validation techniques, and applications.

1.2.2 Develop a technique for identifying appropriate MOE upon which to structure a communications simulation.

1.2.3 Develop a technique for determining the relationships among proposed MOE to be used in a communications network simulation.

1.2.4 Develop a Q&D communications network simulation that is valid, user friendly, timely, and runs on an inexpensive desk top computer.

1.3 Previous Work. Many USAF studies have been conducted and documented on nuclear environment analysis, models, and system design. Because of the abundance of documents in these areas, Appendix A, Bibliography, has been included in

this report to record those documents identified in the literature survey that was conducted.

1.3.1 Appendix A, Section I-PNAC is dedicated to documentation associated with the USAF communications network simulation, "Propagation Network Analysis Code (PNAC)". Section II is dedicated to module modeling that supports PNAC, Section III is dedicated to satellite systems in nuclear environments, and Section IV is dedicated to nuclear environment models and design. Three different contractors accomplished the development of the most of this documentation. They are: Mission Research Corporation (MRC); Berkeley Research Associates (BRA); and, Computer Sciences Corporation (CSC). As will be noted, most of these documents contain classified information.

1.3.2 Nuclear and EW caused degradation of communications networks has been studied from a graph theory aspect by Deckro [4] and from a simulation aspect by Fowler [5] and Thomas [10] for the USAF. Much of the above work is based on the previous work of Tanenbaum [9], Christofides [2], and Frank and Frisch [6].

1.4 Research Efforts. The following paragraphs of the report summarize the research efforts and results accomplished during the 1984 summer at AFWL. Topics include a review of PNAC, techniques for developing communications network MOE, and the development of a communications network computer simulation.

2.0 Propagation Network Analysis Code (PNAC). A review of the documentation listed in Appendix A, Sections I and II, is the basis for the following presentations of PNAC characteristics, validation procedures, and deficiencies.

2.1 PNAC Characteristics. The PNAC characteristics reflect a message oriented simulation. All of the following message oriented outputs are available for any message at any time represented in the simulation: probability of reception, time of reception, time delay between source and destination, message routing, and message throughput rate. In other words, a detailed audit trail of each message is available if so desired. All of these outputs are calculated even if they are not desired as outputs. As might be suspected, the inputs must describe all message protocols and node processes. The PNAC output data must be characterized as having a high level of resolution. Even though PNAC is a message oriented simulation, its output data implicitly contain network robustness quantification. And a network robustness quantification can be obtained by properly analyzing the audit trail data for all messages. This analysis would be in addition to the post-processing of output data already required. Thus it must be concluded that PNAC can be modified to also be a network oriented simulation besides being a message oriented simulation.

2.2 PNAC Validation Technique. The validation procedure for PNAC was to use a building block technique. First the nuclear phenomenology was developed in the MICE/MELT code

and approved by the Defense Nuclear Agency as a benchmark for any simulation requiring nuclear phenomenology. The basis for validating the MICE/MELT code was empirical data collected from the STARFISH and barium release high altitude atmospheric tests. The equipment performance data base was developed from laboratory tests conducted on individual components of communications network equipment and this data base was approved for use in network simulations by AFWL. Next the link performance module was validated by comparing empirical data collected while transmitting a RF signal through four different sets of homogeneous media with that output from the simulation.

2.3 PNAC Deficiencies. The PNAC deficiencies are characterized as user deficiencies and analytical deficiencies. Each are discussed below.

2.3.1 PNAC is not user friendly for policy, doctrine, operational, or procurement users for the following reasons. Users are suspicious or uncertain of the simulation results because a simulation technician has to interpret (post-process) the output data before it can be comprehended by the user. PNAC has such a long "turn-around" time that it is not amenable to playing "what if" games. It will not "fit" on a personal (desk top) computer for intimate interaction with the user.

2.3.2 The PNAC analytical deficiencies are associated with processing time, a mismatch in levels of resolution, and

validation uncertainty. The pre- and post-processing effort and time appears to be excessive because of the cost involved. This cost in time and money makes PNAC impractical for use in what would be considered as most candidate systems. Next the SCENARIO and MICE/MELT module codes use a one-dimensional, one-fluid Lagrangian hydrodynamics algorithm (to reduce grid distortion effects) to simulate a three-dimensional magnetohydrodynamic disturbed environment. This results in a mismatch of levels of resolution between the simulation and the process to be simulated. Because of this mismatch, the MRC authors of the SCENARIO module documentation stated that the code should be viewed with a healthy skepticism. The next deficiency topic is based on validation uncertainty. The equipment performance data base was developed by each component of equipment being tested individually. Combining the MICE/MELT data with the equipment performance data base, the SCENARIO code develops a RF propagation environment. Then the simulation interfaces all of the module outputs using the individual component data and SCENARIO data. This results in a feeling of uncertainty with respect to the simulation validity. Last PNAC only considers nuclear phenomenology effects upon the RF propagation of the signal. The near blast effects and electromagnetic pulse (EMP) effects are not considered in PNAC.

3.0 Measures Of Effectiveness (MOE). MOE's used to quantify communications network robustness, degradation, survivability, etc. have several characteristics which need to be

discussed. The first is level of resolution.

3.1 Level of Resolution. When studying MOE's it becomes apparent that they can be characterized by their level of resolution, or level of meaningfulness as Hightower [8] describes it. Hightower has even quantified, in a tabular form, the level of resolution of several candidate MOE. MOE's that quantify a message's time delay obviously have a high level of resolution. MOE's that quantify a whole network's connectivity obviously have a low level of resolution. Thomas [10] labels high level resolution MOE as source node-to-destination node MOE and low level resolution MOE as network MOE. Ziegler [12] uses component MOE and network MOE. Network and simulation design specifications will be based on whether the mission objectives or operational requirements call for high or low resolution MOE's.

3.2 Information Throughput MOE. Information (or data) throughput MOE is probably the most universal communications network MOE. It is a low level of resolution MOE that implies two other MOE, i.e., source to destination transmission time and connectivity. From this point on, the lineage tree distinctions become hopelessly blurred. And so the need for standardization.

3.3 MOE Definitions. Measures of survivability (MOS), measures of degradation (MOD), component measures of effectiveness (CMOE), and degree of meaningfulness are different titles for MOE. However when MOS, CMOE, or MOD terminology is

used, a special application of MOE is being considered. Thus unless otherwise specified, MOS, CMOE, and MOD will be considered subsets of the universal set, MOE. Since there is no standardization of MOE, it is useful to list the MOE definitions presented by Thomas [11], Ziegler [12], and Hightower [8] as a basis from which to work. The low level resolution MOE will be listed first, followed by the high level resolution MOE.

3.3.1 Thomas [11] provides the following low level resolution MOE definitions and has developed a FORTRAN program, GRAFTHY, for calculating each. Similar programs have been reported by Deckro [4]. Many of the graph theory and network concepts are taken from Frank and Frisch [6] and Tanenbaum [9].

3.3.1.1 Average Delay - The average of the time delay for every possible source-to-destination node pair.

3.3.1.2 Average Throughput - The average of the maximum throughput rate for every possible source-to-destination node pair.

3.3.1.3 Average Reliability - The average of the probability that at least one path exists between every possible source-to-destination node pair.

3.3.1.4 Connectivity - The sum of communicating node pairs after degradation divided by the sum of communicating node pairs prior to degradation.

3.3.1.5 Connected Network Reliability - The probability that every connected node pair before degradation is still connected after degradation.

3.3.1.6 Reliable Throughput - The sum of all link and node reliable throughput probabilities after degradation divided by the sum of all link and node reliable throughput probabilities before degradation.

3.3.1.7 Network Reliability - The product of the Connectivity MOE and Reliable Throughput MOE.

3.3.2 Thomas [11] provides the following high level resolution MOE definitions and has developed a FORTRAN program, GRAFTHY, for calculating each.

3.3.2.1 Shortest Delay Path - The shortest time delay path between a given source-to-destination node pair.

3.3.2.2 Highest Reliable Path - The highest reliability path between a given source-to-destination node pair.

3.3.2.3 Reachability - Affirmation that a given destination can be reached from a given source node along any path of any number of links.

3.3.2.4 Limited Reachability - Affirmation that a given destination node can be reached from a given source node along any path in less than a given number of links.

3.3.2.5 Maximum Throughput (Min-Cut Max-Flow) - The maximum throughput rate between a given source-to-destination

node pair.

3.3.2.6 Number of Link Independent Paths (Arc Connectivity, Degree) - The number of link independent paths between a given source-to-destination node pair.

3.3.2.7 Number of Node Independent Paths (Node Connectivity) - The number of node independent paths between a given source-to-destination node pair.

3.3.2.8 Reliability - The probability that at least one path exists between a given source-to-destination node pair.

3.3.2.9 Availability - The mean-time-between-failures (MTBF) for a given node, link, source-to-destination node pair path, etc.

3.3.3 Ziegler [12] and Hightower [8] developed the high level resolution MOE - Local Connectedness (LC). LC is defined as a measure of the local topological connectedness, link traffic, and link survival probability of a given network link. Since this is a new MOE, Ziegler has presented its development in detail and has developed a FORTRAN program for calculating it.

3.4 Comparison of Three MOE. Ziegler [12] has compared three MOE [local connectedness (LC), network reliability (NR), and average reliability (AR)] for four different network topologies (maximally connected, star, linear, and ring). The results show the LC program running 20 times faster than the AR program, but that the AR MOE has a higher

level of resolution of its quantification, while NR comparatively seems to be a "middle-of-the-road" MOE.

3.5 DELPHI and MOE Classification. Since there is no standardization of MOE definition, identification, or prioritization, Ziegler [12] has presented in detail a DELPHI process that could be used for satellite communications network MOE. The DELPHI process presented follows that which was suggested by Boroson [1] and Dalkey et al [3].

3.6 Factor Analysis and MOE Relationships. Hightower [8] has presented a factor analysis approach [using techniques presented in Fruchter (7)] for determining the clustering relationship or correlation between 9 MOE when applied to 10 different networks. The results verify that link flow MOE are clustered and have essentially no correlation with the cluster of link probability MOE. Hightower [8] has written FORTRAN programs to implement the factor analysis processes.

4.0 Summary. This report considers several network simulation topics and presents an extensive bibliography. The first topic is a review of the Propagation Network Analysis Code (PNAC) simulation, its characteristics, validation technique, and deficiencies. This review points out several reasons for additional research being required in communications network simulation. The second topic is measures of effectiveness (MOE). MOE levels of resolution, definitions, calculation programs, and a newly developed MOE were dis-

cussed. An analytical and graphical comparison of three MOE was discussed. Also presented was a DELPHI sequence to classify MOE and a factor analysis technique to obtain MOE correlation relations. The details of the MOE topics are included in three companion reports [8], [11], and [12].

5.0 Future Research. The development and execution of a DELPHI sequence to identify and classify MOE for a satellite communications network simulation is a prime candidate for future research. A much more nebulous research topic is the development of a factor analysis methodology to show the correlation between simulation inputs and outputs. This technique would be used to validate massive simulations.

6.0 References.

1. Boroson, Warren, and David P. Snyder, "The First Nuclear War", NEXT, Sep/Oct 1980, Vol. 1, Number 4, pgs. 29-37, NEXT Publishing Co., Litton Magazine Inc.
2. Christofides, Nicos, Graph Theory: An Algorithmic Approach, Academic Press Inc., New York, N. Y., 1975.
3. Dalkey, Norman C., Daniel L. Rourke, Ralph Lewis, and David Snyder, Studies in the Quality of Life: DELPHI and Decision-Making, D. C. Heath and Co., Lexington, Mass., 1972.
4. Deckro, Richard F., Modeling Network Disruption, Final Report, USAF/OSR/SCEEE/USAF, Contract No. F49620-79-C-0038, Kirtland AFB, NM, September 1, 1980. (Unpublished)
5. Fowler, Eddie R., HEMP Vulnerability/Survivability Of Computer Networks, Final Report, USAF/OSR/SCEEE/AFWL, Contract No. F49620-82-C-0035, Kirtland AFB, NM, 8 August 1983. (Unpublished)
6. Frank, Howard and Ivan T. Frisch, Communications, Transmission, and Transportation Networks, Addison-Wesley Publishing Co., Inc., Reading, Mass., 1971.
7. Fruchter, Benjamin, Introduction to Factor Analysis, D. Van Nostrand Co., Inc., Princeton, N. J., 1954.
8. Hightower, Ron R., The Factor Analysis Methodology Applied To MOE Categorization And Evaluation, Final Report, USAF/OSR/SCEEE/AFWL, Contract No. F49620-82-C-0035, Kirtland AFB, NM, August 1, 1984. (Unpublished)
9. Tanenbaum, Andrew S., Computer Networks, Prentice-Hall, Inc., Englewood Cliffs, N. J., 1981.
10. Thomas, Russell D., Computer Network Characterization, Final Report, USAF/OSR/SCEEE/AFWL, Contract No. F49620-82-C-0035, Kirtland AFB, NM, 23 August 1983. (Unpublished)
11. Thomas, Russell D., A Computer Network Simulation Utilizing Graph Theory To Calculate Measures Of Effectiveness, Final Report, USAF/OSR/SCEEE/AFWL, Contract No. F49620-82-C-0035, Kirtland AFB, NM, 3 August 1984. (Unpublished)
12. Ziegler, Kurt, Simulation Validation And The Identification Of MOEs, Final Report, USAF/OSR/SCEEE/AFWL, Contract No. F49620-82-C-0035, Kirtland AFB, NM, August, 1984. (Unpublished)

APPENDIX A - BIBLIOGRAPHY

SECTION I - Propagation Network Analysis Code (PNAC)

1. Nichols, W., and G. Cable, Propagation Network Analysis Code (PNAC): Recommended Approach, Final Report, AFWL-TR-80-111, Computer Sciences Corporation, February 1981.
2. Nichols, W., G. Cable, and D. Kellum, Propagation Environment Data Bases for Use with the Propagation Network Analysis Code (PNAC), AFWL-4489-C-007, Computer Sciences Corporation, 6 Apr 81, (U).
3. Nichols, W., G. Cable, J. Ehrhart, and D. Kellum, Propagation Network Analysis Code (PNAC), AFWL-8343-C-002, Computer Sciences Corporation, Nov 83, (U).
4. Nichols, W., G. Cable, J. Ehrhart, and D. Kellum, Propagation Network Analysis Code (PNAC), Operating Instructions, AFWL-8343-C-003, Computer Sciences Corporation, 26 Apr 83, (U).

SECTION II - Module Modeling That Supports PNAC

1. Sappenfield, D. S., and R. W. Stagat, SCENARIO Code Results II: Comparison of Results for a Single Burst with Results Given by the MICE/MELT Nuclear Burst Phenomenology Codes (U), DNA 5860T, MRC-R-619, Mission Research Corporation, March 1981 (SFRD).
2. Sappenfield, D. S., J. P. Incerti, and R. W. Stagat, SCENARIO Code Results I: A Ten-Event Multiburst Scenario Over Eastern Conus (U), DNA 5865T, MRC-R-604, Mission Research Corporation, December 1980 (U).
3. Stagat, R. W., D. S. Sappenfield, and J. P. Incerti, The SCENARIO Code: Modifications in Version II and the Striation Convection Theory, AFWL-TR-80-124, MRC-R-539, Mission Research Corporation, July 1980 (U).
4. Stagat, R. W., and D. S. Sappenfield, SCENARIO: A Program for Satellite Signal Propagation Analysis Applications, AFWL-TR-78-137, MRC-R-404, Mission Research Corporation, July 1978 (U).
5. Fajen, F. E., A. W. Gregersen, R. W. Kilb, R. E. Stoockly, and W. W. White, A MICE/MELT Calculation of Conditions During the Ten Hours Following a Megaton-Range Explosion at 250 km Altitude (U), DNA 4916F, MRC-R-434,

Mission Research Corporation, February 1979 (SFRD).

6. Fajen, F. E., R. E. Stoeckly, and W. W. White, A MICE/MELT Simulation of a Multiburst Scenario (U), DNA 4485T, MRC-R-359, Mission Research Corporation, December 1977 (SFRD).
7. Fajen, D. W., MIXW--An Implicit Difference Scheme for MHD Calculations, DNA 2877I, Mission Research Corporation, March 1972 (U).
8. Fajen, F. E., D. H. Sowle, and D. Smith, Two-Fluid MICE (U), MRC-R-71, Mission Research Corporation, May 1973 (SFRD).
9. Michelet, A. H., Link Performance Data Base I (U), AFWL-TR-79-112, MRC-N-373, Mission Research Corporation, December 1979 (S).
10. Michelet, A. H., Link Performance Data Base II (U), AFWL-TR-80-101, MRC-R-557, Mission Research Corporation, March 1980 (S).
11. Bogusch, R. L., Link Performance Data Base III (U), AFWL-TR-81-95, MRC-R-645, Mission Research Corporation, June 1981 (S).
12. Michelet, A. H., Link Performance Data Base IV, AFWL-TR-82-63, MRC-R-696, Mission Research Corporation, August 1982 (U).

SECTION III - Satellite Systems In Nuclear Environments

1. Finci, A. G., HEMP Hardening Status of the DSCS (U), AMRC-R-195, Mission Research Corporation, 17 Aug 79 (S).
2. Trybus, P. R., Assessment of CONUS Ground Station (CGS) - Final Report (U), AMRC-R-192, Mission Research Corporation, 9 Oct 79 (S).
3. Bogusch, R. L., and A. Michelet, Performance of SSS UHF Low Data Rate Links in Scintillation and Jamming (U), MRC-R-537, Mission Research Corporation, Jan 80 (S).
4. Workman, J., and F. Chu, Nuclear Environment Models for Communication Analysis, AMRC-R-222, Mission Research Corporation, 10 Apr 80.
5. Chodorav, A., G. Morgan, and B. Singaraju, Hardening Recommendations for Two Satellite Antenna Systems, AMRC-R-240, Mission Research Corporation, 12 Sep 80, and rev 1, 29 Oct 80.

6. Chodorow, A. M., and D. A. Schafer, Quick Look EMP Survivability/Vulnerability Assessment of the AN/GSC-49 Satellite Earth Terminal, Mission Research Corporation, February 1984.
7. Bogusch, R. L., and R. W. Hendrick, Effects of Propagation Disturbances on a Specific Satellite Communications Link, Volume II: Models of Propagation Disturbances, AFWL-TR-76-25, Vol. II, MRC-R-156, Mission Research Corporation, October 1976 (U).
8. Wittwer, L. A., The Propagation of Satellite Signals Through Turbulent Media, AFWL-TR-77-183, Air Force Weapons Laboratory, January 1978 (U).
9. Bogusch, R. L., and F. W. Guigliano, Nuclear Survivability Criteria for Satellite Links (U), AFWL-TR-82-18, MRC-R-626, Mission Research Corporation, February 1982 (SRD).
10. Bogusch, R. L., et al., Recent Accomplishments in Effects of Nuclear-Induced Signal Propagation Disturbances on Satellite C and Radar Systems (U), MRC-R-713, (to be published by DNA), June 1982 (S).
11. Ibaraki, R., et al., DSP Satellite Link Survivability Overview in a Nuclear Environment (U), ESL-TM1315, ESL Incorporated, January 1981 (S).
12. Bogusch, R. L., and F. W. Guigliano, DSP Link Survivability Techniques (U), DNA 2914F, MRC-R-439, Mission Research Corporation, March 1979 (SPRD).
13. Nuclear Criteria Group Secretariat Report, Air Force Satellite Link Criterion (U), NCGS 82-1, Nuclear Criteria Group Secretariat, Kirtland AFB, NM, May 1982 (SPRD).
14. Guigliano, F. W., et al., DSP Satellite 14 Link Survivability Study (U), MRC-R-715, Mission Research Corporation, February 1983 (S).
15. Guigliano, F. W., and R. L. Bogusch, Design and Evaluation of Survivable Links for IONDS (U), MRC-R-598, Mission Research Corporation, prepared for USAF Space Division under Contract F04701-79-C-0009, December 1980 (SFRD).
16. Heckman, R., E. Tsui, R. Ibaraki, and C. Prettie, IONDS Downlink Performance Through a Striated Nuclear Environment (U), DNA 5282T, ESL Incorporated, February 1980 (SFRD).
17. Satellite Communication Systems Performance in a Nuclear Propagation Environment (U), Workshop Proceedings published by R&D Associates, RDA-TR-113211-003, November

1980 (SFRD).

18. Bogusch, R. L., D. D. Newman, D. L. Knepp, and A. H. Michelet, MILSTAR Link Design and Performance Trade Studies in Scintillation and Jamming (U), MRC-R-718, Mission Research Corporation, February 1983 (S).
19. Michelet, A. H., Potential Nuclear-Induced Propagation Effects on Satellite Communication Systems, DNA 5582T, MRC-R-587, Mission Research Corporation, July 1980 (U).
20. JRSC Mitigation Modem Design and Performance in a Black-out/Scintillation Channel (U), WW-JRMM-04-08, Headquarters, U.S. Army Communications Command, Fort Huachuca, Arizona, February 1980 (S).
21. Marshall, J., and E. Tsui, Nuclear Environment Link Performance Specification for JRSC (U), USACC WW-JRMM-04-80, ESL Incorporated, February 1980 (S).
22. Knepp, D. L., M. A. Messier, and F. W. Guigliano, GPS Advanced Receiver Design Options (U), MRC-R-697, Mission Research Corporation, prepared for USAF Space Division under Contract F04701-79-C-0009, May 1982 (SFRD).
23. Bogusch, R. L., and D. L. Knepp, Propagation Effects on GPS Receiver Model X (U), AFWL-TR-79-25, MRC-R-373, Mission Research Corporation, September 1979 (S).
24. Bogusch, R. L., Preliminary Analysis of Propagation Effects on GPS (U), AFWL-TR-78-126, MRC-R-305, Mission Research Corporation, July 1979 (S).
25. Tsui, E., et al., The Global Positioning System Navigation Receiver Performance in a Nuclear Environment (U), DNA 4259T, ESL-TM737, ESL Incorporated, November 1976 (SRD).
26. Bogusch, R. L., F. W. Guigliano, D. L. Knepp, A. H. Michelet, and B. E. Sawyer, Propagation Effects on DSCS II Links (U), DNA 4578T, MRC-R-333, Mission Research Corporation, December 1977 (SFRD).
27. Nuclear Effects Vulnerability of Future MILSATCOM Links (U), Workshop proceedings published by R&D Associates, RDA-TR-106507-001, June 77 (SRD).
28. The Prediction of Nuclear Weapon Effects on UHF Satellite Communications (U), Workshop Proceedings published by R&D Associates, RDA-TR-103202-001, January 1977 (SRD).
29. Bogusch, R. L., and R. W. Hendrick, A Detailed Simulation of Message Communication Over a Specific SATCOM Link Under Disturbed Conditions (U), AFWL-TR-76-26, MRC-R-177, Mission Research Corporation, October 1976 (S).

30. Bogusch, R. L., Effects of Propagation Disturbances on a Specific Satellite Communications Link, Volume III: Calculation of Link Performance (U), AFWL-TR-76-25, Vol. III, MRC-R-156, Mission Research Corporation, October 1976 (SFRD).
31. Rino, C. L., J. Owen, and R. C. Livingston, Analysis of Nuclear Propagation Effects Utilizing Wideband Satellite Data, DNA 5807F, SRI International, April 1981 (U).
32. Bogusch, R., F. Guigliano, and D. Knepp, Frequency-Selective Scintillation Effects and Decision Feedback Equalization in High Data-Rate Satellite Links, Proceedings of the IEEE, Vol. 71, No. 6, Mission Research Corporation, Jun 83 (U).
33. Nichols, W., et al, Satellite Communications System Performance Assessment, Final Report, AFWL-4489-C-009, 19 Jun 82 (U).
34. Frazier, J., and G. Krajci, The Performance of an EHF Satellite Communications Link in a Scintillated Environment, AFWL-TR-81-33, Jul 81, (U).
35. Hendrick, R., Propagation Analysis for GPS, MRC-R-307, Apr 77, (U).
36. Bogusch, R., Propagation Effects on Satellite Systems: A Brief Status Report, AFWL-TR-76-46, Sep 76, (U).
37. Hiebert, A., and W. Sollfrey, Techniques for the Analysis of Spectral and Orbital Congestion in Space Systems, R-3046-AF, March 84, (U).
38. Generic Methodology Design Specifications for MILSATCOM Vulnerability Analysis, Bell Technical Operations Corp., BTO M1-2-007, 8 May 81, (U).

SECTION IV - Nuclear Environment Models and Design

1. Nichols, W., Scintillation Mitigation Technology, Conference Report, AFWL-8343-C-004, 8 Feb 84, (U).
2. A Power Model for Plasma Convection, Final Report, Physical Dynamics, Inc., Apr 79, (U).
3. A Gradient Drift Microstructure Model, Physical Dynamics, Inc., DNA 4539T, Feb 78, (U).
4. Appendix 3, Striation Microstructure Model, An Interim Report, Physical Dynamics, Inc., Oct 76, (U).

5. Appendix 2, Striation Convection Model, An Interim Report, Physical Dynamics, Inc., Oct 76, (U).
6. Appendix 1, Extended Neutral Wind Modelling, An Interim Report, Physical Dynamics, Inc., Oct 76, (U).
7. Thomson, J., Striated Fluid Modeling, Physical Dynamics, Apr 73, (U).
8. Workman, J., and S. Chu, Communication System Analysis Modelling, Multiburst Simulation, PD-BRA-78-180, Jul 78, (U).
9. Communication System Analysis Modelling, The Preliminary Phase, PD-B-77-134, Physical Dynamics, Inc., Feb 77, (U).
10. The Numerical Simulation of the High Altitude Nuclear Environment Relevant to Communication System Analysis, Physical Dynamics, Inc., Oct 76, (U).
11. Bogusch, R., F. Guigliano, D. Knepp, and A. Michelet, Frequency Selective Propagation Effects on Spread-Spectrum Receiver Tracking, Proceedings of the IEEE, Vol. 69, No. 7, Jul 81, (U).
12. Kilb, R. W., and D. Glenn, CMHD Simulations of Very High Altitude Nuclear Bursts from 0 to 1 sec (U), DNA 4629F, Mission Research Corporation, June 1978, (SRD).
13. Rino, C. L., Propagation Modeling and Evaluation of Communication System Performance in Nuclear Environments, DNA 5265F, SRI International, February 1980, (U).
14. Bogusch, R. L., and M. J. Stanton, Computer Simulation of the Effects of a Nuclear Environment on Radar (RANC II) (U), 65TMP-54, General Electric-Tempo, October 1965 (SRD).
15. Michelet, A. H., and W. Schlueter, An Advanced MEECN HF Communications System Concept--System Modeling and Propagation Environment Considerations (U), MRC-N-321, Mission Research Corporation, November 1977, (S).
16. Michelet, A. H., and M. R. Frolli, Modeling and Initial Performance Evaluation of the Proposed ITT Adaptive HF/VHF Communication System Concept (U), DNA 4762T, MRC-R-411, Mission Research Corporation, December 1978, (S).
17. Gutsche, S. L., and J. P. Incerti, Relay-Capable Network Performance in Severe Nuclear Environments (U), MRC-R-622, Mission Research Corporation, May 1981, (S).
18. Bernal, R., Dual Modem (LES Mode) Experimental Test with Scintillated Signal Structures (U), Linkabit Corporation, September 1978, (C).

19. Wittwer, L. A., The Performance of Advanced Frequency Shift Key Modulation Techniques in Scintillated Environments II (U), AFWL-TR-78-49, Air Force Weapons Laboratory, April 1978, (S).
20. Wittwer, L. A., The Performance of Advanced Frequency Shift Key Modulation Techniques in Scintillated Environments I (U), AFWL-TR-77-182, Air Force Weapons Laboratory, February 1978, (S).
21. Proceedings of the DNA/LASL High-Altitude Nuclear Weapons Effects Summer Study (U), Volume II-Working Group Reports (U), DNA 4736P-3, edited by D. R. McDaniel (SR11), Defense Nuclear Agency, November 1978, (S).
22. Satellite C3 Nuclear Mitigation Techniques (U), Volume I--Summary from DNA/LASL High-Altitude Nuclear Weapons Effects Summer Study (U), DNA 4736P-1, edited by L. A. Wittwer (DNA) and R. L. Bogusch (MRC), Defense Nuclear Agency, November 1978 (C).
23. Ibaraki, R., et al., CPSK, DPSK, and FSK Demodulator Performance Under Nuclear Stressed Conditions, DNA 5006F, ESL-TM1083, ESL Incorporated, March 1979 (U).
24. Fulks, G., HF/VHF Propagation in a Nuclear Environment: Bomb Mode Phenomenology (U), MRC-R-455, Mission Research Corporation, December 1979 (SFRD).
25. Krajci, G. S., and J. A. Frazier, Jr., Satellite & C3 Link Survivability Program--History I, AFWL-NTYCC-TN-81-7, Air Force Weapons Laboratory, May 1981 (U).
26. Wittwer, L. A., F. W. Guigliano, R. L. Bogusch, and R. W. Kilb, A Reasonable Worst Case Specification of Nuclear Disturbed Radio Signals (U), DNA-IR-82-01, Defense Nuclear Agency, April 1982 (SFRD).
27. Wittwer, L. A., et al., UHF Propagation Effects in Scintillated Environments, AFWL-TR-76-304, Air Force Weapons Laboratory, August 1977 (U).
28. Knepp, D. L., Propagation of Wide Bandwidth Signals Through Strongly Turbulent Ionized Media, DNA-TR-81-78, MRC-R-671, Mission Research Corporation, March 1983 (U).
29. Sowle, D. H., A Phenomenology Model for Late Time Absorption Effects of High Altitude Bursts (U), DNA 4376T, MRC-R-266, Mission Research Corporation, July 1977 (SRD).
30. Baumann, E. J., An Analysis of Upper HF/VHF Propagation Data Resulting from Nuclear-Induced High-Altitude Ionization (U), DNA 5037T, MRC-R-454, Mission Research Corporation, July 1979.

31. Trybus, P. R., A. M. Chodorow and H. Fowles, Final Report on the EMP Hardening and Hardness Validation of Selected C3 and Warning Systems, Mission Research Corporation, April 1982.
32. Technical Staff (MRC), Technical Letter Reports on C3 and Information System Hardening Assessment and Validation Study, Vol. I: Unclassified Letter Reports--II March 1982 to 30 June 1983, Mission Research Corporation, December 1983.
33. Technical Staff, R&D Associates, GWEN Initial Connectivity and Thin Line Network Development, Mission Research Corporation, November 1982.
34. Technical Letter Reports on Ground Based C3 Facilities Hardening and Validation, Vol. I: UNCLAS Letter Reports, Technical Staff, AMRC-R-404, MRC, 17 Aug 82.
35. Same, Vol. II: Classified Letter Reports (U), AMRC-R-404, MRC, 17 Aug 82 (S).
36. Fowles, H. M., A. Chodorow, J. Prewitt, and P. Trybus, Final Report on Ground Based C3 Facilities Hardening and Validation (U), AMRC-R-385, MRC, Aug 82 (S).
37. Hodson, W., and J. Barry (RDA), Survivable Spread Spectrum Communications Network - Annotated Briefing, MRC, 26 May 82.
38. Bogusch, R. L., and A. Michelet, Performance of SSS Low Data Rate Links in Scintillation and Jamming - Phase II, MRC-R-661, MRC 12 Oct 81.
39. Winn, R. (CSC), C4 Survivability/Vulnerability Data Base - Final Report, AMRC-R-310, MRC, 31 August 1981.
40. Fowles, H. M., Preliminary Design of an EMP Hardened Headquarters Command Post (U), AMRC-R-289, MRC, 15 Jul 81 (S).
41. Fowles, H. M., Headquarters EMP Hardening, Task I: Functional Analysis (U), AMRC-N-162, MRC, 19 Feb 81 (S).
42. Morel, R. S. (CSC), Users Guide to the AFWL Survivability/Vulnerability Data Base, MRC, 28 Jan 81.
43. Fowles, H. M. (MRC), B. Harlacher, and J. Harper (IRT) Design and Demonstration of an EMP Hardened SAC Wing Command Post, Final Summary, AMRC-R-241, MRC, 1 Oct 80.
44. Wright W. and W. Gilbert (R&D Associates), Strategic C3 Survivability Issues (U), MRC, 29 Jul 80 (S).

45. Harlacher, B. (IRT), Hardness Evaluation of the Prototype EMP Hardened SAC Wing Command Post, MRC, 3 Jul 80.
46. Harlacher, B., Preliminary Design Requirements for EMP Hardened SAC Wing Command Post, Vol. I, Existing Systems, IRT0060-003, MRC, 25 Oct 78.
47. Chodorow, A. M., and H. M. Fowles, Preliminary Design Requirements for EMP Hardened SAC Wing Command Post, Vol. II, Future Systems, AMRC-R-164, MRC, 20 Nov 78.
48. Harlacher, B., and J. Harper, Design Requirements for EMP Hardened SAC Wing Command Post, Vol. I, IRT-0060-007, MRC, 29 Jan 79.
49. Chodorow, A. M., and H. M. Fowles, Design Requirements for EMP Hardened SAC Wing Command Post, Vol. II, AMRC-R-177, MRC, 9 Mar 79.
50. Harlacher, B., and J. Harper, Design Requirements for EMP Hardened SAC Wing Command Post, Vol. III, IRT-0060-008, MRC, 29 Jan 80.
51. Ground Data Station Analysis Report (U), Vol. I, Autometrics Strategic Systems Division, Rockwell International, MRC, May 79.
52. Trybus, P. R., Ground Data Station Analysis Report (U), Vol. II, AMRC-R-185, MRC, 29 May 79 (S).

1983-84 USAF-SCEEE RESEARCH INITIATION PROGRAM

Sponsored by the

AIR FORCE OFFICE OF SCIENTIFIC RESEARCH

Conducted by the

SOUTHEASTERN CENTER FOR ELECTRICAL ENGINEERING EDUCATION

FINAL REPORT

CONFIDENTIAL REPORT

Prepared by: Dr. Victor Frost

Academic Rank: Assistant Profesor

Department and
University: Electrical Engineering Department
University of Kansas Center for Research, Inc.

Research Location: Rome Air Development Center

Date: December 1984

1983-84 USAF-SCEEE RESEARCH INITIATION PROGRAM

Sponsored by the

AIR FORCE OFFICE OF SCIENTIFIC RESEARCH

Conducted by the

SOUTHEASTERN CENTER FOR ELECTRICAL ENGINEERING EDUCATION

FINAL REPORT

DEVELOPMENT AND EVALUATION OF SCALES FOR THE ORGANIZATIONAL ASSESSMENT

PACKAGE WITH WORK GROUPS AS THE UNIT OF ANALYSIS

Prepared by: Dr. Samuel B. Green

Academic Rank: Associate Professor

Department and
University: Psychology Department
Auburn University

Research Location: Air Force Leadership & Management Development Center

Date: December 1984

Development and Evaluation of Scales for the Organizational
Assessment Package with Work Groups as the Unit of Analysis

Samuel B. Green

Abstract

The objective of the research was to develop and evaluate scales for the Organizational Assessment Package (OAP) using work groups as the unit of analysis and to compare these results to those obtained using within-group, deviation scores. OAP data for four functional groups of non-supervisory, Air Force personnel were selected. They included Civil Engineering (N=3308), Supply (N=1664), Transportation (N=937), and Personnel (N=347). For each functional group, mean item scores were computed, as well as within-group, deviation scores. The OAP data were then used to obtain factors using factor analytic techniques, scales obtained through item analysis techniques, and reliability estimates on these scales. It was concluded that the use of the work group as the unit of analysis is valid on logical grounds and, from this perspective, our results suggested that the use of the individual as the unit of the analysis would tend to distort empirical findings.

Acknowledgements

I would like to thank everyone at the Leadership and Management Development Center for making this research project an enjoyable one. Special thanks are extended to Major Larry Short, Captain Janice Hightower, Major Mickey Danaby, and Colonel Loyd Woodman for their help during the course of this project. Also, I wish to thank my research assistant Dorothy Winther for all the extra hours that she spent on the project. Finally, appreciation is extended to the Air Force Systems Command, Air Force Office of Scientific Research, who made this research project a rewarding experience.

Development and Evaluation of Scales for the Organizational
Assessment Package with Work Groups as the Unit of Analysis

Consultative services are offered by the Leadership and Management Development Center (LMDC). The goals of these services are to improve the leadership and management skills of Air Force personnel and, in the long run, to enhance combat effectiveness through increased motivation and productivity. The consultative process used to achieve these goals involves five steps: (a) request by unit commander for consultative services; (b) assessment of organization using primarily the Organizational Assessment Package Survey (OAP); (c) evaluation by consultants of the organization's strengths and weaknesses based upon the assessment; (d) improvement effort, which essentially consists of providing feedback of mean OAP scores of work groups to their supervisors; and (e) a follow-up assessment of the organization using primarily the OAP. Because the OAP plays a major role within this process, the effectiveness of the improvement effort is directly dependent upon the psychometric quality of its scales.

The OAP is an attitudinal measure and is completed by a stratified, random sample of personnel within an organization. It contains 109 items that are divided into seven modules: (a) Background Information (16 items), (b) Job Inventory (34 items), (c) Job Desires (7 items), (d) Supervision (19 items), (e) Work Group Productivity (5 items), (f) Organization Climate (19

items), and (g) Job Related Issues (9 items). Except for the items on the first module, respondents give their attitudes by responding on a seven-point scale, most frequently anchored at the extremes by "strongly disagree" and "strongly agree." Computer analysis of the OAP yields data on the 109 items, on 20 factors based on a factor analysis of the items, and on 7 factors based on a non-statistical, rational clustering of items.

The psychometric characteristics of the OAP have been evaluated extensively in the past (e.g., Conlon, 1982; Hendrix & Halverson, 1979; Hightower, 1982; Hightower & Short, 1982; Short & Hightower, 1981; Short & Hamilton, 1981; Short & Wilkerson, 1981). These analyses used exclusively the individual rather than the work group as the unit of analysis and, consequently, the conclusions that may be drawn from them are limited to individual scores. In contrast in application, mean scores of a work group are used to describe the strengths and weaknesses of that group to its supervisor and individual scores are rarely if ever interpreted. The objective of the current research is to re-evaluate some of the psychometric characteristics of the OAP using the work group as the unit of analysis. Specifically, OAP scales are developed based upon work-group mean scores and these results are compared to those obtained using within-group, deviation scores obtained by subtracting from each individual's score the mean score for his/her group. Also, internal consistency estimates of reliability are computed for mean and deviation scale scores.

OAP Factors and Past Research

Factor scores are most frequently used by LMDC consultants, although item scores are available on the computer printout and, presumably, occasionally interpreted in practice. Because the attitudinal items address interrelated issues, it would be inefficient for consultants to discuss item scores with the supervisors. Consultants need a way to summarize these item scores, and factor scores which are summed item scores serve this purpose. Ideally, a factor should include items that assess a single construct. The summed score should represent more adequately this construct than any one of the item scores within the composite and, therefore, also should possess greater accuracy or reliability.

Although a number of methods exist for the development of factors or scales, LMDC researchers have used exclusively factor analytic techniques. The results of their factor analyses are reviewed below. This review serves two purposes. (a) A correlation matrix based upon individual scores, the total matrix, is partially a function of two correlation matrices, the between-group matrix based upon work-group means and the within-group matrix based upon within-group, deviation scores (Pedhazur, 1982). Consequently, the factor analyses of total correlation matrices by previous researchers may suggest what factor could be obtained in the present study. (b) A critical review of these studies could suggest what methodological problems we are likely to encounter.

Number of factors. Hendrix and Halverson (1979) factor analyzed the item responses (last six OAP modules) of individuals and obtained the 20 factors that are currently reported on the computer analysis of the OAP. The large number of factors that they found suggested that Air Force personnel have a very multifaceted perspective of their jobs, their work group, and the larger organization. Later studies (Conlon, 1982; Hightower, 1982; Hightower & Short, 1982) indicated that fewer factors may be necessary; however, the number of extracted factors varied across these studies. Although the different results may reflect actual changes in attitudes towards work and the organization, it is more likely that the discrepancy resulted from sampling error and from the different methods employed by the researchers. This later explanation seems plausible because the analyses were conducted within a short period of time and at least some of the analyses were conducted on overlapping samples.

LNDC researchers have used most frequently the eigenvalue-greater-than-one criterion (Kaiser, 1960) for determining the number of extractable factors. Although it is the default option for many factor analytic computer programs, straightforward in application, and supported by some research with simulated data (Nakstian, Rogers, & Cattell, 1982), it is not well-accepted within the factor analytic literature in general (e.g., Zwick & Velicer, 1982). When Conlon (1980) applied the eigenvalue-greater-than-one criterion with individual OAP scores, he found 14 factors, but chose to interpret only

nine of them. He dropped the remaining five factors on the basis of their lack of interpretability. Based on his research, it seems justified to conclude that item scores from individuals may be represented by fewer than the twenty or more factors currently scored. However, the number of factors necessary for this type of data may differ drastically from the number appropriate for analyses with work-group mean scores.

The above discussion probably over-dramatizes the importance of the judgment involving the number of factors and implies that a correct number of factors truly exists. In practice, this assumption seems unwarranted. For example, a typical factor from the Hendrix and Henderson analysis did include items that seemed related conceptually and, therefore, did summarize the item scores without losing much item information. On the other hand, if a fewer number of factors were used, the results may be presented even more efficiently with little additional loss of information. In other words some of the Hendrix and Henderson factors could be combined together to yield better defined factors. For example, Hightower (1982) reported a factor called Task Characteristics in her analyses which subsumed four of the factors from the original factor analyses (with the exception of one item).

Replicability of factors across groups. A great deal of job diversity exists within the Air Force. Some individuals work within hospitals, others fly, while still other maintain supplies. It seems quite likely that these individuals who

perform drastically different duties might not require the same scales to summarize their item scores. Nevertheless, Hightower and Short (1982) were able to demonstrate reasonable consistency of factor analytic results across different groups of individuals who perform different functions and across various demographic groups. Factors which tended to have only a few salient (large) loadings did show poorer replicability across groups.

Interpretability of factor analyses. One difficulty with exploratory factor analysis is that the factors are defined solely on the correlational pattern among items. What has sometimes occurred with factor analyses of the OAP is that items have salient loadings on the same factor even though these items seem to assess distinctly different concepts. More specifically, the modules on the OAP are conceptually distinct (with a few exceptions). For example, the Job Inventory Module addresses questions about a person's job, while the Job Desires Module asks questions about the job that a respondent would like to have. It would seem inappropriate to combine across these two types of items regardless of the correlational pattern among the items.

Reliability of OAP factors. Short and Hamilton (1981) investigated the test-retest reliability of the OAP factor scores. A five week interval separated the two testings. The correlations were moderate in magnitude. Seventy-five percent

of them ranged in value from .70 to .90. However, the sample size was very small (18 or 19 subjects). They also reported results with a much larger sample. These test-retest coefficients were obtained with a six-month interval between the two testings. They were uniformly low; none of the coefficients exceeded .60. On this same sample, Short and Hamilton computed a second type of reliability coefficient, Cronbach's alpha. As expected, the alphas were relatively high for factors with a large number of items and substantially lower (below .60) for factor with a few number of items. These results supported the commonsensical notion that two or three item scales cannot adequately represent an item domain.

In general, it would appear that factor scores for individuals based on only a few items should not be interpreted because they are unreliable. However, these results do not necessarily imply that mean factor scores for work groups would be as unreliable. In fact, because these scores involve an averaging process, we would hypothesize that their reliability would be greater.

Summary and Implications of Past Research

Previous research with the OAP using individuals as the unit of the analysis indicated that its items can be clustered into relatively homogeneous scales. The scales which contain fewer items (i.e., less than 5 items) did not possess good psychometric characteristic. Specifically, they tended to have low

reliabilities and did not generalize across functional and demographic groups. On the other hand, the scales which have a greater number of items did appear to be relatively reliable and generalizable across groups.

Two methodological problems appeared to flaw the previous research. One concerns the focus of the present study, the use of the individual as the unit of analysis. The second was an under-reliance on subjective judgment. This problem was most evident in the development of scales or factors. With a few exceptions, correlation matrices were computed among items; factors were extracted using principal components; they were retained if their eigenvalues were greater than one; the retained factors were rotated using varimax rotation; and the resulting factor structure matrix interpreted. In other words, subjective judgment was reserved for the last step. We believe that this over-reliance on statistical analysis yields results that are more difficult to interpret. In the present study, we will attempt not to rely solely on statistical techniques, but rather try to integrate our judgments with these techniques. For example, not only will factor analytic methods be used to derive scales, but also statistically simpler methods that require judgments by the investigator.

Method

Subjects

The sample, 6256 Air Force personnel, was drawn from the pretest OAP data base. Four types of personnel were selected in order to obtain results that would be generalizable across functional groups. They were Civil Engineering (N=3308), Supply (N=1664), Transportation (N=937), and Personnel (N=347). These particular groups were chosen because it was believed that their jobs tended to be relatively similar across bases.

Individuals were included in the sample only if they were non-supervisory personnel and belonged to work groups which had four members who had taken the OAP. These criteria were imposed for a few reasons. (a) The objective of the study was to assess the OAP using the work group as the unit of analysis. (b) LMDC gives OAP feedback to supervisors only if they have four subordinates who have taken the survey. Consequently, the unit of analysis should be restricted to work groups with four or more respondents. (c) Non-supervisory personnel were chosen to avoid the conceptual and statistical problems associated with data from hierarchical organizations.

The number of work groups varied greatly across the four functional groups: Civil Engineering, 476; Supply, 261; Transportation, 150; and Personnel, 70. The average number of individuals within a work group differed somewhat across

functional groups: Civil Engineering, 6.95; Supply, 6.37; Transportation, 6.25; and Personnel, 4.96.

Measure and Data Preparation

Only the attitudinal items of the OAP were analyzed in the present study. These included 93 items from six of the seven modules: Job Inventory, Job Desires, Supervision, Work Group Productivity, Organization Climate, and Job Related Issues.

Two data sets were created for each of the four functional groups. One set was obtained by computing item means for each work group. The second set was obtained by subtracting from each individual's item score the mean item score for his/her work group. Data analyses were conducted separately for the work-group mean scores and the within-group deviation scores. Analyses conducted on the former scores use the work group as the unit of analysis, while the latter scores use the individual as the unit of analysis (with the effect due to work group removed through the subtraction process).

Subjective Scale Development

In order to use simple item analysis methods and not to rely solely on empirical results, we developed nineteen OAP scales, primarily by carefully reading all OAP items and sorting them into groups on the basis of their content. However, these judgments were influenced by the previous research on the OAP

and, to a lesser extent, on some preliminary analyses conducted on this study's sample. These 19 scales and an abbreviated form of their items are presented in Table 1.

Although these scales were developed subjectively, we did use some guidelines to help us make our judgments. First, we attempted to develop scales within modules primarily because the modules appear to assess different components. Also, previous factor analytic research tended to indicate that correlations between items within modules tended to be higher than those between modules. Secondly, if a module had more than eight or nine items, we attempted to develop multiple scales for that module to allow us to assess if it was multidimensional. Finally, we wanted multiple item scales for precision, but did not want to sacrifice the meaningfulness of the scale by combining items which seemed to assess distinctly different components.

Scale scores were computed by summing items associated with each scale. Mean scale scores were computed for each work group and added to the mean item scores for the four functional groups. In addition, within-group deviation scores were computed for the scales and added to the data sets containing the within-group deviation scores for the items.

Analyses

The data analyses can be divided into three types. Item scores were factor analyzed. The subjectively derived scales

were item analyzed using bivariate correlational methods. Finally, reliabilities were computed on scales developed in the first two steps.

Factor analyses. Factor analyses were conducted separately on the mean and deviation item scores with two of the four functional groups, Civil Engineering and Supply. The remaining two functional groups were not analyzed because of the small number of work-group mean scores (150 for Transportation and 70 for Personnel). Even the sample sizes associated with mean scores for the other two functional groups were rather small (476 for Civil Engineering and 261 for Supply) given the large number of items, ninety-three. However, the data sets containing the deviation scores for these two groups were very large and should have yielded very stable results (3308 for Civil Engineering and 1664 for Supply).

For each of the four analyses (two functional groups and two types of data, means and deviation scores), factors were extracted from a correlation matrix with squared multiple correlations along the diagonal as estimates of communalities using a principal-axis solution. A number of criteria were used to determine the number of factors to rotate and interpret. They included eigenvalue-greater-than-one criterion, parallel analysis method (Montanelli & Humphreys, 1976), scree technique (Gorsuch, 1982), and interpretability of results. Although the four analyses suggested different number of factors, the same number of factors were rotated in order to compare results. The nine

factors were rotated using varimax. (Relatively good simple structure was achieved with the varimax solution so that the extra complexity involved with oblique solutions was successfully avoided.)

Simple Item Analysis. Item analysis of the subjectively developed scales was conducted on the mean and deviation scores for all four functional groups. We might be criticized for using these techniques on the mean data sets because of the small number of observations, but we chose, nevertheless, to perform these analyses for a couple of reasons. First, because we used subjective judgements to combine items into scales prior to the analyses, we reduced the degree that the analyses capitalized on chance in comparison with the factor analyses. Secondly, we minimized capitalization on chance by requiring replication across functional groups.

The item analysis was performed in two steps. (a) Three of the modules (Job Inventory, Supervision, and Organization Climate) contained more than one scale. The scales for each of these module were analyzed separately to determine if they should be eliminated, combined, or kept intact. (b) The three scales which essentially represented the remaining three modules (Job Desires, Work Group Productivity, and Job Related Issues) and the scales that resulted from the first stage of the item analyze were then analyzed together to yield a final set of scales.

For each stage, an item was correlated with its own scale and each of the other scales. When an item was correlated with its own scale, the summed scale score excluded the score for that item; otherwise, the correlation would be spuriously high. For all other correlations, a scale score was the sum of all items belonging to that scale. These correlations were inspected to determine if they were high between an item and its own scale (convergent validity) and lower between an item and the other scales (discrimination validity). A scale which adequately summarizes the items on it should correlate highly with those items. In addition, two scales should be combined if the items on their respective scales correlate highly with the other scale score.

Given the large number of correlations, these results were summarized three ways. To produce a more linear scale, all correlations were transformed using the Fisher r -to- z transformation. Next, the transformed correlations between a scale's items and its total score were averaged. Also, the transformed correlations between a scale's items and total scores for each of the other scales were averaged. These averaged values were then tabled separately for each functional group.

A second type of table included some of the same information: the average transformed correlation between a scale's items and its total score for each functional group. In addition, a second statistic was computed for each functional group by (a) averaging the transformed correlations between a scale's item scores and the total scores for all other scales and

(b) subtracting the resulting value from the average transformed correlation between the same items and its own scale scores. The two statistics attempt to assess, respectively, the convergent and discriminant validity of the items for each scale.

The third type of table is similar to the first except rather than presenting the results separately for each functional group, they are averaged across the four groups.

Reliability

Coefficient alphas, an internal consistency estimate of reliability, were computed on the scales derived from the item analysis procedures. These reliabilities were computed separately for the four functional group's mean scores and with-group deviation scores.

Results and Discussion

Factor Analyses

The mean and deviation item scores for Civil Engineering and Supply were factored. The various criteria for establishing the number of factor to extract did not yield consistent results. For example, the parallel analysis for the mean scores indicated 13 and 8 factors for Civil Engineering and Supply, respectively. With the deviation scores, it indicated more than 20 factors for both groups. On the other hand, the eigenvalue-greater-than-one criterion suggested 15 and 13 factors with the mean scores for

Civil Engineering and Supply, respectively. The same criterion yielded 16 factors with the deviation scores for both groups. On the other hand, the scree technique suggested from 6 to 9 factors across the four data sets. Finally, different number of factors were rotated and evaluated for interpretability. Based primarily on the latter two criteria, we decided to present the nine factor solutions. Admittedly, the decision was somewhat arbitrary.

The salient loadings for the rotated solutions are presented in Tables 3 and 4. The salient loadings are the highest correlations between the items and the factors. The factor structures for the mean scores were relatively similar. The nine factors as numbered in the table tended to have salient loadings on the following sets of items: (1) Supervision Module , (2) Organization Climate and, to a lesser extent, Job Related Issues Modules, (3) Goals and Skill/Wholeness Scales, (4) Autonomy Scale, (5) Work Group Productivity Module, (6) Job Desires Module, (7) Promotion/Recognition Scale, (8) Repetiveness Scale, and (9) Interference Scale.

The factor structures for the within-work-group, deviation scores differed to some extent with each other and also from those for the work-group mean scores. For example, a Satisfaction factor which was separate from Climate emerged only for the Supply deviation scores (factor 8). Also, the items on the Interference and Repetiveness Scales merged into a single factor for Civil Engineering. On the other hand, the factor structures based on deviation scores in general did show a

reasonable degree of overlap with those for mean scores. For example, the factors representing the modules of Supervision, Organization Climate, and Work Group Productivity were found with both the mean and deviation scores.

In general, the factor analytic results for the mean scores appeared interpretable and they replicated across both functional groups. Those associated with the deviation scores also were fairly interpretable, although they did not appear to replicate as well. Finally, items on a subjectively derived scale tended to cluster on a single factor. This finding tends to support both the meaningfulness of the empirically derived factors and the subjectively derived scales.

Item Analyses

Job Inventory Module. The item analysis statistics based on the work-group mean scores are presented in Tables 4 through 6 for the Job Inventory Module, while the comparable statistics based on the within-group deviation scores are given in Tables 7 through 9. Only the items on the Interference Scale tended to show low convergent validity. In terms of discriminate validity, the items on the Interference, Physical Characteristics, and Repetitiveness Scales tended not to correlate very highly with any other scale besides their own scale. Based on these statistics, we decided to eliminate these three scales. Because they did show relatively good discriminate validity, they could

not be combined with any other scale. Yet each of these scales had too few items to remain intact even though two of them possessed good convergent validity.

For the Goals, Skill, Autonomy, and Promotion Scales, not only were the item correlations relatively high within scales, but also moderate in magnitude between scales; however, the correlations between the items of the Autonomy Scale with the other three scales were slightly lower. Nevertheless, it should be noted that all four scales did show discriminate validity; that is, the items on each scale correlated more with its own scale than with the other scales.

We decided that it might be reasonable to reach two different conclusions for these results. Goals, Skill, and Autonomy might be combined together to make an Enrichment Scale and Promotion/Recognition kept as an intact scale. Alternatively, all four scales could remain separate. These decisions need not be mutually exclusive. Enrichment could be viewed as a scale and Goals, Skill, and Autonomy could be considered its subscales. Consequently, Enrichment, Goals, Skill, Autonomy, and Promotion were retained for the second stage of the item analysis.

The correlations for the work-group means, on the average, were larger in magnitude than those for the within-group, deviation scores. The patterns of the correlations for the two types of data were relatively similar, although the correlations

based on the mean item scores did produce somewhat better discriminate validity.

Supervision Module. The item analysis statistics based on the work-group mean scores are presented in Tables 10 through 12 for the Supervision Module, while the comparable statistics based on the within-group, deviation scores are given in Tables 13 through 15. The items on all four Supervision Scales showed high convergent validity. On the other hand, they did not demonstrate adequate discriminant validity. The lack of discrimination for the General Scale was expected in that its items tended to be broad in nature, rather than assess any specific aspect of supervision. For the remaining Supervision Scales, the item correlations within a scale, on the average, were only slightly higher than the item correlations with other scales. These results held across functional groups. Also although the correlations were in general higher for the correlations based on mean scores than those based on deviation scores, the lack of discrimination replicated across type of data. Given these data, we decided to make a single scale called Supervision from the four scales on the Supervision Module. This conclusion is consistent with the factor analytic results.

Organization Climate Module. The item analysis statistics based on the work-group mean scores are presented in Tables 16 through 18 for the Organization Climate Module, while the comparable statistics based on the within-group, deviation scores are given in Tables 19 through 21. The results for the scales on

this module were similar to those for the Supervision Module. The items on all five Organization Climate Scales showed high convergent validity, but three of the five did not demonstrate adequate discriminant validity. Feedback/Recognition and, to a lesser extent, Downward Communication showed some degree of discrimination. We decided to combine all five scales together into a single Organization Climate Scale, although we could have kept Feedback/Recognition as an intact scale. Although the correlations were in general higher for those based on mean scores than those based on deviation scores, the patterns of correlations across the mean and deviation scores were similar.

Item Analysis on Scales from all Modules (Second Stage).

The item analysis statistics based on the work-group mean scores are presented in Tables 22 through 24. The scales for these analyses included those not evaluated in the first stage of the item analysis and the scales that resulted from the first stage except Enrichment. The comparable statistics based on the within-group, deviation scores are given in Tables 25 through 27. The Organization Climate and Supervision Scales showed excellent convergent and discriminant validity. The decision to combine scales to produce these two scales would appear appropriate given the results. In addition, Work Group Productivity also appeared to possess excellent psychometric characteristics. The remaining six scales showed adequate convergent and discriminant validity.

In most cases, the correlations for the work group means were higher than those for the deviation scores. Also, for Organization Climate, Supervision, Satisfaction, and Work Group Productivity, discriminant validity was consistently better for the mean scores than for the deviation scores. On the other hand, for some scales such as Job Desires, the discriminant validity was approximately the same for two types of scores. It appeared that scales which tend to assess group phenomena, such as Supervision or Work Group Productivity, yield statistics that varied in magnitude with the choice of the unit of analysis. Those scales which tend to assess individual constructs, such as Job Desires, did not yield statistics that were greatly affected by the choice of the unit of analysis.

Tables 28 also presents statistics for the mean scores associated with the second stage of the item analysis, but substitutes Enrichment for its component parts: Goals, Skill, and Autonomy Scales. Table 29 presents similar statistics except using within-group, deviation scores. In general, Enrichment did not appear to produce any better statistics than its component parts and, therefore, the Goals, Skill, and Autonomy Scales need not be combined unless it was dictated by the use of the OAP.

Reliability

Table 30 presents the reliabilities for the ten scales that appeared to have good psychometric characteristics based on the item analysis results. Because LMDC uses work-group mean scores as feedback to supervisor, the relevant reliabilities are those

based on these mean scores (in the upper half of the table). The only scales with reliabilities in the .70's were Goals and Job Desires. The scales with a large number of items demonstrated very high reliability. For example, the reliabilities for Organization Climate and Supervision were all above .95.

Except for Job Desires, the reliabilities based on the deviation scores were somewhat lower than those based on the means. These results are similar to those for the convergent validities in that both sets of statistics are directly related to the covariance among items.

Conclusions: Use of Work Group as the Unit of Analysis

The major objective of the research was to evaluate some psychometric characteristics of the OAP using the work group as the unit of analysis. The choice to use this unit of analysis was based on how the OAP is used; that is, the LNDC consultants interpret work-group mean scores and not individual scores. Nevertheless, we were hesitant to conduct the research because sample sizes for the mean scores were relatively small. On the basis of the sample sizes alone, we felt that the results for the work-group mean scores might be much less stable and yield less interpretable results than those for the within-group, deviation scores. However, in general, we did not obtain these findings. In fact, the analyses based on the mean scores yielded more meaningful and replicable results.

The two types of data do reach some parallel findings. Regardless of whether scales were derived using factor analyses or a simpler item analysis technique, some scales such as Supervision emerged for both group mean scores and within-group deviation scores. Such similarities should not be used as an empirical justification for the use of individual scores. We believe that the use of the work group as the unit of analysis is valid on logical grounds and, from this perspective, our results suggested that the use of the individual as the unit of the analysis would tend to yield distorted empirical findings.

References

Conlon, E. J. Determining behavioral consultation effectiveness in the United States Air Force (AFOSR-81-0138). Bolling AFB, D. C., 1982.

Gorsuch, R. L. Factor Analysis (2nd ed.). Philadelphia: Saunders, 1974.

Hakstian, A. R., Rogers, W. T., & Catell, R. B. The behavior of number-of-factor rules with simulated data. Multivariate Behavioral Research, 1982, 17, 193-219.

Hendrix, W. H., & Halverson, V. B. Organizational Survey Assessment Package for Air Force organizations (AFHRL-TR-78-93). Brooks AFB, Tx: Air Force Human Resources Laboratory, 1979.

Hightower, J. M., & Short, L. O. Factor stability of the factor structure of the Organizational Assessment Package (LMDC-TR-82-1). Maxwell AFB, Al: Air Force Leadership and Management Development Center, 1982.

Hightower, J. M. Temporal stability of the factor structure of the Organizational Assessment Package (LMDC-TR-82-2).

Maxwell AFB, Al: Air Force Leadership and Management
Development Center, 1982.

Kaiser, H. F. The application of electronic computers to factor
analysis. Educational and Psychological Measurement, 1960,
20, 141-151.

Montanelli, R. G., Humphreys, L. G. Latent roots of random data
correlation matrices with squared multiple correlations on
the diagonal: A Monte Carlo study. Psychometrika, 1976, 41,
341-348.

Pedhazur, E. L. Multiple Regression in Behavioral Research
(2nd. ed.). New York: Holt, Rinehart, and Winston, 1982.

Short, L. O., & Hamilton, K. L. An examination of the
reliability of the Organizational Assessment Package
(LNDC-TR-81-2). Maxwell AFB, Al: Air Force Leadership and
Management Development Center, 1981.

Short, L. O., & Wilkerson, D. A. An examination of the
construct validity of the Organizational Assessment Package.
Proceedings of the 23rd Annual Conference of the Military
Testing Association (Vol. II). Arlington, Va: U.S. Army
Research Institute, 1981.

Zwick, W. R., & Velicer, W. F. Factors influencing four rules
for determining the number of components to retain.
Multivariate Behavioral Research, 1962, 17, 253.

Table 1
OAP Rationally-derived Scales

Scale	Items
Goals	<p>Job Inventory Module:</p> <p>34. ...what is expected of you in performing your job?</p> <p>35. ...are your job performance goals difficult to accomplish?</p> <p>36. ...are your job performance goals clear?</p> <p>37. ...are your job performance goals specific?</p> <p>38. ...are your job performance goals realistic?</p>
Skill/ Wholeness/ Effect on others	<p>Job Inventory Module:</p> <p>17. ...job require you to do many different things ...?</p> <p>18. ...job involve doing a whole task or unit of work?</p> <p>19. ...job significant, in that it affects others ...?</p> <p>27. ...doing your job well affect a lot of people?</p> <p>28. ...job provide you with the chance to finish completely...?</p> <p>29. ...job require you to use a number of complex skills?</p>
Autonomy	<p>Job Inventory Module:</p> <p>20. ...job ... independence in scheduling your work?</p> <p>21. ...job ... independence in selecting your own procedures ...?</p> <p>22. ...doing your job without feedback from anyone else?</p> <p>26. ...job provide the chance ... responsible for your own work?</p> <p>30. ...job ... do your work as you see fit?</p> <p>31. ...you allowed to make major decisions ... your job well?</p> <p>33. ...accountable to your supervisor in accomplishing your job?</p>
Promotion/ Recognition	<p>Job Inventory Module:</p> <p>41. ... promotion/advancement opportunities that affect you?</p> <p>43. ... progress up your career ladder?</p> <p>44. ... prepared to accept increased responsibility?</p> <p>45. ... people who perform well receive recognition?</p> <p>47. ... learn skills which will improve your promotion potential?</p>
Interfer- ence	<p>Job Inventory Module:</p> <p>23. ... do additional duties interfere with ... job?</p> <p>49. ... details ... interfere with performance ... job?</p> <p>50. ... bottleneck in your organization seriously affect ...?</p>
Physical character- istics	<p>Job Inventory Module:</p> <p>24. ... adequate tools and equipment to accomplish your job?</p> <p>25. ... amount of work space provided adequate?</p> <p>48. ... necessary supplies to accomplish your job?</p>
Repeti- tiveness	<p>Job Inventory Module:</p> <p>39. ... same tasks repeatedly within a short period of time?</p> <p>40. ... same type of problem on a daily basis?</p>

Table 1 (continued)

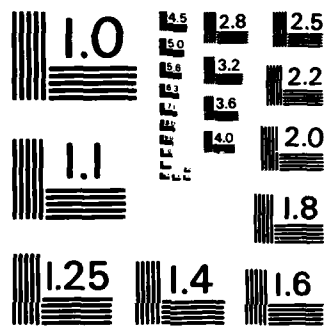
Job	<u>Job_Desires_Module</u> (all items):
Desire	51. Opportunities to have independence in my work. 52. A job that is meaningful. 53. An opportunity for personal growth in my job. 54. Opportunities in my work to use my skills. 55. Opportunities to perform a variety of tasks. 56. A job in which tasks are repetitive. 57. A job in which tasks are relatively easy to accomplish.
General	<u>Supervision_Module</u> : 65. My supervisor performs well under pressure. 66. My supervisor takes time to help me when needed.
Planning/ Goal setting	<u>Supervision_Module</u> : 58. My supervisor is a good planner. 59. My supervisor sets high performance standards. 62. My supervisor establishes good work procedures. 63. My supervisor has made his responsibilities clear 64. My supervisor fully explains procedures 68. My supervisor asks ... ideas on task improvements. 69. My supervisor helps me set specific goals.
Feedback/ Training	<u>Supervision_Module</u> : 70. My supervisor lets me know when I am doing a good job. 71. My supervisor lets me know when I am doing a poor job. 72. My supervisor always helps me improve my performance. 73. My supervisor insures ... job related training when needed. 74. ... performance has improved due to feedback ... supervisor. 75. ... technical advice, I usually go to my supervisor. 76. My supervisor ... feedback on how well I am doing my job.
Upward communica- tion/Team	<u>Supervision_Module</u> : 60. My supervisor encourages teamwork. 61. My supervisor represents the groups at all times. 67. My supervisor asks members for their ideas
Work group productiv- ity	<u>Work_Group_Productivity_Module</u> (all items): 77. The quantity of output of your work group is high. 78. The quality of output of your work group is high. 79. ... group do an outstanding job in handling these situations. 80. Your work group always gets maximum output 81. ... in comparison to similar work groups is very high. <u>Job_Inventory_Module</u> : 42. ... your work group maintain high standards of performance. <u>Job_Related_Issues_Module</u> : 102. ... share the load, and the spirit of teamwork... .
Upward communica-	<u>Organization_Climate_Module</u> : 82. Ideas ... accepted by ... personnel above my supervisor. 86. My complaints are aired satisfactorily. 87. My organization ... interested in the attitudes of 88. My organization ... interest in the welfare of its people.

Table 1 (continued)

Downward communica- tion	<u>Organization Climate Module:</u>
	83. My organization provides ... information for me
	84. My organization provides adequate information
	85. ... group is usually aware of important events
	91. The information in my organization is widely shared
100. My organization provides accurate information	
Feedback/ Recognition	<u>Organization Climate Module:</u>
	92. Personnel in my unit are recognized for ... performance.
	93. I am usually given ... demonstrate my work to others.
98. My organization rewards individuals based on performance.	
Planning/ Goal setting	<u>Organization Climate Module:</u>
	96. My organization has clear-cut goals.
	99. The goals of my organization are reasonable.
Organiza- tion efficacy	<u>Organization Climate Module:</u>
	89. I am very proud to work for this organization.
	90. I feel responsible to my organization in accomplishing
	94. There is a high spirit of teamwork among my co-workers.
95. ... outstanding cooperation between work groups	
97. I feel motivated to contribute by best efforts	
Satisfac- tion	<u>Job-Related Issues Module:</u>
	101. ... welfare through the performance of my job.
	103. ... pride my family has in the work I do.
	104. The OJT instructional methods and instructors' competence.
	105. The technical training I have received to perform
	106. My work schedule; ... regularity of my work schedule;
	107. Job Security
	108. The chance to acquire valuable skills
	109. My job as a whole
	<u>Job Inventory Module:</u>
32. To what extent are you proud of your job?	
46. To what extent does your work give you a feeling of pride?	

Table 2
Salient Loadings on Factors for Civil Engineering

Items	Group mean scores									Deviation scores								
	Factors									Factors								
	1	2	3	4	5	6	7	8	9	1	2	3	4	5	6	7	8	9
<u>Job Inv. Module</u>																		
<u>Goals</u>																		
34.			+					+					+					+
35.									+									+
36.			+					+					+					+
37.			+					+					+					+
38.			+															+
<u>Skill</u>																		
17.			++										++					
18.			+										+					
19.			++										+					
27.			++										+					
28.			+	+									+	+				+
29.			++										+					
<u>Autonomy</u>																		
20.				++										+				
21.				++										++				
22.				+									+	+				
23.			+	+									+	+				
30.				++										+				
31.				++										+				
33.	+		+										+					
<u>Promotion</u>																		
41.								+	+								+	+
43.								+	+								+	+
44.			+					+	+								+	+
45.	+	+						+	+	+	+						+	+
47.			+					+	+								+	+
<u>Interference</u>																		
23.								+										+
49.								+										+
50.																		+
<u>Physical</u>																		
24.								+										+
25.								+										+
48.							++											+
<u>Repetitive</u>																		
39.								++										+
40.								++										+



MICROCOPY RESOLUTION TEST CHART
NATIONAL BUREAU OF STANDARDS-1963-A

Table 2 (continued)
Salient Loadings on Factors for Civil Engineering

Items	GROUP BEST SCORES									Deviation scores								
	Factors									Factors								
	1	2	3	4	5	6	7	8	9	1	2	3	4	5	6	7	8	9
Job Desires Module																		
Job Desires																		
51.				*		*								*				
52.						**								**				
53.						**								**				
54.						**								**				
55.						**								**				
56.								*									*	
57.						-											*	
Supervision Module																		
General																		
65.	**									**								
66.	**									**								
Planning																		
58.	**									**								
59.	**									**								
62.	**									**								
63.	**									**								
64.	**									**								
68.	**									**								
69.	**									**								
Feedback																		
70.	**	*								**								
71.	*									*								
72.	**									**								
73.	**									**								
74.	**									**								
75.	**									**								
76.	**									**								
VR. CORR.																		
60.	**									**								
61.	**									**								
67.	**									**								
Product. Module (except 42 and 102)																		
Product.																		
77.					**					**								
78.	*				**					**								
79.					**					**								
80.					*					*								
81.					**					**								
42.					*					*								
102.	*				*					*								

Table 2
Salient Loadings on Factors for Civil Engineering

Items	GROUP mean scores									Deviation scores								
	Factors									Factors								
	1	2	3	4	5	6	7	8	9	1	2	3	4	5	6	7	8	9
Job Inv. Module																		
Goals																		
34.			*					*				*					*	
35.								*									*	
36.			*					*				*					*	
37.			*					*				*					*	
38.			*														*	
Skill																		
17.			**									**						
18.			*									*						
19.			**									*						
27.			**									*						
28.			*	*								*	*				*	
29.			**									*						
Autonomy																		
20.				**									*					
21.				**									**					
22.				*								*	*					
26.			*	*								*	*					
30.				**								*	*					
31.				**								*	*					
33.	*		*							*								
Promotion																		
41.								*	*								*	*
43.								*	*								*	*
44.			*					*	*								*	*
45.	*	*						*	*	*	*						*	*
47.			*					*	*								*	*
Interference																		
23.								*									*	
49.								*									*	
50.								*									*	
Physical																		
24.								*									*	
25.								*									*	
48.							**										*	
Repetitive																		
39.							**										*	
40.							**										*	

Table 2 (continued)
Salient Loadings on Factors for Civil Engineering

Items	GROUP mean scores									Deviation scores								
	Factors									Factors								
	1	2	3	4	5	6	7	8	9	1	2	3	4	5	6	7	8	9
Client Module																		
Up. comm.																		
82.		+		+														
86.		+	++															
87.			++															
88.			++															
Down. comm.																		
83.			++															
84.			++															
85.			++															
91.			++															
100.			++															
Feedback																		
92.			++															
93.			+															
98.			++															
Planning																		
96.			++															
99.			++															
Efficacy																		
89.			++															
90.			+	+														
94.			+															
95.			++															
97.			++	+														
Job Iss. Module (except 32 and 46)																		
101.			+	+														
103.			+	+														
104.			+	+														
105.			+															
106.			+		+													
107.			+					+										
108.			+	+														
109.			+	+														
32.			++	++														
46.			+	+														

Note. The symbols indicate the sign and magnitude of the factor loading (L): ++ indicates $L > .60$; + indicates $.30 < L < .60$; - indicates $-.60 < L < -.30$.

Table 3
Salient Loadings on Factors for Supply

Items	Group mean scores									Deviation scores								
	1	2	3	4	5	6	7	8	9	1	2	3	4	5	6	7	8	9
Job Inv. Module																		
Goals																		
34.			*										*					
35.								*										*
36.			**										*					
37.			*										**					
38.		*	*										*					
Skill																		
17.				*				*								*	*	
18.			*													*		
19.			*										*					*
27.			*										*					
28.			*	*				-					*					
29.				*				-	*				*	*				*
Autonomy																		
20.				**									*					
21.				**									**					
22.				*									*	*				
26.			*	*									*	*				
30.				**									**					
31.		*		**									*					
33.	*		*	*						*								
Perception																		
41.	*							*								*		
43.								*								*		
44.								*								*		
45.	*	*								*	*					*		
47.	*	*						*								*		
Interference																		
23.	-							*										*
49.								*										*
50.	-							*										*
Physical																		
24.	*		*					*					*					
25.	*		*					*					*					
48.	*		*					*					*					
Repetitive																		
39.								**					*					
40.								**										

Table 3 (continued)
Salient Loadings on Factors for Supply

Items	Group mean scores									Deviation scores								
	Factors									Factors								
	1	2	3	4	5	6	7	8	9	1	2	3	4	5	6	7	8	9
Job Desires Module																		
Job Desires																		
51.					*									*				
52.					**									**				
53.					**									**				
54.					**									**				
55.					**									**				
56.					-													
57.					-													
Supervision Module																		
General																		
65.	**									**								
66.	**									**								
Planning																		
58.	**									**								
59.	**									**								
62.	**									**								
63.	**									**								
64.	**									**								
68.	**	*								**								
69.	**									**								
Feedback																		
70.	**									**								
71.	*									*								
72.	**									**								
73.	**									**								
74.	**									**								
75.	**									**								
76.	**									**								
UP. CORR.																		
60.	**									**								
61.	**									**								
67.	**									**								
Product. Module (except 42 and 102)																		
Product.																		
77.					**					*								
78.					**					**								
79.	*				**					**								
80.	*				*					*								
81.					**					**								
42.	*				*					*								
102.	*	*			*					*						*		*

Table 3 (continued)
Salient Loadings on Factors for Supply

Items	Group mean scores									Deviation scores								
	Factors									Factors								
	1	2	3	4	5	6	7	8	9	1	2	3	4	5	6	7	8	9
Climate Module																		
Up. Cont.																		
82.		**													*			
86.		**								*	*							
87.		**									**							
88.		**									**							
Down. Cont.																		
83.		**									**							
84.		**									**							
85.		**									**							
91.		**									**							
100.		**									**							
Feedback																		
92.		**									**							
93.		**									*							
98.		**									**							
Planning																		
96.		**									**							
99.		**									**							
Efficacy																		
89.		**									**							*
90.		**								*	*							
94.	*	*			*						*			*				
95.		**									**							
97.		**	*								*							*
Job Iss. Module (except 32 and 46)																		
101.		*		*							*							*
103.		*									*							*
104.	*	*					*			*	*							*
105.	*						*				*							*
106.		*		*						*	*							*
107.		*								*	*							*
108.		*					*	-		*	*							*
109.		*					*	-		*	*							**
32.			*	*				-			*		*					*
46.		*	*	*						*	*							*

Note. The symbols indicate the sign and magnitude of the factor loading (L): ** indicates $L > .60$; * indicates $.30 < L < .60$; - indicates $-.60 < L < -.30$.

Table 4
 Job Inventory Items Using Work-group Mean Scores: Mean Z-transformed-r of
 Items from a Scale with their Own Scale and with Each of the Other Scales
 for each Functional Group

Scale of items	Scale Totals						
	Goals	Skill/ Whole	Autonomy	Promote/ Recogn.	Interfer.	Physical chreser.	Repeti- tive
Civil engineering							
Goals	.72	.46	.43	.43	-.08	.22	.11
Skill	.45	.76	.47	.28	.00	.17	-.06
Autonomy	.45	.45	.78	.29	-.12	.22	-.06
Promote	.46	.32	.30	.72	-.05	.36	.03
Inter.	-.09	.01	-.13	-.05	.44	-.15	.11
Physical	.25	.21	.24	.39	-.17	.71	.07
Repeti.	.14	-.02	-.07	.04	.13	.08	.85
Supply							
Goals	.62	.43	.36	.34	-.07	.29	.00
Skill	.47	.81	.59	.46	.02	.34	-.13
Autonomy	.42	.56	.81	.42	-.07	.39	-.17
Promote	.40	.48	.44	.79	-.05	.34	-.15
Inter.	-.08	.01	-.09	-.05	.68	-.24	.24
Physical	.36	.39	.44	.37	-.25	.81	-.03
Repeti.	-.02	-.11	-.21	-.17	.27	-.04	.69
Transportation							
Goals	.72	.52	.55	.45	-.19	.34	-.03
Skill	.56	.89	.69	.45	.02	.14	-.16
Autonomy	.56	.67	.79	.45	-.17	.31	-.18
Promote	.48	.46	.48	.80	-.17	.28	-.07
Inter.	-.17	.00	-.15	-.14	.26	-.23	.13
Physical	.37	.18	.35	.30	-.30	.84	.12
Repeti.	-.05	-.14	-.21	-.08	.17	.13	.68
Personnel							
Goals	.62	.48	.37	.31	-.04	.26	-.05
Skill	.50	.73	.50	.35	-.01	.15	-.26
Autonomy	.40	.48	.67	.36	-.24	.27	-.24
Promote	.31	.33	.36	.58	-.10	.29	-.23
Inter.	-.04	.02	-.28	-.12	.66	-.28	.27
Physical	.31	.30	.32	.38	-.29	.72	-.08
Repeti.	-.07	-.24	-.31	-.30	.29	-.08	.63

Table 5
Job Inventory Items Using Work-group Mean Scores: Averaged Z-transformed-r
of Items with their Own Scale and Difference Obtained by Subtracting this
Mean from Averaged Z-transformed-r of Items with Other Scales

Functional group	Scales						
	Goals Whole	Skill/ Whole	Autonomy	Promote/ Reason	Interfer.	Physical checked	Repeti- tive
Averaged Z-transformed-r of items with own scale							
Civil engineer	.72	.76	.78	.72	.44	.71	.85
Supply	.62	.81	.81	.79	.68	.81	.69
Trans- portation	.72	.89	.79	.80	.26	.84	.68
Personnel	.62	.73	.67	.58	.66	.72	.63
Mean	.67	.80	.76	.72	.51	.77	.71
Difference between own and other scale							
Civil engineer	.46	.54	.58	.48	.49	.54	.80
Supply	.40	.52	.55	.55	.64	.60	.74
Trans- portation	.48	.61	.52	.56	.35	.67	.71
Personnel	.40	.52	.50	.42	.73	.56	.75
Mean	.40	.55	.54	.50	.55	.59	.75

Table 6
 Job Inventory Items Using Work-group Mean Scores: Mean Z-transformed-r of
 Items from a Scale with their Own Scale and with Each of the Other Scales
 Averaged across Functional Groups

Scale of items	Scale Totals						
	Goals	Skill/ Whole	Autonomy	Promote/ Recog.	Interfer.	Physical charac.	Repeti- tive
Goals	.67	.47	.43	.38	-.10	.28	.00
Skill	.50	.80	.56	.38	.01	.20	-.15
Autonomy	.46	.54	.76	.38	-.15	.30	-.16
Promote	.41	.40	.40	.72	-.09	.32	-.10
Inter.	-.10	.01	-.16	-.09	.51	-.22	.19
Physical	.30	.27	.34	.36	-.25	.77	.02
Repetitive	.00	-.13	-.20	-.13	.22	.02	.71

Table 7

Job Inventory Items Using Within-group Deviation Scores: Mean Z-transformed-r of Items from a Scale with their Own Scale and with Each of the Other Scales for each Functional Group

Scale of items	Scale Totals						
	Goals	Skill/Whole	Autonomy	Promote/Record	Interfer.	Physical Change	Repeti-tive
Civil engineering							
Goals	.55	.35	.37	.30	-.01	.24	.06
Skill	.36	.66	.43	.21	.04	.20	.02
Autonomy	.35	.40	.57	.27	-.03	.23	.01
Promote	.31	.22	.29	.57	-.03	.25	-.02
Inter.	-.01	.04	-.03	-.03	.32	-.08	.13
Physical	.27	.23	.28	.28	-.09	.53	.02
Repeti.	.08	.05	.02	-.03	.16	.02	.18
Supply							
Goals	.54	.34	.32	.25	.03	.20	.08
Skill	.34	.62	.41	.21	.09	.20	.03
Autonomy	.30	.37	.53	.25	.02	.20	-.01
Promote	.32	.33	.36	.52	.00	.22	-.03
Inter.	.03	.09	.02	-.03	.32	-.12	.14
Physical	.24	.24	.25	.24	-.13	.53	.01
Repeti.	.11	.07	.01	.01	.16	.01	.13
Transportation							
Goals	.51	.33	.55	.25	-.03	.22	.07
Skill	.33	.63	.42	.21	.07	.18	.07
Autonomy	.34	.39	.53	.25	.06	.37	.02
Promote	.26	.21	.27	.52	-.03	.20	.01
Inter.	-.03	.06	-.06	-.03	.32	-.13	.15
Physical	.26	.23	.34	.24	-.14	.52	.01
Repeti.	.10	.12	.02	.01	.18	.02	.13
Personnel							
Goals	.52	.27	.35	.30	.04	.27	.09
Skill	.25	.62	.30	.22	.09	.12	.06
Autonomy	.32	.32	.53	.21	-.01	.22	-.01
Promote	.30	.23	.23	.55	.04	.21	.07
Inter.	.04	.08	-.01	.05	.32	-.04	.08
Physical	.33	.17	.29	.24	-.05	.52	.06
Repeti.	.11	.10	-.01	.08	.09	.06	.13

Table 8
Job Inventory Items Using Within-group Deviation Scores: Averaged
Z-transformed-r of Items with their Own Scale and Difference Obtained by
Subtracting this Mean from Averaged Z-transformed-r of Items with Other
Scales

Functional group	Scales						
	Goals Whole	Skill/ Autonomy	Promote/ Recogn.	Interfer.	Physical chgrc.	Repeti- tive	
Averaged Z-transformed-r of items with own scale							
Civil engineer	.55	.66	.57	.57	.39	.53	.48
Supply	.54	.62	.53	.59	.39	.55	.43
Trans- portation	.51	.63	.53	.52	.38	.59	.52
Personnel	.59	.52	.53	.55	.39	.58	.46
Mean	.55	.61	.54	.56	.39	.58	.46
Difference between own and other scales							
Civil engineer	.33	.45	.37	.40	.39	.36	.43
Supply	.33	.39	.33	.39	.34	.41	.36
Trans- portation	.31	.42	.31	.37	.39	.43	.44
Personnel	.37	.35	.36	.38	.35	.48	.39
Mean	.33	.40	.34	.38	.37	.42	.40

Table 9
 Job Inventory Items Using Within-group Deviation Scores: Mean
 Z-transformed-r of Items from a Scale with their Own Scale and with Each of
 the Other Scales Averaged across Functional Groups

Scale of items	Scale Totals						
	Goals	Skill/ Whole	Autonomy	Promote/ Recogn.	Interfer.	Physical Charg.	Repeti- tive
Goals	.33	.32	.35	.29	.01	.23	.08
Skill	.32	.61	.39	.24	.07	.18	.04
Autonomy	.33	.37	.54	.26	.01	.23	.00
Promote	.30	.25	.29	.56	.00	.22	.01
Inter.	.01	.07	-.02	.00	.32	-.09	.12
Physical	.28	.22	.29	.25	-.10	.56	.02
Repetitive	.10	.08	.01	.02	.15	.03	.45

Table 10
 Supervision Items Using Work-group Mean Scores: Mean Z-transformed-r of
 Items from a Scale with their Own Scale and with Each of the Other Scales
 for each Functional Group

Scale of items	Scale Totals			
	General	Planning/ Goal setting	Feedback/ training	Upward comun./ Teamwork
Civil engineering				
General	1.05	1.23	1.07	1.18
Planning/ Goal setting	1.13	1.26	1.16	1.22
Feedback/ Training	.90	1.03	1.13	.96
Upward comun./ Teamwork	1.12	1.26	1.09	1.20
Supply				
General	1.05	1.20	1.05	1.10
Planning/ Goal setting	1.07	1.27	1.08	1.11
Feedback/ Training	.89	1.00	1.10	.90
Upward comun./ Teamwork	1.02	1.15	.99	1.07
Transportation				
General	1.13	1.24	1.33	1.18
Planning/ Goal setting	1.13	1.38	1.30	1.21
Feedback/ Training	.94	1.14	1.13	1.01
Upward comun./ Teamwork	1.11	1.24	1.16	1.19
Personnel				
General	.95	1.06	1.05	.97
Planning/ Goal setting	1.01	1.37	1.14	1.05
Feedback/ Training	.88	1.00	1.08	.87
Upward comun./ Teamwork	.91	1.05	.97	1.04

Table 11
 Supervision Items Using Work-group Means: Averaged Z-transformed-r of
 Items with their Own Scale and Difference Obtained by Subtracting this
 Mean from Averaged Z-transformed-r of Items with Other Scales

Functional group	Scales			
	General	Planning/ Goal Setting	Feedback/ Training	Upward commn./ Teamwork
Averaged Z-transformed-r of items with own scale				
Civil engineering	1.06	1.36	1.13	1.20
Supply	1.05	1.27	1.10	1.07
Trans- portation	1.13	1.38	1.13	1.19
Personnel	.95	1.37	1.08	1.04
Mean	1.05	1.34	1.11	1.12
Difference between own and other scales				
Civil engineering	-.16	.19	.17	.04
Supply	-.07	.20	.17	.02
Trans- portation	-.12	.17	.10	.02
Personnel	-.08	.30	.16	.06
Mean	-.10	.22	.15	.04

Table 12
 Supervision Items Using Work-group Mean Scores: Mean Z-transformed-r of
 Items from a Scale with their Own Scale and with Each of the Other Scales
 Averaged across Functional Groups

Scale of items	Scale Totals			
	General	Planning/ Goal setting	Feedback/ training	Upward comm./ Teamwork
General	1.05	1.10	1.12	1.11
Planning/ Goal setting	1.08	1.34	1.17	1.15
Feedback/ Training	.90	1.04	1.11	.94
Upward comm./ Teamwork	1.04	1.10	1.05	1.12

Table 13
 Supervision Items Using Within-group Deviation Scores: Mean
 Z-transformed-r of Items from a Scale with their Own Scale and with Each
 of the Other Scales for each Functional Group

Scale of items	Scale Totals			
	General	Planning/ Goal setting	Feedback/ training	Upward comm./ Teamwork
Civil engineering				
General	.63	.84	.76	.78
Planning/ Goal setting	.74	.94	.81	.84
Feedback/ Training	.64	.76	.85	.68
Upward comm./ Teamwork	.74	.90	.77	.78
Supply				
General	.75	.88	.77	.81
Planning/ Goal setting	.75	.94	.81	.83
Feedback/ Training	.63	.78	.87	.68
Upward comm./ Teamwork	.75	.90	.77	.81
Transportation				
General	.75	.81	.76	.80
Planning/ Goal setting	.69	.92	.76	.84
Feedback/ Training	.61	.71	.81	.65
Upward comm./ Teamwork	.73	.90	.75	.76
Personnel				
General	.67	.91	.75	.79
Planning/ Goal setting	.81	.99	.82	.98
Feedback/ Training	.64	.76	.88	.65
Upward comm./ Teamwork	.77	.98	.76	.90

Table 14
 Supervision Items Using Within-group Deviation Scores: Averaged
 Z-transformed-r of Items with their Own Scale and Difference Obtained by
 Subtracting this Mean from Averaged Z-transformed-r of Items with Other
 Scales

Functional group	Scales			
	General	Planning/ Goal Setting	Feedback/ Training	Upward commun./ Teamwork
Averaged Z-transformed-r of items with own scale				
Civil engineering	.63	.94	.85	.78
Supply	.75	.94	.87	.81
Trans- portation	.75	.92	.81	.76
Personnel	.67	.99	.88	.90
Mean	.70	.95	.85	.81
Difference between own and other scales				
Civil engineering	-.16	.14	.16	-.02
Supply	-.07	.14	.17	.00
Trans- portation	-.05	.16	.15	.11
Personnel	-.15	.16	.20	.06
Mean	-.11	.15	.17	.04

Table 15
 Supervision Items Using Within-group Deviation Scores: Mean
 Z-transformed-r of Items from a Scale with their Own Scale and with Each
 of the Other Scales Averaged across Functional Groups

Scale of items	Scale Totals			
	General	Planning/ Goal setting	Feedback/ training	Upward comm./ Teamwork
General	.70	.86	.76	.80
Planning/ Goal setting	.75	.92	.80	.85
Feedback/ Training	.63	.75	.85	.66
Upward comm./ Teamwork	.75	.92	.76	.81

Table 16
 Organizational Climate Items Using Work-group Mean Scores: Mean
 Z-transformed-r of Items from a Scale with their Own Scale and with Each
 of the Other Scales for each Functional Group

Scale of items	Scale Totals				
	Upward conn.	Downward conn.	Feedback/ Recog.	Planning/ Goal setting	Organizational efficacy
Civil engineering					
Up. conn.	.92	.86	.78	.76	.83
Down. conn.	.89	1.10	.79	.86	.80
Feed/Recog.	.79	.77	1.09	.75	.75
Plan./Goal	.86	.94	.83	.87	.92
Organ. eff.	.78	.73	.69	.76	.84
Supply					
Up. conn.	1.10	.96	.98	.88	1.00
Down. conn.	1.01	1.28	.99	.98	.97
Feed/Recog.	1.02	.98	1.31	.93	.93
Plan./Goal	.96	1.03	.98	1.00	1.08
Organ. eff.	.96	.89	.86	.93	1.06
Transportation					
Up. conn.	1.15	1.07	.92	.89	.95
Down. conn.	1.06	1.18	.84	.85	.91
Feed/Recog.	.93	.85	1.30	.82	.85
Plan./Goal	.95	.90	.87	.91	.94
Organ. eff.	.85	.81	.76	.79	.93
Personnel					
Up. conn.	1.08	.93	.99	.92	.94
Down. conn.	.94	1.18	.88	.93	1.00
Feed/Recog.	.98	.85	1.13	.89	.95
Plan./Goal	1.00	.99	.99	.89	.99
Organ. eff.	.93	.98	.96	.91	1.09

Table 17
 Organizational Climate Items Using Work-group Means: Averaged
 Z-transformed-r of Items with their Own Scale and Difference Obtained by
 Subtracting this Mean from Averaged Z-transformed-r of Items with Other
 Scales

Functional group	Scales				
	Upward Comm.	Downward Comm.	Feedback/ Respons.	Planning/ Goal setting	Organizational efficacy
	Averaged Z-transformed-r of items with own scale				
Civil engineering	.95	1.10	1.09	.87	.88
Supply	1.10	1.28	1.31	1.00	1.06
Trans- portation	1.15	1.18	1.30	.91	.93
Personnel	1.08	1.18	1.13	.89	1.09
Mean	1.07	1.18	1.21	.92	.99
	Difference between own and other scales				
Civil engineering	.14	0.26	0.32	-.02	.14
Supply	.14	.29	.34	-.01	.02
Trans- portation	.19	.26	.44	-.01	.29
Personnel	.14	.24	.21	-.10	.14
Mean	.15	.26	.33	-.03	.15

Table 18
 Organizational Climate Items Using Work-group Mean Scores: Mean
 Z-transformed-r of Items from a Scale with their Own Scale and with Each
 of the Other Scales Averaged across Functional Groups

Scale of items	Scale Totals				
	Upward comm.	Downward comm.	Feedback/ Recogn.	Planning/ Goal setting	Organizational efficacy
Upward comm.	<u>1.07</u>	.96	.92	.86	.93
Downward comm.	.98	<u>1.18</u>	.88	.90	.92
Feedback/ Recogn.	.93	.86	<u>1.21</u>	.85	.87
Planning/ Goal setting	.94	.85	.92	<u>.92</u>	.98
Organization efficacy	.88	.85	.82	.85	<u>0.99</u>

Table 19
 Organizational Climate Items Using Within-group Deviation Scores: Mean
 Z-transformed-r of Items from a Scale with their Own Scale and with Each
 of the Other Scales for each Functional Group

Scale of items	Scale Totals				
	Upward comm.	Downward comm.	Feedback/ Recogn.	Planning/ Goal setting	Organizational efficacy
Civil engineering					
Up. comm.	.78	.70	.60	.54	.61
Down. comm.	.71	.89	.61	.62	.65
Feed/Recog.	.61	.60	.90	.53	.57
Plan./Goal	.61	.69	.59	.68	.72
Organ. eff.	.57	.58	.52	.58	.69
Supply					
Up. comm.	.76	.65	.61	.52	.65
Down. comm.	.67	.90	.61	.62	.64
Feed/Recog.	.63	.60	.93	.55	.62
Plan./Goal	.60	.69	.62	.72	.71
Organ. eff.	.61	.58	.57	.58	.73
Transportation					
Up. comm.	.79	.71	.63	.54	.63
Down. comm.	.73	.89	.62	.61	.65
Feed/Recog.	.63	.61	.91	.54	.56
Plan./Goal	.60	.66	.60	.60	.70
Organ. eff.	.58	.59	.52	.58	.70
Personnel					
Up. comm.	.78	.61	.64	.56	.68
Down. comm.	.58	.73	.49	.50	.50
Feed/Recog.	.60	.49	.80	.51	.57
Plan./Goal	.63	.58	.60	.66	.78
Organ. eff.	.57	.45	.51	.58	.58

Table 20
 Organizational Climate Items Using Within-group Deviation Scores: Averaged
 Z-transformed-r of Items with their Own Scale and Difference Obtained by
 Subtracting this Mean from Averaged Z-transformed-r of Items with Other
 Scales

Functional group	Scales				
	Upward comm.	Downward comm.	Feedback/ Recogn.	Planning/ Goal setting	Organizational efficacy
----- Averaged Z-transformed-r of items with own scale -----					
Civil engineering	.78	.89	.90	.68	.69
Supply	.76	.90	.93	.72	.73
Trans- portation	.79	.89	.91	.60	.70
Personnel	.78	.73	.80	.66	.58
Mean	.78	.85	.88	.66	.68
----- Difference between own and other scales -----					
Civil engineering	.17	.24	.32	.03	.13
Supply	.15	.26	.33	.06	.15
Trans- portation	.16	.24	.33	-.04	.13
Personnel	.16	.21	.26	.01	.05
Mean	.16	.24	.31	.02	.12

Table 21
 Organizational Climate Items Using Within-group Deviation Scores: Mean
 Z-transformed-r of Items from a Scale with their Own Scale and with Each
 of the Other Scales Averaged across Functional Groups

Scale of items	Scale Totals				
	Upward comm.	Downward comm.	Feedback/ Recogn.	Planning/ Goal setting	Organizational efficacy
Upward comm.	.79	.67	.62	.54	.64
Downward comm.	.67	.85	.58	.59	.61
Feedback/ Recogn.	.62	.58	.88	.53	.58
Planning/ Goal setting	.61	.66	.60	.66	.73
Organization efficacy	.58	.55	.53	.58	.68

Table 22

OAP Items Using Work-group Mean Scores: Mean Z-transformed-r of Items from a Scale with their Own Scale and with Each of the Other Scales for each Functional Group

Scale of items	Scale Totals								
	Clinate	Super.	Goal	Skill	Auton.	Promote	Satis.	Product.	Desires
<u>Civil engineering</u>									
Clinate	.98	.50	.42	.30	.41	.46	.66	.52	.17
Supervis.	.56	1.26	.45	.26	.43	.48	.49	.52	.16
Goals	.39	.37	.72	.46	.43	.43	.49	.41	.26
Skill	.29	.23	.45	.76	.47	.28	.45	.34	.30
Autonomy	.40	.38	.45	.45	.78	.29	.42	.45	.30
Promote	.46	.42	.46	.32	.30	.72	.52	.36	.25
Satisfac.	.58	.39	.47	.45	.39	.48	.74	.47	.28
Product.	.53	.48	.46	.36	.48	.38	.54	.91	.27
Desires	.15	.13	.25	.29	.28	.22	.24	.23	.68
<u>Supply</u>									
Clinate	1.14	.46	.45	.42	.47	.58	.78	.57	.21
Supervis.	.47	1.20	.44	.33	.37	.53	.52	.47	.18
Goals	.37	.36	.62	.43	.36	.34	.42	.41	.24
Skill	.39	.29	.47	.81	.59	.46	.51	.43	.37
Autonomy	.43	.34	.42	.56	.81	.42	.56	.38	.28
Promote	.55	.49	.40	.38	.44	.79	.59	.49	.31
Satisfac.	.71	.48	.48	.53	.58	.58	.91	.53	.26
Product.	.58	.46	.51	.51	.42	.53	.58	1.04	.28
Desires	.17	.14	.24	.34	.24	.26	.22	.22	.70
<u>Transportation</u>									
Clinate	1.08	.49	.53	.39	.54	.54	.71	.52	.15
Supervis.	.53	1.29	.46	.31	.47	.62	.43	.51	.11
Goals	.50	.39	.72	.52	.55	.45	.51	.44	.27
Skill	.38	.29	.56	.89	.69	.45	.58	.42	.30
Autonomy	.50	.40	.56	.67	.79	.45	.57	.43	.31
Promote	.54	.56	.48	.46	.48	.80	.44	.42	.19
Satisfac.	.63	.34	.50	.54	.56	.41	.80	.45	.25
Product.	.50	.46	.47	.42	.46	.43	.50	.92	.14
Desires	.13	.09	.26	.28	.29	.17	.24	.12	.70
<u>Personnel</u>									
Clinate	1.11	.48	.51	.42	.49	.52	.83	.60	.23
Supervis.	.50	1.19	.43	.36	.46	.45	.56	.65	.22
Goals	.43	.35	.62	.48	.37	.31	.40	.39	.17
Skill	.38	.31	.50	.73	.50	.35	.44	.37	.29
Autonomy	.42	.39	.40	.48	.67	.36	.50	.39	.21
Promote	.44	.36	.31	.33	.36	.58	.45	.38	.21
Satisfac.	.72	.49	.43	.46	.54	.47	.85	.59	.25
Product.	.61	.63	.48	.43	.46	.47	.66	1.04	.15
Desires	.16	.15	.14	.22	.17	.20	.17	.11	.52

Table 23
 OAP Items Using Work-group Mean Scores: Averaged Z-transformed-r of Items
 from a Scale with their Own Scale and Difference Obtained by Subtracting
 this Mean from Averaged Z-transformed-r of Items with Other Scales

Functional group	Scale Totals								
	Climate	Super.	Goal	Skill	Auton.	Promote	Satis.	Product.	Desires
Averaged z-transformed-r of items with own scale									
Civil Engineer.	.98	1.26	.72	.76	.78	.72	.74	.91	.68
Supply	1.14	1.20	.62	.81	.81	.79	.91	1.04	.70
Trans- portation	1.08	1.29	.72	.89	.79	.80	.80	.92	.70
Personnel	1.11	1.19	.69	.73	.67	.58	.85	1.04	.52
Mean	1.08	1.24	.69	.80	.76	.72	.82	.98	.65
Difference between own and other scales									
Civil Engineer.	.55	.84	.32	.41	.39	.33	.30	.47	.46
Supply	.49	.79	.25	.37	.39	.32	.39	.56	.42
Trans- portation	.60	.86	.27	.43	.30	.35	.34	.50	.50
Personnel	.60	.74	.33	.34	.28	.22	.36	.55	.36
Mean	.56	.81	.29	.39	.34	.30	.35	.52	.44

Table 24
 OAP Items Using Work-group Mean Scores: Mean Z-transformed-r of Items from
 a Scale with their Own Scale and with Each of the Other Scales for each
 Functional Group

Scale of items	Scale Totals								
	Climate	Super.	Goal	Skill	Auton.	Promote	Satis.	Product.	Desires
Climate	<u>1.08</u>	.48	.48	.38	.48	.52	.74	.55	.19
Supervis.	.52	<u>1.24</u>	.44	.32	.43	.52	.50	.54	.17
Goals	.33	.44	<u>.67</u>	.47	.43	.38	.46	.41	.24
Skill	.36	.28	.50	<u>.80</u>	.69	.38	.50	.39	.32
Autonomy	.44	.38	.46	.54	<u>.76</u>	.38	.51	.41	.24
Promote	.50	.46	.41	.40	.40	<u>.74</u>	.50	.41	.24
Satisfac.	.66	.42	.47	.50	.52	.48	<u>.82</u>	.51	.26
Product.	.56	.51	.48	.43	.46	.45	.57	<u>.98</u>	.21
Desires	.15	.13	.22	.28	.24	.21	.22	.17	<u>.65</u>

Table 25
 OAP Items Using Within-group Deviation Scores: Mean Z-transformed-r of
 Items from a Scale with their Own Scale and with Each of the Other Scales
 for each Functional Group

Scale of items	Scale Totals								
	Climete	Superv.	Goals	Skill	Auton.	Promote	Satis.	Product.	Desires
Civil engineering									
Climete	.79	.43	.31	.20	.28	.35	.47	.40	.10
Supervis.	.47	.91	.33	.19	.30	.36	.41	.37	.07
Goals	.31	.30	.55	.35	.37	.30	.34	.25	.18
Skill	.20	.18	.36	.66	.43	.21	.34	.23	.23
Autonomy	.26	.26	.35	.40	.57	.27	.34	.22	.22
Promote	.36	.34	.31	.22	.29	.57	.39	.23	.14
Satisfac.	.43	.35	.31	.31	.33	.35	.60	.34	.16
Product.	.41	.35	.27	.24	.25	.23	.38	.70	.12
Desires	.09	.07	.18	.24	.22	.13	.17	.12	.64
Supply									
Climete	.80	.40	.26	.26	.30	.37	.52	.40	.11
Supervis.	.43	.92	.29	.24	.31	.39	.42	.40	.12
Goals	.25	.26	.54	.34	.32	.30	.31	.24	.21
Skill	.26	.23	.34	.62	.41	.33	.38	.26	.20
Autonomy	.27	.26	.30	.37	.53	.32	.35	.21	.15
Promote	.39	.38	.32	.33	.36	.59	.43	.29	.16
Satisfac.	.50	.37	.31	.36	.37	.40	.66	.37	.14
Product.	.42	.39	.26	.27	.24	.30	.40	.74	.15
Desires	.10	.10	.21	.20	.16	.15	.14	.13	.66
Transportation									
Climete	.79	.42	.25	.20	.32	.37	.50	.38	.12
Supervis.	.45	.88	.26	.16	.31	.35	.35	.36	.11
Goals	.24	.23	.51	.33	.35	.25	.28	.23	.14
Skill	.19	.14	.33	.63	.42	.21	.31	.20	.21
Autonomy	.29	.27	.34	.38	.53	.25	.34	.24	.16
Promote	.37	.32	.26	.21	.27	.52	.38	.22	.14
Satisfac.	.44	.29	.27	.29	.34	.35	.57	.32	.12
Product.	.40	.36	.25	.22	.28	.24	.38	.73	.15
Desires	.12	.10	.14	.22	.17	.13	.12	.14	.64
Personnel									
Climete	.72	.31	.21	.10	.21	.32	.41	.27	.11
Supervis.	.36	.94	.22	.04	.21	.29	.24	.24	.06
Goals	.22	.20	.59	.27	.35	.30	.22	.13	.13
Skill	.09	.02	.25	.52	.30	.22	.20	.07	.18
Autonomy	.20	.17	.32	.32	.53	.21	.30	.15	.18
Promote	.35	.27	.30	.23	.23	.55	.33	.21	.13
Satisfac.	.38	.20	.20	.22	.30	.29	.56	.21	.19
Product.	.28	.21	.12	.10	.15	.20	.23	.63	.02
Desires	.10	.05	.11	.17	.17	.12	.18	.02	.47

Table 26
 OAP Items Using Within-group Deviation Scores: Averaged Z-transformed-r of
 Items from a Scale with their Own Scale and Difference Obtained by
 Subtracting this Mean from Averaged Z-transformed-r of Items with Other
 Scales

Functional group	Scale Totals								
	Climate	Super.	Goal	Skill	Auton.	Promote	Satis.	Product.	Desires
Averaged z-transformed-r of items with own scale									
Civil Engineer.	.79	.91	.55	.66	.57	.57	.60	.70	.64
Supply	.80	.92	.54	.62	.53	.59	.66	.74	.66
Trans- portation	.79	.88	.51	.63	.53	.52	.57	.73	.64
Personnel	.72	.94	.59	.52	.53	.55	.56	.63	.47
Mean	.78	.91	.55	.61	.54	.56	.60	.70	.60
Difference between own and other scale									
Civil Engineer.	.47	.60	.25	.39	.28	.29	.28	.42	.49
Supply	.47	.60	.26	.32	.25	.26	.22	.43	.51
Trans- portation	.47	.63	.25	.38	.25	.25	.27	.46	.50
Personnel	.48	.73	.36	.38	.30	.29	.31	.47	.36
Mean	.47	.64	.29	.37	.27	.27	.27	.44	.46

Table 27
 OAP Items Using Within-group Deviation Scores: Mean Z-transformed-r of
 Items from a Scale with their Own Scale and with Each of the Other Scales
 for each Functional Group

Scale of items	Scale Totals								
	Clinate	Super.	Goal	Skill	Auton.	Promote	Satis.	Product.	Desires
Clinate	.78	.39	.26	.19	.28	.35	.48	.36	.11
Supervis.	.43	.91	.28	.16	.28	.35	.36	.34	.09
Goals	.26	.25	.55	.32	.35	.29	.29	.21	.16
Skill	.18	.14	.32	.61	.39	.24	.31	.19	.20
Autonomy	.26	.24	.33	.37	.54	.26	.33	.20	.18
Promote	.37	.33	.30	.25	.29	.56	.38	.24	.14
Satisfac.	.44	.30	.27	.30	.34	.35	.60	.31	.15
Product.	.38	.33	.22	.21	.23	.24	.35	.70	.11
Desires	.10	.08	.16	.21	.18	.13	.15	.10	.60

Table 28
 OAP Items Using Work-group Mean Scores: Mean Z-transformed-r of Items from
 a Scale with their Own Scale and with Each of the Other Scales for each
 Functional Group

Scale of items	Scale Totals						
	Climate	Supervis.	Enrich.	Promote	Satis.	Product.	Desires
Civil engineering							
Climate	.98	.50	.45	.46	.66	.52	.17
Supervis.	.56	1.26	.45	.48	.49	.52	.16
Enrich.	.36	.32	.65	.34	.45	.40	.29
Promote	.46	.42	.41	.72	.52	.36	.25
Satisfac.	.58	.39	.53	.48	.74	.47	.28
Product.	.53	.48	.53	.38	.54	.91	.27
Desires	.15	.13	.33	.22	.24	.23	.68
Supply							
Climate	1.14	.46	.54	.58	.78	.57	.21
Supervis.	.47	1.20	.44	.53	.52	.47	.18
Enrich.	.39	.33	.66	.41	.50	.41	.30
Promote	.55	.49	.53	.79	.59	.49	.31
Satisfac.	.71	.48	.66	.58	.91	.53	.26
Product.	.58	.46	.57	.53	.58	1.04	.28
Desires	.17	.14	.32	.26	.22	.22	.70
Transportation							
Climate	1.08	.49	.55	.54	.71	.52	.15
Supervis.	.53	1.29	.46	.62	.43	.51	.11
Enrich.	.46	.36	.75	.45	.55	.43	.30
Promote	.54	.56	.53	.80	.44	.42	.19
Satisfac.	.63	.34	.61	.41	.80	.45	.25
Product.	.50	.46	.51	.43	.50	.92	.14
Desires	.13	.09	.31	.17	.24	.12	.70
Personnel							
Climate	1.11	.48	.57	.52	.83	.60	.23
Supervis.	.50	1.19	.50	.45	.56	.65	.22
Enrich.	.40	.35	.63	.34	.44	.38	.22
Promote	.44	.36	.40	.58	.45	.38	.21
Satisfac.	.72	.49	.59	.47	.85	.59	.25
Product.	.61	.63	.54	.47	.66	1.04	.15
Desires	.16	.15	.21	.20	.17	.11	.52

Table 29
 OAP Items Using Within-group Deviation Scores: Mean Z-transformed-r of
 Items from a Scale with their Own Scale and with Each of the Other Scales
 for each Functional Group

Scale of items	Scale Totals						
	Climate	Super	Enrich.	Promote	Satis.	Product.	Desires
Civil engineering							
Climate	.79	.43	.31	.35	.47	.40	.10
Supervis.	.47	.91	.33	.36	.41	.37	.07
Enrich.	.25	.24	.54	.26	.33	.23	.21
Promote	.36	.34	.33	.57	.39	.23	.14
Satisfac.	.43	.35	.40	.35	.60	.34	.16
Product.	.41	.35	.30	.23	.38	.70	.12
Desires	.09	.07	.26	.13	.17	.12	.64
Supply							
Climate	.80	.40	.34	.37	.52	.40	.11
Supervis.	.43	.92	.35	.39	.42	.40	.12
Enrich.	.26	.25	.51	.31	.34	.23	.19
Promote	.39	.38	.42	.59	.43	.29	.16
Satisfac.	.50	.37	.44	.40	.66	.37	.14
Product.	.42	.39	.32	.30	.40	.74	.15
Desires	.10	.10	.23	.15	.14	.13	.66
Transportation							
Climate	.79	.42	.32	.37	.50	.38	.12
Supervis.	.45	.88	.30	.35	.35	.36	.11
Enrich.	.25	.22	.52	.24	.31	.22	.18
Promote	.37	.32	.30	.52	.38	.22	.14
Satisfac.	.44	.29	.37	.35	.57	.32	.12
Product.	.40	.36	.30	.24	.38	.73	.15
Desires	.12	.10	.22	.13	.12	.14	.64
Personnel							
Climate	.72	.31	.22	.32	.41	.27	.11
Supervis.	.36	.94	.20	.29	.24	.24	.06
Enrich.	.17	.13	.48	.24	.25	.12	.17
Promote	.35	.27	.31	.55	.33	.21	.13
Satisfac.	.38	.20	.32	.29	.56	.21	.19
Product.	.28	.21	.16	.20	.23	.63	.02
Desires	.10	.05	.19	.12	.18	.02	.47

Table 30
Coefficient Alphas for the Mean and Deviation Scores of the OAS Scales
for Each Functional Group

Scales	Functional Group			
	Civil Engineering	Supply	Transportation	Personnel
----- Mean scores -----				
Climate	.96	.97	.98	.97
Supervision	.98	.98	.98	.98
Enrich.	.91	.91	.93	.89
Goals	.77	.71	.77	.69
Autonomy	.87	.88	.87	.83
Skill	.83	.84	.87	.82
Promote/Recog.	.82	.85	.85	.75
Satisfaction	.89	.92	.90	.91
Productivity	.90	.93	.90	.92
Job desires	.77	.76	.78	.60
----- Deviation scores -----				
Climate	.96	.94	.94	.92
Supervision	.96	.96	.95	.96
Enrich	.87	.86	.86	.83
Goals	.70	.68	.66	.69
Autonomy	.78	.76	.75	.75
Skill	.79	.77	.78	.70
Promote/Recog.	.75	.76	.71	.73
Satisfaction	.84	.86	.83	.81
Productivity	.84	.85	.85	.79
Job desires	.77	.75	.77	.64

1983-84 USAF-SCEEE RESEARCH INITIATION PROGRAM

Sponsored by the

AIR FORCE OFFICE OF SCIENTIFIC RESEARCH

Conducted by the

SOUTHEASTERN CENTER FOR ELECTRICAL ENGINEERING EDUCATION

FINAL REPORT

REINFORCEMENT INDUCED STEREOTYPE OF SEQUENTIAL BEHAVIOR

Prepared by: Dr. Arthur Gutman

Academic Rank: Associate Professor

Department and
University: School of Psychology
Florida Institute of Technology

Research Location: Air Force Human Resources Laboratory
Training Systems Division

Date: January 1985

I. INTRODUCTION

The purpose of the research conducted on my grant was to interface problems in Air Force technical training with current research findings in the area of learning and memory. This interest stemmed from my tenure as a Research Fellow at Lowry AFB (from 20 Jul 83 to 26 Aug 83). During this interval, I interacted with a team of research psychologists and training officers who dealt with issues of training on a daily basis. I attended their planning sessions and, in addition, read technical reports and training manuals. On the basis of these experiences, the major theme that emerged was the question of need (or lack thereof) of classroom Residence Training (RT) programs for Air Force technicians.

It was interesting to note that a number of the training officers (and research psychologists) felt that RT provides little, if any advantage for ultimate job performance. In other words, the feeling was that most jobs can be adequately learned on the job site. Entering as an impartial observer, I had no stake in the truth or falsity of this belief. I did note, however, that most of the evidence favoring the belief was anecdotal. Clearly, the belief is widely held by the job site supervisors.

My own literature search turned up only a single study bearing directly on the issue. The study (Black and Bottenberg, 1970) dealt with Category-B skills, and its results revealed a myriad of interactions. In essence, some skills benefited from prior RT training, some benefited from on-the-job (OTJ) training, and some benefited from neither.

Thus, it seems clear that the belief that RT is ineffective is not based as much on evidence as it is on hearsay and anecdote. Moreover, it would appear that the Air Training Command (ATC) is committed to development of curriculum to be taught in the classroom setting. So far, major efforts have been on software for computer assisted instruction (CAI), and on delivery systems such as the Unit Mastery approach. Given this, the relevant question becomes how to maximize transfer from the classroom to the job site.

The transfer-of-training issue is itself complicated by two practical considerations. First, with technological advances in hardware and software, the requisites of jobs are often changed in the course of time. Thus, the on-job requirements can easily differ from what was learned in the classroom. Secondly, at the point of training, the trainee's ultimate job site is unknown. Thus, even in the absence of technological changes, it is unlikely that the technician will end up doing (exactly) what was learned in the classroom. Given either of these factors, it would seem that if classroom education is to contribute positively to job site performance, it must produce flexible students.

II. OBJECTIVES OF THE RESEARCH EFFORT

From the point of view of the learning/memory literature, there are a number of topics which interface with the training issues discussed above. These include curriculum development, method of instruction, issues of transfer (e.g., organization of material, state dependency, overlearning, etc.), and a host of others. But to this investigator, the single most relevant issue would appear to be positive reinforcement.

Positive reinforcement (or reward) is used in any CAI program, particularly when the emphasis is on Unit Mastery. Although a large body of evidence suggests that rewards do strengthen the specific behaviors to which they are applied, there is a more current body of literature suggesting that this may be achieved at an undesirable cost (see Lepper & Greene, 1978 and Schwartz, 1981 for a more complete review). Given this, the objectives of the proposed research are twofold:

- (1). to review relevant literature on the deleterious effects of positive reinforcement on initial learning and subsequent transfer; and
- (2). to report the results of an initial study on the effects of positive reinforcement on transfer in sequential learning.

Before stating the actual problem and reviewing the relevant literature, it is important to define two key terms, namely, reinforcement and transfer.

A reinforcer is any stimulus which when presented or removed increases the probability or frequency of the behavior it is contingent upon. The positive reinforcer (or reward) is the presented stimulus (e.g., a pellet of food for the rat's lever press response), and the negative reinforcer is the removed stimulus (e.g., termination or prevention of painful electric shock contingent upon the rat's running response). In the present research effort, emphasis will be on positive reinforcement.

Transfer occurs when either present learning alters future learning (i.e., proactive transfer), or when present learning alters past learning (i.e., retroactive transfer). In either case, transfer is positive when the effect is to facilitate learning, and negative when the effect is to retard learning. In the present research effort, emphasis will be on negative proactive transfer.

III. STATEMENT OF THE PROBLEM

As noted earlier, the ATC is committed to classroom education, and much time and resources have already been spent on CAI software. On face value, this is not a bad idea. Inspection of the various Job Description manuals reveals that most jobs are depicted in steps. For example, a report by Elwood, Warm, Thocher, and Hritz (1983) breaks down the job of refueling the B-52 into 36 distinct steps (i.e., from the review of safety precautions (#1) to disconnection of the LOX Cart Grounding Cable (#36)). From the Unit Mastery perspective, this job, and jobs like it, can be viewed as a sequence of units, each of which is mastered separately, and at one's own pace.

From the learning/memory perspective, there has been, since Skinner's (1938) initial proclamation, well over 40 years of evidence to support the contention that positive reinforcement strengthens specific behaviors. Skinner has always been a strong advocate of rewarding desirable and extinguishing undesirable

behaviors (he argues in several places that punishment is not necessary). It is this belief that led Skinner (1968) to develop the teaching machine, and influenced Keller (1968) to develop the Unit Mastery system. But despite numerous documented successes (see the most recent issues of the Journal of Personalized Instruction), there is a growing body of evidence suggesting that extrinsic rewards produce undesirable side effects. In particular, the evidence suggests three things:

- (1). extrinsic rewards reduce intrinsic motivation to perform;
- (2). extrinsic rewards for specific behaviors retard learning of nonreinforced, but related behaviors; and
- (3). extrinsic rewards for specific sequences of behaviors retards learning of new and/or difference sequences of behaviors

The implications of these possibilities are profound. From the point of view of CAI and Unit Mastery, extrinsic rewards (usually in the form of points or grades) are the cornerstone of the teaching system. From the point of view of the job descriptions, it is sequential behavior that is the goal of technical training (e.g., from step #1 to step #n). Thus, if the aforementioned possibilities are true, then students may be learning very specific jobs and skills at the expense of more generalized knowledge needed while in the field.

IV. REVIEW OF THE RELEVANT LITERATURE

A. Extrinsic Rewards: According to Skinner (1968), successful learning generates intrinsic rewards. That is, properly arranged programs of instruction have built-in incentives for continued efforts to achieve. Unfortunately, in most educational settings, there are always extrinsic rewards (grades or points), and it is the explicitness of these rewards which seems to create the undesirable

side effects. The most basic finding in the literature is that when extrinsic rewards are provided for behaviors that are already preferred, the rewarded behaviors become less preferred.

For example, in a study by Lepper, Greene, and Nisbett (1973), children were first given the opportunity to choose among a list of attractive activities at playtime. Later, they were explicitly rewarded for engaging in the behaviors they most preferred. Relative to a nonrewarded control group, the rewarded group ultimately showed a marked reduction in preference for initially preferred tasks.

This is a common finding that is not limited to children, or to type of task. But the important question relates to the mechanism by which reduced incentive interferes with behavior. Is it simply a reduction in motivation to perform which affects any and all behaviors? Or is there an interaction between extrinsic reward and information processing?

Although early theorizing favored the simple notion of generalized decline in motivation, more recent evidence suggests that extrinsic rewards do, indeed, affect the way in which information is processed. This evidence suggests that extrinsic rewards produce subjects who tend to choose easier problems to solve (Maher & Stallings, 1972). Also, extrinsically rewarded subjects tend to focus only on those aspects of the problem they perceive as being related to the solution (Condry & Chambers, 1976).

The implications of such findings for Unit Mastery Learning are obvious. Given a choice (which students often are), challenging problems will be avoided so that points may be built up. And, even if the system allows for no choices, students will limit their attention to what they believe is relevant to point production. This latter point relates to a phenomenon called "incidental learning", which will be discussed next.

B. Incidental Learning: The incidental learning paradigm is important because it reveals a distinction between what is known vs. what is done (i.e., learning vs. performance). Performance is directly observable, but learning must be inferred from performance. We tend to assume that good performance reflects good learning, and that poor performance reflects poor learning. However, given what is known about incidental learning, the implication of poor performance is not that simple.

The demonstrative study in this area is by Tolman and Honzik (1930). Rats that were rewarded in the goalbox of a complex maze took an average of ten sessions to reach asymptotic performance levels (as measured by time to complete the maze, and by number of errors made). In comparison, nonrewarded rats showed random performance across the same ten-session interval. However, when given reward after ten sessions, the previously nonrewarded rats took only a single session to reach the same asymptotic levels as the rewarded rats. Thus, despite non-reward, and despite random performance during nonreward, these rats had to have learned pathways to the goalbox during nonreward in order to do in one session, what rewarded rats did in ten sessions.

The implications of incidental learning are therefore twofold. First, learning is a cognitive process separable from performance; and secondly, reward, though seemingly necessary for good performance, is not necessary for learning.

In a surprising extension of these early findings with rats, more recent findings with humans suggest that nonrewarded subjects not only learn in the absence of reward, but also, may learn more than their rewarded counterparts.

In the demonstrative human study, Bahrick, Fitts, and Rankin (1952) asked adult subjects to track spatial events in reward and nonreward conditions. Peripheral stimuli unrelated to reward were occasionally turned off. Rewarded subjects not only performed more poorly on the target task, they also missed the incidental event with greater frequency than their nonrewarded counterparts.

This is not an isolated finding (see also Bahrick, 1954; Davis & Lovelace, 1963; Johnson & Thomson, 1962). Moreover, it relates to the general issue of intrinsic vs. extrinsic motivation discussed earlier. If reward focuses attention only on those elements of problem solving directly related to reward, it makes sense that incidental tasks should be overlooked in the pursuit of the target behavior(s).

Returning to the classroom, the implication is that students will not attend to information unless it is an implicit part of the learning objectives. The danger here is that course objectives may not cover all the material that needs to be learned. If so, what is not covered explicitly, needs to be learned incidentally.

C. Sequences of Behavior: The final relevant point in the literature is that sequential behavior, when explicitly rewarded, tends to fixate, or stereotype the response sequence. This point is the one most relevant to technical training, and to the research results to be reported below. The origins are once again in the animal literature.

In a study by Schwartz (1980), pigeons were required to peck at either of two response keys. Rewards (access to grain) were presented after eight total responses, but only if an equal number of pecks were made to both keys. It is important to realize that in this procedure, specific order is not important; any sequence which leads to four pecks at each key is rewarded, and there are 70 such sequences in this particular task. Despite this, pigeons invariably pecked a single (or dominant) sequence 60-90% of the time.

More recently, Schwartz (1982) obtained the same effect with college students pressing either of two keys on a modified terminal keyboard (for money rewards). More importantly, once the subjects showed this stereotypy, they were retarded in learning new rules relative to control subjects who had never

experienced any original training. It must be stressed that the experimental subjects showed negative transfer even though many of the component parts of the transfer task were present in the original learning task.

Once again, there are important implications for classroom education, particularly for the Unit Mastery system. If the goal of training is to obtain performance of one and only one task, and the performance requirements never change, there is no major problem. However, if the nature of the task changes (e.g., due to technological changes), or if the student is asked to learn related, but different tasks, reinforcement-induced stereotypy stands as a strong potential contributor to negative transfer. Thus, the explicit purpose of the research conducted was to explore the conditions under which sequential learning is negatively affected.

V. RESEARCH CONDUCTED

Experiment 1:

The purpose of Experiment 1 was to determine the degree to which Schwartz's procedure induces reliable and strong stereotypy. It used the following methodology.

Subjects: Nine Florida Institute of Technology college students were recruited as paid volunteers.

Apparatus: An Apple computer system served as the only apparatus used in the research project. The monitor for the system was an Amdek-300 green phosphor screen. Programmed on the screen was a 5 x 5 matrix of stars, any of which could be illuminated (i.e., inversed). Responses in all experiments required pressing of two keys on the board, which were labeled "L" and "R" (for left and right at all times. Pressing any other key on the board (including RESET) had no effect on the program. The Basic program used to provide the contingencies in the experiments was also used to collect, reorder, and print out the data.

Procedure: Subjects were greeted and escorted into the experimental room, and shown the apparatus. They were told that their task was to accumulate points by pressing the L and R keys in any way they saw fit, and that they would be paid two cents per point earned. The points accumulated in a counter in the top right-hand portion of the screen. They were further instructed that L and R responses had no effect unless the blinking cursor was on, and that responses on any other keys on the board (at any time) had no consequences whatsoever. Nothing was said about the 5 x 5 light matrix. At the start of a trial, the entire matrix was visible, with the star in the upper left-hand corner illuminated. An L response extinguished the currently illuminated light and lit the one directly below it, and the R response extinguished the currently illuminated light and lit the one directly to the right of it. A single experimental session consisted of four blocks of 50 trials. On each trial, one of two things could happen. First, the subject could make four responses each on L and R (in any order). This would ultimately illuminate the star in the lower right-hand corner of the 5 x 5 matrix. On these trials, reinforcement (i.e., 1 point) occurred randomly, 50% of the time (i.e., R50). On such a reinforced trial, subjects received an inverted message reading "correct". This message remained on the screen for one second, and was followed by an intertrial interval of 2.5 seconds before the next trial. The other possibility was that a key, either L or R, could be pressed for the fifth time, before the other key was pressed the fourth time. In this case, the screen was blanked, the 2.5 second intertrial interval was given, and reinforcement was not earned. In short, only trials which moved the inverse from top left to lower right ended with a point, and this occurred randomly on such trials 50% of the time.

After each 50-trial block, the subject was given a two-minute rest period, while data from this block was being printed out and stored. Each session lasted approximately one hour, and each subject served in three sessions, all taking place within a single week.

Results and discussion:

The results of Experiment 1 are depicted in Table 1. This table contains two pieces of data for each subject. The left-hand column depicts the number of different sequences used in a given 50-day trial block, and the right-hand column depicts the frequency of the dominant sequence. The pattern for good stereotypy would show a gradual decrease in the number of sequences down the left-hand column, and an increase in the frequency of a dominant sequence down the right-hand column. For example, Subject #9 (S9) started with 16 different sequences on trial block 1, and during this trial block, produced what was ultimately the dominant sequence, eight times. Going down the columns, this subject showed one trial block with only a single sequence containing the dominant pattern. In general, the results were mixed with respect to obtainment of stereotypy.

Five of the nine subjects showed little evidence of the effect obtained by Schwartz. The weakest effect was shown by S8, who by the end of trial block 12 showed more than 20 different sequences, with a dominant frequency of between five to seven. This was the only subject that failed to show a dominant pattern more than 20% of the time. Although not nearly as extreme, the other four subjects showed patterns similar to S7. Here, we can see a failure for number of sequences to decrease below ten, and for frequency of the dominant sequence to increase above 15. Patterns similar to this one were shown by S3, S5, and S6. It is interesting to note that S3 and S5 showed early signs of development of strong stereotypy, but this trend did not continue during their later trials.

In comparison, S1, S2, S4, and S9 showed evidence of strong stereotypy, although the results here, were also somewhat variable. For example, S1 showed stronger stereotypy on trial 6 than on trial 12, and S2 inserted a nondominant pattern on 100% of the trials in trial block 11.

In short, there was a general failure to replicate Schwartz's findings. In Schwartz's R50 condition, four of four subjects developed strong stereotypy well within the 12 trial blocks used in this experiment. It is not clear why I was not able to replicate his results, and I will discuss that issue further in the general discussion section.

Experiment 2:

Recall, the goal of the research project was to study transfer of learning relative to a baseline of stereotypy. However, in order to do so, one must first demonstrate the strong stereotypy. Although some of the subjects in Experiment 1 did so, there were enough general failures and mixed patterns to warrant further study of the conditions that produce stereotypy. Thus, rather than proceeding directly into a transfer study, two additional control conditions were tried. The first of these is reported in this experiment.

Subjects: Seven Florida Institute of Technology college students were recruited as paid volunteers.

Apparatus: The apparatus was the same as described in Experiment 1.

Procedure: The procedure was the same as described for the R50 condition in Experiment 1, but with one noteworthy change. In the R50 condition, points were accumulated on 50% of the trials in which a sequence included four responses each on the L and R key. In the new condition, points occurred on 50% of the trials regardless of which sequence was used. In other words, the inverse did not have to be moved to the lower right-hand corner of the screen.

Results and discussion:

The results of Experiment 2 are depicted in Table 2, which is read in the same way as Table 1. It should be noted that only six of the seven subjects

are represented. Due to equipment problems, some data from Subject #7 was lost. However, this subject performed in much the same manner as the other six.

Inspection of Table 2 reveals virtually no evidence of stereotypy. Although S1 did reduce its total number of sequences to the five-six range, and increased the frequency of the dominant sequence to the 15-17 range, this is the only hint of stereotypy effect, and it is quite weak relative to the effects obtained by Schwartz. The remaining five subjects clearly failed to show stereotypy, showing instead, double digits for number of sequences, and for the most part, single digits for the frequency of a dominant sequence.

The condition used in this experiment is, in effect, a variable time schedule, and the reason it was used is because this schedule is believed to induce superstitious behavior (i.e., stereotyped behavior that is the result of adventitious, or accidental reinforcement). Its failure to induce stereotypy is therefore a plus, in that it suggests that the weak effects obtained in Experiment 1 with R50 were due not to general weakness of this condition, but instead, to potential procedural differences relative to Schwartz's R50 condition. I will speak to these procedural differences in the general discussion section.

Experiment 3:

Relative to the R50 condition in Experiment 1, the variable time 50% (VT50) condition in Experiment 2 maintained the 50% reinforcement schedule, but did so independently of the pattern produced on the screen by the subject. In other words, any pattern had the same probability as any other pattern. Experiment 3 extended the VT50 condition such that 50% of all patterns were reinforced, but the subject lacked control over what was occurring on the screen.

Subjects: Seven Florida Institute of Technology college students were recruited as paid volunteers.

Apparatus: The apparatus was the same as in Experiments 1 and 2.

Procedure: The only difference between the procedure in this experiment relative to the VT50 condition in Experiment 2 was that the inversed cursor moved up or down randomly. In other words, regardless of whether the subject pressed L or R, movement of the cursor was under the control of a random 50% generator. This condition is therefore termed VTNL50 (for variable time no lights).

Results and discussion:

The results of Experiment 3 are depicted in Table 2. Notice, there is only one row of data for each subject in this experiment. This row represents number of dominant sequences. Total number of sequences on this condition is partially out of the control of the subject since any random movement of the cursor that takes the inverse off the screen (either to the right or the left) automatically ends the trial. Thus, this could happen on the 5th-8th response of the subject, regardless of which keys were pressed. The data of interest, therefore, are the number of identical sequences through presses 1-5, which is what each row of data represents.

Under this condition, a good example of stereotypy is illustrated by S4. Notice, during the last three trial blocks, the identical pattern was shown on between 48-50 out of 50 trials. The patterns for S2, S3, S5, and S6 were relatively strong (no not as strong as for S4), whereas the patterns for S11 and S7 showed little if any indication of stereotypy.

Thus, if we compare the results of Experiment 3 to those of Experiment 1, there was more clear-cut evidence of a stereotypy effect in VTNL50 than in R50. It must be noted that Schwartz ran neither a VT50 nor a VTNL50 condition. It must also be noted that the results for VTNL50 are not at all unexpected. In effect, VTNL50 is a "learned helplessness" condition (See Maier, Seligman, & Solomon, 1971). In the learned helplessness condition, subjects are presented

with aversive stimuli that they are unable to do so. What is aversive in the VTNL50 procedure (judging from the reports of the subjects), is their inability to control movement of the inverse.

Experiment 4:

The crucial issue in Schwartz's study was the degree to which prior R50 training impeded subsequent rule learning. For example, in the R50 condition, any sequence containing four each of L and R is rewarded 50% of the time. This is a relatively simple rule. In one of Schwartz's conditions, the rule was made more complicated by requiring that a sequence begin with two L responses. In other words, any sequence of four L and R response beginning with LL was rewarded 100% of the time, a condition called LL50. Schwartz reported that subjects receiving prior R50 training had a more difficult time learning the LL50 rule than subjects with no prior training at all (i.e., a hold group). Experiment 4 tested this with the conditions used in the prior three experiments, plus a hold condition.

Subjects: Seven Florida Institute of Technology students were recruited as paid volunteers. In addition, the 23 students serving in the prior three experiments were given additional training.

Apparatus: The apparatus was the same as in the first three experiments.

Procedure: Naive (i.e., hold) and veteran (i.e., prior experience with R50, VT50, or VTNL50) subjects received the same instructions. They were told that they were to figure out what makes the machine give points. They were also told that there were three components to this rule, and that they must get all three. If they did, they would receive the typical two cents a point payoff, plus a bonus dollar. The actual rule had the following three components. First, there is no reward at any time unless the inverse goes to the bottom right-hand corner of the grid. Second, any sequence that satisfies rule #1 and

is not begun with LL is rewarded only 50% of the time. Third, any sequence that satisfies rule #1 and is begun with LL is rewarded 100% of the time.

Subjects were given scratch sheets for notes. These were presented at the beginning and removed at the end of each trial block. They were told when they correctly identified any of the three components of the rule, but otherwise, were told nothing (even if they were close).

Results and discussion:

The results of Experiment 4 are in Table 4, which depicts the trial block number on which the rule was correctly stated. Thus, the seven control (or hold) subjects took between 11 and 16 trial blocks to figure out all three components of the rule. In comparison, the R50 subjects took between 7 and 15 trial blocks. Inspection of the data for these two groups reveals a finding that is not consistent with Schwartz's. Six of the nine R50 subjects performed within the same range as the hold subjects, and the other three performed better (i.e., took only seven trials). Thus, there was clearly no superiority for the hold subjects (as in Schwartz's study). This was confirmed in Mann-Whitney U-test ($U=30$) which showed no significant difference between the two groups.

Of course, it may be argued that a failure to find a negative transfer effect was due to failure to find strong and consistent stereotypy in R50. This, therefore, could explain the obvious large dispersion in rule discovery by this group. However, if this was true, then there should be a relationship between degree of stereotypy and trials to rule discovery. To determine this, a Pearson Product Moment Correlation Coefficient was computed within the R50 group. The comparison was between median number of dominant sequences on the final four trial blocks vs. trials to rule discovery. A relationship between stereotypy

and rule discovery consistent with Schwartz's results would demand that this correlation be high (i.e., the greater the number of dominant sequences, the longer the number of trials to rule discovery). However, this did not happen, as the correlation was extremely small, though slightly positive ($r=+.14$).

On the other hand, inspection of the VT50 data in Table 4 confirms an opposite prediction implied by Schwartz's results. Specifically, this group showed little if any evidence of stereotypy in their baseline training, and thus would be expected to reach rule discovery in the fewest number of trials. These subjects took between 3 and 10 trials, and a Mann-Whitney U-test comparing hold vs. VT50 was significant at the .01 level ($U=1$).

The VTNL50 data paints a more confused picture. Specifically, four of the subjects performed in the VT50 range, and three performed in the hold range. This amount of variability with this few subjects produced a nonsignificant U-test ($U=16.5$) in the comparison between hold vs. VTNL50. As a pure speculation, it can be argued that those performing like hold subjects were more stereotyped in baseline training than those performing like VT50 subjects. However, the correlation between degree of stereotypy and trials to rule discovery was again small and positive ($r=+.29$). In other words, less than ten percent of the variability in the relationship could be accounted for by this factor.

General Discussion:

The purpose of the research project was to use Schwartz's procedure to further investigate the relationship between degree of reinforcement-induced stereotypy and negative transfer in rule learning. The experiments initially proposed were not ultimately performed, because Schwartz's basic findings were never fully replicated. Thus, the experiments performed were more geared toward

determining the generality of the basic finding itself. The data obtained speak to a number of important procedural and conceptual issues.

On the procedural level, comparison between my procedure and Schwartz's reveals two important sources of variability. First, in Schwartz's R50 condition, the lights moved sideways and downward (in conjunction with L and R responses) on a blank screen. In the present procedure, the lights moved in likewise fashion, but on a grid of stars. In other words, the inverse of a star denoted the current position. Although this seems like a modest difference, it may be argued that with the grid of stars, subjects are almost given a view of where the final light position should be. But on the other hand, it may be argued that this final position should make itself apparent even in a blank screen, after only a few trials. This, of course, is open to empirical investigation.

The second, and more important procedural difference, relates to the subjects themselves. Schwartz used very small groups (between three and four subjects per group), and was very careful in selecting them for constancy on factors such as degree of college experience, grade point average, etc. Considering that the task is one that should vary positively with degree of intellectual factors, these should be considered before assigning subjects to the various groups.

Regarding the conceptual differences, the most important finding was the general failure to obtain strong and consistent stereotyped behavior in R50 within the allotted number of baseline trial blocks (i.e., 12). This, of course, can relate to the two procedural differences discussed above, particularly to the fact of careful selection of subjects. But independently of this, it may be the case that Schwartz's hold condition is not the best control group against which to measure negative transfer. From Schwartz's perspective, this is as it should be. When viewed against this baseline, the R50 condition did, indeed, transfer negatively to rule learning, whereas the VTNL50 condition produced an other-or effect.

Closer inspection of the transfer condition (i.e., LL50) reveals that the important conceptual consideration is hypothesis testing. Schwartz reported that while in LL50, subjects concentrated on trying to discover the rules. That is, once they discovered the LL part of the rule, they could have easily lost sight of the task, and just concentrated on earning points on every single trial. This would involve beginning each trial with LL, and then taking various routes to the bottom right-hand corner. If so, a subject would never have the opportunity of testing a hypothesis with respect to the 50% rule. Schwartz monitored this in his subjects, and reported that it did not occur. In the present study, it occurred in at least half the subjects, and there was no relationship between this effect (called confirmation bias) and the group membership. In short, regardless of the group in which the subjects resided, many of the subjects simply earned points for many trial blocks before testing for the 50% component rule.

In summary, therefore, the present results must be considered exploratory. However, they are suggestive of the variables required for generation of strong stereotypy and negative transfer to rule discovery. These variables include:

- (1). blanking the screen to make the inverse position more difficult to discern.
- (2). ensuring greater homogeneity of the subject population, and, in fact, matching on intellectual factors prior to group assignment.
- (3). varying the complexity of the rule task, and taking precautions to ensure that subjects concentrate on discovering the rule rather than earning the points.
- (4). making the baseline a variable length, and using for transfer purposes only those subjects showing a criterion level of stereotypy performance.

There are many other variables of potential interest, but these seem like the major ones. Consequently, the grant period has allowed me to set up ground conditions for exploring a number of variables, and even though this period has ended, these experiments will be conducted.

Subject #1	Subject #2	Subject #3	Subject #4	Subject #5
14 (20)	10 (25)	10 (12)	4 (26)	2 (20)
4 (39)	14 (7)	4 (24)	3 (34)	2 (22)
2 (14)	5 (22)	4 (36)	5 (31)	6 (11)
2 (43)	5 (37)	4 (7)	2 (33)	6 (12)
9 (11)	5 (25)	5 (13)	2 (28)	6 (10)
1 (50)	10 (11)	6 (5)	4 (28)	11 (8)
10 (23)	9 (6)	11 (2)	5 (23)	10 (12)
6 (23)	4 (44)	7 (10)	4 (21)	9 (9)
7 (19)	5 (45)	6 (11)	2 (29)	10 (8)
4 (25)	2 (46)	9 (18)	3 (27)	10 (5)
3 (28)	2 (0)	5 (14)	4 (25)	11 (8)
3 (16)	4 (27)	6 (11)	2 (31)	8 (20)

Subject #6	Subject #7	Subject #8	Subject #9
19 (9)	16 (5)	24 (8)	16 (8)
19 (9)	6 (14)	5 (10)	5 (28)
10 (15)	11 (0)	9 (10)	4 (2)
12 (12)	17 (0)	12 (10)	6 (19)
12 (14)	10 (11)	16 (10)	5 (17)
9 (12)	11 (11)	22 (5)	6 (33)
7 (12)	7 (13)	25 (4)	1 (50)
8 (12)	8 (10)	26 (6)	2 (38)
8 (10)	8 (14)	27 (5)	3 (29)
8 (10)	7 (12)	29 (5)	5 (32)
13 (8)	6 (10)	25 (7)	2 (49)
12 (5)	5 (10)	21 (6)	2 (30)

TABLE 1: Total number of sequences and frequency of the dominant sequence for each of the nine subjects at each of the 12 50-session trial blocks in Experiment 1.

Subject #1	Subject #2	Subject #3
19 (6)	19 (2)	18 (9)
10 (11)	7 (0)	13 (13)
17 (3)	5 (0)	17 (8)
21 (6)	10 (1)	21 (9)
18 (0)	9 (0)	27 (2)
28 (1)	8 (0)	25 (2)
18 (1)	7 (0)	20 (2)
24 (2)	7 (1)	20 (2)
16 (2)	11 (1)	24 (1)
16 (4)	11 (9)	21 (4)
5 (17)	10 (7)	31 (2)
6 (15)	8 (1)	21 (3)

Subject #4	Subject #5	Subject #6
29 (5)	28 (6)	23 (2)
31 (1)	29 (6)	35 (1)
32 (3)	15 (8)	32 (3)
32 (1)	13 (7)	33 (2)
25 (6)	31 (2)	34 (3)
24 (7)	32 (2)	36 (1)
33 (5)	23 (3)	38 (2)
29 (12)	31 (3)	31 (1)
25 (7)	26 (7)	34 (4)
27 (7)	22 (5)	34 (2)
14 (13)	33 (1)	26 (4)
17 (11)	21 (0)	30 (5)

TABLE 2: Total number of sequences and frequency of the dominant sequence for six of the seven subjects at each of the 12 50-session trial blocks in Experiment 2.

	T1	T2	T3	T4	T5	T6	T7	T8	T9	T10	T11	T12
S1	6	18	46	24	9	0	4	5	34	0	16	14
S2	3	0	5	2	32	41	39	23	25	32	29	28
S3	27	4	0	32	20	17	30	27	25	31	19	22
S4	14	24	15	31	41	19	46	17	0	50	49	48
S5	14	31	27	22	29	34	4	12	37	39	31	22
S6	23	25	40	40	32	29	28	17	41	37	44	32
S7	14	22	11	6	12	7	5	17	18	16	8	6

TABLE 3: Frequency of dominant sequence for each of the seven subjects at each of the 12 50-session trial blocks in Experiment 3.

HOLD	R50	VT50	VTNL50
10	11	8	7
16	7	5	6
13	7	3	13
11	15	9	6
11	12	10	16
12	12	9	12
10	15	9	6
	7		
	15		

TABLE 4: Trial block number on which the rule was correctly stated for subjects in the four conditions in Experiment 4.

REFERENCES

- Bahrick, H.P. Incidental learning under two incentive conditions. Journal of Experimental Psychology, 1954, 47, 170-172.
- Bahrick, H.P. Fitts, P.M., & Rankin, R.E. Effects of incentives upon reactions to peripheral stimuli. Journal of Experimental Psychology, 1952, 44, 400-406.
- Black, D. & Bottenberg, R.A. Comparison of technical school and on-the-job training as methods of skill upgrading. 1970, AFHRL-TR70-48.
- Condry, J.C. & Chambers, J.C. How rewards change the problem solving process. Manuscript in preparation, 1976.
- Davis, R.T. & Lovelace, W.E. Variable rewards and peripheral cues in discriminations by irradiated and nonirradiated monkeys. The Journal of Genetic Psychology, 1963, 103, 201-205.
- Elwood, W.F., Warm, R.E., Thocher, L.I., & Hritz, R.L. Validity and reliability assessment of performance evaluation instrument development procedures. Interim Report to AFHRL/ID, Lowry, AFB, 1983.
- Herrnstein, R.J. Stereotypy and intermittent reinforcement. Science, 1961, 133, 2067-2069.
- Johnson, R. & Thomson, C. Incidental and intentional learning under three conditions of motivation. American Journal of Psychology, 1962, 75, 284-288.
- Keller, F.S. Good-bye teacher. Journal of Applied Behavioral Analysis, 1968, 1, 78-89.
- Lepper, M.R. & Greene, D. The Hidden Costs of Reward. John Wiley & Sons, 1978, New York.
- Lepper, M.R., Greene, D., & Nisbett, R.E. Undermining children's intrinsic interest with extrinsic rewards: A test of the overjustification hypothesis. Journal of Personality and Social Psychology, 1973, 23, 129-137.
- Maehr, M.L. & Stallings, W.M. Freedom from external evaluation. Child Development, 1972, 43, 177-185.
- Schwartz, B. Development of complex, stereotyped behavior in pigeons. Journal of the Experimental Analysis of Behavior, 1980, 33, 153-166.
- Schwartz, B. Reinforcement-induced behavioral stereotypy: how not to teach people to discover rules. Journal of Experimental Psychology: General, 1982, 111(1), 23-59.
- Skinner, B.F. The Behavior of Organisms. New York: Appleton-Century-Crofts, 1938.

Skinner, B.F. The Technology of Teaching. New York: Appleton-Century-Crofts, 1968.

Tolman, E.C., & Honzik, C.H. Introduction and removal of reward, and maze performance in rats. University of California Publications in Psychology, 1930, 4, 257-275.

1983-84 USAF-SCEEE RESEARCH INITIATION PROGRAM

Sponsored by the

AIR FORCE OFFICE OF SCIENTIFIC RESEARCH

Conducted by the

SOUTHEASTERN CENTER FOR ELECTRICAL ENGINEERING EDUCATION

FINAL REPORT

NEUTRAL FUNCTIONAL DIFFERENTIAL EQUATIONS

Prepared by: Dr. Terry L. Herdman

Academic Rank: Associate Professor

Department and
University: Mathematics Department
Virginia Polytechnic Institute & State University

Research Location: Air Force Flight Dynamics Laboratory

Date: December 1984

NEUTRAL FUNCTIONAL DIFFERENTIAL EQUATIONS

and UNSTEADY AERODYNAMICS

- by

Terry L. Herdman

Department of Mathematics

Virginia Polytechnic Institute and State University

ABSTRACT

In the classical formulation the aerodynamic loads depend on the instantaneous motion of the vehicle. For example, the lift at time t is modeled as a function of the velocity components at time t but not on any previous values. However, it is well known that the aerodynamic forces depend to some extent on the flow in the wake behind a lifting surface so that some memory effects are expected. The inclusion of these effects in flight-mechanics problems lead to a model including functional differential equations of neutral type. We establish the well-posedness of a class of functional differential equation which have been proposed as a mathematical model for a two-dimensional model for an aeroelastic system. The well-posedness of these equations is not guaranteed by the previous theory because the difference operator here does not have an atom at zero.

I. INTRODUCTION:

In recent years there has been an increased interest in the development of so called state space model for aeroelastic systems in unsteady aerodynamics (see [2], [3], [4], [7]). The

formulation of control and identification methods and the evaluation of potential design establish the need for mathematical models that faithfully predict the dynamic behavior of the aeroelastic system. The inclusion of memory effects in the aeroelastic forces lead to a model that includes functional differential equations (see [3], [7]). Recent advances in the area of functional differential equations make it reasonable to include these memory effects in the mathematical model.

Although the actual model involves three-dimensional, unsteady, viscous, compressible flow we choose (for this research effort) to consider the two-dimensional unsteady flow of an invicid incompressible fluid. In particular, we choose to consider the model proposed by Burns, Cliff and the author of this report (see [3]). The present project concerns the examination of the well-posedness of this model.

II. WELL-POSEDNESS FOR AN AEROELASTIC SYSTEM

The aeroelastic system described in [3] is of the form

$$\frac{d}{dt}[A_0 x(t) + \int_{-r}^0 A_1(s)x(t+s)ds] = B_0 x(t) + \int_{-r}^0 B_1(s)x(t+s)ds, \quad t > 0 \quad (2.1)$$

$$x(s) = \phi(s), \quad -r \leq s \leq 0$$

where A_0 , $A_1(s)$, B_0 , and $B_1(s)$ are 8×8 matrices satisfying the following condition.

Condition A.

(i) $A_0 = \text{diag} (1, 1, \dots, 1, 0)$

- (ii) $B_1(\cdot)$ is continuous on $[-r, 0]$
- (iii) $A_{ij}(s) = 0$ $i=1, 2, \dots, 8; j=1, 2, \dots, 7.$
- (iv) $A_{i8}(s)$ is continuous on $[-r, 0], i=1, 2, \dots, 7$
- (v) $A_{88}(s) = a|s|^{-1/2}B(s)$, where $a > 0$ and $B(s)$ is continuous on $[-r, 0]$ and $B(0) = 0.$

We shall only consider the case where $r < +\infty$. Although we believe that the results that are described below can be extended to cover the infinite delay problem ($r = +\infty$) found in [3], we have not checked all details at this time.

Let A_0, A_1, B_0, B_1 satisfy condition A and define

$$D\phi(\cdot) = A_0\phi(0) + \int_{-r}^0 A_1(s)\phi(s) \quad (2.2)$$

and

$$L\phi(\cdot) = B_0\phi(0) + \int_{-r}^0 B_1(s)\phi(s). \quad (2.3)$$

We can now rewrite system 2.1 as

$$\frac{d}{dt} D x_t = L x_t \quad (2.4)$$

and

$$x_0 = \phi \quad (2.5)$$

where $x_t, t \geq 0$, is defined on $[-r, 0]$ by $x_t(s) = x(t+s).$

The goal of this research effort was to determine appropriate state spaces so that the functional differential equation (2.4) together with initial condition (2.5) is well-posed. We examined this problem via semigroup theory for neutral functional

differential equations. Since A_0 is singular and $A_1(s)$ is integrable, the operator D defined by (2.2) is not atomic at zero and the results of [5] do not apply to the system (2.4)-(2.5).

Define the operator Q by

$$Q(\eta, \phi) = \langle L\phi(\cdot), \dot{\phi}(\cdot) \rangle \quad (2.6)$$

on the domain

$$\mathcal{D}(Q) = \{(\eta, \phi) \mid \phi(\cdot) \in W^{1,p}, D\phi = \eta\}, \quad (2.7)$$

where $W^{1,p}$ denotes the usual Sobolev space (see [1]).

The operator Q defined by (2.6)-(2.7) generates a C_0 -semigroup on $\mathbb{R}^B \times L_p(-r, 0)$ if and only if $\mathcal{D}(Q)$ is dense in $\mathbb{R}^B \times L_p(-r, 0)$, the resolvent $\rho(Q)$ is nonempty and the Cauchy problem

$$\frac{d}{dt}z(t) = Qz(t), \quad z(0) = z_0 \in \mathcal{D}(Q) \quad (2.8)$$

has a continuously differentiable solution on $[0, +\infty)$, (see [8] and page 102 in [9]).

The following result is a corollary to Theorem 2 in [6] (which is included as an appendix to this report).

Theorem. If D and L are defined by (2.2), (2.3) and Condition A is satisfied, then Q defined by (2.6)-(2.7) generates a C_0 -semigroup on $\mathbb{R}^B \times L_p(-r, 0)$ for all p satisfying $1 < p < 2$.

The well-posedness of the system (2.1) on the state spaces $\mathbb{R}^B \times L_p(-r, 0)$, $1 < p < 2$, is an immediate consequence of this theorem.

We plan to extend these results to include the corresponding

infinite delay ($r \rightarrow \infty$) case. In particular, the specific system found in [3] shall be studied. This study is essential to the development of a framework for the study of efficient numerical approximating schemes.

BIBLIOGRAPHY OF PERTINENT LITERATURE

1. R.A. Adams, Sovolev Spaces, Academic Press, New York, 1975.
2. A.U. Balakrisham, Active control of airfoils in unsteady aerodynamics, Applied Math. Optimization, 4 (1978), 171-195.
3. J.A. Burns, E.M. Cliff and T.L. Herdman, State-Space Model for an Aeroelastic System, Proceedings: 22nd IEEE CDC, 1074-1077.
4. J.A. Burns and E.M. Cliff, Hereditary model for airfoils in unsteady aerodynamics, numerical approximations and parameter estimation, AFWAL-TR-81-3173.
5. J.A. Burns, T.L. Herdman and H.W. Stech, Linear functional differential equations as semigroups on product spaces, SIAM J. Math. Anal., Vol. 14, No. 1, (1983), 98-116.
- *6. J.A. Burns, T.L. Herdman and J. Turi, Well-Posedness of functional differential equations with nonatomic D operators, Proceedings: Vith International Conference on Trends in Theory and Practice of Nonlinear Analysis, to appear.
7. J.W. Edwards, Unsteady aerodynamic modelling and active aeroelastic control, SUDARR 504, 1977, Stanford University.
8. E. Hille, Une generalization du probleme de Cauchy, Ann. Inst. Fourier 4 (1952), 31-48.
9. A. Pazy, Semigroups of Linear Operators and Applications to Partial Differential Equations, Springer-Verlag, Applied Mathematical Sciences 44, New York, 1983.

* Included as Appendix A.

WELL-POSEDNESS OF FUNCTIONAL DIFFERENTIAL
EQUATIONS WITH NONATOMIC D OPERATORS

* John A. Burns
** Terry L. Herdman
* Janos Turi

Department of Mathematics
Virginia Polytechnic Institute and State University
Blacksburg, Virginia
U.S.A

We establish the well-posedness of a class of functional differential equations of neutral type which have been proposed as mathematical models for two-dimensional aeroelastic systems. The well-posedness of these equations is not guaranteed by the previous theory because the difference operator does not have an atom at zero.

I. INTRODUCTION

In this paper we consider the question of well-posedness for a functional differential equation (FDE) that has been used to model the elastic motions of a two-dimensional airfoil in unsteady flows. This equation is a neutral functional differential equation (NFDE) for which the D operator is not atomic at $s=0$. Equations of this type also occur in the theory of lossless transmission lines and include many singular integrodifferential equations. It is often advantageous to have a state space model for these systems when addressing certain numerical and control problems. In Section II we present a brief summary of recent results concerning necessary and sufficient conditions for neutral equations to be well-posed in product spaces. In Section III we consider the well-posedness question for the aeroelastic model and close with a discussion of more general equations.

Notation used in the paper is fairly standard. If X and Y are Banach spaces, then the space of all bounded linear operators from X into Y will be denoted by $B(X,Y)$. The usual Lebesgue spaces of \mathbb{R}^n -valued "functions" on $[a,b]$ whose components are integrable when raised to the p th power is denoted by $L_p(a,b) =$

* The work of this author was supported in part by the National Science Foundation under grant ECS-8109245.

** The work of this author was supported in part by the Air Force Flight Dynamics Laboratory under contract F49620-82-0035 and the Air Force Office of Scientific Research under grant AFOSR-84-0326.

$L_p([a,b]; \mathbb{R}^n)$ for $1 \leq p < +\infty$. The usual Banach space $C([a,b]; \mathbb{R}^n)$ of continuous \mathbb{R}^n -valued functions will be denoted by $C(a,b)$ and similarly the Sobolev space $W^{1,p}([a,b]; \mathbb{R}^n)$ will be denoted by $W^{1,p}(a,b)$. Throughout the remainder of the paper $r > 0$ is a fixed real number and we shall simply write L_p , C and $W^{1,p}$ for $L_p(-r,0)$, $C(-r,0)$ and $W^{1,p}(-r,0)$, respectively. If $x: [-r, +\infty) \rightarrow \mathbb{R}^n$, then we define $x_t: [-r, 0] \rightarrow \mathbb{R}^n$ by $x_t(s) = x(t+s)$.

II. NFDEs ON PRODUCT SPACES

During the past few years considerable attention has been given to the study of semigroups generated by linear functional differential equations (see [1,2,5-9]). In 1969 Borisovic and Turbabin [2] considered the retarded equation

$$\dot{x}(t) = Lx_t \quad (2.1)$$

with initial data

$$x(0) = \eta, \quad x_0(s) = \psi(s) \quad -r \leq s < 0 \quad (2.2)$$

where $(\eta, \psi(\cdot)) \in \mathbb{R}^n \times L_p$ and L was a bounded linear operator from C into \mathbb{R}^n , i.e. $L \in B(C, \mathbb{R}^n)$. They defined the operator

$$A(\eta, \psi(\cdot)) = (L\psi(\cdot), \dot{\psi}(\cdot)) \quad (2.3)$$

on the domain

$$D(A) = \{(\eta, \psi(\cdot)) / \psi(\cdot) \in W^{1,p}, \psi(0) = \eta\} \quad (2.4)$$

and noted that A was the infinitesimal generator of the C_0 -semigroup $S(t)$ on $\mathbb{R}^n \times L_p$ defined by

$$S(t)(\eta, \psi(\cdot)) = (x(t), x_t(\cdot)) \quad (2.5)$$

where $x(\cdot)$ is the solution to (2.1)-(2.2). This result was established for a more general L by Vinter in [15] and later Delfour [8] showed that the result remained valid for any $L \in B(W^{1,p}, \mathbb{R}^n)$. In fact, Delfour's result was necessary in that if A defined by (2.3)-(2.4) generated a C_0 -semigroup on $\mathbb{R}^n \times L_p$, then L must be bounded as an operator from $W^{1,p}$ into \mathbb{R}^n . Therefore, Delfour has established the largest class of retarded hereditary systems defining C_0 -semigroups on product spaces of the form $\mathbb{R}^n \times L_p$.

In [6] and [7] Burns, Herdman and Stech extended Delfour's results to a class of NFDEs of the form

$$\frac{d}{dt} Dx_t = Lx_t \quad (2.6)$$

with initial data

$$Dx_0(\cdot) = \eta, \quad x_0(s) = \psi(s) \quad -r \leq s < 0. \quad (2.7)$$

Defining the operator

$$A(n, \phi(\cdot)) = (L\phi(\cdot), \dot{\phi}(\cdot)) \quad (2.8)$$

on the domain

$$\mathcal{D}(A) = \{(n, \phi(\cdot)) \mid \phi(\cdot) \in W^{1,p}, D\phi(\cdot) = n\} \quad (2.9)$$

it was established in [6] that L and D must belong to $B(W^{1,p}, \mathbb{R}^n)$ if A defined by (2.8)-(2.9) generates a C_0 -semigroup on $\mathbb{R}^n \times L_p$. Moreover, it was shown that if $L \in B(W^{1,p}, \mathbb{R}^n)$ and $D \in B(C, \mathbb{R}^n)$ has an atom at $s=0$, then A defined by (2.8)-(2.9) generates a C_0 -semigroup on $\mathbb{R}^n \times L_p$. Recall that $D \in B(C, \mathbb{R}^n)$ is atomic at $s=0$ if there is a matrix valued function μ and a non-singular matrix A_0 such that for $\phi(\cdot) \in C$

$$D\phi(\cdot) = A_0\phi(0) + \int_{-r}^0 d\mu(s)\phi(s) \quad (2.10)$$

where $\mu(\cdot)$ is of bounded variation on $[-r, 0]$ (we shall always assume $\mu(\cdot)$ is normalized to be continuous from the right on $(-r, 0)$ and $\mu(-r)=0$) and

$$\lim_{\epsilon \rightarrow 0^+} \int_{-r}^{-\epsilon} |d\mu(s)| = 0. \quad (2.11)$$

The sufficient conditions cited above lead to the well-posedness for a large class of hereditary systems and allows one to define generalized solutions to the NFDE (2.6)-(2.7) for L_p initial data.

Although the assumption that D belongs to $B(C, \mathbb{R}^n)$ is not very restrictive, the assumption that D has an atom at $s=0$ seemed to rule out a number of equations, including those that occur in certain models of aeroelasticity. It was shown in [6] that the assumption that D be atomic at $s=0$ is not necessary. Let $0 < \alpha < 1$ and consider the integral equation

$$\int_{-r}^0 |s|^{-\alpha} x(t+s) ds = n \quad 0 < t \quad (2.12)$$

where $x(s) = \phi(s)$, $-r \leq s \leq 0$. If L and D are defined by

$$L\phi(\cdot) = 0, \quad D\phi(\cdot) = \int_{-r}^0 |s|^{-\alpha} \phi(s) ds, \quad (2.13)$$

then (2.12) can be viewed as a neutral equation of the form (2.6)-(2.7). Note that $D \in B(C, \mathbb{R})$ and D is not atomic at $s=0$. However, the following result may be found in [6].

THEOREM 1. Assume L and D are defined by (2.13). If $p < 1/(1-\alpha)$, then A defined by (2.8)-(2.9) generates a C_0 -semigroup on $\mathbb{R} \times L_p$ defined by $S(t)(n, \phi(\cdot)) = (n, x_t(\cdot))$ where $x(\cdot)$ is the unique solution to the Abel equation (2.12). If $p \geq 1/(1-\alpha)$, then Abel's equation has a unique solution for each $(n, \phi(\cdot))$ in a dense subset of $\mathbb{R} \times L_p$. However, A does not generate a C_0 -semigroup on $\mathbb{R} \times L_p$.

Theorem 1 above lead Kappel and Zhang [12, 17] to consider more general necessary conditions for well-posedness in C of problems of the form

$$Dx_t = D\phi(t) \quad t \geq 0 \quad (2.14)$$

with initial data

$$x_0(s) = \phi(s) \quad -r \leq s \leq 0 \quad (2.15)$$

where $\phi(\cdot) \in C$ and D is not atomic at $s=0$. For the scalar case only, they defined an operator D to be weakly atomic at $s=0$ if for real λ

$$\lim_{\lambda \rightarrow \infty} |\lambda \Delta_0(\lambda)| = \infty \quad (2.16)$$

where

$$\Delta_0(\lambda) = D(e^{\lambda \cdot}). \quad (2.17)$$

Any D operator that is atomic at $s=0$ is weakly atomic. However, the D operator defined by (2.13) is not atomic at $s=0$ but is weakly atomic at $s=0$. Zhang [17] proved that if (2.14)-(2.15) is well-posed in C , then it is necessary that D be weakly atomic at $s=0$. It was shown in [7] (see Theorem 3.2) that if (2.6)-(2.7) is well-posed in $\mathbb{R}^n \times L_p$, then (2.6)-(2.7) leads to a well-posed problem on C . It follows that if (2.6)-(2.7) is well-posed in $\mathbb{R}^n \times L_p$, then D must be weakly atomic at $s=0$.

For the scalar case considered in [12] and [17], the assumption that D be weakly atomic implies that for all real λ sufficiently large the operator A has λ in its resolvent. This is true because $L\phi(\cdot) = 0$ and $\lambda \in \rho(A)$ if and only if

$$\Delta(\lambda) = \lambda D(e^{\lambda \cdot} I) - L(e^{\lambda \cdot} I) \quad (2.18)$$

is nonsingular (see Lemma 2.3 in [6]). However, for vector equations the problem becomes much more complex. In particular, condition (2.16) does not imply that $\rho(A)$ is not empty.

EXAMPLE 1. Let $L\phi(\cdot) \equiv 0$ and $D \in B(C, \mathbb{R}^2)$ be defined by

$$D\phi(\cdot) = \begin{bmatrix} 1 & 0 \\ 0 & 0 \end{bmatrix} \phi(0).$$

Note that $\|\lambda \Delta_0(\lambda)\| \rightarrow \infty$ but $\Delta(\lambda) = \lambda \Delta_0(\lambda)$ is singular for all λ . Consequently, A defined by (2.8)-(2.9) can not generate a C_0 -semigroup on $\mathbb{R}^n \times L_p$.

In the next section we consider a special problem that occurs in aeroelasticity and establish the well-posedness of this problem. A complete treatment of more general systems (including infinite delay problems) will appear in a forthcoming paper.

III. WELL-POSEDNESS FOR AN AEROELASTIC SYSTEM

We consider the FDE

$$\frac{d}{dt} [A_0 x(t) + \int_{-r}^0 A_1(s) x(t+s) ds] = B_0 x(t) + \int_{-r}^0 B_1(s) x(t+s) ds \quad (3.1)$$

where A_0 , $A_1(s)$, B_0 and $B_1(s)$ are $n \times n$ matrices satisfying the following condition.

CONDITION A.

- i) $A_0 = \text{dia}(1, 1, \dots, 1, 0)$,
- ii) $B_1(\cdot)$ is continuous on $[-r, 0]$,
- iii) $A_{ij}(s) \equiv 0$ $i=1, 2, \dots, n$, $j=1, 2, 3, \dots, n-1$
- iv) $A_{in}(s)$ is continuous on $[-r, 0]$, $i=1, 2, \dots, n-1$
- v) $A_{nn}(s) = a|s|^{-\alpha} + B(s)$, $a > 0$, $0 < \alpha < 1$ and $B(s)$ is continuous on $[-r, 0]$ and $B(0) = 0$.

Note that the aeroelastic system described in [4] is of the form (3.1) and satisfies the above conditions with $\alpha=1/2$, $n=8$ and $r=+\infty$. Although we are only considering the case where $r < +\infty$, the basic ideas below can be extended to cover the infinite delay problem described in [4].

Let, A_0 , $A_1(\cdot)$, B_0 , $B_1(\cdot)$ satisfy CONDITION A and define

$$D\phi(\cdot) = A_0\phi(0) + \int_{-r}^0 A_1(s)\phi(s) \quad (3.2)$$

and

$$L\phi(\cdot) = B_0\phi(0) + \int_{-r}^0 B_1(s)\phi(s). \quad (3.3)$$

Since A_0 is singular and $A_1(s)$ is integrable, the operator D is not atomic at $s=0$. For D and L defined by (3.2)-(3.3) we denote by A the corresponding operator (2.8)-(2.9).

Recall that A generates a C_0 -semigroup on $\mathbb{R}^n \times L_p$ if and only if $\mathcal{D}(A)$ is dense, the resolvent set $\rho(A)$ is nonempty and the Cauchy problem

$$\frac{d}{dt} z(t) = Az(t) \quad z(0) = z_0 \in \mathcal{D}(A) \quad (3.4)$$

has a unique continuously differentiable solution on $[0, +\infty)$ (see [11] and page 102 in [13]). We shall use this equivalence to establish the following result.

THEOREM 2. If D and L are defined by (3.2)-(3.3) and CONDITION A is satisfied, then A generates a C_0 -semigroup on $\mathbb{R}^n \times L_p$ for all p satisfying $1 \leq p < 1/(1-\alpha)$.

Proof. The proof that the Cauchy problem (3.4) has continuously differentiable solution on $[0, +\infty)$ can be found in [14]. Since it is fairly technical and we are limited by space, we shall not repeat it here. It remains to show that A is densely defined and has non-empty resolvent.

Let $B_i: \mathbb{R}^n \times W^{1,p} \rightarrow \mathbb{R}$ be the linear functional defined by

$$B_i(\eta, \phi(\cdot)) = \langle \eta - D\phi(\cdot), e_i \rangle_{\mathbb{R}^n}$$

where $e_i, i=1,2,\dots,n$ is the standard unit vector in \mathbb{R}^n . The domain of A is equal to $\bigcap_{i=1}^n V(B_i)$, where $V(B_i)$ denotes the null space of B_i . It follows from [3] that $\mathcal{D}(A)$ is dense if and only if each non-trivial linear combination $\Lambda = \sum_{i=1}^n w_i B_i$ is unbounded on $\mathbb{R}^n \times L_p$. If any of the $w_i, i=1,2,\dots,n-1$ are non zero then the proof of Lemma 2.2 in [6] can be used to show that Λ is unbounded. On the other hand, if $w_i=0, i=1,2,\dots,n-1$, then $\Lambda = w_n B_n$. However, since $p < 1/(1-\alpha)$, it follows that $w_n B_n(n, \phi(\cdot)) = w_n n - w_n \int_{-r}^0 A_{nn}(s) \phi_n(s) ds$ is not bounded on $\mathbb{R}^n \times L_p$ (note that $A_{nn}(s) \notin L_p$, where $1/p + 1/p' = 1$). Therefore, $\mathcal{D}(A)$ is dense in $\mathbb{R}^n \times L_p$.

To establish that $\rho(A)$ is not empty, recall that $\lambda \in \rho(A)$ if and only if $\Delta(\lambda) = \lambda D(e^{\lambda \cdot} I) - L(e^{\lambda \cdot} I)$ is nonsingular. Let $F(\lambda)$ denote the $n \times n$ diagonal matrix $F(\lambda) = \text{dia}(\lambda^{-1}, \lambda^{-1}, \dots, \lambda^{-1}, \lambda^{-\alpha})$ and observe that (for $1 \leq p < 1/(1-\alpha)$) as $\lambda \rightarrow \infty$

$$F(\lambda) \lambda D(e^{\lambda \cdot} I) \rightarrow \text{dia}(1, 1, \dots, 1, a_\infty)$$

where $a_\infty \neq 0$ and

$$F(\lambda) L(e^{\lambda \cdot} I) \rightarrow 0.$$

Therefore, as $\lambda \rightarrow \infty$ the matrix $F(\lambda) \Delta(\lambda)$ converges to a non-singular matrix and hence for sufficiently large λ , $\Delta(\lambda)$ must be non singular. This completes the proof.

We conclude this paper by noting that the above ideas can be extended and applied to a larger class of equations than those considered here. A detailed treatment of the more general problem will appear elsewhere.

REFERENCES

- [1] H.T. Banks and J.A. Burns, An abstract framework for approximate solutions to optimal control problems governed by hereditary systems, Proceedings: International Conference on Differential Equations, Academic Press, (1975), 10-25.
- [2] Ju. Borisovic and A.S. Turbabin, On the Cauchy problem for linear nonhomogeneous differential equations with retarded arguments, Soviet Math. Dokl., 10 (1969), 401-405.
- [3] R.C. Brown and A.M. Krall, Ordinary differential operators under Stieltjes boundary conditions, Trans. Amer. Math. Soc., 198 (1974), 73-92.
- [4] J.A. Burns, E.M. Cliff and T.L. Herdman, A state-space model for an aeroelastic system, Proceedings: 22nd IEEE CDC, San Antonio, Texas (1983), 1074-1077.
- [5] J.A. Burns and T.L. Herdman, Adjoint semigroup theory for a class of functional differential equations, SIAM J. Math. Anal. 5 (1976), 729-745.

- [6] J.A. Burns, T.L. Herdman and H.W. Stech, Linear functional differential equations as semigroups on product spaces, *SIAM J. Math. Anal.* 14 (1983), 98-116.
- [7] J.A. Burns, T.L. Herdman and H.W. Stech, The Cauchy problem for linear functional differential equations, *Integral and Functional Differential Equations*, Lecture Notes in Pure and Applied Mathematics Vol. 67, T.L. Herdman, S.M. Rankin and H.W. Stech, eds. Marcel Dekker, 1981, 139-149.
- [8] M.C. Delfour, The largest class of hereditary systems defining a C_0 -semigroup on the product space, *Canad. J. Math.*, 32 (1980), 969-978.
- [9] M.C. Delfour and S.K. Mitter, Controllability, observability and optimal feedback control of hereditary systems, *SIAM J. Control*, 10 (1972), 298-328.
- [10] J.K. Hale and K.R. Meyer, A class of functional differential equations of neutral type, *Mem. Amer. Math. Soc.*, 76 (1967).
- [11] E. Hille, Une generalization du probleme de Cauchy, *Ann. Inst. Fourier*, 4 (1952), 31-48.
- [12] F. Kappel and Kang pei Zhang, On neutral functional differential equations with nonatomic difference operator, Report No. 38, Institute for Mathematics, University of Graz (1984).
- [13] A Pazy, *Semigroups of Linear Operators and Applications to Partial Differential Equations*, Springer-Verlag, Applied Mathematical Sciences 44, New York, 1983.
- [14] J. Turi, Ph.D Thesis, Mathematics Department, Virginia Polytechnic Institute and State University, (In Preparation).
- [15] R.B. Vinter, On a problem of Zabczk concerning semigroups generated by operators with non-local boundry conditions, Publication 77/8, Department of Computing and Control, Imperial College of Science and Technology, London (1977).
- [16] D.V. Widder, *The Laplace Transform*, Princeton University Press, Princeton, 1946.
- [17] Kang pei Zhang, On a neutral equation with nonatomic D-operator, Ph.D. Thesis, Institute for Mathematics, University of Graz (1983).

1983-84 USAF-SCEEE RESEARCH INITIATION PROGRAM

Sponsored by the

AIR FORCE OFFICE OF SCIENTIFIC RESEARCH

Conducted by the

SOUTHEASTERN CENTER FOR ELECTRICAL ENGINEERING EDUCATION

FINAL REPORT

SENSOR/ACTUATOR SELECTION IN LINEAR SYSTEMS

Prepared by: Dr. Kathleen C. Howell

Academic Rank: Assistant Professor

Department and
University: School of Aeronautics & Astronautics
Purdue University

Research Location: Air Force Rocket Propulsion Laboratory

Date: January 1985

INTRODUCTION

It is generally accepted that large space systems will be deployed in the near future. In comparison to the predominant type of spacecraft in operation today, the characteristics of importance will need to be reordered for these new systems. One of the most significant is flexibility which brings with it a large number of attractive new options for design and applications. However, it generally needs to be much better understood before an acceptable level of confidence in our ability to design flexible systems is reached. Besides just flexibility, the large size and lightweight structure itself are also making new approaches necessary.

With work proceeding in all areas of the design of large space structures, interest is growing in the attitude control system. Besides the on-orbit functions of attitude control, which includes cancellation of disturbances, pointing and maneuvers, the system will also contribute to stationkeeping and the new requirement of shape control. To meet the increased demands, the control system will likely consist of a number of devices including sensors and actuators which may be some combination of secondary propulsion units and non-propulsive devices. The interaction of these elements with the structure will be very important.

Control law design for a large, flexible structure touches on many areas including the selection of sensors and actuators, i.e. the appropriate type, number and distribution to effectively control the system. This research effort has had the objective of considering the effect on the selection process of certain actuator characteristics.

Much of the control theory necessary to deal with selection of sensors and actuators is still in development. In most analyses so far, the appropriate number and location of the control elements has been done using sophisticated models of the structure with "generic" and "perfect" sensing and actuating devices assuming they have no contributing dynamics, instantaneous response and unconstrained amounts of torque and/or force available. This effort, then, has involved examination of some interaction of the actuators with the structure by modelling some of the contributing dynamics.

To gain some insight into the effects of actuator characteristics required, the following steps are part of the analysis:

- (1) Determination of a method of actuator selection to use in the study.
- (2) Determination of a structure and development of its dynamical model.
- (3) Choice of an actuator characteristic to be examined and its incorporation into the dynamic model.
- (4) Implementation of cost decomposition as a tool to evaluate actuators for their effectiveness.
- (5) Comparison of the selection process with and without the consideration of the given actuator characteristic.

Each step in the analysis is examined more thoroughly below.

ANALYSIS

A. Actuator Effectiveness Determination

Of a number of methods that have been studied to select an appropriate number of actuators for a system and the best locations for

those actuators, cost decomposition with component cost analysis was chosen to use in this analysis. This was not an attempt to test component cost analysis. Rather it was used only as a tool to evaluate if the results concerning the best or most effective actuators in controlling a structure might be influenced by certain actuator characteristics.

1. The Selection Problem

The goal of designing a control system always begins with a dynamic model of the structure. Classical dynamic analysis will lead to partial differential equations to describe the state of the structure. As part of the model, the measurements to be made and the controls available are usually designated. From here a controller is designed either directly from the partial differential equations (PDE) derived or by first converting the system model to a set of ordinary differential equations (ODE). Rather than the separate steps, the selection of the most useful measurements (sensors) and controls (actuators) should ideally be coupled with the control law determined. Also common, in both the PDE and ODE approach is the assumption of "perfect" sensors and actuators which is implicit in the controller design, i.e. sensors and actuators with infinite bandwidths and no phase shifts. The resulting controller is frequently too complex to be implemented which leads to controller reduction.

The theory used here is one now available to aid the selection of the best sensors and actuators during the controller reduction process. It determines the best \bar{m} out of a possible set of m actuators and the most useful \bar{l} of a possible finite l sensors. [1, 2] The work done

to date, however, does not include any of the possibly significant dynamics associated with the available sensors and actuators. This work included a model of a particular actuator characteristic to consider how it might affect the selection results.

In exploring approaches to the problem, it was noted that sensors and actuators which are available can, at best, usually be described only in terms of finite dimensional models written as ordinary differential equations. In augmenting the structure dynamics, it might also be considered that without partial differential equations to describe the sensors and actuators, modeling the structure over an infinite spectrum with PDEs is unnecessary. Therefore, in preparation to assess the effect of sensor/actuator dynamics, a number of methods of sensor/actuator selection were examined with emphasis on ODE approaches [3-10].

One of the recent approaches to the selection problem involves the application of linear-quadratic-gaussian (LQG) control theory with cost decomposition [11-12]. Rather than immediately obtaining a lower order dynamic model and then designing a controller, in the cost decomposition approach, with component cost analysis (CCA), the control input can be included as part of the reduction process. An open-loop cost decomposition method will first reduce the problem to a higher-order evaluation model for which an optimal LQG controller can be designed, but which is still of an order larger than desired. The key then for this application is the controller reduction process again using cost decomposition and CCA.

2. The Control Problem

Cost decomposition requires a linear model of the system. The system equations may originally be derived as PDEs or ODEs. But assuming that the initial linearized reduced evaluation model is available (or derivable), it is written in the following general form

$$\begin{aligned} \dot{x} &= Ax + Bu + Dw, & x \in R^n, & u \in R^m, & w \in R^p \\ D &= [B \ D_0] \\ y &= Cx, & y \in R^k \\ z &= Mx + v, & z \in R^l \end{aligned} \quad (1)$$

where x is the state and y is the vector of outputs to be regulated [6]. The elements of z are the measurement (sensor) information available, v indicates unmodelled or noisy sensors, and u the actuator signals. $D_0 w$ represents unmodelled system behavior and Bw is the unmodelled actuator noise. The unknowns $x(t_0)$, w , v are all assumed as random, zero mean processes with intensities $W > 0$ and $V > 0$. To date, perfect sensors and actuators have been assumed in such a model, but in actuality, finite dimensional models of the auxiliary equipment are, at best, the only thing available. A low-bandwidth sensor is represented as

$$\begin{aligned} \dot{x}_s &= A_s x_s + B_s \delta, & x_s \in R^{n_s} \\ z &= M_s x_s, & z \in R^{l_s} \end{aligned} \quad (2)$$

where x_s is the sensor state and δ is a column vector whose elements indicate deflections of the structure. A finite dimensional actuator appears in the form

$$\begin{aligned} \dot{x}_a &= A_a x_a + B_a u & x_a \in R^{n_a} \\ y_a &= C_a x_a & y_a \in R^{m_a} \end{aligned} \quad (3)$$

where x_a is the actuator state, u is a column vector of m_a signals to m_a actuators. The output forces of the actuators are reflected in y_a . These models can, of course, be made more complex by including coupling with each other as well as other system components, the addition of disturbances, etc. The equations in (1) are to be augmented by those in (2) and/or (3). The general form of Eqn. (1) will not change, however, the system order will be increased.

Once the dynamic model is prepared, the goal is to find the sensor/actuator combinations to meet output specifications, by minimizing the sum of normalized input variances. To keep the output and inputs (controls) within the specified ranges, which are designated as

$$\begin{aligned} -\sigma_i &< y_i(t) < \sigma_i, & i = 1, \dots, k \\ -u_i &< u_i(t) < u_i, & i = 1, \dots, m \end{aligned}$$

the following variance constraints are placed on the variables throughout the procedure,

$$\begin{aligned} \lim_{t \rightarrow \infty} E y_i^2(t) &\stackrel{\Delta}{=} E_{\infty} y_i^2 \leq \sigma_i^2, & i = 1, \dots, k \\ \lim_{t \rightarrow \infty} E u_i^2(t) &\stackrel{\Delta}{=} E_{\infty} u_i^2 \leq u_i^2, & i = 1, \dots, m \end{aligned}$$

where E is the expectation operator. The selection problem then becomes, in the simplest terms, one of using \bar{m} out of m possible

actuators and $\bar{\ell}$ out of ℓ possible sensors, to find the combination which produces the smallest values for

$$\sum_{i=1}^k E_{\infty} y_i^2 / \sigma_i^2 \text{ subject to } E_{\infty} u_i^2 = \mu_i^2$$

in the input constrained problem or

$$\sum_{i=1}^m E_{\infty} u_i^2 / \mu_i^2 \text{ subject to } E_{\infty} y_i^2 = \sigma_i^2$$

in the output constrained problem.

3. Component Cost Analysis

Once the problem is established, a nontraditional approach is taken to solve the selection/control problem. Performance is measured through a cost function V , defined as

$$V = E_{\infty} (y^T Q y + u^T R u) \quad (4)$$

where the weighting matrices Q and R can be chosen to match the problem specifications [13]. Rather than make calculations for each possible combination of sensors and actuators, however, the process of component cost analysis decomposes V into a sum of component costs, V_i

$$V = \sum_{i=1}^n V_i$$

where

$$V_i \triangleq \frac{1}{2} E_{\infty} \left[\frac{\partial (y^T Q y)}{\partial x_i} x_i \right]$$

Components can be ranked by comparing their "effectiveness values", so that

$$V_1 \geq V_2 \geq \dots$$

Differential equations associated with components x_i having the largest component costs are retained in the model.

As components, each possible sensor and actuator may be assigned a component cost,

$$v_i^{\text{act}} = \frac{1}{2} E_{\infty} \left[\frac{\partial (y^T Q y)}{\partial u_i} u_i \right] \quad i = 1, \dots, m$$

$$v_i^{\text{sen}} = \frac{1}{2} E_{\infty} \left[\frac{\partial (y^T Q y)}{\partial z_i} z_i \right] \quad i = 1, \dots, \ell$$

Cost decomposition reduces the number of control and measurement devices by retention of only those with the largest v_i^{act} and v_i^{sen} .

This method has been well developed and has shown significant results. It is much more efficient than methods which rely on testing all possible locations of measurement and control devices. Although the final result may or may not be optimal, a good indication of performance degradation as a function of sensor/actuator number and location results.

The primary objective now is to determine if the selected locations of the \bar{m} sensors and $\bar{\ell}$ acts are affected by inclusion of the above eqns. These will, of course, add to the system order initially. However, any unit deleted through component cost analysis will also mean deletion of its associated differential eqns., so not only will u and z be reduced but the system order as well. Besides locations, any change in conclusions regarding the number of sensors/actuators would be significant. There may possibly be a range of \bar{m}/m and/or $\bar{\ell}/\ell$ over which the effects are more pronounced.

B. Dynamic Models

To make comparisons and draw conclusions from the above theory, it was necessary to detail a particular structure for study. Besides the structure, it was determined to, at least initially, model actuators only and assume that the sensors and actuators would always be colocated. The models were developed as shown below.

1. Dynamic Model of a Flexible Structure

Although there are some very sophisticated models available of large structures currently being evaluated, a simpler model has many advantages during analysis. That includes a higher degree of confidence in understanding of the natural motion of the structure and a better interpretation of the results. Therefore, an unrestrained beam in a nominally circular orbit was selected as the basic structure to be controlled. It has a specified number of actuators and their possible locations were identified.

The nonlinear dynamics of such a structure have been studied previously, most recently by Kane and Levinson [15, 16]. The structure is modelled in terms of variables and coordinate systems introduced in Fig. 1. Assume that the beam orbits the Earth in the plane of the paper and that all subsequent motion of the beam occurs in that plane. Let point O represent the center of the attracting body, i.e. the Earth, assumed spherically symmetric, and assume O is fixed in the inertial frame N . To describe deformations of the beam, introduce the intermediate frame R defined by perpendicular unit vectors \hat{r}_1 and \hat{r}_2 which intersect at point R^* . Note that \hat{r}_2 is always directed from R^* to

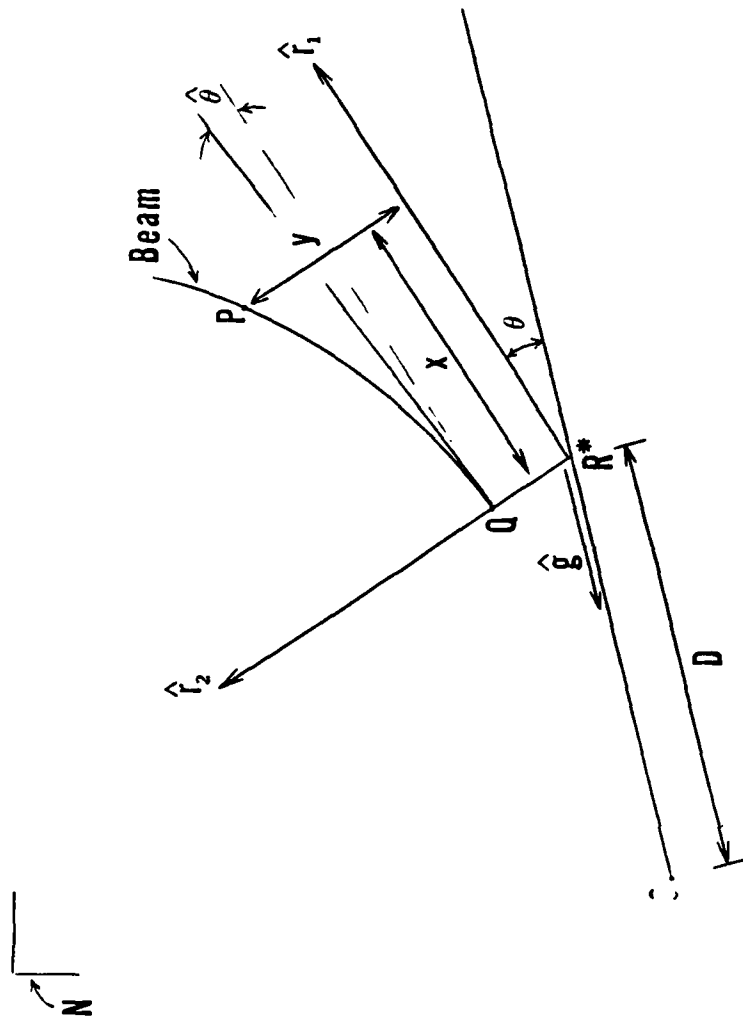


Figure 1. Variables and Coordinate System

point Q at the end of the beam. The unit vector \hat{r}_1 is 90° from \hat{r}_2 and in the plane of motion. \hat{r}_1 thus defines the angle θ . The deformation of a generic particle P of the beam, located at a distance x from point Q, is described in terms of the variable y. It was additionally assumed that the beam had a uniform cross section and that the mass was distributed uniformly along the length. Also, the beam longitudinal deformations were neglected in favor of the lateral deflections.

As is the usual practice, y can be written as a combination of functions of position and time,

$$y(x, t) = \sum_{i=1}^{\nu} \phi_i(x) q_i(t) \quad (5)$$

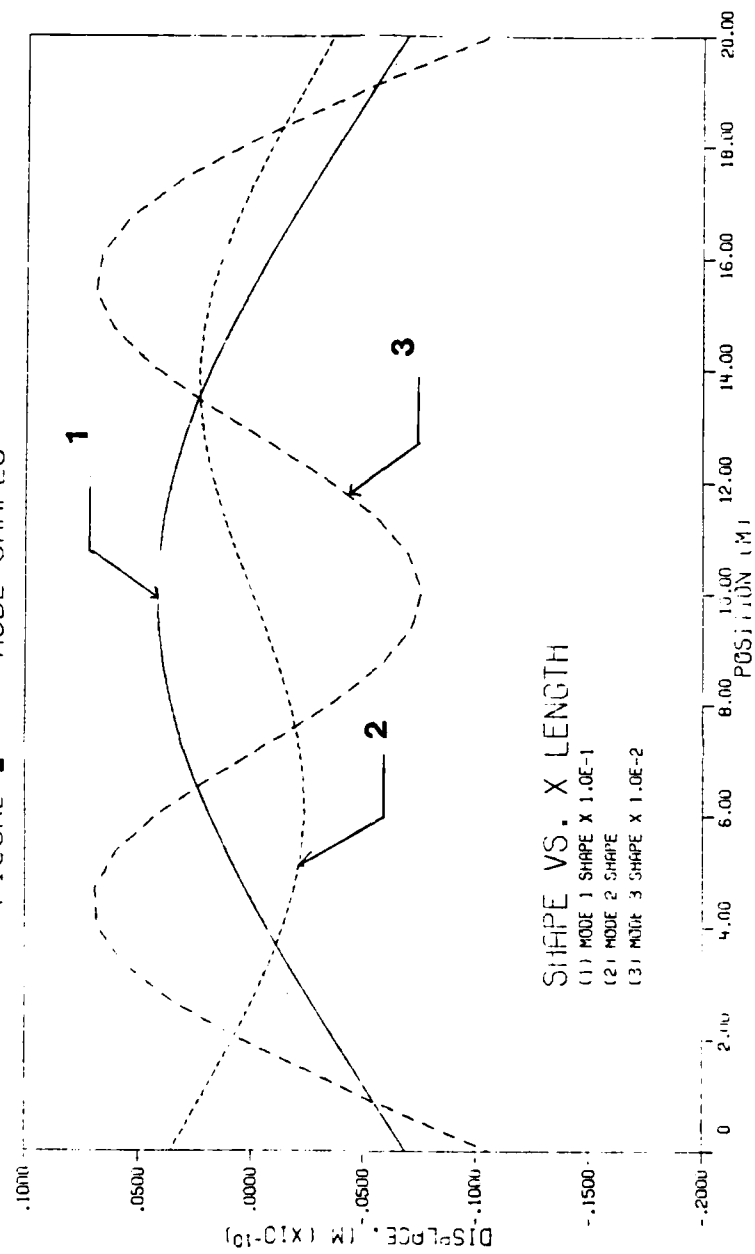
where $1 \leq \nu \leq \infty$. $\phi_i(x)$ are the mode shapes and analytic expressions are known for a free-free beam. Retaining an infinite number of modes is required for a perfect beam representation, but a selected finite number is, of course, the practical alternative. The shapes of the first three modes appear in Fig. 2. The functions $q_i(t)$ are not known and will become state variables whose solution is sought.

To actually write the equations of motion for this structure, generalized variables have been chosen in the following manner. The first three state variables, u_1 , u_2 and u_3 , are defined in terms of the velocity of point R* in the inertial frame and the angular velocity of the reference frame R with respect to the inertial frame,

$$N_{\dot{V}}^{R^*} = u_1 \hat{r}_1 + u_2 \hat{r}_2 \quad (6)$$

$$N_{\dot{W}}^R = u_3 \hat{r}_3 \quad (7)$$

FIGURE 2 MODE SHAPES



The first additional generalized variables are the changes in the time functions, one relationship for each mode selected to be retained for our model,

$$u_{3+i} = \dot{q}_i, \quad i = 1, \dots, v \quad (8)$$

It will be necessary to add θ and D to the list of state variables since they are nonconstant but required for our numerical solution, so

$$u_{4+v} = \theta \quad (9)$$

$$u_{5+v} = D \quad (10)$$

Finally, is added the time functions themselves

$$u_{5+v+i} = q_i, \quad i = 1, \dots, v \quad (11)$$

Therefore, the dynamic model for the structure would be expected to consist of $(5+2v)$ first-order differential equations in terms of the state variables u_ℓ , $\ell = 1, \dots, (5+2v)$. Recalling the actuator locations along the beam have been specified at the positions x_k , the equations governing the system appear as follows:

$$-m_B \dot{u}_1 + u_3 u_2 m_B + u_3^2 e_B + \frac{\gamma}{D^2} [-m_B \cos \theta + \frac{(3 \cos^2 \theta - 1)}{D} e_B] + \sum_{K=1}^{na} F_C(x_K) \sum_{i=1}^v \phi_i'(x_K) q_i = 0$$

$$-m_B \dot{u}_2 - e_B \dot{u}_3 - u_3 u_1 m_B + \frac{\gamma}{D^2} [m_B \sin \theta - \frac{3 \sin \theta \cos \theta}{D} e_B] + \sum_{K=1}^{na} F_C(x_K) = 0$$

$$-u_2 \dot{e}_B - \dot{u}_3 I_B - u_3 u_1 e_B + \frac{\gamma}{D^2} [e_B \sin \theta - \frac{3 \sin \theta \cos \theta}{D} I_B] + \sum_{K=1}^{na} x_K F_C(x_K) = 0$$

$$-\sum_{i=1}^v G_{ij} \dot{u}_{3+i} + u_3^2 \sum_{i=1}^v G_{ij} q_i - \sum_{i=1}^v H_{ij} q_i + \frac{\gamma}{D^2} [-\frac{(1-3 \sin^2 \theta)}{D} \sum_{i=1}^v G_{ij} q_i] + \sum_{K=1}^{na} \phi_j(x_K) F_C(x_K) = 0$$

$$\dot{u}_{4+v} = u_3 - (u_1 \sin \theta + u_2 \cos \theta) / D \quad (12)$$

$$\dot{u}_{5+v} = u_1 \cos \theta - u_2 \sin \theta$$

$$\dot{u}_{5+v+i} = q_i$$

where m_B = mass of the beam

$$e_B = \int_0^L x \rho dx$$

$$I_B = \int_0^L x^2 \rho dx$$

L = beam length

ρ = beam density per unit length

γ = gravitational parameter

$F_C(x_K)$ = force due to actuator located at position x_K

$\phi_i'(x_K)$ = $\partial \phi_i / \partial x$ evaluated at x_K

$$G_{ij} = \delta_{ij}$$

$$H_{ij} = \delta_{ij} \lambda_j$$

λ_j = functions of modal frequencies, known for an unrestrained beam

na = number of actuators

These equations must be solved numerically to provide a solution for the motion of the beam.

2. Actuator Model

To evaluate the effect of actuator characteristics, the initial choice was examination of a time delay in the response of a typical actuator. Each actuator would then have an associated differential equation. The new additional state variables are the actual forces due to each actuator so that

$$u_{5+2\nu+K} = F_c(x_K), \quad K = 1, \dots, n_a \quad (13)$$

The differential equations representing the response delays appear as

$$\dot{u}_{5+2\nu+K} = -a_K u_{5+2\nu+K} + f_K \quad (14)$$

where a_K = slope of response curve

f_K = the desired force in a given actuator determined from the control law.

It is noted that this equation represents the response to a unit step input as seen in Fig. 3. The larger the value of the slope a_K , the

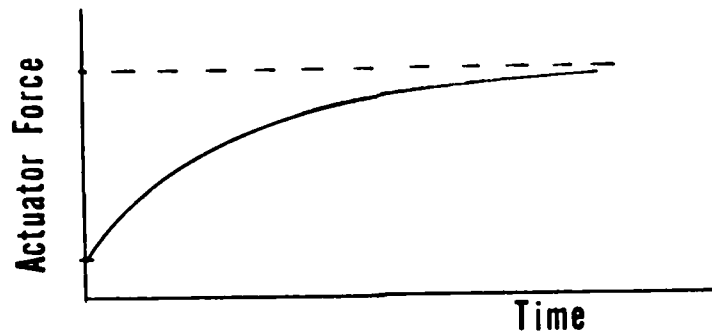


Figure 3. Actual Force in Actuator in Response to a Step Input

closer the Kth actuator approaches the ideal instantaneous reaction. This set adds one first order differential equation for each actuator in the system.

3. Linearized Models

Much of the control theory developed to date for large, flexible systems has used linear dynamic models. For small perturbations and deformations, they provide good approximations to the motion of the structure and practical methods from which to design control laws. A linear model is required of the form in Eqn. (1) to employ the cost decomposition technique. In reducing this model to a linearized version, decoupling will frequently occur between the rigid and flexible modes. For the unrestrained beam in orbit, it will occur for a number of problems in which the ability of the actuators to control the shape in response to small disturbances can be studied. Consider the following case. Assume the nominal motion of the beam center of mass to be a circular orbit with the beam aligned so that its minimum moment of inertia is directed parallel to a radial axis. For a beam of reasonable length it can be assumed that the attitude will not affect the orbit of the center of mass. For small deviations from that nominal solution, the equations in (12) will simplify such that the significant remaining equations will appear [17]

$$\begin{aligned}
 -\ddot{u}_3 - \frac{3\gamma}{D_0^3} \dot{u}_3 - \frac{e_B}{m_B I_B - e_B^2} \sum_{K=1}^{na} F_C(x_K) + \frac{m_B}{m_B I_B - e_B^2} \sum_{K=1}^{na} x_K F_C(x_K) &= 0 \\
 - \sum_{i=1}^v G_{ij} \ddot{u}_{3+i} + (2u_{3_0} \ddot{u}_3 + u_3^2) \sum_{i=1}^v G_{ij} q_i - \sum_{i=1}^v H_{ij} q_i + \sum_{K=1}^{na} \phi_j(x_K) F_C(x_K) &= 0
 \end{aligned} \tag{15}$$

$$\dot{\theta} = u_3$$

$$\dot{u}_{5+v+i} = q_i$$

where u_{3_0} and D_0 are values in the nominal motion. For beams in which the natural mode frequencies ($\sqrt{\lambda_i}$) are much larger than the orbital angular velocity the flexible mode equations completely decouple from the system [17] resulting in state equations

$$-\sum_{i=1}^v G_{ij} \dot{u}_{3+i} - \sum_{i=1}^v H_{ij} q_i + \sum_{K=1}^{na} \phi_j(x_K) F_C(x_K) = 0 \quad (16)$$

$$\dot{u}_{5+v+i} = q_i$$

These of course, actually represent a set of equations, two for each mode being retained in the model. This constitutes our linear dynamic model for the structure. Augment these with the actuator differential equations in (14) when desired. Thus there are $(v + na)$ first-order differential equations in the linear system.

RESULTS

A. Example

To study the effects of nonideal actuators, that is, actuating devices with a finite response time, a beam was arbitrarily chosen with the following characteristics. The beam is of length 20 m and possesses a flexural rigidity EI of 20 N-m^2 and density $\rho = .8 \text{ kg/m}$. The assumed circular orbit about the Earth ($\gamma = 3.986 \times 10^{14} \text{ m}^3/\text{s}^2$) is at an altitude such that the distance from point 0 to the beam center of mass B^* is $7 \times 10^6 \text{ m}$. Mass characteristics include $m_B = 16.0 \text{ kg}$, $e_B = 160.0 \text{ kg-m}$

and $I_B = 2133.3 \text{ kg-m}^2$. The beam was oriented initially as in Fig. 4, for $\theta = 5^\circ$ and $\dot{\theta} = 0$. Note that the beam was initially undeformed. The desired final state included $\theta = 0$ and no beam deformations. This implies that the beam neutral axis should be straight and parallel to a radial vector.

It was assumed that four actuators were available to provide the necessary torque. There were six possible locations at which to place the four actuators, which included x values of 0, 3, 6, 14, 17 and 20 meters. The objective was to: i) Determine the best locations at which to place the actuators and ii) Use those positions to provide the torque necessary to achieve the final state.

B. Actuator Location Determination

To determine the four most effective positions for the actuators from the six locations available, the component cost for each was calculated. Cost decomposition requires use of the linear model, which is good for our initial conditions. Three modes were used to describe the beam. Note that we also used equal weights in the cost function. The actuators were ranked by comparing the cost effectiveness values, V_i , and the four with the largest values are retained. In Fig. 5 those costs are shown, calculated on the assumption of "perfect" actuators, i.e. instantaneous response. Since the possible locations are symmetrically distributed about the beam center, it is not surprising that the costs are also symmetric about the center. Note that, as expected from the mode shapes, the outside actuators are more effective. In Fig. 6, the same analysis is done but now the differential equations

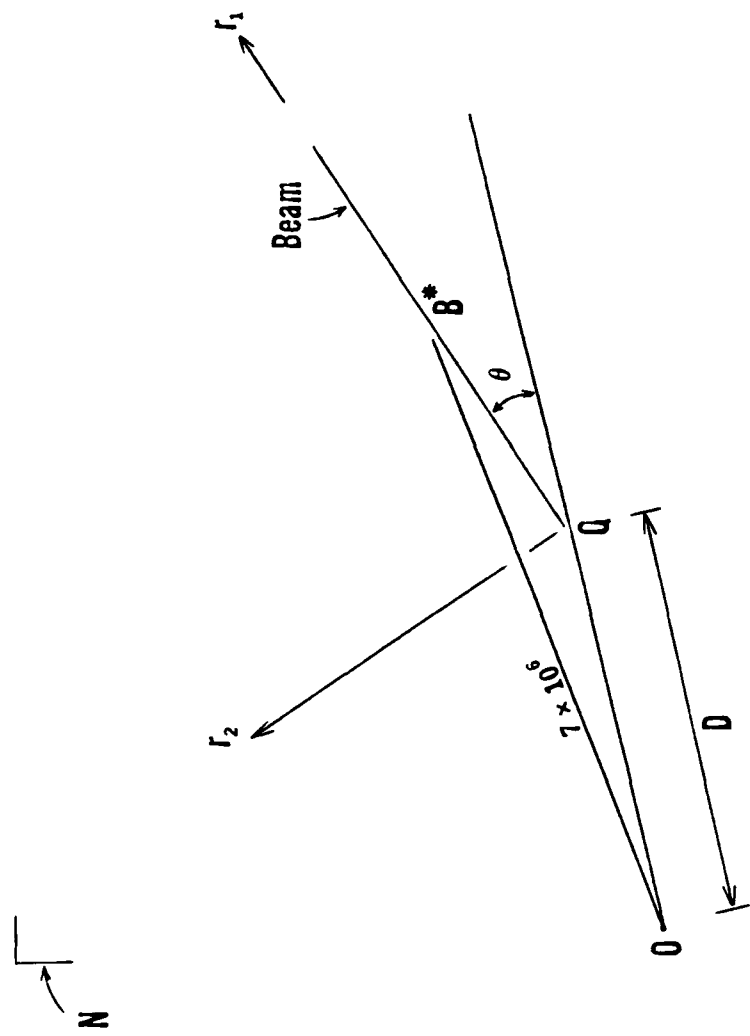


Figure 4. Initial Conditions.

for the nonideal actuators have been included. Although the actuators selected remain the same, the delayed response has made the actuators at $x = 3$ and 17 m "less effective". To explore this further, the response speed was varied by changing the variable a_K in Eqn. (14). A comparison of resulting costs is shown in Fig. 7. The larger the value of a_K , the faster the response. It is of interest to note the following. If only two modes had been considered in the dynamic model, the actuator positions chosen would have been different. Fig. 8 shows costs for only two modes and $a_K = 1.0$. Now the most effective positions are $x = 0, 6, 14$ and 20 m. However, given a specific number of modes to use in the model, the actuator model is clearly seen to affect the costs but does not affect the choice in this example.

C. System Response to Actuators

Initial interest concerned the system response to forces at the specified actuator positions. Although it is an ultimate goal to design an LQG controller, a much less complex controller was initially used here to observe the system response.

1. Control Law

The simple control used is derived from that used in [16]. It appears as

$$F = K_1 \hat{\theta} + K_2 \dot{\hat{\theta}}$$

where $\hat{\theta}$ is defined in Fig. 1. It is the angle between a line tangent to the beam at point Q and a line parallel to \hat{r}_1 . The angle θ itself was not chosen because it can never actually be measured. The gains

K_1 and K_2 are arbitrarily selected to reflect a reduction in θ to half of its initial value in approximately 10 seconds. The value F is a representative force and reflects the torque (F times length) needed from the actuators to return the system to the desired state. The total force F is distributed among the actuators depending on their location.

2. Response Histories

Four actuators were used with the control law above in the example. Three modes were used for the beam. In Fig. 9, the amount of force F required for the torque is represented for two combinations of actuators. Also compared, dynamic models of ideal actuators and models which include actuator differential equations with $a_k = 1$. Clearly there is a difference in the force history when the actuators are a little slow to respond. In all cases, the actuators at the ends of the beams were utilized since they are indeed the most effective. But also compared is the use of actuators at $x = 3$ and 17 m or using $x = 6$ and 14 m as the locations of the second pair. Although there is a perceptible difference, it is less pronounced. Curves #1 and #3 reflect the results of the chosen positions based on cost decomposition and they are seen to be slightly better than their counterparts.

In Fig. 10 the plot shows $\theta(t)$, which is the variable of most interest. The same four cases are presented. All combinations eventually bring θ to an acceptable level. Curve #1 could be interpreted as the most effective although the differences are small. One point is seen in the numerical output and is not obvious in the plot.

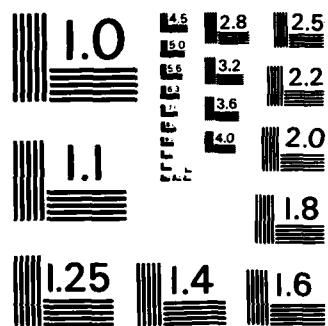
Curves #3 and #4, i.e. the nonideal actuators, oscillate for a significantly longer time before settling out. Finally in Fig. 11, the deflection of point Q, the near end of the beam, away from the neutral axis is plotted. An interesting observation is that the delayed response of the actuator made the maximum deflection of the beam (at approximately 5 seconds) at point Q smaller than in the ideal case. Maximum deflection may or may not be a problem depending on mission requirements. The deflection pattern is different, however, and again curves #3 and #4 take a significantly longer time to settle out.

CONCLUSIONS

It is obvious that much work is yet to be done concerning the attitude control systems for large flexible space structures. Even on the example used here, inclusion of an actuator dynamic characteristic did appear to affect actuator cost as well as system response. Although it did not affect the selection from the cost decomposition in this example, a different result cannot be ruled out for other cases. More study is required on this problem, as well as similar examination of actuator characteristics. Because dynamic effects can be seen, the question concerning actuator-induced instabilities is also still open.

ACKNOWLEDGMENTS

This work was supported through a program sponsored by the United States Air Force.



MICROCOPY RESOLUTION TEST CHART
NATIONAL BUREAU OF STANDARDS - 1963 - A

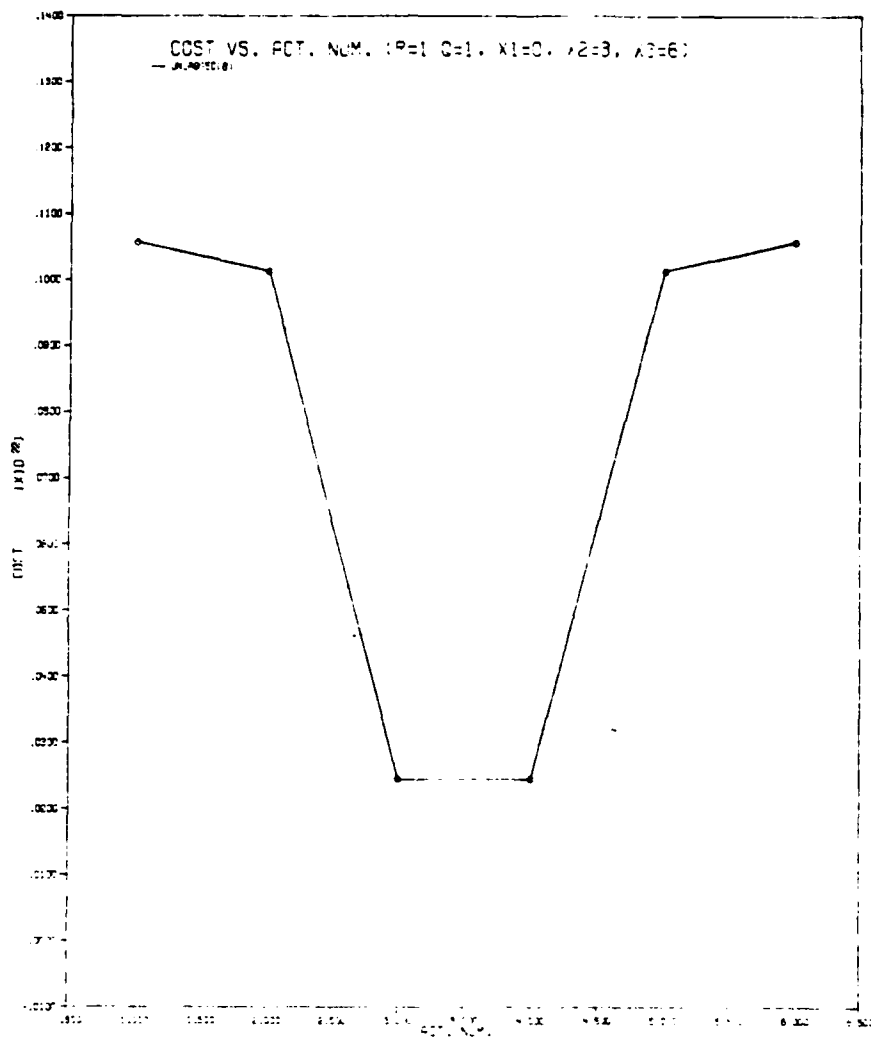


FIGURE 5 UNBUNDLED ACTUATOR FLUTTER COSTS

Curves #3 and #4, i.e. the nonideal actuators, oscillate for a significantly longer time before settling out. Finally in Fig. 11, the deflection of point Q, the near end of the beam, away from the neutral axis is plotted. An interesting observation is that the delayed response of the actuator made the maximum deflection of the beam (at approximately 5 seconds) at point Q smaller than in the ideal case. Maximum deflection may or may not be a problem depending on mission requirements. The deflection pattern is different, however, and again curves #3 and #4 take a significantly longer time to settle out.

CONCLUSIONS

It is obvious that much work is yet to be done concerning the attitude control systems for large flexible space structures. Even on the example used here, inclusion of an actuator dynamic characteristic did appear to affect actuator cost as well as system response. Although it did not affect the selection from the cost decomposition in this example, a different result cannot be ruled out for other cases. More study is required on this problem, as well as similar examination of actuator characteristics. Because dynamic effects can be seen, the question concerning actuator-induced instabilities is also still open.

ACKNOWLEDGMENTS

This work was supported through a program sponsored by the United States Air Force.

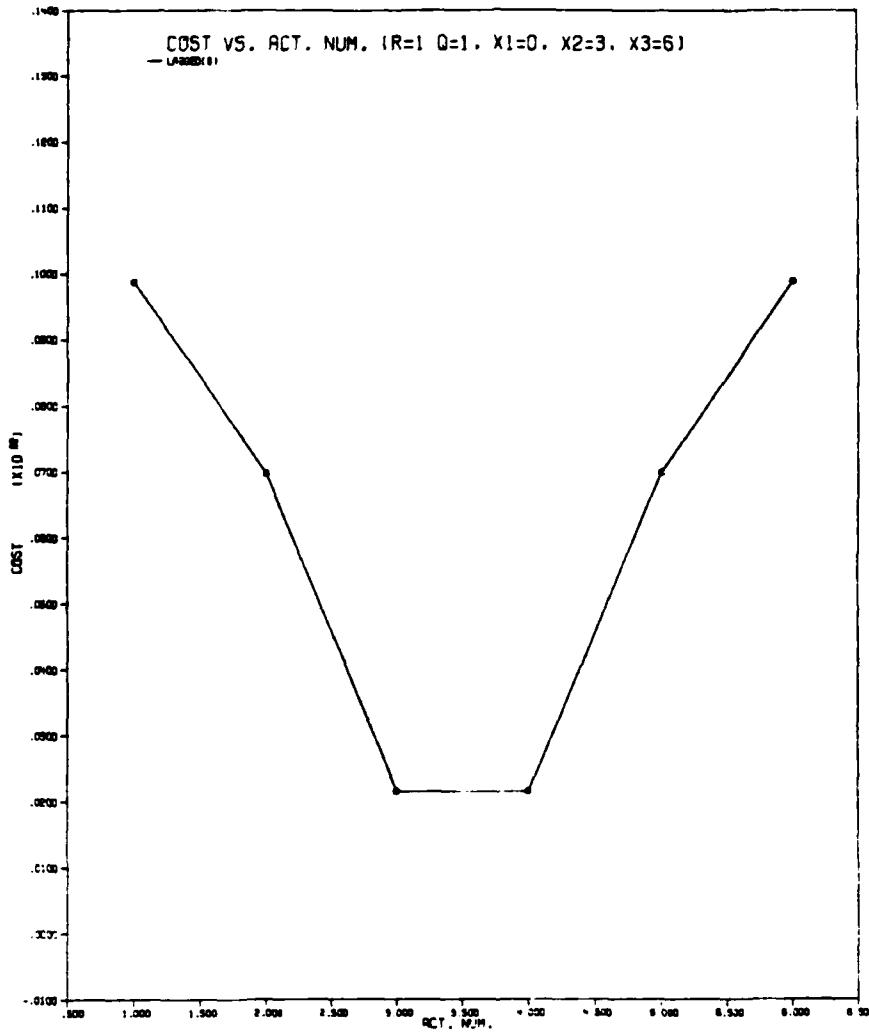
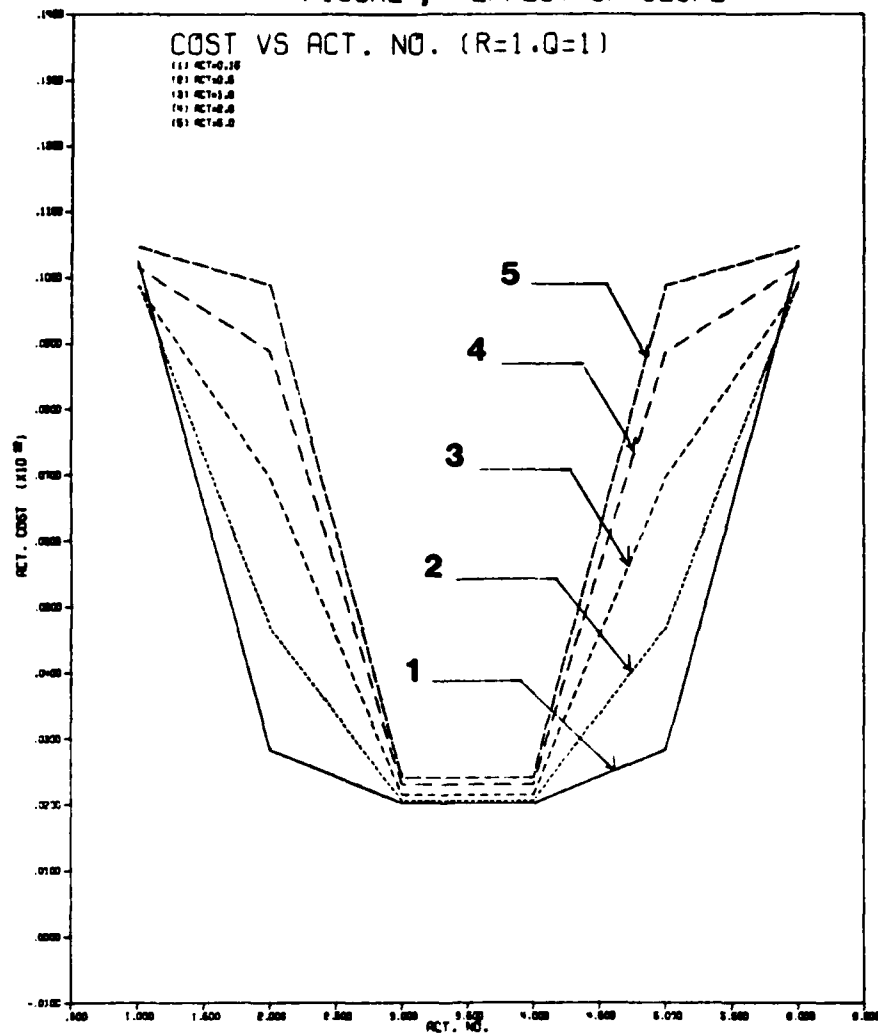


FIGURE 6 DELAYED ACTUATOR SELECTION COSTS

FIGURE 7 EFFECT OF SLOPE



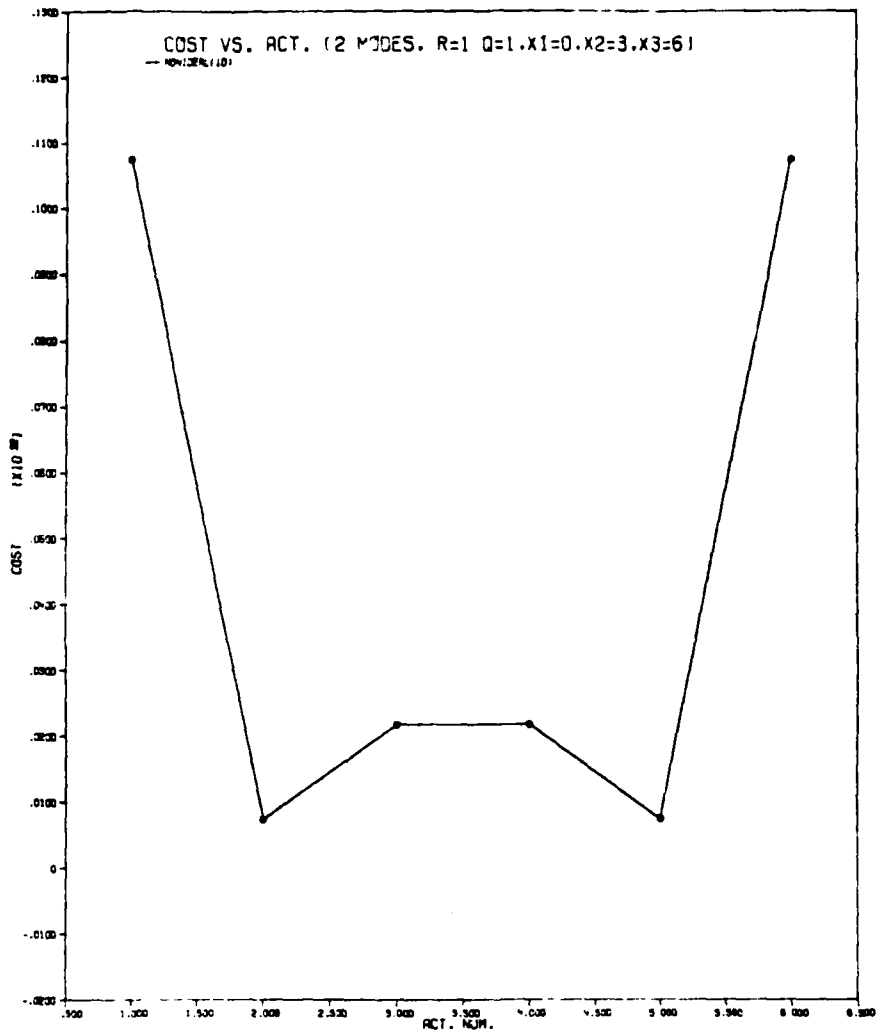


FIGURE 8 NONIDEALIZED ACTUATOR SELECTION COSTS

FIGURE 9 FORCE HISTORIES

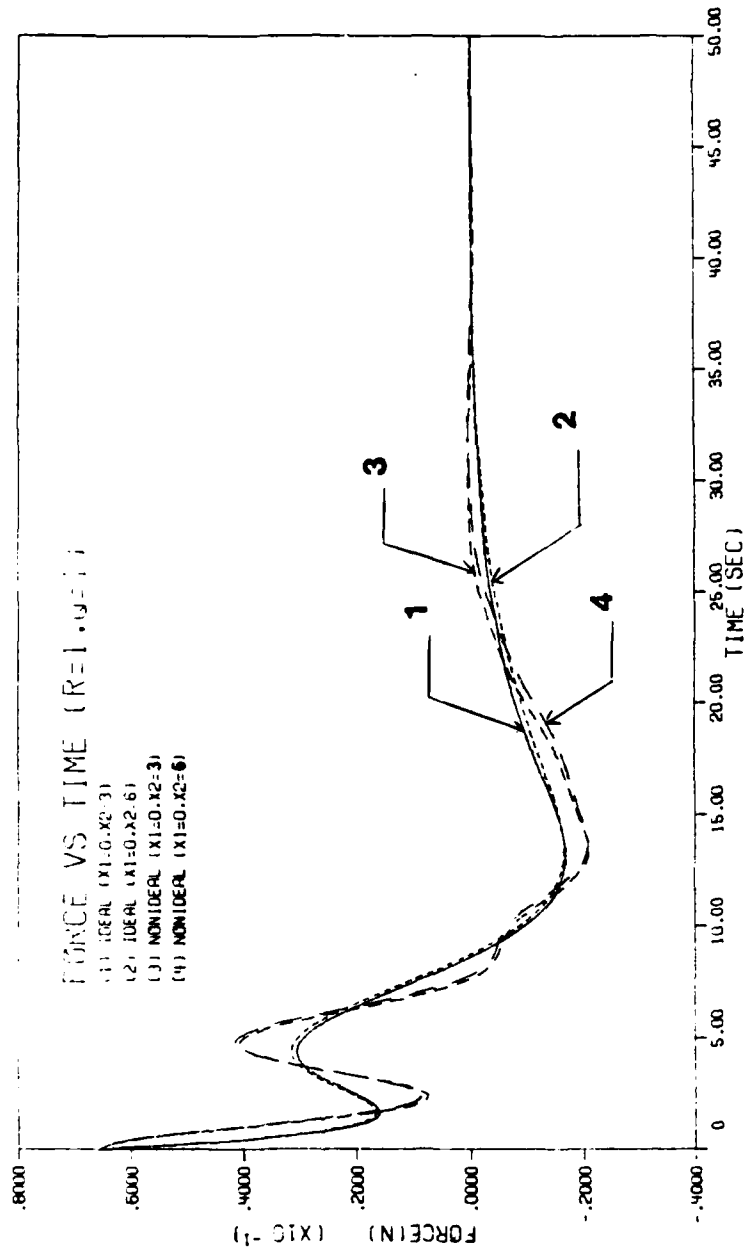


FIGURE 10 THETA HISTORIES

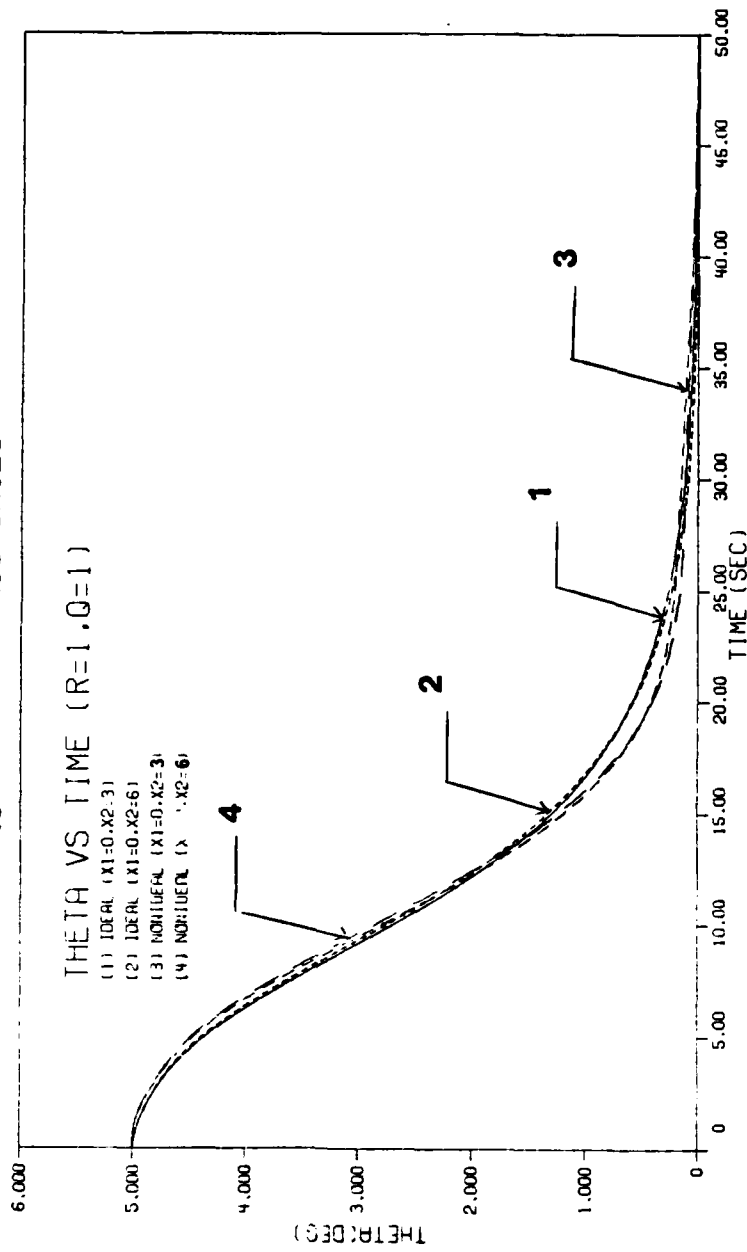
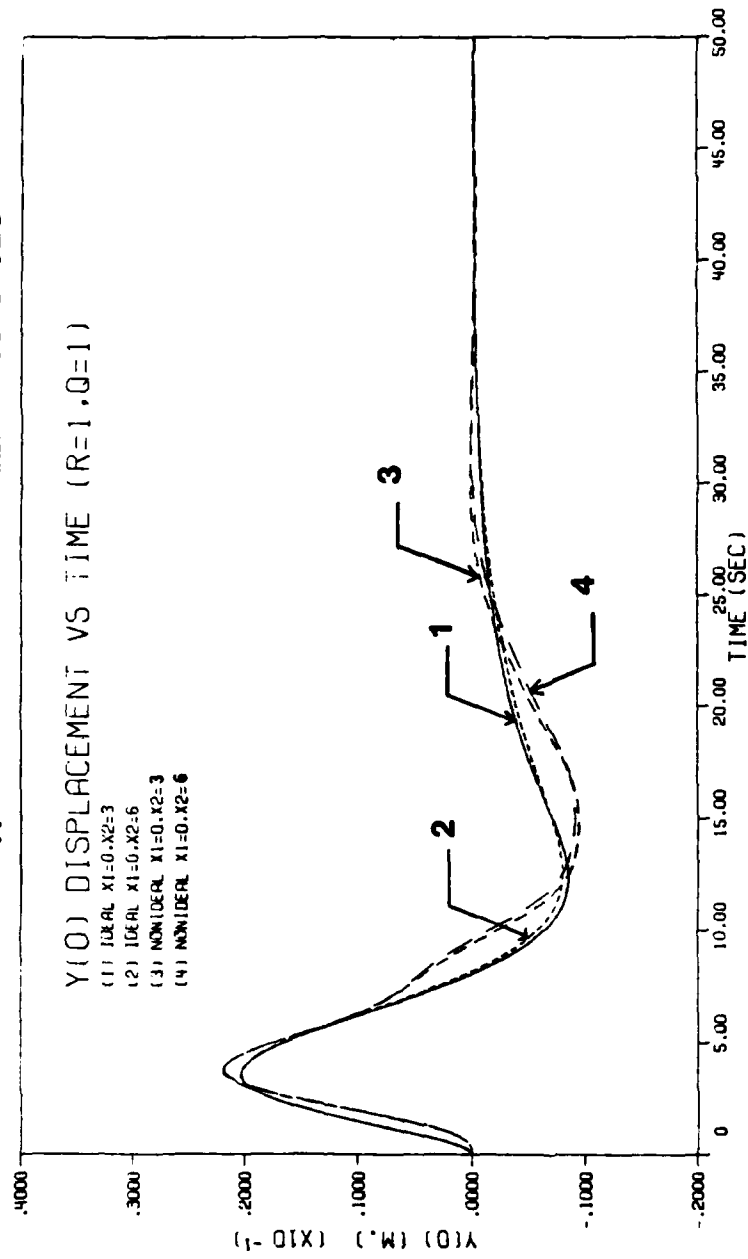


FIGURE 11 END OF BEAM FLEX HISTORIES



REFERENCES

- [1] Chen, W.H. and Seinfeld, J.H., "Optimal Location of Process Measurements," Int. J. Control, 1975, Vol. 21, No. 6, pp. 1003-1014.
- [2] Skelton, R.E., "Cost Decomposition of Linear Systems with Application to Model Reduction," Int. J. Control, Vol. 32, No. 6, 1031-1055, 1980.
- [3] Howell, K.C., "Final Report: Attitude Control Issues for Large Flexible Space Systems," 1983 USAF-SCEEE Summer Faculty Research Program.
- [4] Carignan, C.R. and W.E. Vander Velde, "Number and Placement of Control System Components Considering Possible Failures," Report - NASA Grant #NAG1-126, Dept. of Aeronautics and Astronautics, Massachusetts Institute of Technology, March 1982.
- [5] Chiu, D., "Optimal Sensor/Actuator Selection, Number, and Placement of Linear Stochastic System," Ph.D. Dissertation, School of Aeronautics and Astronautics, Purdue University, West Lafayette, IN, May 1981.
- [6] DeLorenzo, M.L., "Selection of Noisy Sensors and Actuators for Regulation of Linear Systems," Ph.D. Dissertation, School of Aeronautics and Astronautics, Purdue University, West Lafayette, IN., June 1983.
- [7] Hughes, P.C. and R.E. Skelton, "Controllability and Observability for Flexible Spacecraft," Journal of Guidance and Control, Vol. 3, No. 5, Sept. - Oct. 1980, pp. 452-459.
- [8] Juang, J.N. and Rodriguez, G., "Formulations and Applications of Large Structures Actuator and Sensor Placements," Second VPI & SU/AIAA Symposium on: Dynamics and Control of Large Flexible Spacecraft, June 21-23, 1979.
- [9] Lindberg, Jr., R.E., "Actuator-Placement Considerations for the Control of Large Space Structures," Naval Research Laboratory Report 8675, May, 1983.
- [10] Vander Velde, W.E. and C.R. Carigna, "A Dynamic Measure of Controllability and Observability for the Placement of Actuators and Sensors on Large Space Structures," Report-NASA Grant #NAG1-126, Dept. of Aeronautics and Astronautics, Massachusetts Institute of Technology, Jan. 1982.
- [11] Yousuff, A., "Order Reduction of Large Scale Systems," Ph.D. Dissertation, Purdue University, 1981.

- [12] Yousuff, A. and Skelton, R.E., "Controller Reduction by Component Cost Analysis," IEEE Trans. Auto. Control, to appear 1983.
- [13] Skelton, R.E. and DeLorenzo, M.L., "On Selection of Weighting Matrices in the LQG Prob," 20th Annual Allerton Conf. on Communication Control and Computing, Oct. 6-8, 1982, Monticello, Ill.
- [14] Skelton, R.E., "Component Cost Analysis of Large Scale Systems," Final Report, Jet Propulsion Laboratory, Contract No. 955369, School of Aeronautics and Astronautics, Purdue University, January 1982.
- [15] Levinson, D.A. and Kane, J.R., "Simulation of Large Motions of Nonuniform Beams in Orbit: Part I - The Cantilever Beam," Journal of the Astronautical Sciences, 1981, Vol. XXIX, No. 3, pp. 213-244.
- [16] Kane, J.R. and Levinson, D.A., "Simulation of Large Motions of Nonuniform Beams in Orbit: Part II - The Unrestrained Beam," Journal of the Astronautical Sciences, 1981, Vol. XXIX, No. 3, pp. 245-275.
- [17] Kumar, V.K. and Bainum, P.M., "Dynamics of a Flexible Body in Orbit," Journal of Guidance and Control, 1980, Vol. 3, No. 1, pp. 90-92.

1983-84 USAF-SCEEE RESEARCH INITIATION PROGRAM

Sponsored by the

AIR FORCE OFFICE OF SCIENTIFIC RESEARCH

Conducted by the

SOUTHEASTERN CENTER FOR ELECTRICAL ENGINEERING EDUCATION

FINAL REPORT

Prepared by: Dr. Gwendolyn B. Howze

Academic Rank: Associate Professor

Department and
University: Biology Department
Texas Southern University

Research Location: Air Force Aerospace Medical Research Laboratory

Date: May 1984

ABSTRACT

The periosteum is the dense connective tissue coat which covers most of the outer surface of a bone. A similar coat, the endosteum, lines the inner bone cavity. The periosteum and endosteum play major roles in normal bone physiology. The periosteum is the major source of osteoblast for bone growth and bone repair (8).

The rationale for this research consists of three simple hypotheses.

1) During the process of bone demineralization, there are coincident and re-events occurring in the periosteum and endosteum. 2) The putative demineralization related events are manifested as structural changes in the constituent elements such as cells, fibers and blood vessels. 3) The anticipated periosteal changes can be visualized using the scanning electron microscope.

This research has been a continuation of studies done in collaboration with the Biodynamic Effects Branch in the Biodynamics and Bioengineering Division at the Air Force Aerospace Medical Research Laboratory. The subject of the prior study was periosteum from normal rats and Rhesus monkeys. The aim of that study was to obtain a baseline picture of normal periosteum which could be used in analyzing periosteum removed from bone undergoing demineralization.

For reasons of optimization (details given in the objective section), the baseline studies have been continued in this phase of the continuing project. Several new methods have been tested.

I. Introduction

In a live human, a bone such as the femur, for example, is a living organ. It has three main compartments: the matrix, which contains a labyrinth of channels; the periosteum; and the periosteal appendages, the osteocytes, which derive from the periosteum but reside in matrix channel spaces called lacunae (1,2).

When most people speak of bones they have the matrix in mind. It is the most obvious and massive portion (3). The bone matrix, however, is a nonliving secretion product of the periosteum (1, 2). By contrast, the periosteum is a thin unobtrusive tissue which covers the outer surface of the matrix of a bone. In fact, except for the articular surfaces at the joints, the exterior bone surface consists in the periosteum. Though inconspicuous, the periosteum is composed of living cells and their secretion products, the most prominent of which are the collagenous fibers (1, 2). The living periosteum and its appendages, the osteocytes, manufacture and maintain the non-living bone matrix (1, 2).

Interestingly but distressingly, most of the research on bone has been and, even now, is devoted to the characterization of the bone matrix. See for example references 3, 4, and 5. Thus only a minor portion of the massive literature on bone is concerned with the periosteum. This point of view is changing, however, as more and more scientist realize the need for an intense effort to uncover the complete story of periosteal influence on bone function.

Many normal essential Air Force activities place human bones under considerable stress and risk of injury. For example, the three main bone

functions in humans; protection, support and calcium homeostasis are placed under stress by such activities as: parachuting, ejection from aircraft and space flight. Bone injury is usually diagnosed and understood in terms of changes in the matrix. Accordingly, the Air Force has a considerable involvement in the study of bone matrix. In light of the evidence that the periosteum and its appendages, the osteocytes, manufacture and maintain the matrix (1), it is clear that a profound understanding of the periosteum is essential to a successful program of bone health, injury prevention, and repair.

The normal or unstimulated structure of the periosteum has been studied by scanning electron microscopy (SEM) during the tenure of a 1983 AIR Force Summer Faculty Research Fellowship. In the two species studied, rat and Rhesus monkey, five distinct morphological regions were discerned, although sharp boundaries were not visible. The top-most fibrous layer is a coherent layer of fibers in an interknitted array. Intermixed with the fiber bundles are many blood vessels. Below the top layer is a second fibrous layer in which the fibers are more loosely arranged and mixed with a few cells. A third region contains cells, fibers and blood vessels in an apparently random innominate distribution. Cells are plentiful in this region. The fourth layer is highly cellular. In the monkey, the cells are stratified in layers with each layer separated by network of fibrils. The fifth region which is justa-matrix is apparently one cell layer thick and in which the cells are strongly attached to the subjacent bone matrix.

In both species, there are certain thick fibers which are composed of thinner fibrils in parallel array. Because the fibrils which constitute the fibers exhibit a lengthwise structural periodicity, these fibers are tentatively called collagenous fibers. The fibers characteristically are covered with a meshwork, also composed of fibrils, which usually contain pariculate structures of unknown composition. The collagenous fibrils appear to show slight differences in the two species. The differences may be due to the slightly different SEM preparation procedure. In both species, many of the cells contain numerous cytoplasmic processes.

II. Objective

The overall objective of this project is to investigate the possibility that the osteogenic region of the periosteum plays a significant role in the bone demineralization which is induced by hypokinesia or immobilization.

This goal is being approached in two stages. Stage I was carried out in the summer of 1983 at the Air Force Aerospace Medical Research Laboratory at Wright-Patterson Air Force Base. The stage I studies consisted of a scanning electron microscopical (SEM) study of normal periosteum of long bones, such as femur and tibia, from both rat and Rhesus monkey. The specific aim was to obtain a baseline description of the structural organization of normal periosteum. The baseline description is prerequisite to any attempt to detect experimentally induced changes in periosteal structure.

The hypokinesia studies will be conducted in stage II. Rhesus monkeys will be immobilized according to a protocol developed by Mr. C. Oloff of the Biodynamic Effects Branch of Biodynamics and Bioengineering Division at the Air Force Aerospace Medical Research Laboratory (AFAMRL). The hypokinesia or immobilization experiments are expected to induce bone demineralization. Mr. Oloff will give me periosteum biopsy samples from the treated animals. Subsequent to submitting the Research Initiation Program proposal, the Biodynamic Effects group revised the total project as described below. 1) Improvement and refinement of the biopsy procedure. While this has resulted in a delay in starting the hypokinesia experiment, it will improve the reliability of the sampling procedure and sampling speed. 2) Reconsideration of a more accurate bone model. The presently preferred model is the vertebral column which is the major weight bearing axis in man and Rhesus monkeys.

As a result of these changes in the project design, stage I has been prolonged and stage II has been deferred. The stage I baseline study has been continued because of the possibility that periosteum of vertebral bone is significantly different from that of the long bone which we have already studied and described in 1983.

Because the biopsy procedure was still being perfected during the tenure of the RIP grant, Rhesus samples did not become available until May 24th. Consequently, the grant period has been devoted to testing and improving four of the analytical techniques which we hope to use in studying the Rhesus material. The approach, the procedures, and the results obtained will be described in the "RESEARCH PLAN" section of this report.

III. Research Plan

1. The Approach

The baseline studies were continued using rat femur because as already stated Rhesus monkey specimens were not available. The strategy being to test and improve the methods of interest using rat femur. Subsequently the methods can be applied to other specimens when they become available. One old method and three new methods are being adapted. The new methods are: 1) freeze fracture, 2) enzymatic dissociation to survey the cell population, 3) differential Enzymatic hydrolysis as a device to characterize the three types of fibers which have been observed in scanning electron micrographs.

In the method being revised the feasibility of using iso-amyl acetate as a substitute for ether as the solvent for the collodion solutions in the procedure for stripping the periosteum from rat femur was studied. The method is outlined in the summary of methods section called "modified procedure for rat femur."

The usefulness of freeze fracture for viewing the internal structure of periosteum was studied. The details of the method are listed in the summary of methods section called "new methods."

One way to study the cell population in a tissue is to use a high yield tissue dissociation technique and harvest the isolated cells. The cell suspension may be studied by a variety of techniques. In this instance the cells were studied by light microscopy as well as SEM. The method of isolating cells from periosteum is described in the summary of methods section called cell isolation procedure.

As a result of our previous studies which are summarized in the last two paragraphs of the introduction section, three distinct types of fibers were described. One type, the largest, contain thinner fibrils in parallel array . Because the thin fibrils exhibit a lengthwise structural periodicity, the fibers are tentatively referred to as "collagenous fibers". In order to obtain an independent and second line of evidence that the fibrils contain collagen,periosteum specimens were treated with collagenase,an enzyme which hydrolyzes collagen. The reasoning being that if the collagenase were shown to diarupt the fibers, this would be independent evidence that the fibers do contain collagen . The method of enzymatic characterization of the fibers is described in the section called chemical characterization of fibers by enzyme treatment.

2. Summary of Methods

In order to achieve the stated objective, standard scanning electron microscopical procedures (4, 8) have been slightly modified to suit the periosteum. The sequence of steps in summary are the following: 1) obtaining the specimen. 2) preservation of native state by fixation. 3) dehydration. 4) preparation for SEM. 5) observations and producing a permanent record.

Obtaining the specimen: The rats were sacrificed and the femurs were dissected out and washed in buffered saline. The Rhesus monkey periosteas were obtained by biopsy. They were not washed before fixation and unfortunately were contaminated by adhering red blood cells.

Fixation: The specimens were fixed in 2% glutaraldehyde in pH 7.3, 0.2 M phosphate from 3 to 24 hours.

Dehydration: A graded series of ethyl alcohol was used in the dehydration, 35%, 70%, 95% and 100%.

Preparation for SEM: Normally after the dehydration, specimens are transferred to iso-amyl acetate in preparation for the critical point drying procedure. Carbon dioxide was used for the critical point drying. Next the specimens were attached to the stubs with a conductive cement and covered with a gold coat estimated to be 20 nm thick. The observations were made on an ETEC Autoscan Scanning Electron Microscope. Uniformly, the accelerating voltage was 20 Kv. A permanent record was obtained upon Polaroid 55 P/N film. The negatives were used to make the prints exhibited in this report. The printing process resulted in an additional enlargement of 2.21X. This factor should be used in estimating the total magnification in the prints. This procedure was modified slightly for rat specimens.

Modified procedure for rat femur: This procedure was developed for the rat femur, but it probably should be used uniformly since it eliminates certain artifacts, e.g. dissection injury and shrinkage artifacts due to fixation and dehydration. The sequence is as follows: 1) the whole femur is fixed. 2) the dehydration was the same as above, but a subroutine to separate the periosteum from the matrix was inserted before the critical point drying procedure. 3) isolation of the periosteum by embedding it in a collodian membrane. The details of this procedure are listed below. 4) critical point drying and continuation with the standard SEM procedure.

The details of the procedure for isolation of the periosteum are the following:

1. The bones were placed in a 1:1 mixture of absolute ethanol and amyl-acetate, two changes, 15 min each.
2. Next, the bones were placed in 1.5% collodion (dissolved in the ethanol / amyl acetate solvent) for 15 min.
3. They were next transferred to a small container of 5% collodion for 5 minutes.
4. The top of the containers were then removed as the solvent evaporated for 5 min.
5. The bones were removed and held in the air for a minute or more until a definite solid film could be seen, and the smell of solvent had decreased. Caution: do not allow it to dry completely, rotate to insure a uniform film.
6. The semi-dry sample was placed in a container of distilled water for 5 min.
7. A circular cut (through the film down to the matrix) was made at each end. One longitudinal cut extending between the two circular cuts was made.
8. The bone was split along the longitudinal line.
9. The membrane was peeled off the split bone, either as one or two pieces.

Comments: The methods described above were developed during the tenure of the 1983 SFRP. The following section consist of additional modifications and new methods.

Modifications: In order to determine if the use of diethyle ether as a collodion solvent produces surface artifacts in cells and fibers, the procedure for rat femur will be modified in only one aspect. The Collodion will be dissolved in amyl acetate rather than ethmol and diethylether.

New Methods: The freeze fracture procedure (18)

1. The tissue is fixed as usual.
2. Processed through ethyl alcohols
3. After the final 100% ethyl alcohol treatment insert specimens into small cylinder of parafilm contains 100% Ethyl Alcohol.
4. Crimp shut both ends of the cylinder.
5. Hold cylinder under liquid nitrogen until frozen.
6. Place the frozen cylinder containing the frozen tissue on a metal block precooled in liquid nitrogen.
7. Fracture the cylinder with a precooled razor blade.
8. Thaw the specimen in fresh absolute ethanol, and remove from the parafilm cylinder.
9. Dry sample by critical point procedure using 100% ethanol, rather than amyl acetate.
10. The dried tissue fragments are glued onto specimen stubs with silver conductive cement. The fractured surfaces (which are distinctly smoother and shinier when viewed under a dissecting microscope) are oriented upward.
11. Coat specimen on a rotating stage by vaporizing gold to deposit a layer ca. 20 nm thick.

The following two methods employ the enzyme collagenase, in one instance to release cells, in the second case to detect the chemical presence of collagen in fibers.

New Methods: The cell isolation procedure (19,20)

1. Remove femurs as usual.
2. Use the diaphysis, discard the epiphyses.
3. Cut the femur lengthwise and wash the halves with 0.001 M NaEDTA at pH 7.4 to remove blood and marrow cells from the medullary cavity.
4. Place the washed diaphysis in six ml. or less of dissociation fluid (2.5mg/ml. collagenase). **
5. Incubate at 37 degrees C for 30 min.
6. Vortex at intervals and leave in the dissociation fluid for a total of two hours.
7. Collect the cells on millipore filters.
8. Fix the cells attached to the filters.
9. Dehydrate the cells.
10. process for SEM.

** When Rhesus biopsy specimens are used begin at this step, cut the specimen into several pieces.

New Methods: Chemical characterization of fibers by enzyme treatment

1. To six ml. of enzyme solution (2.5 mg/ml enzyme), add small pieces of fresh monkey periosteum or fragments of fresh femur.
2. Incubate at 37 degrees C.
3. Fix samples at intervals of two min., four min., 8 min., 16 min., and 32 min.
4. Dehydrate specimens.
5. Process for SEM.

IV. Results

1. Modification of the stripping procedure

Substitution of iso-amyl-acetate as solvent for the COLLODION, did, as expected, make it easier to detect the banding pattern in the putative collagenous fibrils of rat periosteum.

2. Freeze Fracture

Ideally, freeze fracture seems the best device for opening up the interior of the periosteal mass without at the same time imposing artifacts. The two outer surfaces are very easy to study. In the past when we attempted to study the interior regions, there was a real problem of how reliable the the observations were.. As of this writing, the freeze fracture process has not been successfully used. The problem is technical, in that the fractured material was lost during the critical point drying step. It is expected that working with the larger Rhesus samples and some minor changes will overcome these problems.

3. Enzymic treatments

The enzyme collagenase degrades native helical collagen fibrils. Commercially available collagenase exists in several grades. For tissue dissociation, most researchers employ either crude collagenase or chromatographically purified collagenase. Both of these forms contain non-specific proteolytic activity. The highly purified types are very specific for collagen, containing zero to minimal amounts of non-specific proteolytic activity.

In these experiments , crude collagenase was used in the cell isolation experiments, Sigma type VII, substantially free of non-specific protease, clostripan and tryptic activities, was used in the fiber digestion experiments.

Cell isolation

The cell yield was actually quite good and a variety of types were visible by light microscopy. During the processing for SEM most of the cells were lost from the filters. The cell loss occurred during the critical point drying step. Figure 1 shows examples of the types of cells which remained on the filters after the critical point drying step. It is clear that a way must be found to retain a more representative sample of the cell types indigenous to periosteum.

Fiber digestion

Figure 2 shows two of the three types of fibers which have been detected in periosteum. The small arrow indicates a portion of the ubiquitous meshwork of fibrils which cover and enclose the periosteal components. An example of the putative collagenous fibers is also seen in figure 2, it occupies most of the field, and is indicated by the large arrowhead. The putative collagenous fiber seen in this field is actually composed of bundles of fibrils which are in parallel array. Notice that the fiber is covered by the meshwork. The highly specific collagenase attacks both the meshwork and the putative collagenous fibers. Presumably, both types are composed of collagen.

PLATE A

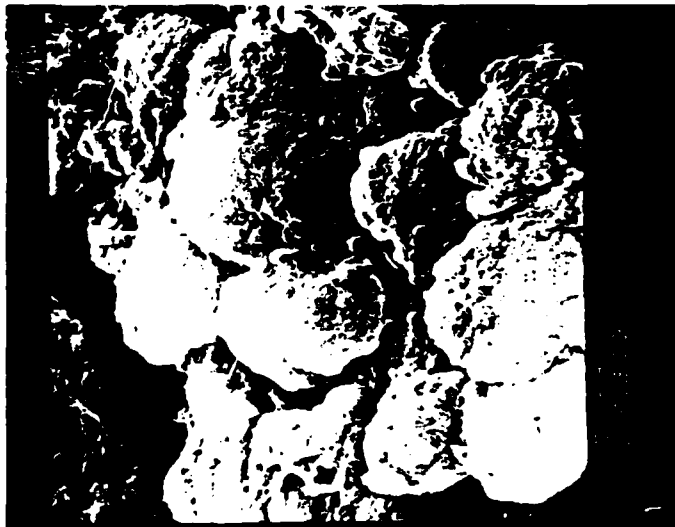


Figure 1. CELL ISOLATION

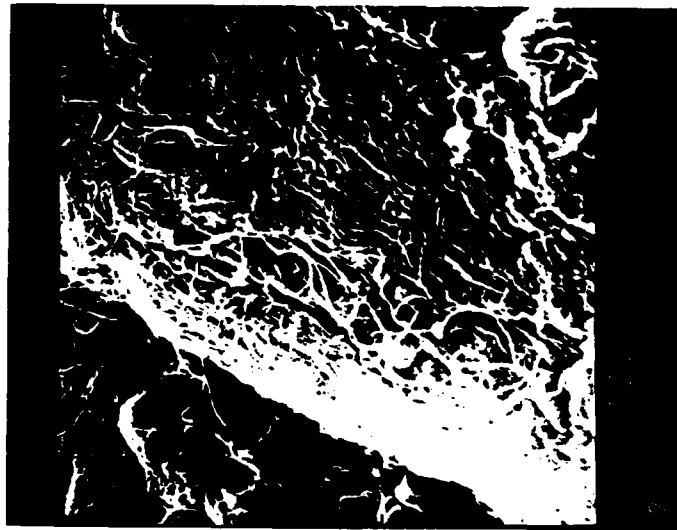


Figure 2. TYPES OF FIBERS DISRUPTED BY COLLAGENASE

REFERENCES

1. Ham, A. W. and D. H. Cornack, Histophysiology of Cartilage, Bone, and Joints, Physiology, J. B. Lippincott Company, 1979.
2. Ham, A. W. and W. R. Harris, "Repair and Transplantation of Bone," In G. H. Bourne (ed.): The Biochemistry and Physiology of Bone, Vol. III, N. Y. Academic Press Inc., 1973.
3. Prtichard, J.J., "General Histology of Bone," In G. H. Bourne (ed.): The Biochemistry and Physiology of Bone, Vol. I., N.Y. Academic Press Inc., 1972.
4. Boyde, A., "Scanning Electron Microscope Studies of Bone" In G. H. Bourne (ed.): The Biochemistry and Physiology of Bone, Vol. I., N.Y. Academic Press Inc., 1972.
5. Cameron, D. A., "Ultrastructure of Bone", In G. H. Bourne (ed.): The Biochemistry and Physiology of Bone, Vol. I., N. Y. Academic Press Inc., 1972.
6. Jones, S. J., A. Boyde and J. B. Pauley, "Osteoblast and Collagen Orientation," Cell Tiss. Res., Vol. 159, pp. 73-80, 1975.
7. Graham, M.D. and H. P. House, "Human Stapes Crura," Arch. Otolaryngol., Vol. 101, pp. 548-551, 1975.
8. Hayat, M.A., Introduction to Biological Scanning Electron Microscopy, Baltimore, University Park Press, 1978.
9. Peck, W. A., J. K. Burks, J. Wilkins, S. B. Rodan, and G. A. Rodan, "Evidence of Preferential Effects of Parathyroid Hormone, Calcitonin and Adenosine on Bone and Periosteum," Vol. 100, pp. 1357-1364, 1977.
10. Whedon G. D., Lutwak, L., Reid, J., Rambaut, P. Whittle,, M., Smith M. and Leach, C., Mineral and Nitrogen Metabolic Studies on Skylab Orbital Space Flight. Trans. Assoc. Am. Phys. 87:95,, 1976.
11. Bassett, L.S., Tzitikalakis, G., Pawluk, R.J., and Bassett, C. A., Prevention of Disuse Osteoporosis in Rats by Means of Pulsing Electromagnetic Fields,, In C.T. Brighton (ed.): Electrical Properties of Bone and Cartilage, Grune and Stratton, New York 1979.
12. Birge, S. J. And Whedon, G. B., Bone, In U. MacNally (ed): Hypodynamics and Hypogravics, Academic Press, New York, 1968.
13. Rajiv, K. and Riggs, B. L., Pathologic Bone Physiology, In M.R. Urist (ed.): Fundamental and Clinical Bone Physiology, J.B. Lippincott Co., Philadelphia, 1980.
14. Kazarian, L. E. and von Gierke, H. E., Bone Loss as a Result of Immobilization and Chelation: preliminary results in Macaca mulatta, Clin. Orthop. 65:65-67, 1969.

15. Kazarian, L. E., Cann, C. Parfitt, M. Simmons D. and Morey-Holton, E., 14-day ground-based hypokinesia study in nonhuman primates- a compilation of results. Nasa-TM- 81268. 1981.
16. Wronski, T.S. , Morey E. R., Inhibition of Cortical and Trabecular Bone Formation in Long Bones of Immobilized Monkey.
17. Morey, E. R. and Baylink, D.J., Inhibition of Bone Formation During Space Flight, Science, 201 1138-1141, 1978.
18. Humphreys, Walter J., B. O. Spurlock and J. S. Johnson. "Critical Point Drying of Ethanol-Infiltreated Cayofractured Biological Specimens for Scanning Electron Microscopy", Scanning Electron Microscopy/1974 (Part I) Proceedings of the Seventh Annual Scanning Electron Microscope Symposium , IIT Research Institute, Chicago, Illinois, 275-282
19. Binderman, Itzhak, D. Duksin, A. Harell, E. Katzir and Leo Sachs, Formation of Bone Tissue in Culture from Isolated Cells, The Journal of Cell Biology, 61:427-439, 1974.
20. Yagiela, John A and D.M. Woodbury, Enzymatic Isolation of Osteoblast from Fetal Rat Calvaria, Anat. Rec. , 188:287-308, 1977.

1983-84 USAF-SCEEE RESEARCH INITIATION PROGRAM

Sponsored by the

AIR FORCE OFFICE OF SCIENTIFIC RESEARCH

Conducted by the

SOUTHEASTERN CENTER FOR ELECTRICAL ENGINEERING EDUCATION

FINAL REPORT

CYCLOCONVERTER MODELING FOR VARIABLE SPEED DRIVES

Prepared by: Dr. Medhat Ibrahim

Academic Rank: Professor

Department and
University: Electrical Engineering Department
California State University

Research Location: Air Force Aero Propulsion Laboratory

Date: December 1984

CYCLOCONVERTER MODELING FOR VARIABLE SPEED DRIVES

by

Medhat A. H. Ibrahim

ABSTRACT

A mathematical model of a cycloconverter was developed. The model was developed for the 36-SCR converter as well as the 18-SCR converter. The output frequency can be changed and the SCR's conduction angle can be controlled between 0-120°. A three phase static load made of resistance in series with an inductance was used for testing the model and the results of simulation were given. A model of the brushless dc motor was suggested for dynamic loading of the cycloconverter. Suggestions for further research in this area, are offered.

ACKNOWLEDGMENTS

The author would like to thank the Air Force Systems Command, the Air Force Office of Scientific Research, and the Southern Center for Electrical Engineering Education for providing the opportunity to conduct part of this research at the Air Force Wright Aeronautical Laboratories, Wright Patterson Air Force Base, Ohio, and to complete this research at California State University under the RISE Program. A special thanks is offered to the Power System Branch of the Aerospace Power Division of the Aero Propulsion Laboratory for providing the excellent place to start this research in the summer of 1983.

Finally, the author would like to thank Dr. William U. Borger for suggesting the topic, and Mr. William L. Smith for helping with programming and Mrs. Marge Cook for typing the report.

I. INTRODUCTION

The constant speed drive represents the lowest installed cost, but may not provide the flexibility or operating efficiency which can be attained from an adjustable speed drive. Adjustable speed drives are needed in aircraft systems as well as countless industrial applications.¹⁻⁶ An adjustable speed drive can be accomplished by prime movers such as: 1) gas turbine, 2) constant speed electric drive with slip coupling, 3) dc motor with adjustable voltage or adjustable field control, 4) ac motor with adjustable voltage or adjustable frequency control. The dc commutator machine is suitable for variable speed and variable torque operation; but due to the brush maintenance and other problems, the machine is not suitable for aircraft application. Fortunately, the brushless dc motor offers the same desirable speed-torque characteristics as the dc commutator machine without the disadvantages. The most common configuration of brushless dc motors is the polyphase permanent magnet synchronous motor with power supply conditioning circuit which is capable of bidirectional power flow. This circuit is a static frequency changer which converts a source frequency to another frequency corresponding to the motor rotation and is called cycloconverter.³⁻⁷ Through the use of the cycloconverter the speed of the motor can be changed by the triggering frequency of the SCR set, and the motor torque is controlled by controlling the length of on-time of the SCRs. The use of cycloconverter as the power conditioning circuit is preferred compared to the use of a dc link.⁵ From the above it is obvious that a good model for the cycloconverter is needed for the simulation of, steady state as well as transient behavior, a generator-motor set coupled through a cycloconverter circuit.

II. OBJECTIVES

The main objective of this project was to develop a model for representing the cycloconverter circuit which is linking a variable frequency variable voltage supply to a passive load made of a resistance

and inductance elements or a permanent magnet brushless dc motor. Due to the research period frame, the loading with brushless dc motor, was left for further studies in the future. In this study the 18-SCRs model as well as the 36-SCRs model were considered and the conduction angle was extended to cover from 0 - 120 degrees.

The specific objectives that were pursued are given:

1. To choose a mathematical model to represent the cycloconverter.
2. To write a computer program to represent the mathematical model.
3. To load the cycloconverter by a passive load.
4. To suggest further studies to be conducted.

III. MATHEMATICAL MODEL USED FOR THE SIMULATION OF THE CYCLOCONVERTER

The cycloconverter is a nonlinear device made of switches, SCRs or transistors, which are either closed or open according to a prescribed function to shape the output wave from the input wave. If the SCRs are triggered and have forward bias, it conducts and continues to conduct after the trigger signal is removed until commutated. With this in mind, the cycloconverter works like a conditioning function which transforms the supply wave into a desired output; or in mathematical terms

$$v_m = F (v_s, i_m) \quad (1)$$

where

v_m : the output wave from the cycloconverter

v_s : the input wave to the device

i_m : the output current from the cycloconverter, i.e.; currents in the different SCRs

F : the cycloconverter transformation function which depends on the triggering function and the commutation in the SCRs.

Because the large number of SCRs used in the cycloconverter, 36-SCRs as in Figure 1 or 18-SCRs as in Figure 2 for the three-phase input three-phase output case, the use of matrices in the formulations is very useful. For the case of the 36-SCRs shown in figure 1, and the 18-SCRs shown in figure 2, transformation function F given in equation 1 can be represented by the matrix D given in equation 2 for the 36-SCRs, while in the 18-SCRs case the upper right 3×3 submatrix and the lower left 3×3 submatrix elements are put to be zeros.

$$D = \begin{bmatrix} d_{11} & d_{12} & d_{13} & | & d_{14} & d_{15} & d_{16} \\ d_{21} & d_{22} & d_{23} & | & d_{24} & d_{25} & d_{26} \\ d_{31} & d_{32} & d_{33} & | & d_{34} & d_{35} & d_{36} \\ \hline d_{41} & d_{42} & d_{43} & | & d_{44} & d_{45} & d_{46} \\ d_{51} & d_{52} & d_{53} & | & d_{54} & d_{55} & d_{56} \\ d_{61} & d_{62} & d_{63} & | & d_{64} & d_{65} & d_{66} \end{bmatrix} \quad (2)$$

The elements of this matrix are related on a one to one basis with the SCRs in the circuit of figure 1 for the 36-SCRs, and figure 2 for the 18-SCRs case. Assuming that the SCRs are ideal switches, the elements of the matrix d_{ij} are either set to "1" when conducting or "0" when not conducting or open.

The state of each element in this matrix depends on three factors which are:

- 1) that the trigger signal is on or off
- 2) that the bias on the SCR is positive or negative
- 3) the commutation state of the SCR after the trigger signal is removed.

Thus it follows that the matrix D can be written as a function of three matrices, D_1 , D_2 , D_3 , which are dependant on the three criteria listed above by the following equation:

$$D = D_1 * D_2 + D_3 \quad (3)$$

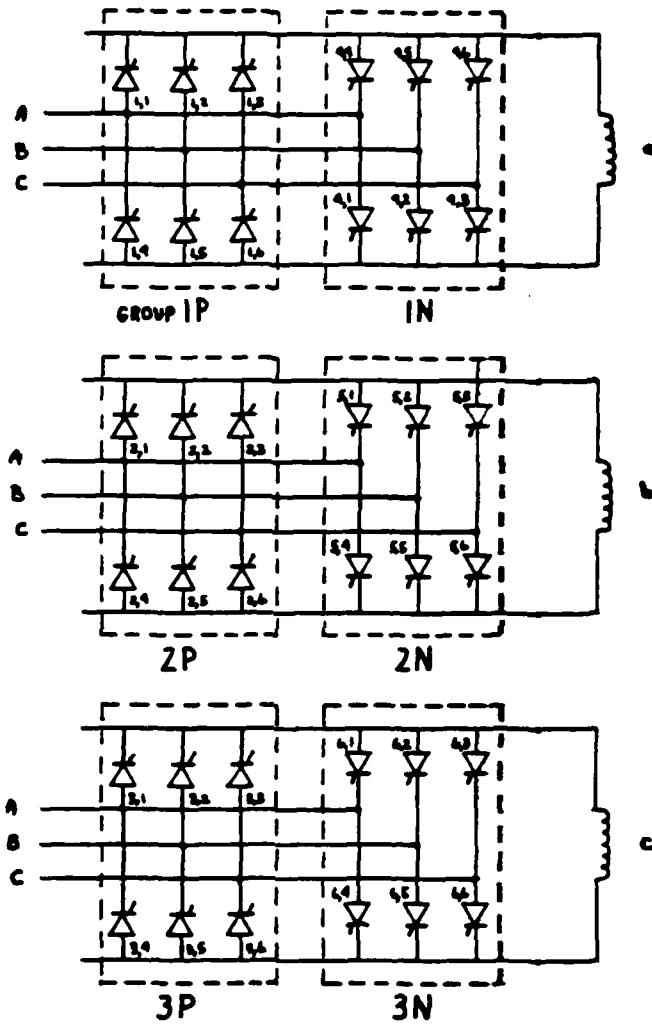


Figure 1 - 36 SCR CYCLOCONVERTER

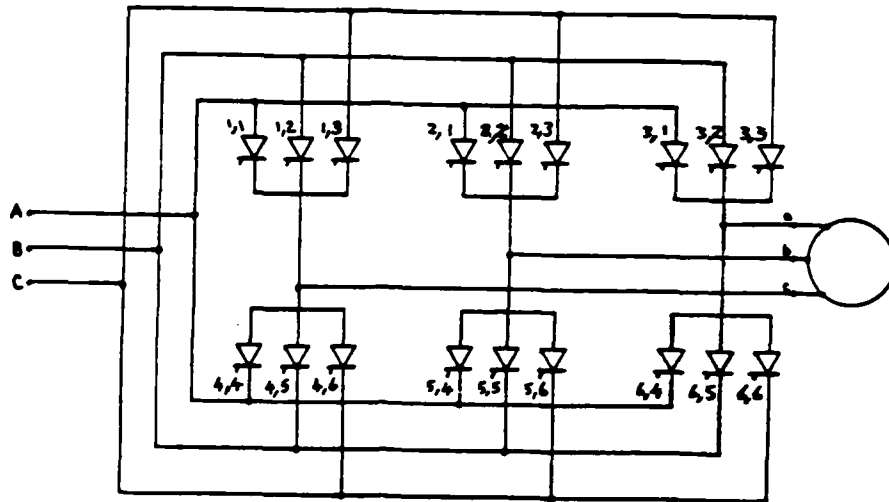


Figure 2 - 18 - SCR CYCLOCONVERTER

In equation 3 the (*) designates corresponding terms multiplications of the two matrices. The elements of these matrices are either "0" or "1" only and the values are set according to the following rules:

Matrix D_1 : The elements of this matrix are set to "1" if the corresponding SCR in the cycloconverter is triggered, and "0" if there is no trigger signal applied.

Matrix D_2 : The elements of this matrix are set to be "1" if biased in the forward direction and to be "0" otherwise.

Matrix D_3 : The elements of this matrix for which the corresponding SCRs are still conducting, after the trigger signal is removed, are set to "1". These elements are then set to "0" following commutation.

The values of the elements of the matrix D, at any given time, are determined by the prearranged control signals to give a specific output voltage wave. From the matrix D and the knowledge of the circuit, a matrix C could be formed:

$$\underline{I}_s = \underline{C} \underline{I}_m \quad (4)$$

where \underline{I}_s : represents the input current to the cycloconverter
 \underline{I}_m : represents the output current from the cycloconverter
C : the connection matrix which is constructed of the elements of the D matrix

From equation 4 and the power equation the output voltages can be obtained:

$$\underline{V}_m = \underline{C}^T \underline{V}_s \quad (5)$$

where \underline{V}_m : the output voltages
 \underline{V}_s : the supply voltages
 \underline{C}^T : the transpose of the matrix C.

The matrix C formation will be demonstrated in the next section for a particular cycloconverter circuit.

IV. CYCLOCONVERTER LOADING AND SIMULATION

A. System Description- A 36-SCRs cycloconverter shown in figure 1, and 18-SCRs shown in figure 2, were simulated by means of a Fortran program. In this simulation the SCRs in one group are simultaneously triggered for a certain portion of the wave. By this method a three-phase output voltage waves, which are 120 electrical degrees apart, were produced. The output voltage frequency and magnitude are determined by the control signal and the input voltage.

B. Cycloconverter - For the circuit shown in figure 1 the matrix C could be written as in equation 6, and for the circuit shown in figure 2, the absent elements are always put to be zeros in 6 .

$$\underline{C} = \begin{bmatrix} d_{11} & -d_{14} & d_{21} & -d_{24} & d_{31} & -d_{34} \\ -d_{41} & d_{44} & -d_{51} & d_{54} & -d_{61} & d_{64} \\ d_{12} & -d_{15} & d_{22} & -d_{25} & d_{32} & -d_{35} \\ -d_{42} & d_{45} & -d_{52} & d_{55} & -d_{62} & d_{65} \\ d_{13} & -d_{16} & d_{23} & -d_{26} & d_{33} & -d_{36} \\ -d_{43} & d_{46} & -d_{53} & d_{56} & -d_{63} & d_{66} \end{bmatrix} \quad (6)$$

To demonstrate the choice of values for the d_{ij} of the matrix C for the 36-SCRs case : for motor angle $0 \leq \theta < \alpha$ (conduction angle) the elements $d_{1j} = 1$ for $j = 1 - 6$, in the matrix D_1 and all the other elements are zeros. Also for a generator or supply angle of $120^\circ \leq \theta < 180^\circ$, v_B is the most positive and v_C is the most negative, $d_{i2} = 1$ for $i = 1 - 6$, and $d_{i6} = 1$ for $i = 1 - 6$ in the matrix D_2 . From this information the matrix D can be obtained which indicates that $d_{12} = d_{16} = 1$ or $I_B = I_b$, $I_C = -I_b$ and $v_a = v_B - v_C$.

C. Static load - The load in this case was made of simple resistance and inductance in series connected to three phase output as shown in figure 1 for the 36-SCRs and as in figure 2 for the 18-SCRs, where the load is wye connected with grounded neutral. This system is a nonlinear system because of the switching operation by the cycloconverters SCRs. The load could be represented by three first order differential equations which are written in the vector form :

$$\frac{di}{dt} = - (R \underline{i} - \underline{v}) / L \quad (7)$$

where i : the current in the load
 R : the resistance in ohms
 L : the inductance in henries
 v : the voltage applied to the load in volts

In figure 3, the flow of and the direction of the current in the different lines will depend on the cycloconverter's SCRs connecting the source to the motor lines at a particular time. For this reason the motor angle between 0 - 360 electrical degrees should be divided in six or more segments, depending on the conduction angle, for the purpose of the simulation.

E. Simulation Results

Due to the time frame and the appropriated funds for this work, only the static load simulation case was performed. The brushless dc motor case is left for future study. The resistance in the load was taken to be 2.6 ohms and the inductance to be 0.175mH. The ratio of input to output frequencies was varied and also different values of conduction angles were considered. The program was extended to include the 18-SCRs as well as 36-SCRs models and the angle was extended to include angles above 60 degrees up to 120 degrees. The program was tested for several cases, some of which is included in this report. Two cases were chosen for the frequency ratio of 2:1 which are:

- Case 1: 36-SCRs, conduction angle = 100 degrees
- Case 2: 18-SCRs, conduction angle = 30 degrees

Two other cases for the frequency ratio of 4:1 were chosen, which are:

- Case 3: 36-SCRs, conduction angle = 59 degrees
- Case 4: 18-SCRs, conduction angle = 75 degrees

The output of these cases are shown in Appendix D. An introduction to the simulation program, flow chart, and Fortran source program are given in Appendices A, B and C.

V. RECOMMENDATIONS

The program was extended to include the 36-SCRs as well as 18-SCRs and the conduction angle was extended to be from 0 - 120 degrees. The extension of the program to dynamic loading by a brushless dc motor was left for further studies.

Also additional research is recommended regarding the following topics:

- A. To study the effect of parameter variation on the steady-state as well as the transient behavior in case of the brushless dc motor loading.
- B. To fabricate a model and verify the test results against the computer simulation.
- C. To study in detail the control circuits needed for the cyclo-converter, including the microprocessor selection or design to best suit the purpose.
- D. To investigate the conditions which might create a discontinuity in the output current of the cycloconverter feeding the dc brushless motor.

REFERENCES

1. Weiss, Herbert W., "Adjustable Speed AC Drive Systems for Pump and Compressor Applications," IEEE Transaction on Industrial Applications, Vol IA-10, Jan/Feb 1974, pp 162 - 167.
2. Hamilton, R. A., and Lezan G. R. , "Thyristor Adjustable Frequency Power Supplies for Hot Strip Mill Run-Out Tables," IEEE Transaction on Industry and General Applications, IGA-3, Mar/Apr 1967, pp 168 - 175.
3. Tsuchiya, T., "Basic Characteristics of Cycloconverter-Type Commutatorless Motors," IEEE Transaction on Industry and General Applications, IGA-6, No. 4, July/August 1970, pp 349 - 360.
4. Jacovides, L. J., "Analysis of a Cycloconverter - Induction Motor Drive System Allowing for Stator Current Discontinuities," IEEE Transaction on Industry and General Applications, Vol. IA-9, No. 2, March/April 1973, pp 206 - 215.
5. Cathey, J. J., "Electrically Compensated Constant Speed Drive," SCEEE Summer Faculty Research Program Final Report 1982.
6. Bowler, P., "The Application of a Cycloconverter to the Control of Induction Motors," IEE Conference Publication 17 on Power Applications of Controllable Semi-Conductor Devices, Nov. 1965, pp 137 - 145.
7. Amato, C. J., "An AC Equivalent Circuit for a Cycloconverter," IEEE Trans on Industry and General Applications, Vol. IGA-2, Sep/Oct 1966, pp 358 - 362.

APPENDIX A

COMPUTER PROGRAM INTRODUCTION

GENERAL DESCRIPTION

"CYCLO" is a FORTRAN language program. It calculates output currents and voltages for a frequency changing SCR circuit. The program is designed for use with either an 18 SCR circuit feeding a wye connected load with a grounded center tap, or a 36 SCR circuit feeding a 3 phase load. The program charts the conducting conditions of the SCR's in a series of 6 X 6 matrices. The program uses positive logic, i.e., a '1' indicates 'on' and a '0' indicates 'off'.

Execution of the program can be under four separate sets of conditions. The program is divided by the circuit type, 18 SCR or 36 SCR, and according to the α angle. The cases are:

- 1) 18 SCR's conduction angle < 60 degrees
- 2) 18 SCR's 60 degrees conduction angle < 120 degrees
- 3) 36 SCR's conduction angle < 60 degrees
- 4) 36 SCR's 60 degrees conduction angle < 120 degrees

The D1 matrix determines which SCR's are triggered. It does so by determining the phase angle of the motor, then assigning '1's to the appropriate positions in the D1 matrix indicating the triggered SCR's.

The D2 matrix determines which SCR's are forward biased. It does so by determining the phase angle of the generator, then assigning '1's to the appropriate positions in the D2 matrix indicating the forward biased SCR's.

The D12 matrix is a combination of the D1 and D2 matrices indicating which SCR's are triggered and forward biased. It does so by multiplying the element of D1 by D2 on a one to one basis. Only an SCR with a '1' in D1, indicating triggered, and a '1' in D2, indicating forward biased, will have a '1' in D12.

Consideration must now be made for the SCR's ability to remain 'on' once it's trigger has been removed, as long as the current did not go to zero. Therefore, each element of the D3 matrix is turned 'on' when it's associated SCR is turned on. The elements of the D3 matrix are then turned off only, if the trigger is off and the SCR is commutated.

The D matrix determines which SCR's are conducting. It does so by inspecting the elements of D12 and D3. If the element in either D12 or D3 is a '1', then a '1' will be assigned to that element in the D matrix.

The basic equations to be solved by CYCLO are the current and voltage through each leg, with respect to time.

The problem is entered into the computer by the general parameters that specify the given conditions. Allowance is made to output the matrices to a file "MATRIX" for further analysis, if desired. The program output is to three separate files, "VOLTS" for the voltages, "CURRENT" for the currents, and "MATRIX" for the matrices.

USER DESCRIPTION

"CYCLO" is primarily designed for use on a time-sharing terminal. Data is entered as requested from the screen, and then printed out for a final check before performing the actual calculations.

Required data input:

SCR FIRING ANGLE?

Respond with the firing angle of the SCR's, in degrees.

NUMBER OF SCRS (18 OR 36)?

Respond with 18 or 36, depending on which circuit you desire.

TIME BETWEEN OUTPUT LINES (IN MICROSECONDS)?

Respond with the time interval, in microseconds, that you desire between each output line. This is an integer number and is simply used as a counter in the program.

FREQUENCY OF GENERATOR?

Respond with desired generator frequency.

FREQUENCY OF MOTOR?

Respond with desired motor frequency.

ENTER 1 IF YOU DESIRE MATRIX OUTPUTS

ENTER 0 IF YOU DO NOT.

Respond with a 1 or a 0, depending on if you wish to utilize the matrix output option.

(The next three questions are asked only if you have indicated a desire for matrix outputs.)

TIME BETWEEN MATRIX OUTPUTS?

Respond, as above, with an integer number. Again, this is used as a counter.

STARTING TIME OF MATRICES (IN MILLISECONDS)?

Respond with a real number, the time of the first matrix output.

STOPPING TIME OF MATRICES (IN MILLISECONDS)?

Respond with a real number.

STARTING TIME (IN MILLISECONDS)?

Respond with the time you wish the voltages and currents to be routed to their respective output files.

STOPPING TIME (IN MILLISECONDS)?

Respond with a real number, the time you wish the program to stop.

The program then displays the data back to the user, allowing the user to check the data before the program body runs. The program then asks:

IF THIS IS CORRECT, TYPE 1

IF NOT, TYPE 0

Responding with a 0 will repeat the entire input section, allowing the user to change the data, otherwise the program will proceed with it's operation.

OUTPUT DESCRIPTION

FILE VOLTS:

This file lists:

TIME, MOTOR ANGLE, VA, VB, VC, VX, VY, VZ

where VA, VB, and VC are motor phase voltages,
and VX, VY, and VZ are generator phase voltages

FILE CURRENT:

This file lists:

TIME, MOTOR ANGLE, X(1), X(2), X(3), XS(1), XS(2), XS(3)

where X(1), X(2), and X(3) are motor phase currents
and XS(1), XS(2), and XS(3) are generator phase currents.

FILE MATRIX:

This file gives the matrices:

D1, D2, D12, D3, D

in each case preceded by the time and motor angle.

LIST OF VARIABLES

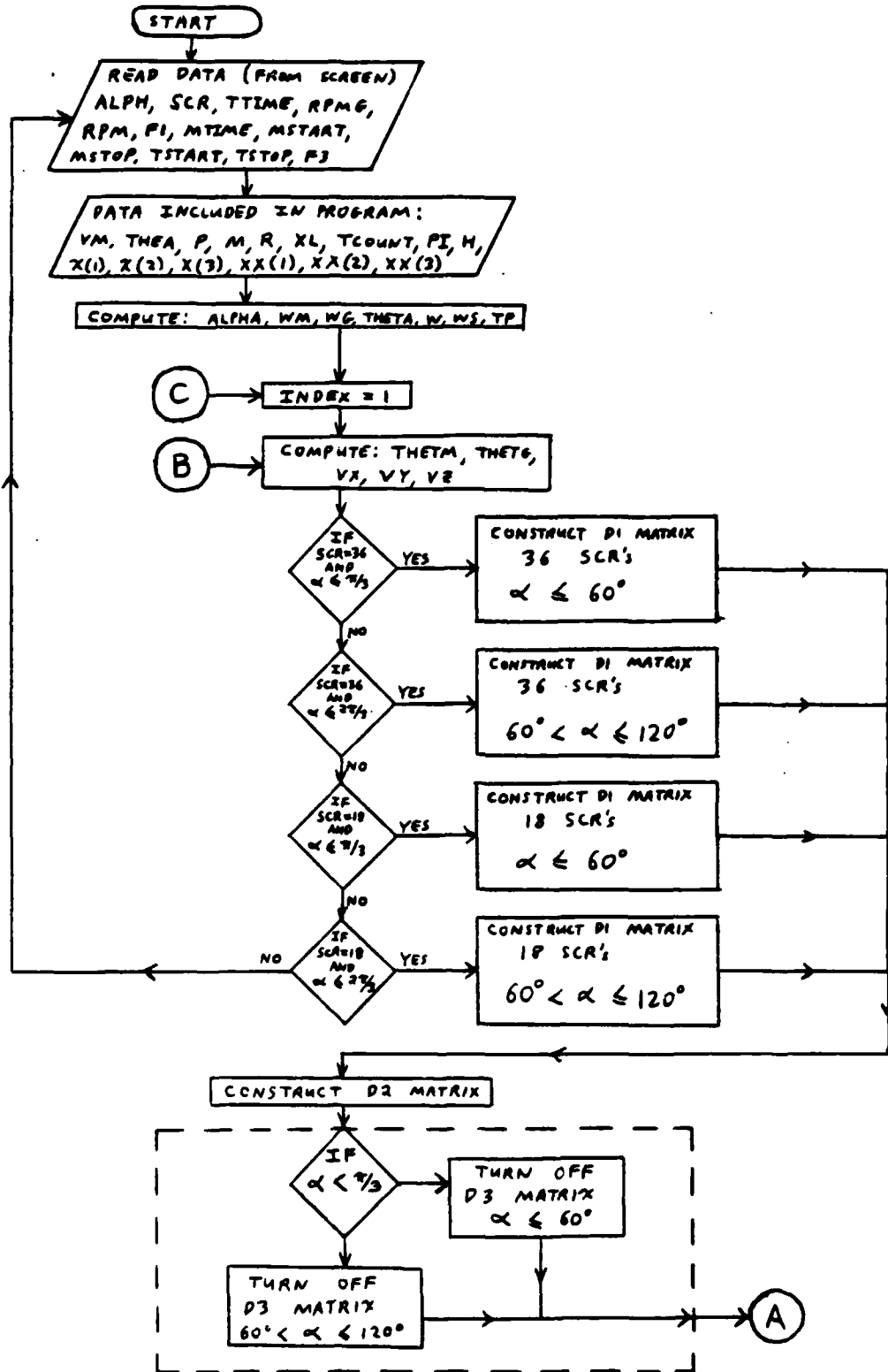
RPM = SPEED OF MOTOR IN RPM
RPMG = SPEED OF THE GENERATOR IN RPM
WM = ANGULAR VELOCITY OF MOTOR IN RAD/S
P = NUMBER OF POLES OF MOTOR
W = ELECTRICAL ANGULAR VEL. OF MOTOR IN RAD/S
WG = ANGULAR VEL. OF GENERATOR DRIVE IN RAD/S
WS = ELECTRICAL ANGULAR VEL. OF GENERATOR IN RAD/S
THETA = START OF CONDUCTION ANGLE IN RAD
THEM = MOTOR ELECT. ANGULAR DISPLACEMENT IN RAD
THEMD = THEM IN DEGREES
THEYS = GENERATOR ELECT. ANGULAR DISPLACEMENT IN RAD
X = CURRENT IN THE DIFFERENT MOTOR PHASES IN AMPS
XS = CURRENT IN THE DIFFERENT GENERATOR PHASES IN AMPS
F = DERIVATIVE OF THE CURRENT
R = PHASE RESISTOR IN OHMS
XL = PHASE INDUCTANCE IN H.
VM = MOTOR VOLTAGE RATING
VA, VB, VC = GENERATOR PHASE VOLTAGES
VX, VY, VZ = MOTOR PHASE VOLTAGES
VN = NODE VOLTAGE (Y INDUCTOR NETWORK, 18 SCR CIRCUIT)
ALPHA, BETA = TRIGGER ANGLE (DEGREES, RADIANS)
BETA = ALPHA + $\pi/3$ (FOR ALPHA > 60 DEGREES)

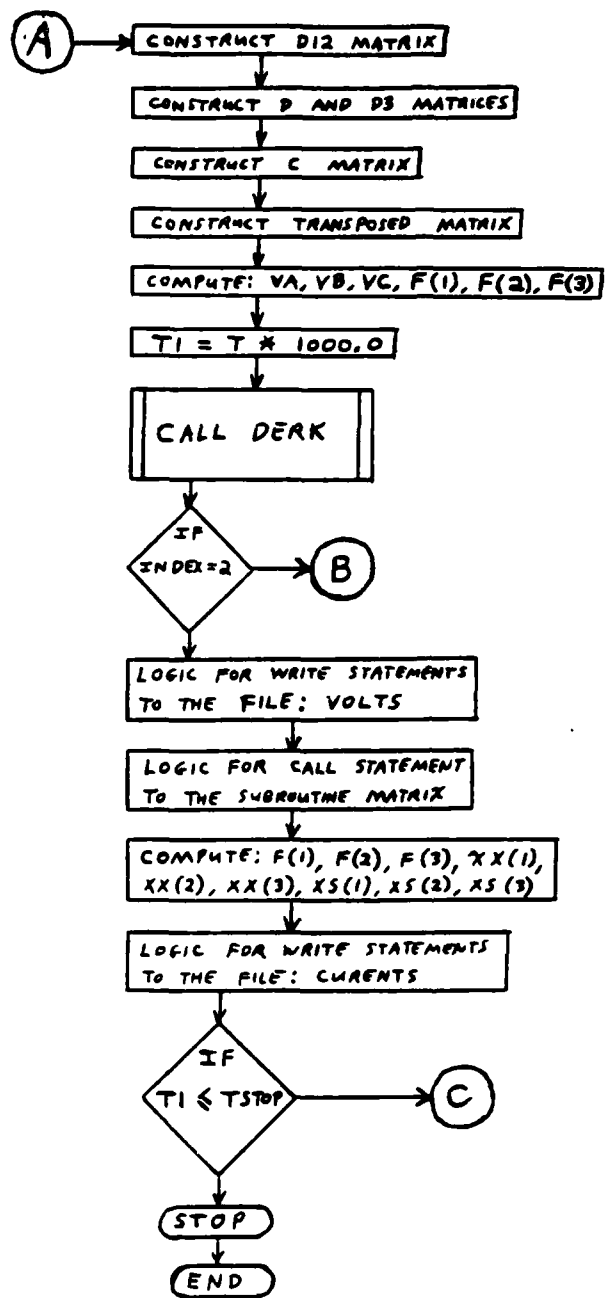
TOTART = STARTS OUTPUT TO FILE
TETOP = STOPS OUTPUT TO FILE
TTIME = TIME BETWEEN OUTPUT LINES
TCOUNT = COUNTER FOR OUTPUT TO FILES
MSTART = STARTS OUTPUT TO MATRIX FILES
METOP = STOPS OUTPUT TO MATRIX FILES
MTIME = TIME BETWEEN MATRIX OUTPUTS
MOUNT = COUNTER FOR MATRIX OUTPUTS

R1 = SHOWS IF OPERATOR WANTS MATRIX OUTPUTS
R2 = FLAG FOR THE INSTANT THE TRIGGER GOES AWAY
R3 = ALLOWS OPERATOR TO REINPUT THE DATA

APPENDIX B

COMPUTER PROGRAM FLOWCHART





APPENDIX C

FORTRAN SOURCE PROGRAM FOR THE CYCLOCONVERTER
SIMULATION

```

0001C      PROGRAM CYCLOS
0002CC C      PROGRAM FOR LOADING THE CYCLOCONVERTER
00030C C
0004CC C
00050C C      RPM = SPEED OF MOTOR IN RPM
00060C C      RPMG = SPEED OF THE GENERATOR IN RPM
00070C C      WM = ANGLLAR VELOCITY OF MOTOR IN RAD/S
00080C C      P = NUMBER OF POLES OF MOTOR
00090C C      W = ELECTRICAL ANGULAR VEL. OF MOTOR IN RAD/S
00100C C      WG = ANGLLAR VEL. OF GENERATOR DRIVE IN RAD/S
00110C C      VS = ELECTRICAL ANGULAR VEL. OF GENERATOR IN RAD/S
00120C C      THETA = START OF CONDUCTION ANGLE IN RAD
00130C C      THETM = MCTOR ELECT. ANGULAR DISPLACEMENT IN RAD
00140C C      THETMO = THETM IN DEGREES
00150C C      THETG = GENERATOR ELECT. ANGULAR DISPLACEMENT IN RAD
00160C C      X = CURRENT IN THE DIFFERENT MOTOR PHASES IN AMPS
00170C C      XS = CURRENT IN THE DIFFERENT GENERATOR PHASES IN AMPS
00180C C      F = DERIVATIVE OF THE CURRENT
00190C C      R = PHASE RESISTOR IN OHMS
00200C C      XL = PHASE INDUCTANCE IN H.
00210C C      VM = MOTOR VOLTAGE RATING
00220C C      VX,VY,VZ = GENERATOR PHASE VOLTAGES
00230C C      VA,VB,VC = MOTOR PHASE VOLTAGES
00240C C      VM = NODE VOLTAGE (Y INDUCTOR NETWORK, 10 SCR CIRCUIT)
00250C C      ALPH,ALPHA = TRIGGER ANGLE (DEGREES,RADIANS)
00260C C      BETA = ALPHA - PI/3 (FOR ALPH > 60 DEGREES)
00270C C
00280C C      TSTART = STARTS OUTPUT TO FILE
00290C C      TSTOP = STOPS OUTPUT TO FILES AND STOPS PROGRAM
00300C C      TTIME = TIME BETWEEN OUTPUT LINES
00310C C      TCOUNT = COUNTER FOR OUTPUT TO FILES
00320C C      MSTART = STARTS OUTPUT TO MATRIX FILES
00330C C      MSTOP = STOPS OUTPUT TO MATRIX FILES
00340C C      MTIME = TIME BETWEEN MATRIX OUTPUTS
00350C C      MCOUNT = COUNTER FOR MATRIX OUTPUTS
00353C C
00354C C      F1 =
00355C C      F2 = FLAG FOR THE INSTANT THE TRIGGER GOES AWAY.
00354C C      F3 =
00360C C
00370C C
00380C C      PROGRAM DEVELOPED BY: MEDHAT A. H. IBRAHIM
00390C C
00400C C
0041CC C      DATE :      NOVEMBER 1984
0042CC C
00430C C
00440C C
00450C C      *****
00460 C      DIMENSION C1(6,6),D2(6,6),D(6,6),C(3,3),CT(3,3)
00470 C      DIMENSION X(6),XX(6),O3(6,6),D12(6,6),F(3),XS(3)
00480 C      REAL VM, VA, VB, VC, VX, VY, VZ, THETA, THETM, THETG
00490 C      REAL MSTART,MSTOP
00500 C      INTEGER SCR,F1,F2,F3
00510 C      DATA VM/150.0,THEA/30.0/,TCOUNT/1/
00520 C      DATA PI/3.1415926536/,CONT/G.0/,T/O.0/,N/O/,MM/O/,P/1.0E-06/
00530 C      DATA X(1)/0.0/,X(2)/0.0/,X(3)/0.0/,XX(1)/0.0/,XX(2)/0.0/,XX(3)/0.0/
00540 C      OPEN(UNIT=9, FILE='CURRENT', STATUS='NEW')
00550 C      OPEN(UNIT=10, FILE='VOLTS', STATUS='NEW')
00560 C      OPEN(UNIT=11, FILE='MATRIX', STATUS='NEW')
00565 C      OPEN(UNIT=12, FILE='DRCRNT', STATUS='NEW')
00570C C*****
00580C C      THIS SECTION READS INPUT VALUES FROM THE SCREEN
00590C C*****

```

```

00600 04 PRINT*, ' SCR FIRING ANGLE'
0061C READ*, ALPH
00620 DATA P/4.0C/,4/3/,R/2.60/,XL/0.000175/
00630 PRINT*, ' NUMBER OF SCRS (18 OR 36)'
00640 READ*, SCR
00650 PRINT*, ' TIME BETWEEN OUTPUT LINES (IN MICROSECONDS)'
00660 READ*, TTIME
00670 PRINT*, ' FREQUENCY OF GENERATOR'
00680 READ*, RPMG
00690 PRINT*, ' FREQUENCY OF MOTOR'
00700 READ*,RPM
00710 PRINT*, 'ENTER 1 IF YOU DESIRE MATRIX OUTPUTS'
00720 PRINT*, 'ENTER 0 IF YOU DO NOT'
00730 READ*,F1
00740 IF(F1.EQ.0) GOTO 06
00750 PRINT*, ' TIME BETWEEN MATRIX OUTPUTS (IN MICROSECONDS)'
00760 READ*, MTIME
00770 PRINT*, ' STARTING TIME OF MATRIXES (IN MILLISECONDS)'
00780 READ*, MSTART
00790 PRINT*, ' STOPPING TIME OF MATRIXES (IN MILLISECONDS)'
00800 READ*, MSTOP
00810 06 PRINT*, ' STARTING TIME IN MILLISECONDS'
00820 PRINT*, ' (NORMALLY 0.0)'
00830 READ*,TSTART
00840 PRINT*, ' STOPPING TIME IN MILLISECOND'
00850 READ*,TSTOP
00860C C*****
00870C C THIS SECTION REPRINTS ALL ENTERED DATA, ALLOWING
00880C C FOR AN ACCURACY CHECK PRIOR TO RUNNING THE MAIN
00890C C BODY OF THE PROGRAM, AND PROVIDING AN OPPORTUNITY
00900C C TO CHANGE THE DATA.
00910C C*****
00920 PRINT*, 'TRIGGER ANGLE: ',ALPH
00930 PRINT*, 'NLMBER OF SCRS: ',SCR
00940 PRINT*, 'TIME BETWEEN OUTPUT LINES (MICROSECONDS): ',TTIME
00950 PRINT*, 'GENERATOR FREQUENCY: ',RPMG
00960 PRINT*, 'MCTOR FREQUENCY: ',RPM
00970 IF(F1.EQ.0) GOTO 03
00980 PRINT*, 'YOU HAVE REQUESTED MATRIXES:'
00990 PRINT*, ' STARTING: ',MSTART
01000 PRINT*, ' STOPPING: ',MSTOP
01010 PRINT*, ' INCREMENT: ',ATIME
01020 03 PRINT*, 'YOU HAVE REQUESTED THE PROGRAM TO:'
01030 PRINT*, ' START OUTPUT: ',TSTART
01040 PRINT*, ' STOP OUTPUT: ',TSTOP
01050 PRINT*, 'IF THIS IS CORRECT, TYPE 1'
01060 PRINT*, 'IF NOT, TYPE 0'
01070 READ*,F3
01080 IF(F3.EQ.0) GOTO 04
01090C C*****
01100C C INITIALIZING VARIABLES
01110C C*****
01120 MCOUNT = MTIME
01130 ALPHA = ALPH * PI / 180.0
01140 WM = RPM * 2.0 * PI / 60.0
01150 WG = RPMG * 2.0 * PI / 50.0
01160 THETA = THEA * PI / 180.0
01170 W = P / 2.C * WM
01180 VS = 2.0 * WG
01190 TP = 2.0 * PI / W
01200C C*****
01210C C INITIALIZES D,C1,D2,D3 MATRIX TO 0.0
01220C C*****
01230 DO 9 I=1,6

```



```

01240      DO 9 J=1,6
01250      D(I,J) = 0.0
01260      D1(I,J) = 0.0
01270      D2(I,J) = C.C
01280      D3(I,J) = C.0
01290      9 CONTINUE
01300C *****
01310C C PRINTS DATA INFORMATION TO
01320C C OUTPUT FILES CURENT AND VOLTS.
01330C *****
01340      WRITE(9,7) SCR,ALPH,RPM,RPMG
01350      WRITE(10,7) SCR,ALPH,RPM,RPMG
01360      7 FORMAT(5X,'SCR = ',I2,5X,'ALPH = ',F5.1,5X,'RPM = ',F7.1,5X,
01370+      'RPMG = ',F7.1)
01380C *****
01390C C THIS BEGINS THE LARGE LOOP OF THE PROGRAM
01400C C AND IS WHERE THE BOTTOM ROUTES BACK TO.
01410C *****
01420      01 INDEX = 1
01430      02 THETM = W * T
01440      IPRIN = INT(THETM / 2.0 / PI)
01450      THETM = THETM - FLOAT(IPRIN) * 2.0 * PI
01460      THETG = WS * T
01470      IPRIN = INT(THETG / 2.0 / PI)
01480      THETG = THETG - FLOAT(IPRIN) * 2.0 * PI
01490      VX = VM * SIN(THETG + THETA)
01500      VY = VM * SIN(THETG - 2.0 * PI / 3.0 + THETA)
01510      VZ = VM * SIN(THETG - 4.0 * PI / 3.0 + THETA)
01520C *****
01530C C THE FOLLOWING ARE BRANCH COMMANDS BASED ON:
01540C C THE ANGLE ALPHA(RADIANS)
01550C C THE NUMBER SCR (SCR'S IN THE CIRCUIT)
01560C *****
01570      IF((SCR.EQ.36).AND.(ALPHA.LE. PI/3.0)) GOTO 200
01580      IF((SCR.EQ.36).AND.(ALPHA.LE.2.0*PI/3.0)) GOTO 300
01590      IF((SCR.EQ.18).AND.(ALPHA.LE. PI/3.0)) GOTO 600
01600      IF((SCR.EQ.18).AND.(ALPHA.LE.2.0*PI/3.0)) GOTO 700
01610C *****
01620C C CONSTRUCTION OF THE D1 MATRIX FOR ALPHA LE 60 DEGREES
01630C C AND 36 SCR'S IN THE CIRCUIT
01640C C
01650C C THE VARIABLE THETM IS DIVIDED INTO 12 PORTIONS
01660C C BASED ON:
01670C C MULTIPLES OF PI/3.0
01680C C AND (MULTIPLES OF PI/3.0) + ALPHA
01690C C
01700C C THE FLAG F2 IS USED TO DETERMINE THE INSTANT
01710C C THE TRIGGER GOES AWAY, INDICATING THE
01720C C MOMENT TO CREATE THE D3 MATRIX.
01730C *****
01740      200 IF(THETM.LT.ALPHA) GOTO 240
01750      IF(THETM.LT.PI/3.0) GOTO 295
01760      IF(THETM.LT.(PI/3.0+ALPHA)) GOTO 250
01770      IF(THETM.LT.2.0*PI/3.0) GOTO 295
01780      IF(THETM.LT.(2.0*PI/3.0+ALPHA)) GOTO 260
01790      IF(THETM.LT.PI) GOTO 295
01800      IF(THETM.LT.(PI+ALPHA)) GOTO 270
01810      IF(THETM.LT.4.0*PI/3.0) GOTO 295
01820      IF(THETM.LT.(4.0*PI/3.0+ALPHA)) GOTO 280
01830      IF(THETM.LT.5.0*PI/3.0) GOTO 295
01840      IF(THETM.LT.(5.0*PI/3.0+ALPHA)) GOTO 290
01850      IF(THETM.LT.2.C*PI) GOTO 295
01860C
01870      240 F2 = 1

```

```

01830      DO 242 J=1,6
01890      D1(1,J) = 1.0
01900      242 CONTINUE
01910      GOTO 70
01920C
01930      250 F2 = 1
01940      DO 252 J=1,6
01950      D1(6,J) = 1.0
01960      252 CONTINUE
01970      GOTO 70
01980C
01990      260 F2 = 1
02000      DO 262 J=1,6
02010      D1(2,J) = 1.0
02020      262 CONTINUE
02030      GOTO 70
02040C
02050      270 F2 = 1
02060      DO 272 J=1,6
02070      D1(4,J) = 1.0
02080      272 CONTINUE
02090      GOTO 70
02100C
02110      280 F2 = 1
02120      DO 282 J=1,6
02130      D1(3,J) = 1.0
02140      282 CONTINUE
02150      GOTO 70
02160C
02170      290 F2 = 1
02180      DO 292 J=1,6
02190      D1(5,J) = 1.0
02200      292 CONTINUE
02210      GOTO 70
02220C
02230C C*****
02240C C   THIS CREATES THE D3 MATRIX THE INSTANT
02250C C   THE TRIGGER GOES AWAY, THEN CLEARS
02260C C   THE D1 MATRIX.
02270C C*****
02280      293 IF(F2.EQ.1) THEN
02290          DO 297 I=1,6
02300          DO 297 J=1,6
02310              D3(I,J) = D(I,J)
02320      297 CONTINUE
02330          F2 = 0
02340          ENDIF
02350          DO 296 I=1,6
02360          DO 296 J=1,6
02370              D1(I,J) = 0.0
02380      296 CONTINUE
02390          GOTO 70
02400C
02410C C*****
02420C C   CONSTRUCTION OF THE D1 MATRIX FOR ALPHA 60-120 DEGREES
02430C C   AND 36 SCR'S IN THE CIRCUIT
02440C C
02450C C   THE VARIABLE THETA IS DIVIDED INTO 6 PORTIONS
02460C C   BASED ON MULTIPLES OF PI/3.0
02470C C
02480C C   THESE ARE THEN SPLIT BY ADDING IN THE VALUE BETA.
02490C C   (WHERE BETA = ALPHA - PI / 3.0)
02500C C
02510C C   LESS THAN BETA: INSURE TWO LINES IN D2 TURNED ON

```

```

02520C C MORE THAN BETA: TURN APPROPRIATE LINE IN D2 OFF
02530C C
02540C C*****
02550 300 BETA = ALPHA - PI / 3.0
02560C
02570 IF(THETM.LT.BETA) GOTO 340
02580C
02590 IF(THETM.GE.PI/3.0) GOTO 304
02600C C*****
02610C C THETM IS NOW GE BETA AND THETM LT PI/3.0
02620C C SO D1(5, ) IS NOW ZERO
02630C C*****
02640 00 302 J=1,6
02650 D3(5,J) = 0(5,J)
02660 D1(5,J) = C.0
02670 302 CONTINUE
02680 GOTO 70
02690C
02700 304 IF(THETM.LT.(PI/3.0+BETA)) GOTO 350
02710C
02720 IF(THETM.GE.2.0*PI/3.0) GOTO 310
02730 00 308 J=1,6
02740 D3(1,J) = 0(1,J)
02750 D1(1,J) = C.0
02760 308 CONTINUE
02770 GOTO 70
02780C
02790 310 IF(THETM.LT.(2.0*PI/3.0+BETA)) GOTO 360
02800C
02810 IF(THETM.GE.PI) GOTO 316
02820 00 314 J=1,6
02830 D3(6,J) = 0(6,J)
02840 D1(6,J) = C.0
02850 314 CONTINUE
02860 GOTO 70
02870C
02880 316 IF(THETM.LT.(PI+BETA)) GOTO 370
02890C
02900 IF(THETM.GE.4.0*PI/3.0) GOTO 322
02910 00 320 J=1,6
02920 D3(2,J) = 0(2,J)
02930 D1(2,J) = C.0
02940 320 CONTINUE
02950 GOTO 70
02960C
02970 322 IF(THETM.LT.(4.0*PI/3.0+BETA)) GOTO 380
02980C
02990 IF(THETM.GE.5.0*PI/3.0) GOTO 328
03000 00 326 J=1,6
03010 D3(4,J) = 0(4,J)
03020 D1(4,J) = C.0
03030 326 CONTINUE
03040 GOTO 70
03050C
03060 328 IF(THETM.LT.(5.0*PI/3.0+BETA)) GOTO 390
03070C
03080 00 332 J=1,6
03090 D3(3,J) = 0(3,J)
03100 D1(3,J) = C.0
03110 332 CONTINUE
03120 GOTO 70
03130C
03140 340 00 342 J=1,6
03150 D1(1,J) = 1.0

```

```

03160      01(5,J) = 1.0
0317C     342 CONTINUE
0318C     GOTO 70
03190C
03200     350 DO 352 J=1,6
03210      01(6,J) = 1.0
03220      01(1,J) = 1.0
03230     352 CONTINUE
03240      GOTO 70
03250C
03260     360 DO 362 J=1,6
03270      01(2,J) = 1.0
03280      01(6,J) = 1.0
03290     362 CONTINUE
03300      GOTO 70
03310C
03320     370 DO 372 J=1,6
03330      01(4,J) = 1.0
03340      01(2,J) = 1.0
03350     372 CONTINUE
03360      GOTO 70
03370C
03380     380 DO 382 J=1,6
03390      01(3,J) = 1.0
03400      01(4,J) = 1.0
03410     382 CONTINUE
03420      GOTO 70
03430C
03440     390 DO 392 J=1,6
03450      01(5,J) = 1.0
03460      01(3,J) = 1.0
0347C     392 CONTINUE
03480      GOTO 70
03490C
03500C     C*****
03510C     C   SEE PRINT STATEMENT BELOW.
03520C     C*****
03530C
03540     600 IF(THETA.LT.ALPHA)          GOTO 650
03550      IF(THETA.LT.PI/3.0)          GOTO 695
03560      IF(THETA.LT.(PI/3.0+ALPHA)) GOTO 655
03570      IF(THETA.LT.2.0*PI/3.0)     GOTO 695
03580      IF(THETA.LT.(2.0*PI/3.0+ALPHA)) GOTO 660
03590      IF(THETA.LT.PI)              GOTO 695
03600      IF(THETA.LT.(PI+ALPHA))      GOTO 670
03610      IF(THETA.LT.4.0*PI/3.0)     GOTO 695
03620      IF(THETA.LT.(4.0*PI/3.0+ALPHA)) GOTO 680
03630      IF(THETA.LT.5.0*PI/3.0)     GOTO 695
03640      IF(THETA.LT.(5.0*PI/3.0+ALPHA)) GOTO 690
03650      IF(THETA.LT.2.0*PI)         GOTO 695
03660C
0367C     650 F2 = 1
03680      DO 652 J=1,3
03690      01(1,J) = 1.0
0370C     652 CONTINUE
03710      GOTO 70
03720C
03730     653 F2 = 1
03740      DO 658 J=4,6
03750      01(6,J) = 1.0
03760     658 CONTINUE
0377C     GOTO 70
03780C
0379C     660 F2 = 1

```

```

0380C      DD 662 J=1.3
03910      D1(2,J) = 1.0
03820      662 CONTINUE
03830      GOTO 76
05245C
03840      670 F2 = 1
03850      DD 672 J=4.6
03860      D1(4,J) = 1.0
03870      672 CONTINUE
03880      GOTO 70
03890C
03900      680 F2 = 1
03910      DD 682 J=1.3
03920      D1(3,J) = 1.0
03930      682 CONTINUE
03940      GOTO 70
03950C
03960      690 F2 = 1
03970      DD 692 J=4.6
03980      D1(5,J) = 1.0
03990      692 CONTINUE
04000      GOTO 70
04010C
04020      695 IF(F2.EQ.1) THEN
04030          DD 697 I=1.6
04040          DD 697 J=1.6
04050          D3(I,J) = D(I,J)
04060      697 CONTINUE
04070          F2 = 0
04080          ENOIF
04090          DD 696 I=1.6
04100          DD 696 J=1.6
04110          D1(I,J) = 0.0
04120      696 CONTINUE
04130          GOTO 70
04140C
04150C      600 PRINT*, ' THE 18 SCR CIRCUIT WILL HAVE NO OUTPUT'
04160C      PRINT*, ' UNDER A TRIGGER CONDITION OF LESS THAN'
04170C      PRINT*, ' 60 DEGREES, SINCE A MOMENT DOES NOT EXIST'
04180C      PRINT*, ' WHEN TWO SCRS ARE TRIGGERED TOGETHER TO'
04190C      PRINT*, ' PROVIDE AN INITIAL PATH FOR CURRENT.'
04200C      GOTO 999
04210C
04220C      C*****
04230C      C   CONSTRUCTION OF THE D1 MATRIX FOR ALPHA 60-120 DEGREES
04240C      C           AND 18 SCRS IN THE CIRCUIT
04250C      C
04260C      C   THE VARIABLE THETA IS DIVIDED INTO 12 PORTIONS
04270C      C           BASED ON:
04280C      C           MULTIPLES OF PI/3.0
04290C      C           AND (MULTIPLES OF PI/3.0) + BETA
04300C      C           (WHERE BETA = ALPHA - PI / 3.0)
04310C      C*****
04320      700 BETA = ALPHA - PI / 3.0
04330C
04340          IF(THETA.LT.BETA) GOTO 740
04350C
04360          IF(THETA.GE.PI/3.0) GOTO 704
04370C      C*****
04380C      C   THETA IS NOW GE BETA AND THETA LT PI/3.0
04390C      C   SO D1(5, ) IS NOW ZERO
04400C      C*****
04410          DD 702 J=1.6
04420          D3(5,J) = C(5,J)

```

```

04430      D1(5,J) = C.0
04440      732 CONTINUE
04450      GOTO 70
04460C
04470      704 IF(THETA.LT.(PI/3.0+BETA)) GOTO 750
04480C
04490      IF(THETA.GE.2.0*PI/3.0) GOTO 710
04500      DO 708 J=1,6
04510      D3(1,J) = C(1,J)
04520      D1(1,J) = C.0
04530      708 CONTINUE
04540      GOTO 70
04550C
04560      710 IF(THETA.LT.(2.0*PI/3.0+BETA)) GOTO 760
04570C
04580      IF(THETA.GE.PI) GOTO 716
04590      DO 714 J=1,6
04600      D3(6,J) = C(6,J)
04610      D1(6,J) = C.0
04620      714 CONTINUE
04630      GOTO 70
04640C
04650      716 IF(THETA.LT.(PI+BETA)) GOTO 770
04660C
04670      IF(THETA.GE.4.0*PI/3.0) GOTO 722
04680      DO 720 J=1,6
04690      D3(2,J) = C(2,J)
04700      D1(2,J) = C.0
04710      720 CONTINUE
04720      GOTO 70
04730C
04740      722 IF(THETA.LT.(4.0*PI/3.0+BETA)) GOTO 780
04750C
04760      IF(THETA.GE.5.0*PI/3.0) GOTO 728
04770      DO 726 J=1,6
04780      D3(4,J) = C(4,J)
04790      D1(4,J) = C.0
04800      726 CONTINUE
04810      GOTO 70
04820C
04830      728 IF(THETA.LT.(5.0*PI/3.0+BETA)) GOTO 790
04840C
04850      DO 732 J=1,6
04860      D3(3,J) = C(3,J)
04870      D1(3,J) = C.0
04880      732 CONTINUE
04890      GOTO 70
04900C
04910      740 DO 742 J=1,3
04920      D1(1,J) = 1.0
04930      D1(5,J+3) = 1.0
04940      742 CONTINUE
04950      GOTO 70
04960C
04970      750 DO 752 J=1,3
04980      D1(1,J) = 1.0
04990      D1(6,J+3) = 1.0
05000      752 CONTINUE
05010      GOTO 70
05020C
05030      760 DO 762 J=1,3
05040      D1(2,J) = 1.0
05050      D1(6,J+3) = 1.0
05060      762 CONTINUE

```

```

05070      6010 70
05080C
05090      770 00 772 J=1,3
05100      01(2,J) = 1.0
05110      01(4,J+3) = 1.0
05120      772 CONTINUE
05130      GOTO 70
05140C
05150      780 00 782 J=1,3
05160      01(3,J) = 1.0
05170      01(4,J+3) = 1.0
05180      782 CONTINUE
05190      GOTO 70
05200C
05210      790 00 792 J=1,3
05220      01(3,J) = 1.0
05230      01(5,J+3) = 1.0
05240      792 CONTINUE
05250      GOTO 70
05260C
05270C C*****
05280C C   CONSTRUCTION OF THE D2 MATRIX
05290C C   THE D2 MATRIX SHOWS WHICH OF THE SCR'S
05300C C   ARE FORWARD BIASED AT ANY GIVEN MOMENT
05310C C
05320C C   IT IS BASED ON THE ANGLE OF THETA AT
05330C C   THE GIVEN MOMENT
05340C C*****
05350      70 IF(THETA.LT.PI/3.0) GOTO 80
05360      IF(THETA.LT.2.0*PI/3.0) GOTO 90
05370      IF(THETA.LT.PI) GOTO 100
05380      IF(THETA.LT.4.0*PI/3.0) GOTO 110
05390      IF(THETA.LT.5.0*PI/3.0) GOTO 120
05400      IF(THETA.LT.2.0*PI) GOTO 130
05410C
05420      80 00 82 I=1,6
05430      02(I,3) = 0.0
05440      02(I,1) = 1.0
05450      02(I,5) = 1.0
05460      82 CONTINUE
05470      GOTO 140
05480C
05490      90 00 92 I=1,6
05500      02(I,5) = 0.0
05510      02(I,1) = 1.0
05520      02(I,6) = 1.0
05530      92 CONTINUE
05540      GOTO 140
05550C
05560      100 00 102 I=1,6
05570      02(I,1) = 0.0
05580      02(I,2) = 1.0
05590      02(I,6) = 1.0
05600      102 CONTINUE
05610      GOTO 140
05620C
05630      110 00 112 I=1,6
05640      02(I,6) = 0.0
05650      02(I,2) = 1.0
05660      02(I,4) = 1.0
05670      112 CONTINUE
05680      GOTO 140
05690C
05700      120 00 122 I=1,6

```

```

05720      D2(I,3) = 1.0
05730      D2(I,4) = 1.0
05740      122 CONTINUE
05750      GOTO 140
05760C
05770      130 DO 132 I=1,6
05780      D2(I,4) = 0.0
05790      D2(I,3) = 1.0
05800      D2(I,3) = 1.0
05810      132 CONTINUE
05820      140 CONTINUE
05830C C*****
05840C C          TURN OFF PORTIONS D3 MATRIX
05850C C*****
05860C
05870      IF(ALPHA.LT.PI/3.0) GOTO 550
05880C
05890C C*****
05900C C  TURNS OFF PORTIONS OF D3 MATRIX FOR
05910C C  60 DEG < ALPHA < 120 DEG
05920C C
05930C C  THE PROGRAM DIVIDES INTO 6 PORTIONS,
05940C C  EACH PORTION THEN CHECKS FOR REVERSE CURRENT.
05950C C
05960C C  IF REVERSE CURRENT, D3 MATRIX IS ZEROED
05970C C
05980C C  IF NOT, THE APPROPRIATE D3 LINE FOR THE CONDUCTING
05990C C  CURRENT IS LEFT ON.
06000C C
06010C C*****
06020      IF(THETA.LT. -PI/3.0+ALPHA) GOTO 545
06030      IF(THETA.LT.  PI/3.0      ) GOTO 520
06040      IF(THETA.LT.      ALPHA) GOTO 520
06050      IF(THETA.LT.2.0*PI/3.0      ) GOTO 525
06060      IF(THETA.LT.  PI/3.0+ALPHA) GOTO 525
06070      IF(THETA.LT.  PI      ) GOTO 530
06080      IF(THETA.LT.2.0*PI/3.0+ALPHA) GOTO 530
06090      IF(THETA.LT.4.0*PI/3.0      ) GOTO 535
06100      IF(THETA.LT.  PI +ALPHA) GOTO 535
06110      IF(THETA.LT.5.0*PI/3.0      ) GOTO 540
06120      IF(THETA.LT.4.0*PI/3.0+ALPHA) GOTO 540
06130      IF(THETA.LT.2.0*PI      ) GOTO 545
06140C
06150      520 IF(X(2).GT.0.0) THEN
06160          DO 521 J=1,6
06170              D3(5,J) = 0.0
06180              DO 521 I=1,3
06190                  D3(I,J) = 0.0
06200      521 CONTINUE
06210      ELSE
06220          DO 522 I=1,3
06230              DO 522 J=1,6
06240                  D3(I,J) = 0.0
06250      522 CONTINUE
06260      ENDIF
06270      GOTO 150
06280C
06290      525 IF(X(1).LT.0.0) THEN
06300          DO 526 J=1,6
06310              D3(1,J) = 0.0
06320              DO 526 I=4,6
06330                  D3(I,J) = 0.0
06340      526 CONTINUE

```



```

06360      ELSE
06370          DO 527 I=4,6
06380          DO 527 J=1,6
06390              D3(I,J) = 0.0
06400 527      CONTINUE
06410          ENDIF
06420          GOTO 150
06430 530 IF(X(3).GT.0.0) THEN
06440          DO 531 J=1,6
06450              D3(6,J) = 0.0
06460          DO 531 I=1,3
06470              D3(I,J) = 0.0
06480 531      CONTINUE
06490          ELSE
06500          DO 532 I=1,3
06510          DO 532 J=1,6
06520              D3(I,J) = 0.0
06530 532      CONTINUE
06540          ENDIF
06550          GOTO 150
06560C
06570 535 IF(X(2).LT.0.0) THEN
06580          DO 536 J=1,6
06590              D3(2,J) = 0.0
06600          DO 536 I=4,6
06610              D3(I,J) = 0.0
06620 536      CONTINUE
06630          ELSE
06640          DO 537 I=4,6
06650          DO 537 J=1,6
06660              D3(I,J) = 0.0
06670 537      CONTINUE
06680          ENDIF
06690          GOTO 150
06700C
06710 540 IF(X(1).GT.0.0) THEN
06720          DO 541 J=1,6
06730              D3(4,J) = 0.0
06740          DO 541 I=1,3
06750              D3(I,J) = 0.0
06760 541      CONTINUE
06770          ELSE
06780          DO 542 I=1,3
06790          DO 542 J=1,6
06800              D3(I,J) = 0.0
06810 542      CONTINUE
06820          ENDIF
06830          GOTO 150
06840C
06850 545 IF(X(3).LT.0.0) THEN
06860          DO 546 J=1,6
06870              D3(3,J) = 0.0
06880          DO 546 I=4,6
06890              D3(I,J) = 0.0
06900 546      CONTINUE
06910          ELSE
06920          DO 547 I=4,6
06930          DO 547 J=1,6
06940              D3(I,J) = 0.0
06950 547      CONTINUE
06960          ENDIF
06970          GOTO 150
05980C

```

```

07000C C   TURNS OFF PORTIONS OF D3 MATRIX FOR
07010C C   ALPHA < 60 DEGREES
07020C C
07030C C   THE PROGRAM DIVIDES INTO 6 PORTIONS,
07040C C   EACH PORTION THEN CHECKS FOR REVERSE CURRENT
07050C C
07060C C   IF REVERSE CURRENT, THAT LINE IS ZEROED IN D3
07070C C
07080C C   IF NOT, NOTHING CHANGES.
07090C C
07100C C   (NOTE: SHOULD THIS CHECK LAST TWO LINES?)
07110C C
07120C C*****
07130 550 IF(THETA.LT. ALPHA) GOTO 580
07140 IF(THETA.LT. PI/3.0 ) GOTO 555
07150 IF(THETA.LT. PI/3.0+ALPHA) GOTO 555
07160 IF(THETA.LT.2.0*PI/3.0 ) GOTO 560
07170 IF(THETA.LT.2.0*PI/3.0+ALPHA) GOTO 560
07180 IF(THETA.LT. PI ) GOTO 565
07190 IF(THETA.LT. PI +ALPHA) GOTO 565
07200 IF(THETA.LT.4.0*PI/3.0 ) GOTO 570
07210 IF(THETA.LT.4.0*PI/3.0+ALPHA) GOTO 570
07220 IF(THETA.LT.5.0*PI/3.0 ) GOTO 575
07230 IF(THETA.LT.5.0*PI/3.0+ALPHA) GOTO 575
07240 IF(THETA.LT.2.0*PI ) GOTO 580
07250C
07260 555 IF(X(1).LE.0.0) THEN
07270 DO 556 J=1,6
07280 D3(1,J) = 0.0
07290 556 CONTINUE
07300 ENDF
07310 GOTO 150
07320C
07330 560 IF(X(3).GE.0.0) THEN
07340 DO 561 J=1,6
07350 D3(6,J) = 0.0
07360 561 CONTINUE
07370 ENDF
07380 GOTO 150
07390C
07400 565 IF(X(2).LE.0.0) THEN
07410 DO 566 J=1,6
07420 D3(2,J) = 0.0
07430 566 CONTINUE
07440 ENDF
07450 GOTO 150
07460C
07470 570 IF(X(1).GE.0.0) THEN
07480 DO 571 J=1,6
07490 D3(4,J) = 0.0
07500 571 CONTINUE
07510 ENDF
07520 GOTO 150
07530C
07540 575 IF(X(3).LE.0.0) THEN
07550 DO 576 J=1,6
07560 D3(3,J) = 0.0
07570 576 CONTINUE
07580 ENDF
07590 GOTO 150
07600C
07610 580 IF(X(2).GE.0.0) THEN
07620 DO 581 J=1,6

```

```

J785U          L3(I,J) = 0.0
U784U  581  CONTINUE
U785U          ENOIF
U786U          GOTO 150
U7870C
U7880C  548  DO 549 I=1,6
U7890C          DO 549 J=1,6
U7900C          D3(I,J) = 0.0
U7910C  549  CONTINUE
U7920C          GOTO 150
U7930C
U7940C  C*****
U7950C  C  CONSTRUCTION OF THE D12 MATRIX
U7960C  C
U7970C          D12 = D1 * D2
U7980C          (TERM BY TERM)
U7990C  C*****
U8000  150  DO 151 I=1,6
U8010          DO 151 J=1,6
U8020          D12(I,J) = D1(I,J) * D2(I,J)
U8030  151  CONTINUE
U8040C
U8050C  C*****
U8060C  C  CONSTRUCTION OF THE D AND D3 MATRIXES
U8070C  C
U8080C          D = 1.0(ON) WHEN EITHER D12 = 1.0(ON)
U8090C          OR D3 = 1.0(ON)
U8100C  C
U8110C          IF D = 1.0(ON) THEN D3 = 1.0(ON)
U8120C          IF D = 0.0(OFF) THEN D3 LEFT ZERO
U8130C  C*****
U8140C  172  DO 169 I=1,6
U8150          DO 169 J=1,6
U8160          IF(D12(I,J).EQ.1.0.OR.D3(I,J).EQ.1.0) THEN
U8170          D(I,J)=1.0
U8180          D3(I,J)=1.0
U8190          ELSE
U8200          D(I,J)=0.0
U8210          END IF
U8220  169  CONTINUE
U8230C
U8240C  C*****
U8250C  C  TO CONSTRUCT THE MATRIX C
U8260C  C*****
U8270C  150  C(1,1) = D(1,1) - D(1,4) - D(4,1) + D(4,4)
U8280C          C(1,2) = D(2,1) - D(2,4) - D(4,1) + D(4,4)
U8290C          C(1,3) = D(3,1) - D(3,4) - D(6,1) + D(6,4)
U8300C          C(2,1) = D(1,2) - D(1,5) - D(4,2) + D(4,5)
U8310C          C(2,2) = D(2,2) - D(2,5) - D(5,2) + D(5,5)
U8320C          C(2,3) = D(3,2) - D(3,5) - D(6,2) + D(6,5)
U8330C          C(3,1) = D(1,3) - D(1,6) - D(4,3) + D(4,6)
U8340C          C(3,2) = D(2,3) - D(2,6) - D(5,3) + D(5,6)
U8350C          C(3,3) = D(3,3) - D(3,6) - D(6,3) + D(6,6)
U8360C  C*****
U8370C  C  TO CONSTRUCT THE C TRANSPOSED MATRIX
U8380C  C*****
U8390C  170  DO 171 I=1,3
U8400C          DO 171 J=1,3
U8410C          CT(I,J) = C(J,I)
U8420C  171  CONTINUE
U8430C  C*****
U8440C  C  CALCULATE THE MOTOR PHASE VOLTAGES FROM THE EQUATION VM = CT * VS
U8450C  C*****

```

```

08270 130 VA = CT(1,1) * VX + CT(1,2) * VY + CT(1,3) * VZ
08280 VB = CT(2,1) * VX + CT(2,2) * VY + CT(2,3) * VZ
08290 VC = CT(3,1) * VX + CT(3,2) * VY + CT(3,3) * VZ
08300C C*****
08310C C CALCULATE THE FIRST DERIVATIVES OF CURRENT
08320C C*****
08330 IF (SCR.EQ.35) GOTO 630
08340C C*****
08350C C 15 SCR CIRCUIT: FIRST DERIVATIVES OF CURRENT
08360C C
08370C C THE CIRCUIT IS IN A WYE CONFIGURATION.
08380C C
08390C C
08400C C
08410C C
08420C C
08430C C
08440C C
08450C C
08460C C*****
08470 IF(THETM.LT. PI/3.0) GOTO 631
08480 IF(THETM.LT.2.0*PI/3.0) GOTO 632
08490 IF(THETM.LT. PI ) GOTO 633
08500 IF(THETM.LT.4.0*PI/3.0) GOTO 634
08510 IF(THETM.LT.5.0*PI/3.0) GOTO 635
08520 GOTO 636
08530 631 IF(X(3).GT.0.0) GOTO 643
08540 X(3) = 0.0
08550C C F(1)=(VA-VB-2.0*X(1)*R)/(2.0*XL)
08560C C F(3)=-R*X(3)
08570C C F(2)=-(F(1)+F(3))
08580 F(1)=(VA-X(1)*R)/XL
08590 F(2)=(VB-X(2)*R)/XL
08600 F(3) = 0.0
08610 GOTO 637
08620 632 IF(X(2).LT.0.0) GOTO 643
08630 X(2) = 0.0
08640C C F(1)=(VA-VC-2.0*X(1)*R)/(2.0*XL)
08650C C F(2)=-R*X(2)
08660C C F(3)=-(F(1)+F(2))
08670 F(1)=(VA-X(1)*R)/XL
08680 F(2) = 0.0
08690 F(3)=(VC-X(3)*R)/XL
08700 GOTO 637
08710 633 IF(X(1).GT.0.0) GOTO 643
08720 X(1) = 0.0
08730C C F(1)=-R*X(1)
08740C C F(2)=(VB-VC-2.0*X(2)*R)/(2.0*XL)
08750C C F(3)=-(F(2)+F(1))
08760 F(1) = 0.0
08770 F(2)=(VB-X(2)*R)/XL
08780 F(3)=(VC-X(3)*R)/XL
08790 GOTO 637
08800 634 IF(X(3).LT.0.0) GOTO 643
08810 X(3) = 0.0
08820C C F(2)=(VB-VA-2.0*X(2)*R)/(2.0*XL)
08830C C F(3)=-R*X(3)
08840C C F(1)=-(F(2)+F(3))
08850 F(1)=(VA-X(1)*R)/XL
08860 F(2)=(VB-X(2)*R)/XL
08870 F(3) = 0.0
08880 GOTO 637
08890 635 IF(X(2).GT.0.0) GOTO 643
08900 X(2) = 0.0

```

```

08910C C F(3)=(VC-VA-2.0*X(3)*R)/(2.0*XL)
08920C C F(2)=-R*X(2)
08930C C F(1)=-F(3)+F(2)
08940 F(1)=(VA-X(1)*R)/XL
08950 F(2)= 0.0
08960 F(3)=(VC-X(3)*R)/XL
08970 GOTO 637
08980 636 IF(X(1).LT.0.0) GOTO 643
08990 X(1)= 0.0
09000C C F(1)=-R*X(1)
09010C C F(3)=(VC-VA-2.0*X(3)*R)/(2.0*XL)
09020C C F(2)=-F(3)+F(1)
09030 F(1)= 0.0
09040 F(2)=(VA-X(2)*R)/XL
09050 F(3)=(VC-X(3)*R)/XL
09060 GOTO 637
09070C C*****
09080C C 36 SCR CIRCUIT: FIRST DERIVATIVES OF CURRENT.
09090C C*****
09100 630 F(1) = VA / XL - R / XL * X(1)
09110 F(2) = VB / XL - R / XL * X(2)
09120 F(3) = VC / XL - R / XL * X(3)
09130 GOTO 637
09140C C638 VN=VB-X(2)*R-F(2)*XL
09150C C GOTO 643
09160C C639 VN=VA-X(1)*R-F(1)*XL
09170C C GOTO 643
09180C C641 VN=VC-X(3)*R-F(3)*XL
09190 643 F(3)=(VC-X(3)*R)/XL
09200 F(2)=(VA-X(2)*R)/XL
09210 F(1)=(VA-X(1)*R)/XL
09220 637 T1 = T * 1000.0
09230 CALL DERK(P, X, F, T, H, INDEX)
09240 IF(INDEX.EQ. 2) GOTO 02
09250C
09260C C*****
09270C C LOGIC FOR DECIDING WHEN TO WRITE
09280C C TO VOLTAGE OUTPUT FILE.
09290C C*****
09300 IF(T1.LT.TSTART) GOTO 195
09310 IF(TCOUNT.EQ.TTIME) GOTO 193
09320 TCOUNT = TCOUNT + 1
09330 GOTO 195
09340C
09350 193 THETMD=(180.0 * THETM) / PI
09360 WRITE(10,160) T1, THETMD, VA, VB, VC, VX, VY, VZ
09370 190 FORMAT(8(6),F10.4))
09374 WRITE(12,166) T1,THETMD,F(1),F(2),F(3)
09375 196 FORMAT(2(3),F10.4),3(3X,F13.4))
09380C
09390 TCOUNT=1
09400C *****
09410C * RETURNS TCOUNT TO 1
09420C *****
09430C C*****
09440C C LOGIC FOR TIMING OF MATRIX OUTPUT
09450C C*****
09460 195 IF(F1.EQ.0) GOTO 194
09470 IF(T1.LT.MSTART.OR.MSTOP.LT.T1) GOTO 194
09480 IF(MCOUNT.LT.MTIME) GOTO 192
09490 CALL MTRIX(01,02,012,03,0,T1,THETM)
09500 MCOUNT=1
09510 GOTO 194
09510 192 MCOUNT = MCOUNT + 1

```

```

09530C
09531C C*****
09532C C COMPUTE CURRENT DERIVATIVES AS
09533C C
09534C C CHANGE IN CURRENT / CHANGE IN TIME
09535C C*****
09540 194 F(1) = (X(1) - XX(1)) / H
09550 F(2) = (X(2) - XX(2)) / H
09560 F(3) = (X(3) - XX(3)) / H
09570 DO 199 KK=1,3
09580 XX(KK) = X(KK)
09590 199 CONTINUE
09591C
09592C C*****
09593C C CALCULATE SUPPLY CURRENTS.
09594C C*****
09600 XS(1) = C(1,1) * X(1) + C(1,2) * X(2) + C(1,3) * X(3)
09610 XS(2) = C(2,1) * X(1) + C(2,2) * X(2) + C(2,3) * X(3)
09620 XS(3) = C(3,1) * X(1) + C(3,2) * X(2) + C(3,3) * X(3)
09630C
09640C C*****
09650C C WILL ONLY WRITE TO FILE IF TCOUNT = 1.0
09660C C AND ALL TIMING PARAMETERS ARE MET,
09670C C WHICH OCCURS DURING THE SAME PASS THROUGH
09680C C THIS SECTION WHEN THE PROGRAM PRINTED
09690C C TO THE OUTPUT FILE VOLTS.
09700C C*****
09710 IF(T1.LT.TSTART) GOTO 113
09720 IF(TCOUNT.GT.1) GOTO 113
09730 WRITE(9,190) T1, THETMD, X(1), X(2), X(3), XS(1), XS(2), XS(3)
09740C
09750C
09760 113 IF(T1.LE.TSTOP) GOTO 01
09770 999 STOP
09780 END
09790 SUBROUTINE DERK(M, X, F, T, H, INDEX)
09800C C
09810C C DERK IS A FOURTH-ORDER, FIXED INCREMENT
09820C C RUNGE-KUTTA INTEGRATION ROUTINE.
09830C C
09840C C M - NUMBER OF SIMULTANEOUS DIFFERENTIAL EQUATIONS
09850C C X - ARRAY OF DEPENDENT VARIABLES
09860C C F - ARRAY OF DERIVATIVES OF INDEPENDENT VARIABLES
09870C C H - INCREMENT
09880C C T - TIME
09890C C INDEX - INDICATOR
09900C C
09910C C 1. IF EXIT WITH INDEX=1, SOLUTION FOUND AT T=T+H
09920C C 2. IF EXIT ROUTINE WITH INDEX=2, GO BACK TO RE-EVALUATE DERIVATES
09930C C
09940 DIMENSION X(6), F(6), O(400)
09950 IF (INDEX.EQ. 2) GOTO 19
09960 18 KXX = 0
09970 INDEX = 2
09980 DO 35 I=1,M
09990 J = I + 300
10000 35 O(J) = X(I)
10010 19 KXX = KXX + 1
10020 GOTO (1, 2, 3, 4), KXX
10030 1 00 3 I=1,M
10040 O(I) = F(I) * H
10050 3 X(I) = X(I) + O(I) / 2.00
10060 T = T + H / 2.00
10070 RETURN

```

```

1008C      2 DO 6 I=1,M
10090      J = I + 10C
10100      K = I + 30C
10110      Q(J) = F(I) * H
10120      6 X(I) = Q(K) + Q(J) / 2.00
10130      RETURN
10140      3 DO 7 I=1,P
10150      J = I + 20C
10160      K = I + 30C
10170      Q(J) = F(I) * H
10180      7 X(I) = Q(K) + Q(J)
10190      T = T + H / 2.00
10200      RETURN
10210      4 DO 8 I=1,P
10220      J = I + 10C
10230      K = I + 20C
10240      L = I + 30C
10250      8 X(I) = Q(L) + ((Q(I) + 2.00*Q(J) + 2.00*Q(K) + F(I)*H) / 6.00)
10260      INDEX = 1
10270      RETURN
10280      END
10290      SUBROUTINE MATRIX(D1,D2,D12,D3,D,T1,THETM)
10300      DIMENSION D1(6,6),D2(6,6),D12(6,6),D3(6,6),D(6,6)
10310      INTEGER N1(6,6),N2(6,6),N12(6,6),N3(6,6),N(6,6)
10320      DO 20 I=1,6
10330      DO 20 J=1,6
10340      N1(I,J)=D1(I,J)
10350      N2(I,J)=D2(I,J)
10360      N12(I,J)=D12(I,J)
10370      N3(I,J)=D3(I,J)
10380      N(I,J)=D(I,J)
10390      20 CONTINUE
10400      WRITE(11,11)T1,THETM*57.2958
10410      11 FORMAT(1X,2(2X,F10.4))
10420      DO 10 I=1,6
10430      WRITE(11,15)N1(I,1),N1(I,2),N1(I,3),N1(I,4),N1(I,5),N1(I,6),
10440+      N2(I,1),N2(I,2),N2(I,3),N2(I,4),N2(I,5),N2(I,6),
10450+      N12(I,1),N12(I,2),N12(I,3),N12(I,4),N12(I,5),N12(I,6),
10460+      N3(I,1),N3(I,2),N3(I,3),N3(I,4),N3(I,5),N3(I,6),
10470+      N(I,1),N(I,2),N(I,3),N(I,4),N(I,5),N(I,6)
10480      15 FORMAT(1X,5(1X,6(I3),1X))
10490      10 CONTINUE
10500      RETURN
10510      END

```

APPENDIX D

RUN OF SOME CASES ON THE PROGRAM

APPENDIX D1

CASE 1(a)

THE OUTPUT REPRESENTS THE SIMULATION FOR
36-SCRs , CONDUCTION ANGLE = 100° , $f_s / f_r = 2$

THE OUTPUT COLUMNS ARE AS FOLLOWS :

TIME(m s), MOTOR ANGLE (Degrees), MOTOR PHASE
CURRENTS X1,X2,X3 (In Amperes).

SCR = 36	ALPH = 100.0	RPM = 10000.0	RPMG = 20000.0	
.0500	6.0000	98.5414	-48.6434	.0000
.1000	12.0000	74.1415	-74.1415	.0000
.1500	18.0000	87.5615	-87.5615	.0000
.2000	24.0000	92.6637	-92.6637	.0000
.2500	30.0000	91.5795	-91.5795	.0000
.3000	36.0000	91.6106	-91.6106	.0000
.3500	42.0000	94.8696	-94.8696	.0000
.4000	48.0000	97.4230	-97.4230	.0000
.4500	54.0000	97.3554	-97.3554	.0000
.5000	60.0000	93.8116	-93.8116	-.2143
.5500	66.0000	92.6725	-86.5382	-48.1433
.6000	72.0000	95.3748	-75.6390	-74.1912
.6500	78.0000	97.6633	-61.5570	-87.5846
.7000	84.0000	97.4697	-44.8046	-92.6747
.7500	90.0000	93.8660	-26.1129	-91.5847
.8000	96.0000	92.6984	-6.2890	-91.6131
.8500	102.0000	95.3872	.0520	-94.8708
.9000	108.0000	97.6692	.0248	-97.4236
.9500	114.0000	97.4725	.0118	-97.3556
1.0000	120.0000	93.8673	.2199	-93.8117
1.0500	126.0000	86.5647	48.1460	-92.6725
1.1000	132.0000	75.6716	74.1912	-95.3749
1.1500	138.0000	61.5630	87.5852	-97.6634
1.2000	144.0000	44.8074	92.6750	-97.4697
1.2500	150.0000	26.1143	91.5849	-93.8660
1.3000	156.0000	6.2897	91.6131	-92.6984
1.3500	162.0000	-.0517	94.8708	-95.3872
1.4000	168.0000	-.0246	97.4236	-97.6692
1.4500	174.0000	-.0117	97.3556	-97.4725
1.5000	180.0000	-.2199	93.8117	-93.8673
1.5500	186.0000	-48.1460	92.6725	-86.5347
1.6000	192.0000	-74.1912	95.3749	-75.6716
1.6500	198.0000	-87.5852	97.6634	-61.5630
1.7000	204.0000	-92.6750	97.4697	-44.8074
1.7500	210.0000	-91.5849	93.8660	-26.1143
1.8000	216.0000	-91.6131	92.6984	-6.2897
1.8500	222.0000	-94.8708	95.3872	.0517
1.9000	228.0000	-97.4236	97.6692	.0246
1.9500	234.0000	-97.3556	97.4725	-.0117
2.0000	240.0000	-93.8117	93.8673	-.2199
2.0500	246.0000	-92.6725	86.5647	48.1460
2.1000	252.0000	-95.3749	75.6716	74.1912
2.1500	258.0000	-97.6634	61.5630	87.5852
2.2000	264.0000	-97.4697	44.8074	92.6750
2.2500	270.0000	-93.8660	26.1143	91.5849
2.3000	276.0000	-92.6984	6.2897	91.6131
2.3500	282.0000	-95.3872	-.0517	94.8708
2.4000	288.0000	-97.6692	-.0246	97.4236
2.4500	294.0000	-97.4725	-.0117	97.3556
2.5000	300.0000	-93.8673	-.2199	93.8117
2.5500	306.0000	-86.5647	-48.1460	92.6725
2.6000	312.0000	-75.6716	-74.1912	95.3749
2.6500	318.0000	-61.5630	-87.5852	97.6634
2.7000	324.0000	-44.8074	-92.6750	97.4697
2.7500	330.0000	-26.1143	-91.5849	93.8660
2.8000	336.0000	-6.2897	-91.6131	92.6984
2.8500	342.0000	.0517	-94.8708	95.3872
2.9000	348.0000	.0246	-97.4236	97.6692
2.9500	354.0000	.0117	-97.3556	97.4725
3.0000	.0000	-.2199	-93.8117	93.8673
3.0500	6.0000	48.1460	-92.6725	86.5347
3.1000	12.0000	74.1912	-95.3749	75.6716

3.2000	24.0000	92.6750	-97.4697	44.8074
3.2500	30.0000	91.5849	-93.5620	26.1143
3.3000	36.0000	91.6131	-92.6984	6.2697
3.3500	42.0000	94.8708	-95.3872	-0.0517
3.4000	48.0000	97.4235	-97.6692	-0.0246
3.4500	54.0000	97.3556	-97.4725	-0.0117
3.5000	60.0000	93.8117	-93.8673	-0.2199
3.5500	66.0000	92.6725	-86.5647	-48.1460
3.6000	72.0000	95.3749	-75.6716	-74.1912
3.6500	78.0000	97.6634	-61.5630	-87.5390
3.7000	84.0000	97.4697	-44.8074	-92.6750
3.7500	90.0000	93.8660	-26.1143	-91.5849
3.8000	96.0000	92.6984	-6.2897	-91.6131
3.8500	102.0000	95.3872	.0517	-94.8708
3.9000	108.0000	97.6692	.0246	-97.4236
3.9500	114.0000	97.4725	.0117	-97.3556
4.0000	120.0000	93.8673	.2199	-93.8117
4.0500	126.0000	86.5647	48.1460	-92.6725
4.1000	132.0000	75.6716	74.1912	-65.3749
4.1500	138.0000	61.5630	87.5852	-97.6634
4.2000	144.0000	44.8074	92.6750	-97.4697
4.2500	150.0000	26.1143	91.5849	-93.8660
4.3000	156.0000	6.2897	91.6131	-92.6984
4.3500	162.0000	-.0517	94.8708	-95.3872
4.4000	168.0000	-.0246	97.4236	-97.6692
4.4500	174.0000	-.0117	97.3556	-97.4725
4.5000	180.0000	-.0056	93.8117	-93.8673
4.5500	186.0000	-47.9421	92.6725	-86.5647
4.6000	192.0000	-74.0942	95.3749	-75.6716
4.6500	198.0000	-87.5390	97.6634	-61.5630
4.7000	204.0000	-92.6530	97.4697	-44.8074
4.7500	210.0000	-91.5744	93.8660	-26.1143
4.8000	216.0000	-91.6082	92.6984	-6.2897
4.8500	222.0000	-94.8685	95.3872	.0517
4.9000	228.0000	-97.4224	97.6692	.0246
4.9500	234.0000	-97.3551	97.4725	.0117
5.0000	240.0000	-93.8114	93.8673	.0056
5.0500	246.0000	-92.6724	86.5647	47.9421
5.1000	252.0000	-95.3748	75.6716	74.0942
5.1500	258.0000	-97.6633	61.5630	87.5390
5.2000	264.0000	-97.4697	44.8074	92.6750
5.2500	270.0000	-93.8660	26.1143	91.5744
5.3000	276.0000	-92.6984	6.2897	91.6082
5.3500	282.0000	-95.3872	-.0517	94.8685
5.4000	288.0000	-97.6692	-.0246	97.4224
5.4500	294.0000	-97.4725	-.0117	97.3551
5.5000	300.0000	-93.8673	-.0056	93.8114
5.5500	306.0000	-86.5647	-47.9421	92.6724
5.6000	312.0000	-75.6716	-74.0942	95.3748
5.6500	318.0000	-61.5630	-87.5390	97.6633
5.7000	324.0000	-44.8074	-92.6530	97.4697
5.7500	330.0000	-26.1143	-91.5744	93.8660
5.8000	336.0000	-6.2897	-91.6082	92.6984
5.8500	342.0000	.0517	-94.8685	95.3872
5.9000	348.0000	.0246	-97.4224	97.6692
5.9500	354.0000	.0117	-97.3551	97.4725
6.0000	360.0000	.0056	-93.8114	95.8673

CASE 1(b)

THE OUTPUT REPRESENTS THE SIMULATION FOR
36-SCRs , CONDUCTION ANGLE = 100°, $f / f = 2$.

THE OUTPUT COLUMNS ARE AS FOLLOWS :
TIME (m s), MOTOR ANGLE (Degrees), MOTOR PHASE
VOLTAGES VA,VB,VC (Volts).

CP # 36	ALPH = 100.0	APR = 1000000		
.3500	6.0000	247.0917	-247.0917	.0000
.4000	12.0000	258.3844	-258.3844	.0000
.4500	18.0000	258.3844	-258.3844	.0000
.5000	24.0000	247.0917	-247.0917	.0000
.5500	30.0000	225.0000	-225.0000	.0000
.6000	36.0000	247.0917	-247.0917	.0000
.6500	42.0000	258.3844	-258.3844	.0000
.7000	48.0000	258.3844	-258.3844	.0000
.7500	54.0000	247.0917	-247.0917	.0000
.8000	60.0000	225.0000	-225.0000	-225.0000
.8500	66.0000	247.0917	-193.0747	-247.0917
.9000	72.0000	258.3844	-152.7111	-258.3844
.9500	78.0000	258.3844	-105.6733	-258.3844
1.0000	84.0000	247.0917	-54.0170	-247.0917
1.0500	90.0000	225.0000	.0000	-225.0000
1.1000	96.0000	247.0917	54.0170	-247.0917
1.1500	102.0000	258.3844	.0000	-258.3844
1.2000	108.0000	258.3844	.0000	-258.3844
1.2500	114.0000	247.0917	.0000	-247.0917
1.3000	120.0000	225.0000	225.0000	-225.0000
1.3500	126.0000	193.0747	247.0917	-247.0917
1.4000	132.0000	152.7111	258.3844	-258.3844
1.4500	138.0000	105.6733	258.3844	-258.3844
1.5000	144.0000	54.0170	247.0917	-247.0917
1.5500	150.0000	.0000	225.0000	-225.0000
1.6000	156.0000	-54.0170	247.0917	-247.0917
1.6500	162.0000	.0000	258.3844	-258.3844
1.7000	168.0000	.0000	258.3844	-258.3844
1.7500	174.0000	.0000	247.0917	-247.0917
1.8000	180.0000	-225.0000	225.0000	-225.0000
1.8500	186.0000	-247.0917	247.0917	-193.0747
1.9000	192.0000	-258.3844	258.3844	-152.7111
1.9500	198.0000	-258.3844	258.3844	-105.6733
2.0000	204.0000	-247.0917	247.0917	-54.0170
2.0500	210.0000	-225.0000	225.0000	.0000
2.1000	216.0000	-247.0917	247.0917	54.0170
2.1500	222.0000	-258.3844	.0000	.0000
2.2000	228.0000	-258.3844	258.3844	.0000
2.2500	234.0000	-247.0917	247.0917	.0000
2.3000	240.0000	-225.0000	225.0000	225.0000
2.3500	246.0000	-247.0917	193.0747	247.0917
2.4000	252.0000	-258.3844	152.7111	258.3844
2.4500	258.0000	-258.3844	105.6733	258.3844
2.5000	264.0000	-247.0917	54.0170	247.0917
2.5500	270.0000	-225.0000	.0000	225.0000
2.6000	276.0000	-247.0917	-54.0170	247.0917
2.6500	282.0000	-258.3844	.0000	258.3844
2.7000	288.0000	-258.3844	.0000	258.3844
2.7500	294.0000	-247.0917	.0000	247.0917
2.8000	300.0000	-225.0000	-225.0000	225.0000
2.8500	306.0000	-193.0747	-247.0917	247.0917
2.9000	312.0000	-152.7111	-258.3844	258.3844
2.9500	318.0000	-105.6733	-258.3844	258.3844
3.0000	324.0000	-54.0170	-247.0917	247.0917
3.0500	330.0000	.0000	-225.0000	225.0000
3.1000	336.0000	54.0170	-247.0917	247.0917
3.1500	342.0000	.0000	-258.3844	258.3844
3.2000	348.0000	.0000	-258.3844	258.3844
3.2500	354.0000	.0000	-247.0917	247.0917
3.3000	.0000	225.0000	-225.0000	225.0000
3.3500	6.0000	247.0917	-247.0917	193.0747
3.4000	12.0000	258.3844	-258.3844	152.7111
3.4500		258.3844	-258.3844	105.6733

3.2000	24.0000	247.0917	-247.0917	54.0170
3.2500	30.0000	225.0000	-225.0000	.0000
3.3000	36.0000	247.0917	-247.0917	-54.0170
3.3500	42.0000	258.3844	-258.3844	.0000
3.4000	48.0000	258.3844	-258.3844	.0000
3.4500	54.0000	247.0917	-247.0917	.0000
3.5000	60.0000	225.0000	-225.0000	-225.0000
3.5500	66.0000	247.0917	-193.0747	-247.0917
3.6000	72.0000	258.3844	-152.7111	-258.3844
3.6500	78.0000	258.3844	-105.6733	-258.3844
3.7000	84.0000	247.0917	-54.0170	-247.0917
3.7500	90.0000	225.0000	.0000	-225.0000
3.8000	96.0000	247.0917	54.0170	-247.0917
3.8500	102.0000	258.3844	.0000	-258.3844
3.9000	108.0000	258.3844	.0000	-258.3844
3.9500	114.0000	247.0917	.0000	-247.0917
4.0000	120.0000	225.0000	225.0000	-225.0000
4.0500	126.0000	193.0747	247.0917	-247.0917
4.1000	132.0000	152.7111	258.3844	-258.3844
4.1500	138.0000	105.6733	258.3844	-258.3844
4.2000	144.0000	54.0170	247.0917	-247.0917
4.2500	150.0000	.0000	225.0000	-225.0000
4.3000	156.0000	-54.0170	247.0917	-247.0917
4.3500	162.0000	.0000	258.3844	-258.3844
4.4000	168.0000	.0000	258.3844	-258.3844
4.4500	174.0000	.0000	247.0917	-247.0917
4.5000	180.0000	.0000	225.0000	-225.0000
4.5500	186.0000	-247.0917	247.0917	-193.0747
4.6000	192.0000	-258.3844	258.3844	-152.7111
4.6500	198.0000	-258.3844	258.3844	-105.6733
4.7000	204.0000	-247.0917	247.0917	-54.0170
4.7500	210.0000	-225.0000	225.0000	.0000
4.8000	216.0000	-247.0917	247.0917	54.0170
4.8500	222.0000	-258.3844	258.3844	.0000
4.9000	228.0000	-258.3844	258.3844	.0000
4.9500	234.0000	-247.0917	247.0917	.0000
5.0000	240.0000	-225.0000	225.0000	.0000
5.0500	246.0000	-247.0917	193.0747	247.0917
5.1000	252.0000	-258.3844	152.7111	258.3844
5.1500	258.0000	-258.3844	105.6733	258.3844
5.2000	264.0000	-247.0917	54.0170	247.0917
5.2500	270.0000	-225.0000	.0000	225.0000
5.3000	276.0000	-247.0917	-54.0170	247.0917
5.3500	282.0000	-258.3844	.0000	258.3844
5.4000	288.0000	-258.3844	.0000	258.3844
5.4500	294.0000	-247.0917	.0000	247.0917
5.5000	300.0000	-225.0000	.0000	225.0000
5.5500	306.0000	-193.0747	-247.0917	247.0917
5.6000	312.0000	-152.7111	-258.3844	258.3844
5.6500	318.0000	-105.6733	-258.3844	258.3844
5.7000	324.0000	-54.0170	-247.0917	247.0917
5.7500	330.0000	.0000	-225.0000	225.0000
5.8000	336.0000	54.0170	-247.0917	247.0917
5.8500	342.0000	.0000	-258.3844	258.3844
5.9000	348.0000	.0000	-258.3844	258.3844
5.9500	354.0000	.0000	-247.0917	247.0917
6.0000	360.0000	.0000	-225.0000	225.0000

CASE 1(c)

HIGH-SPEED DIGITAL PRINTER PLOTS FOR

VA, VB, VC : MOTOR PHASE VOLTAGES

X1, X2, X3 : MOTOR PHASE CURRENTS

VX, VY, VZ : SUPPLY PHASE VOLTAGES **

** VX, VY, VZ ARE THE SAME FOR ALL $f_s / f_r = 2$, AND
THE PEAK PHASE VOLTAGE IS GIVEN TO BE 150 VOLTS.

PLOT OF VA

	-25	-15	-5	5	15	25	Y(1, J)
C	I	I	I	I	I	A I	.22463E+02
	I	I	I	I	I	A I	.23489E+02
	I	I	I	I	I	A I	.23489E+02
	I	I	I	I	I	A I	.22463E+02
	I	I	I	I	I	A I	.20455E+02
	I	I	I	I	I	A I	.22463E+02
	I	I	I	I	I	A I	.23489E+02
	I	I	I	I	I	A I	.23489E+02
	I	I	I	I	I	A I	.22463E+02
10	I	I	I	I	I	A I	.20455E+02
	I	I	I	I	I	A I	.22463E+02
	I	I	I	I	I	A I	.23489E+02
	I	I	I	I	I	A I	.23489E+02
	I	I	I	I	I	A I	.22463E+02
	I	I	I	I	I	A I	.20455E+02
	I	I	I	I	I	A I	.22463E+02
	I	I	I	I	I	A I	.23489E+02
	I	I	I	I	I	A I	.23489E+02
	I	I	I	I	I	A I	.22463E+02
20	I	I	I	I	I A	I	.20455E+02
	I	I	I	I	A I	I	.17532E+02
	I	I	I	I	A	I	.13883E+02
	I	I	I	A	I	I	.96667E+01
	I	I	I	A	I	I	.49106E+01
	I	I	I	A	I	I	.00000E+00
	I	I	I	A	I	I	-.49106E+01
	I	I	I	A	I	I	.00000E+00
	I	I	I	A	I	I	.00000E+00
	I	I	I	A	I	I	.00000E+00
30	I A	I	I	I	I	I	-.20455E+02
	I A	I	I	I	I	I	-.22463E+02
	I A	I	I	I	I	I	-.23489E+02
	I A	I	I	I	I	I	-.23489E+02
	I A	I	I	I	I	I	-.22463E+02
	I A	I	I	I	I	I	-.20455E+02
	I A	I	I	I	I	I	-.22463E+02
	I A	I	I	I	I	I	-.23489E+02
	I A	I	I	I	I	I	-.23489E+02
	I A	I	I	I	I	I	-.22463E+02
40	I A	I	I	I	I	I	-.20455E+02
	I A	I	I	I	I	I	-.22463E+02
	I A	I	I	I	I	I	-.23489E+02
	I A	I	I	I	I	I	-.23489E+02
	I A	I	I	I	I	I	-.22463E+02
	I A	I	I	I	I	I	-.20455E+02
	I A	I	I	I	I	I	-.22463E+02
	I A	I	I	I	I	I	-.23489E+02
	I A	I	I	I	I	I	-.23489E+02
	I A	I	I	I	I	I	-.22463E+02
50	I A	I	I	I	I	I	-.20455E+02
	I A	I	I	I	I	I	-.22463E+02
	I A	I	I	I	I	I	-.23489E+02
	I A	I	I	I	I	I	-.23489E+02
	I A	I	I	I	I	I	-.22463E+02
	I A	I	I	I	I	I	-.20455E+02
	I A	I	I	I	I	I	-.22463E+02
	I A	I	I	I	I	I	-.23489E+02
	I A	I	I	I	I	I	-.23489E+02
	I A	I	I	I	I	I	-.22463E+02
60	I A	I	I	I	I	I	-.20455E+02
	I A	I	I	I	I	I	-.17532E+02
	I A	I	I	I	I	I	-.13883E+02
	I A	I	I	I	I	I	-.96667E+01
	I A	I	I	I	I	I	-.49106E+01
	I A	I	I	I	I	I	.00000E+00
	I A	I	I	I	I	I	.49106E+01
	I A	I	I	I	I	I	.00000E+00
	I A	I	I	I	I	I	.00000E+00

	-25	-15	-5	5	15	25	
60							.20455E+02
							Y(1,1)
C							
I		I	I	I	I	A I	.22463E+02
I		I	I	I	I	A I	.23489E+02
I		I	I	I	I	A I	.23489E+02
I		I	I	I	I	A I	.22463E+02
I		I	I	I	I	A I	.20455E+02
I		I	I	I	I	A I	.22463E+02
I		I	I	I	I	A I	.23489E+02
I		I	I	I	I	A I	.23489E+02
I		I	I	I	I	A I	.22463E+02
I		I	I	I	I	A I	.20455E+02
10							
I		I	I	I	I	A I	.22463E+02
I		I	I	I	I	A I	.23489E+02
I		I	I	I	I	A I	.23489E+02
I		I	I	I	I	A I	.22463E+02
I		I	I	I	I	A I	.20455E+02
I		I	I	I	I	A I	.22463E+02
I		I	I	I	I	A I	.23489E+02
I		I	I	I	I	A I	.23489E+02
I		I	I	I	I	A I	.22463E+02
I		I	I	I	I	A I	.20455E+02
20							
I		I	I	I	I A	A I	.17552E+02
I		I	I	I	A I	I	.13883E+02
I		I	I	I	A I	I	.96667E+01
I		I	I	A I	I	I	.49106E+01
I		I	I	A I	I	I	.00000E+00
I		I	A I	I	I	I	-.49106E+01
I		I	A I	I	I	I	.00000E+00
I		I	A I	I	I	I	.00000E+00
I		I	A I	I	I	I	.00000E+00
I		I	A I	I	I	I	.00000E+00
30							
I	A	I	I	I	I	I	-.22463E+02
I	A	I	I	I	I	I	-.23489E+02
I	A	I	I	I	I	I	-.23489E+02
I	A	I	I	I	I	I	-.22463E+02
I	A	I	I	I	I	I	-.20455E+02
I	A	I	I	I	I	I	-.22463E+02
I	A	I	I	I	I	I	-.23489E+02
I	A	I	I	I	I	I	-.23489E+02
I	A	I	I	I	I	I	-.22463E+02
I	A	I	I	I	I	I	-.20455E+02
40							
I	A	I	I	I	I	I	-.22463E+02
I	A	I	I	I	I	I	-.23489E+02
I	A	I	I	I	I	I	-.23489E+02
I	A	I	I	I	I	I	-.22463E+02
I	A	I	I	I	I	I	-.20455E+02
I	A	I	I	I	I	I	-.22463E+02
I	A	I	I	I	I	I	-.23489E+02
I	A	I	I	I	I	I	-.23489E+02
I	A	I	I	I	I	I	-.22463E+02
I	A	I	I	I	I	I	-.20455E+02
50							
I	A	I	I	I	I	I	-.17552E+02
I	I A	I	I	I	I	I	-.13883E+02
I	I	A	I	I	I	I	-.96667E+01
I	I	I	A I	I	I	I	-.49106E+01
I	I	I	I A	I	I	I	.00000E+00
I	I	I	I	A I	I	I	.49106E+01
I	I	I	I	A I	I	I	.00000E+00
I	I	I	I	A I	I	I	.00000E+00
I	I	I	I	A I	I	I	.00000E+00
I	I	I	I	A I	I	I	.00000E+00

PLOT OF V8

	-25	-15	-5	5	15	25	Y(1, I)
0+	I	I	I	I	I	I	-.22463E+02
	I A	I	I	I	I	I	-.23489E+02
	I A	I	I	I	I	I	-.23489E+02
	I A	I	I	I	I	I	-.22463E+02
	I A A	I	I	I	I	I	-.20455E+02
	I A	I	I	I	I	I	-.22463E+02
	I A	I	I	I	I	I	-.23489E+02
	I A	I	I	I	I	I	-.23489E+02
	I A	I	I	I	I	I	-.22463E+02
10+	I	I	I	I	I	I	-.20455E+02
	I A	I	I	I	I	I	-.17552E+02
	I	I A	I	I	I	I	-.13883E+02
	I	I	I A	I	I	I	-.9667E+01
	I	I	I	I A	I	I	-.49106E+01
	I	I	I	I	I	I	.00000E+00
	I	I	I	I	I A	I	.49106E+01
	I	I	I	I	I	I	.00000E+00
	I	I	I	I	I	I	.00000E+00
	I	I	I	I	I	I	.00000E+00
20+	I	I	I	I	I	I	.20455E+02
	I	I	I	I	I	I A	.22463E+02
	I	I	I	I	I	I A	.23489E+02
	I	I	I	I	I	I A	.23489E+02
	I	I	I	I	I	I A	.22463E+02
	I	I	I	I	I	I A	.20455E+02
	I	I	I	I	I	I A	.22463E+02
	I	I	I	I	I	I A	.23489E+02
	I	I	I	I	I	I A	.23489E+02
	I	I	I	I	I	I A	.22463E+02
30+	I	I	I	I	I	I	.20455E+02
	I	I	I	I	I	I A	.22463E+02
	I	I	I	I	I	I A	.23489E+02
	I	I	I	I	I	I A	.23489E+02
	I	I	I	I	I	I A	.22463E+02
	I	I	I	I	I	I A	.20455E+02
	I	I	I	I	I	I A	.22463E+02
	I	I	I	I	I	I A	.23489E+02
	I	I	I	I	I	I A	.23489E+02
	I	I	I	I	I	I A	.22463E+02
40+	I	I	I	I	I	I	.20455E+02
	I	I	I	I	I A	I	-.17552E+02
	I	I	I	I	I	I	-.13883E+02
	I	I	I	I	I	I	-.9667E+01
	I	I	I	I A	I	I	-.49106E+01
	I	I	I	I	I	I	.00000E+00
	I	I	I	I	I	I	-.49106E+01
	I	I	I	I	I	I	.00000E+00
	I	I	I	I	I	I	.00000E+00
	I	I	I	I	I	I	.00000E+00
50+	I	I	I	I	I	I	-.20455E+02
	I A	I	I	I	I	I	-.22463E+02
	I A	I	I	I	I	I	-.23489E+02
	I A	I	I	I	I	I	-.23489E+02
	I A	I	I	I	I	I	-.22463E+02
	I A	I	I	I	I	I	-.20455E+02
	I A	I	I	I	I	I	-.22463E+02
	I A	I	I	I	I	I	-.23489E+02
	I A	I	I	I	I	I	-.23489E+02

PLOT OF VC

	-25	-15	-5	5	15	25	Y(I,I)
C+	I	I	I	A	I	I	.00000E+00
	I	I	I	A	I	I	.00000E+00
	I	I	I	A	I	I	.00000E+00
	I	I	I	A	I	I	.00000E+00
	I	I	I	A	I	I	.00000E+00
	I	I	I	A	I	I	.00000E+00
	I	I	I	A	I	I	.00000E+00
	I	I	I	A	I	I	.00000E+00
10+	I	A	I	I	I	I	-.20455E+02
	I	A	I	I	I	I	-.22463E+02
	I	A	I	I	I	I	-.23489E+02
	I	A	I	I	I	I	-.23469E+02
	I	A	I	I	I	I	-.22463E+02
	I	A	I	I	I	I	-.20455E+02
	I	A	I	I	I	I	-.22463E+02
	I	A	I	I	I	I	-.23489E+02
	I	A	I	I	I	I	-.23489E+02
	I	A	I	I	I	I	-.22463E+02
20+	I	A	I	I	I	I	-.20455E+02
	I	A	I	I	I	I	-.22463E+02
	I	A	I	I	I	I	-.23489E+02
	I	A	I	I	I	I	-.23489E+02
	I	A	I	I	I	I	-.22463E+02
	I	A	I	I	I	I	-.20455E+02
	I	A	I	I	I	I	-.22463E+02
	I	A	I	I	I	I	-.23489E+02
	I	A	I	I	I	I	-.23489E+02
	I	A	I	I	I	I	-.22463E+02
30+	I	A	I	I	I	I	-.20455E+02
	I	A	I	I	I	I	-.17552E+02
	I	A	I	I	I	I	-.13883E+02
	I	A	I	I	I	I	-.96067E+01
	I	A	I	I	I	I	-.49106E+01
	I	A	I	A	I	I	.00000E+00
	I	A	I	A	I	I	.49106E+01
	I	A	I	A	I	I	.00000E+00
	I	A	I	A	I	I	.00000E+00
	I	A	I	A	I	I	.00000E+00
40+	I	A	I	I	I	A	.20455E+02
	I	A	I	I	I	A	.22463E+02
	I	A	I	I	I	A	.23489E+02
	I	A	I	I	I	A	.23489E+02
	I	A	I	I	I	A	.22463E+02
	I	A	I	I	I	A	.20455E+02
	I	A	I	I	I	A	.22463E+02
	I	A	I	I	I	A	.23489E+02
	I	A	I	I	I	A	.23489E+02
	I	A	I	I	I	A	.22463E+02
50+	I	A	I	I	I	A	.20455E+02
	I	A	I	I	I	A	.22463E+02
	I	A	I	I	I	A	.23489E+02
	I	A	I	I	I	A	.23489E+02
	I	A	I	I	I	A	.22463E+02
	I	A	I	I	I	A	.20455E+02
	I	A	I	I	I	A	.22463E+02
	I	A	I	I	I	A	.23489E+02
	I	A	I	I	I	A	.23489E+02

I	I	I	I	I	A	I	.22463E+02
60	-25	-15	-5	5	15	25	.20455E+02
0							Y(1,1)
I	I	I	I	I	A	I	.17552E+02
I	I	I	I	I	AI	I	.13883E+02
I	I	I	I	A	I	I	.96667E+01
I	I	I	A	I	I	I	.49106E+01
I	I	I	A	I	I	I	.00000E+00
I	I	A	I	I	I	I	-.49106E+01
I	I	I	A	I	I	I	.00000E+00
I	I	I	A	I	I	I	.00000E+00
I	I	I	A	I	I	I	.00000E+00
10	A						-.20455E+02
I	A	I	I	I	I	I	-.22463E+02
I	A	I	I	I	I	I	-.23489E+02
I	A	I	I	I	I	I	-.23489E+02
I	A	I	I	I	I	I	-.22463E+02
I	A	I	I	I	I	I	-.20455E+02
I	A	I	I	I	I	I	-.22463E+02
I	A	I	I	I	I	I	-.23489E+02
I	A	I	I	I	I	I	-.23489E+02
I	A	I	I	I	I	I	-.22463E+02
20	A						-.20455E+02
I	A	I	I	I	I	I	-.22463E+02
I	A	I	I	I	I	I	-.23489E+02
I	A	I	I	I	I	I	-.23489E+02
I	A	I	I	I	I	I	-.22463E+02
I	A	I	I	I	I	I	-.20455E+02
I	A	I	I	I	I	I	-.22463E+02
I	A	I	I	I	I	I	-.23489E+02
I	A	I	I	I	I	I	-.23489E+02
I	A	I	I	I	I	I	-.22463E+02
30	A						-.20455E+02
I	A	I	I	I	I	I	-.17552E+02
I	IA	I	I	I	I	I	-.13883E+02
I	I	A	I	I	I	I	-.96667E+01
I	I	A	I	I	I	I	-.49106E+01
I	I	I	A	I	I	I	.00000E+00
I	I	I	A	I	I	I	.49106E+01
I	I	I	A	I	I	I	.00000E+00
I	I	I	A	I	I	I	.00000E+00
I	I	I	A	I	I	I	.00000E+00
40			A				.00000E+00
I	I	I	I	I	A	I	.22463E+02
I	I	I	I	I	A	I	.23489E+02
I	I	I	I	I	A	I	.23489E+02
I	I	I	I	I	A	I	.22463E+02
I	I	I	I	I	A	I	.20455E+02
I	I	I	I	I	A	I	.22463E+02
I	I	I	I	I	A	I	.23489E+02
I	I	I	I	I	A	I	.23489E+02
I	I	I	I	I	A	I	.22463E+02
50					A		.20455E+02
I	I	I	I	I	A	I	.22463E+02
I	I	I	I	I	A	I	.23489E+02
I	I	I	I	I	A	I	.23489E+02
I	I	I	I	I	A	I	.22463E+02
I	I	I	I	I	A	I	.20455E+02
I	I	I	I	I	A	I	.22463E+02
I	I	I	I	I	A	I	.23489E+02
I	I	I	I	I	A	I	.23489E+02
I	I	I	I	I	A	I	.22463E+02

FLOT OF VZ

	-25	-15	-5	5	15	25	Y(1,I)
0	I	I	I	AI	I	I	.42139E+01
	I	I	I	A	I	I	.14254E+01
	I	I	I	I	I	I	-.14254E+01
	I	I	IA	I	I	I	-.42139E+01
	I	I	A	I	I	I	-.68182E+01
	I	I	A	I	I	I	-.91245E+01
	I	I	A	I	I	I	-.11632E+02
	I	I	A	I	I	I	-.12457E+02
	I	I	A	I	I	I	-.13338E+02
10	I	I	I	I	I	I	-.13338E+02
	I	I	A	I	I	I	-.12457E+02
	I	I	A	I	I	I	-.11632E+02
	I	I	A	I	I	I	-.91245E+01
	I	I	A	I	I	I	-.68182E+01
	I	I	IA	I	I	I	-.42139E+01
	I	I	I	A	I	I	-.14254E+01
	I	I	I	I	I	I	.14254E+01
	I	I	I	AI	I	I	.42139E+01
20	I	I	I	I	A	I	.68182E+01
	I	I	I	I	A	I	.91245E+01
	I	I	I	I	A	I	.11632E+02
	I	I	I	I	A	I	.12457E+02
	I	I	I	I	AI	I	.13338E+02
	I	I	I	I	A	I	.13338E+02
	I	I	I	I	A	I	.12457E+02
	I	I	I	I	A	I	.11632E+02
	I	I	I	I	A	I	.91245E+01
	I	I	I	I	A	I	.68182E+01
30	I	I	I	AI	I	I	.42139E+01
	I	I	I	A	I	I	.14254E+01
	I	I	I	I	I	I	-.14254E+01
	I	I	IA	I	I	I	-.42139E+01
	I	I	A	I	I	I	-.68182E+01
	I	I	A	I	I	I	-.91245E+01
	I	I	A	I	I	I	-.11632E+02
	I	I	A	I	I	I	-.12457E+02
	I	I	A	I	I	I	-.13338E+02
	I	I	A	I	I	I	-.13338E+02
40	I	I	I	I	I	I	-.12457E+02
	I	I	A	I	I	I	-.11632E+02
	I	I	A	I	I	I	-.91245E+01
	I	I	A	I	I	I	-.68182E+01
	I	I	IA	I	I	I	-.42139E+01
	I	I	I	A	I	I	-.14254E+01
	I	I	I	I	I	I	.14254E+01
	I	I	I	AI	I	I	.42139E+01
50	I	I	I	I	A	I	.68182E+01
	I	I	I	I	A	I	.91245E+01
	I	I	I	I	A	I	.11632E+02
	I	I	I	I	A	I	.12457E+02
	I	I	I	I	AI	I	.13338E+02
	I	I	I	I	A	I	.13338E+02
	I	I	I	I	A	I	.12457E+02
	I	I	I	I	A	I	.11632E+02

	I	I	I	I	A	I	I	
60	-25	-15	-9	5	15	25		.91245E+01 .68182E+01 Y(1,I)
0	I	I	I	AI	I	I		.42139E+01 .14254E+01 -.14254E+01 -.42139E+01 -.68182E+01 -.91245E+01 -.11632E+02 -.12457E+02 -.13338E+02
10	I	I	I	I	I	I		-.13338E+02 -.13338E+02 -.12457E+02 -.11632E+02 -.91245E+01 -.68182E+01 -.42139E+01 -.14254E+01 .14254E+01 .42139E+01 .68182E+01
20	I	I	I	I	AI	I		.91245E+01 .11632E+02 .12457E+02 .13338E+02 .13338E+02 .12457E+02 .11632E+02 .91245E+01 .68182E+01
30	I	I	I	I	I	I		.42139E+01 .14254E+01 -.14254E+01 -.42139E+01 -.68182E+01 -.91245E+01 -.11632E+02 -.12457E+02 -.13338E+02 -.13338E+02
40	I	I	I	I	I	I		-.12457E+02 -.11632E+02 -.91245E+01 -.68182E+01 -.42139E+01 -.14254E+01 .14254E+01 .42139E+01 .68182E+01
50	I	I	I	I	AI	I		.91245E+01 .11632E+02 .12457E+02 .13338E+02 .13338E+02 .12457E+02 .11632E+02 .91245E+01
	I	I	I	I	I	I		.42139E+01 .14254E+01 -.14254E+01 -.42139E+01 -.68182E+01 -.91245E+01 -.11632E+02 -.12457E+02 -.13338E+02 -.13338E+02

	I	I	I	A	I	I	I	
60				A				.14625E-02
-25				A				.27488E-01
0								Y(1, I)
	I	I	I		IA	I		.60183E+01
	I	I	I		I	A	I	.92739E+01
	I	I	I		I	A	I	.10948E+02
	I	I	I		I	A	I	.11584E+02
	I	I	I		I	A	I	.11448E+02
	I	I	I		I	A	I	.11452E+02
	I	I	I		I	A	I	.11659E+02
	I	I	I		I	A	I	.12178E+02
	I	I	I		I	A	I	.12169E+02
10								.11726E+02
	I	I	I		I	A	I	.11564E+02
	I	I	I		I	A	I	.11622E+02
	I	I	I		I	A	I	.12208E+02
	I	I	I		I	A	I	.12184E+02
	I	I	I		I	A	I	.11733E+02
	I	I	I		I	A	I	.11587E+02
	I	I	I		I	A	I	.11623E+02
	I	I	I		I	A	I	.12209E+02
	I	I	I		I	A	I	.12184E+02
20								.11733E+02
	I	I	I		I	A	I	.10621E+02
	I	I	I		I	A	I	.94590E+01
	I	I	I		I	A	I	.76634E+01
	I	I	I		I	IA	I	.56009E+01
	I	I	I		I	A	I	.32643E+01
	I	I	I		I	A	I	.78621E+00
	I	I	I		I	A	I	-.64625E-02
	I	I	I		I	A	I	-.30750E-02
	I	I	I		I	A	I	-.14625E-02
30								-.70600E-03
	I	I	AI		I		I	-.59628E+01
	I	I	I		I		I	-.92618E+01
	I	I	A		I		I	-.10942E+02
	I	I	A		I		I	-.11582E+02
	I	I	A		I		I	-.11447E+02
	I	I	A		I		I	-.11451E+02
	I	I	A		I		I	-.11659E+02
	I	I	A		I		I	-.12178E+02
	I	I	A		I		I	-.12169E+02
40								-.11726E+02
	I	I	A		I		I	-.11584E+02
	I	I	A		I		I	-.11622E+02
	I	I	A		I		I	-.12208E+02
	I	I	A		I		I	-.12184E+02
	I	I	A		I		I	-.11733E+02
	I	I	A		I		I	-.11587E+02
	I	I	A		I		I	-.11623E+02
	I	I	A		I		I	-.12209E+02
	I	I	A		I		I	-.12184E+02
50								-.11733E+02
	I	I	A		I		I	-.10621E+02
	I	I	A		I		I	-.94590E+01
	I	I	A		I		I	-.76634E+01
	I	I	AI		I		I	-.56009E+01
	I	I	I		I	A	I	-.32643E+01
	I	I	I		I	A	I	-.78621E+00
	I	I	I		I	A	I	-.64625E-02
	I	I	I		I	A	I	-.30750E-02

I						I	-.12369E+02
80	I	A	I	I	I	I	-.11726E+02
-25	-15	-5	5	15	25		Y(1,1)
0	I	I	I	I	I	I	-.11564E+02
I	I	A	I	I	I	I	-.11522E+02
I	I	A	I	I	I	I	-.12208E+02
I	I	A	I	I	I	I	-.12384E+02
I	I	A	I	I	I	I	-.11733E+02
I	I	A	I	I	I	I	-.11587E+02
I	I	A	I	I	I	I	-.11523E+02
I	I	A	I	I	I	I	-.12209E+02
I	I	A	I	I	I	I	-.12384E+02
10	I	A	I	I	I	I	-.11733E+02
I	I	A	I	I	I	I	-.10821E+02
I	I	A	I	I	I	I	-.94590E+01
I	I	A	I	I	I	I	-.76554E+01
I	I	A	I	I	I	I	-.55009E+01
I	I	A	I	I	I	I	-.32643E+01
I	I	A	I	I	I	I	-.78621E+00
I	I	A	I	I	I	I	.64625E-02
I	I	A	I	I	I	I	.30750E-02
I	I	A	I	I	I	I	.14625E-02
20	I	A	I	I	I	I	.27488E-01
I	I	A	I	I	I	I	.60183E+01
I	I	A	I	I	I	I	.92759E+01
I	I	A	I	I	I	I	.10648E+02
I	I	A	I	I	I	I	.11584E+02
I	I	A	I	I	I	I	.11448E+02
I	I	A	I	I	I	I	.11452E+02
I	I	A	I	I	I	I	.11859E+02
I	I	A	I	I	I	I	.12178E+02
I	I	A	I	I	I	I	.12369E+02
30	I	A	I	I	I	I	.11726E+02
I	I	A	I	I	I	I	.11584E+02
I	I	A	I	I	I	I	.11522E+02
I	I	A	I	I	I	I	.12208E+02
I	I	A	I	I	I	I	.12384E+02
I	I	A	I	I	I	I	.11733E+02
I	I	A	I	I	I	I	.11587E+02
I	I	A	I	I	I	I	.11523E+02
I	I	A	I	I	I	I	.12209E+02
I	I	A	I	I	I	I	.12384E+02
40	I	A	I	I	I	I	.11733E+02
I	I	A	I	I	I	I	.10821E+02
I	I	A	I	I	I	I	.94590E+01
I	I	A	I	I	I	I	.76554E+01
I	I	A	I	I	I	I	.55009E+01
I	I	A	I	I	I	I	.32643E+01
I	I	A	I	I	I	I	.78621E+00
I	I	A	I	I	I	I	-.64625E-02
I	I	A	I	I	I	I	-.30750E-02
I	I	A	I	I	I	I	-.14625E-02
50	I	A	I	I	I	I	-.70000E-03
I	I	A	I	I	I	I	-.59526E+01
I	I	A	I	I	I	I	-.92618E+01
I	I	A	I	I	I	I	-.10642E+02
I	I	A	I	I	I	I	-.11562E+02
I	I	A	I	I	I	I	-.11447E+02
I	I	A	I	I	I	I	-.11451E+02
I	I	A	I	I	I	I	-.11859E+02
I	I	A	I	I	I	I	-.12178E+02
I	I	A	I	I	I	I	-.12369E+02

PLOT OF XZ

	-25	-15	-5	5	15	25	Y(1, I)
0	I	I	AI	I	I	I	-.60C52E+01
	I	I	A	I	I	I	-.92C77E+C1
	I	I	A	I	I	I	-.10445E+02
	I	I	A	I	I	I	-.11563E+02
	I	I	A	I	I	I	-.12447E+02
	I	I	A	I	I	I	-.11451E+02
	I	I	A	I	I	I	-.11499E+02
	I	I	A	I	I	I	-.12178E+02
	I	I	A	I	I	I	-.12169E+02
10	I	I	A	I	I	I	-.11726E+02
	I	I	A	I	I	I	-.10E17E+02
	I	I	A	I	I	I	-.94274E+01
	I	I	A	I	I	I	-.76446E+01
	I	I	AI	I	I	I	-.56C06E+01
	I	I	A	I	I	I	-.32C41E+01
	I	I	A	I	I	I	-.78E13E+C0
	I	I	A	I	I	I	.65600E-02
	I	I	A	I	I	I	.31C00E-02
	I	I	A	I	I	I	.14750E-02
20	I	I	A	I	I	I	.27488E-01
	I	I	A	IA	I	I	.60183E+01
	I	I	A	A	I	I	.92739E+01
	I	I	A	A	I	I	.10448E+02
	I	I	A	A	I	I	.11584E+02
	I	I	A	A	I	I	.11448E+02
	I	I	A	A	I	I	.11452E+02
	I	I	A	A	I	I	.11459E+02
	I	I	A	A	I	I	.12178E+02
	I	I	A	A	I	I	.12169E+02
30	I	I	A	A	I	I	.11726E+02
	I	I	A	A	I	I	.11584E+02
	I	I	A	A	I	I	.11422E+02
	I	I	A	A	I	I	.12208E+02
	I	I	A	A	I	I	.12184E+02
	I	I	A	A	I	I	.11733E+02
	I	I	A	A	I	I	.11587E+C2
	I	I	A	A	I	I	.11423E+02
	I	I	A	A	I	I	.12209E+02
	I	I	A	A	I	I	.12184E+02
40	I	I	A	A	I	I	.11733E+02
	I	I	A	A	I	I	.10E21E+02
	I	I	A	A	I	I	.94590E+01
	I	I	A	IA	I	I	.76454E+01
	I	I	A	A	I	I	.56409E+01
	I	I	A	A	I	I	.32C43E+01
	I	I	A	A	I	I	.76C21E+C0
	I	I	A	A	I	I	-.64C25E-02
	I	I	A	A	I	I	-.30750E-02
	I	I	A	A	I	I	-.14C25E-02
50	I	I	A	A	I	I	-.27488E-01
	I	I	AI	I	I	I	-.60183E+C1
	I	I	A	I	I	I	-.92739E+01
	I	I	A	I	I	I	-.10448E+C2
	I	I	A	I	I	I	-.11584E+C2
	I	I	A	I	I	I	-.11448E+C2
	I	I	A	I	I	I	-.11452E+C2
	I	I	A	I	I	I	-.11459E+02
	I	I	A	I	I	I	-.12178E+02

	I	I	I	I	A	I	I
60+					A		.12184E+02
-25	-15	-5	5	15		25	.11733E+02
							Y(1,I)
0							
I	I	I	I	A	I	I	.10821E+02
I	I	I	I	A	I	I	.94590E+01
I	I	I	I	A	I	I	.76954E+01
I	I	I	I	IA	I	I	.56009E+01
I	I	I	A	I	I	I	.32643E+01
I	I	I	A	I	I	I	.78621E+00
I	I	I	A	I	I	I	-.64625E-02
I	I	I	A	I	I	I	-.30750E-02
I	I	I	A	I	I	I	-.14625E-02
10							
I	I	AI	I	I	I	I	-.27480E-01
I	I	A	I	I	I	I	-.50183E+01
I	I	A	I	I	I	I	-.92739E+01
I	I	A	I	I	I	I	-.10648E+02
I	I	AA	I	I	I	I	-.11584E+02
I	I	AA	I	I	I	I	-.11448E+02
I	I	AA	I	I	I	I	-.11452E+02
I	I	AA	I	I	I	I	-.11659E+02
I	I	AA	I	I	I	I	-.12178E+02
I	I	AA	I	I	I	I	-.12169E+02
20							
I	I	AA	I	I	I	I	-.11726E+02
I	I	AA	I	I	I	I	-.11584E+02
I	I	AA	I	I	I	I	-.11622E+02
I	I	AA	I	I	I	I	-.12208E+02
I	I	AA	I	I	I	I	-.12184E+02
I	I	AA	I	I	I	I	-.11733E+02
I	I	AA	I	I	I	I	-.11567E+02
I	I	AA	I	I	I	I	-.11623E+02
I	I	AA	I	I	I	I	-.12209E+02
I	I	AA	I	I	I	I	-.12184E+02
30							
I	I	AA	I	I	I	I	-.11733E+02
I	I	AA	I	I	I	I	-.10621E+02
I	I	AA	I	I	I	I	-.94590E+01
I	I	AA	I	I	I	I	-.76954E+01
I	I	AA	I	I	I	I	-.56009E+01
I	I	AA	I	I	I	I	-.32643E+01
I	I	AA	I	I	I	I	-.78621E+00
I	I	AA	I	I	I	I	.64625E-02
I	I	AA	I	I	I	I	.30750E-02
I	I	AA	I	I	I	I	.14625E-02
40							
I	I	AA	I	IA	I	I	.70000E-03
I	I	AA	I	IA	I	I	.59628E+01
I	I	AA	I	IA	I	I	.92618E+01
I	I	AA	I	IA	I	I	.10642E+02
I	I	AA	I	IA	I	I	.11582E+02
I	I	AA	I	IA	I	I	.11447E+02
I	I	AA	I	IA	I	I	.11451E+02
I	I	AA	I	IA	I	I	.11659E+02
I	I	AA	I	IA	I	I	.12178E+02
I	I	AA	I	IA	I	I	.12169E+02
50							
I	I	AA	I	IA	I	I	.11726E+02
I	I	AA	I	IA	I	I	.11584E+02
I	I	AA	I	IA	I	I	.11622E+02
I	I	AA	I	IA	I	I	.12208E+02
I	I	AA	I	IA	I	I	.12184E+02
I	I	AA	I	IA	I	I	.11733E+02
I	I	AA	I	IA	I	I	.11567E+02
I	I	AA	I	IA	I	I	.11623E+02
I	I	AA	I	IA	I	I	.12209E+02
I	I	AA	I	IA	I	I	.12184E+02

PLOT OF X3

	-25	-15	-5	5	15	25	Y(1, I)
0+	I	I	I	A	I	I	.00000E+00
	I	I	I	A	I	I	.00000E+00
	I	I	I	A	I	I	.00000E+00
	I	I	I	A	I	I	.00000E+00
	I	I	I	A	I	I	.00000E+00
	I	I	I	A	I	I	.00000E+00
	I	I	I	A	I	I	.00000E+00
	I	I	I	A	I	I	.00000E+00
10+	I	I	A	I	I	I	-.26788E-01
	I	I	A	I	I	I	-.60179E+01
	I	I	A	I	I	I	-.92738E+01
	I	I	A	I	I	I	-.10548E+02
	I	I	A	I	I	I	-.11584E+02
	I	I	A	I	I	I	-.11448E+02
	I	I	A	I	I	I	-.11452E+02
	I	I	A	I	I	I	-.11659E+02
	I	I	A	I	I	I	-.12178E+02
	I	I	A	I	I	I	-.12169E+02
20+	I	I	A	I	I	I	-.11726E+02
	I	I	A	I	I	I	-.11584E+02
	I	I	A	I	I	I	-.11522E+02
	I	I	A	I	I	I	-.12208E+02
	I	I	A	I	I	I	-.12184E+02
	I	I	A	I	I	I	-.11733E+02
	I	I	A	I	I	I	-.11587E+02
	I	I	A	I	I	I	-.11523E+02
	I	I	A	I	I	I	-.12209E+02
	I	I	A	I	I	I	-.12184E+02
30+	I	I	A	I	I	I	-.11733E+02
	I	I	A	I	I	I	-.10821E+02
	I	I	A	I	I	I	-.94590E+01
	I	I	A	I	I	I	-.76554E+01
	I	I	A	I	I	I	-.56009E+01
	I	I	A	I	I	I	-.32643E+01
	I	I	A	I	I	I	-.78621E+00
	I	I	A	I	I	I	.64625E-02
	I	I	A	I	I	I	.30750E-02
	I	I	A	I	I	I	.14625E-02
40+	I	I	A	I	I	I	.27488E-01
	I	I	A	I	I	I	.60183E+01
	I	I	A	I	I	I	.92739E+01
	I	I	A	I	I	I	.10548E+02
	I	I	A	I	I	I	.11584E+02
	I	I	A	I	I	I	.11448E+02
	I	I	A	I	I	I	.11452E+02
	I	I	A	I	I	I	.11659E+02
	I	I	A	I	I	I	.12178E+02
	I	I	A	I	I	I	.12169E+02
50+	I	I	A	I	I	I	.11726E+02
	I	I	A	I	I	I	.11584E+02
	I	I	A	I	I	I	.11522E+02
	I	I	A	I	I	I	.12208E+02
	I	I	A	I	I	I	.12184E+02
	I	I	A	I	I	I	.11733E+02
	I	I	A	I	I	I	.11587E+02
	I	I	A	I	I	I	.11523E+02

APPENDIX D2

CASE 2(a)

THE OUTPUT REPRESENTS THE SIMULATION FOR
18-SCRs , CONDUCTION ANGLE = 30° , $f_s / f_r = 2$.

THE OUTPUT COLUMNS ARE AS FOLLOWS :

TIME (ms) , MOTOR ANGLE (Degrees) , MOTOR PHASE
CURRENTS X1,X2,X3 (Amperes) .

SCR = 12	ALPH = 30.3	RPM = 10000.0	RPM = 20000.0	
.0500	6.0000	18.0585	.0000	.0000
.1000	12.0000	31.2856	.0000	.0000
.1500	18.0000	41.2226	.0000	.0000
.2000	24.0000	48.4430	.0000	.0000
.2500	30.0000	53.1108	.0000	.0000
.3000	36.0000	55.2505	.0000	.0000
.3500	42.0000	54.8769	.0000	.0000
.4000	48.0000	52.0580	.0000	.0000
.4500	54.0000	46.9416	.0000	.0000
.5000	60.0000	39.7631	.0000	-.1429
.5500	66.0000	30.8417	.0000	-30.0508
.6000	72.0000	20.5700	.0000	-42.8880
.6500	78.0000	9.3981	.0000	-46.3543
.7000	84.0000	-.0467	.0000	-44.2281
.7500	90.0000	-.0222	.0000	-38.4721
.8000	96.0000	-.0106	.0000	-30.2275
.8500	102.0000	-.0050	.0000	-20.2778
.9000	108.0000	-.0024	.0000	-9.2590
.9500	114.0000	-.0011	.0000	-.0216
1.0000	120.0000	-.0005	.0714	-.0103
1.0500	126.0000	.0000	18.0925	-.0049
1.1000	132.0000	.0000	31.3019	-.0023
1.1500	138.0000	.0000	41.2303	-.0011
1.2000	144.0000	.0000	48.4466	-.0005
1.2500	150.0000	.0000	53.1126	-.0003
1.3000	156.0000	.0000	55.2513	-.0001
1.3500	162.0000	.0000	54.8772	-.0001
1.4000	168.0000	.0000	52.0582	.0000
1.4500	174.0000	.0000	46.9417	.0000
1.5000	180.0000	-.1429	39.7632	.0000
1.5500	186.0000	-30.0508	30.8417	.0000
1.6000	192.0000	-42.8880	20.5700	.0000
1.6500	198.0000	-46.3543	9.3981	.0000
1.7000	204.0000	-44.2281	-.0467	.0000
1.7500	210.0000	-38.4721	-.0222	.0000
1.8000	216.0000	-30.2275	-.0106	.0000
1.8500	222.0000	-20.2778	-.0050	.0000
1.9000	228.0000	-9.2590	-.0024	.0000
1.9500	234.0000	-.0216	-.0011	.0000
2.0000	240.0000	-.0103	-.0005	.0714
2.0500	246.0000	-.0049	.0000	18.0925
2.1000	252.0000	-.0023	.0000	31.3019
2.1500	258.0000	-.0011	.0000	41.2303
2.2000	264.0000	-.0005	.0000	48.4466
2.2500	270.0000	-.0003	.0000	53.1126
2.3000	276.0000	-.0001	.0000	55.2513
2.3500	282.0000	-.0001	.0000	54.8772
2.4000	288.0000	.0000	.0000	52.0582
2.4500	294.0000	.0000	.0000	46.9417
2.5000	300.0000	.0000	-.1429	39.7632
2.5500	306.0000	.0000	-30.0508	30.8417
2.6000	312.0000	.0000	-42.8880	20.5700
2.6500	318.0000	.0000	-46.3543	9.3981
2.7000	324.0000	.0000	-44.2281	-.0467
2.7500	330.0000	.0000	-38.4721	-.0222
2.8000	336.0000	.0000	-30.2275	-.0106
2.8500	342.0000	.0000	-20.2778	-.0050
2.9000	348.0000	.0000	-9.2590	-.0024
2.9500	354.0000	.0000	-.0216	-.0011
3.0000	360.0000	.0714	-.0103	-.0005
3.0500	6.0000	18.0925	-.0049	.0000
3.1000	12.0000	31.3019	-.0023	.0000
			-.0011	.0000

3.2000	24.0000	48.4466	-.0065	.0000
3.2500	30.0000	53.1125	-.0063	.0000
3.3000	36.0000	55.2313	-.0061	.0000
3.3500	42.0000	54.8772	-.0061	.0000
3.4000	48.0000	52.0582	.0060	.0000
3.4500	54.0000	46.9417	.0060	.0000
3.5000	60.0000	39.7632	.0060	-.1429
3.5500	66.0000	30.8417	.0060	-30.0508
3.6000	72.0000	20.5700	.0060	-42.6680
3.6500	78.0000	9.3981	.0060	-46.3543
3.7000	84.0000	-.0467	.0060	-44.2281
3.7500	90.0000	-.0222	.0060	-38.4721
3.8000	96.0000	-.0106	.0060	-30.2275
3.8500	102.0000	-.0050	.0060	-20.2778
3.9000	108.0000	-.0024	.0060	-9.2590
3.9500	114.0000	-.0011	.0060	-.0216
4.0000	120.0000	-.0005	.0714	-.0103
4.0500	126.0000	.0000	18.0925	-.0049
4.1000	132.0000	.0000	31.3019	-.0023
4.1500	138.0000	.0000	41.2363	-.0011
4.2000	144.0000	.0000	48.4466	-.0005
4.2500	150.0000	.0000	53.1126	-.0003
4.3000	156.0000	.0000	55.2513	-.0001
4.3500	162.0000	.0000	54.8772	-.0001
4.4000	168.0000	.0000	52.0582	.0000
4.4500	174.0000	.0000	46.9417	.0000
4.5000	180.0000	.0000	39.7632	.0000
4.5500	186.0000	-29.9149	30.8417	.0000
4.6000	192.0000	-42.8234	20.5700	.0000
4.6500	198.0000	-46.3235	9.3981	.0000
4.7000	204.0000	-44.2135	-.0467	.0000
4.7500	210.0000	-38.4652	-.0222	.0000
4.8000	216.0000	-30.2242	-.0106	.0000
4.8500	222.0000	-20.2762	-.0050	.0000
4.9000	228.0000	-9.2583	-.0024	.0000
4.9500	234.0000	-.0212	-.0011	.0000
5.0000	240.0000	-.0101	-.0005	.0000
5.0500	246.0000	-.0048	.0000	18.0246
5.1000	252.0000	-.0023	.0000	31.2696
5.1500	258.0000	-.0011	.0000	41.2149
5.2000	264.0000	-.0005	.0000	48.4393
5.2500	270.0000	-.0002	.0000	53.1091
5.3000	276.0000	-.0001	.0000	55.2496
5.3500	282.0000	-.0001	.0000	54.8765
5.4000	288.0000	.0000	.0000	52.0578
5.4500	294.0000	.0000	.0000	46.9416
5.5000	300.0000	.0000	.0000	39.7631
5.5500	306.0000	.0000	-29.9149	30.8417
5.6000	312.0000	.0000	-42.8234	20.5599
5.6500	318.0000	.0000	-46.3235	9.3981
5.7000	324.0000	.0000	-44.2135	-.0467
5.7500	330.0000	.0000	-38.4652	-.0222
5.8000	336.0000	.0000	-30.2242	-.0106
5.8500	342.0000	.0000	-20.2762	-.0050
5.9000	348.0000	.0000	-9.2583	-.0024
5.9500	354.0000	.0000	-.0212	-.0011
6.0000	360.0000	.0000	-.0101	-.0005

AD-A161 907

USAF/SCEEE (UNITED STATES AIR FORCE/SOUTHEASTERN CENTER 11/12

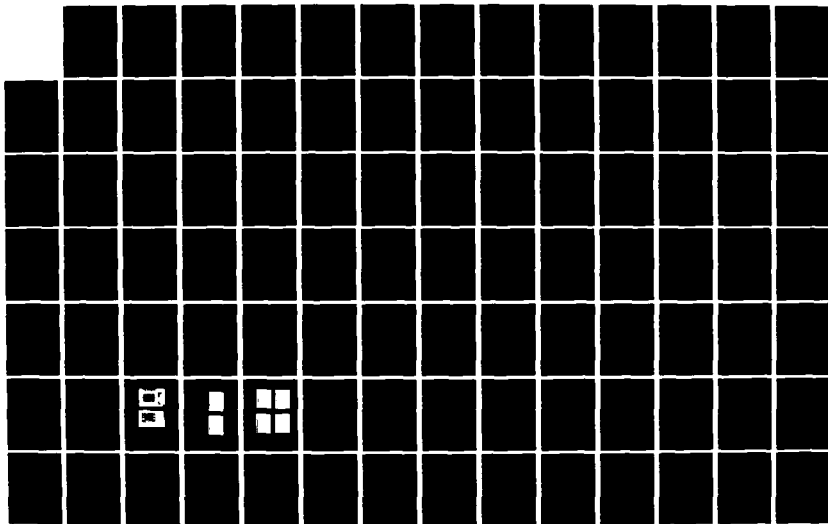
FOR ELECTRICAL EN. (U) SOUTHEASTERN CENTER FOR
ELECTRICAL ENGINEERING EDUCATION INC S. W D PEELE

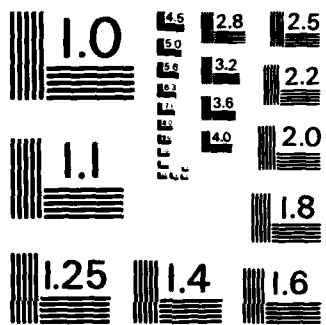
UNCLASSIFIED

MAR 85 AFOSR-TR-85-0904 F49620-82-C-0035

F/G 9/3

NL





MICROCOPY RESOLUTION TEST CHART
NATIONAL BUREAU OF STANDARDS - 1963 - A

CASE 2(b)

THE OUTPUT REPRESENTS THE SIMULATION FOR
18-SCRs, CONDUCTION ANGLE = 30° , $f_s / f_r = 2$.

THE OUTPUT COLUMNS ARE AS FOLLOWS:

TIME(ms), MOTOR ANGLE(Degrees), MOTOR VOLTAGES
VA,VB,VC (Volts) .

ALPH	ALPH	ALPH	ALPH	ALPH
.0500	6.0000	100.3696	.0000	.0000
.1000	12.0000	121.3525	.0000	.0000
.1500	18.0000	137.0318	.0000	.0000
.2000	24.0000	146.7221	.0000	.0000
.2500	30.0000	150.0000	.0000	.0000
.3000	36.0000	146.7221	.0000	.0000
.3500	42.0000	137.0318	.0000	.0000
.4000	48.0000	121.3525	.0000	.0000
.4500	54.0000	100.3696	.0000	.0000
.5000	60.0000	75.0000	.0000	-150.0000
.5500	66.0000	46.3525	.0000	-146.7221
.6000	72.0000	15.6793	.0000	-137.0318
.6500	78.0000	-15.6793	.0000	-121.3525
.7000	84.0000	.0000	.0000	-100.3696
.7500	90.0000	.0000	.0000	-75.0000
.8000	96.0000	.0000	.0000	-46.3525
.8500	102.0000	.0000	.0000	-15.6793
.9000	108.0000	.0000	.0000	15.6793
.9500	114.0000	.0000	.0000	.0000
1.0000	120.0000	.0000	75.0000	.0000
1.0500	126.0000	.0000	100.3696	.0000
1.1000	132.0000	.0000	121.3525	.0000
1.1500	138.0000	.0000	137.0318	.0000
1.2000	144.0000	.0000	146.7221	.0000
1.2500	150.0000	.0000	150.0000	.0000
1.3000	156.0000	.0000	146.7221	.0000
1.3500	162.0000	.0000	137.0318	.0000
1.4000	168.0000	.0000	121.3525	.0000
1.4500	174.0000	.0000	100.3696	.0000
1.5000	180.0000	-150.0000	75.0000	.0000
1.5500	186.0000	-146.7221	46.3525	.0000
1.6000	192.0000	-137.0318	15.6793	.0000
1.6500	198.0000	-121.3525	-15.6793	.0000
1.7000	204.0000	-100.3696	.0000	.0000
1.7500	210.0000	-75.0000	.0000	.0000
1.8000	216.0000	-46.3525	.0000	.0000
1.8500	222.0000	-15.6793	.0000	.0000
1.9000	228.0000	15.6793	.0000	.0000
1.9500	234.0000	.0000	.0000	.0000
2.0000	240.0000	.0000	.0000	75.0000
2.0500	246.0000	.0000	.0000	100.3696
2.1000	252.0000	.0000	.0000	121.3525
2.1500	258.0000	.0000	.0000	137.0318
2.2000	264.0000	.0000	.0000	146.7221
2.2500	270.0000	.0000	.0000	150.0000
2.3000	276.0000	.0000	.0000	146.7221
2.3500	282.0000	.0000	.0000	137.0318
2.4000	288.0000	.0000	.0000	121.3525
2.4500	294.0000	.0000	.0000	100.3696
2.5000	300.0000	.0000	-150.0000	75.0000
2.5500	306.0000	.0000	-146.7221	46.3525
2.6000	312.0000	.0000	-137.0318	15.6793
2.6500	318.0000	.0000	-121.3525	-15.6793
2.7000	324.0000	.0000	-100.3696	.0000
2.7500	330.0000	.0000	-75.0000	.0000
2.8000	336.0000	.0000	-46.3525	.0000
2.8500	342.0000	.0000	-15.6793	.0000
2.9000	348.0000	.0000	15.6793	.0000
2.9500	354.0000	.0000	.0000	.0000
3.0000	.0000	75.0000	.0000	.0000
3.0500	6.0000	100.3696	.0000	.0000
3.1000	12.0000	121.3525	.0000	.0000
3.1500	18.0000	137.0318	.0000	.0000

3.2000	24.0000	146.7221	.0000	.0000
3.2500	30.0000	150.0000	.0000	.0000
3.3000	36.0000	146.7221	.0000	.0000
3.3500	42.0000	137.0318	.0000	.0000
3.4000	48.0000	121.3525	.0000	.0000
3.4500	54.0000	100.3696	.0000	.0000
3.5000	60.0000	75.0000	.0000	-150.0000
3.5500	66.0000	46.3525	.0000	-146.7221
3.6000	72.0000	15.6793	.0000	-137.0318
3.6500	78.0000	-15.6793	.0000	-121.3525
3.7000	84.0000	.0000	.0000	-100.3696
3.7500	90.0000	.0000	.0000	-75.0000
3.8000	96.0000	.0000	.0000	-46.3525
3.8500	102.0000	.0000	.0000	-15.6793
3.9000	108.0000	.0000	.0000	15.6793
3.9500	114.0000	.0000	.0000	.0000
4.0000	120.0000	.0000	75.0000	.0000
4.0500	126.0000	.0000	100.3696	.0000
4.1000	132.0000	.0000	121.3525	.0000
4.1500	138.0000	.0000	137.0318	.0000
4.2000	144.0000	.0000	146.7221	.0000
4.2500	150.0000	.0000	150.0000	.0000
4.3000	156.0000	.0000	146.7221	.0000
4.3500	162.0000	.0000	137.0318	.0000
4.4000	168.0000	.0000	121.3525	.0000
4.4500	174.0000	.0000	100.3696	.0000
4.5000	180.0000	.0000	75.0000	.0000
4.5500	186.0000	-146.7221	46.3525	.0000
4.6000	192.0000	-137.0318	15.6793	.0000
4.6500	198.0000	-121.3525	-15.6793	.0000
4.7000	204.0000	-100.3696	.0000	.0000
4.7500	210.0000	-75.0000	.0000	.0000
4.8000	216.0000	-46.3525	.0000	.0000
4.8500	222.0000	-15.6793	.0000	.0000
4.9000	228.0000	15.6793	.0000	.0000
4.9500	234.0000	.0000	.0000	.0000
5.0000	240.0000	.0000	.0000	.0000
5.0500	246.0000	.0000	.0000	100.3696
5.1000	252.0000	.0000	.0000	121.3525
5.1500	258.0000	.0000	.0000	137.0318
5.2000	264.0000	.0000	.0000	146.7221
5.2500	270.0000	.0000	.0000	150.0000
5.3000	276.0000	.0000	.0000	146.7221
5.3500	282.0000	.0000	.0000	137.0318
5.4000	288.0000	.0000	.0000	121.3525
5.4500	294.0000	.0000	.0000	100.3696
5.5000	300.0000	.0000	.0000	75.0000
5.5500	306.0000	.0000	-146.7221	46.3525
5.6000	312.0000	.0000	-137.0318	15.6793
5.6500	318.0000	.0000	-121.3525	-15.6793
5.7000	324.0000	.0000	-100.3696	.0000
5.7500	330.0000	.0000	-75.0000	.0000
5.8000	336.0000	.0000	-46.3525	.0000
5.8500	342.0000	.0000	-15.6793	.0000
5.9000	348.0000	.0000	15.6793	.0000
5.9500	354.0000	.0000	.0000	.0000
6.0000	360.0000	.0000	.0000	.0000

CASE 2(c)

HIGH-SPEED DIGITAL PRINTER PLOTS FOR

VA, VB, VC : MOTOR PHASE VOLTAGES

X1, X2, X3 : MOTOR PHASE CURRENTS

VX, VY, VZ : SUPPLY PHASE VOLTAGES

(Not included, the same as in case 1(c))

PLDT OF VB

	-25	-15	-5	5	15	25	Y(1, I)
0	I	I	I	A	I	I	.00000E+00
	I	I	I	A	I	I	.00000E+00
	I	I	I	A	I	I	.00000E+00
	I	I	I	A	I	I	.00000E+00
	I	I	I	A	I	I	.00000E+00
	I	I	I	A	I	I	.00000E+00
	I	I	I	A	I	I	.00000E+00
	I	I	I	A	I	I	.00000E+00
10	I	I	I	A	I	I	.00000E+00
	I	I	I	A	I	I	.00000E+00
	I	I	I	A	I	I	.00000E+00
	I	I	I	A	I	I	.00000E+00
	I	I	I	A	I	I	.00000E+00
	I	I	I	A	I	I	.00000E+00
	I	I	I	A	I	I	.00000E+00
	I	I	I	A	I	I	.00000E+00
20	I	I	I	A	I	I	.68182E+01
	I	I	I	I	A	I	.91245E+01
	I	I	I	I	A	I	.11632E+02
	I	I	I	I	A	I	.12457E+02
	I	I	I	I	A	I	.13636E+02
	I	I	I	I	A	I	.13636E+02
	I	I	I	I	A	I	.12457E+02
	I	I	I	I	A	I	.11632E+02
	I	I	I	I	A	I	.91245E+01
	I	I	I	I	A	I	.68182E+01
30	I	I	I	A	I	I	.42139E+01
	I	I	I	A	I	I	.14254E+01
	I	I	I	A	I	I	-.14254E+01
	I	I	I	A	I	I	.00000E+00
	I	I	I	A	I	I	.00000E+00
	I	I	I	A	I	I	.00000E+00
	I	I	I	A	I	I	.00000E+00
	I	I	I	A	I	I	.00000E+00
	I	I	I	A	I	I	.00000E+00
40	I	I	I	A	I	I	.00000E+00
	I	I	I	A	I	I	.00000E+00
	I	I	I	A	I	I	.00000E+00
	I	I	I	A	I	I	.00000E+00
	I	I	I	A	I	I	.00000E+00
	I	I	I	A	I	I	.00000E+00
	I	I	I	A	I	I	.00000E+00
	I	I	I	A	I	I	.00000E+00
	I	I	I	A	I	I	.00000E+00
50	I	I	I	A	I	I	-.13636E+02
	I	A	I	I	I	I	-.13636E+02
	I	A	I	I	I	I	-.12457E+02
	I	A	I	I	I	I	-.11632E+02
	I	A	I	I	I	I	-.91245E+01
	I	A	I	I	I	I	-.68182E+01
	I	A	I	I	I	I	-.42139E+01
	I	A	I	I	I	I	-.14254E+01

1	I	I	A	I	I	I	.00000E+00
60	-----						.00000E+00
-25	-15	-5	5	15	25	Y(1,1)	
C	-----						
I	I	I	A	I	I	I	.00000E+00
I	I	I	A	I	I	I	.00000E+00
I	I	I	A	I	I	I	.00000E+00
I	I	I	A	I	I	I	.00000E+00
I	I	I	A	I	I	I	.00000E+00
I	I	I	A	I	I	I	.00000E+00
I	I	I	A	I	I	I	.00000E+00
I	I	I	A	I	I	I	.00000E+00
10	-----						.00000E+00
I	I	I	A	I	I	I	.00000E+00
I	I	I	A	I	I	I	.00000E+00
I	I	I	A	I	I	I	.00000E+00
I	I	I	A	I	I	I	.00000E+00
I	I	I	A	I	I	I	.00000E+00
I	I	I	A	I	I	I	.00000E+00
I	I	I	A	I	I	I	.00000E+00
I	I	I	A	I	I	I	.00000E+00
20	-----						.68182E+01
I	I	I	I	A	I	I	.91245E+01
I	I	I	I	A	I	I	.11032E+02
I	I	I	I	A	I	I	.12457E+02
I	I	I	I	A	I	I	.13336E+02
I	I	I	I	A	I	I	.13336E+02
I	I	I	I	A	I	I	.12457E+02
I	I	I	I	A	I	I	.11032E+02
I	I	I	I	A	I	I	.91245E+01
30	-----						.68182E+01
I	I	I	A	I	I	I	.42139E+01
I	I	I	A	I	I	I	.14254E+01
I	I	I	A	I	I	I	-.14254E+01
I	I	I	A	I	I	I	.00000E+00
I	I	I	A	I	I	I	.00000E+00
I	I	I	A	I	I	I	.00000E+00
I	I	I	A	I	I	I	.00000E+00
I	I	I	A	I	I	I	.00000E+00
I	I	I	A	I	I	I	.00000E+00
40	-----						.00000E+00
I	I	I	A	I	I	I	.00000E+00
I	I	I	A	I	I	I	.00000E+00
I	I	I	A	I	I	I	.00000E+00
I	I	I	A	I	I	I	.00000E+00
I	I	I	A	I	I	I	.00000E+00
I	I	I	A	I	I	I	.00000E+00
I	I	I	A	I	I	I	.00000E+00
I	I	I	A	I	I	I	.00000E+00
50	-----						.00000E+00
I	I	A	I	I	I	I	-.13336E+02
I	I	A	I	I	I	I	-.12457E+02
I	I	A	I	I	I	I	-.11032E+02
I	I	A	I	I	I	I	-.91245E+01
I	I	A	I	I	I	I	-.68182E+01
I	I	A	I	I	I	I	-.42139E+01
I	I	A	I	I	I	I	-.14254E+01
I	I	A	I	I	I	I	.14254E+01
I	I	A	I	I	I	I	.00000E+00

PLOT OF X2

	-25	-15	-5	5	15	25	Y(1,1)
0+	I	I	I	A	I	I	.00000E+00
	I	I	I	A	I	I	.00000E+00
	I	I	I	A	I	I	.00000E+00
	I	I	I	A	I	I	.00000E+00
	I	I	I	A	I	I	.00000E+00
	I	I	I	A	I	I	.00000E+00
	I	I	I	A	I	I	.00000E+00
	I	I	I	A	I	I	.00000E+00
10+	I	I	I	A	I	I	.00000E+00
	I	I	I	A	I	I	.00000E+00
	I	I	I	A	I	I	.00000E+00
	I	I	I	A	I	I	.00000E+00
	I	I	I	A	I	I	.00000E+00
	I	I	I	A	I	I	.00000E+00
	I	I	I	A	I	I	.00000E+00
	I	I	I	A	I	I	.00000E+00
20+	I	I	I	A	I	I	.89250E-02
	I	I	I	A	I	I	.22616E+01
	I	I	I	A	I	I	.39127E+01
	I	I	I	A	I	I	.51538E+01
	I	I	I	A	I	I	.63558E+01
	I	I	I	A	I	I	.66291E+01
	I	I	I	A	I	I	.69664E+01
	I	I	I	A	I	I	.68597E+01
	I	I	I	A	I	I	.65073E+01
	I	I	I	A	I	I	.58677E+01
30+	I	I	I	A	I	I	.49704E+01
	I	I	I	A	I	I	.38552E+01
	I	I	I	A	I	I	.25713E+01
	I	I	I	A	I	I	.11748E+01
	I	I	I	A	I	I	-.38375E-02
	I	I	I	A	I	I	-.27750E-02
	I	I	I	A	I	I	-.13250E-02
	I	I	I	A	I	I	-.62500E-03
	I	I	I	A	I	I	-.33000E-03
	I	I	I	A	I	I	-.13750E-03
40+	I	I	I	A	I	I	-.62500E-04
	I	I	I	A	I	I	.00000E+00
	I	I	I	A	I	I	.00000E+00
	I	I	I	A	I	I	.00000E+00
	I	I	I	A	I	I	.00000E+00
	I	I	I	A	I	I	.00000E+00
	I	I	I	A	I	I	.00000E+00
	I	I	I	A	I	I	.00000E+00
	I	I	I	A	I	I	.00000E+00
50+	I	I	I	A	I	I	-.17663E-01
	I	I	I	A	I	I	-.37564E+01
	I	I	I	A	I	I	-.53610E+01
	I	I	I	A	I	I	-.57543E+01
	I	I	I	A	I	I	-.55285E+01
	I	I	I	A	I	I	-.48090E+01
	I	I	I	A	I	I	-.37644E+01
	I	I	I	A	I	I	-.25147E+01

I	I	I	A	I	I	I	-.2700E-02
60	-25	-15	-5	5	15	25	-.12775E-02
I	I	I	A	I	I	I	Y(1,1)
I	I	I	A	I	I	I	-.61250E-03
I	I	I	A	I	I	I	-.28750E-03
I	I	I	A	I	I	I	-.13750E-03
I	I	I	A	I	I	I	-.62500E-04
I	I	I	A	I	I	I	-.37500E-04
I	I	I	A	I	I	I	-.12500E-04
I	I	I	A	I	I	I	-.12500E-04
I	I	I	A	I	I	I	.00000E+00
I	I	I	A	I	I	I	.00000E+00
10	I	I	A	I	I	I	.00000E+00
I	I	I	A	I	I	I	.00000E+00
I	I	I	A	I	I	I	.00000E+00
I	I	I	A	I	I	I	.00000E+00
I	I	I	A	I	I	I	.00000E+00
I	I	I	A	I	I	I	.00000E+00
I	I	I	A	I	I	I	.00000E+00
I	I	I	A	I	I	I	.00000E+00
20	I	I	A	I	I	I	.89250E-02
I	I	I	A	I	I	I	.22616E+01
I	I	I	A	I	I	I	.39127E+01
I	I	I	A	I	I	I	.51538E+01
I	I	I	A	I	I	I	.60558E+01
I	I	I	A	I	I	I	.66391E+01
I	I	I	A	I	I	I	.69664E+01
I	I	I	A	I	I	I	.68597E+01
I	I	I	A	I	I	I	.65073E+01
I	I	I	A	I	I	I	.58677E+01
30	I	I	A	I	I	I	.49704E+01
I	I	I	A	I	I	I	.38552E+01
I	I	I	A	I	I	I	.25713E+01
I	I	I	A	I	I	I	.11748E+01
I	I	I	A	I	I	I	-.58373E-02
I	I	I	A	I	I	I	-.27750E-02
I	I	I	A	I	I	I	-.13250E-02
I	I	I	A	I	I	I	-.62500E-03
I	I	I	A	I	I	I	-.30000E-03
I	I	I	A	I	I	I	-.13750E-03
40	I	I	A	I	I	I	-.62500E-04
I	I	I	A	I	I	I	.00000E+00
I	I	I	A	I	I	I	.00000E+00
I	I	I	A	I	I	I	.00000E+00
I	I	I	A	I	I	I	.00000E+00
I	I	I	A	I	I	I	.00000E+00
I	I	I	A	I	I	I	.00000E+00
I	I	I	A	I	I	I	.00000E+00
50	I	I	A	I	I	I	.00000E+00
I	I	I	A	I	I	I	-.37394E+01
I	I	I	A	I	I	I	-.53529E+01
I	I	I	A	I	I	I	-.37904E+01
I	I	I	A	I	I	I	-.55267E+01
I	I	I	A	I	I	I	-.48082E+01
I	I	I	A	I	I	I	-.37760E+01
I	I	I	A	I	I	I	-.25345E+01
I	I	I	A	I	I	I	-.11573E+01
I	I	I	A	I	I	I	-.26500E-02

	I	I	I	A	I	I	I	
60								-.13750E-03
-25								-.62100E-04
								Y(1, I)
0								
	I	I	I	A	I	I	I	.00000E+00
	I	I	I	A	I	I	I	.00000E+00
	I	I	I	A	I	I	I	.00000E+00
	I	I	I	A	I	I	I	.00000E+00
	I	I	I	A	I	I	I	.00000E+00
	I	I	I	A	I	I	I	.00000E+00
	I	I	I	A	I	I	I	.00000E+00
	I	I	I	A	I	I	I	.00000E+00
	I	I	I	A	I	I	I	.00000E+00
10								-.17663E-01
	I	I	IA		I	I	I	-.37164E+01
	I	I	A		I	I	I	-.53610E+01
	I	I	AI		I	I	I	-.57643E+01
	I	I	AI		I	I	I	-.55285E+01
	I	I	A		I	I	I	-.48690E+01
	I	I	IA		I	I	I	-.37784E+01
	I	I	I A		I	I	I	-.25847E+01
	I	I	I A		I	I	I	-.11574E+01
	I	I	I A		I	I	I	-.27000E-02
20								-.12675E-02
	I	I	I	A	I	I	I	-.61250E-03
	I	I	I	A	I	I	I	-.28750E-03
	I	I	I	A	I	I	I	-.13750E-03
	I	I	I	A	I	I	I	-.62500E-04
	I	I	I	A	I	I	I	-.37500E-04
	I	I	I	A	I	I	I	-.12500E-04
	I	I	I	A	I	I	I	-.12500E-04
	I	I	I	A	I	I	I	.00000E+00
	I	I	I	A	I	I	I	.00000E+00
30								.00000E+00
	I	I	I	A	I	I	I	.00000E+00
	I	I	I	A	I	I	I	.00000E+00
	I	I	I	A	I	I	I	.00000E+00
	I	I	I	A	I	I	I	.00000E+00
	I	I	I	A	I	I	I	.00000E+00
	I	I	I	A	I	I	I	.00000E+00
	I	I	I	A	I	I	I	.00000E+00
	I	I	I	A	I	I	I	.00000E+00
40								.00000E+00
	I	I	I	A	I	I	I	.22531E+01
	I	I	I	AI	I	I	I	.39687E+01
	I	I	I	A	I	I	I	.51119E+01
	I	I	I	IA	I	I	I	.60149E+01
	I	I	I	I A	I	I	I	.66386E+01
	I	I	I	I A	I	I	I	.69662E+01
	I	I	I	I A	I	I	I	.68596E+01
	I	I	I	I A	I	I	I	.65672E+01
	I	I	I	IA	I	I	I	.58677E+01
50								.49704E+01
	I	I	I	AI	I	I	I	.38552E+01
	I	I	I	A	I	I	I	.25712E+01
	I	I	I	A	I	I	I	.11748E+01
	I	I	I	A	I	I	I	-.56375E-02
	I	I	I	A	I	I	I	-.27750E-02
	I	I	I	A	I	I	I	-.13250E-02
	I	I	I	A	I	I	I	-.62500E-03
	I	I	I	A	I	I	I	-.30000E-03
	I	I	I	A	I	I	I	-.13750E-03

APPENDIX D3

CASE 3(a)

THE OUTPUT REPRESENTS THE SIMULATION FOR
36-SCRs, CONDUCTION ANGLE = 59°, $f_s / f_r = 4$.

THE OUTPUT COLUMNS ARE AS FOLLOWS:

TIME(ms), MOTOR ANGLE(Degrees), MOTOR CURRENTS
X1, X2, X3 (Amperes).

3.2000	24.0000	91.6439	-.0747	.0000
3.2500	30.0000	92.6377	-.0356	.0000
3.3000	36.0000	93.9387	-.0169	.0000
3.3500	42.0000	96.2635	-.0080	.0000
3.4000	48.0000	93.5920	-.0038	.0000
3.4500	54.0000	96.3782	-.0018	.0000
3.5000	60.0000	94.8903	-.0009	-.2143
3.5500	66.0000	82.8888	-.0004	-49.7641
3.6000	72.0000	59.3592	-.0002	-75.2474
3.6500	78.0000	26.9002	-.0001	-83.5935
3.7000	84.0000	.0747	.0000	-91.6220
3.7500	90.0000	.0356	.0000	.0000
3.8000	96.0000	.0169	.0000	.0000
3.8500	102.0000	.0080	.0000	.0000
3.9000	108.0000	.0038	.0000	.0000
3.9500	114.0000	.0018	.0000	.0000
4.0000	120.0000	.0009	.2143	-94.8903
4.0500	126.0000	.0004	49.7641	-82.8888
4.1000	132.0000	.0002	75.2474	-59.3592
4.1500	138.0000	.0001	83.5935	-26.9002
4.2000	144.0000	.0000	91.6220	-.0747
4.2500	150.0000	.0000	92.6377	-.0356
4.3000	156.0000	.0000	93.9387	-.0169
4.3500	162.0000	.0000	96.2635	-.0080
4.4000	168.0000	.0000	93.5920	-.0038
4.4500	174.0000	.0000	96.3782	-.0018
4.5000	180.0000	.0000	94.8903	-.0009
4.5500	186.0000	-49.7641	82.8888	-.0004
4.6000	192.0000	-75.2474	59.3592	-.0002
4.6500	198.0000	-83.5935	26.9002	-.0001
4.7000	204.0000	-91.6220	.0747	.0000
4.7500	210.0000	-92.6377	.0356	.0000
4.8000	216.0000	-93.9387	.0169	.0000
4.8500	222.0000	-96.2635	.0080	.0000
4.9000	228.0000	-93.5920	.0038	.0000
4.9500	234.0000	-96.3782	.0018	.0000
5.0000	240.0000	-94.8903	.0009	.0000
5.0500	246.0000	-82.8888	.0004	49.7641
5.1000	252.0000	-59.3592	.0002	75.2474
5.1500	258.0000	-26.9002	.0001	83.5935
5.2000	264.0000	-.0747	.0000	91.6220
5.2500	270.0000	-.0356	.0000	92.6377
5.3000	276.0000	-.0169	.0000	93.9387
5.3500	282.0000	-.0080	.0000	96.2635
5.4000	288.0000	-.0038	.0000	93.5920
5.4500	294.0000	-.0018	.0000	96.3782
5.5000	300.0000	-.0009	.0000	94.8903
5.5500	306.0000	-.0004	-49.7641	82.8888
5.6000	312.0000	-.0002	-75.2474	59.3592
5.6500	318.0000	-.0001	-83.5935	26.9002
5.7000	324.0000	.0000	-91.6220	-.0747
5.7500	330.0000	.0000	-92.6377	-.0356
5.8000	336.0000	.0000	-93.9387	-.0169
5.8500	342.0000	.0000	-96.2635	-.0080
5.9000	348.0000	.0000	-93.5920	-.0038
5.9500	354.0000	.0000	-96.3782	-.0018
6.0000	360.0000	.0000	-94.8903	-.0009

CASE 3(b)

THE OUTPUT REPRESENTS THE SIMULATION FOR
36-SCRs, CONDUCTION ANGLE = 59° , $f_s / f_r = 4$.

THE OUTPUT COLUMNS ARE AS FOLLOWS:

TIME(ms), MOTOR ANGLE(Degrees), MOTOR PHASE
VOLTAGES VA,VB,VC (Volts).

.0500	6.0000	258.3844	.0000	.0000
.1000	12.0000	247.0917	.0000	.0000
.1500	18.0000	247.0917	.0000	.0000
.2000	24.0000	258.3844	.0000	.0000
.2500	30.0000	225.0000	.0000	.0000
.3000	36.0000	258.3844	.0000	.0000
.3500	42.0000	247.0917	.0000	.0000
.4000	48.0000	247.0917	.0000	.0000
.4500	54.0000	258.3844	.0000	.0000
.5000	60.0000	225.0000	.0000	.0000
.5500	66.0000	152.7111	.0000	-225.0000
.6000	72.0000	54.0170	.0000	-258.3844
.6500	78.0000	-54.0170	.0000	-247.0917
.7000	84.0000	.0000	.0000	-247.0917
.7500	90.0000	.0000	.0000	-258.3844
.8000	96.0000	.0000	.0000	-225.0000
.8500	102.0000	.0000	.0000	-258.3844
.9000	108.0000	.0000	.0000	-247.0917
.9500	114.0000	.0000	.0000	-258.3844
1.0000	120.0000	.0000	225.0000	-225.0000
1.0500	126.0000	.0000	258.3844	-152.7111
1.1000	132.0000	.0000	247.0917	247.0917
1.1500	138.0000	.0000	247.0917	-54.0170
1.2000	144.0000	.0000	258.3844	54.0170
1.2500	150.0000	.0000	225.0000	.0000
1.3000	156.0000	.0000	258.3844	.0000
1.3500	162.0000	.0000	247.0917	.0000
1.4000	168.0000	.0000	247.0917	.0000
1.4500	174.0000	.0000	258.3844	.0000
1.5000	180.0000	-225.0000	225.0000	.0000
1.5500	186.0000	-258.3844	152.7111	.0000
1.6000	192.0000	-247.0917	54.0170	.0000
1.6500	198.0000	-247.0917	-54.0170	.0000
1.7000	204.0000	-258.3844	.0000	.0000
1.7500	210.0000	-225.0000	.0000	.0000
1.8000	216.0000	-258.3844	.0000	.0000
1.8500	222.0000	-247.0917	.0000	.0000
1.9000	228.0000	-247.0917	.0000	.0000
1.9500	234.0000	-258.3844	.0000	.0000
2.0000	240.0000	-225.0000	.0000	225.0000
2.0500	246.0000	-152.7111	.0000	258.3844
2.1000	252.0000	-54.0170	.0000	247.0917
2.1500	258.0000	54.0170	.0000	247.0917
2.2000	264.0000	.0000	.0000	258.3844
2.2500	270.0000	.0000	.0000	225.0000
2.3000	276.0000	.0000	.0000	258.3844
2.3500	282.0000	.0000	.0000	247.0917
2.4000	288.0000	.0000	.0000	247.0917
2.4500	294.0000	.0000	.0000	258.3844
2.5000	300.0000	.0000	-225.0000	225.0000
2.5500	306.0000	.0000	-258.3844	152.7111
2.6000	312.0000	.0000	-247.0917	54.0170
2.6500	318.0000	.0000	-247.0917	-54.0170
2.7000	324.0000	.0000	-258.3844	.0000
2.7500	330.0000	.0000	-225.0000	.0000
2.8000	336.0000	.0000	-258.3844	.0000
2.8500	342.0000	.0000	-247.0917	.0000
2.9000	348.0000	.0000	-247.0917	.0000
2.9500	354.0000	.0000	-258.3844	.0000
3.0000	.0000	225.0000	-225.0000	.0000
3.0500	6.0000	258.3844	-152.7111	.0000
3.1000	12.0000	247.0917	-54.0170	.0000
3.1500	18.0000	247.0917	54.0170	.0000

3.2000	24.0000	258.3844	.0000	.0000
3.2500	30.0000	225.0000	.0000	.0000
3.3000	36.0000	258.3844	.0000	.0000
3.3500	42.0000	247.0917	.0000	.0000
3.4000	48.0000	247.0917	.0000	.0000
3.4500	54.0000	258.3844	.0000	.0000
3.5000	60.0000	225.0000	.0000	-225.0000
3.5500	66.0000	152.7111	.0000	-258.3844
3.6000	72.0000	54.0170	.0000	-247.0917
3.6500	78.0000	-54.0170	.0000	-247.0917
3.7000	84.0000	.0000	.0000	-258.3844
3.7500	90.0000	.0000	.0000	-225.0000
3.8000	96.0000	.0000	.0000	-258.3844
3.8500	102.0000	.0000	.0000	-247.0917
3.9000	108.0000	.0000	.0000	-247.0917
3.9500	114.0000	.0000	.0000	-258.3844
4.0000	120.0000	.0000	225.0000	-225.0000
4.0500	126.0000	.0000	258.3844	-152.7111
4.1000	132.0000	.0000	247.0917	-54.0170
4.1500	138.0000	.0000	247.0917	54.0170
4.2000	144.0000	.0000	258.3844	.0000
4.2500	150.0000	.0000	225.0000	.0000
4.3000	156.0000	.0000	258.3844	.0000
4.3500	162.0000	.0000	247.0917	.0000
4.4000	168.0000	.0000	247.0917	.0000
4.4500	174.0000	.0000	258.3844	.0000
4.5000	180.0000	.0000	225.0000	.0000
4.5500	186.0000	-258.3844	152.7111	.0000
4.6000	192.0000	-247.0917	54.0170	.0000
4.6500	198.0000	-247.0917	-54.0170	.0000
4.7000	204.0000	-258.3844	.0000	.0000
4.7500	210.0000	-225.0000	.0000	.0000
4.8000	216.0000	-258.3844	.0000	.0000
4.8500	222.0000	-247.0917	.0000	.0000
4.9000	228.0000	-247.0917	.0000	.0000
4.9500	234.0000	-258.3844	.0000	.0000
5.0000	240.0000	-225.0000	.0000	.0000
5.0500	246.0000	-152.7111	.0000	258.3844
5.1000	252.0000	-54.0170	.0000	247.0917
5.1500	258.0000	54.0170	.0000	247.0917
5.2000	264.0000	.0000	.0000	258.3844
5.2500	270.0000	.0000	.0000	225.0000
5.3000	276.0000	.0000	.0000	258.3844
5.3500	282.0000	.0000	.0000	247.0917
5.4000	288.0000	.0000	.0000	247.0917
5.4500	294.0000	.0000	.0000	258.3844
5.5000	300.0000	.0000	.0000	225.0000
5.5500	306.0000	.0000	-258.3844	152.7111
5.6000	312.0000	.0000	-247.0917	54.0170
5.6500	318.0000	.0000	-247.0917	-54.0170
5.7000	324.0000	.0000	-258.3844	.0000
5.7500	330.0000	.0000	-225.0000	.0000
5.8000	336.0000	.0000	-258.3844	.0000
5.8500	342.0000	.0000	-247.0917	.0000
5.9000	348.0000	.0000	-247.0917	.0000
5.9500	354.0000	.0000	-258.3844	.0000
6.0000	360.0000	.0000	-225.0000	.0000

CASE 3(c)

HIGH-SPEED DIGITAL PRINTER PLOTS FOR

VA, VB, VC : MOTOR PHASE VOLTAGES
X1, X2, X3 : MOTOR PHASE CURRENTS
VX, VY, VZ : SUPPLY PHASE VOLTAGES ***

*** VX, VY, VZ ARE THE SAME FOR ALL $f_s / f_r = 4$, AND
THE PEAK PHASE VOLTAGE GIVEN TO BE 150 VOLTS .

PLOT OF VC

	-25	-15	-5	5	15	25	Y(1,1)
0	I	I	I	A	I	I	.00000E+00
	I	I	I	A	I	I	.00000E+00
	I	I	I	A	I	I	.00000E+00
	I	I	I	A	I	I	.00000E+00
	I	I	I	A	I	I	.00000E+00
	I	I	I	A	I	I	.00000E+00
	I	I	I	A	I	I	.00000E+00
	I	I	I	A	I	I	.00000E+00
	I	I	I	A	I	I	.00000E+00
10	A	I	I	I	I	I	-.20455E+02
	I	I	I	I	I	I	-.23489E+02
	I	I	I	I	I	I	-.22463E+02
	I	I	I	I	I	I	-.22463E+02
	I	I	I	I	I	I	-.23489E+02
	I	I	I	I	I	I	-.20455E+02
	I	I	I	I	I	I	-.23489E+02
	I	I	I	I	I	I	-.22463E+02
	I	I	I	I	I	I	-.22463E+02
	I	I	I	I	I	I	-.23489E+02
20	A	I	I	I	I	I	-.20455E+02
	I	I	I	I	I	I	-.13863E+02
	I	I	I	I	I	I	-.49106E+01
	I	I	I	A	I	I	.00000E+00
	I	I	I	A	I	I	.00000E+00
	I	I	I	A	I	I	.00000E+00
	I	I	I	A	I	I	.00000E+00
	I	I	I	A	I	I	.00000E+00
	I	I	I	A	I	I	.00000E+00
	I	I	I	A	I	I	.00000E+00
30	I	I	I	A	I	I	.00000E+00
	I	I	I	A	I	I	.00000E+00
	I	I	I	A	I	I	.00000E+00
	I	I	I	A	I	I	.00000E+00
	I	I	I	A	I	I	.00000E+00
	I	I	I	A	I	I	.00000E+00
	I	I	I	A	I	I	.00000E+00
	I	I	I	A	I	I	.00000E+00
	I	I	I	A	I	I	.00000E+00
40	I	I	I	I	I	A	.20455E+02
	I	I	I	I	I	A	.23489E+02
	I	I	I	I	I	A	.22463E+02
	I	I	I	I	I	A	.22463E+02
	I	I	I	I	I	A	.23489E+02
	I	I	I	I	I	A	.20455E+02
	I	I	I	I	I	A	.23489E+02
	I	I	I	I	I	A	.22463E+02
	I	I	I	I	I	A	.22463E+02
	I	I	I	I	I	A	.23489E+02
50	I	I	I	I	A	I	.20455E+02
	I	I	I	I	A	I	.13863E+02
	I	I	I	A	I	I	-.49106E+01
	I	I	I	A	I	I	.00000E+00
	I	I	I	A	I	I	.00000E+00
	I	I	I	A	I	I	.00000E+00
	I	I	I	A	I	I	.00000E+00
	I	I	I	A	I	I	.00000E+00

PLOT OF X2

	-25	-15	-5	5	15	25	Y(1,I)
0	I	I	I	I	I	I	.00000E+00
	I	I	A	I	I	I	.00000E+00
	I	I	I	A	I	I	.00000E+00
	I	I	I	A	I	I	.00000E+00
	I	I	I	A	I	I	.00000E+00
	I	I	I	A	I	I	.00000E+00
	I	I	I	A	I	I	.00000E+00
	I	I	I	A	I	I	.00000E+00
10	I	I	I	A	I	I	.00000E+00
	I	I	I	A	I	I	.00000E+00
	I	I	I	A	I	I	.00000E+00
	I	I	I	A	I	I	.00000E+00
	I	I	I	A	I	I	.00000E+00
	I	I	I	A	I	I	.00000E+00
	I	I	I	A	I	I	.00000E+00
	I	I	I	A	I	I	.00000E+00
20	I	I	I	A	I	I	.26788E-01
	I	I	I	I	A	I	.62460E+01
	I	I	I	I	A	I	.94161E+01
	I	I	I	I	A	I	.10455E+02
	I	I	I	I	A	I	.11455E+02
	I	I	I	I	A	I	.11580E+02
	I	I	I	I	A	I	.11742E+02
	I	I	I	I	A	I	.12033E+02
	I	I	I	I	A	I	.11699E+02
	I	I	I	I	A	I	.12047E+02
30	I	I	I	I	A	I	.11661E+02
	I	I	I	I	A	I	.10361E+02
	I	I	I	I	A	I	.74195E+01
	I	I	I	A	I	I	.33625E+01
	I	I	I	A	I	I	.93575E-02
	I	I	I	A	I	I	.44200E-02
	I	I	I	A	I	I	.21125E-02
	I	I	I	A	I	I	.10000E-02
	I	I	I	A	I	I	.47500E-03
	I	I	I	A	I	I	.22500E-03
40	I	I	I	A	I	I	.11250E-03
	I	I	I	A	I	I	.50000E-04
	I	I	I	A	I	I	.25000E-04
	I	I	I	A	I	I	.12500E-04
	I	I	I	A	I	I	.00000E+00
	I	I	I	A	I	I	.00000E+00
	I	I	I	A	I	I	.00000E+00
	I	I	I	A	I	I	.00000E+00
	I	I	I	A	I	I	.00000E+00
	I	I	I	A	I	I	.00000E+00
50	I	I	I	A	I	I	-.26786E-01
	I	I	A	I	I	I	-.62460E+01
	I	I	A	I	I	I	-.94161E+01
	I	I	A	I	I	I	-.10455E+02
	I	I	A	I	I	I	-.11455E+02
	I	I	A	I	I	I	-.11580E+02
	I	I	A	I	I	I	-.11742E+02
	I	I	A	I	I	I	-.12033E+02

I	I	A	I	I	I	I	-0.12647E+02
60	-25	-15	-5	5	15	25	-0.11661E+02
							Y(1,1)

I	I	A	I	I	I	I	-0.10361E+02
I	I		A	I	I	I	-0.74199E+01
I	I			A	I	I	-0.33625E+01
I	I				A	I	-0.93375E-02
I	I					A	-0.44500E-02
I	I						-0.21125E-02
I	I						-0.10600E-02
I	I						-0.47500E-03
I	I						-0.22500E-03
10	-----						-0.11250E-03
I	I			A	I	I	-0.50000E-04
I	I				A	I	-0.25000E-04
I	I					A	-0.12500E-04
I	I						0.00000E+00
I	I						0.00000E+00
I	I						0.00000E+00
I	I						0.00000E+00
I	I						0.00000E+00
I	I						0.00000E+00
20	-----						0.26788E-01
I	I				A	I	0.62460E+01
I	I					A	0.94181E+01
I	I						0.10455E+02
I	I					A	0.11455E+02
I	I						0.11580E+02
I	I						0.11742E+02
I	I						0.12033E+02
I	I						0.11699E+02
I	I						0.12047E+02
30	-----						0.11661E+02
I	I				A	I	0.10361E+02
I	I					A	0.74199E+01
I	I						0.33625E+01
I	I			A	I	I	0.93375E-02
I	I			A	I	I	0.44500E-02
I	I				A	I	0.21125E-02
I	I					A	0.10600E-02
I	I						0.47500E-03
I	I						0.22500E-03
40	-----						0.11250E-03
I	I			A	I	I	0.50000E-04
I	I				A	I	0.25000E-04
I	I					A	0.12500E-04
I	I						0.00000E+00
I	I						0.00000E+00
I	I						0.00000E+00
I	I						0.00000E+00
I	I						0.00000E+00
I	I						0.00000E+00
50	-----						0.00000E+00
I	I		A	I	I	I	-0.62205E+01
I	I			A	I	I	-0.94059E+01
I	I		A	I	I	I	-0.10449E+02
I	I			A	I	I	-0.11455E+02
I	I		A	I	I	I	-0.11578E+02
I	I			A	I	I	-0.11742E+02
I	I				A	I	-0.12033E+02
I	I					A	-0.11699E+02
I	I						-0.12047E+02

PLOT OF X3

	-25	-15	-5	5	15	25	Y(1, I)
0	I	I	I	A	I	I	.00000E+00
I	I	I	I	A	I	I	.00000E+00
I	I	I	I	A	I	I	.00000E+00
I	I	I	I	A	I	I	.00000E+00
I	I	I	I	A	I	I	.00000E+00
I	I	I	I	A	I	I	.00000E+00
I	I	I	I	A	I	I	.00000E+00
I	I	I	I	A	I	I	.00000E+00
10	I	I	I	A	I	I	-.26786E-01
I	I	I	A	I	I	I	-.62460E+01
I	I	A	I	I	I	I	-.94181E+01
I	I	A	I	I	I	I	-.10433E+02
I	I	A	I	I	I	I	-.11455E+02
I	I	A	I	I	I	I	-.11580E+02
I	I	A	I	I	I	I	-.11742E+02
I	I	A	I	I	I	I	-.12033E+02
I	I	A	I	I	I	I	-.11699E+02
I	I	A	I	I	I	I	-.12047E+02
20	I	I	A	I	I	I	-.11661E+02
I	I	A	I	I	I	I	-.10261E+02
I	I	A	I	I	I	I	-.74199E+01
I	I	A	I	I	I	I	-.33625E+01
I	I	A	I	I	I	I	-.93373E-02
I	I	A	I	I	I	I	-.44500E-02
I	I	A	I	I	I	I	-.21225E-02
I	I	A	I	I	I	I	-.10000E-02
I	I	A	I	I	I	I	-.47500E-03
I	I	A	I	I	I	I	-.22500E-03
30	I	I	A	I	I	I	-.11250E-03
I	I	A	I	I	I	I	-.50000E-04
I	I	A	I	I	I	I	-.25000E-04
I	I	A	I	I	I	I	-.12500E-04
I	I	A	I	I	I	I	.00000E+00
I	I	A	I	I	I	I	.00000E+00
I	I	A	I	I	I	I	.00000E+00
I	I	A	I	I	I	I	.00000E+00
I	I	A	I	I	I	I	.00000E+00
I	I	A	I	I	I	I	.00000E+00
40	I	I	A	I	I	I	.00000E+00
I	I	A	I	I	I	I	.26786E-01
I	I	A	I	I	I	I	.62460E+01
I	I	A	I	I	I	I	.94181E+01
I	I	A	I	I	I	I	.10455E+02
I	I	A	I	I	I	I	.11455E+02
I	I	A	I	I	I	I	.11580E+02
I	I	A	I	I	I	I	.11742E+02
I	I	A	I	I	I	I	.12033E+02
I	I	A	I	I	I	I	.11699E+02
I	I	A	I	I	I	I	.12047E+02
50	I	I	A	I	I	I	.11661E+02
I	I	A	I	I	I	I	.10261E+02
I	I	A	I	I	I	I	.74199E+01
I	I	A	I	I	I	I	.33625E+01
I	I	A	I	I	I	I	.93373E-02
I	I	A	I	I	I	I	.44500E-02
I	I	A	I	I	I	I	.21225E-02
I	I	A	I	I	I	I	.10000E-02
I	I	A	I	I	I	I	.47500E-03

I	I	I	A	I	I	I	.22500E-03
60+	-25	-15	-5	5	15	25	.11250E-03
0+							Y(1,1)
I	I	I	A	I	I	I	.50000E-04
I	I	I	A	I	I	I	.25000E-04
I	I	I	A	I	I	I	.12500E-04
I	I	I	A	I	I	I	.00000E+00
I	I	I	A	I	I	I	.00000E+00
I	I	I	A	I	I	I	.00000E+00
I	I	I	A	I	I	I	.00000E+00
I	I	I	A	I	I	I	.00000E+00
10+							-.26788E-C1
I	I	A	I	I	I	I	-.62460E+01
I	I	A	I	I	I	I	-.94181E+01
I	I	A	I	I	I	I	-.10455E+02
I	I	A	I	I	I	I	-.11455E+02
I	I	A	I	I	I	I	-.11580E+02
I	I	A	I	I	I	I	-.11742E+02
I	I	A	I	I	I	I	-.12033E+02
I	I	A	I	I	I	I	-.11699E+02
I	I	A	I	I	I	I	-.12147E+02
20+							-.11661E+02
I	I	A	I	I	I	I	-.10361E+02
I	I	A	I	I	I	I	-.74199E+01
I	I	A	I	I	I	I	-.33625E+01
I	I	A	I	I	I	I	-.93375E-02
I	I	A	I	I	I	I	-.44500E-02
I	I	A	I	I	I	I	-.21125E-02
I	I	A	I	I	I	I	-.10000E-02
I	I	A	I	I	I	I	-.47500E-03
I	I	A	I	I	I	I	-.22500E-03
30+							-.11250E-03
I	I	I	A	I	I	I	-.50000E-04
I	I	I	A	I	I	I	-.25000E-04
I	I	I	A	I	I	I	-.12500E-04
I	I	I	A	I	I	I	.00000E+00
I	I	I	A	I	I	I	.00000E+00
I	I	I	A	I	I	I	.00000E+00
I	I	I	A	I	I	I	.00000E+00
I	I	I	A	I	I	I	.00000E+00
I	I	I	A	I	I	I	.00000E+00
40+							.50000E+00
I	I	I	I	A	I	I	.62205E+01
I	I	I	I	A	I	I	.94056E+01
I	I	I	I	A	I	I	.10449E+02
I	I	I	I	A	I	I	.11453E+02
I	I	I	I	A	I	I	.11578E+02
I	I	I	I	A	I	I	.11742E+02
I	I	I	I	A	I	I	.12133E+02
I	I	I	I	A	I	I	.11699E+02
I	I	I	I	A	I	I	.12147E+02
50+							.11661E+02
I	I	I	I	A	I	I	.10361E+02
I	I	I	I	A	I	I	.74199E+01
I	I	I	I	A	I	I	.33625E+01
I	I	I	I	A	I	I	.93375E-02
I	I	I	I	A	I	I	.44500E-02
I	I	I	I	A	I	I	.21125E-02
I	I	I	I	A	I	I	.10000E-02
I	I	I	I	A	I	I	.47500E-03
I	I	I	I	A	I	I	.22500E-03

APPENDIX D4

CASE 4(a)

THE OUTPUT REPRESENTS THE SIMULATION FOR
18-SCRs, CONDUCTION ANGLE = 75° , $f_s / f_r = 4$.

THE OUTPUT COLUMNS ARE AS FOLLOWS:

TIME(ms), MOTOR ANGLE(Degrees), MOTOR PHASE
CURRENTS X1,X2,X3 (Amperes) .

.0500	6.0000	25.6626	-29.2035	.0500
.1000	12.0000	37.5700	-37.7259	.0000
.1500	18.0000	47.8944	-32.2863	.0000
.2000	24.0000	49.8962	-17.7257	.0000
.2500	30.0000	43.2508	.0249	.0000
.3000	36.0000	41.2393	.0118	.0000
.3500	42.0000	47.3594	.0056	.0000
.4000	48.0000	52.9518	.0027	.0000
.4500	54.0000	52.1119	.0013	.0000
.5000	60.0000	44.3050	.0006	-.1429
.5500	66.0000	41.7408	.0000	-24.2715
.6000	72.0000	47.5980	.0000	-37.7582
.6500	78.0000	52.6653	.0000	-35.7376
.7000	84.0000	52.1659	.0000	-41.7440
.7500	90.0000	44.3307	.0000	-49.3851
.8000	96.0000	29.6314	.0000	-52.6986
.8500	102.0000	10.1897	.0000	-48.9037
.9000	108.0000	.0061	.0000	-41.0401
.9500	114.0000	.0329	.0000	-44.2667
1.0000	120.0000	.0014	.0714	-50.5853
1.0500	126.0000	.0007	20.6966	-53.2696
1.1000	132.0000	.0003	37.5862	-49.1754
1.1500	138.0000	.0001	47.9021	-37.7354
1.2000	144.0000	.0000	49.8959	-20.3212
1.2500	150.0000	.0000	43.2526	-.0082
1.3000	156.0000	.0000	41.2401	-.0039
1.3500	162.0000	.0000	47.3598	-.0018
1.4000	168.0000	.0000	52.9520	-.0009
1.4500	174.0000	.0000	52.1120	-.0004
1.5000	180.0000	-.1429	44.3050	-.0002
1.5500	186.0000	-29.2715	41.7408	-.0001
1.6000	192.0000	-37.7582	47.5980	.0000
1.6500	198.0000	-35.7376	52.6653	.0000
1.7000	204.0000	-41.7440	52.1659	.0000
1.7500	210.0000	-49.3851	44.3307	.0000
1.8000	216.0000	-52.6986	29.6314	.0000
1.8500	222.0000	-48.9037	10.1897	.0000
1.9000	228.0000	-41.0401	.0061	.0000
1.9500	234.0000	-44.2667	.0329	.0000
2.0000	240.0000	-50.5853	.0014	.0714
2.0500	246.0000	-53.2696	.0007	20.6966
2.1000	252.0000	-49.1754	.0003	37.5862
2.1500	258.0000	-37.7354	.0001	47.9021
2.2000	264.0000	-20.3212	.0000	49.8959
2.2500	270.0000	-.0082	.0000	43.2526
2.3000	276.0000	-.0039	.0000	41.2401
2.3500	282.0000	-.0018	.0000	47.3598
2.4000	288.0000	-.0009	.0000	52.9520
2.4500	294.0000	-.0004	.0000	52.1120
2.5000	300.0000	-.0002	-.1429	44.3050
2.5500	306.0000	-.0001	-29.2715	41.7408
2.6000	312.0000	.0000	-37.7582	47.5980
2.6500	318.0000	.0000	-35.7376	52.6653
2.7000	324.0000	.0000	-41.7440	52.1659
2.7500	330.0000	.0000	-49.3851	44.3307
2.8000	336.0000	.0000	-52.6986	29.6314
2.8500	342.0000	.0000	-48.9037	10.1897
2.9000	348.0000	.0000	-41.0401	.0061
2.9500	354.0000	.0000	-44.2667	.0329
3.0000	.0000	.0714	-50.5853	.0014
3.0500	6.0000	20.6966	-53.2696	.0007
3.1000	12.0000	37.5862	-49.1754	.0003
3.1500	18.0000	47.8944	-37.7354	.0001

3.2000	24.0000	49.8999	-20.3212	.0001
3.2500	30.0000	43.2526	-.0002	.0000
3.3000	36.0000	41.2401	-.0039	.0000
3.3500	42.0000	47.3598	-.0018	.0000
3.4000	48.0000	52.5520	-.0009	.0000
3.4500	54.0000	52.1120	-.0004	.0000
3.5000	60.0000	44.3050	-.0002	-.1429
3.5500	66.0000	41.7408	-.0001	-29.2719
3.6000	72.0000	47.5980	.0000	-37.7582
3.6500	78.0000	52.6653	.0000	-35.7376
3.7000	84.0000	52.1659	.0000	-41.7440
3.7500	90.0000	44.3307	.0000	-49.3851
3.8000	96.0000	29.6314	.0000	-52.6986
3.8500	102.0000	10.1897	.0000	-48.9037
3.9000	108.0000	.0061	.0000	-41.0401
3.9500	114.0000	.0029	.0000	-44.2667
4.0000	120.0000	.0014	.0714	-50.5853
4.0500	126.0000	.0007	20.6966	-53.2696
4.1000	132.0000	.0003	37.5862	-49.1754
4.1500	138.0000	.0001	47.9021	-37.7354
4.2000	144.0000	.0001	49.8999	-20.3212
4.2500	150.0000	.0000	43.2526	-.0082
4.3000	156.0000	.0000	41.2401	-.0039
4.3500	162.0000	.0000	47.3598	-.0018
4.4000	168.0000	.0000	52.5520	-.0009
4.4500	174.0000	.0000	52.1120	-.0004
4.5000	180.0000	.0000	44.3050	-.0002
4.5500	186.0000	-29.1356	41.7408	-.0001
4.6000	192.0000	-37.6935	47.5980	.0000
4.6500	198.0000	-35.7068	52.6653	.0000
4.7000	204.0000	-41.7294	52.1659	.0000
4.7500	210.0000	-49.3781	44.3307	.0000
4.8000	216.0000	-52.6953	29.6314	.0000
4.8500	222.0000	-48.9022	10.1897	.0000
4.9000	228.0000	-41.0393	.0061	.0000
4.9500	234.0000	-44.2664	.0029	.0000
5.0000	240.0000	-50.5851	.0014	.0000
5.0500	246.0000	-53.2695	.0007	20.6286
5.1000	252.0000	-49.1753	.0003	37.5538
5.1500	258.0000	-37.7354	.0001	47.8867
5.2000	264.0000	-20.3212	.0001	49.8923
5.2500	270.0000	-.0082	.0000	43.2491
5.3000	276.0000	-.0039	.0000	41.2384
5.3500	282.0000	-.0018	.0000	47.3590
5.4000	288.0000	-.0009	.0000	52.5516
5.4500	294.0000	-.0004	.0000	52.1119
5.5000	300.0000	-.0002	.0000	44.3049
5.5500	306.0000	-.0001	-29.1356	41.7408
5.6000	312.0000	.0000	-37.6935	47.5980
5.6500	318.0000	.0000	-35.7068	52.6653
5.7000	324.0000	.0000	-41.7294	52.1659
5.7500	330.0000	.0000	-49.3781	44.3307
5.8000	336.0000	.0000	-52.6953	29.6314
5.8500	342.0000	.0000	-48.9022	10.1897
5.9000	348.0000	.0000	-41.0393	.0061
5.9500	354.0000	.0000	-44.2664	.0029
6.0000	360.0000	.0000	-50.5851	.0014

CASE 4(b)

THE OUTPUT REPRESENTS THE SIMULATION FOR
18-SCRs, CONDUCTION ANGLE = 75° , $f_s / f_r = 4$.

THE OUTPUT COLUMNS ARE AS FOLLOWS :

TIME(ms), MOTOR ANGLE(Degrees), MOTOR PHASE
VOLTAGES VA,VB,VC (Volts) .

SCP - 1A	ALPH - 75.0	REP - 1000000	REP - 1000000	REP - 1000000
.0500	6.0000	121.3525	-137.0316	.0000
.1000	12.0000	146.7221	-100.3696	.0000
.1500	18.0000	146.7221	-46.3525	.0000
.2000	24.0000	121.3525	15.6793	.0000
.2500	30.0000	75.0000	.0000	.0000
.3000	36.0000	121.3525	.0000	.0000
.3500	42.0000	146.7221	.0000	.0000
.4000	48.0000	146.7221	.0000	.0000
.4500	54.0000	121.3525	.0000	.0000
.5000	60.0000	75.0000	.0000	-150.0000
.5500	66.0000	121.3525	.0000	-137.0316
.6000	72.0000	146.7221	.0000	-100.3696
.6500	78.0000	146.7221	.0000	-100.3696
.7000	84.0000	121.3525	.0000	-137.0316
.7500	90.0000	75.0000	.0000	-150.0000
.8000	96.0000	15.6793	.0000	-137.0316
.8500	102.0000	-46.3525	.0000	-100.3696
.9000	108.0000	.0000	.0000	-100.3696
.9500	114.0000	.0000	.0000	-137.0316
1.0000	120.0000	.0000	75.0000	-150.0000
1.0500	126.0000	.0000	121.3525	-137.0316
1.1000	132.0000	.0000	146.7221	-100.3696
1.1500	138.0000	.0000	146.7221	-46.3525
1.2000	144.0000	.0000	121.3525	15.6793
1.2500	150.0000	.0000	75.0000	.0000
1.3000	156.0000	.0000	121.3525	.0000
1.3500	162.0000	.0000	146.7221	.0000
1.4000	168.0000	.0000	146.7221	.0000
1.4500	174.0000	.0000	121.3525	.0000
1.5000	180.0000	-150.0000	75.0000	.0000
1.5500	186.0000	-137.0316	121.3525	.0000
1.6000	192.0000	-100.3696	146.7221	.0000
1.6500	198.0000	-100.3696	146.7221	.0000
1.7000	204.0000	-137.0316	121.3525	.0000
1.7500	210.0000	-150.0000	75.0000	.0000
1.8000	216.0000	-137.0316	15.6793	.0000
1.8500	222.0000	-100.3696	-46.3525	.0000
1.9000	228.0000	-100.3696	.0000	.0000
1.9500	234.0000	-137.0316	.0000	.0000
2.0000	240.0000	-150.0000	.0000	75.0000
2.0500	246.0000	-137.0316	.0000	121.3525
2.1000	252.0000	-100.3696	.0000	146.7221
2.1500	258.0000	-46.3525	.0000	146.7221
2.2000	264.0000	15.6793	.0000	121.3525
2.2500	270.0000	.0000	.0000	75.0000
2.3000	276.0000	.0000	.0000	121.3525
2.3500	282.0000	.0000	.0000	146.7221
2.4000	288.0000	.0000	.0000	146.7221
2.4500	294.0000	.0000	.0000	121.3525
2.5000	300.0000	.0000	-150.0000	75.0000
2.5500	306.0000	.0000	-137.0316	121.3525
2.6000	312.0000	.0000	-100.3696	146.7221
2.6500	318.0000	.0000	-100.3696	146.7221
2.7000	324.0000	.0000	-137.0316	121.3525
2.7500	330.0000	.0000	-150.0000	75.0000
2.8000	336.0000	.0000	-137.0316	15.6793
2.8500	342.0000	.0000	-100.3696	-46.3525
2.9000	348.0000	.0000	-100.3696	.0000
2.9500	354.0000	.0000	-137.0316	.0000
3.0000	.0000	75.0000	-150.0000	.0000
3.0500	6.0000	121.3525	-137.0316	.0000
3.1000	12.0000	146.7221	-100.3696	.0000
3.1500	18.0000	146.7221	-46.3525	.0000

1.2000	24.0000	121.3525	15.6793	.0000
1.2500	30.0000	75.0000	.0000	.0000
1.3000	36.0000	121.3525	.0000	.0000
1.3500	42.0000	146.7221	.0000	.0000
1.4000	48.0000	146.7221	.0000	.0000
1.4500	54.0000	121.3525	.0000	.0000
1.5000	60.0000	75.0000	.0000	-150.0000
1.5500	66.0000	121.3525	.0000	-137.0318
1.6000	72.0000	146.7221	.0000	-100.3696
1.6500	78.0000	146.7221	.0000	-150.3696
1.7000	84.0000	121.3525	.0000	-137.0318
1.7500	90.0000	75.0000	.0000	-150.0000
1.8000	96.0000	15.6793	.0000	-137.0318
1.8500	102.0000	-46.3525	.0000	-100.3696
1.9000	108.0000	.0000	.0000	-100.3696
1.9500	114.0000	.0000	.0000	-137.0318
2.0000	120.0000	.0000	75.0000	-150.0000
2.0500	126.0000	.0000	121.3525	-137.0318
2.1000	132.0000	.0000	146.7221	-100.3696
2.1500	138.0000	.0000	146.7221	-46.3525
2.2000	144.0000	.0000	121.3525	15.6793
2.2500	150.0000	.0000	75.0000	.0000
2.3000	156.0000	.0000	121.3525	.0000
2.3500	162.0000	.0000	146.7221	.0000
2.4000	168.0000	.0000	146.7221	.0000
2.4500	174.0000	.0000	121.3525	.0000
2.5000	180.0000	.0000	75.0000	.0000
2.5500	186.0000	-137.0318	121.3525	.0000
2.6000	192.0000	-100.3696	146.7221	.0000
2.6500	198.0000	-100.3696	146.7221	.0000
2.7000	204.0000	-137.0318	121.3525	.0000
2.7500	210.0000	-150.0000	75.0000	.0000
2.8000	216.0000	-137.0318	15.6793	.0000
2.8500	222.0000	-100.3696	-46.3525	.0000
2.9000	228.0000	-100.3696	.0000	.0000
2.9500	234.0000	-137.0318	.0000	.0000
3.0000	240.0000	-150.0000	.0000	.0000
3.0500	246.0000	-137.0318	.0000	121.3525
3.1000	252.0000	-100.3696	.0000	146.7221
3.1500	258.0000	-46.3525	.0000	146.7221
3.2000	264.0000	15.6793	.0000	121.3525
3.2500	270.0000	.0000	.0000	75.0000
3.3000	276.0000	.0000	.0000	121.3525
3.3500	282.0000	.0000	.0000	146.7221
3.4000	288.0000	.0000	.0000	146.7221
3.4500	294.0000	.0000	.0000	121.3525
3.5000	300.0000	.0000	.0000	75.0000
3.5500	306.0000	.0000	-137.0318	121.3525
3.6000	312.0000	.0000	-100.3696	146.7221
3.6500	318.0000	.0000	-100.3696	146.7221
3.7000	324.0000	.0000	-137.0318	121.3525
3.7500	330.0000	.0000	-150.0000	75.0000
3.8000	336.0000	.0000	-137.0318	15.6793
3.8500	342.0000	.0000	-100.3696	-46.3525
3.9000	348.0000	.0000	-100.3696	.0000
3.9500	354.0000	.0000	-137.0318	.0000
4.0000	360.0000	.0000	-150.0000	.0000

CASE 4(c)

HIGH-SPEED DIGITAL PRINTER PLOTS FOR

VA, VB, VC : MOTOR PHASE VOLTAGES
X1, X2, X3 : MOTOR PHASE CURRENTS
VX, VY, VZ : SUPPLY PHASE VOLTAGES
(not included, the same as in case 3(c))

I	I	I	A	I	I	I	.00000E+00
60			A				.00000E+00
-25	-15	-9		9	15	25	Y(1, I)
0							
I	I	I	A	I	I	I	.00000E+00
I	I	I	A	I	I	I	.00000E+00
I	I	I	A	I	I	I	.00000E+00
I	I	I	A	I	I	I	.00000E+00
I	I	I	A	I	I	I	.00000E+00
I	I	I	A	I	I	I	.00000E+00
I	I	I	A	I	I	I	.00000E+00
10		A					-.13636E+02
I	I	A	I	I	I	I	-.12457E+02
I	I	A	I	I	I	I	-.91245E+01
I	I	A	I	I	I	I	-.91245E+01
I	I	A	I	I	I	I	-.12457E+02
I	I	A	I	I	I	I	-.13636E+02
I	I	A	I	I	I	I	-.12457E+02
I	I	A	I	I	I	I	-.91245E+01
I	I	A	I	I	I	I	-.91245E+01
I	I	A	I	I	I	I	-.12457E+02
20		A					-.13636E+02
I	I	A	I	I	I	I	-.12457E+02
I	I	A	I	I	I	I	-.91245E+01
I	I	A	I	I	I	I	-.42139E+01
I	I	A	I	I	I	I	-.14234E+01
I	I	A	I	I	I	I	.00000E+00
I	I	A	I	I	I	I	.00000E+00
I	I	A	I	I	I	I	.00000E+00
I	I	A	I	I	I	I	.00000E+00
I	I	A	I	I	I	I	.00000E+00
I	I	A	I	I	I	I	.00000E+00
30			A				.00000E+00
I	I	I	A	I	I	I	.00000E+00
I	I	I	A	I	I	I	.00000E+00
I	I	I	A	I	I	I	.00000E+00
I	I	I	A	I	I	I	.00000E+00
I	I	I	A	I	I	I	.00000E+00
I	I	I	A	I	I	I	.00000E+00
I	I	I	A	I	I	I	.00000E+00
I	I	I	A	I	I	I	.00000E+00
40			A				.00000E+00
I	I	I	I	A	I	I	-.11632E+02
I	I	I	I	A	A	I	-.13338E+02
I	I	I	I	A	A	I	-.13338E+02
I	I	I	I	A	A	I	-.11632E+02
I	I	I	I	A	A	I	-.68182E+01
I	I	I	I	A	A	I	-.11632E+02
I	I	I	I	A	A	I	-.13338E+02
I	I	I	I	A	A	I	-.13338E+02
I	I	I	I	A	A	I	-.11632E+02
50				A			-.68182E+01
I	I	I	I	A	I	I	-.11632E+02
I	I	I	I	A	A	I	-.13338E+02
I	I	I	I	A	A	I	-.13338E+02
I	I	I	I	A	A	I	-.11632E+02
I	I	I	I	A	A	I	-.68182E+01
I	I	I	I	A	A	I	-.14234E+01
I	I	I	I	A	A	I	-.42139E+01
I	I	I	I	A	A	I	.00000E+00
I	I	I	I	A	A	I	.00000E+00

PLOT OF X2

	-25	-15	-5	5	15	25	Y(1,1)
0	I	I	IA	I	I	I	-.36504E+01
	I	I	A	I	I	I	-.47157E+01
	I	I	IA	I	I	I	-.40360E+01
	I	I	I A	I	I	I	-.22162E+01
	I	I	I A	I	I	I	.31125E-02
	I	I	I A	I	I	I	.14756E-02
	I	I	I A	I	I	I	.70000E-03
	I	I	I A	I	I	I	.33750E-03
	I	I	I A	I	I	I	.16250E-03
10	I	I	I A	I	I	I	.75000E-04
	I	I	I A	I	I	I	.00000E+00
	I	I	I A	I	I	I	.00000E+00
	I	I	I A	I	I	I	.00000E+00
	I	I	I A	I	I	I	.00000E+00
	I	I	I A	I	I	I	.00000E+00
	I	I	I A	I	I	I	.00000E+00
	I	I	I A	I	I	I	.00000E+00
	I	I	I A	I	I	I	.00000E+00
20	I	I	I A	I	I	I	.59250E-02
	I	I	I A	I	I	I	.25671E+01
	I	I	I A	I	I	I	.46983E+01
	I	I	I A	I	I	I	.59678E+01
	I	I	I A	I	I	I	.62275E+01
	I	I	I A	I	I	I	.34066E+01
	I	I	I A	I	I	I	.51250E+01
	I	I	I A	I	I	I	.59200E+01
	I	I	I A	I	I	I	.65690E+01
	I	I	I A	I	I	I	.65140E+01
30	I	I	I A	I	I	I	.55581E+01
	I	I	I A	I	I	I	.52176E+01
	I	I	I A	I	I	I	.59498E+01
	I	I	I A	I	I	I	.65632E+01
	I	I	I A	I	I	I	.65207E+01
	I	I	I A	I	I	I	.55413E+01
	I	I	I A	I	I	I	.37039E+01
	I	I	I A	I	I	I	.12737E+01
	I	I	I A	I	I	I	.76250E-03
	I	I	I A	I	I	I	.36250E-03
40	I	I	I A	I	I	I	.17500E-03
	I	I	I A	I	I	I	.87500E-04
	I	I	I A	I	I	I	.37500E-04
	I	I	I A	I	I	I	.12500E-04
	I	I	I A	I	I	I	.12500E-04
	I	I	I A	I	I	I	.00000E+00
	I	I	I A	I	I	I	.00000E+00
	I	I	I A	I	I	I	.00000E+00
	I	I	I A	I	I	I	.00000E+00
50	I	I	I A	I	I	I	-.17663E-01
	I	I	I A	I	I	I	-.36266E+01
	I	I	I A	I	I	I	-.47146E+01
	I	I	I A	I	I	I	-.44672E+01
	I	I	I A	I	I	I	-.52180E+01
	I	I	I A	I	I	I	-.61731E+01
	I	I	I A	I	I	I	-.65673E+01
	I	I	I A	I	I	I	-.61250E+01
	I	I	I A	I	I	I	-.51250E+01

	I	AI	I	I	I	I
60						-.55333E+01
-25	-15	-5	5	15	25	-.63232E+01
						Y(1, I)
2		A				-.66587E+01
		A				-.61469E+01
		A				-.47169E+01
		A				-.25402E+01
			A			-.16250E-02
			A			-.48750E-03
			A			-.22500E-03
			A			-.11250E-03
			A			-.50000E-04
10			A			-.25000E-04
			A			-.12500E-04
			A			.00000E+00
			A			.00000E+00
			A			.00000E+00
			A			.00000E+00
			A			.00000E+00
			A			.00000E+00
			A			.00000E+00
20			A			.89250E-02
			A			.25671E+01
			A			.46983E+01
			IA			.59678E+01
			IA			.62375E+01
			A			.54066E+01
			A			.51250E+01
			IA			.59200E+01
			IA			.55490E+01
			IA			.65140E+01
30			A			.55381E+01
			A			.52176E+01
			IA			.59498E+01
			IA			.65832E+01
			IA			.65207E+01
			IA			.55413E+01
			AI			.37639E+01
			A			.12737E+01
			A			.76250E-03
			A			.36250E-03
40			A			.17500E-03
			A			.87500E-04
			A			.37500E-04
			A			.12500E-04
			A			.12500E-04
			A			.00000E+00
			A			.00000E+00
			A			.00000E+00
			A			.00000E+00
			A			.00000E+00
50			A			.00000E+00
		IA				-.36420E+01
		A				-.47217E+01
		IA				-.44634E+01
		A				-.52162E+01
		A				-.61725E+01
		AI				-.65669E+01
		AI				-.61126E+01
		A				-.51299E+01
		A				-.55333E+01

	I	I	I	A	I	I	I	
60				A				.36250E-03
								.17200E-03
	-25	-15	-5		5	15	25	Y(1, J)
0								
I	I	I	I	A	I	I	I	-.87500E-04
I	I	I	I	A	I	I	I	.37500E-04
I	I	I	I	A	I	I	I	.12500E-04
I	I	I	I	A	I	I	I	.12500E-04
I	I	I	I	A	I	I	I	.00000E+00
I	I	I	I	A	I	I	I	.00000E+00
I	I	I	I	A	I	I	I	.00000E+00
I	I	I	I	A	I	I	I	.00000E+00
I	I	I	I	A	I	I	I	.00000E+00
10				A				-.17663E-01
I	I	I	IA		I	I	I	-.36589E+01
I	I	I	A		I	I	I	-.47198E+01
I	I	I	IA		I	I	I	-.44672E+01
I	I	I	A		I	I	I	-.52180E+01
I	I	I	AI		I	I	I	-.61731E+01
I	I	I	A		I	I	I	-.65673E+01
I	I	I	AI		I	I	I	-.61130E+01
I	I	I	A		I	I	I	-.51300E+01
I	I	I	AI		I	I	I	-.55533E+01
20				A				-.63232E+01
I	I	I	AI		I	I	I	-.66587E+01
I	I	I	AI		I	I	I	-.61469E+01
I	I	I	A		I	I	I	-.47169E+01
I	I	I	A		I	I	I	-.25402E+01
I	I	I	I	A	I	I	I	-.10250E-02
I	I	I	I	A	I	I	I	-.48750E-03
I	I	I	I	A	I	I	I	-.22500E-03
I	I	I	I	A	I	I	I	-.11250E-03
I	I	I	I	A	I	I	I	-.50000E-04
30				A				-.25000E-04
I	I	I	I	A	I	I	I	-.12500E-04
I	I	I	I	A	I	I	I	.00000E+00
I	I	I	I	A	I	I	I	.00000E+00
I	I	I	I	A	I	I	I	.00000E+00
I	I	I	I	A	I	I	I	.00000E+00
I	I	I	I	A	I	I	I	.00000E+00
I	I	I	I	A	I	I	I	.00000E+00
I	I	I	I	A	I	I	I	.00000E+00
I	I	I	I	A	I	I	I	.00000E+00
40				A				.00000E+00
I	I	I	I	A	I	I	I	.25766E+01
I	I	I	I	A	I	I	I	.46942E+01
I	I	I	I	IA	I	I	I	.59656E+01
I	I	I	I	IA	I	I	I	.62366E+01
I	I	I	I	A	I	I	I	.54061E+01
I	I	I	I	A	I	I	I	.51548E+01
I	I	I	I	IA	I	I	I	.59199E+01
I	I	I	I	IA	I	I	I	.65690E+01
I	I	I	I	IA	I	I	I	.65140E+01
50				A				.55361E+01
I	I	I	I	A	I	I	I	.52176E+01
I	I	I	I	IA	I	I	I	.59498E+01
I	I	I	I	IA	I	I	I	.65632E+01
I	I	I	I	IA	I	I	I	.65207E+01
I	I	I	I	IA	I	I	I	.55413E+01
I	I	I	I	AI	I	I	I	.37039E+01
I	I	I	I	A	I	I	I	.12737E+01
I	I	I	I	A	I	I	I	.76200E-03
I	I	I	I	A	I	I	I	.36250E-03

1983-84 USAF-SCEEE RESEARCH INITIATION PROGRAM

Sponsored by the

AIR FORCE OFFICE OF SCIENTIFIC RESEARCH

Conducted by the

SOUTHEASTERN CENTER FOR ELECTRICAL ENGINEERING EDUCATION

FINAL REPORT

A NOVEL FDM SYSTEM FOR OPTICAL FIBER COMMUNICATION

Prepared by: Dr. Charles S. Ih

Academic Rank: Professor

Department and
University: Electrical Engineering Department
University of Delaware

Research Location: Air Force Rome Air Development Center

Date: December 1984

Final Report

on

A NOVEL FDM SYSTEM FOR OPTICAL FIBER COMMUNICATION

by

Charles S. Ih
Department of Electrical Engineering
University of Delaware
Newark, De. 19716

ABSTRACT

The transmission characteristics of a novel FDM (Frequency-Division-Multiplexing) system have been investigated. This novel system uses a SWAOM (Standing-Wave-Acousto-Optical-modulator) to produce the carrier frequency and the information is directly modulated onto the laser diode. We have also studied the non-linear characteristics of optical fiber communication systems in general and discovered that the non-linearity is inherent to the optical modulation process. The non-linearity causes serious intermodulations which have prevented FDM systems being widely used for multi-channel information transmission. Our studies show that the proposed FDM system is less susceptible to the non-linear distortion and therefore potentially more efficient in implementing FDM systems.

Final Report

on

A NOVEL FDM SYSTEM FOR OPTICAL FIBER COMMUNICATION

by

Charles S. Ih

University of Delaware

Newark, De. 19716

1.0 Introduction

We proposed to investigate a novel FDM (Frequency-Division-Multiplexing) system for optical fiber communications (OFC). This novel system [1,2] can be implemented in several ways. One implementation uses a SWAOM (Standing-Wave-Acousto-Optical-modulator) to produce the carrier frequency and the information is modulated directly onto the laser diode. Another approach incorporates a Mach-Zehnder interferometer with a TWAOM (Traveling-Wave AOM) and injection-locked lasers [1,2]. Because of the time limitations, We have investigated only the first system. The results are applicable to the second system.

Our objectives were to build and to evaluate the new modulation system and to study its operational characteristics. The important tasks to be accomplished were to study the system nonlinearities and to improve high frequency detections. We have

built a transmitter using the new technique and a receiver employing a parallel resonant circuit as the load to the photo detector. The system performed very well and better than we had ever expected. The picture received by the new system is better than a similar system using the conventional modulation method (Fig. 1) when compared side-by-side in the laboratory. Even though we cannot yet give quantitative comparisons between the two systems, nevertheless, we are confident that this system is suitable for simultaneous analog and digital information transmissions. Previous experiments were done using only digital signals.

We also studied the non-linearity of optical transmission systems. We discovered that the non-linearity, therefore the intermodulation, is resulted from the way the optical signal is modulated and to a less degree on device non-linearities widely believed in the literatures. We have done some experiment to verify our theory. The experimental results are consistent with the theory. This suggests that the new system is more suitable for FDM applications than the conventional method.

2.0 The SWAOM System

The novel modulation system is shown Fig. 2. The laser beam is directly modulated by signal. In our experiment, the signal is a standard TV video analog signal. The modulated laser beam is collimated by the lens L1. A wavefront-correction-optics

(WCO) may be used to correct the wavefront distortion of the laser diode. We did not use the corrector. The collimated laser beam is then passing through a standing wave AO modulator (SWAOM) at the Bragg angle. The diffracted beam is focused by lens L2 and coupled into the optical fiber for transmission. The SWAOM is driven (CW) at one half of the TV carrier frequency. We used channel 6 (82 - 88 MHz). So the SWAOM was driven at 42 MHz. The SWAOM effectively modulate the optical beam at the right carrier frequency (84 MHz) for channel 6. A photo-detector with a parallel resonant circuit as its load was used to detect the signal. We believe the parallel resonant circuit "neutralizes" the capacitance of the photo detector and improved the signal quality. The output of the photo-detector conforms with a standard TV signal which can be either first amplified or connected directly to a TV set. The pictures received are shown Fig. 3. (The original picture was in color).

This system is effectively a DSB (Double-Side-Band) modulation with the carrier being suppressed. We shall call this modulation system as the DBM (Double-Beam-Modulation). The system offers many advantages and we shall discussed some of them later in this report.

An Intra-Action Model SWM-40 modulator (SWAOM) was used for the experiment. The video source was from an Apple II+ computer. We also used TV cameras and other video signal sources and obtained equally good results. The 0.5-Km multimode fiber had an

attenuation of 5 - 6 db/Km at the .83 um.

3. Non-linearity Study

One of the objectives of our studies was to investigate the non-linear characteristics of optical fiber transmission systems in general and for the proposed system in particular. The presence of any system non-linearity will not only distort the signal, but also for a FDM system it introduces severe intermodulations. The source of these intermodulations has widely believed in the current literatures to be from device non-linearities. We have looked this problem from a different point of view and discovered that the non-linearity is of a more fundamental nature than simply from the device non-linearities. We will present a simplified description here.

In electrical circuits and/or communication systems, the electrical quantities which are to be modulated are either the voltage or the current. The same quantities are transmitted according to known physical laws through the medium, such as a cable or in the open air and received and then detected. Therefore it is clear that if there is a non-linearity in the system, it must be from the devices in the transmitter or the receiver. The situation is different in optics. The quantity that can be detected and converted to an electrical signal (current or voltage) is the light intensity but not the amplitude of the electric or magnetic field. Therefore in order to reproduce an un-

distorted electrical signal, we must modulate the intensity of the light linearly, but not the amplitude of the fields. Since the intensity is proportional to the square of the field, the latter is therefore modulated to the square root of the modulating signal. Since it is the fields that propagate and obey the Maxwell' equations, we should look the propagation properties from this point of view.

Indeed, if we look from this point of view, the optical fiber is inherently non-linear. This non-linearity is particularly exemplified in a multi-mode fiber system. A simple explanation is given below. We are now in the process of preparing a paper on this subject.

For a multi-mode fiber system, the information bandwidth is limited by modal dispersions. In electrical communications, we have accustomed to transmit information up to the system's band limit. We continue to operate the optical fiber system in the same fashion. In an optical fiber system, since the electrical field is not linearly modulated, signal transmission near the band limits will introduce distortions. The explanation is simple. A non-linearly modulated electric field contains many higher order harmonics. These high frequency components (harmonics) are attenuated more by the fiber system and therefore not received equally by the receiver. The electric field without the higher order harmonics results in non-linear distortion in the output. If more than one signal are transmitted, the signals re-

ceived suffers not only distortions but also severe intermodulations. This is one of the more important objectives we proposed to investigate. To the best of the author's knowledge, the source of the non-linearity of the optical fiber system has not been discussed in any details in the public literatures.

If the theory we suggested is correct, we can test this easily with experiments. It is clear that if the bandwidth of the fiber system is much large than the maximum frequency of the signal, there should be no or very little non-linearities (except from the electronic devices). On the other hand, if the maximum signal frequencies extend near or belong fiber cut-off frequency, the distortion will become very severe. This is also true for intermodulations. Since the intermodulation is more easily detected, we have designed experiments to verify the theories.

4. Intermodulation Investigations

When two or more signals are send through a non-linear system, such as the optical fiber system, new frequencies are produced. These frequencies cause interferences and are undesirable. This is known as intermodulation. Measuring the intermodulation, i.e., measuring or detecting the new frequencies, is a very efficiency way to evaluate a system's linearities. As we have discussed previously, at low frequencies, an optical fiber system can be considered linear. The non-linearity increases as the signal frequencies approach the cut-off frequency.

The experiments we did were the following. We set up a conventional optical fiber system which consists of a laser diode transmitter, an optical coupler, 1 km (or 400 m) fiber with a cut-off frequency of 50 MHz-km, and an optical detector/amplifier. The test equipment includes signal generators and spectrum analyzers. The experiments were conducted in the following fashion. We first combine two signals of low frequencies (10 kHz and 30kHz). The combined signal was analyzed with the spectrum analyzer. Now appreciable intermodulation was observed. The combine signal was then applied to the input of the laser diode transmitter to modulate the laser beam. The laser beam was then coupled into the optical fiber of 1 km in length and the output at the receiving was detected. The detected signal was analyzed again with the same spectrum analyzer. Again no appreciable intermodulations were observed. The results are shown in Fig. 4. Experiments were also performed at a higher frequency of 70 MHz using slight different method. The original 70 MHz signal was first analyzed to assume that it did not contain spurious harmonics. The detected signal was again analyzed. Large harmonics were indeed observed at 140 and 210 MHz (the second and third harmonics). The results are shown in Fig. 5 and consistent with the theory. We altered the high frequency experiments because we did not have the suitable signal generators and spectrum analyzer at hand at that time. However, at a higher frequency the distortions were quite large and thus could be more easily measured. In all the experiments, we carefully adjusted

the operating point of the laser, so that it was operated in a linear region.

Since all the electronic equipment was operated under nearly identical conditions except at different frequencies, we conclude that the frequency dependent non-linearities must be from the optical fiber system. It is clear from the above discussions that when a laser is modulated at higher frequencies, the signals are subjected to more distortions than those at lower frequencies. In conventional FDM systems, the optical carrier must be modulated at very high frequencies in order to accommodate more channels. This inevitably introduces severe intermodulations which can no longer be tolerated in a practical system. This is why such conventional FDM systems have never been put into practical use. The conventional FDM system has only been used for FM modulated channels. The FM modulated FDM system requires more bandwidth and needs special transmitting and receiving equipment and therefore, is incompatible with the standard TV transmission systems.

On the other hand, for the newly proposed modulation scheme, the optical carrier is modulated at only baseband frequencies and the high frequency carrier is generated by the SWAOM. This high frequency generation method is fundamentally different from the electronic modulation methods. The high frequency is the result of the interference of two optical waves created by the SWAOM. This is electronically equivalent to the suppressed carrier modulation (Double-Side-Band modulation

without the carrier). For the conventional modulation system, more than one half of the laser energy is in the unnecessary carrier which is, however, generated automatically. We therefore conclude that the new modulation system is a more efficient way for optical FDM systems. It has lower non-linear distortions because the laser is modulated at much lower frequencies. It has lower detection noise because the unnecessary carrier is automatically suppressed. A more detailed theory and implementation techniques are being developed.

5. Conclusions and Discussions

We have investigated a new FDM scheme suitable for optical fiber communications. The FDM system employs a novel modulation technique using a SWAOM. The new modulation method was compared with the conventional direct current modulation method. The new method appeared to produce better pictures. The new method also has lower distortion and possible lower noise. We plan to study the related theories in more details and also to do more experimental work. We plan to submit a proposal for the investigations in the near future.

References

1. U.S. Patent No. 4, 210,803, July 1, 1980. Inventor: C.S. Ih
assignee: the University of Delaware.
2. C. S. Ih, Feasibility and Requirements for Dispersion Compensation in Coherent FOC, Optical Waveguide Sciences - Proceedings of the International Symposium, Kweilin, China, June 20 - 23, 1983 Martinus nijhoff Publishers, 1983.

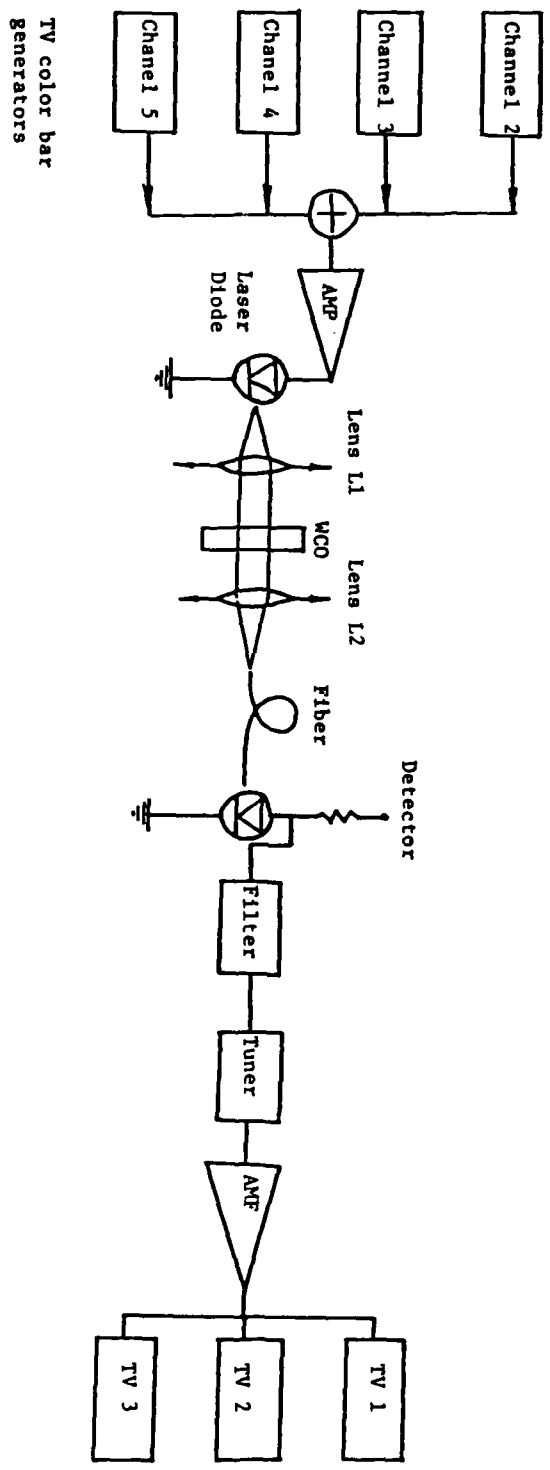


Fig. 1. Conventional optical FDM system.

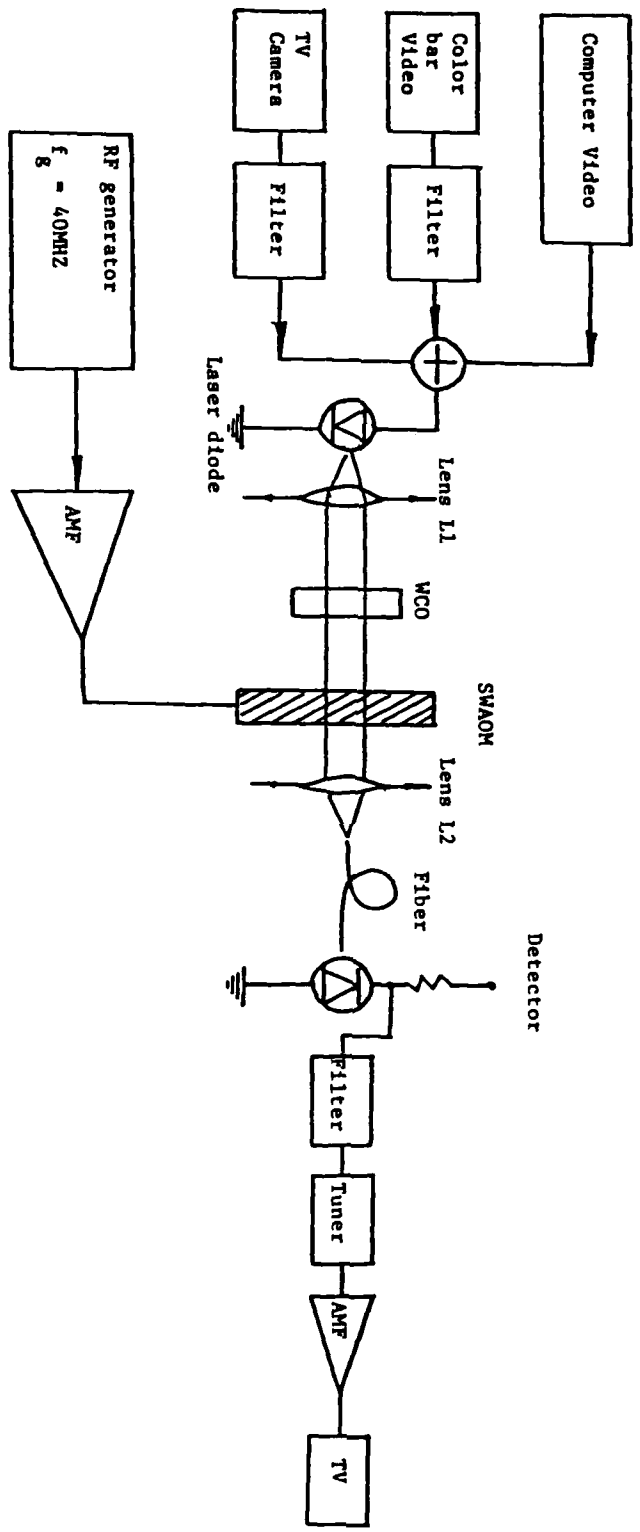
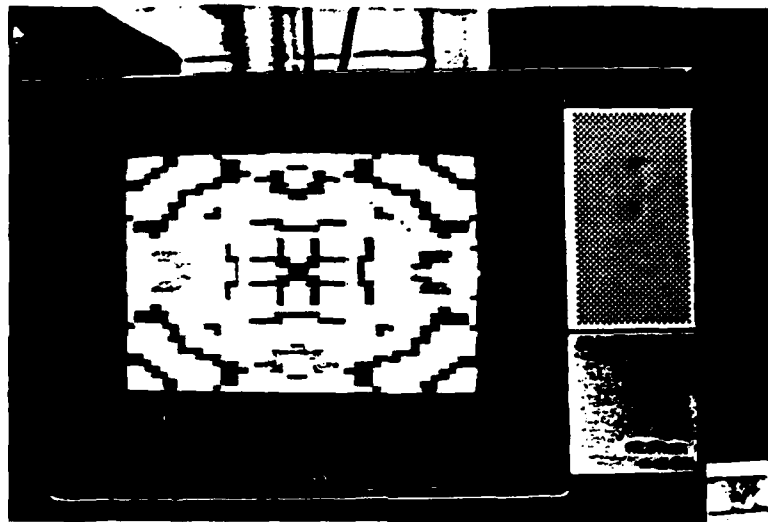


Fig. 2. A novel modulation, SMAOM, optical FM system.



(a)



(b)

Fig. 3

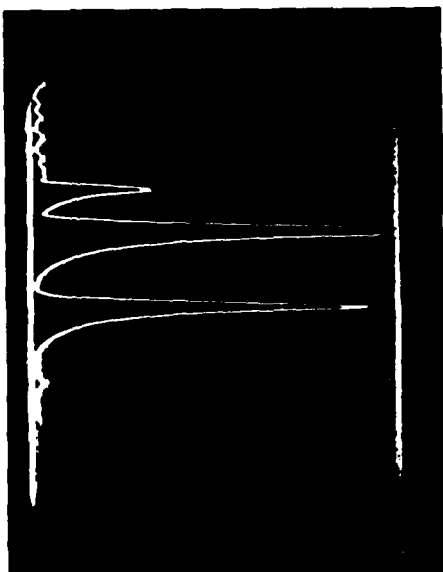
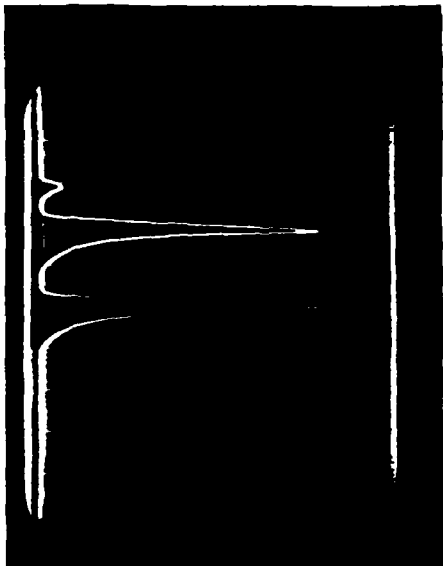
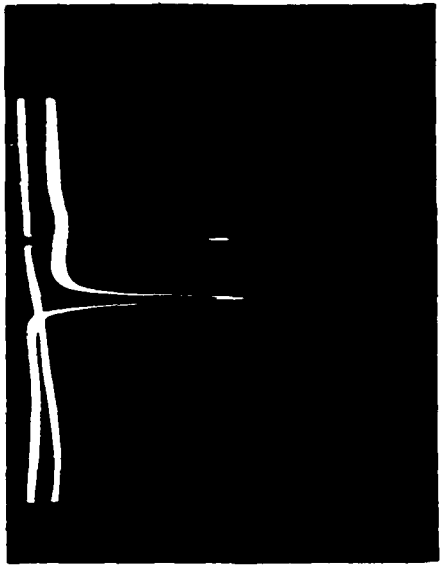
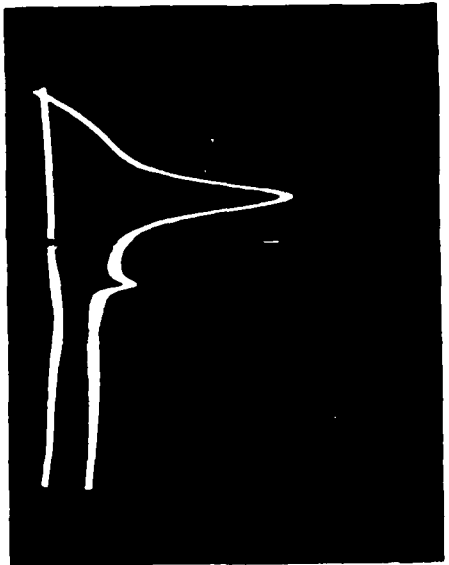


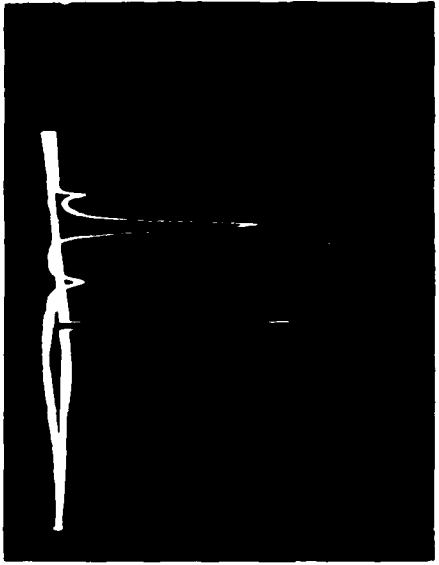
Figure 4



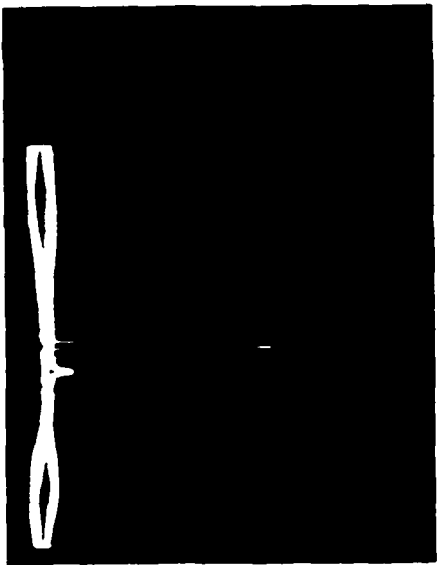
(a)



(b)



(c)



(d)

Fig. 5

1983-84 USAF-SCEEE RESEARCH INITIATION PROGRAM

Sponsored by the

AIR FORCE OFFICE OF SCIENTIFIC RESEARCH

Conducted by the

SOUTHEASTERN CENTER FOR ELECTRICAL ENGINEERING EDUCATION

FINAL REPORT

AN EXPERIMENTAL STUDY OF THE PORTABLE LIQUID-COOLED SYSTEM

Prepared by: Dr. Amir Karimi

Academic Rank: Assistant Professor

Department and
University: Engineering Division
University of Texas at San Antonio

Research Location: Air Force School of Aerospace Medicine

Date: December 1984

AN EXPERIMENTAL STUDY OF THE PORTABLE LIQUID-COOLED SYSTEM

by

Amir Karimi

ABSTRACT

The thermal properties of a portable liquid system have been investigated. The cooling system consists of an ILC-Dover liquid-cooled garment (Model 00016814-D1-01) (LCG), a heat sink/heat exchanger unit (HSHE) and a circulating pump. The overall heat transfer coefficient for the LCG is determined using data from the experiments conducted on human subjects. The requirements for cooling capacity of the HSHE is stated. It is proposed that the heat exchanger should consist of a single shell-multiple aluminum tube pass heat exchanger. The shell contains a frozen medium (ice). The freezing and melting process is fully discussed and relations for the evaluation of the freezing time and melt down period is developed. The arrangement of tubes for the enhancement of the freezing time is configured.

This study suggests that the ILC-Dover garment provides sufficient cooling to satisfy the demands of the groundcrew personnel. It is also shown that the thermal effectiveness of the HSHE unit drops sharply during the initial state of the melt down. It is proposed that the design of heat exchanger should be based on the final stages of melting process.

Acknowledgements

I would like to thank the Air Force System Command, the Air Force Office of Scientific Research and the Southeastern Center for Electrical Engineering Education for providing both funding and the opportunity for me to conduct research under a Research Initiation Program at The School of Aerospace Medicine, Brooks Air Force Base. I would also like to thank the staff of The School of Aerospace Medicine for support during the course of this research. I particularly would like to thank Maj. Charles Flick for his valuable suggestions and discussions and Mr. Chen for his invaluable help and assistance in conducting experiments.

AN EXPERIMENTAL STUDY OF THE PORTABLE LIQUID-COOLED SYSTEM

I. INTRODUCTION

In the event of chemical warfare, the USAF groundcrew personnel are expected to perform their assigned combat duties. A completely impermeable environment must be created to protect these personnel against chemical warfare agents. This requirement can be achieved either by encapsulating the entire operational environment (macro-environment) or by encapsulating each individual groundcrew member in a micro-environment. It is already established that the latter is a more practical and cost effective method of operation. Therefore, the groundcrew personnel are required to wear chemical defense gear while performing their duties during chemical warfare situations.

Although the chemical defense attire is designed to protect the personnel from chemical agents, it also places additional thermal stress on the men, as the metabolic heat generated by the body cannot be directly dissipated into the environment.

Under normal conditions, the cooling of the body is by means of evaporation, convection, conduction and/or irradiation. The studies [1-3] have shown that conductive or liquid cooling provides the most effective method of cooling for the situation under consideration. In fact, the majority of recent efforts have been conducted in this area.

In this conductive method, a liquid-cooled vest is placed in direct contact with the body. The vest contains tubes or channel network panels which come into direct contact with the heat source (body). A cold liquid (cooler than the body temperature) circulates throughout the tubing channel network.

Heat will be conducted through the walls of tubing or channel network of the vest due to the temperature gradient between the body's skin temperature and the inner surface of the tubing. Depending on the relevant heat transfer parameters (surface temperature, liquid mean temperature, the length of tubing, available heat transfer area, etc.), a portion or all of the metabolically generated heat will be removed from the body, thereby reducing or alleviating the thermal stress.

For continuous cooling, it is clear that the cooling system must operate in a cycle. Because of the possibility of chemical contamination of the working fluid in an open cycle, it becomes necessary that the working fluid flow in a closed-looped, cyclic process. The heat gains by the traveling liquid must be removed at some point in the cycle. A refrigeration unit, thus, may be used to achieve this requirement.

Since the groundcrew personnel must be able to move about freely to conduct their combat duties, an additional constraint is placed on the design of the cooling system. Therefore, a portable cooling unit has been suggested. This cooling unit must be both portable and lightweight. Based on weight limitations on the heat sink and the liquid-cooled system as a whole, the

present trend in design is toward the use of re-useable ice packs as heat sinks.

The portable cooling systems, in general, consist of a vest, a pump, a heat exchanger unit (HEU) and a control display unit for the control of temperature and fluid flow. The working fluid is pumped through the vest and removes heat from the body. The warm liquid then enters the heat exchanger unit where it comes into indirect contact with ice (through a bladder, wrapped around the ice cartridge or through a tubing coil that is in contact with the melting ice).

In recent years, the efforts of investigators at the U.S. Air Force have been concentrated on evaluating the effect of cooling on humans by three (3) available portable cooling systems. These included the cooling system designed and manufactured by the Engineering Physics Department of the Royal Aircraft Establishment (RAE) in Farnborough, Hampshire; ILC Dover; and the Life Support Systems, Inc. (LSSI), Mountain View, California. The majority of studies conducted on these systems have dealt with the physiological effects of cooling on humans. The in-viability and impracticality of the ILC cooling system is discussed in [3, 4].

Current USAF efforts are directed toward the re-evaluation and design improvement of liquid-cooled systems.

II. OBJECTIVES

In a study conducted during the summer of 1983 at The School of Aerospace Medicine at Brooks Air Force Base (USAF SAM/VNC) we evaluated the "LSSI" cooling system. A number of design inadequacies were encountered which we reported in [5]. We also made recommendations for the improvement of the system.

We showed that each cartridge of ice used as a heat sink in the "LSSI" cooling system provided 340 kJ of cooling capacity (or 680 kJ of cooling capacity for the two ice cartridges used in the cooling system). We suggested that for the groundcrew personnel performing duties which fall in the range of medium to heavy work, (440-703 W metabolic heat output)[6], the heat sink in this system would provide only 16-26 minutes of cooling (before complete melting occurred) if all metabolically generated heat were removed.

The results of our experiments also indicated that under most favorable conditions, the "LSSI" vest could remove only 170 watts of generated body heat. Dissipation at this rate was not sufficient to relieve the thermal stress of groundcrew personnel performing moderate work. The experiments on personnel involved in some type of activity also showed that both the skin and rectal temperatures rose while this system was utilized. We also investigated other shortcomings of the LSSI system and reported them in [5].

Studies and experiments conducted on human subjects, using the

LSSI cooling system, have indicated that this system does not provide sufficient cooling power and comfort for the groundcrew personnel to conduct combat duties. The basic research conducted within the Crew Technology Division specifies that the liquid condition garment must be capable of removing up to 500 W (430 kCal/hr) of metabolic heat generated by the groundcrew personnel.

The recent efforts by the Crew Technology Division at Brooks Air Force Base have been directed toward the design of a new liquid-cooled system that can satisfy the cooling requirements of the groundcrew personnel. The staff at the Crew Technology Division have conducted a series of experiments on human subjects wearing the ILC Dover liquid-conditioned garment (Model 00016814-D1-01) [7]. The results of these experiments have shown that the ILC Dover is capable of removing up to 535 W (460 kcal/hr) of metabolically generated heat.

In the present effort, the study was divided into the following tasks:

- (1) Evaluation of overall heat transfer coefficient for the ILC Dover liquid-conditioned vest (Model 00016814-D1-01)
- (2) Design consideration of heat sink (heat exchanger)
- (3) Evaluation of the freezing time of the heat sink
- (4) Development of heat transfer relations
- (5) Determination of thermal effectiveness of the system

III. A BRIEF DESCRIPTION OF THE PORTABLE LIQUID-COOLED SYSTEM

The liquid-cooled system under consideration is a closed-loop,

man-mounted, fully portable system which consists of three main units: liquid-conditioned vest and hood; heat sink (heat exchanger unit); and pump and control valve. The liquid-conditioned vest and hood contain a series of short, parallel plastic tubing to be worn in direct contact with the skin. The heat sink (heat exchanger), the pump and the control valve are stationed on a back pack. The vest and hood are connected to the heat sink by an umbilical. The pump is powered by a small, rechargeable battery. This battery must provide at least one hour of continuous operational power.

The coolant fluid (mixture of water and antifreeze) is pumped through the tubing within the system and circulates through the vest, hood and heat sink-heat exchanger system. A schematic description of the system is sketched in Fig. 1.

IV. COOLING CAPACITY OF THE SYSTEM

The cooling capacity of the system is determined by the amount of ice present in the heat sink-heat exchanger unit. The Crew Technology Division specifies that the minimum heat capacity of the heat sink shall be 1280 Btu (1350 kJ). This will provide approximately 45 minutes of cooling at a rate of 500 W heat removal. The medium used in the heat sink is usually ice with some additive to prevent corrosion or to retard expansion in the solidification process. The heat sink, therefore, must have the capacity for at least 4 kg (8.9) of water in order to satisfy this requirement.

V. THERMAL EVALUATION OF THE VEST

The ILC Dover liquid-conditioned vest consists of a series of short tygon tubing parallelly connected. The inside and outside diameter of the tubes are 1/16" and 1/8", respectively. The pressure drop across the vest (without the hood and connectors) is 0.59 Psi at a flow rate of 1.0 l/min. The pressure drop for the vest with the hood and connectors is 1.5 Psi at 1.0 l/min flow rate.

A series of experiments were conducted by the staff at the Crew Technology Division of The School of Aerospace Medicine (Brooks Air Force Base) [7] on human subjects wearing this vest.

The vest was connected to an in-house manufactured heat sink-heat exchanger unit [8] in a closed system loop. A recirculating pump was used to supply the vest with liquid coolant. The coolant was a solution of 20% propylene glycol-80% water mixture. A flow meter was placed in the loop to monitor the flow rate. Two thermisters were used to measure the inlet and the outlet temperatures of the coolant. Additional surface thermisters were placed beneath the vest to monitor the skin temperature. The inlet temperature, outlet temperature, skin temperature and coolant flow rate were observed and recorded periodically.

The rate of heat removal by the vest was calculated, using the relation:

$$\dot{q} = \dot{m} c_p (T_{out} - T_{in}) \quad (1)$$

where

- \dot{q} = the rate of heat removal
- \dot{m} = coolant mass flow rate
- c_p = specific heat of the coolant
- T_{in}, T_{out} = the vest inlet and outlet temperatures, respectively.

During the steady state circulation of the liquid coolant, the inlet temperature varied between 2° C and 12.5° C. The mean skin temperature during this period was in the range $25.5^{\circ}\text{C} \leq T_{sk} \leq 31.5^{\circ}\text{C}$.

The calculated rate of heat removal was in the range 97 to 450 kcal/hr (113-525 W) depending on the garment inlet temperature. Only the data corresponding to the inlet temperatures of 2° C to 6° C were considered in the ongoing analysis, since the higher temperatures indicated that the ice inside the heat sink-heat exchanger was probably completely melted.

The heat transfer rate also may be evaluated from the relation:

$$\dot{q} = UA (\text{LMTD}) \quad (2)$$

where

- U = the overall heat transfer coefficient of the vest
- A = the surface area of tubing in contact with the skin
- LMTD = the log mean temperature difference

$$\text{LMTD} = \frac{(T_{sk} - T_{out}) - (T_{sk} - T_{in})}{\ln [(T_{sk} - T_{out}) / (T_{sk} - T_{in})]} \quad (3)$$

where T_{in} , T_{out} , and T_{sk} are the inlet temperature, outlet temperature and skin mean temperature, respectively.

It is assumed that the skin temperature does not vary much along the contact area with the tubing. Therefore, combining equations (1), (2) and (3), the product of U and A can be written as:

$$UA = \dot{m} c_p \ln [(T_{sk} - T_{in}) / (T_{sk} - T_{out})] \quad (4)$$

The experimental data corresponding to the inlet temperatures in the range of 2°C to 6°C were used in Eq. (4) to evaluate UA . It was determined that in this range of inlet temperatures, the product UA has an average value of $16.64 \pm 2.69 \text{ W}/^{\circ}\text{C}$ ($14.31 \pm 2.31 \text{ kcal/hr.}^{\circ}\text{C}$).

VI. DESIGN CONSIDERATION FOR THE HEAT SINK-HEAT EXCHANGER UNIT (HSHE).

The Crew Technology Division specifications requires that the liquid-cooled garment (LCG) meet the following performance specifications:

- a) provide at least 1,000 Btu/hr (293 W) of cooling when the cooling system is adjusted for maximum cooling;
- b) the inlet temperature of the liquid coolant into the garment shall be less than 50°F (10°C);
- c) the coolant flow rate through the garment shall be 8 GPH (0.5 l/min);
- d) the pressure drop across the garment shall not exceed 10 Psi (69 kPa).

The experimental data on the ILC-Dover LCG indicates that this garment satisfies the above specifications. Therefore, this garment may be adopted for use in a liquid-cooled system and the thermal requirements of this garment shall be considered in the design of the HShe unit.

Harrison and Belyavin [9] have suggested that the efficiency of liquid-cooled garments in heat removal drops when skin temperature drops below 30° C. They argue that when the skin temperature drops below this, the blood vessels in human subjects contract, reducing the blood circulation, and hence reducing the rate of heat removal from the body's core. Thus, for maximum cooling effect, the skin temperature should be maintained in the range of 30-37° C.

The experimental data on the ILC-Dover liquid-cooled garment indicates that for the inlet temperature in the range 2° C to 6° C, the average skin temperature may be correlated as

$$T_{sk} = 27.8 + 0.26 T_{in} , ^\circ C \quad (5-a)$$

or

$$T_{sk} = 73.72 + 0.26 T_{in} , ^\circ F \quad (5-b)$$

It should be noted that the correlation of the average skin temperature data involves a degree of uncertainty. The average skin temperatures were computed from measurements made at only a few skin sites. However, the deviations between the temperature measurements at various sites were small. Thus, although equation (5) is not highly accurate, it provides a useful

approximation for the relation between T_{sk} and T_{in} .

Equation (5) suggests that to maintain the skin temperature above 30° C, the inlet temperature of the coolant into the garment shall not drop below 8.5° C. To provide a cooling effect, the temperature must also be less than 35° C.

The refreezing time period for the HSHE unit is an important logistic concern. Currently, the Crew Technology Division is in the process of developing a fully portable support system for the man-mounted, liquid-cooled system. This support system will be employed for the refreezing of the HSHE unit. The specifications for the refreezing system, therefore, must also be considered in the design of the HSHE unit. The heat sink must meet the following requirements during the refreezing process:

- a) the rate of heat removal shall be at least 1600 Btu/hr (469 W);
- b) the coolant fluid must be the same for both the portable and the support systems;
- c) the inlet temperature of the coolant into the heat sink shall be less than 15° F (-9.5° C);
- d) the coolant flow rate into the heat sink must exceed 50 GPH (3.2 l/min).

The heat sink exchanger unit used in the experiments conducted on the ILC-Dover garment was built in-house at The School of Aerospace Medicine. This single shell, 32 tube pass heat exchanger consisted of two parallel paths of 0.25 in. O.D., 0.18 in. I.D. aluminum tubing. Each path of tubing was 17.5 ft. long

and was formed in a series of U-shapes 8 in. high. The distance between two vertical branches of tubing was approximately 1 in. These tubings were enclosed in a container approximately 10 in. long and 5 in. wide. The container was insulated and was encased in a wooden box. Four kg of water (ice) were used in the container to provide a heat sink medium.

During the freezing period, the tube side of the heat exchanger was connected to a constant temperature bath containing a solution of 50% propylene glycol-50% water mixture. During the freezing period, an attempt was made to maintain the temperature of the bath at -5°C . A pump was used to circulate the coolant through the tubing at a rate of 0.75 l/min. An average of 2 hours and 40 minutes was required to completely solidify the water in the container.

For a given coolant inlet temperature, the rate of heat removal decreases with an increase in the thickness of the ice crust around the tubing. Therefore, the arrangement and the orientation of the tubing in the heat exchanger unit greatly affects the freezing time. To illustrate this point, let us compare the tubing configuration in two heat exchanger units. Horizontal cross sections of tubing in two heat exchanger units are shown in Fig. 2. In Fig. 2(a) the vertical tube branches form a network of squares, while in Fig. 2(b) the center of the tubes form a network of equilateral triangles. In each case, the distance between the center of the two nearest tubes is indicated by p . The shaded area represents the contribution of each tube in the freezing process. r is the distance between the center of

the tubes and the point that freezes last in the heat exchanger. In Fig. 2(a), $r = \sqrt{2} p/2$ and in Fig. 2(b), $r = \sqrt{3} p/3$. It can readily be shown that the shaded area in Fig. 2(a)

$$A = R^2 [2 (r / R)^2 - \pi] \quad (6)$$

and the shaded area in Fig. 2(b)

$$A = R^2 [3 \sqrt{3} (r/R)^2 / 2 - \pi] \quad (7)$$

where R is the outer diameter of the tube. For practical purposes, it is clear that the values of $r/R \geq (\sqrt{2})^{1/2}$ for the first heat exchanger and $r/R \geq [2\pi / (3\sqrt{3})]^{1/2}$ for the second heat exchanger.

The comparison of Eqs. (6) and (7) indicates that the formation of solid per unit length of tubing is larger in the second heat exchanger than the first, if the value of r and R are the same in both heat exchangers. This suggests that the tubing configuration in Fig. 2(b) enhances the complete solidification time. In fact, the tubing arrangement in Fig. 2(b) produces the most efficient heat exchanger since the last point to freeze in the heat exchanger is at equal distance to the centers of all adjacent tubing.

VII. HEAT TRANSFER RELATIONS USED IN THE DESIGN OF HEAT SINK-HEAT EXCHANGER UNIT

When a sub-freezing coolant is passed through the tubing in a heat exchanger filled with a heat sink medium (water), a layer of

ice will form on the outer surface of the tubes. The temperature gradient between the liquid coolant and water in the heat exchanger results in heat flow from the water towards the subfreezing coolant fluid. The removal of the latent heat of solidification, at the liquid-ice interface, is equal to the heat transferred to the coolant if we neglect the heat capacities of the tubing wall and the ice crust. We further assume the liquid to be at freezing temperature. The removal of the latent heat of fusion results in continuous growth of the ice layer around the tubing. This process proceeds until the solidification of water in the heat exchanger is complete.

The temperature distributions for the solidification and melting process around a cylinder are shown in Fig. 3.

If we consider uniform physical properties throughout the solid shell (negligible change of enthalpy), it can be shown that the time, t , required to form a layer of ice of thickness, δ , can be represented by

$$t_s = \frac{\rho_f h_{if} r^2}{2 k_i (T_f - T_b)} \left\{ \ln(r/R_o) + [1 - (R_o/r)^2] \right. \\ \left. \times [(k_i/k_t) \ln(R_o/R_i) + k_i/(R_i \bar{h}_c) - 1/2] \right\} \quad (8)$$

where

- ρ_f = the density of freezing liquid
- h_{if} = the latent heat of fusion for freezing liquid
- k_i, k_t = the thermal conductivities of ice and tubing wall, respectively

- R_i, R_o = the inside and outside radii of tubing, respectively
 r = $R_o + \delta$
 T_f = the freezing point temperature of the heat sink medium
 T_b = the bulk temperature of the circulating coolant
 \bar{h}_c = the average heat transfer of the circulating fluid

For the melting process, a similar equation may be developed and the melt down period may be represented as

$$t_m = \frac{\rho_i h_{if} r^2}{2 k_f (T_b - T_f)} \left\{ \ln(r/R_o) + [1 - (R_o/r)^2] \right. \\
 \left. \times \left[(k_f/k_t) \ln(R_o/R_i) + k_f/(R_i h_c) - 1/2 \right] \right\} \quad (9)$$

where

- ρ_i = the density of frozen medium
 k_f = the thermal conductivity of melt

Equation (8) represents the minimum solidification time since the change of enthalpy was neglected through the solid shell (assumed $c_{pi} \Delta T / h_{if} \ll 1$). The real solidification time is always greater than the one presented by Eq. (8). Martin [10] has suggested an empirical correction relation to calculate the real solidification time from the minimum values calculated by the "quasi steady-state solutions". For cylindrical coordinates this relation can be expressed as

$$t_{s,real}/t_{s,min} = 1 + \frac{1}{2} \left(\frac{Bi}{1 + Bi} \right)^{2/3} \\
 \times \left(\sqrt{1 + \frac{4}{Ph}} - 1 \right) \quad (10)$$

where Bi and Ph are biot and phase change numbers, respectively. For the cylindrical case under study, the dimensionless quantities can be represented as

$$Bi = \frac{(k_t / k_i)}{\ln(R_o/R_i) + k_t/(R_i \bar{h}_c)} \quad (11)$$

and

$$Ph = \frac{\int_f h_{if}}{\rho_i C_{pi} (T_f - T_b)} \quad (12)$$

where C_{pi} is the specific heat of the frozen medium.

The evaluation of the real melt down period is more complicated since, in addition to the change of enthalpy, natural convection occurs in the molten media. However, for practical application, Eq. (9) provides a reasonable approximation for the melt down period. The heat transfer coefficient, \bar{h}_c , in Eqs. (8) and (9) depends on the flow characteristics of the circulating fluid in the tube. For the smallest inside tube diameter ($D_i = 0.065$ in.) and a flow rate of up to 5.0 l/min (78 GPM), the Reynolds number, falls below 10,000. Reynolds number is defined as

$$Re_D = \rho u D / \mu$$

where ρ , u , and μ are the fluid density, average velocity, and viscosity respectively. $Re_D < 10000$ characterizes the fluid flow in the laminar and transition regimes. To obtain turbulent flow, either one must increase the flow rate or reduce the tube diameter, which in either case increases the pumping requirements

of the heat exchanger.

In the transition regime (Re_D between 2,300 and 10,000), the fluid flow is highly unstable and the values for the heat transfer coefficient and friction factors vary considerably from system to system. Thus, it is suggested that the heat transfer equipment be designed so that it operates outside the transition regime [11]. Therefore, only laminar fluid flow treatment was employed in the design of the heat sink/heat exchanger unit. Depending on the fluid properties and tube configurations, the following quantities were used to evaluate the heat transfer coefficients, \bar{h}_C .

- a) for laminar, fully developed isothermal pipe [12]

$$\bar{Nu}_D = \bar{h} D / k = 3.66 \quad (13)$$

if $L/D > 0.05 Re Pr$

where D , L , k and Pr are insidetube diameter, tube length, fluid thermal conductivity and Prandtl number,

$$Pr = \mu c_p / k ,$$

respectively.

- b) for laminar, thermal entry length isothermal pipe [13]

$$\bar{Nu}_D = 1.86 [Pe D/L]^{1/3} (\mu_b / \mu_w)^{0.14} \quad (14)$$

if $L/D < 0.05 Pe$ and $(Pe D/L)^{1/3} (\mu_b / \mu_w)^{0.14} \geq 2.0$.

μ_b and μ_w are the fluid viscosities evaluated at bulk temperature and wall temperature, respectively. Pe is the pecllet number and is defined as

$$Pe = Re Pr$$

With the exception of μ_w all other properties in Eqs. (13) and (14) are evaluated at average bulk temperature.

The pressure drop in a fully developed laminar flow in a pipe ($L/D > 0.05 Re_D$) can be evaluated from the relation

$$P = \rho \frac{u^2}{2} [f (L/D) + \sum K] \quad (15)$$

where u is the average flow velocity, K is constant for minor losses (bends, elbows, etc) and the friction factor, f , for fully-developed flow is defined as

$$f = 64 / Re_D \quad (16)$$

VIII. COOLANT SELECTION

The coolant fluid must possess a melting point that is lower than the freezing point of the heat sink medium so it does not freeze when the system is in operation. Therefore, a coolant that consists of a solution of water and some antifreeze agent can meet this requirement if water is used as the heat sink medium. There are a number of antifreeze solutions available commercially. We considered solutions of propylene glycol-water mixture to be utilized as liquid coolant. The freezing points for 10, 20, 30, 40 and 50% by weight pure-propylene glycol agent are 27, 18, 8, -7, and -25 degrees Fahrenheit, respectively. However,

the Crew Technology Division specifications required that the freezing point of the coolant should not fall below -20° F. Therefore, a solution of 40% propylene glycol-60% water may be used as the working fluid to satisfy the above requirements. The following linear relations were developed to express the variation of specific gravity, specific heat and the thermal conductivity of this coolant fluid as a function of operating mean temperature.

The specific gravity may be expressed by

$$SG = 1.052 - 2.4 \times 10^{-4} T \quad (17)$$

The specific heat may be evaluated from

$$c_p = 0.88 + 1.33 \times 10^{-4} T, \text{ Btu/(lbm.F)} \quad (18)$$

The thermal conductivity is represented by

$$k = 0.235 + 1.0 \times 10^{-4} T, \text{ Btu/(hr.ft.F)} \quad (19)$$

In Eqs. (17), (18) and (19) the temperature, T , is in $^{\circ}$ F.

Andrade equation [15] was used to correlate the viscosity of the coolant. The relationship between the liquid viscosity and the temperature is expressed as

$$\mu = 10^{-6} A \rho^{1/3} \times \exp (C\rho/T) \quad (20)$$

where A and C are constant and can be determined from known properties at two states, using the following relations

$$C = \frac{\ln (\mu_1 / \mu_2) + 1/3 \ln (\rho_2 / \rho_1)}{\rho_1 / T_1 - \rho_2 / T_2} \quad (21)$$

and

$$A = 10^6 (\rho_1)^{-1/3} \exp (-C \rho_1 / T_1) \quad (22)$$

The viscosities of the coolant solution at 32°F and 68°F [14] were used in Eqs. (21) and (22) and the following values were obtained for A and C, respectively.

$$A = 0.804, (\text{lbm})^{2/3}/\text{s} \quad \text{or} \quad 0.4746, (\text{kg})^{2/3}/\text{s}$$

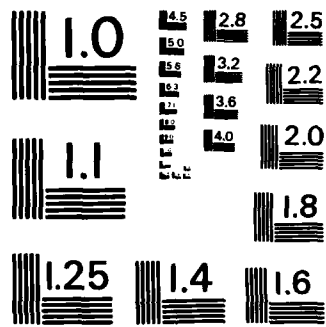
and

$$C = 58.36, \text{ft}^3\text{-R/lbm} \quad \text{or} \quad 2.024, \text{m}^3\text{-K/kg}$$

IX. THERMAL ANALYSIS OF HSHE UNIT DURING REFREEZING PERIOD

The time required to completely refreeze the heat sink medium is of great concern in chemical warfare situations. The complete solidification period depends mainly on the thermal capacity of the refreezer used in the support system. The thermal analysis of the refreezing system is beyond the scope of the present study. However, for a given refreezer, the tube size and arrangement in the HSHE unit greatly influence the complete solidification time. We have demonstrated that tube arrangements illustrated in Fig. 2(b) will enhance the efficiency of HSHE unit for the freezing process. Therefore, the ongoing analysis is based upon such tube configuration.

In preceding discussions we have suggested that extreme caution must be used in thermal analysis of heat transfer equipment that



MICROCOPY RESOLUTION TEST CHART
NATIONAL BUREAU OF STANDARDS - 1963 - A

operate within the transitional range of the fluid flow regime ($2300 < Re_D < 10000$). For a coolant fluid at 10°F and flow rates in the range 0.5 to 5.0 l/min the Reynolds number for fluid flow through a number of commercially available thin-walled aluminum tubes [14] were evaluated and the results are tabulated in Table 1. In order to operate in the laminar flow regime, Table 1 indicates that for a 1/8 in. OD tube, the coolant flow rate has to be below 3.0 l/min. At higher flow rates, the tubing in the heat HSHE unit must be split into two parallel paths.

If it is desired to base the design of the HSHE unit on the freezing time requirement, Eqs. (7,8) and (10-12) may be applied to determine the length and the size of tubing necessary to completely solidify the heat sink medium within this time constraint. We developed a computer program to achieve this goal. The pertinent relations for heat transfer during the freezing period (discussed in the preceding sections) were used in this program. The input variables included the coolant flow rate and operating bulk temperature, and the tube size (I.D. and O.D.). In addition, we based our calculations on a freezing period of one hour -- the time required for complete solidification of 4 kg of water in the HSHE unit.

For each combination of input variables, the length of tubing and the size of the heat sink (volume of ice plus the tubing) were evaluated. Selected results are presented in Figs. 4 and 5 for comparison. For a coolant flow rate of 1.5 l/min and coolant bulk temperatures varying in the range of -5°F to 25°F ,

Fig. 4 represents the size of the heat exchanger (volume of ice and tubing) as a function of the tube size (O.D.). Figure 4 indicates that the heat exchanger volume increases with the size of the tubing.

Based on one hour freezing time and a coolant flow rate of 1.5 l/min, Fig. 5 indicates that the size of the heat exchanger (or the volume of the tubing in the heat exchanger) increases with the coolant operating bulk temperature. Figure 5 also shows that the heat exchanger size increases with the tube size (O.D.). The dependency of the size of the heat exchanger on the tube size is more pronounced at higher coolant bulk temperature.

X. THERMAL ANALYSIS OF SYSTEM DURING MELT DOWN PERIOD.

When in operation, the HSHE unit must satisfy the thermal requirements of the ILC liquid-cooled garment. The rate of heat removal by the garment can be evaluated from the relation

$$\dot{q}_G = \epsilon_G m C_p (T_{sk} - T_{in}) \quad (23)$$

where

m = the mass flow rate of circulating coolant fluid

C_p = the specific heat of coolant fluid

T_{sk} = the average skin temperature (defined in terms of T_{in} by Eq.(5))

T_{in} = the inlet temperature of coolant into the garment

and ϵ_G is the effectiveness of the LCG and can be evaluated from the expression

$$\epsilon_G = 1 - \exp(-NTU)_G \quad (24)$$

NTU is the "number of transfer units" and is defined as:

$$NTU_G = (UA/m c_p)_G \quad (25)$$

It was shown that the average value of UA for the ILC garment is equal to $16.64 + 2.69 \text{ W/}^\circ\text{C}$.

It is clear from Eqs. (24) and (25) that the effectiveness of the LCG varies with the flow rate of the liquid coolant. The effect of coolant flow rate, in the range of 0.1-1.0 l/min, on the thermal effectiveness of the ILC liquid-cooled garment is illustrated in Fig. 6. The figure shows that the garment's effectiveness decreases with an increase coolant flow rate. Assuming an inlet temperature of 8.5°C and employing Eqs. (5) and (23-25), the rate of heat removal was evaluated for coolant flow rates in the range 0.1-1.0 l/min. The results are plotted in Fig. 7. It indicates that the ability of the ILC liquid-cooled garment to remove heat from the body increases with the liquid flow rate. Figure 7 also shows that for coolant flow rates greater than 0.8 l/min, the rate of heat removal by the garment does not change significantly with the flow rate.

The garment outlet temperature can be determined by combining Eqs. (1) and (23) and it is expressed as

$$T_{out} = \epsilon_G (T_{sk} - T_{in}) + T_{in} \quad (26)$$

The rate of heat transfer to the heat sink can be evaluated from the relation:

$$\dot{q}_{hx} = hx (T_{out} - T_i) \quad (27)$$

where T_i is the melting temperature of the frozen medium in the HSHE unit and

$$NTU_{hx} = (UA)_{hx} / m c_p \quad (28)$$

A is the heat transfer area of tubing in the heat exchanger unit and U is the overall heat transfer coefficient, expressed as:

$$U = \frac{1}{\frac{R_o \ln (r/R_o)}{k_f} + \frac{R_o \ln (R_o/R_i)}{k_t} + \frac{R_o}{R_i \bar{h}_c}} \quad (29)$$

where

R_i, R_o = the inside and outside diameter of tubing, respectively

r = the distance between the liquid-solid interface and the center of tubing

k_f, k_t = thermal conductivity of the melt and tube wall, respectively

\bar{h}_c = average convective heat transfer coefficient of the circulating coolant fluid.

Equation (29) suggests that the overall heat transfer coefficient, U , depends on the location of the liquid-solid interface moving boundary in the heat exchanger. Therefore, for a fixed coolant flow, the heat exchanger effectiveness varies with time as the melting process progresses in the heat exchanger unit and as the layers of melt surrounding the tubing

in the heat exchanger grows.

To satisfy the thermal requirements of the ILC garment, the rate of the heat transfer into the heat sink medium must be equal to the rate of heat removal by the garment. Thus, by combining Eqs. (23), (26) and (27), it can be shown that the heat exchanger effectiveness may be represented by:

$$\epsilon_{hx} = \frac{\epsilon_G (T_{sk} - T_{in})}{\epsilon_G (T_{sk} - in) + (T_{in} - T_i)} \quad (30)$$

Therefore, for a given garment flow rate and inlet temperature, the required effectiveness of the HSHS can be determined from Eq. (30). For a garment inlet temperature of 8.5° C, the variation of heat exchanger effectiveness with flow rate is shown in Fig. 6. The required heat transfer surface in the heat exchanger (or the length of tubing) thus can be determined by combining Eqs. (27) and (28).

For a coolant flow rate equal to 0.5 l/min and a garment inlet temperature equal to 8.5° C, the following quantities were determined for the garment:

$$\begin{aligned} NTU &= 0.514 \\ G &= 0.402 \\ q &= 279.9 \text{ W} \\ T_{sk} &= 30^\circ\text{C} \\ T_{out} &= 17.2^\circ\text{C} \end{aligned}$$

For various tube sizes, and based on the garment's thermal requirements we evaluated the minimum requirements for the length

and the volume of tubing in the heat exchanger unit at the start of the melt-down period (the liquid-solid interface at outside surface of tubes). The results are presented in Table 2. This table indicates that the size of the heat exchanger increases with the tube size. The quantities in Table 2 represent the minimum requirements for the design of a heat exchanger at the start of the melt down period. However, the effectiveness of the heat exchanger varies with time. The influence of the melting process on the effectiveness of the heat exchangers is presented in Fig. 8. This figure shows that effectiveness decreases with progress in the melting process.

Notice the sharp drop in the effectiveness of the heat exchanger unit during the initial stage of the melt down period. This suggests that the rate of heat transfer into the heat sink medium drops sharply after a short period of time. Therefore, a liquid-cooled system will not provide sufficient cooling if the design of the HSHE unit is based on the initial state of the melting process. Figure 8 also shows that the variation of effectiveness with time becomes insignificant during the final stages of the melting process. This suggests that, in the design of heat exchangers, the determination of the required length of tubing should be based upon the latter stages of the melting process.

Further observation of Fig. 8 indicates that the use of larger size tubes in the HSHE results in greater effectiveness values during the melt down process. However, we have shown that a larger size tubing increases the size of the heat exchanger. Therefore, there exists a trade-off: the effectiveness vs. the

heat exchanger size. Depending on the requirements, one might be favored over the other.

We have shown that the design of the HSHE involves a number of trade offs. The requirements of freezing time and the rate of heat removal during the melt down period are the greatest concerns of the engineer designing the HSHE unit. Questions arise as to whether the design should be based upon the time requirements for complete solidification of ice, or if it should be based on the rate of heat removal during the system's operational period. We feel that the ability of the liquid-cooled system to remove heat is the main purpose of the design and that it should be the primary concern of the designer to meet this requirement.

XI. SUMMARY AND CONCLUSIONS

- 1) The liquid-cooled system has been described as a closed-loop, fully portable system which consists of three main units:
 - liquid conditioned vest and hood.
 - heat sink/heat exchanger (HSHE) unit.
 - pump and flow control valve.
- 2) The experimental observations have revealed that the ILC Dover liquid cooled garment can provide up to 525 W of cooling power.
- 3) The effective overall heat transfer coefficient for the ILC liquid cooled garment has been determined to be equal to 16.64 ± 2.69 .

- 4) The proposed HSHE unit consists of a single shell, multiple tube pass heat exchanger. Four kg of ice in the shell side provides 1350 kJ of cooling capacity for the system. The coolant passes through the tube side of the heat exchanger.
- 5) The arrangement of tubes in the heat exchanger according to the Fig. 2(b) configuration minimizes the freezing time of the heat sink medium.
- 6) The freezing and melting processes in the heat exchanger have been investigated. Relations for heat transfer during these processes have been developed:
 - The freezing time is given by Eqs.(8) and (10).
 - The melt down period is expressed by Eq. (9).
- 7) The thermal effectiveness of the HSHE unit drops sharply during the initial stages of the melt down period.
- 8) The design of the HSHE unit should be based on the the final stages of the melting process.

REFERENCES

1. Vincent Iacono et. al. "Development of a Microclimate Cooling System for Combat Vehicles," United States Army Natick Research and Development Laboratories, Natick, Massachusetts, February 1982.
2. George C. Rannenber, "Study to Determine the CB Threat and Define Alternative Crew Protective Systems for the Advance Attack Helicopter" (AAH) (Vol. 1), United States Army Natick Research and Development Laboratories, Natick, Massachusetts, June, 1981.
3. S. Livingston et. al. "The Effect of Body Cooling on Aircrew in Hot Humid Environments", (Abstract), ASCC Working Party 61 Symposium, November, 1979.
4. D. M. Terrian and S. A. Nunneley, "A Laboratory Comparison of Portable Cooling Systems for Workers Exposed to Two Levels of Heat Stress," USAFSAM Technical Report, 1982.
5. A. Karimi, "A Thermal Evaluation of the 'LSSI' Liquid-Cooled System: An Engineering Perspective", USAF-SCEEE Summer Faculty Program, Final Report, Vol. 1/2, Report No.48, September, 1983.
6. P. Webb, Editor, "Biastronautics Data Book", NASA SP 3006, National Aeronautics and Space Administration, 1964.
7. Charles A. Flick, Frye, "Thermal Evaluation of Commercially Available Liquid-Cooled Garments", unpublished experimental data.
8. V. T. Chen, "Heat Exchanger Designed at USAFSAM, Brooks AFB."
9. M. H. Harrison and A. J. Belyavin, "Operational Characteristics of Liquid-Conditioned Suits", Aviation, Space and Environmental Medicine, August, 1978, pp. 994-1003.
10. H. Martin, "Melting and Solidification", Heat Exchanger Design Handbook, Hemisphere Publishing Co., 1983, Section 2.4.4.
11. F. Kreith, and W. Black, Basic Heat Transfer, Harper & Row Publishers, New York, 1980, pp. 248.
12. W. M. Kays, Convective Heat and Mass Transfer, McGraw-Hill, New York, 1966.

13. E. N. Sieder and G. E. Tate, "Heat Transfer and Pressure Drop of Liquids in Tubes," Ind. Eng. Chem., Vol. 28, 1936, p. 1429.
14. R. E. Bolz, and G. L. Tuve, Editors, CRC Handbook of Tables for Applied Engineering Science, 2nd edition, Chemical Rubber Co., Cleveland, 1976.
15. E. N. Andrade, "A Theory of Viscosity of Liquids, Part I", Philos. Mag. J. Sci., Vol. 17, pp. 497-511, 1934; Part II, Ibid, Vol. 17, pp. 698-732, 1934.

LIST OF TABLES AND FIGURES

- Table 1. The variation of Re_D with the flow rate and tube size for 40% propylene glycol-60% water solution at $10^\circ F$
- Table 2. The required length and volume of tubing at the start of the melt down period. Garment outlet temperature = $17.15^\circ C$, coolant flow rate = 0.5 l/min
- Fig. 1. The schematic description of a liquid cooled System
- Fig. 2. Comparison of two possible tube Arrangements in a HSHE unit
- Fig. 3. Temperature distribution in the solidification and melting process around a cylinder. For melting process positions of liquid and solid are exchanged and T_D is greater than T_i
- Fig. 4. Variation of HSHE size with the tube size (O.D.). See Table 2 for corresponding I.D. Coolant flow rate = 1.5 l/min.
- Fig. 5. Variation of HSHE size with the coolant operating temperature. Coolant flow rate = 1.5 l/min.
- Fig. 6. The influence of flow rate on thermal effectiveness.
- Fig. 7. The effect of coolant flow rate on the rate of heat removal by ILC Dover liquid cooled garment. $T_{in} = 8.5^\circ C$.
- Fig. 8. The influence of the melting process and the tube size on the thermal effectiveness of the HSHE unit. Coolant flow rate = 0.5 l/min.

Table 1. The variation of Re_D with the flow rate and tube size for 40% propylene glycol-60% water solution at 10° F

O.D.	1/8	3/16	1/4	5/16	3/8	1/2
I.D.	0.1275	0.19	0.2485	0.2485	0.311	0.436
Flow rate l/min	$Re_D = u_{ave} D_i /$					
0.5	410	209	140	107	87	61
1.0	820	418	280	214	171	122
1.5	1230	627	421	322	257	183
2.0	1639	836	561	499	343	244
2.5	2049	1045	701	536	428	306
3.0	2459	1254	841	643	514	367
3.5	2869	1463	982	750	600	428
4.0	3279	1672	1122	858	685	489
4.5	3689	1881	1262	965	771	550
5.0	4099	2090	1402	1072	857	611

Table 2. The required length and volume of tubing at the start of the melt down period. Garment outlet temperature = 17.15°C, coolant flow rate = 0.5 l/min

Tube Size, in.		Length	Volume
O.D.	I.D.	ft.	in. ³
1/8	0.065	16.08	2.37
3/16	0.1275	16.06	5.32
1/4	0.19	16.06	9.46
5/16	0.2485	16.06	14.78
3/8	0.311	16.05	21.28
1/2	0.436	16.05	37.82

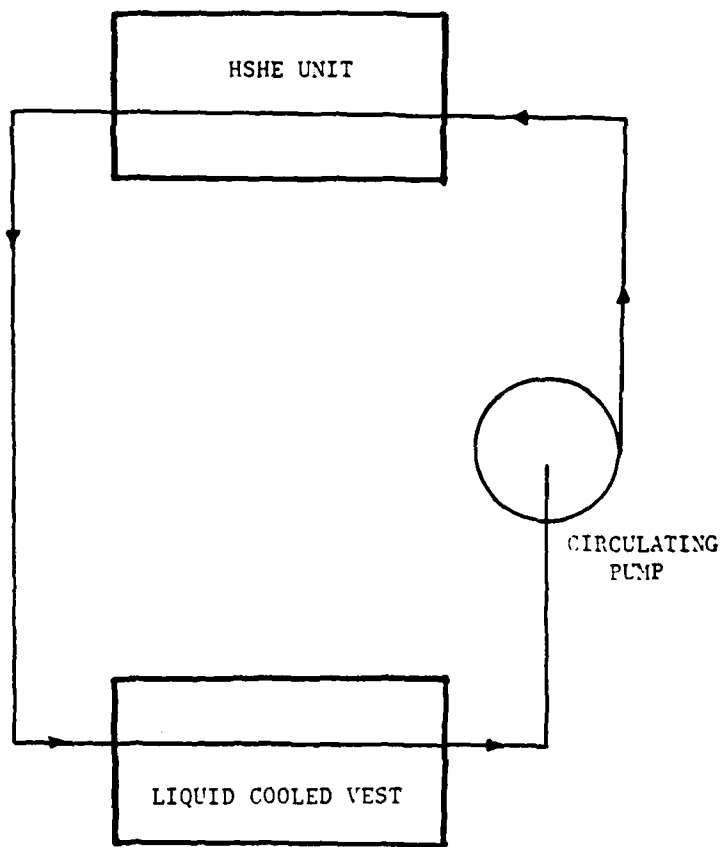
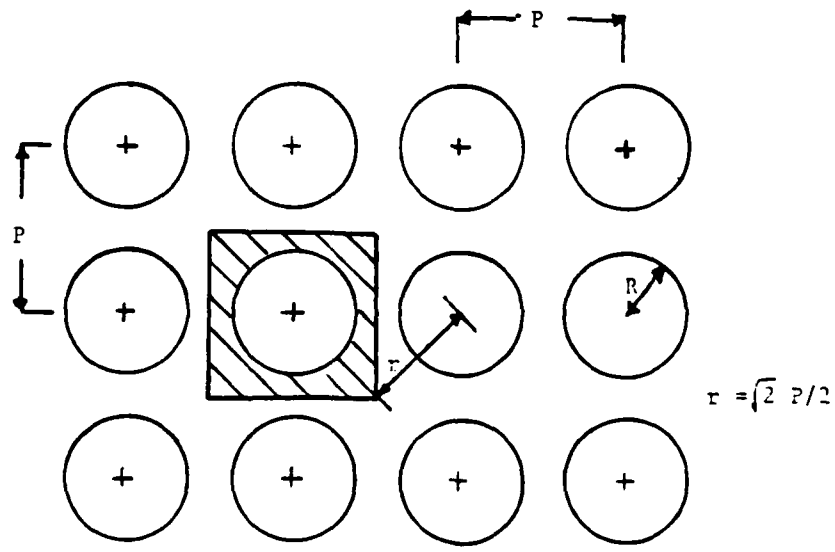
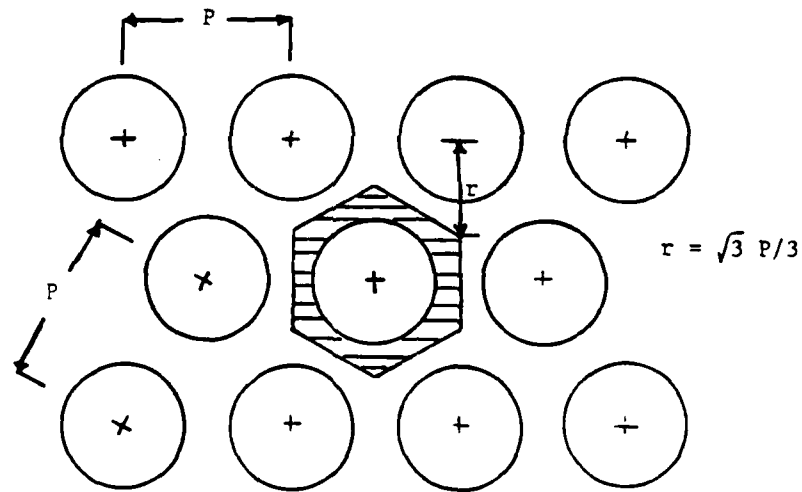


Fig. 1



(a)



(b)

Fig. 2

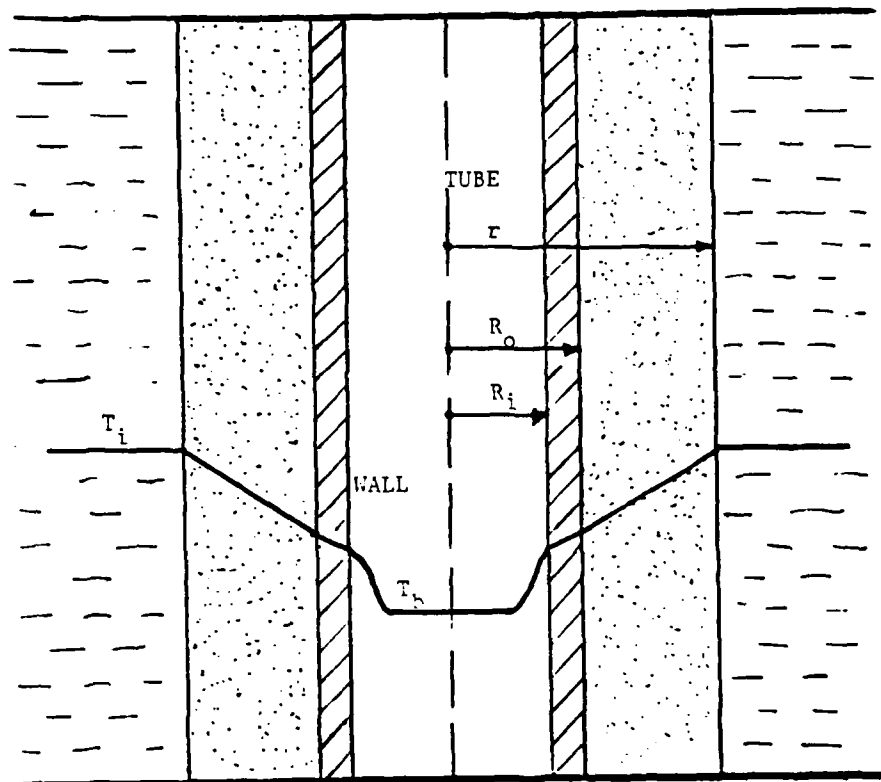


Fig. 3

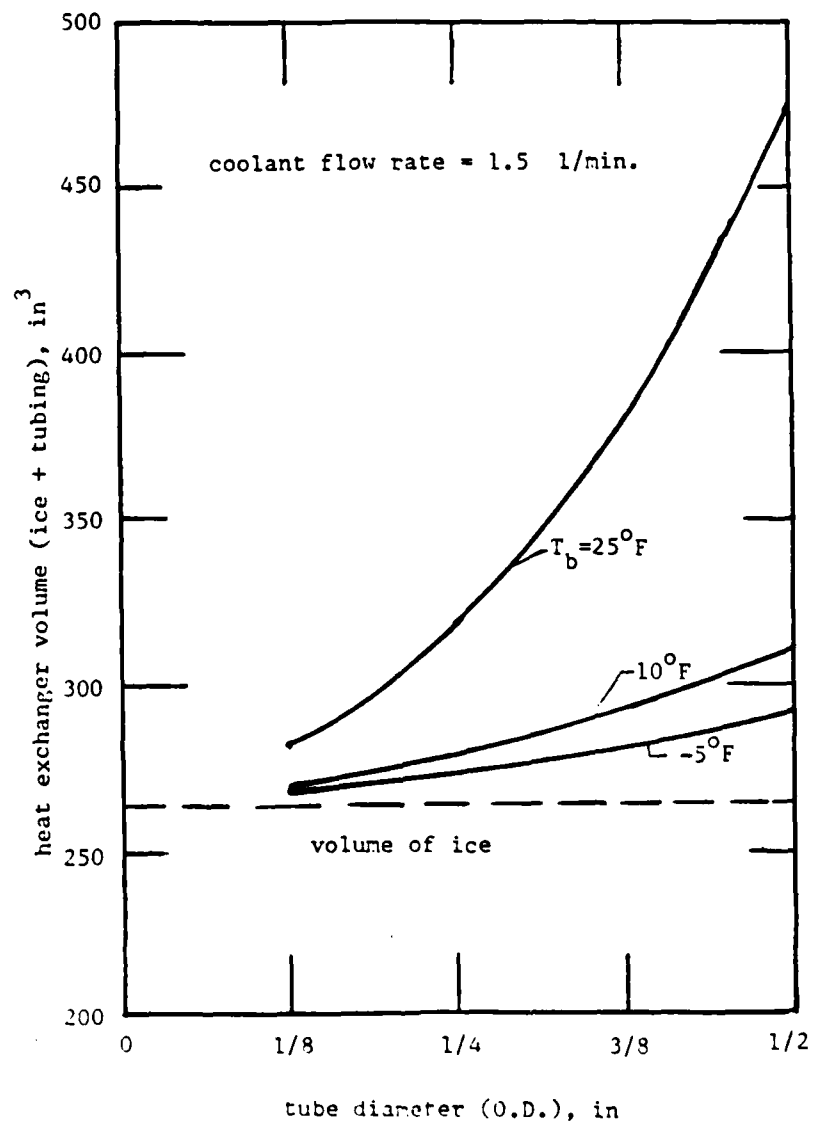


Fig. 4

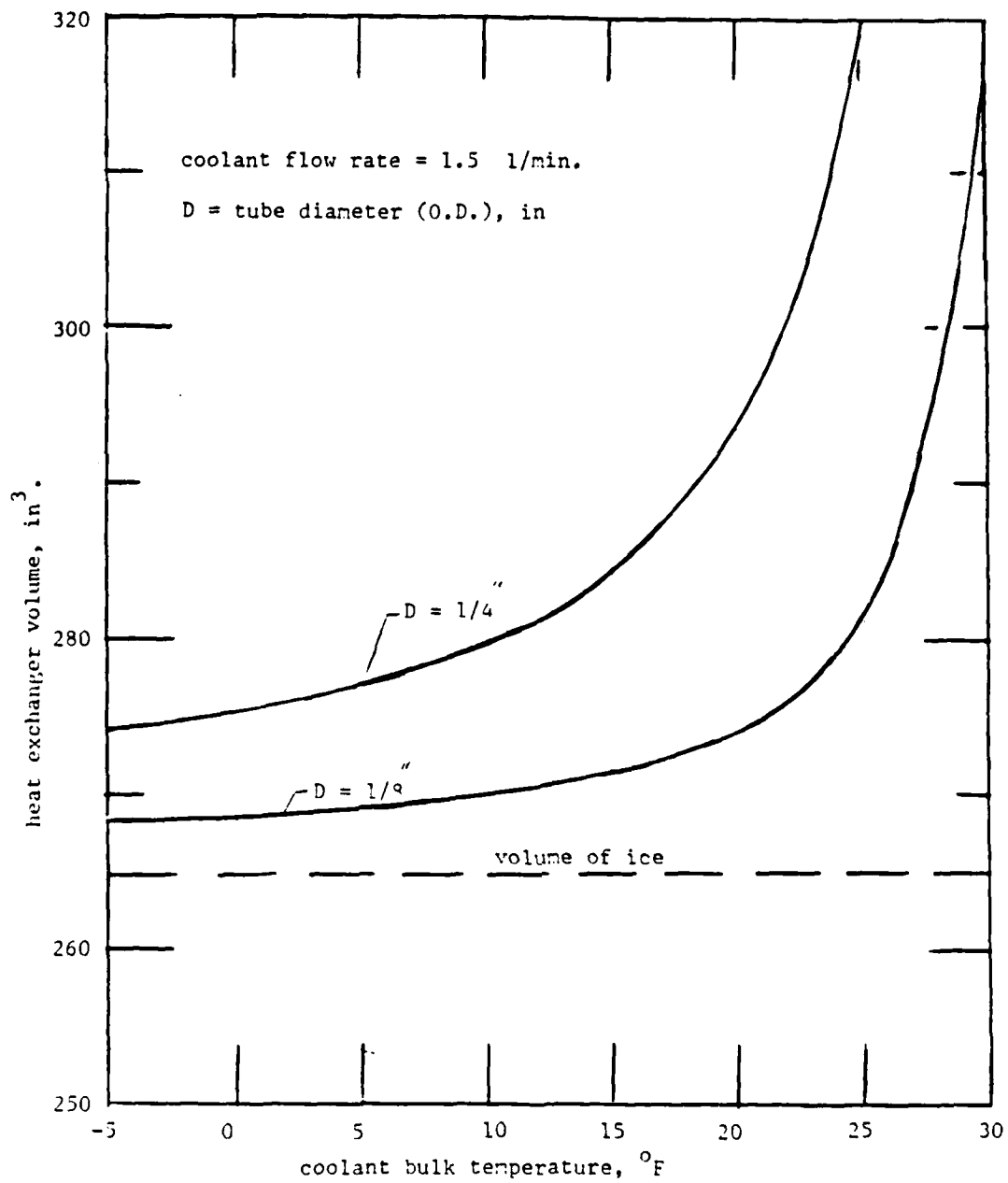


Fig. 5

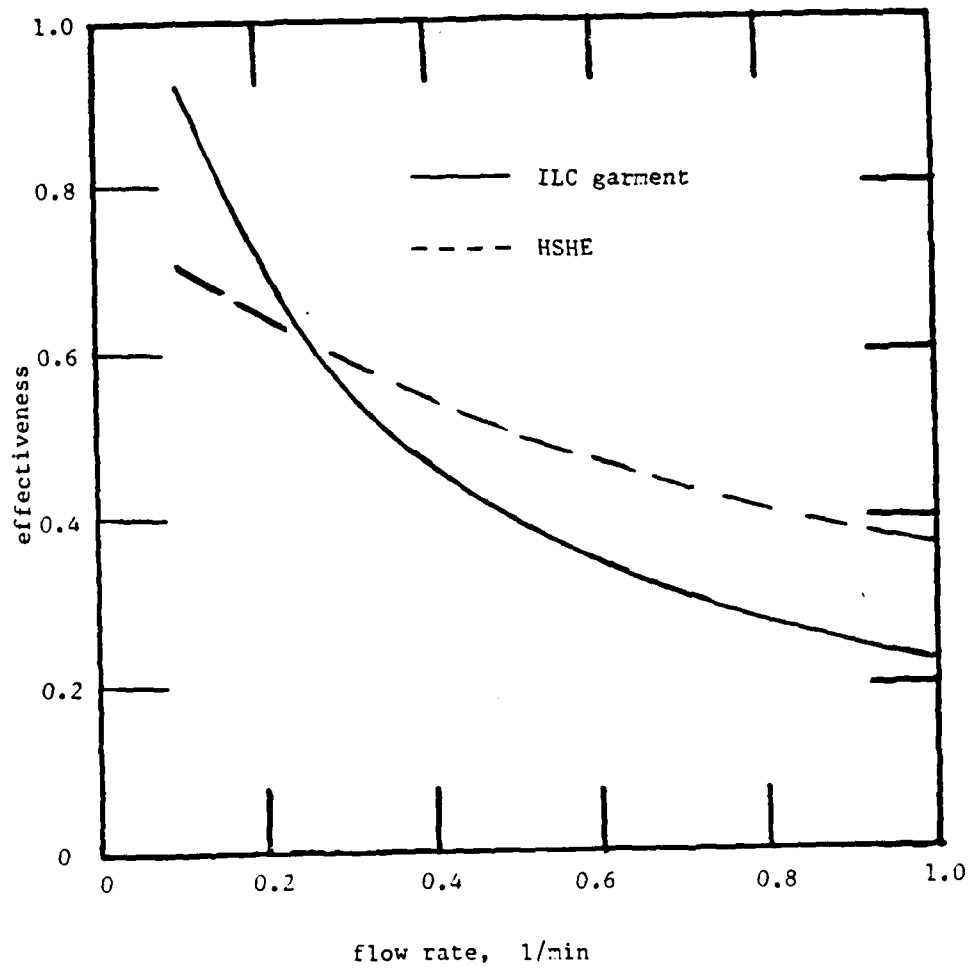


Fig.6

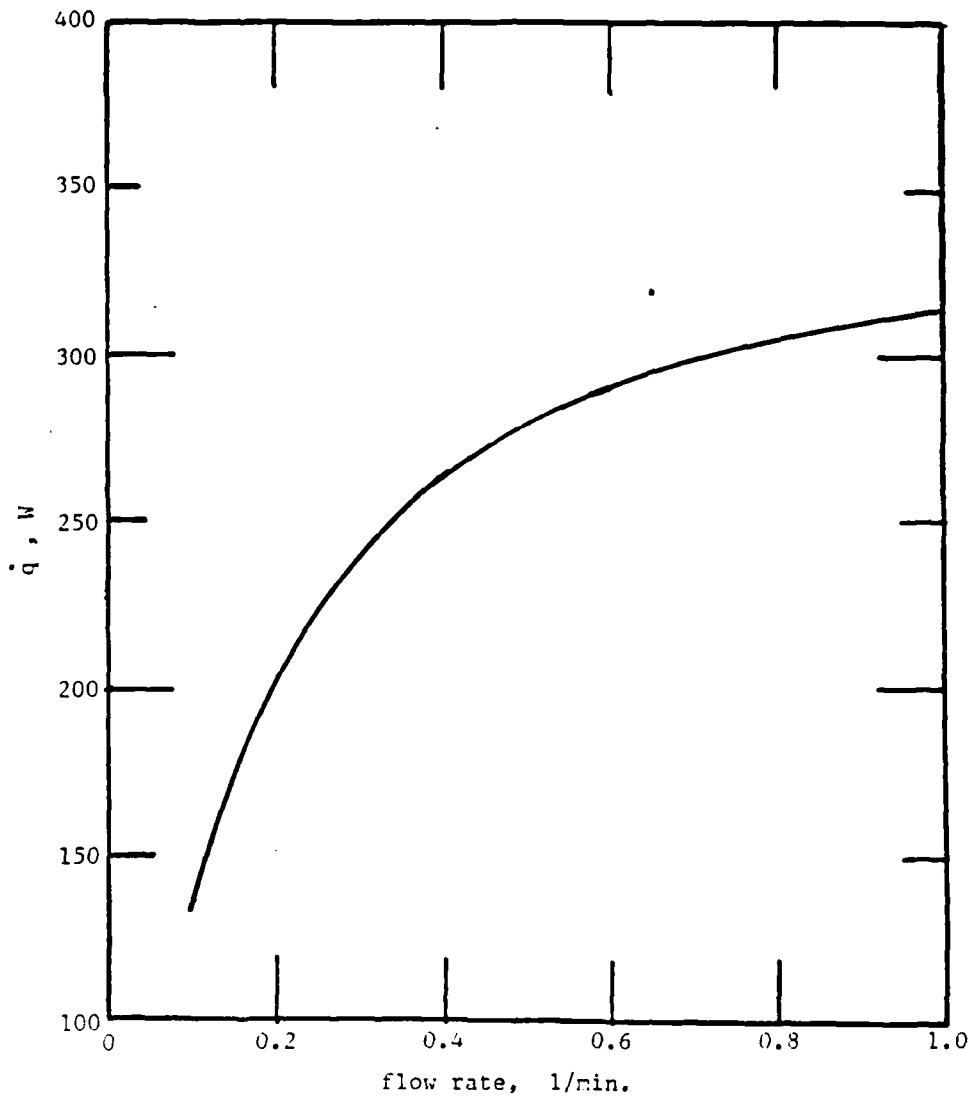


Fig. 7

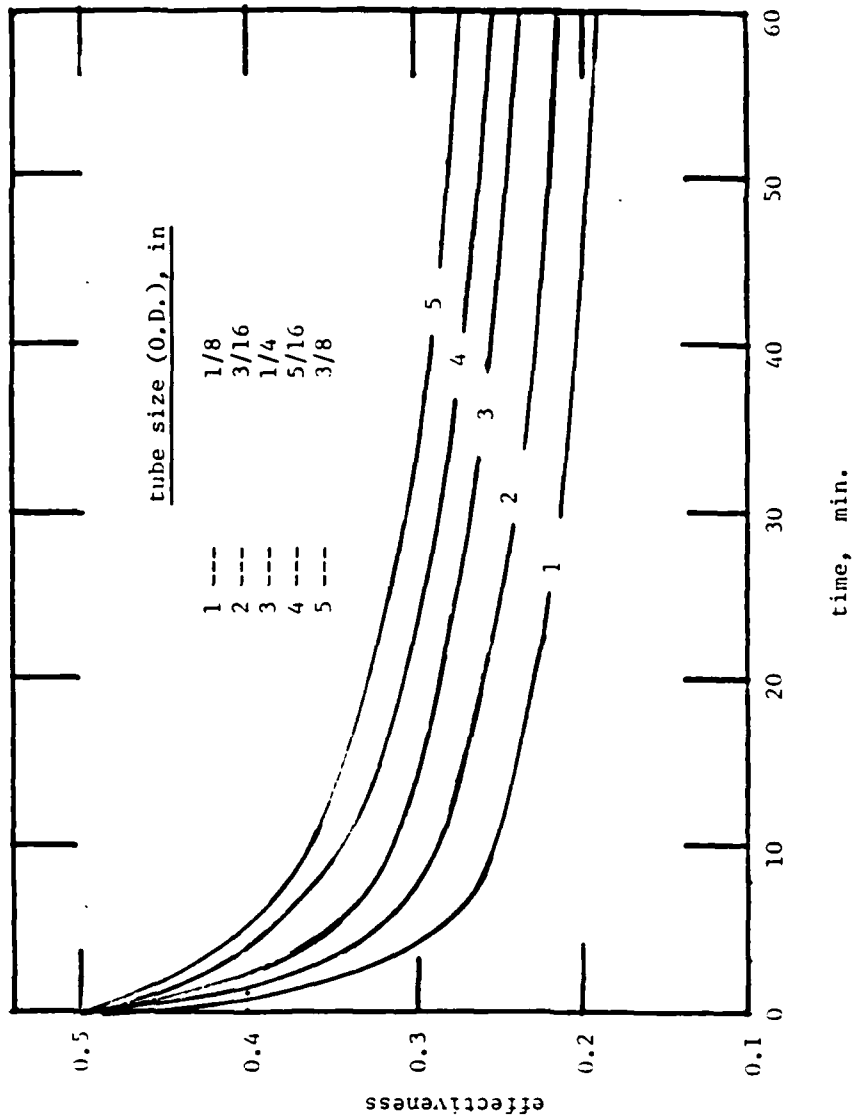


Fig. 8

1983-84 USAF-SCEEE RESEARCH INITIATION PROGRAM

Sponsored by the

AIR FORCE OFFICE OF SCIENTIFIC RESEARCH

Conducted by the

SOUTHEASTERN CENTER FOR ELECTRICAL ENGINEERING EDUCATION

FINAL REPORT

SHORT CRACK BEHAVIOR FOR FLAWS EMANATING FROM FASTENER HOLES

Prepared by: Dr. George Kirby

Academic Rank: Assistant Professor

Department and
University: Mechanical & Aerospace Engineering Department
West Virginia University

Research Location: Air Force Flight Dynamics Laboratory

Date: June 1984

SHORT CRACK BEHAVIOR FOR FLAWS
EMANATING FROM FASTENER HOLES

ABSTRACT

Apparent stress intensity factors are found for short fatigue cracks emanating from filled fastener holes by the Anderson-James backcalculation technique. Empirical formulas for the stress intensity factor as a function of crack length are also derived. For crack lengths of 0.01 inches (0.25 mm) to 0.2 inches (5 mm), the empirical formulas agree well with accepted solutions of cracks radiating from a hole in a plate loaded in remote tension. For crack lengths less than 0.01 inches (0.25 mm) the accepted solutions diverge from those derived herein. It is found that the stress intensity factor is independent of the crack initiation site, load level, fastener fit, load transfer through the fastener and drilling technique. Also, the "short crack effect" reported by other investigators was not corroborated.

ACKNOWLEDGMENT

Work performed on this study was supported through a grant by the Southeastern Center for Electrical Engineering Education under contract number F49620-82-C-0035. The data evaluated in this report was obtained from the "Fastener Hole Quality" report by Noronha, Henslee, Gordon and Wolanski. The authors would like to express their extreme gratitude to John Potter who provided invaluable guidance during the initial stages of an earlier but similar study and who first suggested this study. Finally, the authors would like to thank Sheri Smith for typing the final report.

I. INTRODUCTION

Most fatigue cracks originate in regions of high stress concentrations that are caused by notches, holes, or sudden changes in geometry. Fastener holes are one of the most common sources for the initiation and subsequent growth of fatigue cracks in aircraft structures. For example, the General Dynamics F-16 has over 250,000 fastener holes. Thus, the knowledge of the growth behavior of a flaw from such a stress concentration is self-evident.

Fracture mechanics provides a basis of quantifying the behavior of a crack, from the initiation of the flaw to the final failure of the structural component. The principal assumption of fracture mechanics is that the stress field surrounding the crack tip governs crack behavior. The stress field may be characterized by a quantity known as the stress intensity factor (SIF), which is a measure of magnitude of the stress field in the neighborhood of the crack tip. The SIF is a function of several variables, such as the crack length, the specimen geometry, and the type of loading.

The principal cause of failure of aircraft structural components is the fatigue growth of a microscopic crack to a critical crack size. Because of a major portion of a component's fatigue life occurs during the formation and growth of short cracks, considerable attention has been recently directed to the study of this kind of crack. Various studies suggest an irregularity in the growth of short cracks (1-11). It has been shown by several

authors (6,7) that the growth rate for a short crack is relatively high at the onset of crack propagation and then decreases for a period, after which monotonic growth rates are observed. This is contradictory to the smooth and monotonic growth rates observed for longer cracks (Figure 1).

This study examines the crack growth data from experiments performed by Noronha et al. (12). Using the data from the above work this study then addresses two questions. The first question asks what are the effects of the load level, fastener fit, load transfer and crack initiation sites upon the SIF of a flaw emanating from a fastener hole. The second question asks if conventional SIF solutions to cracks emanating from fastener holes indicate an apparent short crack effect (SCE). The SIF solutions obtained in this study are purely empirical and are derived by statistical methods.

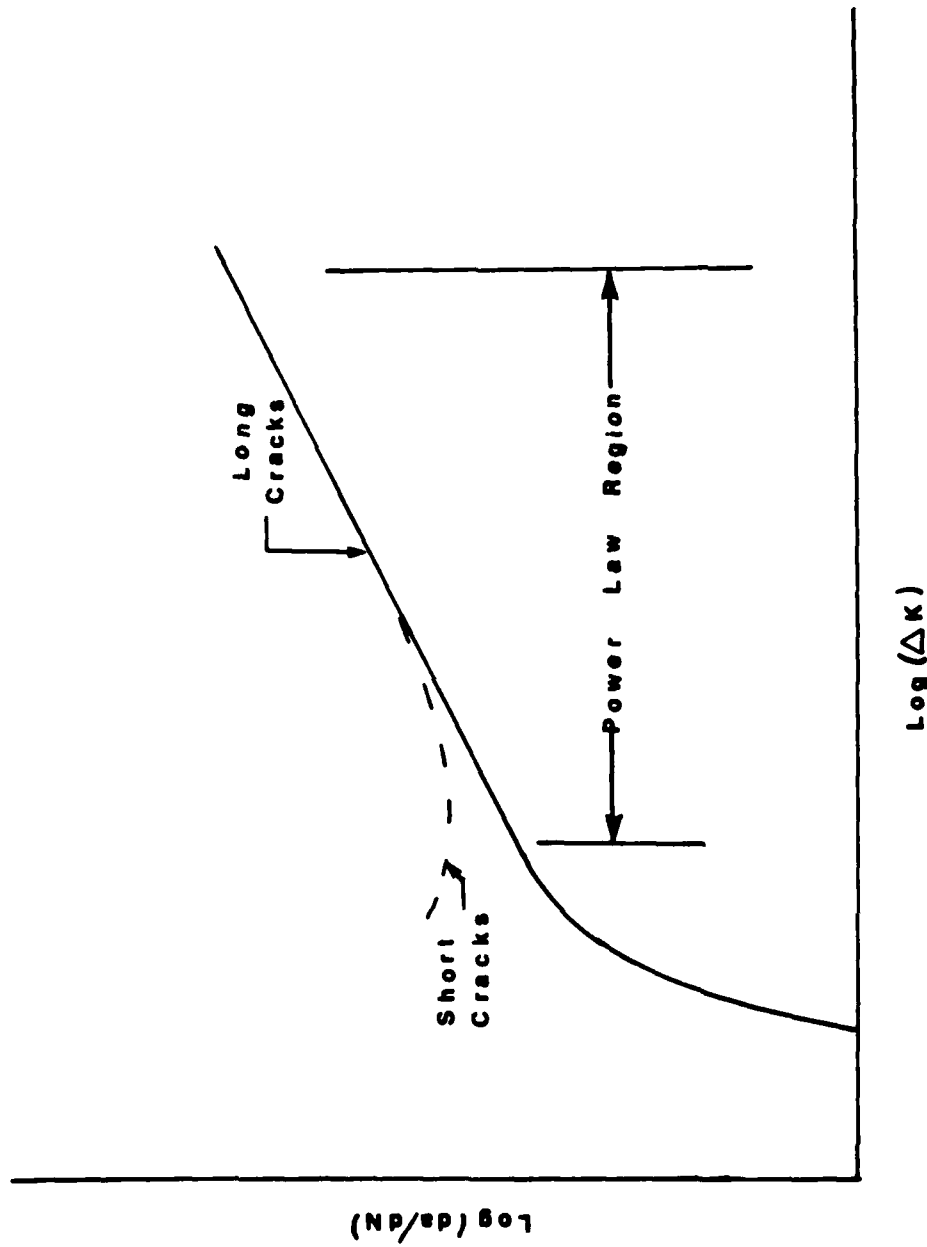


Figure 1. Long Crack Versus Short Crack Growth Behavior

II. LITERATURE REVIEW

2.1 RADIAL CRACK EMANATING FROM A FASTENER HOLE

The first analytical solutions of the stress field surrounding a radial crack emanating from a central circular hole in an infinite plate loaded in remote uniform tension were derived by Bowie (13), and Tweed and Rooke (14). Bowie's solution was based upon a complex mapping technique, while Tweed and Rooke's solution was based upon a Fredholm equation derived from integral equations.

Other solutions to the above problem that are empirical in nature are given by Grandt (15), and Kirby and Potter (11). Grandt represented the SIF solution by a least squares approximation to Bowie's solution. However, no attempt was made by Grandt to account for the three dimensional nature of the flaw. Kirby and Potter used a least squares analysis together with the Paris growth law to obtain an apparent SIF from data of crack length and flight hours. The data used in Kirby and Potter's study was obtained from Noronha et al. (12) and was for cracks emanating from a filled fastener hole with different pin clearances and load transfer through the fastener.

2.2 SHORT CRACK EFFECT (SCE)

Pearson (1) was one of the first investigators to report the short crack effect. He grew surface flaws with initial lengths

of 0.002 inches (0.051 mm) in BS L65 and DTD 5050 aluminum alloys under bending loads. It was found that when the observed crack growth rates were correlated with ΔK , they were not only faster than previously seen for longer cracks, but also displayed a much reduced if not nonexistent threshold. Since the crack front of these short center cracks were semicircular in shape, the conventional SIF for a semicircular crack (16) was used to reduce the fatigue crack growth data.

The SCE has subsequently been confirmed for different materials and conditions (2-7). Explanations to the SCE observed by various authors are crack closure (2,3), violation of the underlying continuum mechanics (4), and the plastic region surrounding the crack (6,7).

Cook and Edwards (2) studied short cracks in notched 2L65 aluminum alloy specimens under constant and variable amplitude loading. Measurements of corner cracks emanating from holes were taken down to crack lengths of 0.0004 inches (0.01 mm) using replicas. Under constant amplitude loading short crack anomalies were identified positively at zero mean stress. However, for fully repeated loading, these anomalies were almost completely absent. Clear short crack anomalies were also identified under variable amplitude loading. Edge cracks emanating from notches were studied by Fisher and Sherratt (3). Typical initial crack lengths of 0.003 inches (0.08 mm) were measured by eddy current methods. Fatigue crack growth was measured in two notched En3A and BS970 mild steel speci-

mens under conditions of constant and random amplitude loading. The analysis showed that constant-amplitude fatigue crack growth rates are principally related to ΔK and random loading fatigue crack growth rates were principally related to the root-mean-square value of ΔK . They also observed apparent high initial crack growth rates.

Another explanation of the SCE other than crack closure is the violation of the continuum requirements (4). It was shown that the use of conventional fracture mechanics concepts to characterize small cracks resulted in behavior which differed from that of long cracks. This difference was attributed to the breakdown of the underlying continuum mechanics assumptions. Thus, in the prediction of short crack growth, Hudak projected that conventional SIF solutions were doomed to fail. However, Lankford (5) tested hot rolled AISI 4340 steel specimens using fractography to measure crack growth rates. He found that by taking into account the debonded inclusions he could correlate the observed crack propagation rates with that predicted by linear elastic fracture mechanics (LEFM) over the entire growth rate region. The correlation was valid down to microstructural dimensions.

The plastic zone around crack tip has also been used to explain the SCE, Leis and Forte (6) studied the behavior of physically short cracks in notched aluminum and steel plates. They observed a decreasing and then increasing crack growth rates in the growth of physically short cracks. It appeared to be caused by the plastic

field at the notch and the control condition local to the crack tip. Leis and Galliher (7) also observed this behavior in 2024 aluminum alloy with initial crack lengths of 0.001 inches (0.025 mm). The solution for the SIF was determined by compounding SIF solutions for corner and through the thickness cracks.

Although the above studies indicate a SCE, there is contradictory evidence. This is seen from two separate sets of papers. El Haddad et al. introduced the notion of an effective crack length l_o (8,9). Other contradictory evidence is given by papers examining the data from a study by Noronha et al. (12).

El Haddad et al. (8) redefined the stress intensity factor in terms of the physical crack length plus an effective crack length l_o . Thus, if the SIF solution is used to correlate short crack results, the discrepancy between short and longer crack results is eliminated. Furthermore, if this effective length is incorporated into the solution then elastic and elastic-plastic fracture mechanics solutions can be modified to predict the SCE. Straight forward calculations of ΔJ values of the G40.11 and 1015 steel data were performed and the results were plotted against the crack growth rate (9). The data obtained from different notches and for different load levels shows excellent agreement with the long crack data for both 1015 steel and G40.11 steel. By recomputing both ΔK and ΔJ to include this l_o concept, a closer correspondence between long and short crack growth rates resulted. However, this technique

is subjected to two objections. First, because of the empirical nature of this effective crack length, it can not be used on a general basis to make short crack data consistent with the trends seen for long cracks. Second, no satisfactory physical significance has been ascribed to this empirical quantity, l_0 .

Noronha et al. (12) obtained data for cracks emanating from filled fastener holes under a 0% and 15% load transfer through the fastener. Because the crack that caused the failure was fractographically traced to its origin, crack lengths of 0.001 inches (0.025 mm) were routinely observed. It should be noted that the fastener holes in these specimens were not preflawed. Thus, the flaw growth behavior in the above study represented the growth behavior of cracks found in service. In a subsequent study using data from Noronha et al. (12), Potter and Yee (10) showed that the crack growth rates were smooth and monotonic and no SCE was observed. They suggested it may be possible that the preflaw procedure was responsible for the SCE seen by other investigators. In another study using the same data, Kirby and Potter (11) determined an empirical relationship between the crack length and an apparent SIF. The results showed that there existed an exponential relationship between the crack length and the apparent SIF. They also observed that the underprediction of the SIF for short cracks could cause an apparent SCE.

III. METHODOLOGY

3.1 FATIGUE TEST DATA

The basic crack growth data for the current study were obtained from the Noronha et al. study (12) which was designed to evaluate the influence of the fastener hole quality on the structural durability of a 7475-T7351 aluminum alloy. The load spectrum used was based upon a fighter load history. At fracture, the flaw causing the failure was fractographically traced to its origin. Fatigue crack growth data were collected periodically at constant time increments of 400 flight hours (the length of the repeating load block). The origination of the failure flaw was also recorded. From the above test, it was observed that flaws initiated from one of the following sites: the bolt hole, the chamfer corner, the radius corner or the mating surface (Figure 2). Four test series (QPF, XQPF, HYWPF, LYWPF) from the Reference 12 were examined. The QPF series had a 0% load transfer through the fastener. The Q stands for a Quackenbush Drilled/Reamed procedure which produced a clearance of 0.0005 inches, the P for proper drill speeds, coolant and feeds, and the F for fighter load history. The XQPF, HYWPF and LYWPF series were 15% load transfer through the fastener. The W stands for a Winslow Spacematic Drill procedure which produced a clearance of 0.002 inches, the H for a high stress level (40.8 ksi), and the L for a low stress level (30.4 ksi). All other test series

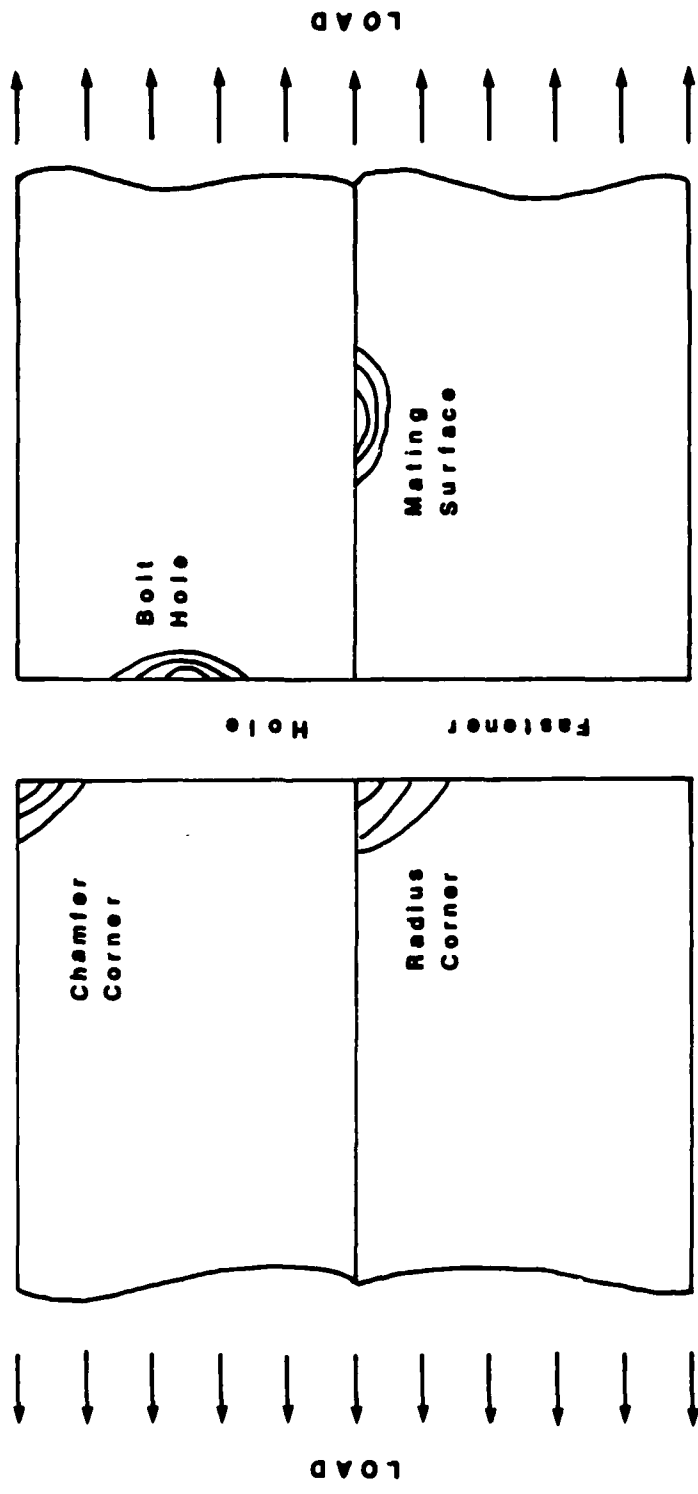


Figure 2. Crack Initiation Sites

had maximum load levels of 34 ksi. The YWPF series used an improved drilling technique in which the bit was allowed to rotate during extraction. This technique minimized the scratches induced on the bolt hole.

3.2 BASELINE DATA

The fatigue growth rate constants C and n were obtained from a study in Wilkinson and Potter (Figure 3). It should be noted that typical growth rates for the specimens examined in this study ranged from 10^{-7} to 10^{-4} inch/ft. hr. Thus, it was necessary to extrapolate the growth rate constants obtained from Wilkinson and Potter (17) to 10^{-7} inch/ft. hr. Examination of the growth rate versus crack length for the specimens studied indicated no abnormal behavior in the growth of these short cracks for the range of growth rates considered. Thus, the extrapolation above is justified. The material used by the above study was 7075-T651 aluminum. The baseline fatigue tests were performed under the same fighter load history spectrum as that in Noronha et al. study.

3.3 APPARENT STRESS INTENSITY FACTORS

The familiar Paris growth law (18) was used to obtain the apparent SIF from the fatigue crack growth data. The crack growth rate is related to the SIF by the following:

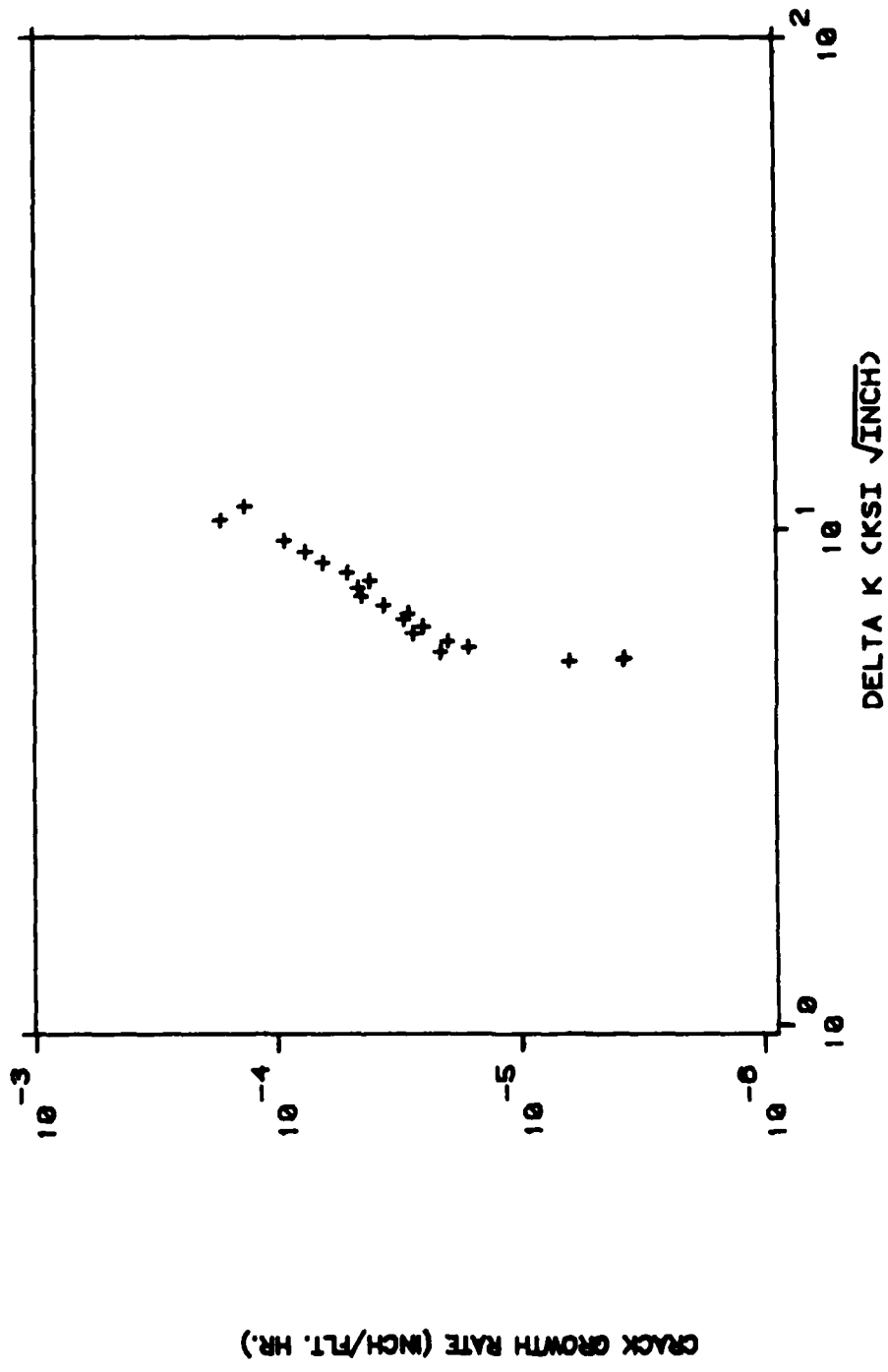


Figure 3. Baseline Growth Rate Data (17).

$$\frac{da}{dF} = C (\Delta K)^n \quad (1)$$

where C and n are growth rate constants. The Anderson-James back-calculation technique (19) was also used to obtain ΔK . The principal assumption of this technique is that at any given instant the crack growth rate is associated with a unique value of the SIF. The procedure for applying the technique is as follows:

- (1) Raw data of crack length and flight hours are obtained.
- (2) The crack growth rate da/dF is determined in terms of the quantities in step 1 by applying the ASTM seven point incremental polynomial method (20).
- (3) With the growth rate constants C and n, and a crack growth rate da/dF associated with individual crack length, the quantity ΔK for each crack length is calculated by:

$$\Delta K = 10^{\frac{1}{n}(\log da/dF - \log C)} \quad (2)$$

This technique has been successfully applied by Schjive (21) to determine the SIF for corner cracks from a loaded pin hole. The apparent SIF (K_{app}) was defined as

$$K_{app} = \frac{\Delta K}{1 - R} \quad (3)$$

where R is the load ratio based upon a root mean square average of the load spectrum. For tests run under constant amplitude loading, K_{app} would correspond to the maximum SIF (K_{max}).

3.4 LINE OF BEST FIT

Upon examination of K_{app} versus crack length in logarithmic space (Figures 4-7), it was apparent that the following relationship existed:

$$K_{app} = A(a)^B \quad (4)$$

The constants A and B were determined by a least squares analysis. The above equation provided a means for comparing the effects of crack initiation site, load transfer, load level and fastener fit on the apparent SIF.

3.5 SHORT CRACK EFFECT

The question of whether short cracks grow differently than long cracks was resolved by examining a plot of the crack growth rate versus the apparent stress intensity factor. Normal crack growth should appear as smooth, continuous and monotonically increasing in the above graph. By examining how conventional SIF would have handled the data by Noronha et al. (12), an explanation to the SCE seen by other investigators may be postulated.

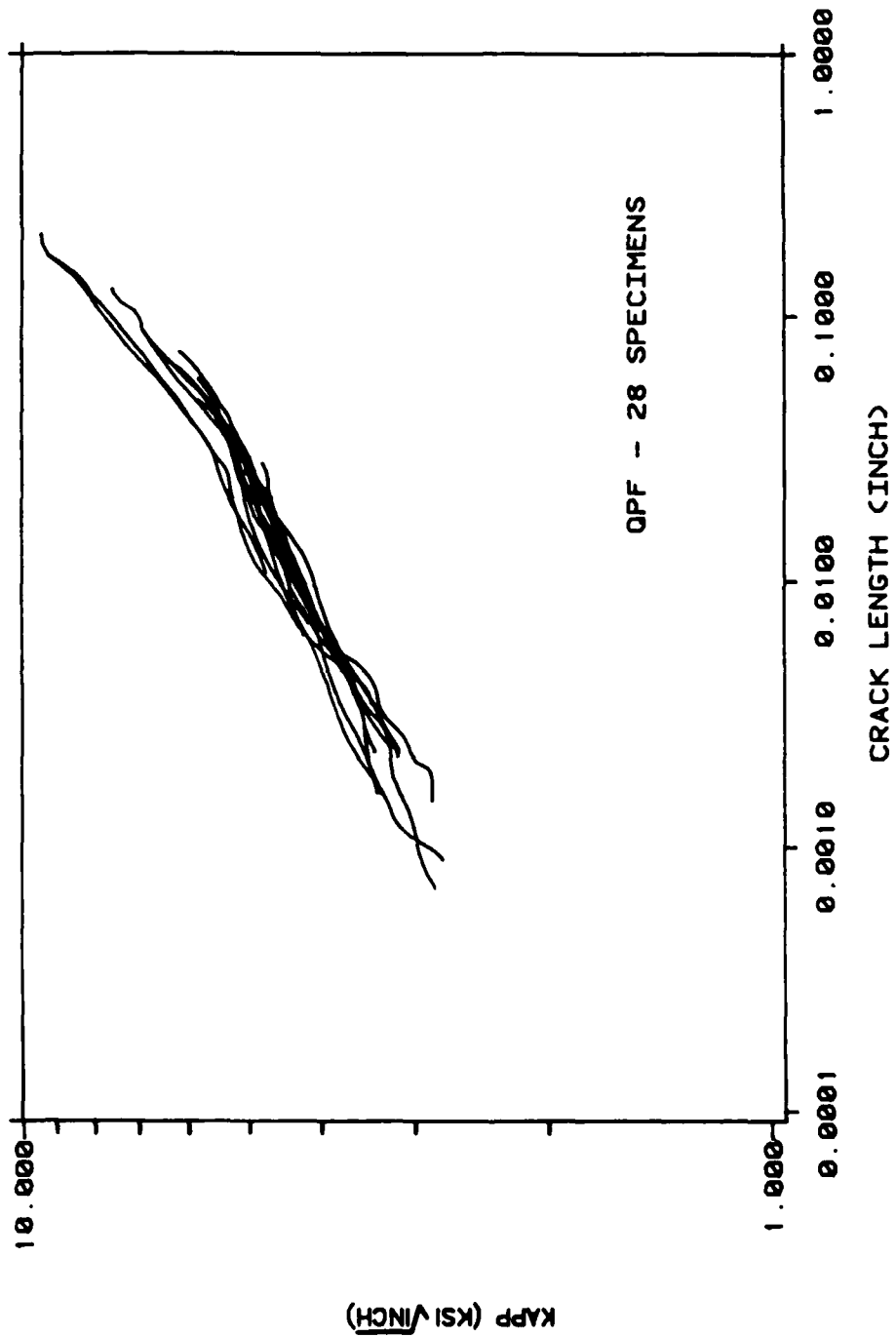


Figure 4. Apparent Stress Intensity Factor for QPF, 28 Specimens.

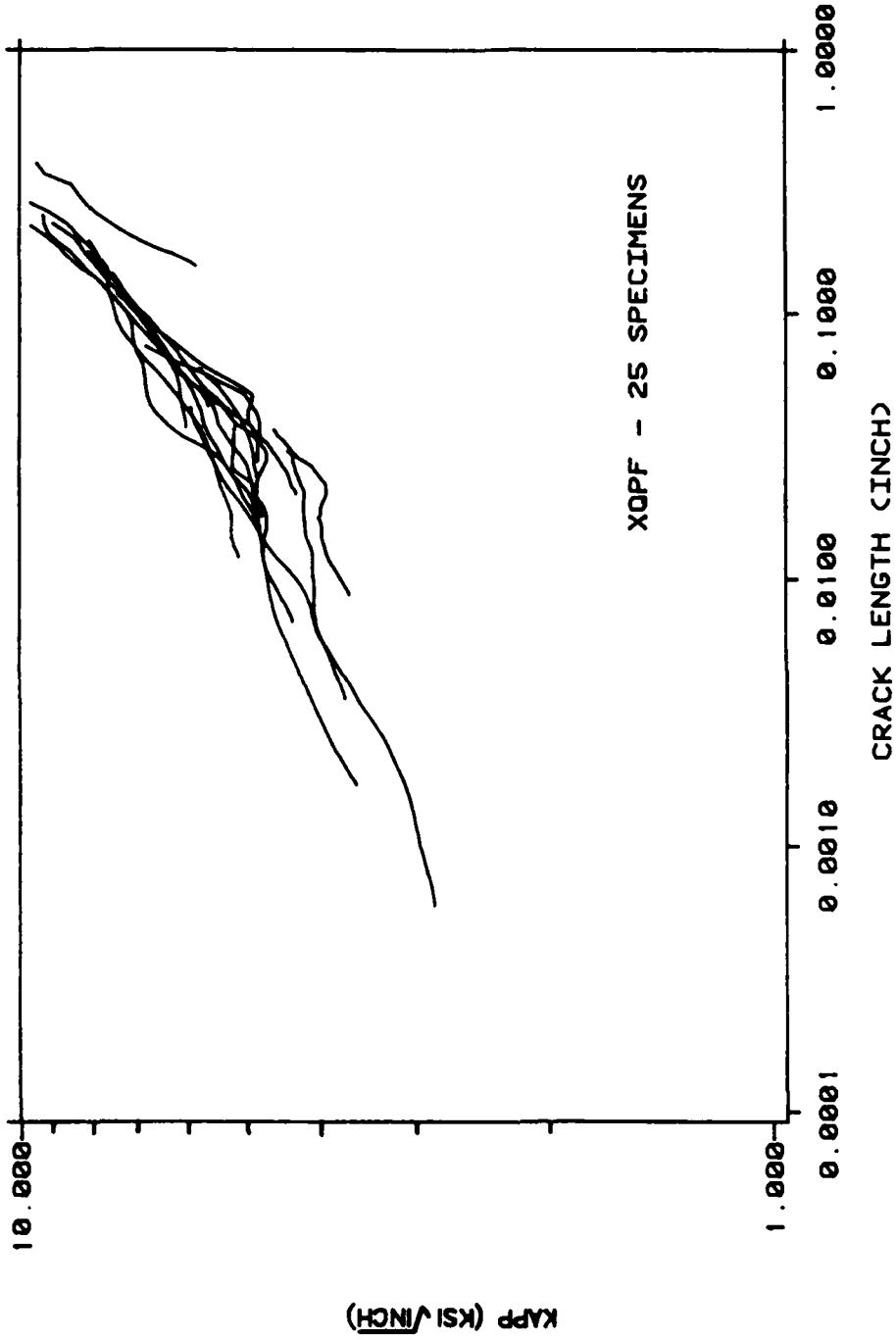


Figure 5. Apparent Stress Intensity Factor for XQPF, 25 Specimens.

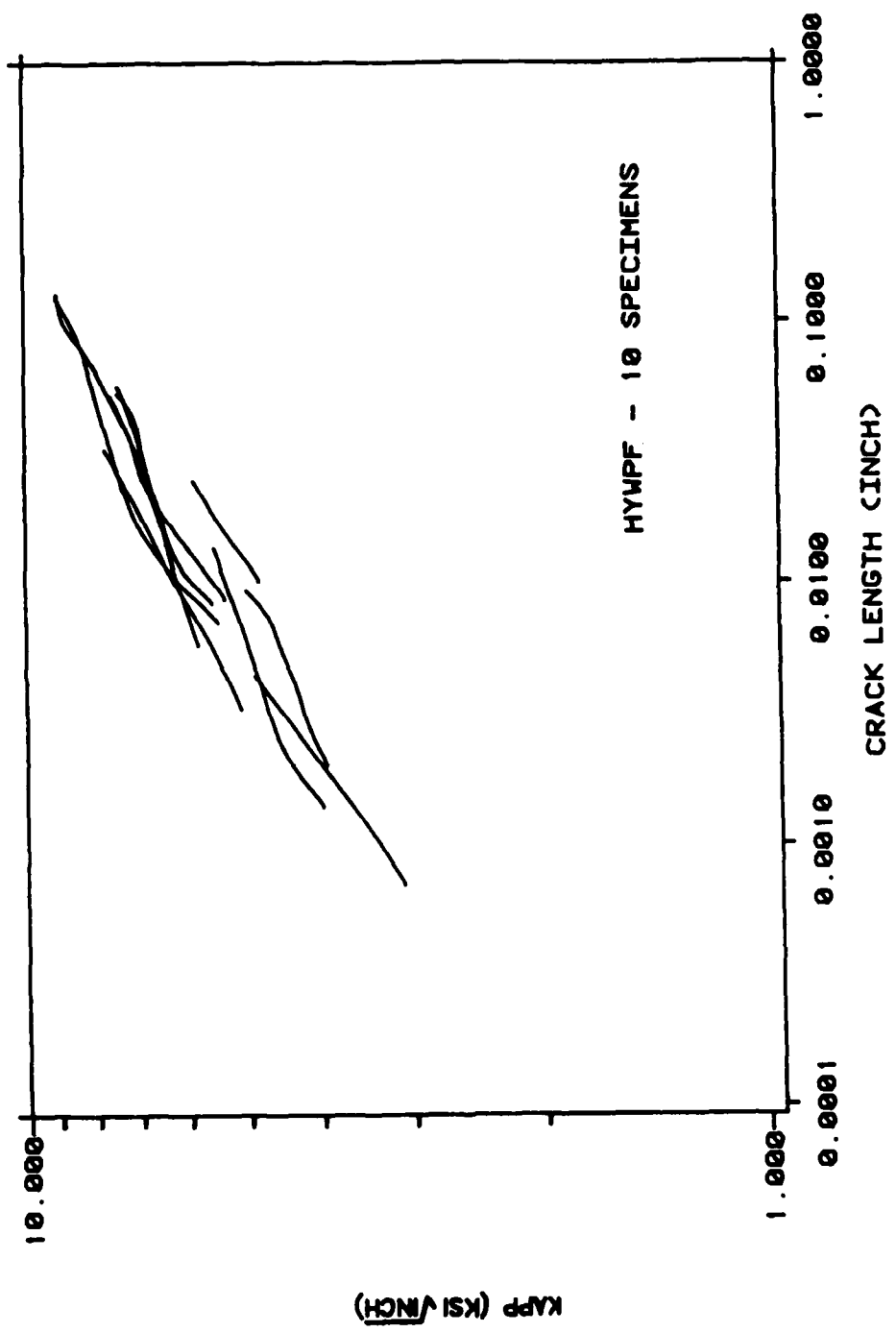


Figure 6. Apparent Stress Intensity Factor for HYWPF, 10 Specimens.

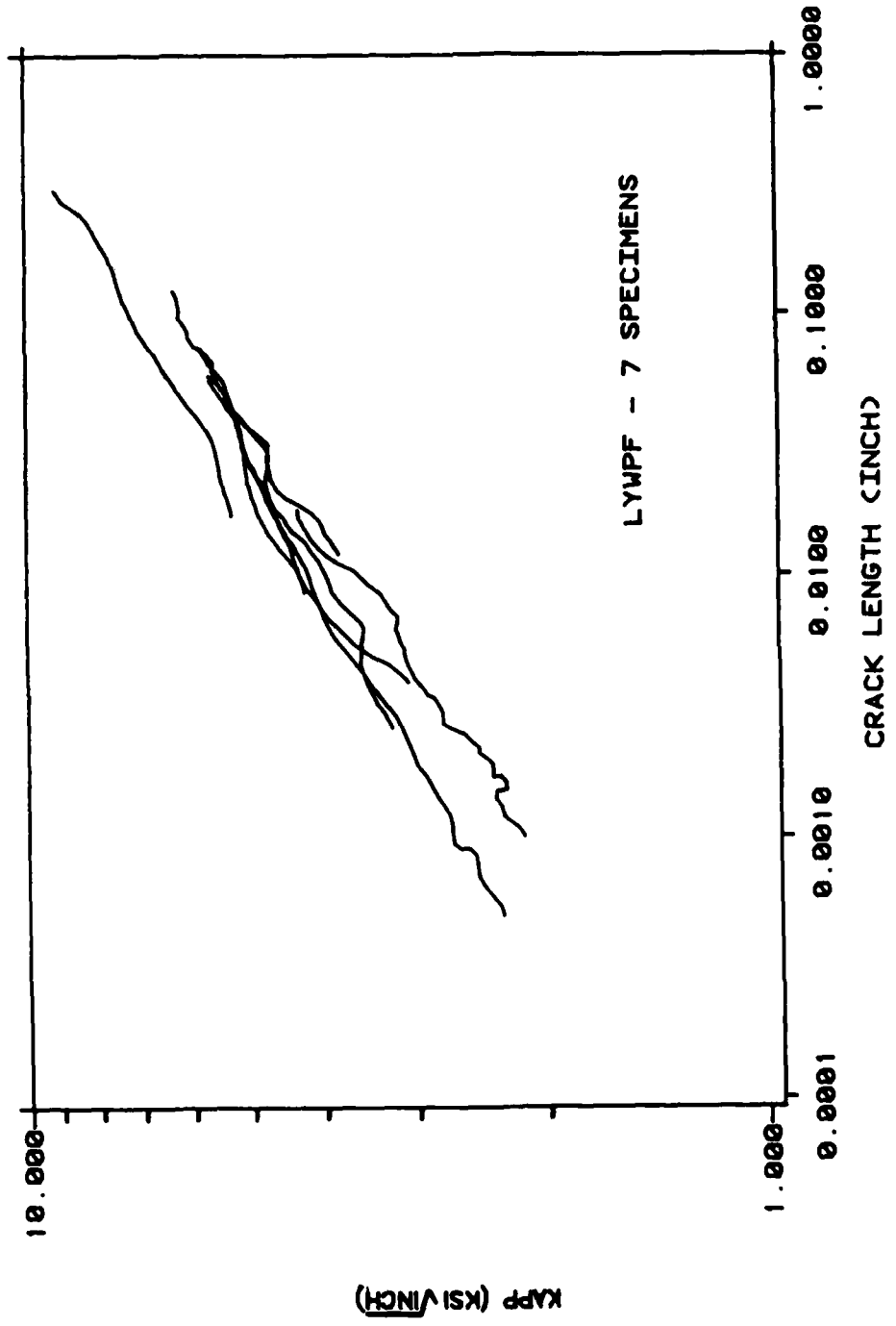


Figure 7. Apparent Stress Intensity Factor for LYWPF, 7 Specimens.

IV. RESULTS

4.1 APPARENT STRESS INTENSITY FACTORS

With regard to an apparent SIF, this study is performed to establish a correlation between the apparent SIF (K_{app}) and the crack length (a). With exception of 9 out of 70 tests as shown by figures 4, 5, 6 and 7, the data for each series (QPF, XQPF, HYWPF, LYWPF) fall within $\pm 10\%$ of the mean behavior of that series. These figures indicate a high degree of repeatability. This is substantiated by the high coefficient of correlation (r) for each set of tests, typically $r = 0.96$. With the exception of 4 out of 14 cases, the coefficient of correlation was greater than 0.95 for each fitted line. Table 1 tabulates the apparent SIF as the line of best fit according to the power relationship given in Equation 4 and the corresponding coefficient of correlation for each series and crack initiation site.

4.2 EFFECT OF CRACK LOCATION

To determine the influence of crack location upon the apparent SIF solution, the crack length versus the apparent SIF was plotted for each of the initiation sites for the three series (XQPF, HYWPF, LYWPF) respectively (figures 8-10). The solid lines represent the empirical relations derived between crack length and K_{app} for

Table 1. Apparent SIF for Crack Initiation Site and Corresponding Coefficient of Correlation

INITIATION SITE	QPF 28 Specimens	XQPF 25 Specimens	HYWPF 10 Specimens	LYWPF 7 Specimens
All Sites	Kapp = 10.034a ^{0.183} r = 0.970	Kapp = 10.791a ^{0.215} r = 0.909	Kapp = 13.936a ^{0.198} r = 0.961	Kapp = 11.017a ^{0.225} r = 0.971
Bolt Hole		Kapp = 12.167a ^{0.238} r = 0.923	Kapp = 14.485a ^{0.204} r = 0.973	Kapp = 9.408a ^{0.183} r = 0.995
Chamfer Corner		Kapp = 12.054a ^{0.262} r = 0.924	Kapp = 9.931a ^{0.101} r = 0.994	Kapp = 9.553a ^{0.190} r = 0.973
Radius Corner			Kapp = 13.844a ^{0.195} r = 0.988	
Mating Surface		Kapp = 9.926a ^{0.194} r = 0.840	Kapp = 13.990a ^{0.232} r = 0.990	Kapp = 11.275a ^{0.217} r = 0.957

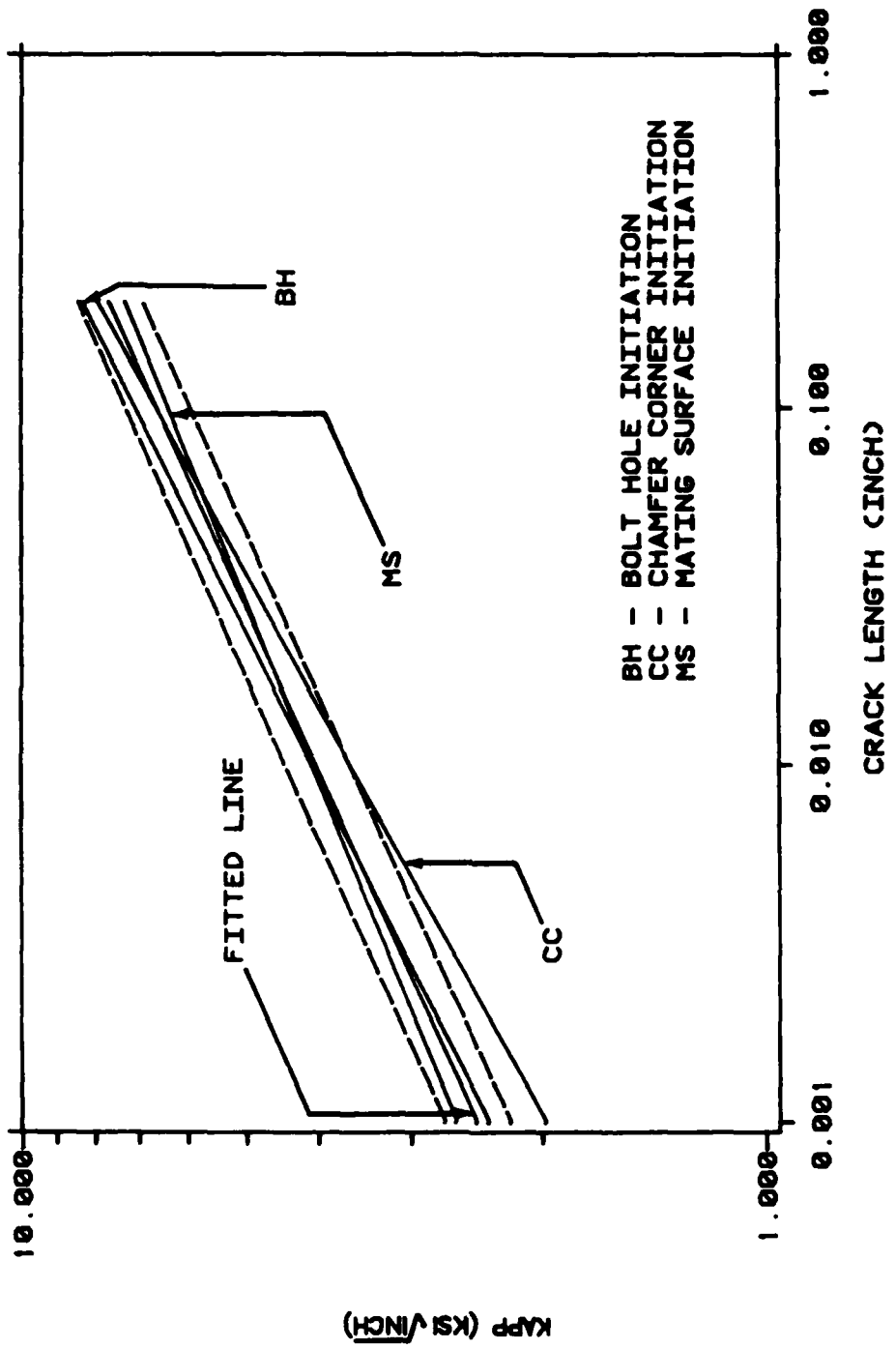


Figure 8. Influence of the Crack Initiation Site Upon the Apparent SIF, XQPF Series.

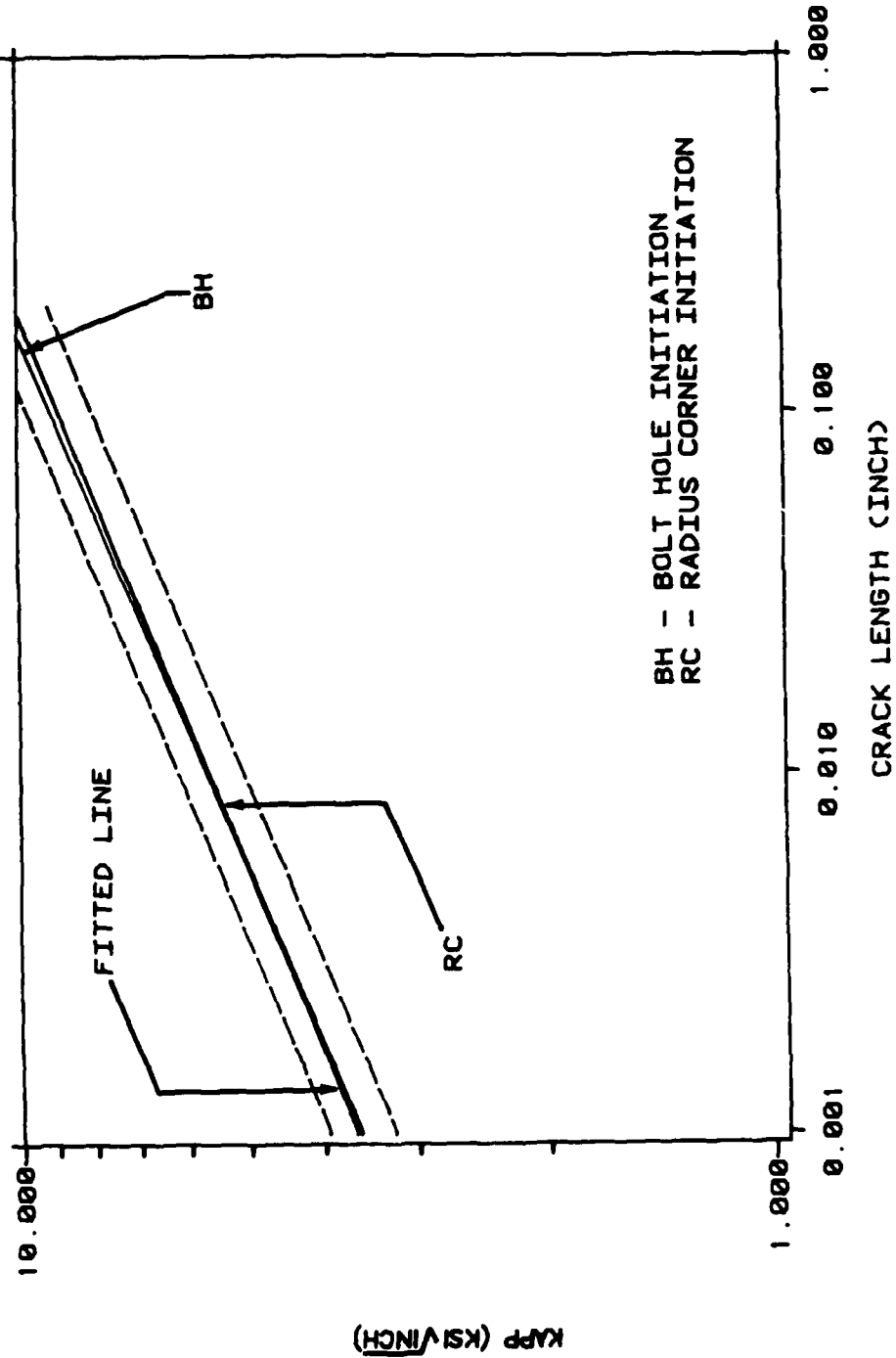


Figure 9. Influence of the Crack Initiation Site Upon the Apparent SIF, HYWPF Series.

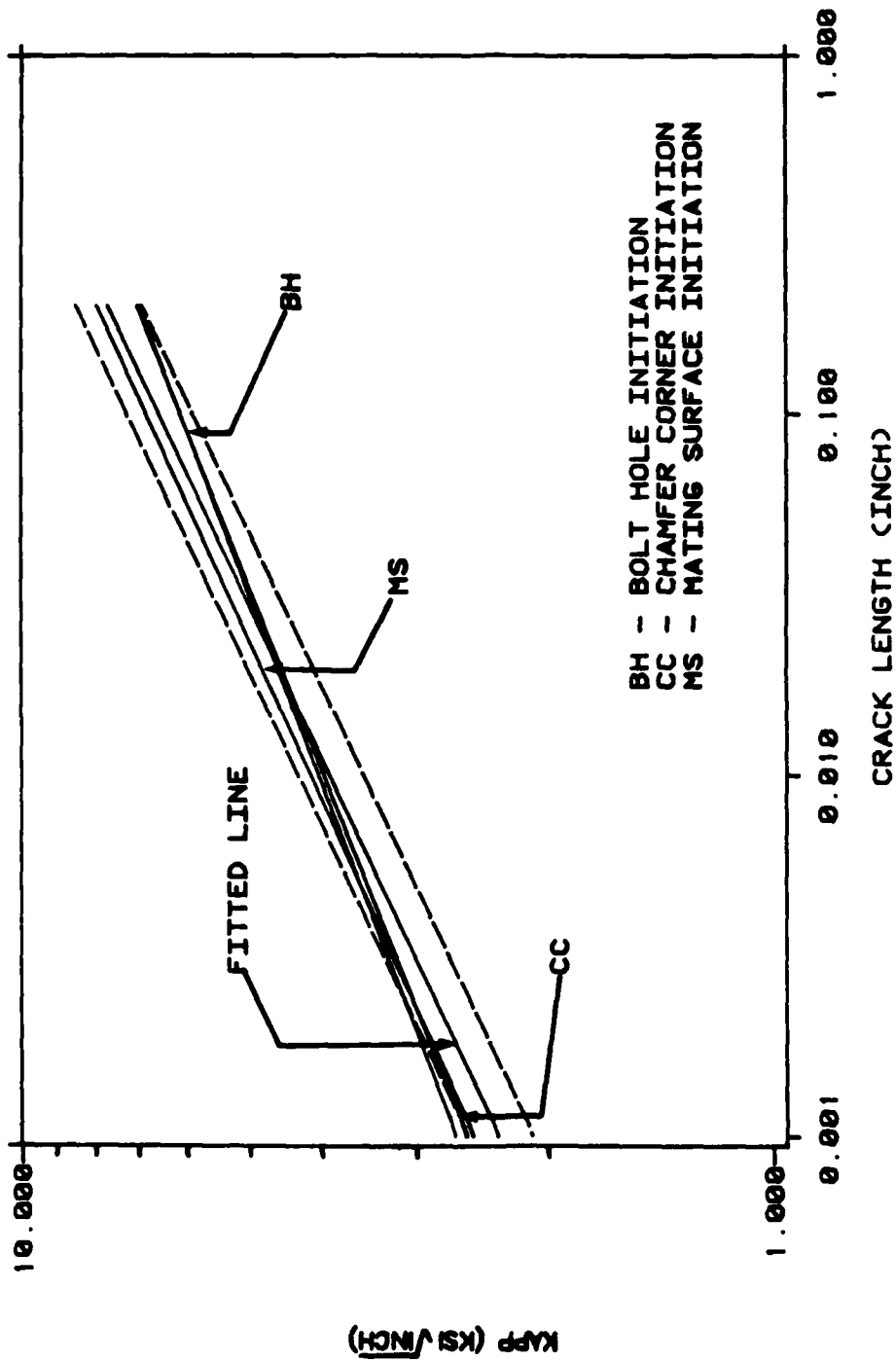


Figure 10. Influence of the Crack Initiation Site Upon the Apparent SIF, LYMPF Series.

the various crack initiation sites. The dashed lines indicate $\pm 10\%$ deviations from the mean empirical solution for all the specimens of each series.

In the XQPF series, as shown by Figure 8, the Kapp solution for crack initiation at the chamfer corner lies outside of the $\pm 10\%$ deviation from the mean solution for crack lengths less than 0.01 inches. The Kapp solutions for the rest of the crack initiation sites lie within the $\pm 10\%$ boundary for the range of crack lengths considered. The corresponding coefficient of correlation for each of the fitted lines is higher than 0.90 except for the case of mating surface initiation which has a coefficient of correlation of 0.84.

In the HYWPF series, as shown by Figure 9, the mean Kapp solutions for the cases of bolt hole and radius corner initiations are very close to the fitted line for all the specimens of this series. Due to the limited number of data points available for the cases of chamfer corner and mating surface crack initiations in this series, no conclusive correlation between Kapp and crack length may be stated. Thus, these two cases will be removed from any further analysis or discussion. For the cases of bolt hole and radius corner initiations the solutions fall within $\pm 5\%$ of the mean. The maximum deviation for this series from the mean was 3%. This occurs for the case of the bolt hole initiation. The coefficients of correlation for the initiation sites considered in this series are higher than 0.95.

In the LYWPF series, as shown by Figure 10, the empirical solution for each crack initiation site falls within $\pm 10\%$ of the mean behavior. The coefficients of correlation of all the cases in this series are higher than 0.95.

Based upon the observation for the above results, one may say that for the short cracks ($0.001 \leq a \leq 0.2$ inches) the apparent SIF is independent of the crack initiation sites.

4.3 EFFECT OF LOAD TRANSFER

The effect of load transfer through the fastener can be found in Figure 11. The figure shows that a maximum difference of 13.8% in K_{app} exists for the range of crack lengths investigated. Thus, one may say that for short cracks the load transfer does not affect K_{app} .

4.4 EFFECT OF LOAD LEVEL

The effect of load level is summarized in Figure 12. The empirical solutions are presented in the form of a K_{app}/σ versus the crack length. The solution for the YWPF series was obtained from Kirby and Potter (11). The denominator σ was required so that cases with different stress levels could be compared. This form of presentation shows clearly the effect of load level.

In the HYWPF, LYWPF and YWPF series, a maximum different of 11.5% in K_{app}/σ was obtained for the range of crack lengths investigated. Thus, one may say that for short cracks the load level

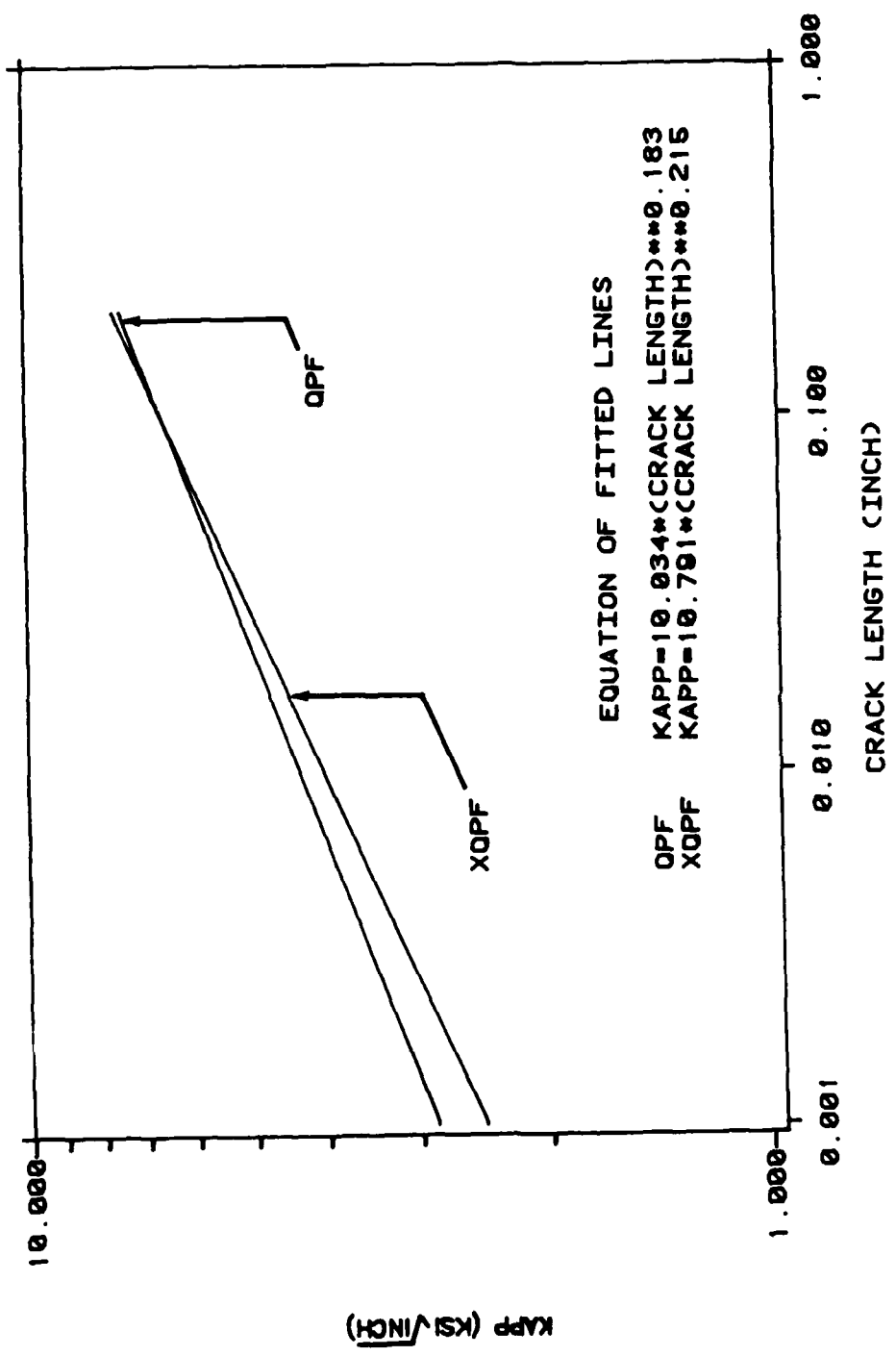


Figure 11. Effect of Load Transfer Through the Fastener Upon the Apparent SIF.

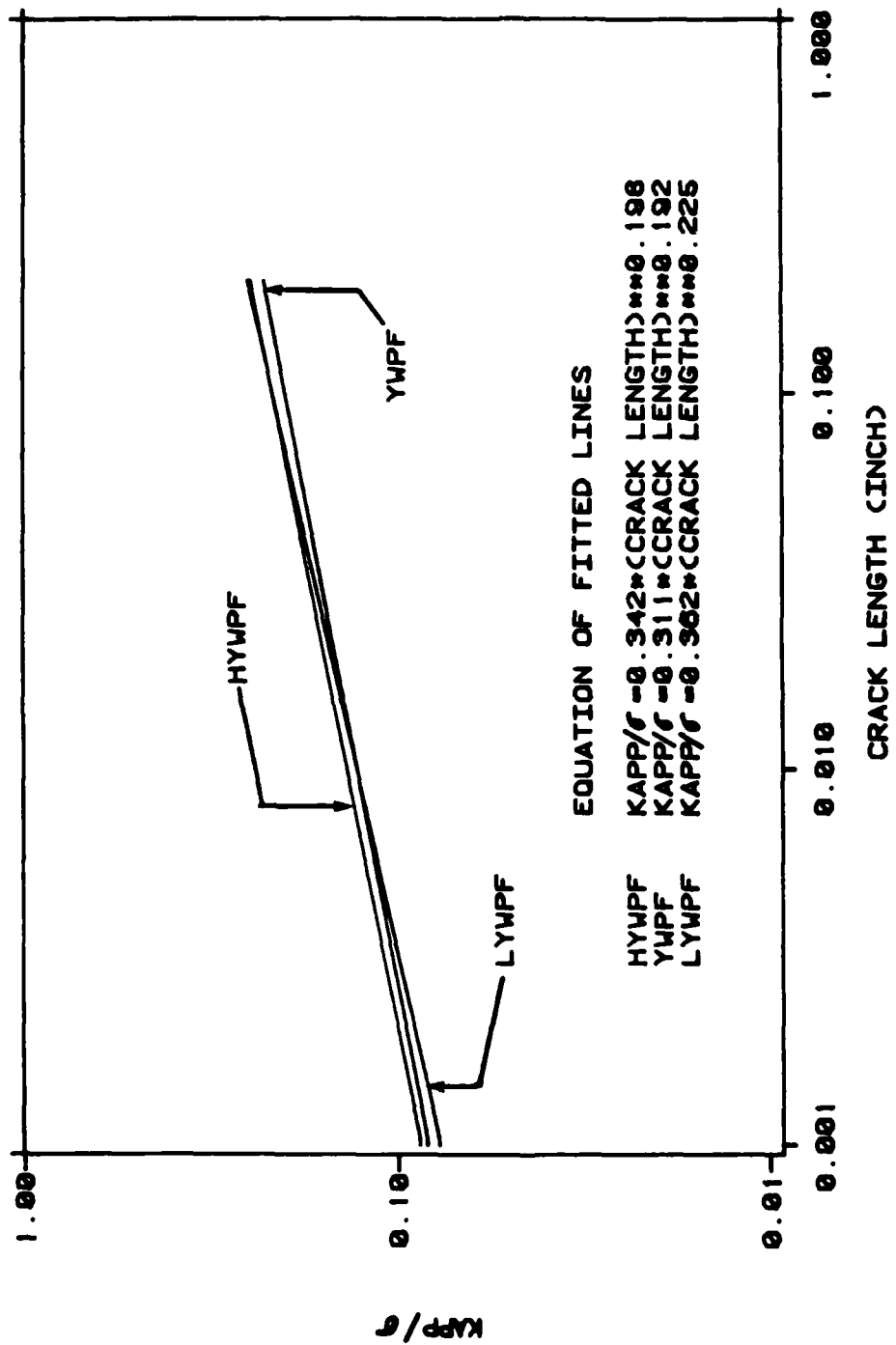


Figure 12. Influence of Load Level Upon the Apparent SIF.

does not affect the apparent SIF solution.

4.5 EFFECT OF FASTENER FIT

To determine the effects of the fastener fit on the SIF, the apparent SIF solutions were compared for the specimens prepared by the Quackenbush drilling procedure and the Winslow drilling procedure. The solutions for the WPF and XWPF was obtained from Kirby and Potter (11). These results may be seen in Figures 13 and 14. In the QPF, WPF series for no-load transfer specimens, a maximum difference of 3% in Kapp was obtained for the range of crack lengths investigated. In the XQPF and XWPF series for low-load transfer specimens, a maximum difference of 13.6% in Kapp was obtained for the range of crack lengths investigated.

Figures 13 and 14 indicate that the Kapp does not change significantly, even though there is a difference in clearance between a fastener hole and the fastener. Thus, one may say that the fastener fit does not affect the apparent SIF solution.

4.6 COMPARISON WITH ANALYTICAL SOLUTION

To complete the analysis of this study, a comparison was made between the results of this study and three analytical SIF solutions from flaws emanating from fastener hole (Figure 15). It should be noted that the present solution was multiplied by 4.18 to achieve agreement of the apparent SIF in the range of crack

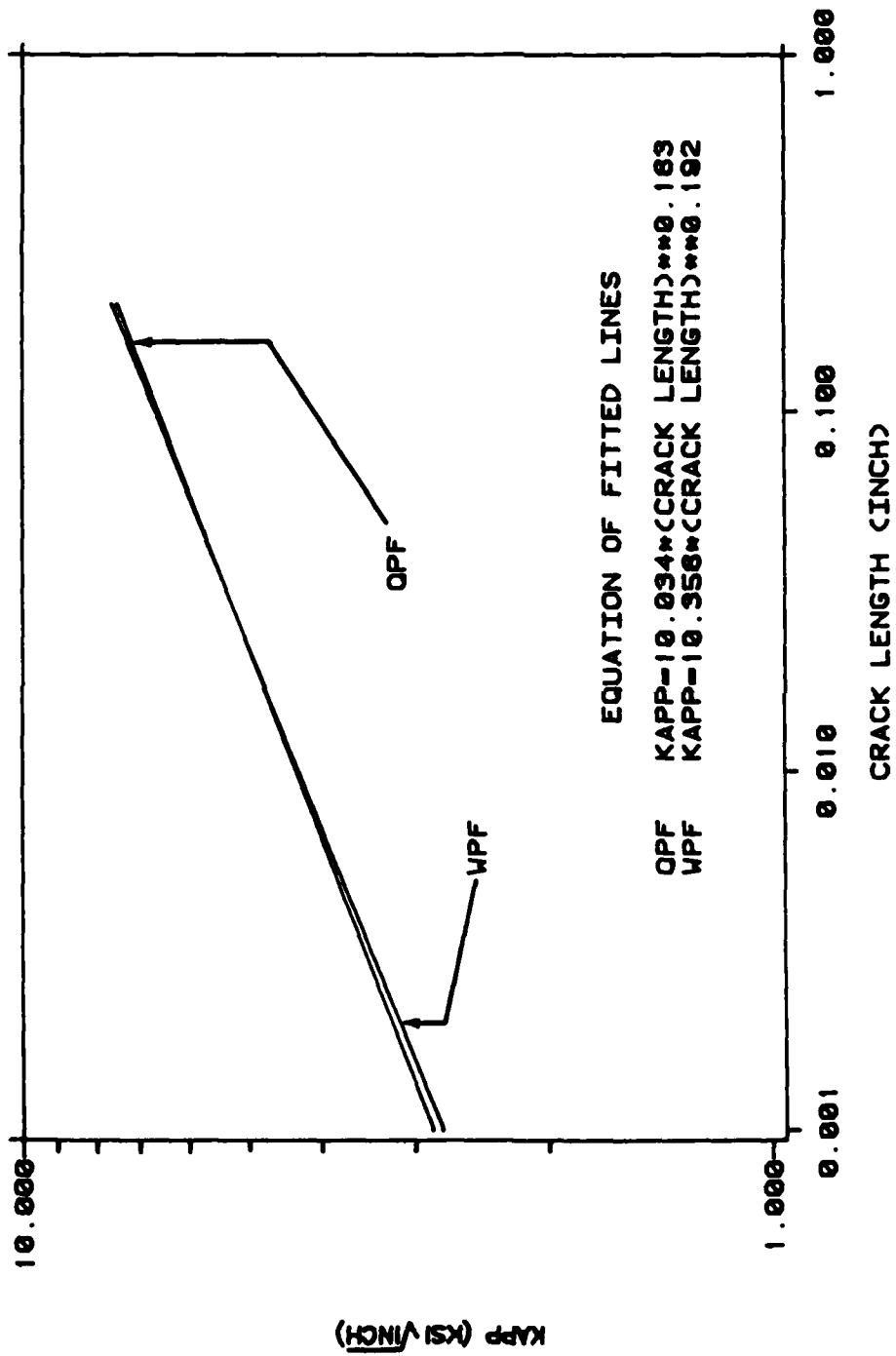


Figure 14. Effect of Fastener Fit Upon the Apparent SIF, No Load Transfer Through the Fastener.

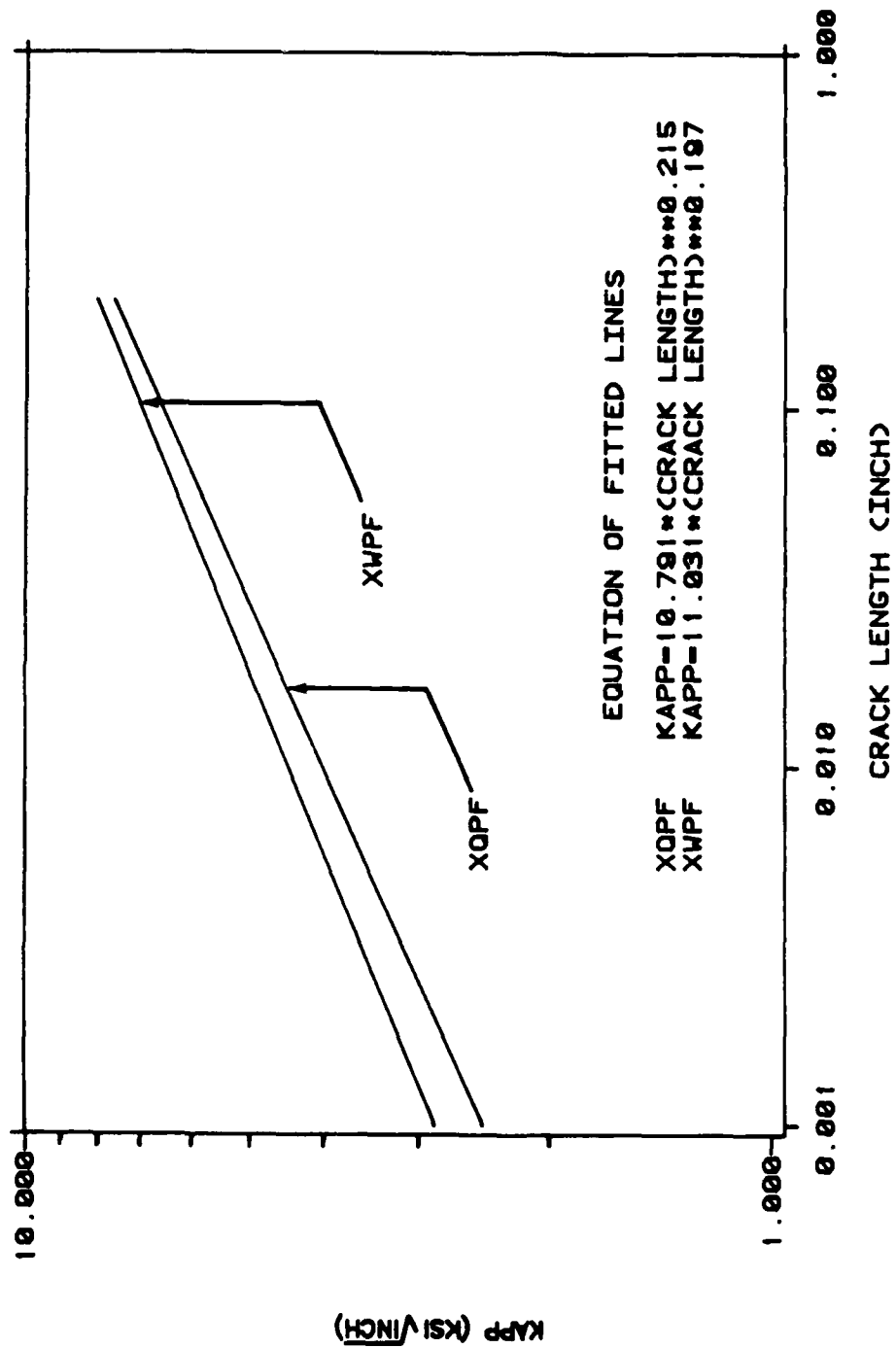


Figure 14. Effect of Fastener Fit Upon the Apparent SIF, 15% Load Transfer Through the Fastener.

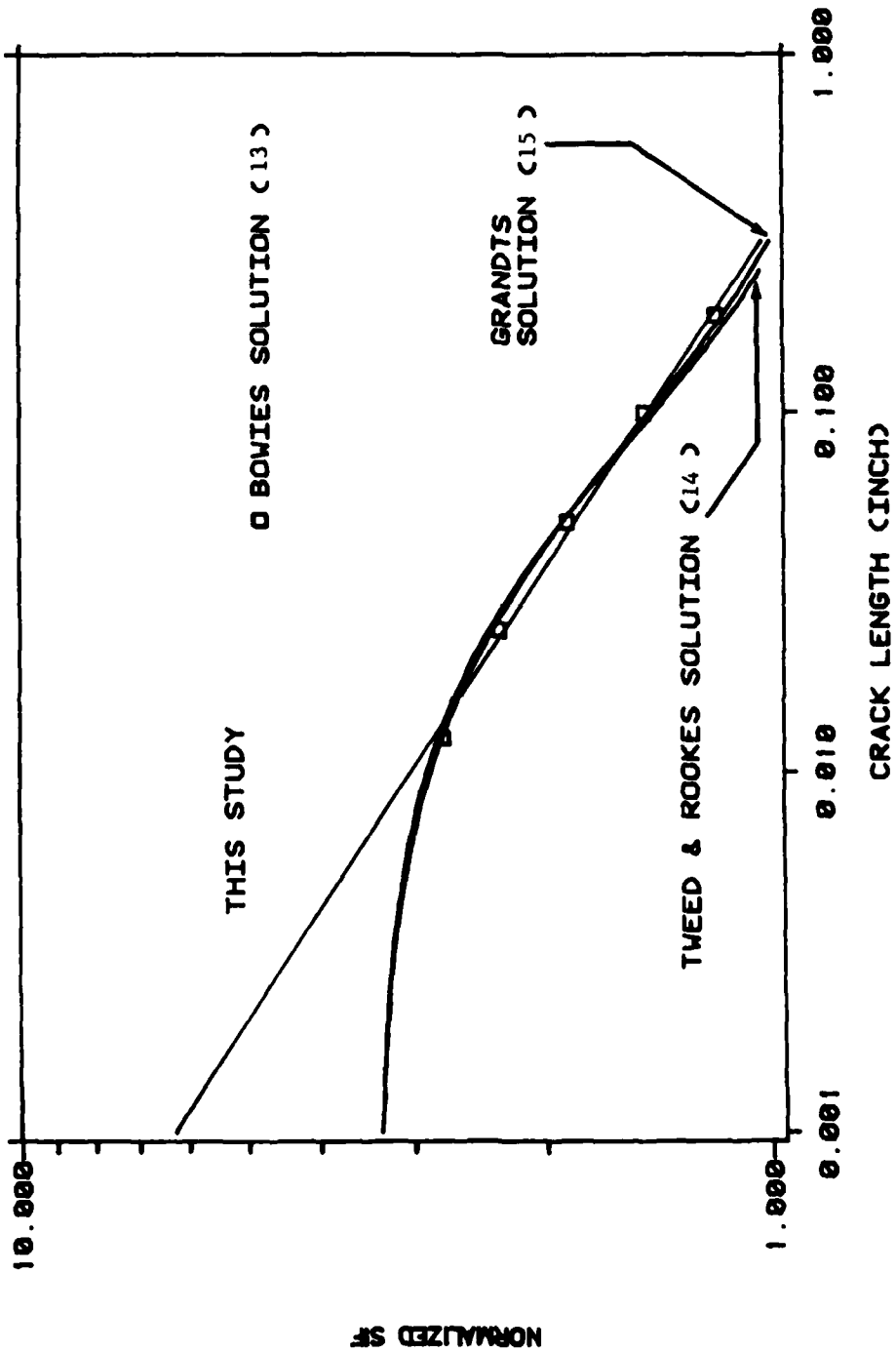


Figure 15. Comparison of This Study of Analytical Solutions to a Radial Crack Emanating From a Fastener Hole.

lengths of 0.01 to 0.1 inches (0.25 to 2.5 mm). In Kirby and Potter's study (11) an adjustment factor of 4.35 was also necessary to achieve agreement in this range. The justification of this correction lies in the ambiguity of the effects of random amplitude loading on the load ratio R . However, this correction does not alter the general trend seen in the study. At crack lengths less than 0.01 inches (0.25 mm), Bowie's (13), Tweed and Rooke's (14) and Grandt's (15) solutions for cracks at holes begin to diverge from the present solution and underpredict K_{app} by approximately 47% for a crack length of 0.001 inches (0.025 mm). This underprediction of K_{app} for short crack lengths may be the cause of the SCE seen by many investigators. For example, using the data from a typical test from Noronha et al. (12), Grandt's solution indicates a presence of a short crack effect (Figure 16), even though it has been established by Potter and Yee (10) that no short crack effect exists in this data.

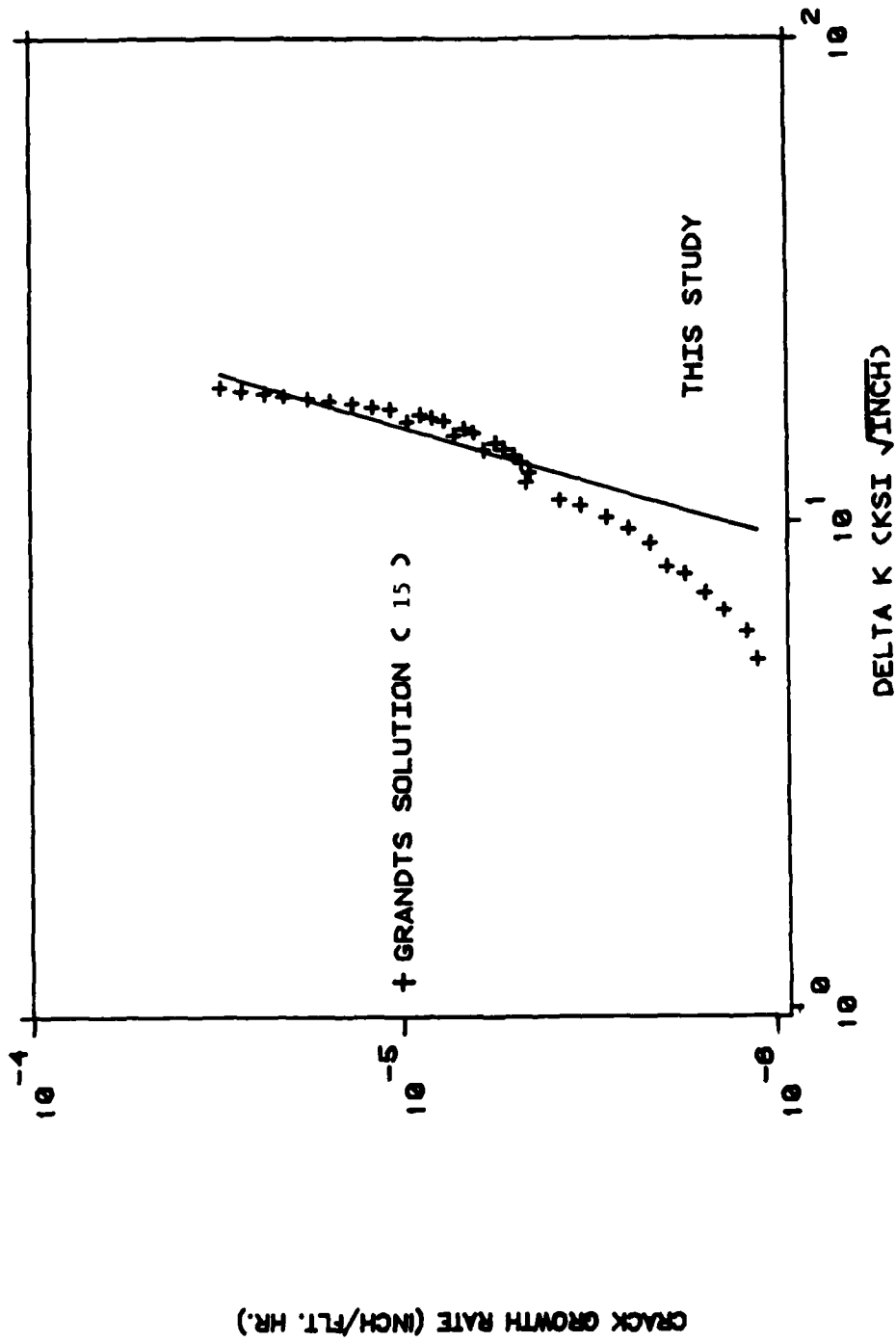


Figure 16. Short Crack Effect Predicted by Grandt's Solution (15) for Noronha et al. Data (12).

V. DISCUSSION OF RESULTS

One unanticipated result from this study is that the apparent SIF is independent of crack initiation site and load transfer for short cracks. One possible explanation for this unexpected behavior is that short cracks cannot feel the presence of the boundaries of the specimen. Thus, all short cracks behave the same regardless of the crack location or load transfer, through the fastener. Although this explanation is satisfactory for cracks having lengths of less than 0.01 inches (0.25 mm), it does not explain this behavior for cracks with lengths of 0.20 inches (5 mm) or greater.

Another unanticipated result is that the apparent SIF is not affected by load level and fastener fit. A possible explanation for this unexpected behavior of fastener fit is that both drilling techniques produce the same degree of fastener fit. A possible explanation for this unexpected behavior of load level is that although the load level does influence the apparent SIF, whatever effects caused by the load level (size of plastic zone, changes in specimen geometry, etc.) do not influence the apparent SIF. It is essential to note that the apparent SIF provides only a convenient measure of load applied to the crack tip region and contains no information on the response of the material to this load.

Even though the flaws investigated in this study are three dimensional elastic problems, the empirical solutions to the

apparent SIF obtained for these flaws were compared to a two dimensional solution. This comparison was done for the following two reasons. First, it was seen that the apparent SIF was independent of the crack initiation sites and thus, the comparison of the solutions derived in this study with two dimensional solutions is justified. Second, it would be impossible to compare the empirical solutions of this study to the appropriate three dimensional solution because of the lack of information of how the flaw shape continuously changes throughout the flaw growth.

VI. CONCLUSION

The following conclusions were drawn from this study:

- (1) The SIF solution for small cracks at fastener holes is an exponential function.
- (2) For short fatigue cracks emanating from fastener holes, the SIF is independent of the crack initiation sties, load transfer through the fastener hole, load level and fastener fit.
- (3) For specimens examined in this study, no short crack effect was seen. However, it was found that fastener hole SIF solutions similar to Bowie's solution (13) underpredict the SIF for crack lengths less than 0.01 inches (0.25 mm). This underprediction of apparent SIF may explain the short crack effect seen by other authors.

It has been suggested that the extrapolation of the growth rate constants to the region of very low growth rates may not be applied with any degree of confidence. Although this extrapolation may be justified by examining Figures 4-7, there are some researchers who are not completely satisfied with this justification. The above controversy may be resolved by determining what the growth rate constants are for the very low growth rates encountered in this study.

REFERENCES

1. S. Pearson, "Initiation of Fatigue Cracks in Commercial Aluminum Alloys and Propagation of Very Short Cracks," Engineering Fracture Mechanics, Vol. 7, pp. 235-247, 1975.
2. R. Cook and P. R. Edwards, "Crack Propagation at Short Crack Lengths Under Variable Amplitude Loading (2nd Report)," Materials and Structures Department, Royal Aircraft Establishment, Farnborough, Hants., England.
3. B. C. Fisher and F. Sherratt, "A Fracture Mechanics Analysis of Fatigue Crack Growth Data for Short Cracks," Fracture Mechanics in Engineering Practice, Proceedings of the Annual Conference, Sheffield, England, Sept., 1976.
4. S. J. Hudak, "Small Crack Behavior and the Prediction of Fatigue Life," Journal of Engineering Materials and Technology, Transactions of ASME, Vol. 103, pp. 26-35, Jan. 1981.
5. J. Lankford, "Initiation and Early Growth of Fatigue Cracks in High Strength Steel," Engineering Fracture Mechanics, Vol. 9, pp. 617-624, 1977.
6. B. N. Leis and T. P. Forte, "Fatigue Growth of Initially Physically Short Cracks in Notched Aluminum and Steel Plates," the 13th National Symposium on Fracture Mechanics, Philadelphia, Penn., June, 1980.

7. B. N. Leis and R. D. Galliher, "Growth of Physically Short Corner Cracks at Circular Notches," Proceedings International Symposium on Low Cycle Fatigue and Life Prediction, ASTM STP (In Press).
8. M. H. El Haddad, K. N. Smith, and T. H. Topper, "Fatigue Crack Propagation of Short Cracks," Journal of Engineering Materials and Technology, Transaction of ASME, Vol. 101, pp. 42-46, 1979.
9. M. H. El Haddad, N. E. Dowling, T. H. Topper, and K. N. Smith, "J-Integral Applications for Short Cracks at Notches," International Journal of Fracture, Vol. 16, pp. 15-30, 1980.
10. J. M. Potter and B. G. W. Yee, "Use of Small Crack Data to Bring About the Quantify Improvements to Aircraft Structural Integrity," AGARD Specialists' Meeting on Behavior of Short Cracks in Aircraft Structures, Toronto, Canada, Sept., 1982.
11. G. C. Kirby and J. M. Potter, "Short Crack Behavior of Flaws Emanating from Fastener Holes," AFWAL-TR-83-3095, Air Force Wright Aeronautical Laboratories, Dayton, Oh., 1983.
12. P. J. Noronha, S. P. Henslee, Z. Wolanski, D. E. Gordon, and B. G. W. Yee, "Fastener Hole Quality," AFFDL-TR-78-206, Vol. I & II, USAF Flight Dynamics Lab., Dayton, Oh., 1979.

13. O. L. Bowie, "Analysis of an Infinite Plate Containing Radial Cracks Originating at the Boundary of an Internal Circular Hole," Journal of Mathematics and Physics, Vol. 35, pp. 60-71, 1956.
14. J. Tweed and D. P. Rooke, "The Distribution of Stress Near the Tip of a Radial Crack at the Edge of a Circular Hole," International Journal of Engineering Science, Vol. 11, pp. 1185-1195, 1973.
15. A. F. Grandt, "Stress Intensity Factors for Some Thru-Cracked Fastener Holes," AFML-TR-74-71, USAF Materials Lab., Dayton, Oh., 1971.
16. F. W. Smith, "Stress Intensity Factors for a Semi-Elliptical Surface Flaw," Boeing Co., Structural Development Research Memorandum, Vol. 17, 1966.
17. R. L. Wilkinson and J. M. Potter, "Effects of Bonding Temperatures on Fatigue Crack Growth," AFWAL-TR-82-3058, Air Force Wright Aeronautical Laboratories, Dayton, Oh., 1982.
18. P. C. Paris and F. Erdogan, "A Critical Analysis of Crack Propagation Laws," Journal of Basic Engineering, Transaction of

ASME, Vol. 85, pp. 528-534, 1963.

19. W. E. Anderson and L. A. James, "A Simple Experimental Procedure for Stress Intensity Calibration," Engineering Journal of Fracture Mechanics, Vol. 1, pp. 565-568, Apr., 1969.
20. ASTM, "Standard Test Method for Constant-Load-Amplitude Fatigue Crack Growth Rates Above 10^{-8} m/cycle," E647-81.
21. J. Schijve, "Comparison Between Empirical and Calculated Stress Intensity Factors of Hole Edge Cracks," Report LR-376, Department of Aerospace Engineering, Delft University of Technology, Feb., 1983.

END

FILMED

1-86

DTIC